Contents

Acknowledgements

The present dissertation is the accomplishment of many years of research. This work would not have been possible without the efficient help and collaboration of many people. Though it is difficult to draw an exhaustive list of all individuals who contributed in some way, I would nevertheless like to take this opportunity to express my gratitude to some of them.
First of all, my thanks go to my present and past colleagues from the *Institut d'Astrophysique et de Géophysique Liège* and more specifically from the *Groupe d'Astrophysique des Hautes Energies* (GAPHE), for many fruitful collaborations, many stimulating discussions (not always on astrophysics) and most of all for their friendship. Here, I would especially like to mention Drs. Jean-Marie Vreux, Eric Gosset and Prof. Jean-Pierre Swings who welcomed me in - what was then called - the *Groupe Étoiles Massives* (GEM) already 14 years ago, and have supported me ever since, also during difficult times. My special thanks go also to my former PhD students, Drs. Yaël Nazé, Hugues Sana and Michaël De Becker. Working with them has been and still is an extremely enriching experience.
Many external collaborators deserve my gratitude. They are far too numerous to list them all here, but a very warm "thank you" goes to Drs. Ian Stevens, Ronny Blomme and Andy Pollock. I would also like to mention the staff supporting the observing facilities on the ground (Observatoire de Haute Provence, European Southern Observatory and Cerro Tololo Interamerican Observatory) as well as in space (European Space Agency and National Aeronautics and Space Administration): their work is essential to make astrophysical observations possible. In this context, I would especially like to thank the people of the *XMM-Newton* Science Operation Centre. They have done a tremendous job to schedule our observations of colliding wind binaries at the right orbital phases.
It is also a pleasure to thank Drs. Yaël Nazé, Michaël De Becker, Damien Hutsemékers, Jean-Pierre Swings and Jean-Marie Vreux for reading and commenting a previous draft of the present dissertation as well as the members of the jury who accepted to devote some of their time to read this manuscript.
Of course, scientific research would be impossible without financial support. Here, I wish to express my gratitude to the *Fonds National de la Recherche Scientifique* (FNRS) and to the *Belgian Science Policy Office* (Belspo).
Finally, I am deeply indebted to my family: to Yaël for her patience and her help in the preparation of this habilitation thesis and most of all to my parents. I would not be working in the fascinating field of astrophysics without their sacrifices and without their constant support over so many years. My thoughts go especially to the person who is no longer here to read these lines.

Gregor Rauw

Introduction

Pour les uns, qui voyagent, les étoiles sont des guides.
Pour d'autres elles ne sont rien que des petites lumières.
Pour d'autres, qui sont savants, elles sont des problèmes.

Antoine de Saint-Exupéry, *Le Petit Prince*

Ever since the dawn of humanity, men have watched the stars, wondering what the cosmos is made of and how it works. Indeed, astronomy – the quest of a deeper understanding of the Universe – was one of the very first scientific activities and has triggered many developments in other disciplines such as mathematics, physics, mechanics,... Our present knowledge in the field builds on the work of many generations of scientists as well as on the tremendous technological progresses that have been achieved mainly over the last century. For instance, spaceborne telescopes have opened up entirely new windows to the Universe, giving us access for the first time to a huge part of the electromagnetic spectrum that could otherwise not be studied from the ground. This allowed to find out about the amazing diversity of the objects that populate the Universe and to discover the variety of phenomena that exist over different scales of distance and time.

The present habilitation thesis is meant to provide a modest contribution to our understanding of some particular objects in the Universe. This work is focused on the study of *massive stars* with emphasis on their *high-energy properties*.

From the point of view of stellar evolution, massive stars are objects that go through all nuclear burning phases (H, He, C, Ne, O and Si burnings) until the formation of an iron core. This definition corresponds to stars more massive than 8 – 10 $M_\odot$ (see e.g. Meynet 2004). Massive stars are extremely rare. In fact, for each star with a mass between 60 and 120 $M_\odot$ there form about 250 stars with masses between 1 and 2 $M_\odot$ and about 640 objects with masses in the range 0.5 to 1.0 $M_\odot$. In addition, from an observational point of view, these stars are quite distant objects. The nearest O-type star, ζ Oph (O9.5 V), and the nearest Wolf-Rayet binary system, γ^2 Vel (WC8 + O7.5 III), are located at distances of 142 ± 15 pc and 263 ± 37 pc respectively (Schröder et al. 2004)[1], whilst the 'prototype' O supergiant ζ Pup (O4 Ief) lies at a distance of 429^{+120}_{-77} pc from Earth (Schaerer et al. 1997). Finally, massive stars have relatively short lifetimes. They exist only for less than 10^7 years, whilst the Sun has an expectation of life of about

[1] Very recently, Millour et al. (2007) redetermined a larger distance of 368^{+38}_{-13} pc for γ^2 Vel from interferometric observations with the AMBER instrument at the *VLTI*.

10^{10} years. So, why bother about massive stars?

In fact, the study of massive stars has broader astrophysical implications, well beyond the mere problem of stellar astrophysics. Actually, massive stars have played and still play a key role in many processes in the Universe. These stars shape their surroundings through their powerful stellar winds, their strong UV radiation field as well as through their spectacular deaths as supernovae.
The first generations of these stars that formed at zero metallicity (so-called Population III stars) were probably significantly more massive than the most massive objects known today: the typical masses of Population III stars were probably $\sim 100\,\mathrm{M}_\odot$, to be compared to a typical mass of $\sim 1\,\mathrm{M}_\odot$ for Population I objects. Their evolution must have been quite different from that of today's massive stars because of the zero metallicity that implies significantly lower mass loss rates. These objects could have played a key role in the formation of intermediate mass block holes[2], with masses between those of *stellar mass* (5 – $15\,\mathrm{M}_\odot$) and *supermassive* (10^6 – $10^9\,\mathrm{M}_\odot$) black holes at redshift $z = 10$ – 20 (for a review see van der Marel 2004). Possibly in conjunction with subsequent accretion in a very dense star cluster, these intermediate mass black holes could have grown to form those supermassive black holes that are believed to be at the core of the active galactic nuclei.
Massive stars might also be linked to another problem that has remained at the focus of astrophysical research for many years: the γ-ray burst (GRB) phenomenon. Indeed, several GRBs were found to be observationally associated with supernovae (see Postnov 2005 for a review). It has been suggested that the explosion of a rapidly rotating Wolf-Rayet star (descending from a progenitor of initial mass $\geq 25\,\mathrm{M}_\odot$) could produce a rotating black hole that accretes the pre-supernova debris and releases a huge amount of energy (10^{51} – 10^{52} erg) through a GRB. This scenario is known as the 'failed type Ib supernova' or 'collapsar' model. Whether or not the collapse leads to a powerful hypernova or a faint supernova probably depends on various physical parameters such as the angular momentum of the collapsing core (e.g. Nomoto et al. 2005).
Also, because of their relatively short lifetime, the previous generations of massive stars have contributed significantly to the chemical enrichment of the interstellar medium. Without previous generations of massive stars, the chemical composition of the Universe would be drastically different. Key elements such as C, N and O would be much less abundant and life such as we know it would probably not be possible.

When applying for observing time, it is commonplace to state that 'despite considerable progress over the last few decades, our understanding of massive stars is still fragmentary'. While this statement is certainly useful to convince the time allocation committees to grant some telescope time, it is nonetheless true in the case of massive stars. Indeed, a number of fundamental questions remain unsolved. Here, I present a brief personal overview of those issues that have not been solved yet and that are relevant for the present work. This is by no means an exhaustive list.
How massive is massive? In other words, what is the upper limit of the mass of a Population I star? On statistical grounds, this limit is expected to be somewhere in the range 120 – $200\,\mathrm{M}_\odot$ (Oey & Clarke 2005). So far, masses larger than $100\,\mathrm{M}_\odot$ have only been derived by indirect means (such as modelling of the spectra with sophisticated non-LTE model atmosphere codes, e.g. Herrero et al. (2000) or by comparison with theoretical evolutionary tracks). However, these results are subject to huge uncertainties. The least model dependent approach to this question is based on the study of spectroscopic (and ide-

[2]While no unambiguous detection of intermediate mass black holes has been reported so far, these objects could be related to the so-called ultra-luminous X-ray sources (e.g. van der Marel 2004).

ally eclipsing) binaries. Therefore, researchers from the *Groupe d'Astrophysique des Hautes Energies (GAPHE)* of the Liège Astrophysics Institute have observed massive binaries for many years. An important part of the present work thus focuses on my contribution to the determination of fundamental stellar parameters through the study of binary systems.
What fraction of massive stars are members of multiple systems? This question is most relevant e.g. for understanding the importance of mass transfer in the evolution of massive stars. A systematic census of binaries in several open clusters has been performed by various members of the GAPHE team. Some results, that I have obtained, are part of this habilitation thesis.
Do massive stars have magnetic fields? Due to the rapid rotation of O-type stars, their spectra display rather broad absorption lines, thus rendering a direct determination of their magnetic fields through the Zeeman splitting extremely difficult (Mathys 1999). Moreover, theoretical models do not provide an unambiguous answer about what could be the origin of such a magnetic field (for a review see De Becker 2005). Still, indirect evidence for moderate magnetic fields has been found for a number of objects, either through their X-ray spectra, their recurrent variability in the optical or their non-thermal (synchrotron) radio emission. Over the last decade, I have participated in several studies related to these subjects and part of this habilitation thesis deals with the results that were obtained in this context.
Where does the X-ray emission of massive stars come from? Although it was already discovered almost thirty years ago, the X-ray emission of early-type stars nevertheless remains a puzzle. In massive binaries, the interaction of the stellar winds of the two components produces an additional variable X-ray emission. Thanks to observations with *ROSAT*, *ASCA*, *Chandra* and, most of all, *XMM-Newton*, I had the opportunity to analyse the X-ray emission of a sample of massive stars (including presumably single objects as well as known binaries).
How do massive stars form? This question is considered as one of the hottest topics in the field. Though the observations discussed in this work do not directly concern massive stars during their formation, clues on the way these stars have formed come also from the lower-mass star formation activity in their vicinity. It is this aspect that I have chosen to develop in the last chapter of this dissertation.

The data discussed in the following were gathered in the framework of a multi-wavelength study covering wavelengths from γ-rays to the radio domain. Many ground-based as well as spaceborne observing facilities were used to collect these observations. Concerning the optical wavelength range, I would like to emphasize that the bulk of the data were taken with small and medium-size telescopes (from 0.5 to 3.5 m). Indeed, many of the targets discussed in this work are relatively bright objects and do not require large collecting areas to obtain high quality data. Still, what is often needed is a monitoring of a specific target over rather long time intervals. This cannot be done in an efficient way with the largest telescopes that are subject to large pressure factors and where the overheads associated with an observation of a bright object would largely exceed the actual integration time on the target. Therefore, while plans are currently being elaborated for ELTs (Extremely Large Telescopes), it is also important to preserve a fair number of smaller telescopes. While smaller telescopes will probably not lead to as large a number of press releases as the ELTs, they will nevertheless provide the means to perform excellent fundamental research work, thereby allowing astronomers to continue the investigation of the Universe that started such a long time ago.

Chapter 1

Massive binaries: fundamental parameters and colliding winds

Wie alles sich zum Ganzen webt,
Eins in dem anderen wirkt und lebt!
Wie Himmelskräfte auf und niedersteigen
Und sich die goldnen Eimer reichen.
Mit segenduftenden Schwingen
Vom Himmel durch die Erde dringen,
Harmonisch all das All durchklingen!

Johann Wolfgang von Goethe, *Faust*

In this first chapter, I discuss the observational properties of a number of early-type (mainly O + O) binary systems as determined from optical spectroscopy and photometry. The investigations of these systems aim at an accurate determination of fundamental parameters such as the masses and the radii of massive stars. In some cases, optical spectroscopy also provides evidence for ongoing interaction processes between the binary components or their stellar winds.

1.1 Introduction

As a general introduction to the topic of early-type binaries, I reproduce hereafter the notes of the invited lecture I gave at the Aussois Thematic School (13 – 18 October 2002) organised by the *Programme National de Physique Stellaire* of the French CNRS (Rauw 2004a). This paper presents our knowledge of massive binaries as it was in October 2002. For some specific points there has been quite some progress in the meantime and the reader will find the corresponding updates throughout the relevant chapters of this thesis. After this general introduction, I briefly address the issue of the incidence of binaries among early-type stars and I provide an overview of some specific techniques that are used in the subsequent sections and chapters to analyse and interpret the observations of massive binaries.

Evolution of Massive Stars, Mass Loss and Winds
M. Heydari-Malayeri, Ph. Stee and J.-P. Zahn
EAS Publications Series, Vol. **13** *(2004) 293-316*

MASSIVE BINARIES AND COLLIDING WINDS

G. Rauw[1]

Abstract. In this contribution, I review recent results from observational investigations of early-type binaries of spectral types O and Wolf-Rayet. These studies aim at an accurate determination of fundamental parameters such as masses and radii of the most massive stars. In addition, multi-wavelength analyses of wind collisions in massive binaries provide constraints on the properties of stellar winds of massive stars and shock physics of cosmic plasmas.

1 Introduction

Although they are rather rare objects, massive early-type stars (initial masses exceeding $20\,M_\odot$) of spectral types O and Wolf-Rayet (WR) play a key role in the evolution of the galaxies. In fact, they are the hottest and most luminous objects of young stellar populations and account therefore for the bulk of the light emitted by distant starburst galaxies. Their stellar winds carry huge quantities of kinetic energy thereby shaping the ambient interstellar medium. Evolved early-type stars release huge amounts of chemically enriched material into space.

Despite considerable progress in our understanding of the physics of these stars, many questions, related to the evolution of these objects and the properties of their winds, still remain unanswered. A number of these questions can be addressed through the study of massive binaries.

This review is organised as follows. Section 2 summarizes some general results obtained from the study of O + O and WR + O systems. Sections 2.1 to 2.4 illustrate a few aspects of the study of massive binaries: how do the mass determinations of stars in binaries compare to other (indirect) techniques, what can we learn about the properties of open clusters harbouring massive binaries, what are the most massive stars in binaries and how can we identify systems that have experienced mass exchange? Section 3 presents a brief introduction to the concept of interacting winds in early-type binaries as well as some observational evidence

[1] Institut d'Astrophysique et de Géophysique, Université de Liège, Allée du 6 Août 17, Bât B5c, 4000 Liège (Sart-Tilman), Belgium

DOI: 10.1051/eas:2004058

for this phenomenon at various wavelengths (from the radio to the X-ray domain). Finally, some conclusions are given in the last section.

2 Early-type spectroscopic binaries

The study of binary systems provides the only direct means to measure the masses of stars all across the Hertzsprung-Russell diagram. If the spectrum of a binary system displays lines belonging to only one of the components, we are dealing with a single-lined spectroscopic binary (SB1). For this category of binaries, measuring the Doppler shift of the lines as a function of the orbital phase allows us to establish the radial velocity curve of the brightest binary component (generally the primary[1]) only. The analysis of this radial velocity curve yields the mass function:

$$f(m) = \frac{m_2^3 \sin^3 i}{(m_1 + m_2)^2} \quad = \quad 1.036 \times 10^{-7} K^3 P_{\rm orb} (1 - e^2)^{3/2} \qquad (2.1)$$

where m_1 and m_2 are the masses (in $M_\odot$) respectively of the primary and secondary component, i is the inclination of the orbital plane with respect to the plane of the sky. K, $P_{\rm orb}$ and e indicate respectively the amplitude of the radial velocity curve (in $\mathrm{km\,s^{-1}}$), the orbital period (in days) and the eccentricity. The mass function contains the only information on the masses of the stars in an SB1 system that can be extracted from the analysis of its radial velocities.

If the spectral signatures of both binary components are visible in the spectrum, we are dealing with an SB2 system. In this case, the simultaneous analysis of the radial velocity curves of both stars allows to derive the values of $m_1 \sin^3 i$ and $m_2 \sin^3 i$, i.e. the absolute masses of the stars multiplied by a factor $\sin^3 i$. The main unknown in this case becomes therefore the orbital inclination i. This parameter can be determined from an analysis of the light curve of the binary provided that i is sufficiently close to 90° so that the binary displays photometric eclipses. In some non-eclipsing close binary systems, it is still possible to constrain i by analysing the light variations due to the changing orientation of tidally deformed stars in so-called ellipsoidal variable stars.

Therefore, eclipsing SB2 binaries provide the main source of direct measurements of stellar masses and radii that serve as test benches for the predictions of the stellar evolution theory. Among the most outstanding results of the investigation of binary systems is the discovery of an empirical mass-luminosity relation for main-sequence stars across the Hertzsprung-Russell diagram. However, for stars more massive than $\sim 25\,M_\odot$, mass loss through stellar winds considerably affects the stellar evolution even during the main sequence lifetime (see e.g. Maeder & Meynet 1994). The relationship between the mass and the luminosity of a single massive star will therefore depend on its evolutionary status (not to speak

[1]Throughout this review, we shall refer to the primary as the more massive component of the binary as observed in its *present-day* configuration. Conversely, the secondary is the binary component which has currently the lower mass.

about the effects of mass exchange in binary systems that are addressed by D. Vanbeveren in his review).

In order to provide useful constraints on the fundamental properties of *single* massive stars, an early-type binary system has to meet several criteria: i) it must be of type SB2, ii) it should display eclipses, iii) the stars should be inside their Roche lobes and iv) the components must be young objects that have not yet suffered any mass exchange through Roche lobe overflow. However, due to the short duration of the main-sequence phase of a massive star (a few million years), the number of observable well detached binaries among the massive systems with short orbital periods is considerably reduced. Conversely, many short period O + O binaries are observed in a stage of their evolution affected by a previous episode of mass exchanges (e.g. Penny *et al.* 1996, Rauw *et al.* 2002b). Mass transfer in a massive binary can be considered roughly instantaneous since it occurs on a time scale of only about ~ 10000 years. However, the rate of mass transfer during this short-lived interaction phase is of order 10^{-3} to $10^{-2}\,M_\odot\,yr^{-1}$ and the result is that the analysis of these binaries after mass exchange will no longer provide information on the properties of single massive stars.

The number of suitable O + O systems is therefore rather low and until the early 1990's, accurate orbital elements for many of them were lacking. The main problems that prevented high quality orbital solutions from being established for a long time were the line-blending mainly due to the rotational broadening of the spectral lines and the contamination of absorption lines by emission lines formed in the stellar wind. Considerable progress has been achieved with the advent of cross-correlation techniques and the possibility of simultaneous multiple Gaussian fitting. In WR + O binaries an additional difficulty arises from the fact that the spectra of WR stars contain no photospheric absorption lines and one has therefore to rely on the radial velocities of broad emission lines to describe their orbital motion. It has to be noted that the orbital parameters of WR stars are sometimes extremely sensitive to the choice of the spectral line adopted for the orbital solution. These effects reflect the relative motion of the line forming regions that are located in the outflowing stellar wind rather than at the level of the WR core.

Generally speaking, the study of massive binaries requires a considerable amount of observations, especially when the orbital periods are very long or ill-conditioned (i.e. shorter than about five days and very close to an integer number of days). Several teams have contributed to the recent effort aiming at a better understanding of the properties of massive binaries. A (by no means exhaustive) list of these teams includes the groups from La Plata (Argentina, e.g. Morrell *et al.* 2001), Atlanta (USA, e.g. Bagnuolo *et al.* 1994), St. Andrews (United Kingdom, e.g. Harries *et al.* 1998), Chilton (United Kingdom, e.g. Stickland *et al.* 1995), Montréal (Canada, e.g. Lamontagne *et al.* 1996) and Liège (Belgium, e.g. Rauw *et al.* 2001a).

Recent compilations of galactic O + OB and WR + OB binaries for which relatively accurate determinations of the masses exist can be found in Gies (2003) and van der Hucht (2001).

2.1 The mass discrepancy

In the absence of an empirical mass-luminosity relation, there are two independent indirect techniques to estimate the mass of a single early-type star. The first approach consists in comparing the position of the star (i.e. its luminosity and effective temperature) in an empirical Hertzsprung-Russell diagram with the predictions of stellar evolution calculations. The second method is based on the modeling of the observed spectrum with a stellar atmosphere code. This modeling yields several stellar parameters including the radius and the gravity and hence the stellar mass (see also the review by P. Crowther in this volume).

However, the model atmosphere codes yield masses that are systematically lower than those inferred from the comparison with the evolutionary models (see e.g. Herrero *et al.* 1992, 2000). This discrepancy mostly affects supergiants that are close to the Eddington limit, but it also exists for O-stars on the main sequence. Herrero *et al.* (2000) pointed out that the use of spherical model atmospheres accounting for mass loss reduces the mass discrepancy but the spectroscopic masses are still systematically lower than the evolutionary ones.

Burkholder *et al.* (1997) and Gies (2003) showed that the agreement between the observed masses of massive stars in detached unevolved binaries and those determined through a comparison with evolutionary models is generally quite satisfactory for masses up to $\sim 57\,M_\odot$, provided that the 'spectral type - effective temperature' calibration of Martins *et al.* (2002) is adopted. Martins *et al.* found that the inclusion of line blanketing leads to a somewhat cooler effective temperature scale than previously suggested by Vacca *et al.* (1996). Consequently, the bolometric luminosities and the masses determined by comparison with evolutionary tracks are also reduced.

Finally, one has to bear in mind that the detailed comparison with evolutionary tracks may require an additional parameter to be considered. Meynet & Maeder (2000) pointed out that rotation can have a significant impact on the evolutionary track of a massive star in the Hertzsprung-Russell diagram (see also the contributions by A. Maeder in this volume). For low gravity objects that evolved from rapidely rotating progenitors, the comparison between models with and without rotation can lead to relative mass differences of order 30%, the inclusion of rotation leading to lower masses for a given luminosity.

2.2 Massive binaries in the young open cluster Trumpler 16

The very young open cluster Trumpler 16 (Massey & Johnson 1993) in the Carina complex is particularly rich in massive binaries (Levato *et al.* 1991). For instance, this cluster harbors the only known galactic binary containing an unevolved star of spectral type O3 V (HD 93205; recently reclassified as O3.5 V ((f$^+$)) by Walborn *et al.* 2002; see also below). On the other hand, the cluster contains also at least two eclipsing binaries (Tr 16-1 and Tr 16-104). In this section, we will briefly review the properties of these objects and the information they provide on the parameters of massive stars and on the properties of the open cluster itself.

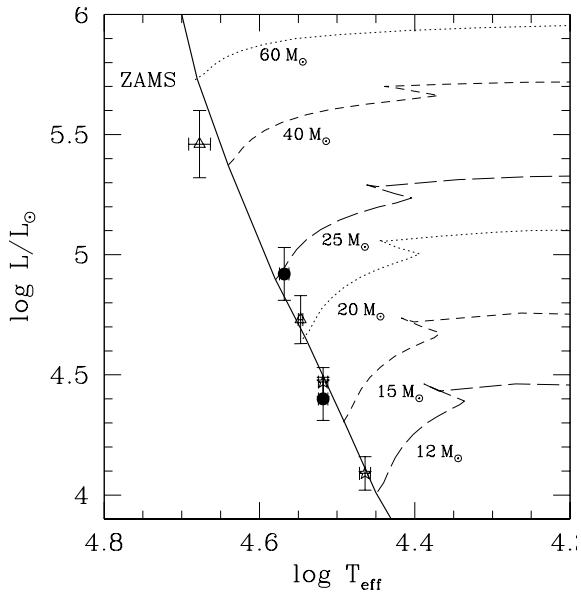

Fig. 1. Hertzsprung-Russell diagram of eclipsing or ellipsoidal early-type binaries in the open cluster Tr 16 of the Carina complex. The evolutionary tracks are taken from Schaller *et al.* (1992) for solar metallicity. The different symbols stand for HD 93205 (triangles), Tr 16-104 (filled dots) and Tr 16-1 (stars).

We have displayed the properties of the components of the eclisping binaries Tr 16-1 (Freyhammer *et al.* 2001) and Tr 16-104 (Rauw *et al.* 2001a) as well as of the ellipsoidal variable HD 93205 (Morrell *et al.* 2001, Antokhina *et al.* 2000) in a Hertzsprung-Russell diagram. We adopted the radii determined from the photometric analyses as well as the temperature scale proposed by Martins *et al.* (2002). In Fig. 1, we have also drawn the evolutionary tracks corresponding to theoretical models from Schaller *et al.* (1992) for solar metallicity. The components of the three binaries are all found to lie pretty close to the zero-age main sequence (ZAMS). This result suggests that Tr 16 contains stars that are probably younger than 1 million years.

Adopting the bolometric corrections from Humphreys & McElroy (1984), we can use the bolometric magnitudes directly obtained from the light curve analyses to compute the absolute magnitudes M_V. The results are given in the sixth column of Table 1, whilst the last column of this table provides the absolute visible magnitudes for stars of this spectral type following the calibration of Humphreys & McElroy (1984). It becomes immediatly clear that the stars on the ZAMS in Tr 16 are about one magnitude fainter than expected from the Humphreys & McElroy calibration. This discrepancy is further enhanced if we compare our observed absolute magnitudes with the absolute magnitudes proposed by Vacca *et al.* (1996).

Table 1. Properties of three short-period eclipsing or ellipsoidal early-type binaries in the young open cluster Trumpler 16. The effective temperatures are based on the calibration of Martins *et al.* (2002). The last column provides the absolute visual magnitudes according to the calibration of Humphreys & McElroy (1984).

System		$R/R_\odot$	$T_{\rm eff}$ (K)	$\log L/L_\odot$	$M_{V,obs}$	$M_{V,cal}$
HD 93205	O3.5 V	8.0 ± 1.2	47500 ± 1500	5.46 ± 0.14	-4.60	-5.50
	O8V	6.3 ± 0.7	35250 ± 250	4.73 ± 0.10	-3.58	-4.80
Tr 16 − 104	O7 V	7.1 ± 0.9	37000 ± 500	4.92 ± 0.11	-3.95	-5.00
	O9.5V	4.9 ± 0.5	33000 ± 500	4.40 ± 0.09	-3.00	-4.20
Tr 16 − 1	O9.5 V	5.3 ± 0.3	33000 ± 500	4.47 ± 0.06	-3.18	-4.20
	B0.3V	4.4 ± 0.3	29100 ± 500	4.09 ± 0.07	-2.58	-3.80

The reason for this discrepancy resides essentially in the stellar radii obtained from the analyses of the light curves. These radii are significantly smaller than what is usually expected for main sequence early-type stars. This result is reminiscent of the finding of Walborn & Blades (1997) who discovered a population of subluminous, so-called O Vz, stars among the youngest objects of the 30 Doradus complex in the Large Magellanic Cloud (LMC). Walborn & Blades suggested that these objects are nearer to the ZAMS than more luminous 'typical' O V stars.

We can use the absolute magnitudes determined from the study of the eclipsing binaries to constrain the distance of the cluster. In fact, comparing the absolute magnitudes to the apparent dereddened magnitudes, we obtain a distance modulus of 11.95 ± 0.06 (corresponding to a distance of 2.45 kpc). This value is smaller than the one determined by Massey & Johnson (1993; 3.2 kpc). Again, this discrepancy may be accounted for by the fact that the O V stars in Tr 16 are subluminous.

As stated above, Tr 16 is extremely rich in massive binaries. Several of these binaries actually belong to multiple (triple, quadruple,...) systems, some of which might be genuine hierarchical systems (e.g. Tr 16-104, Rauw *et al.* 2001a), while others might be line-of-sight associations (this could be the case of Tr 16-110, Albacete-Colombo *et al.* 2002). Tr 16-104 consists of an eclipsing SB2 binary of period 2.15 days and a more distant third component that probably describes a longer period orbit of either 285 or 1340 days around the center of mass of the system. Tr 16-110, on the other hand, consists of an SB2 ($P_{\rm orb} = 3.63$ days) and an SB1 ($P_{\rm orb} = 5.03$ days). However the physical link between the SB2 and the SB1 is not established yet. The genuine multiple systems offer a unique opportunity to test the theory of dynamical interaction in young open clusters as well as to improve our understanding of the formation of massive stars and of the conditions of stability of hierarchical systems.

Another interesting question to address in an open cluster that rich in early-type binaries is to determine the cut-off period for eccentric orbits that is defined as the critical period below which the tidal forces have circularised the orbit of an initially eccentric system. The existing data on binaries in Tr 16 suggest that orbits

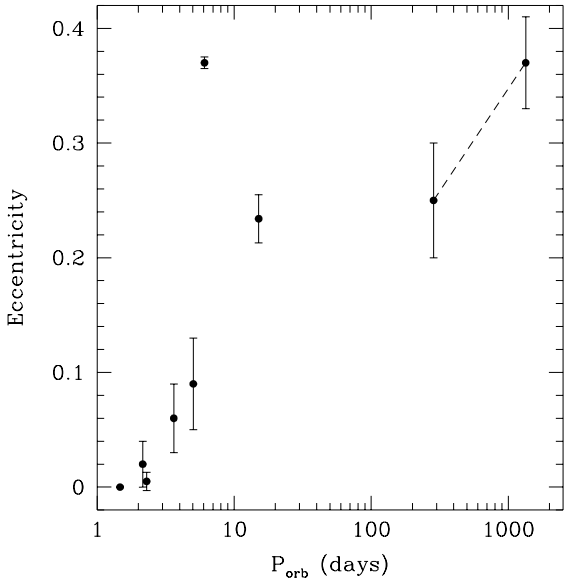

Fig. 2. Distribution of the orbital eccentricity of a sample of early-type binaries in the open cluster Tr 16 as a fonction of their orbital period. The symbols connected by the dashed line refer to the two possible SB1 orbital solutions of the third component in Tr 16-104.

with periods below 2.5 days are indeed circular, whereas eccentricities significant at the $\geq 2\,\sigma$ level are found for periods longer than 3.6 days. The fact that the tidal forces did not have enough time yet to significantly shape the $(\log P_{\rm orb}, e)$ diagram is yet another indication of the extreme youth of the stars in this cluster.

2.3 What are the most massive stars known to date?

An important question in the context of the formation and the stability of very massive stars is that of the mass of the most massive stars. A priori, we would expect to find them among the unevolved objects of spectral type O2 V - O3 V (Walborn *et al.* 2002). Indeed, the evolution of massive objects is largely influenced by their huge mass loss rates and it is therefore expected that they have lost a sizeable fraction of their mass once they reach more advanced evolutionary stages (such as the WN or WC stage).

From a comparison with evolutionary tracks, Walborn *et al.* (2002) infer masses of up to $\sim 200\,{\rm M}_\odot$ for the most luminous O2 stars (Pismis 24-1, Cyg OB2 22A). Do stars that massive really exist? Let us consider the most massive binary systems known so far. First of all, we should point out that, to date, there is no known binary system that harbors an O2-star. One has to bear in mind that the binarity

of such a system might remain undetected if the mass ratio (primary/secondary) were large. In fact, the large mass of the O2 primary would then lead to a low amplitude of its radial velocity curve and a large mass ratio would also imply a large luminosity ratio, such that the spectral signature of the secondary in the composite spectrum would be extremely weak.

The lack of O2 binaries is even more embarrassing considering that the evolutionary masses of O2 V - O3 V stars determined by Walborn *et al.* span an extremely wide range from about 50 to 200 $M_\odot$! Therefore, even if we knew a binary system harboring an O2 star with a mass below say 100 $M_\odot$, we would not be able to draw a general conclusion about the masses of the stars in this spectral class.

Over the last years, the search for the most massive star in a binary system focused on HD 93205, the O3.5 V + O8 V system discussed hereabove. HD 93205 is indeed the only known binary system in our Galaxy that contains such an early main-sequence star. As indicated in Section 2.2, this system consists of two stars that are still on the ZAMS. The orbital solution of Morrell *et al.* (2001) yields a mass ratio of 2.4. Assuming a typical mass of 22 - 25 $M_\odot$ for the O8 V secondary, the mass of the O3.5 V primary would 'only' be of the order of 52 - 60 $M_\odot$. A fit of the ellipsoidal light variations (amplitude 0.02 mag) yields a 'best-fit' orbital inclination of 60° (although the uncertainties on this value are quite large; see Antokhina *et al.* 2000) corresponding to masses of 48 and 20 $M_\odot$ for the O3.5 V and O8 V component respectively. Therefore, the mass of the primary of HD 93205 appears rather 'modest'! What about binaries harboring O3 V stars in other galaxies? Interestingly, there are indeed at least three eclipsing binaries harboring very massive O V stars in the R 136 cluster of the 30 Dor complex in the LMC (Massey *et al.* 2002). The extreme youth of R 136 suggests that these stars are representative of the population of O3 stars on the ZAMS (although at a lower than solar metallicity). The remarkable analysis of Massey *et al.* indicates that the binaries R 136-38 (O3 V + O6 V) and R 136-42 (O3 V + O3 V) have primaries with masses below 57 $M_\odot$, again far from the 200 $M_\odot$ suspected for some O2 stars.

Although we argued above that the most massive stars are to be found among the ZAMS objects, let us nevertheless consider binary systems in more advanced evolutionary stages. For a long time, Plaskett's Star (HD 47129) was thought to be the best candidate for the heavy-weight record-holder. This O7.5 I + O6 I binary with a 14.4 day orbital period consists of two very massive stars whose masses have been estimated to be of the order of 42.5 and 51.0 $M_\odot$ for the primary and secondary respectively (Bagnuolo *et al.* 1992). However, these results must be considered with caution since HD 47129 does not display photometric eclipses allowing an accurate orbital inclination to be determined.

Another extremely massive object is the WN7ha primary in the 80-day period binary WR 22. Rauw *et al.* (1996) derived a minimum mass of 72 $M_\odot$ for this star. Since the system displays atmospheric eclipses when the WNha star passes in front of its secondary (Gosset *et al.* 1991), the orbital inclination is pretty close to 90° (Rauw 1997) and the actual mass should be close to the minimum mass. However, Schweickhardt *et al.* (1999) obtained a more extensive data set of this

system and found a somewhat larger orbital eccentricity than Rauw *et al.* (1996) leading to a downwards revision of the mass of the primary (although with a mass of $55\,M_\odot$ it remains one of the most massive stars known in our Galaxy).

In summary, it appears that so far there is hardly any evidence that stars with masses exceeding $60\,M_\odot$ actually exist in binary systems. Although this does not rule out the existence of stars with larger masses, high-quality radial velocity studies and photometric monitoring of the candidates for these extremely massive objects are urgently needed to investigate their multiplicity and uncover possible binary systems. An important question to address from the theoretical point of view would be whether there could exist a difference in the upper mass limit for the formation of single and binary massive stars.

2.4 Observational evidence for mass exchange in evolved massive binaries?

As stated above the results from the study of early-type binaries can be used to infer the properties of single massive stars only if the binary system has not suffered from any mass exchange. However, many massive binaries are found to be evolved systems. In some cases, the comparison of the properties of their components with evolutionary tracks for single massive stars yields inconsistent results. For instance, in the case of HD 152248 (O7.5 III(f) + O7 III(f)) both stars appear overluminous for their masses (Sana *et al.* 2001) and the evolutionary masses needed to account for the observed luminosity are $\sim 30\%$ larger than the observed masses. Penny *et al.* (1996) argued that this behaviour is an indication of ongoing Roche lobe overflow (RLOF). We note however, that the available light curve solution of HD 152248 (Mayer *et al.* 2001) does not support this idea. The present-day configuration of HD 152248 may have been affected by a past RLOF episode instead (Sana *et al.* 2001). On the other hand, as stated previously the inclusion of rotation in the single star evolutionary models may in fact reduce the discrepancy between the observed and theoretical masses. However, in this system, the observed present-day rotational velocities are not exceptionally large and it remains to be seen whether they are sufficient to account for a large effect on the evolution.

As a second example, we consider the evolved binary HDE 228766. Rauw *et al.* (2002b) found that this system consists of an O7 primary and a WN8ha secondary. Although the secondary is nowadays the less massive star it has clearly the stronger stellar wind and is the most evolved component of the system (as witnessed also by the peculiar chemical abundances in its wind). The secondary star appears therefore as a kind of transition object at the beginning of the WN stage and it must have been the initially more massive component of the system. The easiest way to account for this situation is to assume that the evolution of the whole system has been influenced by mass exchange. Evolutionary tracks from Vanbeveren & de Loore (1994) and de Loore & Vanbeveren (1994) could indeed explain the overluminosity of the secondary. The initially more massive component could have undergone mass loss through Roche lobe overflow and would now appear as the less massive star. Rauw *et al.* (2002b) pointed out that the

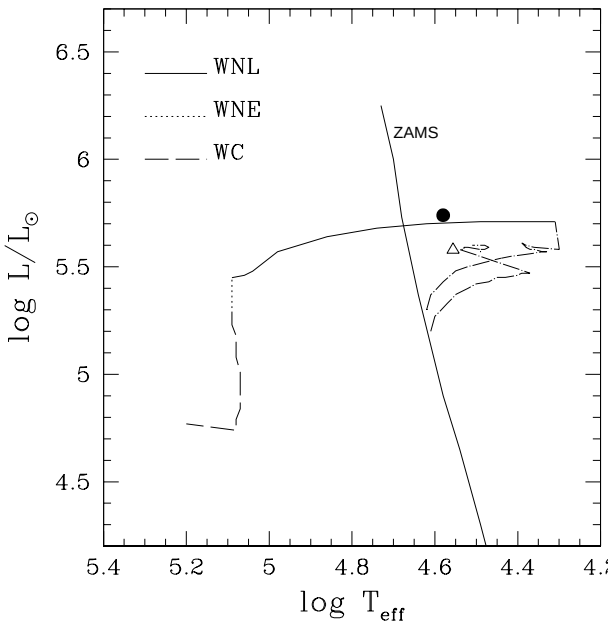

Fig. 3. Comparison of the location of the components of HDE 228766 in the Hertzsprung-Russell diagram with the binary evolution tracks from Vanbeveren & de Loore (1994) and de Loore & Vanbeveren (1994) for a binary of initial masses $40\,M_\odot + 36\,M_\odot$ and an initial orbital period of 25 days. The open triangle stands for the present-day primary whereas the filled dot stands for the present-day secondary. Note that the dash-dotted tracks correspond to the evolution during the main-sequence lifetime.

primary has broader absorption lines and seems therefore to be rotating faster than the secondary. In the framework of a binary evolution model, the larger $v \sin i$ of the present-day primary could be due to spinning up through accretion (Vanbeveren & de Loore 1994). Let us emphasize that according to the binary evolution tracks from Vanbeveren & de Loore and de Loore & Vanbeveren (1994) for a binary of initial masses $40\,M_\odot + 36\,M_\odot$ and an initial orbital period of 25 days, the present-day parameters of both stars in HDE 228766 are consistent with an age of about 5.5 million years. It seems therefore plausible that HDE 228766 is in a post RLOF stage.

3 Interacting winds in early-type binaries

Early-type stars have energetic highly supersonic winds. Whenever two early-type stars find themselves bound by gravitation in a binary system, their winds interact. The wind interaction region is limited by two hydrodynamical shocks, each facing one of the binary components. The compressed stellar winds are separated by a

contact discontinuity which is set by the equilibrium of the stellar wind momenta.

Colliding stellar winds in massive binaries provide an astrophysical laboratory to study the shock physics of cosmic plasmas. The theoretical concept of colliding stellar winds was put forward by Prilutskii & Usov (1976) and Cherepashchuk (1976). The first models based on a numerical solution of the differential equations of the hydrodynamics governing the phenomenon were presented by Lebedev & Myasnikov (1988), Luo *et al.* (1990) and Stevens *et al.* (1992). Although the details of the process are quite complex, some insight into the geometry and the physics of the phenomenon can be gained from rather simple considerations. Below, we will briefly introduce some theoretical aspects of colliding winds. To this aim, we closely follow the developments presented by Stevens *et al.* (1992).

3.1 Some basic theoretical concepts

Consider a system formed by two stars of radii R_1 and R_2. We assume that the stellar winds of both components are spherically symmetric and that the wind velocity at radius r can be described by a so-called β-law:

$$v_j(r) = v_{\infty,j}\,\left(1-\frac{R_j}{r}\right)^{\beta_j}, j=1,2$$

where $v_{\infty,j}$ and R_j stand respectively for the asymptotic wind velocity and the radius of star j. Each wind carries a mass loss rate $\dot{\rm M}_j$. The equation of the contact discontinuity follows from the condition of ram pressure equilibrium:

$$\rho_1(r_1)\,v_1^2(r_1)\cos^2\phi_1 = \rho_2(r_2)\,v_2^2(r_2)\cos^2\phi_2$$

(see Fig. 4) where $\rho_j(r_j)$ stands for the density of the stellar wind of star j at radius r_j. This can be written

$$\frac{\dot{\rm M}_1\,v_1(r)}{4\,\pi\,r_1^2}\,\cos^2\phi_1 = \frac{\dot{\rm M}_2\,v_2(r)}{4\,\pi\,r_2^2}\,\cos^2\phi_2 \tag{3.1}$$

Introducing the wind momentum ratio

$$\mathcal{R} = \left(\frac{\dot{\rm M}_1\,v_{\infty,1}}{\dot{\rm M}_2\,v_{\infty,2}}\right)^{1/2} \tag{3.2}$$

one obtains that

$$\frac{r_1}{r_2} = \lambda\,\frac{\tan\beta\,\cos\theta_1-\sin\theta_1}{\sin\theta_2-\tan\beta\,\cos\theta_2}$$

where $\lambda = \mathcal{R}\,(1-R_1/r_1)^{\beta_1/2}/(1-R_2/r_2)^{\beta_2/2}$.

Finally, after some basic algebra, we obtain the differential equation describing the contact discontinuity:

$$\frac{dz}{dx} = \tan\beta = \frac{(\lambda\,r_2^2+r_1^2)\,z}{\lambda\,r_2^2\,x+r_1^2\,(x-d)} \tag{3.3}$$

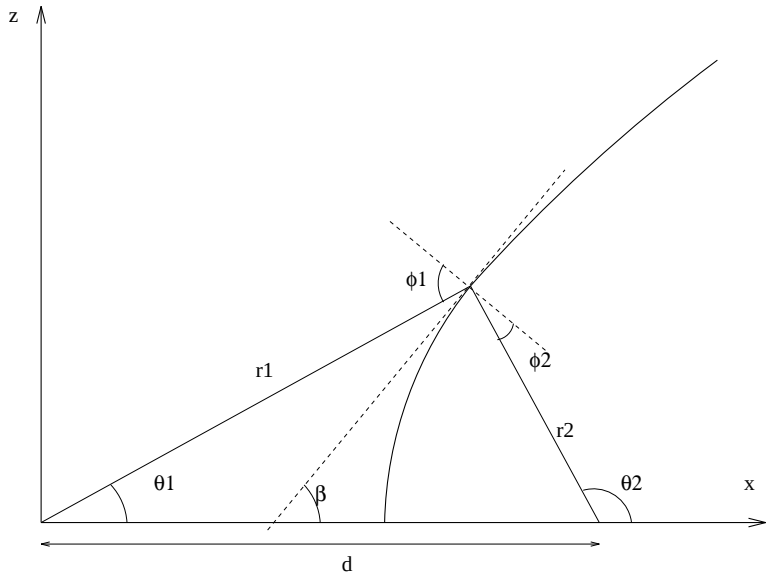

Fig. 4. Schematic view of the contact discontinuity in a colliding wind binary. The star with the more energetic wind is located at the origin of the axes, while the companion is located at a distance d on the x-axis. We assume that the shock region has an axi-symmetric shape around the binary axis.

where $r_1 = \sqrt{x^2 + z^2}, r_2 = \sqrt{(x-d)^2 + z^2}$ and d stands for the distance between the centers of the stars (see Stevens *et al.* 1992). The shape of the contact discontinuity is then obtained through numerical integration of equation 3.3.

If both winds have reached their terminal velocity before they collide, we get $\lambda = \mathcal{R}$. In this case, the intersection between the binary axis and the surface discontinuity will be found at a distance $x^{\rm stag} = \mathcal{R}\, d/(\mathcal{R}+1)$ from the origin (i.e. from the center of mass of the star with the more energetic wind). In a binary system where both winds are of equal strength ($\mathcal{R} = 1$), the contact discontinuity can be approximated by a plane located mid-way between the two stars. In a more general situation with $\mathcal{R} \neq 1$, the contact discontinuity appears as a cone wrapped around the star with the less energetic wind. The half opening angle of this shock cone may be approximated by $\Theta(^\circ) \sim 120(1 - \frac{\mathcal{R}^{-4/5}}{4})\mathcal{R}^{-2/3}$ (Eichler & Usov 1993).

The immediate post-shock properties of the plasma can be described by the Rankine-Hugoniot conditions for strong shocks in a gas with $\gamma = 5/3$: $\rho_{s,j} = 4\,\rho_j$, $v_{s,j} = v_j/4$ and $T_{s,j} = \frac{3\,\overline{m}_j\, v_j^2}{16\,k}$, where $\overline{m}_j$ is the average mass per particle in the wind of star j (see e.g. Stevens *et al.* 1992). For solar abundances, we find that $kT_{s,j} \simeq 1.17\, v_8^2$ (in keV) where v_8 is the pre-shock velocity expressed in $1000\,{\rm km\,s^{-1}}$. Therefore, due to the large pre-shock wind velocities, the post-shock

plasma temperature is very high ($\geq 10^7$ K). Thus the main signature of this shock-heated plasma is expected to occur in the X-ray domain.

The post-shock gas near the axis will be subsonic (due to the high post-shock temperature and the fact that the sound speed increases as $\sqrt{T_s}$). The post-shock gas flows away from the axis at velocities close to the sound speed. The properties of the post-shock gas depend to a large extent on the importance of radiative cooling that can be roughly estimated from the ratio between the characteristic cooling time and the typical escape time from the shock region:

$$\chi = \frac{t_{\rm cool}}{t_{\rm esc}} \simeq \frac{v_8^4\, x_{12}^{\rm stag}}{\dot{\rm M}_{-7}}$$

where $x_{12}^{\rm stag}$ and $\dot{\rm M}_{-7}$ are respectively the distance to the contact surface in units 10^7 km and the mass loss rate in units $10^{-7}\,{\rm M}_\odot\,{\rm yr}^{-1}$ (Stevens *et al.* 1992). If radiative cooling is important ($\chi \ll 1$), the entire thermal energy produced in the shock is radiated immediately away. If the shock is highly radiative, it collapses and the ionization of the material in the interaction region is set by the radiation of the stars rather than by the shock. This rather cool material can contribute to the formation of emission lines in the optical spectrum. Otherwise, if $\chi \geq 1$, the shock region is adiabatic. From the χ parameter defined by Stevens *et al.* (1992), it becomes immediately clear that the larger the mass loss rate (all other things being equal), the more efficient the cooling.

The shocked winds are seldom stable. Different kinds of instabilities may affect the material in the interaction region and these phenomena are usually more pronounced for radiative winds.

We ought to mention that the shocks associated with a wind collision can act as sites for particle acceleration through the first order Fermi mechanism (Eichler & Usov 1993). In this scenario free electrons undergo acceleration to relativistic velocities by crossing the shock front forth and back (see e.g. Longair 1992).

Over the last ten years it became clear that there are several effects that may substantially affect the predictions of the numerical simulations. The most prominent ones are:

- deviations of the wind velocity law from the standard β-law description. There are various reasons why the β-law may not be a good approximation especially in close binary systems: radiative inhibition (Stevens & Pollock 1994) and radiative braking (Gayley *et al.* 1997) are the best understood effects. In addition, X-ray emission from the shock region may also alter the ionization of the wind material and therefore affect its ability to suffer radiative acceleration.

- 3-D effects that are often neglected in the numerical models. The Coriolis force may have an important impact on the shape of the interaction region if the orbital period is short enough for the orbital velocities to become significant compared to the wind velocities (see e.g. Pittard 2000).

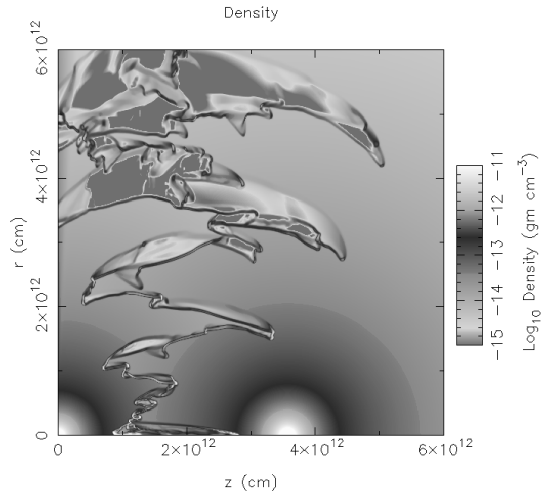

Fig. 5. Snapshot grey-scale images of the density structure of a hydrodynamical simulation of a highly radiative wind collision. The z-axis corresponds to the line of centers whilst r yields the radial distance from this axis. The wind parameters are such that $\mathcal{R} = 1$ and $\chi \simeq 0.07$ for the shocked winds of both stars (courtesy Sana *et al.* 2003, in preparation).

3.2 Observational evidence for colliding winds

3.2.1 In the optical and UV domain...

Optical and ultraviolet spectra of many early-type binaries display emission line profile variability. Examples of evolved O + O star binaries that show such phase-locked profile variations are AO Cas (O9 III + O8 V; Gies *et al.* 1997), 29 CMa (O7.5-8 Iabf + O9.7 Ib; Wiggs & Gies 1993), Plaskett's Star (HD 47129, O7.5 I + O6 I, Wiggs & Gies 1992), HD 93403 (O5.5 I + O7 V; Rauw *et al.* 2002a), HD 149404 (O7.5 I(f) + ON9.7 I; Rauw *et al.* 2001b), HD 152248 (O7.5 III(f) + O7 III(f); Sana *et al.* 2001), V 729 Cyg (O6-7 Ia + Ofpe/WN9; Rauw *et al.* 1999)... Examples of colliding wind WR binaries showing emission line profile variations are HD 5980 (WN? + ?; Breysacher & François 2000), WR 30a (Gosset *et al.* 2001), WR 42 (WC7 + O; Hill *et al.* 2000), WR 79 (WC7 + O; Hill *et al.* 2000), WR 139 (WN5 + O6 III-V, Marchenko *et al.* 1997)...

Many of the WR + O systems (especially the WC + O) display moving subpeaks on top of flat-topped broad emission lines. The line profile variability reflects the loss of spherical symmetry of the winds. In fact, the variations can be due either to geometrical effects produced by the cavity in the emitting/absorbing wind volume or to excess emission coming from the high density material compressed in the wind interaction region. In a highly radiative shock, the material in the interaction region cools sufficiently to reach temperatures where optical and UV

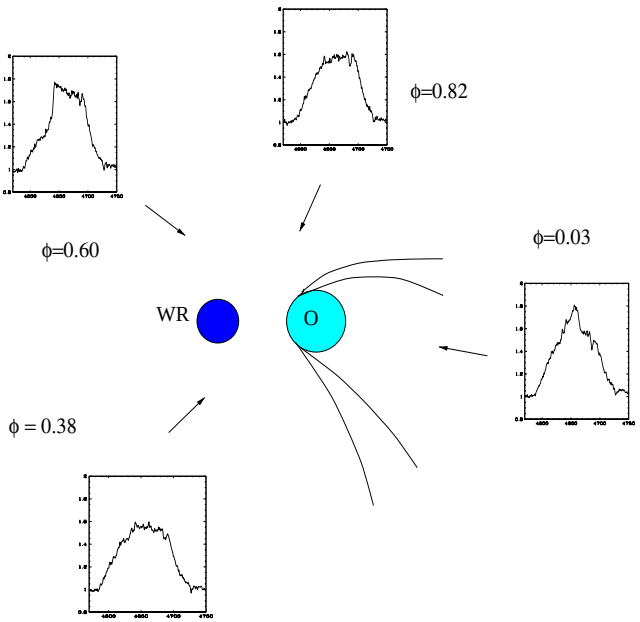

Fig. 6. Orbital variability of the C IV λ 4658 blend in the spectrum of WR 30a. The arrows indicate the projections of the line of sight on the orbital plane at various phases, while the insets display the C IV profiles observed at these phases (see Gosset *et al.* 2001).

recombination lines are formed. Due to the density squared dependence of the emissivity of the recombination process, the high-density material in the post-shock region can contribute significantly to the total line emission spectrum of an early-type binary.

To illustrate this phenomenon, we consider the variations of the C IV λ 4658 blend in the spectrum of the WO4 + O5((f)) binary WR30a (Gosset *et al.* 2001). Two time-series of spectra taken one year apart revealed identical line profile variations clearly demonstrating the phase-locked nature of the phenomenon. The variations result from an apparent extra emission on top of the broad line (see Fig. 6). The phase dependence of this feature is consistent with excess emission produced mainly in the trailing arm of the shock region. Due to the Coriolis effect, the shock cone is probably deflected by about 18° and the emissivity of the wind material is most likely larger in the trailing wake where the shock of the WR wind is more head-on.

Although the most straightforward explanation for the observations related to phase-locked line profile variability in the optical spectra of early-type binaries is indeed a colliding wind scenario, present day hydrodynamic simulations fail to reproduce this feature. The main reason for this failure is the fact that the numerical grids undersample the cooling layers of the shock region.

3.2.2 In the radio domain...

A subset of early-type stars display a non-thermal radio emission in addition to the thermal radio emission produced via free-free emission from the stellar wind. The non-thermal (synchrotron) emission is a definite sign of two things: (i) a magnetic field must be present in the winds of these objects and (ii) relativistic electrons exist in the radio emitting region. As stated above, the relativistic electrons may be accelerated through the first order Fermi mechanism in the shock zone of the wind interaction region (Eichler & Usov 1993). Interestingly, many of the non-thermal radio emitting early-type stars are binary systems. For instance, Dougherty & Williams (2000) pointed out that at least seven out of nine WR stars that display non-thermal radio emission are in fact binaries.

The most famous examples in this category are probably WR 140 (WC7 + O5, e.g. White & Becker 1995) and WR 147 (e.g. Williams *et al.* 1997).

WR 140 has a highly eccentric ($e = 0.84$) orbit with a period of 7.9 yrs and the radio flux displays a phase-locked variation (White & Becker 1995). The radio flux is thermal over large parts of the orbit. However, between phases 0.55 and 0.95 (phase 0.0 corresponding to the periastron passage), the radio flux increases dramatically and displays a non-thermal spectral index. The shape of the radio light curve at different frequencies results basically from a combination of two effects. First, during most of the orbit, the two stars are so close that the region of the wind interaction is burried deep inside the (huge) radio photosphere of the WR star and therefore non-thermal radio emission produced by electrons accelerated in the shock can only be observed at phases near apastron when the shock zone is farthest away from the WR core and moves out of the WR's radio photosphere (remember that the distance of the shock from the WR star, $x^{\rm stag}$ scales with the binary separation d). Second, as a result of the cavity produced by the shock cone in the WR wind, the non-thermal radio emission can reach us when the O-star with its lower density (and thus less opaque) wind passes in front of the WR star.

WR 147 is a visual binary consisting of a WN8 star and a late-O, early-B type star. The radio emission from this system was resolved by MERLIN into two components: a thermal component associated with the wind of the WN8 star and a non-thermal component located in between the WR star and its visual companion (but closer to the latter, see Williams *et al.* 1997). The location of this non-thermal component is consistent with the ram pressure balance of the two stellar winds as expected in a colliding wind scenario. Interestingly, WR 147 is also the first early-type system where Chandra ACIS-I observations revealed evidence for a spatially extended X-ray emission. The X-rays are found to peak close to the position of the radio bow shock (Pittard *et al.* 2002).

3.2.3 In the infrared...

Some WC stars (some of which are known binaries usually with wide orbital separations) exhibit episodic variability of their IR emission. At least in two cases (WR 140 and WR 137) this phenomenon is recurrent. These variations have been attributed to dust formation in the wind collision zone (see Williams 2002 for a

review). However, this wind interaction zone offers a rather hostile environment for dust to form. Although the chemical ingredients to make dust are available in a WC wind, the intense radiation from the WR stars and its O-type companion should prevent dust from forming. Even more critical is the fact that the temperature in the shocked winds of a binary with an adiabatic wind collision is much higher than what is required for dust to form and it remains to be seen whether the density ($\geq 10^{12}\,\mathrm{cm}^{-3}$) and temperature ($\leq 3900\,\mathrm{K}$) conditions required to initiate dust formation (Le Teuff 2002) can be met in the wind interaction zone. Recent hydrodynamical simulations suggest that clumpiness of the WR wind might help to overcome these problems (see Walder & Folini 2003).

At least in the case of WR 140, the IR outbursts (variation by 3 magnitudes at $3.8\,\mu$m) appear to be phase-locked. The outburst events are initiated a few months after periastron passage, indicating that material is swept away from the interaction region, only forming dust at some distance downstream (Williams 2002).

Another, probably related observation is the detection of pinwheel nebulae associated with several WC binaries. In fact, observing with the Keck I telescope in the near infrared, Tuthill *et al.* (1999) discovered that WR 104 displays a spiral shaped nebula that is moving around the center of mass of the binary as the stars are revolving around each other once in 220 days. In this case, it seems that the infrared excess is produced in the tail of the shock region wrapped around the O-star companion. Dust produced in the wake of the O-star would be carried out of the system by the WR wind and the combination of the radial wind with the orbital motion results in a spiral-like feature. Due to the shadowing effect of the inner coil of the spiral, its outer parts are not heated by the central stars and remain therefore invisible in the near IR.

3.2.4 In the X-rays...

As stated above, the main signature of wind interactions, especially in the adiabatic case, is expected in the X-ray domain. However, individual early-type stars are also intrinsic X-ray emitters. To disentangle the shock emission from the intrinsic X-ray emission, we can compare the observed L_X/L_{bol} ratio to the 'canonical' scaling relation derived by Berghöfer *et al.* (1997).

On statistical grounds, early-type binaries are found to be stronger X-ray sources than their single counterparts (Pollock 1987, Chlebowski & Garmany 1991). However, there is a considerable scatter in the L_X/L_{bol} relation. Therefore, it is important to have an additional criterion allowing to establish the link between colliding winds and X-ray emission in early-type binaries. The X-ray emission from colliding wind binaries is expected to display a significant phase-locked modulation (Pittard & Stevens 1997) either as a consequence of changing opacity along the line of sight or as a consequence of a changing separation between the stars in eccentric binaries (for an adiabatic shock, the X-ray luminosity is expected to scale as $L_X \propto \dot{M}^2/d$, Stevens *et al.* 1992). Corcoran (1996) presented the ROSAT-PSPC light curves of sixteen O-type binaries and found evidence for a phase-locked modulation in at least four cases.

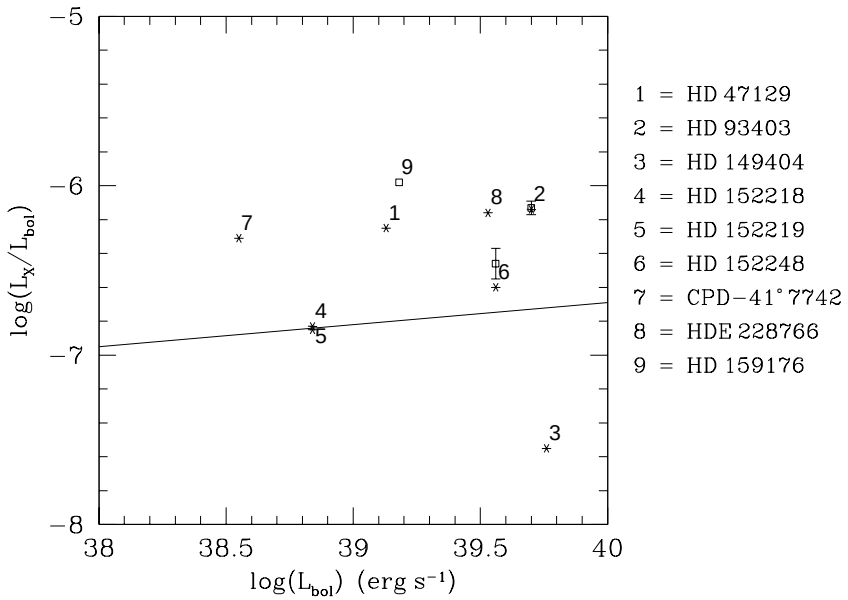

Fig. 7. ROSAT-PSPC and XMM-Newton EPIC X-ray luminosities in the energy range 0.1 to 2.0 keV for a sample of massive close O + O binaries. The solid line shows the empirical scaling relation derived by Berghöfer *et al.* (1997). Stars stand for ROSAT data whereas open squares stand for XMM data. Note the good agreement between ROSAT and XMM data for HD 93403 and HD 152248. While most of the binaries are X-ray over-luminous, two systems (HD 152218 and HD 152219) exhibit no excess emission and HD 149404 even appears underluminous. The 'error bars' on the data points of HD 93403 and HD 152248 indicate the range of orbital variability of their X-ray luminosities.

A textbook example of a WR + O colliding wind binary is the WC8 + O7.5 III binary γ^2 Vel (= WR 11, $P_{\rm orb} = 78.53$ days). Willis *et al.* (1995) gathered ROSAT-PSPC observations of this system that revealed substantial phase-locked variability of the X-ray flux. These authors attributed the increase of the X-ray flux between phases 0.0 and 0.2 to extra emission from a colliding wind interaction. The X-ray emission from the shock is highly absorbed when the dense and opaque WR wind is in front but becomes significantly less absorbed at orbital phases when the cavity around the O-star crosses the line of sight. Stevens *et al.* (1996) showed that a detailed comparison between two ASCA observations of γ^2 Vel and synthetic spectra calculated from hydrodynamic colliding wind models allow to constrain the mass loss rate of the WC8 component.

A number of early-type binaries have been monitored with previous X-ray satellites (for a review see e.g. van der Hucht 2002). Some very recent results have been published based on observations with the XMM-Newton and Chandra observatories. These include Chandra observations of WR 147 (Pittard *et al.* 2002),

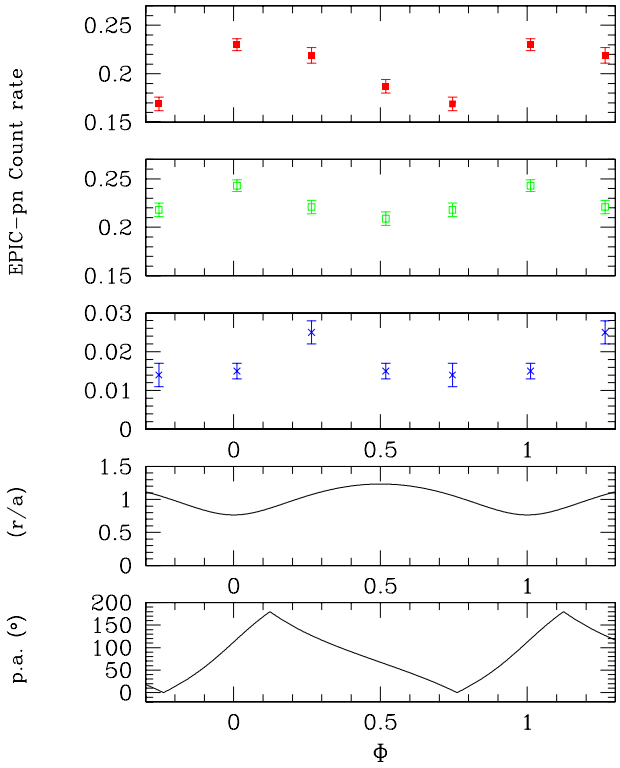

Fig. 8. XMM-Newton light curve of HD 93403. The upper, second and third panels display the EPIC-pn count rates respectively over the 0.5 – 1.0 (soft), 1.0 – 2.5 (medium) and 2.5 – 10.0 keV (hard) energy bands. 1-σ error bars are indicated. The fourth panel yields the relative orbital separation (r/a) between the components of HD 93403 (a stands for the semi-major axis of the orbit). Finally, the lower panel provides the position angle of the binary axis. A p.a. of 0° corresponds to the primary star being 'in front' of the secondary (Rauw *et al.* 2002a).

Chandra and XMM-Newton observations of γ^2 Vel (Skinner *et al.* 2001, Dumm *et al.* 2003), XMM-Newton observations of HD 93403 (Rauw *et al.* 2002a) and WR 22 (Gosset *et al.* 2003).

Rauw *et al.* (2002a) presented XMM-Newton observations of the O-star binary HD 93403 revealing phase-locked variability of its X-ray flux and of its optical spectrum. The colliding wind scenario offers a promising explanation for both phenomena. Below 1.0 keV, the observed X-ray flux is essentially modulated by the opacity of the primary wind. Above 1.0 keV, the observed variation of the X-ray flux is roughly consistent with a $1/d$ dependence expected for an adiabatic colliding wind interaction. However, not all early-type binaries display the $1/d$ dependence of their X-ray flux. For instance, Pittard *et al.* (2000) analyzed two

ASCA observations of ι Ori obtained near periastron and apastron. Strong differences between these phases were a priori expected, but the observations proved otherwise: both the luminosity and the spectral shapes were found to be remarkably similar. This suggests that the bulk of the X-ray emission in ι Ori is in fact intrinsic to one of the components rather than being associated with the wind interaction.

Another interesting X-ray light curve is provided by the XMM-Newton observations of WR 22 (WN7ha + O6.5-8.5). In this system, the X-ray flux decreases smoothly from apastron to periastron. This behaviour is in stark contrast with a $1/d$ variation. However, if the count rates are divided into a soft ($0.5 - 2.0$ keV) and hard ($2.0 - 5.0$ keV) band, it becomes clear that the modulation seen in the broad band light curve essentially results from the variations in the soft band, whereas the harder flux remains essentially constant. Since periastron passage corresponds to the atmospheric eclipse of the O-star by the WR wind (Gosset *et al.* 1991), it seems likely that the observed variations reflect the progressive extinction of the O-star's intrinsic X-ray emission by the opacity of the WR wind. WR 22 offers therefore the possibility to use the X-ray emission of the O-star as a probe to scan the wind opacity of the WN7ha wind.

3.2.5 Predictions for the γ-ray domain

Finally, we consider the situation in the γ-ray domain. Romero *et al.* (1999) found a significant correlation (at the $4\,\sigma$ level) of unidentified EGRET sources with OB associations. Their study further provides evidence that several individual massive binaries, including WR 140 and the multiple system V 729 Cyg, are probable counterparts of γ-ray sources (see also Chen *et al.* 1996; Benaglia *et al.* 2001).

As stated above, the shocks in a colliding wind binary provide an excellent site for the acceleration of charged particles to relativistic energies (Eichler & Usov 1993). Because of the strong UV radiation field of luminous early-type stars, relativistic electrons are expected to dissipate most of their energy through the inverse-Compton scattering mechanism (Mücke & Pohl 2001) and the expected luminosities are of the order of a few times $10^{34}\,\mathrm{erg\,s^{-1}}$ (Benaglia *et al.* 2001).

In addition, relativistic protons lose their energy in the interaction with thermal ions in the densest part of the stellar wind producing neutral pions that decay into γ-rays with a symmetric spectrum peaking around 70 MeV. The total luminosity due to π^0-decay depends on the wind density and hence the mass loss rate (the denser the wind, the more opaque it is to the ion-ion interactions). Theoretical models predict values of about $10^{33}\,\mathrm{erg\,s^{-1}}$ (White & Chen 1992).

As shown by Benaglia *et al.* (2001), the energy contents of the relativistic electron population in the wind interaction region of V 729 Cyg and the local radiation fields could result in a significant keV–MeV inverse-Compton flux from this system. Forthcoming INTEGRAL observations will allow to check these predictions and therefore provide a unique result that has been lacking for even the best-known colliding wind systems in the past.

4 Conclusions

Many fundamental properties of early-type stars can be determined in a direct way through the study of binary systems. Among the most critical problems that should be addressed is the question of the multiplicity of extremely massive star candidates. An observational as well as a theoretical effort are needed to check whether extremely massive stars actually exist in binary systems.

The study of eclipsing binaries further suggests that the 'standard' luminosities of single early-type stars may be overestimated at least for very young main sequence stars. ESA's forthcoming astrometric mission GAIA will allow to establish accurate distances for most of the early-type stars known in our Galaxy. Together with an in-depth study of eclipsing binaries these results will provide constraints on bolometric corrections and other parameters that are still rather uncertain.

Our understanding of wind interactions in early-type binaries is still somewhat fragmentary. The most obvious questions deal with the formation of dust and optical emission lines respectively in adiabatic and radiative colliding wind systems. But a lot of work remains to be done on the X-ray and radio side as well. For instance, multiplicity has still to be established for some of the O or WR stars displaying non-thermal radio emission. Also a deeper understanding of the X-ray emission is needed to distinguish between excess emission from the shocked winds and intrinsic emission from the individual components.

My thanks go to the organizers of the Aussois school for their invitation to present this review and to the participants for many stimulating discussions. I wish to express my gratitude to my colleagues from the Groupe d'Astrophysique des Hautes Energies in Liège and especially to Drs. Jean-Marie Vreux and Jean-Pierre Swings who initially triggered my interest in the study of high energy phenomena associated with massive stars. I am greatly indebted to the Fonds National de la Recherche Scientifique (Belgium) for multiple assistance. This research is also supported in part by contracts P4/05 and P5/36 "Pôle d'Attraction Interuniversitaire" (SSTC-Belgium) and through PRODEX grants linked to the ESA XMM-Newton and INTEGRAL missions.

References

Albacete-Colombo, J.F., Morrell, N.I., Rauw, G., Corcoran, M.F., Niemela, V.S., & Sana, H. 2002, MNRAS, 336, 1099

Antokhina, E.A., Moffat, A.F.J., Antokhin, I.I., Bertrand, J.-F., & Lamontagne, R. 2000, ApJ, 529, 463

Bagnuolo, W.G.Jr., Gies, D.R., & Wiggs, M.S. 1992, ApJ, 385, 708

Bagnuolo, W.G.Jr., Gies, D.R., Hahula, M.E., Wiemker, R., & Wiggs, M.S. 1994, ApJ, 423, 446

Benaglia, P., Romero, G.E., Stevens, I.R., & Torres, D.F. 2001, A&A, 366, 605

Berghöfer, T.W., Schmitt, J.H.M.M., Danner, R., & Cassinelli, J.P. 1997, A&A, 322, 167

Breysacher, J., & François, P. 2000, A&A, 361, 231

Burkholder, V., Massey, P., & Morrell, N. 1997, ApJ, 490, 328

Chen, W., White, R.L., & Bertsch, D. 1996, A&AS, 120, 423

Cherepashchuk, A.M. 1976, Sov. Ast. Lett., 2, 138

Chlebowski, T., & Garmany, C.D. 1991, ApJ, 368, 241

Corcoran M.F. 1996, Rev. Mex. Astron. Astrofis. Conf. Series, 5, 54

de Loore, C., & Vanbeveren, D. 1994, A&A, 292, 463

Dougherty, S.M., & Williams, P.M. 2000, MNRAS, 319, 1005

Dumm, T., Güdel, M., Schmutz, W., Audard, M., Schild, H., Leutenegger, M., & van der Hucht, K.A. 2003, in *"New Visions of the X-ray Universe in the XMM-Newton and Chandra Era"*, ed. F. Jansen, ESA SP-488, in press

Eichler, D., & Usov, V.V. 1993, ApJ, 402, 271

Freyhammer, L.M., Clausen, J.V., Arentoft, J., & Sterken, C. 2001, A&A, 369, 561

Gayley, K.G., Owocki, S.P., & Cranmer, S.R. 1997, ApJ, 475, 786

Gies, D.R. 2003, in *"A Massive Star Odyssey, from Main Sequence to Supernova"*, Proc. IAU Symp. 212, eds. K.A. van der Hucht, A. Herrero & C. Esteban, in press

Gies, D.R., Bagnuolo, W.G.Jr., & Penny, L.R. 1997, ApJ, 479, 408

Gosset, E., Remy, M., Manfroid, J., Vreux, J.-M., Balona, L.A., Sterken, C., & Franco, G.A.P. 1991, IBVS, 3571, 1

Gosset, E., Royer, P., Rauw, G., Manfroid, J., & Vreux, J.-M. 2001, MNRAS, 327, 435

Gosset, E., Rauw, G., Vreux, J.-M., Nazé, Y., Antokhin, I., & Sana, H. 2003, in *"A Massive Star Odyssey, from Main Sequence to Supernova"*, Proc. IAU Symp. 212, eds. K.A. van der Hucht, A. Herrero & C. Esteban, in press

Harries, T.J., Hilditch, R.W., & Hill, G. 1998, MNRAS, 295, 386

Herrero, A., Kudritzki, R.P., Vilchez, J.M., Kunze, D., Butler, K., & Haser, S. 1992, A&A, 261, 209

Herrero, A., Puls, J., & Villamariz, M.R. 2000, A&A, 354, 193

Hill, G.M., Moffat, A.F.J., St-Louis, N., & Bartzakos, P. 2000, MNRAS, 318, 402

Humphreys, R.M., & McElroy, D.B. 1984, ApJ, 284, 565

Lamontagne, R., Moffat, A.F.J., Drissen, L., Robert, C., & Matthews, J.M. 1996, AJ, 112, 2227

Lebedev, M.G., & Myasnikov A.V. 1988, in *"Numerical Methods in Aerodynamics"*, eds. V.M. Paskonov, G.S. Roslyakov, Moscow State University Press, Moscow, 3

Le Teuff, Y.H. 2002 in *"Interacting Winds from Massive Stars"*, eds. A.F.J. Moffat & N. St-Louis, ASP Conf. Series 260, 223

Levato, H., Malaroda, S., Morrell, N., Garcia, B., & Hernández, C. 1991, ApJS, 75, 869

Longair, M.S. 1992, *"High Energy Astrophysics, Vol. 1: Particles, Photons and their Detection"*, Cambridge University Press

Luo, D., McCray, R., & MacLow, M.-M. 1990, ApJ, 362, 267

Maeder, A., & Meynet, G. 1994, A&A, 287, 803

Marchenko, S.V., Moffat, A.F.J., Eenens, P.R.J., Cardona, O., Echevarria, J., & Hervieux, Y. 1997, ApJ, 485, 826

Martins, F., Schaerer, D., & Hillier, D.J. 2002, A&A, 382, 999

Massey, P., & Johnson, J., 1993, AJ, 105, 980

Massey, P., Penny, L.R., & Vukovich, J., 2002, ApJ, 565, 982

Mayer, P., Harmanec, P., Lorenz, R. *et al.* 2001 in *"The Influence of Binaries on Stellar Population Studies"*, ed. D. Vanbeveren, Kluwer Academic Publisher, 567

Meynet, G., & Maeder, A. 2000, A&A, 361, 101

Morrell, N.I., Barbá, R.H., Niemela, V.S. *et al.* 2001, MNRAS, 326, 85

Mücke, A., & Pohl, M. 2001, in *"Interacting Winds from Massive Stars"*, eds. A.F.J. Moffat & N. St-Louis, ASP Conf. Series 260, 355

Penny, L.R., Gies, D.R., & Bagnuolo, W.G.Jr. 1996 in *"Wolf-Rayet Stars in the Framework of Stellar Evolution"*, Proc. 33rd Liège Intern. Astroph. Coll., eds. J.-M. Vreux, A. Detal, D. Fraipont-Caro, E. Gosset & G. Rauw, 289

Pittard, J.M. 2000, *PhD thesis*, University of Birmingham

Pittard, J.M., & Stevens, I.R. 1997, MNRAS, 292, 298

Pittard, J.M., Stevens, I.R., Corcoran, M.F., Gayley, K.G., Marchenko, S.V., & Rauw, G. 2000, MNRAS, 319, 137

Pittard, J.M., Stevens, I.R., Williams, P.M., Pollock, A.M.T., Skinner, S.L., Corcoran, M.F., & Moffat, A.F.J. 2002, A&A, 388, 335

Pollock, A.M.T. 1987, ApJ, 320, 283

Prilutskii, O., & Usov., V. 1976, Sov. Ast.-AJ, 20, 2

Rauw, G. 1997, *PhD thesis*, Université de Liège

Rauw, G., Vreux, J.-M., Gosset, E., Hutsemékers, D., Magain, P., & Rochowicz, K. 1996, A&A, 306, 771

Rauw, G., Vreux, J.-M., & Bohannan, B., 1999, ApJ, 517, 416

Rauw, G., Sana, H., Antokhin, I.I. *et al.* 2001a, MNRAS, 326, 1149

Rauw, G., Nazé, Y., Carrier, F., Burki, G., Gosset, E., & Vreux, J.-M., 2001b, A&A, 368, 212

Rauw, G., Vreux, J.-M., Stevens, I.R., Gosset, E., Sana, H., Jamar, C., & Mason, K.O., 2002a, A&A, 388, 552

Rauw, G., Crowther, P.A., Eenens, P.R.J., Manfroid, J., & Vreux, J.-M. 2002b, A&A, 392, 563

Romero, G.E., Benaglia, P., & Torres, D.F. 1999, A&A, 348, 868

Sana, H., Rauw, G., & Gosset, E. 2001, A&A, 370, 121

Schaller, G., Schaerer, D., Meynet, G., & Maeder, A. 1992, A&AS, 96, 269

Schweickhardt, J., Schmutz, W., Stahl, O., Szeifert, T., & Wolf, B. 1999, A&A, 347, 127

Skinner, S.L., Güdel, M., Schmutz, W., & Stevens, I.R. 2001, ApJ, 558, L113

Stevens, I.R., Blondin, J.M., & Pollock, A.M.T. 1992, ApJ, 386, 265

Stevens, I.R., & Pollock, A.M.T. 1994, MNRAS, 269, 226

Stevens, I.R., Corcoran, M.F., Willis, A.J., Skinner, S.L., Pollock, A.M.T., Nagase, F., & Koyama, K. 1996, MNRAS, 283, 589

Stickland, D.J., Lloyd, C., Koch, R.H., & Pachoulakis, I. 1995, Observatory, 115, 317

Tuthill, P., Monnier, J., & Danchi, W. 1999, Nat, 398, 487

Vacca, W.D., Garmany, C.D., & Shull, J.M. 1996, ApJ, 460, 914

Vanbeveren, D., & de Loore, C. 1994, A&A, 290, 129

van der Hucht, K.A. 2001, New Astronomy Reviews, 45, 135

van der Hucht, K.A. 2002, in *"Multifrequency Behaviour of High Energy Cosmic Sources"*, eds. F. Giovanelli & L. Sabau-Graziati, Mem. S. A. It., 73

Walborn, N.R., & Blades, J.C. 1997, ApJS, 112, 457

Walborn, N.R., Howarth, I.D., Lennon, D.J. *et al.* 2002, AJ, 123, 2754

Walder, R., & Folini, D. 2003, in *"A Massive Star Odyssey, from Main Sequence to Supernova"*, Proc. IAU Symp. 212, eds. K.A. van der Hucht, A. Herrero & C. Esteban, in press

White, R.L., & Becker, R.H. 1995, ApJ, 451, 352

White, R.L., & Chen, W. 1992, ApJ, 387, L81

Wiggs, M.S., & Gies, D.R. 1992, ApJ, 396, 238

Wiggs, M.S., & Gies, D.R. 1993, ApJ, 407, 252

Williams, P.M. 2002 in *"Interacting Winds from Massive Stars"*, eds. A.F.J. Moffat & N. St-Louis, ASP Conf. Series 260, 311

Williams, P.M., Dougherty, S.M., Davis, R.J., van der Hucht, K.A., Bode, M.F., & Setia Gunawan, D.Y.A. 1997, MNRAS, 289, 10

Willis, A.J., Schild, H., & Stevens, I.R. 1995, A&A, 298, 549

1.1.1 The frequency of binaries

Massive stars are quite often found in binary systems. But what exactly means 'quite often'? This is more than just a question of semantics. In fact, the incidence of duplicity is a key parameter to help us distinguish between different scenarios for the formation of massive stars (see also Chapter 5).
Garmany et al. (1980) discussed the multiplicity of 67 O-type stars using photographic spectra with a typical dispersion of $\sim 18\,\text{Å}\,\text{mm}^{-1}$ (radial velocity accuracy of $\sim 20\,\text{km}\,\text{s}^{-1}$). These authors found $(36 \pm 7)\%$ of the stars in their sample to be binaries and 85% of these binaries had a mass ratio $q = m_1/m_2 \leq 2.5$. Garmany et al. therefore argued that very few, if any, short period (days to weeks) O-type binaries with $q > 3$ exist.
Mason et al. (1998) showed that about 41% of the O-stars in clusters and associations are members of astrometric binaries, whilst this percentage is only 20% for field O-stars and drops to 0% for runaways. As far as spectroscopic duplicity of O-stars is concerned, Mason et al. (1998) reported a binary fraction of 61, 50 and 20% in open clusters and associations, among field stars and runaways respectively. While these numbers clearly indicate that the fraction of binaries is larger among O-stars in clusters, a few words of caution are nevertheless necessary:

- the status of many of the spectroscopic binaries used in the survey of Mason et al. is still uncertain. When these SB? systems are excluded from the statistics, the percentages of *confirmed* binaries reduce to 34, 20 and 5% for clusters and associations, field stars and runaways respectively (Mason et al. 1998).

- different young open clusters reveal quite different fractions of binaries among O-stars. Indeed, García & Mermilliod (2001) reported extremely large binary fractions of about 80% in NGC 6231 and IC 1805 (see Sect. 1.3 below). For NGC 2244 and Trumpler 16, these authors claim binary fractions of 50 and 35%, whilst Trumpler 14 is credited with only 1 binary for 7 O-type stars.

Obviously, our census of massive binary systems is subject to a number of observational biases. Due to the typical length of an observing campaign and to the larger amplitude of the radial velocity variations for shorter orbital periods, it is usually easier to uncover spectroscopic binaries with short orbital periods. Also, as a result of the mass-luminosity relation, it is quite difficult to identify spectroscopic binaries with mass ratios $q > 3$ (at least if both components belong to the same luminosity class). Therefore, the scarcity of binary systems with large q or periods of order a few months does not necessarily mean that these systems are indeed rare.
As pointed out above, for some young open clusters, very large fractions of O-star binaries have been reported. The best studied case is probably NGC 6231 for which Sana (2005) established a minimum binary fraction of 63% among the O-star population. All of the known massive binaries in NGC 6231 have orbital periods of less than one year and 6 out of 10 systems have periods of less than 10 days.
To appreciate what these numbers mean, let us consider the fraction of binaries among late-type stars. Halbwachs et al. (2004) and Eggenberger et al. (2004) investigated the frequency of binaries and multiples in a sample of late-type (F7 – K) stars in the solar neighbourhood. While the fraction of spectroscopic binaries with orbital periods P ≤ 10 yrs was found to be $\sim 14\%$ (Halbwachs et al. 2004), the total percentage of binaries with $\log P < 6.31$ (where P is expressed in days) was found to be as large as $\sim 56\%$ (Eggenberger 2004). A large fraction of these systems are either visual binaries or common proper motion pairs.
Therefore, it seems that close binary systems are much more common among early-type stars than among lower mass objects. However, apart from the study of NGC 6231 reported by Sana (2005), most inves-

tigations of the multiplicity of early-type stars in open clusters rely on older, lower quality or heterogeneous data sets (e.g. García & Mermilliod 2001). As a result, some objects that were found to show radial velocity variations, and were thus classified as binaries, might in fact be single stars. This was the case for instance of some early-type stars in IC 1805. For this cluster, García & Mermilliod (2001) quoted an extreme binary fraction of 80% among the O-star population. In Sect. 1.3, I present the results of a dedicated spectroscopic study of the O-stars in IC 1805 which suggests a significantly lower fraction of O + O binaries in this cluster.

1.1.2 Spectral disentangling

For several binaries studied in this work, I have applied a disentangling technique to separate the spectra of the primary and secondary component. The method used for this purpose is based on the papers by Marchenko et al. (1998) and González & Levato (2006). The basic idea behind this technique is that the most natural way to handle spectra for radial velocity measurements is to express them as a function of $x = \ln \lambda$, rather than as a function of λ[1]. In this way, one can express the Doppler shift for a line of rest wavelength λ_0 as

$$\begin{aligned} \ln \lambda &= \ln \left[\lambda_0 \left(1 + \frac{v}{c} \right) \right] \\ &= \ln \lambda_0 + \ln \left(1 + \frac{v}{c} \right) \\ &\simeq \ln \lambda_0 + \frac{v}{c} \\ \Rightarrow x &\simeq x_0 + \frac{v}{c} \end{aligned}$$

The latter relation holds with an accuracy of better than $2\,\mathrm{km\,s^{-1}}$ for radial velocities v that do not exceed about $1000\,\mathrm{km\,s^{-1}}$, which is well above the radial velocities encountered in the binary systems that we study here.

Let $A(x)$ and $B(x)$ be the spectra of the primary and secondary respectively in the heliocentric frame of reference. In the absence of line profile variability, the spectrum observed at any phase ϕ can be written as

$$S(x) = A(x - \frac{v_A(\phi)}{c}) + B(x - \frac{v_B(\phi)}{c})$$

where $v_A(\phi)$ and $v_B(\phi)$ are respectively the radial velocities of star A and B at orbital phase ϕ.

Thus, for a total of n observed spectra, one can compute the spectrum of the primary as the average of the observed spectra from which the secondary spectrum shifted by the appropriate radial velocity (RV) has been subtracted (González & Levato 2006):

$$A(x) = \frac{1}{n} \sum_{i=1}^{n} \left[S_i \left(x + \frac{v_A(\phi_i)}{c} \right) - B \left(x - \frac{v_B(\phi_i)}{c} + \frac{v_A(\phi_i)}{c} \right) \right]$$

And similarly for the secondary:

$$B(x) = \frac{1}{n} \sum_{i=1}^{n} \left[S_i \left(x + \frac{v_B(\phi_i)}{c} \right) - A \left(x - \frac{v_A(\phi_i)}{c} + \frac{v_B(\phi_i)}{c} \right) \right]$$

[1] This formulation has the advantage to clearly separate the Doppler shift from the λ_0 term.

Starting from an initial approximation for $B(x)$ (usually a flat spectrum), $v_A(\phi_i)$ and $v_B(\phi_i)$, one can then iteratively determine the primary and secondary spectra as well as their radial velocities (see González & Levato 2006). The technique is straightforward, easy to implement (it basically consists of interpolations and a cross-correlation technique to determine the improved RVs at the various iterations) and rather cheap in terms of CPU time.

As an illustration of the power of this technique, I show in Fig. 1.1, the results of the disentangling applied to a series of high-resolution FEROS (fiber-fed échelle spectrograph) spectra of HD 165052 (O6.5 V + O7.5 V, $P_{orb} = 2.955$ days). The success of the method to separate the highly blended spectra of the system near conjunction phases is obvious.

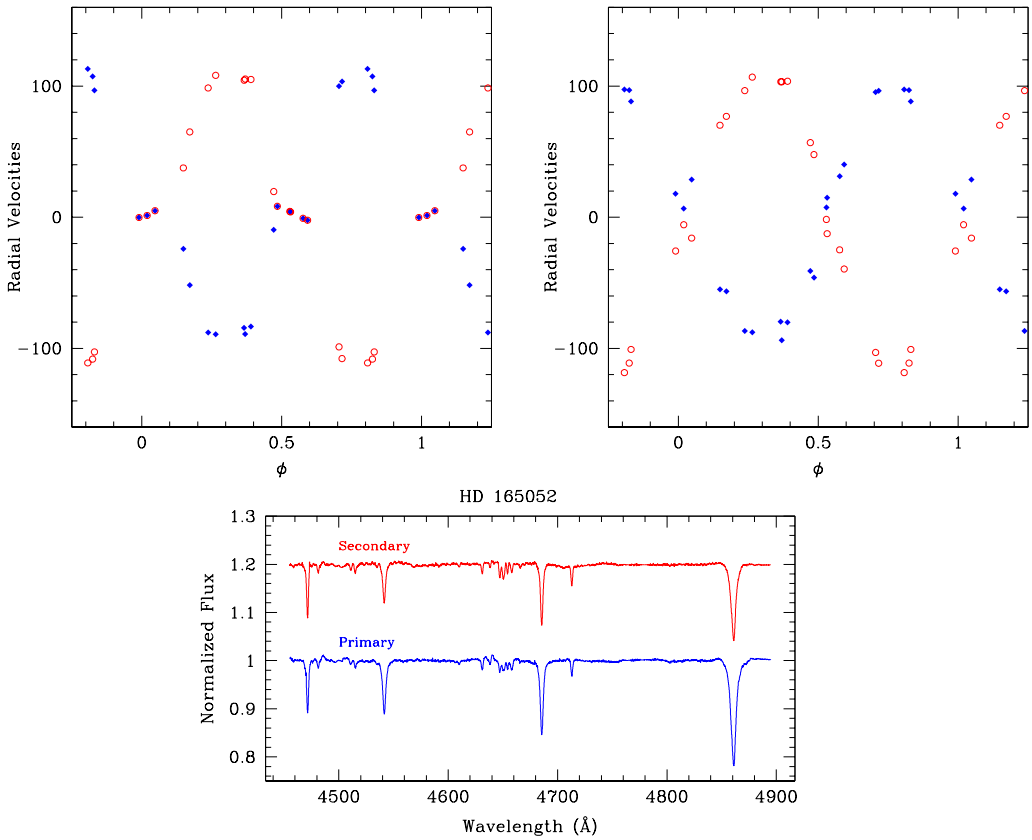

Figure 1.1: Top left: radial velocities of HD 165052 (in km s^{-1}) as determined through Gaussian fitting of prominent absorption lines on the FEROS spectra of the binary. Top right: radial velocities determined through the disentangling technique. Filled and open symbols stand for the radial velocities of the primary and secondary respectively. Lower panel: reconstructed spectra of the primary and secondary in the blue spectral range.

To make this method (or any other disentangling technique) work properly, a good sampling of the orbital cycle is necessary. In addition, the success of the disentangling also depends upon the physical properties of the system: indeed, the observed excursion in radial velocity of the stars should at least be large enough to provide a full sampling of the width of the lines of both components.

1.1.3 Doppler tomography

Some of the early-type binaries in our sample display variable emission lines (Hα, He II λ4686,...) in their optical spectra. The profile variations of these lines reflect the interaction processes between the components of these binaries. Under some assumptions, the study of these variations provides insight into the nature of the interaction. A useful technique to analyse these line profile variations is the so-called Doppler tomography (Horne 1991, Kaitchuk et al. 1994). This method allows to map the line formation region of an emission line in velocity space.

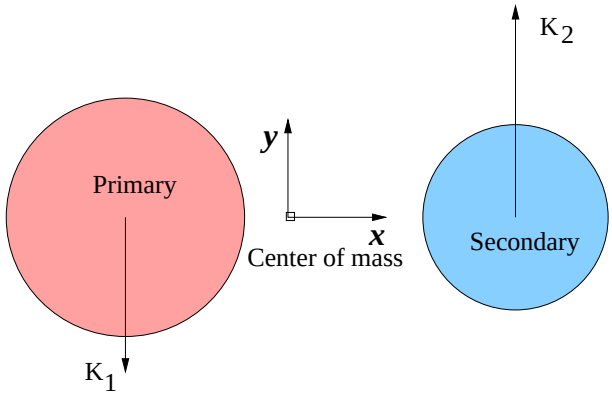

Figure 1.2: Orientation of the axes used in the Doppler tomography.

Let us adopt a reference frame centered on the centre of mass of the binary with the x-axis pointing from the primary to the secondary and the positive y-axis pointing along the direction of the secondary's orbital motion (see Fig. 1.2). The main assumption of the Doppler tomography technique is that the phase dependence of the radial velocity $v(\phi)$ of any gas flow that is stationary in the rotating frame of reference of the binary can be described by a so-called 'S-wave' relation:

$$v(\phi) = -v_x \cos(2\,\pi\,\phi) + v_y \sin(2\,\pi\,\phi) + v_z \tag{1.1}$$

Here ϕ stands for the orbital phase, whilst (v_x, v_y, v_z) are the velocity coordinates of the gas flow. v_x and v_y simply reflect the projected velocity components along the x and y axes: $v_x = V_x \sin i$ and $v_y = V_y \sin i$, where V_x and V_y are the actual velocities in the orbital plane of the binary and i is the orbital inclination. The meaning of the v_z component is somewhat more tricky. This latter component corresponds to the apparent systemic velocity of the line under investigation. In other words, it accounts for several ingredients: the true radial velocity of the centre of mass as well as a global constant velocity shift of the specific line with respect to the actual systemic velocity.
The Doppler map consists of a projection of the S-wave relation Eq. (1.1) onto the (v_x, v_y) plane (for which $v_z = 0$). Therefore, each pixel in a Doppler map, specified by its velocity coordinates is associated with a particular S-wave (see e.g. Horne 1991 for a detailed discussion of the method). From Eq. (1.1) it appears that a Doppler map assumes that profiles observed half an orbital cycle apart are mirror images of each other.
The implementation of the Doppler tomography that I use here is based on a Fourier filtered back projection algorithm (Horne 1991). The Point Spread Function (PSF) of a pure back projection technique in the $v_x - v_y$ plane has a Gaussian core with extended wings having a $1/\sqrt{v_x^2 + v_y^2}$ profile (Horne 1991).

One way to sharpen the PSF is to apply a Fourier filter to the spectra prior to the back projection. To do this, one first computes the Fourier transform of the trailed spectrogram and one then multiplies the result by a filter $\frac{\omega}{\omega_N}\,\exp\left[-\frac{(\omega/\omega_C)^2}{2}\right]$ to suppress the $1/\sqrt{v_x^2+v_y^2}$ tail and to prevent the amplification of high-frequency noise in the spectra. Finally, an inverse Fourier transformation is performed to recover the filtered spectra that are then back projected. ω_N is the Nyquist frequency of the spectra, ω_C is set by the spectral resolution (for further details see e.g. Horne 1991). The back projection produces stripes across the Doppler map at angles corresponding to the binary phases sampled by the data. Therefore, the back projection method can lead to the so-called 'radial-spoke artefact' if the data do not provide a uniform coverage of the orbital cycle.

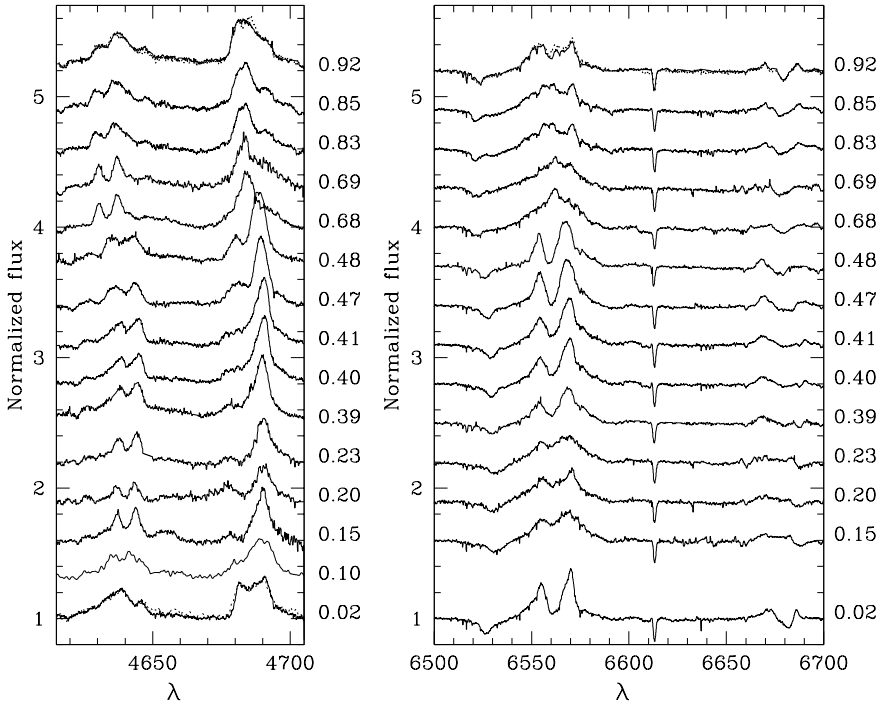

Figure 1.3: Line profile variations of some important emission lines in the optical spectrum of LSS 3074. The orbital phases are given on the right of each panel. The wavelengths are expressed in Å. Note the good agreement between the two spectra (one displayed as a solid line, the other as a dotted line) taken at phase 0.92 as well as the blue spectra taken at phase 0.02, showing that the variations are indeed phase-locked.

To illustrate the Doppler tomography technique, I show in Fig. 1.3 the line profile variations observed in the case of the O4 If$^+$ + O7.5(f) early-type binary LSS 3074 ($P_{\rm orb} = 2.1851$ days, Gosset et al. 2005b) whilst the corresponding Doppler maps are presented in Fig. 1.4. The most prominent emission lines in the optical spectrum of LSS 3074 display indeed strong profile variations (see Fig. 1.3).
For instance, the He II λ4686 line evolves from a broad and skewed emission (around $\phi = 0.0$) into a double-peaked feature with rather narrow individual peaks and the strongest peak closely following the orbital motion of the primary (at phases near 0.5). On the other hand, the Hα emission displays a double-peaked profile on most of our spectra and the profiles observed around the two conjunctions are quite similar. At phases near quadrature, the peaks are broader and less clear cut.

To build the Doppler maps of the He II λ 4686 and Hα emission lines (Fig. 1.4), the data were weighted so as to account for the uneven sampling of the orbital cycle[2]. The Doppler map of the Hα line reveals an extended line formation region in velocity space consisting of two lobes on either side of the Roche lobes. The emission regions in velocity space are quite elongated, extending over almost 1000 km s^{-1} in v_y, but only over 300 – 500 km s^{-1} in v_x. The maximum is found around $(v_x, v_y) = (-310, -110)$ and seems to move with a shift of ~ 0.20 in phase compared to the O7.5 secondary star. A secondary maximum is located near $(400, 200)$. Apparently, there is little or no Hα emission following strictly the orbital motions of either the primary or the secondary stars. While this is not surprising for the secondary (an absorption component moving in phase with the secondary is indeed seen on the profiles; see Fig. 1.3), it is somewhat unexpected for the O4f$^+$ primary since Hα is known to be in strong emission in the spectrum of another O4f$^+$ star, HD 190429A (see Walborn & Howarth 2000). Moreover, in the case of HDE 228766, the secondary has a spectrum quite similar to that of the primary of LSS 3074, but the Doppler tomography reveals that the bulk of the Hα emission is indeed associated directly with the secondary of HDE 228766 (Rauw et al. 2002b, see Sect. 1.4).

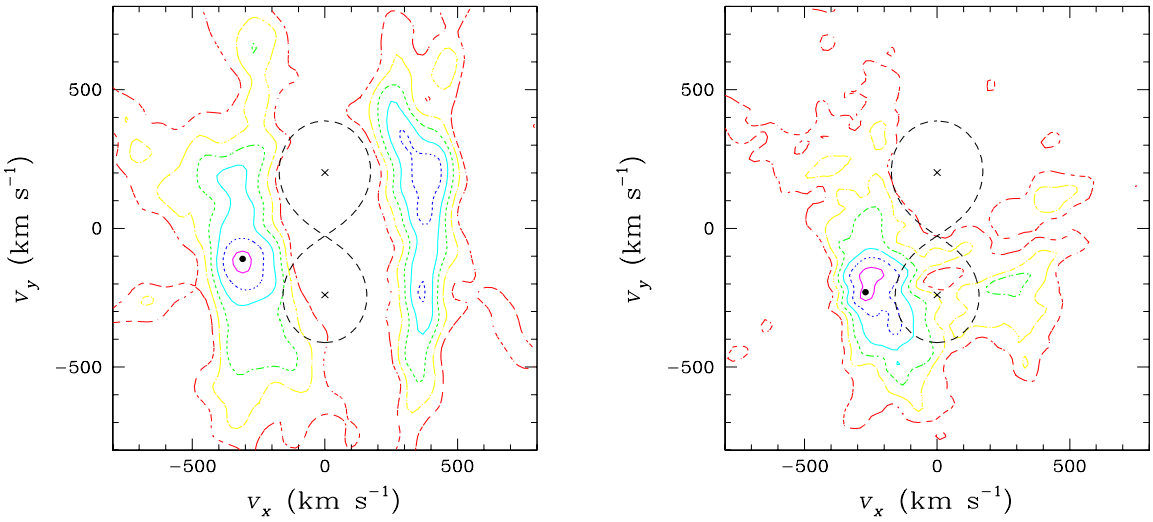

Figure 1.4: Left: Doppler map of the Hα emission line in the spectrum of LSS 3074. The crosses correspond to the radial velocity amplitudes of the center of mass of the primary and secondary. The shape of the Roche lobe in velocity-space (thick dashed line) has been calculated for a mass ratio of 1.19. The Doppler map was computed with v_z set to -50 km s^{-1}. The black dot indicates the position of the highest peak and the contours correspond to levels of 0.95, 0.80, 0.65, 0.50, 0.35 and 0.20 times the maximum emissivity. Right: Same, but for the He II λ 4686 emission.

The Doppler map of the He II λ 4686 line shows its highest peak at about $(-250, -190)$. We see no emission directly moving with the secondary. The strongest emission lobe has again an elongated shape somewhat reminiscent of the Hα Doppler map, but the secondary emission structure is less prominent and less extended. Moreover, both emission structures in the He II λ 4686 Doppler map are connected.

[2]Each spectrum was assigned a weight proportional to the separation in phase from its closest neighbours.

A possible interpretation of the Hα and He II λ 4686 Doppler maps of LSS 3074 could be that, due to the proximity of the two stars, the primary wind only fully develops (and hence emits) in directions away from the secondary (i.e. along the negative x axis). Towards the secondary component, the primary wind would encounter either the wind or the surface of the secondary and hence the only emission from this region should be produced by the material compressed in the wind interaction zone. In this scenario, the emission lobe with negative v_x would correspond to the truncated primary wind, whilst the one with the positive v_x would arise from the shocked wind near the secondary's surface. Between these two physical regions, shock heating could lead to a higher than normal ionisation, thus preventing the formation of optical recombination lines.

1.2 Early-type binaries in and around the Trumpler 16 cluster

The region around η Carina harbours several very young open clusters and is therefore extremely rich in early-type stars (see Fig. 1.5). As a consequence, this area has been the subject of many investigations over the last thirty years.
In the framework of the *X-Mega* project, aiming (among other things) at an intensive monitoring of the region around η Carina with the *ROSAT* X-ray satellite, an international consortium was set up to perform optical support observations. The main actors in this collaboration were the hot star group of La Plata (Argentina) and the Liège group. One of the prime objectives of the *X-Mega* project was to obtain X-ray light curves of a sample of colliding wind binaries. In this context, accurate ephemerides for early-type binary systems were needed and together with the La Plata group, we therefore initiated a spectroscopic monitoring campaign for a number of binaries (or binary candidates) in and around the open cluster Trumpler 16. The campaign mostly relies on data collected at ESO (Boller & Chivens medium resolution spectra and mainly FEROS high-resolution échelle data). Later on, when the observing program for *XMM-Newton* was defined, special emphasis was again put on several objects in this area (η Car, WR 25, HD 93403) and we thus extended our optical monitoring to a few additional targets.
In this section, I present the results obtained in the course of this campaign. I start by reproducing two papers on the orbital solutions of HD 93403 (Rauw et al. 2000b) and Tr 16-104 (Rauw et al. 2001c). Afterwards, I summarize the main results that have been obtained in the study of HD 93205, Tr 16-110, HD 93161, HD 93250, HD 93343 and Tr 16-112 to which I have contributed. The location of the different stars discussed in this section with respect to the Trumpler 14, 15 and 16 clusters is shown in Fig. 1.5.

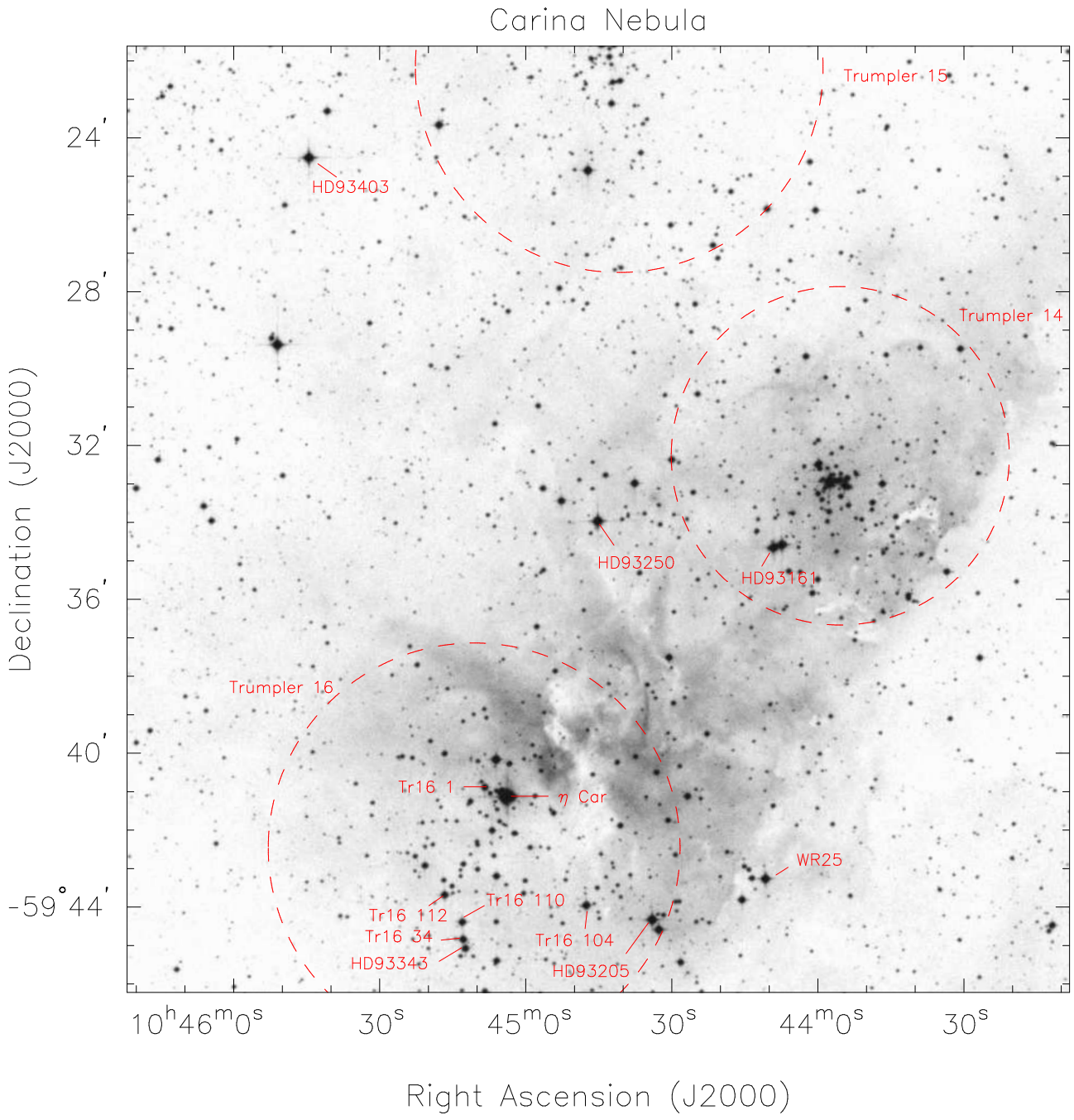

Figure 1.5: Digitized Sky Survey image (30' × 30') of the Carina region showing the location of the O-type stars discussed in this section. The positions and radii of the three open clusters are taken from Tapia et al. (2003). North is up and east is to the left.

Astron. Astrophys. 360, 1003–1010 (2000)

ASTRONOMY AND ASTROPHYSICS

A new orbital solution for the massive binary system HD 93403⋆

G. Rauw⋆⋆,†**, H. Sana, E. Gosset**⋆⋆⋆,†**, J.-M. Vreux, E. Jehin, and G. Parmentier**

Institut d'Astrophysique et de Géophysique, Université de Liège, 5, Avenue de Cointe, 4000 Liège, Belgium

Received 31 January 2000 / Accepted 15 June 2000

Abstract. We present a spectroscopic analysis of the early-type massive binary system HD 93403. Using high resolution optical spectra, we clearly separate the primary and secondary components. For the first time, we are able to provide an orbital solution for both stars. Our new orbital parameters show discrepancies with the previous solution published by Thackeray & Emerson (1969). We further discuss several spectral features of HD 93403. We finally derive qualitative constraints on the inclination of the system and we discuss its evolutionary status and the position of both components in the Hertzsprung-Russell diagram.

Key words: stars: binaries: spectroscopic – stars: early-type – stars: fundamental parameters – stars: individual: HD 93403

1. Introduction

HD 93403 is a relatively bright ($V = 7.3$) early-type star of the southern sky. Lying within the H II region NGC 3372 near η Car, it has long been known to be a single-lined spectroscopic binary (Feast et al. 1955). Walborn (1972) classified the spectrum of HD 93403 as O5 III:f. Based on the ratio of the equivalent widths of the He I λ 4471 and He II λ 4541 absorption lines, Conti & Frost (1977) reported HD 93403 as being an O5.5:f. Based on a tomographic study of a set of IUE spectra by Penny (1997), Thaller (1997) quoted spectral types O5 III + O7 III for HD 93403.

The only published orbital solution for HD 93403 we are aware of is 30 years old (Thackeray & Emerson 1969, TE hereafter). These authors determined an orbital period of 15.093 days, an eccentricity of 0.524 and a mass ratio close to 1.5. However, due to the rather limited quality of their data, TE were unable to disentangle the secondary spectrum, except on a few plates taken when the radial velocity separation between the two components was near maximum. Thackeray & Emerson guessed the spectral type of the fainter component to be O7.5, although they cautioned that this result was quite uncertain. These authors further mentioned photometric observations of HD 93403 that apparently failed to reveal eclipses.

HD 93403 was detected as a fairly bright X-ray source with the EINSTEIN satellite (Seward et al. 1979) and has been selected for observations with ESA's X-ray Multi Mirror (XMM) observatory. The analysis of these X-ray data, especially in terms of a colliding wind interaction (Pittard & Stevens 1997), requires an accurate knowledge of the orbital parameters of the system. As a first step, we derive therefore a new orbital solution for HD 93403. Using high resolution spectra obtained with the CES and FEROS instruments of the European Southern Observatory at La Silla and with the BME spectrograph at CTIO, we clearly separate the primary and secondary spectra, which means that HD 93403 should now be classified as an SB2 system.

This paper is organized as follows: the observations, data reduction and spectral features are discussed in Sect. 2; in Sect. 3, the radial velocities are used to set up a new orbital solution for both components of HD 93403. The fundamental parameters of the system are discussed in Sect. 4. Finally, our conclusions are presented in Sect. 5.

2. Observations and Data Reduction

2.1. Observations

Spectroscopic data on HD 93403 were obtained during several runs spread over a bit more than two years (from February 1998 till May 2000). The data set consists of observations gathered with various instruments at the European Southern Observatory (ESO) at La Silla and at the Cerro Tololo Inter-American Observatory (CTIO). Table 1 presents the journal of the observations.

Twenty high resolution spectra of the He I λ 4471 line were obtained with ESO's 1.4 m Coudé Auxiliary Telescope (CAT) at La Silla, using the Coudé Echelle Spectrometer (CES) equipped with the Long Camera (LC, before March 1998) or the Very Long Camera (VLC, after March 1998). The detector used was ESO CCD#38, a Loral 2688×512 pixel CCD with a pixel size of $15\ \mu$m$\times 15\ \mu$m. The slit width was chosen to achieve a nominal resolution of 70000–80000. The effective resolving power as derived from the FWHM of the lines of the ThAr calibration exposures is 60000–75000. Typical exposure times were of the

Send offprint requests to: G. Rauw (rauw@astro.ulg.ac.be)

⋆ Based on observations collected at the European Southern Observatory (La Silla, Chile) and the Cerro Tololo Inter-American Observatory (CTIO).

⋆⋆ Postdoctoral Researcher FNRS (Belgium)

⋆⋆⋆ Research Associate FNRS (Belgium)

† Visiting Astronomer, CTIO, National Optical Astronomy Observatories (NOAO). NOAO is operated by the Association of Universities for Research in Astronomy, Inc. under contract with the National Science Foundation.

order of 45 minutes and the average S/N ratio is above 100. The wavelength domain is centered on the He I λ 4471 line and is ~ 40 Å and ~ 20 Å wide for spectra taken with the LC and the VLC respectively.

During three observing runs in April – May 1999, end of May 1999 and early May 2000, a set of echelle spectra was gathered with the Fiber-fed Extended Range Optical Spectrograph (FEROS, Kaufer et al. 1999) attached to the ESO 1.52 m telescope at La Silla. Thirty seven orders corresponding to a wavelength domain from 3650 to 9200 Å were observed. Typical exposure times were of the order of 10–15 minutes and the average S/N ratio is about 65, 150 and 110 at 4050, 6000 and 7500 Å respectively. The spectral resolving power of the FEROS instrument is 48000. The detector was an EEV CCD with 2048×4096 pixels of $15\,\mu$m$\times 15\,\mu$m. For a detailed description of the spectrograph, we refer the reader to the paper of Kaufer et al. (1999).

Finally, another set of echelle spectra over the range 3850 to 5790 Å was obtained with the Bench-Mounted Echelle Spectrograph (BME) attached to the 1.5 m CTIO Ritchey-Chretien Telescope, during a 5 night run in June 1999. Forty nine orders were observed using the KPGL2 316 lines mm^{-1} grating as a cross-disperser. The detector was a Tek 2048 CCD with 24 μm pixels. The slit width was set to 70μm corresponding to a resolving power of 45000. Exposure times ranged from one hour to two hours depending on the weather conditions and the S/N ratio in the continuum is about 80.

2.2. Data reduction

The CAT observations were reduced in a standard way using the MIDAS package provided by ESO. The spectra of HD 93403 were rectified by means of an instrumental response curve built from observations of a metal-poor 'reference' star with weak narrow absorption lines. When such a reference spectrum was not available, we performed the normalization by fitting a polynomial to the continuum.

We used the FEROS context working under the MIDAS environment to reduce the FEROS echelle spectra. We slightly adapted the MIDAS routines kindly provided by Dr. O. Stahl in order to match the current configuration of the FEROS instrumentation. The reduction was performed using both *standard* and *optimum* options. It turned out that the *standard* option yields slightly better results, probably due to the important number of bad columns on the CCD. Most of the unavoidable strong fringes that affect the red part of the spectrum (above 6600 Å) are simply corrected by flat-fielding. There are however a few residual fringes near 6670, 7140 and 7385 Å. In order to achieve a good S/N ratio around the order connections in the blue, the orders were merged by averaging the overlapping areas over a 30 Å range. Due to particularly precarious weather conditions, the FEROS observations of the end of May 1999 run result from the addition of several spectra taken during the same night. Finally, the FEROS spectra were normalized over a range of a few hundred Å at once by fitting a polynomial of degree 4 or 5 to the continuum.

Table 1. Journal of the observations of the He I λ 4471 absorption line. The first column gives the Heliocentric Julian Date (HJD) in the format HJD–2450000. The next two columns give the measured radial velocity, expressed in km s^{-1}, for the primary and secondary respectively. For those spectra where we were not able to separate the blended lines, only the radial velocity of the blend is listed. The fourth column reports the method used to measure the RVs: 1=one gaussian fit, 2=two gaussian fit, 3=cross-correlation like method. The fifth column identifies the instrumentation. The last column provides the orbital phases of the observations relative to the time of periastron passage ($T_0 = 2451355.643$) as derived from our new common orbital solution given in Table 5.

Date	$v_{r,1}$	$v_{r,2}$	Method	Intrument.	ϕ
857.868	69.2	−146.0	2	CES+LC	0.019
859.644	−18.2		1	CES+LC	0.137
860.633	−19.6		1	CES+LC	0.203
861.626	−57.8	87.0	2	CES+LC	0.268
862.625	−62.2	104.2	2	CES+LC	0.335
864.607	−70.2	106.2	2	CES+LC	0.466
925.649	−70.3	91.2	2	CES+VLC	0.510
926.605	−52.0	82.8	2	CES+VLC	0.574
928.509	−18.5		1	CES+VLC	0.700
931.486	70.8	−146.4	2	CES+VLC	0.897
932.472	81.1	−171.5	2	CES+VLC	0.962
933.487	59.4	−137.3	2	CES+VLC	0.030
934.484	−23.4		1	CES+VLC	0.096
936.527	−66.4	60.4	3	CES+VLC	0.231
939.468	−70.3	99.7	2	CES+VLC	0.426
995.580	−16.0		1	CES+VLC	0.144
996.537	−50.8	36.4	3	CES+VLC	0.207
998.543	−80.6	96.8	2	CES+VLC	0.340
999.543	−74.6	101.3	2	CES+VLC	0.406
1000.503	−78.4	97.9	2	CES+VLC	0.470
1299.704	−64.7	93.3	2	FEROS	0.294
1300.712	−75.2	97.5	2	FEROS	0.360
1301.692	−75.7	102.2	2	FEROS	0.425
1302.697	−72.8	97.7	2	FEROS	0.492
1304.710	−52.7	49.3	3	FEROS	0.625
1322.507	9.7	−83.5	3	FEROS	0.804
1323.669	66.2	−140.8	2	FEROS	0.882
1327.501	−26.5	−9.1	3	FEROS	0.135
1328.530	−24.6		1	BME	0.206
1329.471	−53.2	55.5	3	BME	0.266
1330.497	−82.0	87.3	2	BME	0.334
1331.575	−82.1	96.6	2	BME	0.405
1332.585	−82.2	89.2	2	BME	0.472
1669.664	27.9	−76.9	3	FEROS	0.806
1670.655	49.9	−130.1	2	FEROS	0.871
1671.657	75.9	−169.3	2	FEROS	0.938
1672.640	78.5	−165.7	2	FEROS	0.003
1673.624	42.2	−121.1	3	FEROS	0.068

The BME data were reduced using the IRAF[1] package and following the recommendations of the BME User's Manual. The pixel to pixel variations were removed using flat field exposures

[1] IRAF is distributed by the National Optical Astronomy Observatories.

Table 2. Radial velocities of several lines measured on FEROS and BME spectra. The notations are identical to those used in Table 1.

Date	O III λ 5592			C IV λ 5801			C IV λ 5812			He I λ 5876		
	$v_{r,1}$	$v_{r,2}$	Method	$v_{r,1}$	$v_{r,2}$	Method	$v_{r,1}$	$v_{r,2}$	Method	$v_{r,1}$	$v_{r,2}$	Method
1299.704	−59.8	90	2	−55.0	90.8	2	−65.0	93.8	2	−63.1	81.4	2
1300.712	−74.1	106.7	2	−71.0	108.9	2	−74.2	105.9	2	−68.9	96.4	2
1301.692	−70.3	116.7	2	−59.7	115.3	2	−70.3	104.0	2	−70.2	108.8	2
1302.697	−71.6	99.0	2	−63.7	103.0	2	−73.1	99.1	2	−68.1	99.2	2
1304.710	−52.8	65.0	3	−20.7		1	−46.3	60.7	3	−43.2	46.2	3
1322.507	42.1	−74.9	3	31.4	−87.7	3	24.9	−91.7	3	19.5	−71.6	3
1323.669	79.0	−134.6	2	68.8	−130.3	2	64.7	−134.0	2	69.3	−132.7	2
1327.501	−21.0	18.1	3	−0.8		1	−15.3	10.7	3	−15.7	−5.8	3
1328.530	−15.8		1									
1329.471	−47.9	64.7	2									
1330.497	−86.2	92.0	2									
1331.575	−72.0	116.3	2									
1332.585	−77.0	113.4	2									
1669.664	25.3	−64.1	3	41.3	−66.5	3	4.3		1	22.6	−64.3	3
1670.655	60.2	−128.0	2	70.8	−136.2	2	55.6	−126.0	2	57.6	−120.0	2
1671.657	92.7	−172.0	2	96.5	−185.1	2	90.8	−158.1	2	84.0	−166.8	2
1672.640	93.1	−169.3	2	97.1	−186.1	2	94.9	−154.8	2	84.8	−160.9	2
1673.624	60.6	−97.1	2	70.7	−89.7	3	59.7	−103.4	2	47.2	−102.1	2

taken with a very bright light source and a diffusing screen placed inside the spectrograph (so-called *milky flats*). A first rectifying of the extracted echelle orders was carried out with the projector flat exposures. Finally, the spectra were normalized by fitting a low-order polynomial to the continuum. As the exposure time of individual spectra was limited to one hour, we added up the spectra taken during the same night in order to reach a higher S/N ratio. For those nights where we have added several exposures, the dates listed in Table 1 and Table 2 correspond to the mean time.

2.3. Radial velocity measurements

The radial velocities (RVs) were measured by fitting two gaussians to the absorption lines whenever the separation was sufficient to do so. When this was not the case, we used a cross-correlation like technique in an attempt to deblend the lines of the two components of the system. To do so, we built a template of the individual absorption lines derived from the fit to the spectra when the separation is maximum and we shifted both fake lines until we achieved an acceptable fit to the blend. Near the conjunctions, this technique yields usually two possible solutions and we selected the most likely one by comparison with the spectra obtained at adjacent orbital phases. Probably as a result of some slight line profile variability, we notice that the templates do not perfectly match the line profiles near conjunction. This leads to intrinsically larger error bars on the RVs measured near conjunction and these RVs were thus assigned a lower weight in the orbital solution (see Sect. 3). The measured RVs and the method used to deblend the lines are reported in Tables 1 and 2. The effective rest wavelengths used in the RV computations are given in column 2 of Table 3 and were adopted from Underhill (1995) except for the He I λ 4471 line where we used the result of Conti et al. (1977).

Table 3. Adopted effective wavelengths, average equivalent width ratios (primary/secondary) measured on our spectra and corresponding luminosity ratios corrected for the different spectral types (see text).

Spectral line	λ_0 (Å)	EW ratio	$L^{\rm prim}/L^{\rm sec}$
He I λ 4471	4471.512	2.15	4.6
O III λ 5592	5592.370	2.64	4.0
C IV λ 5801	5801.330	3.83	4.0
C IV λ 5812	5811.980	4.81	5.0
He I λ 5876	5875.620		

2.4. Spectral features

The FEROS instrument offers the opportunity to investigate nearly the entire optical spectrum of HD 93403. Selected spectral ranges are shown in Fig. 1. The main spectral lines are indicated. The most outstanding spectral features of HD 93403 are described below.

- The He II λ 4686 line consists of a mixture of absorption and emission components. Its profile presents obvious but complex night-to-night variations. A preliminary analysis shows that the wavelength variations of the absorption component follow the secondary RV curve. The emission component appears quite broad and we suspect rather fast profile variations. Whether this is the signature of a wind interaction process is unclear. Additional high quality data are required to clarify the nature of these variations and we have to defer a discussion of the He II λ 4686 line profile variations to a forthcoming paper.
- Both the primary and the secondary spectra show the C III λ 5696 line in emission. We have measured the phase-dependent RVs of both components and the results are in fair agreement with the orbital solutions derived from the absorption lines. This result is in line with a photospheric

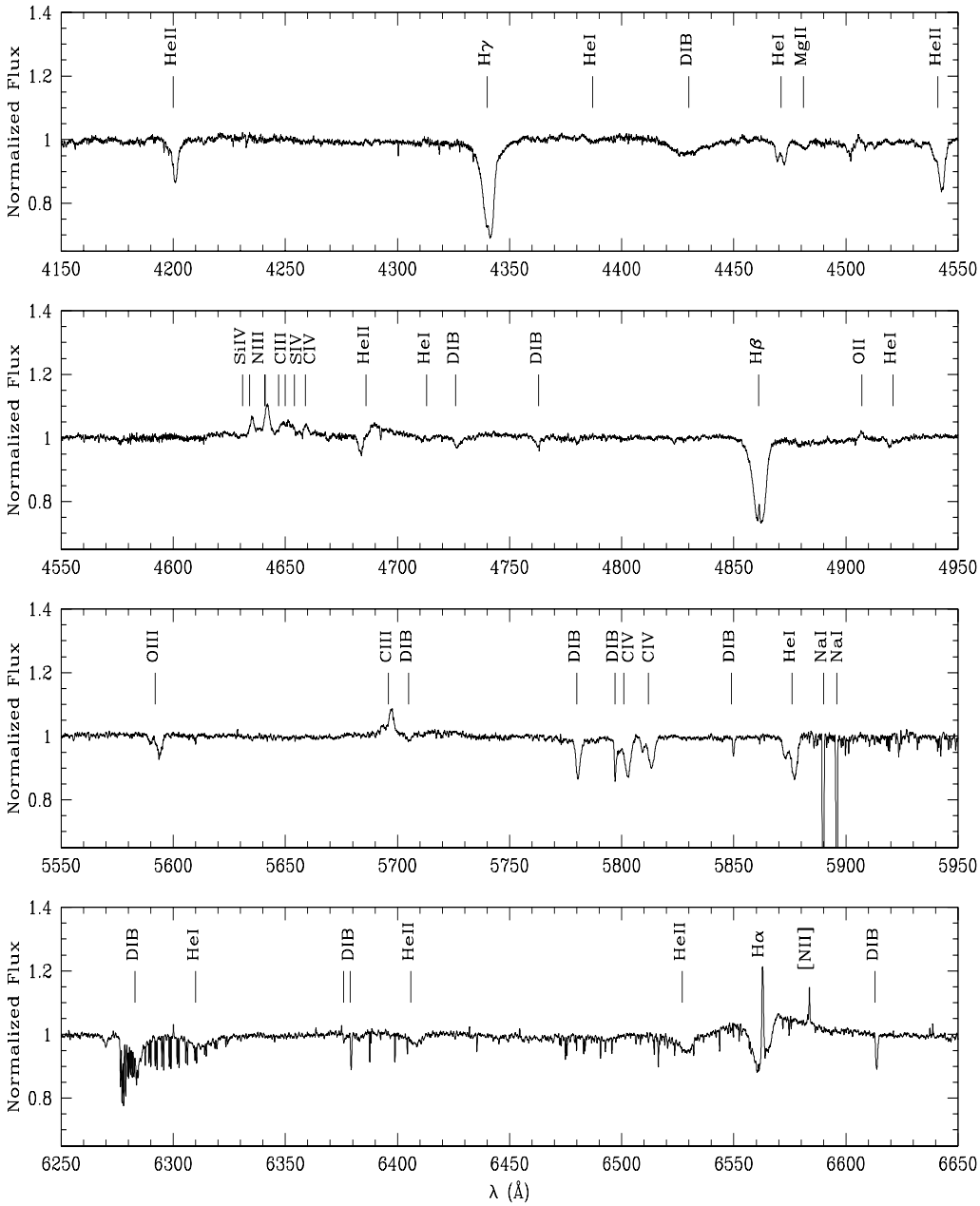

Fig. 1. FEROS spectrum of HD 93403 as observed on HJD 2451323.669.

origin of the C III λ5696 emission line in the spectra of O stars as suggested by Nussbaumer (1971) and Cardona-Núñez (1978) and lends further support to our orbital solution.

– The Hα line profile is rather complex. It is composed of an absorption component superimposed on a broader emission. Thaller (1997) claimed that the Hα profile was variable. However, our data reveal only subtle night-to-night variability and the line profile analysis is further complicated by a rather prominent nebular emission line.

– Finally, we investigate the interstellar Ca II and Na I lines (Fig. 2). Though Walborn & Hesser (1975) report single Ca II H and K lines, we could detect an additional blueshifted fainter component around $-23\,\mathrm{km\,s^{-1}}$. The profile of the stronger Ca II component is most probably formed by two heavily blended lines. The Na I lines also show a fainter blueshifted component, with a velocity similar to that of the

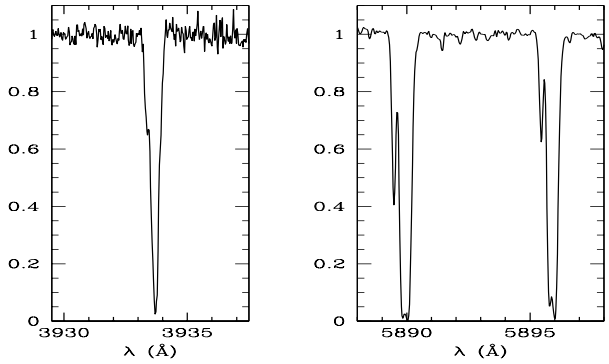

Fig. 2. Interstellar Ca II K and Na I D1 and D2 profiles in the spectrum of HD 93403.

Table 4. Mean RVs and EWs of Ca II and Na I interstellar lines. The quoted uncertainties correspond to the standard deviation of our measurements.

Spectral line	RV (km s^{-1})			EW (mÅ)		
Ca II K λ 3933	-24.0	$\pm$	0.8	50	$\pm$	6
	2.9	$\pm$	0.6	382	$\pm$	9
Ca II H λ 3968	-22.0	$\pm$	1.1	31	$\pm$	6
	2.9	$\pm$	0.2	196	$\pm$	12
Na I D2 λ 5890	-23.6	$\pm$	0.2	108	$\pm$	2
	-7.6	$\pm$	0.3	209	$\pm$	11
	6.0	$\pm$	0.3	337	$\pm$	12
Na I D1 λ 5896	-23.2	$\pm$	0.2	66	$\pm$	1
	-7.6	$\pm$	0.2	166	$\pm$	6
	4.9	$\pm$	0.2	320	$\pm$	8

Ca II one. The strongest Na I component clearly reveals a double peaked profile. We have measured the RVs and the equivalent widths on the FEROS spectra. Our results are listed in Table 4. They are in qualitative agreement with previous measurements (Walborn & Hesser 1975, Walborn 1982). We should emphasize here the good night-to-night stability of the FEROS spectrograph as the dispersion of the measured radial velocities of the interstellar lines is rather low.

3. Orbital Solution

The orbital solution was computed using a modified version of the Wolfe, Horak & Storer algorithm (Wolfe et al. 1967, WHS hereafter). Knowing the observation dates, the RVs and the period, the original WHS method allows to compute the orbital solution associated to one component of the system at once, which is of course sufficient for an SB1 system. Applying this method to SB2 systems leads however to a priori independent orbital elements for both components of the system, as only the RVs associated to one star are taken into account. For instance, this problem typically leads to two distinct values of the eccentricity and of the time of periastron passage. We have therefore modified the WHS method to circumvent this problem and to take into account the primary and secondary RVs simultaneously.

Our approach is based on the following straightforward relation between the RVs of the two components of the binary system:

$$v_2(\phi) = c\, v_1(\phi) + b \tag{1}$$

with $c = -K_2/K_1 = -m_1/m_2$ and $b = \gamma_1\, K_2/K_1 + \gamma_2$.

m_i, $v_i(\phi)$ and K_i are respectively the mass, the radial velocity at orbital phase ϕ and the amplitude of the radial velocity curve of the i-th component of the system. γ_i is the *apparent* systemic velocity as deduced from the spectrum of the i-th component. Since it is not unusual to find quite different apparent systemic velocities for the components of an evolved early-type binary (e.g. Rauw et al. 1999), we will consider a priori distinct values of γ_i for both stars.

We first fit a straight line to the data in the $(v_{r,1}, v_{r,2})$ plane. This is done using an orthogonal regression as both coordinates are affected by errors of the same order of magnitude. The best fit relation immediately provides us with the mass ratio of the system and it further allows us to express the RVs associated with one star of the system as a function of those of its companion. We are then able to convert all the RV data to equivalent RVs of one component and thus to run the WHS code taking into account the complete data set. We adopt a unity weight for the RVs measured by fitting two well separated gaussians, while we set the weight of the RVs near conjunction to a value two to ten times lower, according to the quality of the cross-correlation fit. Those lines that we were not able to deblend were attributed a zero weight.

We first adopted a period of 15.093 days, as derived by TE. Table 5 gives both individual and joint orbital solutions as computed in the way described just here above. We chose the primary to be the most massive and most luminous star of the system. Fig. 3 displays the RV curves of HD 93403.

4. Discussion

Our new orbital solution differs significantly from the one of Thackeray & Emerson (1969), especially with respect to the value of the eccentricity which we find to be about half their value. We re-computed the orbital elements using TE's data and we recovered their published values. We believe that the discrepancy between their solution and ours arises from the fact that they were unable to separate both components on most of their spectra. This could lead to underestimate the primary RVs except near phases of maximum RV separation. As a result the RV curve displays an apparently narrower peak, leading to the determination of a higher eccentricity. Another discrepancy concerns the difference in the longitude of periastron ω of about 34°. Interpreted in terms of an apsidal motion, it would correspond to a rate of apsidal motion of about 1° per year, which is an unexpectedly high value for such a system. Therefore, it seems likely that at least part of this difference is an artefact due to the above mentioned bias in TE's radial velocities.

Table 5. Computed orbital solution for HD 93403 using the RVs of the He I λ 4471 absorption lines. T_0 is the time of the periastron passage.

	Common solution			Individual Solutions					
				Primary			Secondary		
P(days)	15.093 (fixed)			fixed			fixed		
e	0.234	$\pm$	0.021	0.237	$\pm$	0.031	0.229	$\pm$	0.021
$\omega(^o)$	22.5	$\pm$	4.4	22.2	$\pm$	6.4	202.9	$\pm$	4.4
T_0(HJD-2450000)	1355.643	$\pm$	0.158	1355.629	$\pm$	0.231	1355.660	$\pm$	0.162
γ_1 (km s^{-1})	-14.8	$\pm$	1.2	-15.0	$\pm$	1.8			
K_1 (km s^{-1})	79.3	$\pm$	1.1	79.4	$\pm$	1.6			
$a_1 \sin i$ (R$_\odot$)	22.9	$\pm$	0.3	22.9	$\pm$	0.5			
γ_2 (km s^{-1})	-5.4	$\pm$	4.5				-5.8	$\pm$	2.1
K_2 (km s^{-1})	139.0	$\pm$	4.9				138.7	$\pm$	1.8
$a_2 \sin i$ (R$_\odot$)	40.3	$\pm$	1.7				40.3	$\pm$	0.6
$q(m_1/m_2)$	1.753	$\pm$	0.057						
$m_1 \sin^3 i$ (M$_\odot$)	9.52	$\pm$	0.82						
$m_2 \sin^3 i$ (M$_\odot$)	5.43	$\pm$	0.33						
rms$(O-C)$ (km s^{-1})	5.0			5.8			6.7		

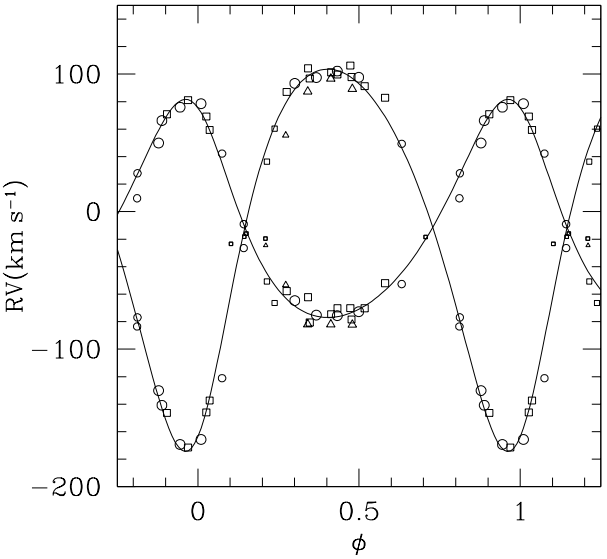

Fig. 3. Radial velocity curve of the HD 93403 binary system. Different symbols refer to different instruments: triangle=BME, square=CES, circle=FEROS. Different sizes indicate different weights assigned to the data points in the orbital solution.

We next turn to the problem of the orbital period of the system. One point was to look for any significant change over the last thirty years. Another was to try to improve TE's value. To do so, we used the method of Lafler & Kinman (1965) and a Fourier analysis to derive the orbital period from our RV data. Both techniques yield values that lie within 0.02 days of TE's value, which is well below the estimated uncertainty (the FWHM of the peak in the power spectrum corresponds to 0.25 days) of our period determination. We then allowed differential corrections for the period while running our orbital solution code (see WHS, 1967). The value found in this way is 15.096 ± 0.002 days, which again is in fair agreement with TE's value. We conclude therefore that there is no evidence for a variation of the period and, owing to the above mentioned bias, we think wise to adopt TE's value of 15.093 days.

In addition to the He I λ 4471 line, four other absorption lines (namely O III λ 5592, C IV λ 5801, C IV λ 5812 and He I λ 5876) reveal the signature of both components except near conjunction. We used the mean RVs associated to these lines and the He I λ 4471 line, measured on FEROS spectra, to derive another orbital solution. The resulting parameters overlap within the errors with those of Table 5.

Four FEROS spectra could be obtained when the separation between the components' lines reached its maximum (around phases 0.9 to 0.1; see Fig. 1). Six more lines could be deblended on these spectra: He I λ 4026, He II λ 4200, Mg II λ 4481, He II λ 4541, He II λ 5412 and He I λ 7065. Following Conti (1973), we then use the ratio of the equivalent widths of the He I λ 4471 and He II λ 4541 lines ($\log W(\frac{\lambda\,4471}{\lambda\,4541})$, see his Table 1) for the primary and the secondary respectively, in order to derive a spectral classification for the two components. We get average values of $\log W^{\rm prim} = -0.40 \pm 0.04$ and $\log W^{\rm sec} = -0.10 \pm 0.03$. According to this criterion, HD 93403 is an O5.5 + O7 system. It is worth noting here that this result is in very good agreement with the spectral types proposed by TE 30 years ago, and with the ones derived by Penny (1997) from UV data.

We can derive a rough estimate of the luminosity ratio between the components of HD 93403 by comparing the intensities of their absorption lines. Using a cross-correlation technique to analyse IUE spectra, Howarth et al. (1997) found a difference in magnitude between the two stars of $\Delta\, m' = 1.1$. This result did however not include a correction for the difference in spectral type between the components of HD 93403 and corresponds to the only two IUE spectra obtained near periastron and which showed well resolved cross-correlation peaks. The mean intensity ratios measured on our observations are listed in Table 3. In order to derive the luminosity ratio, the measured intensity

ratios must be corrected for the spectral type difference of the components. From the results of Conti & Alschuler (1971), we expect an average ratio of ~ 0.47 between the equivalent width of the He I λ 4471 absorption lines of a typical single O5.5 star and a single O7 star. Therefore, the observed line intensity ratio corresponds to a corrected luminosity ratio of ~ 4.6. The trend of the O III λ 5592 and C IV $\lambda\lambda$ 5801, 5812 line intensities with spectral type is less clear cut (Conti 1974, Walborn 1980). We have nevertheless used the equivalent widths tabulated by Conti (1974) to estimate average equivalent width ratios for single stars. The corrected luminosity ratios (Table 3) confirm the result obtained for the He I λ 4471 line. We caution however that the strength of the C IV lines in the spectrum of the secondary star shows a phase dependence and the equivalent widths increase by about a factor of two in the phase interval 0.9–0.1. Whether this phenomenon is related to the so-called 'Struve-Sahade' effect (Stickland 1997) is not clear. These EW variations are much less pronounced for the He I λ 4471 and O III λ 5592 lines. In the following, we adopt the mean value derived from these two lines, yielding a luminosity ratio of 4.3 between the primary and the secondary. It is worth noting that this luminosity ratio is larger than the value expected (~ 1.7, Howarth & Prinja 1989) if both stars were of giant luminosity class as suggested by Penny (1997). Therefore it seems more likely that the two components have different luminosity classes. The fact that He II λ 4686 is found in absorption in the spectrum of the secondary star while the line is not seen in absorption in the primary's spectrum lends further support to this conclusion.

Assuming that the primary is a giant and the secondary a main sequence star and adopting the effective temperature calibration of Chlebowski & Garmany (1991), the spectral types derived above yield $T_{\rm eff} = 41300 \pm 1100$ K and $T_{\rm eff} = 40100 \pm 1100$ K for the primary and the secondary respectively. Given the good agreement between the spectral types derived by different investigators, we assume a typical uncertainty of half a spectral subtype.

Kaltcheva & Georgiev (1993) report $V = 7.30$ and $E(B-V) = 0.49$ for HD 93403. Assuming $A_V = 3.2 \times E(B-V)$ and adopting an average distance modulus of 12.55 to the Tr 16 cluster (Massey & Johnson 1993), we obtain $\log (L_{\rm bol}^{\rm prim}/L_\odot) = 6.08 \pm 0.2$ and $\log (L_{\rm bol}^{\rm sec}/L_\odot) = 5.41 \pm 0.2$ for the primary and secondary respectively. The locations of the components of HD 93403 are plotted in a H-R diagram in Fig. 4 together with the theoretical models of Schaller et al. (1992). The primary star is the most evolved component of the system, whereas the secondary lies still close to the ZAMS. A crude interpolation between the evolutionary tracks of Schaller et al. (1992) yields $M_1 = 75.5^{+8.2}_{-16.4}$ M$_\odot$ and $M_2 = 37.3^{+7.2}_{-4.2}$ M$_\odot$. The theoretical mass ratio of $2.02^{+.51}_{-.69}$ is larger than the observed value (1.753 ± 0.057) but we emphasize that this theoretical mass ratio is rather sensitive to the adopted distance of HD 93403 and to the luminosity ratio between the two stars.

If we repeat the above procedure assuming this time that the primary is a supergiant and the secondary a giant star, we obtain $T_{\rm eff} = 39300 \pm 1100$ K, $\log (L_{\rm bol}^{\rm prim}/L_\odot) = 6.02 \pm 0.2$ and $T_{\rm eff} = 38100 \pm 1100$ K, $\log (L_{\rm bol}^{\rm sec}/L_\odot) = 5.35 \pm 0.2$ for the primary and the secondary respectively. This time, comparison with the models of Schaller et al. (1992) yields masses of $M_1 = 68.5^{+12.3}_{-14.6}$ M$_\odot$ and $M_2 = 34.8^{+4.7}_{-4.4}$ M$_\odot$. Our conclusion about the theoretical mass ratio ($1.97^{+.69}_{-.61}$) remains valid although we find a slightly better agreement with the observed value. Finally, if we assume that the primary is a supergiant and the secondary is a main sequence object, we get a theoretical mass ratio of $1.84^{+.60}_{-.63}$.

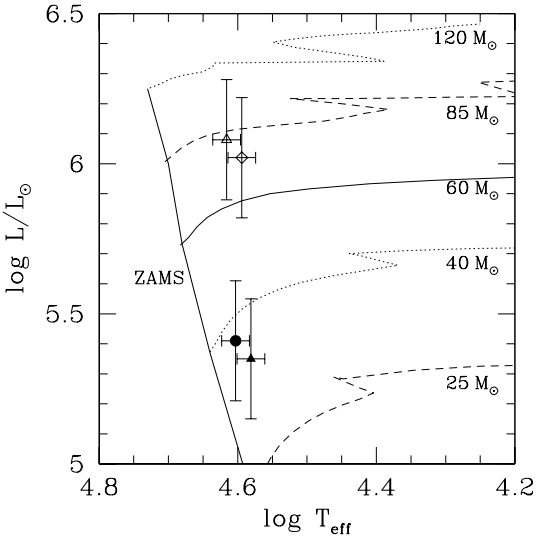

Fig. 4. Hertzsprung-Russell diagram of the HD 93403 system. The open and filled symbols stand for the primary and secondary respectively. Different symbols stand for different assumptions on the luminosity class (and hence the bolometric correction): circles, triangles and diamonds correspond to luminosity classes V, III and I respectively. The evolutionary tracks are from Schaller et al. (1992) for Z=0.020 and adopting 'standard' mass loss rates.

Comparing our results with the typical parameters of O stars listed by Howarth & Prinja (1989), we find the best overall agreement if we assume that the primary is an O5.5 I supergiant and the secondary an O7 V main sequence star.

We can use the above results to discuss some constraints on the geometry of the system adopting typical parameters for O5.5 I and O7 V stars (see e.g. Howarth and Prinja 1989). From the typical radii ($R_{\rm O5.5\,I} \simeq 24\,{\rm R}_\odot$; $R_{\rm O7\,V} \simeq 10\,{\rm R}_\odot$) and assuming that HD 93403 is a non-eclipsing system, we can set an upper limit on the orbital inclination i of 58.2°. Using the minimum masses corresponding to our orbital solution (Table 5) this upper limit on i corresponds to lower limits of 15.5 M$_\odot$ and 8.8 M$_\odot$ for the mass of the primary and secondary respectively. If we further impose that the primary's mass should be less than 120 M$_\odot$, which seems a reasonable limit, we get $i \geq 25°$.

Adopting a mass of 68.5 M$_\odot$ for the O5.5 I primary, we get a first crude estimate for the orbital inclination: $i \approx 31.2°$. Applying the same argument ($M_{\rm O7\,V} \simeq 37.3\,{\rm M}_\odot$) to the secondary yields an inclination of 31.7°, in excellent agreement with the value for the primary star. Though this is a very crude method

to estimate i, it will certainly be useful for the interpretation of the forthcoming X-ray data.

Although the Roche equipotential model is certainly not well justified for a binary system with an eccentricity of 0.234, we can derive first order constraints on the configuration of the binary from the radii of the 'instantaneous' Roche lobe (R_{RL}) around periastron passage. To this end, we adapt Eggleton's formula (Eggleton 1983):

$$\frac{R_{RL}}{a} = (1-e)\,\frac{0.49\,q^{2/3}}{0.6\,q^{2/3}+\ln(1+q^{1/3})} \qquad (2)$$

where a is the total semi-major axis of the binary and q is the mass ratio. Using $a\sin i = 63.2\,\mathrm{R}_\odot$, we get the minimum values of:

$$\begin{cases} R_{RL,1}\sin i = 20.7\,\mathrm{R}_\odot \\ R_{RL,2}\sin i = 16.0\,\mathrm{R}_\odot \end{cases}$$

As the 'typical' radii for O5.5 I and O7 V stars are $24\,\mathrm{R}_\odot$ and $10\,\mathrm{R}_\odot$ respectively, the stars in HD 93403 are unlikely to undergo 'Roche lobe overflow' near periastron. Assuming an inclination of $i \approx 32°$, the primary and secondary should fill respectively about 23% and 4% of their critical volume at periastron passage.

5. Conclusion

We have presented a spectroscopic analysis of the early-type binary HD 93403. As this system is scheduled for observations with ESA's recently launched XMM satellite, one aim of this study was to derive accurate orbital parameters. Using high resolution observations, we have been able to separate the primary and secondary component of the binary. For the first time, an orbital solution for both stars of the system has been computed. This new solution differs significantly from the previous one obtained by TE. This may result from a bias in TE's data due to the fact that they did not separate the primary and secondary spectra.

Based on the He I λ 4471 and He II λ 4541 equivalent width ratio, we derive an O5.5 and O7 spectral type for the primary and secondary respectively. This is in fair agreement with previous spectral-type determinations including the results of the tomographic analysis of IUE data by Penny (1997). Due to the presence of He II λ 4686 in absorption in the secondary spectrum and to the relatively high spectroscopic luminosity ratio between the primary and secondary, we also suggest that the secondary could be a main sequence star and would therefore be the less evolved component of the system whereas the primary is probably a more evolved supergiant.

Using typical parameters for O-type stars, we derived qualitative constraints on the inclination of the system: $25° < i < 58°$ with a 'reasonable' value around $31°$ to $32°$. We further underline that HD 93403 should not be currently undergoing a 'Roche lobe overflow' process. The low orbital inclination makes this system a highly interesting target for studying the effects of a non zero eccentricity on the intrinsic X-ray emission generated in a colliding wind process. In fact, given this low inclination, we expect little variability of the circumstellar column density towards the shock cone as a function of orbital phase. Since the column density remains probably roughly constant, any orbital variability of the X-ray emission would most probably be due to the changing separation between the two stars (Pittard & Stevens 1997).

Finally we note the complex line profile variability of the He II λ 4686 line. Unfortunately our phase coverage of this spectral region is not sufficient to investigate the phase dependence of this variability. More high resolution and high S/N ratio spectra are needed to investigate possible fast line profile variability. In light of a possible wind interaction between the components of HD 93403, the comparison of the line profile variability of He II λ4686 with the forthcoming X-ray data could be of crucial importance to constrain the nature of the interaction process.

Acknowledgements. We wish to thank Dr. O. Stahl for his efficient help in adapting the FEROS reduction package to our data. We are grateful to Y. Nazé and Dr. J. Manfroid for their help in the reduction of the BME data and to A. Kransvelt for his assistance during the commissioning of the VLC instrument. We are greatly indebted to the Fonds National de la Recherche Scientifique (Belgium) for multiple supports. This research is also supported in part by contract P4/05 "Pôle d'Attraction Interuniversitaire" (SSTC-Belgium). Partial support through the PRODEX XMM-OM Project is also gratefully acknowledged. The SIMBAD database has been consulted for the bibliography.

References

Cardona-Núñez O., 1978, PhD Thesis, University of Colorado, Boulder
Chlebowski T., Garmany C.D., 1991, ApJ 368, 241
Conti P.S., 1973, ApJ 179, 181
Conti P.S., 1974, ApJ 187, 539
Conti P.S., Alschuler W.R., 1971, ApJ 170, 325
Conti P.S., Frost S.A., 1977, ApJ 212, 728
Conti P.S., Leep E.M., Lorre J.J., 1977, ApJ 214, 759
Eggleton P.P., 1983, ApJ 268, 368
Feast M.W., Thackeray A.D., Wesselink A.J., 1955, Mem. R. Astr. Soc. 67, 51
Howarth I.D., Prinja R.K., 1989, ApJS 69, 527
Howarth I.D., Siebert K.W., Hussain G.A.J., Prinja R.K., 1997, MNRAS 284, 265
Kaltcheva N.T., Georgiev L.N., 1993, MNRAS 261, 847
Kaufer A., Stahl O., Tubbesing S. et al., 1999, The Messenger 95, 8
Lafler J., Kinman T.D., 1965, ApJS 11, 216
Massey P., Johnson J., 1993, AJ 105, 980
Nussbaumer H., 1971, ApJ 170, 93
Penny L.R., 1997, PASP 109, 848
Pittard J.M., Stevens I.R., 1997, MNRAS 292, 298
Rauw G., Vreux J.-M., Bohannan B., 1999, ApJ 517, 416
Schaller G., Schaerer D., Meynet G., Maeder A., 1992, A&AS 96, 269
Seward F.D., Forman W.R., Giacconi R. et al., 1979, ApJ 234, L55
Stickland D.J., 1997, The Observatory 117, 37
Thackeray A.D., Emerson B., 1969, MNRAS 142, 429
Thaller M.L., 1997, ApJ 487, 380
Underhill A.B., 1995, ApJS 100, 433
Walborn N.R., 1972, AJ 77, 312
Walborn N.R., 1980, ApJS 44, 535
Walborn N.R., 1982, ApJS 48, 145
Walborn N.R., Hesser J.E., 1975, ApJ 199, 535
Wolfe R.H. Jr., Horak H.G., Storer N.W., 1967. In: Modern Astrophysics, Hack M. (ed.), Gordon & Breach, New York, 251

Mon. Not. R. Astron. Soc. **326,** 1149–1160 (2001)

Optical spectroscopy of XMEGA targets in the Carina Nebula – III. The multiple system Tr 16-104 (≡CPD −59° 2603)

G. Rauw,[1★†] H. Sana,[1★] I. I. Antokhin,[1★] N. I. Morrell,[2★‡] V. S. Niemela,[2★§] J. F. Albacete Colombo,[2★¶] E. Gosset[1★‖] and J.-M. Vreux[1★]

[1]*Institut d'Astrophysique & Géophysique, Université de Liège, 5, Avenue de Cointe, B-4000 Liège, Belgium*
[2]*Facultad de Ciencias Astronómicas y Geofísicas, Universidad Nacional de La Plata, Paseo del Bosque, 1900 La Plata, Argentina*

Accepted 2001 May 11. Received 2001 May 10; in original form 2001 February 5

ABSTRACT

We discuss the orbital elements of the multiple system Tr 16-104 which is usually believed to be a member of the open cluster Trumpler 16 in the Carina complex. We show that Tr 16-104 could be a hierarchical triple system consisting of a short-period (2.15 d) eclipsing O7 V + O9.5 V binary bound to a B0.2 IV star. Our preliminary orbital solution of the third body indicates that the B star most probably describes an eccentric orbit with a period of ∼285 or ∼1341 d around the close binary. Folding photometric data from the literature with our new ephemerides, we find that the light curve of the close binary exhibits rather narrow eclipses indicating that the two O stars must be well inside their Roche lobes. Our analysis of the photometric data yields a lower limit on the inclination of the orbit of the close binary of $i \geq 77°$. The stellar radii and luminosities of the O7 V and O9.5 V stars are significantly smaller than expected for stars of this spectral type. Our results suggest that Tr 16-104 lies at a distance of the order of 2.5 kpc and support a fainter absolute magnitude for zero-age main-sequence O stars than usually adopted. We find that the dynamical configuration of Tr 16-104 corresponds to a hierarchical system that should remain stable provided that it suffers no strong perturbation. Finally, we also report long-term temporal variations of high-velocity interstellar Ca II absorptions in the line of sight towards Tr 16-104.

Key words: binaries: close – binaries: spectroscopic – stars: early-type – stars: fundamental parameters – stars: individual: Tr 16-104 – open clusters and associations: individual: Trumpler 16.

1 INTRODUCTION

The study of spectroscopic binary systems in open stellar clusters with well-determined age and distance constitutes an elegant means to constrain the fundamental properties of the binary components and to evaluate the time-scales of tidal circularization. This is especially true for early-type binaries in the youngest open clusters. In principle, the very young Trumpler 16 cluster in the Carina region [log (age) = 6.5, Massey & Johnson 1993] could be one of the best places in our Galaxy to study the multiplicity of massive stars. A previous study of the duplicity in Tr 16 (Levato et al. 1991) revealed the presence of at least five O-type spectroscopic binaries with orbital periods shorter than seven days. Using spectrograms of 43 Å mm^{-1} dispersion, Levato et al. found rather large eccentricities ($e \geq 0.16$) even for the shortest orbital periods. However, higher spectral resolution is required to ascertain the orbital elements of these systems and this is especially true for those systems classified as single-lined spectroscopic binaries (SB1s) where the apparent eccentricity could result from the blend of the spectral lines of the individual components.

Tr 16-104 (≡CPD −59° 2603, Feinstein, Marraco & Muzzio 1973) is a multiple system in the Tr 16 cluster. Walborn (1973) determined an O7 V ((f)) spectral classification for the composite spectrum and suspected multiplicity for this star. Levato et al. (1991) classified Tr 16-104 as a short-period SB1 binary. Their preliminary orbital solution yields an orbital period of 1.81 d, an eccentricity of 0.16 and a semi-amplitude $K = 160$ km s^{-1}.

Howarth et al. (1997) studied the only two *IUE* spectra of this

★E-mail: rauw@astro.ulg.ac.be (GR); sana@astro.ulg.ac.be (HS); antokhin@astro.ulg.ac.be (IIA); nidia@fcaglp.fcaglp.unlp.edu.ar (NIM); virpi@fcaglp.fcaglp.unlp.edu.ar (VSN); albacete@lilen.fcaglp.unlp.edu.ar (JFAC); gosset@astro.ulg.ac.be (EG); vreux@astro.ulg.ac.be (JMV)
†Chargé de Recherches FNRS, Belgium.
‡Member of Carrera del Investigador Científico, CONICET, Argentina.
§Member of Carrera del Investigador Científico, CICBA, Argentina.
¶Fellow of the Comisión de Investigaciones Científicas (CIC), Prov. de Buenos Aires, Argentina.
‖Chercheur Qualifié FNRS, Belgium.

system and found three peaks in their cross-correlation function. According to Howarth et al., only peak A (the most prominent one) had changed its position between the two *IUE* exposures. These authors suggested therefore that star A could be the SB1 binary component that had been studied by Levato et al. (1991) while the other two peaks would not be associated with the binary. This would bring the number of stars in the system to at least four. More recently, a preliminary SB2 orbital solution for Tr 16-104 was proposed by Solivella & Niemela (1999) who derived a period of 2.15291 d from the radial velocities of the He II λ 4686 line as measured on medium resolution spectra.

Besides our will to investigate the multiplicity of Tr 16-104, our observing campaign was motivated by the fact that this system was also observed with the *ROSAT* satellite as part of the XMEGA campaign (http://lheawww.gsfc.nasa.gov/users/corcoran/xmega/xmega.html) to study the X-ray properties of early-type stars (Corcoran, Pittard & Marchenko 1999). Since the *ROSAT* observations could have revealed an excess X-ray emission arising in a wind interaction zone, new accurate ephemerides were needed to fully interpret the X-ray data. In the present paper, we discuss a large set of medium and high resolution optical spectra and we show that Tr 16-104 could actually be a hierarchical triple system consisting of a short period eclipsing O7 V + O9.5 V binary revolving around a third component of spectral type B0.2 IV.

The paper is organized as follows. In Section 2, we present our observations and the properties of the spectrum of Tr 16-104 are discussed in Section 3. Section 4 deals with the orbital solutions of this multiple system and the light curve is analysed in Section 5. The fundamental parameters of the components and the multiplicity of Tr 16-104 are discussed in Section 6. Finally our conclusions are outlined in Section 7.

2 OBSERVATIONS

Blue–violet and yellow medium-resolution spectra of Tr 16-104 were gathered during several observing runs in 1995, 1996 and 1997 with the ESO 1.5-m telescope equipped with a Boller & Chivens (B&C) Cassegrain spectrograph. The data were obtained with a holographic grating (2400 line mm^{-1}) providing a reciprocal dispersion of 32.6 Å mm^{-1}. The detector used in 1995 was a Ford Aerospace 2048L UV-coated CCD with a pixel size of 15 μm, whereas in 1996 and 1997 we used a thinned, UV flooded Loral-Lesser CCD. The slit width was set to 220 μm corresponding to 2 arcsec on the sky. The spectral resolution as measured on the helium–argon calibration spectra is 1.2 Å. Our blue–violet data cover the wavelength ranges 3800–4750 Å (1995 March) and 3850–4800 Å (1996 May and 1997 March). The yellow setting covers the range 5400–6200 Å (1995 March). Part of the B&C data are affected by a strange fringing pattern (Turatto, Tighe & Castillo 1997) that occurs over the wavelength range 4050–4250 Å in the present instrument configuration. Given the variability of the fringing pattern and in order to avoid amplification of the fringes in the stellar spectra, the data were not flat-fielded. All the reductions were performed using the MIDAS software developed at ESO.

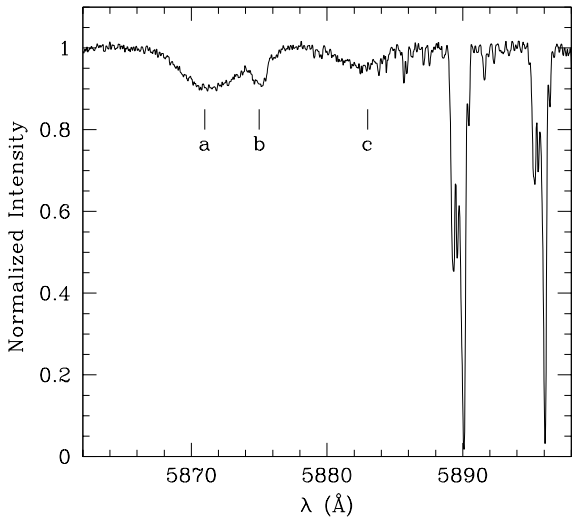

Figure 1. FEROS spectrum of Tr 16-104 around the He I λ 5876 line as observed on HJD 245 1299.602. Note also the very complex structure of the interstellar Na I profiles.

19 CCD echelle spectra were obtained at the Complejo Astronómico El Leoncito (CASLEO),[1] Argentina during five different observing runs between 1997 February and 2001 March. We used the 2.15-m Jorge Sahade Telescope and the modified REOSC SEL[2] Cassegrain spectrograph equipped with a Tek 1024 × 1024 pixel CCD as detector. These spectra cover an approximate wavelength range from 3500 to 6000 Å, at a reciprocal dispersion of 0.17 Å pixel^{-1} at 4500 Å. All the data obtained at CASLEO were reduced and analysed using IRAF[3] routines.

During three observing runs in 1999 April–May, end of 1999 May and 2000 May, a set of echelle spectra was taken with the Fiber-fed Extended Range Optical Spectrograph (FEROS, Kaufer et al. 1999) attached to the ESO 1.5-m telescope at La Silla. 37 orders corresponding to a wavelength domain from 3650 to 9200 Å were observed. The spectral resolving power of the FEROS instrument is 48 000. The detector was an EEV CCD with 2048 × 4096 pixels of 15 × 15 μm. We used the FEROS context working under the MIDAS environment to reduce the FEROS echelle spectra.

3 THE SPECTRUM OF TR 16-104

Our medium- and high-resolution spectra of Tr 16-104 clearly reveal the spectral signature of at least three stellar components. These are best seen in the profiles of the He I absorption lines (Fig. 1). The absorptions of two of the three components are quite broad and their wavelengths change rather quickly as a result of their orbital motion. On the contrary, the lines of the third component are rather narrow and their radial velocity evolves only very slowly. We also notice a fourth, very narrow (FWHM ∼0.23 Å) absorption component of the He I λ 3889 line at a fairly constant radial velocity of $\sim -33 \pm 1$ km s^{-1}. On some of our spectra, a similar feature can be seen in the He I λ 5876 line. This fourth component is most likely of interstellar origin. In fact, interstellar He I λ 3889 absorption at this radial velocity is a common feature in the spectra of early-type stars in the Carina complex (Walborn & Hesser 1975).

In the following, we call component 'a' the star that displays the broadest and strongest absorption lines (see Fig. 1). In particular, component 'a' has the strongest He II absorption lines and is the

[1] CASLEO is operated under agreement between CONICET and the National Universities of La Plata, Córdoba and San Juan.
[2] Spectrograph Echelle Liège (jointly built by REOSC and Liège Observatory and on long-term loan from the latter).
[3] IRAF is distributed by NOAO, operated by AURA, Inc., under agreement with NSF.

Table 1. FWHM of the He I λ 5876 lines of the various components of the Tr 16-104 system. The third column provides the most likely cross-reference with the identifications proposed by Howarth et al. (1997). The last column lists the rotational velocities of the three components as derived by Howarth et al.

Component	$\overline{\text{FWHM}}$ (He I λ 5876) (Å)	Cross-ID	$v_e \sin i$ (km s^{-1})
a	5.0 ± 0.4	A	164
b	1.2 ± 0.2	B	59
c	4.0 ± 0.4	C	111

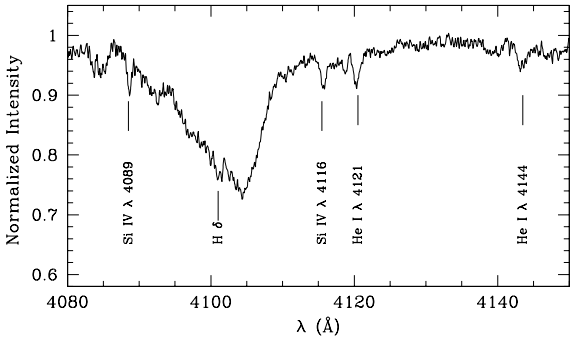

Figure 2. FEROS spectrum of Tr 16-104 in the region around the Hδ line as observed on HJD 245 1300.608. The figure illustrates the relative strengths of the lines of the B0.2–0.5 component that are used for the luminosity classification of this star (see text).

only star in the system that shows C IV $\lambda\lambda$ 5801, 5812 in absorption. A broad and very weak C III λ 5696 emission line appears also to be associated with star 'a'.

In addition to the sharp prominent He I absorption lines, the spectrum of component 'b' displays also narrow absorptions of He II λ 4686 as well as many metal lines (e.g. O II $\lambda\lambda$ 4070, 4072, 4075, 4415, 4417, 4699; Si III $\lambda\lambda$ 4552, 4568; Si IV λ 4089, …).

Star 'c' displays broad absorption lines. While the He I lines have strengths comparable to those of star 'a', the He II lines are considerably weaker and we see no trace of C IV lines associated with this star. Comparing our observations with the relative intensities and the widths of the UV lines reported by Howarth et al. (1997), it seems reasonable to cross-identify the components A = a, B = b and C = c (see Table 1).

3.1 Spectral classification

We have measured the equivalent widths (EWs) of the O-star classification lines He I λ 4471 and He II λ 4542 on those high resolution spectra where they are best separated. Using the Conti (1973b) and Mathys (1988) classification scheme, we find that the primary (i.e. the more massive star, 'a') is of spectral type O7–7.5 ($\log W' = \log \text{EW(He I}\lambda 4471) - \log \text{EW(He II}\lambda 4542) = -0.1$ to $+0.06$), whilst the secondary ('c') yields $\log W' =$ 0.42–0.72, corresponding to a spectral type O9.5–9.7. Our data reveal no trace of the very weak N III emission reported by Walborn (1973). Therefore we cannot confirm the O ((f)) classification of Tr 16-104. It seems likely that the continuum between the absorption features of the triple spectrum had been mistaken for weak emission in the past.

Finally, the Si IV λ 4089 and Si III λ 4552 lines in the spectrum of component 'b' have comparable strengths and the He II λ 4686 line is seen in absorption. According to the criteria of Walborn & Fitzpatrick (1990), these spectral features correspond to a B0.2–0.5 spectral type.

From the dilution of the absorption lines in Tr 16-104 compared to the line strength in the spectra of single stars of the same spectral type, we can infer a very rough estimate of the relative contributions of the various stars in the system to its total optical luminosity (see e.g. Rauw et al. 2000). Assuming that stars 'a' and 'c' have normal He abundances, we compare the observed equivalent widths of the He I $\lambda\lambda$ 4026, 4471 and He II λ 4542 lines to the average EWs of these lines in the spectra of O7 and O9.5 stars as tabulated by Conti & Alschuler (1971) and Conti (1973a). In this way, we obtain $l_a = L_a/L_{tot} \simeq 0.64$ and $l_c = L_c/L_{tot} \simeq 0.29$ in the blue–violet part of the spectrum for orbital phases outside photometric eclipse (see below).

Similarly, using the typical equivalent widths of spectral lines in B-type stars as listed by Didelon (1982), we obtain $l_b = L_b/L_{tot} \simeq 0.15$. Of course, the sum of the relative contributions should not exceed 1.0 and if we normalize our results hereabove, we derive $l_a \simeq 0.59$, $l_b \simeq 0.14$ and $l_c \simeq 0.27$.

From the strengths of the cross-correlation peaks, Howarth et al. (1997) derived raw magnitude differences of 1.2 and 1.3 between the A–B and A–C components respectively. The results of Howarth et al. yield $l_a = 0.61$, $l_b = 0.20$ and $l_c = 0.19$ in the *IUE* spectral range. Given the uncertainties and the different spectral domains, the numbers inferred from both methods (Howarth et al.'s technique and ours) are in fair agreement with each other.

We can use the $\log W'' = \log \text{EW(Si IV}\lambda 4089) - \log \text{EW(He I}\lambda 4144)$ criterion proposed by Conti & Alschuler (1971) to determine the luminosity of the O7 component. From our FEROS spectra, we find that EW(Si IVλ4089) $\simeq 0.16$ Å and EW(He Iλ4144) ≤ 0.15 Å yielding $\log W'' \geq 0.03$. According to Conti & Alschuler (1971), this corresponds to a main-sequence classification, though the fact that we are dealing with a lower limit on W'' leaves some ambiguity between luminosity classes V and III. The strength of the He II λ 4686 absorption and the ratio of He I λ 4388/He II λ 4542 (Walborn & Fitzpatrick 1990) do not allow us to discriminate between luminosity classes V and III either, though they are slightly more consistent with a main-sequence classification. Walborn (1980) pointed out that the strength of the C III λ 5696 emission line in the spectrum of O7–O8 stars increases with luminosity. Therefore, the weak (EW $\simeq 0.1$ Å) C III λ 5696 emission associated with star 'a' is also marginally more consistent with a main-sequence classification of this star.

We use the Mathys (1988) criterion ($\log W^+ = \log \text{EW(He I}\lambda 4388) + \log \text{EW(He II}\lambda 4686)$) for the luminosity classification of the O9.5 secondary (i.e. star 'c'). This criterion yields $\log W^+ = 4.23 - 2 \log l_c$. Inserting the above estimates of $l_c = 0.20$–0.27, we obtain $\log W^+ = 5.37$–5.63 corresponding to a main-sequence star ($\log W^+ > 5.35$, Mathys 1988) though again we cannot completely rule out a luminosity III classification from this result. We emphasize that the primary/secondary optical luminosity ratio clearly indicates that the primary and the secondary should be of the same luminosity class.

From the relative strengths of the Si IV $\lambda\lambda$ 4089, 4116 and He I $\lambda\lambda$ 4121, 4144 lines (Fig. 2) in the spectrum of component 'b', we infer a luminosity class IV (Walborn & Fitzpatrick 1990) for this star, though we cannot rule out a luminosity class III. Again the relative luminosity of the 'b' component implies that this star is most likely of a similar luminosity class than the components of the short-period binary.

In summary, the short-period binary most probably consists of an O7 primary and an O9.5 secondary, whilst the third component is of spectral type B0.2–0.5. The spectroscopic luminosity ratios indicate that all three stars should belong to the same luminosity class. Though some of the criteria yield somewhat ambiguous results, it seems that the stars are of main-sequence luminosity class (we shall return to this point in Section 6.1).

Though the equivalent widths of the absorption lines of the close binary display some variations, we could not find any significant phase-locked variations that might be related to the so-called 'Struve–Sahade' effect (e.g. Stickland 1997). The only possible exception is the He I λ 4471 line that appears stronger in the primary spectrum around orbital phases when the star is approaching, while the EW of the secondary's line does not vary.

3.2 The interstellar absorption lines

The spectrum of Tr 16-104 displays very prominent and complex interstellar absorption lines of Ca II and Na I (see Figs 1 and 3). In the Ca II H and K lines, the strongest absorption features have radial velocities of -216, -34, -18, $+5$, $+25$ and $+100\,\mathrm{km\,s^{-1}}$. The same structures are found in the Na I D1 and D2 lines although the visibility of the fainter higher velocity (-216 and $+100\,\mathrm{km\,s^{-1}}$) components is hampered by the telluric absorption lines. The RVs of the strongest components are in good agreement with those of the double-peaked nebular [O III] $\lambda\lambda$ 4959, 5007 lines (-29, $+8\,\mathrm{km\,s^{-1}}$). The optical and UV interstellar absorption spectrum towards Tr 16-104 has been extensively studied by Walborn (1982), Walborn et al. (1998) and Danks et al. (2001) and we refer to their analyses for further details. Nevertheless, we emphasize that the Ca II profiles in our spectra are slightly different from those published by Walborn (1982). The most outstanding difference concerns the absorption component at $+100\,\mathrm{km\,s^{-1}}$ which appears much stronger in our spectra than in the data of Walborn (1982). Though the variability of interstellar absorptions is an a priori unexpected feature, this is not the first time that such a phenomenon is reported for Tr 16-104. In fact, Danks et al. (2001) recently analysed high-resolution *HST*–STIS observations of the interstellar Mg I and Mg II lines towards Tr 16-104 taken 22 months apart and discovered temporal variations in five distinct interstellar velocity components. These authors suggest that the high-velocity interstellar features are produced through the interaction of the stellar winds with dense surrounding material. In this context, we note that we find no significant variability on the time-scales of the orbital periods of the close binary or of the third component that could indicate an origin of the variations in changing lines of sight to the binary components at different phases.

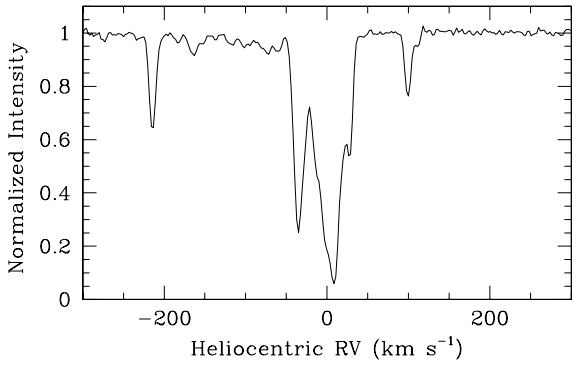

Figure 3. Mean FEROS spectrum of Tr 16-104 around the Ca II K line. Note the complex structure of the line and the sharp component at RV = $+100\,\mathrm{km\,s^{-1}}$ that was only marginally present in the data of Walborn (1982).

4 ORBITAL SOLUTIONS

The radial velocities of the three stellar components in Tr 16-104 were measured by fitting simultaneously up to three Gaussians to the observed line profiles. Because of the varying strength of the different line components (see below), good fits could only be

Table 2. Journal of our spectroscopic observations of Tr 16-104. For each component we list the radial velocity (RV in $\mathrm{km\,s^{-1}}$) as well as the number of spectral lines (n) used to determine these RVs. The last column specifies the instrument used to collect the spectrum: B&C = Boller & Chivens at the 1.5 m ESO, R = REOSC at CASLEO, F = FEROS at the 1.5 m ESO.

HJD	'a'		'b'		'c'		Inst.
−244 0000	RV	n	RV	n	RV	n	
9805.723	−111.1	3	−65.9	1	266.3	3	B&C
9805.799	−104.5	2			233.9	1	B&C
9808.727	229.4	3	−67.5	1	−328.6	1	B&C
9808.787	218.7	3	−68.0	1	−330.5	1	B&C
9808.853	219.9	3	−71.2	1	−307.5	1	B&C
9809.739	−221.9	2	−70.5	1	354.1	1	B&C
10205.696	−212.5	3	27.2	3	260.1	3	B&C
10206.718	74.0	3	34.1	2	−265.5	3	B&C
10207.691	−113.6	1	49.3	2	34.3	1	B&C
10208.688	23.3	3	38.7	2	−182.8	2	B&C
10209.696	5.7	1	24.2	3	−140.9	3	B&C
10210.681	−46.2	1	41.6	2	231.1	2	B&C
10211.552	95.5	2			−280.9	2	B&C
10505.675	−3.0	4	6.0	10	−87.0	4	R
10507.770	−59.0	4	5.0	16	103.0	2	R
10508.648	177.0	12	15.0	5	−247.0	4	R
10534.712	62.9	1					B&C
10535.717	−53.3	3			−173.0	3	B&C
10536.679	149.7	3	36.4	3	−235.4	3	B&C
10537.708	−169.8	4			223.5	4	B&C
10538.747	162.2	3	25.6	3	−292.3	3	B&C
10539.729	−180.7	3			298.5	3	B&C
10841.769	143.0	7	−13.0	6	−204.0	4	R
10844.832	−75.0	3	−18.0	11	83.0	3	R
10846.814	120.0	7	−20.0	9	−124.0	1	R
10851.799	−229.0	7	−3.0	2	322.0	2	R
11209.828	137.0	12	−56.0	9	−156.0	2	R
11210.822	−77.0	4	−55.0	15	72.0	10	R
11211.856	13.0	4	−50.0	9	76.0	3	R
11216.719	234.0	10	−52.0	8	−321.0	6	R
11217.845	−178.0	9	−57.0	8	344.0	5	R
11218.705	230.0	12	−59.0	8	−294.0	5	R
11299.602	−201.6	9	−27.7	14	340.2	10	F
11300.608	222.9	10	−30.6	14	−309.1	7	F
11301.584	−182.7	7	−30.0	13	292.3	8	F
11302.627	193.1	11	−26.6	14	−264.5	8	F
11304.585	98.7	6	−26.4	11	−157.0	3	F
11327.576	−217.9	9	−3.4	15	332.8	8	F
11615.749	−141.0	5	36.0	6	202.0	6	R
11619.507	178.0	5	44.0	5	−280.0	5	R
11620.516	−198.0	12	21.0	6	251.0	6	R
11669.598	−146.4	6	24.4	11	203.2	5	F
11670.556	98.3	9	23.7	13	−109.3	4	F
11671.609	−91.8	6	21.2	11	122.5	4	F
11672.545	−25.5	3	21.2	9	68.3	2	F
11673.543	96.5	5	22.4	11	−67.6	2	F
11969.548	−78.0	5	−5.0	5	97.0	5	R
11970.583	153.0	5	6.0	4	−133.0	5	R
11971.541	−150.0	5	−5.0	4	240.0	5	R

achieved when the depths and widths of the Gaussians were allowed to vary. The formal errors on the central wavelengths of these Gaussian fits in the FEROS spectra are about 4 km s^{-1} for the SB2 components and 2 km s^{-1} for the third star, whilst these formal errors are about three times larger for the lower resolution B&C data. For the O-star lines, we adopted the effective wavelengths from Underhill (1995). For component 'b', the radial velocities of the metal lines provide an independent check of the results of the multiple Gaussian fit used to deblend the He I lines. The radial velocities of the three components are listed in Table 2.

4.1 The orbital periods

We performed a period search on the radial velocity differences (primary – secondary) using the trial period technique of Lafler & Kinman (1965). Since we expect the systemic velocity of the close binary to vary owing to the influence of the third star, these RV differences are better suited for the purpose of period determinations than the actual RVs of the individual components. In fact, the RV differences are not sensitive to possible temporal changes of the systemic velocity γ. The results are listed in Tables 3 and 4. The Lafler & Kinman method yields two minima at ν_2 and $\nu_1 = 0.5 \times \nu_2$. While the FWHM of the dip at ν_2 is roughly equal to the natural width (4.6×10^{-4} d^{-1}) of the peak set by the sampling of our RV time series, we notice that the dip at ν_1 has a FWHM about half this value. Therefore, ν_1 is clearly a classical sub-harmonic artefact of the ν_2 frequency.

The most likely orbital period of the close binary turns out to be 2.15294 d. The natural width of the peak set by the sampling of our time series amounts to 0.00214 d. Assuming that the actual uncertainty equals about one tenth of the natural width, we find that the orbital period would be equal to 2.15294 ± 0.00021 d. Our value is in excellent agreement with the one obtained by Solivella & Niemela (1999) but it is different from the 1.81-d period suggested by Levato et al. (1991). The latter discrepancy is most probably a result of the severe one-day aliasing that affected the Levato et al. data set.

We have applied the 'generalized spectrogram' Fourier method introduced by Heck, Manfroid & Mersch (1985), see also the appendix in Gosset et al. (2001). The strongest peak in the periodogram of the time series of the $RV_a - RV_c$ differences was found at $\nu'_2 = 0.46449$ d^{-1} corresponding to a period of 2.15290 d in excellent agreement with the result above. In the following, we will adopt an orbital period for the close binary of $P_{\rm orb}^{\rm in} = 2.15287$ d, which is slightly different from the best-fitting period derived hereabove, but which lies well within the error bar and provides the best agreement between our spectroscopic data and photometric data from the literature (see Section 5).

Table 2 clearly reveals that the radial velocity of the third component of Tr 16-104 varies slowly as a function of time. We have therefore searched the time series of the RVs of star 'b' for a long term periodicity. The results are also indicated in Tables 3 and 4. The most likely frequencies found with the Lafler & Kinman (1965) technique are ν_3 and $\nu_4 \sim 5 \times \nu_3$ corresponding to periods of respectively 1408.5 ± 91.6 d and 281.7 ± 3.6 d. Again, the quoted uncertainties correspond to one tenth of the natural width. We caution that our data do not allow us to discriminate between the ν_3 and ν_4 frequencies since both dips have a FWHM consistent with the natural width set by the time series (see also Section 4.2). However, our data set covers only about 1.5 cycle of the ν_3 frequency and the existence of a true 1408 d 'periodicity' is thus quite uncertain. Using the Fourier method of Heck et al. (1985) and Gosset et al. (2001), the most prominent peaks appear at frequencies of $\nu'_3 = 0.000746$ d^{-1} and $\nu'_4 = 0.003508$ d^{-1} that differ by less than one tenth of the natural width from ν_3 and ν_4 respectively. We find also a strong one-day alias of ν'_3 at ν'_5. The periods corresponding to ν'_3 and ν'_4 are 1340.5 ± 83.0 and 285.1 ± 3.8 d respectively. In the following, we will focus on the periods derived from the Fourier analysis.

There are two possible explanations for the RV variations of the third component: either the B0.2 star belongs to a rather wide binary that lies along the line of sight towards the close binary or alternatively it is physically connected to the close binary and is revolving around the centre of mass of a genuine triple system. We will address this question in the following subsection.

Table 3. Results of the period search using the Lafler & Kinman technique. $\Theta_{\rm LK}$ corresponds to the value of the criterion defined by Lafler & Kinman (1965) normalized to 1.0. The first two periods refer to the time series of the RV differences between the two components of the close binary, whilst the other two periods correspond to the analysis of the RVs of the third component.

	ν (d^{-1})	$\Theta_{\rm LK}$	P (days)	Data set
ν_1	0.23224	0.0935	4.30589	} $RV_a - RV_c$
ν_2	0.46448	0.0494	2.15294	
ν_3	0.000710	0.0864	1408.5	} RV_b
ν_4	0.003550	0.0898	281.7	

Table 4. Same as Table 3, but using the Fourier method of Heck et al. (1985) and Gosset et al. (2001). A is the amplitude of the RV curve (in km s^{-1}) corresponding to the peaks in the periodogram.

	ν (d^{-1})	A	P (d)	Data set
ν'_2	0.46449	524.8	2.15290	} $RV_a - RV_c$
ν'_3	0.000746	48.8	1340.5	} RV_b
ν'_4	0.003508	49.3	285.1	
ν'_5	0.999332	49.9	1.00067	

4.2 Mass ratios and orbital solutions

An orthogonal regression method applied to the RV data of the 'a' and 'c' components yields a mass-ratio of $m_c/m_a = 0.65 \pm 0.03$ (1σ). Since the systemic velocity of the close binary could change as a function of time (if the binary is physically connected to the B0.2–0.5 star), the value of m_c/m_a derived hereabove is strictly valid only if our observations provide a sufficient sampling of the orbital period of the third star.

Before we turn to the orbital solution of the close binary system, let us first consider the issue of the connection between the close binary and star 'b'. To this aim, we computed

$$v_a + \frac{m_c}{m_a} v_c = \gamma_a + \frac{m_c}{m_a} \gamma_c$$

as a function of time. Here, γ_a and γ_c stand for the *apparent systemic velocities* as derived from the measured RVs of the 'a' and 'c' components respectively. The quantity $v_a + (m_c/m_a)v_c$ provides a direct measure of any time variation of the systemic velocity of the close binary and allows us to test whether or not

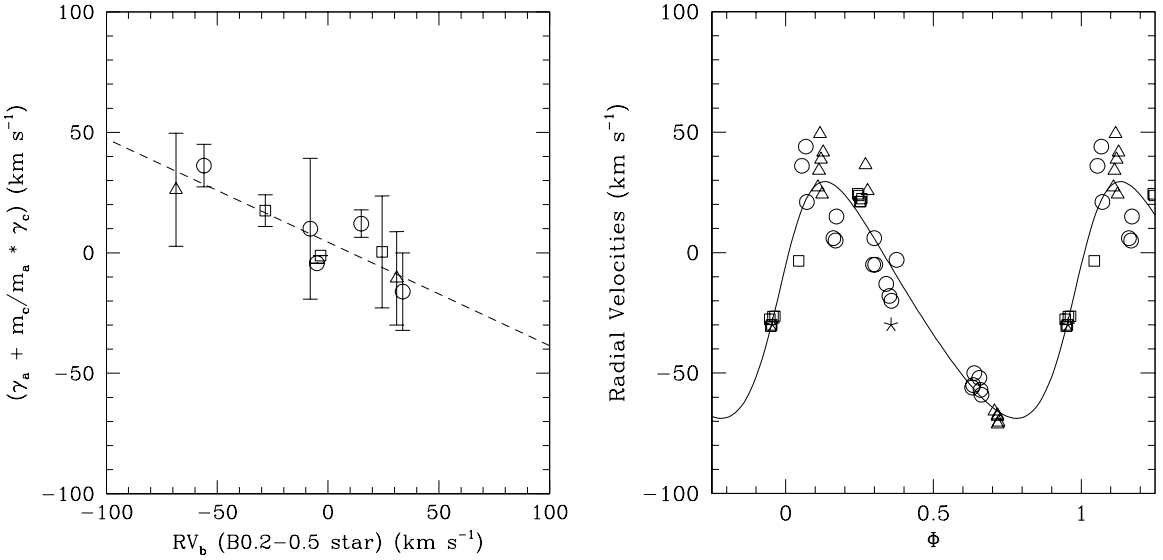

Figure 4. Left: plot of the systemic velocity $\gamma_a + \frac{m_c}{m_a}\gamma_c$ as a function of the RV of the third star. The data points are average values over an observing run. Triangles, circles and squares stand for data obtained respectively with the B&C, REOSC and FEROS instruments. Right: radial velocities of the third component as a function of phase, adopting a period of 285.1 d and assuming $T_0^{\rm out} = 2450174.6$. The continuous line corresponds to the eccentric solution described below (Table 6). The symbols have the same meaning as in the left panel except for the asterisks that indicate rough estimates of the RV of the third component as derived from the cross-correlation functions of Howarth et al. (1997).

Table 5. Orbital solutions derived from the radial velocities of the components of the close binary ('a' + 'c'). The adopted orbital period is $P_{\rm orb}^{\rm in} = 2.15287$ d. Columns 2 and 3 yield the orbital elements derived from a least squares fit, without any a priori correction of the systemic velocity, whereas the last two columns list the orbital parameters obtained from a fit where the RVs have been corrected for the variations of the systemic velocity. The radii of the Roche lobes ($R_{\rm RL}$) are computed using the formula of Eggleton (1983).

	No correction		Corrected γ	
	Primary	Secondary	Primary	Secondary
γ (km s^{-1})	4.0 ± 4.6	-3.2 ± 5.9	-1.5 ± 3.9	-6.7 ± 5.1
K (km s^{-1})	215.3 ± 5.5	331.8 ± 8.4	212.9 ± 5.0	332.8 ± 7.8
$T_0^{\rm in}$ (JD–2450000)	1621.967 ± 0.008		1621.973 ± 0.006	
$a \sin i$ (R$_\odot$)	9.2 ± 0.1	14.1 ± 0.4	9.1 ± 0.1	14.2 ± 0.2
$m \sin^3 i$ (M$_\odot$)	22.2 ± 1.4	14.4 ± 0.9	22.1 ± 1.3	14.1 ± 0.8
$R_{\rm RL}/a_{\rm tot}$	0.417 ± 0.003	0.342 ± 0.003	0.418 ± 0.002	0.341 ± 0.002
$\overline{\lvert O-C \rvert}$ (km s^{-1})	23.1		20.5	

these variations are anti-correlated with the RV variations of the B0.2–0.5 star. Since the error bars on the individual data points are rather large, we averaged the results obtained during a given observing run. To further reduce the errors, we only included RV measurements of the close binary obtained near quadrature. Though the errors are still quite large, Fig. 4 reveals that the systemic velocity varies indeed roughly in anti-correlation with the velocity of the third star indicating that we are probably dealing with a genuine triple system. The dashed line in Fig. 4 yields the best-fitting orthogonal regression to the data excluding the B&C measurement that deviates the most from the general trend. If $\gamma_a = \gamma_c$, then our best-fitting relation corresponds to $(m_a + m_c)/m_b \simeq 3.8$. We caution that the latter result should be regarded only as a rough estimate of the actual mass ratio because of the rather large uncertainties on the radial velocity of the centre of mass of the close binary.

Coming back to the close binary and assuming that its orbit is circular, we obtain the orbital elements listed in Table 5 and the solution shown in Fig. 5. $T_0^{\rm in}$ corresponds to the conjunction with the most massive star (component 'a') being behind its companion. Our first solution was obtained without any correction for the changing systemic velocity. The corresponding orbital elements are in excellent agreement with the preliminary SB2 solution of Solivella & Niemela (1999). Part of the scatter around the orbital solution could result from the use of varying samples of lines from night to night (owing to the various spectral ranges observed). In fact, absorption lines in O-star spectra often show different systemic velocities because they form at different depths in an expanding atmosphere and this could introduce some scatter in the average RVs.

Since Levato et al. (1991) quoted an eccentricity of $e = 0.16 \pm 0.1$ for their SB1 orbit of Tr 16-104, we have also tested the assumption of an elliptical orbit, though the short orbital period seems to rule this out a priori. An eccentric orbital solution for the close binary yields $e = 0.02 \pm 0.02$ (1σ) which is clearly consistent with $e = 0$. The eccentric solution does not provide any improvement of the quality of the fit either. We conclude therefore that the orbit of the close binary system is indeed circular.

The eccentricity found by Levato et al. (1991) was most likely an artefact due to the fact that these authors did not resolve the spectral signatures of the three components of Tr 16-104. This result is not only important for the study of Tr 16-104 as an individual system, but is also relevant for the issue of the ($\log P_{\rm orb}$, e) diagram for OB stars in very young open clusters (e.g. Mermilliod 1996; Mason et al. 1998) and of the determination of the cut-off period below which most orbits are circular due to tidal circularization.

Using the least squares fit between the systemic velocity of the short period binary and the velocity of component 'b', we have also computed an orbital solution where the radial velocities of components 'a' and 'c' have been corrected for the variations of the 'instantaneous' systemic velocity. The results are also listed in Table 5. We see that the corresponding parameters are in excellent agreement with those obtained for the RV solution without correction for the γ velocity variations.

We note that the minimum masses of the two components are quite large which is a good indication that the orbital inclination must be large. In fact, if we compare the values of $m \sin^3 i$ of the primary and secondary components to the 'typical' masses of O7 V and O9.5 V stars as listed by Howarth & Prinja (1989), we derive an orbital inclination of 58° and 62° respectively. Therefore, it seems likely that the close binary system could display photometric eclipses.

Our data do not allow us to decide which of the two frequencies ν_3' or ν_4' provides the best estimate of the orbital period $P_{\rm orb}^{\rm out}$ of the B0.2–0.5 star. While the 1340.5-d period corresponds to a rather asymmetrical ($e \sim 0.37$) radial velocity curve, the 285.1-d period yields a moderate eccentricity of 0.25. We have computed preliminary orbital solutions for both periods which are given in Table 6. We caution however that the scatter around the best-fitting solutions remains quite large (compared to the amplitude K) and we have no means to chose definitively between the two possible orbital periods. One notices that the systemic velocity derived for the third component in the case of the 285.1-d period is in excellent agreement with the mean heliocentric radial velocity ($-23.5\,{\rm km\,s^{-1}}$) of stars in Tr 16 as derived by Levato et al. (1991).

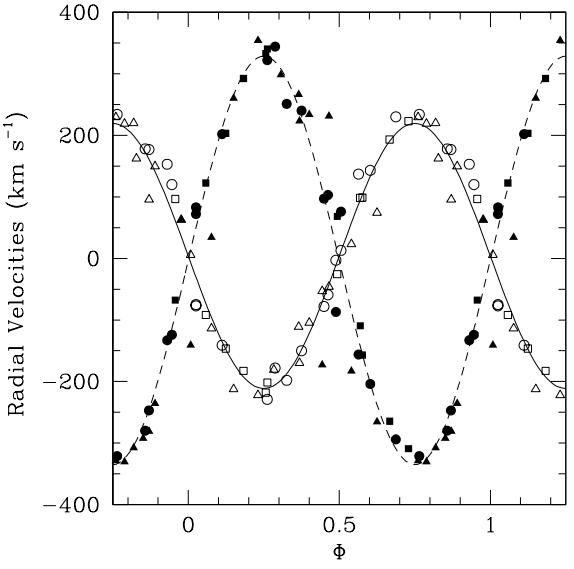

Figure 5. Orbital solution ($e = 0.0$) of the close binary for $P_{\rm orb}^{\rm in} = 2.15287$ days without correction of the systemic velocity. The symbols have the same meaning as in Fig. 4. Open and filled symbols stand for the primary (i.e. star 'a') and secondary (i.e. star 'c') respectively, while the solid and dashed lines show the corresponding best fitting solutions.

5 PHOTOMETRIC VARIABILITY

Inspection of our spectra reveals that the intensities of the lines of the B0.2–0.5 star vary as a function of time. We have measured the EWs of the least blended absorption lines of this star and plotted them as a function of the orbital phase of the close binary system. The result for the Si III λ 4552 and Si III λ 4568 lines is shown in Fig. 6. Though the typical errors of the EW measurements are of

Table 6. Orbital solution from the RVs of the B0.2–0.5-type star (component 'b') in the spectrum of Tr 16-104 assuming a period of 285.1 or 1340.5 days. $T_0^{\rm out}$ denotes the time of periastron passage and ω the longitude of periastron. $X_0^{\rm min}$ indicates the value of the stability criterion of Eggleton & Kiseleva (1995), see Section 6.3.

$P_{\rm orb}^{\rm out}$ (d)	285.1	1340.5
γ (km s^{-1})	-23.2 ± 1.5	-8.7 ± 1.5
K (km s^{-1})	49.1 ± 2.7	46.4 ± 1.7
e	0.25 ± 0.05	0.37 ± 0.04
ω (°)	287.0 ± 19.6	238.3 ± 8.1
$T_0^{\rm out}$ (JD–2450000)	174.6 ± 12.5	1264.8 ± 18.2
$a \sin i$ ($R_\odot$)	267.5	1129.6
$a \sin i$ (AU)	1.25	5.27
$f(m)$ ($M_\odot$)	3.20	11.2
$\overline{\lvert O-C \rvert}$ km s^{-1}	8.5	6.6
$X_0^{\rm min}$	29.7	35.4

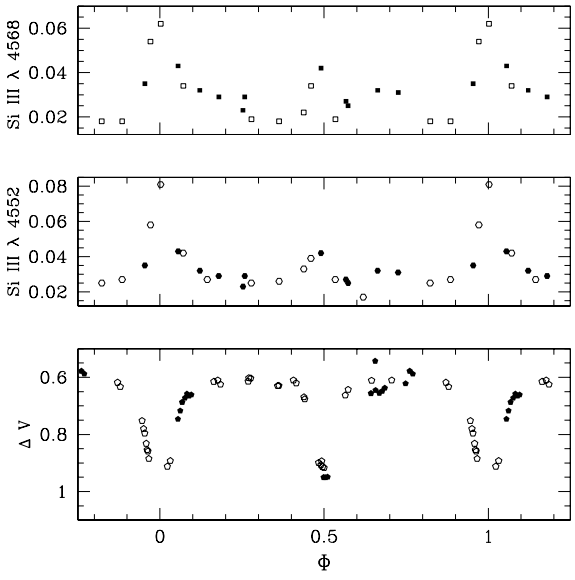

Figure 6. Top and middle panels: EWs (in Å) of two rather unblended absorption lines of component 'b' in the spectrum of Tr 16-104 as a function of the orbital phase of the close binary. Open and filled symbols stand for the EWs measured on the B&C and FEROS spectra respectively. Lower panel: V-band light curve of Tr 16-104 as derived from the data of Antokhin & Cherepashchuk (1993) assuming an orbital period of 2.15287 days. The photometric data are given as differential magnitudes with respect to HDE 303308. The open and filled symbols in the V light curve stand for the 1980 and 1991 data respectively.

the order of 0.005 Å near maximum EW and about twice as large near minimum EW, we see a clear increase of the EWs at phases around 0.0 and 0.5, i.e. around conjunction of the close binary system. The most straightforward interpretation of this phenomenon is that the continuum light of the close binary (and hence the dilution of the B0.2–0.5 star's lines) is reduced at these phases because of photometric eclipses.

Antokhin & Cherepashchuk (1993) presented *UBV* photometry of a set of stars in the Carina complex including Tr 16-104. These data were gathered in 1980 and 1991 at the Siding Spring Observatory. The authors reported photometric variability of Tr 16-104 between two light levels with the brightness changes occurring over rather short time-scales. Antokhin & Cherepashchuk were not aware of the multiplicity of this system and although they considered the possibility of an eclipsing binary, they found it rather unlikely since the radii of the binary components had to be very small.

We have folded the data of Antokhin & Cherepashchuk (1993) using the 2.15290-d period derived from our RV time series. The resulting light curve displays two rather narrow eclipses around the conjunction phases. We find a slight shift in phase between the eclipses and the conjunctions ($\Delta\Phi \simeq 0.044$) for this value of the period. This shift is extremely small given that half of the photometric data were taken about 15 yr (i.e. more than 2500 cycles!) before our spectroscopic data were obtained. From the preliminary orbital solution of the third component and assuming that star 'b' is indeed bound to the close binary, we find that the changes in the projected distance result in a light time effect with a peak-to-peak amplitude of about 1400 s at most (for $P_{\rm orb}^{\rm out} = 1340.5$ d). This translates into a phase shift for the minima of the eclipsing binary of 0.007. Therefore, we can safely rule out the light time effect as the origin of the $\Delta\Phi \simeq 0.044$ phase difference. The most likely reason for this shift is therefore a small error on the orbital period. Unfortunately a period search on the photometric time series is not very helpful in this case because of the huge number of aliases that have the same importance. We found however that a period of 2.15287 d allows us to simultaneously fit the light curve and the RV solution and we therefore used this period to derive the ephemerides of the close binary in Section 4.2. The *V* light curve obtained by folding the Antokhin & Cherepashchuk (1993) data according to the ephemeris

$$\mathrm{HJD}(\Phi = 0) = 245\,1621.973 + 2.152\,87E$$

is shown in Figs 6 and 7. We estimated the typical uncertainties from the 1σ dispersion of the differential magnitudes of HD 93204 with respect to HDE 303308 as observed by Antokhin & Cherepashchuk. In this way, we obtain estimates of the uncertainties on the individual data points of $(\sigma_U, \sigma_B, \sigma_V) = (0.033, 0.022, 0.020)$ and (0.051, 0.044, 0.046) for the 1980 and 1991 data respectively.

Although the light curve is somewhat sparse, we can nevertheless use it to derive constraints on the physical parameters of the components of the close binary in Tr 16-104. In fact, we notice that the eclipses are rather narrow and there is no evidence for a strong phase-locked photometric variability outside the eclipses unlike what would be expected for a contact or semi-detached binary. This is strong evidence that both components of the close binary should have rather spherical shapes and must be well inside their Roche lobes.

From the light curve, we find that the full width of both eclipses is about 0.164 in phase. At the 'first contact' (i.e. when the projections of the stars on the plane of the sky touch for the first time), the projected separation of the centres of the stars is equal to the sum of their radii. If the stars are indeed spherical, this condition can be expressed by the relation

$$R_{\rm a} + R_{\rm c} = a_{\rm tot}(1 - \sin^2 i \cos^2\theta_1)^{1/2}$$

where θ_1 is the position angle (with respect to conjunction) of the stars at first contact. The *UBV* light curves yield $\theta_1 \simeq 29\overset{\circ}{.}5$. From our orbital solution, we obtain

$$R_{\rm a} + R_{\rm c} = 23.3(1 - 0.758\sin^2 i)^{1/2}(\sin i)^{-1}$$

where the radii are given in $\mathrm{R}_\odot$. This relation expresses a model-independent constraint on the absolute dimensions of the stars. However, we caution that this is only valid if the stars have a roughly spherical shape, i.e. if they are well inside their Roche lobes (which seems to be the case for the components of the close binary in Tr 16-104).

Assuming that stars 'a' and 'c' were in synchronous rotation, the projected rotational velocities derived by Howarth et al. (1997), yield $R_a/R_c = 1.48$, $R_a \sin i = 6.96\,\mathrm{R}_\odot$ and $R_c \sin i = 4.71\,\mathrm{R}_\odot$. Comparison of the latter values with the first contact relation requires a rather large inclination of $\sim 83\overset{\circ}{.}8$ and hence very small radii. If we assume that the ratio of the radii of the components is indeed given by $R_a/R_c = 1.48$, we find that the first contact relation yields a radius of the secondary that is always smaller than the radius of its Roche lobe provided that $i \geq 37\overset{\circ}{.}5$, whereas the primary is only inside its Roche lobe for $i \geq 55\overset{\circ}{.}3$ (see Fig. 8). The validity of the first contact relation is thus restricted to $i > 55°$. For inclinations between 55° and 90°, the sum of the radii varies between 19.9 and $11.5\,\mathrm{R}_\odot$. This result clearly demonstrates that the components of the close binary must be on the main sequence, in very good agreement with our luminosity classification hereabove.

To proceed one step further, we have calculated a grid of synthetic light curves using the numerical code of Antokhina

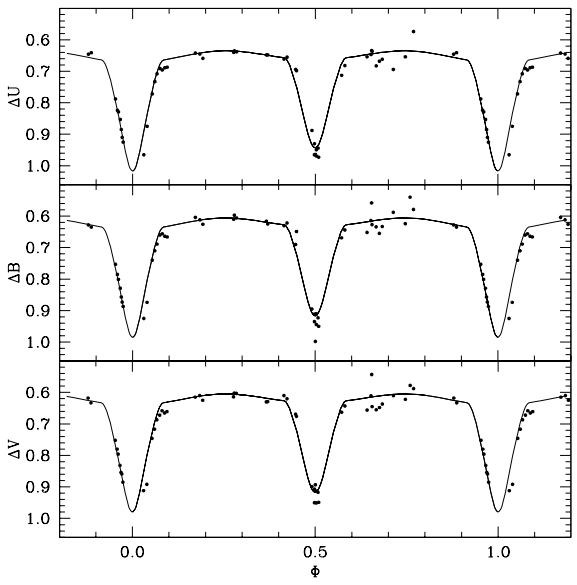

Figure 7. Best fitting synthetic light curves for $i = 82\overset{\circ}{.}5$ compared to the *UBV* photometric data of Antokhin & Cherepashchuk (1993).

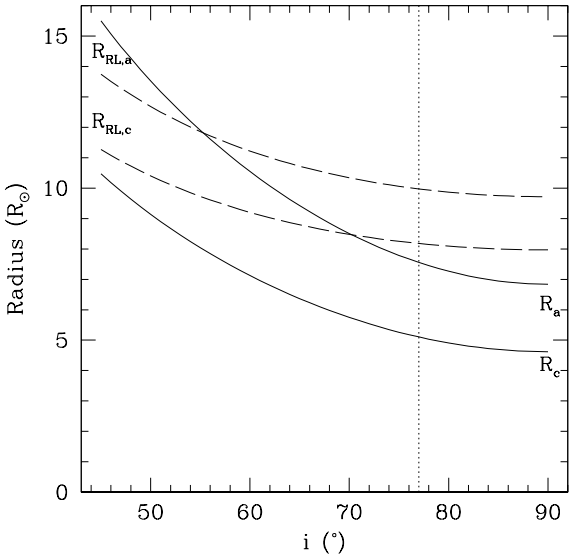

Figure 8. Constraints on the radii and the inclination of the close binary system in Tr 16-104 as derived from the first contact relation. The continuous lines yield the radii of the O7 V primary and the O9.5 V secondary assuming $R_a/R_c = 1.48$, whilst the dashed lines indicate the radii of the Roche lobe of the primary and secondary as calculated from our orbital solution (Table 5). The dotted vertical line corresponds to the minimum inclination of the orbit as derived from our best fitting models of the light curve (see text).

Table 7. Absolute parameters of the O7 V + O9.5 V close binary in Tr 16-104 as derived from the best fitting light curve model at $i = 82.^\circ5$. The third light contribution was assumed to be $l_b = 0.14$ in all three filters. R stands for the mean radius (slightly larger than the polar radius, R^P) of the star.

	Primary	Secondary	
$T_{\rm eff}$ (K)	37500	32750	adopted
i	$82.^\circ5$		
m ($M_\odot$)	22.7	14.5	
μ	0.75 ± 0.10	0.65 ± 0.07	
R ($R_\odot$)	7.11 ± 0.94	4.93 ± 0.53	
$v_e \sin i$ (km s^{-1})	166	115	
$\log(L_{bol}/L_\odot)$	4.96	4.41	
M_{bol}	−7.65	−6.27	

(1988) (see also Antokhina et al. 2000). Adopting the calibration of Humphreys & McElroy (1984), we fixed the effective temperatures of the primary and the secondary at $T^a_{\rm eff} = 37500$ K and $T^c_{\rm eff} = 32750$ K respectively. Assuming a typical uncertainty of half a spectral type, these effective temperatures should be accurate within about 1500 K for the primary and 1250 K for the secondary. We further assumed that the stars are in synchronous rotation and we adopted a third light contribution of $l_b = 0.14$. The albedo ($A^a = A^c = 1.0$, Wilson 1994) and gravity darkening coefficients ($\beta^a = \beta^c = 0.25$, von Zeipel 1924) were fixed and we adopted a square-root limb darkening law (Diaz-Cordovés & Giménez 1992) with the corresponding coefficients taken from the work of van Hamme (1993). Finally, the orbital parameters were taken from our corrected-γ orbital solution in Table 5. Therefore, the only remaining free parameters are the orbital inclination i and the Roche lobe filling factors[4] of the two stars μ_a and μ_c.

In our grid of models, we generated theoretical *UBV* light curves for $i \in [50^\circ, 90^\circ]$ with a step $\Delta i = 2^\circ$ up to $i = 78^\circ$ and $\Delta i = 0.^\circ5$ between $i = 78^\circ$ and $i = 90^\circ$. The Roche lobe filling factors were varied in the range $\mu_a, \mu_c \in [0.1, 1.0]$ with $\Delta\mu = 0.05$. The synthetic light curves in all three filters were compared to the observations of Antokhin & Cherepashchuk (1993). We find that the best-fitting models with $i \geq 79^\circ$ have almost identical χ^2-values. At the 99 per cent confidence level, all values of the inclination in the range $i \in [77^\circ, 90^\circ]$ are acceptable. We remind the reader that these results were obtained under a number of assumptions (e.g. synchronous rotation, adopted effective temperatures) and depend also on the actual value of the third light contribution. Some additional uncertainties might result from the poor phase coverage of the observed light curve around the primary minimum. However, the conclusion that the orbital inclination must be larger than $\sim 75^\circ$ is quite robust. In fact, below this inclination, the synthetic light curves predict that the bulk of the photometric variability should be owing to the ellipticity of the components rather than to genuine eclipses and this is clearly not the case for the close binary in Tr 16-104. We will discuss the implications of these results in Section 6.1.

The lowest χ^2 value was obtained for $i = 82.^\circ5$, $\mu_a = 0.75$ and $\mu_c = 0.65$. The corresponding absolute parameters of the close binary are listed in Table 7 and the model light curves are shown in Fig. 7. We emphasize the almost perfect agreement between the projected rotational velocities derived from our best-fitting light curve model and those measured by Howarth et al. (1997) and listed in Table 1 above.

6 DISCUSSION

6.1 Fundamental parameters

Several authors obtained photometric measurements of Tr 16-104 (Antokhin & Cherepashchuk 1993; Massey & Johnson 1993; Kaltcheva & Georgiev 1993). In the Antokhin & Cherepashchuk (1993) data, the differential magnitude of Tr 16-104 outside eclipse with respect to HDE 303308 is $\Delta V \simeq 0.64$. From the results of Massey & Johnson (1993), we derive a differential magnitude of 0.63, whereas the photometry of Kaltcheva & Georgiev (1993) yields $\Delta V = 0.74$. Therefore, it seems likely that the data of Kaltcheva & Georgiev were affected by the eclipse of the close binary. In the following, we adopt a V magnitude of 8.82 as obtained by Massey & Johnson. Splitting the total brightness of the system according to the spectroscopic brightness ratios derived hereabove, we infer magnitudes of $m^a_V = 9.39$, $m^b_V = 10.95$ and $m^c_V = 10.24$. The distance of the Tr 16 cluster remains a controversial issue. Using *UBV* photometry, Massey & Johnson (1993) obtained a distance modulus of $DM = 12.49 \pm 0.09$. On the other hand, Kaltcheva & Georgiev (1993) derived the distance of individual stars in Tr 16 from the relation between the Strömgren β index and the absolute magnitude M_V (Balona & Shobbrook 1984). Assuming a normal extinction law, these authors found a large dispersion in the distance moduli that might reflect a real range in distance. Since the line of sight towards Tr 16 is almost parallel to the molecular cloud ridge in the Carina spiral arm, Kaltcheva &

[4] The Roche lobe filling factor $\mu = R^p/R^p_{\rm RL}$ corresponds to the ratio between the actual polar radius and the polar radius for complete filling of the Roche lobe (see Antokhina 1988).

Georgiev question the existence of an open cluster and suggest that the stars could rather lie along an extended star formation region which is projected on a small area on the sky. For Tr 16-104, Kaltcheva & Georgiev (1993) derived $DM = 13.24$ from their Strömgren photometry. However, as pointed out hereabove, the data of Kaltcheva & Georgiev were most probably obtained during an eclipse of the close binary and it is not clear how this affects the strength of the Hβ line and the corresponding β index.

As a first step, we assume that the distance modulus of Tr 16-104 amounts to 12.49 as suggested by Massey & Johnson (1993). Accounting for a colour excess $E(B-V) = 0.43$, we obtain absolute visual magnitudes of $M_V^{\rm a} = -4.5$, $M_V^{\rm b} = -2.9$ and $M_V^{\rm c} = -3.6$. Components 'a' and 'c' are about 0.5 mag fainter than expected for a typical O7 V and O9.5 V star (see e.g. Humphreys & McElroy 1984). An even larger discrepancy ($\sim$1.5 mag) holds for the B0.2-0.5 IV star. Of course, the most straightforward solution to this problem would be to adopt a larger distance modulus than suggested by Massey & Johnson (1993). As a second step we could therefore adopt the distance modulus $DM = 13.24$ as derived by Kaltcheva & Georgiev (1993). In this way, we obtain absolute visual magnitudes of $M_V^{\rm a} = -5.2$, $M_V^{\rm b} = -3.7$ and $M_V^{\rm c} = -4.4$, slightly brighter than for typical stars of the same spectral type. However, such a large distance leads to a large discrepancy with the results of our light-curve analysis (see below).

Alternatively there could be a problem with the absolute magnitude–spectral type calibration. Lamers et al. (1997) discussed the absolute visual magnitude of a sample of OB V-III stars as determined from the parallaxes measured by *Hipparcos*. Slowly rotating stars (i.e. $v_{\rm e} \sin i < 100\,{\rm km\,s^{-1}}$) were found to be fainter by up to 1.5 mag than the standard M_V-spectral type relation, whereas the differences were much smaller for rapid rotators of the same spectral type. Lamers et al. (1997) attributed this phenomenon to the influence of rotation on the assignment of the luminosity class. In the case of the O7 V and O9.5 V stars in Tr 16-104, we are dealing with rather fast rotators (in the terminology of Lamers et al. 1997) and we expect therefore a priori that this effect should be small. However, the influence of rotation could be considerably larger for the B0.2–0.5 IV component ($v_{\rm e} \sin i = 59\,{\rm km\,s^{-1}}$) and this could probably account for part of the larger discrepancy found for this star. In fact, comparing the absolute magnitude of star 'b' to the *Hipparcos* absolute magnitude of ϕ^1 Ori (B0.2 IV, $v_{\rm e} \sin i = 39\,{\rm km\,s^{-1}}$, $M_V = -3.39$, Lamers et al. 1997), the discrepancy is reduced to about 0.5 mag which is pretty much the same value than for the other components of Tr 16-104.

Now, a more serious dilemma arises if we compare the bolometric luminosities derived from our light curve analysis with those obtained for the two values of the distance modulus and adopting the bolometric corrections of Humphreys & McElroy (1984). In fact, the bolometric luminosities of the O7V and O9.5V stars corresponding to the Massey & Johnson (1993) distance modulus would be $\log L_{\rm bol}^{\rm a}/{\rm L}_\odot = 5.14$ and $\log L_{\rm bol}^{\rm c}/{\rm L}_\odot = 4.64$. These values are about 50 per cent larger than those derived from the light curve analysis (Table 7). Of course, adopting the Kaltcheva & Georgiev (1993) distance will increase this discrepancy to about a factor 3. If the bolometric corrections are correct, then the luminosities derived from our light curve analysis suggest a distance of about 2.5 kpc for Tr 16-104, in agreement with the recent determination of the distance of the eclipsing binary Tr 16-1 ($\equiv$CPD -59° 2628) by Freyhammer et al. (2001). In this context, we emphasize that the complex structure of the interstellar absorption lines in the spectrum of Tr 16-104 demonstrates that the star is either behind or immersed in the region where the interstellar lines originate. The fact that we observe interstellar He I absorptions further indicates that this star is inside a hot gas bubble. Therefore Tr 16-104 must be at the same distance as most of the stars of the Tr 16 cluster. Walborn (1995) pointed out that the distance determinations of the open clusters in the Car OB1 association are in fact very sensitive to the assumption on the ratio R of total-to-selective extinction. Indeed, the results of Walborn (1995) indicate that for $R = 3$ and 4, the distance of Tr 16-104 would be respectively 2.8 and 2.25 kpc. Walborn (1995) further noted that the inclusion of a number of main-sequence O and B stars, that might be closer to the ZAMS – and hence less luminous – than the 'typical' calibrators, could artificially raise the distance modulus as determined by Massey & Johnson (1993). Finally it is worth mentioning that a spectroscopic study of the Homunculus Nebula by Davidson et al. (2001) yielded a distance of 2250 ± 180 pc for η Car which is believed to be associated with Tr 16.

The low luminosities of the stars as inferred from the light curve stem from the fact that the radii of the O7V and O9.5V components that we derived in Section 5 are surprisingly small. As stated above, the values of the Roche lobe filling factors inferred from the light curve analysis depend on several assumptions that are difficult to check. Nevertheless, the rather large orbital inclination ($i \geq 77^\circ$ at the 99 per cent confidence level) and the first contact relation (see Fig. 8) obviously imply radii and luminosities that are certainly much smaller than the 'typical' values listed by Howarth & Prinja (1989) or than the radii inferred from the analysis of a sample of interacting (and probably more evolved) O-star binaries (Harries, Hilditch & Hill 1998). In this context, it is interesting to point out that the analyses of the light curves of HD 93205 (Antokhina et al. 2000), ι Orionis (Marchenko et al. 2000) and Tr 16-1 (Freyhammer et al. 2001) also yield radii that are comparatively small for the spectral types and luminosity classes inferred from the spectroscopic data. The light variations in HD 93205 and ι Ori are due to the changing shapes of the stars during the eccentric orbit rather than to geometric eclipses and the uncertainties on the orbital inclination and hence on the radii are thus somewhat larger than in our case. Tr 16-1, on the other side, was found to be an eclipsing binary system consisting of an O9.5 V primary and a B0 V secondary and the parameters of the O9.5 V star in Tr 16-1 as derived by Freyhammer et al. (2001) are in excellent agreement with those of the O9.5 V secondary in Tr 16-104 (star 'c'). Our results for the close binary in Tr 16-104 as well as the results of Freyhammer et al. (2001) suggest therefore that the luminosities of main-sequence O-stars in very young clusters such as Tr 16 could be systematically smaller than usually believed. These results are in line with the conclusions of Lamers et al. (1997) and cast some doubt on distance determinations using the 'standard' M_V – spectral type calibration. In this context, we point out that Walborn & Blades (1997) reported the existence of a number of subluminous so-called O Vz stars among the youngest objects of the 30 Doradus complex. The O Vz stars stand out through a very strong He II λ 4686 absorption line and Walborn & Blades (1997) suggested that they are nearer to the ZAMS than more luminous 'typical' O V stars.

6.2 X-ray data

So far, Tr 16-104 has not been detected at X-ray energies. Seward & Chlebowski (1982) only quoted an upper limit of $0.23 \times 10^{-3}\,{\rm count\,s^{-1}}$ on the *EINSTEIN*-HRI count rate. The XMEGA observation (rh202331) provides the deepest *ROSAT*-HRI pointing on the Carina region including Tr 16-104. We have analysed these

data with the XSELECT software (v1.4b). Inside a radius of 40 arcsec around the position of Tr 16-104, we obtain a net background-corrected HRI count rate of $\sim 1.55 \times 10^{-3}$ count s^{-1} which corresponds to a marginal detection against the strong diffuse X-ray emission from the Carina Nebula. Assuming a thermal plasma model (Raymond & Smith 1977) of temperature $kT = 0.5$ keV and adopting the interstellar H I column density of $N_{\rm H} = 2.9 \times 10^{21}$ cm^{-2} (Diplas & Savage 1994), we derive a dereddened flux of 9.5×10^{-14} erg cm^{-2} s^{-1} in the 0.5–2.0 keV energy range. Adopting a distance of 2.5 kpc (see Section 6.1), we infer $L_{\rm x} = 7.0 \times 10^{31}$ erg s^{-1}. Using the bolometric luminosities derived from our light curve solution yields $\log L_{\rm x}/L_{\rm bol} = -6.85$. The latter value is in excellent agreement with the predicted ratio $\log L_{\rm x}/L_{\rm bol} = -6.90$ between the sum of the individual X-ray luminosities of components 'a' and 'c' compared to the sum of their bolometric luminosities. The theoretical X-ray luminosities of star 'a' and 'c' were derived from the empirical $\log L_{\rm x}/L_{\rm bol}$ relation for single OB stars proposed by Berghöfer et al. (1997). Therefore, we conclude that there is no indication of any significant X-ray emission that could be attributed to a colliding wind interaction in Tr 16-104, but this is not surprising for a close binary consisting of two main-sequence stars (Chlebowski & Garmany 1991).

6.3 The multiplicity of Tr 16-104

Let us briefly return to the cross-identification of the optical and UV components of the system. Extrapolating our ephemerides back to the epoch of the *IUE* observations, we obtain predicted radial velocities of $\mathrm{RV_a} = 206$ km s^{-1} and $\mathrm{RV_c} = -331$ km s^{-1} for SWP7022 (JD 244 4174.737, $\Phi = 0.787$) as well as $\mathrm{RV_a} = 151$ km s^{-1} and $\mathrm{RV_c} = -244$ km s^{-1} for SWP7988 (JD 244 4289.024, $\Phi = 0.873$). Comparing these results with the cross-correlation functions of Howarth et al. (1997) (see their fig. 2), we find that the RVs of their component 'A' is in good agreement with our component 'a', whereas we find a rough agreement between our component 'c' and star 'C' in the Howarth et al. naming. The RVs of star 'B' are also in rough agreement with those expected from our preliminary ephemerides of star 'b' (see Fig. 4). A slight discrepancy is not surprising given the preliminary nature of the orbital solution and the large uncertainties on the orbital period of this star. All in all, the comparison between our ephemerides and the *IUE* data further confirms our cross-identification initially based on the relative widths and strengths of the lines (Section 3).

Our data discussed here provide some evidence that the third component is physically related to the system. In fact, the radial velocity of star 'b' varies with a 'period' of 285.1 or 1340.5 d. Though we cannot completely rule out that Tr 16-104 could be a quadruple (or line of sight binary + binary) system consisting of an SB2 binary ('a' + 'c') with an orbital period of 2.15 d and an SB1 ('b' + ?) with a longer period, the fact that the variations of the close binary's γ systemic velocity are essentially anti-correlated with those of the third component indicates that Tr 16-104 is most probably a hierarchical triple system. The mass of star 'b' inferred from this anti-correlation and the best-fitting parameters of the close binary (Table 7) would be 9.8 $\mathrm{M}_{\odot}$. We emphasize that we found no spectral indication of any additional component in our present data.

So far there are only a few other examples of hierarchical multiple systems containing early-type stars. HD 167971 consists of a close O-type eclipsing binary ($P_{\rm orb}^{\rm in} = 3.3$ d) and a third more distant Of companion that dominates the optical and UV spectrum and could actually be a line-of-sight object (Leitherer et al. 1987).

Niemela, Seggewiss & Moffat (2001) found that Sk-67° 18 in the LMC is a multiple system harbouring at least two pairs of short-period binaries (an O3f* + O binary with $P_{\rm orb} = 2.001$ d and another system with $P_{\rm orb} = 19.3$ d). However, the physical connection between these binaries is not clear and they could just lie along the same line of sight.

SZ Cam (Lorenz, Mayer & Drechsel 1998; Harries et al. 1998) consists of an O9 IV+B0.5 V eclipsing binary ($P_{\rm orb}^{\rm in} = 2.7$ d) that is physically bound ($P_{\rm orb}^{\rm out} \sim 50$–$60$ yr) to a third component which is itself a short-period SB1 binary. A visual companion (which is also a binary) seems also related to the system, bringing the total number of stars in this system to six.

The τ CMa system (van Leeuwen & van Genderen 1997) is slightly more similar to Tr 16-104. This system consists of a close eclipsing binary ($P_{\rm orb}^{\rm in} = 1.3$ d) connected in an eccentric orbit ($e = 0.3$, $P_{\rm orb}^{\rm out} = 155$ d) to a third component. However, the fundamental parameters of the stars in τ CMa are rather poorly constrained since this system remains so far an SB1 binary with no indication of the spectral signature of the other two stars.

IU Aur is believed to be a genuine triple system consisting of a semi-detached B0.5+B0.5 binary with a period of 1.9 d and a gravitationally bound tertiary with a period of $P_{\rm orb}^{\rm out} = 294$ d. However, the third component has been resolved by speckle interferometry (Mason et al. 1998) and this suggests that the system might actually be quadruple (see Harries et al. 1998). Therefore, the properties of Tr 16-104 (eclipsing 'SB3' system) make this system a rather unique example of its kind that deserves more studies (especially long-term monitoring of the third component).

N-body simulations indicate that hierarchical triple systems and double binaries can be produced by collisions of hard binaries in open clusters (e.g. Leonard & Duncan 1990; Kiseleva et al. 1996), although clusters consisting of a large number of stars have an aversion to forming triple systems (Leonard & Duncan 1990). Kaltcheva & Georgiev (1993) argued that the stars in Tr 16 are not members of a real open cluster but belong rather to a huge stellar complex seen in projection on the line of sight. As pointed out in Section 6.1, the distance towards Tr 16-104 is most probably significantly smaller than the value suggested by Kaltcheva & Georgiev and the interstellar spectrum suggests that Tr 16-104 is located at the same distance as most of the stars of Tr 16. Alternatively, it could be that Tr 16-104 came out of a small compact cluster or that the third component was formed from the outer circumstellar envelope of the protostellar cloud of the close binary.

Hierarchical triple systems may be quite stable for significant times if the external perturbations are small. According to Eggleton & Kiseleva (1995), hierarchical systems are stable provided that their configuration is such that $P_{\rm orb}^{\rm out}/P_{\rm orb}^{\rm in} \geq X_0^{\rm min}$ where $X_0^{\rm min}$ is a function of the mass ratios $q_{\rm in} = m_{\rm a}/m_{\rm c}$ and $q_{\rm out} = (m_{\rm a} + m_{\rm c})/m_{\rm b}$ and the eccentricities of the inner and outer orbits. Substituting our orbital parameters of Tr 16-104 into the stability criterion of Eggleton & Kiseleva (1995), we obtain the results listed in Table 6. Obviously a system such as Tr 16-104 with $P_{\rm orb}^{\rm out}/P_{\rm orb}^{\rm in} \simeq 132 \gg X_0^{\rm min} = 29.7$ (assuming an outer orbital period of 285.1 d) or $P_{\rm orb}^{\rm out}/P_{\rm orb}^{\rm in} \simeq 623 \gg X_0^{\rm min} = 35.4$ (assuming an outer orbital period of 1340.5 d) should form a stable configuration.

7 CONCLUSIONS

We have shown that Tr 16-104 could be a rather rare case of a hierarchical triple system consisting of an eclipsing binary bound

to a third component in a slightly eccentric orbit. This system offers an interesting opportunity for studying the fundamental parameters of unevolved early-type main-sequence stars. In fact, we have shown that the components of the close binary must be well inside their Roche lobes and therefore, their parameters are most probably not yet affected by evolution through mass transfer. Our analysis of the photometric data yields a lower limit on the inclination of the orbital plane of the close binary of $i \geq 77°$. The corresponding stellar radii and luminosities are significantly smaller than usually believed for stars of the same spectral type. This conclusion points towards a problem in the absolute magnitude versus spectral type calibration for O-stars and accurate distance determinations from future astrometric observations (e.g. with ESA's planned *GAIA* satellite) should help to clarify this situation. Our results suggest that Tr 16-104 (and probably also the Tr 16 cluster) lies at a distance of the order of 2.5 kpc i.e. slightly closer than the mean distance of Tr 16 as suggested by Massey & Johnson (1993). The triple system Tr 16-104 could either have emerged from a single protostellar cloud or alternatively it could have been formed by the collision of a hard binary either with a single star or with another binary in the Tr 16 open cluster. In the latter case, the fourth star would probably have been dynamically ejected from the system (Leonard & Duncan 1990).

ACKNOWLEDGMENTS

This paper is based on observations collected at the European Southern Observatory, La Silla (Chile) and the Complejo Astronómico El Leoncito (Argentina). We are greatly indebted to Dr E. A. Antokhina for providing her code for the lightcurve analysis. We thank Dr N. R. Walborn for discussion and the referee Dr D. R. Gies for helpful comments. GR, HS, EG, IA and JMV acknowledge support by the Fonds National de la Recherche Scientifique (Belgium), by contract P4/05 'Pôle d'Attraction Interuniversitaire' (SSTC-Belgium) and by the PRODEX XMM-OM and INTEGRAL projects. NIM, VSN and JFAC acknowledge use at CASLEO of the CCD and data acquisition system supported under US NSF grant AST-90-15827 to R. M. Rich and wish to thank the director and staff of CASLEO for the use of their facilities and kind hospitality during several observing runs. The SIMBAD data base has been consulted for the bibliography.

REFERENCES

Antokhin I. I., Cherepashchuk A. M., 1993, Astron. Rep., 37, 152
Antokhina E. A., 1988, SvA, 32, 608
Antokhina E. A., Moffat A. F. J., Antokhin I. I., Bertrand J.-F., Lamontagne R., 2000, ApJ, 529, 463
Balona L. A., Shobbrook R. R., 1984, MNRAS, 211, 375
Berghöfer T. W., Schmitt J. H. M. M., Danner R., Cassinelli J. P., 1997, A&A, 322, 167
Chlebowski T., Garmany C. D., 1991, ApJ, 368, 241
Conti P. S., 1973a, ApJ, 179, 161
Conti P. S., 1973b, ApJ, 179, 181
Conti P. S., Alschuler W. R., 1971, ApJ, 170, 325
Corcoran M. F., Pittard J. M., Marchenko S. V., 1999, in van der Hucht K. A., Koenigsberger G., Eenens P. R. J., eds, Proc. IAU Symp. 193, Wolf-Rayet Phenomena in Massive Stars and Starburst Galaxies. Astron. Soc. Pac., San Francisco, p. 772
Danks A. C., Walborn N. R., Vieira G., Landsman W. B., Gales J., García B., 2001, ApJ, 547, L155
Davidson K., Smith N., Gull T. R., Ishibashi K., Hillier D. J., 2001, AJ, 121, 1569
Diaz-Cordovés J., Giménez A., 1992, A&A, 259, 227
Didelon P., 1982, A&AS, 50, 199
Diplas A., Savage B. D., 1994, ApJS, 93, 211
Eggleton P. P., 1983, ApJ, 268, 368
Eggleton P. P., Kiseleva L. G., 1995, ApJ, 455, 640
Feinstein A., Marraco H. G., Muzzio J. C., 1973, A&AS, 12, 331
Freyhammer L. M., Clausen J. V., Arentoft T., Sterken C., 2001, A&A, 369, 561
Gosset E., Royer P., Rauw G., Manfroid J., Vreux J.-M., 2001, MNRAS, in press
Harries T. J., Hilditch R. W., Hill G., 1998, MNRAS, 295, 386
Heck A., Manfroid J., Mersch G., 1985, A&AS, 59, 63
Howarth I. D., Prinja R. K., 1989, ApJS, 69, 527
Howarth I. D., Siebert K. W., Hussain G. A. J., Prinja R. K., 1997, MNRAS, 284, 265
Humphreys R. M., McElroy D. B., 1984, ApJ, 284, 565
Kaltcheva N. T., Georgiev L. N., 1993, MNRAS, 261, 847
Kaufer A., Stahl O., Tubbesing S., Nørregaard P., Avila G., François P., Pasquini L., Pizzella A., 1999, The Messenger, 95, 8
Kiseleva L. G., Aarseth S. J., Eggleton P. P., de La Fuente Marcos R., 1996, in Milone E. F., Mermilliod J.-C., eds, ASP Conf. Ser. 90, The Origins, Evolutions and Destinies of Binary Stars in Clusters. Astron. Soc. Pac., San Francisco, p. 433
Lafler J., Kinman T. D., 1965, ApJS, 11, 216
Lamers H. J. G. L. M., Harzevoort J. M. A. G., Schrijver H., Hoogerwerf R., Kudritzki R. P., 1997, A&A, 325, L25
Leitherer C. et al., 1987, A&A, 185, 121
Leonard P. J. T., Duncan M. J., 1990, AJ, 99, 608
Levato H., Malaroda S., Morrell N., Garcia B., Hernández C., 1991, ApJS, 75, 869
Lorenz R., Mayer P., Drechsel H., 1998, A&A, 332, 909
Marchenko S. V. et al., 2000, MNRAS, 317, 333
Mason B. D., Gies D. R., Hartkopf W. I., Bagnuolo W. G, Jr., ten Brummelaar T., McAlister H. A., 1998, AJ, 115, 821
Massey P., Johnson J., 1993, AJ, 105, 980
Mathys G., 1988, A&AS, 76, 427
Mermilliod J.-C., 1996, in Milone E. F., Mermilliod J.-C., eds, ASP Conf. Ser. 90, The Origins, Evolutions and Destinies of Binary Stars in Clusters. Astron. Soc. Pac., San Francisco, p. 95
Niemela V. S., Seggewiss W., Moffat A. F. J., 2001, A&A, 369, 544
Rauw G., Sana H., Gosset E., Vreux J.-M., Jehin E., Parmentier G., 2000, A&A, 360, 1003
Raymond J. C., Smith B. W., 1977, ApJS, 35, 419
Seward F. D., Chlebowski T., 1982, ApJ, 256, 530
Solivella G. R., Niemela V. S., 1999, Rev. Mex. Astron. Astrofis. Ser. de Conf., 8, 145
Stickland D. J., 1997, The Observatory, 117, 37
Turatto M., Tighe R., Castillo R., 1997, ESO Technical Report, No. E15-TRE-ESO-22201-00001
Underhill A. B., 1995, ApJS, 100, 433
van Hamme W., 1993, AJ, 106, 2096
van Leeuwen F., van Genderen A. M., 1997, A&A, 327, 1070
von Zeipel H., 1924, MNRAS, 84, 684
Walborn N. R., 1973, ApJ, 179, 517
Walborn N. R., 1980, ApJS, 44, 535
Walborn N. R., 1982, ApJS, 48, 145
Walborn N. R., 1995, Rev. Mex. Astron. Astrofis. Ser. de Conf., 2, 51
Walborn N. R., Hesser J. E., 1975, ApJ, 199, 535
Walborn N. R., Fitzpatrick E. L., 1990, PASP, 102, 379
Walborn N. R., Blades J. C., 1997, ApJS, 112, 457
Walborn N. R. et al., 1998, ApJ, 492, L169
Wilson R. E., 1994, PASP, 106, 921

This paper has been typeset from a TEX/LATEX file prepared by the author.

1.2.1 Some additional results on binary systems in the Carina region

In this section, I summarize some additional results on early-type binaries and binary candidates in the Carina complex. I was actively involved in all of these studies.

Morrell et al. (2001) revised the orbital solution of the O3.5 V + O8 V binary system HD 93205, the only known Galactic SB2 system hosting an O3.5 V star. The orbital period of HD 93205 is 6.0803 day and the orbit is eccentric with $e = 0.37$. The most important results of this study are the rather high mass ratio $m_{\rm sec}/m_{\rm prim} = 0.42$ and the rather low minimum mass of the O3.5 V primary ($m_{\rm prim}\ \sin^3 i = 31\,{\rm M}_\odot$). If the secondary is a typical O8 V star (with a mass of 22 – 25 $\rm M_\odot$), then the actual mass of the O3.5 V star would amount to about 52 – $60\,{\rm M}_\odot$. Most of the consequences of these results were already discussed in Rauw (2004a, see Sect. 1.1). Another important point in the analysis of Morrell et al. (2001) was the detection of a significant apsidal motion with a period of 185 ± 16 yr, mainly due to tidal and rotational distortions.

Albacete Colombo et al. (2002) investigated the spectrum of Tr 16-110. They found that this system consists of at least three stars: an O7 V and an O8 V forming an SB2 binary with orbital period 3.628 days and an O9 V star that is an SB1 binary with a period of 5.034 days. Unlike the situation of Tr 16-104, in Tr 16-110, there are no apparent changes in the systemic velocity of the SB2 with the orbital period of the SB1 that could hint towards a physical link between the two binaries. It therefore seems likely that the system contains at least 4 stars: two belonging to the SB2 binary plus another two stars in the SB1 binary system for which we only see the brightest component in the combined spectrum.

Nazé et al. (2005) investigated yet another multiple system of the Carina complex. HD 93161 is a visual binary with a separation of 2 arcsec which is itself only 13 arcsec away from HD 93160. While HD 93161A was found to be an O8 V + O9 V SB2 binary system of orbital period 8.566 days, the status of HD 93161B is less clear. The latter star is of spectral type O6.5 V(f) and displays RV variations, but these could be due to atmospheric motions. Comparing the minimum masses derived from the SB2 orbital solution with evolutionary masses, Nazé et al. (2005) argued that the orbital inclination of HD 93161A could be large enough to allow eclipses. However, we found no indication whatsoever for photometric eclipses in the literature.

Finally, we note that neither Tr 16-110 nor HD 93161 present a large X-ray excess or flux variability that could hint towards a significant contribution of a colliding wind interaction to the X-ray emission of these stars. Using mass-loss recipes for HD 93161, Nazé et al. (2005) estimated that the colliding wind interaction in this system should produce a detectable X-ray emission. The non-detection of such an extra emission suggests that the mass loss rates of these stars could actually be lower than estimated from the theoretical Vink et al. (2000, 2001) formulae. This finding is in line with the results of Martins et al. (2005b) who found that for some O-type dwarfs the actual mass loss rates are indeed much lower than expected from the Vink et al. (2000, 2001) relation.

Based on 10 low-resolution spectra, Levato et al. (1991) reported Tr 16-112 to be an eccentric ($e = 0.23$), single-lined spectroscopic binary with an orbital period of 4.02 days. They classified the star as O4.5 V((f)). Five additional radial velocities were reported by Luna et al. (2003), but given the poor quality of their data, they did not improve the orbital solution of this system. During her undergraduate thesis under my supervision, Lanotte (2006) analysed a set of high-resolution high-quality FEROS spectra of this star collected by our group and detected for the first time the spectral signature of the companion. Indeed, weak secondary absorption features were found in the He I lines, while no trace of the secondary was seen in He II, pointing towards a B spectral type for this component. The orbital period was established to be $4.0155 \pm 5.8 \times 10^{-4}$ days and the detection of the secondary star allowed to derive the

Table 1.1: Orbital properties of the short-period spectroscopic binaries in the Carina complex (from Morrell et al. 2001, Albacete Colombo et al. 2002, Nazé et al. 2005 and Lanotte 2006).

System	P_{orb} (days)	e	ω (°)	K (km s^{-1})	$m \sin^3 i$ ($M_\odot$)	$a \sin i$ ($R_\odot$)	$f(m)$ ($M_\odot$)
HD 93205	6.0803	0.370 ± 0.005	50.8 ± 0.9	132.6 ± 2.0 313.6 ± 1.8	31.5 ± 1.1 13.3 ± 1.1	14.8 ± 0.3 35.0 ± 0.3	
Tr 16 − 110	3.6284	0.06 ± 0.03	355 ± 15	184 ± 4 192 ± 4	10.1 ± 1.0 9.7 ± 1.0	13.2 ± 0.2 13.7 ± 0.2	
	5.034	0.09 ± 0.04	209 ± 30	48 ± 5		4.8 ± 0.4	0.06 ± 0.02
HD 93161A	8.566	0.0		152.9 ± 1.7 200.6 ± 2.2	22.2 ± 0.6 17.0 ± 0.4	25.9 ± 0.2 33.9 ± 0.4	
Tr 16 − 112	4.0155	0.176 ± 0.009	355.3 ± 3.9	91.4 ± 0.9 328.1 ± 15.9	22.9 ± 2.1 6.4 ± 0.5	7.1 ± 0.1 25.6 ± 1.2	

very first SB2 orbital solution for Tr 16-112 (see Fig. 1.6) with a mass ratio $q = m_1/m_2 = 3.59 \pm 0.17$. The spectral type of the primary was determined to be O5.5-6 V((f)), whilst the parameters (mass and luminosity) of the secondary suggest a B2 V type for the latter component.

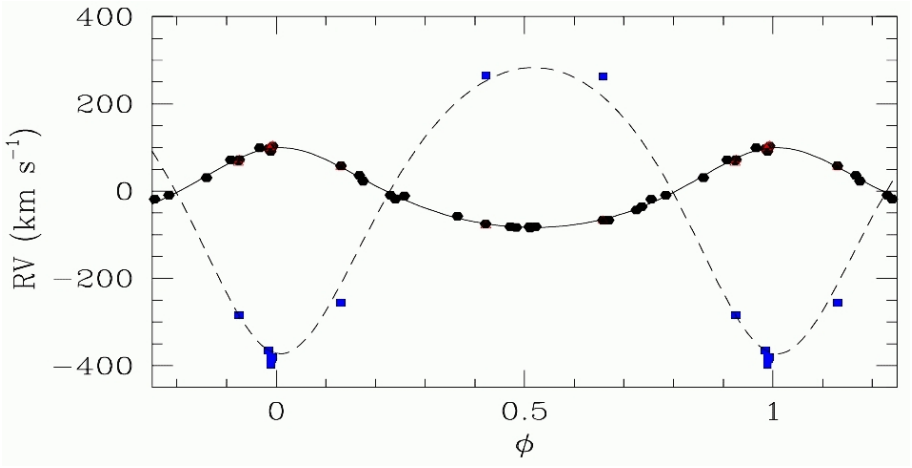

Figure 1.6: SB2 orbital solution of Tr 16-112. From Lanotte (2006).

In their study of the spectroscopic binaries in Trumpler 16, Levato et al. (1991) reported RV variations of HD 93343 (O8 Vn) although they could not provide firm evidence for the multiplicity of the star. Nine FEROS spectra of this star spread over four years were analysed by Lanotte (2006). These data revealed the SB2 nature of this star: one of the components of HD 93343 has narrow absorption lines (FWHM ~ 125 km s^{-1}), whilst the companion displays much broader lines (FWHM ~ 500 km s^{-1}!). The star with the sharper lines is of spectral type O8, whilst its companion is probably somewhat earlier (O7-7.5). The RVs of the O7-7.5 component are affected by large uncertainties due to the width of the lines. Unfortunately, the existing data are not sufficient to establish an orbital solution for this system. The nature of HD 93343 thus remains a puzzle: are we really dealing with a binary harbouring a slow

rotator along with a very fast rotator, or is HD 93343 actually a triple system? To answer this question an intensive monitoring campaign of this star is required.

Six FEROS high-resolution spectra of HD 93250 were analysed by Lanotte (2006). The spectrum of this star displays several emission lines: N III $\lambda\lambda$ 4634-40, C III $\lambda\lambda$ 5696, 6721, 6727-31 and Si IV $\lambda\lambda$ 4089, 4116 are the most prominent ones. A weak N IV λ 4058 emission is also seen, whilst He II λ 4686 is in strong absorption ($\overline{EW} = 0.54 \pm 0.06$ Å) with a slightly asymmetric profile. These features indicate that HD 93250 is an O V((f$^+$)) star. Walborn et al. (2002) introduced the new O3.5 spectral type and proposed HD 93250 to be a prototype of this category. This result is in good agreement with the ratio of the equivalent widths of the He I λ 4471 ($\overline{EW} = 0.119 \pm 0.008$ Å) and He II λ 4542 ($\overline{EW} = 0.690 \pm 0.018$ Å) classification lines. Indeed, the Conti (1973) criterion yields $\log W' = -0.76 \pm 0.03$ corresponding to an O4 spectral type[3]. In summary, HD 93250 hence appears to be an O3.5 V((f$^+$)) star.

Levato et al. (1991) reported HD 93250 to have a constant radial velocity. This statement was based on 8 low-resolution spectra obtained on 8 consecutive nights. The 1-σ dispersion of their measurements was 11.6 km s^{-1}. The RV measurements of Lanotte (2006) indicate 1-σ RV dispersions of less than 2.0 km s^{-1} for the He II $\lambda\lambda$ 4026, 4542 and 5412 absorption lines. These measurements sample time scales of 3 - 5 days as well as of several years. The lack of significant RV variations therefore indicates that HD 93250 is most likely not a spectroscopic binary with an orbital period of order a few days to a few weeks or a few years. Finally, it should be noted that Mason et al. (1998) did not report a visual companion to HD 93250. In conclusion, HD 93250 is most likely a single O3.5 V((f$^+$)) star.

However, some indication of a possible binarity were found in the radio and X-ray domains. In fact, Leitherer et al. (1995) reported on an Australia Telescope Compact Array (ATCA) radio observation of HD 93250. The star was detected only at the 8.64 GHz frequency. Assuming the radio flux to be of thermal origin and adopting a distance of 2.2 kpc, Leitherer et al. inferred a mass loss rate of $\log \dot{M} \sim -4.39 \pm 0.15$. This value is considerably larger than the mass loss rate derived from analyses of the optical spectra of this star[4]. Therefore, Leitherer et al. (1995) suggested that the radio emission is essentially non-thermal. Since non-thermal (synchrotron) radio emission is nowadays commonly believed to arise from a wind-wind collision in an early-type binary (see e.g. De Becker 2005 and Chapter 3), one would thus expect HD 93250 to be a binary system. Moreover, *XMM-Newton*-EPIC observations of HD 93403 include also HD 93250 (see Sect. 2.3). The EPIC light curve of HD 93250 displays some slight variability between the four pointings, whilst most of the other sources (apart from HD 93403) did not show significant variability. The EPIC spectra of HD 93250 can be fitted with a two-temperature optically thin thermal plasma `mekal` model with temperatures around 0.60 keV and 1.08 – 1.74 keV. These results, i.e. the existence of a relatively hard thermal component and the slight X-ray variability could be seen as further evidence for HD 93250 being a colliding wind binary. I will come back to the lack of RV variations and its implications in the context of the non-thermal radio emission in Chapter 3.

1.2.2 The Hertzsprung-Russell diagram of the massive binaries in the Carina region

The properties of the eclipsing or ellipsoidal variables (Tr 16-1, Tr 16-104 and HD 93205) were already discussed in Sect. 1.1. These systems are particularly useful since their light curve and orbital solution provide absolute parameters. In addition, the eclipsing systems allow us to constrain their distance. In this section, I assume that all the stars investigated in this part of the Carina complex actually lie at the same distance (i.e. 2.5 kpc). With this assumption, let us see what additional information can be obtained

[3]Note that Conti (1973) did not consider an O3.5 spectral type in his classification scheme.

[4]Indeed, Martins et al. (2005b) recently derived $\log \dot{M} = -6.25 \pm 0.7$.

from the other (non-eclipsing) SB2 systems. To provide a homogeneous Hertzsprung-Russell diagram of the massive stars in the Carina complex, I also revise the temperatures and bolometric luminosities of the eclipsing systems using the most recent temperature calibration of O-type stars.

Let us start with HD 93161 (Nazé et al. 2005). Using the 'observed' temperature scale of Martins et al. (2005a), the spectral types of the various components of the system translate into effective temperatures of 37900 ± 1000 K, 34900 ± 1000 K and 32900 ± 1000 K for HD 93161B, HD 93161Aa and HD 93161Ab respectively. The uncertainties on these temperatures correspond to half a subclass for the components of HD 93161A and to the range of temperatures for the O6.5 V class according to Martins et al. (2005a) for HD 93161B. In order to derive the luminosities, one needs the observed magnitude, the reddening, the brightness ratios between the different components, the bolometric corrections and an estimate of the distance. The WEBDA database lists the results of several photometric studies that provide the apparent V magnitude of the entire (Aa + Ab + B) system HD 93161 (Walborn 1973, Feinstein et al. 1973, Kaltcheva & Georgiev 1993, Forte 1978, Massey & Johnson 1993). On average, we find $V = 7.84 \pm 0.02$ for the entire HD 93161 system. Vázquez et al. (1996) quote $V = 8.56$ and $V = 8.60$ for HD 93161A and HD 93161B respectively. These magnitudes yield $V = 7.83$ for the entire system in good agreement with the mean V value hereabove. On the other hand, Mason et al. (1998) found $V = 9.0$ for HD 93161A and $V = 9.1$ for HD 93161B. If these values were correct, the total magnitude of HD 93161 should be 8.3 in contradiction with the actual observations. In the following, I thus adopt apparent magnitudes of 8.56 ± 0.02 and 8.60 ± 0.02 for HD 93161A and B respectively.

The $(B-V)$ colour-indices of HD 93161A and HD 93161B were found to be 0.20 and 0.23 respectively (Vázquez et al. 1996). We hence adopt $E(B-V) = 0.52$ and $E(B-V) = 0.55$ for HD 93161A and HD 93161B respectively.

The relative brightness of the components of HD 93161A in the visible spectral range, can be estimated from the ratio of the EWs of the primary and secondary lines. This was done on the FEROS spectra obtained in 2004 (i.e. the least contaminated by light from the nearby HD 93161B component). Nazé et al. (2005) used the He I $\lambda\lambda$ 4471, 5876, He II λ 4542 and O III λ 5592 lines to estimate a brightness ratio of 1.7 ± 0.3 between the primary and secondary of HD 93161A. This results in apparent magnitudes of 9.06 ± 0.07 and 9.68 ± 0.12 for the primary and secondary component of HD 93161A respectively.

Carraro et al. (2004) presented a study of the clusters Tr 14, Tr 16 and Collinder 232 based on $UBVRI$ photometry. These authors argued that a unique reddening law is not appropriate to study the whole region and they estimated different values of the selective extinction $R_V = A_V/E(B-V)$ for each cluster. For HD 93161, they infer $R_V = 3.83 \pm 0.33$, whereas they estimate $R_V = 3.60 \pm 0.27$ for HD 93160, its close neighbour on the sky. Adopting the mean value for the two stars $R_V = 3.72 \pm 0.16$, we obtain absolute magnitudes of -4.86 ± 0.11, -4.24 ± 0.15 and -5.44 ± 0.09 for HD 93161Aa, Ab and B respectively. Finally, adopting the bolometric corrections from Martins et al. (2005a) yields the bolometric luminosities quoted in Table 1.2. Note that the luminosity of HD 93161B might be overestimated if the star turned out to be indeed another binary system.

One can do the same job for the components of Tr 16-110. Using the spectral types and relative luminosities derived by Albacete Colombo et al. (2002) along with the reddening estimate by Carraro et al. (2004), the spectral type - effective temperature calibration and bolometric corrections of Martins et al. (2005a) yields the results presented in Table 1.2.

For HD 93343, the WEBDA database yields on average $V = 9.57 \pm 0.05$ and $(B-V) = 0.24 \pm 0.03$. Considering that $(B-V)_0 = -0.32$ and making the same assumptions on the reddening law and distance as for HD 93250, one obtains an absolute magnitude of $M_V = -4.38 \pm 0.22$ for the binary system. From the dilution effect of the equivalent widths of the primary (O8 V) and secondary (O7-

Table 1.2: Revised temperatures and bolometric luminosities of the components of eclipsing (upper part) and non-eclipsing (middle part) binaries in the Carina complex (see text). The lower part yields the properties of the probably single star HD 93250.

System	Spectral type	$T_{\rm eff}$ (K)	$\log L/L_\odot$
HD 93205a	O3.5 V	43900 ± 1000	5.32 ± 0.14
HD 93205b	O8 V	34900 ± 1000	4.71 ± 0.10
Tr 16-104a	O7 V	36900 ± 1000	4.92 ± 0.11
Tr 16-104c	O9.5 V	31900 ± 1000	4.34 ± 0.09
Tr 16-1a	O9.5 V	31900 ± 1000	4.41 ± 0.06
Tr 16-1b	B0.3 V	29100 ± 500	4.09 ± 0.07
HD 93161Aa	O8 V	34900 ± 1000	5.16 ± 0.04
HD 93161Ab	O9 V	32900 ± 1000	4.85 ± 0.06
HD 93161B	O6.5 V(f)	37900 ± 1000	5.50 ± 0.04
HD 93343a	O8 V	34900 ± 1000	4.40 ± 0.10
HD 93343b	O7-7.5 V	36400 ± 1000	4.89 ± 0.09
HD 93403a	O5.5 I	37700 ± 900	5.72 ± 0.05
HD 93403b	O7 V	36900 ± 1000	4.97 ± 0.22
Tr 16-110a	O7 V	36900 ± 1000	4.86 ± 0.06
Tr 16-110b	O8 V	34900 ± 1000	4.69 ± 0.06
Tr 16-110c	O9 V	32900 ± 1000	4.55 ± 0.07
Tr 16-112a	O5.5-6 V	39400 ± 1000	5.27 ± 0.11
Tr 16-112b	B2 V	22000 ± 3000	3.64 ± 0.27
HD 93250	O3.5 V((f$^+$))	44000 ± 300	6.09 ± 0.07

7.5 V) components of the He I λ 4471 and He II λ 4542 lines, Lanotte (2006) inferred a brightness ratio of $p = f_{V,1}/f_{V,2} = 0.36 \pm 0.05$. This yields the results summarized in Table 1.2. An identical analysis of Tr 16-112, which has on average $V = 9.28 \pm 0.04$ and $(B-V) = 0.28 \pm 0.05$, indicates an absolute magnitude of $M_V = -4.84 \pm 0.27$ for the binary system. Using the equivalent widths of the He I λ 4471 lines of the primary and secondary as well as the dilution of the primary's He II λ 4542 line, Lanotte (2006) estimated a brightness ratio of 12.5 ± 6.3. Again, the final results are given in Table 1.2.

At this stage, it is also worth re-assessing the parameters of HD 93403, adopting a distance modulus of 12.0 as well as the revised temperature scale for O-stars (Martins et al. 2005a). This yields the parameters listed in Table 1.2. The evolutionary masses are revised downwards to $48.9^{+2.6}_{-2.6}$ and $26.4^{+5.1}_{-3.0}$ $M_\odot$ for the primary and secondary respectively. These values correspond to an evolutionary mass ratio of 1.85 ± 0.30, in broad agreement with the observed mass ratio (1.75 ± 0.06).

Finally, the measurements listed in the WEBDA database yield $V = 7.37 \pm 0.02$ and $(B-V) = 0.17 \pm 0.01$ for the probably single O3.5 V((f$^+$)) star HD 93250. With $R_V = 3.48 \pm 0.33$ (Carraro et al. 2004) and a distance of 2.5 kpc, one gets an absolute magnitude of -6.37 ± 0.17. Martins et al. (2005b) inferred an effective temperature of 44000 K and a bolometric correction of -4.10 for HD 93250. Using the latter value yields $\log L/L_\odot = 6.09 \pm 0.07$ in very good agreement with the luminosity $\log L/L_\odot = 6.12^{+.25}_{-.17}$ inferred by Martins et al. (2005b) using a different method.

In Fig. 1.7, I have plotted the components of the various binary systems discussed hereabove and the probably single star HD 93250 in a Hertzsprung-Russell diagram along with the evolutionary tracks from

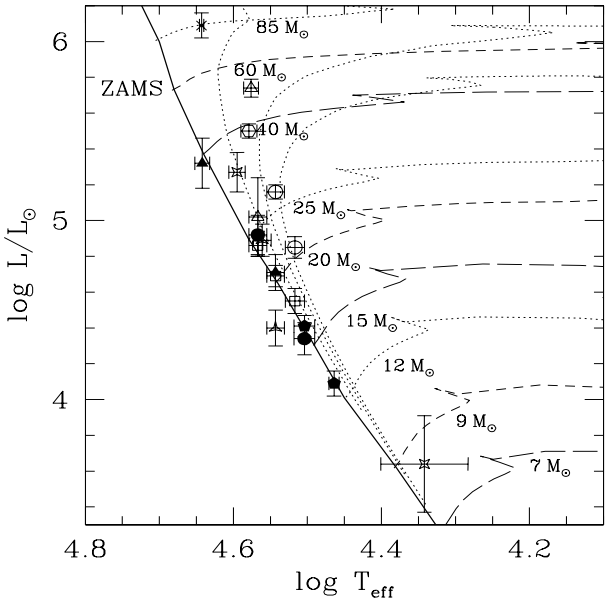

Figure 1.7: Location of the components of various main-sequence binary systems of the Carina region and HD 93250 in the Hertzsprung-Russell diagram. Eclipsing binaries are shown by filled symbols, whilst non-eclipsing systems are indicated by open symbols and the asterisk stands for the probably single star HD 93520. The evolutionary tracks are from Schaller et al. (1992) for $Z = 0.0$. Isochrones for 2, 3 and 4 Myr are indicated.

Schaller et al. (1992) for solar metallicity. Provided that the stars are indeed all at the same distance from Earth, this diagram suggests that the stars in HD 93161 and HD 93403 (open circles and open triangles respectively) are evolved off the zero age main-sequence with an age of about 2 – 3 Myr, unlike the components of the eclipsing binaries and of Tr 16-110 which are found very close to the ZAMS (see also Rauw 2004a).
It should be noted that HD 93250, HD 93403 and HD 93161 are actually rather far away from the core of the Tr 16 cluster (see Fig. 1.5) and might thus not be physically related to this cluster.

1.2.3 Tidal interactions and multiple systems

Using all the available orbital solutions for early-type binary systems in or around Trumpler 16, I constructed the period – eccentricity diagram shown in Fig. 1.8. This figure provides an update of Fig. 2 of Rauw (2004a) (see Sect. 1.1) and confirms our assertion from Fig. 1.7 that HD 93161A must be older and more evolved than the main-sequence stars in the core of Tr 16. In fact, for the latter, significant eccentricities are found for orbital periods as short as ~ 4 days, indicating that tidal interactions have not yet had the time to circularize the eccentric orbits.
At least three systems of multiplicity three or higher were found among the early-type binaries in the Carina complex. Concerning the fraction of systems of multiplicity three and higher, Tokovinin (2004) found that about 43% of the nearby low-mass (0.5 - 1.5 $M_\odot$) spectroscopic binaries with $P < 10$ days quoted in the Eighth Catalogue of Spectroscopic Binaries have indeed a tertiary component. The third component provides a natural sink for the angular momentum that needs to be removed from a binary system in order to make it a close one. Tokovinin (2004) quotes an empirical stability limit for a triple

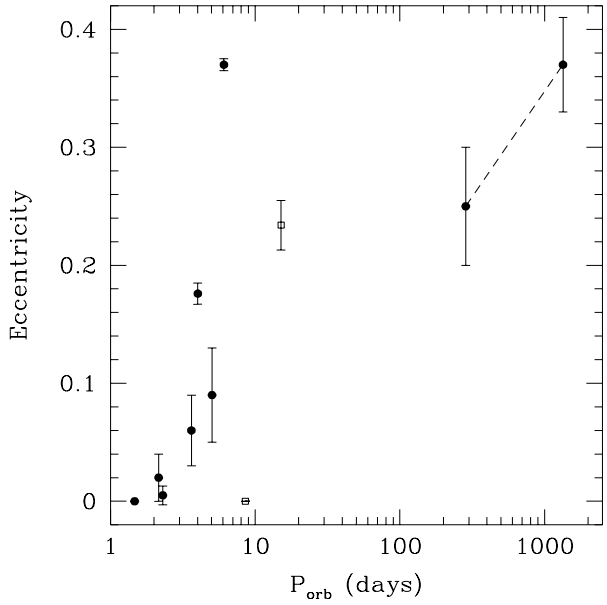

Figure 1.8: Eccentricity of the orbits of a sample of early-type binaries in the Carina complex as a function of the orbital period. The probable members of Tr 16 are shown by filled symbols, whereas the two binary systems outside the cluster (HD 93403 and HD 93161A) are indicated by open symbols.

system:

$$P_{\rm out}\,(1-e_{\rm out})^3 > 5\,P_{\rm in}$$

where $P_{\rm in}$, $P_{\rm out}$ and $e_{\rm out}$ correspond respectively to the orbital period of the close binary, the orbital period of the third star around the centre of mass of the close binary and the eccentricity of the third star's orbit. Both possible orbital solutions for the third component in Tr 16-104 largely satisfy this criterion, whilst the orbital period of the SB1 component in Tr 16-110 assumed to correspond to $P_{\rm out}$ of a triple system obviously cannot meet this condition, thus confirming the idea that there should exist a fourth (unseen) component in this system.

1.3 Early-type stars in the core of IC1805

IC 1805, located at the core of the Cas OB6 association, is another very young open cluster that has been suggested to harbour a large number of early-type binaries. The Liège team has conducted an extensive observing campaign of the brightest O-type stars of the cluster using the telescopes and spectrographs of the Observatoire de Haute Provence (OHP, France).
In the following pages, I reproduce the first paper reporting the results of a spectroscopic investigation of the O-type stars in IC 1805 (Rauw & De Becker 2004a). This paper deals with three mid-O stars that were all previously considered to be spectroscopic binaries, although no orbital solution existed for any of them.
As a next step, I provide an update on the SB2 system BD+60° 497 and I summarize some additional results obtained by our team on the earliest-type stars of this cluster. Finally, I discuss the fraction of binaries among the O-type stars in IC 1805.

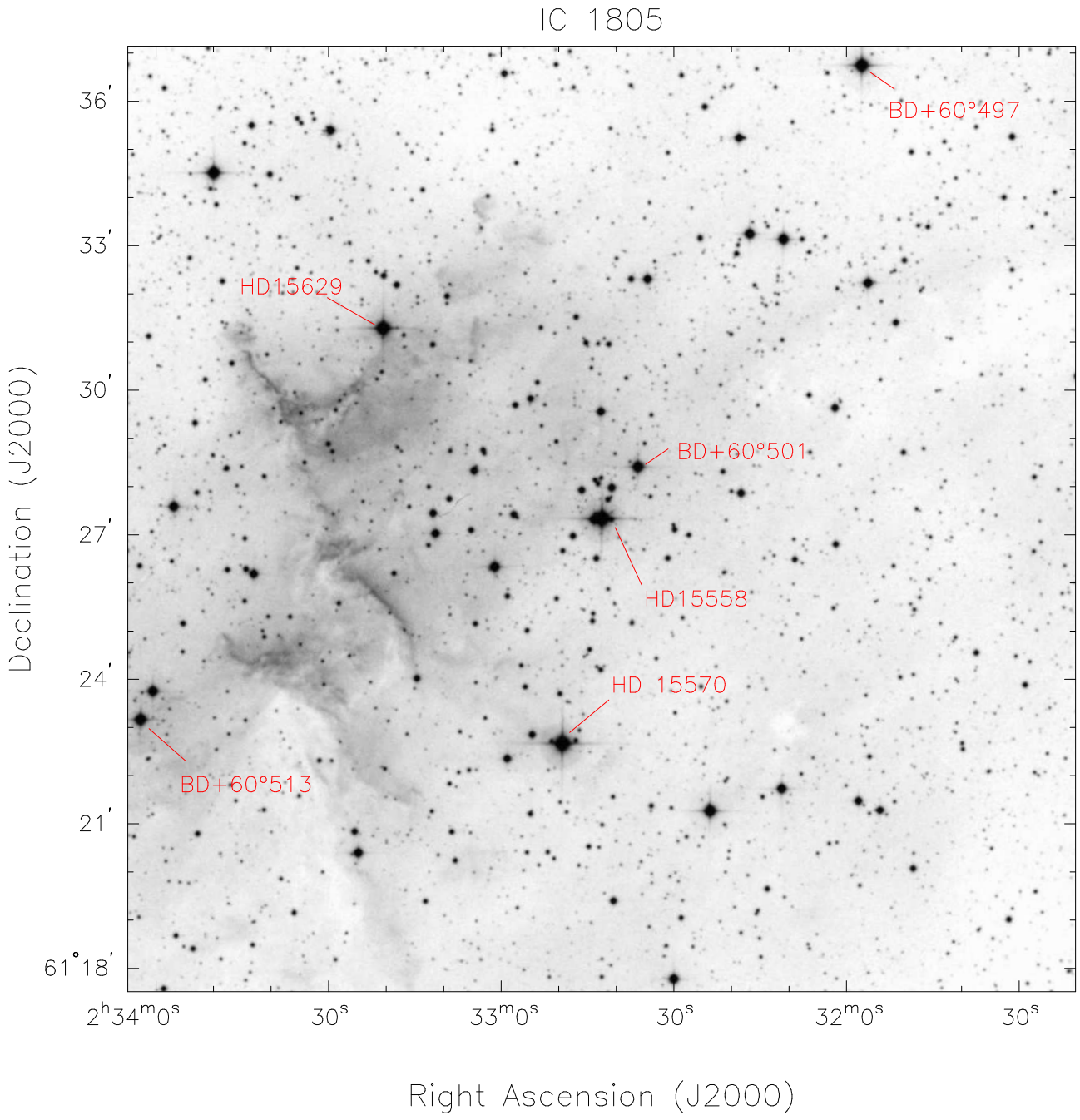

Figure 1.9: Digitized Sky Survey image (20' × 20') of the core of the IC 1805 cluster showing the location of the O-type stars discussed in this section. North is up and east is to the left.

A&A 421, 693–702 (2004)
DOI: 10.1051/0004-6361:20040255

Astronomy & Astrophysics

Early-type stars in the young open cluster IC 1805

I. The SB2 system BD+60° 497 and the probably single stars BD+60° 501 and BD+60° 513⋆

G. Rauw⋆⋆ and M. De Becker

Institut d'Astrophysique et de Géophysique, Université de Liège, Allée du 6 Août, Bât. B5c, 4000 Liège, Belgium

Received 12 February 2004 / Accepted 30 March 2004

Abstract. We investigate the multiplicity of three O-type stars in the very young open cluster IC 1805. All our targets were previously considered as spectroscopic binaries, but no orbital solution was available for any of them. Our results confirm the binarity of BD+60° 497 and we provide the very first orbital solution for this double-lined spectroscopic binary. This is only the second O-star binary in IC 1805, and the first SB2 system, for which an orbital solution is now available. BD+60° 497 has an orbital period of 3.96 days and consists of an evolved O6.5 V((f)) primary and an O8.5-9.5 V((f)) secondary with minimum masses of $m_1 \sin^3 i = 13.9\ M_\odot$ and $m_2 \sin^3 i = 10.9\ M_\odot$. The observed primary/secondary mass ratio (1.28) appears lower than expected from a comparison with single star evolutionary models (1.60–1.74). For the other two stars, BD+60° 501 and BD+60° 513, we find no significant radial velocity variations, suggesting that they are most probably single. Although a fraction of binaries among the early-type stars of IC 1805 as high as 80% has been advocated in the literature, our results suggest that this number might be overestimated.

Key words. stars: binaries: spectroscopic – stars: early-type – stars: fundamental parameters – stars: individual: BD+60° 497 – stars: individual: BD+60° 501 – stars: individual: BD+60° 513

1. Introduction

Studying early-type binaries in very young open clusters has the potential to provide important information on many fundamental problems of stellar astrophysics including the star and cluster formation processes, dynamical interactions in clusters and stellar evolution in general. This is especially crucial for the still poorly understood formation of the most massive stars. Unfortunately, our present knowledge of the binary properties of massive stars is still fragmentary (Mermilliod 1996). For many binaries reliable orbital solutions are still lacking and the binarity of the majority of the early-type stars has simply never been investigated.

Several years ago, our group started an investigation of a number of early-type binaries in the open clusters Trumpler 16 and NGC 6231 in the southern hemisphere. Our extensive observing campaigns already led to the discovery of several triple systems and allowed us to considerable improve the orbital solutions for a number of binaries (Rauw et al. 2000, 2001; Morrell et al. 2001; Sana et al. 2001, 2003; Albacete Colombo et al. 2002). In this context, we have also undertaken a spectroscopic monitoring of the most massive members of the IC 1805 cluster in the northern hemisphere.

IC 1805 is a rich cluster in the core of the Cas OB6 association which in turn is embedded in the molecular cloud W 4 in the Perseus spiral arm of our Galaxy. All in all, the cluster harbors about forty early-type stars from spectral type O4 through B2 (Shi & Hu 1999) and their energetic winds have created a "galactic chimney" – i.e. a cone-shaped cavity in the interstellar medium – that allows efficient transport of hot gas from the galactic disk into the halo (Normandeau et al. 1996).

Among the 10 O-stars in IC 1805, García & Mermilliod (2001, see also Ishida 1970) estimated an extremely high binary frequency of 80%. However, to date, an orbital solution is available for only one of them: HD 15558 (O5 III(f)). HD 15558 is the optically brightest star in the cluster. It is an eccentric single-line binary (SB1) system with an orbital period of 440 days, the longest of any known O-star binary (Garmany & Massey 1981).

In this paper, we present the first double-line (SB2) orbital solution for another O-type binary (BD+60° 497 = LSI +61 274) in IC 1805. Although, Underhill (1967) and Walborn (1973) already reported the presence of a secondary spectrum in their observations of BD+60° 497, no detailed investigation of this system has apparently ever been performed. Underhill (1967) further noted that Trumpler (1930)

Send offprint requests to: G. Rauw,
e-mail: rauw@astro.ulg.ac.be

⋆ Based on observations collected at the Observatoire de Haute Provence (France).

⋆⋆ Research Associate FNRS (Belgium).

had suspected BD+60° 497 to be an SB1 with an orbital period of 25.48 days.

We also analyse the spectra and radial velocities of two other O-type stars in IC 1805: BD+60° 501 (=LSI +61 282) and BD+60° 513 (=LSI +61 296) for which we find no evidence of binarity in contradiction with previous reports of radial velocity changes for the former and apparent double lines for the latter (Underhill 1967). Our results on the earliest O-type stars in this cluster will be the subject of a forthcoming paper.

In Sect. 2, we present our new data on the program stars and we derive their spectral classification. The orbital solution of BD+60° 497 and the radial velocities of the other two targets are discussed in Sect. 3 whilst the fundamental parameters of the BD+60° 497 system are the subject of Sect. 4. Section 5 presents a brief discussion of the *ROSAT* X-ray observations of our program stars and finally, our conclusions are given in Sect. 6.

2. Spectral classification

2.1. Observations and data reduction

Spectroscopic observations were collected during several observing campaigns in 2002 and 2003 at the Observatoire de Haute-Provence (OHP). We used the Aurélie spectrograph attached to the 1.52 m telescope. The detector was a 2048 × 1024 CCD EEV 42-20#3, with a pixel size of 13.5 μm squared. Our spectra cover the wavelength range from 4455 to 4905 Å with a reciprocal dispersion of 16 Å mm^{-1}. Depending on the atmospheric conditions, the exposure times were of order 30 to 45 min (respectively 45 to 60 min.) for BD+60° 497 and BD+60° 501 (respectively BD+60° 513). The mean signal to noise ratio of individual spectra is about 200−300 in the continuum.

The data were reduced using the MIDAS software developed at ESO. For each observation, the Aurélie CCD data consist of five images of the object's spectrum obtained by means of a Bowen image slicer (see Gillet et al. 1994). These five images were treated individually, i.e. they were bias-subtracted, flat-fielded and extracted. After removing the cosmic ray events from the individual images, we combined them into a weigthed average. The resulting spectrum was wavelength-calibrated using a Th-Ar comparison exposure taken shortly before or after the observation on the sky. Finally, the spectra were normalized using properly chosen continuum windows.

2.2. BD+60° 497

The blue spectra of BD+60° 497 are dominated by He I, He II and the Hβ absorption lines of the primary. Weak metal lines due to C III, N III, O II, Mg II, Si III and Si IV are also present. Their changing wavelengths indicate that they mainly follow the orbital motion of the primary. The secondary spectrum is seen in the He I absorption lines. The visibility of the secondary lines changes with orbital phase (see Fig. 1 and below).

Several authors provided spectral classifications for BD+60° 497: O7 (Underhill 1967), O6 V(n) (Walborn 1973), O7 V (Mathys 1989), O7 V((f)) (Massey et al. 1995) and O7 V (Shi & Hu 1999). It should be noted that these results are in fair agreement with each other whilst older classifications included early B-types (see Ishida 1970, and references therein). Ishida (1970) suggested that the spread in older spectral types (from B3 to O7) might indicate a possible change of some spectral features. However, this is not confirmed by the more recent results (including our own data).

In order to determine the spectral type of both components of BD+60° 497, we deblended the classification lines by simultaneously fitting two Gaussian profiles. The average equivalenth width (*EW*) of the He I λ 4471 line in the spectrum of the primary (resp. secondary) determined in this way amounts to 0.34 ± 0.02 Å (resp. 0.22 ± 0.03 Å). For the He II λ 4542 line the situation is less clear: due to the stronger intensity contrast between the primary and secondary in this line, it was only at a few phases that we were able to deblend the lines. For the primary (resp. secondary) we find *EW* = 0.54 Å (resp. 0.08 Å) for this line. Due to the orbital variation of the secondary line strength (see below) and the fact that we could only deblend this line at phases when the secondary is approaching, the *EW* of the secondary line could be a lower limit. The equivalent width ratio of the He I λ 4471 and He II λ 4542 classification lines places the primary of BD+60° 497 right at the border between spectral type O6 and O6.5 (Conti 1973b), whilst the secondary would be of spectral type O9−9.5 (or of somewhat earlier spectral type if the measured *EW* of He II λ 4542 is indeed a lower limit). We have also compared the blue spectrum of BD+60° 497 to the atlas of Walborn & Fitzpatrick (1990). The primary's spectrum is intermediate between those of HD 101190 of type O6 V((f)) and HD 93146 of type O6.5 V((f)), but slightly closer to the latter. For the secondary, comparison with the spectra provided by Walborn & Fitzpatrick suggests that this star should have a spectral type later than about O8.5.

The He II λ 4686 absorption line is in rather strong absorption in the spectrum of BD+60° 497, suggesting a main sequence luminosity class for both stars (see however also Sect. 4 below). We note the presence of a very weak N III λ 4641 emission line. The line roughly moves in phase with the primary component though with a reduced radial velocity (*RV*) amplitude. We further note that the width of the line changes as a function of phase. At some phases near $\phi = 0.25$, the line deblends into two components suggesting that the reduced *RV* amplitude and the changing width are due to a blend between two emission lines associated with both components. This means that both stars probably have this line in weak emission in their spectrum.

In summary, we thus classify the primary and secondary of BD+60° 497 as O6.5 V((f)) and O8.5−9.5 V((f)) respectively.

Finally, let us briefly turn to the apparent change in the strength of the secondary's absorption lines as a function of orbital phase. Though in the mean spectra displayed in Fig. 1 the He I λ 4713 line doubles its *EW* between approaching and receding quadrature, we must note that the effect is much less clear cut in the He I λ 4471 line and moreover, the dispersion of the *EW* of He I λ 4713 measured on individual spectra at

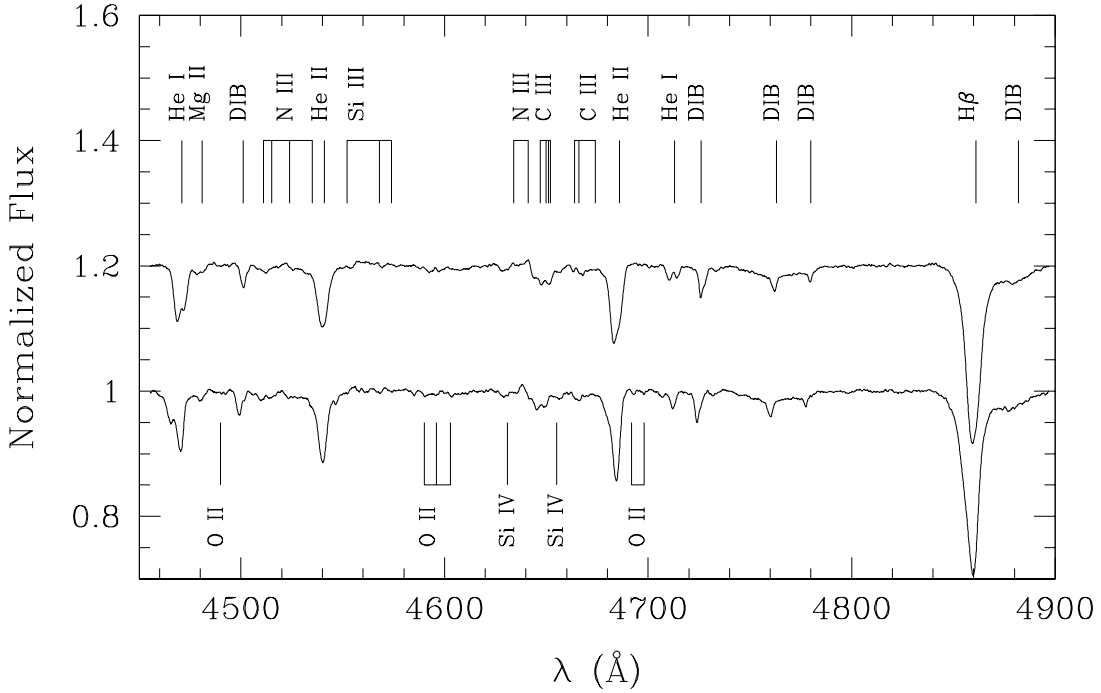

Fig. 1. Average spectrum of BD+60° 497 as observed around the phases of quadrature. The average spectrum around phases 0.65−0.85 is shifted vertically by 0.2 units with respect to the average spectrum around phases 0.1−0.35. The most prominent stellar features as well as the diffuse interstellar bands (DIBs) are identified. Note the aspect of the He I λ4471 and λ4713 lines that reveal clearly the signature of the secondary star. The relative importance of the secondary lines varies between the two quadratures (see text).

similar orbital phases is uncomfortably large. If real, the effect seen in Fig. 1 is such that the secondary's lines appear stronger at phases when the secondary is moving away from us compared to their intensity at approaching phases. This is the opposite situation of the so-called "Struve-Sahade" effect (SSe) which is defined as the apparent strengthening of the secondary lines at those orbital phases when the secondary is approaching and the corresponding weakening of its lines when it is receding (see e.g. Bagnuolo et al. 1999). BD+60° 497 is not the only binary where such an opposite SSe is seen. In fact, a similar behaviour was reported by Howarth et al. (1997) for HD 100213 (O7.5 V + O9.5 V).

2.3. BD+60° 501

The blue spectrum of BD+60° 501 is very similar to that of BD+60° 497 except for sharper and somewhat deeper absorptions (see Fig. 2). No indication of a secondary spectrum is found. The average *EW*s of the He I λ4471 and He II λ4542 classification lines are 0.57 ± 0.02 Å and 0.68 ± 0.04 Å respectively (in good agreement with the values quoted by Mathys 1989). According to the criterion provided by Conti (1973b), the ratio of these equivalent widths indicates an O7 classification. This result is confirmed by a comparison with the spectral atlas of Walborn & Fitzpatrick (1990). The strong He II λ4686 absorption further indicates a main sequence luminosity class. Finally, we note some evidence of a very weak N III λ4641 emission. In summary we thus assign an O7 V((f)) spectral type to BD+60° 501.

The spectral types given in the literature range from O6.5 V (Underhill 1967; Ishida 1970; Conti & Alschuler 1971) to O7 V (Walborn 1973; Mathys 1989; Shi & Hu 1999) and O7 V((f)) (Massey et al. 1995). Our result appears thus fully consistent with these classifications.

2.4. BD+60° 513

The spectrum of BD+60° 513 is similar to that of BD+60° 501 except for the much broader lines in the former (see Fig. 2). This is not unexpected since the projected rotational velocity is significantly larger for BD+60° 513 ($v \sin i \sim 300\,\mathrm{km\,s^{-1}}$) than for BD+60° 501 ($v \sin i \sim 200\,\mathrm{km\,s^{-1}}$; see Mathys 1987; Conti & Ebbets 1977). We note that the absorption lines in the spectrum of BD+60° 513 display some low-level profile variability, but no obvious indication of a secondary spectrum is found (see below). The average *EW*s of the He I λ4471 and He II λ4542 lines are 0.61 ± 0.04 Å and 0.56 ± 0.02 Å respectively. These values and the strength of the He II λ4686 absorption yield an O7.5 V classification (Conti 1973b; Walborn & Fitzpatrick 1990). Again, the possibility of a very weak N III λ4634-41 emission, finally leads to an O7.5 V((f)) spectral type for BD+60° 513.

The spectral types quoted in the literature include O7 V (Shi & Hu 1999), O7 Vn (Walborn 1973), O7.5 V (Mathys 1989; Conti & Ebbets 1977), O8 V((f)) (Massey et al. 1995),

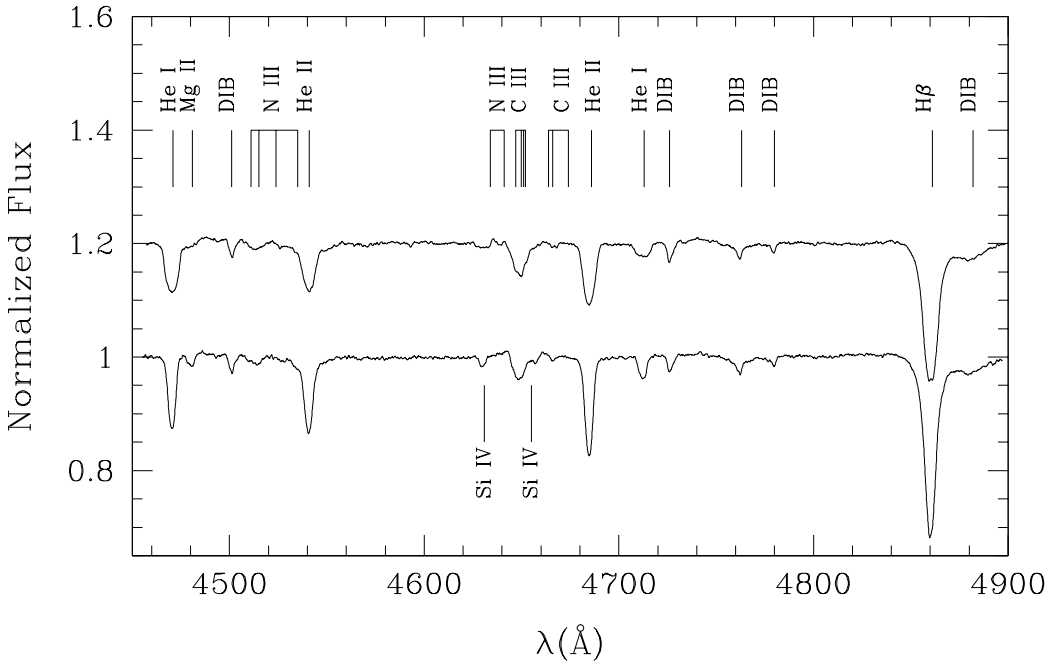

Fig. 2. Average spectra of BD+60° 501 (*bottom*) and BD+60° 513 (shifted vertically by 0.2 units). The lines of BD+60° 513 are significantly broader than those of BD+60° 501 (see text).

O9 V (Ishida 1970) and B0 (Underhill 1967). This rather wide range of spectral types most probably results from the difficulties related to the broad lines of this star and possibly some confusion problems between BD+60° 513 and BD+60° 512 in older studies (as pointed out by Conti & Leep 1974 and Mathys 1987).

3. Radial velocities and orbital solutions

3.1. BD+60° 497

Radial velocities of the components of BD+60° 497 were determined from simultaneous fits of several Gaussian profiles and through cross-correlation with a template spectrum. The results of both techniques generally agree within the uncertainties. Most lines of the binary components remain blended over large parts of the orbital cycle and the intensities of the secondary's lines change as a function of the orbital phase (Fig. 1). The secondary's signature is best seen in the He I λ4471 and λ4713 lines as well as, at some orbital phases, in Mg II λ4481. These three absorptions provide therefore the best lines to derive the radial velocities (*RV*s) of the binary components. We adopt the rest wavelengths for these lines from Underhill (1994) and the resulting *RV*s (determined by means of simultaneous Gaussian fitting) are listed in Table 1. For most measurements the typical uncertainties are of order 10−15 km s^{-1}. About twice as large uncertainties affect the data points indicated by a colon in Table 1.

We applied the generalized spectrogram technique of Heck et al. (1985; see also Gosset et al. 2001) and the trial method of Lafler & Kinman (1965) to the timeseries of our RV_1-RV_2 data. Both methods consistently yield 3.96 days as the best estimate for the orbital period. This result was confirmed by a 2D period search technique (see e.g. Rauw et al. 2003) applied to the line profile changes in the spectrum of BD+60° 497. Assuming that the uncertainty on the corresponding frequency amounts to one tenth of the width of the peak in the periodogram, we estimate an uncertainty of 0.09 day on the orbital period. Our orbital period is clearly at odds with the much longer value (25.48 days) suggested by Trumpler (1930, as reported by Underhill 1967). In the following we adopt 3.96 days as the orbital period of BD+60° 497.

A circular orbital solution of BD+60° 497 yields a mass ratio $q = m_1/m_2 = 1.28$ and the minimum masses of the stars are found to be $m_1 \sin^3 i = 13.9\,M_\odot$ and $m_2 \sin^3 i = 10.9\,M_\odot$ for the primary and the secondary respectively. The systemic velocities obtained for each component are in broad agreement with each other and with the mean radial velocity of other IC 1805 cluster members (see Underhill 1967 and the cases of BD+60° 501 and BD+60° 513 below). Allowing for an eccentric orbital solution yields $e = 0.14 \pm 0.14$. Given the large errors on the eccentricity and though we cannot completely rule out a small eccentricity, in the following we assume $e = 0.0$.

3.2. BD+60° 501

We measured the *RV*s of the He I λ4471, He II $\lambda\lambda$4542, 4686 and Hβ lines in the spectra of BD+60° 501 by fitting Gaussians. These fits are of good quality and the position of the line centre is determined with an accuracy of about 1−2 km s^{-1}. The resulting mean *RV*s are listed in Table 3. Again, the rest wavelengths were adopted from Underhill (1994).

Table 1. Radial velocities of BD+60° 497 as derived from our Aurélie spectra. The orbital phases are computed with respect to HJD 2 452 935.977 with a period of 3.96 days (see Table 2).

HJD−2 450 000	ϕ	RV_1 (km s^{-1})	RV_2 (km s^{-1})
2520.644	0.118	−151.1	94.4:
2523.600	0.864	76.3	−285.2:
2524.552	0.105	−142.0:	91.9:
2527.555	0.863	92.0	−286.1
2528.533	0.110	−158.7:	77.0:
2529.562	0.370	−156.9	74.0
2531.543	0.870	91.1	−264.6
2532.534	0.120	−179.1	79.9
2533.638	0.399	−146.6	44.4
2916.583	0.103	−185.9	108.5
2918.667	0.629	50.0:	−210.6:
2919.632	0.872	78.4	−203.8
2922.677	0.641	74.3	−176.1
2925.665	0.396	−155.8:	−16.3:
2928.641	0.147	−236.3	118.0
2934.545	0.638	67.4	−189.4

Table 2. Orbital solution for BD+60° 497 assuming a circular orbit. T_0 refers to the time of conjunction with the primary being behind. γ, K and $a \sin i$ denote respectively the systemic velocity, the amplitude of the radial velocity curve and the projected separation between the centre of the star and the centre of mass of the binary system. $R_{\rm RL}$ stands for the radius of a sphere with a volume equal to that of the Roche lobe computed according to the formula of Eggleton (1983).

	Primary	Secondary
P(days)	3.96 (fixed)	
e	0.0 (adopted)	
T_0(HJD-2 450 000)	2935.977 ± 0.152	
γ (km s^{-1})	−53.7 ± 9.2	−68.9 ± 11.9
K (km s^{-1})	171.9 ± 11.9	220.6 ± 14.9
$a \sin i$ ($R_\odot$)	13.4 ± 0.9	17.3 ± 1.7
$q = m_1/m_2$	1.28 ± 0.12	
$m \sin^3 i$ ($M_\odot$)	13.9 ± 2.5	10.9 ± 2.0
$R_{\rm RL} \sin i$ ($R_\odot$)	12.3 ± 0.8	11.0 ± 0.7

We find no significant variations neither over the data taken in September 2002 nor between the September 2002 and the October 2003 campaigns. This suggests that the star has a constant radial velocity over time scales of days, weeks and probably years. This result is at odds with the SB1 status (with an orbital period of 3.69 days) that Trumpler assigned to this system (see Underhill 1967). Underhill (1967) measured *RV*s of +1 and −57 km s^{-1} on two spectra taken two years apart. We note however that the velocities of the interstellar Ca II K-line reported by Underhill for these spectra also differ by as much as 39 km s^{-1}, confirming the caveat given by Underhill that the accuracy of her *RV*s was not very high.

Table 3. Radial velocities of BD+60° 501 as derived from our Aurélie spectra (see text).

HJD−2 450 000	RV (km s^{-1})
2518.633	−54.1
2520.611	−49.5
2524.527	−44.8
2527.617	−48.5
2531.572	−51.3
2532.573	−50.3
2533.602	−49.6
2919.602	−50.6
2922.588	−50.3
Mean	−49.9 ± 2.5

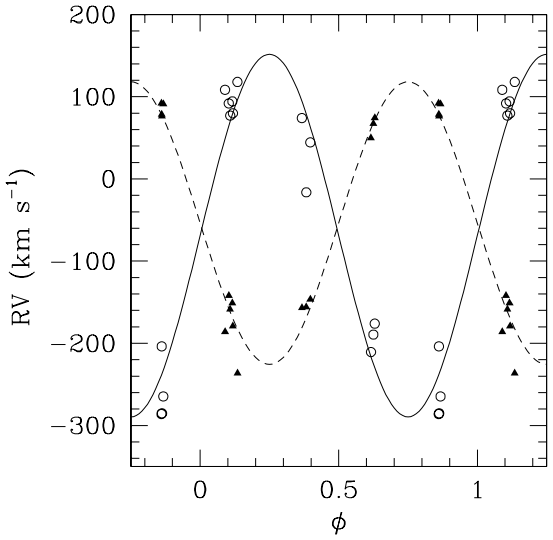

Fig. 3. Radial velocity curve of the BD+60° 497 binary system as derived from the He I $\lambda\lambda$ 4471, 4713 and Mg II λ 4481 absorption lines (see Table 1). Filled triangles and open circles stand for the primary and secondary *RV*s respectively. The circular orbital solution of Table 2 is shown by the solid and dashed lines.

Finally, in order to search for low level line profile variability – that could be due e.g. to non-radial pulsations, wind structures or binary effects – we have computed the time variance spectrum (TVS, Fullerton et al. 1996) of our entire data set over the spectral range 4460 to 4890 Å. The TVS hardly exceeds the expected level due to normalization errors and the S/N ratio of the data. Therefore, we conclude that no significant line profile variability is present in our data of BD+60° 501.

In summary, the *RV*s of BD+60° 501 as well as the lack of profile variability suggest that this is a single O7 V((f)) star.

Table 4. Same as Table 3 but for BD+60° 513.

HJD−2 450 000	RV (km s^{-1})
2520.569	−59.2
2524.609	−57.5
2527.662	−55.8
2529.602	−43.3
2531.612	−36.4
2532.619	−37.5
2533.580	−39.1
2918.631	−28.8:
2922.633	−48.9
2934.664	−36.8
Mean	−44.3 ± 10.5

3.3. BD+60° 513

Following the same procedure as for BD+60° 501 we measured the *RV*s of the He I λ 4471, He II $\lambda\lambda$ 4542, 4686 and Hβ lines in the spectra of BD+60° 513 by fitting Gaussians. Due to the much broader line profiles in the spectrum of BD+60° 513, these fits are however of much poorer quality than in the case of BD+60° 501 (this is especially true for He I λ 4471 and He II λ 4542) leading to uncertainties of $\sim$10 km s^{-1} on the line centroids. The mean *RV*s of BD+60° 513 are provided in Table 4.

Though the *RV*s show a much wider spread than in the case of BD+60° 501, they do not reveal a clear binary behaviour. Actually, the $\sim$10 km s^{-1} dispersion in our *RV* data most probably reflects the difficulties related to the broadening of the lines and their distortion due to the profile variability (essentially for Hβ), whilst the star likely has a roughly constant radial velocity.

Most importantly, we do not detect any evidence for double lines contrary to the results of Trumpler reported by Underhill (1967). Underhill measured *RV*s of +27 and −63 km s^{-1} on two spectra separated by one year. The same remarks as for BD+60° 501 hold for these *RV*s especially as a result of the difficulties related to the line broadening.

An alternative possibility to explain the line broadening and the lack of significant *RV* changes with a binary scenario would be to assume that we observed the binary at phases between quadrature and conjunction, when the lines of the individual components are still blended. In this case, the shape of the lines (i.e. the lack of an obvious blue/red asymmetry in any of the stronger lines) would suggest that the putative binary components have to be of the same spectral type. BD+60° 513 would therefore consist of two roughly identical O7.5 V stars. It seems however rather unlikely that all our observations sample a unique orbital phase (unless the orbital period would be very long). Therefore, because of the orbital motion, we would expect the *RV* separation of both stars and hence the width of the various absorption lines to change. This is not the case in our data.

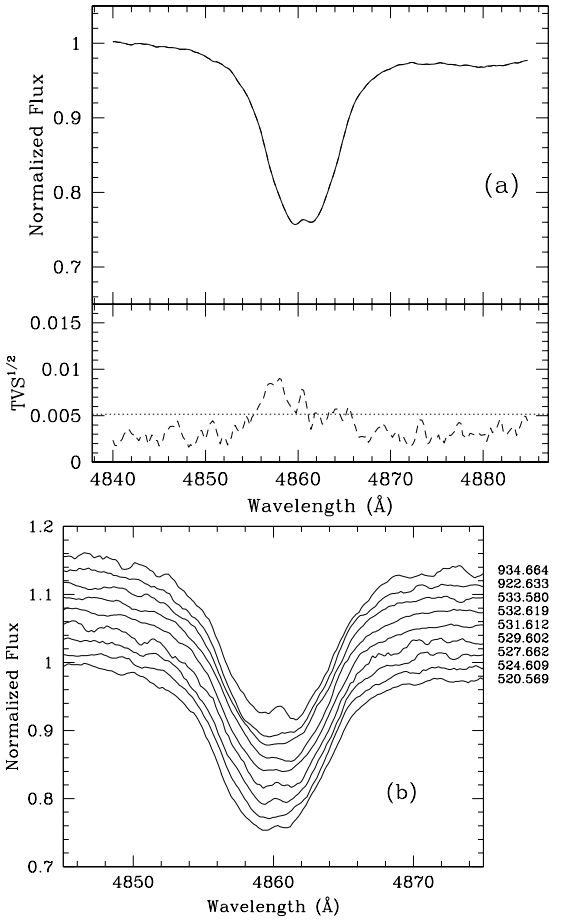

Fig. 4. Variability of the Hβ line in the spectrum of BD+60° 513. Panel **a)** yields the mean profile over our entire data set along with the square root of the TVS. The dotted line on the TVS$^{1/2}$ plot illustrates the thresholds for variations significant at the 99% level. Panel **b)** illustrates the variations of the Hβ profile as a function of time. The heliocentric Julian days are given in the format HJD−2 452 000 on the right of each spectrum. Note that the weak central emission peak in the core of the Hβ absorption is due to the contamination by the nebular emission from the IC 1805 nebula.

As mentioned above, there is some low-level line profile variability in the spectrum of BD+60° 513. In order to quantify this variability, we have computed the time variance spectrum over the entire spectral range from 4460 to 4890 Å as well as for individual lines. The TVS yields the most significant detection of variability in the blue wing of the Hβ line (see Fig. 4). The existence of this variability turns out to be robust in the sense that it remains if we omit individual spectra (one at the time) and reapply our analysis to the remaining time series. A 2D Fourier analysis (see e.g. Rauw et al. 2003) suggests time scales of 1.4 or 3.5 days for this variability. The former "period" is too short to be due to an orbital motion (there would not be enough room for a pair of O7.5 V stars in such a system). The 3.5 days period would not suffer from this problem. However, as stated above, for a short orbital period our data set would sample very different orbital phases and we

would thus expect to see variations of the apparent line widths, which we do not observe here. We note that the presence of other strong peaks in the 2D periodograms suggests that the line profile variability could occur over significantly longer or shorter time scales (depending on the choice of the right alias). Unfortunately, our time series does not allow to properly investigate profile variability on these time scales.

In summary, the *RV*s of BD+60° 513 as well as the lack of line width changes suggest that this is a rather rapidly rotating single O7.5 V((f)) star. The low-level profile variability of the Hβ line could be due to non-radial pulsations maybe occuring on a time scale too short to be sampled by our data set. In fact, the rather low mass loss rate ($2.8 \times 10^{-7}\ M_\odot\ \mathrm{yr}^{-1}$) inferred by Llorente de Andrés et al. (1982) suggests that the stellar wind density might be too low to trigger an appreciable variability in optical lines.

4. Fundamental parameters of BD+60° 497

Moffat & Vogt (1974) quote a V magnitude of 8.84 and a $B-V$ colour of 0.51 for BD+60° 497 (their star # 27011). On the other hand, Reed (1998) presents a compilation of *UBV* measurements from different bibliographic sources (see references in Reed 1998) that yield V in the range 8.76 to 8.80 and a $B-V$ colour of 0.57. Massey et al. (1995) finally quote $V = 8.85$ and $B-V = 0.54$. In the following we adopt an average value of $V = 8.80$ and $B-V = 0.57$. The latter value yields $E(B-V) \simeq 0.90$. Using near infrared photometry, Sagar & Qian (1990) showed that $R_V = 3.0$ should be appropriate for BD+60° 497. We thus obtain an extinction of $A_V \simeq 2.70$ in excellent agreement with the value (2.73 ± 0.05) that Sagar & Qian independently derived from their IR photometry.

Using photometry and spectroscopy of a large set of cluster members, Massey et al. (1995) inferred a distance modulus of $DM = 11.85 \pm 0.08$ and an age of 1–3 Myr for IC 1805. They also derived a mean colour excess $\overline{E(B-V)} = 0.87 \pm 0.02$ with a spread in colour excess from 0.68 to 1.29. The distance is in good agreement with the result ($DM = 11.9 \pm 0.1$) of Guetter & Vrba (1989). Therefore, we obtain an absolute V magnitude of $M_V = -5.75 \pm 0.12$ for the BD+60° 497 binary.

In order to position the components of BD+60° 497 in the Hertzsprung-Russell diagram, we need to derive the bolometric luminosity of the individual components. To do so, we first infer their relative brightness in the blue spectral range by comparing the measured *EW*s of the two components of the He I λ 4471 line to the mean *EW* of this line in the spectra of single stars of same spectral type. The latter were evaluated from the compilation of *EW*s provided by Conti & Alschuler (1971) and Conti (1973a). In this way, we find that the primary must be about three times brighter than the secondary in the optical spectral range: $M_{V,1} - M_{V,2} \sim -1.14 \pm 0.16$. Combining this result with the absolute magnitude of the binary system inferred above yields $M_{V,1} = -5.42 \pm 0.13$ and $M_{V,2} = -4.28 \pm 0.17$. Finally, adopting the bolometric corrections from Humphreys & McElroy (1984), we obtain bolometric luminosities of $\log L_{\mathrm{bol},1}/L_\odot = 5.55 \pm 0.05$ and $\log L_{\mathrm{bol},2}/L_\odot = 4.94 \pm 0.07$ for the primary and secondary respectively.

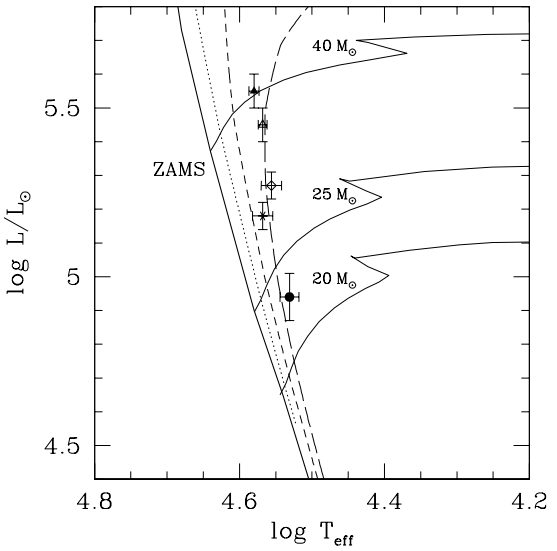

Fig. 5. Position of the primary (filled and open triangle respectively for a bolometric correction for luminosity class V or III) and secondary (filled circle) of BD+60° 497 in the Hertzsprung-Russell diagram. The evolutionary tracks for single stars of initial mass 20, 25 and 40 $M_\odot$ as well as the isochrones corresponding to ages of 1, 2 and 3 Myr are from Schaller et al. (1992) for solar metallicity. The locations of BD+60° 501 and BD+60° 513 are indicated by the star and open diamond respectively.

Following the temperature scale of main sequence O-type stars proposed by Martins et al. (2002), the effective temperature of the primary and secondary should be respectively (38 000 ± 500) K and (34 000 ± 1000) K. The location of the two components in the H-R diagram is illustrated in Fig. 5. Both stars appear to have evolved off the zero age main sequence (ZAMS). More precisely, whilst the absolute magnitude and the bolometric luminosity that we derived for the secondary are in good agreement with typical values of late O main sequence stars (see e.g. Howarth & Prinja 1989), the parameters of the primary are intermediate between those of a main sequence and a giant O6.5 star. Therefore, we may wonder whether it would not be more appropriate to use a luminosity class III bolometric correction for the primary. If we do so, we obtain $\log L_{\mathrm{bol},1}/L_\odot = 5.45 \pm 0.05$ and $T_{\mathrm{eff},1} = (37\,000 \pm 500)$ K. The corresponding position for the primary is also shown in Fig. 5.

In Fig. 5 we compare the properties of the components of BD+60° 497 to the single star evolutionary models of Schaller et al. (1992). We find that the primary lies almost exactly on the 40 $M_\odot$ initial mass evolutionary track, whilst the secondary lies between the tracks for an initial mass of 20 and 25 $M_\odot$. A crude interpolation between the various models yields evolutionary masses of $M_1 = (39.6 \pm 2.5)\,M_\odot$ and $M_2 = (22.7 \pm 1.0)\,M_\odot$ for the primary (adopting the main sequence bolometric correction) and secondary respectively. The corresponding evolutionary mass ratio (1.74 ± 0.13) of the system appears thus significantly larger than the observed mass ratio of 1.28 ± 0.12. This discrepancy (although slightly less severe) subsists if we

adopt instead the luminosity class III bolometric correction for the primary ($M_1 = (36.3 \pm 1.5)\ M_\odot$; $M_1/M_2 = 1.60 \pm 0.10$).

The evolutionary tracks of Schaller et al. (1992) account for the effect of mass loss but do not include rotational mixing. Meynet & Maeder (2000) quantified the importance of rotation on the output of stellar evolution models at solar metallicity. As a consequence of rotational mixing, fast rotators appear more luminous than non-rotating stars of the same mass. However in the region of the H-R diagram where the components of BD+60° 497 are located (i.e. near the main sequence), this effect should have a rather modest impact on the stellar luminosity ($\leq$0.1 in $\log L_{\rm bol}/L_\odot$ according to Fig. 8 of Meynet & Maeder 2000), probably not sufficient to reconcile the mass ratio estimated from the single star evolutionary tracks with the observed mass ratio, especially since the primary absorption lines do not reveal evidence for an exceptionally large rotational velocity.

These problems in the comparison of massive binaries to single star evolutionary theories are actually not new. Penny et al. (1996) already described the same sort of conflicts for binary systems where one component is suspected to currently undergo Roche lobe overflow (RLOF). These authors suggested that during case A RLOF, the mass-losing star is apparently hotter and more luminous than its mass would predict. Could this imply that the primary in BD+60° 497 is currently losing mass through RLOF?

From the luminosities and temperatures derived above we can estimate the radii of the two components to be (13.6 ± 0.9) $R_\odot$ and (8.5 ± 0.8) $R_\odot$ for the primary[1] and secondary respectively. Whilst the secondary probably fits well inside its critical volume, the primary component might fill its Roche lobe if the inclination is as large as 65° (or 74° for the giant parameters). BD+60° 497 is not known to display eclipses that might help to constrain the orbital inclination. Halbedel (1986) monitored BD+60° 497 over 43 night as one of two comparison stars during her observing campaign on BD+60° 562. The differential photometry failed to reveal significant variability of the program star or the comparison stars. Although for a short orbital period that close to an integer number of days the orbital cycle could under some circumstances be poorly sampled, it appears unlikely that BD+60° 497 displays strong variability attributable to photometric eclipses. We further checked this on the data of the Northern Sky Variability Survey (NSVS[2], Woźniak et al. 2004). The NSVS contains time series of data obtained in a single unfiltered photometric band with the Robotic Optical Transient Search Experiment. Though these data indicate a dispersion of 0.018 mag for BD+60° 497, they fail to reveal phase-locked variations attributable to eclipses or ellipsoidal variations. The lack of eclipses yields the condition $a \cos i \geq R_1 + R_2$. Substituting the numerical values from Table 2 and the radii of the components, we obtain $i \leq (54 \pm 2.5)^\circ$ (or $i \leq (55 \pm 2.5)^\circ$ for the giant parameters). For these values of the inclination, the Roche lobe radii (computed from the results in Table 2) would be sufficiently large so that none of the stars should be filling its Roche lobe. Moreover, though a direct comparison with binary evolutionary models is always tricky (due to the huge parameter space to explore), we note that models predict a rather complex behaviour for the evolutionary tracks during RLOF (e.g. de Loore & Vanbeveren 1994; Wellstein et al. 2001) and an overluminosity of the mass losing star during RLOF does not seem to be a general feature.

We thus conclude that there is no indication at present that the primary in BD+60° 497 is undergoing Roche lobe overflow. Alternatively, we caution that the numerical results obtained in this section (including the evolutionary masses) rest upon the various calibrations that we adopted. Recent results suggest that the effective temperature scale of mid-O stars might have to be revised downwards by as much as 6000 K (Bianchi & Garcia 2002) compared to the calibration of Martins et al. (2002) and this could of course impact on the properties derived in this section and account for some of the discrepancy between the observed and evolutionary mass ratios.

Using the same calibrations as above, we have also plotted the locations of BD+60° 501 and BD+60° 513 in the H-R diagram. For BD+60° 501, we infer on average $V = 9.58 \pm 0.03$ and $B - V = 0.46 \pm 0.01$ (Massey et al. 1995; Reed 1998). With $R_V = 3.0$, we thus obtain $A_{\rm V} \simeq 2.34$ in good agreement with the value (2.24 ± 0.18) of Sagar & Qian (1990). The absolute V magnitude and bolometric luminosity of BD+60° 501 thus become $M_V = -4.61 \pm 0.11$ and $\log L_{\rm bol}/L_\odot = 5.18 \pm 0.04$, whilst the effective temperature of an O7 V star should be (37 000 ± 500) K according to Martins et al. (2002). For BD+60° 513, we obtain in a similar fashion $V = 9.40 \pm 0.01$ and $B - V = 0.49 \pm 0.01$. From these values we derive $M_V = -4.88 \pm 0.11$ and $\log L_{\rm bol}/L_\odot = 5.27 \pm 0.04$ and the effective temperature is estimated as (36 000 ± 500) K. It can be noted from Fig. 5 that the location of these stars in the H-R diagram is in good agreement with the 1–3 Myr age of the cluster as determined by Massey et al. (1995).

5. *ROSAT* data

O-type stars are rather soft intrinsic X-ray emitters with luminosities that roughly follow an empirical relation between $L_{\rm X}$ and $L_{\rm bol}$ (see Berghöfer et al. 1997 and references therein). Due to an excess X-ray emission produced in the wind interaction zone, some binary systems display an X-ray luminosity above the level expected from this empirical relation. X-ray observations therefore have the potential to provide some additional hints on the multiplicity of early-type stars.

IC 1805 was observed for 8.8 ks with the PSPC instrument onboard the *ROSAT* satellite on 22–23 August 1992 (sequence number rp201263n00). We have extracted these data from the LEDAS archive and processed them using the XSELECT and XSPEC softwares. BD+60° 497 and BD+60° 501 are clearly detected with net (i.e. background corrected) count rates of $(4.6 \pm 1.3) \times 10^{-3}$ and $(6.4 \pm 1.1) \times 10^{-3}$ cts s^{-1}. BD+60° 513 is not detected in this observation and a save upper limit on its net count rate (determined from the count rate of the faintest source detected in this field) is $\sim 2 \times 10^{-3}$ cts s^{-1}.

[1] If we adopt the luminosity III bolometric correction for the primary, the radius becomes (12.8 ± 0.8) $R_\odot$.

[2] The NSVS was created jointly by the Los Alamos National Laboratory and the University of Michigan and was funded by the US Department of Energy, NASA and the NSF.

Although the X-ray spectra of BD+60° 497 and BD+60° 501 are of poor quality, we managed to fit them with an absorbed `mekal` optically thin thermal plasma model (Mewe et al. 1985).

For BD+60° 497 we fixed the neutral hydrogen column density at the interstellar value of $N_{\rm H}^{\rm ISM} = 0.52 \times 10^{22}$ cm^{-2} and we obtained a best fitting temperature $kT = 0.34^{+.43}_{-.14}$ keV with a flux of 4.2×10^{-14} erg cm^{-2} s^{-1} in the energy band 0.1−2.0 keV. The corresponding dereddened X-ray flux over the same energy range is 3.6×10^{-13} erg cm^{-2} s^{-1}. Adopting a distance of 2.3 kpc (see above), we obtain an X-ray luminosity of $L_{\rm X} = 2.4 \times 10^{32}$ erg s^{-1} in the 0.1−2.0 keV domain. From the empirical $L_{\rm X}/L_{\rm bol}$ relation of Berghöfer et al. (1997) and the bolometric luminosities of the individual binary components derived hereabove, we expect an X-ray luminosity of the binary of 2.6×10^{32} erg s^{-1} in excellent agreement with the value derived from the *ROSAT* data. Therefore, we conclude that BD+60° 497 does not display any excess X-ray emission that could be attributed to a wind interaction in the binary.

For BD+60° 501 the hydrogen column density was fixed at $N_{\rm H}^{\rm ISM} = 0.45 \times 10^{22}$ cm^{-2} and the best fitting temperature was found at $kT = 0.93^{+.75}_{-.59}$ keV. The corresponding observed and unabsorbed fluxes are 4.6×10^{-14} and 1.8×10^{-13} erg cm^{-2} s^{-1} in the 0.1−2.0 keV band. This corresponds to an X-ray luminosity of $L_{\rm X} = 1.1 \times 10^{32}$ erg s^{-1}. Again this value is in good agreement with the empirical $L_{\rm X}/L_{\rm bol}$ relation of Berghöfer et al. (1997) from which we expect an X-ray luminosity of 0.8×10^{32} erg s^{-1}. On the other hand, given the bolometric luminosity of BD+60° 513 estimated above, the non-detection of the latter in the *ROSAT* data is somewhat surprising. We note that this non-detection – and consequently the lack of an X-ray luminosity excess – provides further evidence against a close binary scenario for BD+60° 513. In fact, the O7 V + O7 V binary HD 159176 displays an X-ray excess of about a factor 7 (De Becker et al. 2004) and one would expect a very similar result if BD+60° 513 were an O7.5 V + O7.5 V binary.

In summary, the *ROSAT* data do not provide any evidence for multiplicity of BD+60° 501 or BD+60° 513.

6. Summary and conclusions

Using a set of spectroscopic data we have investigated the multiplicity of three mid-O (O6−8.5) stars in the very young open cluster IC 1805. We have found that BD+60° 497 is an SB2 system consisting of an O6.5 V((f)) primary and an O8.5-9.5 V((f)) secondary. From the radial velocities of its components, we have inferred an orbital period of 3.96 ± 0.09 days and we have presented the very first orbital solution for this system. The mass ratio of the binary 1.28 ± 0.12 is smaller than the value expected from a comparison with single star evolutionary tracks. We suggest that this discrepancy stems mainly from the uncertainties that affect the current calibrations of O-star temperatures, bolometric corrections and luminosities.

The other two targets of our present study, BD+60° 501 and BD+60° 513, do not display significant radial velocity changes, suggesting that these are probably single stars. This is in contradiction with previous reports of these stars showing *RV* changes or double lines.

So far, the only confirmed spectroscopic binaries in IC 1805 are the SB1 system HD 15558 (Garmany & Massey 1981) and the SB2 system BD+60° 497 studied in the present paper. The stars investigated here provide a complete sample of mid-O type stars in IC 1805. The fraction of confirmed binaries in this mass range is thus 1/3. Our results imply therefore that the lower limit[3] on the binary fraction among the early-type stars of IC 1805 is reduced to 60% rather than the 80% quoted by Ishida (1970) and García & Mermilliod (2001) who included BD+60° 501 and BD+60° 513 in their census of massive binary stars in IC 1805. Therefore the binary fraction in this cluster appears less extreme than previously thought. Additional data on the earliest O-type stars (HD 15558, HD 15570 and HD 15629) of IC 1805 are currently being analysed and will help to further constrain the binary fraction among O-type stars in this cluster. This will be the subject of a forthcoming paper (De Becker et al. in preparation).

Acknowledgements. We are greatly indebted to the FNRS (Belgium) for multiple assistance including the financial support for the rent of the OHP telescope in 2002 through contract 1.5.051.00 "Crédit aux Chercheurs". The travels to OHP and the rent of the telescope in 2003 were supported by the Ministère de l'Enseignement Supérieur et de la Recherche de la Communauté Française. This research is also supported in part by contract P5/36 "Pôle d'Attraction Interuniversitaire" (Belgian Federal Science Policy Office) and through the PRODEX XMM-OM and INTEGRAL contracts. We would like to thank the staff of OHP for their support. The SIMBAD and WEBDA databases have been consulted for the bibliography. We thank Dr. J.-C. Mermilliod for additional information on the WEBDA database as well as the referee Dr. C. Foellmi for a careful reading of the manuscript.

References

Albacete Colombo, J. F., Morrell, N. I., Rauw, G., et al. 2002, MNRAS, 336, 1099
Bagnuolo, W. G. Jr., Gies, D. R., Riddle, R., & Penny, L. R. 1999, ApJ, 527, 353
Berghöfer, T. W., Schmitt, J. H. M. M., Danner, R., & Cassinelli, J. P. 1997, A&A, 322, 167
Bianchi, L., & Garcia, M. 2002, ApJ, 581, 610
Conti, P. S. 1973a, ApJ, 179, 161
Conti, P. S. 1973b, ApJ, 179, 181
Conti, P. S., & Alschuler, W. R. 1971, ApJ, 170, 325
Conti, P. S., & Leep, E. M. 1974, ApJ, 193, 113
Conti, P. S., & Ebbets, D. 1977, ApJ, 213, 438
De Becker, M., Rauw, G., Pittard, J. M., et al. 2004, A&A, 416, 221
de Loore, C., & Vanbeveren, D. 1994, A&A, 292, 463
Eggleton, P. P. 1983, ApJ, 268, 368
Fullerton, A. W., Gies, D. R., & Bolton, C. T. 1996, ApJS, 103, 475
García, B., & Mermilliod, J.-C. 2001, A&A, 368, 122
Garmany, C. D., & Massey, P. 1981, PASP, 93, 500
Gillet, D., Burnage, R., Kohler, D., et al. 1994, A&AS, 108, 181
Gosset, E., Royer, P., Rauw, G., Manfroid, J., & Vreux, J.-M. 2001, MNRAS, 327, 435

[3] This fraction is a lower limit since we cannot rule out the existence of binaries seen under a low inclination (thus preventing us from detecting any *RV* changes).

Guetter, H. H., & Vrba, F. J. 1989, AJ, 98, 611
Halbedel, E. M. 1986, IBVS, 2884, 1
Heck, A., Manfroid, J., & Mersch, G. 1985, A&AS, 59, 63
Howarth, I. D., & Prinja, R. K. 1989, ApJS, 69, 527
Howarth, I. D., Siebert, K. W., Hussain, G. A. J., & Prinja, R. K. 1997, MNRAS, 284, 265
Humphreys, R. M., & McElroy, D. B. 1984, ApJ, 284, 565
Ishida, K. 1970, PASJ, 22, 277
Lafler, J., & Kinman, T. D. 1965, ApJS, 11, 216
Llorente de Andrés, F., Burki, G., & Ruiz del Arbol, J. A. 1982, A&A, 107, 43
Martins, F., Schaerer, D., & Hillier, D. J. 2002, A&A, 382, 999
Massey, P., Johnson, K. E., & De Gioia-Eastwood, K. 1995, ApJ, 454, 151
Mathys, G. 1987, A&AS, 71, 201
Mathys, G. 1989, A&AS, 81, 237
Mermilliod, J.-C. 1996, in The Origins, Evolution and Destinies of Binary Stars in Clusters, ed. E. F. Milone, & J.-C. Mermilliod, ASP Conf. Ser., 90, 97
Mewe, R., Gronenschild, E. H. B. M., & van den Oord, G. H. J. 1985, A&AS, 62, 197
Meynet, G., & Maeder, A. 2000, A&A, 361, 101
Moffat, A. F. J., & Vogt, N. 1974, Veröff. Astron. Inst. Bochum, 2
Morrell, N. I., Barbá, R. H., Niemela, V. S., et al. 2001, MNRAS, 326, 85
Normandeau, M., Taylor, A. R., & Dewdney, P. E. 1996, Nature, 380, 687
Penny, L. R., Gies, D. R., & Bagnuolo, W. G. Jr. 1996, in WR Stars in the Framework of Stellar Evolution, Proc. 33rd Liège Int. Astroph. Coll., ed. J.-M. Vreux, A. Detal, D. Fraipont-Caro, E. Gosset, & G. Rauw, 289
Rauw, G., Sana, H., Gosset, E., et al. 2000, A&A, 360, 1003
Rauw, G., Sana, H., Antokhin, I. I., et al. 2001, MNRAS, 326, 1149
Rauw, G., De Becker, M., & Vreux, J.-M. 2003, A&A, 399, 287
Reed, B. C. 1998, ApJS, 115, 271
Sagar, R., & Qian, Z.-Y. 1990, ApJ, 353, 174
Sana, H., Rauw, G., & Gosset, E. 2001, A&A, 370, 121
Sana, H., Hensberge, H., Rauw, G., & Gosset, E. 2003, A&A, 405, 1063
Schaller, G., Schaerer, D., Meynet, G., & Maeder, A. 1992, A&AS, 96, 269
Shi, H. M., & Hu, J. Y. 1999, A&A, 136, 313
Trumpler, R. J. 1930, Lick Obs. Bull., 14, 154
Underhill, A. B. 1967, in Determination of Radial Velocities and their Applications, ed. A. H. Batten, & J. F. Heard (London: Academic Press), Proc. IAU Symp., 30, 167
Underhill, A. B. 1994, ApJ, 420, 869
Walborn, N. R. 1973, AJ, 78, 1067
Walborn, N. R., & Fitzpatrick, E. L. 1990, PASP, 102, 379
Wellstein, S., Langer, N., & Braun, H. 2001, A&A, 369, 939
Woźniak, P. R., Vestrand, W. T., Akerlof, C. W., et al. 2004, AJ, 127, 2436

1.3.1 The SB2 binary BD+60° 497

I have applied the disentangling method introduced in Sect. 1.1.2 to the spectra of BD+60° 497. While radial velocities were determined for all spectra, the spectral reconstruction was restricted to those spectra that have the highest signal to noise ratio and the most secure normalisation (i.e. twelve spectra out of the sixteen used by Rauw & De Becker 2004a). The resulting individual spectra of the primary and secondary component are illustrated in Fig. 1.10. The slow apparent intensity increase of the secondary spectrum between 4800 and 4850 Å results from the difficulties of the disentangling method of González & Levato (2006) to deal with low frequency features (due to residual uncertainties of the normalisation) in the composite spectra of the SB2 binary.

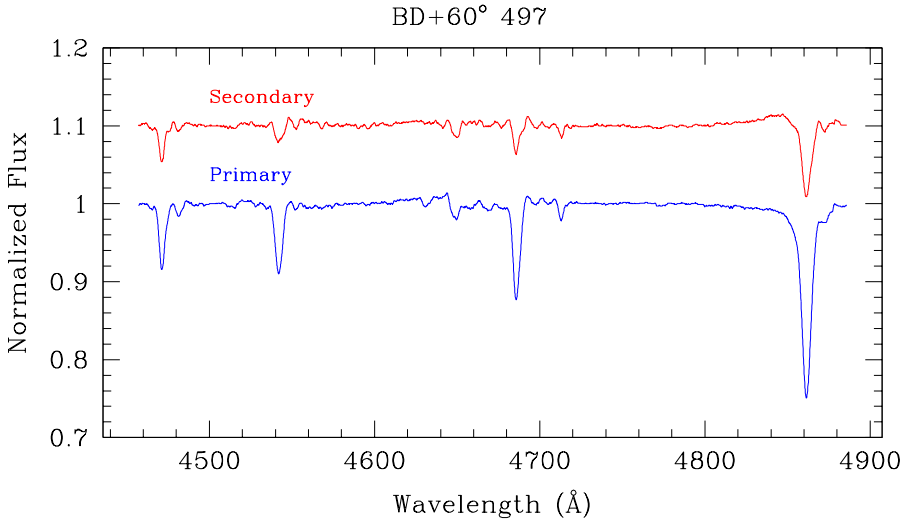

Figure 1.10: Disentangled primary and secondary spectra of BD+60° 497. Note that the level of the continuum has been set arbitrarily whilst the line intensities correspond to the actual line strengths in the composite spectrum. Also, the narrow diffuse interstellar bands were removed before the disentangling method was applied.

Although the spectral reconstruction is far from being perfect, we find a rather good agreement with the disentangled spectra of the same binary from Hillwig et al. (2006). As pointed out by González & Levato (2006), it is important to have a good coverage of the full radial velocity excursion in order for the disentangling method to produce the highest S/N in the separated spectra. However, as can be seen from Fig. 1.10, the data set does not provide such an optimal phase coverage of the orbital cycle, and therefore one expects to see some residuals in the disentangled spectra. For instance, our data miss the phases near quadrature with the most extreme radial velocity excursions and this will likely generate artefacts in the line wings of the reconstructed primary and secondary spectra.
I have measured the equivalent widths (EWs) of the He I λ 4471 and He II λ 4542 classification lines in the disentangled spectra. For the primary and secondary component, I find respectively EW(4471) = 0.36 Å and 0.22 Å as well as EW(4542) = 0.43 Å and 0.10 Å. These He I/He II line intensity ratios yield spectral types O7 and O9 for the primary and secondary respectively, in fair agreement with the classifications proposed by Rauw & De Becker (2004a). We expect the spectral types of the reconstructed spectra to be more accurate than those inferred from the Gaussian deblending technique used by Rauw & De Becker. The main reason is that the disentangling method uses (almost) all our data, whilst the Gaussian fits could only be applied to a few spectra taken near the quadrature phases. One notes that the

primary spectrum displays a weak N III emission complex near 4634-40, in agreement with the O((f)) classification proposed by Rauw & De Becker (2004a). Hillwig et al. (2006) derived slightly earlier spectral types (O6 V + O8 V) for the components of this binary system through comparison with the Walborn & Fitzpatrick (1990) spectral atlas. The optical brightness ratio (0.35 ± 0.08) that Hillwig et al. inferred is in perfect agreement with the result of Rauw & De Becker (2004a).

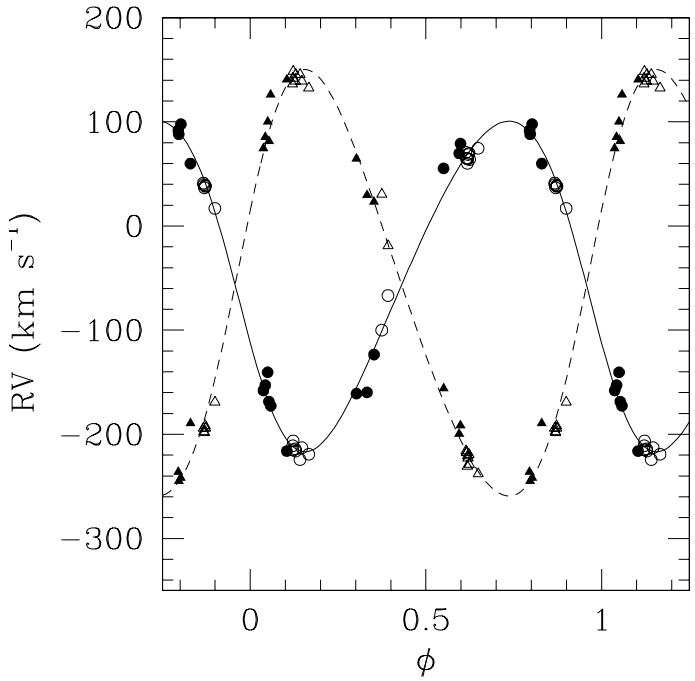

Figure 1.11: Revised orbital solution of BD+60° 497 using the RVs determined through the spectral disentangling technique (filled symbols) along with the RVs derived by Hillwig et al. (2006) (open symbols).

The RVs of the stars were determined by cross correlation with a mask consisting of those three lines measured by Rauw & De Becker (He I $\lambda\lambda$ 4471, 4713 and Mg II λ 4481). When analysed alone, the newly derived RVs yield a circular orbit with parameters that are in reasonably good agreement with the orbital solution found by Rauw & De Becker (2004a), although with slightly reduced error bars. Allowing for a non-zero eccentricity yields $e = 0.06 \pm 0.10$ and does not improve the quality of the solution.

However, recently Hillwig et al. (2006) presented a new set of radial velocities as well as a revised orbital solution for BD+60° 497. The main difference compared to the Rauw & De Becker solution was that Hillwig et al. found a significant orbital eccentricity. I have combined their RVs with the values derived from the spectral disentangling method. The corresponding orbital solution is shown in Fig. 1.11. A significant eccentricity is indeed confirmed by these data and the figure now indicates why this was missed by the Rauw & De Becker (2004a) data. In fact, our data did not sample those phases that are most sensitive to e. We note that, as a result of the non-zero eccentricity, the minimum masses of the new solution are reduced compared to those of the circular solution.

The detection of a significant eccentricity is an interesting result suggesting that BD+60° 497 is a very young binary system that has not yet undergone Roche lobe overflow. This is important in the context

Table 1.3: Revised orbital parameters of BD+60° 497 using the RVs determined through the spectral disentangling method along with the Hillwig et al. (2006) data (see Fig. 1.11). The orbital solution of Hillwig et al. is provided for comparison.

	New RVs + Hillwig et al.		Hillwig et al. (2006)	
	Primary	Secondary	Primary	Secondary
P(days)	3.9590 ± 0.0002		3.95863 ± 0.00021	
e	0.135 ± 0.010		0.156 ± 0.019	
T_0(HJD)	2452916.352 ± 0.069		2452916.233 ± 0.015	
$\omega(^\circ)$	109.8 ± 6.4		100 ± 11	
γ (km s^{-1})	-50.8 ± 2.0	-63.8 ± 2.2	-53.8 ± 1.7	-67.5 ± 2.3
K (km s^{-1})	158.7 ± 2.2	204.8 ± 2.8	159.9 ± 2.2	207.7 ± 2.9
$a \sin i$ ($R_\odot$)	12.3 ± 0.2	15.9 ± 0.2	12.39 ± 0.12	16.0 ± 0.16
$q = m_1/m_2$	1.29 ± 0.04		1.30 ± 0.08	
$m \sin^3 i$ ($M_\odot$)	10.8 ± 0.3	8.4 ± 0.2	11.1 ± 0.5	8.6 ± 0.4
$R_{RL} \sin i$ ($R_\odot$)	11.30 ± 0.05	10.06 ± 0.05		

of the discrepancy between the observed mass ratio and the evolutionary one pointed out by Rauw & De Becker (2004a). In fact, the youth of the system rules out a mass-exchange as the origin of this discrepancy. How could this issue be solved instead? There are two avenues that we can explore. First of all, the new O7 spectral type inferred from the disentangled spectra hereabove should reduce the evolutionary mass ratio slightly. Second, Hillwig et al. (2006) suggested that the distance of IC 1805 should be about 1.9 kpc instead of the commonly adopted value of 2.4 kpc (e.g. Sung & Lee 1995). This lower distance was found to be consistent with the observations of the eclipsing binary DN Cas (= BD+60° 470, O8 V + B0.2 V). If we use the calibration of Martins et al. (2005a) and the same values of the reddening and observed magnitude as Rauw & De Becker, we infer $\log L_{\rm bol}/L_\odot = 5.28 \pm 0.05$ and 4.68 ± 0.07 for the primary and secondary respectively, assuming both stars to be on the main-sequence. Interpolating in the evolutionary tracks of Schaller et al. (1992) yields evolutionary masses of 32.3 ± 1.1 and $19.0 \pm 0.5\,M_\odot$ and hence a mass ratio of 1.70 ± 0.10. This is still significantly larger than the observed value of 1.29 ± 0.23. The discrepancy thus remains unsolved with our current knowledge of this binary system.

1.3.2 Of-stars in IC 1805

De Becker et al. (2006a) recently investigated time series of spectra of the three earliest O-type stars (HD 15558, HD 155570 and HD 15629) in IC 1805. All these stars have large spectroscopic masses (between 60 and 90 $M_\odot$, Herrero et al. 2000) and were reported to display radial velocity variations in the literature. Furthermore, Romero et al. (1999) suggested that these Of stars might be associated with the unidentified EGRET source 3EG J0229 +6151.

HD 15570 and HD 15629 were classified as O4 If$^+$ and O5 V((f)) respectively (De Becker et al. 2006a, see Fig 1.12). For both stars, line profile variations were seen in the He II λ 4686 and Hβ lines (De Becker 2005). In the case of HD 15629, the Fourier analysis of the radial velocities yielded the highest peaks at $\nu = 0.08$ and $0.16\,d^{-1}$ for He I λ 4471 and He II λ 4542 respectively (De Becker et al. 2006a). However,

the corresponding amplitude of the RV variations was found to be less than $5\,\mathrm{km\,s^{-1}}$ (i.e. less than the typical measuring uncertainty of about $10\,\mathrm{km\,s^{-1}}$). For HD 15570, the Fourier analysis of the He II $\lambda\,4542$ radial velocities yielded the highest peak at $\nu \sim 0.71\,\mathrm{d^{-1}}$ with an amplitude of $\sim 4\,\mathrm{km\,s^{-1}}$, again significantly less than the typical error (De Becker et al. 2006a). In summary, we found no indication of multiplicity for these two stars on time scales of a few days up to two weeks or a few years.

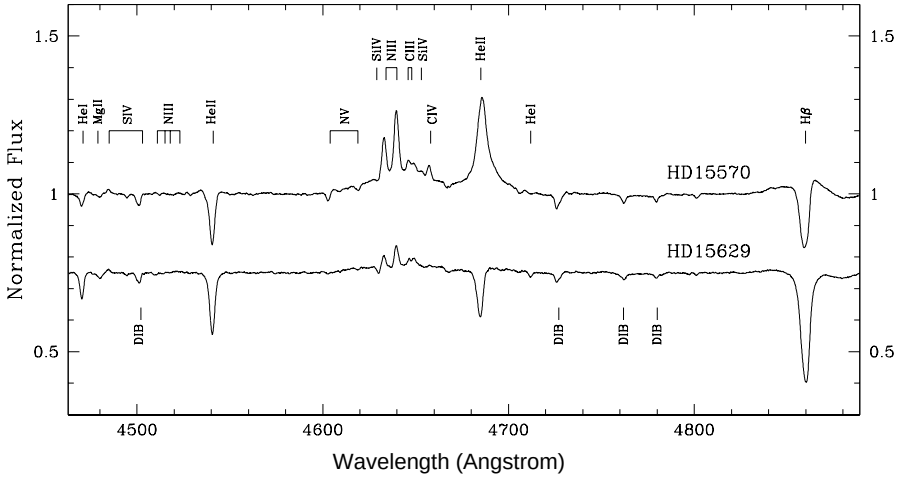

Figure 1.12: Average spectra of HD 15570 and HD 15629 as observed with the Aurélie spectrograph at OHP.

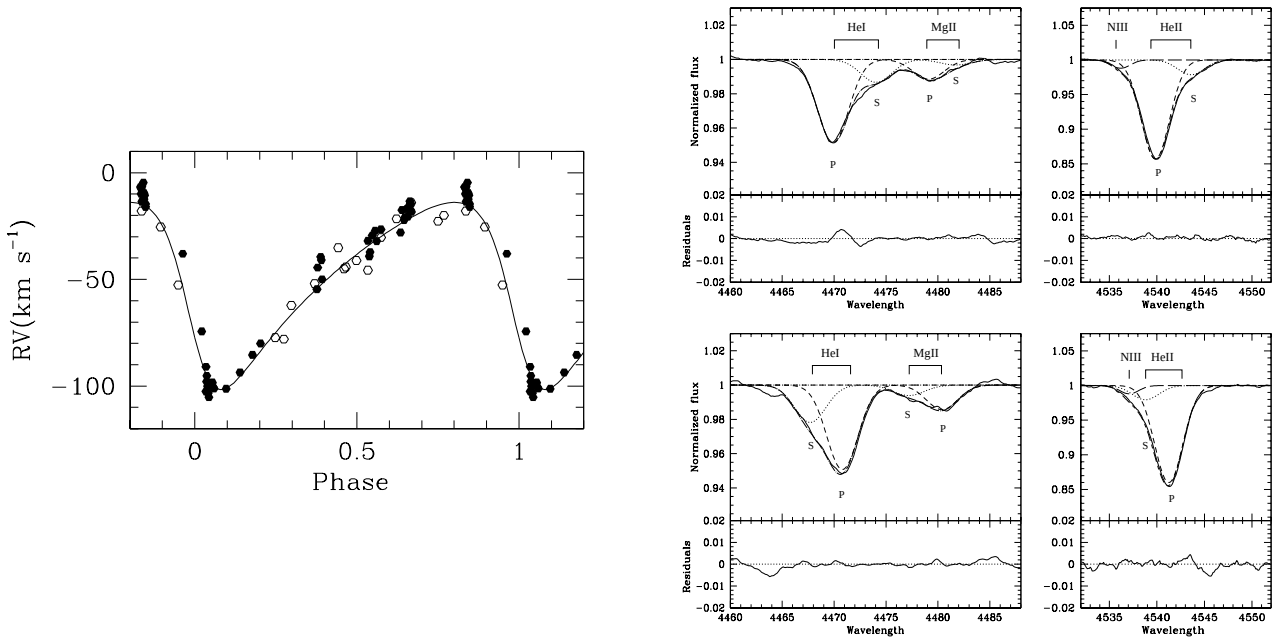

Figure 1.13: Left: SB1 orbital solution of HD 15558. Right: simultaneous fit of two Gaussians to the He I $\lambda\,4471$ and He II $\lambda\,4542$ lines near phases of maximum RV separation (De Becker et al. 2006a). The wavelengths are given in Å.

The third star, HD 15558 is a known multiple system consisting of a long period (~ 440 days) eccentric ($e \sim 0.5$) spectroscopic binary (Garmany & Massey 1981) and a visual companion (Mason et al. 1998). No SB2 orbital solution was available for this system. Interestingly, HD 15558 displays a non-thermal radio emission (Lamers & Leitherer 1993) that might originate in a wind interaction zone of the system (see also Chapter 3).

Seventy spectra of HD 15558 were obtained at OHP (53 and 17 with the Aurélie and Elodie spectrographs at the 1.52 m and 1.93 m telescopes respectively). From the He II λ 4542 radial velocities of this extensive time series, De Becker et al. (2006a) derived an orbital period of 442.5 ± 12.2 days and obtained an SB1 orbital solution (see Fig. 1.13 and Table 1.4).

Possible signatures of the secondary are seen near the maximum and minimum of the RV curve. De Becker et al. used a simultaneous Gaussian fitting process to separate the lines of the binary components (Fig. 1.13). This allowed us to classify the stars as O5.5 III(f) + O7 V. The mass ratio of the system was estimated to be around 3. So far, the SB2 orbital solution is of rather poor quality, still the mass ratio is probably quite robust as it was confirmed through spectral disentangling with the method outlined in the previous sections. The corresponding minimum masses are extremely large (Table 1.4). The minimum mass of the primary star is difficult to reconcile with its spectral type (O5.5 III(f)), especially since the initial mass of the primary would have to be even more extreme (a 120 $M_\odot$ star loses about 30% of its initial mass before it becomes an O5.5 giant, Schaller et al. 1992).

An interesting feature of HD 15558 is that the He II λ 4686 line displays line profile variations on time scales of a few days (see Fig. 1.14) although the exact recurrence time is still ill-defined (De Becker 2005). In the context of the large minimum masses inferred above, these variations could indicate that HD 15558 is actually a hierarchical triple system with a shorter period binary (the primary of the 440-day system) seen nearly face on.

Table 1.4: Orbital solutions of HD 15558 using the RVs of the He II λ 4542 line (De Becker et al. 2006a). The SB1 solution is shown in Fig. 1.13.

	SB1 solution	SB2 solution	
		Primary	Secondary
P(days)	442.478 (fixed)	442.478 (fixed)	
e	0.40 ± 0.03	0.37 ± 0.07	
T_0(HJD-2450000)	1798.39 ± 7.21	1796.27 ± 12.97	
$\omega(^\circ)$	121 ± 7	120 ± 12	
γ (km s^{-1})	-40.1 ± 1.1	-51.5 ± 12.3	-10.2 ± 15.3
K (km s^{-1})	41.3 ± 1.8	43.3 ± 6.3	135.9 ± 19.7
$a \sin i$ ($R_\odot$)	331.2 ± 15.2	351.4 ± 52.0	1101.3 ± 163.0
$f(m)$ ($M_\odot$)	2.5 ± 0.3		
$q = m_1/m_2$		3.13 ± 0.71	
$m \sin^3 i$ ($M_\odot$)		159.5 ± 58.4	50.9 ± 14.4

1.3.3 The fraction of binaries in IC 1805

Recently, Hillwig et al. (2006) studied a sample of O-stars in Cas OB 6, including some targets in IC 1805. These authors found a binary fraction of 50% in their sample. They confirmed our result that

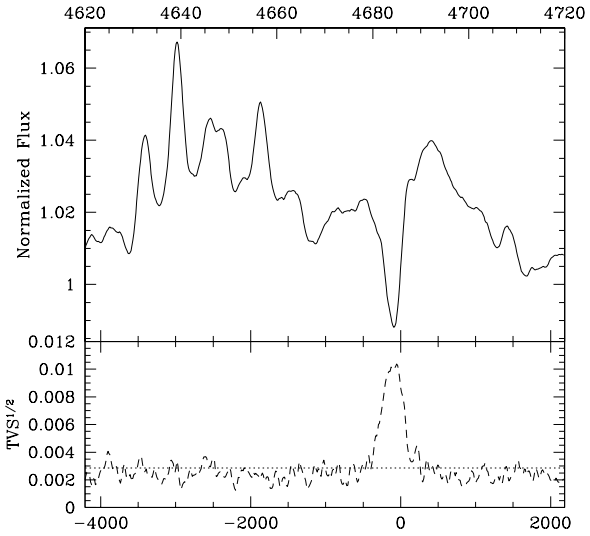

Figure 1.14: Average spectrum of HD 15558 as observed in September 2000 with the Aurélie spectrograph at OHP. The time variance spectrum (TVS) shown in the bottom panel reveals a highly significant peak in the absorption component of the He II λ 4686 line. The dotted horizontal line in the lower panel yields the 99% significance level. The abscissa is given as the wavelength (in Å) at the top and as radial velocities (in km s^{-1}) in the frame of the He II λ 4686 line in the bottom scale.

BD+60° 501, BD+60° 513, HD 15570 and HD 15629 have most probably a constant radial velocity. Rauw & De Becker (2004a) established a 1-$\sigma_{\rm RV}$ dispersion of 2.5 and 10.5 km s^{-1} on the radial velocities of BD+60° 501 and BD+60° 513 respectively. For the He II λ 4542 lines in HD 15570 and HD 15629, the 1-$\sigma_{\rm RV}$ dispersions were found to be 5.9 and 5.2 km s^{-1} (De Becker et al. 2006a). From the lack of significant RV variations, we concluded that these stars are most likely single. The RV data used in these papers allow us to check time scales of a few days up to a few weeks as well as longer time scales of the order of one or a few years.

How secure is the statement that these objects are indeed single stars? To answer this question, let us first recall the observational biases that might affect the detection of a spectroscopic binary. The first problem that comes to mind is that the orbital inclination might be close to zero, thus reducing the amplitude of the radial velocity variations below our detection threshold. Second, the mass ratio ($q = m_1/m_2$) could be quite large, again reducing the amplitude of the primary's radial velocity curve and hampering the detection of the secondary's spectral signature. Third, we might have explored the wrong time scales. Obviously if the orbital periods were rather long, the amplitudes of the radial velocity variations would be small.

One can use the approach of Garmany et al. (1980) to evaluate the probability that we have missed a spectroscopic binary as a result of a low orbital inclination and for a given period and mass ratio. For this purpose, I take the rather conservative assumption that the semi-amplitude of the radial velocity curve K should be smaller than $2 \times \sigma_{\rm RV}$.

The mass function of the primary component can be written:

$$f(m) = \frac{m_1 \, \sin^3 i}{q \, (1+q)^2} = 1.0355 \times 10^{-7} \, K^3 \, P \, (1-e^2)^{3/2}$$

where m_1 is the primary mass (in M$_\odot$), K is expressed in km s^{-1}, e is the orbital eccentricity and P is

the orbital period (in days). This relation can be easily transformed to express the orbital inclination as a function of the other parameters. Inserting the upper limit on K and assuming $e = 0$ then yields an upper limit on $\sin i$:

$$\sin i \leq 9.392 \times 10^{-3}\, \sigma_{\rm RV} \left(\frac{P\, q\, (1+q)^2}{m_1} \right)^{1/3} \tag{1.2}$$

For BD+60° 501 and BD+60° 513, Rauw & De Becker (2004a) inferred spectral types of O7 V((f)) and O7.5 V((f)) respectively and I shall thus adopt masses of $m_1 = 30$ and $m_1 = 27\,{\rm M}_\odot$ respectively. For HD 15570 (O4 If$^+$) and HD 15629 (O5 V((f))), I consider masses of $m_1 = 70$ and $40\,{\rm M}_\odot$ respectively. Assuming a random distribution of the orbital directions in space, the probability that the orbital inclination is indeed smaller than the value obtained from Eq. (1.2) can be evaluated as

$$\int_0^{i_{\rm up}} \sin i\, di = 1 - \cos i_{\rm up}$$

Table 1.5: Probability that i be lower than the upper limit evaluated from Eq. (1.2) for different values of the orbital period P and the mass ratio q.

	$P = 3$ days			$P = 15$ days		
	$q = 1$	$q = 5$	$q = 10$	$q = 1$	$q = 5$	$q = 10$
BD+60° 501	1.5×10^{-4}	1.9×10^{-3}	6.8×10^{-3}	4.4×10^{-4}	5.6×10^{-3}	2.0×10^{-2}
BD+60° 513	2.8×10^{-3}	3.6×10^{-2}	13.7×10^{-2}	8.3×10^{-3}	11.1×10^{-2}	49.6×10^{-2}
HD 15570	4.7×10^{-4}	6.0×10^{-3}	2.2×10^{-2}	1.4×10^{-3}	1.8×10^{-2}	6.5×10^{-2}
HD 15629	5.3×10^{-4}	6.8×10^{-3}	2.4×10^{-2}	1.6×10^{-3}	2.0×10^{-2}	7.3×10^{-2}

From the results in Table 1.5 it appears that the probability that BD+60° 501 be a spectroscopic binary with a period of less than 15 days and a secondary component earlier than A0 (i.e. $q \leq 10$) is only $\leq 2\%$. For the same range of orbital periods, the probability that the companion be a star earlier than spectral type B5 ($q \leq 5$) would be $\leq 0.6\%$. For significantly longer orbital periods (less well sampled by the RV data of Rauw & De Becker 2004a), the results are of course less stringent. Therefore, we may conclude that for orbital periods between a few days and about one month, the probability of BD+60° 501 being a spectroscopic binary is indeed very small.

For BD+60° 513, the larger RV dispersion (resulting mainly from the broader spectral lines and their profile variability) yields poorer constraints. Assuming a period of ≤ 15 days, the probability of having an O-type companion would be rather small. However, there could still be an 11% chance of having an inclination small enough to hide a binary system with a B5 secondary. Therefore, if BD+60° 513 was a binary with a period of less than about one month, it would most probably have to be a system with a rather large mass ratio and hence a late-type companion.

In a similar fashion, the probability that HD 15570 and HD 15629 would be binaries with late O - early B companions and periods of less than 15 days is very low ($\leq 2\%$).

We thus conclude that the fraction of binaries among the O-type stars (earlier than O9) in the core of IC 1805 is likely of the order of one third, much less than previously claimed (e.g. García & Mermilliod 2001).

1.3.4 The location of the stars in the Hertzsprung-Russell diagram

The 2005 update of the online catalogue of Reed (1998) lists about ten values for the photometry of each of the three brightest O stars in IC 1805. The mean values and standard deviations of the V magnitudes and $B-V$ colours are respectively 7.87 ± 0.05 and 0.51 ± 0.02 for HD 15558, 8.11 ± 0.03 and 0.70 ± 0.06 for HD 15570 and 8.42 ± 0.03 and 0.42 ± 0.01 for HD 15629. Assuming $R_V = 3.1$ and adopting the distance of 1.9 kpc advocated by Hillwig et al. (2006), yields absolute magnitudes of $M_V = -6.09$, -6.41 and -5.29 for HD 15558, HD 15570 and HD 15629 respectively. From the ratio of the EWs quoted by De Becker et al. (2006a), I infer a brightness ratio of 4.9 ± 2.0 for the primary and secondary in HD 15558. Accounting for this brightness ratio and using the calibration of Martins et al. (2005a) finally yields $\log L_{\rm bol}/L_\odot = 5.72 \pm 0.03$ and 4.95 ± 0.07 for the primary and the secondary of HD 15558 respectively. In the same manner, one finds $\log L_{\rm bol}/L_\odot = 5.96 \pm 0.08$ and $\log L_{\rm bol}/L_\odot = 5.52 \pm 0.02$ for HD 15570 and HD 15629 respectively.

The location of the O-type stars of IC 1805 investigated here in the Hertzsprung-Russell diagram is shown in Fig. 1.15. The most massive and most evolved O-stars of the cluster suggest an age of about 2 Myr. Note that adopting a cluster distance of 2.4 kpc instead of 1.9 kpc would shift the stars upwards in $\log L_{\rm bol}/L_\odot$ by 0.20. With the distance determined by Hillwig et al. (2006), we see that the masses of the primary and secondary of HD 15558 would be about 50 and 25 $M_\odot$ respectively, i.e. much less than the minimum masses inferred from the SB2 solution of De Becker et al. (2006a). This result casts further doubt on the reality of these large minimum masses.

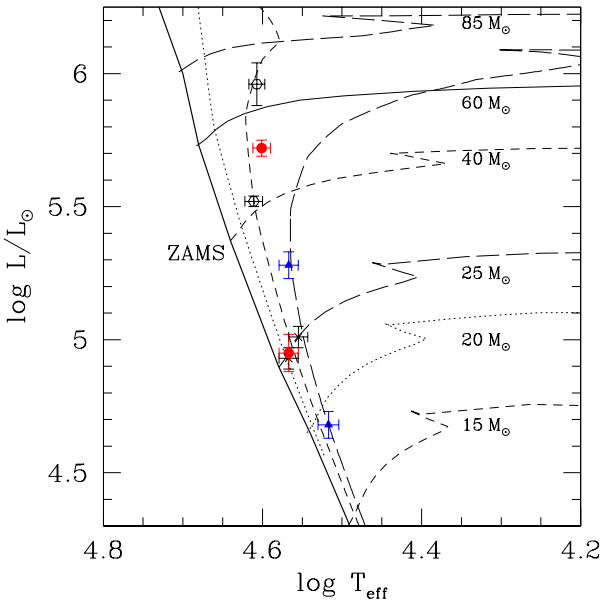

Figure 1.15: Observational Hertzsprung-Russell diagram of the O-type stars in IC 1805. Filled symbols stand for known spectroscopic binaries, whilst open symbols represent presumably single stars.

1.4 Evolved, post Roche lobe overflow early-type binaries

While the previous sections were mainly devoted to relatively unevolved main-sequence O-type binaries, I turn now to the cases of two evolved systems. In this section, I present the observational study of HD 149404 (Rauw et al. 2001b) and HDE 228766 (Rauw et al. 2002b): both systems are shown to be likely in a post Roche lobe overflow (RLOF) evolutionary stage.
Roche lobe overflow occurs when a component of a binary system (usually the more massive star, except in X-ray binaries or cataclysmic variables) expands during its evolution and fills up its critical volume. From a theoretical point of view, one can distinguish various types of RLOF (e.g. Vanbeveren 2004):

- case A corresponds to RLOF of the more massive star while it is still in the core-hydrogen burning phase;
- case B RLOF occurs when the more massive star fills its critical volume while it is in the hydrogen shell burning stage;
- and finally, if the more massive star goes into RLOF after core helium exhaustion and during the hydrogen and helium shell burning phase, one speaks about a case C.

The systems discussed in this section are most likely in a post case-A or B evolutionary stage.

A&A 368, 212–224 (2001)
DOI: 10.1051/0004-6361:20000527

Astronomy & Astrophysics

The strange case of the massive binary HD 149404⋆

G. Rauw[1,⋆⋆,‡], Y. Nazé[1,⋆⋆⋆], F. Carrier[2], G. Burki[2], E. Gosset[1,†,‡], and J.-M. Vreux[1]

[1] Institut d'Astrophysique et de Géophysique, Université de Liège, 5 avenue de Cointe, 4000 Liège, Belgium
[2] Observatoire de Genève, 1290 Sauverny, Switzerland

Received 30 October 2000 / Accepted 15 December 2000

Abstract. We report the analysis of an extensive set of high-resolution spectroscopic observations of the massive binary system HD 149404. We compare different techniques to measure the radial velocities of the heavily blended absorption lines and we derive a new orbital solution. The absorption lines display strong variability that slightly affects the orbital solution and the determination of the spectral types of the components of the binary. We find that the primary is probably of spectral type O7.5 I(f), while the secondary is most likely an ON9.7 I supergiant. The secondary seems to be the most evolved component of the system and its current evolutionary status could best be explained if the system has undergone a Roche lobe overflow episode during the past. The secondary could actually still be rather close to filling its critical volume and this could lead to an enhanced mass loss of the secondary. The spectrum of HD 149404 displays many emission lines some of which show phase-locked line profile variations. In particular, the Hα line displays a double-peaked morphology at orbital phases near conjunction. We investigate the radial velocity behaviour of the emission lines and we find that some of them must be formed in an interaction region. We propose a simple model where some of the optical emission lines arise in a heavily bended shock region.

Key words. stars: early-type – binaries: spectroscopic – stars: individual: HD 149404

1. Introduction

Over the last decade, substantial progress has been achieved in our understanding of the interaction processes in early-type binary systems. It has been shown that some of the emission lines in the spectra of O-star binaries are at least partially formed in the wind interaction region (e.g. Thaller 1997). Observations of the phase-locked emission line profile variability can be used to constrain the geometry of the interaction region and allow us in principle to distinguish between a colliding wind phenomenon and a Roche lobe overflow (RLOF) process (e.g. Wiggs & Gies 1993; Rauw et al. 1999). A detailed analysis of the interaction phenomena in binaries in different evolutionary stages is therefore crucial for our understanding of stellar evolution as well as for a determination of the properties of the stellar winds of the binary components.

In the present paper, we discuss an extensive set of spectra of HD 149404 (= HR 6164 = V 918 Sco). Walborn (1972) assigned an O9 Ia spectral type to the global spectrum of this system. Later on, it was discovered that some lines were actually double, but heavily blended (Conti et al. 1977). A first orbital solution was derived by Massey & Conti (1979) from a set of optical spectra, and another one was obtained by Stickland & Koch (1996) from IUE observations (see Table 4). Several spectral features of HD 149404 point towards an interaction between the two components. In fact, Massey & Conti (1979) noticed the double-peaked structure of the Hα emission profile in the spectrum of HD 149404 and they interpreted this feature as a signature of an ongoing Roche lobe overflow process. More recently, Thaller (1998) suggested that the behaviour of the two Hα peaks was due to a colliding wind interaction. HD 149404 is also known to display the so-called "Struve-Sahade effect" (Stickland 1997). So far, the origin of this effect remains unclear although Gies et al. (1997) suggest that it could result from photospheric heating by the X-ray emission generated in the wind interaction region.

This paper is organized as follows: the observations and the data reduction are presented in Sect. 2 and the

Send offprint requests to: G. Rauw,
e-mail: rauw@astro.ulg.ac.be

⋆ Based on observations collected at the European Southern Observatory (La Silla, Chile) and at the Cerro Tololo Inter-American Observatory (CTIO).
⋆⋆ Postdoctoral Researcher FNRS (Belgium).
⋆⋆⋆ Research Fellow FNRS (Belgium).
† Research Associate FNRS (Belgium).
‡ Visiting Astronomer, CTIO, National Optical Astronomy Observatories (NOAO). NOAO is operated by the Association of Universities for Research in Astronomy, Inc. under contract with the National Science Foundation.

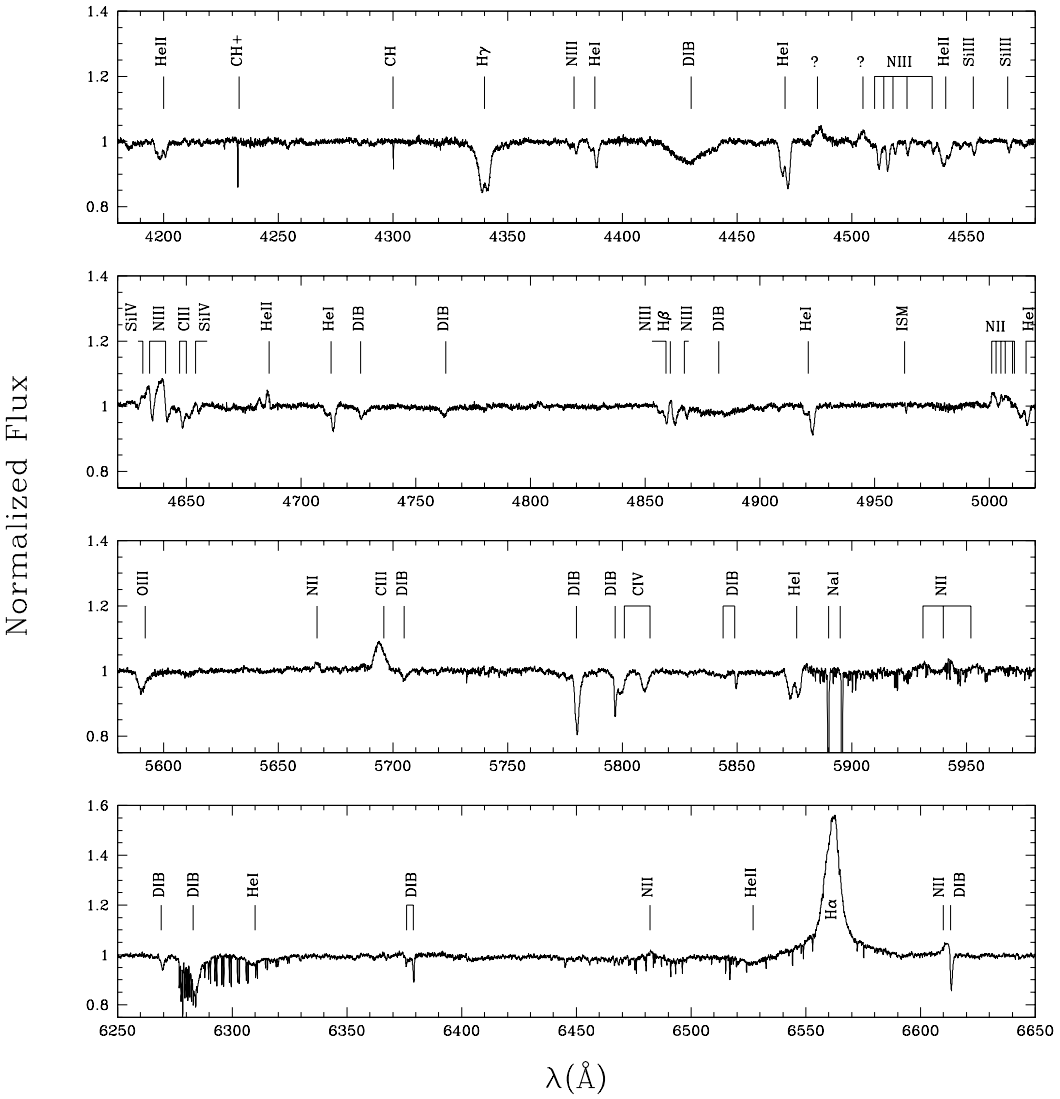

Fig. 1. Spectrum of HD 149404 as observed with the FEROS spectrograph on HJD 2451299.800 ($\phi = 0.23$). At this orbital phase, the spectrum of the most massive star is shifted towards the blue

spectral features of HD 149404 are discussed in Sect. 3. Different techniques are used to measure the radial velocities of the absorption lines and a new orbital solution is derived in Sect. 4. In Sect. 5, we discuss the luminosity ratio of the binary components. As a next step, we examine the variations of the emission lines (Sect. 6). Finally, we discuss a possible model for the interaction in HD 149404 as well as the evolutionary status of the system (Sect. 7).

2. Observations and data reduction

We observed HD 149404 over a period of 3 years with various instruments. A first set of spectra, covering roughly 45 Å centred on the He I λ4471, He II λ4686 and N III $\lambda\lambda$4634-41 lines, was obtained in June 1997 with the 1.4 m Coudé Auxiliary Telescope (CAT) at ESO, La Silla, feeding the Coudé Echelle Spectrometer (CES) and the Long Camera (LC). Additional data (covering 20 Å around the He I λ4471 and He II λ4686 lines) were taken with the same spectrograph equipped with the Very Long Camera (VLC) in April–May 1998 and July 1998. In all cases, the detector was ESO CCD#38, a Loral 2688×512 CCD with pixel size 15 μm × 15 μm. The nominal resolving power was 70 000–80 000. Typical exposure times were of the order of 15 min and the average signal-to-noise ratio was about 150.

In May 1999 and May 2000, we observed HD 149404 with the Fiber-fed Extended Range Optical Spectrograph (FEROS, Kaufer et al. 1999) at the ESO 1.52 m telescope at La Silla. The spectra cover the wavelength range 3650–9200 Å with a resolving power of 48 000. The detector was a 2k × 4k EEV CCD with pixel size 15 μm × 15 μm.

The typical exposure time was 2 min and the S/N ratio at 6000 Å is about 160.

Five more spectra were taken in May–June 1999 with the Bench-Mounted Echelle spectrograph (BME) fed by the 1.5 m Ritchey-Chrétien telescope at CTIO. These data covered the spectral range 3750–5800 Å. The typical S/N ratio was 120 at 4620 Å for exposure times of about 20 min. The detector used was a TEK CCD with 2048 × 2048 pixels of 24 μm × 24 μm and the resolving power was 45 000.

Finally, twelve echelle spectra were obtained in February 2000 with the 1.2 m Euler Swiss telescope at La Silla, equipped with the Coralie spectrograph and a 2k × 2k CCD with pixel size 15 μm × 15 μm. The Coralie instrument is an improved version of the Elodie spectrograph (Baranne et al. 1996). These observations covered the spectral range 3875–6800 Å with a resolving power of 50 000. The integration times varied between 30 and 45 min and the typical S/N ratio at 5000 Å was 120–150.

The CAT data were reduced in a standard way with the MIDAS software developed at ESO. The spectra were normalized by fitting a low order polynomial to the continuum. The FEROS spectra were reduced using the appropriate context of the MIDAS environment together with several dedicated routines kindly provided by Dr. O. Stahl. The extracted FEROS spectra were rectified by fitting a polynomial of degree 4 or 5 to the continuum over a range of a few hundred Å at once.

The CTIO data were reduced using the IRAF[1] package, following the recommendations of the BME User's Manual. We used the smoothed projector flat field exposures as a first guess of the continuum, and the spectra were finally normalized using a low-order polynomial.

The Coralie data were reduced at the telescope, using the INTER-TACOS (INTERpreter for the Treatment, the Analysis and the COrrelation of Spectra) software developed by D. Queloz and L. Weber at the Geneva Observatory (Baranne et al. 1996). Next, the normalisation was done by dividing by the blaze fits and finally by fitting a polynomial to the continuum.

Whenever several exposures were available for the same night, we averaged them to increase the S/N ratio. Some preliminary results based on our data were already presented by Nazé et al. (2000).

3. The spectrum of HD 149404

A FEROS spectrum of HD 149404 is shown in Fig. 1. Besides the lines of the upper Balmer series (above Hγ), the spectrum reveals many typical O-star absorption lines of He I, He II, N III, Si III, Si IV, C IV and O III. The less massive star exhibits strong N III absorptions whereas N III is seen as a weak absorption or emission (N III $\lambda\lambda$4634-41) in the primary's spectrum. The spectrum reveals also a number of diffuse interstellar bands (DIBs), as well as interstellar absorptions due to Na I, Ca II, CH and CH^+. However, the most remarkable feature of HD 149404 is the important number of emission lines in its spectrum: Hα, Hβ, He II λ4686, C III λ5696, as well as several N II and Si IV lines. We will come back to some of these features in the next sections. Throughout this paper we will refer to the more massive star as the primary.

[1] IRAF is distributed by the National Optical Astronomy Observatories.

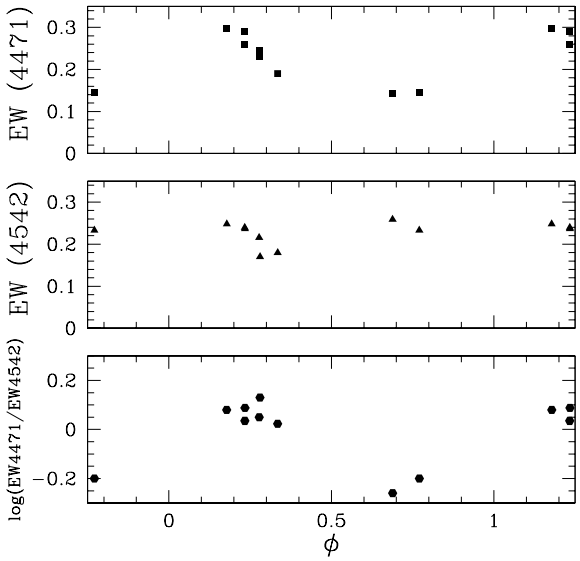

Fig. 2. Variations of the equivalent width of the He I λ4471 and He II λ4542 lines and of the log(W') criterion for the primary star as a function of orbital phase

3.1. Spectral types

Only the least blended spectra are suitable for the spectral classification. Following Conti & Alschuler (1971), Conti & Frost (1977) and Mathys (1988, 1989), we adopt the $\log W' = \log(EW(4471)/EW(4542))$ classification criteria. We caution that the equivalent width (EW) of the He II λ4542 line of the individual components is rather difficult to measure in the case of HD 149404 because of the severe blending.

For the secondary, we find $\log W'$ between 0.51 and 0.83, corresponding to a spectral type O9.7 (using the Mathys criteria). The O9.7 classification is also supported by the fact that the He II λ4542 and Si III λ4552 absorptions have about the same strength (Walborn & Fitzpatrick 1990).

For the primary, we obtain $\log W'$ between −0.26 and 0.13. More specifically, we find an O6.5 spectral type for orbital phases near 0.75, i.e. when the primary is moving towards us (see Fig. 2), and an O7.5 type half a period later. In fact, Fig. 2 indicates that the orbital variation of $\log W'$ is essentially due to the variation of the equivalent width of the He I λ4471 line. It is interesting to note that the He I λ4471 absorption of the secondary displays

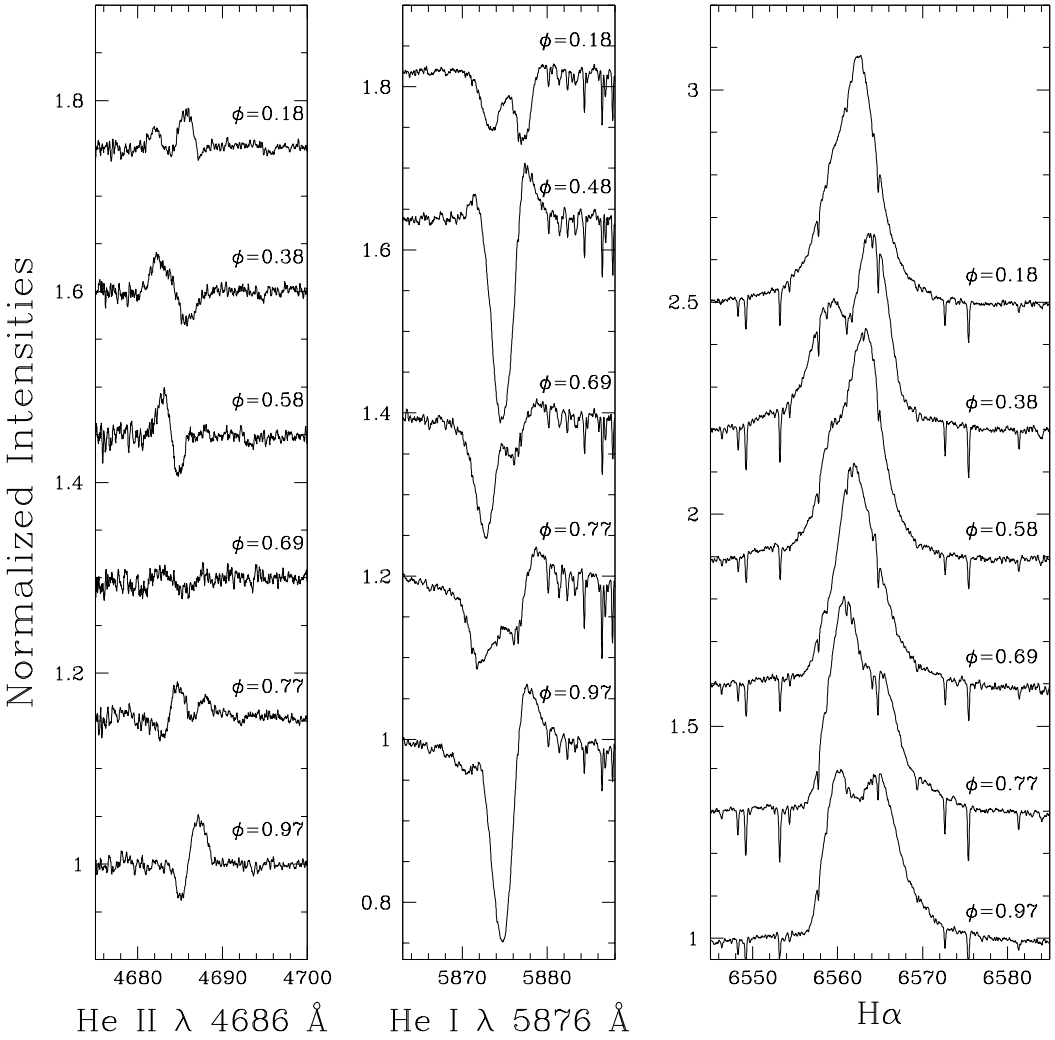

Fig. 3. Variation of the He II λ4686, He I λ5876 and Hα lines with phase

the opposite behaviour[2], i.e. it appears stronger around $\phi = 0.75$ and weaker near $\phi = 0.25$ (Nazé et al. 2000). The behaviour of both absorption components at He I λ4471 could therefore at least partially reflect the blending with a weak, slightly red-shifted emission component that does not follow the orbital motion of neither star. Such an emission feature is indeed seen in the He I λ5876 line (see Fig. 3) and we actually detect a weak emission on some of the He I λ4471 spectra taken near conjunction. At phases near 0.75, the emission is blended with the primary's absorption, hence reducing its equivalent width. The reverse situation occurs half a cycle later, when the secondary's absorption is blended with the emission. As the primary's EW is most probably less affected by the emission feature around $\phi = 0.25$, we adopt the O7.5 classification for this star (see also Nazé et al. 2000).

For the luminosity classification, we rely on the $\log W'' = \log(EW(\mathrm{Si\,IV}\ \lambda4089)/EW(\mathrm{He\,I}\ \lambda4143))$ criterion introduced by Conti & Alschuler (1971). This turned out to be even more difficult than the spectral classification. In fact, He I λ4143 could be deblended on a few spectra only and we could only set an upper limit of ≤ 0.07 Å on the EW of the primary's He I λ4143 line. For the secondary, we find $\log W''$ between 0.36 and 0.65 corresponding to a supergiant classification. In the same way, our upper limit on the primary's EW(He I λ4143) yields $\log W'' \geq 0.4$ (at all orbital phases), also corresponding to luminosity class I. We caution that a similar effect as for the He I λ4471 line could alter the EWs of the He I λ4143 lines, although we do not expect this effect to significantly affect our conclusions.

On the other hand, He II λ4686 could be in absorption in the spectrum of both stars (see below), an

[2] We caution however that the variation of the $\log W'$ criterion of the secondary results also from variations of the EW of the He II λ4542 line that are more pronounced than for the primary.

Table 1. Radial velocities (in $\mathrm{km\,s^{-1}}$) of the most prominent interstellar lines in the spectrum of HD 149404. The quoted uncertainties correspond to the 1-σ dispersion of the RVs measured during the same observing run

Line	FEROS 1999	Coralie	FEROS 2000
Ca II λ3933	-3.9 ± 0.2	-4.5 ± 0.3	-2.7 ± 0.1
Ca II λ3968	-3.8 ± 0.3	-5.3 ± 0.5	-3.8 ± 0.1
CH^+ λ3958	-2.4 ± 0.6	-3.6 ± 2.9	-2.3 ± 0.8
CH^+ λ4233	-1.6 ± 0.6	-2.7 ± 0.4	-1.9 ± 0.4
CH λ4300	-0.4 ± 0.2	-1.0 ± 0.3	-0.4 ± 0.4
Na I λ5890	-7.8 ± 0.3	-8.4 ± 0.4	-8.2 ± 0.0
Na I λ5896	-7.9 ± 0.3	-8.2 ± 0.3	-7.9 ± 0.0

unlikely feature for luminosity class I stars, especially for Ia stars (Walborn 1971). Finally, the N III $\lambda\lambda$4634-41 emission lines appear to follow more or less the motion of the primary. Therefore we add an (f) tag to the spectral classification of the primary.

3.2. Interstellar lines

We have measured the radial velocities (RVs) of the most prominent interstellar lines (Table 1). Both Ca II lines exhibit a blueshifted much fainter component which is only visible on the FEROS spectra.

We emphasize the very good night-to-night stability of the FEROS and Coralie spectrographs as revealed by the small 1-σ dispersions of the RVs in Table 1. There is a slight difference of the order of $0.5\,\mathrm{km\,s^{-1}}$ between the RVs derived from the FEROS and the Coralie data. Moreover, we notice that there is a slight RV-difference between the Ca II and Na I lines. Stickland & Koch (1996) adopted a radial velocity of $-7.5\,\mathrm{km\,s^{-1}}$ for the interstellar features in their *IUE* spectra, which is consistent with our results for the Na I lines.

4. Orbital solution

4.1. Radial velocity determination

Since He I λ4471 is the most extensively covered absorption line in our data set and since it is also usually the least blended one, we decided to use the RVs of this line to determine a new orbital solution. Other lines are either weak (e.g. He II λ4542), blended with other weaker absorptions (He II λ4200 blended with N III λ4196) or affected by a rather strong emission component (He I λ5876). These features are thus not well suited to measure the RVs of the binary components.

We notice that the intensities of the absorption lines (including He I λ4471, see Fig. 2 and Nazé et al. 2000) change with phase. This phenomenon is not unexpected since HD 149404 is known to display variations of the line strength in the UV that could be related to the so-called "Struve-Sahade effect" (Stickland 1997).

The radial velocities were determined by fitting two Gaussians whenever it was possible to do so. However, the lines remain heavily blended over the main part of the orbit and even around quadrature the lines are not completely separated. Therefore, two different techniques were tested to determine the radial velocities when Gaussian fitting turned out to be impossible. In both cases we use a template line profile built from the spectra at maximum separation.

(1) When the lines are partially blended, the "outer" wing of the strongest line is rather unaffected by the other line. Fitting the corresponding wing of the template spectrum to the observed profile yields the position of the strongest line. Next, the template profile of the strongest line is shifted to the correct position and subtracted from the observed spectrum. The position of the weaker line is finally obtained by fitting a Gaussian to the residuals;
(2) Alternatively we have attempted a simultaneous fit of the positions of the lines of both components. To this aim we have shifted both templates independently and simultaneously until we found a best fit to the observed profile.

The resulting radial velocities are presented in Table 2.

Given the difficulties due to the severe blending of the lines, we also used another method developed at the Geneva observatory to determine the radial velocities. The velocities are obtained by cross-correlation of the FEROS and Coralie spectra with a mask built from a synthetic spectrum. This method is well known for less massive stars, but this is the first attempt to extend it to the optical spectra of O-type stars. A synthetic O-star spectrum in the 3875–6820 Å spectral domain was generated using the SYNSPEC (Hubeny et al. 1994) code with the model atmospheres interpolated from the Kurucz ATLAS9 (1994) grid. The Vienna Atomic Line Database was used to create a line list for the spectrum synthesis (Kupka et al. 1999). The spectrum synthesis programme uses an LTE-model which is certainly not appropriate to determine the properties of O-stars, but should be sufficient for the radial velocity determinations. Many tests were conducted and eventually, a synthetic spectrum with $T_{\rm eff} = 42\,500$ K was adopted because it provided the most narrow cross-correlation peak. Blended lines as well as emission lines or lines that occur in the synthetic spectrum but are absent from the actual spectrum were removed from the mask. Therefore, the final mask no longer corresponds to a single $T_{\rm eff}$ but should be valid over a rather broad temperature range from about 35 000 to 42 500 K. The radial velocities were finally obtained from the cross-correlation function by fitting two Gaussians. The results are presented in the last two columns of Table 2.

4.2. Period determination

We used the generalized Fourier spectrogramme technique of Heck et al. (1985, hereafter HMM, see their Eq. (1)) and

Table 2. Barycentric radial velocities obtained for He I λ4471 and by a correlation with a synthetic mask. The dates of the observations are given in the format HJD–2450000 and the orbital phases are those corresponding to the circular orbital solution derived from the cross-correlation RVs (see Table 3). The method used to derive the RVs of the He I λ4471 line is specified in the sixth column: d(nbr of Gaussians) = Gaussian fit, $c1$ ($c2$) = 1st (2nd) technique (see text), m = mean of techniques listed in brackets

Instr.	Date	ϕ	He I λ4471			cross-correlation	
			RV_1 km s^{-1}	RV_2 km s^{-1}	Method	RV_1 km s^{-1}	RV_2 km s^{-1}
LC	622.588	0.23	−107.0	71.7	$d(2)$		
LC	623.595	0.34	−107.1	35.5	$m(c1, c2)$		
LC	624.552	0.43	−86.9	−14.2	$m(c1, c2)$		
LC	625.593	0.54	−58.2	−58.2	$d(1)$		
LC	626.556	0.64	−12.3	−109.4	$c1$		
VLC	925.944	0.14	−103.4	26.8	$m(d(2), c1)$		
VLC	926.944	0.24	−124.2	47.6	$d(2)$		
VLC	930.884	0.65	0.2	−136.9	$m(d(2), c1)$		
VLC	932.946	0.86	−21.2	−124.6	$m(d(2), c1)$		
VLC	937.914	0.36	−111.9	13.7	$m(d(2), c1)$		
VLC	995.635	0.24	−116.6	72.5	$d(2)$		
VLC	996.565	0.34	−96.9	31.3	$m(c1, c2)$		
VLC	997.581	0.44	−66.3	4.1	$m(c1, c2)$		
VLC	998.572	0.54	−73.9	−73.9	$d(1)$		
VLC	999.572	0.64	−48.5	−147.4	$m(c1, c2)$		
VLC	1000.544	0.74	36.7	−160.6	$d(2)$		
FER.	1299.800	0.23	−117.8	52.9	$d(2)$	−108.0	55.5
FER.	1300.793	0.34	−118.8	43.5	$d(2)$	−109.0	49.7
FER.	1301.797	0.44	−79.6	−23.6	$c2$	−67.1	3.0
FER.	1302.788	0.54	−67.5	−67.5	$d(1)$	−39.2	−70.5
FER.	1304.796	0.74	28.5	−127.6	$d(2)$	12.4	−138.5
FER.	1323.741	0.67	43.8	−119.7	$d(2)$	15.4	−124.0
FER.	1327.766	0.08	−77.6	4.6	$c2$	−75.0	2.5
BME	1328.700	0.18	−135.5	−0.5	$c2$		
BME	1329.705	0.28	−131.3	46.0	$d(2)$		
BME	1330.707	0.38	−92.9	0.6	$c2$		
BME	1331.717	0.49	−52.5	−52.5	$d(1)$		
BME	1332.728	0.59	−32.8	−120.5	$c2$		
COR.	1578.866	0.67	38.8	−115.1	$d(2)$	6.8	−123.1
COR.	1579.879	0.77	38.0	−139.7	$d(2)$	18.8	−146.6
COR.	1580.872	0.87	−45.5	−122.1	$c2$	−9.6	−111.9
COR.	1581.864	0.97	−58.8	−58.8	$d(1)$	−34.2	−64.0
COR.	1582.869	0.08	−70.5	11.2	$d(2)$	−80.6	−3.7
COR.	1583.877	0.18	−92.8	63.5	$d(2)$	−98.0	54.7
COR.	1584.857	0.28	−101.0	65.9	$d(2)$	−99.7	58.1
COR.	1585.845	0.38	−84.4	8.9	$d(2)$	−85.9	8.2
COR.	1586.870	0.48	−46.6	−46.6	$d(1)$	−65.0	−30.9
COR.	1587.861	0.58	−48.2	−104.7	$c2$	−10.0	−89.8
COR.	1588.886	0.69	31.8	−133.8	$d(2)$	8.1	−132.9
COR.	1590.886	0.89	−49.8	−108.3	$c2$	−9.1	−98.5
FER.	1668.892	0.84	−44.2	−150.0	$c2$	−4.4	−127.2
FER.	1669.769	0.93	−73.5	−73.5	$d(1)$	−18.1	−82.2
FER.	1670.770	0.03	−46.1	−46.1	$d(1)$	−61.0	−15.0
FER.	1671.775	0.13	−95.3	27.8	$d(2)$	−85.5	27.9
FER.	1672.766	0.23	−104.6	67.4	$d(2)$	−102.5	64.8
FER.	1673.895	0.35	−106.7	18.8	$d(2)$	−89.6	33.7

the methods of Renson (1978) and Lafler & Kinman (1965, hereafter LK) to determine an improved value of the orbital period. To this aim, we applied the period search techniques to the time series of the $RV_1 - RV_2$ radial velocity differences as determined from the He I λ4471 line in our data. To improve the accuracy of the result, we included also the data of Stickland & Koch (1996). The HMM method yields an orbital period of 9.81475 days (in agreement with the results of the Renson method) whilst the LK method yields 9.81431 days. The estimation of

the error on a period is not a straightforward problem. A secure upper limit on the error can be estimated from the width of the peak (which regardless of the method is of the order $1/\Delta T$ where ΔT is the total time spanned by the data set) i.e. 0.014 day in the present case. Empirically, the error is usually a substantial fraction of it. Under the hypothesis that the data are well distributed over ΔT and that the sampling does not suffer from any particular problem, we can use Eq. (20) of Lucy & Sweeney (1971) to compute a formal error. In the present case this yields $\sigma_{\rm P} = 0.00084$ day. The three methods hereabove yield values of the period that overlap within the errors and in the following we will adopt the period obtained with the HMM technique.

4.3. Orbital elements

We used our radial velocity measurements to determine a new orbital solution. As a first step, we considered the possibility of an eccentric solution. The *RV*s determined by cross-correlation of our echelle spectra with a mask yield a very small eccentricity of $e = 0.02 \pm 0.02$. We notice that the *RV*s of the He I λ4471 line alone yield a larger value of $e = 0.20 \pm 0.05$, but this result is most probably due to the systematic deviation of the He I λ4471 *RV*s at certain orbital phases with respect to the *RV*s derived by cross-correlation. In the following, we will focus on the non-eccentric solutions. The orbital elements determined using the various datasets are listed in Table 3 and the curves shown in Figs. 4 and 5.

A simple inspection of the solutions listed in Table 3 shows that most of the orbital elements overlap within their errors. The errors on the cross-correlation solution are however much smaller and the data points show little scatter around the best fit solution. This illustrates the power of the mask cross-correlation technique to handle the orbital solutions of heavily blended early-type binaries and, in the following, we will use the orbital elements determined from this solution. The orbital phases used throughout this paper refer to the ephemerides from this latter solution.

The *RV*s determined for the He I λ4471 line are usually in rough agreement with those determined by mask cross-correlation if we account for the slight difference in the γ velocities. A major disagreement is apparent around $\phi \sim 0.75$ for the *RV*s of the primary star that cluster systematically some $40\,{\rm km\,s^{-1}}$ above the best fit curve (Fig. 4). It is interesting to note that the most discrepant He I λ4471 *RV*s occur precisely in the range of orbital phases when the primary's lines display a reduced *EW*. The discrepant *RV*s of the primary near $\phi \sim 0.75$ lead to a somewhat larger mass ratio inferred from the *RV*s of the He I λ4471 line than from the cross-correlation *RV*s. In this context, we note that an orbital solution derived from the *RV*s of the He II λ5412 line yields a mass ratio of 0.619 (Nazé et al. 2000), in better agreement with the value obtained from the cross-correlation method.

Our orbital solutions yield apparent systemic velocities for the two components that are somewhat different with the primary showing the more negative γ. This could indicate that the primary's wind is slightly stronger than that of the secondary. However, the effect is much smaller for HD 149404 than for some other evolved early-type binaries (e.g. Rauw et al. 1999, 2000b).

Table 4 provides an overview of the orbital solutions of HD 149404 available in the literature. We notice that the mass ratio determined from our solution is intermediary between the values proposed by Massey & Conti (1979) and by Stickland & Koch (1996). Several authors argue that the actual mass ratio might be close to unity. In fact, Massey & Conti (1979) suggested a value of $q \sim 1$ based on the *RV*s of the N III $\lambda\lambda$4634-41 emission lines which they attributed to the primary star. Though it has been shown that the N III emissions might actually form in the photosphere of Of-type stars (Mihalas & Hummer 1973), our observations of HD 149404 reveal a rather complex behaviour of these lines that is not consistent with a purely photospheric origin (see below). A mass ratio near unity was also suggested by Hutchings & van Heteren (1981) based on a preliminary analysis of four IUE spectra and by Penny et al. (1996) from a comparison of the location of the components of HD 149404 in the H-R diagram with theoretical evolutionary tracks of single stars. It is worth mentioning that all the prominent absorption lines in the spectrum of HD 149404 (He II λ4542, He I λ4713, He I λ4921, N III $\lambda\lambda$4510-24, ...) yield a mass ratio in agreement with our orbital solution.

Finally, we note that including the Stickland & Koch (1996) data in our orbital solution yields orbital elements very similar to those found from our data alone.

4.4. Inclination

Massey & Conti (1979) report a photometric study of HD 149404 by Dr. N. Morrison that revealed some variability at a rather low level (0.03 mag). The lightcurve could probably be explained by ellipsoidal variations but there are not enough data points to draw any firm conclusion (Morrison 2000).

Luna (1988) obtained polarimetric observations of HD 149404 that yield only an upper limit of 50° on the orbital inclination. Vanbeveren & de Loore (1980) propose an inclination of 28° based on the orbital solution of Massey & Conti (1979) and on a comparison of the primary parameters with typical masses of O7 stars. Penny et al. (1996) derived an upper limit of 31° from the condition that neither of the two stars should fill its Roche lobe, and a lower limit of 15° by setting an upper limit of 150 $M_\odot$ on the primary's mass.

Comparing our minimum masses from Table 3 with "typical" masses of O9.7 I and O7.5 I supergiants (e.g. Howarth & Prinja 1989), we find an inclination of 20.3° for the primary and 21.0° for the secondary. Adopting 21° as a "realistic" estimate, the Roche lobe radii are equal to

Table 3. Orbital solutions adopting a period of $P = 9.81475$ days and assuming $e = 0.0$. T_0 corresponds to the conjunction with the secondary in front. The quoted errors correspond to $1\,\sigma$ uncertainties

	He I λ4471		cross-correlation	
	Prim.	Second.	Prim.	Second.
T_0(HJD–2450000)	1680.188 ± 0.531		1680.279 ± 0.174	
γ (km s^{-1})	-54.0 ± 5.2	-46.4 ± 11.5	-46.6 ± 1.7	-41.6 ± 3.5
K (km s^{-1})	62.8 ± 6.0	99.1 ± 9.0	59.7 ± 2.0	98.7 ± 3.2
$a \sin i\,(R_\odot)$	12.2 ± 1.2	19.2 ± 1.9	11.6 ± 0.4	19.1 ± 0.6
$m \sin^3 i\,(M_\odot)$	2.64 ± 0.66	1.68 ± 0.42	2.52 ± 0.21	1.52 ± 0.13
$q = m_2/m_1$	0.634 ± 0.085		0.605 ± 0.027	
$R_{\rm RL}/(a_1 + a_2)$	0.42 ± 0.01	0.34 ± 0.01	0.42 ± 0.01	0.34 ± 0.01
$R_{\rm RL} \sin i\,(R_\odot)$	13.2	10.7	13.0	10.3
rms (O–C) (km s^{-1})	18.3		6.1	

Table 4. Orbital solutions from the literature. T_0 corresponds to the conjunction with the less massive star in front

	Massey & Conti		Stickland & Koch	
	Prim.	Second.	Prim.	Second.
P (days)	9.813		9.81452	
T_0 (HJD-2440000)	2503.607		4446.849	
e	0 (adopted)		0 (adopted)	
γ (km s^{-1})	-28.0	-37.0	-60.0	-52.5
K (km s^{-1})	60.0	101.0	64.3	98.1
$a \sin i\,(R_\odot)$	11.60	19.63	12.47	19.04
$m \sin^3 i\,(M_\odot)$	2.7	1.6	2.64	1.73
$q = m_2/m_1$	0.595		0.655	
Spectral types	O7 III(f)	O8.5 I		

36 $R_\odot$ and 29 $R_\odot$ for the primary and secondary respectively. According to Howarth & Prinja (1989), the typical radii of O9.7 I and O7.5 I supergiants are 21 and 26 $R_\odot$ respectively. With that inclination, it seems a priori unlikely that any of the two components fills its Roche lobe. However, we will come back to this point in Sect. 7.1.

5. Spectroscopic luminosity ratio

In principle, a rough estimate of the visible luminosity ratio of the binary components can be inferred from the ratio of the equivalent widths of absorption lines in the primary's and secondary's spectra (e.g. Rauw et al. 2000a):

$$\frac{I_{\rm prim}}{I_{\rm sec}} = \left(\frac{EW_{\rm prim}}{EW_{\rm sec}}\right)_{\rm obs} \times \left(\frac{EW_{\rm O9.5I}}{EW_{\rm O7.5I}}\right)_{\rm typ}$$

where $\left(\frac{EW_{\rm O9.5I}}{EW_{\rm O7.5I}}\right)_{\rm typ}$ stands for the ratio of the EWs of the lines as observed in typical single O9.5 I (as a best substitute for O9.7 I) and O7.5 I stars. We measured the EW ratios of the He I $\lambda\lambda$4026, 4471, He II λ4542 and Si IV $\lambda\lambda$4089, 4116 absorption lines (see Table 5). The typical EW ratios were derived from the compilation of O-star equivalent widths published by Conti & Alschuler (1971) and Conti (1973, 1974).

In the case of HD 149404, the main limitation of the method stems from the strong orbital variability of the line strength (see Table 5). For instance, the strength of the primary's Si IV lines around $\phi \sim 0.75$ is reduced by a factor 2 with respect to $\phi \sim 0.25$, while the strength of the secondary's Si IV lines simultaneously increases by about a factor 1.3. An easy way to account for the fading of the primary's lines around $\phi \sim 0.75$ and the simultaneous strengthening of the secondary's absorptions would be to assume that one of the two stars was brighter on the front side than on the rear. However, since the amplitude of the photometric variations is only a few percent, it seems rather unlikely that the observed EW variations reflect actual variations of the brightness of one of the binary components, otherwise a larger amplitude of the light curve would be expected.

We notice that the total EW (primary + secondary) varies by only about 5% for the absorptions considered here. On the other side, we know that the He I lines are most probably affected by an emission component and the EW of the primary's He I lines are reduced around

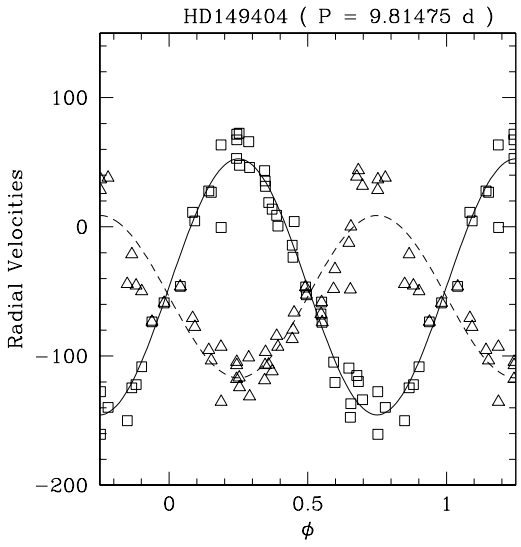

Fig. 4. Radial velocity curve of the He I λ4471 line in the spectrum of HD 149404 as a function of the orbital phase and assuming $e = 0.0$ (see Table 3). The triangles correspond to the primary's RVs while the squares indicate the RVs of the secondary

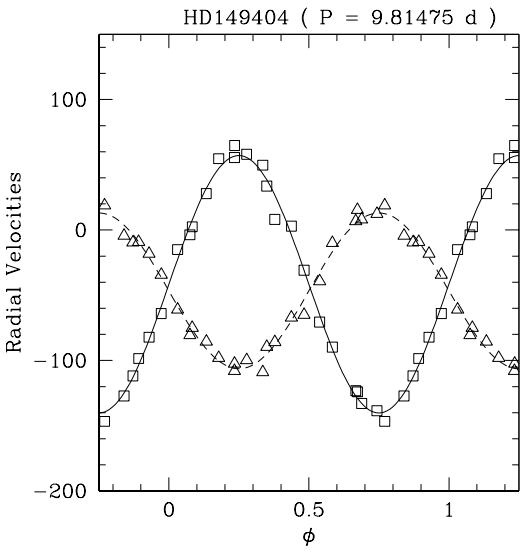

Fig. 5. Radial velocity curve determined by the mask cross-correlation method as a function of the orbital phase (assuming a circular orbit, see Table 3)

$\phi \sim 0.75$ (see Fig. 2). Therefore, blending with a most probably slightly red-shifted emission component not associated with either of the two stars could be an explanation for the observed variations.

Similar difficulties are encountered in the UV. Howarth et al. (1997) derived a mean raw UV magnitude difference of 0.8 with the secondary being the brighter component. Correcting this magnitude difference for the different spectral types, we obtain a UV luminosity ratio (primary/secondary) of roughly 0.6. Stickland & Koch (1996) reported a luminosity ratio of about 1.0 when the primary is moving towards us (our phase 0.25) and about 0.5 when it is moving away (our phase 0.75). Using the results for the He II and Si IV lines from Table 5, we calculate a mean luminosity ratio of about 1.4 ± 0.4 near $\phi \sim 0.25$ and 0.5 ± 0.1 near $\phi \sim 0.75$.

Assuming that the observed EWs are indeed reduced by a red-shifted emission component, we can derive the "actual" spectroscopic luminosity ratio using the mean EWs of each star's line when the star is moving towards us. In this way, we find an average ratio of $\overline{I}_{\rm prim}\,(0.25)/\overline{I}_{\rm sec}\,(0.75) = 0.90 \pm 0.16$ (see Table 5).

Alternatively, the absorption enhancement seen when the lines are blueshifted could be due to material from a wind interaction region that would be swept up by the star during its orbital motion. In this case, the front sides of the stars would display abnormal line strengths and the actual luminosity ratio would best be derived from the mean EWs of the lines observed when the stars are moving away from us. This assumption yields an average ratio of $\overline{I}_{\rm prim}\,(0.75)/\overline{I}_{\rm sec}\,(0.25) = 0.75 \pm 0.23$ (see Table 5). This result overlaps within the errors with the value of the $\overline{I}_{\rm prim}\,(0.25)/\overline{I}_{\rm sec}\,(0.75)$ ratio. In this second scenario, each star would have to sweep up about the same amount of material in order to explain the roughly constant total EWs of the lines. Therefore, it seems more likely that the variations of the apparent luminosity ratio are rather due to an unresolved emission component and in the following we shall thus adopt a spectroscopic luminosity ratio of 0.90 ± 0.16.

6. Emission lines

The spectrum of HD 149404 exhibits many emission lines some of which display strong orbital variability.

- The unidentified $\lambda\lambda$4486, 4504 emission lines appear to be associated with the secondary star as shown by Nazé et al. (2000). These emission lines are a common feature in the spectra of the most luminous stars between spectral type O7 and O9.5 (Conti 1973; Walborn & Fitzpatrick 1990);
- N III $\lambda\lambda$4634-41: the bulk of the emission seems to follow the primary whilst the lines are observed in absorption in the secondary's spectrum. The RV behaviour of the N III emissions itself is however rather complex and the lines are quite broad and display strong profile variability probably indicating that these lines are not purely stellar features;
- He II λ4686 (see Fig. 3) consists of a mixture of emission and absorption lines and the line morphology displays strong phase-locked variations. The emissions do not follow the orbital motion of the stars. Instead, both stars exhibit this line in weak absorption though the visibility of these absorption features varies strongly with phase and the absorption lines vanish near phases 0.2 and 0.7;
- A similar situation is observed for the Hβ line. As for He II λ4686, the stellar Hβ lines are again in (rather weak) absorption and the composite line profile suffers strong variability with an emission feature that does not follow the motion of either star. We caution that the Hβ profile is blended with the N III $\lambda\lambda$4858-67 absorption lines and this blend probably affects the radial velocity measurements of the Hβ emission components;
- Our echelle spectra reveal N II emission features at $\lambda\lambda$5001-12, 5667, 5932, 5940-42, 5952, 6482 and 6611, that are associated with the O9.7 secondary. Walborn (1980) reported weak N II $\lambda\lambda$5940-42, 6482 emission in the ON9.7 Iae star HD 105056. The presence of the N II emissions and the strength of the N III absorption lines in the spectrum of the secondary of HD 149404 could therefore indicate that nitrogen is enhanced in the atmosphere of this star. Further support for an ON classification of the secondary comes from the relative weakness of the C III $\lambda\lambda$4647-50 absorption compared to the intensity of this line in "normal" O9.7 supergiants (see Walborn & Fitzpatrick 1990);

Table 5. Luminosity ratios (primary/secondary) derived for different lines at different orbital phases. Typical uncertainties on the observed EW ratios are less than 10%. The colons indicate those measurements that have larger uncertainties due to heavier blending. The last two columns list the luminosity ratios derived from the mean EWs measured when the components are moving towards us (Col. 7) or when they are moving away from us (Col. 8); see the text for further details

HJD–2450000	1299.800	1584.857	1672.766	1304.796	1579.879		
ϕ	0.234	0.278	0.235	0.743	0.771	$\overline{I}_{\rm prim}\,(0.25)/\overline{I}_{\rm sec}\,(0.75)$	$\overline{I}_{\rm prim}\,(0.75)/\overline{I}_{\rm sec}\,(0.25)$
He I λ4026	1.70	1.13	1.95	0.28	0.41	0.86	0.66
He I λ4471	1.35	1.19	1.51	0.35	0.47	0.84	0.60
He II λ4542	1.71	1.22:	1.95		1.15:	1.19	0.66
Si IV λ4089	1.07	0.90	1.11	0.39	0.91:	0.83	0.61
Si IV λ4116	1.40	1.25	1.57	0.54		0.80	1.21

- The C III λ5696 emission is probably formed by two independent features. The strongest component follows the orbital motion of the primary. This trend is confirmed by the variations of the line peak position (see Nazé et al. 2000). At some orbital phases (e.g. $\phi = 0.67$), a second emission peak appears with a velocity indicating that it is most probably associated with the secondary;
- In addition to the absorption lines, He I λ5876 displays a variable emission which is particularly strong at phases near 0.0 and 0.5 (see Fig. 3). This emission is probably present in other He I lines too, maybe causing part of the intensity and EW variations;
- The strongest emission feature in the visible spectrum of HD 149404 is Hα (see Fig. 3). The line exhibits a double peaked structure at certain phases, more or less in quadrature with the orbital motion. Though the visibility of the emission peaks in the Hβ profile is hampered by the blending with the stellar absorption lines, they seem nevertheless to follow more or less the behaviour of the Hα peaks, pointing towards a similar origin. In Sect. 7.2, we will discuss the variability of the Hα emission line in terms of a wind interaction model.

To further analyse the emission features, we apply a so-called "S-wave analysis" (see e.g. Richards et al. 1996). We adopt two axes centred on the center of mass of the binary; the x axis points towards the secondary star while the direction of the y axis is given by the orbital motion of the secondary. We measured the RVs of the peaks of the most prominent emission lines and fitted a sine-wave expression

$$v(\phi) = -v_x\,\cos(2\pi\phi) + v_y \sin(2\pi\phi) + v_z$$

to these points (see e.g. Rauw et al. 1999). The results are summarized in Table 6 and a projected Doppler map is presented in Fig. 6. We caution that the quality of the fit to the RVs of the N III $\lambda\lambda$4634-41 lines is rather poor, mainly because of the variable shape of these lines.

The positions of the $\lambda\lambda$4486, 4504, C III λ5696, N III $\lambda\lambda$4634-41 and N II $\lambda\lambda$5932, 5942 emission regions in velocity space indicate that the bulk of these emissions arises most probably within the atmospheres of the stars.

Table 6. Results of the S-wave analysis: Coralie observations are not included for the N III emissions

	v_x	v_y	v_z
? λ4486	−0.1	87.3	−39.1
? λ4504	2.7	80.6	6.5
N III λ4634	−9.6	−73.6	−36.9
N III λ4641	−16.9	−105.8	−52.8
C III λ5696	22.3	−62.6	−42.5
N II λ5932	8.3	108.0	−81.7
N II λ5942	16.3	109.7	−44.8
He II λ4686	−128.6	−82.4	−99.7
He II λ4686	80.6	−65.3	16.4
Hβ	−123.8	−153.2	−47.1
Hβ	136.7	57.0	−47.8
Hα	−119.2	−75.1	−44.4
Hα	106.2	24.0	−53.4

On the other side, our analysis reveals that this is not the case for the Hα, Hβ and He II λ4686 emissions. The latter lines exhibit a double peaked structure at orbital phases near conjunction and a single peak around quadrature. Assuming that the two peaks actually cross over, we have fitted their RVs with the above sine-wave expression. We caution here that only the Hα peaks are free from blends with absorption lines. The Hβ and He II λ4686 lines are usually "polluted" by absorption lines and the results for these lines should therefore be regarded only as trends roughly confirming the behaviour of the Hα peaks.

7. Discussion

7.1. The evolutionary status

Adopting the effective temperature calibration of Chlebowski & Garmany (1991), the spectral types we have derived yield $T_{\rm eff} = 35\,100 \pm 1000$ K and $T_{\rm eff} = 30\,500 \pm 400$ K for the primary and the secondary respectively. HD 149404 has an apparent V magnitude of 5.47 (Drilling 1991). Assuming that the star is a member of the Ara OB1a association ($DM = 10.7$, Humphreys 1978) and adopting a colour excess $E(B-V) = 0.68$ (Shull & Van Steenberg 1985) and a spectroscopic luminosity

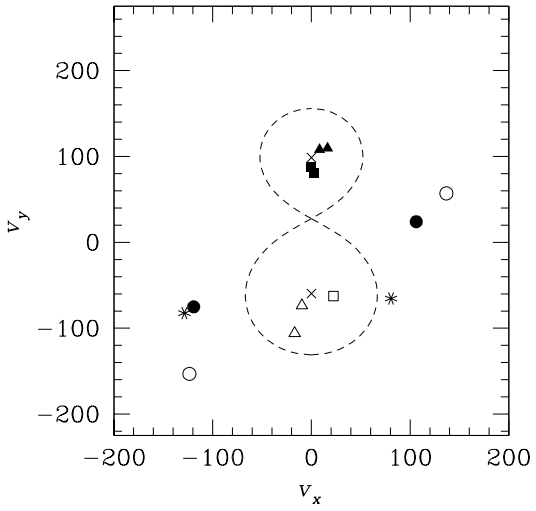

Fig. 6. Doppler map showing the results of our S-wave analysis projected on the (v_x, v_y) velocity plane. The crosses indicate the velocity of the center of mass of the binary components as derived from our orbital solution while the dashed line is the equivalent of the Roche lobe in velocity space. The different symbols stand for different emission lines: filled circles = Hα; open circles = Hβ; filled triangles = N II $\lambda\lambda$5932, 5942; open triangles = N III $\lambda\lambda$4634-41; filled squares = $\lambda\lambda$4486, 4504; open square = C III λ5696 and stars = He II λ4686

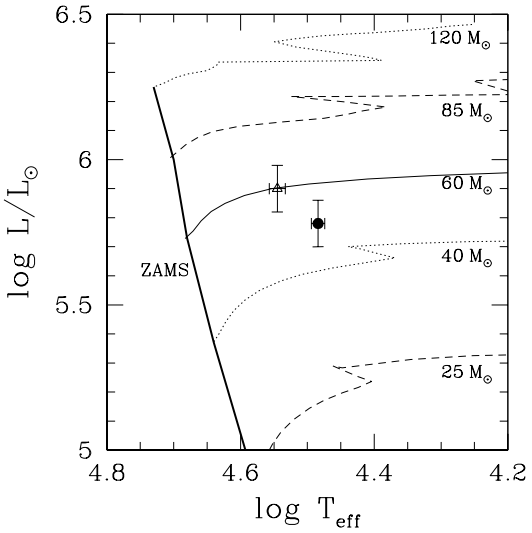

Fig. 7. Hertzsprung-Russell diagram of HD 149404. The open triangle stands for the primary star whilst the filled circle yields the position of the secondary star

ratio of 0.90±0.16 (see above), we derive $\log(L_{\rm bol}^{\rm prim}/L_\odot) = 5.90\pm0.08$ and $\log(L_{\rm bol}^{\rm sec}/L_\odot) = 5.78\pm0.08$ for the primary and secondary respectively. We caution that the error bars on the luminosities correspond only to the estimated error on the luminosity ratio and an uncertainty of half a spectral class for the bolometric correction. Our error bars account by no means for the (probably large) uncertainties on the distance of HD 149404.

The resulting locations of the components of HD 149404 in a H-R diagram are shown in Fig. 7 together with the theoretical evolutionary tracks of Schaller et al. (1992). We notice that the secondary star (i.e. the least massive star) seems to be the most evolved component though it lies on an evolutionary track of lower initial mass than the primary. This was already found by Penny et al. (1996), though these authors adopted different spectral types and hence derived different positions for the stars in the H-R diagram. As pointed out in Sect. 6, the strong N III absorptions and the N II emission lines seen in the secondary's spectrum could indicate that nitrogen is slightly enhanced in the atmosphere of this star, which would be a further indication that this star must be an evolved object. A possibility to account for the evolutionary status of the secondary would be to suppose that this star was initially the more massive component of the binary and has lost (or transferred) a considerable fraction of its mass through Roche lobe overflow in the past (see also Penny et al. 1996).

The temperatures and luminosities derived here correspond to radii of 24.3 and 28.1 $R_\odot$ for the primary and the secondary respectively. Therefore, the radius of the secondary star appears larger than we would expect from the "typical" parameters listed by Howarth & Prinja (1989). Howarth et al. (1997) derived projected rotational velocities of $v_{\rm e}\sin i = 91\,{\rm km\,s^{-1}}$ and $100\,{\rm km\,s^{-1}}$ for the O7.5 and the O9.7 component respectively. Assuming that the stars have the same angular rotational velocity (though the rotation needs not necessarily be synchronous with the orbital motion), we can derive the ratio of the stellar radii from the ratio of the projected rotational velocities. The value obtained in this way $R_{\rm prim}/R_{\rm sec} = 0.91$ is in very good agreement with the ratio of the radii derived above (0.86).

At this point, we need to return to the question of a current RLOF. In fact, the radius of the secondary star derived hereabove[3] (28.1 $R_\odot$) is only slightly smaller than the radius of its Roche lobe (29 $R_\odot$) for an inclination of 21°. Therefore a small error on the (poorly constrained) inclination has a large impact on our conclusion about the current configuration of HD 149404. Indeed, it could be that the secondary has just finished RLOF and is now settling down on a "normal" evolutionary track corresponding to its current mass. Alternatively, the secondary could still be filling its critical volume and could be suffering an enhanced mass loss through the inner Lagrangian point.

7.2. Towards a model for the wind interaction

In Sect. 6 we have shown that the Hα, Hβ and He II λ4686 emission lines are not formed in the atmospheres of the stars but must be formed somewhere between the stars.

[3] We caution that the actual value of $R_{\rm sec}$ depends on the adopted luminosity ratio between the two stars and the adopted distance towards HD 149404.

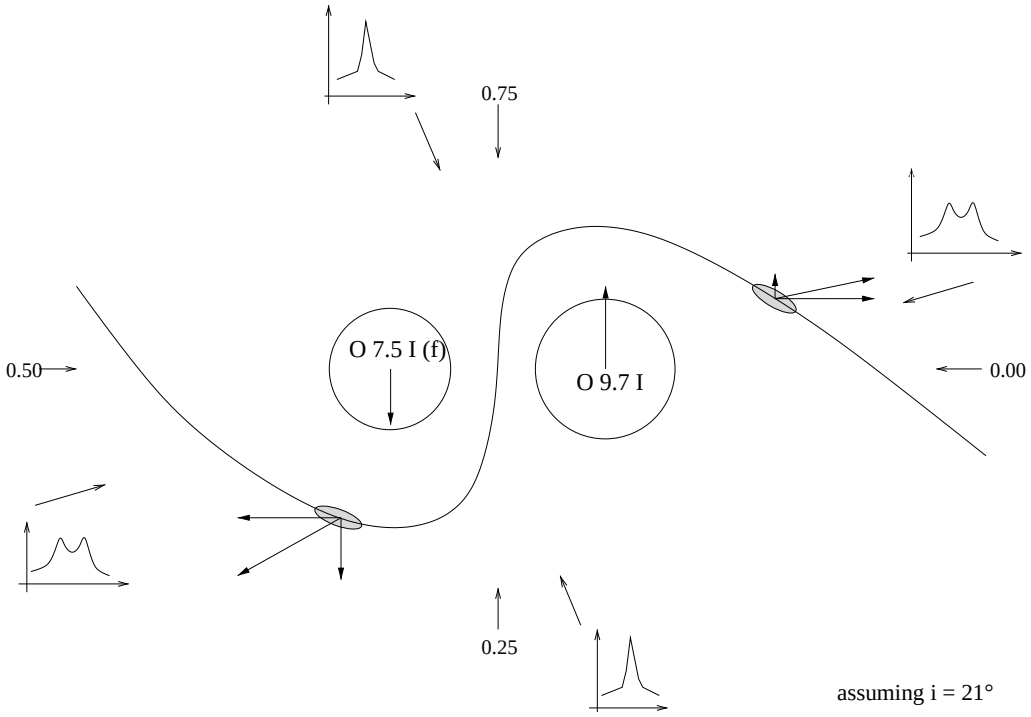

Fig. 8. Schematic view of the wind interaction in the HD 149404 system projected on the orbital plane. The changing morphology of the Hα line at some specific orbital phases is also sketched as a function of the line of sight. The relative dimensions of the orbit and the stars correspond to an inclination of $i = 21°$

Thaller (1998) suggested that the Hα emissions were coming from two focused stellar winds flowing towards a colliding wind interaction between the stars. Though the radius of the secondary star derived in Sect. 7.1 supports the possibility of an enhanced mass loss from the secondary focused towards the primary, it is not clear how the model suggested by Thaller (1998) could account for the *RV* behaviour found in Sect. 6. We favour an alternative model where the Hα emissions arise in the arms of a colliding wind shock region. Figure 8 displays a schematic view of such a wind interaction. As pointed out above, the secondary might actually be suffering a stronger mass loss than would be expected for a "normal" O9.7 I star. Therefore, we assume that the two stars have roughly equally strong winds. The Coriolis force bends the arms of the shock region around both stars. In this model, the Hα emission forms through recombination in the hatched areas where the density is enhanced due to the shock (Fig. 8). The arrows indicate the velocity components of the Hα emission regions as inferred from our S-wave analysis. The velocity components result from the combination of the orbital motion and the flow velocity of the plasma in the shock region.

In Fig. 8, the projections of the line of sight on the plane of the orbit are indicated for orbital phases near conjunction and quadrature. We see that this rather simple model can at least qualitatively account for the changing morphology and the *RV* behaviour of the Hα emission line in the spectrum of HD 149404.

We have analyzed *ROSAT* observations of HD 149404 to search for a signature of the wind interaction in the X-ray domain. HD 149404 was observed twice with *ROSAT*. A first exposure was obtained as part of the *ROSAT* All Sky Survey (Berghöfer et al. 1996). Another 3 ksec PSPC exposure was obtained on JD 2449056.813 ($\phi = 0.70$). We have retrieved this latter observation (rp201266) from the ARNIE database at Leicester University. The data were reduced using the XSELECT and XSPEC softwares. The background corrected PSPC count rate is $8.0\,10^{-2}$ cts s^{-1}. The PSPC spectrum is quite hard, as the ratio of the count rates in the ranges 0.5–2 keV and 0.1–0.5 keV is about 25. Despite the limited S/N ratio, we could fit an absorbed Raymond-Smith model (Raymond & Smith 1977) to the PSPC spectrum fixing the neutral hydrogen column density to its interstellar value $N_{\rm H}^{\rm ISM} = 2.5\,10^{21}$ cm^{-2} (Shull & Van Steenberg 1985). The best fit yields an X-ray temperature of 0.84 ± 0.10 keV and a luminosity in the 0.1–2.0 keV energy range of $L_{\rm X} = 1.6\,10^{32}$ erg s^{-1} corresponding to a ratio $L_{\rm X}/L_{\rm bol}$ of $3.0\,10^{-8}$, slightly lower than for typical O stars. This result is in agreement with the value found by Berghöfer et al. (1996). Thus the snapshot *ROSAT* observations reveal no indication of a strong X-ray excess that could be attributed to a colliding wind emission. This is in line with

the results of Chlebowski & Garmany (1991) who found no significant X-ray excess in those O-star binaries that are in a semi-detached or a contact configuration.

7.3. Summary and conclusions

We have used an extensive set of high resolution spectra to derive new orbital elements for the early-type binary HD 149404. We have shown that the mask cross-correlation technique developed at the Geneva observatory can be successfully applied to disentangle heavily blended lines in massive binaries. Our results allowed us to propose a new spectral classification for the components. We find that the primary is of spectral type O7.5 I(f), while the secondary is most likely an ON9.7 I supergiant. The secondary seems to be the most evolved component of the system and its current evolutionary status could best be explained if the system has undergone a Roche lobe overflow episode during the past. The secondary could actually still be rather close to filling its critical volume and this could lead to an enhanced mass loss of the secondary.

The behaviour of the emission lines in the spectrum of HD 149404 points towards a wind interaction between the two stars. We propose a simple model where some of the optical emission lines arise in a heavily bended shock region. It seems likely that HD 149404 is currently in a rather short-lived evolutionary stage where the wind interaction could be strongly affected by an enhanced mass loss of the secondary star. We caution, however, that this rather simple picture of the interaction could be seriously complicated if the secondary actually filled its critical volume. In this context, we emphasize that some of the crucial parameters of HD 149404 such as its distance and the orbital inclination remain poorly constrained. All future observations that could help to determine these parameters would be extremely useful to fully understand this system.

Acknowledgements. We are grateful to H. Sana for taking the May 2000 spectra and for his help in the reduction of the FEROS data, and to Dr. E. Jehin and G. Parmentier for taking some of the CAT + VLC observations. We also thank an anonymous referee for his helpful comments. We are greatly indebted to the Fonds National de la Recherche Scientifique for multiple support. This research is also largely supported by contract P4/05 "Pôle d'Attraction Interuniversitaire" (SSTC-Belgium) and through the PRODEX XMM-OM and Integral Projects. Part of this work has been supported by the Swiss National Found for the Scientific Research. The SIMBAD database has been consulted for the bibliography.

References

Baranne, A., Queloz, D., Mayor, M., et al. 1996, A&AS, 119, 373
Berghöfer, T. W., Schmitt, J. H. M. M., & Cassinelli, J. P. 1996, A&AS, 118, 481
Chlebowski, T., & Garmany, C. D. 1991, ApJ, 368, 241
Conti, P. S. 1973, ApJ, 179, 181
Conti, P. S. 1974, ApJ, 187, 539
Conti, P. S., & Alschuler, W. R. 1971, ApJ, 170, 325
Conti, P. S., & Frost, S. A. 1977, ApJ, 212, 728
Conti, P. S., Leep, E. M., & Lorre, J. J. 1977, ApJ, 214, 759
Drilling, J. S. 1991, ApJS, 76, 1033
Gies, D. R., Bagnuolo, W. G. Jr., & Penny, L. R. 1997, ApJ, 479, 408
Heck, A., Manfroid, J., & Mersch, G. 1985, A&AS, 59, 63
Howarth, I. D., & Prinja, R. K. 1989, ApJS, 69, 527
Howarth, I. D., Siebert, K. W., Hussain, G. A. J., & Prinja, R. K. 1997, MNRAS, 284, 265
Hubeny, I., Lanz, T., & Jeffery, C. S. 1994, TLUSTY and SYNSPEC: A User's Guide, Newsletter on Analysis of Astronomical Spectra (Univ. of St. Andrews)
Humphreys, R. M. 1978, ApJS, 38, 309
Hutchings, J. B., & van Heteren, J. 1981, PASP, 93, 626
Kaufer, A., Stahl, O., Tubbesing, S., et al. 1999, The Messenger, 95, 8
Kupka, F., Piskunov, N., Ryabchikova, T. A., Stempels, H. C., & Weiss, W. W. 1999, A&AS, 138, 119
Kurucz, R. L. 1994, Solar abundance model atmospheres for 0, 1, 2, 4, 8 km s^{-1}, CD-ROM No. 19, Smith. Astroph. Obs.
Lafler, J., & Kinman, T. D. 1965, ApJS, 11, 216
Lucy, L. B., & Sweeney, M. A. 1971, AJ, 76, 544
Luna, H. G. 1988, A&AS, 74, 427
Massey, P., & Conti, P. S. 1979, in IAU Symp. 83, Mass Loss and Evolution of O-Type Stars, ed. P. S. Conti, & C. W. H. de Loore, 271
Mathys, G. 1988, A&AS, 76, 427
Mathys, G. 1989, A&AS, 81, 237
Mihalas, D., & Hummer, D. G. 1973, ApJ, 179, 827
Morrison, N. D. 2000, private communication
Nazé, Y., Carrier, F., & Rauw, G. 2000, in Interacting Winds from Massive Stars, ed. A. F. J. Moffat, & N. St.-Louis, ASP Conf. Ser., in press
Penny, L. R., Gies, D. R., & Bagnuolo, W. G. Jr. 1996, in Proc. 33rd Liège Int. Astroph. Coll., Wolf-Rayet Stars in the Framework of Stellar Evolution, ed. J.-M. Vreux et al., 289
Rauw, G., Vreux, J. M., & Bohannan, B. 1999, ApJ, 517, 416
Rauw, G., Sana, H., Gosset, E., et al. 2000a, A&A, 360, 1003
Rauw, G., Sana, H., Vreux, J.-M., Gosset, E., & Stevens, I. R. 2000b, in Interacting Winds from Massive Stars, ed. A. F. J. Moffat, & N. St.-Louis, ASP Conf. Ser., in press
Raymond, J. C., & Smith, B. W. 1977, ApJS, 35, 419
Renson, P. 1978, A&A, 63, 125
Richards, M. T., Jones, R. D., & Swain, M. A. 1996, ApJ, 459, 249
Schaller, G., Schaerer, D., Meynet, G., & Maeder, A. 1992, A&AS, 96, 269
Shull, J. M., & Van Steenberg, M. E. 1985, ApJ, 294, 599
Stickland, D. J., & Koch, R. H. 1996, The Observatory, 116, 145
Stickland, D. J. 1997, The Observatory, 117, 37
Thaller, M. L. 1997, ApJ, 487, 380
Thaller, M. L. 1998, in Proc. Boulder-Munich II Worksh., Properties of Hot, Luminous Stars, ed. I. D. Howarth, ASP Conf. Ser., 131, 417
Vanbeveren, D., & de Loore, C. 1980, A&A, 86, 21
Walborn, N. R. 1971, ApJS, 23, 257
Walborn, N. R. 1972, AJ, 77, 312
Walborn, N. R. 1980, ApJS, 44, 535
Walborn, N. R., & Fitzpatrick, E. L. 1990, PASP, 102, 379
Wiggs, M. S., & Gies, D. R., 1993, ApJ, 407, 252

A&A 392, 563–574 (2002)
DOI: 10.1051/0004-6361:20020927

Astronomy & Astrophysics

The evolved early-type binary HDE 228766 revisited⋆

G. Rauw[1], P. A. Crowther[2], P. R. J. Eenens[3], J. Manfroid[1,⋆⋆], and J.-M. Vreux[1]

[1] Institut d'Astrophysique et de Géophysique, Université de Liège, Allée du 6 Août, Bât. B5c, 4000 Liège (Sart Tilman), Belgium
[2] Department of Physics & Astronomy, University College London, Gower Street, London WC1E 6BT, UK
[3] Departemento de Astronomia, Universidad de Guanajuato, Apartado 144, 36000 Guanajuato Gto, Mexico

Received 6 May 2002 / Accepted 18 June 2002

Abstract. We use an extensive set of spectroscopic observations to reinvestigate the properties of the massive binary HDE 228766. Conventional classification criteria suggest that HDE 228766 consists of an O7 primary and an Of$^+$ secondary. However, several spectral features of the secondary, such as the simultaneous presence of N III, N IV and N V emissions, make it a rather unusual object. We find that the orbital motion of the secondary is probably best described by the radial velocities of the narrow N III emission lines. Our orbital solution yields $m_1 \sin^3 i = 31.7$ and $m_2 \sin^3 i = 25.5\ M_\odot$ for the primary and secondary respectively. The He II λ 4542 absorption in the secondary's spectrum appears considerably blue-shifted with respect to the narrow emission lines, indicating that the absorption is probably formed in the accelerating part of the secondary's wind. We use a tomographic technique to investigate the profile variability of the broader emission lines. In addition to a strong emission from the secondary, the Hα line displays a weak emission feature that is probably associated with a wind interaction region located near the surface of the primary star. Finally, our analysis of the spectrum with a non-LTE code indicates that the secondary is an evolved object that exhibits some CNO processed material in its atmosphere and has a large mass loss rate. Assuming a distance of 3.5 kpc (which follows from adopting $M_{V,s} = -6$ for the secondary) we infer $\dot{M} \simeq 10^{-5}\ M_\odot\ \mathrm{yr}^{-1}$ for the secondary. Our results suggest that HDE 228766 could be in a post-Roche lobe overflow stage. The secondary may be classified as WN8ha and is currently in a transition stage between a "normal" Of star and a WNL-type Wolf-Rayet star.

Key words. binaries: spectroscopic – stars: early-type – stars: fundamental parameters – stars: individual: HDE 228766

1. Introduction

HDE 228766 (=BD+36° 3991) was first reported to be a spectroscopic binary with a period of about 10.6 d by Hiltner (1951). In addition to absorption lines of H I, He I and He II, the spectrograms collected by Hiltner revealed the presence of emission lines of He II λ 4686 and N IV λ 4058 and this author classified HDE 228766 thus as "WN7 or slightly earlier". The Wolf-Rayet classification of this system was soon questioned by several authors. In fact, Roman (1951) noted that the emission lines in the spectrum of HDE 228766 were rather narrow, unlike what was observed for typical Wolf-Rayet stars, and therefore Roman suggested that HDE 228766 should be called an Of star. Hiltner & Schild (1966) reclassified HDE 228766 as an Of-type system and this result was also supported by Walborn (1973) who suggested that the system consists of an early Of star and a rapidely rotating late O supergiant. Very recently, Walborn et al. (2002) classified the combined spectrum of HDE 228766 as O3.5 If*.

A leap forward in the study of this system came with the work of Massey & Conti (1977, hereafter MC77). These authors derived an O7.5 + O5.5 f classification for the primary and secondary respectively. More importantly, they succeeded for the first time to resolve some of the absorption lines in the spectrum of HDE 228766 into two components. In fact, earlier investigators (Hiltner 1951; Hart 1957) failed to resolve these lines and assigned the entire absorption spectrum to the late O primary star. The older orbital solutions hence only provided upper limits on the true orbital motion of the late O component. MC77 found the apparent systemic velocity of the secondary's absorptions to be considerably blue-shifted relative to the primary, while the He II λ 4686 emission line appeared red-shifted.

Beside its interest for our understanding of stellar evolution, HDE 228766 could also be considered a promising target for studies of stellar wind interactions. The fact that this binary was quoted as a moderately bright X-ray source (Chlebowski et al. 1989) makes it indeed a good candidate for a colliding wind phenomenon. These considerations prompted us to reinvestigate the properties of this binary system with a particular emphasis on the search for phase-locked emission line profile variability that is often associated with a wind-wind collision.

In this paper, we present an extensive set of new spectroscopic observations of HDE 228766. In Sect. 3, we discuss

Send offprint requests to: G. Rauw, e-mail: rauw@astro.ulg.ac.be

⋆ Based on observations collected at the Observatoire de Haute Provence (France) and the Observatorio Astronómico Nacional of San Pedro Mártir (Mexico).

⋆⋆ Directeur de Recherches FNRS (Belgium).

the spectral features of HDE 228766. Radial velocity measurements are used in Sect. 4 to derive new orbital solutions. The emission line profile variability is analysed in Sect. 5. Finally, a discussion of the fundamental parameters of this system and of the wind interaction phenomenon is presented in Sect. 6.

2. Observations and data reduction

The bulk of our observations were collected during several observing campaigns at the Observatoire de Haute-Provence (OHP). We used the Carelec and Aurélie spectrographs respectively attached to the 1.93 and 1.52 m telescopes at OHP. Table 1 provides a summary of the various spectral ranges covered and the corresponding reciprocal dispersions.

For the Carelec observations until 1990, we used a thin back illuminated RCA CCD with 323×512 pixels of 30 μm squared. In 1995, the detector was a Tektronix TK512 CCD with a pixel size of 27 μm. Aurélie was equipped with a Thomson TH7832 linear array with a pixel size of 13 μm until 1999. From 2000 on, the detector of the Aurélie instrument was replaced by a 2048×1024 CCD EEV 42-20#3, with a pixel size of 13.5 μm squared.

All the data were reduced in the standard way using the IHAP (for data taken before 1995) and MIDAS softwares developed at ESO.

We derived a template of the telluric absorption spectrum that affects the spectral ranges centered on Hα and He I λ 5876 from observations of a rapidely rotating star obtained at very different airmasses. This template was then used to achieve a first order correction of the telluric features on the spectra of HDE 228766. Finally, the spectra were normalized using properly chosen continuum windows.

Three spectra of HDE 228766 were obtained in October 2001 with the echelle spectrograph at the 2 m telescope of the Observatorio Astronómico Nacional of San Pedro Mártir (SPM). The detector was a Site CCD with 1024×1024 pixels of 24 μm squared. The slit width was set to 150 μm corresponding to 2″ on the sky. The data were reduced using the MIDAS echelle package and the wavelength-calibrated spectra were rectified using the SPEFO code (Horn et al. 1996).

3. The spectrum of HDE 228766

As already pointed out by previous investigators, the spectrum of HDE 228766 displays a fair number of emission lines (see Fig. 1) that are essentially associated with the secondary (see Sect. 4). The most prominent ones are He II $\lambda\lambda$4686, 10124; He I λ 10830; Hα; N III $\lambda\lambda$ 4379, 4634, 4641; N IV $\lambda\lambda$ 4058, 7103–11, 7123–29 and Si IV $\lambda\lambda$ 4089, 4116. The spectral region from 4500 to 4540 Å displays numerous faint N III emission lines, but we find no trace of the two "unidentified Of" emission lines at 4485 and 4504 Å that were recently associated with S IV transitions (Werner & Rauch 2001). The Hβ and He I λ 5876 lines consist of a mixture of absorption and probably P-Cygni type emission lines. The presence of the N V $\lambda\lambda$ 4603, 4620 lines is also a remarkable feature suggesting a very early spectral type (O3–O4) for the secondary (e.g. Walborn & Fitzpatrick 1990; Walborn 2001). Beside the "typical" O-star absorption lines (e.g. Hγ; He I λ 4471; He II $\lambda\lambda$ 4200, 4542; ...) there are a number of interstellar absorptions as well as diffuse interstellar bands (DIBs). The strongest interstellar lines in our data are Na I $\lambda\lambda$ 5890, 5896; CH^+ λ 4233 and CH λ 4300.

Table 1. Overview of our observing campaigns. The second column indicates the instrument used for the observations: A = Aurélie at the OHP 1.52 m, C = Carelec at the OHP 1.93 m, SPM = echelle spectrograph at the SPM 2 m telescope. *N* yields the number of nights when HDE 228766 was observed.

Campaign	Inst.	Spectral range (Å)	Recipr. disp. (Å mm^{-1})	*N*
Aug. 1989	C	6500–10 400	260	1
Sep. 1989	C	8350–11 150	260	1
Aug. 1990	C	6780–7200	33	1
Aug. 1990	C	8300–11 100	260	1
Jul. 1995	C	4530–4720	17	1
Jul. 1999	A	4100–4950	33	7
Aug. 1999	A	4100–4950	33	13
Sep. 2000	A	4455–4905	16	9
Sep. 2000	A	6340–6790	16	9
Sep. 2000	A	5580–6030	16	2
Sep. 2000	A	3980–4440	16	1
Sep. 2001	A	6340–6790	16	7
Oct. 2001	SPM	3700–7370	10	3

The near-IR spectrum of HDE 228766 reveals a rather prominent and probably variable He II λ 10124 emission feature that was first reported by Vreux & Andrillat (1979). Whereas this line is commonly observed in emission in the spectra of Wolf-Rayet (WR) stars, He II λ 10124 is usually seen in absorption in the spectra of Of stars. Emission in this line has been reported only for some of the hottest and most luminous Of stars. These include Of^+ stars (Vreux & Andrillat 1979), several OIafpe transition objects (Crowther & Bohannan 1996) as well as peculiar objects such as the Oef stars ζ Pup and λ Cep and the high mass X-ray binaries Cyg X-1 (Conti & Howarth 1999) and HD 153919 (Bohannan & Crowther 1999). The strong He I λ 10830 emission was first noted by Andrillat & Vreux (1979) and is also indicative of a large mass loss rate or an extreme wind extension (Conti & Howarth 1999).

The equivalent width (EW) ratios of the usual O-star classification lines He I λ 4471 and He II λ 4542 ($W' = EW$(He I λ4471)/EW(He II λ4542), Conti 1973) point towards an O7 spectral type for both components ($\log W' = -0.03 \pm 0.07$ and $\log W' = -0.04 \pm 0.16$ for the primary and secondary respectively). The presence of Si IV $\lambda\lambda$ 4089, 4116 in emission in addition to the "classical" N III $\lambda\lambda$ 4634-41 and He II λ 4686 Of emission lines indicates an Of^+ classification (see e.g. Walborn & Fitzpatrick 1990) for the secondary star. Though these results are in crude agreement with the classification proposed by MC77 (O7.5 + O5.5f) based on photographic spectra, we caution that the spectral types are rather uncertain due to the serious blending of the classification lines of both stars. Moreover, an O7 classification for the secondary

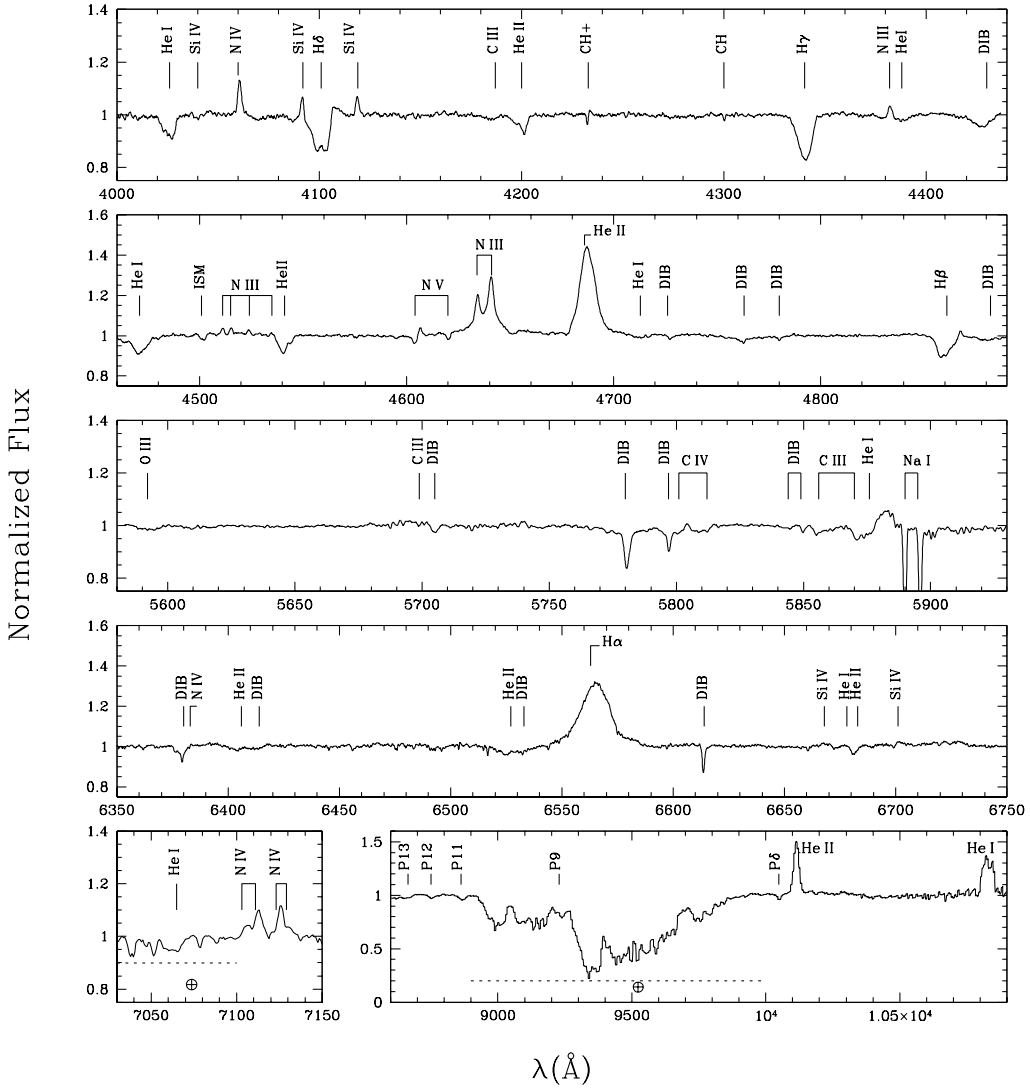

Fig. 1. Composite spectrum of HDE 228766 from the near ultraviolet to the near infrared. All the observations shown here were taken in September 2000 except for the spectral ranges 7030–7150 and 8600–10 900 that were observed in August 1990. The most prominent stellar and interstellar features are identified. The ⊕ symbol indicates spectral regions that are considerably affected by telluric absorptions and for which no first order correction was applied.

is obviously at odds with the early spectral type implied by the presence of the N IV and N V lines (see also Sect. 6.1).

At this stage, it is worth pointing out that the He I λ 4471 absorption is likely to be affected by wind emission. In fact, the He I λ 5876 line appears as a mixture of emission and absorption features and a slightly weaker emission at He I λ 4471 could essentially remain undetected though it would affect the *EW*s of this line in the spectrum of both stars. The He II λ 4542 line in the spectrum of the secondary might not be of purely photospheric origin either. Indeed, our orbital solution (see the forthcoming Sect. 4) reveals a surprisingly large difference of 150 km s^{-1} between the apparent systemic velocities of the two stars with the secondary being the star with the more negative γ. Since most of the emission lines are also associated with the secondary, the blueshift of the secondary's He II λ 4542 absorption could be the result of the strong wind of this star. In this context, Crowther & Bohannan (1997) showed that in extreme Of stars, the usual diagnostic lines such as He II $\lambda\lambda$ 4542, 5412 are significantly affected by wind contamination and as a consequence the distinction between the most extreme Of stars and the least extreme WN stars becomes a rather tricky issue. It is worth noting that Hackwell et al. (1974) did not find a significant infrared excess in the spectrum of HDE 228766. Such an excess is often seen for Wolf-Rayet stars and is attributed to free-free emission from the dense stellar wind. The relative weakness of the infrared free-free emission in HDE 228766 is consistent with an Of or a weak-lined WN spectral type for the secondary.

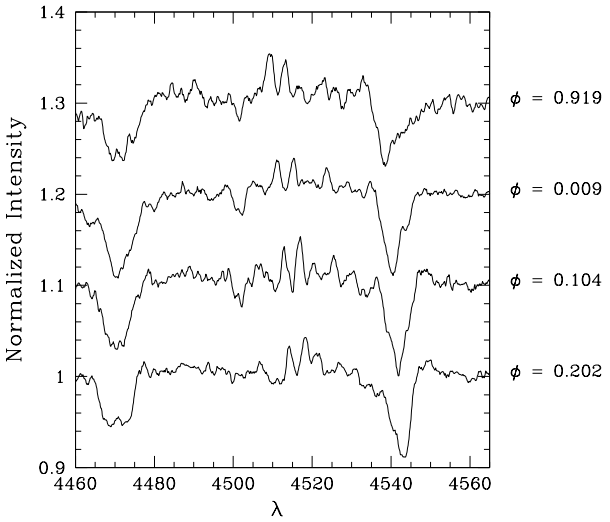

Fig. 2. Examples of the blue-violet spectra of HDE 228766 as a function of phase illustrating the severe blending of the absorption lines even around $\phi = 0.2$. Note also the numerous weaker N III emission lines.

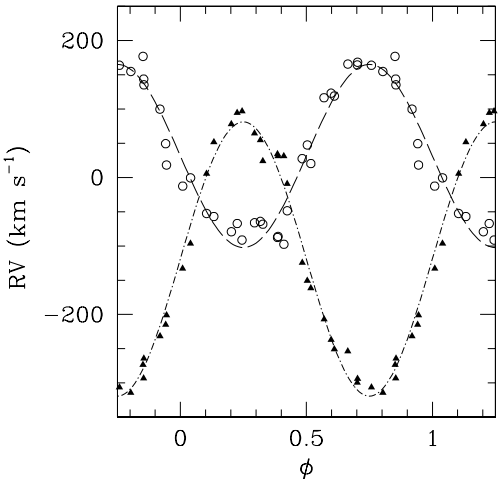

Fig. 3. Radial velocity curve of the HDE 228766 binary system as derived from the He II λ 4542 absorption line (see Table 3). Open circles and filled triangles stand for the primary and secondary *RV*s respectively.

4. Orbital solution

The most extensive and most accurate compilation of radial velocities (*RV*s) of HDE 228766 in the literature concerns the He II λ 4686 emission line. We measured the *RV*s of this line on our spectra by fitting a Gaussian. Adopting the orbital period of 10.7424 d as derived by MC77, we used our He II λ 4686 *RV*s to determine a new orbital solution for this line (see Rauw et al. 2002). Apart from a small phase-shift, this new solution is in excellent agreement with the results of Hart (1957) and MC77. This finding prompted us to take advantage of the entire *RV* dataset of He II λ 4686 available in the literature to derive a better estimate of the orbital period of HDE 228766. We applied the generalized spectrogram technique of Heck et al. (1985; see also Gosset et al. 2001) and the trial method of Lafler & Kinman (1965) to this timeseries and both methods consistently yield 10.7426 d as the best estimate for $P_{\rm orb}$. Assuming that the uncertainty on this result amounts to one tenth of the natural width of the peak in the periodogram, we estimate an uncertainty of 6×10^{-4} d. Therefore, our new orbital period confirms the previous determinations. In the following, all the orbital solutions are computed adopting our new value of 10.7426 d.

A close inspection of our data reveals that most of the absorption lines of the binary components remain blended over the main part of the orbital cycle (Fig. 2). The only absorption feature that seems reasonably well suited to establish an orbital solution for both stars is the He II λ 4542 absorption line. The He I λ 4471 and Hγ absorptions are seldom completely deblended and suffer most probably from a contamination by a variable wind emission.

To determine the radial velocities of the He II λ 4542 absorption lines, we have built a template of the line in the spectrum of each star by fitting two Gaussians to the blend around maximum separation. At the other orbital phases, we used these templates within a cross-correlation like technique to deblend the lines of the two components. We define phase 0.0 as the phase of conjunction with the secondary star being in front of the primary and we adopt the 10.7426 d orbital period derived above.

Allowing for an eccentric orbital solution yields $e = 0.06 \pm 0.02$ for the *RV*s derived from the He II λ 4542 absorption lines. However, the radial velocity curves of the He II λ 4686 and N III $\lambda\lambda$ 4634, 4641 emission lines all indicate an eccentricity below 0.03 with correspondingly large errors (~0.01, 1 σ). Therefore, although we cannot completely rule out a very small eccentricity, in the following we assume $e = 0.0$.

Our He II λ 4542 radial velocity measurements yield a significantly larger mass ratio ($q = 1.50$) than the value ($q = 1.04$) obtained by MC77. This larger mass ratio results from a slightly lower K_1 (134 vs. 150 km s^{-1}) and a significantly larger K_2 (200 vs. 156 km s^{-1}). We find a huge difference of 150 km s^{-1} between the *apparent* systemic velocities of the two components of the system with the secondary line being blue-shifted with respect to the primary. Our non-LTE analysis of the spectrum of HDE 228766 (Sect. 6.1 below) confirms that this shift of the apparent γ-velocities can be ascribed to wind contamination of the secondary's helium lines. This blue-shift of the secondary's absorption was already discovered by Massey & Conti (1977) but these authors reported a difference of "only" 45 km s^{-1}. MC77 used the mean *RV*s of several absorption lines to derive their orbital solution. Due to the severe blending problems, these authors cautioned that their *RV* measurements of the absorption lines on their photographic plates were at least partly subjective. Our *RV*s obtained through a cross-correlation technique are in principle less subjective, but refer to the sole He II λ 4542 line thus rendering a direct comparison of our γ velocities with the ones of MC77 difficult.

Table 2. Journal of observations of HDE 228766 in the blue-violet range obtained with the Carelec and Aurélie spectrograph at OHP. The orbital phases are computed with respect to HJD 2451822.052 with a period of 10.7426 d (see Table 3). The last column yields the equivalent width of the He II λ 4686 emission line integrated from 4665 to 4705 Å.

HJD-2 440 000	ϕ	He II λ 4542		N III λ 4634	N III λ 4641	He II λ 4686	
		RV_1 (km s^{-1})	RV_2 (km s^{-1})	RV (km s^{-1})	RV (km s^{-1})	RV (km s^{-1})	EW (Å)
9917.412	.702	164.2	−299.4	−224.6	−222.0	−190.2	−5.33
11373.492	.245	−91.3	96.7	221.3	196.6	283.8	−5.61
11374.379	.327	−68.2	24.0	178.6	168.6	254.7	−5.72
11375.415	.424	−48.7	−9.3	96.1	67.3	159.7	−5.49
11376.425	.518	20.3	−161.4	−19.9	−47.1	32.5	−5.22
11377.428	.611	119.0	−250.7	−153.0	−171.2	−107.5	−5.60
11378.417	.703	168.3	−293.9	−224.0	−244.5	−187.2	−5.74
11379.494	.803	154.7	−314.1	−220.2	−236.7	−172.6	−5.57
11396.488	.385	−87.6	34.3	142.3	125.5	214.3	−5.49
11397.543	.484	27.5	−124.5	9.9	−14.9	80.6	−4.99
11398.473	.570	116.4	−207.1	−107.2	−120.4	−50.2	−5.66
11399.486	.664	165.6	−253.7	−207.7	−218.1	−159.3	−5.36
11401.537	.855	135.2	−264.2	−185.8	−207.2	−141.1	−5.53
11402.465	.942	49.3	−214.9	−98.6	−118.9	−36.5	−5.34
11403.524	.040	−0.6	−96.5	39.3	15.2	119.0	−5.36
11404.518	.133	−57.0	51.7	151.4	124.8	236.3	−5.43
11405.514	.226	−67.2	94.4	207.7	189.3	298.0	−5.52
11406.500	.317	−64.2	54.5	208.5	190.8	266.5	−5.61
11407.503	.411	−97.5	31.1	106.0	88.3	197.9	−5.24
11408.503	.504	47.4	−150.7	−6.5	−30.5	54.6	−5.21
11409.517	.598	123.0	−236.8	−138.5	−163.3	−101.8	−5.88
11810.440	.919	99.7	−231.7	−122.5	−123.3	−71.4	−5.88
11811.408	.009	−12.6	−132.8	2.5	−3.4	96.1	−4.36
11812.427	.104	−52.5	5.6	122.8	120.8	191.0	−5.81
11813.484	.202	−79.2	77.9	200.9	202.5	281.1	−5.78
11814.469	.294	−66.2	64.5	210.3	210.0	279.2	−5.92
11815.473	.388	−86.2	31.3	142.1	137.8	216.9	−5.77
11819.453	.758	163.8	−306.2	−234.4	−233.3	−202.2	−5.99
11820.460	.852	176.8	−273.4	−194.9	−180.0	−143.2	−5.71
11820.487	.854	143.7	−293.3	−186.9	−181.3	−144.4	−5.43
11821.461	.945	18.2	−201.0	−89.4	−87.7	−20.5	−5.66

We have measured the radial velocities of the N III $\lambda\lambda$ 4634, 4641 and He II λ 4686 emission lines (Table 2). The lines appear to follow closely the orbital motion of the secondary star without any significant phase lag (Table 3). The semi-amplitude of our N III RV-curves overlap within 3 km s^{-1} with previous results, whereas the semi-amplitude of our He II λ 4686 RV-solution (244 km s^{-1}) is intermediate between the values of 218 and 260 km s^{-1} obtained respectively by MC77 and Hart (1957). It is worth mentioning that the absorption components of the N V $\lambda\lambda$ 4604, 4620 lines as well as the N V λ 4604 P-Cygni emission also follow the motion of the secondary star with a semi-amplitude of 223–227 km s^{-1} (see also Table 4 below).

A tricky question that occurs frequently for binary systems harboring Wolf-Rayet or extreme Of stars is which of the spectral lines reflects the actual orbital motion of the WR or Of star. In the case of HDE 228766, it seems likely that the absorption lines of the secondary are formed in the stellar wind rather than in the photosphere. The γ velocity of the He II λ 4542 absorption is blue-shifted by more than 100 km s^{-1} with respect to the RV-curve of the N III emission lines. This blue-shift suggests that the absorption forms in the wind, where the outflow has already reached larger velocities than in the formation area of the narrow emission lines. This situation is reminiscent of the case of the WN7ha + O binary WR 22 for which the H9 absorption appears blue-shifted by 80 km s^{-1} with respect to the N IV λ 4058 emission (Rauw et al. 1996). For WR 22, it was found that the narrow N IV emission provides the best indicator of the orbital motion of the WN7ha star. It seems likely that the same holds for the N III, N IV and N V emission lines of the secondary in HDE 228766. Indeed, the various narrow emission lines yield the same K and their γ velocities are in reasonable agreement with that of the primary's He II λ 4542 absorption line.

The line formation region of the He II λ 4686 emission is probably more extended and hence more affected by the presence of the primary and/or by a wind interaction phenomenon than that of the nitrogen lines.

Table 3. New orbital solutions for HDE 228766. The *RV*s of the emission lines vary almost perfectly in phase with the *RV* of the secondary's He II λ 4542 absorption line. T_0 refers to the time of conjunction with the primary being behind. $R_{\rm RL}$ stands for the radius of a sphere with a volume equal to that of the Roche lobe computed according to the formula of Eggleton (1983).

	He II λ 4542		N III λ 4634	N III λ 4641	He II λ 4686
	Primary	Secondary			
P (days)	10.7426 (fixed)			(fixed)	
e	0.0 (adopted)			0.0 (adopted)	
T_0 (HJD-2 450 000)	1822.052 ± 0.305		1822.081 ± 0.044	1822.034 ± 0.100	1822.040 ± 0.072
γ (km s^{-1})	31.4 ± 7.3	−119.0 ± 8.2	−10.1 ± 0.7	−22.4 ± 1.5	52.0 ± 1.2
K (km s^{-1})	133.7 ± 7.6	200.2 ± 10.9	224.9 ± 1.0	222.1 ± 2.1	244.5 ± 1.7
$a \sin i$ ($R_\odot$)	28.4 ± 1.6	42.5 ± 2.3	47.7 ± 0.2	47.1 ± 0.4	51.9 ± 0.4
$q = m_1/m_2$	1.50 ± 0.11				
$m \sin^3 i$ ($M_\odot$)	24.8 ± 1.8	16.6 ± 2.4			
$R_{\rm RL} \sin i$ ($R_\odot$)	29.3 ± 1.5	24.4 ± 1.2			

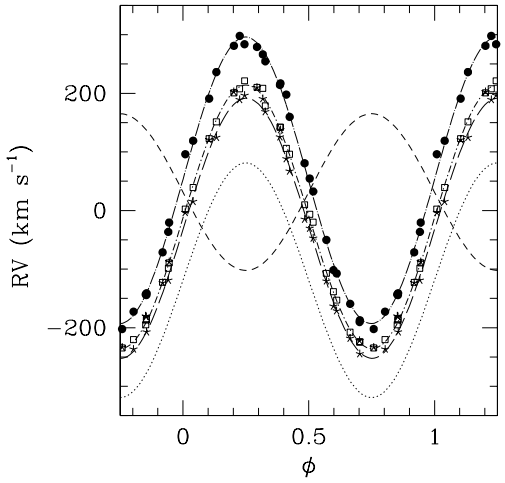

Fig. 4. Radial velocity curves of the N III λ 4634 (open squares), N III λ 4641 (stars) and He II λ 4686 (black dots) emission lines in the spectrum of HDE 228766. The He II λ 4542 orbital solutions of the primary (dashed line) and secondary (dotted line) are shown for comparison.

Therefore, we suggest that the true $K_2 \simeq K_{\rm N\,III} \simeq 225$ km s^{-1}. Adopting this value yields a mass ratio of $q = 1.67$, a projected separation of $(a_1 + a_2) \sin i = 76\ R_\odot$ and minimum masses of $m_1 \sin^3 i = 31.7$ and $m_2 \sin^3 i = 25.5\ M_\odot$ for the primary and secondary respectively. The rather large minimum masses suggest that the inclination i could be large and HDE 228766 might display photometric variability. Unfortunately, it seems that there has been no photometric investigation of this system so far and no light-curve is available that could allow to constrain i.

5. Line profile variability

5.1. He II λ 4686

The He II λ 4686 line appears as a strong emission with a nearly symmetric profile, the blue wing being only slightly steeper than the red wing. The full width at half maximum of the line amounts to about 7 Å (i.e. ∼450 km s^{-1}).

This line displays no significant phase-locked line profile variations contrary to what is observed in several other interacting wind Of binary systems (e.g. Rauw et al. 1999; Sana et al. 2001). There are however some intensity variations. We have measured the equivalent width of the line integrated between 4665 and 4705 Å. There is a large scatter in the data points, without any clear dependence on the orbital phase (though the lowest *EW*s correspond to the two conjunction phases). The mean *EW* of the He II λ 4686 emission is −5.52 Å with variations between −4.36 and −5.99 Å (see Table 2). Despite this large peak to peak variation, the 1 σ dispersion on the mean *EW* is only 0.32 Å, i.e. 6%. This result is in good agreement with the assertion of Massey & Conti (1977) that the *EW* of this line does not show variations of more than 15%.

Though the emission peak follows the orbital motion of the secondary, there could be higher order variations in the line profile reflecting an interaction with the primary. Unveiling such variations requires an analysis of the entire profile. For this purpose, we have applied a Doppler tomography technique to map the line formation region of the He II λ 4686 emission line in velocity space (see e.g. Thaller et al. 2001 for an example of the application of this method to early-type binaries). Our method uses a Fourier filtered back projection algorithm (Horne 1991). The radial velocity of any gas flow that is stationary in the rotating frame of reference of the binary can be described by a so-called "S-wave" relation:

$$v(\phi) = -v_x \cos(2\pi\phi) + v_y \sin(2\pi\phi) + v_z \quad (1)$$

ϕ stands for the orbital phase, whereas (v_x, v_y, v_z) are the velocity coordinates of the gas flow. The S-wave relation assumes that the x-axis runs between the stars, from the primary to the secondary, whilst the positive y-axis points in the direction of the secondary's orbital motion. Finally, the z-axis is perpendicular to the orbital plane. The Doppler map consists of a projection of the S-wave relation on the (v_x, v_y) plane. Therefore, each pixel in a Doppler map, specified by its velocity coordinates is associated with a particular S-wave (see e.g. Horne 1991 for a detailed discussion of the method).

Our data were weighted so as to account for the uneven sampling of the orbital cycle. The resulting Doppler map (Fig. 5) reveals an extended line formation region centered on the secondary without any obvious trace of a structure that

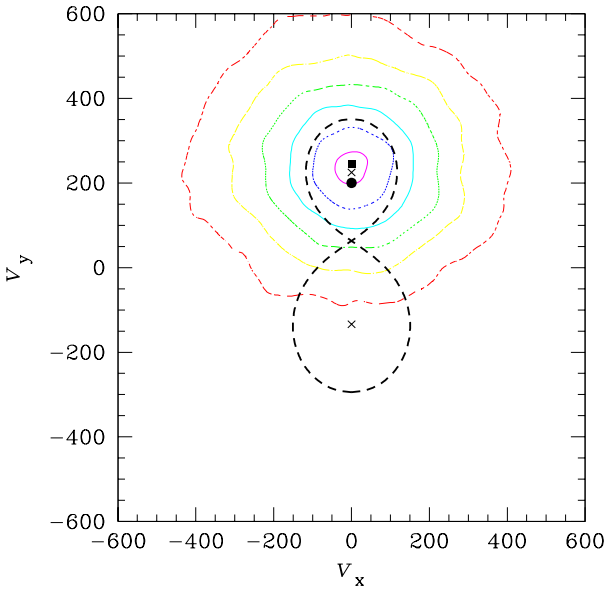

Fig. 5. Doppler map of the He II λ 4686 emission line in the spectrum of HDE 228766. The crosses correspond to the *RV*s of the center of mass of the primary and secondary as derived from the He II λ 4542 absorption and N III λ 4634 emission respectively. The shape of the Roche lobe in velocity-space (thick dashed line) has been calculated for a mass ratio of 1.67. The black dot and the black square correspond to the *RV* curves of the secondary's He II λ 4542 absorption and the peak of the He II λ 4686 emission line respectively. The Doppler map was computed with v_z set to 52 km s^{-1}.

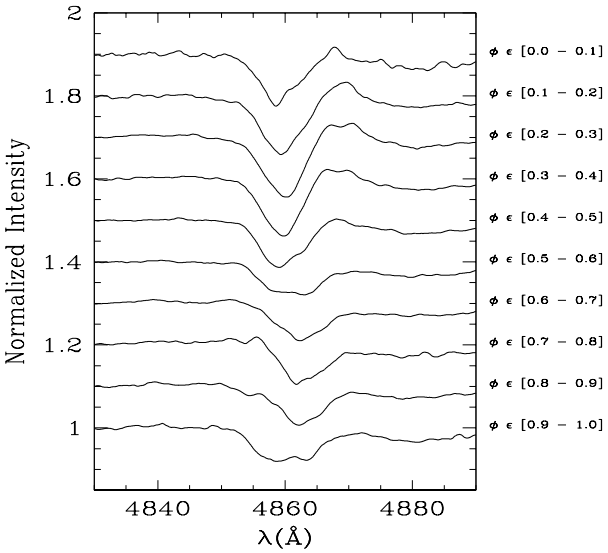

Fig. 6. Normalized profile of the Hβ line in the spectrum of HDE 228766 as observed in July and August 1999. The various spectra have been binned into phase intervals of 0.1. The broad absorption around 4880 is due to a diffuse interstellar band.

could be attributed to a wind interaction or a Roche lobe overflow. Therefore, it seems likely that the bulk of the He II λ 4686 emission arises in a relatively unperturbed part of the stellar wind of the secondary.

5.2. Hβ

The profile variations of the Hβ line are clearly phase-locked and stable over time scales of at least two years. The line displays a weak P-Cygni emission component between phases $\phi = 0.0$ and $\phi = 0.5$, i.e. when the lines of the secondary are red-shifted (see Fig. 6). The emission component vanishes when the secondary's lines are blue-shifted. This situation strongly suggests that the emission component is associated with the secondary star and that the bulk of the profile variations result from blending effects with the primary's absorption line.

5.3. Hα

Figure 7 reveals Hα emission consisting of at least two components. The stronger component roughly follows the orbital motion of the secondary whilst the weaker component moves roughly in anti-phase. The two emission components are best seen at quadrature phases.

MC77 reported the presence of a blue-shifted absorption feature in the Hα line near $\phi \sim 0.3$. Although we do not observe an absorption feature that goes below the continuum level, we note that the double-peaked structure of the line around $\phi \sim 0.3$ could be interpreted as a blend of a blue-shifted absorption (associated with the primary) with a red-shifted emission (belonging to the secondary). However, in this case, we would expect the Hα profile to display a double-peaked profile with a roughly central absorption at conjunction phases, which is not observed. Therefore, it seems more likely that the weaker component seen near quadrature corresponds to a genuine emission component that moves independently of the stronger component.

The Doppler map of this line (Fig. 8) reveals a more complex structure than in the case of He II λ 4686. The bulk of the emission still follows the secondary star though with a significantly larger *RV* amplitude. There is a secondary "peak" in the map associated with the weaker emission component seen in the spectra. This structure does not seem to belong to any of the stars. The equivalent width of this feature usually corresponds to less than 15% of the *EW* of the total Hα emission. The remaining ~85% of the flux follow the motion of the secondary star.

Finally, we have also carried out a simple S-wave analysis of the *RV*s of the peaks of the various emission lines in the spectrum of HDE 228766, i.e. we fitted the *RV*s of the peaks following Eq. (1). The results are given in Table 4. We note that the weaker Hα component is the only spectral feature that presents a significant v_x component and has a negative v_y. All other lines investigated in Table 4 display an orbital motion consistent with line formation in the wind of the secondary.

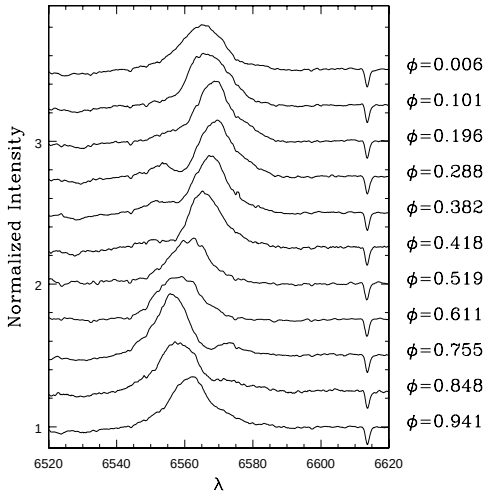

Fig. 7. Montage of the Hα line profile variability. All data are from the September 2000 campaign apart from the spectra at $\phi = 0.418$ (Sep. 2001) and $\phi = 0.519, 0.611$ (Oct. 2001).

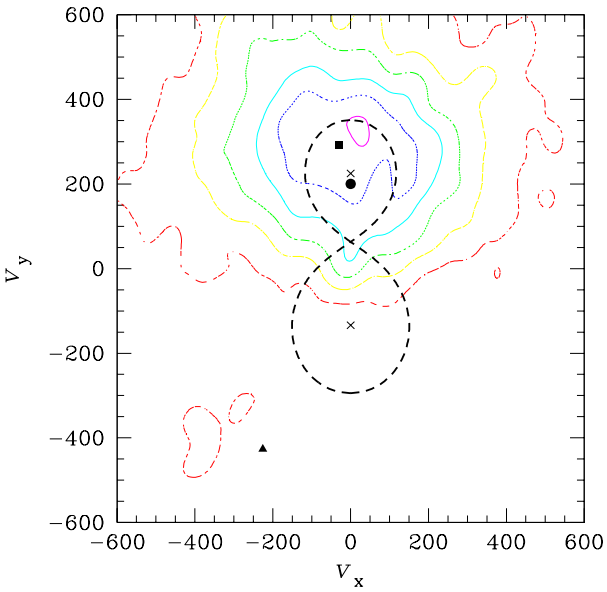

Fig. 8. Same as Fig. 5, but for the Hα emission with v_z set to -8.3 km s^{-1}. The symbols have the same meaning as before except for the filled square and the filled triangle that stand for the S-waves of the dominant peak (filled square) and the secondary peak (filled triangle) of the Hα profile.

Table 4. Summary of the S-wave analysis of the *RV*s of the peaks of various emission features in the spectrum of HDE 228766. The absorption components of the N v P-Cygni profiles are also included. The (v_x, v_y, v_z) velocity components and the mean |O − C| residuals are given in km s^{-1}.

Line	v_x	v_y	v_z	$\overline{\lvert O-C \rvert}$
Hα (strong)	−29.1	292.2	−8.3	23.2
Hα (weak)	−225.3	−426.3	−51.2	60.3
He II λ4686	−1.7	244.5	52.0	9.1
N III λ4511	16.1	224.6	0.4	8.3
N III λ4515	10.3	220.1	0.0	10.9
N III λ4634	3.8	224.9	−10.1	5.1
N III λ4641	−2.3	222.1	−22.4	11.5
N v λ4604 (A)	4.0	226.5	−37.6	9.1
N v λ4604 (E)	5.8	222.8	165.8	9.9
N v λ4620 (A)	3.2	223.3	−12.6	11.4

6. Discussion

6.1. The fundamental parameters of HDE 228766

Massey & Conti (1977) inferred the relative brightness of the components of HDE 228766 from the ratio of the intensities of their H8 and H9 lines. In this way, they derived a roughly equal brightness ($\Delta m_V \leq 0.5$ mag). We used the *EW*s of the He I λ 4471 and He II λ 4542 lines as measured on the spectra of maximum *RV*-separation and compared them with the *EW*s of single O-stars quoted by Conti & Alschuler (1971). The results depend of course on the (rather uncertain) spectral types adopted for each star, but they essentially confirm the results of MC77: the line ratios suggest in fact that both stars have more or less the same brightness with the secondary being somewhat brighter ($m_{V,\rm p} - m_{V,\rm s} \sim 0.3$).

Unfortunately, the distance of HDE 228766 is extremely uncertain. Popova & Kraicheva (1984) associated the system with the open cluster Dolidze 3. Zakirov (1999) determined a distance of 1.9 kpc for the eclipsing binary KV Cyg near the center of Dolidze 3. However, the membership of HDE 228766 in Dolidze 3 seems questionable since the system lies at ∼38′ from the cluster center (according to Ruprecht et al. 1983). On the other hand, HDE 228766 lies in the region of the sky spanned by the Cyg OB1 association for which Humphreys (1978) quoted a mean distance of 1.82 kpc. Let us start by assuming that HDE 228766 lies indeed at a distance of 1.9 kpc. Adopting the $V = 9.14$ magnitude and $B - V = 0.65$ colour ($E_{B-V} \simeq 0.95$) quoted by Hiltner (1956) and assuming a ratio of total-to-selective extinction $R = 3.2$, we find that the absolute magnitude of HDE 228766 should be −5.29. Note that the magnitude (9.15) and colour (0.60) found by Demers & Fernie (1964) yield an absolute magnitude of −5.12. These absolute magnitudes are at odds with the idea that HDE 228766 consists of two O-type giants or supergiants which should rather have a combined absolute magnitude of ∼−6.6 to ∼−7.2 (Schmidt-Kaler 1982). It appears rather unlikely that a peculiar extinction law could account for the entire discrepancy. Therefore, it seems more plausible that the actual distance of the system is larger than 1.9 kpc. For instance, if we assume an absolute magnitude of $M_{V,\rm s} = -6.0$ for the secondary and $M_{V,\rm p} = -5.7$ for the primary, we obtain a distance of 3.5 kpc for HDE 228766.

To determine the stellar properties of HDE 228766 we have modelled the combined spectrum of HDE 228766 by means of model atmosphere codes. For the primary's photospheric spectrum we have adopted a TLUSTY non-LTE model (Hubeny & Lanz 1995) corresponding to the O8 III star λ Ori. The relevant

model parameters are $T_{\rm eff,p} = 36\,000$ K, $R_{*,\rm p} = 16\,R_\odot$ ($L_{\rm bol,p} = 380\,000\,L_\odot$), $\log g = 3.5$ and $v \sin i = 200$ km s^{-1}. At this stage, it is worth emphasizing that the value of the projected rotational velocity of the primary has to be significantly larger than 100 km s^{-1} (the value that matches the secondary, see below) to achieve a good fit of the primary's lines.

For the secondary, we have utilised the non-LTE code of Hillier & Miller (1998) which solves the radiative transfer equation subject to the constraints of statistical and radiative equilibrium, in a spherical, extended atmosphere. Line blanketing is incorporated directly through the use of a super-level approach. We use a similar atomic model to that employed by Crowther et al. (2002) in their study of early-type O supergiants, including H I, He I-II, C III-IV, N III-V, O III-VI, Si IV, P IV-V, S IV-VI and Fe IV-VII (see Crowther et al. for further details).

The velocity in the supersonic part of the wind is described by a standard β-law:

$$v(r) = v_\infty \left(1 - \frac{R_{*,\rm s}}{r}\right)^\beta$$

whilst the atmospheric structure, connecting the spherically extended hydrostatic layers to the β-law wind is achieved via a parameterized scale height, h (see Hillier et al. 2002 for details), for which $h = 0.001$ yields a reasonable match to He I and Balmer line wings, consistent with $\log g = 3.5$.

The synthetic photospheric spectrum of the primary and the synthetic photospheric + wind spectrum of the secondary are combined allowing for the visual brightness ratio ($m_{V,\rm p} - m_{V,\rm s} = 0.3$) and the parameters of the secondary model are fine-tuned to match the observed line profiles. We adjust the stellar temperature[1] and mass-loss rate of an individual model until the "photospheric" He II λ 4542 and He I λ 4471 lines are reproduced. Simultaneously, we vary the mass-loss rate until Hα is also matched. The exponent of the β-law is adjusted until the shape of Hα is well reproduced – for HDE 228766 we find $\beta \sim 1.5$. Since HDE 228766 is very heavily reddened and no UV spectra are available, we adopt a representative terminal wind velocity of $v_\infty = 1800$ km s^{-1}. Our calculations assume a microturbulence $v_{\rm turb} = 10$ km s^{-1} and, due to the severe blending of the lines, we nominally adopt $v \sin i = 100$ km s^{-1} for the secondary.

As discussed by Hillier et al. (2002), it is extremely difficult to determine accurate He/H abundances in O supergiants. Consequently, we adopt He/H = 0.2 by number, whilst C and N abundances are varied until diagnostic optical line profiles are reproduced. In Fig. 9, we present selected optical line profile fits. Overall, agreement for $T_{\rm eff,s} = 38\,000$ K is good. He I λ 4471 provides our main temperature constraint since other blue optical He I lines are weak or absent. Alternatively, we considered using He I λ 5876 (or He I λ 10830) together with the He II λ 4686 line. However, this method (followed by Crowther & Bohannan 1997) yields significantly (~4000 K) lower stellar temperatures, and suffers from inconsistencies involving the ionization balance of UV/optical metal lines. Therefore, we have greater confidence in our adopted diagnostics, which do not suffer from such problems.

[1] Defined, as is usual for an extended atmosphere, as the effective temperature corresponding to the radius at a Rosseland optical depth of 20.

Table 5. Summary of the main parameters of our non-LTE analysis of the spectrum of HDE 228766.

	Primary	Secondary
$T_{\rm eff}$ (K)	36 000	38 000
$\log (L_{\rm bol}/L_\odot)$	5.58	5.74
$R_* (R_\odot)$	16	17
$\log g$	3.5	
$\dot{M}$ ($M_\odot$ yr^{-1})		10^{-5}
$v \sin i$ (km s^{-1})	200	100

A reasonable fit of the combined spectrum is achieved for $R_{*,\rm s} = 17\,R_\odot$ ($L_{\rm bol,s} = 550\,000\,L_\odot$). Assuming the secondary to solely contribute to the Hα and He II λ 4686 emission, its mass-loss rate is $10^{-5}\,M_\odot$ yr^{-1}. We note that our value of the mass loss rate is in perfect agreement with the estimate of MC77 who used the strength of the Hα line to infer $\dot{M} = 10^{-5}\,M_\odot$ yr^{-1}. Moderate clumping would reduce this value by a factor of ~2.

Our primary nitrogen abundance diagnostics is N III $\lambda\lambda$ 4634–41 which implies $\epsilon_{\rm N} = 6\,\epsilon_{\rm N,\odot}$. Carbon is somewhat more difficult to constrain, with an upper limit to the strength of C III $\lambda\lambda$ 4647–51 of $\epsilon_{\rm C} = 0.08\,\epsilon_{\rm C,\odot}$. As discussed elsewhere (e.g. Hillier et al. 2002), oxygen is exceedingly difficult to constrain in mid-O supergiants due to the lack of suitable optical diagnostics.

While the synthetic model fits the H I Balmer, He II (including He II λ 10124), N III and N IV lines pretty well, the fit of the He I λ 4471 profile is less good and the model fails to reproduce the observed He I $\lambda\lambda$ 5876, 10830 emission profiles as well as the N V $\lambda\lambda$ 4604, 4620 lines. To match the He I profiles, the temperature of the model would have to be much lower and would therefore be in disagreement with the value derived from the optical nitrogen lines. While a significant fraction of the He I emission could be associated with the primary wind (He I λ 10830 emission is common among O supergiants, e.g. Andrillat & Vreux 1979) or with an interaction region, our S-wave analysis clearly indicates that the N V lines belong to the same star (i.e. the secondary) as the N III and N IV lines. The effective temperature of the secondary indicates an O6-7 spectral type, in agreement with the results derived from the EW ratio of the He I λ 4471 and He II λ 4542 lines. However, the puzzling presence of the N V $\lambda\lambda$ 4604, 4620 lines cannot be explained by this temperature. A higher temperature of approximately 40 000–42 000 K would be needed to fit the N V lines. However, the temperature cannot be much larger than 38 000 K because otherwise the N IV line gets too strong.

The spectrum of HDE 228766 is remarkably similar to that of the O4If$^+$ star HDE 269698 in the LMC. HDE 269698 also displays N III, N IV and N V lines in its spectrum and Crowther et al. (2002) derive $T_{\rm eff} = 40\,000$ K for this star, which also provides a good match to He I/He II, UV, and far-UV lines.

The structure of the secondary's atmosphere in HDE 228766 could be intermediate between the winds of HDE 269698 and of the WN7ha star in WR 22. The latter star

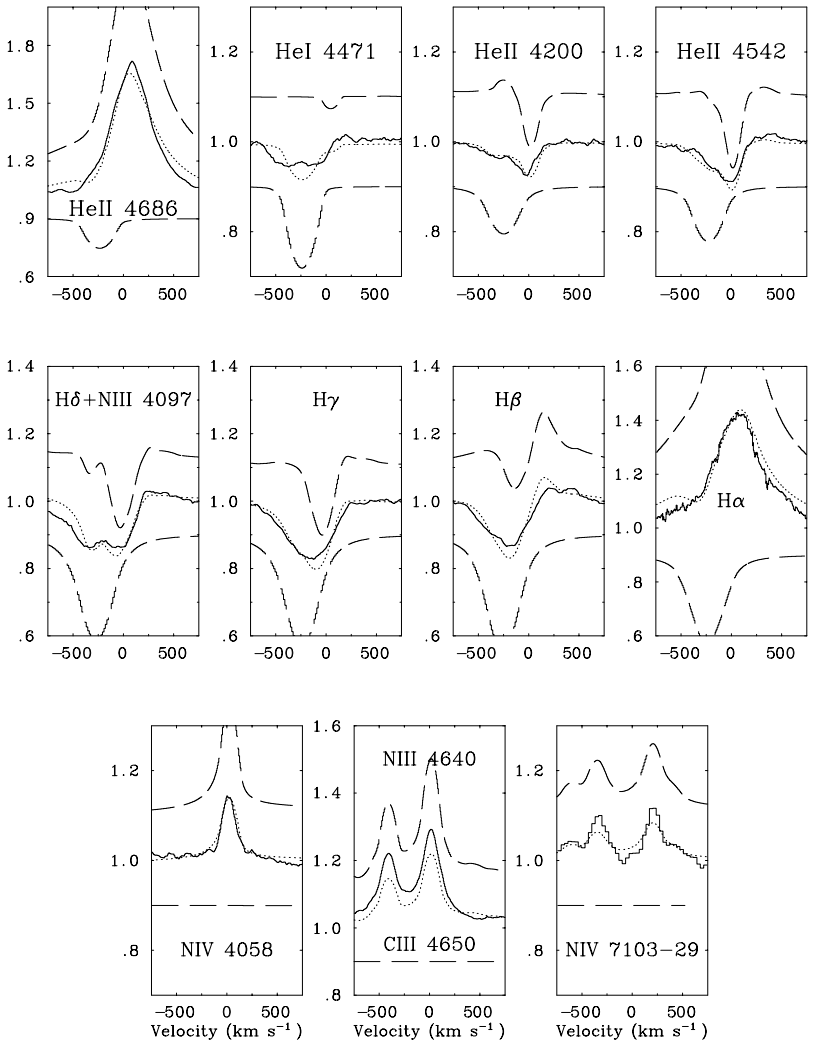

Fig. 9. Fit of the spectrum of HDE 228766 as observed in September 2000 (except for the N IV $\lambda\lambda$ 7103–29 lines observed in August 1990) with a non-LTE model atmosphere code. The combined synthetic model is shown by the dotted line, whilst the observations are displayed by the continuous line. The individual normalized synthetic spectra are shown by the dashed lines offset by −0.1 and +0.1 for the primary and the secondary respectively. The synthetic spectra have been shifted in velocity to match the radial velocities of the two components at the orbital phases of the observations.

also displays N III, N IV and N V emission lines in its spectrum (Rauw et al. 1996). Note that an analysis of the H I, He I and He II spectrum of WR 22 with a non-LTE code yielded a rather low stellar temperature (T_* = 31 900 K, Crowther et al. 1995), whereas the He II, N III and N IV lines profiles were reasonably well reproduced using a higher stellar temperature (T_* = 36 500 K, Crowther et al. 1995).

Combining the results of our tomographic analysis, the mean EW of the He II λ 4686 line in the observed spectrum of HDE 228766 and the optical brightness ratio we infer that the EW of the intrinsic He II λ 4686 emission in the secondary's spectrum is of order ∼10 Å. This puts the secondary's intrinsic emission strength beyond the nominal Of range, but below that of regular WNL stars. However a WNLha classification (see Smith et al. 1996) could account for the observed line strength. In fact, comparing with the observed spectra of the presumably single WNLha stars WR 25 (WN7ha) and WR 108 (WN9ha), we find the secondary in HDE 228766 to be intermediate in excitation between these two objects, but similar in wind strength. These results suggest that a WN8ha classification might be appropriate.

6.2. Evolutionary status

Although the parameters derived hereabove depend on the unknown distance of HDE 228766 and the poorly constrained optical brightness ratio, our analysis clearly reveals an evolved secondary star as witnessed by the large mass loss rate and the peculiar abundances. The secondary star in HDE 228766

appears therefore most likely as a kind of transition object at the beginning of the WR stage.

Adopting the parameters inferred hereabove, we can compare the properties of the stars in HDE 228766 with the evolutionary tracks of Schaller et al. (1992). The most stricking feature is that the secondary appears to be the most evolved component and is clearly overluminuous for its present-day mass. Hence, the secondary must have been the initially more massive component of the system. The only way to account for this situation in the framework of single star evolutionary models would be if the secondary were moving bluewards after an excursion towards the lower temperature regime. Note that in this case, the evolutionary model suggests that the secondary would be a fully developed WN Wolf-Rayet star.

Alternatively, the evolution of the whole system could have been influenced by mass exchange. Evolutionary tracks from Vanbeveren & de Loore (1994) and de Loore & Vanbeveren (1994) could indeed account for the overluminosity of the secondary. The initially more massive component could have undergone mass loss through Roche lobe overflow (RLOF) and would now be the less massive star. We note also that the primary has broader lines and seems to be rotating faster than the secondary. If the stars were in synchronous rotation, they should roughly have the same $v \sin i$. In the framework of a binary evolution model, the larger $v \sin i$ of the present-day primary could be due to spinning up through accretion (Vanbeveren & de Loore 1994). It seems therefore plausible that HDE 228766 is in a post RLOF stage. The evolutionary tracks of Vanbeveren & de Loore (1994) indicate that the secondary should be in the WNL stage.

6.3. A wind interaction in HDE 228766?

Our data reveal a weak Hα emission feature that could be an indication of a wind interaction in the optical spectrum of HDE 228766. A colliding wind phenomenon could also produce a signature in the X-ray domain through a phase-dependent excess X-ray emission (e.g. Stevens et al. 1992).

We have therefore searched the ROSAT archive for observations of HDE 228766. Unfortunately there is only a single pointed observation (rp500248a01) where the star happened to lie within the field of view of the ROSAT-PSPC (though it was outside the inner ring of the PSPC detector). Using our new ephemeris we find that the orbital phase of HDE 228766 at the time of the PSPC observation was $\phi = 0.64$. We extracted a background corrected spectrum using the XSELECT software. We have fitted this spectrum with an absorbed single-temperature optically thin plasma model (Raymond & Smith 1977) within the XSPEC software. Fixing the neutral hydrogen column density at the interstellar value of $N_{\rm H}^{\rm ISM} = 0.53 \times 10^{22}$ cm^{-2}, we obtain a best fitting temperature $kT = 0.88^{+.25}_{-.16}$ keV. The corresponding dereddened X-ray flux in the energy band 0.1–2.0 keV is 1.6×10^{-12} erg cm^{-2} s^{-1} yielding an unabsorbed X-ray luminosity[2] of $L_{\rm X} = 2.34 \times 10^{33}$ erg s^{-1} for a distance of 3.5 kpc. If the total bolometric luminosity of the binary amounts to $L_{\rm bol} = 9.3 \times 10^5\ L_\odot$ (see above), we obtain $\log L_{\rm X}/L_{\rm bol} = -6.18$. The $L_{\rm X}/L_{\rm bol}$ ratio appears a factor ~3.6 larger than expected from the empirical relation for single O-stars given by Berghöfer et al. (1997). Although the snapshot ROSAT observation does not provide any information about the variability of the X-ray flux, it seems tempting to associate the X-ray "overluminosity" with a binary interaction.

[2] We caution that our fit does not account for any intrinsic – i.e. circumstellar wind – absorption.

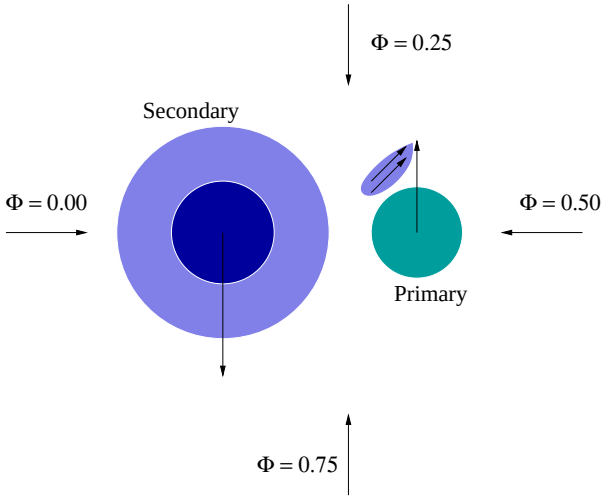

Fig. 10. Schematic view of the Hα emission region in the HDE 228766 binary system. The projection of the line of sight onto the plane of the orbit is indicated at four orbital phases. The bulk of the emission arises in the wind of the secondary star. An additional contribution comes from the small shaded area close to the primary's surface. The arrows indicate the direction of the orbital motion of the stars and of the velocity of the material in the small emitting region.

Adopting the mass ratio $q = 1.67$ derived in Sect. 4, we can estimate the minimum radii of the Roche lobes of the components using the formula of Eggleton (1983). In this way we find $R_{\rm RL} \sin i = 32.2$ and 25.5 $R_\odot$ for the primary and secondary respectively. From our non-LTE model hereabove, we infer a radius of 17 $R_\odot$ for the secondary. Therefore it appears rather unlikely that any of the components currently fills up its critical volume. The interaction in HDE 228766 is therefore more likely associated with a wind collision rather than an ongoing Roche lobe overflow.

Since the secondary wind is by far more energetic than that of the primary, it is likely that the former crashes onto the surface of the primary star. Such a shock could in turn compress the primary wind resulting in a high density region near the point of head-on wind collision, where the weak Hα emission would be formed through recombination. Figure 10 illustrates a possible model for the location of the Hα emitting material in HDE 228766. While the bulk of the emission is produced in the stellar wind of the secondary, the weaker emission component could arise in a plasma volume which is passing by the primary's surface. This geometry could at least qualitatively account for the double-peaked line shape observed near the quadrature phases.

6.4. Final remarks and conclusions

Our analysis of HDE 228766 suggests that the secondary star is the most evolved component of the system and accounts for almost all the emission features seen in the spectrum. The only exception to this rule comes from a weak Hα emission component that moves in anti-phase with the secondary and arises most probably in a wind interaction region near the surface of the primary.

HDE 228766 offers the unique opportunity to study the fundamental properties of a massive star which is just in the transition between an Of$^+$ and a WNL Wolf-Rayet star. However, a couple of crucial ingredients are missing that prevent us from deriving absolute values for some parameters. The most obvious parameter that needs to be determined is the distance. Future astrometric observations (e.g. with ESA's planned *GAIA* satellite) will hopefully allow to solve this problem. Moreover, a photometric monitoring of the binary over an entire orbital cycle is badly needed to clarify whether or not the system displays photometric eclipses. Our orbital solutions suggest that the orbital inclination i might be large enough for such eclipses to occur. If this is the case, then an analysis of the light curve should allow to constrain not only the inclination, but also the radii of the stars and their relative brightness. This would make HDE 228766 a cornerstone for our understanding of massive star evolution.

Acknowledgements. The authors would like to thank the referee Dr. H. Henrichs for a careful reading of the manuscript. The Liège team is greatly indebted to the Fonds National de la Recherche Scientifique (Belgium) for multiple assistance including the financial support for the rent of the OHP telescope in 1999 and 2000 through contract 1.5.051.00 "Crédit aux Chercheurs" FNRS. The travels to OHP for the observing runs were supported by the Ministère de l'Enseignement Supérieur et de la Recherche de la Communauté Française. This research is also supported in part by contracts P4/05 and P5/36 "Pôle d'Attraction Interuniversitaire" (SSTC-Belgium) and through the PRODEX XMM-OM Project. PAC acknowledges financial support from the Royal Society. GR would like to thank the staff of the Observatoire de Haute Provence for their technical support during the various observing runs. The SIMBAD database has been consulted for the bibliography.

References

Andrillat, Y., & Vreux, J.-M. 1979, A&A, 76, 221
Berghöfer, T. W., Schmitt, J. H. M. M., Danner, R., & Cassinelli, J. P. 1997, A&A, 322, 167
Bohannan, B., & Crowther, P. A. 1999, ApJ, 511, 374
Chlebowski, T., Harnden, F. R. Jr., & Sciortino, S. 1989, ApJ, 341, 427
Conti, P. S. 1973, ApJ, 179, 181
Conti, P. S., & Alschuler, W. R. 1971, ApJ, 170, 325
Conti, P. S., & Howarth, I. D. 1999, MNRAS, 302, 145
Crowther, P. A., Hillier, D. J., & Smith, L. J. 1995, A&A, 293, 403
Crowther, P. A., & Bohannan, B. 1996, in Wolf-Rayet Stars in the Framework of Stellar Evolution, Proc. 33rd Liège Int. Astroph. Coll., ed. J.-M. Vreux, A. Detal, D. Fraipont-Caro, E. Gosset, & G. Rauw, 437
Crowther, P. A., & Bohannan, B. 1997, A&A, 317, 532
Crowther, P. A., et al. 2002, ApJ, submitted
de Loore, C., & Vanbeveren, D. 1994, A&A, 292, 463
Demers, S., & Fernie, J. D. 1964, PASP, 76, 350
Eggleton, P. P. 1983, ApJ, 268, 368
Gosset, E., Royer, P., Rauw, G., Manfroid, J., & Vreux, J.-M. 2001, MNRAS, 327, 435
Hackwell, J. A., Gehrz, R. D., & Smith, J. R. 1974, ApJ, 192, 383
Hart, A. B. 1957, ApJ, 126, 463
Heck, A., Manfroid, J., & Mersch, G. 1985, A&AS, 59, 63
Hillier, D. J., & Miller, D. L. 1998, ApJ, 496, 407
Hillier, D. J., et al. 2002, ApJ, in press
Hiltner, W. A. 1951, ApJ, 113, 317
Hiltner, W. A. 1956, ApJS, 2, 389
Hiltner, W. A., & Schild, R. E. 1966, ApJ, 143, 770
Horn, J., Kubát, J., Harmanec, P., et al. 1996, A&A, 309, 521
Horne, K. 1991, in Fundamental Properties of Cataclysmic Variable Stars: 12th North American Workshop on Cataclysmic Variables and Low Mass X-ray Binaries (SDSU Press), ed. A. W. Shafter, 23
Hubeny, I., & Lanz, T. 1995, ApJ, 439, 875
Humphreys, R. M. 1978, ApJS, 38, 309
Lafler, J., & Kinman, T. D. 1965, ApJS, 11, 216
Massey, P., & Conti, P. S. 1977, ApJ, 218, 431
Popova, M., & Kraicheva, Z. 1984, Astrof. Issled. Izv. Spets. Astr. Obs., 18, 64
Rauw, G., Vreux, J.-M., Gosset, E., Hutsemékers, D., Magain, P., & Rochowicz, K. 1996, A&A, 306, 771
Rauw, G., Vreux, J.-M., & Bohannan, B. 1999, ApJ, 517, 416
Rauw, G., Sana, H., Vreux, J.-M., Gosset, E., & Stevens, I. R. 2002, in Interacting Winds from Massive Stars, ASP Conf. Ser. 260, ed. A. F. J. Moffat, & N. St.-Louis, 449
Raymond, J. C., & Smith, B. W. 1977, ApJS, 35, 419
Roman, N. G. 1951, ApJ, 114, 492
Ruprecht, J., Balazs, B., White, R. E., & Sharov, A. S. 1983, SvA, 27, 358
Sana, H., Rauw, G., & Gosset, E. 2001, A&A, 370, 121
Schaller, G., Schaerer, D., Meynet, G., & Maeder, A. 1992, A&AS, 96, 269
Schmidt-Kaler, T. 1982, Physical Parameters of the Stars, Landolt-Börnstein Numerical Data and Functional Relationships in Science and Technology, New Series, Group VI (Springer Verlag, Berlin)
Smith, L. F., Shara, M. M., & Moffat, A. F. J. 1996, MNRAS, 281, 163
Stevens, I. R., Blondin, J. M., & Pollock, A. M. T. 1992, ApJ, 386, 265
Thaller, M. L., Gies, D. R., Fullerton, A. W., Kaper, L., & Wiemker, R. 2001, ApJ, 554, 1070
Vanbeveren, D., & de Loore, C. 1994, A&A, 290, 129
Vreux, J.-M., & Andrillat, Y. 1979, A&A, 75, 93
Walborn, N. R. 1973, ApJ, 186, 611
Walborn, N. R. 2001, in Eta Carinae and Other Mysterious Stars: The hidden opportunities of emission spectroscopy, ASP Conf. Ser., 242, ed. T. R. Gull, S. Johannson, & K. Davidson, 217
Walborn, N. R., & Fitzpatrick, E. L. 1990, PASP, 102, 379
Walborn, N. R., Howarth, I. D., Lennon, D. J., et al. 2002, AJ, 123, 2754
Werner, K., & Rauch, T. 2001, in Eta Carinae and Other Mysterious Stars: The hidden opportunities of emission spectroscopy, ASP Conf. Ser. 242, ed. T. R. Gull, S. Johannson, & K. Davidson, 229
Zakirov, M. M. 1999, Astron. Lett., 25, 229

HD 149404 and HDE 228766: some additional remarks

Simultaneously with and independently of our investigation of HD 149404 (Rauw et al. 2001b reproduced above, see also Nazé et al. 2002), Thaller et al. (2001) studied a sample of Hα spectra of this binary system. Their data were obtained in 1995 at the ESO CAT telescope and in 1996 and 1997 at the Mount Stromlo observatory. The overall shape and phase-locked variations of the Hα profile were in good agreement with those reported by Rauw et al. (2001b, see Fig. 3 in this paper). In addition, Thaller et al. (2001) claimed the detection of long- and short-term emission strength variations unrelated to the orbital cycle. However, since the data were obtained with two different instruments over narrow wavelength ranges that render the normalisation of the spectra quite difficult, the long-term variations could also result from instrumental effects.
Thaller et al. (2001) performed a Doppler tomography analysis of the Hα emission line. The Doppler map of their ESO data reveals an extended emission volume roughly centered on the centre of mass with two peaks, the main peak near $(v_x, v_y) = (-96, -48)$ and a secondary peak near $(116, 110)$. The Doppler tomography of the Mount Stromlo data yielded qualitatively the same results although the positions of the peaks were slightly different. Whilst these results are in qualitative agreement with the S-wave analysis of Rauw et al. (2001b), the phase coverage of the Thaller et al. data (especially the Mount Stromlo spectra) is not optimal. Therefore, I decided to perform a tomographic analysis of our own Hα data.
To establish the Doppler map from our FEROS + CORALIE data, I have re-normalised the FEROS data. This step was necessary to remove the broad wings of the Hα line which are apparent in the FEROS data but cannot be correctly determined in the CORALIE spectra because of the narrow wavelength range of the échelle orders of the latter. Despite this re-normalisation, FEROS and CORALIE data taken at close orbital phases can show some low-level (at most a few percent of the continuum) residual normalisation discrepancies in the line wings (i.e. essentially above absolute velocities of $\sim 1200\,\mathrm{km\,s^{-1}}$). I then built the Doppler map of the Hα line using all our available data and the tomography method outlined in Sect. 1.1.3. The resulting Doppler map is illustrated in Fig. 1.16.
The Hα tomogram is in excellent agreement with the results of Thaller et al. (2001). Even the details of the map nicely agree. This is remarkable since the Thaller et al. map and ours were obtained from different data sets and using different tomography methods. Figure 1.16 further illustrates a good agreement between the position of the peaks of the map and the results of the S-wave analysis presented by Rauw et al. (2001b) and Nazé et al. (2002).

Thaller et al. (2001) argued that the bulk of the Hα emission arises in focused stellar winds flowing from both stars into the shock region between the stars. The positions of the peaks in the Doppler map would result from the combination of the wind velocity and the rotational velocity. This illustrates the ambiguity to convert information from the velocity space into constraints on the geometrical location of the emitting gas. While the Thaller et al. model qualitatively agrees with the Doppler map, it seems unclear why only the material flowing into the shock region should produce Hα emission. Since the gas in the wind interaction zone should cool rather rapidly, material flowing away from the shock region is also likely to contribute (as we suggested in Rauw et al. 2001b). It seems therefore likely that emission from both the focused winds and the arms of the shock contributes to the observed Hα emission and its orbital variability.

Penny et al. (1999) analysed the *Hipparcos* photometry of HD 149404 finding small ($\Delta H \simeq 0.04$ mag) ellipsoïdal variations consistent with an orbital inclination of $i \simeq (30 \pm 5)^\circ$. Combined with our cross-

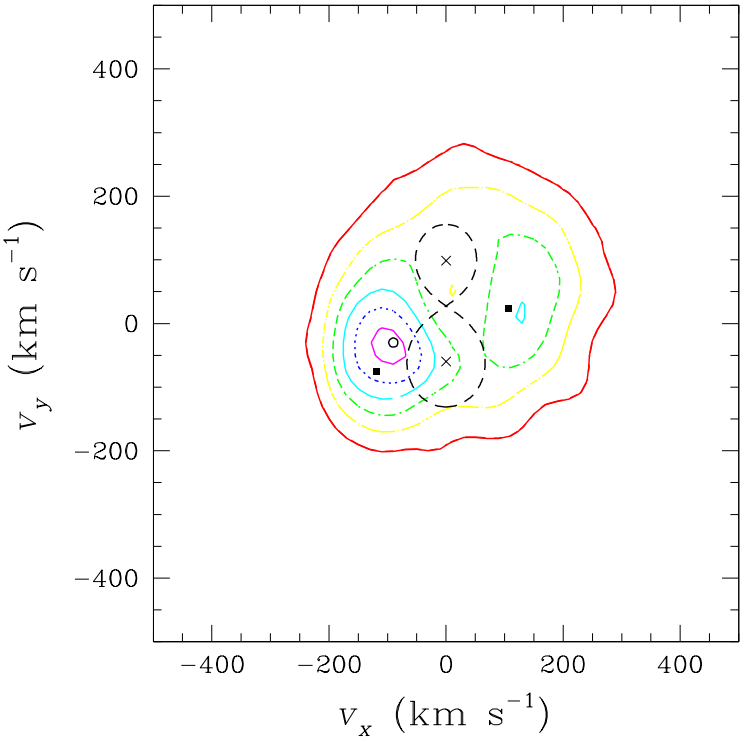

Figure 1.16: Doppler map of the Hα line in HD 149404 for $v_z = -50\,\mathrm{km\,s^{-1}}$. All the data presented by Rauw et al. (2001b) were used to establish this map. The crosses indicate the positions of the centres of mass of the stars in velocity space. The filled dots yield the results of the S-wave analysis presented by Rauw et al. (2001b) and Nazé et al. (2002). The Roche lobe in velocity space was computed for a mass ratio of 0.605. The different contours of the map correspond to 95, 80, 65, 50, 35 and 20% of the maximum level which is reached at $(v_x, v_y) = (-90, -30)\,\mathrm{km\,s^{-1}}$ (shown as an open circle in the plot).

correlation orbital solution, this inclination yields masses of 20.1 ± 9.3 and $12.2 \pm 5.6\,\mathrm{M}_\odot$ for the O7.5 I(f) primary and the ON9.7 I secondary respectively. These values are well below the evolutionary masses one would obtain from a comparison with single star evolutionary tracks (see Fig. 7 of Rauw et al. 2001b). This discrepancy is a further indication that the evolution of this system must have been affected by one or several Roche lobe overflow episodes. It should be noted that a similar situation (surprisingly low masses for evolved O-type stars) was encountered in the study of LSS 3074 (Gosset et al. 2005b).

I checked the All Sky Automated Survey (ASAS, Pojmanski 2002) database for photometric data of HD 149404. Unfortunately, although I selected only quality A data and despite the fact that the typical formal errors on the photometry quoted on the ASAS web page are quite small (of order 0.02 mag), the actual dispersion of the data is rather substantial (of order 0.3 mag). This is due to saturated data which are not flagged individually (G. Pojmanski 2006, private communication). This situation renders any attempt to study the ellipsoïdal variations with ASAS photometry hopeless at this point in time.

Finally, a few words about HDE 228766. Rauw et al. (2002b) argued that the large minimum masses of HDE 228766 could indicate that the system displays photometric eclipses. To check this, I considered the data from the Northern Sky Variability Survey (NSVS, Wozniak et al. 2004). While the data suggest

that the system indeed displays some variability ($\sigma_V = 0.030$ mag to be compared to formal photometric errors of 0.010 mag) with a minimum near $\phi = 0.0$, we find no unambiguous modulation attributable to photometric eclipses (see Fig. 1.17).

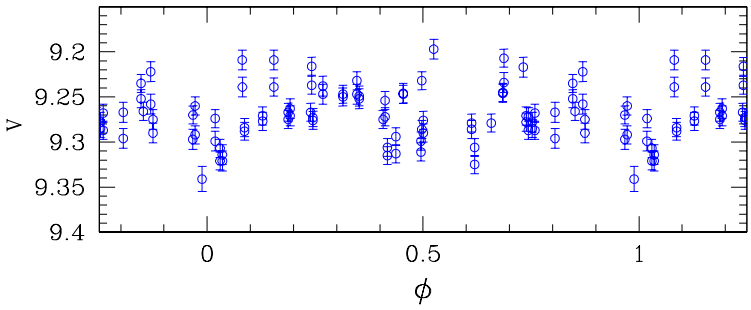

Figure 1.17: NSVS photometric data for HDE 228766 as a function of orbital phase using the ephemeris from Rauw et al. (2002b).

The radii of the components estimated by Rauw et al. (2002b) indicate that no eclipses, but only ellipsoïdal variations with a peak-to-peak amplitude of about 0.02 mag are expected for an inclination of less than $\sim 68°$.

In Sect. 1.5.3, I suggest that the simultaneous presence of prominent N III, N IV and N V lines in the spectrum of WR 20a stems from the surface temperature differences that exist as a result of gravity darkening. Since the spectrum of HDE 228766 also displays these features (associated with the secondary component in this case), one may wonder whether gravity darkening could also play a decisive role here. Using the von Zeipel theorem and adopting the stellar and binary parameters from Rauw et al. (2002b) together with $i = 65°$, the maximum difference in temperature between the polar region and the equator due to gravity darkening amounts to ~ 1500 K (assuming a mean effective temperature of 38000 K for the secondary). Rauw et al. (2002b) estimated that a temperature of 40000 - 42000 K would be needed to fit the N V lines. Whilst gravity darkening could provide some of the temperature difference, it may not be sufficient to account for the 2000 - 4000 K temperature elevation needed here. However, one should bear in mind that the actual impact of the gravity darkening effect strongly depends on the Roche lobe filling factor of the secondary which is difficult to constrain in the absence of photometric eclipses.

1.5 WR 20a and the quest for very massive stars

As outlined in the introduction above (Sect. 1.1), an important question in the field of massive star research is what is the upper mass limit of Population I stars. In some cases, analyses of the spectra of early-type stars in the Local Group galaxies led to extremely large masses. Let us first see how the mass of a single star can be constrained by studying its spectrum. A stellar atmosphere code is used to generate a model spectrum that is then fitted to an observed high-resolution spectrum of the star. In this way, the effective temperature $T_{\rm eff}$ and the surface gravity $\log g$ of the best fit model are determined. Using the photometry of the star along with some assumptions on its distance and reddening, the bolometric luminosity and hence the stellar radius can be inferred. The surface gravity then yields the *spectroscopic* mass determination.
There are several potential problems with this technique:

- the determination of the bolometric luminosity can be subject to large uncertainties. First of all, the star might not be single. For instance, R 136a at the centre of the 30 Dor complex in the LMC was once believed to be a single extremely massive (several thousand $M_\odot$) star. However, high resolution images (e.g. Weigelt & Baier 1985, Weigelt et al. 1991, Campbell et al. 1992) revealed that R 136a is actually a very compact stellar cluster. In some cases, the luminosities can also be overestimated due to binarity. A major uncertainty on the luminosities stems from the usually rather poorly known distances and reddenings. This is especially the case for objects in our own Galaxy.

- the inclusion or not of effects such as line blanketing in the model atmosphere code can significantly alter the values of the fundamental parameters (effective temperature, gravity, bolometric correction...) determined for a given star. This obviously has also an impact on the spectroscopic mass determinations.

- the latter issue is directly related to the so-called 'mass-discrepancy', i.e. the difference between the spectroscopic mass determination and evolutionary mass estimates (see Sect. 1.1). While this problem seems now solved for Galactic objects, it still remains for Magellanic Cloud stars and in this case for both dwarfs and supergiants (see the discussion by Herrero & Najarro 2005).

The *spectroscopic masses* obtained in this way must therefore be considered with caution. One potentially very luminous (and hence very massive) star identified in this way is the LBV-type object known as 'Pistol Star' in the Quintuplet cluster near the Galactic centre. Figer et al. (1998) analysed the near-infrared spectrum of the star with a model atmosphere code and concluded that its initial mass must have been around 200 – 250 $M_\odot$. However, the same limitations as above regarding the un-determined multiplicity also apply to Pistol Star.

The least model-dependent way to measure the mass of a star is through the study of eclipsing spectroscopic binaries. However, this is not a trivial exercise. First of all, one has to identify the best candidates to search for very massive stars. At first sight, O2 and O3 stars appear to be the obvious targets for such a campaign. Still, it is interesting to consider some results from stellar evolution theory. In fact, according to single star evolutionary models, there exists a minimum initial mass ($M_{\rm OWR}$) for a single star to become a Wolf-Rayet star already during its main-sequence (MS) lifetime (i.e. while the star is still burning hydrogen in its core). A star more massive than $M_{\rm OWR}$ would evolve directly during its MS lifetime into a WNL stage without going through an LBV phase. Meynet (2004) quotes a value

of $M_{OWR} = 62\,M_\odot$ for a non-rotating stellar model at $Z = 0.020$. For a star with an initial rotation velocity of $300\,km\,s^{-1}$ at $Z = 0.020$, this minimum mass would be $45\,M_\odot$. Therefore, some of the most massive Population I stars might actually be found among hydrogen rich late-type WN stars (so-called WNLha stars). Indeed, WR 22 and WR 20a, two of the most massive binary systems, contain WN7ha and WN6ha stars and therefore most probably belong to this category.

Before we turn to the case of WR 20a, let us briefly review some recent results related to the issue of the upper mass limit that were not included in the Aussois lecture notes (Rauw 2004a, see Sect. 1.1). Ostrov (2001) analysed photometry and spectroscopy of the eclipsing binary MACHO*05:34:41.3−69:31:39 (O3 If* + O6: V, $P_{orb} = 1.40$ day). The components of this system have masses of 41.2 ± 1.2 and $27.0 \pm 1.2\,M_\odot$ for the O3 If* primary and the O6: V secondary respectively. These values are surprisingly low for such hot stars (especially for the primary). However, this specific binary system is in overcontact and its current evolutionary status can thus not be explained by single star models, implying also that these mass determinations cannot be used to constrain the mass-luminosity relation of single early-type stars.

Ostrov (2002) discussed the SB2 system LH 54-425 in the LMC. This binary of spectral type O3 III(f*) + O5 has a short orbital period of about 2.25 days and displays ellipsoidal light variations with a peak to peak amplitude of ~ 0.1 mag. The analysis of the light curve performed by Ostrov (2002) assuming an absolute magnitude of the binary yields $i \simeq 45°$ – 50°. The author also reports 6 RV measurements obtained near quadrature phases, which then suggest masses of $M_1 = 108 \pm 3\,M_\odot$ and $M_2 = 52 \pm 3\,M_\odot$. However, values of the orbital inclination between 39 and $58°$ are acceptable which then correspond to uncomfortably large ranges of masses of 64 – 160 $M_\odot$ and 31 – 80 $M_\odot$ for the primary and secondary respectively.

De Becker et al. (2006a) presented the first SB2 orbital solution of the long-period (440 days) binary system HD 15558 (O5 III(f)). While this orbital solution suggests minimum primary masses well in excess of $100\,M_\odot$, it is unfortunate that the scatter of the RV measurements of the secondary is rather large, leading to large errors on the minimum masses ($m \sin^3 i$). If the primary mass was actually that large, that would be an unexpected result for several reasons: first, the spectral type of the primary is rather late for such a very massive star and second, the luminosity (assuming HD 15558 actually belongs to IC 1805) is rather low for such a very high mass (see the discussion in De Becker 2005, De Becker et al. 2006a and Section 1.3.2). Therefore, although there is no clear spectroscopic evidence for such a scenario (apart maybe from the spectral variability of the primary that occurs on time scales of a few days), the most likely explanation would be that this is actually a triple system, where the O5 III(f) star would be a short period binary (De Becker et al. 2006a).

Finally, it is worth recalling that several recent studies suggest that there exists indeed an upper limit on the mass of a Population I early-type star. For instance, on statistical grounds, this limit is expected to be somewhere in the range 120 – 200 $M_\odot$ (Oey & Clarke 2005). Figer (2005) studied the population of massive stars in the Arches cluster near the Galactic centre. He found no star with an initial mass exceeding $\sim 130\,M_\odot$ in this cluster, whilst the Initial Mass Function would predict the existence of 18 such objects. These considerations led him to suggest that a firm upper limit on the mass of a star in our galaxy should be around $150\,M_\odot$.

1.5.1 The discovery of the binarity of WR 20a

The Wolf-Rayet nature of WR 20a was discovered by Shara et al. (1991). We obtained a first high-quality spectrum of the star in March 2002. This spectrum suggested that WR 20a is a binary system. Our team therefore obtained a more extensive data set in February 2004, allowing us to establish the binary

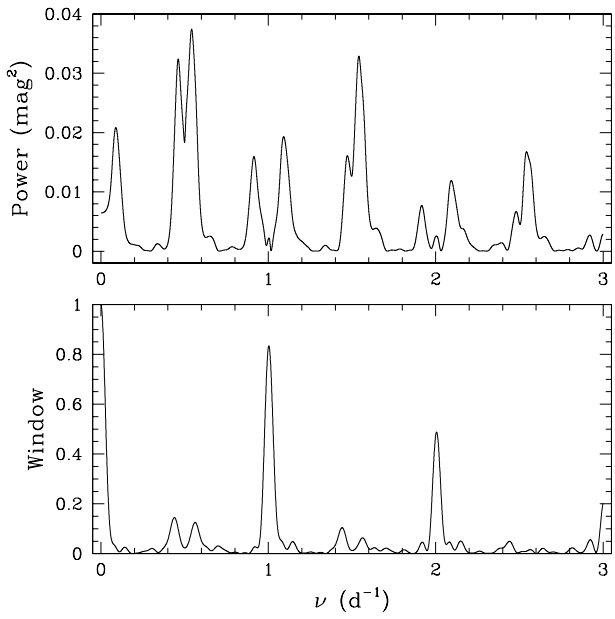

Figure 1.18: Power spectrum of the I band OGLE photometric data of WR 20a presented by Bonanos et al. (2004).

nature of the system. Our data allowed us to measure the radial velocities of the components of WR 20a and to search for an orbital solution. While the most likely orbital period was found to be 3.675 days (corresponding to extremely large minimum masses), our RV time series did not allow us to completely rule out the alternative aliases for the orbital period of 4.419 and 1.293 days (see Rauw et al. 2004b). Since the exact orbital period is very important to establish the minimum masses of the components, and since we expected WR 20a to be an eclipsing binary, we were planning to obtain photometric data of the system. However, a few days after we posted the results of our spectroscopic campaign on astro-ph, the OGLE team started a photometric monitoring of WR 20a over about three weeks. They found that the star is indeed an eclipsing binary and they actually established that the orbital period is close to 3.686 days (Bonanos et al. 2004). This situation nicely demonstrates the amazing possibilities of a team benefiting from an unrestricted access to a private telescope.

The power spectrum of the photometric data obtained by Bonanos et al. 2004 is illustrated in Fig. 1.18. This power spectrum clearly indicates that the most likely orbital period of WR 20a is indeed near 3.7 days. In fact, the frequency of the highest peak in the power spectrum is 0.54176 day^{-1}. Since both components of WR 20a have nearly equal properties, both eclipses have essentially equal depths and we thus expect the highest frequency of the power spectrum to be at $\nu = \frac{2}{P_{\rm orb}}$, leading to $P_{\rm orb} = 3.692$ days.

The following pages reproduce the letter (Rauw et al. 2004b) that announced our discovery of the multiplicity of WR 20a and presented its first orbital solution suggesting that this system likely contains two very massive stars. This is followed by a second paper (Rauw et al. 2005c) reporting a thorough analysis of the optical spectrum of this important system. The most prominent emission lines, Hα and He II λ 4686, are shown to display strong phase-locked profile variability probably related to a wind interaction phenomenon. A non-LTE model atmosphere code is used to derive the fundamental parameters of the

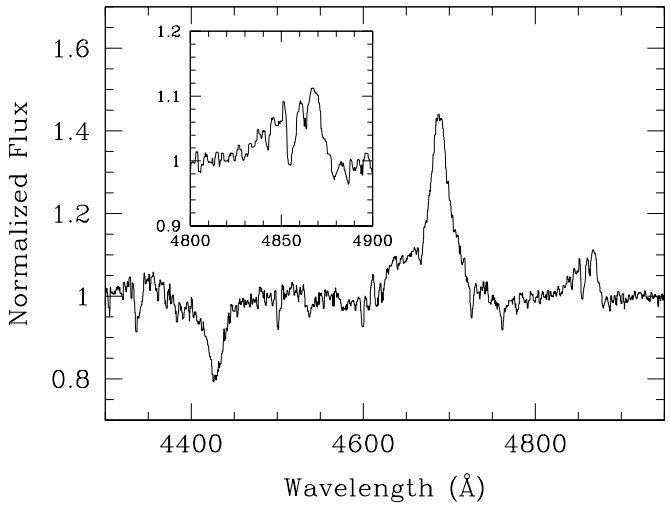

Figure 1.19: Normalized spectrum of WR 20a as observed on JD 2453457.640. The insert shows a zoom on the Hβ line profile.

WN6ha components and some clues on the evolutionary stage of the binary are presented.
Finally, one additional medium resolution spectrum covering the domain from 4200 to 4950 Å was obtained with the EMMI instrument at the NTT on HJD 2453457.640 ($\phi = 0.361$ using the ephemeris from Bonanos et al. 2004). The spectrum is presented in Fig. 1.19. The He II λ 4686 line profile is in very good agreement with the one obtained on HJD 2453033.739 (i.e. at $\phi = 0.358$, but 115 cycles earlier) as shown in Fig. 2 of our second paper (Rauw et al. 2005c). This indicates that the line profile variations are indeed phase-locked. In addition, the Hβ profile shows a central absorption in nice agreement with the synthetic spectrum shown in Fig. 6 of Rauw et al. (2005c).

A&A 420, L9–L13 (2004)
DOI: 10.1051/0004-6361:20040150

Astronomy & Astrophysics

WR 20a: A massive cornerstone binary system comprising two extreme early-type stars⋆

G. Rauw[1,⋆⋆], M. De Becker[1], Y. Nazé[1,⋆⋆⋆], P. A. Crowther[2], E. Gosset[1,⋆⋆], H. Sana[1,⋆⋆⋆], K. A. van der Hucht[3,4], J.-M. Vreux[1], and P. M. Williams[5]

[1] Institut d'Astrophysique et de Géophysique, Université de Liège, Allée du 6 Août, Bât. B5c, 4000 Liège, Belgium
[2] Department of Physics & Astronomy, University of Sheffield, Hicks Building, Hounsfield Rd., Sheffield S3 7RH, UK
[3] SRON National Institute for Space Research, Sorbonnelaan 2, 3584 CA Utrecht, The Netherlands
[4] Astronomical Institute Anton Pannekoek, University of Amsterdam, Kruislaan 403, 1098 SJ Amsterdam, The Netherlands
[5] Institute for Astronomy, University of Edinburgh, Royal Observatory, Blackford Hill, Edinburgh EH9 3HJ, UK

Received 25 March 2004 / Accepted 25 April 2004

Abstract. We analyse spectroscopic observations of WR 20a revealing that this star is a massive early-type binary system with a most probable orbital period of ~3.675 days. Our spectra indicate that both components are most likely of WN6ha or O3If*/WN6ha spectral type. The orbital solution for a period of 3.675 days yields extremely large minimum masses of 70.7 ± 4.0 and $68.8 \pm 3.8\ M_\odot$ for the two stars. These properties make WR 20a a cornerstone system for the study of massive star evolution.

Key words. binaries: spectroscopic – stars: early-type – stars: fundamental parameters – stars: individual: WR 20a

1. Introduction

Although it is generally accepted that Wolf-Rayet (WR) stars are evolved descendants of massive O-stars, many open questions remain about the evolution of these objects. Among the most fundamental issues is the importance of mass transfer in the evolution of massive O + O binaries (e.g. Vanbeveren et al. 1998). It is therefore of prime interest to achieve as complete a census of WR binaries as possible and to investigate the fundamental properties of individual massive binary systems.

Among the 227 objects listed in the VIIth Catalogue of Galactic Wolf-Rayet Stars (van der Hucht 2001), there are only 52 known spectroscopic binaries and only 32 of them have reliable orbital solutions. In addition to these confirmed binaries, van der Hucht (2001) provides a list of 30 rather faint and poorly studied objects that are potential WR + OB binaries. Most of these binary candidates were classified as such because of their comparatively weak emission lines that could be the result of the dilution by the continuum light of an OB-type companion. In order to search for a composite spectrum – and hence confirm multiplicity – we performed a snapshot spectroscopic survey of a sample of WR binary candidates. One of the most interesting objects that emerged from our survey was WR 20a.

WR 20a (=THA 35-II-036 = SMSP2) was catalogued by Thé (1966) in an Hα emission line survey, and first discovered to be a WR star by Shara et al. (1991) in the course of a deep narrow and broadband photometric survey for galactic Wolf-Rayet stars in the southern Milky Way. The latter authors also obtained a low-resolution (2 pixel resolution of 7 Å) spectrum of the star and proposed a WN7 spectral type, although they noted the lack of a He II λ 5411 emission line. Shara et al. (1991) suggested that WR 20a had a rather high H/He abundance ratio. Later, the object was re-classified as WN7: h/WC by Shara et al. (1999). The star is believed to be a member of the young open cluster Westerlund 2 in the core of the H II region RCW 49 (Moffat et al. 1991).

In this letter, we first present our blue/violet observations of WR 20a (Sect. 2). The spectral features as well as the nature of WR 20a are revisited in Sect. 3.1, whilst Sect. 3.2 deals with an analysis of the radial velocities. Finally, we briefly discuss the implications of our results in Sect. 4.

2. Observations

Two snapshot spectra of WR 20a were obtained in March 2002 with the EMMI instrument mounted on ESO's 3.5 m New Technology Telescope (NTT) at La Silla. The EMMI instrument was used in the BLMD medium dispersion spectroscopic mode with grating # 3 (1200 lines mm^{-1}) providing a wavelength coverage of 460 Å per set-up. The central wavelength was set to 4080 Å (violet setting) or 4530 Å (blue setting). The exposure times were 30 min for each setting and the

Send offprint requests to: G. Rauw,
e-mail: rauw@astro.ulg.ac.be

⋆ Based on observations collected at the European Southern Observatory (La Silla, Chile).
⋆⋆ Research Associate FNRS (Belgium).
⋆⋆⋆ Research Fellow FNRS (Belgium).

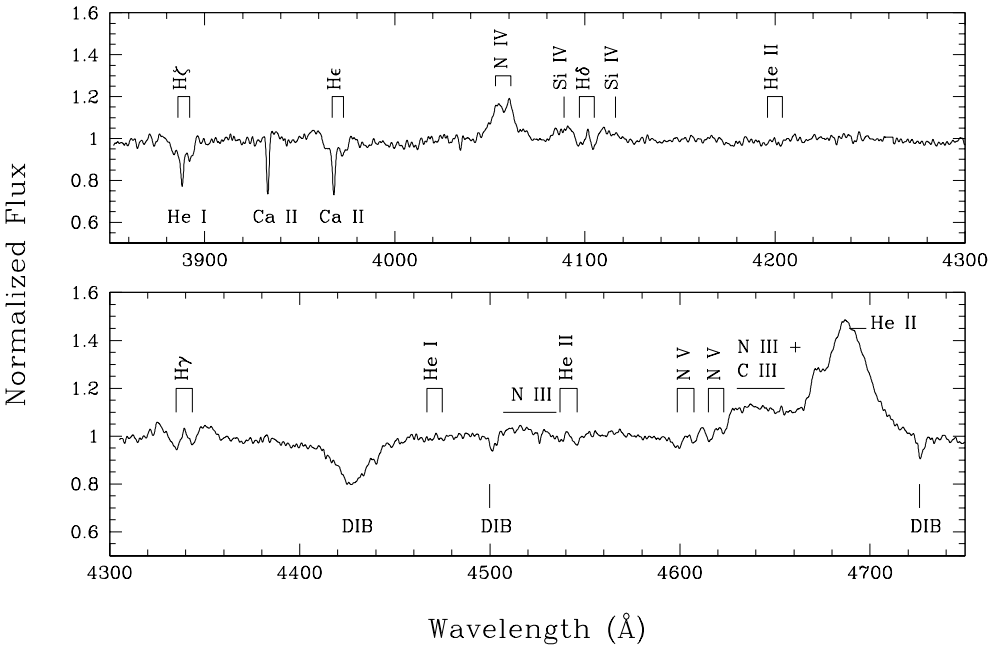

Fig. 1. Spectrum of WR 20a as observed on HJD 2 453 034.715 (violet setting, *top panel*) and 2 453 034.741 (blue setting, *lower panel*). Note the double N IV λ 4058 emission line as well as the double N V λ 4604 and N V λ 4620 absorptions. The stellar lines are labelled above the spectrum, whereas the interstellar lines and diffuse interstellar bands (DIBs) are indicated below.

corresponding *S/N* was about 100. The spectral resolution as determined from the FWHM of the lines of the Th-Ar comparison spectra was about 1.25 Å. The data were reduced in the standard way using the long context of the MIDAS package. The violet spectrum taken on HJD 2 452 355.60 revealed double absorption lines of hydrogen and helium as well as a moderately strong double-peaked NIV λ 4058 emission. On the other hand, the blue spectrum obtained on HJD 2 452 354.56 showed single absorption lines of hydrogen, He II and N V. These properties suggested that WR 20a could be a short period binary consisting of two very early extreme Of-type stars (Driesens 2003). We thus organized a follow-up observing campaign to confirm the binarity of WR 20a. The star was monitored over 12 consecutive nights in January–February 2004 with the same instrumentation as in March 2002. The weather conditions were good except for the last two nights where the seeing and the transparency were poor. The data were reduced in the same way as in 2002 and the complete journal of the useable observations is given in Table 1.

3. Results

3.1. The spectrum of WR 20a

Our data reveal that WR 20a is indeed a short-period binary system (see below). All prominent spectral features appear double with nearly identical intensities on most of our spectra (see e.g. Fig. 1) indicating that the components of WR 20a must have identical spectral types and a visible brightness ratio of ~1. The spectrum of WR 20a displays many absorption lines of H I, He II and N V unlike what we would expect if WR 20a were indeed a "classical" WN7 star (see however below). Only a few (rather narrow) emission lines are seen in the blue/violet spectrum: N IV λ 4058, He II λ 4686 as well as a broad complex probably due to N III $\lambda\lambda$ 4634-41, C III $\lambda\lambda$ 4647-50 and possibly C IV λ 4658. The Balmer absorption lines also display some broad underlying emission wings on several spectra. The emissions seen around the Hδ absorption in Fig. 1 could actually be due to Si IV $\lambda\lambda$ 4089, 4116, but the spectra obtained on other nights do not allow us to unambiguously confirm this identification. In addition to the strong diffuse interstellar bands, we note the presence of the interstellar He I λ 3889 absorption line. This latter feature was also observed in the spectra of several early-type stars of the Carina Nebula (Walborn & Hesser 1975). This line is not usually seen in interstellar sightlines (cf. ζ Oph, Shulman et al. 1974) and may be formed locally as in the case of the Carina stars.

No stellar He I lines are clearly seen in the spectrum. Together with the presence of rather strong N V absorption lines, this would suggest a very early O-type classification for the components of WR 20a. The presence of He II λ 4686 in strong emission further suggests a supergiant luminosity class. Comparing our spectra to the classification scheme of Walborn et al. (2002, see also Walborn 2001), we would propose an O3 If* spectral type for both stars. However, distinguishing an extreme Of star from a weak-lined WNL star is a very tricky issue. In this context, Crowther & Dessart (1998) proposed *EW*(He II λ 4686) = 12 Å as a boundary between O3 If*/WN and WN5-6 stars. For WR 20a, we determine *EW*(He II λ 4686) = 13.1 Å with a 1-σ dispersion of 1.3 Å, right at the borderline proposed by Crowther & Dessart. Since

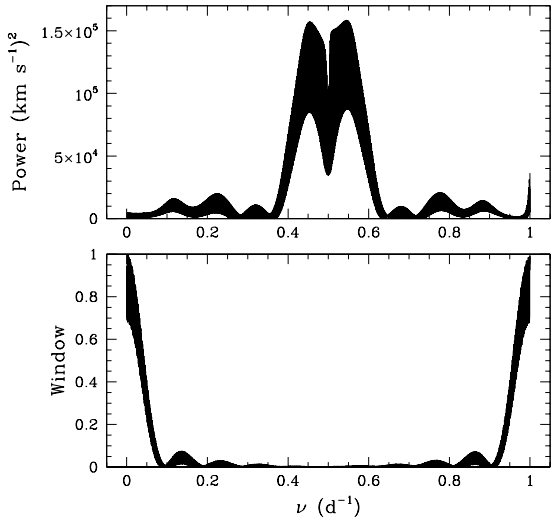

Fig. 2. *Top panel*: power spectrum of our $|RV_1 - RV_2|$ time series of WR 20a. The bottom panel provides the corresponding power spectral window.

the He II λ4686 emission could contain a contribution from a wind interaction process, we consider this an upper limit on the actual strength of the line. Comparing the spectrum of WR 20a obtained near conjunction with the spectra of several extreme Of and weak-lined WN stars, we find that the components of WR 20a are indeed intermediate between Mk 42 (O3If*/WN) and HD 97950C (=WR 47c, WN6ha). Finally, the spectrum of WR 20a presented by Shara et al. (1991) indicates that the Hβ line is in weak emission. The latter feature favours a WN6ha spectral type. We shall thus adopt a WN6ha classification for both components of WR 20a, though we cannot fully exclude an O3 If*/WN6ha type. The Shara et al. (1991) spectrum of WR 20a suggested the presence of a C IV λ5808 emission with a normalized intensity stronger relative to He I λ5876 than in normal WN stars, thus leading to the WN/WC classification proposed by Shara et al. (1999). Note that our blue/violet spectra do not provide support for such a hybrid type.

3.2. Orbital solution

We have measured the radial velocities (*RV*s) of the components of WR 20a by fitting Gaussians. The typical uncertainties on individual *RV* measurements are of order 10−15 km s^{-1} for those phases when the components are resolved[1].

A major issue in determining the orbital period arises from the fact that the spectral types of both stars are identical. In fact, the spectra do not allow us to distinguish the components a priori. Therefore, we performed a period search on the absolute values of the radial velocity differences $|RV_1 - RV_2|$. In this way, we expect to find the highest peak in the periodogram at $\nu_1 = 2/P_{\rm orb}$. Using the Fourier technique of Heck et al. (1985, see also Gosset et al. 2001), we find that the most likely value of ν_1 is 0.544 ± 0.009 day^{-1}. However, there is a strong ambiguity with the $1 - \nu_1$ alias at 0.453 ± 0.009 day^{-1} which produces only a slightly smaller (formal) peak in the periodogram (see Fig. 2). Our preferred value for the orbital period is therefore 3.675 ± 0.030 days, but we cannot discard the alternative value of 4.419 ± 0.044 days. Alternatively, if the (slightly smaller) peak at the $1 + \nu_1$ alias (1.547 day^{-1}) were to be selected, the orbital period would be ∼1.29 days, i.e. even shorter than the 1.64 day period of CQ Cep, the shortest period WN binary system known to date (see e.g. van der Hucht 2001).

As a next step, we determined the apparent systemic velocity of each spectral line from an orbital solution obtained for the *RV*s of the specific line. In this way, we found apparent systemic velocities of −75, −18, −77, −42, −51 and −26 km s^{-1} for the Hγ, He II λ4542, N V λ4604, N V λ4620, N IV λ4058 and Hδ lines respectively. Finally, we averaged the *RV*s of the different lines listed above after subtracting their systemic velocities. The results are listed in Table 1.

Due to the ambiguity about the right alias in the periodogram, we caution that the orbital phases as well as the primary/secondary identifications in Table 1 are only valid if the orbital period is indeed 3.675 days. Adopting this period, we have derived the orbital solution of WR 20a using the technique described by Sana et al. (2003). Since the *RV*s show no indication of a significant orbital eccentricity, we assumed a circular orbit. The results are provided in Table 2 and the *RV* curve is illustrated in Fig. 3. We emphasize that orbital solutions derived from the *RV*s of individual spectral lines overlap within the errors with the results in Table 2.

The most important results are the large minimum masses of 68.8 ± 3.8 and 70.7 ± 4.0 $M_\odot$ derived for the secondary and primary component respectively. It should be emphasized that these values strongly depend on the adopted orbital period. In fact, the alternative orbital period (4.419 days) would lead to even larger minimum masses of 80.8 ± 5.1 and 84.0 ± 5.3 $M_\odot$ respectively. If, on the contrary, the $1 + \nu_1$ alias corresponding to an orbital period of 1.293 days were selected, the minimum masses would be much lower (24.9 ± 1.4 and 25.9 ± 1.4 $M_\odot$). We note however, that in the latter case, the orbital solution is of significantly lower quality than the one obtained for an orbital period of 3.675 days.

4. Discussion and future perspectives

The WN6ha or O3 If*/WN6ha spectral type of the components of WR 20a is significantly earlier than those of the earliest members (O6:V−O7:V) of Westerlund 2 analysed by Moffat et al. (1991).

Several authors have estimated the distance of Westerlund 2: $7.9^{+1.2}_{-1.0}$ kpc (Moffat et al. 1991); 5.7 ± 0.3 kpc (Piatti et al. 1998); 6.4 ± 0.4 kpc (Carraro & Munari 2004). Adopting a visual brightness ratio of 1 together with the photometry of Moffat et al. (1991; $V = 13.58$, $B - V = 1.51$) the various distance estimates yield absolute magnitudes M_V in the range −5.0 to −6.1. This is fainter than the average of

[1] Note that we also determined the heliocentric radial velocities of the sharp interstellar features: we obtain *RV*s of −16.6 ± 15.0, −7.8 ± 10.5 and −10.2 ± 14.0 km s^{-1} for the He I λ3889, Ca II λ3934 and Ca II λ3968 lines. The 1σ dispersions listed here provide some rough indication of the accuracy of our wavelength calibration.

Table 1. Journal of our spectroscopic observations of WR 20a. The first and second columns provide the heliocentric Julian date (in the format HJD−2 450 000) and the orbital phase assuming a period of 3.675 days and adopting phase $\phi = 0.0$ as given in Table 2. The third column indicates whether the blue (B) or violet (V) spectral range was observed. The recentred and averaged primary and secondary radial velocities are given in Cols. 4 and 5 respectively (see text). Finally, the last column yields the weight that we assigned to the various RV data in the orbital solution.

Date	ϕ	Set-up	RV_1 (km s^{-1})	RV_2 (km s^{-1})	Weight
2354.560	0.542	B	−11.7	−11.7	0.1
2355.600	0.825	V	290.7	−319.3	0.7
3032.716	0.074	B	−131.9	182.9	0.2
3032.742	0.081	V	9.1	9.1	0.1
3033.715	0.346	V	−288.4	277.4	0.7
3033.739	0.353	B	−285.1	292.6	1.0
3034.715	0.618	V	235.8	−219.1	0.7
3034.741	0.625	B	287.6	−265.5	1.0
3035.719	0.892	V	269.3	−222.7	0.7
3035.746	0.899	B	245.2	−219.4	1.0
3036.719	0.164	V	−259.7	287.0	0.7
3036.743	0.170	B	−302.6	309.5	1.0
3037.738	0.441	V	−78.3	−78.3	0.1
3037.762	0.447	B	−74.0	−74.0	0.1
3038.723	0.709	V	363.5	−354.0	0.7
3038.746	0.715	B	374.6	−375.9	1.0
3039.718	0.980	V	12.4	12.4	0.1
3039.752	0.989	B	−28.0	−28.0	0.1
3040.717	0.252	V	−309.3	368.4	0.7
3040.741	0.258	B	−336.1	394.0	1.0
3041.722	0.525	V	4.3	4.3	0.1
3041.747	0.532	B	22.9	22.9	0.1
3042.714	0.795	B	375.4	−374.4	0.2

three WN6ha stars in NGC 3603, namely −6.9 to −7.7 mag[2], such that only the largest published distance of Westerlund 2 would be in marginal agreement with the photometry of WR 20a, allowing for a cosmic scatter of 0.5−0.7 mag on M_V. This problem would be less severe if the absolute magnitudes of the components of WR 20a were more typical of O3 I stars ($M_V = -5.9$ according to Crowther & Dessart 1998). Alternatively, WR 20a could actually be unrelated to Westerlund 2 (though the rarity of early-type stars and the angular proximity of WR 20a to the cluster strongly suggest membership) or the photometry of Moffat et al. could be affected by photometric eclipses. Concerning the last possibility, we note that given the extremely large minimum masses of the components in WR 20a, it appears very likely that the system could display eclipses. A photometric monitoring of this binary is therefore of the utmost importance in order to help derive its absolute magnitude, to get rid of the aliasing problem of the RV data and to constrain the orbital inclination. We intend to organize such a campaign in the near future.

[2] Moffat et al. (1994) derived an average M_V of −7.7 for the three H-rich WN stars in NGC 3603, whilst Crowther & Dessart (1998) re-evaluated their distance and reddening and obtained an average of −6.9 mag.

Table 2. Orbital solution for WR 20a assuming a circular orbit and an orbital period of 3.675 days. T_0 refers to the time of conjunction with the primary being behind. γ, K and $a \sin i$ denote respectively the systemic velocity, the amplitude of the radial velocity curve and the projected separation between the centre of the star and the centre of mass of the binary system. R_{RL} stands for the radius of a sphere with a volume equal to that of the Roche lobe computed according to the formula of Eggleton (1983). All error bars indicate 1-σ uncertainties.

	Primary	Secondary
T_0(HJD−2 450 000)	3043.480 ± 0.014	
γ (km s^{-1})	18.8 ± 5.6	−3.5 ± 5.7
K (km s^{-1})	353.1 ± 8.6	362.6 ± 8.8
$a \sin i$ ($R_\odot$)	25.6 ± 0.2	26.3 ± 0.6
$q = m_1/m_2$	1.03 ± 0.03	
$m \sin^3 i$ ($M_\odot$)	70.7 ± 4.0	68.8 ± 3.8
$R_{RL} \sin i$ ($R_\odot$)	19.8 ± 0.2	19.5 ± 0.2

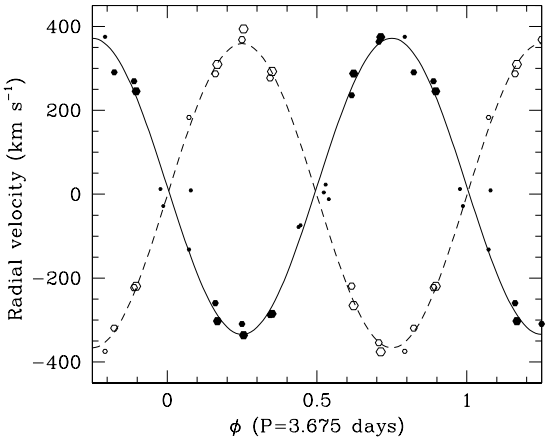

Fig. 3. Radial velocity curve of WR 20a for an orbital period of 3.675 days. The filled (resp. open) symbols stand for the primary (resp. secondary) RVs. The sizes of the symbols reflect the relative weight assigned to the various points in the orbital solution (see Table 1). The solid line and the dashed line yield our best fit orbital solution assuming a circular orbit (see Table 2).

An important issue in the context of the formation and the evolution of very massive stars is that of the mass of the most massive ones. Masses up to ∼200 $M_\odot$ have been inferred for the most luminous O2 stars from a comparison with evolutionary tracks (Walborn et al. 2002). However, to date, none of the O2 stars is known to belong to a binary system that would allow to determine its mass in a less model dependent way. The most massive main-sequence stars in binary systems known so far were found in R 136-38 (O3 V + O6 V) and R 136-42 (O3 V + O3 V). Massey et al. (2002) determined

masses of 57 and 40 $M_\odot$ respectively for the O3 V primary stars of these systems. Another extremely massive object is the WN7ha primary in the 80-day period binary WR 22 (Rauw et al. 1996; Schweickhardt et al. 1999) with a minimum mass of 55 $M_\odot$. WR 20a thus probably consists of two of the most massive stars with a direct mass determination known so far. Therefore, WR 20a is certainly a cornerstone system for future investigations of massive star evolution.

Finally, we note that the emission lines in the spectrum of WR 20a display strong phase-locked profile variability. This aspect will be discussed along with an analysis of the spectrum with a model atmosphere code in a forthcoming paper.

Acknowledgements. The Liège team is greatly indebted to the Fonds National de la Recherche Scientifique (Belgium) for multiple assistance. This research is also supported in part by contract P5/36 "Pôle d'Attraction Interuniversitaire" (Belgian Federal Science Policy Office) and through the PRODEX XMM-OM and INTEGRAL projects. The SIMBAD database has been consulted for the bibliography.

References

Carraro, G., & Munari, U. 2004, MNRAS, 347, 625
Crowther, P. A., & Dessart, L. 1998, MNRAS, 296, 622
Driesens, L. 2003, Master thesis, University of Liège
Eggleton, P. P. 1983, ApJ, 268, 368
Gosset, E., Royer, P., Rauw, G., Manfroid, J., & Vreux, J.-M. 2001, MNRAS, 327, 435
Heck, A., Manfroid, J., & Mersch, G. 1985, A&AS, 59, 63
Massey, P., Penny, L. R., & Vukovich, J. 2002, ApJ, 565, 982
Moffat, A. F. J., Shara, M. M., & Potter, M. 1991, AJ, 102, 642
Moffat, A. F. J., Drissen, L., & Shara, M. M. 1994, ApJ, 436, 183
Piatti, A. E., Bica, E., & Clariá, J. J. 1998, A&AS, 127, 423
Rauw, G., Vreux, J.-M., Gosset, E., et al. 1996, A&A, 306, 771
Sana, H., Hensberge, H., Rauw, G., & Gosset, E. 2003, A&A, 405, 1063
Schweickhardt, J., Schmutz, W., Stahl, O., Szeifert, T., & Wolf, B. 1999, A&A, 347, 127
Shara, M. M., Moffat, A. F. J., Smith, L. F., & Potter, M. 1991, AJ, 102, 716
Shara, M. M., Moffat, A. F. J., Smith, L. F., et al. 1999, AJ, 118, 390
Shulman, S., Bortolot, V. J., & Thaddeus, P. 1974, ApJ, 193, 97
Thé, P. S. 1966, Contributions Bosscha Observatory, 35, 1
Vanbeveren, D., de Loore, C., & van Rensbergen, W. 1998, A&ARv, 9, 63
van der Hucht, K. A. 2001, New Astron. Rev., 45, 135
Walborn, N. R. 2001, in Eta Carinae and Other Mysterious Stars, ed. T. Gull, S. Johansson, & K. Davidson, ASP Conf. Ser., 242, 217
Walborn, N. R., & Hesser, J. E. 1975, ApJ, 199, 535
Walborn, N. R., Howarth, I. D., Lennon, D. J., et al. 2002, AJ, 123, 2754

A&A 432, 985–998 (2005)
DOI: 10.1051/0004-6361:20042136

Astronomy & Astrophysics

The spectrum of the very massive binary system WR 20a (WN6ha + WN6ha): Fundamental parameters and wind interactions⋆

G. Rauw[1,⋆⋆], P. A. Crowther[2], M. De Becker[1], E. Gosset[1,⋆⋆], Y. Nazé[1], H. Sana[1,⋆⋆⋆], K. A. van der Hucht[3,4], J.-M. Vreux[1], and P. M. Williams[5]

[1] Institut d'Astrophysique et de Géophysique, Université de Liège, Allée du 6 Août 17, Bât. B5c, 4000 Liège, Belgium
e-mail: rauw@astro.ulg.ac.be
[2] Department of Physics & Astronomy, University of Sheffield, Hicks Building, Hounsfield Rd., Sheffield, S3 7RH, UK
[3] SRON National Institute for Space Research, Sorbonnelaan 2, 3584 CA Utrecht, The Netherlands
[4] Astronomical Institute Anton Pannekoek, University of Amsterdam, Kruislaan 403, 1098 SJ Amsterdam, The Netherlands
[5] Institute for Astronomy, University of Edinburgh, Royal Observatory, Blackford Hill, Edinburgh, EH9 3HJ, UK

Received 7 October 2004 / Accepted 23 November 2004

Abstract. We analyse the optical spectrum of the very massive binary system WR 20a (WN6ha + WN6ha). The most prominent emission lines, Hα and He II λ 4686, display strong phase-locked profile variability. From the variations of their equivalent widths and from a tomographic analysis, we find that part of the line emission probably arises in a wind interaction region between the stars. Our analysis of the optical spectrum of WR 20a indicates a reddening of $A_V \simeq 6.0$ mag and a distance of ∼7.9 kpc, suggesting that the star actually belongs to the open cluster Westerlund 2. The location of the system at ∼1.1 pc from the cluster core could indicate that WR 20a was gently ejected from the core via dynamical interactions. Using a non-LTE model atmosphere code, we derive the fundamental parameters of each component: $T_{\rm eff} = 43\,000 \pm 2000$ K, $\log L_{\rm bol}/L_\odot \simeq 6.0$, $\dot{M} = 8.5 \times 10^{-6}\,M_\odot\,{\rm yr}^{-1}$ (assuming a clumped wind with a volume filling factor $f = 0.1$). Nitrogen is enhanced in the atmospheres of the components of WR 20a, while carbon is definitely depleted. Finally, the position of the binary components in the Hertzsprung-Russell diagram suggests that they are core hydrogen burning stars in a pre-LBV stage and their current atmospheric chemical composition probably results from rotational mixing that might be enhanced in a close binary compared to a single star of same age.

Key words. stars: binaries: spectroscopic – stars: early-type – stars: fundamental parameters – stars: individual: WR 20a – stars: Wolf-Rayet

1. Introduction

In a recent letter, our team reported the discovery of the binary nature of WR 20a (Rauw et al. 2004, hereafter Paper I). We found that the system consists most probably of two WN6ha stars with almost identical spectra revolving around each other in ∼3.7 days. Our orbital solution indicated very large minimum masses of about 70 $M_\odot$ for each star and we predicted that the binary should display photometric eclipses (Paper I). These results triggered a prompt photometric study of WR 20a by Bonanos et al. (2004) who actually detected the eclipses in their I-band photometry hence confirming, and slightly improving, the orbital period of the system. Combining the value of the orbital inclination of 74.5° ± 2° derived by Bonanos et al. with the radial velocity data from Paper I yields masses of about 80 $M_\odot$ for both stars, thus making WR 20a the most massive binary with well determined masses so far.

In this paper, we present an in-depth study of the spectrum of WR 20a in order to constrain the properties of its Wolf-Rayet (WR) components. Information on the mass-loss rates and the chemical composition of the stellar winds as well as on the stellar temperatures and luminosities are crucial for understanding the evolutionary stage of such an exceptional system. In addition, given the extreme properties of the stars in WR 20a and their small separation, various interactions such as Roche lobe overflow or a wind-wind collision may occur in this system. These interactions imply the motion of high-density material between the stars that can best be traced through a study of the phase-locked variations of the emission lines that are formed through recombination in the high-density material.

This paper is organised as follows. Our observations are presented in Sect. 2, whilst we discuss the features of the green and red spectrum of WR 20a in Sect. 3. Section 4 deals with the analysis of the line profile variability that affects the Hα

⋆ Based on observations collected at the European Southern Observatory, La Silla, Chile.
⋆⋆ Research Associate FNRS, Belgium.
⋆⋆⋆ Research Fellow FNRS, Belgium.

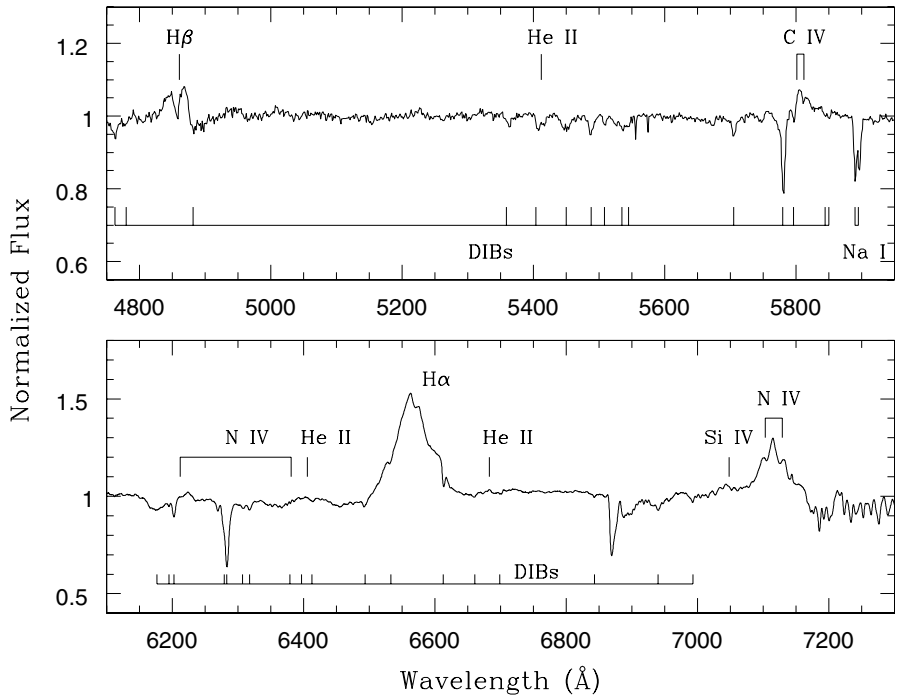

Fig. 1. Green and red spectrum of WR 20a. The top panel corresponds to the spectrum observed at phase 0.895 (HJD 2 453 179.472), whilst the lower panel corresponds to phase 0.798 (HJD 2 453 042.734). In addition to the telluric absorptions, the bulk of the absorption features in these spectral domains are due to diffuse interstellar bands (the identifications are taken from Herbig 1995). The stellar spectrum is dominated by strong emission lines of Hα and several blends due to N IV lines. Note also the absence of He I λ 5879 and the presence of C IV $\lambda\lambda$ 5801, 5812 in emission.

and He II λ 4686 emissions. In Sect. 5, we use a state of the art model atmosphere code to derive the fundamental properties of the stars and their winds. Finally, in Sect. 6, we discuss the implications of our results and we highlight some future perspectives to solve some of the still open questions related to WR 20a.

2. Observations

In addition to the blue and violet spectra presented in Paper I, we analyse here a set of red spectra of WR 20a. Ten medium resolution spectra were obtained in January–February 2004 with the EMMI instrument mounted on ESO's 3.5 m New Technology Telescope (NTT) at La Silla. The EMMI instrument was used in the RILD low dispersion spectroscopic mode with grism # 6 (600 grooves mm^{-1}) providing a wavelength coverage from about 5750 to 8670 Å. The slit width was set to 1 arcsec and the exposure times were 10–15 min yielding a *S/N* ratio of about 200. The spectral resolution as determined from the *FWHM* of the lines of the He-Ar comparison spectra was about 4.0 Å. The data were reduced in the standard way using the *long* context of the MIDAS package.

Another low resolution spectrum was obtained on June 22, 2004 with the same equipment except for the grism, where we used grism #5 instead (600 grooves mm^{-1}), which provides a wavelength coverage from 3800 to 7020 Å and a spectral resolution of 5.0 Å (*FWHM* of the He-Ar lines). The weather conditions during that night were very good and we also obtained an observation of the spectro-photometric standard star LTT 9239 (Stone & Baldwin 1983; Hamuy et al. 1992) that we used to perform a relative flux calibration of the spectrum of WR 20a.

3. The optical spectrum of WR 20a

The blue-violet spectrum of WR 20a is illustrated in Paper I and the reader is referred to that paper for a detailed description. In this section we shall rather focus on the spectral features at wavelengths from 4800 to 7200 Å that provide important clues on the nature of the stars. This part of the spectrum is illustrated in Fig. 1.

First of all, we note the important number of relatively strong diffuse interstellar bands (DIBs) that account actually for most of the absorption features in the green – red spectrum of WR 20a. Although the strength of most DIBs and the $E(B-V)$ colour excess are not systematically correlated, except for a few features (Herbig 1995), the strengths of the DIBs in the spectrum of WR 20a is a clear indication of a rather heavy interstellar absorption. Indeed, we can get a lower limit to the colour excess of WR 20a by comparing the strength of those DIBs that correlate best with $E(B-V)$ (at 5780 and 5797 Å) with their strength in the well studied interstellar spectrum of HD 183143 (B7 I, $E(B-V) = 1.28$, see Herbig 1995): since the DIBs are stronger in the spectrum of WR 20a, we conclude that $E(B-V) \geq 1.3$ at least.

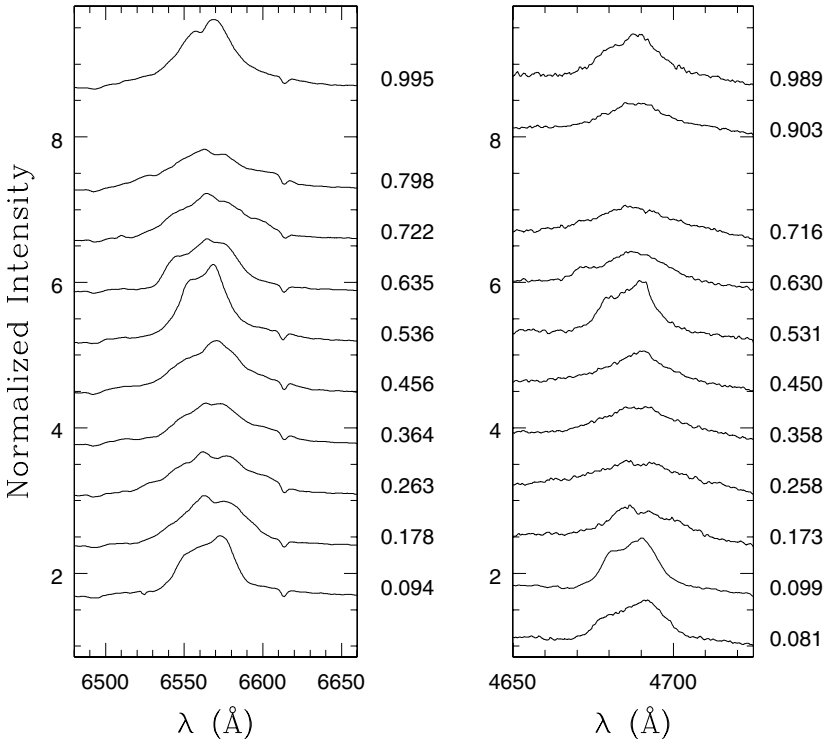

Fig. 2. Line profile variability of the Hα (*left*) and He II λ 4686 (*right*) emission lines in the spectrum of WR 20a. The normalized spectra are vertically shifted by 0.7. The orbital phases of the observations, computed using the ephemeris of Bonanos et al. (2004), are given on the right of each panel. Note the striking similarity between the profiles of the two lines at similar orbital phases.

The most prominent stellar features are emission lines of Hα, Hβ, C IV $\lambda\lambda$ 5801, 5812 and N IV $\lambda\lambda$ 6212–20, 6381, 7103–29. The Hβ line was observed at orbital phase 0.895, i.e. shortly before conjunction, and the double-peaked morphology of the line can therefore not be attributed to the deblending of the lines of the two components. Without a knowledge of the variations of this line, it is difficult to provide a unique interpretation of the double-peaked profile. It could either originate in a wind interaction zone, as is likely to be the case of the two peaks seen in Hα and He II λ 4686 (see Sect. 4), or alternatively it could be intrinsic to the stars. The latter interpretation would be supported by the shape of the line in the spectrum of WR 25, another WN6ha star (see e.g. Crowther et al. 1995) as well as by the synthetic profile simulated with a model atmosphere code (see Sect. 5 and Fig. 6). The presence of Hβ in emission further favours a WN6ha rather than an O3 If*/WN classification for both components of WR 20a.

The C IV $\lambda\lambda$ 5801, 5812 blend has an equivalent width of about 1.0 ± 0.1 Å on our spectrum[1]. The presence of this line in the spectrum of WR 20a along with the weakness of He I λ 5876 was first noted by Shara et al. (1999) who classified WR 20a accordingly as a WN7:h/C star. Finally, we note that the He II λ 5412 line is seen in absorption. This is not surprising since the blue spectra presented in Paper I already indicated that He II λ 4542 is also in absorption.

[1] We note that this value is likely to be a lower limit on the actual line strength because of the contamination of the blend by several DIBs.

4. Line profile variability

As pointed out in Paper I, the He II λ 4686 emission line in the spectrum of WR 20a displays a prominent profile variability that appears definitely phase-locked. This variability is not restricted to this line, but is also seen in Hα. Analysing these modulations should help us to understand the interactions between the two stars.

4.1. The Hα line

The variations of the Hα line are illustrated in Fig. 2. At phases near conjunction ($\phi \simeq 0.0$ and $\phi \simeq 0.5$), the line displays a rather narrow double-peaked profile with the red peak being somewhat stronger. On the other hand, at phases near quadrature the line appears broader with some indication of more than two peaks. This behaviour suggests the existence of one or several emission components possibly arising from an interaction between the components of WR 20a.

We have measured the equivalent width (*EW*) of the Hα line integrated between 6499 and 6646 Å as a function of orbital phase. The results are reported in Table 1. We estimate that the uncertainties affecting our *EW* measurements are of order ∼5%. In Fig. 3, the *EW*s are compared to the *I*-band light curve

Table 1. Journal of our red spectroscopic observations of WR 20a. The first and second columns provide the heliocentric Julian date (in the format HJD−2 450 000) and the orbital phase computed using the ephemeris of Bonanos et al. (2004). Phase $\phi = 0.0$ corresponds to the "primary eclipse" with the slightly less massive star in front. Columns 3 and 4 respectively indicate the grism used for the observation (see text) and the equivalent width of the Hα emission line as integrated between 6499 and 6646 Å (see Sect. 4).

Date	ϕ	Grism	EW(Hα) (Å)
3032.766	0.094	#6	33.6
3033.762	0.364	#6	28.7
3034.760	0.635	#6	31.4
3036.762	0.178	#6	31.4
3037.784	0.456	#6	35.1
3038.765	0.722	#6	31.9
3039.772	0.995	#6	42.2
3040.760	0.263	#6	31.4
3041.747	0.536	#6	40.6
3042.734	0.798	#6	31.0
3179.472	0.895	#5	26.6

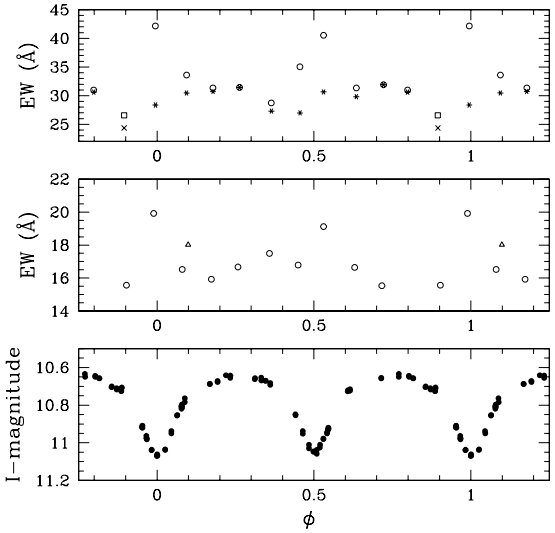

Fig. 3. *Upper panel*: variations of the measured EW of the Hα emission line between 6499 and 6646 Å (open symbols) and of the EWs corrected for the variations of the continuum (asterisks). The open square and the cross correspond respectively to the measured and the corrected EW of the line in the June 2004 spectrum. *Middle panel*: variations of the measured EW of the He II λ4686 line between 4656 and 4723 Å (see text). The triangle refers to the measurement from our 2002 campaign (see text). *Lower panel*: photometric light curve of WR 20a in the I-band as reported by Bonanos et al. (2004).

presented by Bonanos et al. (2004). There is a net increase in the apparent line strength by ∼40% during photometric eclipses. Using the I-band light curve, we have performed a first order correction of the EWs for the variations of the continuum level. The results are also shown in Fig. 3 by the asterisks and the cross. Apart from a slow modulation with a peak to peak amplitude of about 20%, the corrected EW of the Hα line is almost constant. The remaining modulation might be real and could then reflect partial occultations of the line emitting regions by the stellar bodies. In fact, the minima in the corrected EWs occur about 0.05–0.10 in phase before the actual photometric eclipses.

In summary, apart from the small modulation described above, the variations of the EW of the Hα line are consistent with a rather constant line flux superposed on a variable continuum level. This suggests that the bulk of the emission arises from an extended region that is only marginally affected by occultations that occur before the actual photometric eclipses.

To interpret the strong profile variability of the Hα line, we have further applied the Doppler tomography technique described by Rauw et al. (2002) to map the line formation region in velocity space (see also e.g. Thaller et al. 2001, for an example of the application of Doppler tomography to early-type binaries). Our method uses a Fourier filtered back projection algorithm (Horne 1991). The radial velocity of any gas flow that is stationary in the binary's rotating frame of reference can be described by a simple relation:

$$v(\phi) = -v_x \cos(2\pi\phi) + v_y \sin(2\pi\phi) + v_z \quad (1)$$

where ϕ stands for the orbital phase, whilst (v_x, v_y, v_z) are the projected velocity coordinates of the gas flow. The above relation assumes that the x-axis runs between the stars, from the primary to the secondary, whilst the positive y-axis points in the direction of the secondary's orbital motion. The projected v_x and v_y velocities are related to the absolute velocity coordinates through the relation $(v_x, v_y) = (V_x \sin i, V_y \sin i)$. Finally, the z-axis is perpendicular to the orbital plane. The Doppler map consists of a projection of relation (1) on the (v_x, v_y) plane. Therefore, for a given value of v_z, each pixel in a Doppler map, specified by its velocity coordinates is associated with a particular form of Eq. (1) (see e.g. Horne 1991, for a detailed discussion of the method).

To avoid a bias due to the lower resolution of the June 2004 spectrum, we use only the data from the January–February observing run. Our data were weighted so as to account for the uneven sampling of the orbital cycle as well as for the effect of the photometric eclipses. To provide a rough indication of the "point spread function" in velocity space, we have computed the Doppler map of a constant discrete emission feature convolved with the instrumental response and "observed" with the same sampling as the actual data (shown by the insert in Fig. 4).

The v_z parameter can be seen as some sort of – a priori unknown – apparent systemic velocity of the Hα line. In Paper I we found a wide range (from −77 to −18 km s^{-1}) in apparent systemic velocities for different spectral lines. All the lines studied in Paper I (including the Hδ and Hγ Balmer lines) are in absorption apart from the N IV λ4058 emission. In the spectra of WNL stars, the latter line is often considered as the most reliable indicator of the true stellar velocity. Its apparent systemic velocity being −51 km s^{-1}, we have thus adopted $v_z = -50$ km s^{-1} in the Doppler map (Fig. 4) presented here. We have also carried out our analysis for values of v_z in the range −80 to +20 km s^{-1}. While some details of the map change, we find that its general appearance does not depend

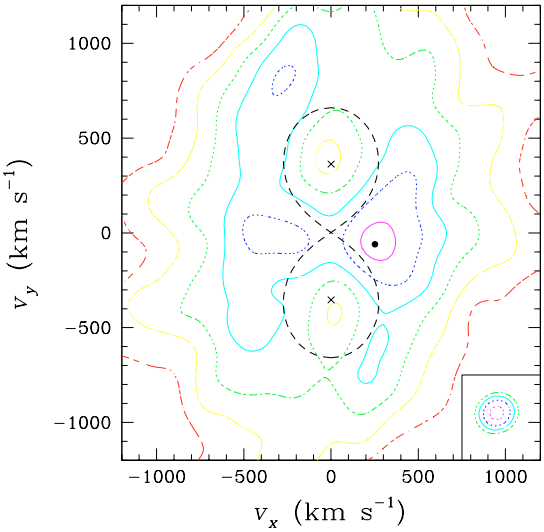

Fig. 4. Doppler map of the Hα emission line in the spectrum of WR 20a. The crosses correspond to the radial velocity amplitudes of the centre of mass of the primary (*bottom*) and secondary (*top*) as derived from our orbital solution in Paper I. The shape of the Roche lobe in velocity-space (thick dashed line) has been calculated for a mass ratio of 0.99. The Doppler map was computed with v_z set to -50 km s^{-1}. The black dot indicates the position of the highest peak and the contours correspond to levels of 0.95, 0.80, 0.65, 0.50, 0.35 and 0.20 times the maximum emissivity. The insert in the lower right corner illustrates the Doppler map of a constant Gaussian with a *FWHM* corresponding to the spectral resolution of our data and observed with the same sampling as the actual data. This figure appears in colour in the electronic version of the journal.

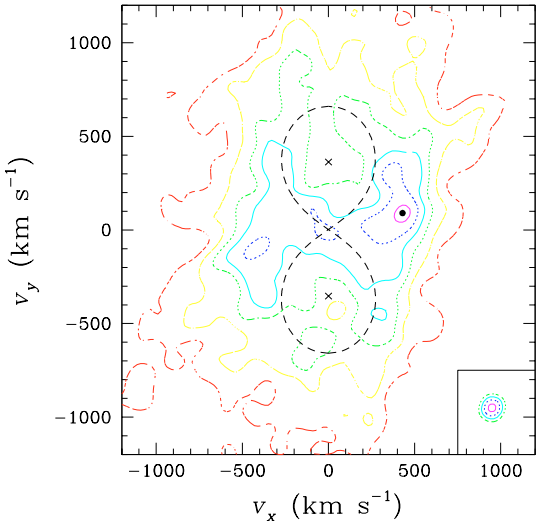

Fig. 5. Same as Fig. 4, but for the He II λ 4686 emission.

on the adopted value of v_z within the range of values explored here.

The Doppler map reveals an extended line formation region in velocity space with a primary maximum around $(250, -60)$. A secondary maximum is found near $(-330, -10)$. Thus the maximum emission arises from plasma that moves with a phase shift of almost exactly $\pi/2$ compared to the orbital motion of the two stars. It should also be stressed that the velocities of the centres of mass of the two stars are actually associated with local minima of the emissivity in the Doppler map.

4.2. The He II λ 4686 line

The analysis of the variations of He II λ 4686 is less secure than for Hα, mainly because of the blends with a broad emission bump on the blue side between 4640 and 4660 Å. However, the He II λ 4686 profile and its variations are extremely similar to those of Hα (see Fig. 2) suggesting that the two lines form in the same physical regions.

The *EW* of the He II λ 4686 line, as measured between 4656 and 4723 Å, changes as a function of orbital phase. The variations are apparently less pronounced than in the case of Hα (Fig. 3), though they are certainly significant compared to the estimated uncertainties on the measurements of ~5–10%. We caution however that the impression of more erratic variations is to a large extent due to the point at phase 0.099 (the triangle in Fig. 3), which comes from our 2002 campaign (see Paper I). Extrapolating the photometric ephemeris back to the epoch of this observation could result in rather large uncertainties on the orbital phase. If we omit this point, the variations of the *EW* are quite reminiscent of those of the Hα line. Note that we have chosen not to correct the observed *EW*s for the modulation of the continuum level since the light curve in the *I*-band filter might not be representative of the actual variations of the continuum in the blue spectral range.

Finally, the Doppler map of this line (Fig. 5) is again quite similar to the one of Hα. To avoid too severe contamination of the Doppler map by the emission bump bluewards of He II λ 4686, we have restricted the velocity interval in the back projection to $[-2000, 2000]$ km s^{-1}. The highest peaks (at about $(425, 90)$ and $(-400, -95)$) are again found at a phase shift of almost $\pi/2$ compared to the orbital motion.

5. Fundamental parameters

Adopting the orbital period of 3.686 days as derived by Bonanos et al. (2004), we have recalculated an orbital solution[2] using our data from Paper I (with the same weights as in Paper I, but reversing the primary/secondary identifications for the data of HJD 2 452 355.6). This new solution yields $K_1 = 362.5 \pm 9.0$ km s^{-1}, $K_2 = 365.6 \pm 9.1$ km s^{-1}, $\gamma_1 = 20.1 \pm 5.8$ km s^{-1}, $\gamma_2 = -5.2 \pm 5.9$ km s^{-1}, $(a_1 + a_2) \sin i = 53.0 \pm 0.7\,R_\odot$, $m_1 \sin^3 i = 74.0 \pm 4.2\,M_\odot$ and $m_2 \sin^3 i = 73.3 \pm 4.2\,M_\odot$[3]. Combining these results with the orbital inclination ($74.5° \pm 2.0°$) inferred by Bonanos et al. yields absolute masses of 82.7 and 81.9 $M_\odot$ for the primary and secondary respectively.

[2] Bonanos et al. already recalculated an orbital solution, adopting a priori a single value for the systemic velocity of both stars. Since the lines measured to evaluate the radial velocities form in moving stellar winds, this could in principle bias the amplitude of the orbital solution.

[3] All error bars in this paper correspond to 1σ uncertainties.

The light curve solution of Bonanos et al. provides also some constraints on the stellar radii. These authors found that the surfaces of the stars are described by a Roche potential of $\Omega = 3.92$, which corresponds to heavily deformed objects with average radii of $\sim 19.7 \pm 0.3\,R_\odot$. Wolf-Rayet stars typically have optically thick stellar winds, such that their stellar radii and corresponding temperatures are generally quoted at Rosseland optical depth of order 10 instead of the usual 2/3. Therefore, since the light curve model of Bonanos et al. does not account for an extended atmosphere, it is not clear a priori whether these observational values refer to the hydrostatic radius or to some specific value of the optical depth. However, in the case of WR 20a, the wind densities of the WN6ha components are only slightly larger than for typical O supergiants, such that their radii at Rosseland optical depths $\tau = 2/3$ and $\tau = 10$ differ by less than $0.1\,R_\odot$.

Bonanos et al. (2004) argue that the *I*-band light curve of WR 20a indicates a slightly deeper primary eclipse and they attribute this to a lower effective temperature (40 300 K) for the secondary compared to the primary (42 000 K). From the spectroscopic point of view, the primary and secondary cannot be distinguished (see Paper I). While it is true that a small difference in effective temperature (or stellar radius) may not necessarily be detectable in the spectrum, we caution that the difference in depth of the eclipses in the light curve of Bonanos et al. could also be due to the scatter of the data around the light curve solution. New photometric observations, especially including additional filters are needed to confirm the difference in eclipse depth and discriminate between a difference in temperature or other model parameters such as the radii. Therefore, in the following, we consider that both stars have identical properties.

To determine the stellar properties of WR 20a we have utilized the non-LTE code of Hillier & Miller (1998) which solves the radiative transfer equation subject to the constraints of statistical and radiative equilibrium, in a spherical, extended atmosphere. Line blanketing is incorporated directly through the use of a super-level approach. We use a similar atomic model to that employed by Walborn et al. (2004) in their study of early-type O stars, including H I, He I–II, C III–IV, N III–V, O III–VI, Ne III–V, Si IV, P V, S IV–VI, Ar III–VI, Fe V–VII and Ni V–VII (see Walborn et al. for further details).

The velocity in the supersonic part of the wind is described by a standard β-law

$$v(r) = v_\infty \left(1 - \frac{R_*}{r}\right)^\beta \qquad (2)$$

with $\beta = 1$. Since no ultraviolet spectra of WR 20a are available, we adopt a representative terminal wind velocity of $v_\infty = 2800\,\mathrm{km\,s^{-1}}$. While this value is larger than for other Galactic WN6ha stars (Crowther & Dessart 1998), we note that lower values of v_∞ would result in a poorer match of the He II λ4686 profile. We further adopted $v_{\rm eq} \sin i = 200\,\mathrm{km\,s^{-1}}$ for the line fits.

For stars such as the WN6ha components in WR 20a, He I lines are weak or absent and we are hence forced to use the nitrogen lines to establish the ionization balance (as in Walborn et al. 2004). There is no obvious indication of an enriched He abundance in the spectrum of WR 20a. On the other hand, it is extremely difficult to determine accurate He/H abundances for extreme stars such as the WN6ha components in WR 20a. Therefore, we have adopted a He/H number abundance ratio of 0.1.

The mass-loss rate ($8.5 \times 10^{-6}\,M_\odot\,\mathrm{yr^{-1}}$) was determined from the strength of the Hα line assuming a clumped wind with a volume filling factor $f = 0.1$. The Hα line forming region in our model peaks at about $1.4\,R_*$, but extends to beyond $10\,R_*$. If the wind volume filling factor in this region were different, the actual $\dot{M}$ would scale roughly as $\sqrt{f}$. For instance, a smooth wind model would require a mass-loss rate of $2.5 \times 10^{-5}\,M_\odot\,\mathrm{yr^{-1}}$ to match the Hα and He II λ4686 lines. Given the extent of the line formation region, it seems likely that the extra emission from the wind interaction zone contributes only a moderate fraction (10 to 20 per cent) of the total Hα emission. Finally, we note that the spectra we have fitted are in principle the least affected by the emission from the wind interaction zone, but were taken at phases affected by the photometric eclipse. Therefore, the equivalent width of the Hα line could be overestimated by $\sim$15%, implying a reduction of $\dot{M}$ of order 10%.

For $T_{\rm eff} = 43\,000 \pm 2000$ K, we find an overall agreement for the nitrogen lines: weak P-Cygni lines in N V, strong emission in N IV and weak emission in N III (see Fig. 6). The nitrogen abundance is found to be 0.5% (by mass), i.e. six times solar. The C IV 5801, 5812 lines can in principle be used to constrain the carbon abundance although these lines are rather sensitive to the extreme UV flux distribution. As stated above, the equivalent width of this blend on our spectra is about 1.0 Å. For an assumed carbon abundance of 0.1 (respectively 0.04) times solar, our model yields an equivalent width of 4.8 Å (respectively 2 Å), too large compared to the observed value. While the lack of other diagnostics prevents us from deriving a more precise abundance, we conclude nevertheless that C is severely depleted in the components of WR 20a. For oxygen, there is no good diagnostic line in the optical and we thus cannot constrain its abundance with our present data set.

The parameters of our best model are given in Table 2. Note that the value of the gravity does not directly follow from the model atmosphere code (which uses a crude treatment of the photospheric structure at depth), but stems from the binary mass determination and the stellar parameters derived from our model. To get a first approximation of $L_{\rm bol}$, we either adopted R_* from the light curve solution of Bonanos et al. (2004) or $M_V = -6.5$ (see also Sect. 6.2). Both assumptions consistently yield $\log L_{\rm bol}/L_\odot \simeq 6.0$. The number of Lyman ionising photons produced by each of the WN6ha stars in WR 20a would be $Q_0 = 7.2 \times 10^{49}\,\mathrm{s^{-1}}$.

Our derived temperature provides a bolometric correction of -3.91 mag. This value is somewhat larger than the mean bolometric correction of -3.70 ± 0.08 derived from the analysis of five WN6ha stars by Crowther & Dessart (1998). The latter value was based on lower temperature unblanketed models and a re-analysis of the WN6ha stars in NGC 3603 and R 136 with contemporary models might therefore lead to bolometric corrections comparable to that of WR 20a.

Table 2. Fundamental parameters of the WN6ha stars of WR 20a and of their stellar winds as determined from our spectral analysis. Note that the luminosity and mass-loss rate are given for a single component. The mass loss rate is based on a clumped wind model with a volume filling factor of $f = 0.1$.

Parameter	Value
Mass ($M_\odot$)	82.7 ± 5.5 (primary)
Mass ($M_\odot$)	81.9 ± 5.5 (secondary)
$L_{\rm bol}$ ($L_\odot$)	$(1.15 \pm 0.15) \times 10^6$
$T_{\rm eff}$ (K)	43 000 ± 2000
$\dot{M}$ ($M_\odot$ yr^{-1})	8.5×10^{-6}
R_* ($R_\odot$)	19.3 ± 0.5
v_∞ (km s^{-1})	2800 (adopted)
$\log g$	3.8
$(B-V)_0$	−0.33
$(V-I)_0$	−0.36
$E(B-V)$	1.94 ± 0.05
$A_{\rm V}$ (mag)	6.02 ± 0.16
d (kpc)	7.9 ± 0.6

6. Discussion and future perspectives

6.1. Wind interactions in WR 20a

6.1.1. The optical emission lines

The Hα Doppler map and the profile variations are reminiscent of those of the O-star binary HD 149404 (Thaller et al. 2001; Rauw et al. 2001) and we can interpret this as a signature of an interaction between the winds of the two stars. In the case of WR 20a, both stars have roughly identical spectral types (see Paper I) and should thus have winds of similar strengths. In such a case, we expect the wind interaction zone to be roughly symmetrical about the centre of mass of the binary system[4].

First of all, we stress that part of the profile variations of Hα and He II λ 4686 is most probably simply due to the loss of spherical symmetry of the winds in this binary system. For instance, it is likely that the properties of the stellar winds along the binary axis between the two stars deviate from those of the winds along other directions. Effects such as "wind focusing" and "radiative inhibition" (Stevens 1988; Stevens & Pollock 1994) are likely to impact on the mass-loss between the stars. Following the formalism of Stevens & Pollock, one would expect that for a binary consisting of two stars of equal mass and equal luminosity, the mass-loss rate per unit solid angle along the binary axis (the so-called stagnation mass-loss rate) might be reduced compared to the corresponding single star mass-loss rate. In fact, in this case, the inhibition effect of the companion's radiation field should dominate over the effect of its gravitational field. However, it must be stressed that the radiative flux from each star reflects off the surface of its companion in radiative equilibrium and as a result of this effect, the actual mass loss might essentially be unchanged by inhibition (Gayley et al. 1999). On the other hand, it is likely that the stagnation wind velocity law differs from that along other directions and the winds should reach only moderate velocities before they collide. Finally, the "radiative braking" mechanism described by Gayley et al. (1997) only occurs in binaries with strongly unequal wind strengths and should thus not play a significant role in the wind interaction region of WR 20a.

In Fig. 7, we provide a very schematic view of the possible wind interaction in WR 20a. In this figure, we have plotted the stars with their shape corresponding to a Roche potential $\Omega = 3.92$ as found in the light curve solution of Bonanos et al. (2004). It is obvious that, due to the proximity of the stars in the binary system and to the radiative inhibition mechanism, the winds do not have the time to accelerate to large velocities before they collide. In the absence of orbital motion, we would expect the wind contact surface to be roughly planar. Given the large orbital velocities and the comparatively low pre-shock wind velocity (both of order 500 km s^{-1}), we expect the wind interaction zone to be heavily skewed by the Coriolis force instead. To first order, we can estimate the deflection angle to be $\psi = \arctan(v_{\rm orb}/v_{\rm wind}) \simeq \pi/4$.

Both the Doppler tomography and the variations of the equivalent widths provide constraints on the possible location of the formation regions of the Hα and He II λ 4686 emission peaks. The fact that the line emitting region might be partially occulted at phases of about 0.05–0.1 before the actual conjunctions (see Sect. 4 above) suggests that the Hα emission peaks arise in plasma that is located in two regions that are shifted by ∼20–35° from the binary axis. Since we do not observe similar occultations at phases 0.05–0.1 after conjunction, the line emitting region must be rather elongated (as illustrated in Fig. 7) such that the strongest occultation occurs at these phases. The (v_x, v_y) coordinates in the Doppler map are then a combination of the orbital motion and the bulk motion (tangential to the shock) of the post-shock plasma. While it is clear that a detailed modelling of the wind interaction in WR 20a is needed to confirm (or reject) our scenario, we tentatively suggest that the wind-wind collision produces a high density zone where the plasma undergoes a very efficient cooling, thus favouring the formation of excess optical emission lines (such as the peaks seen in Hα or He II λ 4686) through recombination. A detailed model of the wind interaction in WR 20a (accounting for the orbital motion and the efficient radiative cooling of the post-shock plasma) should tell us where in the interaction zone the X-ray emission arises and how this impacts on the formation of optical recombination lines. A weakness of our simple model is that it suggests that the material that produces the red-shifted emission peak should be occulted whilst the blue-shifted emission peak should not undergo occultations by the stellar bodies. This seems at odds with the fact that the red peak is usually the strongest one (see Fig. 2). The latter feature clearly calls for sophisticated hydrodynamic simulations including optical line emission diagnostics as well as new observations that should describe the orbital variations of the two peaks with a better phase resolution.

Alternatively, one could also imagine that the Hα and He II λ 4686 line emissions arise in jets impacting on the rear sides of the stars. For instance, Lubow & Shu (1975) have shown that in a RLOF situation, material flowing from the inner Lagrangian point should impact on the rear side of the

[4] Given the lack of information on magnetic fields of early-type stars, we do not consider the impact of magnetic fields on the interaction in WR 20a.

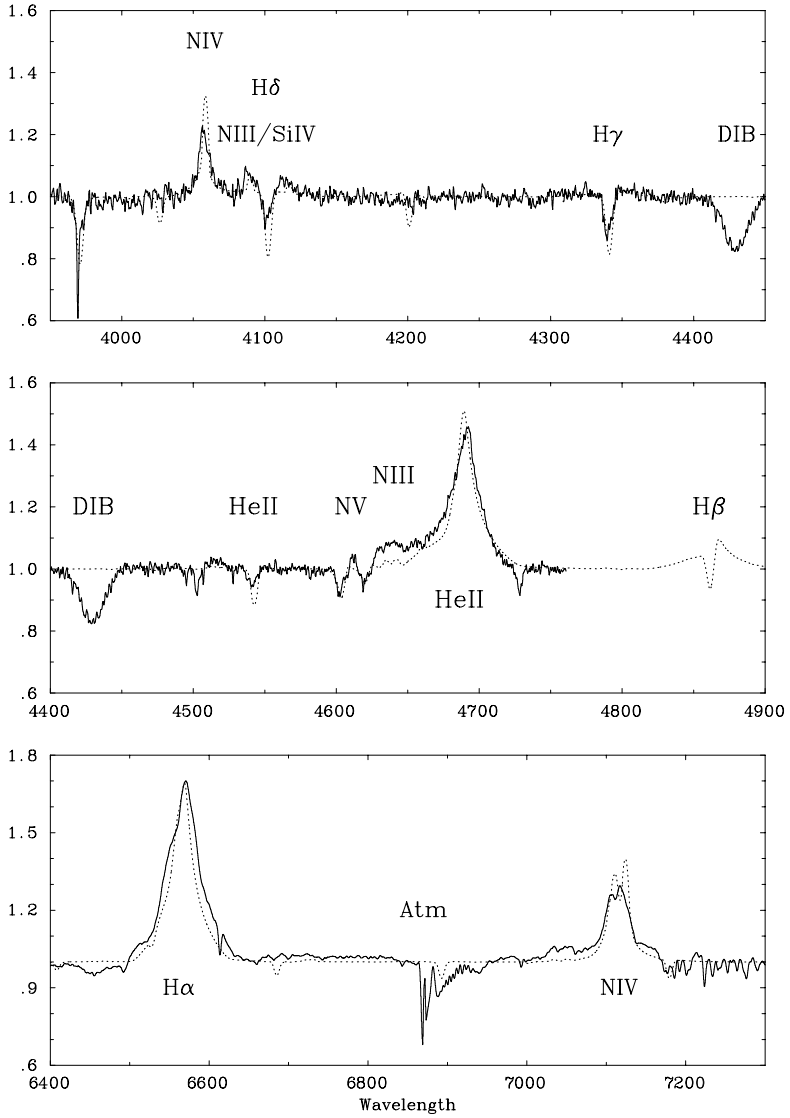

Fig. 6. Comparison between the observed spectrum at phase ~0.46 (solid line) and the predictions from our best atmospheric model (dashed line).

companion star. However, in WR 20a, the light curve solution suggests that both stars are still within their Roche lobe. Moreover, it is not clear how one could explain the existence of two such jets (one moving from the primary to the secondary and the second one in the opposite direction) in such a scenario.

6.1.2. X-ray emission from WR 20a

Wind-wind collisions in early-type binaries are commonly believed to produce an excess X-ray emission (compared to the total intrinsic X-ray emission from the two stars) arising in the hot shocked plasma between the stars (e.g. Stevens et al. 1992).

Little is known so far about the X-ray emission of WR 20a: Pollock et al. (1995) reported a 4σ detection during the *ROSAT* All Sky Survey with a PSPC count rate of $(5.8 \pm 1.4) \times 10^{-2}$ cts s^{-1}, whilst diffuse X-ray emissions from the H II region RCW 49 and from the stars of Westerlund 2 were noted by Mereghetti & Belloni (1995). Apparent diffuse emission from this cluster was previously also reported based on *EINSTEIN*-IPC observations (Goldwurm et al. 1987). Goldwurm et al. attributed this feature either to a wind-blown bubble or a supernova remnant.

We have checked the *ROSAT* archive for pointed observations of WR 20a and we found two HRI and one PSPC data sets. The PSPC observation (rp400329n00) corresponds to the data analysed by Mereghetti & Belloni (1995). Only one of the HRI pointings (rh201611a01) has a sufficient duration (18 ks) to provide useful information. The HRI image (see Fig. 8) indicates that WR 20a is detected with a count rate of $(2.3 \pm 0.5) \times 10^{-3}$ cts s^{-1}. However, this image also reveals a

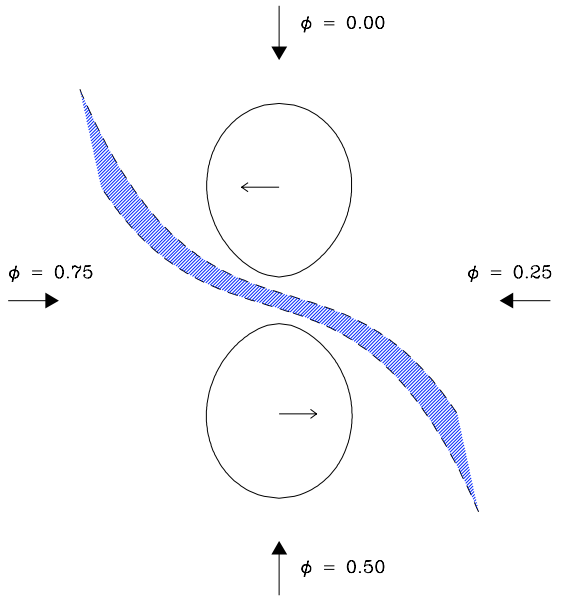

Fig. 7. Schematic view of a possible wind interaction process in WR 20a. The direction of the line of sight is projected on the orbital plane for the phases of quadrature and conjunction. The peaks of the Hα and He II λ 4686 emissions arise in the shaded area, though the full emitting region could extend beyond the limits of our figure.

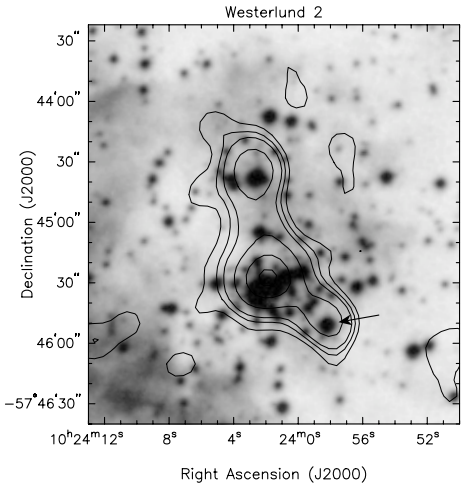

Fig. 8. *ROSAT*-HRI X-ray contours overlaid on a DSS image of the Westerlund 2 cluster. The X-ray emission associated with WR 20a (10h23min58s, −57°45′49″, J2000; indicated by the arrow) is clearly seen. The bright X-ray source to the north of the cluster core appears to be most likely associated with star No. 18 (O7:V) of Moffat et al. (1991).

somewhat brighter source, associated with the core of Westerlund 2, and located at ∼40″ North-East from WR 20a. While the two sources can be almost separated with the HRI, they are not resolved with the PSPC (as becomes also clear from the elongated shape of the PSPC source) and the count rate reported by Pollock et al. (1995) is therefore most likely due to the combined X-ray emission from Westerlund 2 and WR 20a (see also Mereghetti & Belloni 1996).

The X-ray source associated with the cluster core is responsible for most of the apparently diffuse emission discussed by Goldwurm et al. (1987). We note also that star No. 18 of Moffat et al. (1991) is apparently associated with an X-ray source that might be significantly brighter than what would be expected based on the spectral type of this star (O7:V) and on the canonical relation between X-ray and bolometric luminosity (see Berghöfer et al. 1997). This could indicate that star no. 18 is actually a colliding wind binary.

Westerlund 2 was recently observed with the ACIS-I instrument onboard *Chandra*. These observations confirm indeed the existence of a diffuse X-ray emission (Townsley et al. 2004) and allow for the first time the study of many point sources that were previously not resolved. Tsujimoto et al. (2004) report a fit of the ACIS-I X-ray spectrum of WR 20a using an optically thin thermal plasma model with $kT = 2.1$ keV and a neutral hydrogen column density of 2.1×10^{22} cm^{-2}. The latter value is about twice as large as the interstellar neutral hydrogen column density ($N_{\rm H} = 1.1 \times 10^{22}$ cm^{-2}) evaluated from the $E(B-V)$ value determined in Sect. 6.2. This feature is not unusual for Wolf-Rayet stars: extra X-ray absorption is produced by the material in the stellar wind and is observed for instance in the case of the WN6ha star WR 25 (Raassen et al. 2003). Even worse, in the case of the WN8 star WR 40, the wind absorption is probably so large that no X-ray emission is actually escaping (Gosset et al. 2005). The best-fit plasma temperature found by Tsujimoto et al. (2004) is rather high for early-type stars, which could be a signature of the colliding wind interaction. Correcting for the entire hydrogen column density, Tsujimoto et al. infer an unabsorbed flux of $(1.1^{+0.9}_{-0.3}) \times 10^{-12}$ erg cm^{-2} s^{-1} in the 0.9–8 keV energy range. Unfortunately WR 20a fell rather close to a gap of the ACIS-I detector in the *Chandra* observation, which complicates the analysis (Tsujimoto et al. 2004). If instead of correcting for the entire column density we correct only for the absorption of the ISM material, we infer an X-ray flux of 6.3×10^{-13} erg cm^{-2} s^{-1} in the 0.5–8 keV energy range.

Turning back to the *ROSAT* observations, we can use the *Chandra* spectral parameters to convert the HRI count rate into observed and ISM-corrected X-ray fluxes. Doing so, we estimate an ISM corrected X-ray flux of 1.0×10^{-12} erg cm^{-2} s^{-1} in the 0.5–8 keV energy band. This number is about 1.5 times larger than the *Chandra* result, though it is still within the rather large error bars of the latter. This difference might be either attributable to the uncertainties in the flux determinations or to actual variations of the X-ray flux from WR 20a. For a distance of 7.9 kpc, we derive an X-ray luminosity of 7.5×10^{33} erg s^{-1} from the *ROSAT*-HRI result. With a total bolometric luminosity of $2.3 \times 10^6\,L_\odot$ (see Sect. 5), this yields $\log(L_{\rm X}/L_{\rm bol}) = -6.07$.

Comparing these results to the luminosities of presumably single WN stars (Wessolowski 1996), we find that the X-ray luminosity of WR 20a, although not exceptionally large, is clearly among the highest values of the sample. Moffat et al. (2002) reported X-ray luminosities of three WN6ha stars in NGC 3603 as observed with ACIS-I. For NGC 3603 stars A1, B and C, these authors obtain $>10^{34}$, 2–3 $\times 10^{33}$

and $>4 \times 10^{34}$ erg s^{-1} respectively (the lower limits for stars A1 and C are due to pile-up in the *Chandra* data). Although it remains to be established what fraction of their X-ray fluxes arises from colliding wind interactions, we note that the two X-ray brightest Wolf-Rayet objects in NGC 3603 are either confirmed or suspected binary systems (see the discussion in Moffat et al. 2002). Since the wind properties of the components of WR 20a are more typical of extreme Of stars than of classical Wolf-Rayet stars, we compare the observed X-ray luminosity of WR 20a also to the empirical $L_X - L_{bol}$ relation for OB stars derived by Berghöfer et al. (1997). The Berghöfer et al. relation applies to the X-ray luminosity in the 0.1–2.0 keV energy range. Over this energy band, our estimate of the ISM absorption corrected X-ray flux amounts to 2.9×10^{-13} erg cm^{-2} s^{-1} and the corresponding X-ray luminosity is only about 30% larger than the value expected from the Berghöfer et al. $L_X - L_{bol}$ relation. This is well within the intrinsic scatter of the latter relation, thus suggesting that there is only little if any excess emission in the *ROSAT* band. However, only additional X-ray observations with *Chandra* combining spectral information and a high spatial resolution and monitoring the possible variations of the X-ray flux over the full orbital cycle will allow us to check the existence of an excess X-ray emission and of a possible modulation of the X-ray flux.

Finally, we can compare our estimated L_X to the expected X-ray luminosity from a colliding wind binary with equal winds (e.g. Pittard & Stevens 2002, and references therein). Adopting the β velocity law from Sect. 5, we estimate $v \simeq 500$ km s^{-1} at the stagnation point of the wind-wind collision. This implies $L_X^{theor} \simeq 2.2 \times 10^{35}$ erg s^{-1} which is about a factor 30 larger than the observed L_X. Therefore, the actual X-ray luminosity must be much smaller than the theoretical prediction. Again, radiative inhibition (Stevens & Pollock 1994) could play a key role here. This effect could indeed lower the pre-shock velocity substantially, thereby reducing the expected X-ray luminosity of the wind interaction zone.

6.2. The relationship between WR 20a and Westerlund 2

In Paper I we pointed out that, mainly because of the possibility of eclipses, the existing photometric data did not allow us to draw a firm conclusion on the relationship between WR 20a and the open cluster Westerlund 2. With the new information available on WR 20a, we can now readdress this issue.

6.2.1. The reddening towards WR 20a

Moffat et al. (1991) gathered *UBV* CCD photometry of Westerlund 2, thereby discovering the high differential reddening towards this cluster. Following their Fig. 12, WR 20a is apparently located in a region of high extinction ($E(B-V) \geq 1.80$).

Unfortunately, most photometric data of WR 20a quoted in the literature are of little use to constrain the distance and reddening of this system. As a matter of fact, in most cases, the orbital phase at which the observations were obtained is unknown and the data could thus be affected by the eclipses. Even worse, some of these observations were apparently obtained on different nights (i.e. at different phases). The latter limitation does not hold, however, for the study of Bonanos et al. (2004) and for the most recent photometric study of Westerlund 2 by Carraro & Munari (2004). Bonanos et al. measured $V = 13.45$ and $V - I = 2.80$ during maximum light. From the analysis of the WR 20a spectrum in Sect. 5, we find $(V-I)_0 = -0.36$, which is close to the intrinsic $V-I$ colour index of O supergiants (-0.39 to -0.41, see Clark et al. 2004). With $E(V-I) = 3.16$ and using the reddening law of Savage & Mathis (1979), we estimate $E(B-V) = 1.98$ and $A_V = 6.12$ mag.

Carraro & Munari (2004) obtained their *UBVRI* photometry of Westerlund 2 during a single night in June 1992. They found that the $E(B-V)$ colour excess varies between 1.5 and 2.1 across the field of view of the cluster. According to the complete photometric data provided by Carraro (2004), WR 20a had $V = 13.28 \pm 0.05$, $B - V = 1.63 \pm 0.04$, $U - B = 0.29 \pm 0.04$ and $V - I = 2.52 \pm 0.04$. Quite surprisingly, the V magnitude of Carraro & Munari is slightly brighter ($\Delta V = 0.17$) than the magnitude at maximum light determined by Bonanos et al. (2004). Also, the $V - I$ index determined by Carraro & Munari is significantly lower than the colour quoted by Bonanos et al. Therefore, if we adopt $V - I = 2.52$, we find $E(B-V) = 1.80$ with the above technique. Alternatively, from our non-LTE analysis in Sect. 5 we have found that $(B-V)_0 = -0.33$ and the $B - V$ colour of Carraro & Munari then results in $E(B-V) = 1.96 \pm 0.04$ and $A_V = (6.08 \pm 0.14)$ mag.

A completely independent estimate of the reddening can be obtained from our flux-calibrated spectrum of WR 20a. In fact, Morris et al. (1993) showed that the intrinsic continuum energy distribution of Wolf-Rayet stars in the 1500 Å–1 μm range can be approximated by a power law relation $F_\lambda^0 \sim \lambda^{-\alpha}$ with $\alpha = 2.87 \pm 0.38$ for Galactic WNL stars. We have dereddened our flux-calibrated spectrum of WR 20a using the interstellar reddening law of Savage & Mathis (1979) for different values of $E(B-V)$ with a step of 0.02 in $E(B-V)$. We have then fitted the continuum between 4100 and 6800 Å of this dereddened energy distribution with a power law. In this way, we find that the slope is in agreement with the results of Morris et al. (1993) for $E(B-V) = 1.89 \pm 0.11$. The latter value of the colour excess is in very good agreement with the value inferred from the photometric data. Morris et al. (1993) also provide a tight relation between the $(b-v)_0$ colour index[5] and α which indicates that the slope for a WN6ha star could be as steep as $\alpha = 3.33$. Such a large α would shift the best fit $E(B-V)$ value towards the upper end of the confidence range.

In summary, the three reddening estimates that are in closest agreement with each other yield $E(B-V) = 1.94 \pm 0.05$ and $A_V = (6.02 \pm 0.16)$ mag.

[5] The $(b-v)_0$ index refers to the Smith (1968) *ubvr* photometric system. This system was designed for Wolf-Rayet stars and is based on a set of essentially emission line-free narrow band filters. The intrinsic $(b-v)_0$ colour index of five WN6ha stars studied by Crowther & Dessart (1998) amounts to -0.29 ± 0.02.

6.2.2. The distance

Let us first consider the distance of Westerlund 2. Several (somewhat) conflicting determinations of the cluster distance exist in the literature. Moffat et al. (1991) derived a distance of $7.9^{+1.2}_{-1.0}$ kpc for this cluster. Piatti et al. (1998) obtained integrated spectroscopy of Westerlund 2 and arrived at a distance of 5.7 ± 0.3 kpc and an age of 2–3 Myr. Most recently, Carraro & Munari (2004) analysed *UBVRI* photometry of the cluster. Comparing their colour-magnitude diagrams to isochrones from the Padova group, they inferred a distance of 6.4 ± 0.4 kpc and an age ≤ 2 Myr. We note also that distances between 2.3 and 5.8 kpc have been inferred for the RCW 49 H II region either based on ionization or kinematic arguments (see the discussion by Churchwell et al. 2004).

We can now compare this to the distance of WR 20a. In the following we shall use the photometric data of Carraro & Munari (2004) assuming that they represent the colours and magnitudes of WR 20a at maximum light. From our model atmosphere in Sect. 5, we derive a bolometric magnitude of −10.40 for each component and a bolometric correction of −3.91. The absolute M_V magnitude of each component of WR 20a would thus be −6.49 ± 0.08, in reasonable agreement with a mean $M_v = -6.5$ for WN6ha stars (van der Hucht 2001, Table 27)[6]. With $A_V = 6.02 \pm 0.16$ derived hereabove and $V = 13.28 \pm 0.05$, we arrive at a distance modulus $DM = 14.50 \pm 0.17$ ($d = (7.9 \pm 0.6)$ kpc) for the WR 20a system. While this result is in excellent agreement with the cluster distance as determined by Moffat et al. (1991), our distance of WR 20a is significantly larger than the cluster distance of Carraro & Munari (2004). We caution that the result of Carraro & Munari could be somewhat biased towards shorter distances if a significant fraction of the brightest stars in Westerlund 2 were binary systems.

In conclusion, we find that our distance determination of WR 20a is in reasonable agreement with (some) other distance estimates of the cluster, supporting the idea that the binary is a probable member of the cluster.

6.2.3. WR 20a as a member of Westerlund 2

An important issue is the formation of a very massive system like WR 20a in a cluster like Westerlund 2. Though the formation of massive stars still remains an essentially unsolved problem, many observations support the idea that most (if not all) massive stars form in clusters. In very young open clusters such as NGC 6231 and IC 1805, the most massive stars appear to be concentrated in the cluster core. The observed mass segregation in these very young objects is probably not the result of the dynamical evolution of the clusters but seems rather related to the formation process of their most massive members (Raboud & Mermilliod 1998). A possible explanation for this situation involves a massive star formation scenario that combines competitive gas accretion and stellar collisions in the very dense core of the cluster (Bonnell et al. 1998; Portegies Zwart et al. 1999; Bonnell & Bate 2002). The massive stars formed in this way are expected to be often found in a close binary system. At first sight, this scenario could apply to WR 20a. However, WR 20a is actually located slightly outside the core of Westerlund 2. According to the study of Moffat et al. (1991), the core of the Westerlund 2 cluster consists of a rather compact group containing at least five O6-7:V stars within a radius of 15 arcsec. WR 20a appears to be rather isolated, lying at about 30 arcsec from the centre of the cluster. At a distance of 7.9 kpc, this corresponds to a projected distance of ∼1.1 pc. In this context, we note that the Two Micron All Sky Survey point source catalogue (2MASS, Skrutskie et al. 1997) does not reveal any concentration of sources around WR 20a that could hint towards a heavily obscured group of (proto-) stars.

The position of WR 20a within Westerlund 2 could in principle be explained by the fact that turbulence in a molecular cloud can lead to several sites of massive star formation (Bonnell et al. 2004). Nevertheless, it is surprising that the most massive pair known in Westerlund 2 is not found in the cluster centre and that the cluster core apparently does not contain stars earlier than – and hence more massive than – spectral type O6. Clearly, our knowledge of the stellar population of Westerlund 2 is still too fragmentary. Future studies of this cluster should aim at a determination of the spectral types of the stars in the core as well as of their multiplicity. Also, it would be important to look for a possible population of low-mass pre-main sequence stars that could provide further insight into the star formation history of this cluster.

An alternative possibility would be that WR 20a actually formed in the cluster core, but got ejected through dynamical interactions (Bonnell 2004). In fact, *N*-body simulations of typical young clusters indicate that they can produce dynamically ejected runaways as a result of encounters involving hard binaries (i.e. binaries with binding energies that exceed the cluster binding energy by a significant factor, Leonard & Duncan 1990). Depending on the details of the collision, the outcome of such an event can be either two binaries, a single star and a hierarchical triple system, two single stars and a binary, or four single stars. Among the dynamically ejected stars (or binaries), those with the lowest mass reach the highest velocities. In the first and third case, the surviving massive hard binary system(s) will normally only get a moderate velocity kick.

WR 20a could actually have formed in the centre of Westerlund 2 and might have ejected some lower mass stars. As a result of these interactions, WR 20a might have received a small recoil velocity that kicked it out of the cluster core. Considering an age of ∼1.5 Myr for WR 20a (see Sect. 6.3) and a projected distance from the cluster core of 1.1 pc (see above), a strict lower limit on the average velocity required for WR 20a to reach its present position would be 0.5–1.0 km s^{-1}. Such a rather low value (of the same order as the rms velocity in a typical young open cluster) would most probably not be sufficient to make the binary leave the cluster. Nevertheless, the initial "ejection" velocity could have been significantly larger and a detailed model of the cluster's gravitational potential should allow to estimate the binary's present-day velocity. However, since we are lacking many ingredients (the total

[6] The latter result refers again to the Smith (1968) *ubvr* photometric system. We have corrected the absolute magnitude given in Table 27 of van der Hucht (2001) for the revised distance of NGC 3603 by Sagar et al. (2001) compared to Crowther & Dessart (1998).

mass of the stars in the cluster, the total amount of gas in the cluster core, the exact 3D location of WR 20a with respect to Westerlund 2,...) building such a model is beyond the scope of the present paper. In any case, we note that systemic velocities of the order of (or even a factor of a few larger than) a typical cluster rms velocity are well below the detection threshold (especially for a WR binary for which it is almost impossible to establish the true systemic velocity). The less massive stars that got ejected through dynamical interactions with WR 20a would have travelled at significantly larger velocities (average velocities of ≥10–100 km s^{-1}) and would probably be many parsecs away from the cluster centre by now.

Finally, it should be stressed that the radio emission of the RCW 49 H II region reveals two wind-blown bubbles, one around WR 20b (WN7; Shara et al. 1991) and the other (blister-like structure) around the Westerlund 2 cluster (Whiteoak & Uchida 1997). Whiteoak & Uchida suggested that the mechanical luminosity of the WR 20a wind exceeds the combined mechanical luminosity of the other stars in Westerlund 2 by a factor of about three. The dynamics of the latter bubble would therefore be largely dictated by WR 20a. However, Whiteoak & Uchida (1997) estimated that the Lyman continuum flux provided by the known early-type stars in Westerlund 2 could only account for the observed radio flux of RCW 49, if the distance of RCW 49 were of order 2.3 kpc, i.e. much smaller than other estimates of the distance towards Westerlund 2 (see Sect. 6.2.2).

Whiteoak & Uchida evaluated the ionising flux required to explain the entire radio flux density of RCW 49 (210 Jy at 0.843 GHz). If instead we consider only the shell around Westerlund 2, the radio flux density at 0.843 GHz amounts to 110 Jy. Using the formalism of Martín-Hernández et al. (2003) and adopting an electron temperature of 7300 K (Whiteoak & Uchida 1997) and d = 7.9 kpc, we infer a Lyman continuum photon flux of $\sim 3.0 \times 10^{50}$ s^{-1}. Moffat et al. (1991) classified the spectra of two O6:V and five O7:V stars in Westerlund 2 and from their photometry, we estimate that the cluster contains at least two more O7 V stars. According to the model grids of Smith et al. (2002), we find that these objects together provide an ionising photon flux of about 9.5×10^{49} s^{-1}. For the two WN6ha stars in WR 20a, we evaluate a total ionising flux of 1.45×10^{50} s^{-1}. Adding up these numbers, and taking into account the likely presence of a population of somewhat later O-type stars as well as a correction for an unknown fraction of binaries, we see that the early-type stars of Westerlund 2 could probably at least account for the ionisation of this shell. Once again, we emphasize the need for a detailed investigation of the stellar content of Westerlund 2 to address this issue.

6.3. The evolutionary status of WR 20a

Since WR 20a is a close binary system with a rather short period (3.686 days), one could expect a priori that Roche lobe overflow (RLOF) might have played a role in its evolution. For the most massive stars ($M \geq 50\,M_\odot$) in close binaries however, it is likely that they evolve through a Luminous Blue Variable (LBV) phase (Vanbeveren 1991; Langer 1995) associated with a stellar wind mass-loss large enough to avoid mass transfer. As a result of this strong mass-loss, the binary period increases and at the end of the LBV phase, the binary should have a period longer than ~10 days. The LBV phase would correspond to the hydrogen shell burning phase and the post-LBV star should thus be a core helium burning WN star with an atmospheric hydrogen abundance of $X_{\rm atm} \sim 0.2$–0.3 (Vanbeveren 1991).

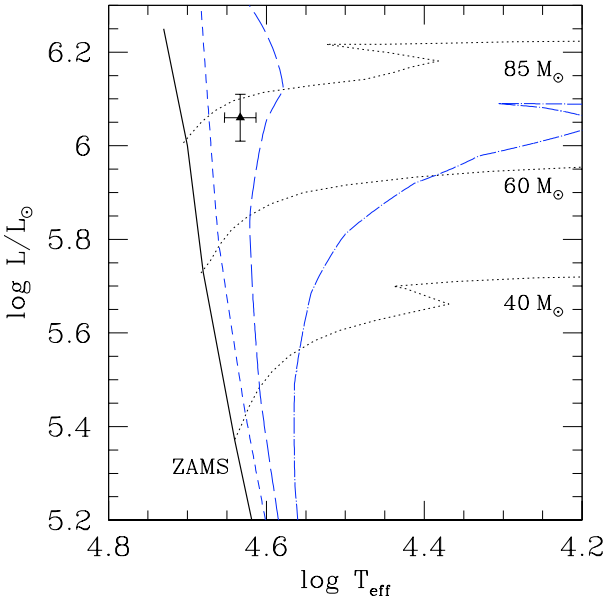

Fig. 9. Position of the components of WR 20a in the Hertzsprung-Russell diagram. The evolutionary tracks for single stars of initial mass 40, 60 and 85 $M_\odot$ as well as the isochrones corresponding to ages of 1, 2 and 3 Myr are from Schaller et al. (1992) for metallicity $Z = Z_\odot$.

In the context of this scenario, it seems more likely that the WN6ha stars in WR 20a are in a pre-LBV rather than post-LBV evolutionary stage. In fact, no LBV ejected nebula around WR 20a has been reported in the literature, the current orbital period of the system is too short for a post-LBV system (see above) and the atmospheric hydrogen fraction is significantly larger than the value expected at the end of an LBV phase. Therefore, the WN6ha stars in WR 20a are likely to be core hydrogen burning stars and their evolution to date should have been similar to that of single stars of equal mass.

The location of the WN6ha components of WR 20a in the Hertzsprung-Russell diagram is illustrated in Fig. 9 along with the single star, solar metallicity and standard mass-loss rate, evolutionary models of Schaller et al. (1992). These evolutionary tracks account for the effect of mass-loss but do not include rotational mixing or magnetic fields.

Assuming that the components of WR 20a are currently evolving redwards in the HRD, we find that they lie between the 60 and 85 $M_\odot$ initial mass evolutionary tracks. The stars appear to have evolved off the zero age main sequence and are actually between the 1 and 2 Myr isochrones in the Schaller et al. models. The agreement between the age as determined from the single star isochrones and the age estimates for the

Westerlund 2 cluster (Carraro & Munari 2004; Piatti et al. 1998) is surprisingly good. A crude interpolation between the various models of Schaller et al. (1992) yields an evolutionary mass of $(76.6 \pm 4.0)\,M_\odot$, which is slightly lower than the observationally determined masses. A major difference concerns the chemical composition of the stars. Whilst the single star tracks of Schaller et al. do not predict any peculiar surface abundances for a star of this mass and age, the spectrum of WR 20a clearly reveals enhanced nitrogen and depleted carbon abundances. Could this be a result of rapid rotation ($v_{\rm eq} \geq 300\,{\rm km\,s^{-1}}$) leading to an efficient rotational mixing (Meynet & Maeder 2000)? Assuming synchronous rotation in WR 20a, we estimate $v_{\rm eq} \sim 265\,{\rm km\,s^{-1}}$ from the current orbital period and adopting a mean radius of $19.3\,R_\odot$. Such a rotation velocity is probably sufficient to produce an efficient mixing that might contribute to the chemical enrichment of the stellar atmosphere.

Alternatively, the temperature and luminosity of the components of WR 20a could also be consistent with those of a single star evolving back towards the blue. However there are several reasons why this cannot be the case for WR 20a. In fact, in this case, the stars would fall almost exactly on the blue-wards loop of a star with initial mass $60\,M_\odot$, but the current evolutionary mass of a star on this track would only be $\sim 30\,M_\odot$, much less than observed, and the atmospheric hydrogen abundance predicted by this model would be $X_{\rm atm} \leq 0.2$, significantly lower than what we find for WR 20a. Moreover, if the stars were currently evolving blue-wards, they should have reached large radii sometimes during their red-wards excursion and as a result they would have gone through a RLOF phase.

Finally, we note that if the initial orbital period is short enough, very massive stars in binary systems could evolve through a case-A RLOF (i.e. mass exchange would occur while the primary would still be in the core hydrogen burning phase). In the case of WR 20a, this is unlikely to be the case since the properties of the mass gainer and the mass loser should be quite different in a post case-A RLOF system, whereas the components of WR 20a have (almost) identical properties.

In summary, the current evolutionary status of the WN6ha stars in WR 20a would be most readily explained if the stars were core hydrogen burning objects in a pre-LBV phase (Vanbeveren 1991). The observed atmospheric chemical composition is likely a result of an efficient rotational mixing due to the large rotational velocities. While WR 20a has most probably not been affected by Roche lobe overflow, we emphasize that there is however one major difference between the evolution of the components of WR 20a and that of a single star of equal mass. In fact, whereas the rotational velocity of a very massive single star is expected to decrease rapidly as a result of the removal of angular momentum by the stellar wind (Meynet & Maeder 2000), the situation in a (synchronised) close binary is probably somewhat different since the evolution of the stellar rotation velocity is also coupled to that of the angular momentum of the orbital motion. Tassoul (1987; see also Tassoul & Tassoul 1990) investigated the effect of tidally induced meridional circulation that tends to synchronise the rotational and orbital motions. Using Eq. (10) of Tassoul (1987), we estimate a spin-down (or spin-up) time scale of about 40 yrs for the components of WR 20a. Even if the actual synchronisation time were an order of magnitude larger than this spin-down time, it would still be sufficiently short so that it seems plausible that both stars could achieve a high degree of synchronism. Therefore, we could expect that the rotational velocity might remain quite large over a longer time scale and the rotational mixing might thus be even more efficient than in the case of a single star.

7. Summary and concluding remarks

We have analysed the optical spectrum of the very massive binary WR 20a. We find that the Hα and He II λ 4686 emission lines have very similar profiles and display strong phase-locked variations suggesting that part of the line emission probably arises in a wind interaction region between the stars.

Combining photometric and spectroscopic measurements, we derive a reddening of $A_{\rm V} \simeq 6.0$ and a distance of ~7.9 kpc. While the latter result is in reasonable agreement with the distance estimates of the Westerlund 2 cluster, it is significantly larger than most distance estimates for the H II region RCW 49. In order to solve this issue, a detailed census of the stellar population (spectral types and multiplicity) of Westerlund 2 is urgently needed. Such a study should not only help explain the ionisation of RCW 49, but should also provide clues on the formation of a very massive binary such as WR 20a and on its relation to Westerlund 2.

WR 20a is clearly detected in the X-rays, although the exact X-ray luminosity and its variability will only be determined by future X-ray observations, combining high sensitivity and a sufficient angular resolution to resolve WR 20a from the emission of Westerlund 2 and covering a large part of the orbital cycle.

We have used a model atmosphere code to derive some fundamental parameters of the WN6ha components in WR 20a. While we find that nitrogen is clearly enhanced and carbon is depleted in the atmospheres of these stars, little can be said about other elements with the present data set. More constraints on the chemical composition might come from future high-resolution high-quality optical spectra as well as UV observations.

Acknowledgements. It is a pleasure to thank Dr. D. Vanbeveren for discussion on massive close binary evolution, Dr. I. A. Bonnell for comments on dynamical interactions in open clusters, Dr. G. Carraro for providing us with his calibrated photometry of Westerlund 2 as well as Drs. L. K. Townsley and M. Tsujimoto for sharing their *Chandra* results with us prior to publication. We are also grateful to Dr. A. Moffat for discussion and to the referee Dr. K. Gayley for valuable comments that helped to improve our manuscript. The Liège team is greatly indebted to the Fonds National de la Recherche Scientifique (Belgium) for multiple assistance. This research is also supported in part by contract P5/36 "Pôle d'Attraction Interuniversitaire" (Belgian Federal Science Policy Office) and through the PRODEX XMM-OM and INTEGRAL projects. The SIMBAD database has been consulted for the bibliography.

References

Berghöfer, T. W., Schmitt, J. H. M. M., Danner, R., & Cassinelli, J. P. 1997, A&A, 322, 167

Bonanos, A. Z., Stanek, K. Z., Udalski, A., et al. 2004, ApJ, 611, L33

Bonnell, I. A. 2004, private communication

Bonnell, I. A., & Bate, M. R. 2002, MNRAS, 336, 659

Bonnell, I. A., Bate, M. R., & Zinnecker, H. 1998, MNRAS, 298, 93

Bonnell, I. A., Vine, S. G., & Bate, M. R. 2004, MNRAS, 349, 735

Carraro, G. 2004, private communication

Carraro, G., & Munari, U. 2004, MNRAS, 347, 625

Churchwell, E., Whitney, B. A., Babler, B. L., et al. 2004, ApJS, 154, 322

Clark, J. S., et al. 2004, in preparation

Crowther, P. A., Hillier, D. J., & Smith, L. J. 1995, A&A, 293, 403

Crowther, P. A., & Dessart, L. 1998, MNRAS, 296, 622

Gayley, K. G., Owocki, S. P., & Cranmer, S. R. 1997, ApJ, 475, 786

Gayley, K. G., Owocki, S. P., & Cranmer, S. R. 1999, ApJ, 513, 442

Goldwurm, A., Caraveo, P. A., & Bignami, G. F. 1987, ApJ, 322, 349

Gosset, E., Nazé, Y., Claeskens, J.-F., et al. 2005, A&A, 429, 685

Hamuy, M., Walker, A. R., Suntzeff, N. B., et al. 1992, PASP, 104, 533

Herbig, G. 1995, ARA&A, 33, 19

Hillier, D. J., & Miller, D. L. 1998, ApJ, 496, 407

Horne, K. 1991, in Fundamental Properties of Cataclysmic Variable Stars: 12th North American Workshop on Cataclysmic Variables and Low Mass X-ray Binaries (SDSU Press), ed. A. W. Shafter, 23

Langer, N. 1995, in Wolf-Rayet Stars: Binaries, Colliding Winds, Evolution, ed. K. A. van der Hucht, & P. M. Williams, Proc. IAU Symp., 163, 15

Leonard, P. J. T., & Duncan, M. J. 1990, AJ, 99, 608

Lubow, S. H., & Shu, F. H. 1975, ApJ, 198, 383

Martín-Hernández, N. L., van der Hulst, J. M., & Tielens, A. G. G. M. 2003, A&A, 407, 957

Mereghetti, S., & Belloni, T. 1995, in Wolf-Rayet Stars: Binaries, Colliding Winds, Evolution, ed. K. A. van der Hucht, & P. M. Williams, Proc. IAU Symp., 163, 76

Mereghetti, S., & Belloni, T. 1996, in Röntgenstrahlung from the Universe, ed. H. U. Zimmermann, J. Trümper, & H. Yorke, MPE Rep., 263, 53

Meynet, G., & Maeder, A. 2000, A&A, 361, 101

Moffat, A. F. J., Shara, M. M., & Potter, M. 1991, AJ, 102, 642

Moffat, A. F. J., Corcoran, M. F., Stevens, I. R., et al. 2002, ApJ, 573, 191

Morris, P. W., Brownsberger, K. R., Conti, P. S., Massey, P., & Vacca, W. D. 1993, ApJ, 412, 324

Piatti, A. E., Bica, E., & Clariá, J. J. 1998, A&AS, 127, 423

Pittard, J. M., & Stevens, I. R. 2002, A&A, 388, L20

Pollock, A. M. T., Haberl, F., & Corcoran, M. F. 1995, in Wolf-Rayet Stars: Binaries, Colliding Winds, Evolution, ed. K. A. van der Hucht, & P. M. Williams, Proc. IAU Symp., 163, 512

Portegies Zwart, S. F., Makino, J., McMillan, S. L. W., & Hut, P. 1999, A&A, 348, 117

Raassen, A. J. J., van der Hucht, K. A., Mewe, R., et al. 2003, A&A, 402, 653

Raboud, D., & Mermilliod, J.-C. 1998, A&A, 333, 897

Rauw, G., Nazé, Y., Carrier, F., et al. 2001, A&A, 368, 212

Rauw, G., Crowther, P. A., Eenens, P. R. J., Manfroid, J., & Vreux, J.-M. 2002, A&A, 392, 563

Rauw, G., De Becker, M., Nazé, Y., et al. 2004, A&A, 420, L9

Sagar, R., Munari, U., & de Boer, K. S. 2001, MNRAS, 327, 23

Savage, B. D., & Mathis, J. S. 1979, ARA&A, 17, 73

Schaller, G., Schaerer, D., Meynet, G., & Maeder, A. 1992, A&AS, 96, 269

Shara, M. M., Moffat, A. F. J., Smith, L. F., & Potter, M. 1991, AJ, 102, 716

Shara, M. M., Moffat, A. F. J., Smith, L. F., et al. 1999, AJ, 118, 390

Skrutskie, M. F., Schneider, S. E., Stiening, R., et al. 1997, in The Impact of Large Scale Near-IR Sky Surveys, ed. F. Garzon et al. (Dordrecht: Kluwer Acad. Pub.), 25

Smith, L. F. 1968, MNRAS, 140, 409

Smith, L. J., Norris, R. P. F., & Crowther, P. A. 2002, MNRAS, 337, 1309

Stevens, I. R. 1988, MNRAS, 235, 523

Stevens, I. R., & Pollock, A. M. T. 1994, MNRAS, 269, 226

Stevens, I. R., Blondin, J. M., & Pollock, A. M. T. 1992, ApJ, 386, 265

Stone, R. P. S., & Baldwin, J. A. 1983, MNRAS, 204, 347

Tassoul, J.-L. 1987, ApJ, 322, 856

Tassoul, J.-L., & Tassoul, M. 1990, ApJ, 359, 155

Thaller, M. L., Gies, D. R., Fullerton, A. W., Kaper, L., & Wiemker, R. 2001, ApJ, 554, 1070

Townsley, L. K., Feigelson, E. D., Montmerle, T., et al. 2004, in X-ray and Radio Connections [arXiv:astro-ph/0406349]

Tsujimoto, M., Townsley, L. K., Feigelson, E. D., et al. 2004, ApJ, submitted

Vanbeveren, D. 1991, A&A, 252, 159

van der Hucht, K. A. 2001, New Astron. Rev., 45, 135

Walborn, N. R., Morrell, N. I., Howarth, I. D., et al. 2004, ApJ, 608, 1028

Wessolowski, U. 1996, in Röntgenstrahlung from the Universe, ed. H. U. Zimmermann, J. Trümper, & H. Yorke, MPE Rep., 263, 75

Whiteoak, J. B. Z., & Uchida, K. I. 1997, A&A, 317, 563

1.5.2 WR 20a in the context of very massive stars

The results of our first paper on WR 20a (Rauw et al. 2004b, see previous subsection) combined with the analysis of the light curve presented by Bonanos et al. (2004) indicate that both components of WR 20a are hydrogen rich WN6ha stars and both are more massive than the minimum mass required for an O star to enter the WR phase during core hydrogen burning, $M_{\rm OWR}$ (Meynet 2004, see also above). Considering the definition of $M_{\rm OWR}$, it seems reasonable to consider that the stars in WR 20a actually evolved into the WN6ha phase while they were still on the main-sequence.
We may therefore wonder how the properties of WR 20a fit into the mass-luminosity relation of massive stars. Using results from Gies (2003), Hilditch et al. (1996) and Massey et al. (2002), Crowther (2004) derived an empirical mass-luminosity relation for massive stars. In the range 10 – 30 $M_\odot$, he found that $L \propto M^{2.5}$, whilst for masses above 30 $M_\odot$ (actually limited to 57 $M_\odot$), he derived $L \propto M^{1.75}$. However, we should first ask ourselves, whether it is reasonable to combine data from binary systems in different galaxies (having different metallicities), as done by Crowther (2004) to infer an empirical relation. To answer this question, I have plotted the theoretical mass-luminosity relation for stars with masses in the range 10 – 120 $M_\odot$ and for three different metallicities (Z = 0.020, 0.008 and 0.001) as predicted by the Geneva non-rotating single star models (Schaller et al. 1992, Schaerer et al. 1993). This relation depends of course upon the evolutionary status of the star and I have therefore considered two extreme situations: first the properties of the star on the zero-age main-sequence (ZAMS) and second the situation at the time of hydrogen exhaustion in the core (corresponding to the end of the MS lifetime, terminal-age main-sequence TAMS). The results are presented in Fig. 1.20. This figure clearly shows that there are almost no significant differences between the ZAMS relations for the three metallicities, whilst the differences are somewhat larger for the TAMS with the highest metallicity models indicating the largest luminosities[5]. Generally speaking, the differences are rather small indicating that from a theoretical point of view, one does not expect any strong metallicity dependence of the mass-luminosity relation on the MS.
I have therefore combined data from several compilations of O-star parameters of *detached eclipsing main-sequence* massive binary systems irrespective of whether these stars belong to the Milky Way, the Large Magellanic Cloud or the Small Magellanic Cloud. For our Galaxy, I used the data from Gies (2003), along with recent results for CPD-41° 7742 (Sana et al. 2005), DN Cas (Hillwig et al. 2006) and of course WR 20a (Rauw et al. 2005c)[6]. For the LMC, I used the results of Massey et al. (2002). Finally, for the SMC, I used only detached systems from the compilation of Hilditch et al. (1996). In fact, Harries et al. (2003) and Hilditch et al. (2005) studied the light curve and orbital solutions for a total of 50 eclipsing OB binaries in the SMC with periods below ~ 5 days. Among these systems, 21 are detached binaries, 28 are semi-detached and one is a contact system. For the detached systems, Hilditch et al. (2005) found that the evolutionary masses deduced from a comparison with single star evolutionary tracks are in excellent agreement with the observed masses. In the semi-detached systems, these authors often note an extra depression in the light curve before first contact of the primary eclipse. They interpret this as photometric evidence for absorption by a gas stream flowing from the secondary (i.e. the Roche lobe filling component) towards the primary. Therefore, these systems are likely to be in the slow case-A

[5]This can be understood through the metallicity dependence of the mass loss rates. The higher the metallicity, the larger $\dot{M}$ and hence the lower the mass at the end of the MS lifetime. At the same time this means that for larger metallicities, layers that were originally deeper in the stellar interior are now exposed at the surface and the star thus appears more over-luminous.

[6]It should be noted here that I have assumed the same bolometric luminosity for the two components of WR 20a as suggested by the optical spectrocopy. The light curves of Bonanos et al. (2004) and Rauw et al. (2007a, see Sect. 1.5.3 below) suggest a small difference in the surface brightness of the components of the binary. However, this result is rather marginal and could depend on the assumptions made (e.g. identical Roche lobe filling factors for the two stars).

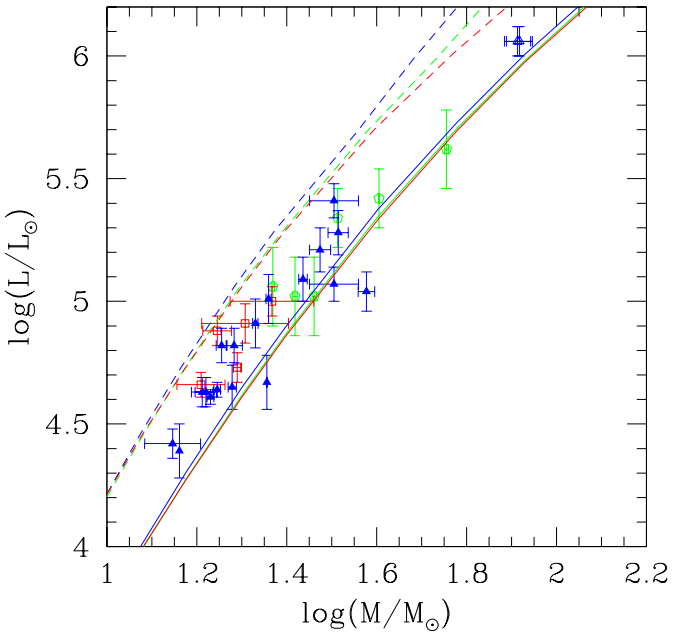

Figure 1.20: Mass-luminosity relation for O-type stars in detached eclipsing binary systems. The different symbols have the following meaning: open squares = SMC objects, open pentagons = LMC binaries, filled triangles = binaries in our Galaxy and open triangles = WN6ha stars in WR 20a. See the references in the text. The solid lines illustrate the theoretical ZAMS relation for different metallicities: 0.020 (blue), 0.08 (green) and 0.01 (red) as determined from the Geneva models (Schaller et al. 1992 and Schaerer et al. 1993). The dashed lines indicate the same relation for stars at the end of their MS lifetime.

mass transfer phase and should thus not be used in the comparison with the mass-luminosity relation of single stars, although Hilditch et al. (2005) claim that the mass gainers have $T_{\rm eff}$ and $L_{\rm bol}$ in agreement with the expectations for single stars of their current mass. The latter result suggests that the mass gainers are not underluminous for their mass and that their cores have been rejuvenated (i.e. well mixed with hydrogren from the newly acquired mass). The fact that the number of semi-detached binaries is sligthly larger than the number of detached systems indicates that the slow phase of case-A mass-transfer must have a duration comparable to the detached phase that precedes it.

The results of combining the data from the different detached eclipsing MS binary systems are presented in Fig. 1.20. As can be seen from this figure, most objects - including WR 20a - fit extremely well into the theoretical MS mass-luminosity relation. As far as the WN6ha stars in WR 20a are concerned, this result fully supports our suggestion that these stars are still burning hydrogen in their core.

From the different results presented in this section, it appears that WR 20a is to date the most massive binary system with well determined parameters. As we have seen there are several other candidates (Pistol Star, HD 15558, LH 54-425) but so far there exist no unambiguous mass determinations for any of these.

1.5.3 The surroundings of WR 20a and the stellar content of the cluster Westerlund 2

This subsection deals with the connection between the Wolf-Rayet binary star WR 20a, the very young open cluster Westerlund 2 and the surrounding giant H II region RCW 49. The main results of a spectroscopic and photometric observing campaign of the cluster are presented in the paper by Rauw et al. (2007a) that is reproduced below. Fig. 1.21 (taken from a press release by the *Spitzer* GLIMPSE consortium) illustrates the RCW 49 complex as seen by the Infrared Array Camera (IRAC) onboard the *Spitzer* observatory. The stellar winds and ionizing radiation of the early-type stars in Westerlund 2 have evacuated the central part of the nebula. RCW 49 is believed to host an intensive star formation activity, probably triggered by the early-type stars that populate the cluster core.

Figure 1.21: *Spitzer* IRAC image of RCW 49 (Churchwell et al. 2004). The colours correspond to emission in different wavebands: 3.6 μm (blue), 4.5 μm (green), 5.8 μm (orange) and 8.0 μm (red). The size of the image is approximately $1^\circ \times 1^\circ$.

Astronomy & Astrophysics manuscript no. aa6495-06
December 21, 2006

Early-type stars in the core of the young open cluster Westerlund 2⋆⋆⋆

G. Rauw[1,⋆⋆⋆], J. Manfroid[1,†], E. Gosset[1,⋆⋆], Y. Nazé[1,‡], H. Sana[2,1], M. De Becker[1], C. Foellmi[3,2], and A.F.J. Moffat[4]

[1] Institut d'Astrophysique et de Géophysique, Université de Liège, Allée du 6 Août, Bât B5c, 4000 Liège, Belgium
[2] European Southern Observatory, Alonso de Cordova 3107, 19 Vitacura, Santiago, Chile
[3] Observatoire de Grenoble, 414, Rue de la Piscine, BP 53, 38041 Grenoble, France
[4] Département de Physique, Université de Montréal, QC, H3C 3J7, and Observatoire du Mont Mégantic, Canada

Received date / Accepted date

ABSTRACT

Aims. The properties of the early-type stars in the core of the Westerlund 2 cluster are examined in order to establish a link between the cluster and the very massive Wolf-Rayet binary WR 20a as well as the H II complex RCW 49.
Methods. Photometric monitoring as well as spectroscopic observations of Westerlund 2 are used to search for light variability and to establish the spectral types of the early-type stars in the cluster core.
Results. The first light curves of the eclipsing binary WR 20a in B and V filters are analysed and a distance of 8 kpc is inferred. Three additional eclipsing binaries, which are probable late O or early B-type cluster members, are discovered, but none of the known early O-type stars in the cluster displays significant photometric variability above 1% at the 1-σ level. The twelve brightest O-type stars are found to have spectral types between O3 and O6.5, significantly earlier than previously thought.
Conclusions. The distance of the early-type stars in Westerlund 2 is established to be in excellent agreement with the distance of WR 20a, indicating that WR 20a actually belongs to the cluster. Our best estimate of the cluster distance thus amounts to 8.0 ± 1.4 kpc. Despite the earlier spectral types, the currently known population of early-type stars in Westerlund 2 does not provide enough ionizing photons to account for the radio emission of the RCW 49 complex. This suggests that there might still exist a number of embedded early O-stars in RCW 49.

Key words. Open clusters and associations: individual: Westerlund 2 – Stars: early-type – binaries: eclipsing – Stars: fundamental parameters – Stars: individual: WR 20a

1. Introduction

The open cluster Westerlund 2 (Westerlund 1961) lies in a blowout region of the giant H II complex RCW 49 (Rodgers et al. 1960). The stellar winds and ionizing radiation of the early-type stars in Westerlund 2 have evacuated the dust in the central part of RCW 49 and filled the cavity with very hot low density gas. Unfortunately, so far, our knowledge of the stellar content of Westerlund 2 was rather fragmentary. Photometric studies were performed by Moffat & Vogt (1975), Moffat et al. (1991) and Carraro & Munari (2004). To date, the only spectroscopic study of the cluster was presented by Moffat et al. (1991) who obtained low resolution spectra of six O-stars in Westerlund 2 and classified them as O6-7:V objects (although, as indicated by the colon, these spectral classifications were rather uncertain).

Recently, interest in the stellar population of Westerlund 2 was triggered by two independent observational studies. On the one hand, RCW 49 was observed with the Infrared Array Camera (IRAC) aboard *Spitzer* in the framework of the GLIMPSE legacy survey (Whitney et al. 2004, Churchwell et al. 2004, Churchwell 2005). These observations revealed strong evidence for ongoing star formation activity and underlined the need for a detailed study of the properties of the early-type stars in the cluster core and their impact on the surrounding nebula. On the other hand, WR 20a - one of the two Wolf-Rayet stars in RCW 49 - was found to be a very massive eclipsing binary consisting of two WN6ha stars with individual masses of about 80 $M_\odot$ (Rauw et al. 2004, 2005, Bonanos et al. 2004). Since previous spectroscopic studies revealed only one O6: and six O7: stars, in the cluster core (Moffat et al. 1991), the existence of a pair of stars that massive was somewhat unexpected. These results therefore called for a re-investigation of the population of early-type stars in Westerlund 2.

2. Observations

2.1. Photometry

Photometric monitoring of the core of Westerlund 2 was performed in service mode with the ANDICAM instrument at the

Send offprint requests to: G. Rauw
⋆ Based on observations collected at the Cerro Tololo Interamerican Observatory and at the European Southern Observatory (La Silla, Chile)
⋆⋆ Tables 2, 3 and 4 are only available in electronic form at the CDS via anonymous ftp to cdsarc.u-strasbg.fr (130.79.128.5) or via http://cdsweb.u-strasbg.fr/cgi-bin/qcat?J/A+A/
⋆⋆⋆ Research Associate FNRS (Belgium)
† Research Director FNRS (Belgium)
‡ Postdoctoral Researcher FNRS (Belgium)
Correspondence to: rauw@astro.ulg.ac.be

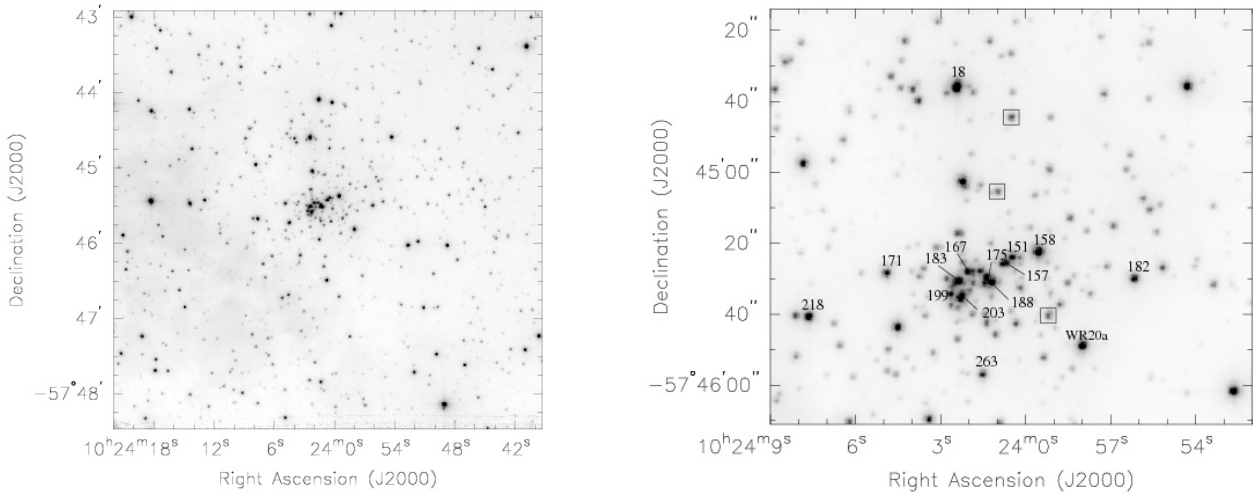

Fig. 1. *Left panel*: average image (combining the best B and V filter observations, i.e. those with a seeing of less than 1.25 arcsec) of the region around Westerlund 2 as observed with the ANDICAM instrument. *Right panel*: zoom on the central part of the cluster. The labels correspond to the numbering scheme introduced by Moffat et al. (1991) and identify those stars for which we obtained spectra. Note that MSP 158 and 218 are late-type foreground stars that are unrelated to the cluster (see Sect. 3.1). The boxes indicate the three newly discovered eclipsing binary systems discussed below.

1.3 m telescope at CTIO operated by the SMARTS[1] consortium. The primary goal of this campaign was the study of the light curves of early-type stars and more specifically of the very massive eclipsing binary WR 20a. Whenever possible, the cluster was observed twice per night (separated by several hours) through the B and V filters of the ANDICAM instrument. Each pointing consisted of integration times of 2×200 and 2×75 s for the B and V filters respectively. The detector was a Fairchild 447 CCD of 2048×2048 pixels. In the standard mode of the instrument the pixels are binned by 2×2. Each binned pixel corresponds to 0.37″on the sky and the total field of view of the instrument is about 6×6 arcmin^2, well suited for monitoring simultaneously most of the early-type stars in the central part of Westerlund 2 (see Fig. 1).

Our campaign covered 45 consecutive nights from 3 December 2004 to 17 January 2005. The median seeing of our data is 1.4 arcsec. During photometric nights, observations of Landolt (1992) standard star fields were also performed. All the data were pipeline processed (bias subtraction and division by a normalized flat field) by the SMARTS consortium at Yale before they were delivered to us.

The photometric reduction was done in three steps. First, instrumental magnitudes were extracted with DAOPHOT (Stetson 1987) under IRAF[2] using aperture and PSF-fitting techniques. To avoid possible flat-fielding errors (Manfroid 1995, Manfroid et al. 2001) the atmospheric extinction and zero-point were determined for the best photometric nights, using only the central part of the fields, by a multi-night, multi-star, multi-filter method as described by Manfroid (1993). The implementation of this reduction procedure allows the construction of a consistent natural system, which contains the extra-atmospheric instrumental magnitudes of all constant stars included in the computation procedure. Stars from all observed fields were included in the building of the natural system. To prevent adverse PSF effects, this procedure was carried out with the widest aperture photometry and restricted to relatively bright, isolated stars. The external calibration is based on two Landolt (1992) standard fields, T Phe and Rubin 149, revisited by Stetson [3]. These fields were observed at air masses ranging between 1.0 and 2.7. The `rms` error on the extinction coefficients of each night is 0.018. The error on the zero points is 0.028 mag, whilst the `rms` deviation of the mean magnitudes of the standard stars is slightly less than 0.003 mag. Finally, an extended set of constant stars was built to provide a calibration for all the frames, including those of relatively poor quality, and over the whole field. This procedure (Manfroid 1995) yields robust differential data. As the centering of the fields was quite consistent over the whole data set, inaccuracies in the overall flat-field calibration could not be evaluated, but they can be tolerated since they only consist of a systematic space-dependent shift and do not affect the variable component of the light curves.

Comparing our PSF photometry to the values reported by Moffat et al. (1991) - calibrated by the photomultiplier aperture photometry of Moffat & Vogt (1975) - for 59 objects in common (excluding a few outliers) and Carraro & Munari (2004) for 82 objects in common, we obtain:

$$(B-V)_{MSP} = (0.860 \pm 0.024)(B-V) + (0.089 \pm 0.037)$$

$$(B-V)_{CM} = (0.958 \pm 0.016)(B-V) + (0.025 \pm 0.020)$$

$$V_{MSP} - V = (0.052 \pm 0.029)(B-V) - (0.086 \pm 0.044)$$

$$V_{CM} - V = (0.062 \pm 0.024)(B-V) - (0.183 \pm 0.029)$$

where magnitudes and colours without an index refer to our data. As noted by Carraro & Munari (2004), the colour effects in the Moffat et al. (1991) data are large. Whilst our V zero-point agrees with the one of Moffat et al., the discrepancy with the zero-point of Carraro & Munari cannot be easily understood since most of the 82 stars in common are not affected by blends.

[1] Small and Moderate Aperture Research Telescope System

[2] IRAF is distributed by the National Optical Astronomy Observatories, which are operated by the Association of Universities for Research in Astronomy, Inc., under cooperative agreement with the National Science Foundation.

[3] http://cadcwww.hia.nrc.ca/standards/

2.2. Spectroscopy

For the spectroscopic analysis, we adopt the MSP numbering convention introduced by Moffat et al. (1991, see also Fig. 1). Medium-resolution long-slit spectroscopy of fourteen of the brightest stars in the central part of the Westerlund 2 cluster was obtained with the EMMI instrument at the ESO New Technology Telescope (NTT) on 27 March 2005. We excluded star MSP 91 for which Moffat et al. (1991) obtained a spectral type G0 V-III as well as MSP 273, another suspected non-member which lies rather far away from the cluster core. All seven O-type stars observed by Moffat et al. (1991) were included among our targets. Finally, MSP 168 was included in our target list, but could not be observed due to a lack of time.

The red arm of EMMI was used in the REMD mode with grating #6 (1200 grooves mm^{-1}). The useful wavelength domain ranged from 4200 to 4950 Å. The spectral resolution of the instrument configuration as measured from the FWHM of the lines in the ThAr calibration exposures was about 1 Å. Exposure times ranged from 20 min to 1 hour. The spectra were bias-subtracted, flat-fielded, sky-subtracted, wavelength-calibrated and normalized using the MIDAS software developed at ESO. The S/N ratios of the calibrated spectra ranged between 60 and 150 for the faintest and brightest sources respectively, with an average of $\sim$ 100 for a $V = 14.5$ star. Since the observations were taken only two days after full moon, the level of the background sky was rather high. Although we extracted the sky spectrum as close as possible to the source, some residual sky features are seen in the final spectra of the faintest source that we observed under somewhat poorer conditions (MSP 263).

3. Spectral classifications

3.1. Late-type foreground stars

Two stars (MSP 158 and 218) have spectral types significantly later than B0 (see Fig. 2). In order to establish the MK spectral types of these two objects, we make use of the digital spectral classification atlas compiled by R.O. Gray and available on the web[4].

The spectrum of MSP 218 (10:24:07.7, −57:45:41, J2000) is dominated by strong and broad H I Balmer lines. Weak absorption lines of He I $\lambda\lambda$ 4388, 4471, Mg II λ 4481 and Si III λ 4552 are also seen. The He I λ 4471/Mg II λ 4481 intensity ratio indicates a spectral type B8-A0. The appearance of some weak metallic lines favours an A0 classification, whilst the width of the Balmer lines suggests a giant luminosity class. We therefore adopt an A0 III spectral type. Our photometric data yield $V = 14.13 \pm 0.03$ and $B - V = 0.34 \pm 0.04$. If the intrinsic colours and absolute magnitudes of MSP 218 are those of a typical A0 III star (Schmidt-Kaler 1982), then $A_V \sim 1.15$ and the star must be located at a distance of about 4.0 kpc.

The spectrum of MSP 158 (10:23:59.5, −57:45:23, J2000) shows a prominent G-band as well as a strong Ca I λ 4227 line indicating a late (G-K) spectral type. The intensity ratios between the Fe I λ 4325 and Hγ lines as well as the ratio between Cr I λ 4254 and the neighbouring Fe I $\lambda\lambda$ 4250, 4260 lines suggest a spectral type G8. The Y II λ 4376/Fe I λ 4383 line ratio and the CN bandhead at 4216 Å indicate a giant luminosity class. We thus assign a G8 III spectral type. From our photometric data, we infer $V = 13.03 \pm 0.03$ and $B - V = 1.09 \pm 0.05$. Assuming magnitudes and colours typical for a G8 III star (Schmidt-Kaler 1982), we derive a reddening of $A_V = 0.47$ and a distance of about 2.25 kpc.

Both stars are foreground objects unrelated to the Westerlund 2 cluster, as suspected by Moffat et al. (1991) based on their UBV photometry. This is also confirmed by the absence of the strong diffuse interstellar band at 4430 Å which is prominent in the spectra of the O-type members of the cluster (see Fig. 3). As we will show below, the O-stars of Westerlund 2 are subject to substantially larger reddening (A_V from about 4.8 to 5.8 mag) and their distance is significantly larger. Comparing the reddening of the G8 III, A0 III and the O-type stars (see below), we note that the A_V of the cluster members exceeds the value estimated from a crude empirical linear $A_V(d)$ relation derived from the foreground stars. Though such a linear relation provides only a first approximation, the result suggests that much of the reddening that affects the cluster could be local (e.g. due to material from the molecular cloud out of which the cluster has formed).

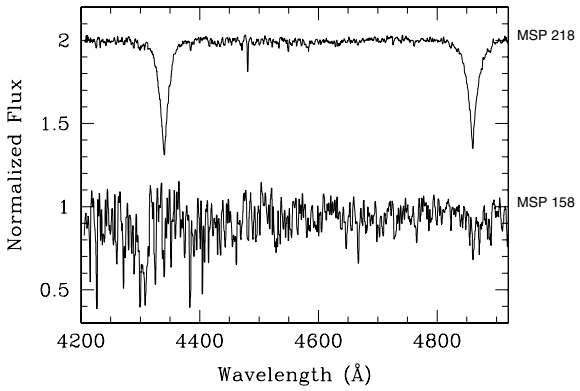

Fig. 2. Medium resolution spectra of the stars MSP 158 and 218 in the field of Westerlund 2. Both stars are likely foreground objects unrelated to the cluster.

3.2. Early-type stars

Twelve of our targets display spectra typical of O-type stars (see Fig. 3). The spectral types were derived from the ratio of the equivalent widths of the He I λ 4471 and He II λ 4542 classification lines by means of the criteria first introduced by Conti (1973, see also Mathys 1988). The results are displayed in Table 1. For star MSP 203, we were only able to derive an upper limit on the equivalent width of the He I λ 4471 line. All stars have rather strong He II λ 4686 absorption lines (equivalent widths in the range 0.4 to 1.1 Å, the extremes corresponding to MSP 167 and 263 respectively) suggesting they are main-sequence or giant objects. Mathys (1988) proposed $EW = 0.56$ Å as the demarcation between weak and strong He II λ 4686 absorption corresponding to luminosity classes III and V respectively. Using this criterion, we have assigned the luminosity classes in Table 1.

We then compared our spectra to the digital atlas of Walborn & Fitzpatrick (1990) and Walborn et al. (2002). The results are also indicated in Table 1. The classifications according to the two criteria agree to better than one subtype. We note that because the He I λ 4471 classification line is quite weak or broad in the spectra of MSP 167, 175 and 203, these objects could also be

[4] http://nedwww.ipac.caltech.edu/level5/Gray/frames.html

Table 1. Spectral classifications of the O-type stars in Westerlund 2. The first and fourth columns yield the number of the star in the numbering scheme of Moffat et al. (1991) as well as the spectral type proposed by these authors. The fifth and sixth columns provide our newly derived spectral types, determined using the Conti (1973) + Mathys (1988) and Walborn & Fitzpatrick (1990) classification criteria. Columns 7, 8 and 9 respectively yield our mean V magnitude, the $B-V$ colour index and the extinction derived assuming the intrinsic colours from Martins & Plez (2006) and $R_V = 3.1$. The individual spectro-photometric distance moduli based on the calibration of Martins & Plez (2006) are listed in column 10. Column 11 provides the effective temperature as derived from our spectral classification and the calibration of Martins et al. (2005a). Finally, the bolometric luminosities given in the last column were computed for an adopted distance modulus of $DM = 14.52 \pm 0.38$ ($d = (8.0 \pm 1.4)$ kpc, see Sect. 5.1).

Star #	RA (J2000)	DEC (J2000)	Spectral type MSP	Spectral type This work: Conti crit.	Spectral type This work: W&F crit.	V	$B-V$	A_V	DM	$T_{\rm eff}$ (K)	$\log L_{\rm bol}/L_\odot$
MSP 18	10:24:02.4	−57:44:35	O7:V	O5.5 V-III	O5 V-III((f))	12.88	1.23	4.68	13.74	40100 ± 800	5.89 ± 0.16
MSP 151	10:24:00.5	−57:45:24	O6:V	O7 III	O6 III	14.33	1.36	5.05	14.97	37100 ± 1000	5.37 ± 0.17
MSP 157	10:24:00.8	−57:45:26	O6:V	O5.5 V	O6.5 V	14.33	1.31	4.93	14.39	38900 ± 1000	5.37 ± 0.17
MSP 167	10:24:02.1	−57:45:28	O7:V	O6 III	O6 III	15.18	1.42	5.24	15.71	38200 ± 500	5.14 ± 0.16
MSP 171	10:24:04.9	−57:45:28		O5 V	O4-5 V	14.47	1.45	5.36	14.53	41900 ± 1000	5.58 ± 0.17
MSP 175	10:24:01.4	−57:45:30		O5.5 V-III	O6 V-III	13.98	1.29	4.87	14.55	39000 ± 800	5.49 ± 0.16
MSP 182	10:23:56.2	−57:45:30		O4 V-III	O4 V-III((f))	14.45	1.32	4.96	15.30	42600 ± 1000	5.45 ± 0.16
MSP 183	10:24:02.4	−57:45:31	O7:V	O4 V	O3 V((f))	13.57	1.50	5.52	13.77	43900 ± 1000	6.07 ± 0.17
MSP 188	10:24:01.2	−57:45:31	O7:V	O4 V-III	O4 V-III	13.41	1.37	5.12	14.10	42600 ± 1000	5.93 ± 0.16
MSP 199	10:24:02.7	−57:45:34		O3 V	O3-4 V	14.37	1.40	5.21	14.88	43900 ± 1000	5.61 ± 0.17
MSP 203	10:24:02.3	−57:45:35	O7:V	O6 V-III	O6 V-III	13.31	1.37	5.10	13.59	38600 ± 800	5.84 ± 0.16
MSP 263	10:24:01.5	−57:45:57		O6.5 V	O6 V	15.01	1.61	5.84	14.09	38350 ± 500	5.45 ± 0.16

classified as O5 rather than O6 stars. Henceforth, we adopt the conservative hypothesis that these objects are actually O6 stars, but we will nevertheless consider the implications of a somewhat earlier classification for these stars when discussing the ionization of RCW 49.

Three stars (MSP 18, 182 and 183) display a strong He II λ 4686 absorption accompanied by weak N III $\lambda\lambda$ 4634-40 emission, which leads to an ((f)) classification. The earliest star in our sample is MSP 183 which displays prominent N V $\lambda\lambda$ 4604, 4620 absorption lines. Except for the weaker N III $\lambda\lambda$ 4634-4640 lines, the spectrum of MSP 183 very much resembles that of HD 64568 (O3 V((f*)), Walborn et al. 2002). We therefore classify MSP 183 as O3 V((f)).

On average the spectral types that we determine are significantly earlier than those inferred by Moffat et al. (1991). The implications of these revised classifications are discussed in Sect. 5. Uzpen et al. (2005) recently inferred an O4 V((f)) spectral type for MSP 18. Our data have a superior resolution (1 Å) than their observations (4.2 Å) and are thus better suited to measure the strength of the weak He I classification lines. We therefore favor the O5 V((f)) spectral classification for this star.

Though our data set is obviously not ideal for this purpose, we note that our spectra do not reveal strong evidence for multiplicity. None of the stars has an obvious composite spectrum nor displays assymmetric, very broad or double lines that could make it a spectroscopic binary candidate. A higher resolution, high S/N spectroscopic monitoring of these stars is however needed to confirm or infirm this impression.

In Table 1, we list the observed V magnitudes and the $B-V$ colours for the spectroscopically identified O-type stars in our sample. For stars that are well isolated on the sky, the aperture and PSF photometry agree very well with each other and we adopted the magnitude obtained with an aperture of 8 pixels (i.e. 3.0″) radius which has the smallest errors. On the other hand, for stars in the crowded core of the cluster, it was mandatory to use the PSF photometry instead. Comparing the observed colour indices with the intrinsic colours of Martins & Plez (2006), we have inferred the extinction A_V, adopting $R_V = 3.1$. Assuming that these objects have absolute magnitudes typical of main-sequence or giant O-type stars (Martins & Plez 2006), we estimate an average distance modulus of 14.47 ± 0.65 (1-σ standard deviation). If we exclude the three stars with the lowest (MSP 18, 183 and 203) and the star with the largest (MSP 167) value of the distance modulus, we get on average $DM = 14.60 \pm 0.43$ in excellent agreement with the value (14.5 ± 0.3) of Moffat et al. (1991) based on their UBV photometry and ZAMS fitting. This suggests therefore a distance of (8.3 ± 1.6) kpc to-

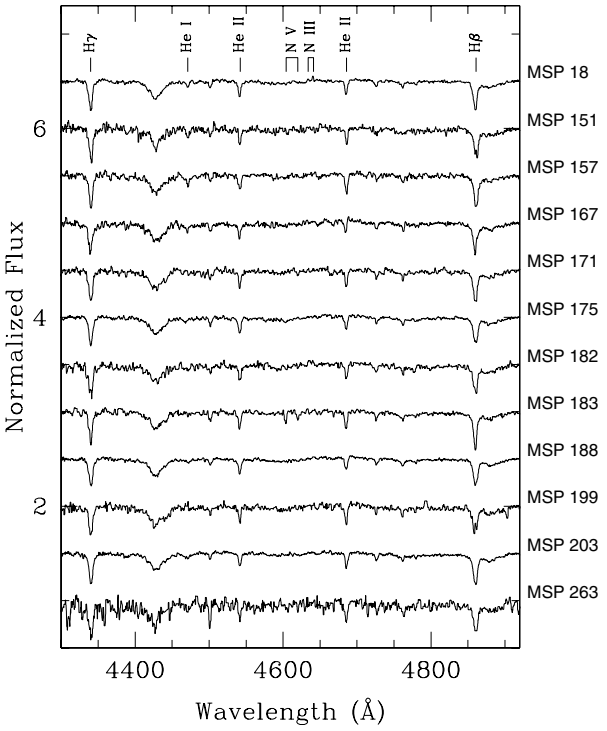

Fig. 3. Medium resolution spectra of O stars in Westerlund 2. Note the very strong diffuse interstellar band (DIB) at 4430Å. Some residual nebular Hβ line emission affects the spectra of MSP 151, 182 and 199.

wards Westerlund 2 in very good agreement with the distance estimate of ∼ 8.0 kpc towards WR 20a (see Rauw et al. 2005 and Sect. 4.1). We note that adopting the intrinsic colours from Schmidt-Kaler (1982) and the absolute magnitudes from Martins et al. (2005a) would reduce the distance modulus by 0.23 mag (i.e. a reduction of the distance by 800 pc).

4. Photometric variability

4.1. WR 20a

As pointed out in the introduction, one of the initial motivations of our observing campaign was the study of the photometric eclipses of the extremely massive binary WR 20a. Bonanos et al. (2004) reported *I* band observations showing that the system displays indeed eclipses on the orbital period of 3.686 days. The Fourier periodogram (computed using the method of Heck et al. 1985, revised by Gosset et al. 2001) of our photometric time series of this system displays the highest peak at $\nu'_1 = 0.5426\,\mathrm{d}^{-1}$ for both filters (*B* and *V*) and irrespective of whether we consider the aperture or PSF photometry (see e.g. Fig. 4). The natural width of the peaks in the Fourier periodogram of our time series is equal to $0.0222\,\mathrm{d}^{-1}$. Assuming that the position of the highest peak can be determined with an accuracy of 5% of this width, we infer an uncertainty of $0.0011\,\mathrm{d}^{-1}$ on ν'_1.

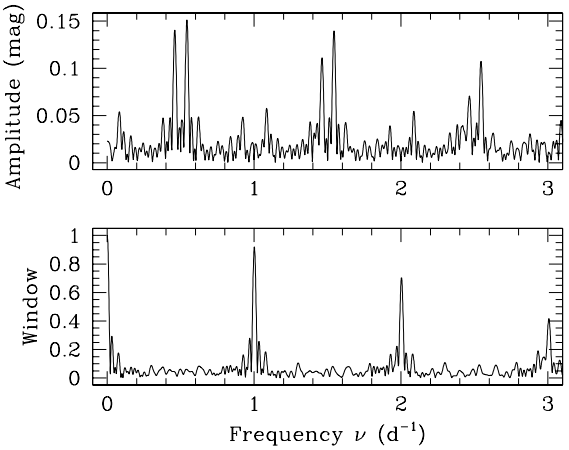

Fig. 4. Periodogram showing the half amplitude of the best-fit sine wave (top panel) and spectral window (bottom panel) derived from the Fourier analysis of the photometric time series of WR 20a. The results are shown for the measurements in the *B* filter (8 pixels radius aperture photometry). For the *V* filter, the results are identical. The highest peak in the periodogram is located at $0.5426\,\mathrm{d}^{-1}$.

Since the two components of WR 20a have roughly equal temperature and brightness, the eclipses are of essentially equal depth and shape. Thus ν'_1 actually corresponds to twice the orbital frequency. Therefore, our data yield an orbital period of (3.6859 ± 0.0075) days, in very good agreement with the value (3.686 ± 0.010 days) found by Bonanos et al. (2004). The whole periodogram (Fig. 4) can be interpreted on the basis of this sole periodicity. Indeed, no peak is visible at $\nu \sim 0.27\,\mathrm{d}^{-1}$ because most of the power is contained in the ν'_1 harmonic. The higher harmonic at $\nu \sim 1.08\,\mathrm{d}^{-1}$ is induced by the shape of the eclipses whereas the harmonics at $\nu \sim 0.82\,\mathrm{d}^{-1}$ (not to be confused with $\nu = 0.93\,\mathrm{d}^{-1}$, the one-day alias of $1.08\,\mathrm{d}^{-1}$) is related to the slight difference in eclipse depths.

Folding the light curve of WR 20a with the derived period, we have evaluated the magnitudes of the system at phases outside of the eclipses: $B = 14.999 \pm 0.021$, $V = 13.416 \pm 0.024$ and $I = 10.658 \pm 0.015$ (the latter value was computed from the Bonanos et al. data). Our estimate of the period can be further refined by comparing our light curves with that of Bonanos et al. Subtracting the above outside-eclipse magnitudes from the observed light curves, we can combine all the data and perform a Fourier analysis. In this way, we find that the highest peak in the periodogram has $\nu_1 = (0.54277 \pm 0.00019)\,\mathrm{d}^{-1}$. Therefore, the newly determined value of the orbital period is (3.68475 ± 0.00129) days. The value of the uncertainty is probably too conservative: comparing the time of primary minimum determined by Bonanos et al. (2004) with our best estimate of the primary minimum results in a more realistic estimate of the uncertainty on the orbital period of 0.00020 days.

The light curves of WR 20a folded with the above period and adopting a time of primary minimum of HJD 2453330.930 are displayed in Fig. 5. We have fitted our *B* and *V* light curve along with the *I* band light curve from Bonanos et al. (2004) using the NIGHTFALL[5] software developed and maintained by R. Wichmann, M. Kuster & P. Risse. We fixed the mass ratio at the value ($m_{\rm sec}/m_{\rm prim} = 0.99$) derived from the radial velocity curve. There exist a number of combinations of the model parameters that fit the light curve but do not provide a physically self-consistent description of the system. For instance, if the filling factors (defined as the ratio of the polar radius of the star to the polar radius of the Roche lobe) of both components are allowed to differ in the fit of the light curve, the luminosities of the primary and secondary star are found to differ by more than 50% which is clearly at odds with the fact that the two stars have identical spectral types and spectral features of identical strength (Rauw et al. 2004, 2005). We have therefore constrained some of the fitting parameters. For instance, we searched for models which have primary and secondary temperatures in agreement with the value (43000 ± 2000 K) derived from an analysis with a model atmosphere code (see Rauw et al. 2005). Following the same strategy as Bonanos et al. (2004), we have assumed that both stars have identical (Roche lobe) filling factors. For a grid of values of the filling factors and the primary (resp. secondary) temperature, we iterated the NIGHTFALL code for the best fit inclination and secondary (resp. primary) temperature. The best constrained model parameter is the orbital inclination which quickly converges to $i = (74.5 \pm 1.0)^\circ$ in excellent agreement with the value derived by Bonanos et al. (2004). Moreover, the shape of the wings of the eclipses and the light variations outside of the eclipses require that the filling factor be between 0.89 and 0.92 with a preferred value of 0.91. The absolute temperatures of the components cannot be constrained by the analysis of the light curve. In principle, the depths of the eclipses constrain the relative surface brightnesses and hence the relative temperatures. Under the above assumptions of equal radii, we find that the primary should be hotter than the secondary by about 2000 – 3000 K (assuming a primary temperature in the range found from the spectroscopic analysis), although models with identical temperatures for both components are of almost equivalent quality. The best fit light curves for a filling factor of 0.91 for

[5] http://www.hs.uni-hamburg.de/DE/Ins/per/Wichmann/Nightfall.html
Note that the NIGHTFALL code does not include stellar wind effects, but given the proximity of the stars in WR 20a, the light curve should be dominated by the geometrical effects.

both stars, an orbital inclination of 74.5°, and temperatures of $T_{eff,p} = 43000$ K and $T_{eff,s} = 40500$ K are illustrated in Fig. 5.

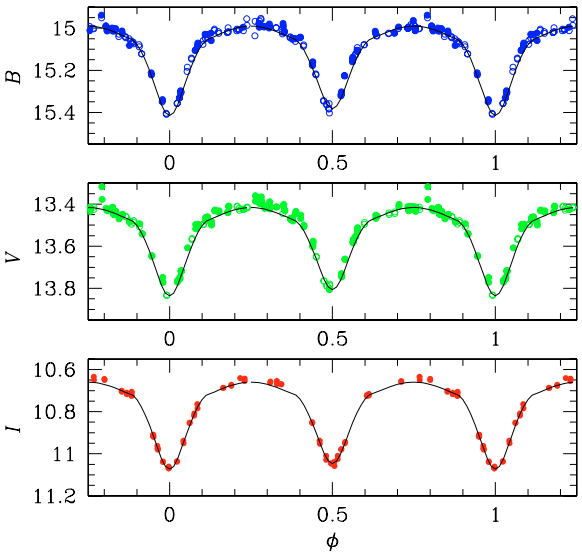

Fig. 5. Light curve of WR 20a in the B, V and I (the latter data from Bonanos et al. 2004) filters folded with the 3.68475 day period and adopting a time of primary minimum of HJD 2453330.930. The B and V data correspond to the photometry obtained through PSF fitting and are given in Table 2 (available in electronic form at the CDS). Filled symbols stand for data with a FWHM of the PSF of less than 4.0 pixels, whilst the open symbols yield data taken under poorer seeing conditions. The continuous curve represents the best fit theoretical light curve determined with the NIGHTFALL code for a filling factor of 0.91 for both stars, an orbital inclination of 74.5°, and temperatures of $T_{eff,p} = 43000$ K and $T_{eff,s} = 40500$ K.

The parameters of the above solution correspond to an average stellar radius of $(18.7 \pm 0.9)\,R_\odot$, roughly 5% smaller than the values found by Bonanos et al. (2004). If the primary temperature amounts to (43000 ± 2000) K as found by Rauw et al. (2005), then its bolometric luminosity would be $\log L/L_\odot = 6.03 \pm 0.09$, whilst for the secondary we obtain $\log L/L_\odot = 5.93 \pm 0.10$. For the entire binary system, we thus find $\log L/L_\odot = 6.28 \pm 0.10$. With the bolometric correction of −3.91 (Rauw et al. 2005), we therefore infer an absolute V magnitude of $M_V = -7.04 \pm 0.25$. The out of eclipse magnitudes listed above yield $B - V = 1.58 \pm 0.03$, hence $E(B - V) = 1.91 \pm 0.03$ (evaluated using the intrinsic colour index from Rauw et al. 2005) and $A_V = 5.93 \pm 0.09$. This leads to $DM = 14.52 \pm 0.27$ corresponding to $d = (8.0 \pm 1.0)$ kpc. This result concurs with the estimate of Rauw et al. (2005; $d = (7.9 \pm 0.6)$ kpc), and agrees perfectly well with the estimate of the distance of the O-type star population presented above. We will come back to this issue in Sect. 5.

Although the periodogram of Fig. 4 can be fully explained by the orbital period and its harmonics, we decided to search for additional variations, in order to extract the maximum information from the data. Moreover, it is reasonable to think that such massive stars might display additional variations such as pulsations (see Sterken & Breysacher 1997, and Fig. 3 of Pamyatnykh 1999). Consequently, we have whitened the B, V photometry time series for the binary variations by removing the orbital period and its harmonics. The time series of the residuals have again been Fourier analysed. No peak exceeding a semi-amplitude of 0.008 mag has been found, indicating that no other periodicity is present in the photometric variations of WR 20a at this level.

4.2. O-type stars

Using our photometric time series, we have searched for variability among the objects identified as early-type O-stars in our spectroscopic campaign. For targets that are rather well isolated, the aperture photometry yields 1-σ dispersions on the B and V magnitudes of order 0.005 to 0.010 mag. A Fourier analysis of our time series, excluding the data points with the poorest seeing reveals no significant peak in the periodogram. The highest peak is usually found near $\nu = 1\,d^{-1}$ which is actually due to the interplay between the sampling of our time series and a few deviating data points.

For objects in the crowded region of the cluster core, we find that the variations of the aperture photometry time series reflect the variations of the seeing during the observing campaign as could be expected. Excluding those points with the poorest observing conditions from the aperture photometry time series, we find that there is no photometric variability exceeding the 1-σ level of 0.010 mag. The Fourier analysis yields the same conclusions as for the isolated objects. Although the PSF photometry provides more accurate absolute photometry, PSF photometry time series usually yield somewhat larger 1-σ dispersions. We conclude that none of the early O-type stars in the cluster core displays a significant variability and in particular, we find no evidence for photometric eclipses.

4.3. Other variables in the field of view

We have searched our photometric time series for additional variables. The light curves of those objects that display a photometric variability exceeding significantly the level of photon noise in the B and V band were extracted and were analysed with the Fourier technique over the frequency range between 0.0 and 5.0 d^{-1}. Only data points obtained when the seeing was better than 4 pixels (i.e. 1.5″) were included in this process. For most objects, the Fourier analysis yields the highest peaks at frequencies near 0 or an integer number of day^{-1}. These features stem from the combination of the actual sampling of the time series with a few deviating data points and do not reflect a genuine periodic behaviour. The only exceptions are the three stars discussed below.

MSP 223 (10:23:59.2 −57:45:40, J2000) is an apparently red star ($V = 15.75$, $B - V = 1.50$) that shows drops in its light curve that are consistently seen in the B and V filter and occur on a recurrence time of 14.61 days. The variations are reminiscent of an eclipsing binary. In this case, the system either lacks a secondary eclipse (maybe as a result of an eccentric orbit or of an insufficient sampling of the light curve near that phase) or the true orbital period could be 29.21 days. We folded the light curve with this latter period and adopting a time of primary minimum of HJD 2453369.85. The eclipses are rather narrow and the secondary eclipse could be slightly shallower than the primary one. The system presents some slight slow variations outside the eclipses (see Fig. 6). Though the photometric data are not sufficient to provide a full solution, test calculations with the NIGHTFALL code suggest that the system consists of a pair of stars of comparable surface brightness that are well inside their Roche lobe and are seen under a high inclination angle. The variations

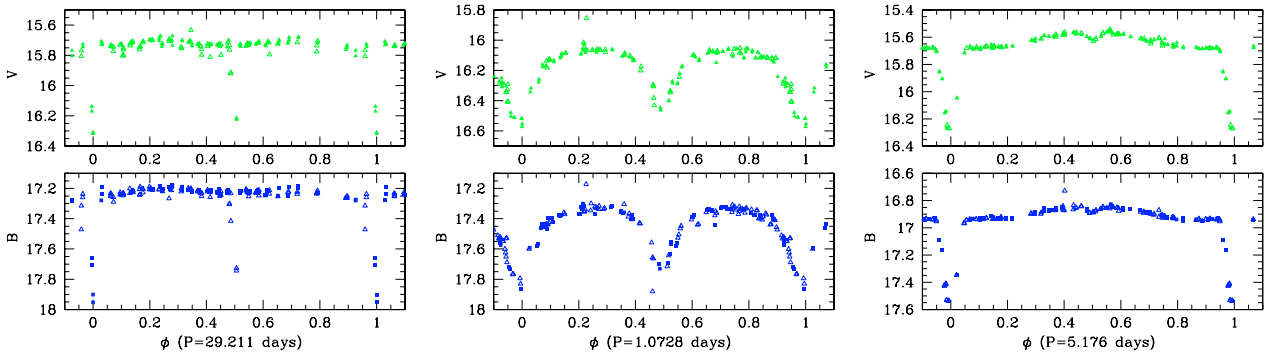

Fig. 6. *Left:* light curves of MSP 223 as obtained from our B and V PSF photometry time series folded with a period of 29.211 days and T_0 = 2453369.85. The filled and open symbols stand for data obtained with a seeing of less than and more than 4.0 pixels (FWHM) respectively. *Middle:* same as left panel, but for MSP 96, a period of 1.0728 days and T_0 = 2453370.6973. *Right:* same as left panel, but for MSP 44, a period of 5.176 days and T_0 = 2453371.75.

outside eclipse cannot be explained by ellipsoidal variations and rather suggest the existence of a non-uniform surface brightness for at least one component. MSP 223 could thus be a kind of magnetically active binary.

The periodogram of the photometry of MSP 96 (10:24:01.0 −57:45:06, J2000; V = 16.17, $B-V$ = 1.27) displays a prominent peak at 1.864 day^{-1}, although its one-day aliases are only slightly weaker. Again the light curve suggests an eclipsing binary and the true period is probably 1.0728 day. The eclipses are rather broad (see Fig. 6) and the ellipsoidal variations suggest that at least one of the two stars must be close to filling its Roche lobe. Also, the different depths of the eclipses indicate that one of the stars must be significantly hotter than its companion.

The periodograms of MSP 44 (10:24:00.5 −57:44:45, J2000; V = 15.67, $B-V$ = 1.25) display their highest peak at 0.1932 day^{-1}, although the $1-\nu$ alias is almost equally strong. The light curve folded with a period of 5.176 days and T_0 = 2453371.75 displays a strong minimum at phase 0.0 as well as a much weaker secondary minimum at phase 0.5. Outside these rather narrow minima the light curve is not flat, but displays a strong modulation (see Fig. 6). As for MSP 223, the narrow eclipses are the signature of a pair of relatively compact stars seen under high inclination, whilst the strong modulation of the flux outside eclipse requires a non-uniform surface brightness (spots or reflection effects) probably for both components. The light curve of MSP 44 is reminiscent of those of RS CVn systems therefore making this a candidate for a magnetically active binary system. Alternatively, MSP 44 could be a detached binary with components that differ quite substantially in temperature. The seemingly symmetric variability outside of the eclipse would then result from a strong reflection effect or surface heating.

To further constrain the nature of MSP 44, 96 and 223, we examine the $(B-V, V)$ colour-magnitude diagram of the stars[6] in the ANDICAM field of view around Westerlund 2 (see Fig. 7). Figure 7 clearly reveals two populations of stars: the foreground field stars which have relatively blue colours and the cluster stars which have an $E(B-V)$ colour excess between 1.51 and 1.88. The O-type stars and WR 20a fall in the region of the cluster main-sequence (see also Sect. 5.2). Two of the three foreground stars MSP 91 and 218 clearly occupy the locus of field stars. The third one (MSP 158, G8 III) falls close to the cluster main sequence, suggesting that the locus of the cluster stars might be polluted by cluster non-members. The three eclipsing binaries fall on the locus of the cluster main-sequence. Moffat et al. (1991) actually labelled all three stars as probable OB members of Westerlund 2 based on their UBV photometry. In this case, the primary components of these binaries would be late O or early B-type stars which would contradict our suggestion of two of these systems being magnetically active late-type binaries. A spectroscopic follow up of these objects will not only help clarify their nature, but will also bring valuable constraints on the general cluster properties.

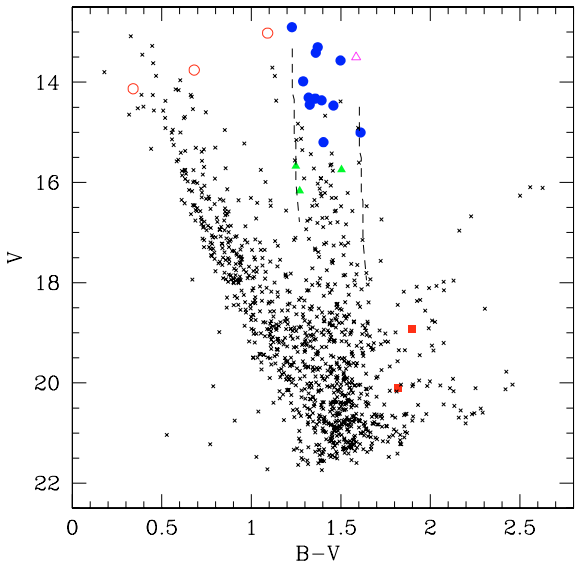

Fig. 7. Colour-magnitude diagram of the stars in the ANDICAM field of view around Westerlund 2. The filled circles and the open triangle correspond to the twelve O-type stars observed in spectroscopy (see Table 1) and the WR 20a binary, respectively. The dashed lines correspond to the main-sequence between spectral types O3 and B2 for a distance modulus of 14.52 and reddened with A_V = 4.68 (leftmost curve) or 5.84 (rightmost curve) and assuming R_V = 3.1. The open circles yield the late-type foreground objects MSP 91, 158 and 218 whilst the filled triangles indicate the three eclipsing binaries discussed in Sect. 4.3. Finally, the two squares correspond to the two non-periodic variables.

[6] Tables 3 and 4 with the light curves of the eclipsing binaries and the mean $(B-V, V)$ data are provided at the CDS.

Finally, Kolmogorov-Smirnov and χ^2 tests were also performed to identify non-periodic variables. Two more stars emerged from these tests and both were found to display a strong apparently non-periodic variability. These objects are located at 10:23:58 −57:47.7 and 10:24:00 −57:44.9 (J2000) and have magnitudes and colours of $V = 20.01$, $B - V = 1.83$ and $V = 18.93$, $B - V = 1.88$, respectively. Both objects are about 1 mag fainter (in B and V) at the beginning of our campaign than later and these 'minima' last about 14 and 18 days respectively. No other event of this type is seen over the rest of the campaign. These objects are either irregular or long-term (period > 45 days) variables or eclipsing binaries with periods very close to 1 or 2 days.

5. The link between Westerlund 2, WR 20a and RCW 49

5.1. The distance

The distance towards Westerlund 2 and RCW 49 has been a very controversial issue (see e.g. the discussions in Churchwell et al. 2004 and Rauw et al. 2005) and distance estimates for the cluster range from about 2.5 kpc to 8 kpc. The line of sight towards RCW 49 is roughly tangential to the Carina arm, leading to a wide range of possible distances. Using a galactic rotation curve along with H I line velocity measurements, Russeil (2003) recently determined a kinematic distance of $4.7^{+0.6}_{-0.2}$ kpc towards RCW 49. Russeil cautioned however that velocity deviations from the circular Galactic rotation model exist all along the Carina spiral arm.

Based on spectro-photometric parallaxes of the early O-type stars, we have estimated $d = (8.3 \pm 1.6)$ kpc, whilst the analysis of the light curve of the eclipsing binary WR 20a yields $d = (8.0 \pm 1.0)$ kpc. The weighted mean of these two distance estimates amounts to $d = (8.0 \pm 1.4)$ kpc. These results clearly rule out a distance below ∼ 6 kpc. Moreover, the excellent agreement between our two distance determinations indicates that WR 20a very likely belongs to Westerlund 2. Various effects that could bias our distance determinations are briefly discussed in Appendix A.

Based on *Spitzer* data, Uzpen et al. (2005) found that MSP 18 displays an IR excess which they attributed to thermal bremsstrahlung from the stellar wind. These authors fitted the V, *Spitzer* and 2MASS photometry with a Kurucz ATLAS9 model. In this procedure, the scaling factor of the surface flux depends on the angular diameter (i.e. on the ratio of the stellar radius and the distance) of the star. In this way, they inferred a spectro-photometric distance of 3233^{+540}_{-535} pc and an extinction of $A_V = 5.63^{+0.01}_{-0.30}$. These authors suggest therefore that the actual distance of Westerlund 2 is 3.2 kpc. The extinction is significantly larger than our value (4.68), whilst their distance is less than 50% of our best estimate of the cluster distance. To understand the origin of this discrepancy, we fitted our B, V magnitudes along with the U magnitude from Moffat et al. (1991) and the 2MASS photometry using a simple (static, plane-parallel atmosphere in LTE) model atmosphere code[7]. Test fits including the 2MASS data suggest that the large A_V value of Uzpen et al. (2005) is likely due to the near-IR domain already being affected by the IR excess emission. Freezing the reddening at the value of $E(B - V) = 1.56$ found above, the temperature at 40 kK compatible with the optical spectrum and fitting only the U B V data clearly confirms this idea. The angular diameter derived from the latter fit amounts to 6×10^{-11} rad. Assuming a typical radius of $12.0\,R_\odot$ for the O5 V-III star then yields a distance of 9.0 kpc. We thus conclude that the discrepancy between the Uzpen et al. (2005) result and our estimate stems from the near-IR photometry which is already affected by excess emission.

In summary, we find that the distance of WR 20a and Westerlund 2 is probably (8.0 ± 1.4) kpc.

[7] The software, developed by S. Jeffery at Armagh Observatory, is available at http://star.arm.ac.uk/~csj/software.store.

5.2. The Hertzsprung-Russell diagram of Westerlund 2

To position the O-type stars in the Hertzsprung-Russell diagram, we have adopted the 'observed' spectral-type – effective temperature calibration and bolometric corrections of Martins et al. (2005a) and Martins & Plez (2006), respectively. The observed V magnitude and A_V extinction of each star were taken from Table 1. The bolometric luminosities are quoted in the last column of Table 1 and were evaluated accounting for the uncertainties in spectral type and luminosity class and assuming a distance of (8.0 ± 1.4) kpc.

In Fig. 8, we compare the location of the O-stars in the Hertzsprung-Russell diagram with the evolutionary tracks and isochrones from Schaller et al. (1992) for solar metallicity. Keeping in mind the possibility that some of the luminosities might be overestimated due to binarity, we note that the O-stars that we have observed should have masses ranging from about 30 to 85 $M_\odot$ and ages of less than ∼ 2.5 Myr.

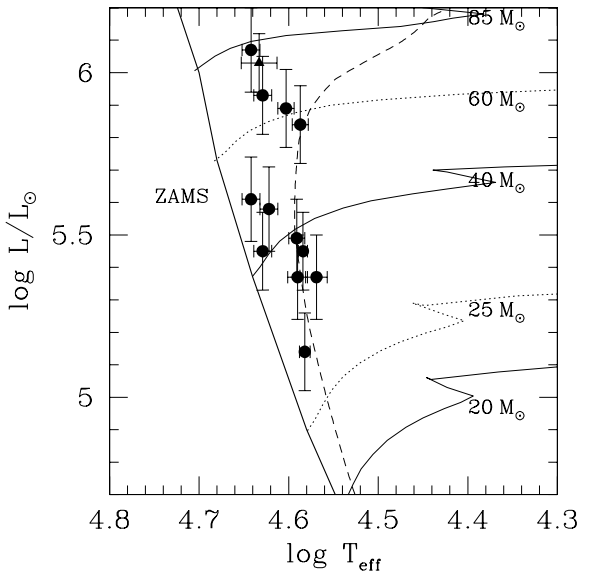

Fig. 8. Hertzsprung-Russell diagram of the O-type stars in Westerlund 2. Evolutionary tracks are from Schaller et al. (1992). The dashed line yields the 2.5 Myr isochrone corresponding to an upper limit on the age of the O-stars. The filled triangle indicates the position of the WN6ha stars of WR 20a.

5.3. The ionization of RCW 49

Several authors have presented radio observations of RCW 49. The continuum radio emission of H II regions is free-free emission that can, in principle, be used to evaluate the minimum number of Lyman continuum photons. In the case of RCW 49, the ob-

served radio luminosity (evaluated for a distance near 8 kpc) was usually found to be too large compared to the Lyman ionizing flux from the known O-star population. For instance, Whiteoak & Uchida (1997) evaluated a flux density of 210 Jy at 0.843 GHz for the entire RCW 49 complex, whilst the flux density of the shell around Westerlund 2 was found equal to 110 Jy. Based on these numbers and the census of O-type stars of Moffat et al. (1991), Whiteoak & Uchida (1997) further argued that the Lyman continuum flux of the early-type stars could only explain the observed radio emission of RCW 49 if the distance were of order 2.3 kpc.

In this context, we emphasize that adopting a lower distance for the nebula and the cluster does not solve the issue of the missing ionizing photons. In fact, both, the radio flux and hence the required number of ionizing photons on the one hand and the bolometric luminosity of the stars on the other hand scale with the distance squared. Assuming a lower distance as was done by Whiteoak & Uchida (1997) would thus imply a drastic underluminosity of the stars compared to typical objects of the same spectral type. Therefore, the ionizing flux would also be reduced compared to the values for typical stars.

For a distance of 8.0 kpc, the number of Lyman continuum photons required to account for the total 0.843 GHz flux of RCW 49 and the flux of the shell near Westerlund 2 as quoted by Whiteoak & Uchida (1997) would be 11.5×10^{50} and $6.0 \times 10^{50}\,s^{-1}$, respectively. In a similar way, scaling the result of Churchwell et al. (2004) to our preferred distance estimate yields a minimum UV photon luminosity of $20.7 \times 10^{50}\,s^{-1}$ to account for the 5 GHz flux density of 335 Jy (as determined by Goss & Shaver 1970). We note that lower determinations of the 5 GHz flux can be found in the literature: 178.8 Jy (Smith et al. 1978) and 263.2 Jy (Kuchar & Clark 1997), which imply photon numbers in the range $11.1 - 16.3 \times 10^{50}\,s^{-1}$. On average, we find $(14.9 \pm 4.5) \times 10^{50}\,s^{-1}$. These numbers actually represent a lower limit on the ionizing flux since they neglect the possible leakage of some UV radiation from the nebula (see Churchwell et al. 2004) and they were estimated for a dust-free nebula using the formalism of Mezger et al. (1974). Near- and mid-IR images of the RCW 49 complex reveal however the existence of dust in this nebula, although the stellar winds and radiations of the O-type stars have cleared the region immediately surrounding Westerlund 2 (e.g. Conti & Crowther 2004 and Churchwell et al. 2004). Using the formalism of Smith et al. (1978) to account for the impact of dust, we estimate that about 58% of the UV continuum flux is actually used to ionize the nebula. As a result, the total number of Lyman photons required to maintain the ionization of RCW 49 would have to be $(25.7 \pm 7.9) \times 10^{50}\,s^{-1}$.

With the newly determined spectral types and bolometric luminosities at hand, we have evaluated the number of ionizing photons produced by the O-type stars of Westerlund 2. To this aim, we have scaled the numbers of Lyman ionizing photons emitted per second (Q_0) as tabulated by Martins et al. (2005a) by the ratio of the above determined bolometric luminosity divided by the 'typical' theoretical bolometric luminosity. For a distance of 8.0 kpc, the total number of Lyman ionizing photons produced by the twelve O-type stars in our sample amounts to $3.2 \times 10^{50}\,s^{-1}$. Assuming that stars in the spectral range O6.5 – O3 have masses between 28 and 60 $M_\odot$, and adopting a Salpeter IMF, we have estimated that Westerlund 2 should harbour about 20 stars with spectral types in the range O9.5 – O7 (masses of 15.5 – 28 $M_\odot$). These late O-type stars would contribute about $7 \times 10^{49}\,s^{-1}$ (i.e. $\sim$ 20% of the early-type O-stars) to the total number of Lyman ionizing photons. Adding the ionizing flux of the WR 20a pair of WN6ha stars ($1.45 \times 10^{50}\,s^{-1}$, Rauw et al. 2005) we arrive at a total of $5.4 \times 10^{50}\,s^{-1}$, i.e. a fifth of the photon flux required to explain the radio emission of RCW 49 (or slightly more than one third of the required flux if we neglect the impact of the dust). In Sect. 3.2, we noted that three stars of our sample (MSP 167, 175 and 203) might actually be somewhat earlier than their classification listed in Table 1. Assuming these objects to be of type O5, rather than O6, would increase the amount of ionizing photons by $1.5 \times 10^{49}\,s^{-1}$, i.e. by about 3%. This latter remark does certainly not alter our conclusion about the lack of a sufficient number of ionizing photons.

Of course, our estimate provides only a lower limit on the actual production of ionizing photons inside the RCW 49 complex. For instance, we have not included WR 20b in our account. This star was classified as WN7:h by Shara et al. (1999). By analogy with the ionizing fluxes of WN6ha stars in NGC 3603 (Crowther & Dessart 1998), the components of WR 20a (Rauw et al. 2005) and the models of Smith et al. (2002), we estimate that $\log(Q_0) \leq 50.0$. Thus this star alone cannot solve the issue of the missing ionizing photons. Some of the early-type stars might still be hidden from our view by the material of their natal cloud. Indeed, observations indicate that star formation is ongoing in Westerlund 2. Whitney et al. (2004) reported *Spitzer* IRAC near-IR colours of the stars in RCW 49 that are typical of a star formation region. They estimated the total number of young stellar objects to be $\sim$ 7000. Star formation occurs preferentially within $\sim 5'$ from the cluster core, where the stellar winds of the massive stars in Westerlund 2 have swept up gas and dust. This suggests that the ongoing star formation activity may be induced by the action of the early-type stars in Westerlund 2. The spectral energy distributions of two stars were fitted with models of B2 V and B5 V stars surrounded by accretion disks and a large envelope feeding the disk (Whitney et al. 2004, Churchwell 2005). However, these stars are apparently not massive enough to contribute significantly to the ionization of the nebula. If the predictions of stellar atmosphere models are correct, then we conclude that we must still be missing an important fraction of the early-type stars in RCW 49.

The influence of the early-type stars in the cluster core is not limited to the ionization of the nebula. The stellar winds of these stars also strongly impact on their surroundings. The signature of this process has been detected as diffuse X-ray emission with *Chandra* (Townsley et al. 2005). This feature is probably due to the thermalisation of the stellar winds either resulting from the collisions between the winds of individual early-type cluster members or from the shocks with the ambient interstellar medium. Townsley et al. (2005) found that this emission has temperatures between $kT \sim 0.8$ and 3.1 keV. Assuming a distance of 2.3 kpc, these authors inferred a total intrinsic (i.e. absorption corrected) X-ray luminosity of $3 \times 10^{33}\,erg\,s^{-1}$ over the 0.5 – 8.0 keV energy range. For a distance of 8.0 kpc, this X-ray luminosity becomes $3.6 \times 10^{34}\,erg\,s^{-1}$. From the temperatures and emission measures of the best-fit X-ray models proposed by Townsley et al. (2005), we estimate that a total thermal energy of $6.5 - 20.4 \times 10^{49}$ erg (for a filling factor of 0.1 and 1.0 respectively) is required to produce the observed diffuse X-ray emission.

Considering a Salpeter IMF and the typical masses of O-stars as tabulated by Martins et al. (2005a), we estimate that Westerlund 2 should contain about 4500 $M_\odot$ in the form of stars with masses between 1 and 120 $M_\odot$. We used the STARBURST99 code (v5.0; Leitherer et al. 1999, Vázquez & Leitherer 2005) to

estimate the total mechanical energy injected through the stellar winds. For an age of 2 Myr, no supernova explosion should have occured. However, the total wind luminosity should be about 5.4×10^{37} erg s^{-1} and the cumulative energy input from stellar winds would be about 3.6×10^{51} erg. This exceeds the thermal energy that produces the X-ray emission by more than one order of magnitude. Since RCW 49 is a blister-like structure, the latter result is not surprising. Recent models accounting for the effects of clumping indicate that the mass loss rates of O-type stars might have been overestimated and are probably lower by a factor 3 – 4 (e.g. Martins et al. 2005b, Bouret et al. 2005). Lower mass loss rates would imply a reduction of the cumulative energy input from the stellar winds, although the latter number would still exceed the thermal energy responsible for the X-ray emission by at least a factor of a few.

In summary, while the currently known population of O-type stars in Westerlund 2 does apparently not provide enough ionizing photons to explain the radio emission of RCW 49, the dynamical energy provided by the stellar winds of these stars seems sufficient to explain the observed diffuse X-ray emission.

6. Summary and conclusions

Our spectroscopic observations indicate that the core of Westerlund 2 harbours at least twelve O-type stars of spectral type earlier than O7, the earliest object being of type O3 V((f)). These spectral types are significantly earlier than previous classifications. The spectro-photometric distance of these O-type stars is found to be 8.3 ± 1.6 kpc. This number is in excellent agreement with the result obtained from the study of the B and V light curve of the very massive Wolf-Rayet binary WR 20a and the distance based on ZAMS fitting of the UBV photometry of Moffat et al. (1991). The weighted distance of Westerlund 2 and WR 20a amounts to 8.0 ± 1.4 kpc. This distance determination implies that the radio emission of the giant H II region RCW 49 must be larger than previously estimated. Despite the earlier spectral types inferred in this paper, the currently known population of early-type stars in Westerlund 2 provides only between one fifth and one third of the ionizing photons required to account for the radio emission of RCW 49. Future observations should aim at establishing a complete census of the O-type stars population in RCW 49, although our colour-magnitude diagram (Fig. 7) indicates that at least within the field of view of the ANDICAM instrument, there are only a few candidates for early O-type stars other than those objects we have classified here.

None of the early O-type stars in the cluster core displays a significant photometric variability on time scales from a day to a month and a half. None of these objects displays an obvious signature of multiplicity in our snapshot spectra. However, we have identified three eclipsing binaries (in addition to WR 20a) that are probably late O or early B-type stars belonging to the Westerlund 2 cluster. This suggests that there might in fact be many more (non-eclipsing) binaries. A spectroscopic follow-up of these systems as well as of some of the O-type stars that appear somewhat overluminous (MSP 18, 183 and 203) would bring precious information on their nature as well as on the general properties of the cluster.

Finally, we emphasize that the results reported here indicate that WR 20a actually belongs to the Westerlund 2 cluster and further suggest that the cluster contains enough massive stars to explain the location of the Wolf-Rayet binary through the effect of a dynamical interaction scenario as suggested by Rauw et al. (2005).

Appendix A: Uncertainties of the distance determinations

The distance of WR 20a stems from the luminosity determined in the light curve analysis. Under the assumptions made in Sect. 4.1, the radii of the stars in WR 20a are rather robust. The issue of the effective temperature is a bit trickier. This parameter is essentially determined by the spectroscopic analysis with a non-LTE model atmosphere code (Rauw et al. 2005). The strengths of the N III, N IV and N V features provide the most stringent constraints. The model atmosphere code used by Rauw et al. (2005) assumes a spherically symmetric star. In a binary system such as WR 20a, the stars are however not spherical. Their shape is rather set by the Roche potential. Moreover, the gravity varies over the stellar surface, being maximum near the poles and minimum on the portion of the surface facing the companion star. As a result, gravity darkening renders the surface temperature non-uniform: the star is hotter near the poles and cooler near the equator. Adopting the fitting parameters of the light curve shown in Fig. 5 and assuming a gravity darkening exponent $\beta = 1.0$, we estimate that the temperature near the primary's poles should be about 1900 K hotter than the average effective temperature (43000 K), while it would be lower by $\sim$ 5300 K over the part of the stellar surface facing the secondary. Whilst these numbers may be overestimated, for instance because we neglected reflection effects, they nevertheless suggest that part of the difficulties encountered when trying to fit simultaneously N III, N IV and N V lines might actually arise from a non-uniform surface temperature distribution in a close binary system. Concerning the distance of WR 20a, we estimate that the effect of gravity darkening could produce a 4 – 5% uncertainty on the effective temperature which would then correspond to a 10% margin on the distance.

Alternatively, our distance estimate of the early O-type stars in Westerlund 2 could be biased. In this respect, we note the rather large dispersion (0.65 mag) of our spectro-photometric distance moduli. The primary suspects to bias our result would be binary systems. However, our photometric monitoring campaign failed to reveal any eclipsing binary system among these O-type stars with a period between a few days and a few weeks. Furthermore, we do not find evidence for multiplicity in our spectroscopic data either, although these snapshot data are certainly not suited to provide firm constraints on the number of spectroscopic binaries. Therefore, it seems unlikely that the majority of the O-type stars that we have observed are binaries. If we nevertheless consider that some of them might be multiple objects, the smaller distance moduli of MSP 18, 183 and 203 make them the best binary candidates. Discarding these three objects from the mean yields $DM = 14.72 \pm 0.54$ (1-σ standard deviation). Note that the dispersion about the mean remains quite large, though comparable to the cosmic scatter of absolute magnitudes based on the spectral types.

Another possible reason for the dispersion of DM could be that some of the main-sequence O-stars are slightly evolved off the main sequence and are thus intrinsically brighter than 'typical' main-sequence stars. Our luminosity class determination based on the strength of the He II λ 4686 line suggests that some of the stars are indeed giants. Those stars that have an EW of the He II λ 4686 line at the border-line between the two luminosity classes are labelled with a V-III luminosity class in Table 1. For these objects, we evaluated the distance by comparison with an interpolation of the main-sequence and giant absolute magnitudes of Martins & Plez (2006). Some other objects could have

intermediate evolutionary stages and might thus be responsible for part of the dispersion.

Finally, as suggested in Sect. 3.1, some part of the reddening that affects the stars in Westerlund 2 might be produced by material from the parental molecular cloud. Therefore, we cannot rule out a priori that, at least for this material, R_V differs from the canonical value of 3.1. In fact, in some clusters with a higher mean density interstellar medium, it has been argued that R_V could range from 3 to 6 (see e.g. Turner 1994). If that were the case for Westerlund 2, all the distance determinations in this paper would have to be revised downwards. To determine the value of R_V requires at least UBV photometry. Since we do not have our own new U-band measurements, we would have to rely on the data of Moffat et al. (1991) or Carraro & Munari (2004). Unfortunately, both data sets seem to have problems (see Sect. 2.1) and their U magnitudes disagree. Our attempts to use these archive photometric data failed to produce conclusive results and we have to conclude that the reddening law cannot be quantified with the data currently available.

Acknowledgements. We are grateful to the collaborators of the SMARTS consortium for obtaining the data of our photometric monitoring campaign. We thank Chang-Hui Rosie Chen (UIUC) for providing us with the STARBURST99 simulations, Prof. David Turner (Saint Mary's University) for discussion about the reddening law and the anonymous referee for his/her comments that helped us improve our manuscript. The Liège group acknowledges financial support from the FNRS (Belgium), as well as through the XMM and INTEGRAL PRODEX contract and contract P5/36 PAI (Belspo). AFJM acknowledges financial support from NSERC (Canada) and FQRNT (Québec).

References

Bonanos, A.Z., Stanek, K.Z., Udalski, A., et al. 2004, ApJ, 611, L33
Bouret, J.-C., Lanz, T., & Hillier, D.J. 2005, A&A, 438, 301
Carraro, G., & Munari, U. 2004, MNRAS, 347, 625
Churchwell, E., GLIMPSE Team 2005, Rev. Mex. Astron. Astrof. Serie de Conferencias, 23, 53
Churchwell, E., Whitney, B.A., Babler, B.L., et al. 2004, ApJS, 154, 322
Conti, P.S. 1973, ApJ, 179, 181
Conti, P.S., & Crowther, P.A. 2004, MNRAS, 355, 899
Crowther, P.A., & Dessart, L. 1998, MNRAS, 296, 622
Goss, W.M., & Shaver, P.-A. 1970, Aust. J. Phys. Astrophys. Suppl., 14, 1
Gosset, E., Royer, P., Rauw, G., Manfroid, J., & Vreux, J.-M. 2001, MNRAS, 327, 435
Heck, A., Manfroid, J., & Mersch, G. 1985, A&AS, 59, 63
Kuchar, T.A., & Clark, F.O. 1997, ApJ, 488, 224
Landolt, A.U. 1992, AJ, 104, 340
Leitherer, C., Schaerer, D., Goldader, J.D., et al. 1999, ApJS, 123, 3
Manfroid, J. 1993, A&A, 271, 714
Manfroid, J. 1995, A&AS, 113, 587
Manfroid, J., Royer, P., Rauw, G., & Gosset, E. 2001, in *Astronomical Data Analysis Software and Systems X*, eds. F. Harnden, F. Primini, & H. Payne, ASP Conf. Ser., 238, 373
Martins, F., Schaerer, D., & Hillier, D.J. 2005a, A&A, 436, 1049
Martins, F., Schaerer, D., Hillier, D.J., Meynadier, F., Heydari-Malayeri, M., & Walborn, N. 2005b, A&A, 441, 735
Martins, F., & Plez, B. 2006, A&A, in press
Mathys, G. 1988, A&AS, 76, 427
Mezger, P.G., Smith, L.F., & Churchwell, E. 1974, A&A, 32, 269
Moffat, A.F.J., & Vogt, N. 1975, A&AS, 20, 125
Moffat, A.F.J., Shara, M.M., & Potter, M. 1991, AJ, 102, 642
Pamyatnykh, A.A. 1999, Acta Astronomica, 49, 119
Rauw, G., De Becker, M., Nazé, Y., et al. 2004, A&A, 420, L9
Rauw, G., Crowther, P.A., De Becker, M., et al. 2005, A&A, 432, 985
Rodgers, A.W., Campbell, C.T., & Whiteoak, J.B. 1960, MNRAS, 121, 103
Russeil, D. 2003, A&A, 397, 133
Schaller, G., Schaerer, D., Meynet, G., & Maeder, A. 1992, A&AS, 96, 269
Schmidt-Kaler, T. 1982, in *Physical Parameters of the Stars*, Landolt-Börnstein Numerical Data and Functional Relationships in Science and Technology, Group VI, vol. 2b
Smith, L.F., Biermann, P., & Mezger, P.G. 1978, A&A, 66, 65
Smith, L.J., Norris, R.P.F., & Crowther, P.A. 2002, MNRAS, 337, 1309
Shara, M.M., Moffat, A.F.J., Smith, L.F., Niemela, V.S., Potter, M., & Lamontagne, R. 1999, AJ, 118, 390
Sterken, C., & Breysacher, J. 1997, A&A, 328, 269
Stetson, P.B. 1987, PASP, 99, 191
Townsley, L., Feigelson, E., Montmerle, T., Broos, P., Chu, Y.-H., Garmire, G., & Getman, K. 2005, in *X-ray and Radio Connections*, eds. Sjouwerman L.O. & Dyer, K.K., http://www.aoc.nrao.edu/events/xraydio/meetingcont/3.4_townsley.pdf
Turner, D.G. 1994, RevMexAA, 29, 163
Uzpen, B., Kobulnicky, H.A., Olsen, A.G. 2005, ApJ, 629, 512
Vázquez, G.A., & Leitherer, C. 2005, ApJ, 621, 695
Walborn, N.R., & Fitzpatrick, E.L. 1990, PASP, 102, 379
Walborn, N.R., Howarth, I.D., Lennon, D.J., et al. 2002, AJ, 123, 2754
Westerlund, B. 1961, Arkiv for Astronomi, 2, 419
Whiteoak, J.B.Z., & Uchida, K.I. 1997, A&A, 317, 563
Whitney, B.A., Indebetouw, R., Babler, B.L., et al. 2005, ApJS, 154, 315

1.5.4 TeV γ-ray emission from WR 20a and Westerlund 2

Very recently, an extremely interesting result was reported by the consortium that operates the HESS Cherenkov telescopes. In fact, from March to July 2006, the HESS array acquired 13 hours of good-quality data on the RCW 49 complex. This led to the detection (at the 9-σ level) of a TeV source in the vicinity of WR 20a and the Westerlund 2 cluster (Aharonian et al. 2007, O. Reimer 2006, private communication; see Fig. 1.22). This source, named HESS J1023 575, was found to be slightly extended (0.2° accounting for the size of the PSF of the HESS telescopes). At a distance of 8 kpc, this corresponds to a linear size of about 28 pc. While this is much larger than the dimension of the wind-wind interaction zone of WR 20a, it is of the order of the expected size of a wind-blown bubble. Shocks and turbulence inside the bubble or at its interface with the surrounding medium could accelerate particles and the TeV emission could then be produced by hadronic collisions. Aharonian et al. (2007) attribute the position and the morphology of the source to the blister-like structure (Whiteoak & Uchida 1997) where the bubble powered by WR 20a and the other early-type stars in the cluster opens up and the hot gas expands into the low-density interstellar medium.

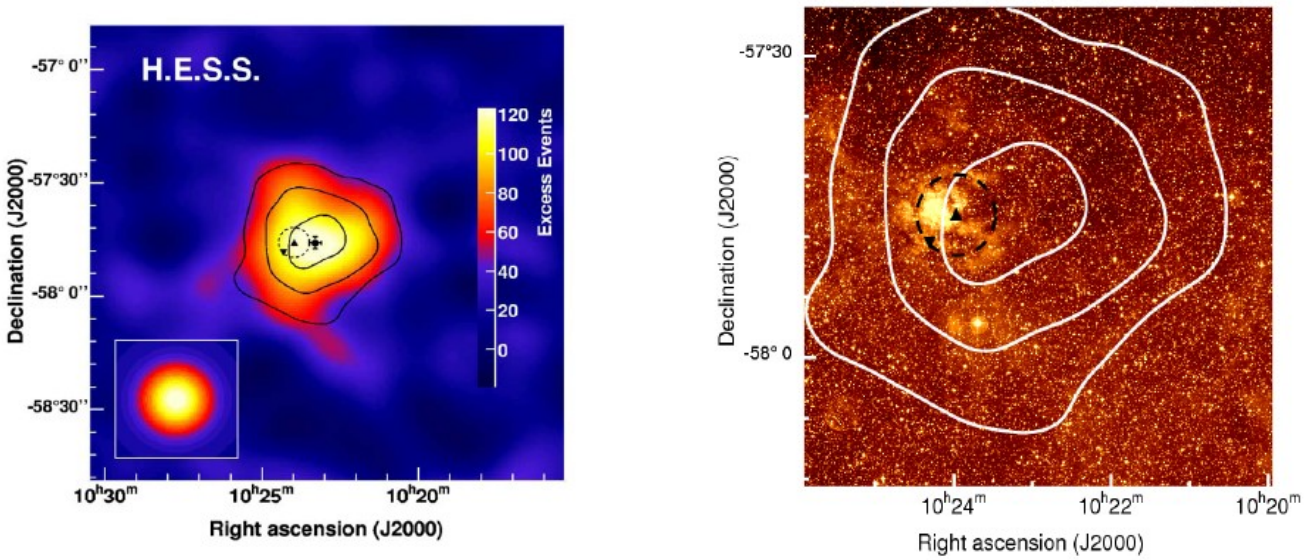

Figure 1.22: Left: HESS TeV map of RCW 49 (Aharonian et al. 2007). The contours correspond to significance levels of 5, 7 and 9 σ. The centroid of the TeV source is shown by the black dot with error bars. The upright and downright triangles indicate the positions of WR 20a and WR 20b respectively. The insert in the lower left corner illustrates the PSF of the HESS array. Right: HESS significance contours overlaid on a B-band image from the Palomar Observatory Sky Survey.

1.6 Concluding remarks on massive binaries

In this chapter, I have presented several results we obtained on individual massive binary systems. Most of these objects are rather young systems where the properties of the stars have not (yet) been affected by mass exchange through Roche lobe overflow. Such binaries are extremely useful to constrain the general properties (masses, radii, luminosities,...) of early-type stars and hence to build an empirical mass-luminosity relation in this rather poorly known part of the Hertzsprung-Russell diagram. As most O-type

stars appear in young open clusters, the study of spectroscopic and eclipsing binaries further allows to derive constraints on the distances of these clusters which are essentially model independent. However, there is still a lot of work to be done: the number of data points in the empirical mass-luminosity relation still needs to be increased and we further need to improve our understanding of mass transfer in early-type binaries. These objectives can only be achieved through additional observational efforts with state-of-the-art high-resolution facilities. While these studies may at first sight appear as boring routine programs, they are actually of fundamental importance and can sometimes reveal quite surprising and unexpected results.

Indeed, it was more or less by chance that during one of our spectroscopic campaigns, we discovered the multiplicity of WR 20a, the most massive binary system to date with well determined masses. While this was not our primary objective a that time, it is clear that a system such as WR 20a is indeed of fundamental importance in the context of massive stars. One important message that its discovery has told us is that one should not restrict the search for extremely massive Population I stars to the sole group of O2 – O3 stars. In fact, some of the most massive objects are likely to display a Wolf-Rayet cloak – or more precisely a WNL spectrum with hydrogen lines in absorption – while they are still on the main sequence. It is probably fair to say that our discovery triggered new interest in the search for the most massive stars as was nicely illustrated by various presentations at the December 2006 workshop in Cariló (Argentina). At the time of writing of this habilitation thesis, several teams are indeed monitoring a number of potential candidates such as Pismis 24-1 (a visual pair of spectral types O3.5 If* + O4 IIIf$^+$, the latter star likely being itself a spectroscopic binary, Maíz Apellániz et al. 2007), HD 93129A (another tight visual binary of type O2 If*, Maíz Apellániz et al. 2007), NGC 3603/A1 (WNLha, Moffat 2007), R 145 (WNLha, Moffat 2007) as well as several O2-O3 stars in the core of R 136 in 30 Dor (Morrell et al. 2007). These ongoing campaigns may eventually reveal another 'record-holder' even more massive than the stars in WR 20a.

Another important aspect of the study of early-type binaries is the phase-locked profile variability that is seen in their emission lines. While this feature was already well known for Wolf-Rayet stars, we now realise that quite similar effects occur also in O + O binaries with sufficiently strong winds. The main contributions in this field have come from the work of the Atlanta and Liège groups. Beyond the 'simple' effect of blendings, this variability also tells us a lot about the interactions that exist between the winds of the binary components. The previous subsections have illustrated what techniques can be used in practise to study these effects. However, while the observational results can be nicely represented by Doppler maps or grey-scale techniques, a consistent theoretical modelling of the effects of wind interactions on emission lines in the optical domain is still lacking. Such models will be extremely helpful for the interpretation of the observational results and should be developed as soon as the progress of computing facilities allows to overcome the numerical limitations of current hydrodynamical models.

Chapter 2

X-ray emission from colliding wind binaries

L'essentiel est invisible pour les yeux.

Antoine de Saint-Exupéry, *Le Petit Prince*

In this chapter, I report and discuss the X-ray signature of wind-wind interactions in several early-type binaries. Since the topic of colliding winds was already introduced in Sect. 1.1, the introduction of this chapter rather addresses the general issue of X-ray emission from early-type stars (including both single stars and binary systems).

2.1 X-ray emission from early-type stars

To introduce the topic of X-ray emission from early-type stars, I reproduce hereafter a review paper that I presented at the ESA conference "The X-ray Universe 2005" held in El Escorial (Spain) in September 2005 (Rauw 2006) as well as a review presented at the 2nd MSSL workshop on "High Resolution X-ray Spectroscopy: towards *XEUS* and *Con-X*" held at the Mullard Space Science Laboratory (United Kingdom) in March 2006 (Rauw et al. 2006).

7

X-RAY EMISSION FROM EARLY-TYPE STARS: NEW RESULTS AND NEW CHALLENGES

Gregor Rauw*

Institut d'Astrophysique, Université de Liège, Allée du 6 Août, 17, Bât B5c, B-4000 Liège (Sart Tilman), Belgium

ABSTRACT

Early-type stars of spectral types O and Wolf-Rayet are moderately bright X-ray sources. The X-ray emission is usually attributed to a shock-heated plasma. In single stars the shocks could arise from the intrinsic instability of the stellar winds, whilst in binary systems, the collision of the two stellar winds can provide an additional emission. *XMM-Newton* and *Chandra* have observed a number of these stars, obtaining spectra of unprecedented quality. These observations provide new insight into the properties of the hot plasma in early-type stars winds, but raise also new questions that challenge our 'standard' model for the X-ray emission of hot stars. In this review, I highlight some of the most important results obtained over the last six years.

Key words: binaries: general – Stars: early-type – Stars: Wolf-Rayet – Stars: winds, outflow – X-rays: stars.

1. WHAT WE (THOUGHT WE) KNEW

O stars are massive ($\geq 20\,M_\odot$), hot ($T_{\rm eff} \simeq 30\,000 - 90\,000$ K) and luminous ($L/L_\odot \simeq 3\times10^4 - 3\times10^6$) objects that play a key role in many astrophysical contexts. Among the most remarkable features of these early-type stars are their tremendous stellar winds that associate large terminal velocities ($v_\infty \sim 1000 - 3000\,{\rm km\,s^{-1}}$) along with high mass loss rates (of the order of $\dot{M} \simeq 10^{-6} - 10^{-4}\,M_\odot\,{\rm yr}^{-1}$). Wolf-Rayet (WR) stars are believed to represent a late stage of the evolution of massive O stars and the winds of WR stars display a composition resulting from nuclear burning of hydrogen (WN subclass) or helium (WC subclass).

X-ray emission from early-type stars was first discovered serendipitously with *EINSTEIN* (Harnden et al. (1979), Seward et al. (1979)). Subsequent studies with *EINSTEIN* and *ROSAT* indicated that the observed X-ray luminosity of O-type stars roughly scales with their bolometric luminosity as $L_X/L_{bol} \approx 10^{-7}$ (e.g. Berghöfer et al. (1997) and references therein).

Various attempts have been made to explain the X-ray emission from single O and WR stars. By analogy with late-type stars, early models involved a corona at the base of the wind (e.g. Cassinelli & Olson 1979). However, from observations of high-mass X-ray binaries harbouring a neutron star orbiting near the surface of an O-type star (e.g. HD 153919), it is known that the stellar winds of O-type stars are optically thick to soft X-rays. Therefore, any X-ray emission from a base corona of an early-type star should exhibit a dramatic absorption by the cool stellar wind below 1 keV (see the discussion in Pollock & Oskinova 2002). Low and medium dispersion X-ray spectroscopy of massive stars with *ROSAT* and *ASCA* revealed instead relatively soft thermal spectra with little evidence for strong circumstellar absorption. Furthermore, the lack of an outer convective zone in hot stars and the lack of a correlation between the X-ray luminosity and the stellar rotation rate suggest that X-rays of early-type stars are not produced by magnetic activity associated with a solar-type dynamo.

Alternatively, in what has become now the 'standard' model for X-ray emission from single early-type stars, the X-rays are thought to arise from a shock-heated plasma distributed throughout the stellar wind (e.g. Lucy (1982)). In fact, the winds of O-type stars are driven by the radiation pressure of the numerous UV spectral lines, and this mechanism is intrinsically unstable. These instabilities lead to hydrodynamic shocks that could heat the post-shock material to temperatures consistent with the ~ 0.5 keV emission observed for most presumably single early-type stars. The most recent models of this kind yield predicted X-ray luminosities that are in rough agreement with the observed values (see Feldmeier et al. (1997) and references therein).

One difficulty of these wind shock models is that they predict a strong X-ray variability on rather short timescales which has so far not been observed for single O-stars (Berghöfer & Schmitt, 1994). Another shortcoming of this model is that simple theoretical considerations indicate that the most natural scaling of the X-ray luminosity should be with the wind density parameter $\dot{M}/v_\infty$ rather than with L_{bol} (Owocki & Cohen, 1999). Owocki & Cohen (1999) indeed found that a rather subtle balance of X-ray absorption and emission is required to account for the empirically inferred L_X/L_{bol} scaling.

*Research Associate FNRS (Belgium)

Interestingly, Wolf-Rayet stars do not show a clear empirical correlation between L_X and either L_{bol} or $\dot{M} v_\infty$ (Wessolowski, 1996). Ignace & Oskinova (1999) interpreted the lack of a clear scaling relation as a result of the larger optical depth in the stellar winds of WR stars compared to O-star winds. On average, presumably single WN stars tend to be slightly more X-ray luminous than presumably single WC stars. In addition, WR binaries are found to be X-ray brighter than single WR stars (Pollock, 1987).
In a similar way, the first extensive surveys of early-type stars with *EINSTEIN* revealed that O + O binary systems display systematically larger L_X/L_{bol} ratios than single O stars (Chlebowski & Garmany, 1991). This X-ray 'overluminosity' of massive binaries is usually attributed to the emission from a plasma heated by the collision of the stellar winds of the two stars (e.g. Stevens et al. (1992) and references therein). In some cases, massive binaries exhibit a phase-locked modulation of their X-ray flux (e.g. Willis et al. (1995), Corcoran (1996)) that reflects either the variation, during the orbital motion, of the circumstellar opacity along the observer's sightline through the winds or the variation of the separation between the stars in eccentric systems.

2. WHAT WE HAVE LEARNED

2.1. Line diagnostics

Previous X-ray observatories lacked the high-resolution facilities and the sensitivity to study the spectra of early-type stars in great detail. With the launches of *Chandra* and *XMM-Newton*, both equipped with grating spectrometers, it became possible for the first time to study individual lines in the X-ray spectra of these stars. Two types of line diagnostics are commonly used to derive constraints on the properties of the X-ray emitting plasma: the ratio of line intensities in helium-like ions and the detailed morphology of individual lines.
In helium-like ions, the transitions from the $n = 2$ levels to the ground level give rise to a triplet consisting of a *resonance* ($1s2p\,^1P_1 \rightarrow 1s^2\,^1S_0$), an *intercombination* ($1s2p\,^3P_1 \rightarrow 1s^2\,^1S_0$) and a *forbidden* ($1s2s\,^3S_1 \rightarrow 1s^2\,^1S_0$) line. In the coronae of late-type stars, the ratio $\mathcal{R} = f/i$ of the intensities of the forbidden and intercombination lines is essentially sensitive to the electron density. However, in a hot plasma surrounding an early-type star, the stellar UV radiation field introduces a radiative coupling between the upper level of the forbidden line and the upper level of the intercombination lines. In this way, $\mathcal{R}$ is determined by the UV radiation field and provides a sensitive diagnosis of the dilution factor $w(r) = \frac{1}{2}\left(1 - \sqrt{1 - \left(\frac{R_*}{r}\right)^2}\right)$ of the UV radiation field, and hence of the distance r from the centre of the star where the X-rays are emitted (e.g. Blumenthal et al. (1972), Porquet et al. (2001)). High-quality grating spectra therefore yield strong constraints on the location of the X-ray emitting plasma in a stellar wind. In fact, X-ray line emission is proportional to the density squared: in a stellar wind with outwardly decreasing density, it thus occurs as near to the stellar surface as possible. Therefore, if the X-ray emitting material is distributed throughout the wind, the X-ray lines should form near the radius of monochromatic optical depth unity $r(\tau_\lambda = 1)$.
Crucial information about the origin of the X-ray emission can also be obtained from the shape of the strongest emission lines. Various predictions have been made in the context of the 'standard' wind-shock model. For instance, X-ray emission lines formed in an optically thin plasma[1] (assuming a uniform distribution of X-ray emitters and a constant wind speed) without photoelectric absorption by the cool wind, are expected to show a flat-topped profile (e.g. Feldmeier et al. (2003)). When the photoelectric absorption by the wind is included in the profile calculation, it mostly affects the emission from the material that moves away from us (Owocki & Cohen, 2001), thus leading to blue-shifted line profiles. Ignace & Gayley (2002) investigated the effect of line opacity on the line profiles. For strong lines of abundant metals, newly created photons may undergo resonance scattering in the same line. This leads to broad emission profiles that have blue-shifted centroids, but are considerably less asymmetric than in the optically thin case. Feldmeier et al. (2003) investigated the effects of absorption in a fragmented wind. In fact, as a result of the same instabilities that are thought to produce the X-ray emission, the stellar wind is expected to be rather clumpy, instead of being smooth and homogeneous. Once more, it was found that the red-shifted part of the profile should be heavily absorbed while the blue-shifted part remains flat-topped. Interestingly, if the X-rays were emitted at the reverse shock on the starward side of the fragments, one would expect absorption by the natal fragment, leading to a zero flux at the line centre. This should then produce a double-peaked profile, which, however, has never been observed so far.

The high-resolution X-ray spectra of O-type stars that have been obtained so far show a variety of situations. The two most extreme cases are probably ζ Pup and θ^1 Ori C.
The spectrum of ζ Pup (O4Ief) displays strongly broadened (1000 – 1500 km s^{-1}), asymmetric and blue-shifted (e.g. 400 ± 80 km s^{-1} for O VIII Lyα) lines (Kahn et al. (2001), Cassinelli et al. (2001)). No photoelectric absorption edges with $\tau_0 \geq 0.5$ were detected in the RGS spectrum, indicating that the X-rays cannot be concentrated at the base of the wind. The $\mathcal{R} = f/i$ ratio of the S XV, Si XIII, Mg XI, Ne IX and O VII helium-like triplets suggest formation radii that are consistent with their associated radius of optical depth unity (Cassinelli et al. (2001), Kahn et al. (2001)). All these results are in rather good agreement with the expectations for the 'standard' wind-shock model (Kramer et al., 2003), thereby making ζ Pup the prototype of an O-star for which the X-rays probably arise from shocks distributed throughout the wind.

[1] Here it is important to distinguish the optical depth of the hot X-ray emitting plasma from that of the overlying cool wind. The latter is mainly due to photoelectric absorption.

Kramer et al. (2003) presented fits of individual X-ray lines, finding that there is less attenuation of the red wings than expected for a smooth overlying cool wind. This is tentatively attributed to the clumping of the stellar wind.

An alternative to the wind-shock scenario comes from the magnetically channeled wind shock model, originally designed for the special case of θ^1 Ori C (Babel & Montmerle (1997), ud-Doula & Owocki (2002)). In fact, a large-scale magnetic field may confine the stellar wind into the equatorial region. The wind confinement is measured by the so-called confinement parameter $\eta = (B_0^2\, R_*^2)/(\dot{M}\, v_\infty)$ where B_0 is the equatorial field strength, all other parameters having their usual meaning. For $\eta \ll 1$, the field is stretched out by the wind, whereas for $\eta \gg 1$, the wind is confined by the magnetic field. In the latter case, high velocity flows from the two hemispheres meet near the magnetic equator producing a head-on collision that heats the plasma to temperatures much higher than typically expected for single stars in the 'standard' model. Gagné et al. (2005) discuss four *Chandra* grating observations of the oblique magnetic rotator θ^1 Ori C (O4-6 Vp), that sample its rotational cycle. In this star, the strong dipole magnetic field ($B_0 = 530$ G implying $\eta = 7.5$, Donati et al. (2002), Gagné et al. (2005)) is inclined by $\sim 45°$ with respect to the rotation axis. As the star rotates, our viewing angle towards the confined wind changes, resulting in a modulation of the observable X-ray flux (Gagné et al., 2005). The four high-resolution spectra of θ^1 Ori C reveal rather narrow spectral lines with almost constant line widths, whilst the f/i ratios of the He-like ions indicate that the hot plasma must be located quite close to the stellar photosphere. All these features as well as the temperature and total luminosity of the X-ray plasma are extremely well reproduced by the magnetically channeled wind model (Gagné et al., 2005).

Intermediate situations between ζ Pup and θ^1 Ori C were found for several other O-type stars.
For instance, the RGS spectrum of the O4 V((f$^+$)) star 9 Sgr is quite similar to that of ζ Pup, showing broad blue-shifted Lyα lines of Ne X, O VIII and to some extent N VII (Rauw et al. (2002b), see Fig. 1). While it is now established that 9 Sgr is indeed a long-period binary system (Rauw et al., 2005a), at least the bulk of its soft X-ray emission likely arises in the wind of the primary component of the system. Indeed, the X-ray spectrum is dominated by a rather soft thermal emission ($kT_1 \sim 0.26$ and $kT_2 \sim 0.70$ keV). The EPIC spectrum exhibits also a hard tail which could be either thermal ($kT_3 \geq 1.5$ keV) or non-thermal emission ($\Gamma \geq 2.9$) and arises most probably in the wind interaction zone (Rauw et al., 2002b).
ζ Ori (O9.7 Ib) was observed with the gratings onboard *Chandra* (Waldron & Cassinelli, 2001). The spectral lines are broadened to 900 ± 200 km s^{-1}, but unlike the situation in ζ Pup, they are symmetric and show no blueshift. The He-like triplets of O VII, Ne IX and Mg XI indicate that these lines are produced high in the wind. On the other hand, the Si XIII f/i ratio indicates that the latter triplet forms very close to the stellar surface. This is surprising since the wind velocity should be too small

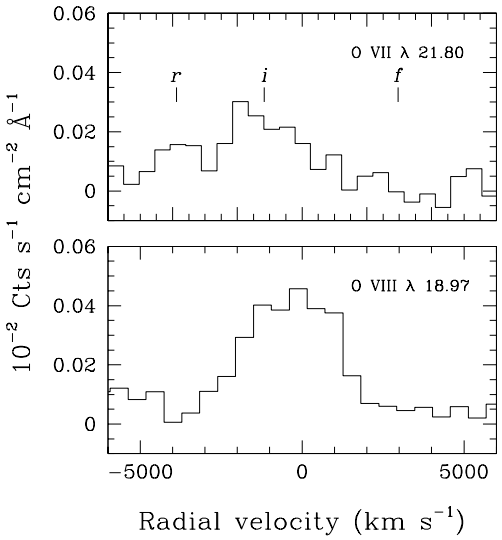

Figure 1. O VII *and O* VIII *lines in the RGS spectrum of 9 Sgr. Note the broadening of the O* VIII *Ly* α *line and the absence of the* f *component in the He-like triplet (Rauw et al. 2002b).*

to produce a shock jump so close to the star. Again, it is found that the X-ray emission lines originate primarily from just above $r(\tau_\lambda = 1)$. However, the shape of the lines is not that expected for a shock-heated plasma distributed throughout the wind. Waldron & Cassinelli (2001) therefore propose a composite model involving wind shocks as well as some magnetic confinement of turbulent hot plasma in a non-symmetric wind.
In the spectrum of δ Ori (O9.5 II + B0.5 III + ...), the lines are broadened to only 430 ± 60 km s^{-1} (HWHM), which is much less than $v_\infty \simeq 2000$ km s^{-1} (Miller et al., 2002a). The characteristic wind optical depth of the O9.5 II stellar wind is intermediate between those of ζ Ori and ζ Pup and one would thus expect to observe line profiles intermediate between these two stars. However, the lines are narrow, essentially unshifted and symmetric. Either the wind is porous or the mass loss rate has been overestimated. An alternative explanation could be that the X-ray emission is dominated by the colliding wind region in this multiple system. The shocked material would be roughly at rest with respect to the observer, thus explaining the narrow lines. Furthermore, most of the X-ray emission would suffer similar wind absorption (leading to symmetric lines). However, in such a configuration, one would expect to see eclipses in the X-ray light curve, which is not the case (Miller et al., 2002b).

2.2. Colliding wind binaries

As pointed out in the introduction, early-type binaries are often more X-ray luminous than what is expected from their bolometric luminosity (see also Fig. 2). If the winds

reach rather high pre-shock velocities, the X-ray emission produced in a wind interaction is a priori expected to be quite hard. In addition, the changing optical depth along the line of sight and/or the changing separation between the two stars can lead to a substantial phase-locked variability of the flux level. A key parameter of a colliding wind interaction is the efficiency of radiative cooling. In close binary systems where the densities in the wind interaction zone are high, the shock-heated plasma cools down rapidely via radiative recombination. In wide binary systems or binaries with low density winds, radiative cooling is much less efficient: the plasma cools only through adiabatic expansion and the resulting X-ray emission is expected to scale roughly as $1/d$, where d is the orbital separation between the two components (Stevens et al., 1992).

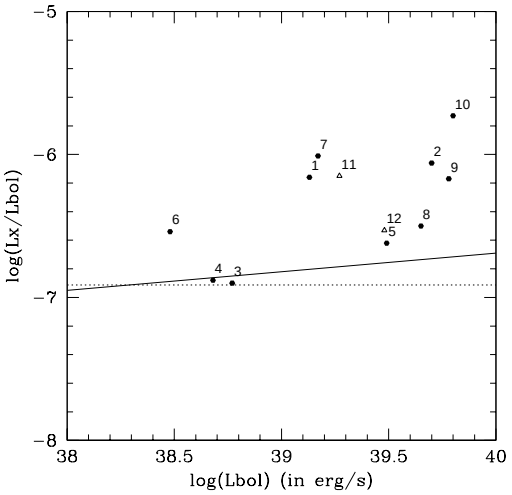

Figure 2. $\log(L_X/L_{bol})$ *(in the 0.5 – 10 keV energy range) for a number of O-type binaries as a function of* $\log L_{bol}$. *All data were obtained with XMM-Newton. The filled dots stand for binary stars: 1 = HD 47129 (Linder & Rauw 2005), 2 = HD 93403 (Rauw et al. 2002a), 3 = HD 152218 and 4 = HD 152219 (Sana et al. 2005b), 5 = HD 152248 (Sana et al. 2004), 6 = CPD-41° 7742 (Sana et al. 2005a), 7 = HD 159176 (De Becker et al. 2004a), 8 = 9 Sgr (Rauw et al. 2002b), 9 = HD 167971 (De Becker et al. 2005), 10 = Cyg OB2 #8a (De Becker & Rauw 2005). Open triangles indicate two suspected binaries: 11 = HD 108 (Nazé et al. 2004a) and 12 = HD 168112 (De Becker et al. 2004b). The solid and dashed lines yield the empirical scaling relations of Berghöfer et al. (1997) and Sana et al. (2005b) respectively.*

XMM-Newton has gathered phase-resolved X-ray spectroscopy of several O star binaries spanning a wide range of stellar wind parameters as well as orbital periods, thereby providing a more detailed description of the colliding wind phenomenon.

The early-type binary with the shortest orbital period that has been (almost) completely covered by *XMM-Newton* is the eclipsing system CPD$-41°$ 7742 (O9 V + B1-1.5 V, $P_{orb} = 2.44$ days, Sana et al. (2005a)). The light curve shows a broad occultation as well as a narrow eclipse respectively when the secondary or the primary star is in front. Sana et al. (2005a) interpreted the main features of this light curve with a simple geometrical model where the primary wind crashes into the photosphere of the secondary.

Six phase-resolved *XMM* observations of HD 152248 (O7.5 III(f) + O7 III(f), $P_{orb} = 5.8$ days, $e = 0.13$) were analysed by Sana et al. (2004). The EPIC spectra are surprisingly soft ($kT \leq 0.71$ keV), most probably because the winds collide well before they have reached their terminal velocities. The flux of this system displays an asymmetric modulation with phase, which is clearly a phase-locked phenomenon as confirmed by archive *ROSAT* data. This variation is most probably due to the changing optical depth along our line of sight towards the wind interaction zone (Sana et al., 2004).

With an orbital period of 15 days, the eccentric ($e = 0.23$) system HD 93403 (O5.5 I + O7 V) provides an interesting illustration of both the effects of the changing optical depth and the changing orbital separation. Indeed, using four *XMM* pointings, Rauw et al. (2002a) found that the soft X-ray emission is essentially modulated by the opacity of the primary star, while the flux at higher energies varies roughly as $1/d$, pretty much as expected for a shock producing a roughly adiabatic post-shock plasma.

De Becker et al. (2004a) investigated an X-ray spectrum of the short period binary HD 159176 (O7 V + O7 V, $P_{orb} = 3.37$ days). The EPIC spectrum could be fitted by a model consisting of two rather soft thermal components (0.2 and 0.58 keV) along with a non-thermal power-law component with a photon index of $\Gamma \sim 2.5$. The latter component could be produced through inverse Compton scattering by a population of relativistic electrons accelerated in the shock region. Since the wind interaction zone is expected to be in the radiative regime, all the kinetic power of the wind affected by the collision should be radiated away almost instantaneously. Interestingly, a steady-state colliding wind model based on the latter assumption, while reproducing the overall shape of the thermal spectrum, overestimates the observed X-ray luminosity by at least a factor 4. The origin of this discrepancy is at present still unkwnon. Part of the kinetic power could actually be used to accelerate relativistic electrons in the shock region.

In the latter context, Cyg OB2 #8a (O6f + O5.5(f), $P_{orb} = 21.9$ days, $e = 0.24$) provides an extremely interesting test case. Indeed, this binary is a known non-thermal radio source where a phase-modulated synchrotron radio emission is produced by relativistic electrons accelerated in the wind interaction zone (Blomme, 2005). The radio flux is maximum near periastron (i.e. at $\phi \sim 0$) and reaches a minimum shortly after $\phi \sim 0.6$. On the other hand, *XMM-Newton*, *ROSAT* and *ASCA* data reveal a phase-locked variation of the X-ray flux by about a factor 1.5, with a minimum shortly after $\phi = 0.0$ and a maximum near $\phi \sim 0.75$ (De Becker & Rauw, 2005). Therefore, the X-ray emission varies essentially in the opposite sense of the radio flux. The EPIC spectra can be represented by a thermal model with three temperatures of

0.26, 0.78 and 1.7 keV and reveal a strong overluminosity (about a factor 10). This hard and bright X-ray emission is a clear indication of a colliding wind interaction. Given these properties, a full phase-coverage of the orbital cycle of Cyg OB2 #8a with *XMM-Newton* could provide unprecedented insight into the connection between colliding winds, particle acceleration and non-thermal radio emission.

Because of its rather hard and strong X-ray emission, WR 25 (WN6ha), one of the X-ray brightest WR stars, was often suspected to be a colliding wind binary system. An analysis with a differential emission measure thermal plasma model of *XMM-Newton* spectra by Raassen et al. (2003) revealed two dominant components at 0.6 and 2.8 keV and a rather extreme $\log \mathrm{L}_X/\mathrm{L}_{\mathrm{bol}} = -5.62$. Quite recently a radial velocity study (Gamen (2005), Gosset et al. (2006)) showed that WR 25 is indeed a rather long period spectroscopic binary. A preliminary analysis of all the available EPIC data (Gosset et al., 2006) reveals a rather strong variation of the X-ray flux (by about a factor two), roughly consistent with a $1/d$ modulation.
A textbook example of a WR + O colliding wind binary is γ^2 Vel (WC8 + O7.5 III, $\mathrm{P}_{\mathrm{orb}} = 78.5$ days). At most orbital phases, the X-ray emission of γ^2 Vel is highly absorbed by the dense and opaque WC8 wind. However, shortly after conjunction when the O-star is in front (i.e. when the collision zone can be seen through a rarefied cavity around the O-star), the flux is significantly enhanced (see Willis et al. (1995)). The system was observed with *XMM-Newton* at two phases (0.1, i.e. high state and 0.4, i.e. low state). The spectrum consists of a high energy emission that is absorbed by a variable column density and a presumably constant emission line spectrum at low energies. The low energy emission displays a radiative recombination continuum of C VI and C V at 25.3 Å. Schild et al. (2004) constrained the temperature of the recombining electrons to be in the range 20 000 to 60 000 K which could indicate that the feature arises from WR material in the outer wind photoionized by the X-rays from the wind-wind collision. Skinner et al. (2001) analysed a *Chandra* HETG observation of γ^2 Vel at phase $\phi = 0.08$, i.e. when the O-star component is almost in front of the WC8 star. They found no evidence for Doppler shifts of the line centroids of the strongest lines, as well as no detectable photo-excitation effect in the He-like triplets of Si XIII, Mg XI and Ne IX. This indicates that these emission lines are probably formed at several tens of stellar radii above the surface of the O-star and not at $\sim 2\,\mathrm{R}_*$ as expected from the location of the colliding wind shock (Skinner et al. (2001), Schild et al. (2004)). This result suggests that these lines actually represent the intrinsic X-ray emission from the O-star itself, rather than the emission from the wind-wind interaction zone.
Finally, the long-period (7.9 yrs), highly eccentric ($e = 0.88$) WC7 + O4-5 binary WR 140 was observed with the HETG at two phases around periastron passage (Pollock et al., 2005). Pollock et al. argue that the lower line widths of cool ions indicate that the plasma in the wind interaction zone is not in equilibrium. They suggest that this is due to the collisionless nature of the shock and the slow character of the energy exchange between electrons and ions in the postshock plasma. This would imply that a quantitative interpretation of the X-ray emission from colliding wind binaries actually requires the use of non-equilibrium plasma models.

2.3. Presumably single Wolf-Rayet stars

As stated in the introduction, no clear relationship between L_{X} and $\mathrm{L}_{\mathrm{bol}}$ was found for WR stars. One of the intriguing questions that came up over the last couple of years is whether single WR stars actually do emit X-rays.

Oskinova et al. (2003) reported on an *XMM-Newton* exposure on the presumably single WC5 star WR 114. Despite the sensitivity of the EPIC cameras and a 15.9 ksec exposure time, the star was not detected. Assuming a plasma temperature of 1 keV yields an upper limit of $2.5 \times 10^{30}\,\mathrm{erg\,s^{-1}}$ on the X-ray luminosity of WR 114 (corresponding to $\mathrm{L}_{\mathrm{X}}/\mathrm{L}_{\mathrm{bol}} \leq 4 \times 10^{-9}$). This non-detection prompted Oskinova et al. (2003) to investigate the X-ray emission of single WC stars in general. The result was that no single WC star has so far been convincingly detected in X-rays. All WC stars that are known to emit X-rays are binaries and even here, only about 20% of the WC binaries are detected. Either X-rays are not produced in WC winds, or they are totally absorbed by the opaque stellar winds. The latter possibility seems quite plausible since the winds of WC stars are dense and metal-rich, making them optically thick out to several hundred stellar radii.
Gosset et al. (2005) analysed a 20 ksec *XMM-Newton* observation of the WN8 star WR 40. The star was not detected and Gosset et al. derived a very conservative upper limit on the X-ray luminosity of $4 \times 10^{31}\,\mathrm{erg\,s^{-1}}$ leading to $\mathrm{L}_{\mathrm{X}}/\mathrm{L}_{\mathrm{bol}} \leq 2.6 \times 10^{-8}$. At first sight, this result is quite surprising given the considerable optical variability (both photometric and spectroscopic) of WR 40 that suggests the existence of numerous structures and instabilities in its wind which could trigger a substantial X-ray emission. However, Gosset et al. (2005) showed that the wind opacity of WR 40 is very large and is probably sufficient to block out all the flux below 2.5 keV that would be emitted within $20\,\mathrm{R}_*$ from the stellar surface.
On the other hand, Ignace et al. (2003) presented a 9 ksec *XMM-Newton* observation of WR 1 (WN4). The star was detected at energies up to 4 keV. The lack of a hard emission component suggests that there is no contribution of a colliding wind emission in this case. Modelling with thermal models failed to reproduce the spectrum around 0.6 and 2.6 keV (i.e. at energies coincident with the K-shell photo-ionization edges of N VI and S IV – VI respectively). For the sulphur feature, Ignace et al. derive an associated optical depth $\tau_\lambda \sim 6$. Therefore, at least some of the X-ray emitting gas in WR 1 must reside below the radius of optical depth unity.
Finally, Skinner et al. (2002) reported on a 25 ksec *XMM-Newton* observation of the WN5-6 star WR 110. While WR 110 is not a known binary system, the X-ray spectrum of the star exhibits a soft ($kT_1 \sim 0.5$ keV) com-

ponent along with a hard one that could either be thermal ($kT_2 \geq 3$ keV) or non-thermal ($\Gamma = 2.2$) emission. Skinner et al. slightly favour the interpretation of the hard component as being thermal emission originating in a wind interaction between the WR star and a yet undetected companion.

In summary, existing observations suggest that single Wolf-Rayet stars do indeed produce X-rays, but the level of observable emission strongly depends on the actual wind opacity. Denser or more metal rich winds probably absorb the entire X-ray emission that is produced in the inner regions of the wind.

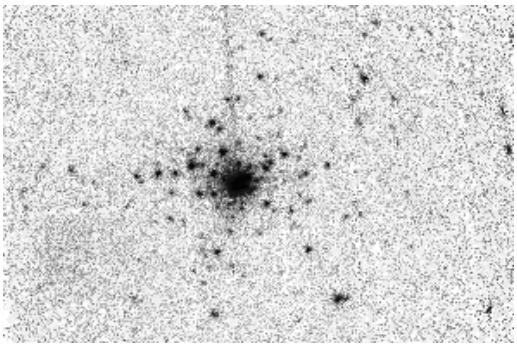

Figure 3. Grey scale image of the NGC6383 cluster as observed with XMM-Newton (Rauw et al. 2003). The EPIC images were exposure corrected before they were combined. The central source is the O-type binary HD 159176 (i.e. the sole O-type object in this cluster). Note the number of faint X-ray sources near HD 159176. Most of them have optically faint counterparts with optical and near-IR colours indicating that they are likely PMS stars. The X-ray brightest of these PMS candidates have quite hard spectra and at least in one case the light curve displays a strong flare (Rauw et al. 2003).

2.4. The surroundings of massive stars

Early-type stars frequently belong to young (a few Myr) open clusters. *XMM-Newton* and *Chandra* observations of these stars often reveal a wealth of faint serendipitous sources. These faint X-ray sources exhibit properties (flares, high spectral temperatures, large L_X/L_{bol} ratios) quite typical of low-mass pre-main sequence (PMS) stars (e.g. NGC 6383, Rauw et al. (2003), see Fig. 3; NGC 6530, Rauw et al. (2002c), Damiani et al. (2004); NGC 6231, Sana et al. (2006); Cyg OB2, Rauw et al. (2005b)). The study of the counterparts of these sources allows to investigate the star formation history of the clusters and the relationship between low-mass and massive members. Interestingly enough, it is often found that low-mass stars apparently form prior to the massive stars. These observations are crucial to constrain the still ill-defined formation mechanisms of the most massive stars.

Some clusters of massive stars are surrounded by an apparently diffuse X-ray emission. This feature is expected as a result of the shocked gas that fills the superbubble blown by the combined stellar winds of the cluster members into the ambient interstellar medium. However, in many cases, simple models based on the energetics of the stellar winds cannot explain all the properties of this diffuse emission. For instance, in the case of the giant H II region N 11 in the LMC, several other ingredients likely contribute to the apparently diffuse soft X-ray emission. In addition to the emission from the superbubble, hidden supernova remnants (SNRs), as well as unresolved point sources associated with either massive stars or PMS objects probably play a role (Nazé et al., 2004b).
Townsley et al. (2004) review the diffuse X-ray emission observed with *Chandra* from the star forming regions M 17 and RCW 49. M 17 hosts a blister H II region that is triggering star formation in an associated giant molecular cloud. M 17 contains about 100 OB stars, among which there are 14 O-type stars. A 40 ksec *Chandra* observation revealed 900 point sources around the so-called 'ring of fire' (consisting of a concentration of early O stars). The diffuse emission does not display an appreciable temperature gradient with distance from the O-stars, thus indicating that the hot gas flows into the interstellar medium without substantial cooling. In the case of RCW 49, over 500 X-ray point sources were found with *Chandra* and the diffuse X-ray emission appears centered on the open cluster Westerlund 2 at the core of RCW 49. The spectrum of this diffuse emission can be modelled by a three temperature thermal emission. The hardest ($kT = 3.1$ keV) component may also be fitted with a non-thermal model (power-law with $\Gamma = 2.3$). If thermal, the hard component might be due to the concentration of stars in Westerlund 2. On the other hand, if non-thermal, it could reveal the signature of embedded SNRs.

3. WHAT WE STILL DON'T KNOW

Over the first six years of their missions, *XMM-Newton* and *Chandra* have already contributed significantly to our understanding of the X-ray emission of massive stars. Much progress has been achieved, but a lot more work remains to be done. Indeed, the new results discussed above have also led to new challenges, that call for additional observations as well as for new theoretical models.

To date, roughly half a dozen presumably single O-type stars have been observed at high spectral resolution. These data reveal a variety of line profiles, some of which are in agreement with the expectations of either the standard wind-shock model or the magnetically channeled wind model. However, more data are needed to put these results on firmer grounds and to find out which of the two situations is the most typical. In the framework of the second model, high-resolution X-ray spectroscopy could provide unprecedented information on the importance of large scale magnetic fields in early-type stars, thereby helping to solve the long-standing issue of magnetic fields in early-type stars. Alternative sce-

narios to the 'standard' model and the channeled wind model are currently being developed (Pollock & Raassen, 2005). High-quality high-resolution spectra will be crucial to test these new ideas.

As pointed out in the introduction, hydrodynamical simulations of the intrinsic instabilities of O-star winds often predict a short-term variability of the X-ray emission (e.g. Feldmeier et al. (2003)). However, observations of presumably single O-stars reveal a rather constant X-ray flux. A possible exception to this rule is ζ Oph (O9.5 V) for which Oskinova et al. (2001) found a 20% modulation of the X-ray flux as observed with *ASCA*. The time-scale (0.77 day) of this variation might be related to the recurrence time of discrete absorption components (DACs) seen in the UV lines of this star. If confirmed, such a correlation would provide important clues on the connection between the X-ray emission and the large-scale wind structures that are thought to produce recurrent DACs.

While the O-star $L_X - L_{bol}$ relation inferred from the *ROSAT* All Sky Survey (Berghöfer et al., 1997) displays a considerable scatter, the corresponding relation obtained from *XMM-Newton* observations of the open cluster NGC 6231 (Sana et al. (2005b), see also Sana et al., these proceedings) reveals an amazingly small scatter. Could this feature be explained by the fact that the Sana et al. relation is drawn from a homogeneous population of O-stars, while the *ROSAT* results refer to a mix of stars all over the Galaxy? Future observations of open clusters harbouring massive stars should allow to further constrain this relationship and to find out whether other parameters (such as metallicity, age, galactocentric distance...) play a role in this relation.

XMM-Newton and *Chandra* have allowed for the first time to collect high quality observations for a number of colliding wind binaries. These data have shed new light on the orbital variability of the X-ray flux of these systems, thereby providing a better description of the colliding wind interaction over a broad range of physical parameters. Many features that have been found are in excellent agreement with the theoretical expectations for colliding wind systems. Some other properties, such as the role of non-thermal processes are as yet more difficult to interpret. A key question that remains to be answered is what happens to the kinetic power in radiative shocks and what fraction of it is used to accelerate relativistic particles. Another issue concerns the nature of the shocks. Pollock et al. (2005) and Pollock & Raassen (2005) suggest that the shocks are collisionless and that the post-shock plasma is not in equilibrium. If this is the case, then the qualitative interpretation of the X-ray spectra of colliding wind binaries (and probably early-type stars in general) requires the design of new dedicated models including collisionless shocks, particle acceleration as well as non-equilibrium plasma conditions.

Finally, hard X-ray emission in early-type stars is often attributed to the presence of a wind interaction zone. However, in some cases, stars that display a hard X-ray emission and that are X-ray overluminous (e.g. the Of?p star HD 108, Nazé et al. (2004a), see also Nazé et al., these proceedings) do not show any obvious indication of multiplicity at other wavelengths. More data, both in X-rays and other energy domains, are needed to clarify the origin of this hard emission.

ACKNOWLEDGEMENTS

I take this opportunity to thank the staff of the *XMM-Newton* SOC for the excellent job they are doing in scheduling time constrained observations of early-type binaries. I'm most grateful to the organisers of this conference for inviting me to present this review, as well as to my colleagues of the Liège high-energy astrophysics group for their help in preparing this work. This research is supported by the FNRS (Belgium), through contract P5/36 IAP (Belspo) and through PRODEX grants linked to the ESA *XMM-Newton* and *INTEGRAL* missions.

REFERENCES

Babel, J., & Montmerle, T. 1997, ApJ, 485, L29

Berghöfer, T.W., & Schmitt, J.H.M.M. 1994, A&A, 290, 435

Berghöfer, T.W., Schmitt, J.H.M.M., Danner, R., & Cassinelli, J.P. 1997, A&A, 322, 167

Blomme, R. 2005, in *Massive Stars and High Energy Emission in OB Associations*, JENAM 2005, in press

Blumenthal, G.R., Drake, G.W.F., & Tucker, W.H. 1972, ApJ, 172, 205

Cassinelli, J.P., & Olson, G.L. 1979, ApJ, 229, 304

Cassinelli, J.P., Miller, N.A., Waldron, W.L., MacFarlane, J.J., & Cohen, D.H. 2001, ApJ, 554, L55

Chlebowski, T., & Garmany, C.D. 1991, ApJ, 368, 241

Corcoran, M.F. 1996, Rev. Mex. Astron. Astrofis. Conf. Ser., 5, 54

Damiani, F., Flaccomio, E., Micela, G., et al. 2004, ApJ, 608, 781

De Becker, M., Rauw, G., Pittard, J.M., et al. 2004a, A&A, 416, 221

De Becker, M., Rauw, G., Blomme, R., et al. 2004b, A&A, 420, 1061

De Becker, M., Rauw, G., Blomme, R., et al. 2005, A&A, 437, 1029

De Becker, M., & Rauw, G. 2005, in *Massive Stars and High Energy Emission in OB Associations*, JENAM 2005, in press

Donati, J.-F., Babel, J., Harries, T.J., et al. 2002, MNRAS, 333, 55

Feldmeier, A., Puls, J., & Pauldrach, A.W.A. 1997, A&A, 322, 878

Feldmeier, A., Oskinova, L., & Hamann, W.-R. 2003, A&A, 403, 217

Gagné, M., Oksala, M.E., Cohen, D.H., et al. 2005, ApJ, 628, 986

Gamen, R. 2005, private communication

Gosset, E., Nazé, Y., Claeskens, J.-F., et al. 2005, A&A, 429, 685

Gosset, E., et al. 2006, in preparation

Harnden, F.R.Jr., Branduardi, G., Elvis, M., et al. 1979, ApJ, 234, L51

Ignace, R., & Oskinova, L.M. 1999, A&A, 348, L45

Ignace, R., & Gayley, K.G. 2002, ApJ, 568, 954

Ignace, R., Oskinova, L.M., & Brown, J.C. 2003, A&A, 408, 353

Kahn, S.M., Leutenegger, M.A., Cottam, J. et al. 2001, A&A, 365, L312

Kramer, R.H., Cohen, D.H., & Owocki, S.P. 2003, ApJ, 592, 532

Linder, N., & Rauw, G. 2005, in *Massive Stars and High Energy Emission in OB Associations*, JENAM 2005, in press

Lucy, L.B. 1982, ApJ, 255, 286

Miller, N.A., Cassinelli, J.P., Waldron, W.L., MacFarlane, J.J., & Cohen, D.H. 2002a, ApJ, 577, 951

Miller, N.A., Cassinelli, J.P., Waldron, W.L., MacFarlane, J.J., & Cohen, D.H. 2002b, ASPC, 262, 63

Nazé, Y., Rauw, G., Vreux, J.-M., & De Becker, M. 2004a, A&A, 417, 667

Nazé, Y., Antokhin, I.I., Rauw, G., et al. 2004b, A&A, 418, 841

Oskinova, L.M., Clarke, D., & Pollock, A.M.T. 2001, A&A, 378, L21

Oskinova, L.M., Ignace, R., Hamann, W.-R., Pollock, A.M.T., & Brown, J.C. 2003, A&A, 402, 755

Owocki, S.P., & Cohen, D.H. 1999, ApJ, 520, 833

Owocki, S.P., & Cohen, D.H. 2001, ApJ, 559, 1108

Pollock, A.M.T. 1987, ApJ, 320, 283

Pollock, A.M.T., & Oskinova, L.M. 2002, in *Stellar Coronae in the Chandra and XMM-Newton Era*, eds. F. Favata & J.J. Drake, ASPC, 277, 563

Pollock, A.M.T., Corcoran, M.F., Stevens, I.R., & Williams, P.M. 2005, ApJ, 629, 482

Pollock, A.M.T., & Raassen, A.J.J. 2005, in *Massive Stars and High Energy Emission in OB Associations*, JENAM 2005, in press

Porquet, D., Mewe, R., Duban, J., Raassen, A.J.J., & Kaastra, J.S. 2001, A&A, 376, 1113

Raassen, A.J.J., van der Hucht, K.A., Mewe, R., et al. 2003, A&A, 402, 653

Rauw, G., Vreux, J.-M., Stevens, I.R., et al. 2002a, A&A, 388, 552

Rauw, G., Blomme, R., Waldron, W.L., et al. 2002b, A&A, 394, 993

Rauw, G., Nazé, Y., Gosset, E., et al. 2002c, A&A, 395, 499

Rauw, G., De Becker, M., Gosset, E., Pittard, J.M., & Stevens, I.R. 2003, A&A, 407, 925

Rauw, G., Sana, H., Gosset, E., et al. 2005a, in *Massive Stars and High Energy Emission in OB Associations*, JENAM 2005, in press

Rauw, G., De Becker, M., & Linder, N. 2005, in *Massive Stars and High Energy Emission in OB Associations*, JENAM 2005b, in press

Sana, H., Stevens, I.R., Gosset, E., Rauw, G., & Vreux, J.-M. 2004, MNRAS, 350, 809

Sana, H., Antokhina, E., Royer, P., et al. 2005a, A&A, 441, 213

Sana, H., Rauw, G., Nazé, Y., Gosset, E., & Vreux, J.-M. 2005b, MNRAS, submitted

Sana, H., Rauw, G., Sung, H., Gosset, E., & Vreux, J.-M. 2006, in preparation

Schild, H., Güdel, M., Mewe, R. et al. 2004, A&A, 422, 177

Seward, F.D., Forman, W., Giacconi, R., et al. 1979, ApJ, 234, L55

Skinner, S.L., Güdel, M., Schmutz, W., & Stevens, I.R. 2001, ApJ, 558, L113

Skinner, S.L., Zhekov, S.A., Güdel, M., & Schmutz, W. 2002, ApJ, 572, 477

Stevens, I.R., Blondin, J.M., & Pollock, A.M.T. 1992, ApJ, 386, 265

Townsley, L., Feigelson, E., Montmerle, T., et al. 2004, in *X-ray and Radio Connections*, http://www.aoc.nrao.edu/events/xraydio

ud-Doula, A., & Owocki, S.P. 2002, ApJ, 576, 413

Waldron, W.L., & Cassinelli, J.P. 2001, ApJ, 548, L45

Wessolowski, U. 1996, in *Röntgenstrahlung from the Universe*, eds. H.U. Zimmerman, J.E. Trümper & H. Yorke, MPE Report, 263, 75

Willis, A.J., Schild, H., & Stevens, I.R. 1995, A&A, 298, 549

High resolution X-ray spectroscopy: towards XEUS and Con-X – MSSL, 27 - 28 March 2006 1

High-resolution X-ray spectroscopy of early-type stars

G. Rauw* [a], A.M.T. Pollock [b], & Y. Nazé†[a]

[a]Institut d'Astrophysique, Université de Liège, Allée du 6 Août, 17, Bât B5c, B-4000 Liège (Sart Tilman), Belgium

[b]ESA *XMM-Newton* Science Operation Centre, ESAC, 28080 Madrid, Spain

Although X-ray emission from massive, early-type stars has been known for almost thirty years, it is only with the advent of the high-resolution spectrographs aboard *Chandra* and *XMM-Newton* that a detailed investigation of the X-ray spectra of these stars has become possible. The existing observations of both single and binary early-type stars have been used to study the properties of their stellar winds. While some results agree with the expectations from theoretical models, other spectra show unexpected features. In this contribution, we review our current knowledge on the X-ray emission of stars of spectral type O and Wolf-Rayet and discuss the possibilities to test some new ideas with future high-resolution X-ray observations.

1. X-ray emission from early-type stars

Early-type stars of spectral type O or Wolf-Rayet (WR) are hot and luminous objects ($T_{\rm eff} \geq 30\,000\,{\rm K}$, $L_{\rm bol} \geq 4 \times 10^6\,L_\odot$) with initial masses on the main sequence of more than about $15\,M_\odot$. The strong radiation fields of these stars drive energetic stellar winds with mass loss rates in the range $\dot{M} \simeq 10^{-7} - 10^{-4}\,M_\odot\,{\rm yr}^{-1}$ and terminal velocities of order $v_\infty \simeq 1000 - 3000\,{\rm km\,s}^{-1}$. These winds not only affect the evolution of the stars themselves, but they have also a tremendous impact on their surroundings (see e.g. [1] for a general review). Stellar winds of O-type stars are driven by the transfer of momentum from the photospheric radiation field through photon scattering by strong UV resonance lines [2]. In this mechanism, only a fraction of the ions are directly accelerated. The other charged particles that constitute the stellar wind are dragged along by Coulomb interactions.

X-ray emission from early-type stars had been expected on theoretical grounds since the presence of certain ions (O VI and N V) in the UV spectra of these stars could be explained by Auger ionisation [3]. In the late seventies, when the *EINSTEIN* satellite observed regions near Cyg X-3 and η Car, a number of secondary X-ray sources were discovered and identified with O and WR stars of the Cyg OB2 and Car OB1 associations [4,5]. The first low-resolution broad-band X-ray spectra of these early-type stars indicated plasma temperatures of about $kT \simeq 0.5\,{\rm keV}$ and luminosities of $\sim 10^{-7}\,L_{\rm bol}$. The first theoretical attempts to explain this X-ray emission supposed that it arises from a dynamo-driven corona at the base of a cool wind [3,6]. However, as the stellar winds of massive stars in high-mass X-ray binaries produce strong absorption of the X-ray emission from the compact companion [7], one would expect to see similarly strong absorption for X-rays arising from a base corona. Since this is not the case, alternatives to the base corona model were sought. The most popular current scenario for X-ray emission from single O-stars stems from the fact that the transfer of momentum via scattering by resonance lines is a highly unstable process (see e.g. [8,9]). This microscopic line-force instability is thought to trigger macroscopic hydrodynamic shocks distributed throughout the wind; X-rays from the shock-heated plasma could better account for the overall properties of the low-resolution spectra of early-type stars as seen with *EINSTEIN*, *ROSAT* and *ASCA* [10].

With the advent of *XMM-Newton* and *Chandra*, the current generation of X-ray observatories combine high throughput and high-resolution spectroscopy, and new insight into the X-ray emission of early-type stars has been obtained. Since this conference deals primarily with high-resolution X-ray spectroscopy, we will focus on the results that have been obtained with the *Chandra* and *XMM-Newton* grating instruments. A general review of X-ray properties of early-type

*Research Associate FNRS (Belgium)
†Postdoctoral Researcher FNRS (Belgium)

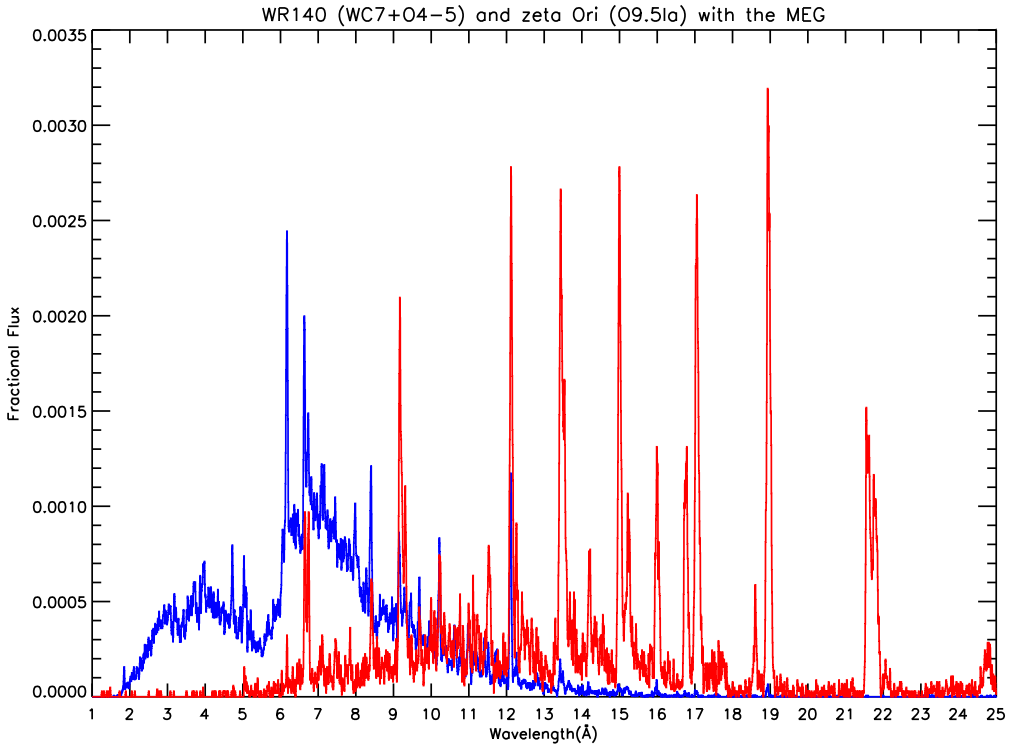

Figure 1. HETG-MEG spectra of ζ Ori (red) and the colliding wind binary WR 140 (blue). Note the prominent bremsstrahlung continuum in WR 140 and the obvious difference in plasma temperature between the two stars. The WR 140 spectrum is the pre-periastron observation discussed by [17].

stars can be found for instance in [11].

The first massive stars to be observed with these high-resolution spectrographs [1] were the supergiants ζ Pup (= HD 66811; O4 Ief) and ζ Ori (= HD 37742; O9.7 Ib) (see [12–14]), revealing X-ray spectra dominated by numerous emission lines (see Fig. 1). These individual lines or groups of lines provide for the first time the opportunity to apply detailed diagnostics of the physical properties of the X-ray emitting plasma. Half a dozen single O-stars have been observed to date with either HETG or RGS and their spectra show a variety of line morphologies, from rather narrow to broad, from symmetric to asymmetric, from blue-shifted to un-shifted, although there seems to be a reasonably smooth transition from ζ Pup at one extreme to σ Ori (= HD 37468; O9.5 V) at the other [15].

While single O-type stars are found to display intrinsic X-ray emission that scales roughly with bolometric luminosity (see e.g. [16] and references therein), some early-type binaries are considerably brighter, hotter and more variable. This is attributed to the interaction of the stellar winds of the binary components. A few of these systems (such as WR 140, [17] see also Fig. 1) are among the brightest hot-star X-ray sources and we review some of the results from high-resolution spectroscopy in Sect. 4.

2. The standard wind-shock model for single O stars

As outlined above, the most popular current interpretation of the intrinsic X-ray emission from

[1] $\Delta\lambda$ = 0.012, 0.024, $\sim$ 0.06Å for the HETG/HEG, HETG/MEG and the RGS instruments respectively

single early-type stars relies on the wind-shock model based on the idea that stellar winds driven by the transfer of momentum from the radiation field through scattering in UV resonance lines are highly unstable. In this scenario, the X-ray emitting plasma should be distributed across the stellar wind and as a result of the bulk expansion of the wind material the spectral lines are expected to be significantly broadened. In addition, photoelectric absorption by the overlying cool wind, assumed smooth and spherically symmetric, should mostly affect the emission coming from the wind material that is moving away from the observer. Hence the red wing of an X-ray line should be more heavily absorbed than the blue wing (see Fig. 2). The lines are thus expected to be broad, blue-shifted and asymmetric with a steeper blue wing (see Fig. 2). Moreover, the line emission is expected to arise from radii above the surface of optical depth unity ($\tau = 1$). Due to the wavelength dependence of photoelectric absorption, longer wavelength transitions should come from farther out in the wind than lines at shorter wavelengths.

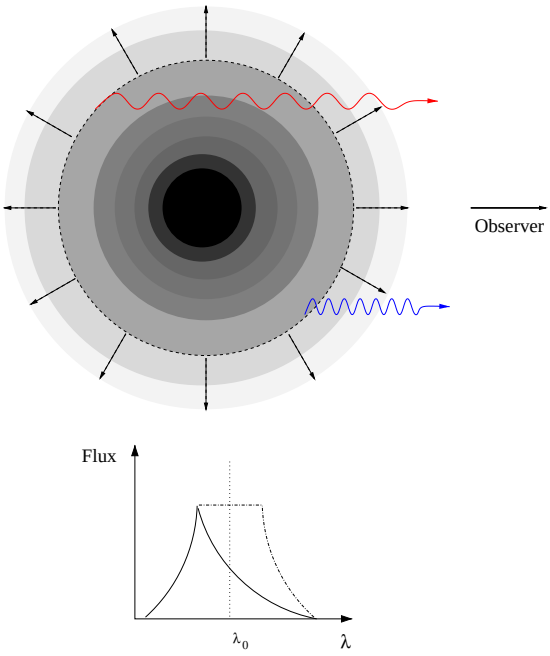

Figure 2. Schematic view of emission-line formation in the standard wind-shock model for a smooth spherically symmetric wind. Consider line photons arising on the dashed surface in an expanding wind. Since the X-ray emitting material is assumed to move along with the cool wind material, for an observer located to the right in our cartoon, a photon coming from the rear side of the wind will be red-shifted, whereas photons from the front side will be blue-shifted. In the absence of photoelectric absorption by the cool wind material, we expect to observe a roughly flat-topped line profile (dash-dotted line profile). However, as a result of the much larger column density seen by the red photons, the red part of the line suffers much stronger absorption than the blue and the resulting profile is blue-shifted and asymmetric, as shown by the solid line profile.

There is growing evidence (e.g. [18]) that stellar winds of O-type stars are not smooth but clumpy. This can have important consequences on the wind absorption, as discussed further below. Several authors have computed synthetic line profiles for various situations (optically thin vs. optically thick lines, homogeneous vs. clumped stellar wind,...) based on the wind-shock model ([19–21]; see also Oskinova *et al.*, these proceedings).

The high-resolution X-ray spectra of the supergiant ζ Pup [13,14] are reasonably well reproduced by these models: the broad emission lines are resolved by the RGS and HETG instruments and appear significantly blueshifted and skewed. The broadening implies Doppler velocities of less than v_∞, indicating that the lines originate from within the wind acceleration zone. The observed line morphologies agree with the theoretical profiles computed for a standard model configuration. Eight individual spectral lines were fitted with a simple spherically symmetric wind-shock line profile model by [22]. The free parameters of their model were

- the inner radius of the emission zone R_0. All the X-ray line emission is assumed to arise from plasma located at $r \geq R_0$.
- the filling factor of the hot plasma (assumed to vary as r^{-q} with q being a fitting parameter.
- the typical wind optical depth τ_* at the

wavelength of the line. For a smooth spherically symmetric wind, this parameter should be equal to $\frac{\kappa \dot{M}}{4\,\pi\,v_\infty\,R_*}$, where κ is the absorption coefficient of the overlying cool wind material.

While for most lines the values of R_0 cluster around $1.4\,R_*$, the most surprising result from this study was that the wind attenuation parameter τ_* was found to be significantly smaller than might have been expected from the commonly adopted $\dot{M}$ and assuming a spherically symmetric homogeneous wind. Moreover, no obvious dependence of τ_* on the line wavelength was found, suggesting that over the observed wavelength domain between 6 and 25Å, the absorption is essentially grey [22].

Another diagnostic of the plasma conditions is provided by the ratio of the intensities of the forbidden and intercombination lines of He-like triplets. For X-ray emitting plasmas surrounding early-type stars which have a strong UV radiation field, this ratio is essentially determined by the dilution of the UV radiation field [23,24]. For the RGS and HETG spectra of ζ Pup this technique indicates that the lines form at several stellar radii above the photosphere as expected for plasma embedded in the wind.

While ζ Pup seems to fit well into the wind-shock paradigm, the morphology of the X-ray line profiles of some other O-type stars observed with the HETG and RGS spectrographs does not conform at first sight so well to expectations. A controversial case is ζ Ori, whose lines are narrower than those of ζ Pup [12,25–27]. In the first paper dealing with the HETG spectra of this star [12], it was argued that the Si XIII He-like triplet arises very close to the stellar surface and that the strongest X-ray lines are symmetric and do not show any evidence of blue-shifted line centroids. They concluded that this result was at odds with the wind-shock model and they proposed instead that the X-ray emission comes from magnetic loops near the stellar surface. Recently, the same data have been reanalysed in a variety of ways, yielding quite different conclusions [27,25–27]. [27] obtained a good fit to the entire spectrum with the same asymmetric triangular velocity profile for every line. They found that the X-ray lines of ζ Ori show some asymmetry with the line centre being blue-shifted by $\sim -300\,\mathrm{km\,s^{-1}}$. Similarly, it has been shown by [25] that Gaussian fits with zero velocity shift such as used by [12] produce systematic residuals that can be reduced if the Gaussians are allowed to have a blue-shifted centroid. [25] also went on to use a model-independent non-parametric method, based on the moments of the lines, to confirm the existence of a significant blue-shift. Finally, they used the same method as [22] to fit seven individual lines with synthetic profiles for a spherically symmetric wind-shock model (see above). Good fits were obtained that indicated values of R_0 of about $1.5\,\mathrm{R_*}$, a roughly constant filling factor and a typical optical depth parameter of $\tau_* \simeq 0.25$ – 0.5, about one order of magnitude lower than expected for a homogeneous wind with the assumed mass loss rate. The R_0 parameter indicates that much of the line emission actually arises from regions in the wind below the $\tau = 1$ surface for a homogeneous wind (see Fig. 3). This situation, along with the fact that, once again, no obvious trend of the optical depth with wavelength was observed (as for ζ Pup [22], see also Fig. 3) could indicate that the mass loss rate of ζ Ori is lower than previously reported and that clumping impacts significantly on the value of τ_*.

The effect of clumping has been investigated further by several authors [26,29,30]. [26,29] fitted the observed HETG spectral lines of ζ Pup, ζ Ori, ξ Per (= HD 24912; O7.5 III(n)((f))) and ζ Oph (= HD 149757; O9.5 V) with a clumped wind model. From these studies, it appears that clumping can have serious effects on the shape of the X-ray lines in the standard model.

First of all, mass loss rates of early-type stars are mostly determined by fitting the optical, UV and near-IR spectra with a model atmosphere code. Accounting for the clumping of a fragmented stellar wind reduces the mass loss rates by a factor of a few to a few tens compared to smooth wind models. This will obviously lead to a reduced optical depth for X-ray photons. The line emission will thus be less attenuated and the line asymmetry will be less pronounced than in a smooth wind.

Second, if the clumps are nearly optically thick, the dependence of τ_* on λ vanishes and the opacity eventually becomes grey. This can easily be understood if we consider that the optical depth

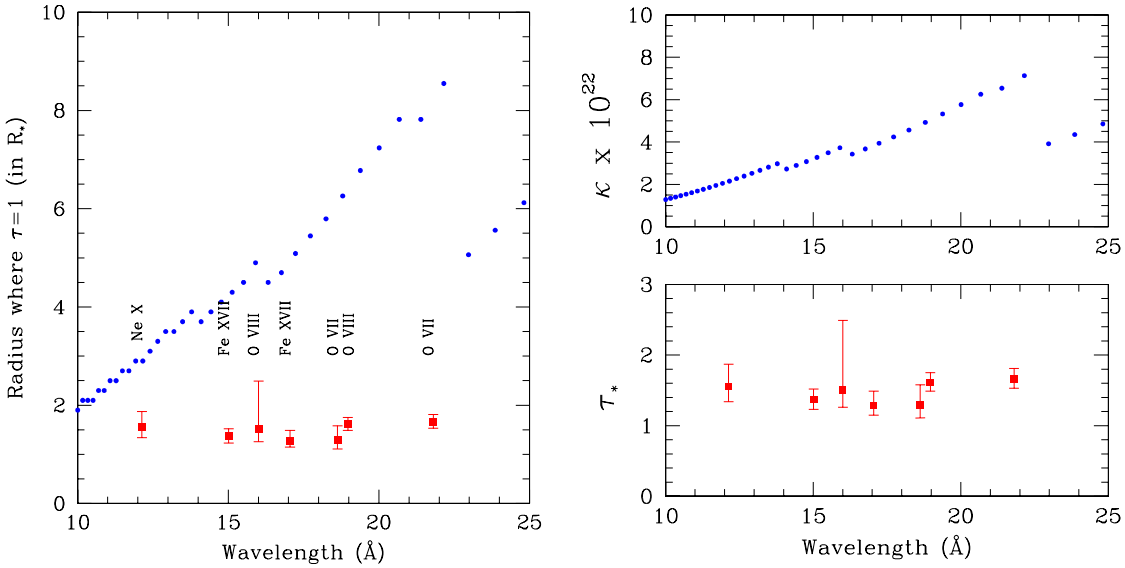

Figure 3. *Left:* comparison of the observed minimum radii of line formation with the 'X-ray photosphere' of ζ Ori. The square dots with error bars indicate the R_0 parameter from the fits of [25] to the line profiles observed in the HETG spectrum as a function of wavelength. The dotted line yields the theoretical radius of $\tau = 1$ for the stellar and wind parameters of ζ Ori ($T_{\rm eff} = 28\,500$ K, $\dot{M} = 2.5 \times 10^{-6}\,M_\odot\,{\rm yr}^{-1}$, $v_\infty = 2100\,{\rm km\,s}^{-1}$, $R_* = 31\,R_\odot$, $M_* = 49\,M_\odot$) calculated with the wind opacity model of [28]. *Right, upper panel:* predicted photoelectric absorption coefficient of the wind material around ζ Ori using the same wind opacity model as for the left panel. *Right, lower panel:* effective wind optical depth of ζ Ori as determined from the fits of individual lines [25].

now reflects the probability that any line of sight from the X-ray emission zone outwards intersects a clump. This probability obviously depends on the average separation between the fragments, which is a wavelength independent, purely geometrical parameter. For a large enough spacing between the clumps, the stellar wind becomes porous and the shape of an emission line is sensitive to the spatial distribution of the clumps rather than to the amount of material along the line of sight. A detailed investigation of the effects of porosity has been presented by [30]. These authors show that in order to produce a substantial reduction of the effective optical depth, the so-called porosity length $h = l/f$ must be large. In this relation, l is the characteristic size of the clumps, whilst $f = l^3/L^3$ is the clumping factor, L being the mean distance between the clumps. A long porosity length implies that either the clumps must have very large characteristic sizes, or the volume filling factor must be small or a combination of both properties. These requirements on the clump sizes and filling factors seem *a priori* at odds with the properties of the small-scale wind structures expected from 1-D hydrodynamical simulations of the intrinsic instability of line driven stellar winds.

At this stage, it is worth emphasizing that any conclusions about the opacity of stellar winds should also be able to account for the wind absorption in high-mass X-ray binaries such as Vela X-1 (see e.g. Paerels, these proceedings). In these systems, the wind of an apparently normal O star provides material for both accretion and absorption, the absorption showing no obvious signs of anything but a normal photoelectric law.

Understanding the nature of wind opacity is also highly relevant for the study of chemical

abundances and vice-versa. As a result of the combined action of stellar evolution and mass loss through the stellar wind, the surface composition of evolved massive stars is significantly altered. In principle, high-resolution X-ray spectroscopy offers the possibility to constrain abundances of some elements that are difficult to derive from other wavelength domains. The relative emission measures of various lines in the RGS spectrum of ζ Pup were investigated by [14]. They found that the abundances of CNO elements were non-solar with nitrogen overabundant, and carbon and oxygen depleted. It should be stressed that this kind of analysis strongly depends on the knowledge of the wavelength dependence of the optical depth. In fact, if the wind is clumpy and the optical depth effectively grey [25,26], then no correction of the wind absorption is needed, although corrections are still required for ISM absorption. If on the other hand, the opacity is non-grey, the differences in optical depth for the different lines must be accounted for. Another crucial point is the fact that the X-ray emitting plasma is usually not isothermal. Therefore, the conversion of line strength into actual abundances critically depends upon our knowledge of the emission measure distribution (see e.g. Behar, these proceedings).

Finally, we stress that the X-ray emission from embedded shocks is usually expected to be rather soft. This is because the X-rays arise from within the wind acceleration zone where the winds have not yet reached v_∞, thus reducing the velocity jump (and hence the increase in plasma temperature) across a hydrodynamical shock. In ζ Pup, for instance, both the line spectrum and the continuum emission, modelled as thermal bremsstrahlung, are consistent with $kT \simeq 0.6$ keV [29]. It is thus usually considered that the wind-shock model cannot explain the existence of significant quantities of X-ray emitting plasma at temperatures above ~ 1 keV in early-type stars. When such hard emission dominates the X-ray spectrum, it is often interpreted in terms of either a magnetically confined wind or a wind-wind collision in a binary system (see e.g. Fig. 1).

3. Magnetically confined winds

In the early 1990's, extensive optical as well as UV monitoring campaigns of θ^1 Ori C (= HD 37022; O4-6 Vp) revealed a periodic (P = 15.42 days) modulation of its spectrum ([31] and references therein). It was suggested that these variations could indicate a rotational modulation of the emission in an oblique magnetic rotator [31]. The same periodicity was subsequently discovered in the *ROSAT* HRI X-ray count rate of this extremely young star [32]. To explain these features, a model where a large-scale dipolar magnetic field confines the stellar wind near the magnetic equator has been proposed [33] (see Fig. 4). This model quantitatively reproduces the X-ray and optical variations of θ^1 Ori C. The existence of a dipolar magnetic field with an equatorial field strength of $B_0 = 530$ G and inclined by $\sim 45°$ with respect to the rotation axis was discovered by [34]. The magnetic field channels wind material from both hemispheres towards the magnetic equator thereby producing a head-on collision of two high velocity flows that heats the plasma to temperatures of $\sim 30 \times 10^6$ K. As the star rotates, our viewing angle towards the confined wind varies, thus resulting in a modulation of the observable X-ray flux as well as of the optical emission lines [33,35]. Recently, [36] reported on four *Chandra* HETG spectra that were obtained in such a way as to sample the 15.42 days cycle. These four spectra display narrow spectral lines with Doppler widths ranging from ~ 250 to $\sim 625\,\mathrm{km\,s^{-1}}$. Furthermore, the line strengths of the He-like triplets seen in the HETG spectra indicate that the X-ray emitting plasma must be located rather close to the stellar surface (between about 1.5 and 2.0 R_*). As shown by [36], these are actually the properties expected for the X-ray emission of a magnetically channeled wind.

The question that comes to mind is how unique an object θ^1 Ori C is. So far, there are two other massive stars for which the detection of a large-scale magnetic field has been claimed in the literature. These are the peculiar Of?p object HD 191612 for which [37] reported a dipolar field strength of 1.5 ± 0.2 kG and the very young B0.2 V star τ Sco (= HD 149438) which has an average field strength of 300 G over the stellar surface [38]. High-resolution X-ray spectra of τ Sco and HD 191612 have been obtained and discussed by [39,40] and [41] respectively. The X-ray properties of τ Sco fit indeed rather well into the overall picture of the magnetically confined wind scenario. In fact, the star displays an unusually hard X-ray spectrum (with temperatures

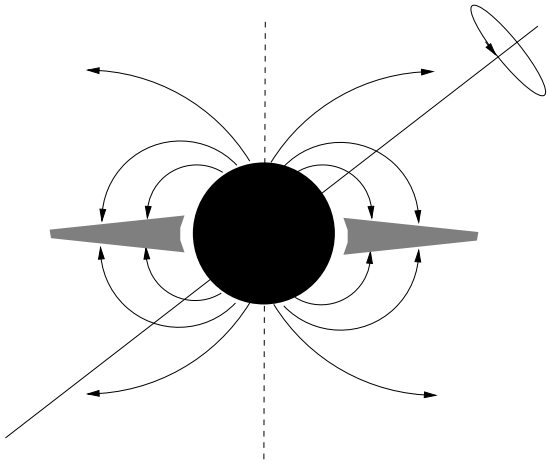

Figure 4. Schematic view of the magnetically confined wind model for an oblique magnetic rotator such as θ^1 Ori C. The magnetic axis (dashed line) is inclined with respect to the rotation axis (solid line). The dipolar magnetic field channels the wind material towards the magnetic equator where it collides with the material from the opposite magnetic hemisphere. This collision generates a hot, high-density plasma near the magnetic equator, where copious amounts of relatively hard X-rays are emitted. During the rotational cycle the viewing angle towards the confined wind region changes resulting in the observed modulation of the X-ray emission as well as of the emission at other wavelengths.

up to 20×10^6 K) and a comparatively large X-ray luminosity ($\sim 3 \times 10^{31}$ erg s^{-1}) for a B0-type object. The average HWHM of the lines in the HETG and RGS spectra is ~ 300 km s^{-1} (much less than $v_\infty \simeq 2400$ km s^{-1}), even less than for θ^1 Ori C. The Si XIII He-like triplet of τ Sco indicates a formation radius of less than $1.5\,R_*$ [39,40]. Therefore, [39] pointed out the similarities between τ Sco and θ^1 Ori C. The discovery of a magnetic field [38] lends further support to this interpretation, although the magnetic topology of τ Sco appears significantly more complex than a simple dipole. Such a complex magnetospheric structure results in a heavily distorted torus of closed magnetic loops where the wind flows collide and produce a hot X-ray emitting plasma. Thus the magnetosphere of τ Sco might resemble that of the Solar corona, although the mechanism responsible for the heating of the plasma would obviously be different [38].

The situation is however quite different for HD 191612. RGS spectra of this star at three different phases of its 538 day cycle were obtained by [41]. While the overall spectrum of the star is rather hard, including emission at temperatures of $12 - 18 \times 10^6$ K, it appears significantly cooler than θ^1 Ori C, where plasma as hot as 30×10^6 K has been observed. In addition, the O VIII Lyα and Fe XVII λ15.014 lines have `FWHM` of $2000 - 2600$ km s^{-1}, whilst the average `FWHM` of the X-ray lines of HD 191612 amounts to 1800 ± 400 km s^{-1}. These lines are thus significantly broader than those of τ Sco or θ^1 Ori C. These properties are therefore at odds with the X-ray emission of HD 191612 arising from a magnetically confined wind. While [37] suggested that the confinement of the stellar winds in θ^1 Ori C and HD 191612 as estimated from the parameter $\eta = \frac{(B_0^2\,R_*^2)}{(\dot{M}\,v_\infty)}$ should be similar, we caution that the large mass loss rate of HD 191612 probably means that the optical depth of the wind is also significantly larger. Therefore, it could be possible that the larger optical depth prevents us from seeing the X-rays from the magnetically compressed wind that should essentially be located below the Alfvén radius. However, this interpretation would contrast with the idea that the X-ray wind attenuation is reduced by wind clumpiness and that most of the X-ray lines form between ~ 1.5 and $\sim 2.5\,R_*$ as inferred for ζ Pup and ζ Ori for instance.

4. Colliding Wind binaries

In early-type binaries, the interaction of stellar winds can produce X-ray emission that comfortably exceeds the intrinsic emission of the companion stars (see e.g. [42]). The eccentric ($e = 0.88$) long-period ($P = 7.94$ yrs) WC7 + O4-5 binary WR 140 (= HD 193793) probably provides the best example of a colliding wind binary system. Signatures of the wind interaction can be seen in wavelengths ranging from radio to X-rays. For instance, the system is known to display non-thermal synchrotron radio emission that varies as a function of orbital phase. Spectacular images of the radio emission obtained with the *VLBA* [43]

show clearly that the non-thermal radio emission comes from the wind-wind collision zone between the stars.

The X-ray emission of WR 140 [17] is also highly variable as a function of orbital phase because of both the changing orbital separation and variable absorption along the line-of-sight to the shock region. WR 140 was observed twice with the *Chandra* HETG close to the 2001 peristron, once before and once after. The spectra reveal a strong continuum ($kT \sim 4$ keV) and many emission lines (see Fig. 1). The pre-periastron X-ray luminosity in the energy range 0.5 – 10 keV was $\sim 1.5 - 2.0 \times 10^{34}$ erg s^{-1}, about a factor of 10 – 100 larger than the typical X-ray luminosity of single O stars.

The remarkably strong neon lines in the X-ray spectrum of WR 140 are probably due to the chemical enrichment of the stellar wind of the WC component. Since the strong bremsstrahlung continuum is largely produced by free electrons from carbon and helium, the most abundant elements in the WC wind, the equivalent widths of lines directly reflect the relative abundance of the corresponding elements with respect to He and C, allowing accurate abundances to be derived.

The spectral lines of WR 140 were blue-shifted during the pre-periastron observation with velocity widths increasing with ionization potential. Given the orbital configuration of the binary at the time of the observation, the blue-shift directly indicates that the X-ray emission arose from material flowing along the shock cone wrapped around the O-star. The changing line-widths, on the other hand, were interpreted as a consequence of the lack of equilibrium caused by the slowness of relaxation behind collisionless shocks in the low-density interacting flows between the stars.

Beside the long-period colliding wind binaries like WR 140 and η Car ([44]), many other shorter period early-type interacting wind binaries have been observed with *XMM-Newton*, mainly O + O systems with periods of days to weeks. In these close systems, the winds interact before they have reached their terminal velocities and many display phase-modulated X-ray flux [45–48]. Because of the lower pre-shock wind velocities, the X-ray emission from the wind interaction zone is softer and weaker than in wider systems such as WR 140. For a review of the X-ray observations of these systems, we refer to [11].

5. A new paradigm for X-ray emission from single early-type stars

Some of the thinking applied to WR 140 has triggered the development of a alternative interpretation to the standard wind-shock model [27,49] that could be far-reaching in its implications. The ions and electrons of the stellar wind interact through slow, long-range Coulomb collisions. As pointed out above, these are relevant in the wind-driving mechanism for transferring momentum from the small minority of directly driven ions to the flow of all ions and electrons. In addition, they will also help determine the way in which any shocks in the wind might develop. [27,49] drew attention to the fact that the ion-ion collisional mean free path scales as v^4/n_i, where v is the ion velocity and n_i the density. Whilst this mean free path is small near the stellar photosphere, it increases rapidly with radius in the stellar wind as v increases and n_i decreases. For instance, in ζ Ori, it reaches about 1 R$_*$ at $r = 10$ R$_*$. These authors suggest, therefore, that in common with most other astrophysical plasmas, much of a stellar wind is a collionless plasma and that any shocks which develop are regulated instead by plasma waves and are thus of magnetic origin. In such collisionless shocks, it is expected that predominantly ions are heated, whilst electrons remain cold. Given the even slower rate of energy exchange between ions and electrons, equilibrium is unlikely to be established and X-ray ionization could be due to protons rather than electrons. The width of the emission lines would then result from the thermalized motion of the ions in the post-shock region, rather than reflecting the bulk motion of the emitting plasma. [27,49] also discussed the possibility that the sluggishness of Coulomb interactions could prevent the microscopic instability of the driving mechanism developing into macroscopic shocks. If the shocks producing the X-rays in both single and binary stars are indeed collisionless, high-resolution X-ray observations of early-type stars provide a novel testbench for the study of magnetic fields and plasma physics.

6. Conclusions and Future Prospectives

High-resolution spectroscopy with *Chandra* and *XMM-Newton* has opened up an entirely new view on the X-ray emission of early-type stars. However, there is still a long way to go before the X-ray spectra of hot stars reach the same level of accuracy as in *IUE* UV spectra. Moreover, high-resolution X-ray spectroscopy of early-type stars is so far restricted to only about a dozen objects. In order to formulate general conclusions, it is mandatory to enlarge this sample. This is especially true since different objects apparently require different models to account for their X-ray spectra. Using longer integration times with the current facilities to observe fainter sources is not enough. Instead, a quantum leap in effective area is required, such as expected for the *XEUS* and *Con-X* , in order to increase significantly the number of early-type stars that can be studied at high resolution.

Beside the large effective area and good spectral resolution, future X-ray spectrographs should also have angular resolution at least as good as that of the current EPIC instruments aboard *XMM-Newton*. As the majority of the early-type stars are located in open clusters, poor angular resolution would condemn X-ray spectroscopists to work with spectra suffering from confusion by the light from either neighbouring massive stars or from the abundance of low-mass pre-main sequence stars that congregate around early-type stars.

Future high-resolution spectra of massive stars will provide the first detailed X-ray line profiles, possibly allowing the study of variability on time-scales down to the hours typical wind flow times. In the UV and optical domain, emission-line-profile variability on such time-scales is common and has been attributed to either small-scale, such as clumps, or large-scale structures in the winds.

XEUS and *Con-X* observations will also provide tests for the various ideas outlined above. For instance, they will allow to search for satellite lines that could indicate the presence of non-thermal electrons via inner-shell ionization. Relativistic particles are expected to be accelerated in the shocks probably responsible for the X-ray emission in both single and binary stars. All-in-all, these observations promise deeper insight into the high-energy mechanisms that occur inside the stellar winds of hot stars and will provide fundamental information on many processes that occur in astrophysical plasmas. In many respects, the *golden age* of X-ray astronomy of early-type stars is yet to come.

REFERENCES

1. Nazé, Y. 2006, Bulletin of the Royal Scientific Society Liège, 75, 20, `http://www.srsl-ulg.net/`
2. Lamers, H.J.G.L.M., & Cassinelli, J.P. 1999, *Introduction to Stellar Winds*, Cambridge University Press
3. Cassinelli, J.P., & Olson, G.L. 1979, ApJ, 229, 304
4. Harnden, F.R.Jr., Branduardi, G., Elvis, M., *et al.* 1979, ApJ, 234, L51
5. Seward, F.D., Forman, W., Giacconi, R., *et al.* 1979, ApJ, 234, L55
6. Waldron, W.L. 1984, ApJ, 282, 256
7. Sato, N., Hayakawa, S., Nagase, F., *et al.* 1986, PASJ, 38, 731
8. Lucy, L., & White, R.L. 1980, ApJ, 241, 300
9. Dessart, L., & Owocki, S.P. 2005, A&A, 437, 657
10. Feldmeier, A., Puls, J., & Pauldrach, A.W.A. 1997, A&A, 322, 878
11. Rauw, G. 2006, in *The X-ray Universe 2005*, ESA SP-604, 7
12. Waldron, W.L., & Cassinelli, J.P. 2001, ApJ, 548, L45
13. Cassinelli, J.P., Miller, N.A., Waldron, *et al.* 2001, ApJ, 554, L55
14. Kahn, S.M., Leutenegger, M.A., Cottam, J., *et al.* 2001, A&A, 365, L312
15. Pollock, A.M.T. 2005, in *6 Years of Science with Chandra*, `http://cxc.harvard.edu/symposium_2005/proceedings/files/pollock_andy.pdf`
16. Sana, H., Rauw, G., Nazé, Y., *et al.* 2006, MNRAS, in press
17. Pollock, A.M.T., Corcoran, M.F., Stevens, I.R., & Williams, P.M. 2005, ApJ, 629, 482
18. Fullerton, A.W., Massa, D.L., & Prinja, R.K. 2006, ApJ, 637, 1025
19. Owocki, S.P., & Cohen, D.H. 2001, ApJ, 559, 1108
20. Ignace, R., & Gayley, K.G. 2002, ApJ, 568, 954
21. Feldmeier, A., Oskinova, L., & Hamann, W.-R. 2003, A&A, 403, 217
22. Kramer, R.H., Cohen, D.H., & Owocki, S.P. 2003, ApJ, 592, 532
23. Blumenthal, G.R., Drake, G.W.F., & Tucker, W.H. 1972, ApJ, 172, 205

24. Porquet, D., Mewe, R., Dubau, J., *et al.* 2001, A&A, 376, 1113
25. Cohen, D.H., Leutenegger, M.A., Grizzard, K.T., *et al.* 2006, MNRAS, in press, astro-ph/0602599
26. Oskinova, L.M., Feldmeier, A., & Hamann, W.-R. 2006, MNRAS, submitted, astro-ph/0603286
27. Pollock, A.M.T., & Raassen, A.J.J. 2005, in *Massive Stars and High Energy Emission in OB Associations*, Proc. JENAM 2005 *Distant Worlds*, eds. G. Rauw et al., 35
28. Nazé, Y., Rauw, G., Vreux, J.-M., *et al.* 2004, A&A, 417, 667
29. Oskinova, L.M., Feldmeier, A., & Hamann, W.-R. 2006, in *The X-ray Universe 2005*, ESA SP-604, 57
30. Owocki, S.P., & Cohen, D.H. 2006, ApJ, submitted, astro-ph/0602054
31. Stahl, O., Kaufer, A., Rivinius, T., *et al.* 1996, A&A, 312, 539
32. Gagné, M., Caillaut, J.-P., Stauffer, J.R., *et al.* 1997, ApJ, 478, L87
33. Babel, J., & Montmerle, T. 1997, ApJ, 485, L29
34. Donati, J.-F., Babel, J., Harries, T.J., *et al.* 2002, MNRAS, 333, 55
35. ud-Doula, A., & Owocki, S.P. 2002, ApJ, 576, 413
36. Gagné, M., Oksala, M.E., Cohen, D.H., *et al.* 2005, ApJ, 628, 986 (Erratum ApJ, 634, 712)
37. Donati, J.-F., Howarth, I.D., Bouret, J.-C., *et al.* 2006a, MNRAS, 365, L6
38. Donati, J.-F., Howarth, I.D., Jardine, M.M., *et al.* 2006b, MNRAS, submitted
39. Cohen, D.H., de Messières, G.E., MacFarlane, J.J., *et al.* 2003, ApJ, 586, 495
40. Mewe, R., Raassen, A.J.J., Cassinelli, J.P., *et al.* 2003, A&A, 398, 203
41. Nazé, Y., Rauw, G., Pollock, A.M.T., *et al.* 2006, in preparation
42. Stevens, I.R., Blondin, J.M., & Pollock, A.M.T. 1992, ApJ, 386, 265
43. Dougherty, S.M., Beasley, A.J., Claussen, *et al.* 2005, ApJ, 623, 447
44. Leutenegger, M.A., Kahn, S.M., & Ramsay, G. 2003, ApJ, 585, 1015
45. Rauw, G., Vreux, J.-M., Stevens, I.R., et al. 2002a, A&A, 388, 552
46. Sana, H., Stevens, I.R., Gosset, E., Rauw, G., & Vreux, J.-M. 2004, MNRAS, 350, 809
47. Sana, H., Antokhina, E., Royer, P., et al. 2005a, A&A, 441, 213
48. De Becker, M., & Rauw, G. 2005, in *Massive Stars and High Energy Emission in OB Associations*, Proc. JENAM 2005 *Distant Worlds*, eds. G. Rauw et al., 73
49. Pollock, A.M.T., & Raassen, A.J.J. 2006, A&A, submitted

ACKNOWLEDGEMENTS

The authors are grateful to the organisers of this workshop for the invitation to present this review. GR and YN are supported by the FNRS (Belgium), through contract P5/36 IAP (Belspo) and through PRODEX grants linked to the ESA *XMM-Newton* and *INTEGRAL* missions.

2.2 Phase dependent X-ray emission from γ^2 Vel

γ^2 Vel (WR 11) is a spectroscopic binary system consisting of a WC8 star and an O7.5 III primary (De Marco & Schmutz 1999, De Marco et al. 2000) orbiting around each other with a period of 78.5 days and an eccentricity $e = 0.4$. Phase-locked variable X-ray emission has been detected with *ROSAT* (Willis et al. 1995, see also Fig. 2.1). The harder X-ray flux in the *ROSAT* band significantly increases over a relatively short phase interval when the O-star passes in front of the WC8 secondary.
This result was interpreted in the framework of a wind-wind collision, the X-ray emission being strongly absorbed when the WC star with its dense and metal enriched stellar wind is in front and much less attenuated at phases when the less opaque O-star wind is in front. In this section, I report the analysis of three *ASCA* observations of this system obtained at key phases of the orbital cycle (Rauw et al. 2000a, see Fig. 2.2).

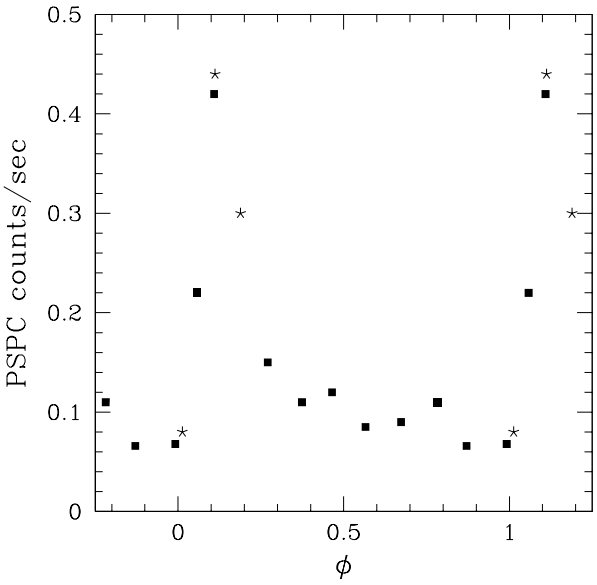

Figure 2.1: X-ray light curve of γ^2 Vel as presented by Willis et al. (1995). Phase $\phi = 0.0$ corresponds to periastron passage. While the black dots indicate *ROSAT*-PSPC data obtained during a single orbital cycle of γ^2 Vel, the stars stand for three target of opportunity pointings that Willis et al. obtained during a later cycle to confirm the phase-locked modulation of the X-ray flux.

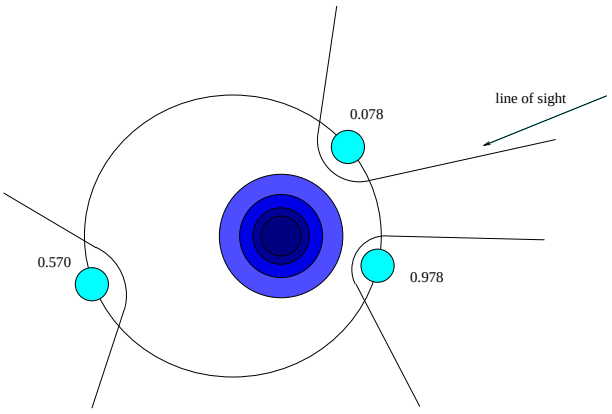

Figure 2.2: Cartoon of the γ^2 Vel binary system at the three orbital phases corresponding to the *ASCA* observations analysed by Rauw et al. (2000a). The orbit of the O-star around the WC8 component is illustrated along with the shock cone produced by the wind-wind collision at the various orbital phases.

Mon. Not. R. Astron. Soc. **316**, 129–136 (2000)

ASCA spectroscopy of the hard X-ray emission from the colliding wind interaction in γ^2 Velorum

G. Rauw,[1,2★†] I. R. Stevens,[2★] J. M. Pittard[2,3★] and M. F. Corcoran[4★]

[1]*Institut d'Astrophysique & Géophysique, Université de Liège, 5, Avenue de Cointe, B-4000 Liège, Belgium*
[2]*School of Physics & Astronomy, University of Birmingham, Edgbaston, Birmingham B15 2TT*
[3]*Department of Physics & Astronomy, University of Leeds, Woodhouse Lane, Leeds LS2 9JT*
[4]*USRA/LHEA, Goddard Space Flight Center, Greenbelt, MD 20771, USA*

Accepted 2000 February 16. Received 2000 January 31; in original form 1999 July 9

ABSTRACT

We discuss an *ASCA* observation of the eccentric WC8 + O7.5 III binary γ^2 Velorum near apastron. The X-ray spectrum is compared with two previous observations obtained when the system was near periastron. All three spectra display a hard-emission component that undergoes strong variability over the orbital cycle. The properties of the hard X-ray emission of γ^2 Vel are constrained by taking into account the contribution from contaminating soft X-ray sources in the vicinity of γ^2 Vel. We find that the observed variations are in qualitative agreement with the predictions of colliding wind models. We investigate for the first time the effect of uncertainties in the chemical composition of the X-ray emitting plasma on our understanding of the high-energy properties of the wind interaction region. Our results indicate that these uncertainties significantly affect the derived shock temperature and absorption column, but play a smaller role in determining the intrinsic X-ray luminosity of the colliding wind zone. We further find that the intrinsic luminosity from the hard X-ray component in γ^2 Vel does not follow the $1/D$ distance relation expected from simple models of adiabatic shocks.

Key words: binaries: general – stars: individual: γ^2 Vel – stars: mass-loss – stars: Wolf–Rayet – X-rays: stars.

1 INTRODUCTION

The eccentric Wolf–Rayet binary γ^2 Velorum (=HD 68273 =WR 11, $P_{\rm orb} = 78.53$ d, $e = 0.326$) is a cornerstone for our understanding of many fundamental aspects of the Wolf–Rayet phenomenon and of massive stars in general, and has therefore been studied extensively at many different wavelengths.

Recently, the distance of γ^2 Vel was determined from *Hipparcos* parallax measurements to be 258^{+41}_{-31} pc (Schaerer, Schmutz & Grenon 1997; van der Hucht et al. 1997). Consequently, the former classification of the O-star component as a supergiant (Conti & Smith 1972) had to be revised and γ^2 Vel is now classified as WC8+O7.5 III (De Marco & Schmutz 1999). The revised distance also leads to a smaller radio mass-loss rate of $\dot{M} = (2.8 \pm 1.0) \times 10^{-5}\,{\rm M}_\odot\,{\rm yr}^{-1}$ for the WC8 star (Leitherer, Chapman & Koribalski 1997; Schaerer et al. 1997). In light of these results, the properties of the O-star component were investigated by De Marco & Schmutz (1999). From a hydrodynamic atmosphere/wind model, these authors derive a mass-loss rate of $\dot{M} = (1.8 \pm 0.4) \times 10^{-7}\,{\rm M}_\odot\,{\rm yr}^{-1}$ for the O-star.

Over the last two decades, observations of γ^2 Vel have provided strong evidence for an interaction between the winds of the WC8 star and its O-star companion. St.-Louis, Willis & Stevens (1993) have studied an extensive set of high-resolution *IUE* spectra of γ^2 Vel. These authors report strong phase-locked line profile variability that they describe as a result of the combination of selective atmospheric eclipses and the effect of a cavity in the WR wind produced by the wind collision.

Radio and millimetre observations of γ^2 Vel revealed essentially a thermal spectrum (Abbott et al. 1986; Williams et al. 1990b; Leitherer et al. 1997) with no clear indication of a non-thermal component arising in the shock region, contrary to what is observed in the very wide WC7+O4–5 binary WR 140 (Williams et al. 1990a). However, Chapman et al. (1999) found a steepening of the radio spectral index of γ^2 Vel between 3 and 20 cm. This could possibly indicate a highly attenuated non-thermal component originating deep within the wind.

Further support for a wind collision in γ^2 Vel comes from the *ROSAT* PSPC observations of this star gathered by Willis, Schild & Stevens (1995). These authors discovered substantial phase-locked variability of the X-ray flux from γ^2 Vel. The X-ray flux

★ E-mail: rauw@astro.ulg.ac.be (GR); irs@star.sr.bham.ac.uk (IRS); jmp@ast.leeds.ac.uk (JMP); corcoran@barnegat.gsfc.nasa.gov (MFC)
† Chargé de Recherches FNRS, Belgium.

strongly increases at orbital phases when the O-star passes in front of the WC8 component. Willis et al. (1995) attribute this increase to extra X-ray emission from a shock front between the two wind components. The X-ray emission from the shock is highly absorbed when the dense and opaque WR wind is in front. However, the colliding wind X-ray emission becomes significantly less absorbed at orbital phases when the cavity around the O-star crosses the line of sight. Stevens et al. (1996) discussed two *ASCA* observations of γ^2 Vel obtained at orbital phases when the O-star is in front of the WC8 component, and used a hydrodynamic model of colliding winds to calculate synthetic spectra that are then fitted to the *ASCA* spectra. They derive a mass-loss rate that is in reasonable agreement with the value derived from radio observations accounting for the revised distance determination (Schaerer et al. 1997).

In the present paper, we discuss an *ASCA* spectrum of γ^2 Vel obtained near apastron and we compare it with the two archival observations that were obtained near periastron. For the first time, we take into account the contamination by nearby point sources as derived from the *ROSAT* PSPC data of Willis et al. (1995). The data analysis is presented in Section 2. Different attempts to fit the spectra with thermal plasma models are discussed in Section 3, and our conclusions are given in Section 4.

2 *ASCA* OBSERVATIONS AND DATA REDUCTION

γ^2 Velorum has been observed with *ASCA* at three different orbital phases; two near-periastron exposures lasted over ~20 ks each, while the apastron observation covered about 30 ks. Throughout this paper we adopt the orbital phases with respect to periastron according to the ephemeris of Schmutz et al. (1997, hereafter S97):

$$\mathrm{JD(periastron)} = 245\,0120.00 + 78.53E$$

(see Table 1). To allow comparison with previous work (Willis et al. 1995; Stevens et al. 1996), Table 1 also provides the orbital phases according to the ephemeris of Moffat et al. (1986) with respect to conjunction (WR star in front).

For all three observations we retrieved the screened event files from the ARNIE data base at Leicester University, and we combined the high bit-rate and medium bit-rate data in our analysis. The raw light curves of these data were inspected and in one case (the apastron observation) we found on several occasions a sudden rise of the overall count rate shortly before the spacecraft entered the South Atlantic Anomaly. After testing different criteria to re-screen the data, it turned out that the most efficient way to remove these sudden background increases was to filter out the time intervals of low data quality. The remaining useful exposure times at $\phi = 0.570$ are 25 700 and 28 000 s for the SIS and GIS instruments, respectively.

Table 1. Journal of γ^2 Vel observations with the *ASCA* satellite.

Date JD-244 0000	ϕ (S97)	PA	ϕ' (M86)	Total elapsed phase interval
9 490.213	0.978	−38°	0.404	0.013
9 497.890	0.078	32°	0.502	0.008
10 164.773	0.570	172°	0.997	0.012

For each observation, we list the JD at mid-exposure and the corresponding orbital phase (with respect to periastron) and the mean position angle (with respect to the line of sight) according to the ephemeris of S97. A PA of 0° corresponds to the O-star being in front of the WR component. To make comparison with previous work easier, the fourth column provides the phase with respect to the conjunction (WR star in front) according to the ephemeris of Moffat et al. (1986). The last column lists the total phase interval elapsed between the start and stop times of the *ASCA* exposure.

The data reduction was performed with the XSELECT software (version 1.4b).

2.1 SIS spectra

For the two near-periastron observations, the source spectra were extracted from a circular region of 4-arcmin radius on the SIS0 detector. Since the source image is located slightly closer to the edge of chip 3 in the SIS1 frame, the extraction radius was reduced to 3.2 arcmin.

During the apastron observation, the source was located closer to the edge of the chip of the SIS0 and SIS1 detectors. The extraction radius was therefore limited to 3 and 2.2 arcmin, respectively. Consequently, up to about 15 per cent of the flux in the wings of the point spread function (PSF) could be lost for the SIS1 apastron spectrum.

We tested several methods of background subtraction:

(i) using the background from the whole chip outside the source region;

(ii) using a circular region on the chip, free from any (obvious) source contamination;

(iii) using archive blank-sky observations and extracting the background in the same circular region as the source.

Background subtraction methods (i) and (ii) provide nearly identical background corrections. A fit with a two-temperature Raymond–Smith-type plasma model (Raymond & Smith 1977) yielded overlapping fit parameters for both background-corrected spectra. Since the extraction region used in method (i) is larger than in method (ii), the number of background counts is larger and the statistical errors of the background spectrum derived by method (i) are slightly lower. In the following analysis of the SIS data we use the background spectra obtained by method (i).

2.2 GIS spectra

For the two near-periastron observations, the GIS2 source spectrum was extracted from a circular region of 6-arcmin radius. For the GIS3 data, a slightly smaller radius of 5.25 arcmin was used in order to avoid overlap of the source region with the background region, which was chosen to be diametrically opposite on the GIS detector.

During the apastron observation, the source was located slightly closer to the centre of the GIS field of view. We used extraction radii of 5 and 4.5 arcmin for the GIS2 and GIS3 data, respectively.

Two methods of background subtraction have been tested:

(i) using a circular region that is diametrically opposite to the source region (i.e. the background region has the same radius and same off-axis angle as the source region);

(ii) adding up archive blank-sky observations of different cut-off rigidity; the background spectrum is then extracted from the same circular region as the source but on the resulting blank-sky image.

The two background methods yield results that overlap within the

errors of the two-temperature fits. In the following we focus on the results obtained with the first background subtraction method.

2.3 Contaminating sources

The *ROSAT* PSPC observations of the γ^2 Vel field presented by Willis et al. (1995) reveal eight X-ray point sources within a radius of 4 arcmin around γ Vel. These sources are not resolved with *ASCA* and therefore contribute to the spectra extracted from the *ASCA* observations. As discussed by Stevens et al. (1996), there is very little information available on the nature of most of the contaminating sources. Two of them are known to be B-type stars and one is classified as a foreground Am star (Abt et al. 1976). However, no classification is known for the other sources.

Comparison between a SIS0 image in a hard energy band (2.0–6.0 keV) and in a soft energy band (0.5–2.0 keV) indicates that the harder emission is slightly more concentrated near the position of γ^2 Vel than the soft emission. This result suggests that, at all three orbital phases, γ^2 Vel is the main hard X-ray source in the field of view, whereas the nearby sources contribute a significant fraction of the soft emission. For instance, depending on the phase-dependent count rate of γ^2 Vel, the surrounding sources provide between 35 and 78 per cent of the total *ROSAT* PSPC count rate from a 4-arcmin radius region centred on γ^2 Vel.

In order to quantify this contamination, we retrieved the relevant *ROSAT* data from the ARNIE archive. We combined all the PSPC event lists and built the mean spectrum of the contaminating sources from two annular regions centred on γ^2 Vel with an inner radius of 1 arcmin and an outer radius of 3 or 4 arcmin, respectively. The PSPC background spectrum was extracted over four source-free circular regions of 10-arcmin radius each. The integrated PSPC count rate of the contaminating sources displays time variability by $\sim$10 per cent, i.e. at the 2σ level.

We fitted a two-temperature Raymond–Smith model to the mean PSPC spectrum of the sources around γ^2 Vel. The best-fitting parameters for extraction radii of 3 and 4 arcmin are listed in Table 2. We notice that these fits yield a column density towards the softer component that is only slightly larger than the interstellar column [$N_{\rm H}({\rm ISM}) = 8 \times 10^{19}\,{\rm cm}^{-2}$: Stevens et al. 1996] towards γ^2 Vel. A two-temperature plasma model with two distinct column densities was necessary to achieve a good fit to the PSPC spectrum of the contaminating sources. Adopting a single column density for both plasma components resulted in a poorer fit ($\chi^2_\nu = 1.48$ for model II), a column density close to $N_{\rm H}$(ISM) and a rather high kT_2 of 1.35 keV, much larger than the typical $kT \simeq 0.5$ keV of most B-type stars (e.g. Berghöfer, Schmitt & Cassinelli 1996).

Table 2. Best-fitting parameters of the mean PSPC spectrum of the contaminating sources. Models I and II correspond to an outer extraction radius of 3 and 4 arcmin, respectively. Within XSPEC, the emission measure EM is defined as $\int_V n_{\rm e} n_{\rm H}\,{\rm d}V$, where $n_{\rm e}$ and $n_{\rm H}$ are the electron and hydrogen densities, respectively. The emission measure corresponds to the *Hipparcos* distance of γ^2 Vel of 258 pc. The last row lists the integrated PSPC count rate of the contaminating source. For comparison the observed PSPC count rate of γ^2 Vel varies between 0.066 and 0.440 count s^{-1} depending on the orbital phase (see Willis et al. 1995).

Model	I	II
Outer extr. rad. (arcmin)	3	4
$(N_{\rm H})_1$ (10^{22} cm^{-2})	$(2.0^{+0.9}_{-0.6}) \times 10^{-2}$	$(1.7^{+0.7}_{-0.6}) \times 10^{-2}$
kT_1 (keV)	$0.16^{+0.04}_{-0.02}$	$0.17^{+0.04}_{-0.02}$
EM$_1$ (10^{55} cm^{-3})	3.52×10^{-2}	4.21×10^{-2}
$(N_{\rm H})_2$ (10^{22} cm^{-2})	$0.81^{+0.21}_{-0.25}$	$0.75^{+0.11}_{-0.25}$
kT_2 (keV)	$0.59^{+0.26}_{-0.25}$	$0.63^{+0.24}_{-0.15}$
EM$_2$ (10^{55} cm^{-3})	2.48×10^{-1}	2.58×10^{-1}
χ^2_ν (dof)	0.48 (14)	1.00 (14)
PSPC count rate (count s^{-1})	0.187	0.240

3 THE *ASCA* SPECTRUM OF γ^2 VEL

The SIS0 spectra of γ^2 Vel are displayed in Fig. 1. This figure illustrates the dramatic changes of the intensity and the spectral shape as a function of orbital phase. One also notices the prominent iron line at $\sim$6.7 keV, visible on all three spectra.

3.1 Spectral fitting

We modelled the extracted spectra using the XSPEC software (version 10.00). The spectra were rebinned to have at least 10 counts per bin and fitted with different models. It became immediately clear that a physically meaningful fit could only be achieved when the contaminating sources were taken into account. In fact, we tested various types of single-temperature and two-temperature Raymond–Smith and Mewe–Kaastra (Mewe, Gronenschild & van den Oord 1985; Kaastra 1992) models that did not take into account the effect of the nearby sources. Given the different sensitivities of the SIS and GIS instruments, we obtained quite different fit results for the SIS and GIS data sets. Part of these differences could actually reflect an instrumental effect leading to an increasing divergence of SIS and GIS spectra in the energy range below 1 keV (Hwang et al. 1999). Moreover, the physical interpretation of two-temperature fits in terms of X-ray emission from γ^2 Vel is rather difficult owing to the contamination by the nearby sources that is expected to affect mainly the softer component of the fits. In the following, we therefore include the effect of the contaminating sources in the spectral fits.

Assuming that the contaminating sources could be represented by the parameters listed in Table 2 at the time of the *ASCA* observations, we fitted the *ASCA* spectra with a three-temperature Raymond–Smith model keeping the parameters of two of the model components fixed at the values derived above (Table 2) for the contaminating sources. For this purpose, we used the spectral parameters of either the 3- or 4-arcmin (outer-radius) annulus depending on the actual radius used to extract the *ASCA* source spectrum (see Section 2). Only the parameters of the third component were varied in the fit, and the hard variable X-ray emission of γ^2 Vel was thus effectively fitted with a single-temperature Raymond–Smith model. Our fits reveal no trace of the very soft ($kT \simeq 0.19$ keV) emission component found by Willis et al. (1995) in the *ROSAT* PSPC spectra of γ^2 Vel. Because of the very different sensitivities of the *ROSAT* and *ASCA* instruments at energies below $\sim$1 keV, the *ROSAT* fit to the contaminating sources may slightly overestimate their actual contribution to the soft emission in the *ASCA* fits. Alternatively, it could be that the very soft component found by Willis et al. (1995) is itself variable and was weaker at the time of the *ASCA* observations.

The chemical composition of WC winds has been studied by means of ultraviolet (UV), optical and infrared (IR) spectroscopy revealing extremely non-solar abundances: H and N are totally

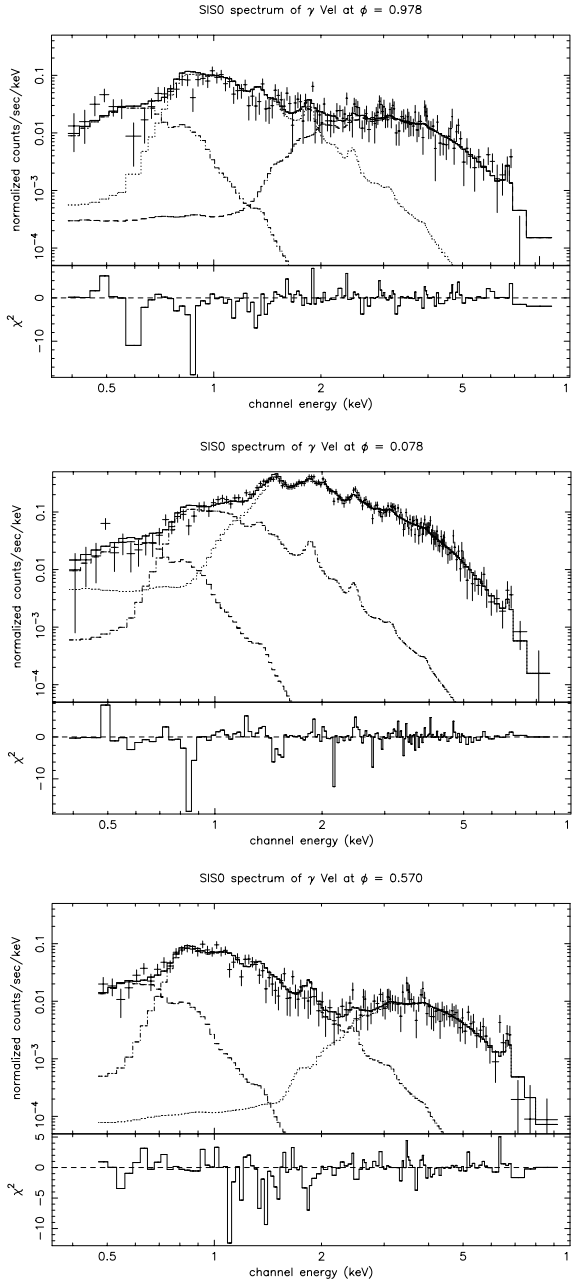

Figure 1. SIS0 spectra of γ^2 Vel at orbital phases $\phi = 0.978$ (top panel), 0.078 (middle panel) and 0.570 (bottom panel). The solid lines correspond to fits with a Raymond–Smith model including the effect of the contaminating sources and assuming a mixture between WC and O-star material of 50/50 by mass (see text). Note the prominent iron K line visible at all three orbital phases, whereas the other emission lines discussed in Section 3.2 are only visible on the $\phi = 0.078$ spectrum.

absent, whereas He, C and O are overabundant. From evolutionary considerations (e.g. Schaller et al. 1992), Ne, Mg and Si are also expected to be overabundant with respect to the solar abundances. Therefore, it seems natural to attempt an analysis of the *ASCA* spectra with non-solar abundance models.

There are, however, several limitations. Unfortunately, the

Table 3. Parameters of the hard component in the spectral fits of the SIS and GIS spectra of γ^2 Vel using a Raymond–Smith model accounting for the spectrum of the contaminating sources and assuming solar abundances. The label of the contaminating sources (I or II) refers to the two-temperature model parameters in Table 2. L_X and L_X^{int} are, respectively, the absorbed and intrinsic (i.e. absorption corrected) luminosities of the hard component in the energy range 0.5–10 keV. The emission measure and luminosities correspond to the *Hipparcos* distance of 258 pc.

Contam. sources	$\phi = 0.978$ II	$\phi = 0.078$ II	$\phi = 0.570$ I
varabs(0/100)*vray(0/100)			
N_H (10^{22} cm^{-2})	$7.5^{+0.9}_{-0.9}$	$2.40^{+0.06}_{-0.05}$	$11.9^{+1.7}_{-1.5}$
$\int \rho\, dz$ (10^{-2} g cm^{-2})	$17.82^{+2.12}_{-2.12}$	$5.72^{+0.14}_{-0.12}$	$28.36^{+4.05}_{-3.57}$
kT (keV)	$1.56^{+0.17}_{-0.12}$	$1.25^{+0.02}_{-0.02}$	$1.81^{+0.26}_{-0.23}$
EM (10^{55} cm^{-3})	1.85	6.16	1.43
χ^2_ν (dof)	1.14 (542)	1.35 (939)	1.28 (588)
L_X (10^{32} erg s^{-1})	0.27	1.51	0.20
L_X^{int} (10^{32} erg s^{-1})	2.49	9.01	1.92

ASCA data of γ^2 Vel are rather ill-suited to derive any constraints on the chemical abundances of the X-ray emitting plasma. The main reason is that the emission lines from the CNO elements are located in an energy region below 0.7 keV where the sensitivity of the instruments onboard *ASCA* is rather low and, moreover, the spectrum of γ^2 Vel in this energy range is seriously contaminated by the X-ray emission from the nearby soft sources. High-resolution spectroscopy with the *XMM* observatory might help to constrain the chemical abundances of the X-ray emitting plasma.

Another serious limitation comes from the fact that the colliding wind plasma, which is believed to produce the hard X-ray emission, consists of a mixture of WR and O-star wind material, with a priori unknown proportions. Although the pre-shock WC8 wind is denser, a greater fraction of the O-star wind is compressed and hence the O-star wind material affects the composition of the shocked plasma.

Moreover, the abundance anomalies of some key elements as predicted by the evolutionary models of WC stars depend critically on the ingredients (mixing, rotation, etc.) of these models (see, e.g., Meynet 1999). Thus any empirical model of the colliding wind plasma strongly depends on the assumed composition of the WC8 wind and the adopted mixture of the two winds. Similar remarks apply to the absorbing column towards the X-ray source, although in this case it seems likely that the absorption at phase $\phi = 0.570$ arises mostly from the WC8 wind material, whereas at phase $\phi = 0.078$ it probably arises from the sole O-star wind.

In view of these limitations, we opted for the following approach: we adopted average chemical abundances as listed by van der Hucht et al. (1986) except for the Ne abundance, which was taken from the recent results of Morris et al. (1999) derived from *ISO* SWS observations of γ^2 Vel. To simulate the chemical composition of the shocked plasma, we assumed a mixture between WC and O-star material of 0/100, 50/50 and 90/10 by mass, respectively. The photoelectric absorption was modelled using the cross-sections calculated by Bałucińska-Church & McCammon (1992) and adopting either the same abundances as for the emitting plasma or solar abundances.

Starting with the assumption that the bulk of the shocked gas comes from the O-star wind, we first used a 0/100 (i.e. solar abundance) model. In fact, it is possible that the majority of the X-ray emitting material might come from the shocked O-star wind

Table 4. As Table 3 except that we used non-solar abundances to model the composition of the emitting plasma and the absorbing column. The chemical composition of the shocked plasma was simulated assuming a mixture between WC- and O-star material of 50/50 and 90/10 by mass, respectively.

Contam. Sources	$\phi = 0.978$ II	$\phi = 0.078$ II	$\phi = 0.570$ I
varabs(50/50)*vray(50/50)			
$\int \rho \mathrm{d}z$ (10^{-2} g cm^{-2})	$1.40^{+0.19}_{-0.17}$	$0.46^{+0.01}_{-0.02}$	$2.17^{+0.27}_{-0.27}$
kT (keV)	$1.92^{+0.27}_{-0.23}$	$1.27^{+0.03}_{-0.03}$	$2.75^{+0.64}_{-0.39}$
EM (10^{55} cm^{-3})	0.20	0.91	0.12
χ^2_ν (dof)	1.14 (542)	1.46 (939)	1.30 (588)
L_X (10^{32} erg s^{-1})	0.27	1.49	0.20
$L_\mathrm{X}^\mathrm{int}$ (10^{32} erg s^{-1})	1.43	7.23	0.88
varabs(90/10)*vray(90/10)			
$\int \rho \mathrm{d}z$ (10^{-2} g cm^{-2})	$0.87^{+0.15}_{-0.09}$	$0.29^{+0.01}_{-0.01}$	$1.40^{+0.18}_{-0.17}$
kT (keV)	$1.97^{+0.23}_{-0.30}$	$1.27^{+0.03}_{-0.03}$	$2.74^{+0.67}_{-0.43}$
EM (10^{55} cm^{-3})	0.03	0.13	0.02
χ^2_ν (dof)	1.16 (542)	1.55 (939)	1.32 (588)
L_X (10^{32} erg s^{-1})	0.27	1.47	0.20
$L_\mathrm{X}^\mathrm{int}$ (10^{32} erg s^{-1})	1.34	7.00	0.87

Table 5. Best-fitting parameters of the most important emission lines in the $\phi = 0.078$ SIS and GIS spectrum of γ^2 Vel. Note that the equivalent widths are not corrected for the contribution of the serendipitous sources.

Ion	Line energy (keV)	Equiv. width (keV)
Mg XI	$1.45^{+0.02}_{-0.02}$	0.51
Si XIII	$1.89^{+0.01}_{-0.01}$	1.22
S XV	$2.42^{+0.02}_{-0.02}$	1.11
S XVI	$3.03^{+0.07}_{-0.06}$	0.56

Table 6. Properties of the iron line in the spectrum of γ^2 Vel as a function of the orbital phase.

	$\phi = 0.978$	$\phi = 0.078$	$\phi = 0.570$
Line energy (keV)	6.66 ± 0.08	6.67 ± 0.04	6.62 ± 0.03
Equiv. Width (keV)	0.85	0.82	1.18

since the shock front is expected to be wrapped around the O7.5 component.

We found good agreement between the fitting parameters derived for the various SIS and GIS data sets. The results of the simultaneous fits of the SIS and GIS data are listed in Table 3. To allow a comparison with non-solar abundance models, the column densities in Table 3 are given as N_H and $\int \rho \mathrm{d}z$ (in g cm^{-2}, where $\int \rho \mathrm{d}z = 2.38 \times 10^{-24} N_\mathrm{H}$ for a solar-composition material). Our fits yield column densities that are systematically larger than the interstellar value [$N_\mathrm{H}(\mathrm{ISM}) = 8 \times 10^{19}$ cm^{-2}], indicating that most of the absorption must be caused by circumstellar material.

The spectral fits to the *ASCA* data obtained with the 50/50 and 90/10 models and assuming identical compositions for the emitting and absorbing plasmas are described in Table 4. These spectral fits have about the same quality as those obtained assuming solar abundances, except for the $\phi = 0.078$ spectrum. For the $\phi = 0.078$ spectrum, the poorer fit quality results mainly from the fact that the non-solar abundance models fail to reproduce the observed relative intensity of the S XV and XVI lines with respect to the Mg XI and Si XIII lines (see Section 3.2).

The parameters in Table 4 yield systematically higher temperatures (especially for the apastron spectrum) and lower column densities than the solar abundance models. Given the much higher opacities of the WC-wind material, the lower column densities are not unexpected.

3.2 The emission lines

The X-ray spectrum of γ^2 Vel near the phase $\phi = 0.078$ contains several strong emission lines including a rather prominent iron K emission at ~ 6.7 keV (see Fig. 1). We measured the energy and the equivalent width of these lines by fitting a power-law continuum + four Gaussians to the spectrum extracted between 0.7 and 4.0 keV and a power law + Gaussian to the spectrum extracted between 5.0 and 8.0 keV. The results for the four most prominent lines in the 0.7–4.0 keV band measured on the $\phi = 0.078$ spectrum are listed in Table 5. The typical uncertainties on the equivalent width are of the order of 10 per cent for the stronger lines and 15 per cent for the weaker ones. Unfortunately, the limited signal-to-noise ratio of the spectra obtained at an orbital phase $\phi = 0.978$ and 0.570 does not allow us to measure any emission line on these spectra apart from the iron K-shell line.

The Mg, Si and S lines are also detected in the spectrum of the WN5+O6 binary V444 Cyg (Maeda et al. 1999), although with considerably lower equivalent widths and slightly different energies.

Unlike the four lines listed in Table 5, the iron Kα emission at $\sim$6.7 keV is detected in all *ASCA* spectra of γ^2 Vel. Most massive stars have X-ray spectra with temperatures below 1 keV and lack any iron K-shell line near 6.7 keV. The line is, however, seen in the spectra of the colliding wind systems WR 140 (Koyama et al. 1994) and V444 Cyg (Maeda et al. 1999).

The equivalent width of the iron line as a function of orbital phase is listed in Table 6. The strength and energy of this line are rather well reproduced by our best-fitting thermal models. The latter result contrasts with the situation in WR 140, where the power-law shape of the continuum and the strong variability of the iron Kα line point towards a non-thermal phenomenon in the winds of WR 140 (Pollock, Corcoran & Stevens 1999).

4 DISCUSSION AND CONCLUSION

Taking into account the contamination of the X-ray spectrum by the nearby sources, the *ASCA* spectrum of γ^2 Vel mainly consists of a hard thermal emission component that displays strong phase-dependent variability (Fig. 2). The bulk of this variability can be attributed to the changing column density towards the X-ray source, in qualitative agreement with theoretical models of colliding wind binaries (Stevens, Blondin & Pollock 1992; Pittard & Stevens 1997; Walder, Folini & Motamen 1999).

However, the variability also affects the temperature and the luminosity of the hard X-ray emission. In terms of a colliding wind interaction, the difference in temperature of the $\phi = 0.570$ and 0.978 spectrum could be interpreted as a consequence of the wider separation between the two stars at apastron. In fact, the winds are expected to reach higher pre-shock velocities at apastron, while they collide with considerably lower velocities near periastron. [In the strong-shock limit, the post-shock

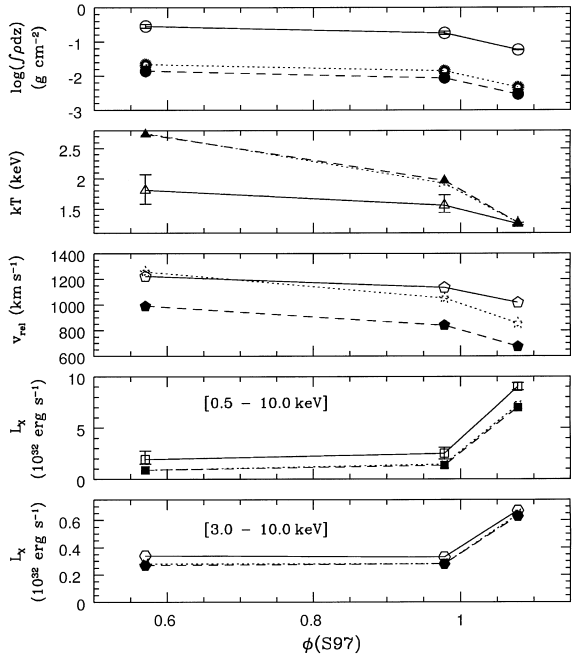

Figure 2. Changes in column density, temperature, relative pre-shock velocity and absorption-corrected luminosity of the hard-emission component in the *ASCA* spectrum of γ^2 Vel as a function of orbital phase (according to the S97 ephemeris). The two lower panels display the intrinsic (absorption-corrected) luminosity in the energy ranges 0.5–10 and 3.0–10 keV. The continuous line indicates the solar composition models, whereas the dotted and dashed lines correspond to the 50/50 and 90/10 non-solar abundance models, respectively. For clarity only the error bars on the parameters of the solar-abundance models have been drawn. The error bars on the luminosities correspond to the 1σ confidence range of the absorbing column density.

temperature is given by the relation $kT = (3/16)\bar{m}v_{\rm rel}^2$ (Stevens et al. 1992), where $\bar{m}$ is the average mass per particle and $v_{\rm rel}$ is the relative pre-shock velocity. In principle, this relationship allows us to derive the relative pre-shock velocities from the temperature of the colliding wind X-ray emission. The values of $v_{\rm rel}$ corresponding to our different models (Tables 3 and 4) are shown in Fig. 2. However, we caution that the actual pre-shock velocity decreases with increasing off-axis angle along the shock front and the temperature of the resulting X-ray emission thus only reflects an average value that certainly underestimates the actual on-axis pre-shock velocity.]

The softest and intrinsically most luminous spectrum is observed at $\phi = 0.078$. A possible explanation could be that the shock region consists of a plasma spanning a rather wide range of temperatures. In this case, a substantial fraction of the softer X-rays may be completely absorbed by the circumstellar material at phases $\phi = 0.978$ and 0.570 and become visible only at a phase $\phi = 0.078$ when the cavity of the O-star wind crosses the line of sight. Alternatively, the lower temperature and higher luminosity at $\phi = 0.078$ could indicate that, at this orbital phase only, the intrinsic emission from the O7.5 III primary star, which we expect to be softer, is significantly contributing to the observed emission. Assuming a bolometric luminosity of the O-star of $2.1 \times 10^5\,L_\odot$ (De Marco & Schmutz 1999) and adopting the canonical $L_{\rm X} - L_{\rm bol}$ relation valid for single O-stars (Berghöfer et al. 1997), we find that the intrinsic X-ray emission of the O-star should contribute a

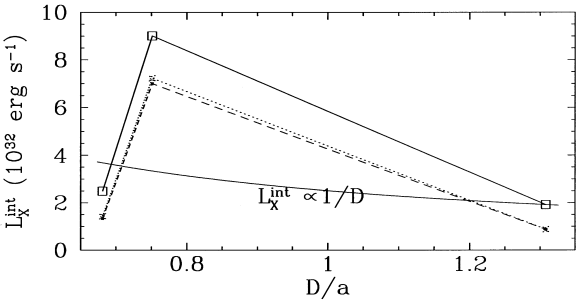

Figure 3. Changes in the absorption-corrected luminosity (0.5–10 keV) of the hard-emission component as a function of orbital separation (according to the S97 ephemeris). The different lines have the same meaning as in Fig. 2. The continuous line labelled $L_{\rm X}^{\rm int} \propto 1/D$ corresponds to the scaling law for adiabatic colliding winds normalized to the luminosity of the solar-abundance apastron model.

luminosity of the order of $1.2 \times 10^{32}\,{\rm erg\,s^{-1}}$. Since Berghöfer et al.'s (1997) relation holds for X-ray luminosities that are not corrected for intrinsic wind absorption, the above estimate should be compared with the $L_{\rm X}$ value at phase $\phi = 0.078$ (Tables 3 and 4). We find that the intrinsic emission from the O-star could indeed account for a significant fraction of the observed X-ray luminosity at a phase of $\phi = 0.078$.

Using the orbital solution of S97 and the scaling law for X-ray emission from largely adiabatic colliding winds, $L_{\rm X} \propto 1/D$, where D is the orbital separation between the stars (Stevens et al. 1992), we would expect a luminosity ratio of 1.7 between the $\phi = 0.078$ and 0.570 spectra and 1.9 between the $\phi = 0.978$ and 0.570 spectra. While the observed ratio between the luminosities at $\phi = 0.078$ and 0.570 is much larger than the 'theoretical' value, whatever the assumed plasma composition, the reverse situation holds for the ratio between the luminosities at $\phi = 0.978$ and 0.570 (see Fig. 3). Fig. 2 also illustrates the variations of the absorption-corrected X-ray flux in the energy band between 3.0 and 10.0 keV which is less affected by the wind absorption and is therefore less sensitive to the uncertainties in the chemical composition of the wind. We find that the disagreement between the measured intrinsic luminosity and the $1/D$ relation persists in the harder energy range. A plausible explanation for the discrepancy between the observed $\phi = 0.978$ versus $\phi = 0.570$ luminosity ratio and the theoretical predictions might be the higher density of the shocked winds near periastron. In fact, as a consequence of the higher density, radiative cooling probably affects the shock properties more efficiently at periastron and hence reduces the hard X-ray emission with respect to the simple scaling law for adiabatic colliding winds. Moreover, the X-ray emission at phase $\phi = 0.978$ could be altered by the shock crushing on to the O-star surface at that orbital phase.

As a result of the large wind momentum ratio between the WR and the O-star wind, St.-Louis et al. (1993) suspected a possible collapse of the shock between the two winds on to the surface of the O-star, at least near periastron. However, Gayley, Owocki & Cranmer (1997) propose that sudden radiative braking might prevent the shock from collapsing on the O-star surface. Using the most recent determination of the wind parameters of the system (Schaerer et al. 1997; De Marco & Schmutz 1999) and the homology relations of Gayley et al. (1997), we find indeed that radiative braking is needed at most orbital phases to prevent a photospheric collision. On the other hand, the temperature and

intrinsic luminosity changes around periastron could also be affected by a time delay between the orbital phase and the occurrence of the expected effects on the wind collision. For instance, the shock could be crushed on to the O-star surface near the periastron passage and might take some time to lift off again.

Corcoran (1996) discussed the variations of the spectral parameters of WR 140 as derived from *ROSAT* PSPC data obtained around periastron passage of this system. We note that in contrast to the γ^2 Vel behaviour displayed in Fig. 2, the temperature of the X-ray spectrum of WR 140 increases strongly around periastron passage.

Considering the position angle of the binary axis with respect to the conjunction at the orbital phases of the *ASCA* observations (Table 1), we notice that the cavity arising from the O-star is probably deflected by the effects of the Coriolis forces (Walder et al. 1999). Willis et al. (1995) suggest a half-opening angle of the shock cone of 25°, while the asymmetry of their *ROSAT* PSPC light curve reflects the effect of the orbital motion. The position angle of the $\phi = 0.078$ *ASCA* observation (Table 1) suggests that the trailing arm of the shock is located at least 32° from the axis of the binary.

We can use the observed column density to the hot component at phase $\phi = 0.570$ when the WC8 star is in front to obtain a rough estimate of the mass-loss rate of this star. Adopting the orbital solution of S97, assuming an orbital inclination of 65° and using the momentum ratio corresponding to the wind parameters of the system (Schaerer et al. 1997; De Marco & Schmutz 1999), we find that the stagnation point (assuming a pure ram-pressure balance) is located at $\sim 32\,R_\odot$ from the centre of the O-star. From this result, we find that the observed column of $\int \rho\,dz = 2.836 \times 10^{-1}\,g\,cm^{-2}$ in the case of the solar-abundance models corresponds to a mass-loss rate of roughly $2 \times 10^{-5}\,M_\odot\,yr^{-1}$. This value is in reasonable agreement with the recent mass-loss determinations by Schaerer et al. (1997) and Stevens et al. (1996). One should, however, notice that this value is strongly dependent on the adopted chemical composition of the absorbing gas and yields probably an *upper limit* on the actual mass-loss rate. Indeed, the non-solar-abundance models yield column densities, and hence mass-loss rates, that are a factor 13 and 20 lower for the 50/50 and 90/10 non-solar-abundance models, respectively.

Maeda et al. (1999) report the analysis of three *ASCA* observations of the short-period (4.2 d) eclipsing binary V444 Cyg (WN5+O6). The fits to these spectra require two-temperature Raymond–Smith models with a soft component at $kT_1 \simeq 0.6$ keV and a harder component at $kT_2 \simeq 2.0$ keV. Maeda et al. find that the column density towards the harder component varies with orbital phase and is largest when the WN5 star is in front. The absorption-corrected luminosity of the hard component in V444 Cyg displays a minimum when the O-star is in front, in agreement with the X-ray source being located between the two stars and rather close to the surface of the O-star. Outside this minimum, the absorption-corrected luminosity (in the 0.7–10 keV energy range and assuming a distance of 1.7 kpc) is of the order of $(1.1\text{–}1.4) \times 10^{33}\,erg\,s^{-1}$, i.e. larger than what is observed for γ^2 Vel.

In contrast to our γ^2 Vel data, the *ASCA* spectra of V444 Cyg reveal no evidence for changes of the temperature of the hard component as a function of orbital phase. In the framework of a colliding wind model, the temperature is indeed expected to remain constant in a binary system with a circular orbit such as V444 Cyg. Let us recall that in the case of the γ^2 Vel data, acceptable fits are achieved with a single-temperature Raymond–Smith model once the contamination by the nearby soft sources is taken into account. In the case of V444 Cyg, there is an additional soft component ($kT_1 \simeq 0.6$ keV) that Maeda et al. (1999) attribute to the intrinsic emission from the WN5 or O6 component. In the case of γ^2 Vel we find no compelling evidence for such a component (except perhaps at phase $\phi = 0.078$).[1] This is not surprising since individual WC stars are on average fainter X-ray sources than individual WN stars (Pollock 1987), and the opaque WC wind material is probably more efficient in absorbing the intrinsic X-ray emission from the O-star in γ^2 Vel.

In summary, our analysis of the three *ASCA* observations of γ^2 Vel reveals a hard-emission component that undergoes strong variability over the orbital cycle. We have constrained the properties of this hard component by accounting for the softer emission from the sources in the vicinity of γ Vel. Our analysis reveals that the uncertainties in the chemical composition of the X-ray emitting plasma significantly affect the derived shock temperature and absorption column, but play a smaller role in determining the intrinsic X-ray luminosity of the colliding wind zone. The observed variations of the hard component are in qualitative agreement with the predictions of colliding wind models, and the column density of the apastron spectrum assuming solar abundances yields an upper limit on the mass-loss rate of the WC8 star of the order of $2 \times 10^{-5}\,M_\odot\,yr^{-1}$ in fair agreement with other recent determinations.

ACKNOWLEDGMENTS

The authors thank an anonymous referee for a careful reading of the manuscript. GR is greatly indebted to the Fonds National de la Recherche Scientifique (Belgium) for support. GR is also supported in part by contract ARC 94/99-178 'Action de recherche concertée de la Communauté Française' (Belgium) and by contract P4/05 'Pôle d'Attraction Interuniversitaire' (SSTC-Belgium). Partial support through the PRODEX XMM-OM Project is also gratefully acknowledged. IRS acknowledges funding from a PPARC Advanced Fellowship. The data reduction was performed on the Starlink node at the University of Birmingham. This research has made use of data obtained from the Leicester Data base and Archive Service at the Department of Physics & Astronomy, Leicester University, UK. The SIMBAD data base has been consulted for the bibliography.

REFERENCES

Abbott D. C., Bieging J. H., Churchwell E., Torres A. V., 1986, ApJ, 303, 239
Abt H. A., Landolt A. U., Levy S. G., Mochnacki S., 1976, AJ, 81, 541
Bałucińska-Church M., McCammon D., 1992, ApJ, 400, 699
Berghöfer T. W., Schmitt J.H.M.M., Cassinelli J. P., 1996, A&AS, 118, 481
Berghöfer T. W., Schmitt J.H.M.M., Danner R., Cassinelli J. P., 1997, A&A, 322, 167
Chapman J. M., Leitherer C., Koribalski B., Bouter R., Storey M., 1999, ApJ, 518, 890
Conti P. S., Smith L. F., 1972, ApJ, 172, 623
Corcoran M. F., 1996, in Niemela V. S., Morrell N., eds, Workshop on Colliding Winds in Binary Stars to honor Jorge Sahade, Rev. Mex. Astron. Astrofis. Ser. Conf., 5, 54
De Marco O., Schmutz W., 1999, A&A, 345, 163
Gayley K. G., Owocki S. P., Cranmer S. R., 1997, ApJ, 475, 786

[1] Willis et al. (1995) fitted the *ROSAT* PSPC data of γ^2 Vel at phases when the O-star is behind the WC8 stellar wind with a blackbody model with $kT \simeq 0.19$ keV. *ASCA* is obviously not the best instrument to detect such a very soft component, especially since the soft energy range is strongly affected by the nearby sources. See also our discussion in Section 3.1.

Hwang U., Mushotzky R. F., Burns J. O., Fukazawa Y., White R. A., 1999, ApJ, 516, 604
Kaastra J. S., 1992, An X-Ray Spectral Code for Optically Thin Plasmas, Internal SRON-Leiden Report
Koyama K., Maeda Y., Tsuru T., Nagase F., Skinner S., 1994, PASJ, 46, L93
Leitherer C., Chapman J. M., Koribalski B., 1997, ApJ, 481, 898
Maeda Y., Koyama K., Yokogawa J., Skinner S., 1999, ApJ, 510, 967
Meynet G., 1999, in van der Hucht K. A., Koenigsberger G., Eenens P. R. J., eds, Wolf–Rayet Phenomena in Massive Stars and Starburst Galaxies, Proc. IAU Symp., Vol. 193. Astron. Soc. Pac., San Francisco, p. 218
Mewe R., Gronenschild E. H. B. M., van den Oord G. H. J., 1985, A&AS, 62, 197
Moffat A. F. J., Vogt N., Paquin G., Lamontagne R., Barrera L. H., 1986, AJ, 91, 1386
Morris P. W., van der Hucht K. A., Willis A. J., Dessart L., Crowther P. A., Williams P. M., 1999, in van der Hucht K. A., Koenigsberger G., Eenens P. R. J., eds, Wolf–Rayet Phenomena in Massive Stars and Starburst Galaxies, Proc. IAU Symp., Vol. 193. Astron. Soc. Pac., San Francisco, p. 77
Pittard J. M., Stevens I. R., 1997, MNRAS, 292, 298
Pollock A. M. T., 1987, ApJ, 320, 283
Pollock A. M. T., Corcoran M. F., Stevens I. R., 1999, in van der Hucht K. A., Koenigsberger G., Eenens P. R. J., eds, Wolf–Rayet Phenomena in Massive Stars and Starburst Galaxies, Proc. IAU Symp., Vol. 193. Astron. Soc. Pac., San Francisco, p. 388
Raymond J. C., Smith B. W., 1977, ApJS, 35, 419
Schaerer D., Schmutz W., Grenon M., 1997, ApJ, 484, L153
Schaller G., Schaerer D., Meynet G., Maeder A., 1992, A&AS, 96, 269
Schmutz W. et al., 1997, A&A, 328, 219 (S97)
St.-Louis N., Willis A. J., Stevens I. R., 1993, ApJ, 415, 298
Stevens I. R., Blondin J. M., Pollock A. M. T., 1992, ApJ, 386, 265
Stevens I. R., Corcoran M. F., Willis A. J., Skinner S. L., Pollock A. M. T., Nagase F., Koyama K., 1996, MNRAS, 283, 589
van der Hucht K. A., Cassinelli J. P., Williams P. M., 1986, A&A, 168, 111
van der Hucht K. A. et al., 1997, New Astron., 2, 245
Walder R., Folini D., Motamen S. M., 1999, in van der Hucht K. A., Koenigsberger G., Eenens P. R. J., eds, Wolf–Rayet Phenomena in Massive Stars and Starburst Galaxies, Proc. IAU Symp., Vol. 193. Astron. Soc. Pac., San Francisco, p. 298
Williams P. M., van der Hucht K. A., Pollock A. M. T., Florkowski D. R., van der Woerd H., Wamsteker W. M., 1990a, MNRAS, 243, 662
Williams P. M., van der Hucht K. A., Sandell G., Thé P. S., 1990b, MNRAS, 244, 101
Willis A. J., Schild H., Stevens I. R., 1995, A&A, 298, 549

This paper has been typeset from a TEX/LATEX file prepared by the author.

2.2.1 More results on the wind-wind collision in γ^2 Vel

Recently, γ^2 Vel has been observed with the high-resolution grating spectrographs onboard *Chandra* and *XMM-Newton*. These observations have shed new light on the X-ray emission of this system. Here, I briefly summarize the main results obtained from these observations.
Skinner et al. (2001) and Henley et al. (2005) discussed the same *Chandra* HETG grating spectra obtained at orbital phase $\phi = 0.08$, i.e. 6 days after periastron and 4 days after the conjunction with the O-star being in front. The HETG spectra reveal strong emission lines of Si, S, Mg, Fe and Ne, along with an underlying continuum emission. These emission lines reach their maximum strength for plasma temperatures between 4 and 25 MK (kT = 0.3 – 2.2 keV). The lines are broadened with a FWHM of about 1200 km s^{-1}. The ratios $\mathcal{R} = f/i$ between the forbidden and intercombination lines of the He-like triplets apparently suggest that these lines arise in a low-density medium at a large distance from the photosphere of the O-star. This is unexpected if the X-rays do indeed form in a wind interaction zone that should be located rather close to the surface of the O-star, given the large wind momentum ratio $\frac{(\dot{M}\,v_\infty)_{\rm WR}}{(\dot{M}\,v_\infty)_{\rm O}} \simeq 33$ (De Marco et al. 2000). Even more surprising were the lack of a Doppler shift of the lines, as well as their Gaussian shape (Henley et al. 2005). At this specific orbital phase, the material in the shock cone of the wind interaction zone is expected to be flowing towards the observer and should hence display emission lines blueshifted by a few hundred km s^{-1} (Henley et al. 2005). The latter authors suggested that the properties of the emission lines can be explained if the opening angle of the shock cone is about 87°, a value much larger than expected from the wind momentum ratio, which could only be explained as the result of sudden radiative braking, i.e. the deceleration of the WR wind when it encounters the radiation field of the O-star (Gayley et al. 1997). However such a wide opening angle is at odds with the *ROSAT* light curve of Willis et al. (1995), which rather suggests a value of $\sim 50^\circ$, as well as with the column densities inferred from the *ASCA* spectra (Rauw et al. 2000a).

The discrepancy between the observed line properties and the expectation for a colliding wind binary outlined above cast some doubt on the origin of the X-ray emission of γ^2 Vel. The wind – wind collision creates a cavity in the wind of the WC star and this cavity certainly produces a phase-dependent absorption of the intrinsic X-ray emission of the O star primary. But does the wind – wind collision also generate X-ray emission itself? In fact, much of the X-ray emission might actually be intrinsic to the O-star. Skinner et al. (2001) pointed out that the HETG spectrum ressembles that of the peculiar (but probably single) O-star θ^1 Ori C and questioned the colliding wind origin of this emission. However, assuming that the X-rays come solely from the wind of the O-star does not solve the issue of the large $\mathcal{R}$ values of the He-like triplets. Henley et al. (2005) further argue that the intrinsic X-ray luminosity (corrected for the total, interstellar + circumstellar, absorption) of γ^2 Vel at phase $\phi = 0.08$ is much larger than expected from the usual $L_X/L_{\rm bol} \sim 10^{-7}$ ratio for O-stars. However, this argument is not correct since the $L_X/L_{\rm bol}$ relation applies to X-ray luminosities corrected for the interstellar absorption only and can thus not be compared to the intrinsic X-ray emission evaluated by Henley et al. (see also the discussion in Rauw et al. 2000a).

Schild et al. (2004) presented two *XMM-Newton* observations of γ^2 Vel obtained at phases $\phi = 0.12$ (near maximum flux) and 0.37 (at a lower flux level). These spectra are identical at very low (< 0.7 keV) and very high (> 4.5 keV) energies, but the $\phi = 0.37$ spectrum is strongly depressed at intermediate energies by the effect of a strong extra absorption (in good agreement with the results reported by Rauw et al. 2000a). Assuming that the X-ray emission arises in the wind-wind collision zone, the column density of the extra absorption provides a direct measure of the mass loss rate of the WC8 star. In this way, Schild

et al. (2004) infer a mass loss rate of $8 \times 10^{-6}\,\mathrm{M}_\odot\,\mathrm{yr}^{-1}$ for the WC8 star, i.e. four times less than that found by De Marco et al. (2000) assuming a homogeneous wind. Schild et al. (2004) interpreted this as evidence for clumping in the Wolf-Rayet wind with a filling factor of only 6%. It is worth noting that this implies a reduced wind momentum ratio (and hence probably a larger cone opening angle of about 76°) compared to the results of De Marco et al. (2000). The cone opening angle is again larger than the 40 – $60°$ range inferred by Willis et al. (1995), but this result is only valid if the mass loss rate of the O star is indeed equal to $1.8 \times 10^{-7}\,\mathrm{M}_\odot\,\mathrm{yr}^{-1}$ as inferred by De Marco et al. (2000) and is not reduced by clumping.
Schild et al. (2004) found that the low energy part of the RGS X-ray spectrum exhibits weak radiation recombination continua of C VI and C V consistent with an electron temperature of about 38000 K. This indicates that these recombination continua arise in a photoionized plasma which must be unaffected by the variable absorption. In summary, Schild et al. (2004) proposed that the highly variable X-ray emission component (with temperatures of 8 and 19 MK corresponding to kT of 0.7 and 1.6 keV respectively) arise in the central part of the colliding wind region which is deeply embedded in the WR wind, whilst a cooler component (0.25 keV) probably represents the intrinsic emission of the O-star primary. Finally, they confirm the lack of a $1/D_{\mathrm{sep}}$ dependence of the X-ray luminosity found by Rauw et al. (2000a).

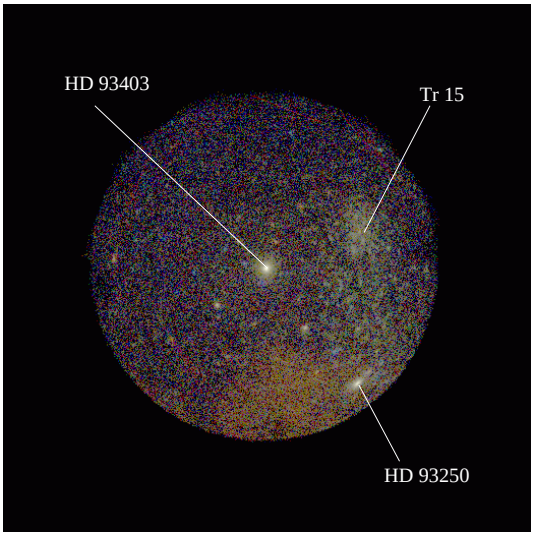

Figure 2.3: Three colour EPIC image of the Carina region around HD 93403. Red, green and blue colours correspond to average energies of 0.7, 1.5 and 2.5 keV. The radius of the EPIC field of view is about 15 arcmin.

2.3 X-ray emission from O-star binaries

The eccentric O-star binary HD 93403 (see Sect. 1.2) was the first O + O type binary for which phase-resolved X-ray spectroscopy was obtained with *XMM-Newton*. Four pointings of HD 93403 were obtained as part of the guaranteed time programme of the *XMM*-OM consortium. The average exposure times per observation were 9.4 and 5.0 ksec for the EPIC-MOS and -pn instruments respectively and the observations were scheduled at binary phases 0.26, 0.52, 0.75 and 0.01 (phase 0.00 corresponding to the periastron passage, see Rauw et al. 2000b). The main results of this campaign, along with a study of the

signature of the wind interaction in the optical spectrum of HD 93403, are reported in the paper by Rauw et al. (2002a) reproduced below.

An image of the EPIC field of view is shown in Fig. 2.3. Beside some soft diffuse emission from the outskirts of the Carina Nebula, the image reveals also a number of point sources, some of which being coincident with other early-type stars (e.g. HD 93250), as well as X-ray emission from the open cluster Trumpler 15.

Rauw et al. (2002a) evaluated the X-ray luminosity of HD 93403 assuming a distance of 3.2 kpc and using the bolometric luminosities of Rauw et al. (2000b). These parameters have been revised in the meantime (see Sect. 1.2). Using the distance of 2.5 kpc, we infer an X-ray luminosity of 2.4×10^{33} erg s^{-1} in the 0.5 – 10 keV energy domain. The bolometric luminosity of the binary as determined in Sect. 1.2 amounts to 2.4×10^{39} erg s^{-1} and hence $\log L_{\rm X}/L_{\rm bol} \simeq -6.0$.

A&A 388, 552–562 (2002)
DOI: 10.1051/0004-6361:20020523

Astronomy & Astrophysics

Phase-resolved X-ray and optical spectroscopy of the massive binary HD 93403⋆

G. Rauw[1], J.-M. Vreux[1], I. R. Stevens[2,1], E. Gosset[1,⋆⋆], H. Sana[1,⋆⋆⋆], C. Jamar[3], and K. O. Mason[4]

[1] Institut d'Astrophysique, Université de Liège, Allée du 6 Août, Bât B5c, 4000 Liège (Sart Tilman), Belgium
[2] School of Physics & Astronomy, University of Birmingham, Edgbaston Birmingham B15 2TT, UK
[3] Centre Spatial de Liège, Université de Liège, Avenue du Pré-Aily, 4031 Angleur, Belgium
[4] Mullard Space Science Laboratory, University College London, Holmbury St. Mary, Dorking, Surrey, RH5 6NT, UK

Received 24 July 2001 / Accepted 3 April 2002

Abstract. We report the first results of a campaign aimed at the study of early-type binaries with the *XMM-Newton* observatory. Phase-resolved EPIC spectroscopy of the eccentric binary HD 93403 reveals a clear orbital modulation of the X-ray luminosity as a function of the orbital phase. Below 1.0 keV, the observed X-ray flux is modulated by the opacity of the primary wind. Above 1.0 keV, the observed variation of the X-ray flux is roughly consistent with a $1/r$ dependence expected for an adiabatic colliding wind interaction. HD 93403 appears less overluminuous in X-rays than previously thought and a significant fraction of the total X-ray emission arises probably within the winds of the individual components of the binary. Optical monitoring of the system reveals strong variability of the He II λ 4686 and Hα line profiles. The He II λ 4686 line displays a broad asymmetrical emission component which is found to be significantly stronger between phases 0.80 and 0.15 than around apastron. This suggests that part of the emission arises in the interaction region and most probably in the trailing arm of a shock cone wrapped around the secondary. Some absorption lines of the secondary's spectrum display equivalent width variations reminiscent of the so-called Struve-Sahade effect. The differences in behaviour between individual lines suggest that the temperature may not be the only relevant parameter that controls this effect.

Key words. stars: early-type – binaries: spectroscopic – stars: individual: HD 93403 – stars: winds, outflows – X-rays: stars

1. Introduction

Early-type binaries, consisting either of a Wolf-Rayet (WR) star with an O-star companion or of two O-stars, can be the scene of a strong interaction between the stellar winds of the two components. This wind collision is expected to produce an X-ray emission that displays significant phase-locked variability either as a consequence of the changing wind opacity along the line of sight towards the shock or as a result of the changing orbital separation in eccentric binaries (see e.g. Stevens et al. 1992; Pittard & Stevens 1997). A comparison of the observed spectra and light curves with predictions from numerical simulations should help us to better understand the hydrodynamics of stellar winds.

While a number of WR + O binaries have been extensively monitored with previous and current X-ray satellites (for a recent review see e.g. van der Hucht 2002), so far only a few colliding wind O + O binaries have been studied in detail in the X-ray domain. Corcoran (1996) presented the ROSAT-PSPC light curves of sixteen O-type binaries (not including HD 93403, the system discussed in this paper) and found evidence for a phase-locked modulation in at least four cases. Pittard et al. (2000) analyzed two *ASCA* observations of the highly eccentric system ι Ori obtained near periastron and apastron. Strong differences between these phases were a priori expected, but the observations proved otherwise: both the luminosity and the spectral shapes were found to be remarkably similar. This suggests that the bulk of the X-ray emission in ι Ori is intrinsic to one of the components rather than being associated with the wind interaction.

The signatures of wind interaction phenomena in O + O binaries may also be found in their optical spectra. Indeed, phase-locked variability of the profiles of optical

Send offprint requests to: G. Rauw,
e-mail: rauw@astro.ulg.ac.be

⋆ Based on observations with XMM-Newton, an ESA Science Mission with instruments and contributions directly funded by ESA Member states and the USA (NASA). Also based on observations collected at the European Southern Observatory (La Silla, Chile).

⋆⋆ Research Associate FNRS (Belgium).

⋆⋆⋆ Research Fellow FNRS (Belgium).

Table 1. Journal of the *XMM-Newton* observations of HD 93403. The first column lists the spacecraft revolution number, the second and third columns provide the date and the corresponding orbital phase of HD 93403 relative to periastron passage (according to the ephemeris of Rauw et al. 2000) at mid-exposure for the EPIC-MOS instruments. Note that the pn exposures started about 4000 s later than the MOS observations. The following six columns list the effective exposure time (in seconds) and the background corrected count rate (cts s^{-1}) of HD 93403 for energies above 0.5 keV. The last two columns provide the relative orbital separation between the components (in units of the semi-major axis) and the position angle (PA) of the binary axis. A PA of 0° corresponds to the O5.5 I primary star being "in front".

Rev.	JD	Φ	MOS1		MOS2		pn		r/a	PA
	−2450000.0		Exp.	Count rate	Exp.	Count rate	Exp.	Count rate		(°)
191	1902.995	0.265	8865	0.208 ± 0.005	8869	0.213 ± 0.005	4472	0.466 ± 0.011	1.060	127
193	1906.815	0.518	8666	0.191 ± 0.005	8670	0.186 ± 0.005	4344	0.419 ± 0.011	1.233	63
195	1910.234	0.745	8763	0.199 ± 0.005	8766	0.199 ± 0.005	4416	0.405 ± 0.011	1.073	5
212	1944.435	0.011	11492	0.228 ± 0.005	11491	0.220 ± 0.005	6871	0.487 ± 0.009	0.767	119

emission lines such as Hα or He II λ 4686 provides a powerful diagnostic that can be used to constrain the geometry of the interaction regions in these systems (e.g. Thaller et al. 2001; Rauw et al. 1999, 2001; Sana et al. 2001).

In this paper, we present the results of our *XMM-Newton* observing campaign of the eccentric massive binary HD 93403 (O5.5 I + O7 V, $P_{\rm orb} = 15.093$ days, $e = 0.234$, Rauw et al. 2000) in the Carina complex. HD 93403 is an ideal system to investigate the effects of the eccentricity on the X-ray emission generated in a colliding wind process. In fact, because of the probably rather low orbital inclination ($i \simeq 30°$, Rauw et al. 2000), we expect little variability of the circumstellar column density towards the shock and any phase dependence of the X-ray emission therefore most probably reflects the changing separation between the two stars.

EINSTEIN observations of HD 93403 revealed an exceptionally large X-ray excess luminosity above the "canonical" $L_{\rm X}/L_{\rm bol}$ relation for single O-stars, making HD 93403 one of the most extreme O + O binary systems in the sample of Chlebowski & Garmany (1991). In our present analysis, we derive however a significantly lower value for $L_{\rm X}/L_{\rm bol}$ (see Sect. 3.3).

In the following, we focus on the EPIC medium resolution spectra of HD 93403. We discuss the X-ray light curve in conjunction with the results of a ground-based campaign that revealed variability in the optical spectrum of HD 93403. Some preliminary results of the optical monitoring were already presented by Rauw et al. (2002a).

2. Observations and data reduction

2.1. XMM-Newton observations

Four phase-constrained observations of HD 93403 were obtained with the *XMM-Newton* observatory (Jansen et al. 2001) as part of the guaranteed time observation programme of the *XMM* Optical Monitor consortium (Mason et al. 2001). The journal of observations is given in Table 1. The first three pointings were scheduled during the same orbital cycle of HD 93403, while the last pointing was obtained two cycles later. The two EPIC MOS instruments were operated in the full frame mode (Turner et al. 2001) whilst the EPIC-pn camera was used in the extended full frame mode (Strüder et al. 2001). All three EPIC instruments used the thick filter to reject optical and UV light.

We used the *XMM-Newton* Science Analysis System (SAS, version 5.0.1) to process the raw EPIC data. For the MOS (resp. pn) observations only events with pattern 0–12 (resp. 0) were considered (Turner et al. 2001). We checked that the data were not affected by any strong background flares. No indication of pile-up was found in our data. The spectrum of HD 93403 was accumulated over a radius of 60″ and the background spectrum was obtained over an annulus around the source region (outer radius 85″). For the pn detector, we truncated the extraction region to include only events from CCD 1. We adopted the redistribution matrices provided by the EPIC instrument teams (versions available in May 2001). We used the SAS to build the appropriate ancillary response file for each observation. The spectra were binned to reach a minimum of 25 counts per channel and the background corrected spectra were analyzed using the XSPEC software (version 11.00).

A preliminary discussion of the X-ray sources in the EPIC field of view around HD 93403 can be found in Rauw et al. (2002b).

2.2. Optical spectra

In the present paper, we use a set of sixteen echelle spectra of HD 93403 obtained with the Fiber-fed Extended Range Optical Spectrograph (FEROS, Kaufer et al. 1999) attached to the ESO 1.52 m telescope at La Silla. The data were collected during four observing runs in April–May 1999, May 1999, 2000 and 2001 (the whole dataset being spread over 49 orbital cycles). The observations and reductions of the first three observing runs (13 spectra) are described in Rauw et al. (2000). In May 2001, three additional spectra were obtained on HJD 2452037.607, 2452038.571 and 2452040.554 corresponding to phases $\Phi = 0.184$, 0.248 and 0.379 respectively. The latter data were reduced with a modified version of the FEROS context working under the MIDAS environment. The MIDAS routines were adapted following recommendations by Dr. H. Hensberge in order to optimize the blaze correction.

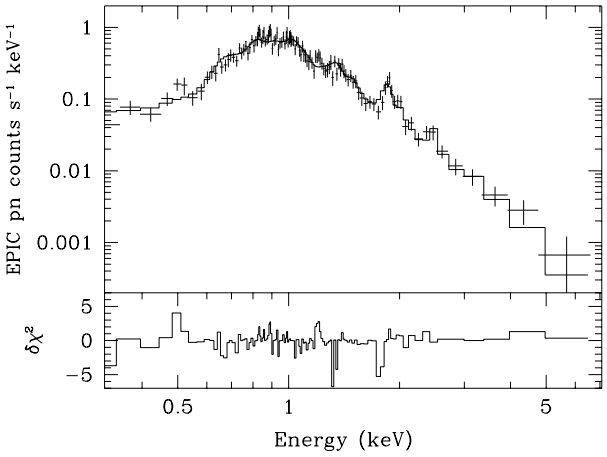

Fig. 1. EPIC pn spectrum of HD 93403 at $\Phi = 0.011$ and best-fitting 2-T MEKAL model (from Table 2). The lower panel yields the contribution to the χ^2 per energy bin with the sign of the (O–C) residual.

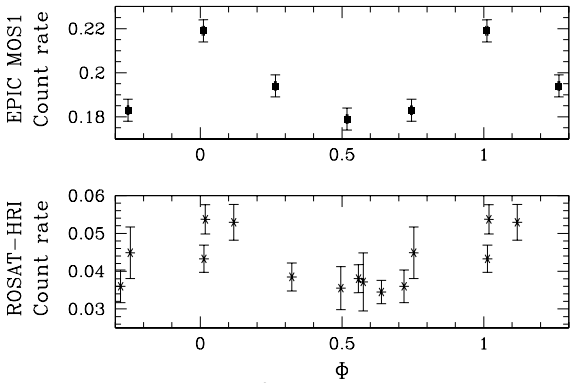

Fig. 2. X-ray light curve of HD 93403. The top panel yields the EPIC MOS1 count rate in the 0.5–2.5 keV band. 1-σ error bars are indicated. The MOS2 and pn data display very similar variations. The lower panel illustrates the *ROSAT*-HRI light curve extracted from observation rh202331n00 (see text).

3. The X-ray data

3.1. Spectral fits

To quantify the properties of the X-ray emission from HD 93403, we fitted the EPIC spectra with a variety of simple models. The spectral fits were restricted to energies above 0.5 keV. This analysis is only meant to characterize the overall spectral shape and its variability as a function of orbital phase. The models used here are certainly too simplistic to accurately describe the physical conditions in the emitting plasma and the best fit parameters should therefore not be overinterpreted. The most evident flaw of this simple spectral modelling is that the cross sections of the absorbing column do not take into account the ionization of the wind material[1]. What prevents us from applying a proper wind absorption model such as the one of Waldron et al. (1998) is that in a colliding wind binary, like HD 93403, the geometry of the emitting and absorbing regions is far more complex than in a single star. An accurate modelling of this situation requires the use of sophisticated 3-D hydrodynamic models (e.g. Pittard 2000). This is beyond the scope of the present work and will be the subject of a forthcoming paper.

Since the best fits obtained for the three EPIC instruments are very similar, we focus here on the results obtained for a simultaneous fit of the data from all EPIC instruments.

First we tried to fit the EPIC spectra of HD 93403 with solar metallicity thermal plasma MEKAL models (Mewe et al. 1985; Kaastra 1992). Single temperature models do not provide a decent fit to the data ($\chi_\nu \geq 2.2$). As a next step, we fitted the spectra using two temperature solar abundance MEKAL models allowing distinct column densities for both components, but requiring them to be larger than the interstellar HI column density. Chlebowski & Garmany (1991) measured the interstellar Lyα line as observed on *IUE* spectra of HD 93403 to estimate $N_{\rm H,ISM} = 0.367 \times 10^{22}\,{\rm cm}^{-2}$. For the fits in Table 2, we thus forced the individual columns of our 2-T model to be larger than $0.37 \times 10^{22}\,{\rm cm}^{-2}$. Apart from the X-ray fluxes, the best-fitting spectral parameters in Table 2 reveal surprisingly little variability over the orbital cycle.

Finally, we also tested a two component model consisting of a 1-T MEKAL thermal model + a power-law spectrum. The fits are of comparable quality to those obtained with the 2-T MEKAL models and yield $kT \simeq 0.60$ keV and a photon index $\Gamma \geq 3.0$. Theoretical models predict that strong shocks in stellar winds, either due to intrinsic instabilities (Chen & White 1991) or to colliding wind interactions in binaries (Eichler & Usov 1993), can accelerate free electrons to relativistic energies through the first-order Fermi mechanism. This process is expected to account for the non-thermal radio emission observed in a subset of early-type stars[2]. Given the enormous supply of photospheric UV photons in the winds of O-stars, inverse-Compton scattering by relativistic electrons is expected to generate a non-thermal X-ray emission. However, the best-fitting photon indices we derive are much steeper than the values expected from theoretical models of the first order Fermi mechanism ($\Gamma \simeq 1.5$, Chen & White 1991). The existence of a non-thermal component in the X-ray spectrum of HD 93403 is therefore unlikely.

3.2. Phase-locked variability

The fits of the EPIC spectra indicate surprisingly little variability of the spectral shape as a function of orbital phase. However, they do reveal a phase-dependence of the observed X-ray flux. In fact, the fluxes given in Table 2 and the count rates plotted in Fig. 2 indicate that

[1] We note however that restricting the fits to energies above 0.5 keV should considerably reduce the impact of this assumption.

[2] No detection of a radio emission (be it thermal or non-thermal) from HD 93403 is reported in the literature.

Table 2. Best fitting parameters of the solar metallicity 2-T MEKAL fits (`wabs`$_{\rm ISM}$`*(wabs`$_1$`*mekal`$_1$`+wabs`$_2$`*mekal`$_2$`)`) to the EPIC spectra of HD 93403. The quoted column densities do not include the interstellar column set to 0.37×10^{22} cm^{-2}. The normalization coefficients correspond to $\frac{10^{-14}}{4\,\pi\,d^2}\int n_{\rm e}\,n_{\rm H}\,{\rm d}V$, where d, $n_{\rm e}$ and $n_{\rm H}$ are respectively the distance of HD 93403 (in cm), the electron density and the hydrogen density (in cm^{-3}) in the X-ray emitting plasma. Error bars correspond to the 90 per cent confidence ranges. $f_{\rm X}^{\rm a}$ and $f_{\rm X}^{\rm b}$ yield the observed (i.e. absorbed) fluxes (in 10^{-12} erg cm^{-2} s^{-1}) integrated over the energy bands 0.5–2.5 keV and 0.5–10.0 keV respectively.

Φ	$N_{\rm H,1}$ (10^{22} cm^{-2})	kT_1 (keV)	norm$_1$	$N_{\rm H,2}$ (10^{22} cm^{-2})	kT_2 (keV)	norm$_2$	χ^2_ν	dof	$f_{\rm X}^{\rm a}$	$f_{\rm X}^{\rm b}$
0.265	$0.45^{+.08}_{-.10}$	$0.24^{+.03}_{-.02}$	1.30×10^{-2}	$0.88^{+.36}_{-.24}$	$1.25^{+.10}_{-.09}$	1.55×10^{-3}	1.13	191	1.14	1.36
0.518	$0.50^{+.09}_{-.09}$	$0.21^{+.02}_{-.02}$	1.96×10^{-2}	$0.85^{+.36}_{-.17}$	$1.01^{+.08}_{-.06}$	1.74×10^{-3}	1.12	169	1.03	1.18
0.745	$0.51^{+.08}_{-.09}$	$0.21^{+.02}_{-.02}$	1.70×10^{-2}	$0.80^{+.17}_{-.12}$	$1.05^{+.06}_{-.06}$	2.01×10^{-3}	1.04	179	1.07	1.25
0.011	$0.36^{+.09}_{-.10}$	$0.25^{+.03}_{-.02}$	0.76×10^{-2}	$0.77^{+.11}_{-.10}$	$0.92^{+.04}_{-.06}$	2.18×10^{-3}	0.99	260	1.24	1.38

the system appears about 20% brighter (in the 0.5–2.5 keV band) around periastron compared to the apastron observation.

To check that this behaviour is stable on time scales that are much longer than the orbital period, we have extracted archive *ROSAT* observations. HD 93403 was observed at several occasions with either the PSPC or the HRI instrument. The *ROSAT* pointings were usually centered on η Car. Therefore, HD 93403 lies rather close to the inner ring of the PSPC mesh and the source was sometimes shadowed by the mesh as a result of the spacecraft wobbling. Because of these difficulties we shall not consider the PSPC data any further and we will focus on the HRI exposures instead.

The background- and exposure-corrected HRI count rates were measured using the ASTERIX software. Figure 2 illustrates the light curve corresponding to observation rh202331n00 (obtained between JD 2450805.8 and JD 2450844.2). Despite the rather large error bars on individual data points the variability of the HRI count rate is significant at the >99.5% level (fitting a constant count rate to the HRI data yields $\chi^2_\nu = 2.87$ for 9 d.o.f.): HD 93403 appears brighter near $\Phi = 0.0$ and fainter around $\Phi = 0.5$, in fair agreement with our EPIC light curve. The overall HRI light curve (including all HRI observations) yields very similar results.

Our *XMM-Newton* data provide the most complete phase-resolved X-ray spectroscopy of an O + O colliding wind system to date. In Fig. 3 we have plotted the MOS1 count rates over different energy bands as a function of phase. Also illustrated in this figure are the orbital separation and the position angle as a function of phase Φ. The count rate in the medium energy band (that yields the dominant contribution to the global flux) follows the trend already seen for the entire energy range in Fig. 2. On the other side, the flux in the soft band is minimum at $\Phi = 0.75$. From Table 2 and Fig. 3, we find that phase 0.75 corresponds to the time of conjunction with the O5.5 I primary, and its denser wind, being in front (PA = 5°). Although the orbital inclination is rather low, it seems likely that the increase of the wind column density along the line of sight at $\Phi = 0.75$ is responsible for the observed drop in the soft flux. Finally, the variations in the hard band are less significant (at the 80% level).

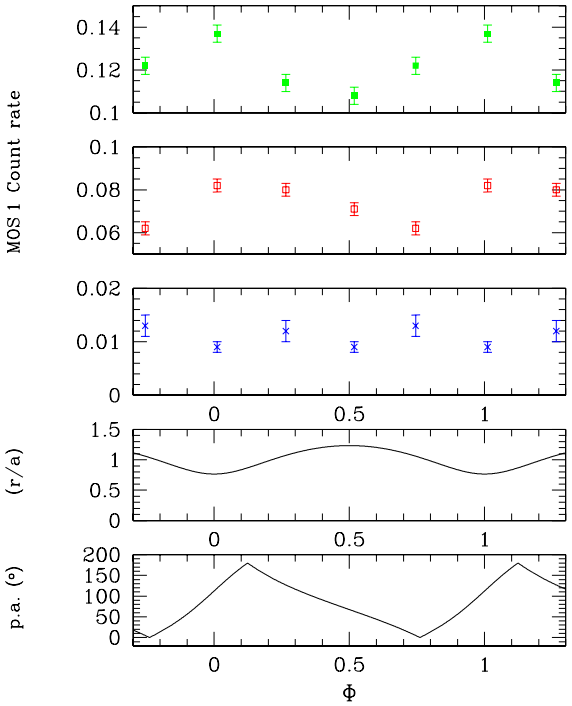

Fig. 3. X-ray light curve of HD 93403 over different energy ranges. The upper, second and third panels display the MOS1 count rates respectively over the 1.0–2.5 (medium), 0.5–1.0 (soft) and 2.5–10.0 keV (hard) energy bands. 1-σ error bars are indicated. The MOS2 and pn data yield very similar light curves. The fourth panel yields the relative orbital separation (r/a) between the components of HD 93403. Finally, the lower panel provides the position angle of the binary axis. A PA of 0° corresponds to the primary star being "in front" of the secondary.

3.3. Discussion

As pointed out above, the EPIC spectra of HD 93403 reveal surprisingly little variability: the model temperatures kT_1 and kT_2 vary by less than 20% and 35%

Table 3. Wind properties of the components of HD 93403 (see text for details). $\mathcal{R}$ yields the "wind momentum ratio" (e.g. Stevens et al. 1992). The last two rows provide the radii of the "instantaneous Roche lobes" at periastron and apastron.

	Primary	Secondary
Spectral type	O5.5 I	O7 V
$T_{\rm eff}$ (K)	39300	40100
$\log(L_{\rm bol}/L_\odot)$	6.02	5.41
$\log \dot{M}\,(M_\odot\,{\rm yr}^{-1})$	−5.29	−6.36
v_∞ (km s^{-1})	2600	2600
$\mathcal{R} = \sqrt{\frac{\dot{M}_1\, v_{\infty,1}}{\dot{M}_2\, v_{\infty,2}}}$	3.3	
$R_{\rm RL}\,\sin i\,(\Phi = 0.0)$ $(R_\odot)$	20.7	16.0
$R_{\rm RL}\,\sin i\,(\Phi = 0.5)$ $(R_\odot)$	33.3	25.8

respectively. At first sight, this is somewhat reminiscent of the case of ι Ori (Pittard et al. 2000). *ASCA* observations of ι Ori (O9 III + B1 III, $e = 0.764$, Marchenko et al. 2000) failed to reveal the expected variability between the periastron and apastron phases. However, in the case of HD 93403, we do observe a phase-dependence of the observed X-ray flux.

To better understand the origin of the variations at different energies we need to first consider some fundamental properties of the components of HD 93403 listed in Table 3. To estimate the mass loss rates of the components, we use the empirical formula proposed by Lamers & Leitherer (1993). The effective temperatures and luminosities are adopted from the estimates of Rauw et al. (2000). Howarth et al. (1997) determined a terminal velocity of 2616 km s^{-1} for the combined stellar wind of HD 93403. Here we assume that both components have the same v_∞ of 2600 km s^{-1}.

High resolution X-ray spectroscopy of single massive stars indicates that the emitting plasma is distributed out to large radii in the stellar wind. Analyses of the He-like triplets of various ions suggest that the bulk of the line emission arises from regions just outside the radius of optical depth unity for the respective wavelength (e.g. Kahn et al. 2001).

We can use the parameters in Table 3 to estimate the radius of optical depth unity in the winds of the two stars at different energies. Assuming homogeneous and spherically symmetric winds, we find that, for photons of energy 0.5 keV, $\tau = 1$ occurs at 9 R_* ($\simeq$216 $R_\odot$) and 2 R_* ($\simeq$20 $R_\odot$) for the primary and secondary of HD 93403 respectively. At 1.5 keV, the primary wind remains optically thick out to 47 $R_\odot$. Comparing these figures to the orbital dimensions ($a \sin i = 63.2\,R_\odot$), we see that even for inclinations of order 30°, the whole orbit lies inside the $\tau = 1$ radius at 0.5 keV except of course for the solid angle occupied by the cavity created by the secondary wind (see Fig. 4). This situation has two important consequences:

– any soft X-ray emission produced in the inner region of the wind interaction zone will be heavily absorbed by the winds

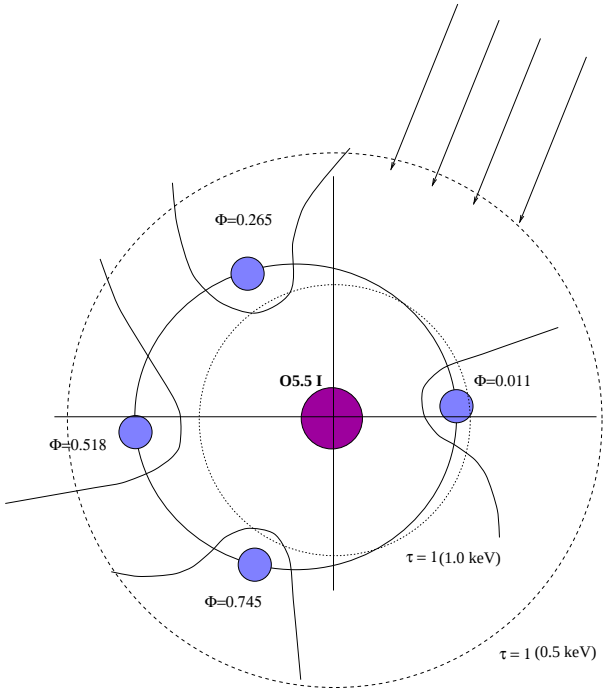

Fig. 4. Schematic view of the HD 93403 binary at the time of the four *XMM* observations. The dimensions of the stars and the orbital separation correspond to an orbital inclination of 30°. The arrows indicate the direction of the observer's line of sight projected on the orbital plane. The dashed and the dotted circles correspond to the surfaces of optical depth unity for the primary wind at 0.5 keV and 1.0 keV respectively.

– the soft (0.5–1.0 keV) X-ray emission observed in the EPIC spectra of HD 93403 most likely arises in the outer regions of the individual stellar winds and the variability in this energy range is probably associated with pure opacity effects.

In the medium energy band (1.0–2.5 keV), optical depth effects are much smaller and should have less impact on the light curve. Figure 3 shows that at least in this energy range, the variation is roughly consistent with a $1/r$ modulation, where r stands for the instantaneous separation between the stars. Such a behaviour is indeed expected in some colliding wind binaries. In fact, if the plasma in the wind interaction zone is adiabatic, the X-ray luminosity of a wind collision is expected to scale roughly as $L_{\rm X} \propto v^{-3.2}\,r^{-1}$ (Stevens et al. 1992), where v stands for the preshock velocity of the gas.

Referring to the cooling parameter χ introduced by Stevens et al. (1992) and the wind parameters listed in Table 3, we find that the plasma in the wind interaction zone of a system such as HD 93403 is a priori most probably adiabatic ($\chi \sim 3$–5), except perhaps around periastron ($\chi \sim 0.4$ for the secondary wind) where radiative cooling could become effective (e.g. Pittard & Stevens 1997). From the sole dependence of $L_{\rm X}$ on the orbital

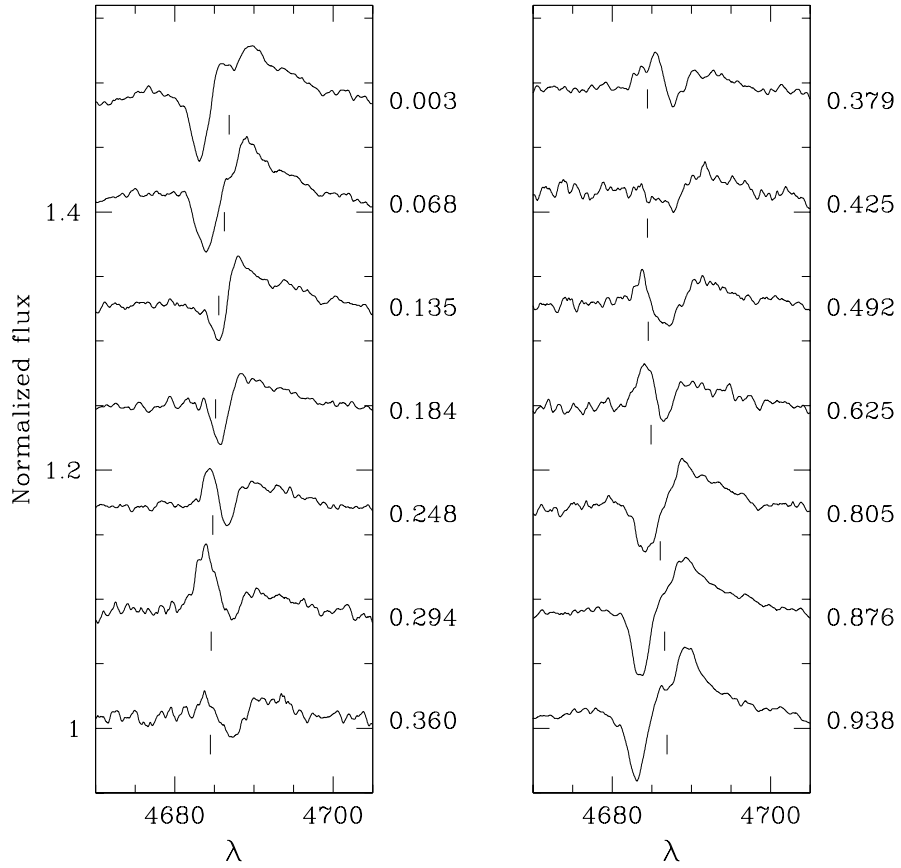

Fig. 5. Profile variations of the He II λ4686 line in the spectrum of HD 93403 as a function of orbital phase. The labels indicate the orbital phases while the small ticks yield the position of the primary's line as derived from the orbital solution of Rauw et al. (2000). Note that the *RV*s of the absorption component are in excellent agreement with the orbital motion of the secondary star.

separation, we would expect a variation of the colliding wind X-ray flux by a factor 1.6 between apastron and periastron (see Fig. 3). The fact that the observed modulation in the medium energy band is clearly lower than a factor 1.6 could indicate that a sizeable fraction of the X-ray emission from HD 93403 is intrinsic to the winds of the individual components or that radiative cooling affects the properties of the plasma to some extent (see also below). Other factors such as radiative braking (Gayley et al. 1997) could also play a role in the wind interaction.

For solar abundances the postshock temperature of the shocked material is expected to be $1.36 \times 10^7\, v^2$ (K) where the preshock velocity is expressed in $1000\,\mathrm{km\,s^{-1}}$ (Stevens et al. 1992). As indicated by the wind momentum ratio $\mathcal{R}$ in Table 3, the wind of the primary most probably dominates that of the secondary and the wind collision region should be wrapped around the secondary star. Since the shock occurs within the wind acceleration zones, the winds collide with velocities below v_∞. If we assume a "standard" β-velocity law for the winds in HD 93403, we find that the postshock temperature should be about 40–50% higher at apastron than at periastron. Though the variations in the hard (2.5–10.0 keV) band are clearly less significant than in the soft and medium bands, variability at these energies is expected to result from the combination of the global $1/r$ modulation and the changes of the temperature of the emitting plasma.

Assuming a distance of 3.2 kpc and correcting the observed flux for an interstellar column density of $0.37 \times 10^{22}\,\mathrm{cm^{-2}}$, we obtain an average dereddened luminosity of $L_\mathrm{X} = 3.7 \times 10^{33}\,\mathrm{erg\,s^{-1}}$ in the 0.5–2.5 keV range. Adopting the bolometric luminosity of the binary as derived by Rauw et al. (2000) yields $\log(L_\mathrm{X}/L_\mathrm{bol}) = -6.13$. This ratio is less extreme than the value (-5.83) derived by Chlebowski & Garmany (1991) from their *EINSTEIN* data. The larger ratio quoted by Chlebowski & Garmany mainly reflects their value of L_X which is about 2.5 times larger than the luminosity we obtain from our EPIC spectra.

It is worth emphasizing that the HRI count rates of HD 93403 are in extremely good agreement with the luminosities and count rates inferred from our EPIC data. For instance, the parameters of the $\Phi = 0.265$ EPIC spectra can be converted into a theoretical HRI count rate

of 4.1×10^{-2} cts s^{-1} in excellent agreement with the results of the *ROSAT* observations obtained three to eight years prior to the *XMM* data. This seems to rule out a long term variation of the X-ray luminosity as the cause of the discrepancy between the *XMM* and *EINSTEIN* results. Part of the difference in L_X therefore most probably arises from the fact that Chlebowski & Garmany (1991) used luminosities from Chlebowski et al. (1989) that assume an optically thin plasma with $kT = 0.5$ keV and affected by interstellar absorption only.

The fact that our $\log(L_X/L_{bol})$ value is not much larger than the "canonical" value for single stars provides further evidence that the X-ray emission is not totally due to colliding wind emission and hence single star emission is likely to play a significant role.

4. The optical data

4.1. Emission lines

The He II λ4686 line consists of a mixture of emission and absorption features (see Fig. 5). Observations taken at the same orbital phase but during different observing runs, separated by several years, display the same overall morphology.

As pointed out by Rauw et al. (2002a), the radial velocities (RVs) of the absorption component closely matches the orbital motion of the secondary star. The He II λ4686 line appears thus in absorption in the spectrum of the O7 secondary, lending further support to the main sequence luminosity class proposed for this star (Rauw et al. 2000). We notice that the strength of the secondary's absorption varies as a function of orbital phase. The absorption appears stronger around $\Phi \simeq 0.9$ and weaker near phase 0.4. Some of these variations might be due to the blending with the emission component(s), but it seems unlikely that the whole phenomenon could be attributed to blending effects.

The emission component displays strong phase-locked variability. Between phases 0.805 and 0.135, we observe a broad asymmetric emission with a prominent extended red wing. Between phases 0.248 and 0.625, the emission is blue-shifted and appears fainter, much narrower and more symmetric. Between $\Phi = 0.360$ and 0.492, the emission strength is considerably reduced and at some phases there is virtually no emission at all. The tickmarks in Fig. 5 indicate the RVs of the primary component. We see that the RV of the emission peak varies roughly in phase with the primary, though with a larger amplitude and a larger systemic velocity: the emission peak is clearly red-shifted with respect to the primary between phases 0.805 and 0.184 and slightly blue-shifted at phases 0.248, 0.294, 0.492 and 0.625. Some hints that the primary spectrum contributes a faint narrow emission to the He II λ4686 line are found at $\Phi = 0.876$, 0.938, 0.003 and 0.068. This stellar emission may also contribute to the narrow line seen between $\Phi = 0.248$ and 0.625.

The Hα profile appears quite complex with a mixture of absorptions and emissions (see Fig. 6). The line seems to consist of an absorption belonging to the secondary and a blue-shifted absorption that is most probably associated with the primary. Underlying these features, there is a broad, roughly symmetric, emission line extending over about 70 Å. The profile is further polluted by a rather strong nebular Hα emission and by telluric water vapor absorptions. The intensity of both of these latter features depends on the weather conditions during the observations. In our normalized spectra, the relative intensity of the nebular emission increases when the atmospheric turbulence increases. In fact, a larger seeing means that the fiber of the FEROS instrument misses part of the stellar flux while the nebular photons that come from a diffuse extended region enter the fiber without significant losses.

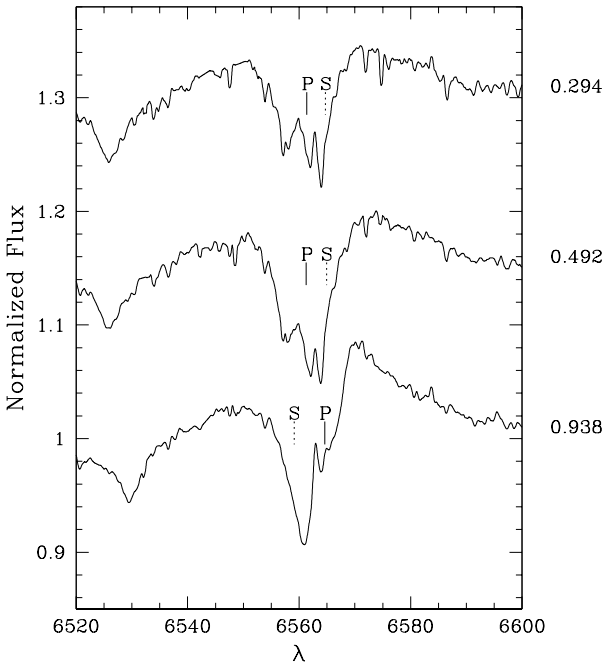

Fig. 6. Example of the line profiles of the Hα line in the spectrum of HD 93403. The P and S labels indicate the position of the lines of the primary and secondary respectively as expected from the orbital solution. Note the sharp nebular emission line at 6562.9 Å.

Despite these complications, we find that the overall variations of the Hα profile are reminiscent of those of He II λ4686. Figure 6 displays a red-shifted emission at $\Phi = 0.938$, while there is no trace of such a feature at the other two phases shown in this plot. Conversely, the strength of the blue-shifted absorption appears reduced at phase 0.294 (i.e. when we observe a narrow, blue-shifted, emission peak in the He II λ4686 line).

4.2. Absorption lines

In addition to the effects discussed hereabove, the spectrum of HD 93403 displays also variations of the relative strength of the absorption lines of the two stars. Whereas

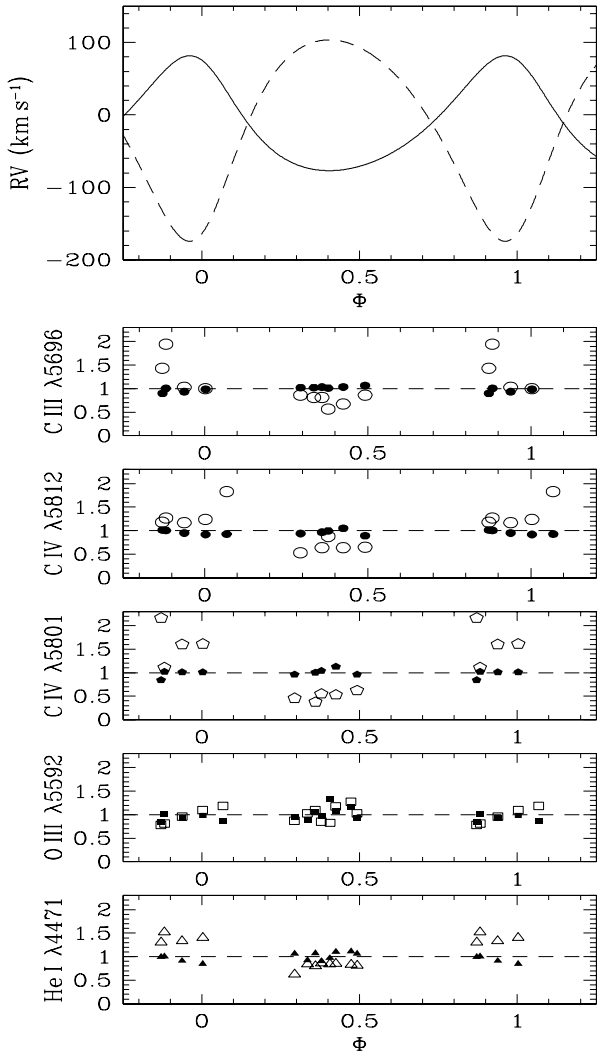

Fig. 7. Upper panel: orbital solution of HD 93403 as derived from the He I λ 4471 absorption line (Rauw et al. 2000). Phase 0.0 corresponds to periastron passage. The other panels display the ratio of the equivalent width of individual lines with respect to the mean *EW* averaged over all available phases. Filled symbols stand for the primary's lines, whereas open symbols correspond to the secondary's lines.

the intensities of the primary's absorptions remain roughly constant over the orbital cycle, we observe substantial changes in the equivalent width (*EW*) of the secondary's lines. Figure 7 displays the ratio between the individual equivalent widths of the different lines that could be deblended at a given orbital phase and the corresponding mean *EW* averaged over all available phases. In general, the secondary's lines appear stronger at orbital phases when the secondary is moving towards us[3] ($\Phi \in [0.8, 0.1]$). This is very similar to the "Struve-Sahade" effect (SSE) described for instance by Stickland (1997) and Bagnuolo et al. (1999).

[3] This is very similar to what we observe for the absorption component of the He II λ 4686 blend.

Table 4. Properties of the absorption lines in the optical spectrum of the secondary star investigated for the Struve-Sahade effect. I.P. stands for the ionization potential of the species corresponding to one ionizing stage below that of the relevant ions. E.P. yields the excitation potential of the lower level of the transition.

Line	I.P. (eV)	E.P. (eV)	SSE
He I λ 4471	0.0	21.0	Yes
O III λ 5592	35.1	33.8	No
C III λ 5696	24.4	32.1	Yes
C IV λ 5801	47.9	37.5	Yes
C IV λ 5812	47.9	37.5	Yes

The Struve-Sahade effect in the optical spectrum of HD 93403 appears most prominent for the C IV $\lambda\lambda$ 5801, 5812 lines whereas it is slightly less pronounced for He I λ 4471 and essentially absent in O III λ 5592. This latter result is somewhat surprising since the C IV doublet and the O III line have all a rather high excitation potential and involve ions that require large ionization potentials (see Table 4). These lines are thus most probably all formed quite deep within the photospheric layers. Another remarkable feature is the fact that the C III λ 5696 *emission* line also displays a moderate SSE.

4.3. Discussion

The variability of the He II λ 4686 line indicates a dependence of the intensity of the broader emission on the orbital separation; the emission is strongest around phases 0.80–0.15 and vanishes when the stars are heading towards apastron. A possible explanation could be that the broader emission component is generated in the interaction between the two stars and scales roughly with some power of $1/r$.

These variations could reflect a change of the primary's mass loss rate due to some sort of tidal interaction. The fact that the emission has a larger *RV* amplitude ($\sim$180 km s^{-1}) than the orbital motion of the primary (79 km s^{-1}) could imply that this emission arises in the tidal bulge on the side of the primary not facing the secondary. Indeed, in order to follow the orbital motion, the material in this part of the wind would have to move at larger velocities than the center of mass of the primary. The lack of significant emission from the bulge on the side facing the secondary could be due to the X-ray emission from a wind collision. These X-rays could ionize this part of the wind and hence prevent the formation of the He II λ 4686 emission line. Since the X-ray luminosity is largest around periastron, it should have the largest ionizing power at this phase. Nevertheless, it is around periastron that the He II λ 4686 emission appears strongest. This could indicate that the emission comes from the "rear"

side of the primary with an intensity that scales as some power of $1/r$ reflecting the dependence of the tidal interaction on the orbital separation.

There are however a couple of problems with this explanation. For instance, it is surprising that our data reveal a stronger emission at phases prior to periastron passage (e.g. $\Phi = 0.876$) than at the symmetric phases after periastron passage (e.g. $\Phi = 0.135$). Simulations of the tidal interactions in an eccentric massive binary (Moreno & Koenigsberger 1999) yield an asymmetrical "time-profile" of the amplitude of the maximum radial displacement of the surface layers of the primary star: the tidal bulge is on average smaller prior to periastron than afterwards. Though the model parameters used by Moreno & Koenigsberger were adjusted to match the ι Ori binary ($e = 0.764$) and although it is not clear how the wind emission lines react to a tidal bulge, it seems likely that the emission should be on average stronger after periastron also in HD 93403, which is not what we observe. Another comment concerns the Roche lobe radii listed in Table 3. For reasonable values of the orbital inclination, the primary's Roche lobe radius at periastron is significantly larger than the "typical" radius of an O 5.5 supergiant ($\sim 24\,R_\odot$) and it seems thus unlikely that a strong tidal interaction could take place in HD 93403.

Alternatively, the broad He II λ 4686 emission could arise in the high density parts of a colliding wind interaction. Let us recall that radiative cooling is expected to be most efficient around periastron and it is therefore around these phases that the optical line emission (arising from relatively cool material) should reach its maximum. The easiest way to account for most of the properties of the broad emission component is to assume that the excess emission is coming from the trailing arm of the shock. Stevens & Howarth (1999) pointed out that the trailing edge of the shock region should produce more line emission because of the greater density at this site. Due to the Coriolis deflection, the shock zone in a wind interaction is expected to be strongly curved. If this effect is strong enough, then the trailing arm of the shock could be roughly perpendicular to the binary axis (see our sketch in Fig. 4) and we would expect a redshifted emission between phases 0.8 and 0.13 which is pretty much what we observe. It is worth pointing out that our observations of the He II λ 4686 line display indeed qualitative similarities to the synthetic line profile variations simulated by Stevens & Howarth (1999). We caution however that a very strong bending of the shock is required to explain the red wing that we observe at $\Phi = 0.184$. Without a strong bending, the redward extension of the emission should already be considerably reduced at this phase.

Though the Struve-Sahade effect was already reported by Struve in the late 1930's (Struve 1937), its origin is still not established and different binaries sometimes lead to contradictory pictures (see e.g. Bagnuolo et al. 1999). Sahade (1959) proposed that a gas stream from the primary that sweeps past the trailing side of the secondary could cause an obscuration of the secondary at orbital phases when it is receding. Alternatively, Abhyankar (1959) suggested that the lines could strengthen during approaching phases due to an enhanced density on the leading hemisphere of the secondary. Gies et al. (1997) proposed that the SSE could result from photospheric heating by the X-rays emitted by a colliding wind interaction. Due to the Coriolis force, the bow shock is deflected in such a way that it would preferentially heat the leading hemisphere which is best seen during orbital phases of secondary approach. More recently, Gayley (2002) suggested that the SSE could result from external irradiation of the stellar surface that induces a transverse radiative force and hence transverse supersonic flows in the secondary's atmosphere. These transverse flows could break the receding/approaching symmetry of the secondary velocity structure and lead to shallower and broader absorption lines at phases when the secondary is receding.

Our observations of HD 93403 indicate that lines corresponding to highly excited species do not necessarily display the same behaviour. An obscuration effect of the secondary by the trailing arm of the wind collision zone can therefore be ruled out as the cause of the SSE in HD 93403. Such an effect should indeed affect all the lines of the secondary in the same way, which is not the case.

Let us remind what is known about the formation of the lines investigated here. The *EW* of the He I λ 4471 line in O-star spectra is rather well correlated with the spectral type and hence the effective temperature though there is also a moderate dependence on gravity (see e.g. Voels et al. 1989 and references therein). On the other hand, the *EW*s of the C IV $\lambda\lambda$ 5801, 5812 and O III λ 5592 lines in O-star spectra do not reveal any clear-cut dependence neither on the spectral type nor on the luminosity (Conti 1974). Finally, the strength of the C III λ 5696 emission is known to increase with luminosity (Walborn 1980). This emission most probably forms in the stellar photosphere; Cardona-Núñez (1978) showed that the upper level $3d\,^1D$ of the λ 5696 transition is overpopulated with respect to the lower level $3p\,^1P^0$ through a combination of direct and dielectronic recombination processes and cascades from upper states.

The lack of variations of the primary's *EW*s suggests that there are no significant variations of the dilution of the primary's lines and thus that the secondary's continuum flux remains constant. It seems unlikely that an increase of the local surface temperature could be the sole effect controlling the SSE in HD 93403. In fact, a local heating of the secondary's surface by the wind interaction zone, without a notable brightening of the secondary, is expected to reduce the *EW* of the He I λ 4471 line when the secondary is moving towards us, which is the opposite of what we observe. Therefore, the SSE in HD 93403 must be caused by some perturbation of the physical conditions in the atmosphere of the secondary that affects the formation processes of some (but not all) lines but does not alter the overall brightness of the secondary.

5. Final remarks and conclusion

We have presented observations of HD 93403 that reveal phase-locked variability of the X-ray flux and of the optical spectrum of this massive binary system. The colliding wind scenario offers a promising explanation of this variability. The bulk of the medium band X-ray emission probably arises in the wind interaction region near the point of head-on collision. The shocked wind material in this region is probably too hot to emit substantial optical emission and the cooling is essentially adiabatic. On the other hand, the optical line emission most probably forms in the trailing arm of the shock region where the density is higher and the plasma cools more efficiently through radiative cooling. It seems therefore that the X-ray and optical data probe two distinct regions of the same interaction phenomenon.

An interesting question is whether the ram pressure of the secondary's wind is sufficient to hold off the primary's wind. In fact, if the primary's wind crushed on the secondary's surface, it would strongly perturb the local physical conditions (e.g. temperature, density, velocity field...) in the secondary's atmosphere. For a wind momentum ratio of $\mathcal{R} = 3.33$ (Table 3) and assuming a standard velocity law with $\beta = 1$ for both stars, we find that the shock should remain detached from the surface of the secondary star over the entire orbit. Although the figures in Table 3 provide only a crude estimate of the stellar parameters, we note that the shock should remain detached for values of $\mathcal{R}$ as large as 4.5. Therefore it seems unlikely that a direct impact of the primary's wind on the secondary's surface could be responsible for the Struve-Sahade effect.

Our results suggest some tracks for future investigations of the wind interactions in O-type binaries. Comparing the *XMM-Newton* spectra of HD 93403 and other early-type binaries, spanning a wide range of spectral types and orbital parameters, with detailed numerical simulations (e.g. Pittard 2000) should enable us to constrain the hydrodynamics of stellar winds and to investigate the effects of radiative braking and thermal conduction on the wind collision. Concerning the Struve-Sahade effect, it will be important to gather optical echelle spectroscopy of a sample of binaries, allowing to investigate a number of lines individually at high spectral resolution and with a high S/N ratio. From a theoretical point of view, quantitative predictions of the behaviour of these lines under the different scenarios (particularly the Gayley 2002 scenario) are needed to allow a comparison with observations and hence to solve this long standing enigma.

Acknowledgements. The authors wish to thank the *XMM*-SOC team for their efforts to schedule the pointings at the right orbital phases and for their assistance in using the SAS software. Our thanks go also to Alain Detal for his help in installing the SAS, to Dr. Herman Hensberge for advising us in the reduction of the FEROS data and to Yaël Nazé for performing wind opacity calculations upon our request. We are greatly indebted to the Fonds National de la Recherche Scientifique (Belgium) for multiple assistance. This research is also supported in part by contract P4/05 "Pôle d'Attraction Interuniversitaire" (SSTC-Belgium) and through the PRODEX *XMM*-OM and *Integral* Projects.

References

Abhyankar, K. D. 1959, ApJS, 4, 157
Bagnuolo, W. G. Jr., Gies, D. R., Riddle, R., & Penny, L. R. 1999, ApJ, 527, 353
Cardona-Núñez, O. 1978, Ph.D. Thesis, University of Colorado, Boulder
Chen, W., & White, R. L. 1991, ApJ, 366, 512
Chlebowski, T., Harnden, F. R. Jr., & Sciortino, S. 1989, ApJ, 341, 427
Chlebowski, T., & Garmany, C. D. 1991, ApJ, 368, 241
Conti, P. S. 1974, ApJ, 187, 539
Corcoran, M. F. 1996, Rev. Mex. Astron. Astrofis. Conf. Ser., 5, 54
Eichler, D., & Usov, V. 1993, ApJ, 402, 271
Gayley, K. G. 2002, in Interacting Winds from Massive Stars, ed. A. F. J. Moffat, & N. St-Louis, ASP Conf. Ser., 260, 583
Gayley, K. G., Owocki, S. P., & Cranmer, S. R. 1997, ApJ, 475, 786
Gies, D. R., Bagnuolo, W. G. Jr., & Penny, L. R. 1997, ApJ, 479, 408
Howarth, I. D., Siebert, K. W., Hussain, G. A. J., & Prinja, R. K. 1997, MNRAS, 284, 265
Jansen, F., Lumb, D., Altieri, B., et al. 2001, A&A, 365, L1
Kaastra, J. S. 1992, An X-ray spectral code for optically thin plasmas, Internal SRON-Leiden Report
Kahn, S. M., Leutenegger, M. A., Cottam, J., et al. 2001, A&A, 365, L312
Kaufer, A., Stahl, O., Tubbesing, S., et al. 1999, The Messenger, 95, 8
Lamers, H. J. G. L. M., & Leitherer, C. 1993, ApJ, 412, 771
Marchenko, S. V., Rauw, G., Antokhina, E. A., et al. 2000, MNRAS, 317, 333
Mason, K. O., Breeveld, A., Much, R., et al. 2001, A&A, 365, L36
Mewe, R., Gronenschild, E. H. B. M., & van den Oord, G. H. J. 1985, A&AS, 62, 197
Moreno, E., & Koenigsberger, G. 1999, Rev. Mex. Astron. Astrofis., 35, 157
Pittard, J. M. 2000, Ph.D. Thesis, University of Birmingham
Pittard, J. M., & Stevens, I. R. 1997, MNRAS, 292, 298
Pittard, J. M., Stevens, I. R., Corcoran, M. F., et al. 2000, MNRAS, 319, 137
Rauw, G., Vreux, J.-M., & Bohannan, B. 1999, ApJ, 517, 416
Rauw, G., Sana, H., Gosset, E., et al. 2000, A&A, 360, 1003
Rauw, G., Nazé, Y., Carrier, F., et al. 2001, A&A, 368, 212
Rauw, G., Sana, H., Vreux, J.-M., Gosset, E., & Stevens, I. R. 2002a, in Interacting Winds from Massive Stars, ed. A. F. J. Moffat, & N. St-Louis, ASP Conf. Ser., 260, 449
Rauw, G., Vreux, J.-M., Antokhin, I., et al. 2002b, in New Visions of the X-ray Universe in the XMM-Newton and Chandra Era, ed. F. Jansen, ESA SP-488, in press
Sahade, J. 1959, PASP, 71, 151
Sana, H., Rauw, G., & Gosset, E. 2001, A&A, 370, 121
Stevens, I. R., Blondin, J. M., & Pollock, A. M. T. 1992, ApJ, 386, 265

Stevens, I. R., & Howarth, I. D. 1999, MNRAS, 302, 549
Stickland, D. J. 1997, The Observatory, 117, 37
Strüder, L., Briel, U., Dennerl, K., et al. 2001, A&A, 365, L18
Struve, O. 1937, ApJ, 85, 41
Thaller, M. L., Gies, D. R., Fullerton, A. W., Kaper, L., & Wiemker, R. 2001, ApJ, 554, 1070
Turner, M. J. L., Abbey, A., Arnaud, M., et al. 2001, A&A, 365, L27
van der Hucht, K. A. 2002, in Multifrequency Behaviour of High Energy Cosmic Sources, ed. F. Giovanelli, & L. Sabau-Graziati, Mem. Soc. Astro. Italia, in press
Voels, S. A., Bohannan, B., Abbott, D. C., & Hummer, D. G. 1989, ApJ, 340, 1073
Walborn, N. R. 1980, ApJS, 44, 535
Waldron, W. L., Corcoran, M. F., Drake, S. A., & Smale, A. P. 1998, ApJS, 118, 217

2.3.1 Other O-star binaries studied by the GAPHE

The High-Energy Astrophysics Group (GAPHE) of the Liège University has studied the X-ray emission of a number of massive binaries with the objective to improve the understanding of wind – wind interactions. I have been actively involved in all these studies. The results related to O-star binaries are summarized in this section.

A phase-resolved observing campaign consisting of six *XMM-Newton* pointings of the O7.5(f) III + O7(f) III binary system HD 152248 (5.816 day orbital period, $e = 0.13$) was reported by Sana et al. (2004). The observed X-ray flux appears enhanced by $\sim 60\%$ at $\phi = 0.66$ i.e. shortly after apastron. Although the variations are largest in the harder energy bands, they are also present at lower energies and Sana et al. (2004) confirmed their phase-locked behaviour and their long-term stability by analysing *ROSAT* data taken 10 years earlier and which nicely confirm the trend seen in the *XMM* data (Fig. 2.4).

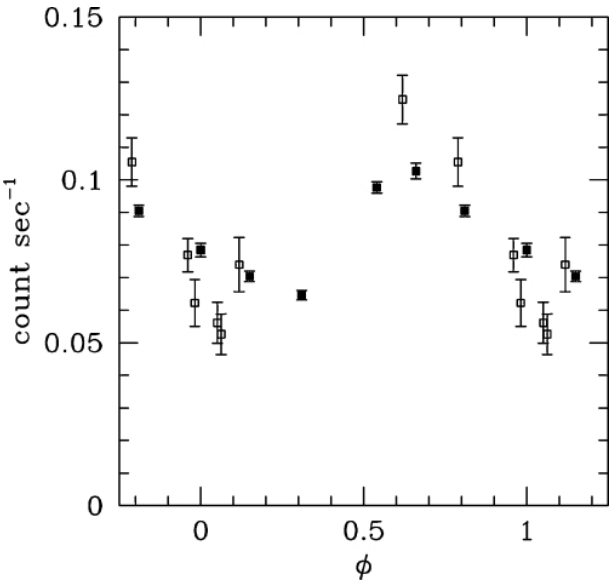

Figure 2.4: X-ray light curve of HD 152248. Filled symbols: *XMM-Newton* EPIC measurements converted into equivalent *ROSAT*-PSPC count rates. Open symbols: actual PSPC measurements taken between March 1991 and February 1993. From Sana et al. (2004).

It must be stressed that the X-ray emission is harder at phases near apastron. Hydrodynamical simulations of the wind – wind interaction in HD 152248 suggest that the intrinsic X-ray emission actually increases at apastron, mainly because of the larger pre-shock velocities at this phase compared to periastron (the winds having more time to accelerate before they collide). While the model predicts a variation of the intrinsic X-ray flux of the wind interaction zone by about 40 %, a much stronger variation (one order of magnitude) is expected for the observed flux from the wind – wind collision as a result of eclipses and the changing amount of circumstellar material. The observed variations are actually lower and this is probably due to the dilution by the (roughly constant) intrinsic X-ray emission of the winds of the individual binary components.

To first approximation, the X-ray spectrum of this binary can be described by a two-temperature (2-T) thermal plasma model with $kT \sim 0.2$ and 0.7 keV. However, fitting the hard tail of the spectrum

requires an additional steep power law component ($\Gamma = 3.7$). This could be either genuine non-thermal emission produced through inverse Compton scattering by relativistic electrons or it could hint at a non-equilibrium plasma as for Plaskett's star (see below). The X-ray luminosity (corrected for the ISM absorption only) amounts to 8.0 – 12.0×10^{32} erg s^{-1} depending on the orbital phase.
Finally, it is worth emphasizing that an intensive optical monitoring campaign of this binary revealed variable optical emission lines (He II λ 4686 and Hα) in its spectrum. The variations of these lines actually suggested that the system harbours a roughly planar wind interaction zone mid-way between the stars (Sana et al. 2001). As for HD 93403, the signature of the wind interaction is therefore seen both in X-rays and in the optical. The wind – wind interaction in HD 152248 is expected to be highly radiative and the shock-heated material should thus cool down rather quickly allowing it to reach the temperature regime where optical emission lines are formed.

De Becker et al. (2004a) reported the analysis of an *XMM-Newton* observation of HD 159176 (O7 V + O7 V, $P_{\rm orb} = 3.367$ days, $e = 0.0$) obtained shortly after quadrature when the primary star is approaching. The RGS spectrum of this system reveals line emission from a comparatively cool plasma (2 to 6 MK, $kT \sim 0.15$ – 0.6 keV) while the EPIC spectrum suggests the existence of somewhat hotter (1 keV) plasma. This rather soft emission (see Fig. 2.5) could indicate that either the X-ray spectrum of HD 159176 is dominated by the intrinsic emission from its components or that the stellar winds collide at a velocity much lower than their terminal velocity. The colliding wind origin of the X-ray emission is supported by the fact that with $L_X \sim 1.5 \times 10^{33}$ erg s^{-1} the system appears X-ray overluminous by about a factor 7 compared to the X-ray emission expected from the bolometric luminosities of its components (De Becker et al. 2004a). No trace of short-time variability (due to hydrodynamical instabilities) was found in the X-ray flux of this system.

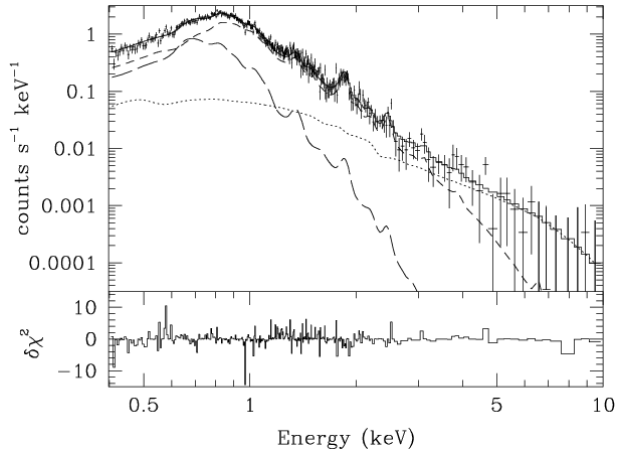

Figure 2.5: EPIC-pn spectrum of HD 159176 fitted with a model consisting of the sum of a soft thermal plasma emission (designed to represent the intrinsic emission of the components, long-dashed line), a colliding wind model (short-dashed line) and a power-law component with $\Gamma = 2.5$ (dotted line). From De Becker et al. (2004a).

The O VIII Lyα line was observed to be quite broad (FWHM ~ 2500 km s^{-1}) and blue-shifted by about 300 – 600 km s^{-1}. The O VII He-like triplet revealed no trace of the forbidden line, a situation that is quite expected for a system where the X-ray plasma is subject to the strong, almost un-diluted, radiation fields of two O-type stars.

Finally, De Becker et al. (2004a) attempted to fit the EPIC spectrum with the semi-analytical model of Antokhin et al. (2004). This model was designed for the calculation of X-ray emission from a steady, fully radiative, wind-wind interaction. The results of this model were that

- the softest component in the X-ray spectrum of HD 159176 likely stems from the intrinsic emission of the individual stars,
- the mass loss rates of the stars are probably of order $2 \times 10^{-7}\,\mathrm{M}_{\odot}\,\mathrm{yr}^{-1}$, and
- an additional power-law component is apparently needed to fit the hard tail of the EPIC spectrum of HD 159176.

De Becker et al. (2004a) interpreted the latter finding as the signature of a non-thermal X-ray emission produced through inverse Compton scattering by relativistic electrons. An alternative explanation might be that the shock-heated plasma is out of equilibrium and therefore optically thin thermal plasma codes such as the one used by Antokhin et al. (2004) might not be appropriate (Pollock & Raassen 2005, see also the case of Plaskett's star below). In this case, the hard tail could actually be thermal bremsstrahlung arising at a higher temperature than the excitation temperature of the ions that produce the line emission.

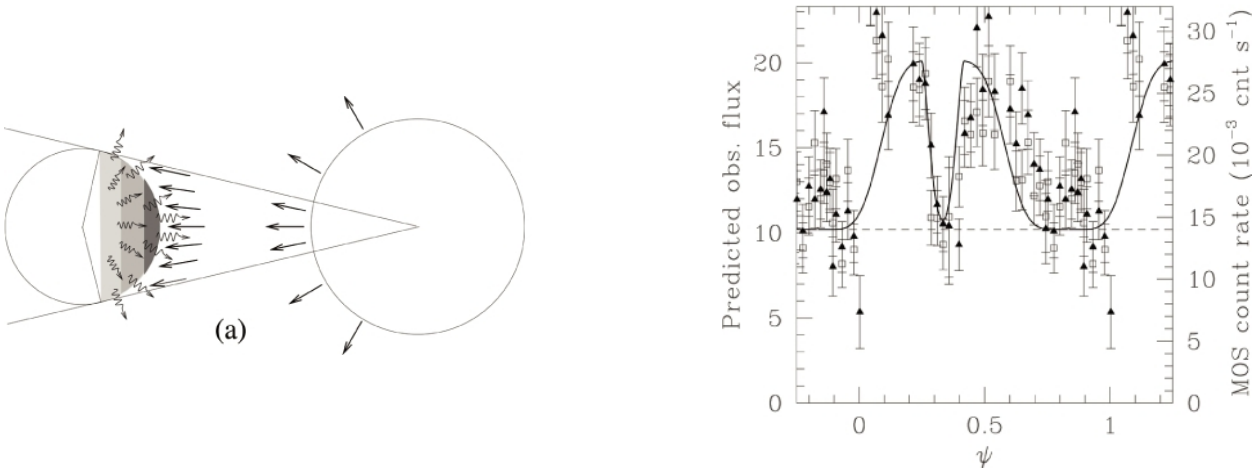

Figure 2.6: Left: cartoon of the wind – photosphere interaction in CPD-41° 7742. In this schematic model, the X-ray emission arises directly on the surface of the secondary at the impact of the overwhelming primary wind. Right: comparison between the observed EPIC-MOS light curve of CPD-41° 7742 and the predicted variations for the phenomenological model shown in the left panel.

CPD-41° 7742 in the NGC 6231 cluster was not expected *a priori* to be a key system for the study of X-ray emission from colliding wind binaries. In fact, this eclipsing system consists of an O9 V primary and a B1-1.5 V secondary revolving around each other in 2.4407 days. The spectral types and orbital parameters are not really the most promising for a strong wind interaction to take place. Still, Sana et al. (2005) found rather strong modulation of the X-ray flux of this system, rather hard emission (kT of 0.6 and 1.0 keV) and a comparatively high X-ray luminosity (8.9×10^{31} erg s^{-1}). The X-ray light curve shows an eclipse at the time of the optical secondary eclipse as well as a much broader minimum when the secondary star is in front. These features can best be explained if there exists an extra emission near or on the surface of the secondary star facing the primary (see Fig. 2.6). Sana et al. (2005) accordingly

suggested that the wind of the primary star overwhelms that of the secondary, resulting either in a wind – photosphere interaction or a shock slightly lift-off from the secondary surface by the effect of radiative braking.

Linder et al. (2006) analysed two *XMM-Newton* observations of Plaskett's star (HD 47129), an O7.5 I + O6 I binary with an orbital period of 14.3966 days ($e = 0.0$). The O6 I secondary is actually the more massive component but has broader and shallower lines rendering its signature in the optical spectrum more difficult to see. The broad lines of this star have been interpreted as the signature of a large rotational velocity ($310\,\mathrm{km\,s^{-1}}$). The primary has a much lower rotational velocity ($90\,\mathrm{km\,s^{-1}}$) and its optical spectrum reveals an enhanced nitrogen abundance (Bagnuolo & Barry 1996). These properties most probably indicate that the system is in a post-RLOF state, with the secondary being the mass gainer and the primary being the initially more massive star. Optical spectra of HD 47129 reveal evidence for a wind – wind interaction with the shock being wrapped around the primary and being Coriolis deflected by $\sim 50°$ (Wiggs & Gies 1992).

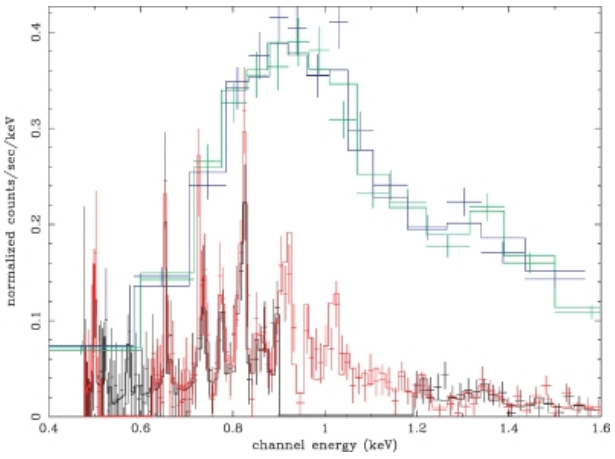

Figure 2.7: EPIC-MOS and RGS spectra of Plaskett's star ($\phi = 0.63$) fitted with a bremsstrahlung model and 85 individual emission lines. From Linder et al. (2006).

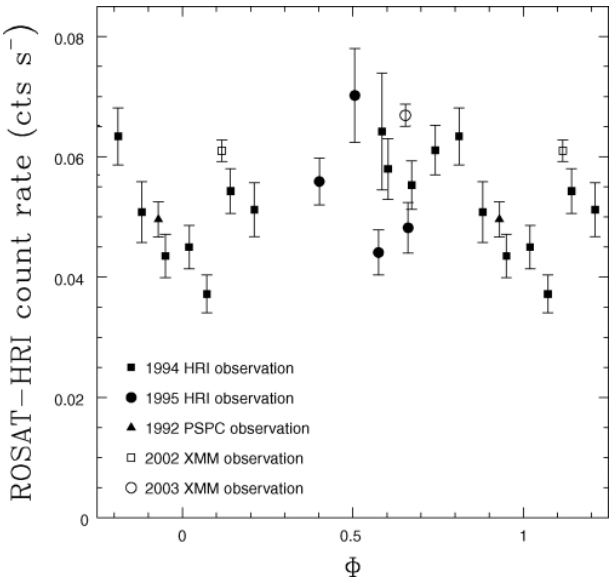

Figure 2.8: Equivalent *ROSAT*-HRI count rate of HD 47129 as a function of orbital phases. The *XMM-Newton* and *ROSAT*-PSPC best-fitting models were converted into equivalent HRI count rates using the HRI response matrix. From Linder et al. (2006).

The *XMM-Newton* observations of Linder et al. (2006) have been obtained at orbital phases $\phi = 0.10$ and 0.63 where $\phi = 0.0$ corresponds to the conjunction with the primary being in front. When considered separately, the EPIC and RGS spectra yield quite different results for the best-fit spectral model when conventional thermal plasma models are used. A possible reason for this discrepancy is that the shock-heated plasma is not in equilibrium, and Linder et al. (2006) therefore used an alternative model consisting of a bremsstrahlung continuum (with an electron temperature of 2.2 keV) and 85 individual lines which have a temperature of maximum emissivity (evaluated under the assumption of thermal equi-

librium) spanning a range in kT between 0.18 and 1.4 keV. This model provides a good fit (Fig. 2.7) and the X-ray luminosity is found to be 8.3×10^{32} erg s^{-1}.
The RGS spectrum reveals a quite strong N VII Lyα line at 24.8Å which indicates a nitrogen overabundance of a factor 6 - 7 in agreement with the qualitative finding of Bagnuolo & Barry (1996). The EPIC data reveal no short term variability (over the duration of the *XMM-Newton* observation) of the X-ray flux but, using archive *ROSAT* data, Linder et al. (2006) find a considerable modulation of the X-ray emission on the orbital time scale (Fig. 2.8). The X-ray flux is minimum at phase 0.0, and Linder et al. (2006) interpret this as the effect of the occultation of the wind – wind collision zone by the body of the primary in a similar way as for CPD-41° 7742. Indeed, the wind momentum ratio $\frac{(\dot{M}\,v_\infty)_{\rm seco}}{(\dot{M}\,v_\infty)_{\rm prim}} \simeq 2$ suggests that the wind collision zone must be located closer to the surface of the primary. However this interpretation suggests a Coriolis deflection of less than 50°; otherwise, the X-ray minimum would not be centered on $\phi = 0.0$.

2.4 General discussion of X-ray emission from Colliding Wind Binaries

In this chapter, I have presented some results on the X-ray emission from colliding wind binary systems obtained with the current generation of X-ray observatories. Several questions arise from these studies:

- Are early-type binaries X-ray overluminous?

  There are many claims in the literature of colliding wind binary systems being X-ray overluminous compared to single stars of the same bolometric luminosity (e.g. Chlebowski & Garmany 1991, Pollock 1987). For Wolf-Rayet stars, it has been shown that their intrinsic X-ray emission is often very low or even inexistent (see Gosset et al. 2005a and references therein). Therefore, the statement most probably holds for WR binaries, although the observable amount of X-ray emission critically depends upon the opacity of the WR wind and the orientation of the system at the time of the observation. In this context, it is interesting to note that WR 25, which had been suspected to be a colliding wind system for many years based on its X-ray brightness, was indeed shown to be a binary system by the Liège and La Plata groups (Gamen et al. 2006, see also below).

  O-stars on the other hand have an intrinsic emission that scales as $L_{\rm X} = (1.2 \times 10^{-7}) L_{\rm bol}$ (Sana et al. 2006b). As shown on Fig. 2 of Rauw (2006) and on Fig. 2.9, many O star binaries are indeed overluminous compared to this relation. However, not all binaries are significantly brighter in X-rays (e.g. HD 152218 and HD 152219) and not all O-stars that are X-ray bright are colliding wind binaries (e.g. θ^1 Ori C).

  Some trends seen on Fig. 2.9 can be understood qualitatively. In fact, the $L_{\rm X}/L_{\rm bol}$ ratio increases with $L_{\rm bol}$ as a result of the general increase of the mass loss rate of the stars with luminosity and the fact that the X-ray emission in the radiative regime is expected to increase with $\dot{M}\,v^2$, whilst in the adiabatic regime this dependence is expected to be $\dot{M}^2\,v^{-3.2}\,D_{\rm sep}^{-1}$ where $D_{\rm sep}$ is the separation between the stars and v the pre-shock velocity. On the other hand, the $L_{\rm X}/L_{\rm bol}$ ratio increases with orbital period for systems in the radiative regime since the pre-shock velocity increases when the orbital separation increases. For longer periods, i.e. for adiabatic systems, the ratio is expected to decrease again due to the $D_{\rm sep}^{-1}$ dependence of the colliding wind X-ray emission. For instance, 9 Sgr which has an orbital period of about 8 – 9 years (the longest in our sample) has a rather modest overluminosity for its bolometric luminosity, though one should obviously not over-interpret this result based on a single case.

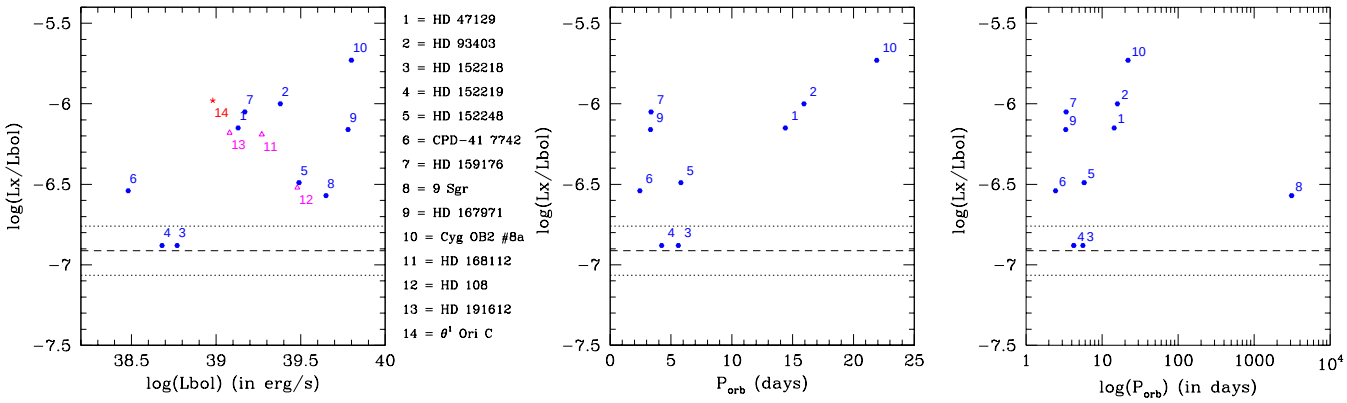

Figure 2.9: Left panel: $L_{\rm X}/L_{\rm bol}$ ratio as a function of $L_{\rm bol}$ for 10 confirmed O-type binaries (filled dots), one binary candidate (HD 168112), two Of?p stars (HD 108 and HD 191612) and the peculiar object θ^1 Ori C. Middle panel: $L_{\rm X}/L_{\rm bol}$ ratio as a function of the orbital period for the confirmed binary systems. Right panel: same but with the orbital periods on a logarithmic scale. The dashed horizontal line yields the empirical $L_{\rm X}/L_{\rm bol}$ relation from Sana et al. (2006b), whilst the dotted lines yield the corresponding error bars on this relation.

- Does the X-ray emission of adiabatic systems vary with $D_{\rm sep}^{-1}$?

  We have found that such a relation might apply to the eccentric system HD 93403, but not to HD 152248. This could simply reflect the fact that the latter system has a shorter orbital period and is hence in the radiative regime. If this explanation is correct, then due to the larger mass loss rates of Wolf-Rayet stars, the transition from the radiative to the adiabatic regime in WR + O binaries should occur at longer orbital periods. Indeed, no $D_{\rm sep}^{-1}$ scaling was seen in γ^2 Vel nor in WR 22 (Gosset et al. 2003) which have both orbital periods near 80 days.

  Recently, the first orbital solution was obtained for WR 25 (WN6ha, see Gamen et al. 2006). Folding the observed X-ray fluxes of WR 25 through the ephemeris of this long-term system ($P_{\rm orb} = 208$ days, $e \simeq 0.35$) suggests that the X-ray emission from this binary indeed undergoes a $D_{\rm sep}^{-1}$ modulation (Fig. 2.10).

- Where does the optical line emission in colliding wind binaries come from?

  At least in two O-star binaries (HD 93403 and HD 152248), optical emission lines and X-ray emission are thought to arise from the wind interaction region. To bring the post-shock plasma from temperatures of several 10^6 K (typical of the X-ray emission) to some 10^4 K (typical of optical emission lines) requires a substantial cooling. Current hydrodynamical models do not have a sufficient resolution to adequately sample the short scale-lengths of those parts of the wind interaction zone where cooling is most efficient. This is a major challenge for forthcoming generations of hydrodynamical models of colliding wind binaries. In the meantime, observations can provide additional constraints. A very promising target in this respect is WR 20a which exhibits profile variations in the He II λ 4686 and Hα emission lines (see Sect. 1.5.1) suggesting that these emissions arise at least partly in the wind interaction region. At the time of writing of this habilitation thesis, *Chandra* is monitoring WR 20a for us (programme 07200285, P.I. G. Rauw). Two 50 ksec observations scheduled at specific orbital phases of this eclipsing binary will allow to map the X-ray emission zone and hence to compare its location with the optical line emission regions.

- Is the X-ray plasma in a wind interaction zone in thermal equilibrium?

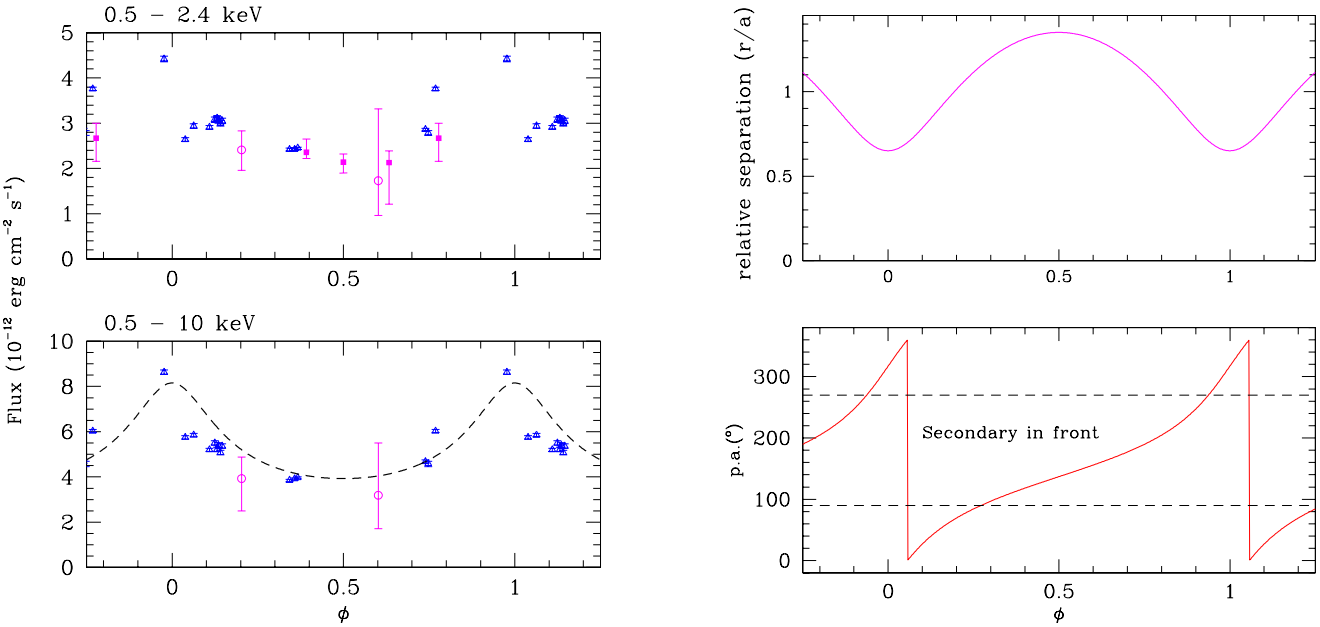

Figure 2.10: Left panel: X-ray light curve of WR 25 (Nazé 2005, private comm.) over two different energy ranges (the *ROSAT* and *XMM-Newton* bands) as a function of orbital phase (using the ephemeris from Gamen et al. 2006). Right panel: variation of the separation between the components of WR 25 and of the position angle of the binary. The $1/D_{\rm sep}$ relation is also shown in the lower left panel for illustration (note that this is not a fit to the data).

Several lines of evidence suggest that the shock-heated plasma might not be in thermal equilibrium (Pollock & Raassen 2005). This could provide an explanation for the hard emission tails that are frequently seen in the X-ray spectra of early-type binaries. This is a crucial issue for a proper understanding and interpretation of X-ray emission from early-type stars in general and from massive binaries in particular. Besides theoretical developments, high-spectral resolution observations are needed to address this question. Unfortunately, the current X-ray observatories lack the sensitivity to gather high-quality high-resolution spectra for a large sample of massive binaries and this issue will therefore have to be postponed until the next generation facilities such as *XEUS* (ESA) and/or *Con-X* (NASA) become available... which will hopefully be the case in a decade or so.

Chapter 3

Non-thermal phenomena in the atmospheres of early-type stars

Qu'est-ce que cette étoile?
Et on lit son nom dans un livre, et on croit la connaître.

Jules Renard, *Journal*

The topic of non-thermal radio, X-ray and γ-ray emissions from massive stars and more specifically from colliding wind binary systems has triggered a number of theoretical and observational investigations over the last few years. In this chapter, I focus on the contributions of the GAPHE team to this field. I was actively involved in all of the results presented here.

3.1 Introduction

As a general introduction to the problem of non-thermal phenomena in the winds of early-type stars, I reproduce below an invited review I delivered at the conference on the 'Multiwavelength Approach to Unidentified Gamma-Ray Sources' that was organised in Hong-Kong from 1 to 4 June 2004 (Rauw 2004b). This review was published as a chapter of the book 'Cosmic Gamma-Ray Sources' edited by K.S. Cheng and Gustavo E. Romero. Some additional results that became available after the Hong-Kong conference are described throughout this chapter.

CHAPTER 5
NON-THERMAL EMISSION FROM EARLY-TYPE BINARIES

Gregor Rauw*
Institut d'Astrophysique et de Géophysique, Université de Liège,
Allée du 6 Août 17, Bât B5c, 4000 Liège (Sart-Tilman), Belgium
rauw@astro.ulg.ac.be

Abstract In this chapter, I review the properties of high-energy particles in the stellar winds of hot early-type stars. Relativistic electrons are responsible for the synchrotron radio emission observed from a subsample of these stars. Most of the objects in the latter category are found to be binaries and the collision between the stellar winds of the binary components is thought to play a crucial role in the acceleration of the relativistic electrons. The interplay between these high-energy electrons and the intense stellar radiation field could produce a substantial non-thermal emission at X-ray and γ-ray energies through inverse Compton scattering. Other mechanisms, such as π^0 decay might also contribute to the production of non-thermal emission from hot stars. These various effects could possibly account for some of the yet unidentified *EGRET* sources found to be correlated with OB associations in our Galaxy. Finally, I review recent results from *XMM-Newton* observations and discuss the prospects of forthcoming γ-ray observations with *INTEGRAL* and *GLAST*.

Introduction

Early-type stars of spectral types O and Wolf-Rayet (hereafter WR) have energetic, highly supersonic, winds associating huge mass loss rates (of order $\dot{\mathrm{M}} \sim 10^{-6}$ and $10^{-5}\,\mathrm{M}_\odot\,\mathrm{yr}^{-1}$ for O-type and WR stars respectively) and large terminal velocities ($v_\infty \sim 2000\,\mathrm{km\,s}^{-1}$). When two such stars form a binary system, their winds collide: the resulting wind interaction region is limited by two hydrodynamical shocks, each shock facing one of the binary components. The compressed stellar winds in

*Research Associate at the Fonds National de la Recherche Scientifique (Belgium)

the interaction region are separated by a contact discontinuity set by ram pressure equilibrium.

The theoretical concept of colliding stellar winds was put forward by Prilutskii & Usov (1976) and Cherepashchuk (1976). The first models based on a numerical solution of the differential equations of the hydrodynamics describing the phenomenon were presented by Lebedev & Myasnikov (1988), Luo et al. (1990) and Stevens et al. (1992). For a general introduction to theoretical aspects of this process, we refer to the paper of Stevens et al. (1992).

Over the last two decades, ample observational evidence for colliding wind interactions has been accumulated. For instance, optical and ultraviolet spectra of many early-type binaries display phase-locked emission line profile variability (e.g. Wiggs & Gies 1993, Rauw et al. 1999, Gosset et al. 2001...). Some wide WC + O binaries also exhibit episodic (recurrent) variability of their IR emission attributed to dust formation in the wind collision zone (see Williams 2002 for a review). Another distinctive signature of wind interactions is the excess X-ray emission produced in the shock-heated plasma. On statistical grounds, early-type binaries are indeed found to be stronger X-ray sources than their single counterparts (Pollock 1987a, Chlebowski & Garmany 1991). The X-ray emission from colliding wind binaries is expected to display a significant phase-locked modulation (Pittard & Stevens 1997) either as a consequence of a changing optical depth along the line of sight or as a result of a changing separation between the stars in eccentric binaries. Such variations have indeed been reported for a number of O + O and WR + O binaries (e.g. Corcoran 1996, Willis et al. 1995, Rauw et al. 2002a).

In this chapter, I will focus on another aspect of the wind interaction in early-type binaries, i.e. the acceleration of relativistic particles near the hydrodynamical shock and the signatures of these particles throughout the spectra of these binaries. This chapter is organised as follows. Section 1 provides a brief introduction to the concept of wind - wind collisions and their potential role in the acceleration of relativistic particles. In Section 2, I consider the synchrotron radiation seen in the radio emission of some O and WR stars, whilst Sect. 3 is devoted to a discussion of the possible observational signature of relativistic particles at X-ray and γ-ray energies through inverse Compton scattering. Section 4 contains a brief overview of other mechanisms related to hot massive stars that may produce γ-ray radiation. Finally, the main conclusions as well as future perspectives are highlighted in Sect. 5.

1. Some basic considerations

1.1 Wind interactions in early-type binaries

Consider a system formed by two stars with spherically symmetric stellar winds (in the absence of the wind interaction). Let $\dot{\mathrm{M}}_j$ and $v_{\infty,j}$ be respectively the mass loss rate and the asymptotic wind velocity of star j. In a wide binary system, both winds reach their terminal velocity before they collide and the shape of the contact discontinuity is set by the wind momentum ratio defined as

$$\mathcal{R} = \left(\frac{\dot{\mathrm{M}}_1 \, v_{\infty,1}}{\dot{\mathrm{M}}_2 \, v_{\infty,2}} \right)^{1/2}$$

(see e.g. Eichler & Usov 1993, Stevens et al. 1992). The intersection between the binary axis and the contact discontinuity lies at a distance $x^{\mathrm{stag}} = \mathcal{R}\, d/(\mathcal{R}+1)$ from the center of mass of the star with the more energetic wind. Here d stands for the orbital separation between the centers of the stars. In a binary system where both winds are of equal strength ($\mathcal{R} = 1$), the contact discontinuity can be approximated by a plane located mid-way between the two stars. In a more general situation with $\mathcal{R} \neq 1$, the contact discontinuity appears as a cone wrapped around the star with the less energetic wind (see Fig. 1).

Immediately behind the shock, the plasma is heated to a temperature of order

$$T_{s,j} = \frac{3\,\overline{m}_j \, v_j^2}{16\,k}$$

where $\overline{m}_j$ is the average mass per particle in the wind of star j and v_j stands for the pre-shock wind velocity (see e.g. Stevens et al. 1992). Due to the large pre-shock wind velocities, the post-shock plasma temperature is very high ($\geq 10^7$ K).

The properties of the post-shock gas depend to a large extent on the importance of radiative cooling that can be roughly estimated from the ratio between the characteristic cooling time and the typical escape time from the shock region:

$$\frac{t_{\mathrm{cool}}}{t_{\mathrm{esc}}} \simeq \frac{v_8^4 \, x_{12}^{\mathrm{stag}}}{\dot{M}_{-7}}$$

where v_8, x_{12}^{stag} and $\dot{M}_{-7}$ are respectively the pre-shock velocity in units $10^3\,\mathrm{km\,s^{-1}}$, the distance to the contact surface in units 10^7 km and the mass loss rate in units $10^{-7}\,\mathrm{M_\odot\,yr^{-1}}$ (Stevens et al. 1992). If radiative cooling is important ($t_{\mathrm{cool}}/t_{\mathrm{esc}} \ll 1$), the entire thermal energy produced in the shock is radiated away almost immediately. These highly radiative shocks collapse and the rather cool material in the interaction zone

can contribute to the formation of optical emission lines. Otherwise, if $t_{\rm cool}/t_{\rm esc} \geq 1$, the shock region is essentially adiabatic.

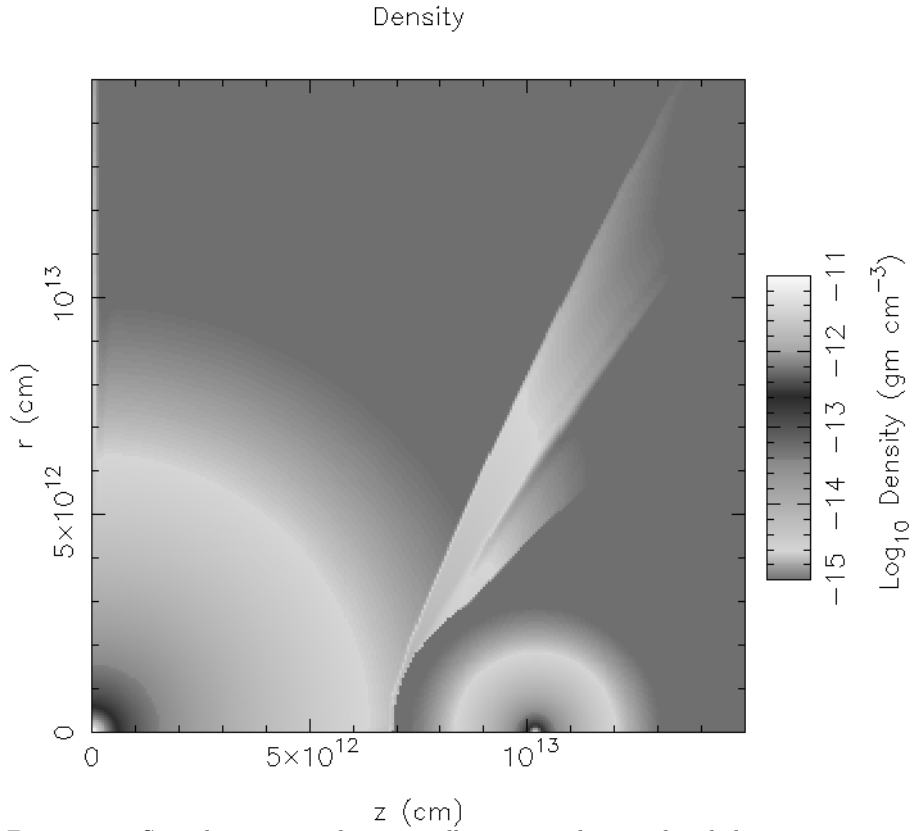

Figure 1. Snapshot gray-scale image illustrating the simulated density structure of an adiabatic wind collision. The center of mass of the primary lies at the origin of the axes, whereas the center of the secondary is located at $z \simeq 10^{13}$ cm. The wind parameters are such that $\mathcal{R} = 3.3$ and $(t_{\rm cool}/t_{\rm esc})_1 = 7$ and $(t_{\rm cool}/t_{\rm esc})_2 = 25$ for the primary and secondary post-shock winds respectively (Sana 2002, private communication).

An important feature associated with the wind collision in an early-type binary is the fact that the shock can act as a site for particle acceleration (Eichler & Usov 1993). In the following sections we will discuss the implications of the presence of relativistic particles in the winds of early-type stars and early-type binaries in particular.

1.2 Relativistic particles in stellar winds

Synchrotron radio emission has been observed for a number of early-type stars (see Section 2 below). The detection of such a non-thermal

emission from these stars implies that a population of relativistic particles is present in their winds. Let us consider what are the main ingredients required to account for this feature.

1.2.1 The acceleration of relativistic particles. Various scenarios have been suggested to explain the presence of relativistic electrons in the atmospheres of early-type stars. Most of them actually require the presence of hydrodynamical shocks. Indeed, free electrons and protons can be accelerated through the first order Fermi mechanism by crossing the shock front forth and back (see e.g. Bell 1978a, Longair 1992). As a result, relativistic electrons should have a power law differential energy distribution $N(\gamma) \propto \gamma^{-n}$, γ being the Lorentz factor of the relativistic electrons. The spectral index n is related to the shock compression ratio χ by

$$n = \frac{\chi + 2}{\chi - 1}$$

(Bell 1978a). If the shocked plasma radiates efficiently, the shock is quasi-isothermal and the compression ratio becomes very large. In this case one expects a value of $n \sim 1$. If instead the shock is adiabatic, then χ should not exceed 4 (for a strong shock) and $n \sim 2$.

Hydrodynamical shocks are found both in *single* and *binary* early-type stars. For instance, in the case of single stars, the intrinsic instabilities of radiatively driven stellar winds (see e.g. Runacres & Owocki 2002 and references therein) lead to the formation of shocks distributed throughout the stellar winds. Therefore, White (1985) and Chen & White (1991a, 1994) suggested that relativistic electrons can be accelerated in the winds of single hot stars. In his model, White (1985) considered that relativistic particles accelerated in shocks in the inner wind region lose energy only through adiabatic expansion and could hence travel out to large distances. However, the interplay between relativistic electrons and the intense stellar radiation field implies strong energy losses through inverse Compton scattering and the electrons accelerated in the inner regions of the stellar wind cannot survive out to large radii. As a consequence, the relativistic electrons responsible for the radio synchrotron emission must be accelerated in situ, i.e. outside the radio photosphere (Chen & White 1994, see also Sect. 2 below). Another consequence of the inverse Compton cooling might be a substantial non-thermal emission at X-ray and γ-ray energies (Pollock 1987b, Chen & White 1991a, b).

In the case of massive binaries, particles can be accelerated through the Fermi mechanism in the shock region of the wind interaction zone (Eichler & Usov 1993). An alternative scenario related to colliding wind

binaries has been proposed by Jardine et al. (1996). These authors considered the current sheets that result from the collision of magnetized stellar winds. The compression of magnetic field lines in the current sheets leads to enhanced local field strengths and the resulting electric fields in the current sheet can accelerate particles also in the atmospheres of stars with rather modest surface magnetic fields.

Finally, one should note that the flow time associated with a shock inside a stellar wind is rather short (of the order of hours to a few days). Compared to the situation in a supernova remnant, where there is ample time to accelerate thermal particles to relativistic energies (Bell 1978b), the particles in a stellar wind spend less time in the vicinity of a shock. More theoretical work is therefore needed to check whether the mechanism proposed by Bell (1978b) for the initial acceleration of particles in supernova remnants works also in stellar winds. Also, while the relativistic electrons may well be injected with a power-law spectrum, various energy loss mechanisms (ionization losses, inverse Compton scattering, synchrotron losses...) will distort this distribution (see for instance the work of Melrose & Crouch 1997 on the effect of synchrotron losses) and might even inhibit the acceleration of the electrons.

1.2.2 Magnetic fields. The question of the existence of magnetic fields in the stellar winds of early-type stars is still a controversial issue. Indeed, early-type stars do not have a convective zone beneath the photosphere that could generate a strong magnetic activity such as seen in the coronae of late-type stars. Non-thermal radio emission, if due to synchrotron radiation, is consistent with surface magnetic fields (B_*) of the order of a hundred Gauss (Chen & White 1994). However, the broad absorption lines in the spectra of OB stars render any direct determination of B_* through Zeeman splitting extremely difficult. So far, magnetic fields have only been measured directly for a few early-type OB stars ($\sim 360\,\mathrm{G}$ in $\beta\,\mathrm{Cep}$ (B1 IV) and $\sim 1100\,\mathrm{G}$ in $\theta^1\,\mathrm{Ori\,C}$ (O4–6 V) see Donati et al. 2001, 2002). For most OB stars, the non-detection of the Zeeman effect puts an upper limit of order $\sim 100\,\mathrm{G}$ on B_* (Mathys 1999). In the case of WR stars, the optical spectra display broad emission lines that are formed throughout the stellar wind and no direct measurement of the magnetic fields of a WR star has been possible to date.

Indirect evidence for magnetic fields in early-type stars has been obtained from the rotational modulation of the stellar winds of some objects. In fact, the periodic variability seen in the spectra of some of these stars has been attributed to corotating structures in the stellar wind. One possibility to generate such corotating structures would be a

stellar magnetic field. The field strength can be estimated by assuming that the outer radius of corotation of the stellar wind is equal to the Alfvén radius (see e.g. Rauw et al. 2001).

The existence of the stellar wind alters the geometry of the magnetic field lines of an otherwise dipolar field. Following the description of Eichler & Usov (1993), the radial dependence of the magnetic field strength at large distance r from the star should be described by a toroidal field:

$$B(r) = B_* \, \frac{v_{\rm rot}}{v_\infty} \, \frac{R_*^2}{R_{\rm A} \, r}$$

(see Fig. 2) where $R_{\rm A}$ is the Alfvén radius, R_* the stellar radius and $v_{\rm rot}$ is the rotation velocity at the stellar equator.

Magnetic fields are important both for the acceleration and emission mechanisms. For instance, the mean free path of a relativistic electron of energy $\gamma \, m_e \, c^2$ is given by

$$\lambda(r) \propto \frac{\gamma \, m_e \, c^2}{e \, B(r)}$$

(where e is the charge of the electron and all parameters are expressed in Gaussian units) and this parameter has implications for the value of the cut-off energy of the relativistic electron distribution. In addition, the local magnetic field is of course an essential ingredient in the synchrotron emission process.

2. Non-thermal radio emission from early-type stars

The bulk of the radio emission from early-type stars is attributed to thermal free-free radiation produced in their stellar winds. Theoretical considerations indicate that these objects should have a radio spectral index[1] of $\alpha \simeq 0.6$ (e.g. Wright & Barlow 1975). Note that actual millimeter and radio observations suggest slightly larger spectral indices of 0.7 – 0.8 for the free-free emission of WR and O stars (Williams 1996).

At radio wavelengths, the winds of early-type stars are optically thick and the optical depth at a radius r is given through the following relation:

$$\tau_\nu(r) = \int_r^\infty K(\nu, T) \, q \, \left(\frac{\dot{\rm M}}{4 \, \pi \, \mu \, m_H \, v_\infty} \right)^2 \, \frac{dx}{x^4}$$

where $K(\nu, T)$ is the linear free-free absorption coefficient (see Wright & Barlow 1975, Leitherer et al. 1995), q is the ratio between the electron and ion number densities, μ and m_H are the mean atomic weight and the

112

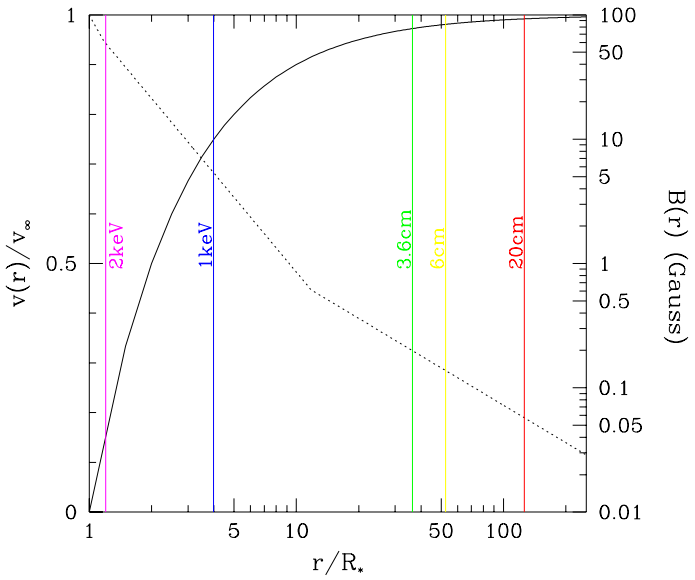

Figure 2. Illustration of the wind structure of a typical O star. The parameters are for 9 Sgr ($\dot{M} = 2.4\,10^{-6}\,M_\odot\,yr^{-1}$, $v_\infty = 2950\,km\,s^{-1}$, $R_* = 16\,R_\odot$, $v_{rot} = 250\,km\,s^{-1}$, see the references in Rauw et al. 2002b). The solid curve yields the wind velocity as a function of radius, assuming a so-called standard β velocity law with $\beta = 1$. The dotted line shows the radial dependence of the magnetic field assuming $B_* = 100\,G$ and adopting the formalism of Eichler & Usov (1993). The vertical lines indicate the location of surfaces of optical depth unity for various energies or wavelengths (given by the labels).

mass of the hydrogen atom respectively. For an isothermal O star wind of temperature 20000 K consisting mainly of ionized hydrogen with $\dot{M} = 3\times10^{-6}\,M_\odot\,yr^{-1}$ and $v_\infty = 2000\,km\,s^{-1}$, we find that $\tau_\nu = 1$ corresponds to radii of 850, 1250 and 3000 $R_\odot$ (corresponding to about 50, 75 and 175 R_*) at radio wavelengths of 3.6, 6 and 20 cm respectively. Note that these radii are even larger for Wolf-Rayet type stars. Therefore, any observable radio flux of an early-type star must arise in the outer regions of its stellar wind. In the case of massive binaries with spherically symmetric winds (outside of the colliding winds region), this condition translates into a critical value of the orbital period: below periods of the order of a month, the heavy wind opacity would prevent us from seeing any non-thermal radio radiation that might be produced in the shock front of a colliding wind WR + O binary (Eichler & Usov 1993).

A subset of OB and WR stars display unusually high radio flux levels with spectral indices that deviate significantly ($\alpha \leq 0.0$) from the canonical value expected for purely thermal free-free emission (e.g. Abbott et al. 1984, Bieging et al. 1989). This feature is attributed to a

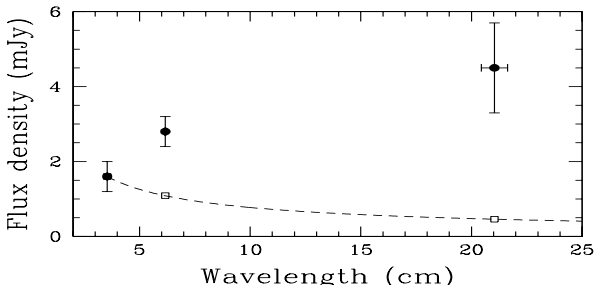

Figure 3. *VLA* radio fluxes of 9 Sgr as reported by Rauw et al. (2002b). The observed fluxes are shown as filled circles. The dotted line and the open squares show the energy distribution that would be observed if the radio emission were thermal with a spectral index $\alpha = 0.7$ (normalized to the observed flux at 3.6 cm).

non-thermal, most probably synchrotron, emission component on top of the thermal wind emission. In fact, synchrotron radiation produced by relativistic particles should produce a power law spectrum with a spectral index $\alpha = -(n-1)/2 \sim -0.5$. The non-thermal radio emission is often variable both in intensity and in spectral index (see e.g. Williams 1996). The observed synchrotron radiation is a definite sign of two things: (i) a magnetic field and (ii) a population of relativistic electrons must exist in the radio emitting region (i.e. outside the radio photosphere).

From an observational point of view, it is worth pointing out that most, if not all, of the WR stars that display a non-thermal radio emission are in fact binaries (see Dougherty & Williams 2000). The situation is however less clear for non-thermal OB stars (see Table 1). While three stars out of eight are binary or triple systems, the multiplicity of the remaining five objects has not yet been fully investigated. However, at least in the case of 9 Sgr (Rauw et al. 2002b) and HD 93250 (Rauw et al. 2003), observational hints towards multiplicity were found in the optical or X-ray domain.

HD 167971 (O7.5 f + O) has the strongest non-thermal radio emission among the OB stars detected in the survey of Bieging et al. (1989). Leitherer et al. (1987) describe HD 167971 as a close eclipsing O star binary ($P_{orb} = 3.32$ days) with a third more distant and much brighter Of companion (which could be a line of sight object).

Cyg OB2 #5 is another multiple system. This system consists of a 6.6-day period close binary harboring an Of supergiant and a more evolved Ofpe/WN9 transition object (Rauw et al. 1999). A third star (probably early B-type) was found to lie 0.95" away from the close binary (see Contreras et al. 1997). The system displays a variable, partly non-thermal radio emission. The radio emission consists of two compo-

nents: a primary associated with the close binary system and a secondary slightly elongated (non-thermal) component with a location consistent with emission from the bow shock between the winds of the close binary and the third component (Contreras et al. 1997). It is worth mentioning that the radio variability of the system is mainly due to the primary radio component (Dougherty 2000, private communication) that shifts between a purely thermal low state and a partly non-thermal high state on an apparent time scale of about 7 years (Miralles et al. 1994).

Table 1. Multiplicity of OB stars known to display a non-thermal radio emission.

Star	Spect. type	Binarity	Reference
HD 15558	O5 III (f)	SB1	[1]
HD 93250	O3 V	X-ray variable	[2]
HD 164794 (= 9 Sgr)	O4 V ((f$^+$))	RV variable	[3]
HD 168112	O5 III	single?	–
HD 167971	O7.5 f + O	triple	[4]
Cyg OB2 #5	O7 Ianf + Ofpe/WN9	triple	[5]
Cyg OB2 #8A	O6 Ib(f)	single?	–
Cyg OB2 #9	O5 f	single?	–

References: [1] Garmany & Massey (1981), [2] Rauw et al. (2003), [3] Rauw et al. (2002b), [4] Leitherer et al. (1987), [5] Contreras et al. (1997).

The observed radio emission of an early-type star can be written

$$S_\nu = S_{ff,\nu_0} \left(\frac{\nu}{\nu_0}\right)^{0.7} + A_{nt,\nu_0}(t) \left(\frac{\nu}{\nu_0}\right)^{\alpha(t)} \exp\left[-\tau_\nu(t)\right]$$

Here S_{ff,ν_0} stands for the thermal emission due to the free-free process at frequency ν_0, whereas $A_{nt,\nu_0}(t)$ and $\alpha(t) = -(n-1)/2$ are respectively the non-thermal flux level at frequency ν_0 and the spectral index. The latter two properties may display significant time variability. Likewise, if the position of the non-thermal source inside the wind changes, the optical depth τ_ν due to free-free absorption towards the region of the non-thermal emission may also vary with time. Note that the spectral indices inferred from radio observations are rather steep, consistent with the electrons being accelerated in rather weak shocks. Finally, below a frequency $\nu_R \sim 20\, n_e/B$ the synchrotron emission is cut off by the *Razin effect* that suppresses the beaming of the synchrotron radiation. Here n_e stands for the electron density (Ginzburg & Syrovatskii 1965).

Non-thermal radio emission is observed essentially in wide binaries where the shock region is located outside the radio photosphere. In

close binaries, synchrotron emission could still be produced, but it might remain undetectable because of the optically thick wind. At least in the case of eccentric binaries, these considerations account for the observed phase-locked variability of the radio flux.

The most famous examples of non-thermal radio emitters associated with colliding wind WR + O binaries are probably WR 140 (WC7 + O5, e.g. Williams et al. 1990, White & Becker 1995) and WR 147 (e.g. Williams et al. 1997).

WR 140 has a highly eccentric ($e = 0.84$) orbit with a period of 7.9 yrs and the non-thermal radio flux displays a prominent phase-locked variation (e.g. White & Becker 1995). Between phases 0.4 and 0.95 (phase 0.0 corresponding to periastron passage), the emission at 6 cm increases dramatically displaying a broad maximum around phase 0.8. The higher frequency emissions rise, peak and decline somewhat earlier than emission at longer wavelengths (White & Becker 1995). The shape of the radio light curve at different frequencies results from a combination of two effects (Williams et al. 1990, 1994). First, the region of the wind interaction is burried deep inside the huge radio photosphere of the WR star, except at phases away from periastron when the shock zone is farther away from the WR core and eventually moves out of the WR's radio photosphere. In addition, as a result of the cavity produced by the shock cone in the WR wind, the non-thermal radio emission becomes observable when the O star with its lower density (and thus less opaque) wind passes in front of its WR companion.

WR 147 is a visual binary consisting of a WN8 star and a late-O, early-B type companion. The radio emission from this system was resolved by *MERLIN* into a thermal component associated with the wind of the WN8 star and a non-thermal component located in between the WR star and its visual companion (see Williams et al. 1997). The location of the non-thermal component (closer to the OB star) as well as its morphology are consistent with the expectations of a colliding wind scenario (Dougherty et al. 2003). Interestingly, WR 147 is also the first early-type system where high resolution *Chandra* ACIS-I observations provided evidence for a spatially extended X-ray emission. The X-rays are found to peak close to the position of the radio bow shock (Pittard et al. 2002).

3. Inverse Compton scattering

Synchrotron radio-emission is expected to account only for a fraction of the total non-thermal energy budget. In fact, given the enormous

116

supply of photospheric UV photons in the winds of OB stars, inverse Compton (IC) scattering becomes a major energy loss mechanism for relativistic electrons and non-thermal X-ray and low-energy γ-rays should be generated, resulting approximately in a power law spectrum from keV to MeV energies (Pollock 1987b, Chen & White 1991a,b). In the Thomson regime, the average energy of a photon after inverse Compton scattering with respect to its initial energy is of order $h\,\nu_{IC} \sim \frac{4}{3}\gamma^2\,h\,\nu_*$. Given the average photon energy $h\,\nu_*$ of the radiation field of a typical early-type star, Lorentz factors of order 10^2 – 10^4 are sufficient to produce IC X-ray and γ-ray radiation. The spectrum resulting from IC scattering by a power law electron distribution of index n is a power law of photon index $\Gamma = (n+1)/2$. The critical question is whether the IC X-ray and γ-ray flux levels are high enough to be detected.

In their model, Chen & White (1991a) considered electrons accelerated in strong wind instability shocks with $\chi = 4$ giving $n = 2$ and $\Gamma = 1.5$. These shocks are distributed throughout the wind of single O stars and these authors therefore treated the IC process in the isotropic approximation. Note that in the case of single stars, the IC X-ray, γ-ray and synchrotron radio emission are not necessarily correlated because they arise in physically distinct regions. Indeed, whilst photoelectric absorption by the circumstellar material can affect the X-ray spectra of early-type stars up to energies of $\sim 1\,$keV, it has little impact on the higher energy X-rays. Therefore, the optical depth to hard X-rays and soft γ-rays throughout the wind is small[2]. Moreover, inverse Compton scattering is expected to be most efficient within a few stellar radii where the UV radiation density is highest. On the other hand, as a consequence of the large free-free optical depth at radio frequencies, radio synchrotron emission can only be observed from the outer regions of the wind (beyond about fifty stellar radii, see Fig. 2). The properties of the expected non-thermal emission of single stars at different energies thus reflect the radial distribution of the relativistic electron spectrum throughout the wind.

Chen & White (1991b) investigated the γ-ray luminosities due to inverse Compton scattering in the atmospheres of O stars. These authors estimated total IC luminosities of $\sim 8\,10^{33}$ and $63\,10^{33}\,$erg s^{-1} for the O4 stars $\zeta\,$Pup and 9 Sgr respectively. However, their predictions depend strongly on the interpretation of the hard X-ray emission (at energies above 3 keV) seen in $\zeta\,$Ori with the Solid State Spectrometer onboard the *EINSTEIN* observatory (see however below).

In a colliding wind situation, the shock region is located closer to the surface of the star with the less energetic wind (see Fig. 1). Therefore,

the seed photons for inverse Compton scattering will mainly come from the UV radiation of this star. In this case, it is the same population of relativistic electrons (accelerated in the wind interaction zone) that produces the synchrotron and IC emission. The inverse Compton scattering emission must be computed in the non-isotropic case (using for instance the head-on approximation, see Reynolds 1982, Mücke & Pohl 2002).

3.1 Non thermal X-ray emission from early-type stars?

Rauw et al. (2002b) performed a multi-wavelength investigation of 9 Sgr. Their *VLA* data obtained simultaneously with an *XMM-Newton* observation indicate a definite non-thermal radio emission (see Fig. 3). The X-ray spectra of 9 Sgr reveal a hard X-ray component that can be fitted equally well by a multi-temperature thermal model including some plasma at kT $\geq$ 1.46 keV or by a rather steep power law ($\Gamma \geq 2.9$) component (see Fig. 4). When interpreted in the framework of the theory of Bell (1978a), such a steep power law corresponds to acceleration by shocks with a low compression ratio ($\chi \leq 1.8$).

The 9 Sgr data discussed by Rauw et al. (2002b) provide the tightest constraints so far on the properties of a hard X-ray power law tail in an O star. In fact, the *EINSTEIN*-SSS observations of the Orion Belt stars that motivated the work of Chen & White (1991a) may have been affected by calibration issues involving the formation of ice on the instrument entrance window and subsequent *ASCA* observations of δ Ori failed to confirm the existence of a hard power law tail in its X-ray spectrum (Corcoran et al. 1994).

It is worth pointing out that the *VLA* observations of 9 Sgr also suggest a low compression ratio of $\chi \simeq 1.7$. In this context, it must be stressed that the compression ratios inferred from the X-ray and radio data should be seen as typical or average values. Rather than having a unique compression ratio, the shocks in the wind are likely to have a distribution of compression ratios, as is also suggested by hydrodynamical models.

Interestingly, Skinner et al. (2002) reported the existence of a hard X-ray component in the *XMM*-EPIC spectra of the presumably single Wolf-Rayet star WR 110. This hard component could be either thermal (kT $\geq$ 3 keV) or non-thermal emission produced by inverse Compton scattering. In the former case, the hard X-rays could arise in a wind collision zone of a WR + O binary with an as yet undetected O star companion. In the latter hypothesis, the hard component can be fitted with a photon index

118

$\Gamma = 2.2$, not too different from the theoretical value for strong adiabatic shocks ($\Gamma \sim 1.5$, see above). The radio emission from WR 110 yields no indication of a synchrotron component. However, the lack of non-thermal radio emission does not rule out the existence of a non-thermal X-ray emission since, as pointed out above, the two phenomena may not be correlated if the synchrotron radio emission forms deep within the wind where it would be strongly absorbed by the huge free-free opacity.

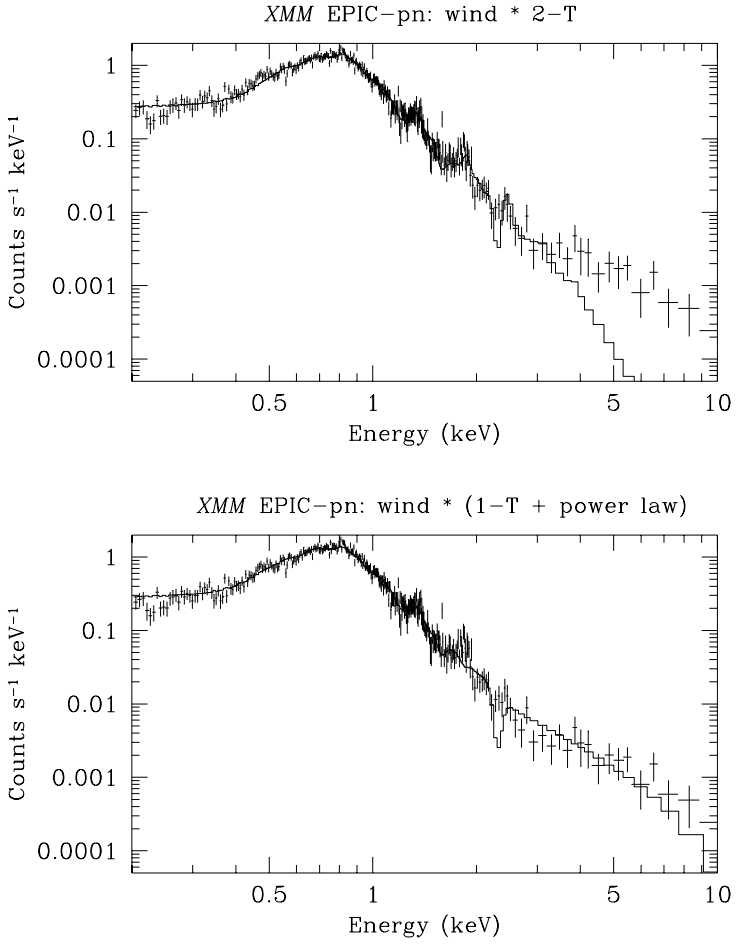

Figure 4. X-ray spectrum of 9 Sgr as observed with the EPIC-pn instrument on-board $XMM - Newton$. The upper panel illustrates the fit of the spectrum with a 2-T thermal plasma model with proper wind absorption cross sections. The model fails to reproduce the hard tail of the spectrum (beyond $\sim$ 3 keV). A better fit is obtained with a 1-T thermal model + non-thermal power law component as shown in the lower panel. For details see Rauw et al. (2002b).

3.2 A possible connection with unidentified γ-ray sources?

At this stage, it is interesting to briefly consider the overall distribution of early-type stars in our Galaxy. The latest version of the *Catalog of Galactic O Stars* (Cruz-González et al. 1995) lists a total of 644 known O stars of luminosity class V. As far as WR stars are concerned, the *VIIth Catalogue of Galactic Wolf-Rayet Stars* (van der Hucht 2001) includes 227 entries. The actual total number of early-type stars in the Milky Way is certainly much larger: many hot massive stars are expected to populate the highly obscured inner regions of the Galaxy. Reed (2000) and van der Hucht (2001) estimated the total Galactic population of O-B2 stars and WR stars at respectively ~ 60000 and ~ 6500.

Gies (1987) investigated the kinematical and binary properties of an essentially complete sample of 195 Galactic O-type stars brighter than $V = 8.0$. 80% of the stars in this sample are found at a Galactic latitude $|b_{II}| \leq 5^\circ$ and their distribution traces the spiral arms of the Galaxy. Gies also showed that 70% of all stars in his sample are members of open clusters or OB associations. In a subsequent study, Gies et al. (1998) found that among the O stars in clusters and associations, 75% are either visual or spectroscopic binaries. The fraction of binaries is significantly lower among field stars and only a small fraction of binaries was found among runaway O stars. The situation is less clear among WR stars where considerable observational biases affect the binary census. Nevertheless, van der Hucht (2001) estimated the binary fraction among WR stars at $\sim 39\%$ (including probable binaries).

In summary, there exists a large number of single and binary early-type stars distributed over the Galactic Plane. Whether or not they produce a detectable emission at γ-ray energies strongly depends on the parameters of the individual systems.

From an observational point of view, many of the yet unidentified *EGRET* sources must be of Galactic origin and appear correlated with the massive stars population (e.g. Montmerle 1979, Manchanda et al. 1996, Romero et al. 1999).

Romero et al. (1999) studied the possible association between sources in the third EGRET catalogue (Hartman et al. 1999) and catalogues of WR and Of stars, supernova remnants (SNRs) and OB association (believed to be essentially pulsar tracers). Marginally significant correlations were found for the WR and Of stars, whereas highly significant correlations were found for SNRs and OB associations. An a posteriori analysis led Romero et al. to conclude further that among the positive

correlations with massive stars, WR 142, WR 140 and Cyg OB2#5 were most likely actual γ-ray sources associated respectively with the sources 3EG J2021+3716, 3EG J2022+4317 and 3EG J2033+4118.

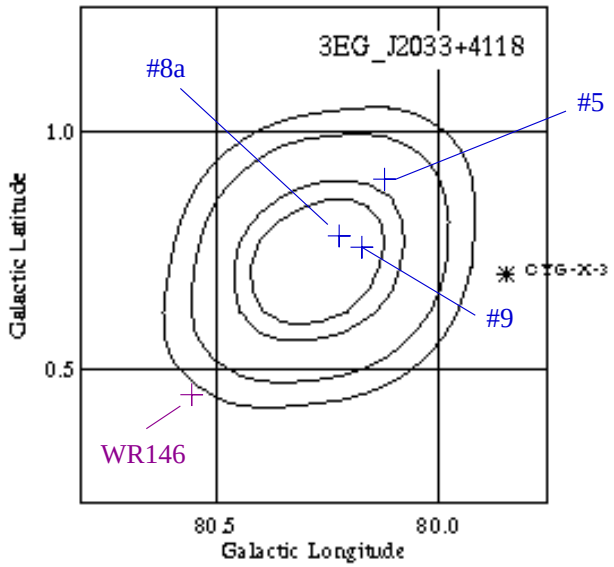

Figure 5. Location of the EGRET source 3EG J2033+4118 in Galactic coordinates (from Hartman et al. 1999). The contours illustrate 50%, 68%, 95% and 99% statistical probability that a single source lies within the given contour. The plus signs indicate the positions of the three Cyg OB2 stars that display a non-thermal radio emission.

Let us consider the case of 3EG J2033+4118 a bit more in detail. This source lies at $l_{II} = 80.27°$ and $b_{II} = 0.73°$ and has a flux of $(7.3 \pm 0.7)\,10^{-7}$ photons cm^{-2} s^{-1} at energies above 100 MeV with a photon index of $\Gamma = 1.96 \pm 0.10$ (Hartman et al. 1999). Chen et al. (1996) studied the possible connection between this source and the Cyg OB2 association. Cyg X-3 lies just outside the error box of the source (see Fig. 5), but the γ-ray flux does not display the 4.8 hrs period of Cyg X-3 and it seems therefore more likely that it is associated with the Cyg OB2 stars. Assuming the source lies at the distance of Cyg OB2, it should have a luminosity of $2.4\,10^{35}$ erg s^{-1} in the EGRET energy range. It is extremely interesting that three Cyg OB2 stars displaying non-thermal radio emission fall into the 95% confidence contour (Fig. 5). These are Cyg OB2 #5 (see below), #8a (Waldron et al. 1998) and #9 (e.g. Phillips & Titus 1990).

Benaglia et al. (2001) studied the possible contribution of the triple system Cyg OB2 #5 to 3EG J2033+4118. The authors found that in-

verse Compton scattering of UV photons by relativistic electrons ($\gamma \sim 3\,10^3 - 4\,10^4$) accelerated in the wind interaction zone between the close binary and the nearby optical companion is likely to be the main contributor to the γ-ray emission of the system, accounting for a luminosity of $\sim 8\,10^{34}\,\mathrm{erg\,s^{-1}}$. π^0 decay of relativistic protons accelerated in the inner regions of the winds of the close binary (see Sect. 4) could contribute another $\sim 5\,10^{34}\,\mathrm{erg\,s^{-1}}$. Due to the lower cut-off energy ($\gamma \leq 10^3$), inverse Compton scattering in the close binary system probably does not play an important role in the γ-ray emission at EGRET energies, it might however contribute at lower energies (i.e. in the *INTEGRAL* energy range).

As another example, Benaglia & Romero (2003) investigate the relation between the 3EG J2022+4317 EGRET source and the colliding wind binary WR 140. The EGRET source has a flux of $(24.7\pm5.2)\,10^{-8}$ photons $\mathrm{cm^{-2}\,s^{-1}}$ and a photon index of $\Gamma = 2.31 \pm 0.19$. Assuming it lies at the distance of WR 140, this flux corresponds to a luminosity of $3.2\,10^{34}\,\mathrm{erg\,s^{-1}}$. WR 140 is the only high energy source in the vicinity of this EGRET source. Benaglia & Romero estimate total IC luminosities between 100 MeV and 20 GeV of about $2.1\,10^{34}\,\mathrm{erg\,s^{-1}}$. π^0 decay from relativistic protons interacting with the HI bubble found near WR 140 could provide an additional extended emission contributing to the EGRET detection.

3.3 Variability

Since the IC process in a colliding wind binary is anisotropic, variability of the γ-ray emission could arise from the fact that the emitted power per volume element is dependent on the scattering angle. As the two stars of the binary revolve around each other, the angle under which the interaction zone is seen changes, therefore leading to a modulation of the observable IC γ-ray emission. Mücke & Pohl (2002) first modelled this effect for a wide WR + O colliding wind system. Adopting the geometrical model of Eichler & Usov (1993) and assuming an injection particle spectrum $\propto \gamma^{-n}$, these authors demonstrate that the observed γ-ray flux could vary by an order of magnitude.

An additional variability of the IC radiation at γ-ray energies could result from the orbital modulation of the UV flux in the case of an eccentric colliding wind binary.

122

4. Other γ-ray emission mechanisms

Several other mechanisms related to early-type stars have been proposed to produce observable amounts of γ-ray emission.

White & Chen (1992) proposed that a small fraction of thermal ions could be accelerated through the first order Fermi mechanism to relativistic energies by the shocks embedded in the highly unstable radiatively driven winds. These relativistic ions interact with the thermal ions to produce γ-rays via π^0 decay with an energy peak around 67 MeV. These authors estimated that individual Cyg OB2 stars could be marginally detectable with EGRET, whilst the combined γ-rays from the Cyg OB2 cluster could be substantial. However, the number density of non-thermal ions (and therefore the production rate of γ-rays at its peak energy) depend strongly on the poorly constrained B_*. In fact, in this model, the high energy cut-off of the particle distribution is quite sensitive to the maximum particle mean free path ($\propto B^{-1}$).

Montmerle (1979) showed that about half of the unidentified COS B sources lie in regions harboring young objects such as SNRs and OB associations. In his scenario, high energy protons are injected by young stars into SNRs where they undergo Fermi acceleration up to relativistic energies. These relativistic protons subsequently interact with the protons in the parent molecular cloud of the OB association to produce a diffuse γ-ray emission through π^0 decay. Alternatively, Cassé & Paul (1980) argued that particles could be accelerated at the terminal shock of the stellar winds without the need of a SNR.

Manchanda et al. (1996) suggested that the combined winds of the stars in young open clusters interact with the gas in the cluster therefore creating a system of bow shocks at the interface between cluster members. At these shocks, protons could be accelerated to relativistic velocities and produce γ-ray emission through π^0 decay.

Finally, Pollock (1987b) proposed that γ-rays may also be produced through bremsstrahlung in the dense winds of WR stars.

5. Conclusions and future perspectives

Synchrotron radio emission observed from a subset of the early-type stars forms only the *tip of the non-thermal iceberg*. As outlined in this chapter, relativistic electrons most probably interact with the intense UV radiation field of these stars to generate a substantial inverse Compton radiation at X-ray and γ-ray energies. The latter radiation may be detectable with the *INTEGRAL* and *GLAST* observatories. In fact, Benaglia & Romero (2003) evaluated the expected γ-ray fluxes in the energy bands of these satellites for three colliding wind binaries (WR 140,

WR 146, WR 147). WR 140 and WR 147 were estimated to have fluxes of $8.3\,10^{-4}$ and $1.2\,10^{-3}$ photons cm^{-2} s^{-1} in the 15 keV – 10 MeV IBIS sensitivity range and $1.1\,10^{-6}$ and $9.4\,10^{-7}$ photons cm^{-2} s^{-1} in the 20 MeV – 300 GeV *GLAST* sensitivity range. For instance, according to the *INTEGRAL* Observing Time Estimator, WR 140 and WR 147 could be detected at the $3\,\sigma$ level in the 30 – 50 keV range within an exposure time of 15 ksec with the IBIS imager. With its unprecedented angular resolution, *INTEGRAL* is especially well suited to disentangle the IC emission from individual early-type stars in open clusters. Many new exciting results are therefore expected from the ongoing *Galactic Plane Survey* observing programme of the *INTEGRAL* satellite.

Finally, let us stress that the simultaneous observation of synchrotron radio emission and IC γ-ray emission of colliding wind binaries offers the exciting perspective of determining the magnetic field strength at the location of the wind interaction zone which can be related back to the surface field.

Notes

1. The radio spectral index is defined by $F_\nu \propto \nu^\alpha$.

2. Note however that high-energy γ-ray photons in the TeV energy range could most probably not escape the base of the stellar winds because they would interact with the stellar photons causing electron/positron pair production: $\gamma + \gamma \rightarrow e^+ + e^-$ (see Reimer 2003).

Acknowledgments

It is a pleasure to thank Professors G.E. Romero and K.S. Cheng for their invitation to contribute this chapter. I wish to express my gratitude to my colleagues from the Groupe d'Astrophysique des Hautes Energies in Liège and to Drs. R. Blomme (Brussels), A. Reimer (Bochum) and A. Pollock (ESA) for discussion. My thanks go also to the Fonds National de la Recherche Scientifique (Belgium) for multiple assistance. This research is also supported in part by contracts P4/05 and P5/36 "Pôle d'Attraction Interuniversitaire" (SSTC-Belgium) and through PRODEX grants linked to the ESA *XMM-Newton* and *INTEGRAL* missions.

References

Abbott, D.C., Bieging, J.H., & Churchwell, E.B. 1984, ApJ, 280, 671
Bell, A.R. 1978a, MNRAS, 182, 147
Bell, A.R. 1978b, MNRAS, 182, 443
Benaglia, P., Romero, G.E., Stevens, I.R., & Torres, D.F. 2001, A&A, 366, 605
Benaglia, P., & Romero, G.E. 2003, A&A, 399, 1121
Bieging, J.H., Abbott, D.C., & Churchwell, E.B. 1989, ApJ, 340, 518
Cassé, M., & Paul, J.A. 1980, ApJ, 237, 236

124

Chen, W., & White, R.L. 1991a, ApJ, 366, 512
Chen, W., & White, R.L. 1991b, ApJ, 381, L63
Chen, W., & White, R.L. 1994, Ap&SS, 221, 259
Chen, W., White, R.L., & Bertsch, D. 1996, A&AS, 120, 423
Cherepashchuk, A.M. 1976, Sov.Ast. Lett., 2, 138
Chlebowski, T., & Garmany, C.D. 1991, ApJ, 368, 241
Contreras, M.E., Rodríguez, L.F., Tapia, M., Cardini, D., Emanuele, A., Badiali, M., & Persí, P. 1997, ApJ, 488, L153
Corcoran, M.F. 1996, Rev. Mex. Astron. Astrof. Conf. Series, 5, 54
Corcoran, M.F., Waldron, W.L., MacFarlane, J.J., et al. 1994, ApJ, 436, L95
Cruz-González, C., Recillas-Cruz, E., Costero, R., & Peimbert, M. 1995, VizieR Online Data Catalog: III/84B, originally published in 1974, Rev. Mex. Astron. Astrof., 1, 211
Donati, J.-F., Wade, G.A., Babel, J., Henrichs, H.F., de Jong, J.A., & Harries, T.J. 2001, MNRAS, 326, 1265
Donati, J.-F., Babel, J., Harries, T.J., Howarth, I.D., Petit, P., & Semel, M. 2002, MNRAS, 333, 55
Dougherty, S.M., & Williams, P.M. 2000, MNRAS, 319, 1005
Dougherty, S.M., Pittard, J.M., Kasian, L., Coker, R.F., Williams, P.M., & Lloyd, H.M. 2003, A&A, 409, 217
Eichler, D., & Usov, V.V. 1993, ApJ, 402, 271
Garmany, C.D., & Massey, P. 1981, PASP, 93, 500
Gies, D.R., 1987, ApJS 64, 545
Gies, D.R., Hartkopf, W.I., Mason, B.D., Bagnuolo, W.G.Jr., ten Brummelaar, T., & McAlister, H.A. 1998, in *Boulder-Munich II: Properties of Hot Luminous Stars*, ed. I.D. Howarth, ASP Conf. Series, 131, 382
Ginzburg, V.L., & Syrovatskii, S.I. 1965, ARA&A, 3, 297
Gosset, E., Royer, P., Rauw, G., Manfroid, J., & Vreux, J.-M. 2001, MNRAS, 327, 435
Hartman, R.C., Bertsch, D.L., Bloom, S.D., et al. 1999, ApJS, 123, 79
Jardine, M., Allen, H.R., & Pollock, A.M.T. 1996, A&A, 314, 594
Lebedev, M.G., & Myasnikov, A.V. 1988, in *Numerical Methods in Aerodynamics*, eds. V.M. Paskonov & G.S. Roslyakov, Moscow State University Press, Moscow, 3
Leitherer, C., Forbes, D., Gilmore, A.C., et al. 1987, A&A, 185, 121
Leitherer, C., Chapman, J.M., & Koribalski, B. 1995, ApJ, 450, 289
Longair, M.S. 1992, *High Energy Astrophysics, Vol. 1: Particles, Photons and their Detection*, Cambridge University Press
Luo, D., McCray, R., & MacLow, M.-M. 1990, ApJ, 362, 267
Manchanda, R.K., Polcaro, V.F., Norci, L., et al. 1996, A&A, 305, 457
Mathys, G. 1999, in *Variable and Non-spherical Stellar Winds in Luminous Hot Stars*, eds. B. Wolf, O. Stahl, & A.W. Fullerton, Lecture Notes in Physics, 523, 95
Melrose, D., & Crouch, A. 1997, Publ. Astron. Soc. Aust., 14, 251
Miralles, M.P., Rodríguez, L.F., Tapia, M., Roth, M., Persí, P., Ferrari-Toniolo, M., & Curiel, S. 1994, A&A, 282, 547
Montmerle, T. 1979, ApJ, 231, 95
Mücke, A., & Pohl, M. 2002, in *Interacting Winds from Massive Stars*, eds. A.F.J. Moffat & N. St-Louis, ASP Conf. Series, 260, 355
Phillips, R.B., & Titus, M.A. 1990, ApJ, 359, L15
Pittard, J.M., & Stevens, I.R. 1997, MNRAS, 292, 298

Pittard, J.M., Stevens, I.R., Williams, P.M., Pollock, A.M.T., Skinner, S.L., Corcoran, M.F., & Moffat, A.F.J. 2002, A&A, 388, 335
Pollock, A.M.T. 1987a, ApJ, 320, 283
Pollock, A.M.T. 1987b, A&A, 171, 135
Prilutskii, O., & Usov., V. 1976, Sov.Ast.-AJ, 20, 2
Rauw, G., Vreux, J.-M., & Bohannan, B., 1999, ApJ, 517, 416
Rauw, G., Morrison, N.D., Vreux, J.-M., Gosset, E., & Mulliss, C.L. 2001, A&A, 366, 585
Rauw, G., Vreux, J.-M., Stevens, I.R., Gosset, E., Sana, H., Jamar, C., & Mason, K.O. 2002a, A&A, 388, 552
Rauw, G., Blomme, R., Waldron, W.L., et al. 2002b, A&A, 394, 993
Rauw, G., Vreux, J.-M., Antokhin, I.I., et al. 2003, in *New Visions of the X-ray Universe in the XMM-Newton and Chandra Era*, ed. F. Jansen, ESA SP-488, in press
Reed, B.C. 2000, AJ, 120, 314
Reimer, A. 2003, in *Proceedings of the 28th International Cosmic Ray Conference*, in press
Reynolds, S.P. 1982, ApJ, 256, 38
Romero, G.E., Benaglia, P., & Torres, D.F. 1999, A&A, 348, 868
Runacres, M.C., & Owocki, S.P. 2002, A&A, 381, 1015
Skinner, S.L., Zhekov, S.A., Güdel, M., & Schmutz, W. 2002, ApJ, 572, 477
Stevens, I.R., Blondin, J.M., & Pollock, A.M.T. 1992, ApJ, 386, 265
van der Hucht, K.A. 2001, New Astron. Reviews, 45, 135
Waldron, W.L., Corcoran, M.F., Drake, S.A., & Smale, A.P. 1998, ApJS, 118, 217
White, R.L. 1985, ApJ, 289, 698
White, R.L., & Becker, R.H. 1995, ApJ, 451, 352
White, R.L., & Chen, W. 1992, ApJ, 387, L81
Wiggs, M.S., & Gies, D.R. 1993, ApJ, 407, 252
Williams, P.M. 1996, in *Radio Emission from the Stars and the Sun*, eds. A.R. Taylor & J.M. Paredes, ASP Conf. Series, 93, 15
Williams, P.M. 2002 in *Interacting Winds from Massive Stars*, eds. A.F.J. Moffat & N. St-Louis, ASP Conf. Series, 260, 311
Williams, P.M., van der Hucht, K.A., Pollock, A.M.T., Florkowski, D.R., van der Woerd, H., & Wamsteker, W.M. 1990, MNRAS, 243, 662
Williams, P.M., van der Hucht, K.A., & Spoelstra, T.A.T. 1994, A&A, 291, 805
Williams, P.M., Dougherty, S.M., Davis, R.J., van der Hucht, K.A., Bode, M.F., & Setia Gunawan, D.Y.A. 1997, MNRAS, 289, 10
Willis, A.J., Schild, H., & Stevens, I.R. 1995, A&A, 298, 549
Wright, A.E., & Barlow, M.J. 1975, MNRAS, 170, 41

3.2 Recent modelling efforts

The subject of non-thermal processes in the winds of early-type stars has triggered quite some theoretical work over the last few years. Here, I briefly review the models that were published after the June 2004 Hong-Kong meeting. Some of the most sophisticated theoretical models for non-thermal phenomena in colliding wind binaries were presented by Pittard et al. (2006) and Pittard & Dougherty (2006).

Pittard et al. (2006) studied the effect of inverse Compton (IC) cooling on the population of relativistic electrons in a long-period binary system with an adiabatic wind interaction. Since particle acceleration is restricted to the vicinity of the shock front, IC cooling becomes increasingly important downstreams when the relativistic electrons flow away from the shock. Because of the $\propto \gamma^2$ dependence of IC cooling, where γ is the Lorentz factor of the electrons, this should lead to a position-dependent break in the power-law distribution of the electron energy. As a result those electrons with the highest values of γ should be confined near the shocks that bound the wind-wind collision zone. Hence, the synchrotron radio emission is expected to be brightest near the shock fronts and somewhat dimmer near the contact discontinuity.

Pittard & Dougherty (2006) studied the effects of modified shocks and the possibility of re-acceleration of non-thermal particles. Shock modification occurs as the result of the diffusion of the non-thermal particles upstream of the shock. In fact, these non-thermal particles exert a significant backpressure on the pre-shock flow which therefore decelerates, forming a smooth precursor ahead of the shock. The main consequence is a reduction of the velocity jump across the shock compared to a classical strong shock, thus also a reduction of the post-shock thermal temperature and a steeper particle energy distribution than for a classical shock (i.e. $n > 2$). In the re-acceleration scenario, on the other hand, particles are first accelerated in wind-embedded shocks before they undergo further acceleration at the shocks bounding the wind collision region. This mechanism produces a particle energy distribution flatter than for diffusive shock acceleration by a single strong shock (i.e. $n < 2$).

Pittard & Dougherty (2006) fitted a radio observation of WR 140 using their model and found that these observations suggest $n < 2$ which would require re-acceleration. However, models of the synchrotron radio emission including the Razin effect, inverse Compton scattering and relativistic bremsstrahlung are ill-constrained by the radio data alone. High-energy data provide clues on how to discriminate between the different models. Still, the current sensitivity and/or angular resolution of γ-ray observatories are not sufficient to derive actual measurements of the high-energy emission of colliding wind systems. For instance, using the IBIS instrument onboard *INTEGRAL*, only upper limits of the soft γ-ray flux could be inferred for most systems except perhaps for η Car + WR 25 and WR 115 (Leyder 2006).

Reimer et al. (2006) presented model calculations of γ-ray emission from long-period colliding wind binaries. They assume a simplified geometry (a cylindric slab) for the wind interaction region. In their model, they include synchrotron emission, inverse Compton scattering accounting for the Klein-Nishina effects, bremsstrahlung, Coulomb losses, particle diffusion out of the acceleration zone as well as γ-ray absorption due to pair production. They conclude that in most configurations, IC scattering should be the dominant emission mechanism, provided that the electron energy spectrum extends to energies beyond 10^4 MeV. Since the stellar photons enter the wind interaction zone from a preferred direction, the anisotropic nature of the IC scattering process must be taken into account. This then leads to predicted temporal variations of the flux level by several orders of magnitude even for colliding wind binaries with circular orbits. Again, in most cases, the predicted level of high-energy emission falls short of the actual sensitivity of current instrumentation.

Finally, it has to be stressed that colliding wind binaries could also produce an unusual radio emission of fully thermal origin. This effect was already pointed out by Stevens (1996) and is accounted for in the

models of Pittard et al. (2006). In fact, the hot and dense plasma in the wind interaction region produces an excess thermal radio emission. For an adiabatic wind collision with a unity wind momentum ratio, the radio emission could increase by about 50% compared to the sum of the emission of the individual stars if they were single. In a short period binary where radiative cooling is important, the effect could be even substantially larger. Some orbital variability is further expected as a result of the changing line-of-sight free-free optical depth. However, as shown by Pittard et al. (2006), while the spectral index of the observable radio emission might be less than the canonical $+0.6$ for thermal emission of a single massive star, it will not become negative. Therefore, the detection of a negative radio spectral index can only be attributed to genuine non-thermal emission mechanisms.

3.3 X-ray observations of non-thermal radio emitters

As outlined in Sect. 3.1, the interplay between the wealth of photospheric UV photons ($h\,\nu_* \geq 10\,\mathrm{eV}$) emitted by early-type stars and relativistic electrons could produce inverse Compton X-rays and γ-rays. In the Thomson regime, inverse Compton scattering produces radiation with an energy $h\,\nu_{IC} \sim \frac{4}{3}\,\gamma^2\,h\,\nu_*$. Lorentz factors of $\gamma \sim 10^2 - 10^4$ are thus sufficient to generate high-energy radiation in the energy range of observatories such as *INTEGRAL*, *EGRET* or *GLAST*. The critical question is whether or not the non-thermal high-energy fluxes are sufficiently high to be detectable with current instrumentation[1]. To test this idea in the X-ray domain at energies of order 5 – 10 keV, I have initiated an *XMM-Newton* observing campaign of several early-type stars known to display a synchrotron radio emission. The targets were 9 Sgr, HD 168112 and HD 167971 which were observed during AO1 (programme 882) and the stars of Cyg OB2 which were observed four times during AO3 (programme 20045). The results of these observations are reported below.

3.3.1 9 Sgr

The first target of this campaign that was observed with *XMM-Newton* was 9 Sgr. For the purpose of this project, observations were gathered in the X-ray, optical and radio domains and theoretical models of stellar winds for single and binary massive stars were considered. This project was conducted in tight collaboration with our colleagues from the hot star group of the Royal Observatory of Belgium in Uccle. The results are reported in the paper by Rauw et al. (2002c) reproduced below.

[1]It should be emphasized though that diffusive shock acceleration transfers more energy into non-thermal ions than into relativistic electrons. This implies that fluxes and spectral slopes of *EGRET* sources, which might preferentially reflect π^0-decay, cannot necessarily be extrapolated towards lower energies to estimate the flux in the energy domain of instruments such as IBIS onboard *INTEGRAL* where IC scattering should be the dominant process.

A&A 394, 993–1008 (2002)
DOI: 10.1051/0004-6361:20020926

Astronomy & Astrophysics

A multi-wavelength investigation of the non-thermal radio emitting O-star 9 Sgr⋆

G. Rauw[1,⋆⋆], R. Blomme[2], W. L. Waldron[3], M. F. Corcoran[4], J. M. Pittard[5], A. M. T. Pollock[6,7], M. C. Runacres[2], H. Sana[1,⋆⋆⋆], I. R. Stevens[8], and S. Van Loo[2]

[1] Institut d'Astrophysique, Université de Liège, Allée du 6 Août, Bât. B5c, 4000 Liège (Sart Tilman), Belgium
[2] Royal Observatory of Belgium, Avenue Circulaire 3, 1180 Brussels, Belgium
[3] L-3 Communications Analytics Corporation, 1801 McCormick Drive, Suite 170, Largo, MD 20774, USA
[4] USRA/HEASARC Goddard Space Flight Center, Greenbelt, MD 20771, USA
[5] Department of Physics & Astronomy, University of Leeds, Leeds LS2 9JT, UK
[6] Computer & Scientific Co. Ltd., 230 Graham Road, Sheffield S10 3GS, UK
[7] European Space Agency, Vilspa, Apartado 50727, 28080 Madrid, Spain
[8] School of Physics & Astronomy, University of Birmingham, Edgbaston Birmingham B15 2TT, UK

Received 21 May 2002 / Accepted 27 August 2002

Abstract. We report the results of a multi-wavelength investigation of the O4 V star 9 Sgr (= HD 164794). Our data include observations in the X-ray domain with *XMM-Newton*, in the radio domain with the VLA as well as optical spectroscopy. 9 Sgr is one of a few presumably single OB stars that display non-thermal radio emission. This phenomenon is attributed to synchrotron emission by relativistic electrons accelerated in strong hydrodynamic shocks in the stellar wind. Given the enormous supply of photospheric UV photons in the wind of 9 Sgr, inverse Compton scattering by these relativistic electrons is a priori expected to generate a non-thermal power law tail in the X-ray spectrum. Our EPIC and RGS spectra of 9 Sgr reveal a more complex situation than expected from this simple theoretical picture. While the bulk of the thermal X-ray emission from 9 Sgr arises most probably in a plasma at temperature $\sim 3 \times 10^6$ K distributed throughout the wind, the nature of the hard emission in the X-ray spectrum is less clear. Assuming a non-thermal origin, our best fitting model yields a photon index of ≥ 2.9 for the power law component which would imply a low compression ratio of ≤ 1.79 for the shocks responsible for the electron acceleration. However, the hard emission can also be explained by a thermal plasma at a temperature $\geq 2 \times 10^7$ K. Our VLA data indicate that the radio emission of 9 Sgr was clearly non-thermal at the time of the *XMM-Newton* observation. Again, we derive a low compression ratio (1.7) for the shocks that accelerate the electrons responsible for the synchrotron radio emission. Finally, our optical spectra reveal long-term radial velocity variations suggesting that 9 Sgr could be a long-period spectroscopic binary.

Key words. radiation mechanisms: non-thermal – stars: early-type – stars: individual: 9 Sgr – stars: winds, outflows – X-rays: stars

1. Introduction

X-ray emission from single early-type stars consists mainly of thermal emission from hot plasma at a few million Kelvin located within the stellar wind. Although the origin of the thermal X-rays is still not fully established, most of the current models focus on shock structures resulting from the line-driven instability as possible loci of the emitting plasma (see Feldmeier et al. 1997 and references therein).

However, the *EINSTEIN*-SSS spectra of three Orion belt stars, revealed X-ray fluxes above 2 keV that were apparently in excess of the thermal flux (Cassinelli & Swank 1983). This led Chen & White (1991, hereafter CW91) to propose that this hard X-ray emission might reflect a non-thermal X-ray component produced through inverse-Compton scattering.

The most prominent indication of non-thermal processes in stellar winds comes from the radio domain (e.g. Bieging et al. 1989). The bulk of the radio emission of luminous OB stars is attributed to thermal free-free radiation produced in the optically thick stellar winds of these objects. However, a subset of OB stars display an often variable non-thermal component on top of their free-free wind emission (see e.g.

Send offprint requests to: G. Rauw,
e-mail: rauw@astro.ulg.ac.be

⋆ Based on observations with XMM-Newton, an ESA Science Mission with instruments and contributions directly funded by ESA Member states and the USA (NASA). Also based on observations collected at the European Southern Observatory (La Silla, Chile) and with the Very Large Array. The VLA is a facility of the National Radio Astronomy Observatory which is operated by the Associated Universities Inc. under cooperative agreement with the National Science Foundation.

⋆⋆ Research Associate FNRS (Belgium).

⋆⋆⋆ Research Fellow FNRS (Belgium).

Williams 1996). In wide massive binaries, non-thermal radio emission is likely to arise in the region of stellar wind collision (Eichler & Usov 1993). In the case of single stars, the non-thermal component is believed to result from synchrotron radiation associated with a small population of relativistic electrons accelerated by Fermi processes in shocks located in the outer regions of the stellar wind (e.g. Chen & White 1994). Non-thermal radio emission, if due to synchrotron radiation, is consistent with surface magnetic fields of the order of a hundred Gauss (Chen & White 1994). However, synchrotron radio-emission is expected to account only for a small fraction of the total non-thermal energy budget. In fact, given the enormous supply of photospheric UV photons in the winds of OB stars, inverse-Compton scattering becomes the major energy loss mechanism for relativistic electrons and substantial levels of non-thermal X-ray and low energy γ-rays should be generated, resulting approximately in a power law spectrum from keV to MeV energies (CW91).

The non-thermal X-ray and radio emissions probably arise in distinct regions of the wind. Indeed, the optical depth to hard X-rays throughout the wind is small and inverse-Compton scattering is expected to be most efficient within a few stellar radii where the UV radiation density is highest. On the other hand, as a consequence of the large free-free optical depth at radio frequencies, radio synchrotron emission can only be observed from the outer regions of the wind (beyond about fifty stellar radii). The properties of the non-thermal emission at different energies thus reflect the radial distribution of the relativistic electron spectrum throughout the wind. Detailed models of this distribution rely on stellar parameters, most of which can be well determined from observations in the optical domain. The most noticeable exception in this respect is the stellar magnetic field B_*[1].

In this context, 9 Sgr (= HD 164794) appeared as a promising target to search for non-thermal X-ray emission. 9 Sgr was considered a probable single O4 V((f)) star by Garmany et al. (1980, but see also Sect. 6). Abbott et al. (1984) discovered non-thermal radio emission with a spectral index[2] of $\alpha = -0.8$. This non-thermal radio emission varies on ill-determined time scales (Bieging et al. 1989). 9 Sgr has been extensively studied at UV and visible wavelengths and has well determined wind properties. Table 1 lists the parameters adopted in our analysis. Note that the mass loss rate ($\dot{M} = 2.4 \times 10^{-6}\,M_\odot\,\mathrm{yr}^{-1}$) taken from Lamers & Leitherer (1993) was obtained from the Hα recombination line rather than from the radio flux which is dominated by the non-thermal emission. Finally, previous X-ray observations of 9 Sgr revealed that this is a relatively bright X-ray source (e.g. Berghöfer et al. 1996).

To search for hard non-thermal X-ray emission in the spectrum of 9 Sgr, we obtained a 20 ksec observation of this target with the *XMM-Newton* observatory. Simultaneously, 9 Sgr was observed at radio wavelengths with the Very Large Array (VLA). A preliminary analysis of the data from this campaign was presented by Rauw et al. (2002). In Sect. 2 of the present paper, we introduce the data from our multi-wavelength campaign including radio, optical and X-ray observations. Sections 3 and 4 deal with the RGS and EPIC spectra of 9 Sgr while the radio and optical data are analysed in Sects. 5 and 6 respectively. Finally, we discuss the overall picture of 9 Sgr that emerges from our campaign and present our conclusions in Sect. 7.

Table 1. Relevant model parameters for 9 Sgr adopted in this paper. The numbers are taken from Conti & Ebbets (1977, CE), Bohannan et al. (1990, BVHA), Lamers & Leitherer (1993, LL) and Shull & van Steenberg (1985, SvS).

Parameter		Ref.
$v_{\rm rot}\ \sin i\,(\mathrm{km\,s^{-1}})$	128	CE[a]
$T_{\rm eff}$ (K)	43 000	BVHA
$R_*\,(R_\odot)$	16	BVHA
$\log L_{\rm bol}\,(\mathrm{erg\,s^{-1}})$	39.49	BVHA
d (kpc)	1.58	BVHA
$v_\infty\,(\mathrm{km\,s^{-1}})$	2950	LL
$\dot{M}\,(M_\odot\,\mathrm{yr}^{-1})$	2.4×10^{-6}	LL
$\log N_{\rm H,ISM}\,(\mathrm{cm}^{-2})$	21.34	SvS

[a] Note that Penny (1996) derived a somewhat lower $v_{\rm rot}\ \sin i$ of $102\,\mathrm{km\,s^{-2}}$, but this does not alter any of our conclusions in the following.

2. Observations

2.1. X-ray data

9 Sgr was observed with *XMM-Newton* (Jansen et al. 2001) during revolution 228 on March 8, 2001 (JD 2451976.978–2451977.239). The two EPIC MOS instruments were operated in the full frame mode (Turner et al. 2001) whilst the EPIC-pn camera was used in the extended full frame mode (Strüder et al. 2001). All three EPIC instruments used the thick filter to reject optical light. The two RGS instruments were operated in the default spectroscopy mode (den Herder et al. 2001).

We used version 5.1 of the *XMM-Newton* Science Analysis System (SAS) to reduce the raw EPIC data. For the MOS (resp. pn) observations only events with pattern 0–12 (resp. 0) were considered (Turner et al. 2001). No indication of pile-up was apparent in the data.

The RGS observations were processed with version 5.0.1 of the SAS. Appropriate response matrices were generated using the "rgsrmfgen" SAS task.

The EPIC data are significantly affected by straylight photons from the LMXB GX 9 +1 (= Sgr X-3) located at 1° from the center of the FOV. For the pn detector the straylight features appear as arcs that are not exactly concentric due to the slight imperfections of the mirror module alignment. On the MOS images the arcs are truncated because of the Reflection Grating Assemblies (RGAs) which are mounted on the mirror modules associated with the MOS instruments. In addition, the

[1] So far, magnetic fields have only been detected for a few early-type OB stars (~360 G in β Cep and ~1100 G in θ^1 Ori C see Donati et al. 2001, 2002). For most OB stars, the non-detection of the Zeeman effect puts an upper limit of order ~100 G on B_* (Mathys 1999).

[2] The radio spectral index α is defined by $F_\nu \propto \nu^\alpha$. Purely thermal sources have $\alpha \simeq 0.6$ (Wright & Barlow 1975).

Table 2. Effective exposure times and background corrected count rates of 9 Sgr as measured with the instruments onboard *XMM* (see the text for details on the source and background extraction). The count rates for the EPIC instruments are given in the energy range 0.2–10 keV.

	MOS1	MOS2	pn	RGS1	RGS2
Exp. (s)	21 880	21 881	17 474	23 100	23 100
Rate (cts s^{-1})	0.269 ± 0.004	0.280 ± 0.004	0.819 ± 0.007	$(3.61 \pm 0.39) \times 10^{-2}$	$(5.16 \pm 0.51) \times 10^{-2}$

straylight arcs in the MOS images display some extended tails. The intensity of these tails decreases with increasing angular distance from GX 9 +1 (see Fig. 1).

The straylight is produced by photons that are singly reflected by the mirror hyperbolas. Although the straylight collecting area is only a few square centimeters (Stockman et al. 1998), the brightness of GX 9 +1 compared to the sources in our field of view leads to a serious contamination of our data. The straylight photons are rather hard. In fact, images extracted in the soft energy range PI $\in$]200, 1500[($\sim E \in$]0.2, 1.5[keV) reveal a negligible contamination level (see Fig. 2).

Because of the complex reflection pattern, one can expect the spectrum of the straylight features to be distorted compared to the actual spectrum of GX 9 +1. Schulz (1999) fitted the ROSAT spectrum of GX 9 +1 using a blackbody model with $N_{\rm H} = 1.36 \times 10^{22}$ cm^{-2} and $kT = 0.98 \pm 0.06$ keV. The spectrum of the brightest straylight arc in the MOS1 detector is shown in the left panel of Fig. 2. Generally speaking, the best fitting spectral parameters depend slightly on the instrument and on the location of the straylight feature considered. In all the cases the straylight spectrum is best fitted by a heavily absorbed blackbody model with $N_{\rm H}$ in the range 2.05×10^{22} (MOS2) – 3.46×10^{22} cm^{-2} (pn) and with a temperature kT between 0.99 (pn) and 1.21 keV (MOS2).

2.2. Radio data

We observed 9 Sgr with the NRAO Very Large Array (VLA) simultaneously (JD 2451977.012–.037) with the *XMM-Newton* observations. Data were collected at 3.6 cm (*X*-band), 6 cm (*C*-band) and 20 cm (*L*-band). At each wavelength, we observed the flux calibrator 3C 286 = 1331+305 (J2000). The observation on 9 Sgr took 8 min for each wavelength, and was preceded and followed by an observation of the phase calibrator 1751-253 (J2000). All observations were made in two sidebands (denoted IF1 and IF2), each of which has a bandwidth of 50 MHz. The VLA was in the B configuration, with the antenna at position N 32 missing.

The data reduction was done using the Astronomical Image Processing System (AIPS, version 31DEC01), developed by the NRAO. From the observed visibilities of the calibrators, the instrumental gains are determined and discrepant points flagged. The gains are interpolated in time and applied to the 9 Sgr visibilities. Applying the Fourier transform to these calibrated visibilities turns them into an intensity map (called the dirty map). The weighting scheme used is robust uniform (Briggs 1995). The images are then deconvolved to remove the effect of the beam, using the CLEAN algorithm as implemented in AIPS (Cornwell & Braun 1989). In the reduction procedure we applied the available baseline corrections. The fluxes assigned to the flux calibrator are given in Table 3.

Table 3. Fluxes of the flux calibrator 3C 286. The fluxes are based on the 1995.2 VLA coefficients (Perley & Taylor 1999). The two values for each entry correspond to the two 50 MHz sidebands (IF1 and IF2).

λ (cm)	Frequency (GHz)	Flux (Jy)
3.6	8.4351	5.2158
	8.4851	5.1947
6	4.8351	7.5100
	4.8851	7.4620
20	1.3851	14.9031
	1.4649	14.5108

The major problem in the reduction of our VLA data is the presence of other, high-intensity, sources in the field. First of all, 9 Sgr is just in front of the Lagoon Nebula (M 8), which appears as a spatially extended source with a high radio flux. Due to the filtering properties of a radio-interferometer, a large part of this flux will not be seen by the instrument. While observations made in the VLA A-configuration show almost no residual background from M 8, our observations (made in the B-configuration) do show some M 8 flux. As the spatial resolution decreases with wavelength, this effect is worst at 20 cm. Secondly, there are strong compact sources in the field (associated with the Hourglass H II region). The sidelobes of these sources can be seen on the dirty map to extend beyond the position of 9 Sgr. At 20 cm, sidelobes from TXS 1801-245 are also important.

To eliminate the effect of the M 8 nebula, we dropped all observational data taken on the shortest baselines (using the keyword `uvrange` in the AIPS task "imagr"). To eliminate the sidelobes of the Hourglass and TXS 1801-245 we made sure that these sources were included in the field on which the cleaning algorithm was applied.

2.3. Optical data

A set of echelle spectra of 9 Sgr was gathered with the Fiber-fed Extended Range Optical Spectrograph (FEROS, Kaufer et al. 1999) attached to the ESO 1.52 m telescope at La Silla, during two observing runs in May 2000 and 2001. Typical exposure times were of the order of five minutes. The spectral resolving power of the FEROS instrument is 48 000. The detector was an EEV CCD with 2048 $\times$ 4096 pixels of 15 μm $\times$ 15 μm. For a detailed description of the spectrograph, we refer to the paper of Kaufer et al. (1999). We used a slightly modified version of the FEROS context within the MIDAS package provided by ESO to reduce the data.

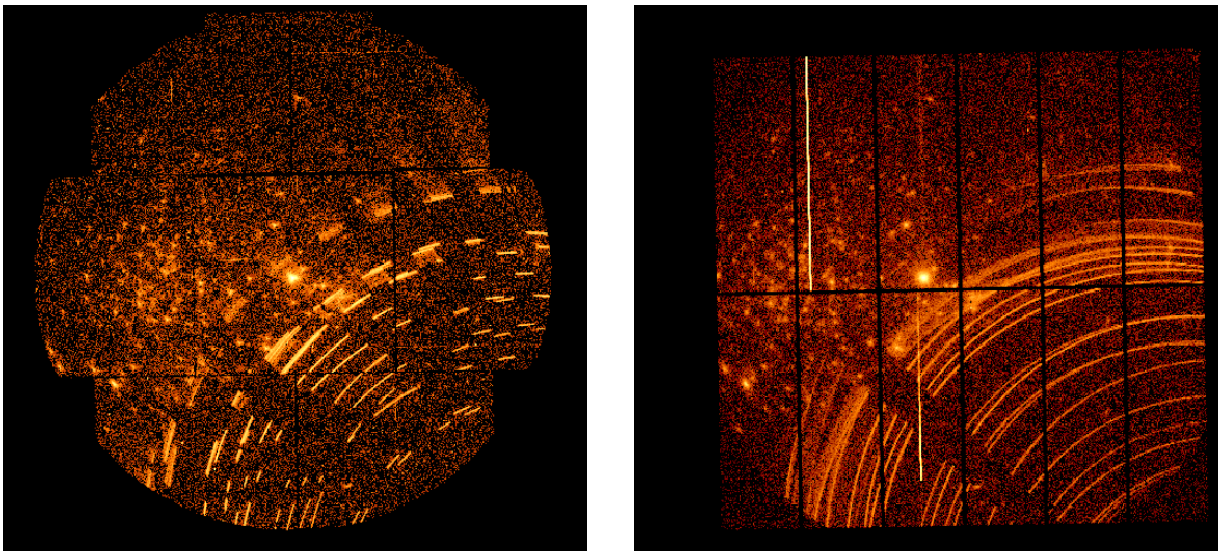

Fig. 1. EPIC MOS2 (left panel) and EPIC-pn (right panel) broad-band images around 9 Sgr. The images are displayed with a logarithmic scale.

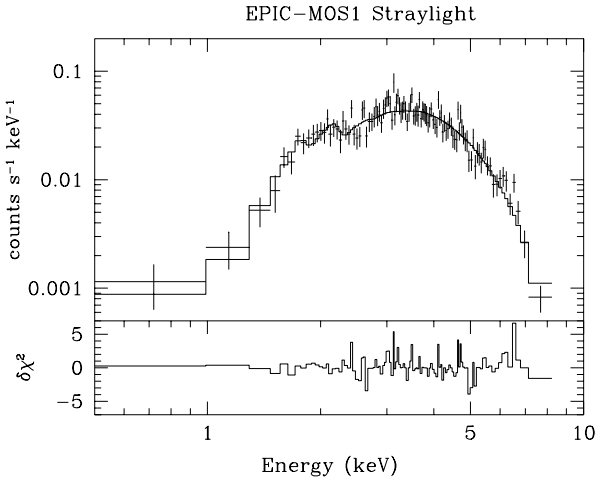

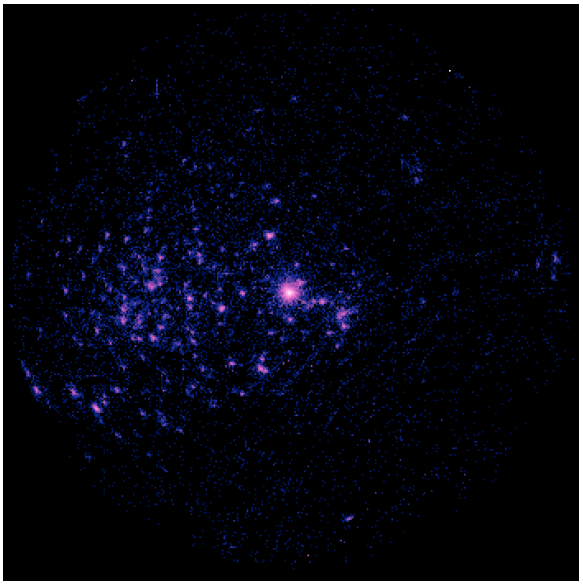

Fig. 2. Left panel: spectrum of the brightest straylight feature in the EPIC-MOS1 image. The energy distribution can be fitted with a heavily absorbed ($N_{\rm H} = (3.1 \pm 0.3) \times 10^{22}$ cm^{-2}) blackbody model of temperature $kT = 1.04 \pm 0.05$ keV. Right panel: combined EPIC MOS1 + MOS2 image extracted over the PI range from 200 to 1500. The image is displayed with a logarithmic scale. The faint sources near 9 Sgr are associated with the young open cluster NGC 6530 inside the Lagoon Nebula. These sources are discussed in a separate paper.

3. The RGS spectrum of 9 Sgr

At first glance, the RGS spectrum of 9 Sgr is reminiscent of that of the O4 Ief star ζ Pup (Kahn et al. 2001) and of the *Chandra*-HETG spectrum of ζ Ori (O9.7 Ib, Waldron & Cassinelli 2001). We observe the He-like triplets of Ne IX and O VII, the Lyα lines of Ne X, O VIII and N VII as well as several L-shell lines of Fe XVII. One difference between ζ Pup and 9 Sgr concerns the relative strength of the nitrogen and oxygen lines: while in ζ Pup, the N/O ratio is enhanced with respect to solar abundances, we find no indication of such an effect in 9 Sgr.

Given the limited S/N of our RGS spectra, little can be said about the detailed morphology of the emission lines. However, we fitted the emission line profiles with Gaussians to determine the line fluxes and centroids (Table 4). The continuum strength was determined from fluxes on each side of the line. We caution that unresolved blends of weak emission lines could mimic a pseudo-continuum that would affect the net line intensities. In this case, our fitted line intensities should provide lower limits to the actual line fluxes.

Table 4. Fluxes and centroid shifts of the most prominent emission lines in the spectrum of 9 Sgr.

	Flux (photons cm^{-2} s^{-1})	Velocity shift ($km\,s^{-1}$)
Ne x λ 12.13	$(3.5 \pm 1.6) \times 10^{-5}$	-660 ± 290
Fe xvii $\lambda\lambda$ 16.78–17.10	$(8.1 \pm 2.0) \times 10^{-5}$	-730 ± 280
O viii λ 18.97	$(8.2 \pm 1.5) \times 10^{-5}$	-540 ± 230
N vii λ 24.78	$(4.1 \pm 1.7) \times 10^{-5}$	-60 ± 600

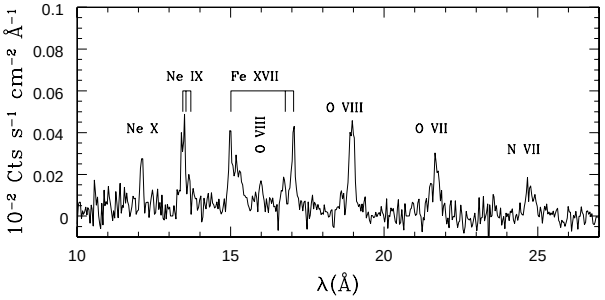

Fig. 3. Combined RGS1+2 first order spectrum of 9 Sgr.

The lines are broad with half widths at half maximum in the range 500–1600 $km\,s^{-1}$. Our data reveal a slight blue-shift of the line centroids in all strong lines. The blue-shift is expected for lines formed in an accelerating stellar wind since radiation from the approaching side of the wind should be less attenuated by continuum opacity than that from the receding part (Owocki & Cohen 2001).

Grating spectra obtained with *XMM-Newton* and *Chandra* have provided new insight into the X-ray properties of hot early-type stars. For instance, the He-like resonance (r), intercombination (i) and forbidden (f) lines have been used to infer the location of the X-ray emitting material within the stellar wind (see e.g. Waldron & Cassinelli 2001). In the presence of a strong ultraviolet radiation field, as in the atmospheres of early-type stars, the transition $2\,^3S \rightarrow 2\,^3P$ is essentially excited by the UV radiation. Hence the ratio $\mathcal{R} = f/i$ is no longer determined by the density of the plasma but rather by the intensity of the UV radiation (e.g. Porquet et al. 2001).

In the case of 9 Sgr, the f component is clearly detected in the Ne ix triplet whilst it is not detected for O vii (Table 5). The non-detection of the O vii f line leaves us with an upper limit of 0.2 on the corresponding $\mathcal{R}$ ratio.

We compared the observed $\mathcal{R}$ ratio of Ne ix with the theoretical values of Porquet et al. (2001) corresponding to radiation temperatures[3] of 30 000 and 40 000 K and an electron temperature of 3×10^6 K (consistent with the temperature inferred from our EPIC spectra of 9 Sgr, Tables 6–8). This comparison suggests that the Ne ix line forms at rather low values of the dilution factor $w = 0.5\,(1 - \sqrt{1 - R_*/r}) \sim 0.01$ and thus far out in the wind (probably beyond several R_*).

We used the formalism outlined by Waldron & Cassinelli (2001) to further constrain the location of the line emitting plasma. The predicted radial dependence of the $\mathcal{R}$ ratios for various ions in the wind of 9 Sgr was computed including the effects of collisions and radiative transitions, accounting for the photospheric UV flux at $T_{\rm eff} = 43\,000$ K. The results are shown in Fig. 4. The observed 90% confidence range of $\mathcal{R}$ for the Ne ix

[3] Torres (1987) showed that the UV energy distribution of 9 Sgr can be matched with model atmospheres corresponding to temperatures of 35 000 and 40 000 K. A radiation temperature of 30 000 K thus probably yields a lower limit to the actual temperature.

Table 5. Line intensity ratios of the He-like fir triplets in the RGS spectra of 9 Sgr. The error bars correspond to the 90% confidence ranges as determined from our fits.

	Ne ix	O vii
f/i	0.31 ± 0.27	<0.2
r/i	0.74 ± 0.43	0.37 ± 0.33

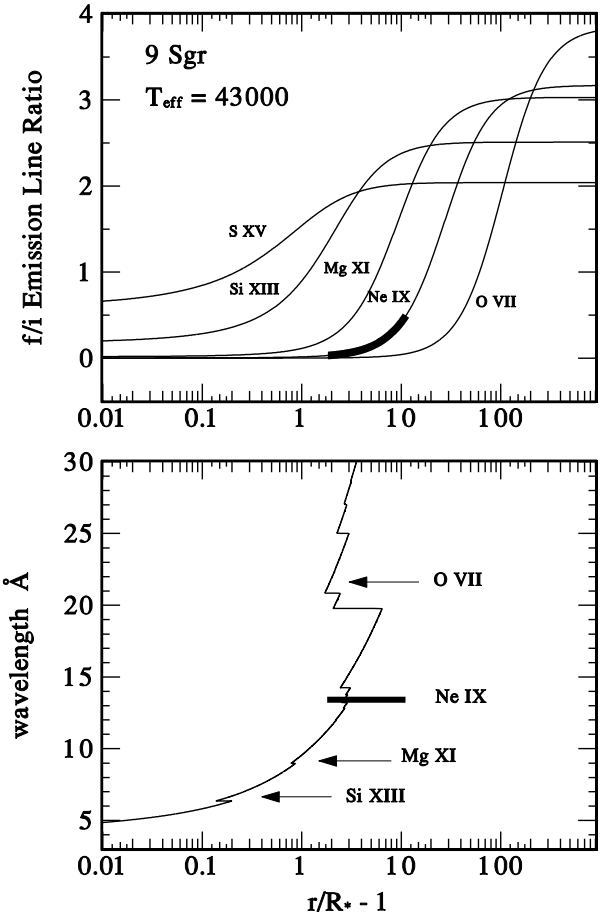

Fig. 4. Upper panel: predicted dependence of the $\mathcal{R} = f/i$ ratio for helium-like triplets of various ions in the stellar wind of 9 Sgr. The heavy solid line indicates the 90% confidence range on $\mathcal{R}$ for the Ne ix triplet. Lower panel: radius of radial optical depth unity as a function of wavelength. The wavelengths of various helium-like triplets are indicated and the probable location of the Ne ix line formation region (corresponding to the uncertainty range on the $\mathcal{R}$ ratio) is indicated by the heavy line.

triplet is displayed by the heavy line. The results of our analysis suggest that the Ne IX line forms somewhere between 3 and 11 R_*.

At radii below ~50 R_*, the $\mathcal{R}$ ratio of O VII varies very slowly as a function of radius (Fig. 4). Hence, the upper limit of $\mathcal{R} < 0.2$ is consistent with the oxygen triad forming anywhere between the stellar surface and about 25 R_*.

A word of caution is necessary though: in addition to the Ne IX triplet, the spectral range 13.3 to 13.8 Å harbors a huge number of iron lines from various ionization stages: Fe XVIII – XXI. Most of these lines have maximum emissivities that are more than a factor ten lower than those of the Ne IX lines (see e.g. the line list of the SPEX plasma code at `http://www.sron.nl/divisions/hea/index.html`, Kaastra et al. 2002). Although the EPIC spectra suggest a multi-temperature plasma that could give rise to a rather broad range of ionization stages, the RGS data only reveal strong iron lines corresponding to Fe XVII. Blends with lines from Fe XX and Fe XXI probably do not have a significant impact on the neon triplet since other iron lines of these species that are expected to be strong are either absent or only marginally detected. The strongest contamination could arise from the Fe XIX lines at 13.51 and 13.52 Å that are blended with the Ne IX intercombination line and have maximum emissivities exceeding that of the *i* line. Conversely, the 13.73–13.74 Å lines of the Fe XIX ion affect the Ne IX *f* line but these lines have maximum emissivities that are about a factor ten lower than those of the lines at 13.51 and 13.52 Å. In any case, the lack of a significant Fe XIX emission at 14.67 and 16.11 Å suggests that the effect of this ion on the Ne IX $\mathcal{R}$ ratio should be pretty low.

The bottom panel of Fig. 4 displays the radius of continuum optical depth unity in the stellar wind of 9 Sgr as a function of wavelength. The circumstellar opacity was computed using the wind absorption model of Waldron et al. (1998) adopting the parameters from Table 1 and assuming a homogeneous and spherically symmetric wind. As can be seen from this figure, the bulk of the Ne line emission arises from outside the radius of radial optical depth unity. This result is quite similar to the situation for other O-stars (see e.g. in ζ Pup, Kahn et al. 2001; Cassinelli et al. 2001; ζ Ori, Waldron & Cassinelli 2001).

Let us briefly return to the blue-shift of the lines seen in Table 4. Within the large error bars, it is hard to uncover any trend (e.g. between the velocity shift and the ionization potential of the specific ions): all velocity shifts are roughly consistent with the same value. Our results from the *fir* analysis above suggest that the bulk of the line emission will have to come from radii beyond $\tau = 1$ (though not too far outwards because of the dependence of the line emission measure on the square of the density). From Fig. 4, it appears that $\tau = 1$ occurs between ~3 and 7 R_* for the four lines listed in Table 4. However, there appears no correlation between the velocity shift and $R(\tau = 1)$ neither. For instance, the N VII and Ne X lines correspond roughly to the same $R(\tau = 1) \in [3, 4]\,R_*$ but have different velocity shifts, although their error bars do overlap.

4. The EPIC spectrum of 9 Sgr

The contamination of the EPIC data by the straylight considerably complicates the extraction of the spectrum of 9 Sgr and of the background. The worst situation is probably encountered for the MOS1 camera.

For all three EPIC cameras, the source spectrum was accumulated over a radius of 45″ excluding the intersection with a small circular region centered on a faint point-like source at RA = 18 : 03 : 50 and DEC = −24 : 21 : 10 (Equinox 2000.0). For the pn detector, the extraction region was further truncated to avoid the gap between the CCDs. Let us recall that the straylight is essentially concentrated in the arcs except for the extended tails in the MOS images described in Sect. 2.1. Figure 5 reveals that the source spectrum of 9 Sgr should be free from any contamination at least in the MOS2 and pn data. However, a low level contamination of the MOS1 source spectrum of 9 Sgr cannot be fully excluded.

The background spectra for the different data sets were obtained over rectangular areas trying to avoid the straylight features (see Fig. 5). We have also tested a different background subtraction technique using the blank sky event lists provided by the *XMM*-SOC. The resulting background subtracted spectra of 9 Sgr do not show any significant differences compared to those obtained with the technique described hereabove.

We adopted the redistribution matrices (rmfs) provided by the EPIC instrument teams (versions available in May 2001) and we used the SAS to build the appropriate ancillary response file (arf) for each EPIC instrument. The spectra were binned to reach a minimum of 10 counts per channel and the background corrected spectra were analyzed using the XSPEC software (version 11.00). Because of the strong noise in the pn detector below 0.2 keV and the calibration uncertainties of the EPIC instruments at low energies, we ignored the binned energy channels below 0.2 keV for the XSPEC fits.

4.1. Fitting simple models

We tested a couple of rather simple models. In these fits, we always fixed the interstellar H I column density at 0.22×10^{22} cm^{-2}. The latter value was adopted from the work of Shull & van Steenberg (1985). These authors evaluated the neutral hydrogen column density towards 9 Sgr using high-resolution *IUE* observations of the interstellar Lyα line. Their result, $N_{\rm H,ISM} = (0.22 \pm 0.03) \times 10^{22}$ cm^{-2}, is in fair agreement with the observed $E(B-V)$ colour excess of 9 Sgr assuming a "normal" gas to dust ratio and the results of a similar study by Diplas & Savage (1994) who determined $N_{\rm H,ISM} = (0.19^{+0.04}_{-0.02}) \times 10^{22}$ cm^{-2}. As a first approximation, we modelled the circumstellar (i.e. wind) absorption using neutral ISM opacities[4].

The background-corrected EPIC spectra of 9 Sgr display a break around ~2.5 keV with extra emission above it. Absorbed single-temperature `mekal` models for optically thin plasmas (Mewe et al. 1985; Kaastra 1992) hence do not provide

[4] This is a crude approximation. Below we use a proper model to simulate the wind absorption.

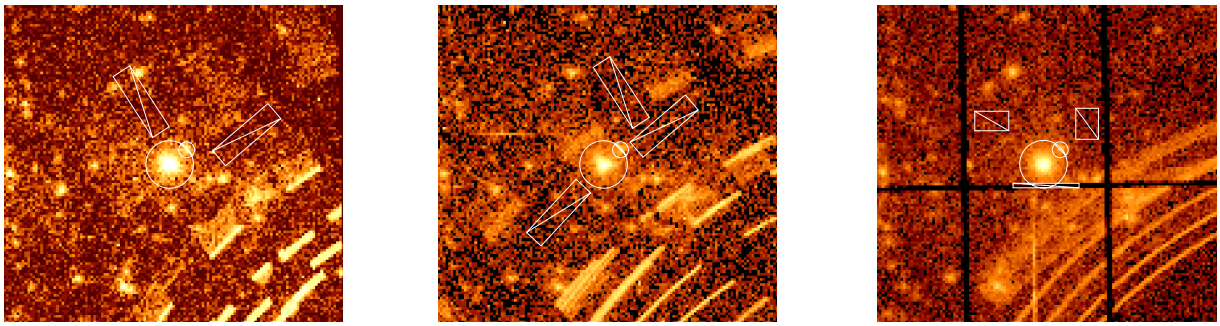

Fig. 5. Zoom on the source and background regions for the three EPIC instruments. From left to right, the images correspond to the MOS1, MOS2 and pn data. Note that the images are displayed with a logarithmic scale. The small circular region around the faint point source to the NW of 9 Sgr was excluded from the source region.

acceptable fits for any of the instruments. Two temperature `mekal` models still yield a reduced $\chi^2_\nu > 2$ except for the pn spectrum ($\chi^2_\nu = 1.49$). The best fit temperatures are about 0.23 and ~0.6 keV for all three instruments. It should be noted that the best-fit column density of the softest `mekal` component is always zero. This is most probably a consequence of the poor representation of the wind absorption by the neutral ISM opacities.

The quality of the fits improves for 1-T `mekal + power law` models (χ^2_ν between 1.31 and 1.79). However, these fits systematically yield photon indices ($\Gamma \geq 3.8$) much larger than the value (~1.5) expected from the Chen & White (1991) model. One reason for this steep power law could be that the thermal plasma model underestimates the observed flux at energies below 0.5 keV and the power law has to provide some flux to compensate this. One should also note that the column density of the power law component is again very close to or equal to zero.

Note that requiring a value of $\Gamma = 1.5$ in the 1-T `mekal + power law` models yields an unacceptably large $\chi^2_\nu \simeq 2$ for all EPIC spectra. We have also tested 2-T `mekal + power law` models. Again requiring $\Gamma = 1.5$, we obtain $\chi^2_\nu = 1.64$ for a simultaneous fit of the EPIC + RGS data set with two temperatures of 0.22 and 0.59 keV. Allowing the photon index to deviate from 1.5, a better fit ($\chi^2_\nu = 1.34$) is achieved for $\Gamma = 3.9$, $kT_1 = 0.18$ and $kT_2 = 0.51$ keV.

To simulate a possible contamination of the EPIC spectra of 9 Sgr by the straylight, we have also tested models where we included an absorbed blackbody with a column density between 2.0 and 3.5×10^{22} cm^{-2} and a temperature in the range 0.99–1.21 keV. Including a straylight component in the fits does not improve their quality and does not alter the best fitting parameters of the `mekal` and/or power law components.

Including the RGS spectra in the fits allows to better constrain the lower energy components of the model. However, since our RGS data do not reveal any feature longwards of ~27 Å (either because of the interstellar + circumstellar absorption or because of the intrinsic lack of lines in the source spectrum at these wavelengths), they cannot help constrain the contribution of the power law component to the flux at low energies ($E < 0.5$ keV).

Since there could be some uncertainties on the EPIC calibration at lower energies, we have also repeated the spectral fitting ignoring all the energy channels below 0.5 keV. The best fitting `mekal + power law` model turns out to be rather insensitive to these energy channels and we recover the same parameters as above.

Finally, we have also fitted 1-T `mekal + broken power law` models. For the broken power law models, we adopted

$$\eta = \eta(E_0) \qquad \text{for } E \leq E_0$$
$$\eta = \eta(E_0)\,(E/E_0)^{-\Gamma+1} \qquad \text{for } E > E_0$$

where η stands for the spectral emissivity and Γ corresponds to the photon index of the power law above the low energy cut-off E_0. Due to various cooling processes and the interaction with thermal electrons, one expects the energy spectrum of relativistic electrons in stellar winds to possess a low energy cut-off. CW91 argue that for O-star winds, this cut-off should translate into an inverse Compton low energy cut-off of order 0.2 keV. However, the exact value depends on a number of stellar parameters and we can therefore not rule out the existence of a low energy cut-off in the inverse Compton power law spectrum within the energy range covered by our EPIC spectra.

We fitted the EPIC data setting E_0 to 0.5, 1.0 or 2.0 keV. By requiring a flat spectrum below E_0, we strongly limit the contribution of the non-thermal component to the flux at low energies. For $E_0 = 0.5$ keV, we obtain a good fit ($\chi^2_\nu = 1.26$ for the pn data set) with $\Gamma \simeq 4.0$ while the parameters of the thermal component remain unchanged. For increasing values of E_0, the value of Γ increases while the quality of the fit decreases.

4.2. Using a wind absorption model

To solve the problems due to the poor modelling of the circumstellar opacity, we have used a wind absorption model (Waldron et al. 1998) computed with the parameters from Table 1. The EPIC spectra of 9 Sgr are fitted with models accounting for the absorption by the ionized wind in addition to the neutral ISM material (the latter corresponds to a fixed column density of 0.22×10^{22} cm^{-2}). The fits are obtained by varying the temperature (or power law index), the wind column density and the emission measure.

We started by testing 2-T `mekal` models including the effects of wind opacity. The results are listed in Table 6 below. The inclusion of the wind absorption cross section significantly improves the quality of the fits at energies below 0.5 keV. However, above 2 keV the model still underestimates the observed energy distribution.

We subsequently fitted the EPIC-pn spectrum of 9 Sgr with a 1-T `mekal + broken power law` model. The results are listed in Table 7. We note that the overall quality of the fits is quite comparable to that of the 2-T fits. However, while the power law models fit the high energy tail, the 2-T models yield a better fit to the Si XIII lines at ∼1.86 keV. Again, we note that Γ depends on the value of the low energy cut-off. However, the values of $\Gamma \geq 2.9$ obtained here are lower than those obtained with the models that assume a neutral absorption column. The inclusion of a proper wind absorption column allows to fit the low energy part of the spectrum by the sole contribution of the thermal component, while this was not the case for the models in Sect. 4.1. Therefore in the current fits, the power law component is far less sensitive to the low energy part of the spectrum than in the fits of Sect. 4.1.

Finally, we note that the EPIC-pn spectrum suggests the presence of an Fe Kα line, although this feature is not seen in the MOS spectra and its existence needs thus to be confirmed by other observations. The possible presence of an Fe Kα line suggests that the hard X-ray continuum could be thermal. These considerations prompted us to fit the EPIC spectra of 9 Sgr with 3-T thermal models. The derived best fit parameters are roughly equal for all three instruments. The third, high temperature, component is however not well constrained. In Fig. 6, we used $kT_3 = 8.6$ keV and $N_{\rm wind,3} = 4.5 \times 10^{22}$ cm^{-2} (corresponding to the maximum wind column density for 9 Sgr). These values provide the best fit, but from a statistical point of view, the fit is not much different from that corresponding to the lower limit values of Table 8.

In summary, we find that, provided the wind absorption is properly treated, the EPIC spectra of 9 Sgr can be fitted equally well either by a multi-temperature thermal model including plasma at a temperature exceeding $\sim 2 \times 10^7$ K, or by a model including a non-thermal power law component with a photon index $\Gamma \geq 2.9$.

5. Simultaneous VLA radio observations

We used the AIPS task "jmfit" to measure the flux on the cleaned radio maps by fitting an elliptical Gaussian to the source. The Gaussian has the same shape as the cleaned beam, so the position and total flux are the only parameters fitted. A comparison between the peak intensity and the flux resulting from the fit shows that 9 Sgr is indeed a point source. Each flux determination is given an error bar equal to the rms in the field.

However, the major source of error in the fluxes is not the statistical noise in the map, but rather the uncertainty in the background subtraction. Various combinations of `uvrange` and depth of cleaning (see Sect. 2.2) give cleaned maps that are acceptably smooth, showing that all background and sidelobe effects have been removed (see Fig. 7). Rather than using a single combination of `uvrange` and depth of cleaning to determine the flux, we opted to look at the whole range spanned by all acceptable combinations. In doing so we did not clean deeper than was necessary for a given `uvrange` (cleaning too deep can easily lower the flux by 1 σ). The resulting fluxes (see Table 9) are then determined by taking the average of the highest and the lowest value of the range. We added to the highest value its rms, and we subtracted from the lowest value its rms. The resulting error bar is given by the range between the average and lowest/highest value. The error bars are sufficiently large that we consider them to include the 1–5% calibration error.

To judge the robustness of our flux determination, we repeated the reduction, tapering the weights of longer baselines, or using natural weighting instead of robust uniform weighting. As almost all results fall within the error bar, we conclude that the error bars we derived correctly reflect the accuracy of the result.

The spectral indices (α) are given in Table 9, as well as the error bars which were derived from the theory of propagation of errors. For a thermal spectrum due to free-free radiation in the wind, one expects $\alpha \simeq +0.6$ (e.g. Wright & Barlow 1975). The 9 Sgr spectral indices are negative, clearly indicating the non-thermal character of the radio emission.

The radio flux of 9 Sgr is known to be variable (Bieging et al. 1989). Our 6 cm flux is high compared to previous values, but the error bar still overlaps the range covered by values in the literature (see Table 9). Our value for 20 cm seems higher than the Bieging et al. ones (3.6–3.9 mJy): however, when we re-reduce their dataset, we tend to derive higher fluxes than they did. As far as we know, no 3.6 cm fluxes have been published. We did have a look at some of the 3.6 cm observations in the VLA archive. The present observation falls within the range of the archive data, but is again in the very upper part of that range.

5.1. A simple model

In this section we attempt to fit the VLA observations of 9 Sgr with a simple theoretical model. As pointed out in the introduction, the non-thermal radio emission is believed to be synchrotron radiation from relativistic electrons (White 1985). In the presence of shocks and of a magnetic field, electrons are accelerated to high energies (Bell 1978) through the first-order Fermi mechanism (Fermi 1949), resulting in a power law distribution for the momentum p of the accelerated particles. The radio flux originating from a distribution $N(p, r)$ of relativistic electrons, can be expressed as

$$F_\nu = \frac{1}{4\pi D^2} \int_{R_\nu}^{R_{\rm max}} {\rm d}r\, 4\pi r^2 \int_{p_0}^{\infty} {\rm d}p\, N(p, r)\, P_\nu(B(r), p) \qquad (1)$$

where P_ν is the emissivity for a single relativistic electron (Rybicki & Lightman 1979), integrated over solid angle, $B(r)$ the magnetic field at radius r and D the distance to the star. For the lower momentum cut-off of the power law, we took $p_0 = 1$ MeV/c (CW91). $B(r)$ is related to the surface field B_* through

$$B(r) = B_* \frac{v_{\rm rot}}{v_\infty} \frac{R_*}{r}. \qquad (2)$$

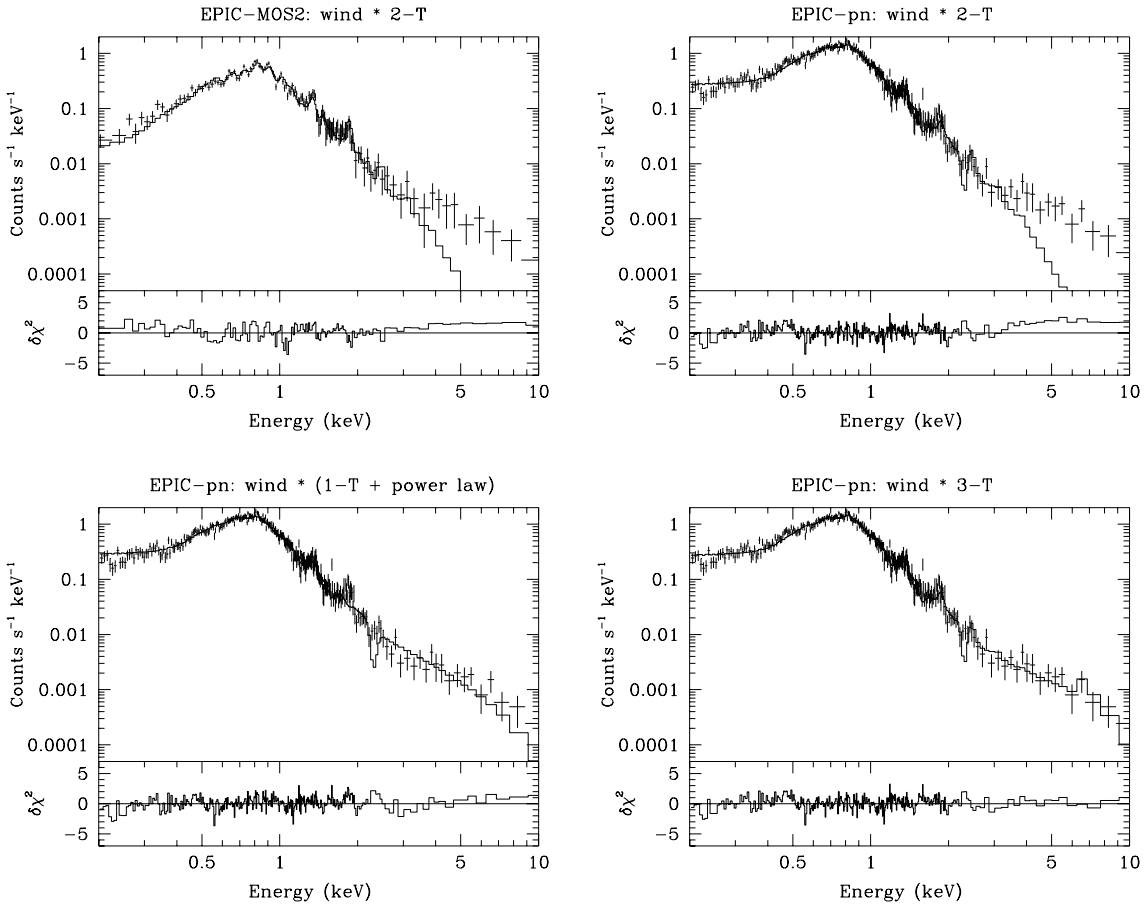

Fig. 6. The EPIC spectrum of 9 Sgr together with different best-fitting models. The different panels illustrate the best fitting 2-T thermal model with realistic wind absorption cross sections for the MOS2 (upper left panel) and the pn (upper right panel), the 1-T + broken power law model together with a wind absorption model (lower left panel) and the 3-T thermal model with wind absorption (lower right panel).

Table 6. Best fitting parameters of the 2-T thermal model fits with a wind opacity model ($\texttt{wabs}_{\rm ISM}$*($\texttt{wabs}_{\rm wind,1}$*$\texttt{mekal}_1$ + $\texttt{wabs}_{\rm wind,2}$*$\texttt{mekal}_2$)). A fixed interstellar column density of 0.22×10^{22} cm^{-2} has been applied to the model. The metallicity was fixed at solar. EM is the emission measure defined by $EM = \int_V n_{\rm e}\, n_{\rm H}\, {\rm d}V$ where $n_{\rm e}$ and $n_{\rm H}$ stand respectively for the electron and proton density in the X-ray emitting plasma. The observed spectral flux measured at Earth at energy E is then given by $f(E) = \frac{1}{4\pi D^2}\,\eta(E,T)\,EM$, where $\eta(E,T)$ stands for the emissivity as a function of temperature and energy. $f_{\rm X}$ yields the observed (i.e. absorbed) flux integrated over the energy band 0.2–10.0 keV (in units 10^{-12} erg cm^{-2} s^{-1}). The number of degrees of freedom is provided between brackets in Col. 8.

Inst.	$N_{\rm wind,1}$ (10^{22} cm^{-2})	kT_1 (keV)	log EM_1 (cm^{-3})	$N_{\rm wind,2}$ (10^{22} cm^{-2})	kT_2 (keV)	log EM_2 (cm^{-3})	χ^2_ν	$f_{\rm X}$
MOS1	0.34 ± 0.16	0.26 ± 0.01	56.22	1.10 ± 0.71	0.78 ± 0.17	55.47	1.86 (122)	1.64
MOS2	0.29 ± 0.14	0.25 ± 0.01	56.19	0.97 ± 0.63	0.71 ± 0.15	55.56	1.44 (124)	1.71
pn	0.28 ± 0.09	0.26 ± 0.01	56.20	1.64 ± 0.62	0.69 ± 0.27	55.79	1.19 (316)	1.84

Table 7. Same as Table 6, but for the best fitting parameters of 1-T `mekal + broken power law` fits to the EPIC-pn spectrum of 9 Sgr. Γ stands for the photon index of the power law above the low energy cut-off E_0 (below E_0 the photon index is equal to 1), while K yields the normalization factor of the broken power law (in photons s^{-1} cm^{-2} keV^{-1} at 1 keV).

E_0 (keV)	$N_{\rm H,1}$ (10^{22} cm^{-2})	kT (keV)	log EM (cm^{-3})	$N_{\rm H,2}$ (10^{22} cm^{-2})	Γ	K	χ^2_ν	$f_{\rm X}$
0.5	0.28 ± 0.09	0.26 ± 0.01	56.16	<0.9	2.92 ± 0.59	7.11×10^{-4}	1.14 (316)	1.84
1.0	0.28 ± 0.09	0.26 ± 0.01	56.19	<1.3	3.40 ± 0.80	8.17×10^{-4}	1.14 (316)	1.83
2.0	0.28 ± 0.09	0.26 ± 0.01	56.20	<2.0	4.33 ± 2.18	2.18×10^{-4}	1.26 (316)	1.81

Table 8. Best fitting parameters of 3-T thermal model fit with a wind opacity model ($\texttt{wabs}_{\rm ISM}$*($\texttt{wabs}_{\rm wind,1}$*$\texttt{mekal}_1$ + $\texttt{wabs}_{\rm wind,2}$*$\texttt{mekal}_2$ + $\texttt{wabs}_{\rm wind,3}$*$\texttt{mekal}_3$)). A fixed interstellar column density of 0.22×10^{22} cm^{-2} has been applied to the model. The metallicity was fixed at solar.

Inst.	$N_{\rm wind,1}$ (10^{22} cm^{-2})	kT_1 (keV)	log EM_1 (cm^{-3})	$N_{\rm wind,2}$ (10^{22} cm^{-2})	kT_2 (keV)	log EM_2 (cm^{-3})	$N_{\rm wind,3}$ (10^{22} cm^{-2})	kT_3 (keV)	log EM_3 (cm^{-3})	χ^2_ν
M1	0.34 ± 0.16	0.26 ± 0.01	56.22	1.06 ± 0.68	0.71 ± 0.15	55.48	>0.63	>1.46	54.71	1.70 (118)
M2	0.29 ± 0.14	0.25 ± 0.01	56.23	0.86 ± 0.56	0.73 ± 0.16	55.52	>0.63	>1.46	54.71	1.33 (120)
pn	0.28 ± 0.09	0.26 ± 0.01	56.22	1.65 ± 0.62	0.67 ± 0.26	55.83	>0.63	>1.46	54.68	1.08 (312)

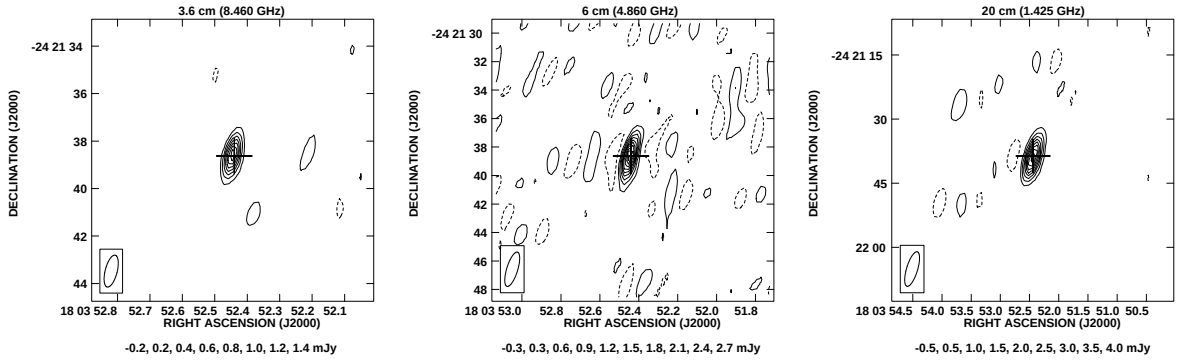

Fig. 7. Maps of 9 Sgr at 3.6, 6 and 20 cm (from left to right). Below each map the contour levels are listed. The negative contour is indicated by the dashed line. The crosses indicate the optical position (ICRS 2000.0) from the Simbad database. The beamsizes are $1.4'' \times 0.5''$ (position angle = 166°) at 3.6 cm, $2.5'' \times 0.8''$ (PA = 163°) at 6 cm and $8.4'' \times 2.6''$ (PA = 163°) at 20 cm. Note the different spatial scale for each of the maps.

This expression, adopted from Weber & Davis (1967), is valid only at large distances from the star ($r \geq 10\,R_*$), which covers the region where the synchrotron radiation is emitted. We follow White (1985) in assuming $v_{\rm rot} = 250\,{\rm km\,s^{-1}}$. This value is plausible, as $v_{\rm rot}\,\sin i = 128\,{\rm km\,s^{-1}}$ (see Table 1). Free-free absorption in the wind is taken into account by setting the lower spatial boundary to the effective radius R_ν of the radio emission (Wright & Barlow 1975).

Besides the power law in momentum space (with exponent n), we also assume a power law (with exponent δ) for the spatial dependence of the distribution:

$$N(p,r) = f_*\, n_{\rm e}^*\,(n-1)\left(\frac{p_0}{m_{\rm e}c}\right)^{n-1}\left(\frac{r}{R_*}\right)^{-\delta} p^{-n} \qquad (3)$$

where f_* and $n_{\rm e}^*$ are the fraction of relativistic electrons and the total electron number density at the stellar surface.

Equation (1) is to be integrated numerically. We take into account the Razin effect, due to the presence of a background plasma (Razin 1960). This effect causes synchrotron radiation to be suppressed at higher wavelengths.

5.2. Fitting the observations

We adopt the stellar parameters listed in Table 1. For the surface magnetic field we assume a value of $B_* = 100$ Gauss (Chen & White 1994). In Fig. 8 we present a model that fits our observations. We set $\delta = 1$, and then adapted n, f_* and $R_{\rm max}$, which gives $n = 5.5$, $R_{\rm max} = 160\,R_*$ and $f_* = 4.5 \times 10^{-3}$. Of these parameters $R_{\rm max}$ appears to be the most critical. As expressed in Eq. (1), $R_{\rm max}$ sets the outer boundary of the synchrotron emission region. It has been shown by CW91 that, due to the efficiency of Compton cooling, relativistic electrons cannot carry much of their energy out of the region where they are accelerated. Thus $R_{\rm max}$ can be interpreted as the position of the terminal shock. The index n is determined by the compression ratio χ of the shock: $n = (\chi+2)/(\chi-1)$. A value of $n = 5.5$ corresponds to weak shocks with a compression ratio of about 1.7.

Table 9. A comparison of our radio flux determination with values from the literature (Florkowski et al. 1985; Bieging et al. 1989). Our error bars are dominated by the uncertainty in the background correction. The spectral indices derived from our data are also listed.

λ (cm)	Literature range flux (mJy)	Our data flux (mJy)	Spectral index
3.6		1.6 ± 0.4	
6	1.0(±0.4) – 2.5(±0.3)	2.8 ± 0.4	−1.1 ± 0.6
20	3.6(±0.3) – 3.9(±0.4)	4.5 ± 1.2	−0.4 ± 0.3

Given the large number of parameters fitting a limited number of observations, the solution is not unique. For instance, a model with $\delta = 0.4$, $n = 4.5$, $R_{\rm max} = 165\,R_*$ and $f_* = 8.9 \times 10^{-6}$ fits the observations equally well.

At this stage, it is worth pointing out that $R_{\rm max}$ is substantially larger than the radius of the formation region of the Ne IX and O VII triplets. Although the VLA data tell us that the shocks that produce radio emission exist out to large distances, these shocks do not contribute a significant fraction of the thermal X-rays. Since the emission measure of the X-ray line emission

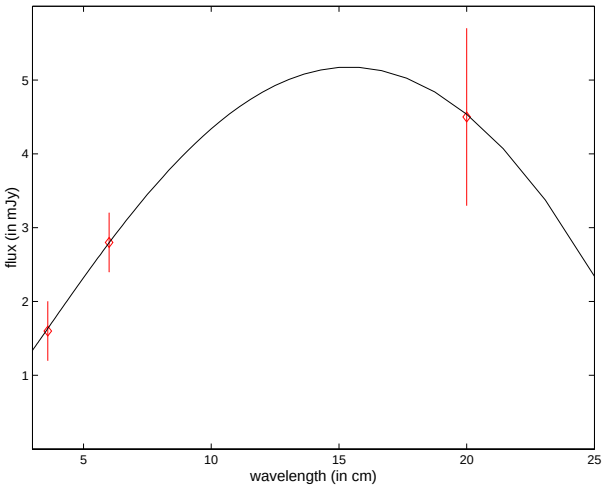

Fig. 8. Theoretical synchrotron radiation calculated with parameters $\delta = 1$, $n = 5.5$, $R_{\max} = 160\,R_*$ and $f_* = 4.5 \times 10^{-3}$. The observations are displayed as open diamonds.

scales with the square of the density, the observed X-ray emission is dominated by the densest regions that lie outside the optical depth unity surface. The density in the outer shocks is obviously too low to compete with the emission from the shocks further in.

6. The optical spectrum

The optical spectrum of 9 Sgr displays a wealth of absorption lines from H I, He I, He II as well as from some metal ions (e.g. O III, C IV, N III, N IV, N V, ...). There are also a few narrow emission lines: N III $\lambda\lambda$ 4634–41, C III λ 5696 and Si IV λ 4116.

The equivalent width ratio of the He I λ 4471 and He II λ 4542 absorption lines ($W' = EW(4471)/EW(4542) = 0.19$) yields an O4 spectral type, while the strength of the He II λ 4686 absorption ($EW = 0.75$ Å) suggests a main-sequence luminosity class. These classifications are in agreement with results published in the literature (e.g. Mathys 1988). The presence of Si IV in emission in addition to the N III emissions and He II λ 4686 absorption indicates an O4 V ((f^+)) classification (see Walborn et al. 2002). The lack of any line at Si IV λ 4089 is usually interpreted as the λ 4089 absorption and emission canceling each other (see Walborn 2001).

We found no significant line profile variability in our spectra of 9 Sgr. This is in agreement with the conclusions of Fullerton (1990) and Fullerton et al. (1996), who did not detect profile variability in the C IV λ 5801 and He I λ 5876 lines.

Garmany et al. (1980) investigated the multiplicity of 9 Sgr from a set of eleven photographic spectra with a dispersion of 16.9 Å mm^{-1}. They concluded that 9 Sgr is probably single and that the variations of about 30 km s^{-1} they detected arise most likely in the atmosphere of the star.

We have measured the radial velocities (*RV*s) of the strongest absorption lines in our spectra of 9 Sgr. We then averaged the *RV*s of nine of them (He II $\lambda\lambda$ 4200, 4542, 4686, 5412; He I $\lambda\lambda$ 4471, 5876; C IV $\lambda\lambda$ 5801, 5812 and O III λ 5592). The results listed in Table 10 do not reveal any significant *RV* changes. The mean *RV* averaged over the entire data set amounts to 15.1 ± 1.3 km s^{-1}. None of the individual lines displays a $1\,\sigma RV$ dispersion over our data set exceeding 3.8 km s^{-1}. We conclude therefore that our data are consistent with a constant *RV* in May 2000 and 2001.

However, our mean *RV*s of the C IV λ 5801 ($\overline{RV} = 23.2 \pm 2.5$ km s^{-1}), C IV λ 5812 ($\overline{RV} = 15.9 \pm 2.5$ km s^{-1}) and He I λ 5876 ($\overline{RV} = 12.7 \pm 1.9$ km s^{-1}) lines are about 42 km s^{-1} more positive than the values quoted by Fullerton (1990) and Fullerton et al. (1996)[5]. The data of Fullerton et al. were collected over seven consecutive nights in June 1986 with a spectral resolving power of ~25 000 and their 1σ dispersions on the mean *RV* of individual lines are comparable to our values. Therefore, although the time scale of the *RV* variations of 9 Sgr is certainly poorly constrained, we conclude that *RV* variations probably occur on time scales of several months or most probably several years.

Both datasets (i.e. Fullerton's and ours) rule out *RV* variations on time-scales of a few days and probably up to several weeks. This is in stark contrast with the results of Garmany et al. (1980) who reported variations of 20 km s^{-1} within two days that they ascribed to the stellar wind. Given the low amplitude of the *RV* variations, only high-quality, high-resolution spectroscopic data are suited to probe the binarity of 9 Sgr and a long-term monitoring of this star is clearly required to unveil *RV* variations such as those occuring over relatively short time intervals around periastron passage in highly eccentric binaries.

Fullerton (1990) already suspected 9 Sgr to be a spectroscopic binary and pointed out that the mean profiles of both the C IV and He I absorptions were asymmetric, displaying a prominent extension towards their red wing (see his Fig. A133). We do not observe such an asymmetry in our data. The lack of this feature in our data could indicate that we are indeed seeing a long-period double-lined spectroscopic binary which was near conjunction in May 2000 and 2001, whereas it was near quadrature in June 1986.

7. Discussion

Let us start by summarizing the most important results of our multi-wavelength investigation of 9 Sgr. The present VLA data show that at the time of the *XMM-Newton* observation, the radio emission of 9 Sgr was definitely non-thermal and the level of emission was in the high end of the range hitherto observed for this star. Our EPIC spectra reveal a hard X-ray component that can be fitted equally well by a multi-temperature thermal model including some plasma at $kT \geq 1.46$ keV or by a rather steep power law ($\Gamma \geq 2.9$) component. Our RGS spectra of 9 Sgr seem consistent with the overall picture of X-ray emission due to shocks distributed throughout the stellar wind. Finally, our optical spectra indicate no *RV* variations on time

[5] We can safely rule out that the velocity shift could be caused by wavelength calibration uncertainties. Indeed, our mean *RV* of the interstellar Na I λ 5890 line (-12.3 ± 0.2 km s^{-1}) is in good agreement with the mean of Fullerton's (1990) data (-13.4 ± 0.2 km s^{-1}).

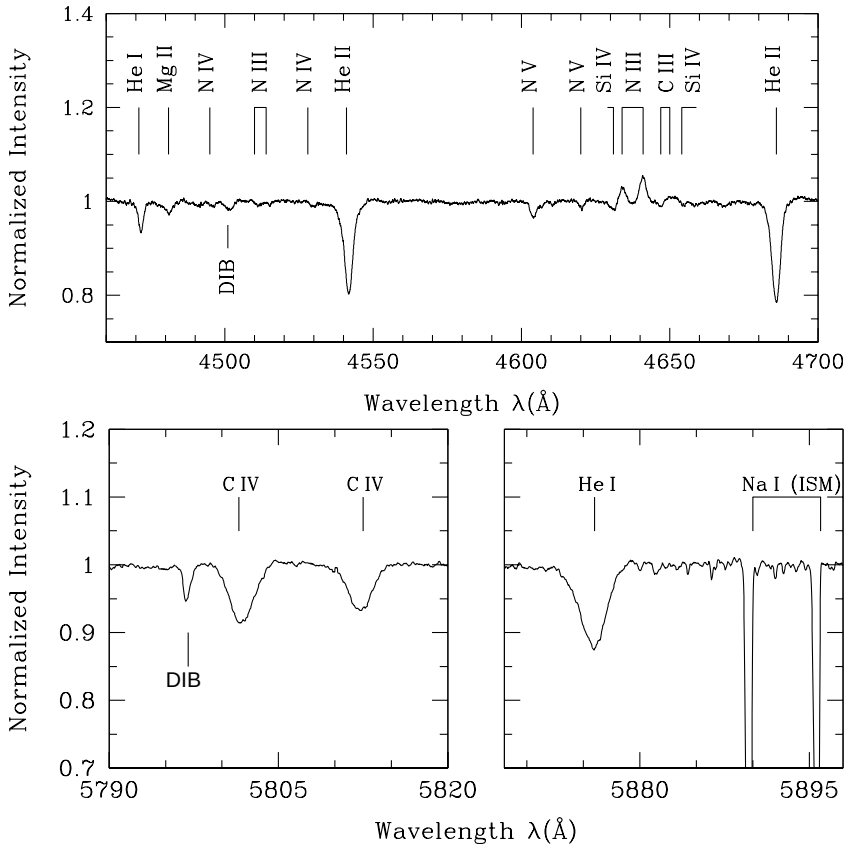

Fig. 9. Upper panel: FEROS spectrum of 9 Sgr in the blue wavelength range. Lower panel: average FEROS spectrum of 9 Sgr around the C IV $\lambda\lambda$ 5801, 5812 lines and the He I λ 5876 line. Contrary to what happened in the data of Fullerton (1990), there is no outstanding asymmetry in the red wing of these line profiles.

scales of weeks but reveal a significant *RV* change compared to data taken fifteen years before.

7.1. Long term variability of the X-ray flux of 9 Sgr?

First, we briefly consider the issue of long term variability of the X-ray emission of 9 Sgr. 9 Sgr was observed at three occasions with the PSPC instrument onboard the *ROSAT* satellite. The observations took place between 1991 and 1993. We have extracted these observations from the archive and analysed them using the XSELECT software. The counts of 9 Sgr were extracted within a radius of 36″ and the background was evaluated over an annulus around the source region. The background corrected count rates are provided in Table 11. These data do not provide evidence for strong variability of the X-ray flux. Note also that converting the best fitting parameters of the 1-T `mekal + power law` model discussed hereabove into theoretical *ROSAT*-PSPC count rates yields 0.157 cts s^{-1}. Given the different sensitivities of the PSPC, EPIC and RGS instruments, this value is in pretty good agreement with the observed count rates. We conclude that the available data provide no indication of a strong variability of the soft X-ray flux of 9 Sgr.

Table 10. Radial velocities of 9 Sgr as measured on our FEROS data.

Date HJD − 2 450 000	$\overline{RV}$ (km s^{-1})
1669.718	14.9
1670.703	17.6
1671.710	15.5
1672.691	15.8
2037.731	14.6
2039.934	13.6
2040.694	14.1

7.2. What is the distribution of relativistic electrons in the wind of 9 Sgr?

According to Bell (1978), a hydrodynamic shock with a compression ratio χ produces a population of relativistic electrons with energies following a power law distribution of index $n = (\chi+2)/(\chi-1)$. When these electrons undergo inverse Compton scattering, they produce a power law spectrum of photon index

Table 11. *ROSAT*-PSPC count rates of 9 Sgr as obtained from three pointings of the star.

Sequence number	Duration (s)	Date	PSPC rate (cts s^{-1})
rp200194n00	1638	17 Mar. 1991	.173 ± .012
rp201261n00	4500	4 Oct. 1992	.164 ± .006
rp900374n00	10 432	1 Apr. 1993	.160 ± .004

$\Gamma = (n+1)/2$ (CW91). In their model, CW91 consider a distribution of relativistic electrons with $n = 2$ (i.e. $\chi = 4$) resulting in a power law spectrum with photon index $\Gamma = 1.5$. Using the parameters from Table 1 and Eq. (33) from CW91, we would expect a flux of $\sim 10^{-5}\eta/B_*$ photons s^{-1} cm^{-2} at 1 keV, where η stands for the ratio of the electron acceleration efficiency to that of ions. This spectral shape is clearly at odds with our X-ray observations of 9 Sgr.

Our data provide the tightest constraints on the properties of a hard X-ray power law tail in an O-star so far. We note that the *EINSTEIN*-SSS observations of the Orion Belt stars that motivated the work of CW91 may have been affected by calibration issues involving the formation of ice on the entrance window of this instrument. Indeed, subsequent *ASCA* observations of δ Ori failed to confirm the existence of a hard power law tail in its X-ray spectrum (Corcoran et al. 1994).

Assuming that the $\Gamma \geq 2.9$ power law component in our spectral fits is indeed due to inverse Compton scattering by a population of relativistic electrons, we find that $n \geq 4.8$ and thus $\chi \leq 1.79$ are implied. It is interesting to note that our VLA data also suggest a low compression ratio of $\chi \simeq 1.7$. The latter ratios are much smaller than the strong shock value $\chi = 4$ used by CW91. Let us emphasize that the shocks responsible for the acceleration of the electrons that produce the synchrotron radio emission must be located at rather large radii. In fact, the surfaces of radial optical depth unity lie at 36, 53 and 125 R_* for emission at 3.6, 6 and 20 cm respectively (assuming a homogeneous, spherically symmetric, wind). On the other hand, hard X-rays can arise from very close to the stellar surface and it would thus not be too surprising to have different compression ratios for the different energy domains.

Our results suggest that if the hard X-ray emission in the spectrum of 9 Sgr is indeed due to a non-thermal phenomenon, then the acceleration of relativistic electrons in the atmosphere of this star cannot be described by the model of Chen & White (1991). The theory of CW91 is based on a number of assumptions on the shock properties which may need to be revised. The elaboration of such a model is beyond the scope of the present paper and we defer this work to a future paper.

At this stage, let us stress that the compression ratios we infer from the X-ray and radio data should be seen as typical or average values. Rather than having one definite compression ratio, the shocks in the wind are likely to have a distribution of compression ratios, as is also suggested by hydrodynamical models (e.g. Feldmeier et al. 1997). In this regard, it is natural that the values we find are lower than the maximum value of $\chi = 4$.

7.3. Is 9 Sgr a binary system?

Assuming instead that the high energy spectrum of 9 Sgr is of thermal origin, a possible explanation to account for the strong non-thermal radio emission and the lack of non-thermal X-rays is to imagine that the radio emission arises from electrons accelerated in a shock region far away from the photosphere of the O4 star where inverse Compton scattering would be less efficient. This could be the case if 9 Sgr were a binary system. As pointed out above, our data hint at a variation of the RV of 9 Sgr over time scales of months or probably years.

Abbott et al. (1984) suggested that non-thermal radio emission might arise from accretion onto an undetected compact companion in a so-called *X-ray quiet* binary system. However, as pointed out by these authors, the extreme youth of 9 Sgr (age ~1.5 Myr, Sung et al. 2000) argues against this hypothesis. In fact, even extremely massive stars of 120 $M_\odot$ would not have the time to complete their evolution and end up as a compact object within 1.5 Myr (e.g. Maeder & Meynet 1994). However, 9 Sgr may be a post mass-exchange binary, in which the present-day primary was rejuvenated through mass accretion and mimics a younger age. This possibility cannot be fully discarded although one would probably expect some peculiar abundances in the photosphere of the star. The analysis of Bohannan et al. (1990) did not reveal evidence for such peculiar abundances.

Another mechanism to produce non-thermal radio emission in a binary system relies on the colliding wind scenario (Eichler & Usov 1993). Dougherty & Williams (2000) showed that seven out of nine non-thermal radio emitting Wolf-Rayet (WR) stars are visual or spectroscopic binaries. Therefore, these authors argue that most, if not all, of the Wolf-Rayet stars that display non-thermal radio emission could be colliding wind binaries. Could 9 Sgr be a colliding wind binary system then? Let us point out that the X-ray luminosity of 9 Sgr $L_X \simeq 1.4 \times 10^{33}$ erg s^{-1} (corrected for an interstellar column of 0.22×10^{22} cm^{-2} and assuming $d = 1.58$ kpc) is not exceptional for a star of this bolometric luminosity (e.g. Berghöfer et al. 1997). The ratio $\log(L_X/L_{bol}) = -6.35$ reveals no outstanding excess attributable to a wind interaction. In order to produce such a modest X-ray luminosity, a colliding wind binary would need to be either very wide (shocked winds adiabatic, see e.g. Pittard & Stevens 1997) or very close (winds collide before they accelerate to large velocities). The latter case can be ruled out because the wind collision region (and hence the electron acceleration site) would be located deep inside the opaque radio photosphere making it very difficult to observe any non-thermal radio emission. Also we would expect to observe substantial *RV* changes on time scales of a few days or weeks, unless the orbital inclination would be almost zero degrees. The possible long-term *RV* variations that we have uncovered suggest that this is not the case. Therefore, it seems more likely that 9 Sgr is a wide long-period spectroscopic binary.

If the asymmetry in the C IV and He I lines reported by Fullerton (1990) reveals indeed an SB2 binary at a phase near quadrature, then the companion of the O4 V star must be

another O-type star[6]. Of course more observations are needed to ascertain this scenario, but it is worth pointing out that the combined optical brightness of two main-sequence O-stars may lead to an interesting problem with the distance of 9 Sgr. Throughout this paper we have assumed a distance of 1.58 kpc, while Sung et al. (2000) derived $d = 1.78$ kpc for the NGC 6530 cluster. Therefore, it remains to be seen whether there is 'enough room' in the optical brightness of 9 Sgr for an O-type companion.

Mason et al. (1998) performed speckle observations of a sample of O-stars including 9 Sgr. The speckle camera used by these authors can detect binaries with angular separations in the range $0.035'' < \rho < 1.5''$ and with an optical brightness ratio of $\Delta m_V \leq 3$. Let us assume that the non-detection of a visual companion by Mason et al. allows us indeed to rule out the presence of a companion at more than $0.035''$. At a distance of 1.58 kpc, this corresponds to a linear separation of 55 AU. Now, assuming that 9 Sgr consists of an O4 V primary of mass $M \sim 55\,M_\odot$ and an ∼O8 V secondary of $M \sim 25\,M_\odot$, we find that the non-detection of Mason et al. (1998) sets an upper limit of 45 yrs on the orbital period of a binary seen at quadrature phase and assuming a circular orbit.

Could a wind-wind collision in a long-period binary produce the observed X-ray spectrum? Wide colliding wind systems have an adiabatic wind collision where the X-ray luminosity scales as the inverse of the orbital separation. Most wide systems (with orbital periods greater than one year) that we know about are WR + O binaries, and the higher mass-loss rate of the WR component helps to keep the X-ray emission fairly strong (e.g. WR 140). However, in an O + O binary, the X-ray luminosity should be drastically reduced (since L_X scales as $\dot{M}^2$, Pittard & Stevens 1997). In an O + O binary with a period of a few years or more, one expects that the soft X-ray emission would remain dominated by the intrinsic emission from each star while the wind-wind collision would only dominate at high energies (e.g. $E > 3$ keV) where there is no contribution from intrinsic wind shocks. We have carried out hydrodynamic simulations (e.g. Pittard & Stevens 1997; Pittard 2000) of the X-ray emission of a colliding wind system consisting of an O4 primary ($\log \dot{M} = -5.6$, $v_\infty = 2950\,\mathrm{km\,s^{-1}}$, $M = 55\,M_\odot$) and an O8 secondary ($\log \dot{M} = -6.6$, $v_\infty = 2950\,\mathrm{km\,s^{-1}}$, $M = 25\,M_\odot$). For an assumed orbital period of 10 yrs (orbital separation 20 AU) the hydrodynamic model predicts a luminosity of $\sim 5 \times 10^{32}\,\mathrm{erg\,s^{-1}}$. The corresponding flux at 3 keV is $6.7 \times 10^{-14}\,\mathrm{erg\,cm^{-2}\,s^{-1}\,keV^{-1}}$ which is about a factor 3 too high compared to the observed flux of 9 Sgr. However, increasing the orbital separation by the same factor 3 would reduce the predicted flux to match the observed value, which would then imply an orbital period of approximately 50 yrs. It can also be seen that the simulated colliding wind spectrum (see Fig. 10) does not fall off as fast as the hard energy tail of the observed spectrum. Reducing the pre-shock wind velocity, particularly of the primary star, would reduce this discrepancy.

We note that confirming the presence of an iron Kα line in future observations would suggest that the hard X-ray continuum is thermal too and would lend further support to the colliding wind interpretation.

Finally, let us point out that among the seven non-thermal radio emitting O-type stars listed by Williams (1996), there are at least three confirmed binary or multiple systems (HD 15558, HD 167971 and Cyg OB2 No. 5). Cyg OB2 No. 5 consists of a short period colliding wind binary (Rauw et al. 1999) with a more distant third component. The non-thermal radio emission has been resolved with the VLA and has been suggested to be associated with the wind interaction zone between the short period binary and the third component (Contreras et al. 1997). HD 167971 (O8 Ib(f)p) has the strongest non-thermal radio emission among the OB stars detected in the survey of Bieging et al. (1989). Leitherer et al. (1987) describe HD 167971 as a close eclipsing O-star binary ($P_{\rm orb} = 3.32$ days) with a third more distant and much brighter O8 I companion (which could be a line of sight object). HD 15558 is the spectroscopic O-star binary with the longest orbital period hitherto known ($P_{\rm orb} = 439.3$ days, $e = 0.54$, Garmany & Massey 1981).

7.4. Conclusions and final remarks

Our multi-wavelength investigation of 9 Sgr confirms the non-thermal origin of its radio emission. However, the X-ray data do not reveal the $E^{-1.5}$ hard power law tail predicted by the model of CW91. Instead, we find that the X-ray spectra can be fitted if we include a steep power law component in the fits. If this model component is real, then the relativistic electrons that produce it must be accelerated in weak shocks with a very low compression ratio.

In this context, it is interesting to point out that Skinner et al. (2002) reported the existence of a hard X-ray component in the presumably single Wolf-Rayet star WR 110. This hard component could be either thermal ($kT \geq 3$ keV) or non-thermal emission. In the former case, Skinner et al. (2002) propose a model where the Wolf-Rayet wind crashes onto an as yet undetected close companion. In the latter case, the hard component can be fitted with a photon index $\Gamma = 2.2^{+0.4}_{-0.3}$, not too different from the theoretical value of CW91 corresponding to strong shocks. Skinner et al. caution that the radio emission from WR 110 yields no indication of a synchrotron component. However, the lack of non-thermal radio emission does not rule out the existence of a non-thermal X-ray emission since the synchrotron radio emission formed within the wind could be strongly absorbed by the huge free-free opacity. Therefore it could be that non-thermal X-ray emission is actually more common among early-type stars than expected from their radio properties. More observations of both thermal and non-thermal radio emitting early-type stars with *XMM-Newton* as well as the elaboration of new theoretical models are needed to clarify the nature of the hard X-ray emission component.

However, our optical data suggest that 9 Sgr could be a long-period spectroscopic binary. Therefore, it seems that a colliding wind scenario provides a plausible alternative and that the hard X-rays could be emitted in a very hot thermal plasma of a wind interaction region. A long-term high resolution spectroscopic monitoring of 9 Sgr is therefore indicated

[6] The C IV lines are strongest at types O6 – O7 (Walborn 1980).

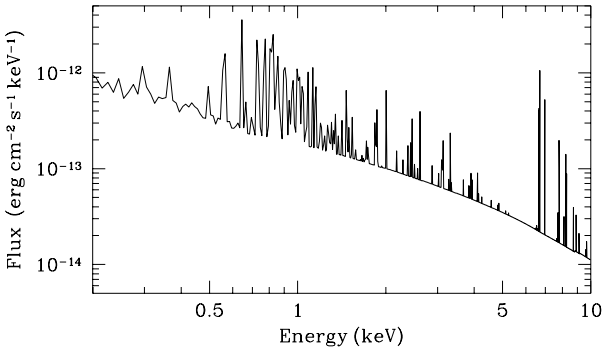

Fig. 10. Simulated unabsorbed X-ray emission from a wind-wind collision in an O4 + O8 binary system with orbital period 10 yrs. Interstellar and wind absorption would greatly reduce the flux below 1 keV, but the ISM column should only absorb a few per cent of the flux at 3 keV. See the text for details.

to unambiguously clarify the multiplicity of this star. Also it would be valuable to perform a multi-wavelength monitoring campaign to determine whether broad-band variations (like those seen in the radio, IR and X-rays for WR 140) can be established for 9 Sgr.

Acknowledgements. The authors wish to thank an anonymous referee for carefully reading our manuscript. We thank Dr. Yvan Stockman from the Centre Spatial de Liège (CSL) for useful information about the straylight behaviour of the *XMM-Newton* mirror modules. We are grateful to Dr. Barry Clark for kindly scheduling the VLA radio observation simultaneously with the *XMM* observation. Our thanks go also to Alain Detal (Liège) for his help in installing the SAS and to Dr. Herman Hensberge (Royal Observatory of Belgium) for advising us in the reduction of the FEROS data. The Liège team acknowledges support from the Fonds National de la Recherche Scientifique (Belgium) and through the PRODEX XMM-OM and Integral Projects. This research is also supported in part by contracts P4/05 and P5/36 "Pôle d'Attraction Interuniversitaire" (OSTC-Belgium). WLW was supported in part by NASA contract # NAG 5-10113. MCR acknowledges support from ESA-Prodex project No. 13346/98/NL/VJ(ic). SVL acknowledges the financial support of the Belgian OSTC. JMP gratefully acknowledges funding from PPARC for a PDRA position. This research has made use of the SIMBAD database, operated at CDS, Strasbourg, France and NASA's Astrophysics Data System Abstract Service.

References

Abbott, D. C., Bieging, J. H., & Churchwell, E. B. 1984, ApJ, 280, 671
Bell, A. R. 1978, MNRAS, 182, 147
Berghöfer, T. W., Schmitt, J. H. M. M., & Cassinelli, J. P. 1996, A&AS, 118, 481
Berghöfer, T. W., Schmitt, J. H. M. M., Danner, R., & Cassinelli, J. P. 1997, A&A, 322, 167
Bieging, J. H., Abbott, D. C., & Churchwell, E. B. 1989, ApJ, 340, 518
Bohannan, B., Voels, S. A., Hummer, D. G., & Abbott, D. C. 1990, ApJ, 365, 729
Briggs, D. S. 1995, Ph.D. Thesis, The New Mexico Institute of Mining and Technology, Socorro, New Mexico
Cassinelli, J. P., & Swank, J. H. 1983, ApJ, 271, 681
Cassinelli, J. P., Miller, N. A., Waldron, W. L., MacFarlane, J. J., & Cohen, D. H. 2001, ApJ, 554, L55
Chen, W., & White, R. L. 1991, ApJ, 366, 512 (CW91)
Chen, W., & White, R. L. 1994, Ap&SS, 221, 259
Conti, P. S., & Ebbets, D. 1977, ApJ, 213, 438
Contreras, M. E., Rodríguez, L. F., Tapia, M., et al. 1997, ApJ, 488, L153
Corcoran, M. F., Waldron, W. L., MacFarlane, J. J., et al. 1994, ApJ, 436, L95
Cornwell, T., & Braun, R. 1989, in Synthesis Imaging in Radio Astronomy, ed. R. A. Perley, F. R. Schwab, & A. H. Bridle, ASP Conf. Ser., 6, 167
den Herder, J. W., Brinkman, A. C., Kahn, S. M., et al. 2001, A&A, 365, L7
Diplas, A., & Savage, B. D. 1994, ApJS, 93, 211
Donati, J.-F., Wade, G. A., Babel, J., et al. 2001, MNRAS, 326, 1265
Donati, J.-F., Babel, J., Harries, T. J., Howarth, I. D., Petit, P., & Semel, M. 2002, MNRAS, 333, 55
Dougherty, S. M., & Williams, P. M. 2000, MNRAS, 319, 1005
Eichler, D., & Usov, V. 1993, ApJ, 402, 271
Feldmeier, A., Puls, J., & Pauldrach, A. W. A. 1997, A&A, 322, 878
Fermi, E. 1949, Phys. Rev., 75, 1169
Florkowski, D. R., Johnston, K. J., Wade, C. M., & de Vegt, C. 1985, AJ, 90, 2381
Fullerton, A. W. 1990, Ph.D. Thesis, University of Toronto
Fullerton, A. W., Gies, D. R., & Bolton, C. T. 1996, ApJS, 103, 475
Garmany, C. D., Conti, P. S., & Massey, P. 1980, ApJ, 242, 1063
Garmany, C. D., & Massey, P. 1981, PASP, 93, 500
Jansen, F., Lumb, D., Altieri, B., et al. 2001, A&A, 365, L1
Kaastra, J. S. 1992, An X-ray spectral code for optically thin plasmas, Internal SRON-Leiden Report
Kaastra, J. S., Mewe, R., & Raassen, A. J. J. 2002, in New Visions of the X-ray Universe in the XMM-Newton and Chandra Era, ed. F. Jansen, ESA SP-488, in press
Kahn, S. M., Leutenegger, M. A., Cottam, J., et al. 2001, A&A, 365, L312
Kaufer, A., Stahl, O., Tubbesing, S., et al. 1999, The Messenger, 95, 8
Lamers, H. J. G. L. M., & Leitherer, C. 1993, ApJ, 412, 771
Leitherer, C., Forbes, D., Gilmore, A. C., et al. 1987, A&A, 185, 121
Maeder, A., & Meynet, G. 1994, A&A, 287, 803
Mason, B. D., Gies, D. R., Hartkopf, W. I., et al. 1998, AJ, 115, 821
Mathys, G. 1988, A&AS, 76, 427
Mathys, G. 1999, in Proc. IAU Coll. 169, Variable and Non-spherical Stellar Winds in Luminous Hot Stars, ed. B. Wolf, O. Stahl, & A. W. Fullerton, Lect. Notes Phys., 523, 95
Mewe, R., Gronenschild, E. H. B. M., & van den Oord, G. H. J. 1985, A&AS, 62, 197
Owocki, S. P., & Cohen, D. H. 2001, ApJ, 559, 1108
Penny, L. R. 1996, ApJ, 463, 737
Perley, R. A., & Taylor, G. B. 1999, The VLA Calibrator Manual (`http://www.aoc.nrao.edu/~gtaylor/calib.html`)
Pittard, J. M. 2000, Ph.D. Thesis, The University of Birmingham, UK
Pittard, J. M., & Stevens, I. R. 1997, MNRAS, 292, 298
Porquet, D., Mewe, R., Dubau, J., Raassen, A. J. J., & Kaastra, J. S. 2001, A&A, 376, 1113
Rauw, G., Vreux, J.-M., & Bohannan, B. 1999, ApJ, 517, 416
Rauw, G., Blomme, R., Waldron, W. L., et al. 2002, in New Visions of the X-ray Universe in the XMM-Newton and Chandra Era, ed. F. Jansen, ESA SP-488, in press
Razin, V. A. 1960, Radiophysica, 3, 584

Rybicki, G. B., & Lightman, A. P. 1979, Radiative Processes in Astrophysics (John Wiley & Sons)
Schulz, N. S. 1999, ApJ, 511, 304
Shull, J. M., & van Steenberg, M. E. 1985, ApJ, 294, 599
Skinner, S. L., Zhekov, S. A., Güdel, M., & Schmutz, W. 2002, ApJ, 572, 477
Stockman, Y., Barzin, P., Hansen, H., et al. 1998, in Proceedings of the First XMM Workshop on Science with XMM held at Noordwijk, The Netherlands, ed. M. Dahlem (http://xmm.vilspa.esa.es/news/ws1/ws1_papers.html)
Strüder, L., Briel, U., Dennerl, K., et al. 2001, A&A, 365, L18
Sung, H., Chun, M.-Y., & Bessell, M. S. 2000, AJ, 120, 333
Torres, A. V. 1987, ApJ, 322, 949
Turner, M. J. L., Abbey, A., Arnaud, M., et al. 2001, A&A, 365, L27
Walborn, N. R. 1980, ApJS, 44, 535
Walborn, N. R. 2001, in Eta Carinae and Other Mysterious Stars: The hidden opportunities of emission spectroscopy, ed. T. R. Gull, S. Johannson, & K. Davidson, ASP Conf. Ser., 242, 217
Walborn, N. R., Howarth, I. D., Lennon, D. J., et al. 2002, AJ, 123, 2754
Waldron, W. L., Corcoran, M. F., Drake, S. A., & Smale, A. P. 1998, ApJS, 118, 217
Waldron, W. L., & Cassinelli, J. P. 2001, ApJ, 548, L45
Weber, E. J., & Davis, L. Jr. 1967, ApJ, 148, 217
White, R. L. 1985, ApJ, 289, 698
Williams, P. M. 1996, in Radio Emission from the Stars and the Sun, ed. A. R. Taylor, & J. M. Paredes, ASP Conf. Ser., 93, 15 (San Francisco)
Wright, A. E., & Barlow, M. J. 1975, MNRAS, 170, 41

Although I will show below that 9 Sgr is a colliding wind binary system, the bulk of its soft X-ray emission most probably arises from the intrinsic emission of the individual stars (actually the emission from the O4 V primary component should dominate). There are several indications that support this assumption. First, compared to the 'canonical' $L_{\rm X}/L_{\rm bol}$ ratio of single O-type stars, the X-ray luminosity does not exhibit a significant excess emission that would be expected from a colliding wind system. Second, the archive *ROSAT* data did not reveal a significant variability of the soft X-ray flux. Finally, the morphology of the X-ray lines seen in the RGS spectrum is compatible with the expectations for the emission produced by a plasma embedded in the wind of a single early-type star. To illustrate this purpose, I have used a numerical code to simulate X-ray line profiles (see Appendix A) and compared the result to the observed profiles of the O VIII and N VII Lyα lines (see Fig. 3.1). This 'exospheric' model has four free parameters: the inner radius of the X-ray emission region R_0, the radial dependence of the X-ray plasma filling factor (characterized by the exponent q of a power law in radius r^{-q}), the terminal wind velocity v_∞ and the typical optical depth of the wind τ_* at the wavelength of the line (see Appendix A for details).

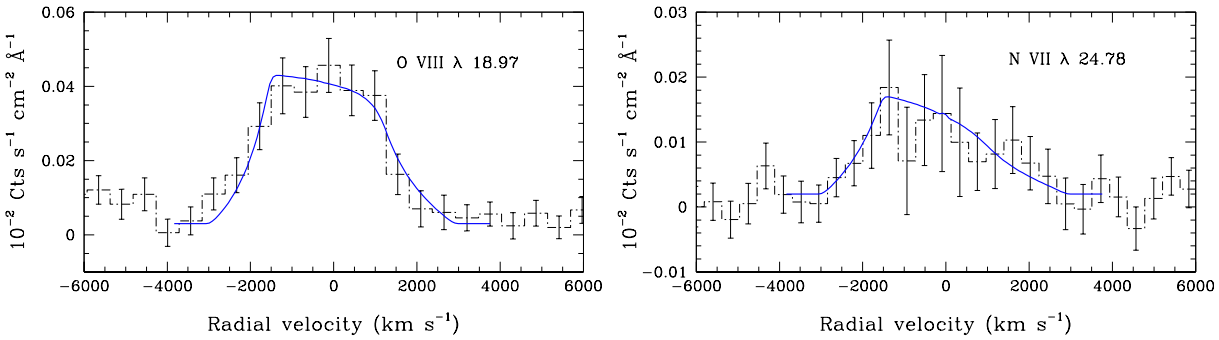

Figure 3.1: Comparison between the observed O VIII Lyα (left) and N VII Lyα lines (right) of 9 Sgr (dashed histogram with error bars) and synthetic line profiles (solid line) computed for $R_0 = 2\,R_*$, $v_\infty = 2950\,{\rm km\,s^{-1}}$, $q = 0.0$ and $\tau_* = 0.2$ for the oxygen line and $\tau_* = 1.0$ for the nitrogen line (see Appendix A for the details of the assumptions of the line profile calculations).

Assuming a flat distribution of the plasma filling factor ($q = 0$, see Appendix A), the width of the observed oxygen line profile suggests that $1.5 \leq R_0/R_* \leq 2.5$, whilst its symmetry indicates $0.15 \leq \tau_* \leq 0.25$. The latter value is surprisingly low for an O4 V star, even compared to the results found for ζ Pup and ζ Ori. This result could indicate that the mass loss rate assumed in Rauw et al. (2002c) was overestimated. For the nitrogen line, the error bars are larger and the optical depth can only be poorly constrained: $0.3 \leq \tau_* \leq 3.0$, whilst R_0 should again be close to $2\,R_*$.

3.3.2 HD 168112

In addition to the data of 9 Sgr, our *XMM-Newton* AO1 campaign on non-thermal radio emitters included another presumably single O5.5 III(f$^+$) star, HD 168112. The results of two quasi-simultaneous *XMM-Newton* and *VLA* observations were presented by De Becker et al. (2004b). The X-ray observations were taken on 6 April and 9 September 2002, whilst the radio measurements were obtained on 24 March and 11 September 2002. The EPIC spectra of the star could be fitted either by a purely thermal model with two temperatures of 0.3 and 2–3 keV or a model including a soft thermal ($\sim 0.3\,$keV) component and a power law with $\Gamma \simeq 3$. The likely presence of an Fe K line favours the thermal model. The ISM absorption corrected luminosity during the *XMM-Newton* observations was found to be $9 \times 10^{32}\,{\rm erg\,s^{-1}}$,

only a factor 2 larger than expected from the canonical $L_{\rm X}/L_{\rm bol}$ relation. However, De Becker et al. (2004b) noted a 25 – 30% decrease of the X-ray flux between April and September 2002. Archive *ROSAT* and *EINSTEIN* data suggest an even stronger variability of the X-ray flux (see Fig. 3.2). The radio data revealed an even more puzzling situation, since the star was in a low emission state in March 2002 with a 6 cm flux density of 0.3 mJy and a radio spectral index of $\alpha = 0.0 \pm 0.9$, whilst the 6 cm flux density and spectral index in September 2002 amount to 2.1 mJy and $\alpha = -0.3 \pm 0.4$ respectively.

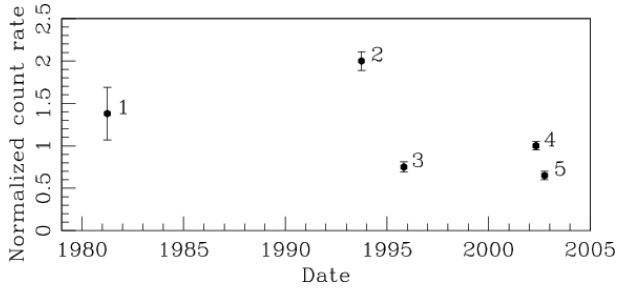

Figure 3.2: Normalized X-ray count rates of HD 168112 as observed with different satellites/instruments. The various points correspond to: 1 = *EINSTEIN*-IPC (March 1981), 2 = *ROSAT*-PSPC (September 1993), 3 = *ROSAT*-HRI (September - October 1995), 4 & 5 = *XMM-Newton*-EPIC (April and September 2002 respectively). To compare these rather heterogeneous data, the best fit model of the EPIC spectra of April 2002 was folded through the response matrices of the different instruments yielding a fake count rate. The actual (i.e. observed) count rate was then divided by this fake rate to produce the normalized count rates shown in this figure. From De Becker et al. (2004b).

Although no significant radial velocity changes nor photometric variations were detected, De Becker et al. (2004b) suggested that HD 168112 could be an eccentric binary system with an orbital period somewhere in the range 1.7 to 8.9 years.

An extensive analysis of archive *VLA* and *ATCA* radio data of HD 168112 was subsequently presented by Blomme et al. (2005). These authors found that the radio emission varies between a low state (observed twice in twenty years) and a high state (observed three times over the same period). In the low state, the 2 – 6 cm spectral index amounts to $\alpha = 0.6 \pm 0.6$, whilst its value in the high state is $\alpha = -1.1 \pm 0.4$. The flux density at 6 cm is a factor twenty larger during the high state than in the low state. Still, even in the low state, the flux density remains a factor ten larger than expected for the thermal emission (0.03 mJy) estimated from the Hα-determined mass loss rate. Blomme et al. (2005) further showed that the spectral shape and flux level of HD 168112 can be explained in the single star scenario, provided that the shock velocity jump of a single shock amounts to $> 500\,{\rm km\,s^{-1}}$, significantly larger than the value ($< 50\,{\rm km\,s^{-1}}$) expected from hydrodynamical simulations of the wind instability of single stars. Alternatively, if the shock velocity jump is restricted to $50\,{\rm km\,s^{-1}}$, then more than 1700 shocks are required in the radio emission region of the wind to explain the observed flux level. This number is much larger than expected from the simulations. The model that best explains all the observed properties is therefore the colliding wind binary scenario. Blomme et al. (2005) accordingly propose that HD 168112 could be an eccentric binary system ($e \geq 0.5$) with a period between 1 and 2 years. The radio variability would then result from the colliding wind shock moving in and out of the radio photosphere of the binary components. Including the results of the X-ray light curve of De Becker et al. (2004b) and assuming a $1/D_{\rm sep}$ dependence of the X-ray flux, Blomme et al. (2005) inferred a best estimate of the period of 1.4 year (see Fig. 3.3) and an orbital inclination of $\leq 15°$.

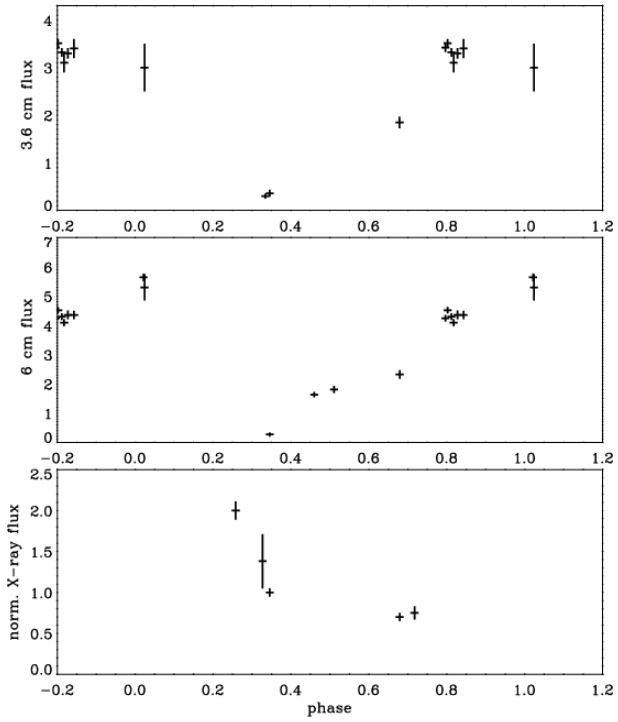

Figure 3.3: Upper and middle panel: 3.6 and 6 cm archive radio light curves of HD 168112 folded with a 1.4 yr period. The bottom panel yields the X-ray light curve with the same period. Phase 0.0 was arbitrarily set to JD 2444000. From Blomme et al. (2005).

3.3.3 HD 167971

Simultaneously with HD 168112, another non-thermal radio emitter, HD 167971, was observed in the same EPIC field of view. HD 167971 is a multiple system consisting of an O5-8 V + O5-8 V eclipsing binary in a 3.32 day orbit along with a more distant O8 I star. The X-ray data were analysed by De Becker et al. (2005). The soft part of the EPIC X-ray spectra of this object can be fitted with two thermal components of temperatures 0.17 and 0.75 keV. The hard tail could be either thermal (2 - 4 keV) or non-thermal ($\Gamma = 3$). If thermal, the hard tail is most likely produced in the colliding wind region between the close binary and the third component. Compared to the canonical $L_{\rm X}/L_{\rm bol}$ relation, the system appears moderately overluminous by a factor 4. Between the two *XMM-Newton* observations, the soft flux decreased by about 12%, which could be due to the eclipses in the close binary. From archive X-ray data, De Becker et al. (2005) noted the possibility of some higher amplitude variations, although this result calls for confirmation. Blomme et al. (2006) reported variations of the 6 cm radio flux of HD 167971 between about 7 and 25 mJy on a time scale of more than 20 years, which they interpret as the orbital period of the O8 I star around the eclipsing binary. They also note the existence of variations on shorter time scales (a few days), but the 3.3 day orbital period of the eclipsing binary does not seem to be present.

3.4 The multiplicity of non-thermal radio emitters

As suggested in the previous sections, non-thermal (i.e. synchrotron) radio emission could *a priori* arise from the 'wind-embedded' shocks that are expected to exist in the winds of single O-type stars as a consequence of the intrinsic instability (the so-called 'line-deshadowing instability') of radiatively driven winds. Relativistic electrons are likely to be accelerated near these shocks. The high-energy cut-off of the electron energy distribution depends essentially on the balance between acceleration and cooling (mainly inverse Compton cooling). Away from the shock, IC cooling removes the energy rather quickly and therefore the synchrotron emission is likely to come from a thin layer behind each shock. The synchrotron emissivity scales with the third power of the shock velocity jump (Van Loo et al. 2006). An important ingredient in the production of an *observable* non-thermal radio emission is the free-free opacity that absorbs any radio emission (thermal or non-thermal) from the base of the wind. Since the free-free opacity increases with wavelength, the radius where the optical depth $\tau = 1$ depends strongly on the wavelength considered (see e.g. Rauw 2004b). Taking into account the results from 1-D hydrodynamical models of the 'line-deshadowing instability', Van Loo et al. (2006) studied the expected properties of non-thermal radio emission of single O-stars. As a result of the radial decrease of the shock velocity jump and the shock compression ratio, predicted by the hydrodynamical simulations, and the wavelength dependence of the optical depth, strong shocks relatively close to the star contribute more to the observed flux at shorter wavelengths than at longer wavelength. These models therefore tend to predict a positive spectral index (Van Loo et al. 2006), whilst observations reveal $\alpha \leq 0$. To produce a negative spectral index would require an emissivity that would decrease only weakly with radius. Van Loo et al. (2006) studied several escape routes (such as reduced mass loss rates - and hence reduced free-free opacity - due to wind clumpiness, re-acceleration of electrons by crossing successive shocks...) but concluded that none was really physically acceptable. These authors therefore argue that the observed synchrotron emission rather arises from shocks in colliding wind binaries.

A spectacular confirmation of the link between non-thermal radio emission and colliding winds in a well known binary system came from *VLBA* observations of WR 140 (WC7 + O4-5, 7.9 yr, $e = 0.88$) presented by Dougherty et al. (2005). These observations actually resolve an arc-shaped emission that rotates as the stars orbit around each other. The shape of this feature results from the combination between the bow-shock shape of the wind interaction zone and the effect of free-free absorption by the winds of the two stars.
As outlined in the introduction, the multiplicity of non-thermal O-stars is less constrained than that of WR stars. For instance, De Becker (2007) lists a total of 17 WR stars with a non-thermal or composite radio spectrum, 12 of which are confirmed spectroscopic or visual binaries and two are suspected binaries. In the same way, De Becker (2007) lists 16 O-type stars with a non-thermal radio emission. Only eight of these objects were known as confirmed binary or multiple systems prior to our studies.
It is therefore important to perform optical monitoring of these stars to look for radial-velocity variations that could reveal binary systems. Below, I report the results of such a study for 9 Sgr and HD 168112 that were first presented at the JENAM 2005 conference in Liège (Rauw et al. 2005a). Whilst Garmany et al. (1980) argued that 9 Sgr is most likely a single star presenting low-amplitude RV variations due to perturbations of its stellar atmosphere, no radial velocity study had been performed for HD 168112 prior to our campaign.

On the multiplicity of the non-thermal radio emitters 9 Sgr and HD 168112*

Gregor Rauw[1†], Hugues Sana[1‡], Eric Gosset[1†], Michaël De Becker[1], Julia Arias[2], Nidia Morrell[3], Philippe Eenens[4] and David Stickland[5]

[1]Institut d'Astrophysique, Université de Liège, Belgium
[2]Facultad de Ciencias Astronómicas y Geofísicas, Universidad Nacional de La Plata, Argentina
[3]Las Campanas Observatory, The Carnegie Observatories, La Serena, Chile
[4]Departamento de Astronomia, Universidad de Guanajuato, Mexico
[5]Rutherford Appleton Laboratory, Chilton, UK

Abstract: We discuss the first results of our ongoing optical spectroscopic monitoring campaign of the two O-type stars 9 Sgr and HD 168112. Both objects display a non-thermal radio emission and were considered as single stars. Based on a large set of high-resolution spectra, we find that 9 Sgr is clearly an eccentric SB2 binary with an orbital period of several years. On the other hand, no evidence for radial velocity variations attributable to binary motion is found in our spectra of HD 168112.

1 Introduction

One of the most intriguing features of early-type stars is the non-thermal radio emission that is observed for some of them. This emission is interpreted as synchrotron radiation, implying that the winds of these stars harbour a population of relativistic electrons. The most likely acceleration sites of these relativistic electrons are hydrodynamic shocks. Such shocks are known to exist at the interface between the stellar winds of the components of early-type binary systems and over the last few years, it has become more and more obvious that many of the non-thermal radio emitters are indeed binary systems (Dougherty & Williams 2000 and references therein; see also Van Loo, these proceedings).

Over the last few years, we have been investigating the multi-wavelength (radio, optical, X-ray and γ-ray) properties of a sample of non-thermal radio emitting O-type stars (see e.g. Rauw et al. 2002, De Becker et al. 2004a, 2004b, 2005, Blomme et al. 2005). Some of our targets (9 Sgr, HD 168112, Cyg OB2 #8a) were previously considered as single stars. We therefore initiated a spectroscopic monitoring of these stars, to uncover yet unknown binary systems.

*Based on data collected at the European Southern Observatory (La Silla, Chile), the Complejo Astronómico El Leoncito (Argentina) and the Observatorio Astronómico Nacional of San Pedro Mártir (Mexico)
†Research Associate FNRS (Belgium)
‡Research Fellow FNRS (Belgium)

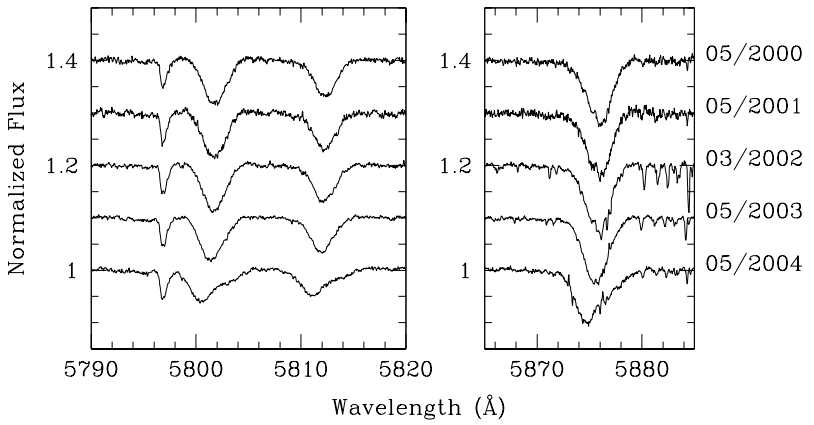

Figure 1: Variations of the C IV $\lambda\lambda$ 5801, 5812 and He I λ 5876 line profiles in the FEROS spectra of 9 Sgr.

A first result of this campaign was presented by De Becker et al. (2004b) who showed that Cyg OB2 #8a is in fact an eccentric spectroscopic binary system with a period of 21.9 days. Here, we discuss preliminary results for 9 Sgr and HD 168112.

2 9 Sgr

In the course of our ongoing monitoring campaign of the O4 V((f$^+$)) star 9 Sgr, we have gathered a total of 31 spectra with the FEROS echelle spectrograph (R = 48000). The data were obtained between 1999 and 2002 at the ESO 1.5 m and since 2003 at the 2.2 m telescopes at La Silla (Chile). In addition, one spectrum was taken with the EMMI instrument in echelle mode (R = 7700) at the New Technology Telescope (La Silla) in 2002. The data taken in 2004 reveal a clear SB2 signature in the C IV $\lambda\lambda$ 5801, 5812 and He I λ 5876 lines: the core of these lines is clearly shifted towards the blue, whilst the red wing shows the presence of a fainter secondary component (see Fig. 1). The ESO data are complemented by 5 spectra obtained in 1995 with the REOSC echelle spectrograph (R = 15000) at CASLEO. Despite their rather low signal to noise ratio, these data play a crucial role since they reveal an SB2 signature similar to that observed in 2004 and to the one already observed in 1987 by Fullerton (1990).

To measure the radial velocities of the two components of 9 Sgr, we have first applied a simultaneous fit of two Gaussians to the spectra obtained during 2004 i.e. near maximum separation. For the other spectra, we have measured the radial velocity (RV) of the line core. The latter values most likely reflect the primary RVs. As a next step, we then applied the spectral disentangling method of González & Levato (2005) to separate the spectra of the primary and secondary component and to determine the RVs. In this approach, we have used the primary RVs derived hereabove as the starting values of the iterative procedure. The results are shown in Fig. 2. Note that secondary RVs obtained when the RV separation is small are quite uncertain. Our results indicate that 9 Sgr is most probably an eccentric SB2 binary system with an orbital period of order 8 – 9 years.

The disentangled spectra of the primary and secondary components yield a brightness ratio of about 4 ± 1 ($\Delta m_V \simeq 1.5 \pm 0.3$) from the ratio of the EWs of the C IV and He I absorptions.

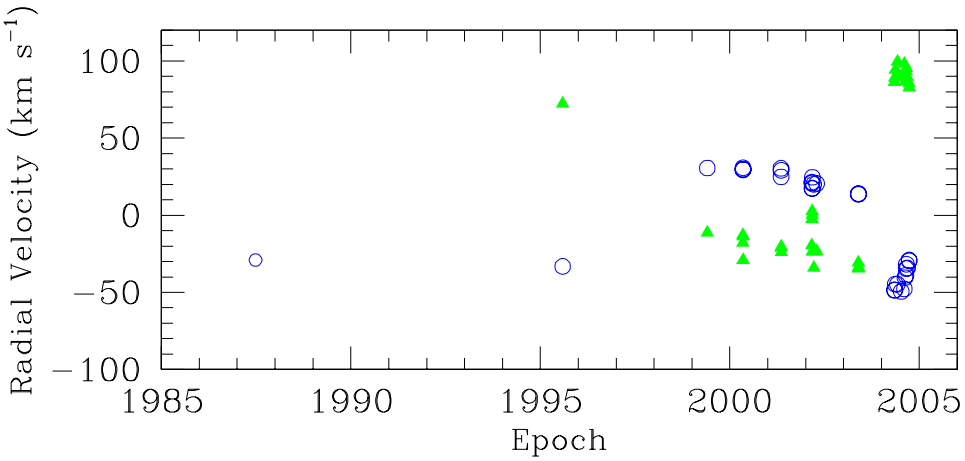

Figure 2: Radial velocities of 9 Sgr as determined using the González & Levato (2005) disentangling method (except for the first observation taken from Fullerton 1990). Open circles and filled triangles indicate the RVs of the primary and secondary components respectively. All RVs were obtained from the C IV $\lambda\lambda$ 5801, 5812 and He I λ 5876 lines.

3 HD 168112

In addition to the data discussed by De Becker et al. (2004a), we have obtained 15 new FEROS spectra spread over six months in 2004. This brings the total number of our echelle spectra of HD 168112 to 25 spanning a total time interval of 1233 days. Our present time series allows us to investigate variations on time scales from a few days to about 10 months as well as from about 1.5 to 4 years. Due to the sampling, periods shorter than one day, between about 10 and 15 months or longer than about 4 years are not well constrained by our data.

We have measured the heliocentric RVs of the strongest absorption lines in our spectra. The RVs of individual lines show little evidence for variability. The 1-σ dispersions range from 1.6 km s^{-1} for the He II λ 5412 line to 6.5 km s^{-1} for He II λ 4686, the latter line being probably affected by wind variations. We averaged the RVs of the Hγ, Hβ, He II $\lambda\lambda$ 4200, 4542, 4686, 5412; He I λ 5876 and C IV $\lambda\lambda$ 5801, 5812 lines. The results are shown in Fig. 3. No obvious trend is apparent on the RV data. The 1-σ dispersion amounts to 3.3 km s^{-1}.

For the time scales covered by our data, we assume that the amplitude of RV variations K is less than $2 \times \sigma = 6.6$ km s^{-1}. Using Kepler's law for a binary system of eccentricity e, period P, mass ratio $q = m1/m2$ yields

$$K = \frac{\sin i}{\sqrt{1-e^2}} \left(\frac{2\,\pi\,G\,m_1}{P\,q\,(1+q)^2} \right)^{1/3}$$

Assuming a mass of 50 $M_\odot$ for the O5.5 III(f$^+$) star in HD 168112, we focus on three different values of the mass ratio: $q = 1$, $q = 5$ (corresponding roughly to a B2 V secondary) and $q = 10$ ($\sim$ B6 V secondary). Some results are illustrated in Table 1 below. This table provides the largest acceptable inclination that can be accommodated within our upper limit on K, as well as the probability to have such a low inclination for a random distribution of orbital inclinations.

Of particular interest are the values for $P = 500$ days in Table 1. Indeed, this corresponds roughly to the 1.4 year period suggested by Blomme et al. (2005) to match both the radio and X-ray light curve. We see that in order to have a colliding wind interaction (which probably

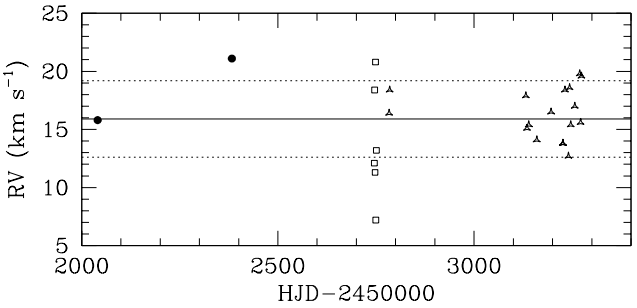

Figure 3: Average RVs of 9 absorption lines in the spectrum of HD 168112. Different symbols stand for data obtained with different instruments. The solid and dotted lines yield the mean as well as the mean ± 1-σ respectively.

requires $q \leq 5$) for such a period, the inclination would have to be less than about 20°. Using Kepler's law and assuming a 1.4 year orbital period, we estimate that $a > 4.61$ AU, which at a distance of 2 kpc yields an angular separation of > 2.3 mas, which should make the companion detectable with the VLTI. A no detection would be a serious challenge for the binary scenario for non-thermal radio emission in O-type stars.

Table 1: Upper limits on the orbital inclination if HD 168112 were a binary with $e = 0$ for different values of P and q. Also indicated is the probability that i be lower than $i_{\rm lim}$ assuming a random distribution of orbital directions in space.

P	10 days			100 days			500 days			1000 days		
q	1	5	10	1	5	10	1	5	10	1	5	10
$i_{\rm lim}(^\circ)$	1.6	5.9	11.1	3.6	12.7	24.6	6.1	22.1	45.4	7.7	28.4	63.7
$p(i \leq i_{\rm lim})(\%)$	0.04	0.5	1.9	0.2	2.5	9.1	0.6	7.4	29.7	0.9	12.0	55.7

Acknowledgements

The Liège team is greatly indebted to the F.N.R.S. for multiple assistance. This research is also supported in part by contract P5/36 "PAI" and through the PRODEX projects.

References

Blomme R., Van Loo S., De Becker M., et al., 2005, A&A, 436, 1033
De Becker M., Rauw G., Blomme R., et al., 2004a, A&A, 420, 1061
De Becker M., Rauw G., Manfroid J., 2004b, A&A, 424, L39
De Becker M., Rauw G., Blomme R., et al., 2005, A&A, 437, 1029
Dougherty S.M., Williams P.M., 2000, MNRAS, 319, 1005
Fullerton A.W., 1990, PhD thesis, University of Toronto
González J.F., Levato H., 2005, A&A, in press
Rauw G., Blomme R., Waldron W.L., et al., 2002, A&A, 394, 993

3.4.1 More results on 9 Sgr and HD 168112

Some additional results of our monitoring campaign of 9 Sgr and HD 168112 have become available since the publication of the JENAM proceedings. The observations of 9 Sgr are still ongoing. Putting all the data available in October 2006 together, I have first attempted to derive the mass ratio between the two stars from their radial velocities derived using the disentangling method outlined in Sect. 1.1.2. The preliminary[2] least square fit of these RVs indicates $RV1(t) = -0.56 * RV2(t) - 10.9$ (in km s^{-1}), thus indicating a mass ratio of $m_2/m_1 = 0.56$. This result needs of course to be confirmed with our forthcoming data, but it is encouraging that this preliminary mass ratio is actually quite consistent with the tentative O7 spectral type proposed for the secondary star[3] by Rauw et al. (2002c). We have then used the above relation between the RVs of the primary and secondary to repeat the disentangling method. The resulting RV curve and the disentangled spectra are shown in Fig. 3.4. Of course, the reconstruction of the primary and secondary spectra is still far from perfect. The main reason is the lack of a clear bluewards excursion of the secondary star in the spectra that we have obtained. Depending on the orientation of the orbit (mainly the longitude of periastron) such a configuration might never occur. The final answer to this question has to await the completion of our monitoring campaign. The ratio between the equivalent widths of the He I λ 5876 lines of the primary and secondary star suggests a brightness ratio of about 5 (not corrected for the difference in spectral types) between the primary and the secondary.

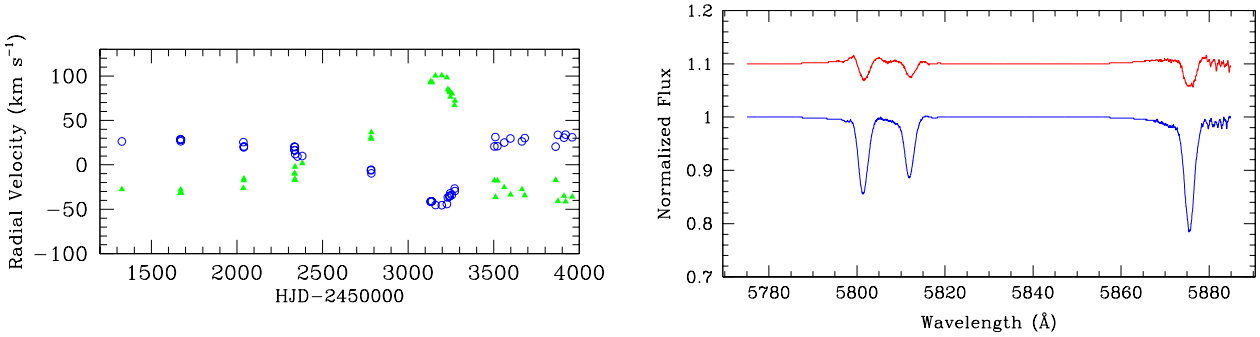

Figure 3.4: Left: Radial velocities of the primary (open circles) and secondary (filled triangles) components of 9 Sgr as obtained in our monitoring campaign. The RVs were obtained through the disentangling method assuming the relation between the primary and secondary RVs quoted in the text. Right: normalized reconstructed spectra of the primary and secondary components around the C IV $\lambda\lambda$ 5801, 5812 and He I λ 5876 lines. The secondary spectrum is shifted upwards by 0.1 unit. Interstellar features have been excluded from the reconstruction. The noise-like features around the He I λ 5876 line are due to the telluric absorption features.

As far as HD 168112 is concerned, the last data set was obtained during ESO period 75 (October 2005 – March 2006). Since no significant RV variations were detected (see Table 3.1 below), we decided to stop the spectroscopic monitoring of this system.
The final sample consists of 32 échelle spectra spread over 1642 days, allowing us to investigate variations on time scales from a few days to about 10 months as well as from about 1.5 to 4 years. Due to the sampling, periods shorter than one day, between about 10 and 15 months or longer than about 5 years are not well constrained by these data. The heliocentric radial velocities (RVs) of the strongest absorption lines show little evidence for variability. The 1-σ dispersions range from 2.0 km s^{-1} for the He II λ 5412 line to 7.6 km s^{-1} for He II λ 4686. The mean RVs of nine absorption lines (Hγ, Hβ, He II $\lambda\lambda$ 4200,

[2]The final relation will be determined once the entire data set of our campaign covering a full orbital cycle will be available.
[3]According to Martins et al. (2005a) the mass ratio between an O4 V and O7 V star should be 0.54.

Table 3.1: Average radial velocities of nine absorption lines in the spectrum of HD 168112 as measured on our échelle data. The third column yields the instrumentation used for the observation: échelle spectrograph at San Pedro (SPM), FEROS at the ESO 1.5 m (F1.5) or FEROS at the ESO/MPE 2.2 m (F2.2).

Date HJD − 2450000	$\overline{RV}$ (km s^{-1})	Inst.	Date HJD − 2450000	$\overline{RV}$ (km s^{-1})	Inst.
2040.721	15.8	F1.5	3226.689	13.8	F2.2
2382.900	21.1	F1.5	3231.620	18.4	F2.2
2745.919	12.1	SPM	3240.574	12.7	F2.2
2746.875	18.4	SPM	3243.544	18.6	F2.2
2747.867	11.3	SPM	3246.602	15.4	F2.2
2748.842	20.8	SPM	3256.574	17.0	F2.2
2749.876	7.2	SPM	3269.526	19.8	F2.2
2750.864	13.2	SPM	3271.548	15.6	F2.2
2783.820	16.4	F2.2	3273.535	19.6	F2.2
2784.815	18.4	F2.2	3503.859	18.8	F2.2
3131.873	17.9	F2.2	3521.764	16.0	F2.2
3134.925	15.1	F2.2	3561.757	14.9	F2.2
3139.708	15.4	F2.2	3597.633	15.7	F2.2
3159.758	14.1	F2.2	3601.650	20.6	F2.2
3196.567	16.5	F2.2	3664.541	13.8	F2.2
3226.615	13.8	F2.2	3682.522	16.4	F2.2

4542, 4686, 5412; He I λ 5876 and C IV $\lambda\lambda$ 5801, 5812) are listed in Table 3.1 and are plotted in Fig. 3.5. No obvious trend is apparent and the 1-σ dispersion on these mean RVs amounts to 2.9 km s^{-1}.
Table 3.2 provides an update of Table 1 of Rauw et al. (2005a). The conclusions from the latter paper are unchanged: from the existing RV data, it appears very unlikely that HD 168112 be a spectroscopic binary with a period shorter than 500 days, a mass ratio less than 5 and an inclination larger than $20°$. This result represents a serious challenge for the colliding wind scenario to explain the origin of the synchrotron radio emission of this star. I will come back to this issue in Sect. 3.6.

3.4.2 HD 93250

As reported in Sect 1.2.1, the RV measurements of Lanotte (2006) indicate 1-σ RV dispersions of less than 2.0 km s^{-1} for the He II $\lambda\lambda$ 4026, 4542 and 5412 absorption lines in the spectrum of HD 93250 for time scales of 3 – 5 days as well as of several years. The lack of significant RV variations therefore suggests that HD 93250 be a single star. What is the probability that we might have missed the binarity of HD 93250? For an O3.5 V((f$^+$)) star, we can assume a mass of $50\,M_\odot$. Assuming further a random distribution of the orbital directions in space, the probability that the orbital inclination be indeed smaller than the value obtained from Eq. (1.2) can be evaluated as (for details see Sect. 1.3.3)

$$\int_0^{i_{\rm up}} \sin i \, di = 1 - \cos i_{\rm up}$$

The probability that HD 93250 be a spectroscopic binary with a period of less than 10 days and a secondary component earlier than B5 (i.e. a mass ratio $q = m_1/m_2 \simeq 10$) is only $\leq 7\%$. For the same

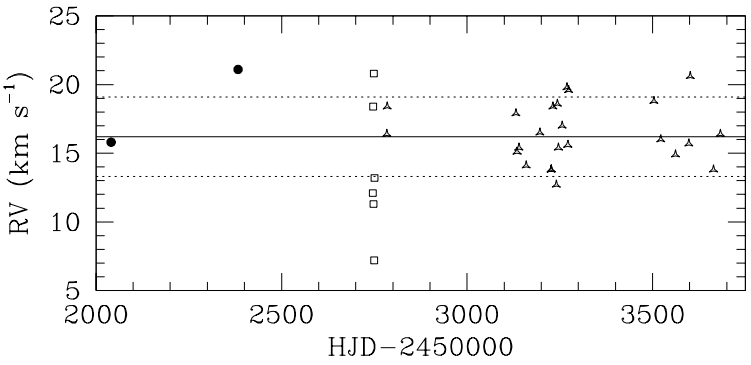

Figure 3.5: Average RVs of nine absorption lines in the spectrum of HD 168112 (see Table 3.1. The different symbols stand for different instruments: filled dots (F1.5), open squares (SPM), triangles (F2.2), see Table 3.1.

Table 3.2: Upper limits on the orbital inclination if HD 168112 were a binary for different values of e, P and q. Also indicated is the probability that i be lower than $i_{\rm lim}$ assuming a random distribution of orbital directions in space.

P	10 days			100 days			500 days			1000 days		
q	1	5	10	1	5	10	1	5	10	1	5	10
	$e = 0.0$											
$i_{\rm lim}(^\circ)$	1.4	5.2	9.8	3.1	11.2	21.4	5.3	19.3	38.7	6.7	24.7	52.0
$p(i \leq i_{\rm lim})(\%)$	0.03	0.4	1.5	0.15	1.9	6.9	0.4	5.6	22.0	0.7	9.1	38.4
	$e = 0.5$											
$i_{\rm lim}(^\circ)$	1.3	4.5	8.5	2.7	9.7	18.5	4.6	16.7	32.8	5.8	21.2	43.0
$p(i \leq i_{\rm lim})(\%)$	0.02	0.3	1.1	0.11	1.4	5.1	0.3	4.2	15.9	0.5	6.7	26.9

Table 3.3: Probability that the inclination of a putative binary system HD 93250 be lower than the upper limit estimated from Eq. (1.2) for different values of the orbital period P and the mass ratio q.

P (days)	$q = 1$	$q = 5$	$q = 10$
3	6.8×10^{-5}	8.6×10^{-4}	2.2×10^{-2}
10	1.5×10^{-4}	1.9×10^{-3}	6.9×10^{-2}

range of orbital periods, the probability that the companion be a star earlier than spectral type B2 ($q \simeq 5$) would be $\leq 0.2\%$.

3.5 A multi-wavelength study of Cyg OB2

One of the best places in our Galaxy to study non-thermal phenomena in early-type stars is certainly the Cyg OB2 association. At least three bright members of this extraordinary cluster exhibit synchrotron radio emission. To study their properties, I have initiated an *XMM-Newton* observing campaign (pro-

gramme 20045) that was performed during AO3. Four observations of an average duration of 23 ksec each were obtained with a separation of about ten days between two consecutive pointings. In parallel to this effort, ground-based optical spectroscopy was collected mostly at the 1.52 m OHP telescope and radio observations were obtained at the *VLA* by our colleagues of the Royal Observatory in Uccle.

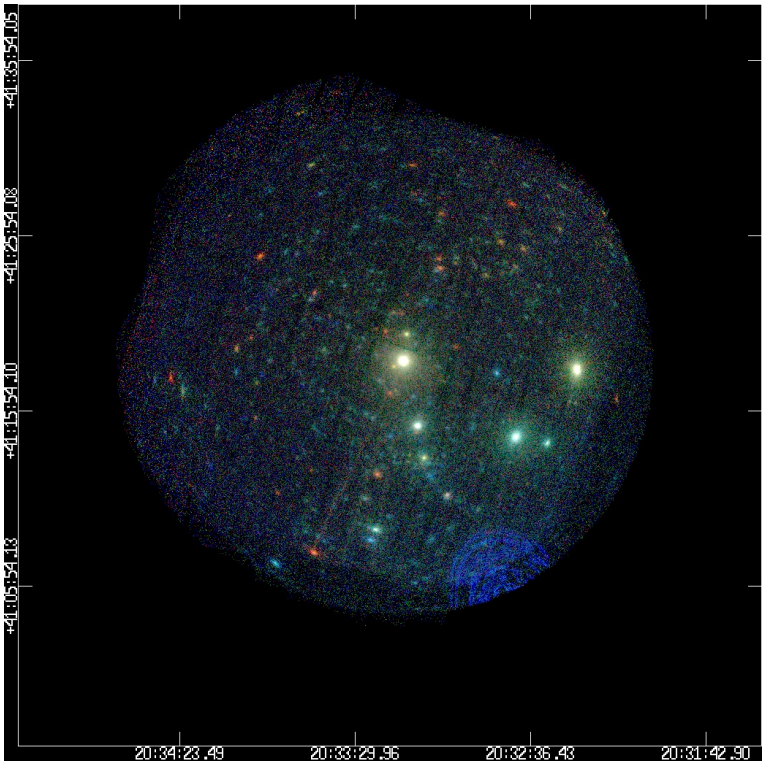

Figure 3.6: Combined three colour image of the Cyg OB2 association as seen with the *XMM-Newton* EPIC instruments in the fall of 2004. The red, green and blue colours correspond to the [0.5,1.0], [1.0,2.0] and [2.0,8.0] keV energy intervals respectively. For each energy domain, the images from the different pointings and cameras were combined into a single image that was corrected for the exposure map. The blue arcs that are seen in the lower right corner of the image are straylight features produced by singly reflected photons from Cyg X-3.

The four X-ray brightest sources in the EPIC field of view (Fig. 3.6) are stars Cyg OB2 #8a (at the centre of the image), #5, #9 and #12. The first three are known non-thermal radio sources. Many fainter secondary sources appear also on this image and they will be discussed later on in this section. Below, I summarize the results that were obtained for the stars of Cyg OB2 in the framework of this multi-wavelength campaign.

3.5.1 Cyg OB2 #8a

De Becker et al. (2004c) studied a series of 35 blue spectra of Cyg OB2 #8a (= BD$+40^\circ$ 4227) obtained with the Aurélie spectrograph at the 1.52 m telescope at OHP. The spectra revealed a clear SB2 signature notably in the He I λ 4471 line (see Fig. 3.7). The star was therefore found to be an O6 I + O5.5 III spectroscopic binary with an orbital period of 21.9 days and an eccentricity of 0.24 ± 0.04. The brightness ratio between the two stars was estimated from the ratio of the EWs of the lines of both components to

be $\simeq 2$, whilst the mass ratio was found to be $m_1/m_2 = 1.16 \pm 0.06$. The rather low minimum masses (6.4 ± 0.6 and $5.5 \pm 0.5\,\mathrm{M}_\odot$ for the primary and secondary respectively) derived from the orbital solution hint at a low orbital inclination. The comparatively short orbital period leads to another problem: is the wind-wind collision located outside the huge radio photospheres ($\geq 1000\,\mathrm{R}_\odot$ and $\geq 700\,\mathrm{R}_\odot$ for the primary and secondary respectively)? The obvious answer to that question is no, at least if the assumption of homogeneous spherically symmetric winds holds in this case. Indeed, the orbital separation is much less than the $\tau = 1$ radius at 6 cm. Even if the mass loss rates were a factor 10 lower than expected from the spectral types of the stars (if no clumping correction is applied), the orbit of the binary would still fit entirely into the radio photosphere.

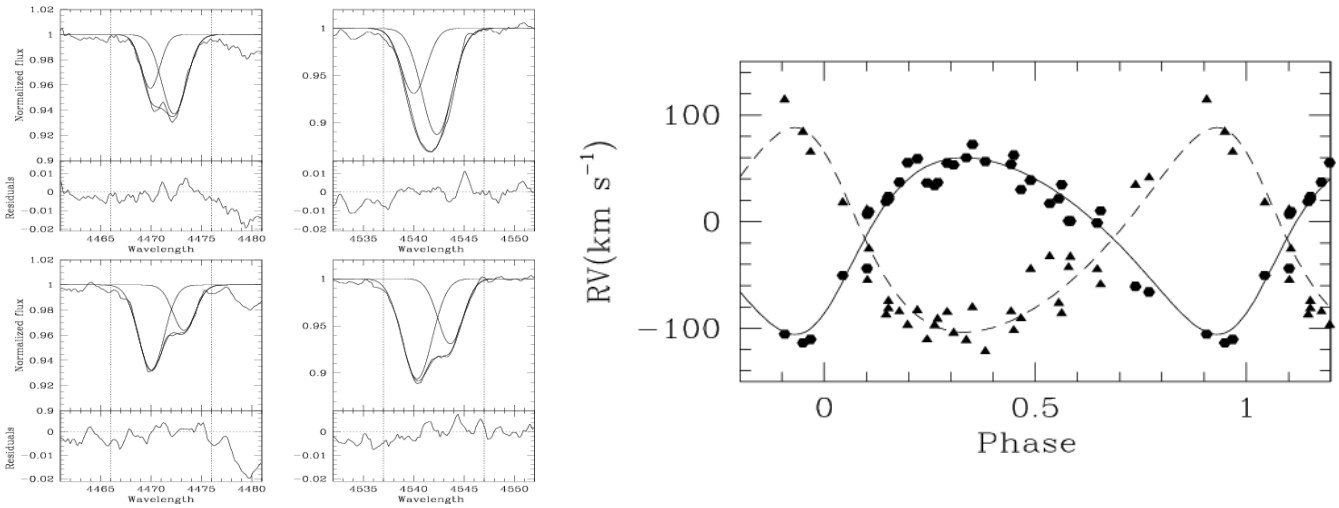

Figure 3.7: Left: Results of the fit of two Gaussians to the He I λ4471 and He II λ4542 lines at opposite quadrature phases ($\phi = 0.307$ and 0.907 for the upper and lower panels respectively).The individual components are overplotted and residuals of the fit (performed over the wavelength range limited by the dashed vertical lines) are shown below the profiles. Right: Radial velocity curve of Cyg OB2 #8a for an orbital period of 21.908 days. The hexagons and triangles stand for the primary and secondary RVs respectively. From De Becker et al. (2004c).

Table 3.4: Orbital parameters of Cyg OB2 #8a from De Becker et al. (2004c).

	Primary	Secondary
P(days)	21.908	
e	0.24 ± 0.04	
T_0(HJD)	2451807.139 ± 0.894	
$\omega(^\circ)$	220 ± 12	
γ (km s^{-1})	-8.1 ± 3.3	-25.0 ± 3.6
K (km s^{-1})	82.8 ± 3.5	95.8 ± 4.0
$a \sin i$ ($\mathrm{R}_\odot$)	34.8 ± 1.5	40.3 ± 1.7
$q = m_1/m_2$	1.16 ± 0.06	
$m \sin^3 i$ ($\mathrm{M}_\odot$)	6.4 ± 0.6	5.5 ± 0.5
$\mathrm{R_{RL}} \sin i$ ($\mathrm{R}_\odot$)	13.6 ± 0.2	14.8 ± 0.2

De Becker et al. (2006b) analysed the four AO3 *XMM-Newton* observations of Cyg OB2 #8a. The

EPIC spectra were modelled using an absorbed three temperature `mekal` model. The X-ray luminosity was found to be $1.02 - 1.45 \times 10^{34}$ erg s^{-1}, i.e. exceeding by a factor 19 – 28 the level of intrinsic emission estimated from the empirical canonical relation proposed by Sana et al. (2006b). The best fit temperatures of the Cyg OB2 #8a EPIC spectra were found to be ~ 0.25, ~ 0.85 and 1.6 – 2.0 keV. The strong Fe Kα line near 6.7 keV indicates that the hard emission is of thermal origin rather than being of non-thermal nature. A fit of the RGS spectrum also confirms the existence of a bremsstrahlung continuum with a temperature of order 1.9 keV. The observed X-ray flux of the star was found to vary by about 20%. Using simultaneously the new *XMM-Newton* data with archive *ASCA*-SIS and *ROSAT*-PSPC data, De Becker et al. (2006b) confirmed that the modulation of the observed X-ray flux is phase-locked. The system displays a decrease of its X-ray flux between apastron and periastron which is most obvious in the hard (2.0 – 10.0 keV) energy band. The lower kT and the lower emission level near periastron ($\phi = 0.0$) were interpreted as evidence for a lower pre-shock velocity at periastron. Generally speaking, the variations are probably due to a combination between a varying circumstellar wind absorption (due to the changing orientation of the line of sight as a function of orbital phase) and the varying separation between the stars.

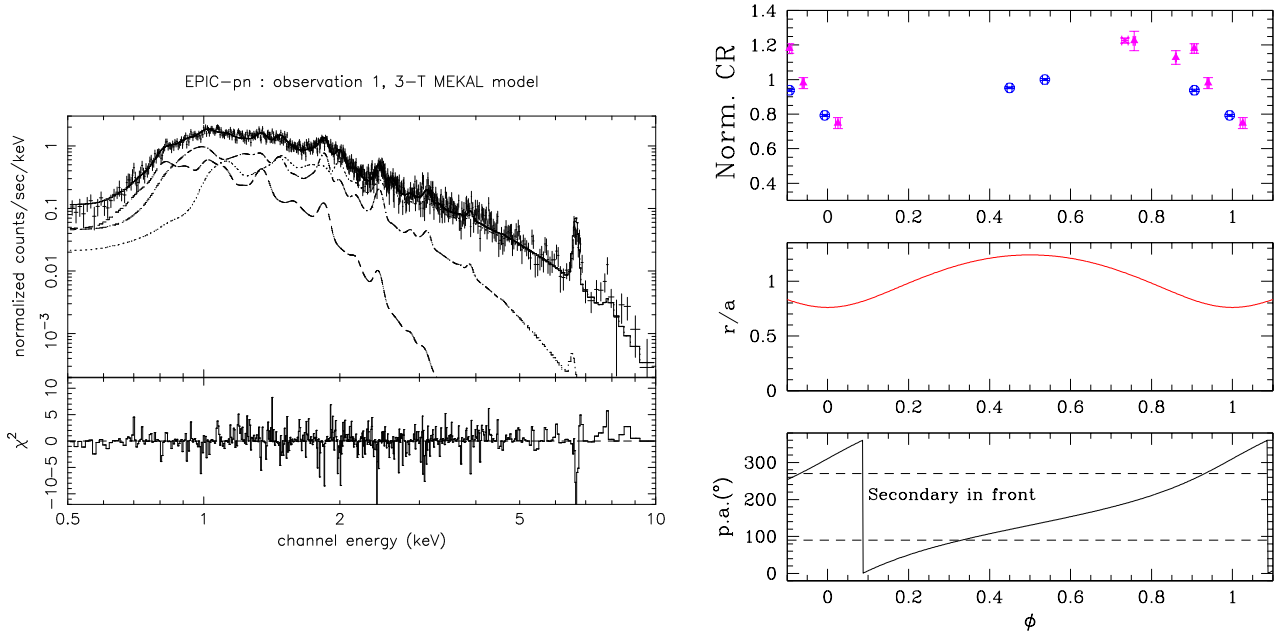

Figure 3.8: Left: EPIC spectra of Cyg OB2 #8a as observed on 29 October 2004. The data were fitted with an absorbed 3-T optically-thin thermal plasma model with temperatures of about 3, 9 and 20 MK. Right: the top panel shows the X-ray light curve of Cyg OB2 #8a. The circles, the triangles and the cross correspond respectively to *XMM-Newton*, *ROSAT* and *ASCA* data. The middle panel shows the variation with orbital phase of the separation between the two stars in this eccentric system. The lower panel shows the position angle (p.a. = 0° corresponding to the primary star being in front). The secondary star is in front between phases 0.3 and 0.95 (see De Becker et al. 2006b).

The 6 cm *VLA* data, that our team collected in coordination with the X-ray data, also display a phase-locked modulation as can be seen on the light curve presented by Blomme (2005, see Fig. 3.9). Obviously, the properties of this light curve cannot be explained by the changing optical depth along the line of sight: in fact both stars should have rather similar mass loss rates and wind densities and the maximum

emission actually occurs at a phase when the star with the slightly denser wind is in front. It seems much more likely that in this case, a variation of the intrinsic synchrotron radio emission produced by the wind interaction as a function of orbital separation plays a role.
All these properties make Cyg OB2 #8a a unique system to study the physics of wind interactions and particle acceleration. In fact, a similar combination of X-ray and radio properties is only found for the long period (8 yrs) Wolf-Rayet binary WR 140. However, with its much shorter orbital period, Cyg OB2 #8a is certainly a much easier target for such a study.

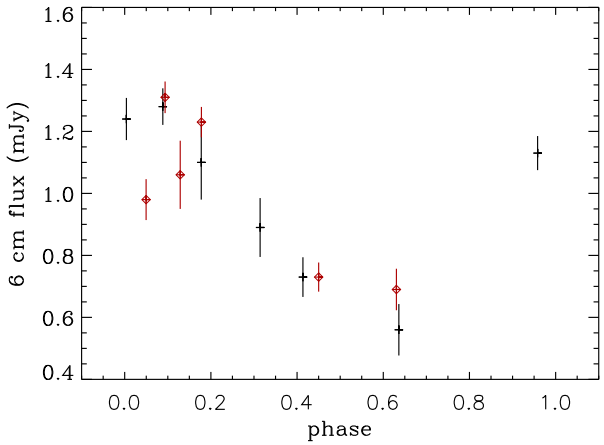

Figure 3.9: *VLA* radio light curve at 6 cm of Cyg OB2 #8a. From Blomme (2005).

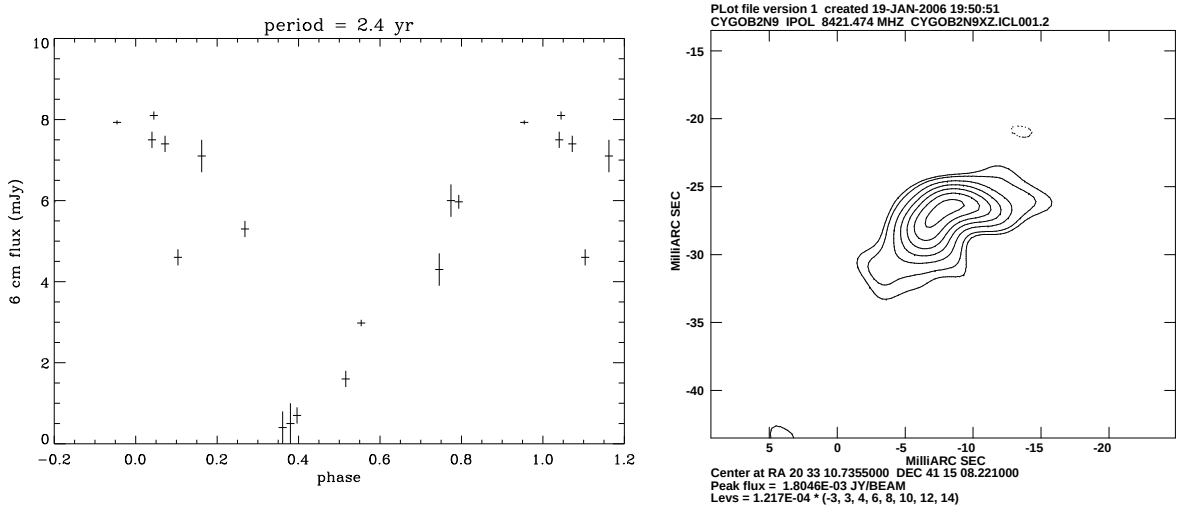

Figure 3.10: Left: 6 cm *VLA* radio light curve of Cyg OB2 #9 folded with a period of 2.4 yrs (from Van Loo 2005). Right: *VLBA* image of Cyg OB2 #9 as obtained in November 2005. The shape of the source suggests a bow-shock due to a wind-wind collision (courtesy Dr. Sean Dougherty, private communication).

3.5.2 Cyg OB2 #9

This is probably one of the most mysterious O-type stars displaying a non-thermal radio emission. De Becker (2005) studied a series of 20 spectra of Cyg OB2 #9 centered on the Hα line, finding only low

level line profile variability and no indication of significant radial velocity variations on time scales of a few months or a year. The radio emission is clearly variable, both in flux and spectral index. Arguing that synchrotron emission from wind-embedded shocks cannot account for the observed properties of the radio emission, Van Loo (2005) rather proposed a binary scenario. From an analysis of archive radio observations, he derived a most likely period of 2.4 yrs for the variability (see Fig. 3.10).

Following this result, the GAPHE and Royal Observatory teams took part in a *VLBA* proposal led by Dr. Sean Dougherty. The idea was to resolve the bow-shock of the colliding wind interaction inside Cyg OB2 #9. The project was accepted and the star was observed in November 2005 (see Fig. 3.10). The radio emission was indeed resolved and the morphology is very much reminiscent of that of the wind-wind interaction zone in WR 140. The ultimate proof of the colliding wind origin of this emission is however still missing. We have therefore submitted another *VLBA* proposal to re-observe the system and check that the emitting region is indeed rotating as the stars in this putative binary system orbit around each other.

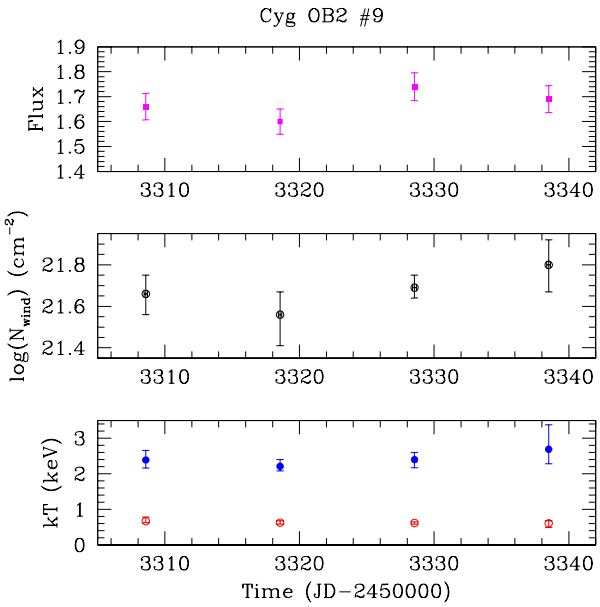

Figure 3.11: Variations of the best fit parameters of the 2-T thermal plasma model fitted to the EPIC spectra of Cyg OB2 #9. The observed flux in the 0.4 – 10 keV energy range is given in units of 10^{-12} erg cm^{-2} s^{-1}.

Evidence for multiplicity is also coming from the same X-ray data as for Cyg OB2 #8a. In fact, while the EPIC spectra are rather well fitted by a 2-T optically thin thermal plasma model, the best fitting parameters (especially the temperature) are unusual for a single O-type star. No significant changes of the fluxes were found over the time interval of the *XMM-Newton* campaign (see Fig. 3.11). Note that if the orbital period were indeed 2.4 yrs, no variations of the X-ray flux would be expected over a one month interval.

Some more results of the (ongoing) analysis of the *XMM-Newton* observations of Cyg OB2 are given below in the proceedings paper of the JENAM 2005 workshop by Rauw et al. (2005b).

XMM-Newton observations of the Cyg OB2 association*

Gregor Rauw†, Michaël De Becker and Natacha Linder

Institut d'Astrophysique, Université de Liège, Belgium

Abstract: We present the first results of an observing campaign of the Cyg OB2 association with the *XMM-Newton* observatory. The brightest OB-type stars exhibit rather hard spectra suggesting that at least part of their X-ray emission arises in a wind-wind interaction. The EPIC images reveal a large number of fainter X-ray sources most of which are probably low-mass pre-main sequence stars belonging to Cyg OB2.

1 Introduction

The Cyg OB2 association is one of the richest and most massive young open clusters known in our Galaxy. These properties make it an ideal target for observations over a broad range of wavelengths from the radio to the γ-ray domain. Optical studies (e.g. Massey & Thompson 1991) are hampered by the heavy and patchy absorption by dense molecular clouds. A far more complete census of the cluster population can be obtained in the near infrared: Knödlseder (2000) analysed 2MASS data of Cyg OB2 finding that the cluster probably harbours about 2600 ± 400 OB stars among which 120 ± 20 O-stars. He accordingly suggested that Cyg OB2 could be a young globular cluster. Four cluster members have been extensively studied in the radio domain. Three of them are non-thermal radio emitters (Cyg OB2 #5, #8a and #9, see e.g. Waldron et al. 1998 and references therein), whilst the fourth one (Cyg OB2 #12) could be one of the most luminous stars in our Galaxy. At the other end of the electromagnetic spectrum, the error box of the unidentified *EGRET* γ-ray source 3EG J2033+4118 overlaps to a large extent with the cluster (Romero et al. 1999, Rauw 2004). Finally, X-ray emission from Cyg OB2 was discovered serendipitously when *EINSTEIN* was pointed at Cyg X-3 (Harnden et al. 1979). This was actually the first report of X-ray emission from OB stars. Since then, Cyg OB2 has been observed by every major X-ray satellite.

Here, we present the very first results of an observing campaign with the EPIC instruments onboard *XMM-Newton*.

*Based on observations with *XMM-Newton*, an ESA Science Mission with instruments and contributions directly funded by ESA Member states and the USA (NASA).

†Research Associate FNRS (Belgium)

"Massive Stars and High Energy Emission in OB Associations"; Proc. JENAM 2005 *Distant Worlds*, Liège (Belgium), eds. Rauw et al., p. 103-106

2 *XMM-Newton* observations of Cyg OB2

Four pointings centered on Cyg OB2 #8a and separated by 10 days each were obtained in October - November 2004. The raw data were processed with SAS version 6.0. After rejecting some bad time intervals affected by high background events (so-called soft-proton flares), the remaining total exposure time was 75 ksec. A few stray-light features (due to singly reflected photons) from Cyg X-3 are visible in the lower right corner of the images. However, they do not affect the most interesting part of the field of view. The SAS routines detected a total of 221 sources in the combined EPIC images (outside the region affected by the stray-light) with fluxes down to 2×10^{-14} erg cm^{-2} s^{-1}. The EPIC spectra of the brightest X-ray sources were analysed with the `xspec` software. The spectra and the light curve of Cyg OB2 #8a are discussed by De Becker & Rauw (these proceedings) and we will not repeat this analysis here.

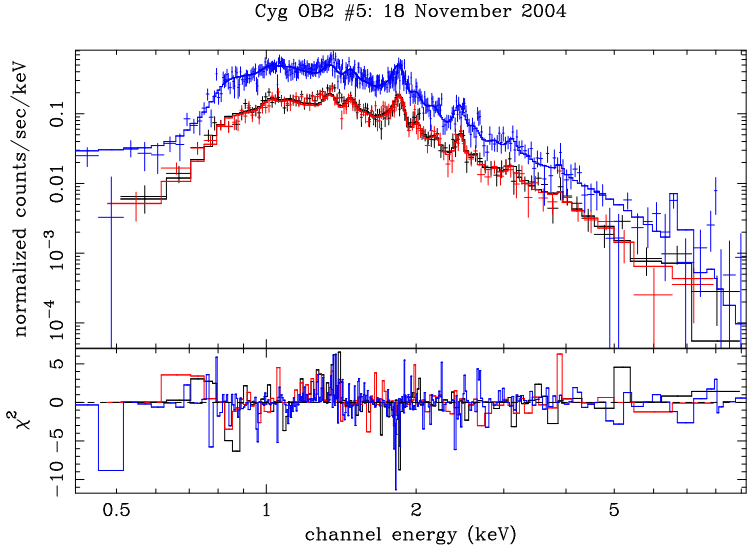

Figure 1: EPIC spectra of Cyg OB2 #5 as observed on 18 November 2004. The data were fitted with an absorbed two temperature optically-thin thermal plasma model (see text).

2.1 Cyg OB2 #5

Cyg OB2 #5 (= BD+40° 4220) is in fact a multiple system consisting (at least) of a short-period colliding wind binary (O6-7 Ia + Ofpe/WN9, Rauw et al. 1999) and a third visual component (most probably a B star, Contreras et al. 1997). The EPIC spectra of this source are well fitted with an absorbed two-temperature thermal plasma model (Fig. 1). In addition to the absorption by the neutral interstellar medium, we included a wind absorption model computed following the technique of Nazé et al. (2004). While the lower temperature of the fit ($kT_1 = 0.63 \pm 0.01$ keV) is quite typical of the intrinsic X-ray emission of early-type stars, the second component is much hotter ($kT_2 = 1.7 \pm 0.2$ keV) and arises most probably in a wind interaction zone. In fact, this multiple system most probably harbours several potential wind-wind collision regions. Unfortunately, the four observations of this system do not provide a good coverage of the 6.6 day orbital period of the close binary system, so that we presently cannot make any statement about the existence or absence of a phase-locked variability.

2.2 Cyg OB2 #9

This O5 If star is a variable non-thermal radio emitter (see also the contributions by Van Loo and by Blomme in these proceedings). Although the non-thermal emission is strongly believed to arise in a wind interaction zone, no spectroscopic evidence for binarity has been reported so far. As for Cyg OB2 #5 , the EPIC spectra are rather well fitted by an absorbed 2-T thermal plasma model (see Fig. 2). While the lower temperature ($kT_1 = 0.63 \pm 0.03$ keV) is again rather typical for O-type stars, the second temperature reaches $kT_2 = 2.4$ keV which corresponds by far to the hottest plasma in the O-type stars of Cyg OB2. This feature is quite consistent with a colliding wind scenario in a binary system where the winds reach their terminal velocities before they collide.

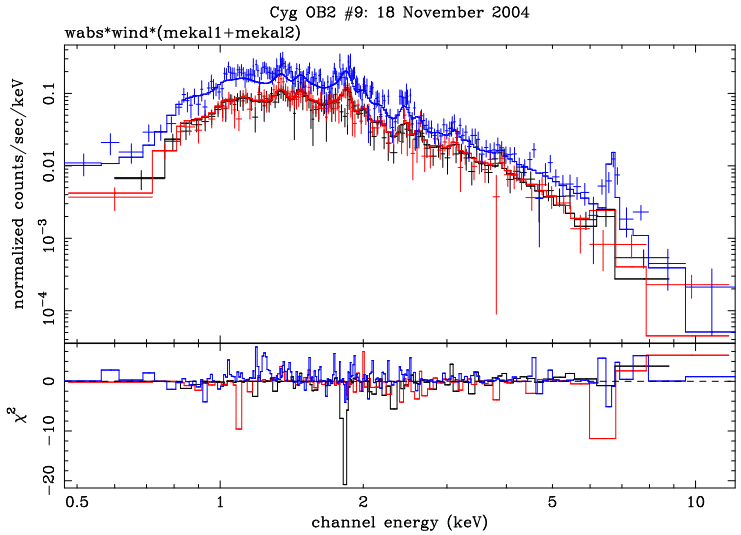

Figure 2: Same as Fig. 1 but for Cyg OB2 #9. Note the prominent Fe K line at 6.6 keV.

2.3 Cyg OB2 #12

The spectral type of this star is rather ill-defined and is probably variable. However, most investigations agree that Cyg OB2 #12 is an extremely luminous B supergiant that could be related to the LBV phenomenon. The EPIC spectra are well fitted with a thermal plasma model with $kT_1 = 0.73 \pm 0.16$ and $kT_2 = 1.8 \pm 0.4$ keV. The latter temperature is surprisingly high given the fact that the wind of the star is rather slow ($\sim 150\,\mathrm{km\,s^{-1}}$, Klochkova & Chentsov 2004). Kolchkova & Chentsov presented evidence for a line radial velocity gradient that they interpreted as an indication for infall of matter. However, even assuming head-on collisions of two flows, each at a velocity of $150\,\mathrm{km\,s^{-1}}$, the post-shock temperature would not be sufficient to account for the hard X-ray spectrum. Therefore, the most likely scenario seems again to be a colliding wind binary where the wind of the companion would have to be much faster.

2.4 Secondary sources

We have cross-correlated the positions of our 221 X-ray sources with the 2MASS point source catalogue. We found near-IR counterparts for 185 of them. Among these, there are 15 known

O-type stars. Beside these early-type objects, most X-ray sources have rather faint near-IR counterparts ($K > 11$). Their location in a ($J - K$, K) colour-magnitude diagram (Fig. 3) suggests that they actually belong to Cyg OB2 and could be low-mass pre-main sequence stars. This latter interpretation is also supported by the flaring activity of some of these secondary sources. Evidence for an active star formation process in Cyg OB2 was already reported based on *IRAS* observations (e.g. Parthasarathy et al. 1992). The *XMM-Newton* results will help to shed more light on the star formation history of this extremely interesting cluster.

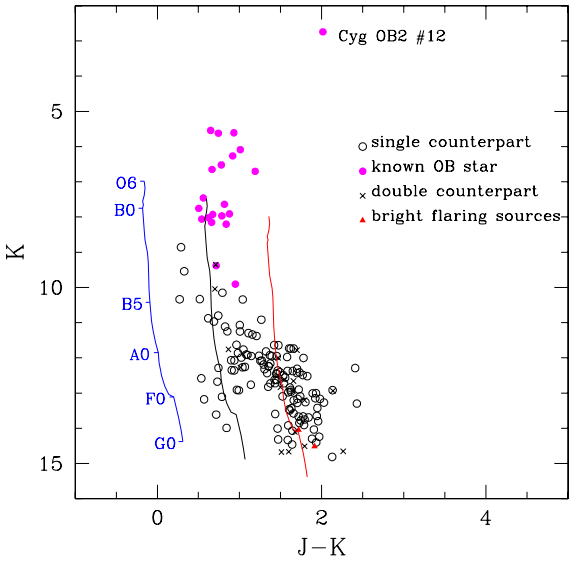

Figure 3: Near-IR colour-magnitude diagram of the 2MASS counterparts of the X-ray sources in Cyg OB2. The location of the main-sequence is shown for three different values of the reddening: from left to right, $A_V = 0$, 5 and 10 mag.

Acknowledgements

This research is supported in part by contract P5/36 IAP (Belspo) and through the XMM/INTEGRAL PRODEX contract.

References

Contreras M.E., Rodríguez L.F., Tapia M., et al., 1997, ApJ, 488, L153
Harnden F.R.Jr., Branduardi G., Elvis M., et al., 1979, ApJ, 234, L51
Knödlseder J., 2000, A&A, 360, 539
Kolchkova V.G., Chentsov E.L., 2004, Astronomy Reports, 48, 1005
Massey P., Thompson A.B., 1991, AJ, 101, 1408
Nazé Y., Rauw G., Vreux J.-M., De Becker M., 2004, A&A, 417, 667
Parthasarathy M., Jain S.K., Bhatt H.C., 1992, A&A, 266, 202
Rauw G., 2004, in *Cosmic Gamma-Ray Sources*, eds. K.S. Cheng & G. Romero, ASSL 304, 105
Rauw G., Vreux J.-M., Bohannan B., 1999, ApJ, 517, 416
Romero G.E., Benaglia P., Torres D.F., 1999, A&A, 348, 868
Waldron W.L., Corcoran M.F., Drake S.A., Smale, A.P., 1998, ApJS, 118, 217

3.6 Conclusions on non-thermal phenomena in early-type stars

The main results of this chapter can be summarized as follows:

- There is no clear detection to date of a high-energy counterpart of the synchrotron radio emission of early-type stars over the energy range of the current generation X-ray telescopes. Furthermore, a 2 Msec *INTEGRAL* observation of the Cygnus region failed to detect hard X-rays or soft γ-rays from the Cyg OB2 association (De Becker 2005). In a few cases (η Car+WR 25 and WR 115) such an emission has possibly been detected (Leyder 2006), but these objects are not known as non-thermal radio emitters and, in the case of WR 115, there is no information available about the multiplicity. Current hard X-ray and γ-ray instruments apparently lack the sensitivity to detect the emission at the level that is expected from theoretical models. At the higher energy end, *GLAST* will bring strong constraints on the position and fluxes of *EGRET* sources that have been tentatively associated with massive stars. In the meantime, to explain the lack of a clear correlation between synchrotron emission and non-thermal X-rays, De Becker et al. (2005) suggested that only long period binaries with a wide separation can show a detectable synchrotron radio emission. However, these binaries would probably not show a detectable inverse Compton high-energy emission, since the hard thermal emission from the colliding wind region should dominate the power law component at energies between a few keV and 10 keV. In addition, the dilution of the photospheric UV radiation in a wide binary system reduces the efficiency of the inverse Compton scattering mechanism. Further theoretical arguments for the lack of simultaneous detections of non-thermal radio and high-energy emissions were given by Pittard et al. (2006). These authors noted that although the intrinsic synchrotron radio emission should increase when the orbital separation decreases, this increase will be more than compensated by the more efficient inverse Compton cooling, the much increased free-free absorption and the increased Razin effect. All these effects taken together imply that no synchrotron radio emission should be observable from a short period colliding wind system.

- While we have shown that 9 Sgr and Cyg OB2 #8a are binary systems, our optical spectroscopic campaigns failed to reveal clear indications for multiplicity of HD 168112, HD 93250 and Cyg OB2 #9. These objects thus challenge the currently favoured explanation of a colliding wind origin of the relativistic electrons. The reason could be that their orbital periods are quite long and their orbital inclinations quite low. For Cyg OB2 #9, the GAPHE team has therefore initiated a long-term radial velocity monitoring campaign together with Italian colleagues at the Asiago observatory (P.I. Y. Nazé). For HD 168112 and HD 167971, the GAPHE team is exploring the possibilities of current and future *VLTI* instruments to resolve the binary components and thus establish the multiplicity of these stars (P.I. M. De Becker). Together with the results of the spectroscopic monitoring described above, these observations will provide crucial tests for our current understanding of non-thermal phenomena in the winds of massive stars. So far, on observational grounds, the possibility that some of the synchrotron radio emitting O-stars might be single cannot be fully discarded.

- The orbital period of Cyg OB2 #8a is surprisingly short, implying a rather small orbital separation. Based on the classical argumentation of the radio opacity of the winds of its components, one would not expect to detect any observable synchrotron emission from this system. The clear detection of such an emission is therefore puzzling. Could this be the result of a porous wind consisting of optically thick clumps? Such a scenario might help to solve this issue, but would also imply that the statement that synchrotron radio emission has to come from the outer regions of the wind does

not hold in all cases. Therefore, one of the major arguments against single O-type stars being non-thermal radio emitters would break down. To attempt to answer this question, it is crucial to obtain radio light curves of Cyg OB2 #8a at different wavelength. The variations at longer wavelength will help us to set constraints on the size of the radio photosphere as a function of wavelength, therefore telling us whether the winds are porous (producing an essentially grey opacity) or not (in this latter case, one would expect a strong wavelength dependence of the wind opacity).

- Finally, relativistic particles might be ubiquitous in colliding wind binaries, including systems that are not known to be non-thermal radio emitters. The presence of such particles could significantly alter the properties of the shocks and hence account for some of the discrepancies between theoretical models of the X-ray emission from colliding wind binaries on the one hand and actual observations on the other hand.

Chapter 4

O-type stars with non-spherical winds?

There are more things in heaven and earth, Horatio,
Than are dreamt of in your philosophy.

William Shakespeare, *Hamlet*

4.1 Introduction

State of the art model-atmosphere codes for early-type stars usually rely on the assumption that the stellar winds of stars of spectral types O and Wolf-Rayet are essentially spherically symmetric. However, over the last decades, detailed monitoring of a number of these stars led to the discovery of a significant variability in their spectra and/or photometry. Here, one has to distinguish between those variations occurring at the level of the photosphere (such as absorption line profile variability arising from non radial pulsations, e.g. Kambe et al. 1997) and modulations rooted in the stellar wind. It is the latter category that is at the focus of this chapter. On the one hand, some of this variability most probably stems from the intrinsic instabilities of line-driven stellar winds that produce stochastic small scale structures (e.g. Dessart 2004). However, individual clumps generated by these instabilities are believed to be comparatively small and are thus not expected to lead to a substantial and systematic deviation from a spherical wind geometry. On the other hand, in some cases, recurrent spectroscopic modulations occur on time scales consistent with the stellar rotational period (e.g. Fullerton 1999). The latter feature is usually explained in terms of large scale corotating structures in the stellar wind.
The origin of such large scale structures is however uncertain. Several scenarios have been proposed, such as non-radial pulsations that induce a perturbation at the base of the wind or magnetic fields. For instance, the peculiar O5.5 Vp star θ^1 Ori C displays a periodic modulation of its spectral lines (including the Hα emission and UV P-Cygni profiles, Stahl et al. 1996) as well as of its X-ray emission (Gagné et al. 2005). This behaviour was interpreted in terms of an oblique magnetic rotator model, where the magnetic field of the star funnels the stellar wind from both hemispheres towards the magnetic equator where the material piles up and forms a magnetically confined wind. Indeed a bipolar magnetic field of ~ 1000 G has been detected for θ^1 Ori C through spectro-polarimetric measurements (Donati et al. 2002).
Because of the prominence of wind features (such as resonance lines) in the ultraviolet, many studies of the variability of stellar winds were actually perfomed with the high-resolution spectrographs onboard

the *International Ultraviolet Explorer*. *IUE* observations revealed that OB stars often display so-called *Discrete Absorption Components* (DACs) in the absorption components of their P-Cygni profiles. These DACs were found to migrate from lower to higher velocities. Intensive monitoring campaigns of some specific objects with *IUE* showed that DACs as well as modulations of the overall intensity of the absorption troughs of P-Cygni profiles also occur with "periodicities" that could be linked to the stellar rotation period (e.g. Fullerton et al. 1997). This led to the concept of *corotating interaction regions*, where it is assumed that a faster outflow from some part of the surface of a rotating star collides with a slower outflow from other parts, thereby leading to the formation of a sort of higher density spiral feature that rotates with the star and could modulate the line of sight opacity towards the star (e.g. Cranmer & Owocki 1996, Owocki 1999 and references therein).
Since neither *IUE* nor any other equivalent UV space observatory are available anymore, intensive spectroscopic monitoring to characterize the variability must nowadays be done in the optical domain. Obviously the success of such an endeavour depends upon the quality of the spectroscopic time series that is obtained. This either requires multi-site campaigns (to fill part of the daily gaps) or long-term programs from a single observatory. Both approaches can become rather frustrating when it comes down to coordinate the schedules of several observatories or to convince the time allocation committees that yet another observing run is needed to complete the study. Still, such projects are certainly worth the effort since our current understanding of stellar wind variability relies on a rather small number of well-studied cases that are considered as 'prototypes'.
In this chapter, I present the results obtained from the optical monitoring of a sample of O stars for which the overall aspect of the spectrum suggests that the geometry of the stellar wind might actually deviate from spherical symmetry.

4.2 Periodic modulations of the wind of HD 192639

In this section, I reproduce two papers that report the results of an intensive monitoring campaign of the O(f) supergiant HD 192639 (Rauw & Vreux 1998, Rauw et al. 2001a).
This campaign led to the discovery of a modulation of the He II λ4686 and the Hα lines on time scales of a few days. The He II λ4686 line displays strong variability, changing from a P-Cygni profile with a double-peaked emission component to a pure blue-shifted emission line. The variability of most of the absorption lines is shown to be correlated with the deformation of the He II λ4686 line. A Fourier analysis of the time-series reveals a recurrent variability with a "period" of roughly 4.8 days. This cyclic modulation is most visible in the absorption components of the He II λ4686 and Hα P-Cygni profiles, but it is also found in the blue wing of several absorption lines (e.g. Hβ) as well as in the double-peaked He II λ4686 and Hα emission components. It is suggested that this phenomenon stems from a periodic modulation of the amount of stellar wind material along the line of sight towards the stellar photosphere. The most likely explanation for the 4.8-day modulation is that this cycle reflects the stellar rotational period (or half this period). The most important observational properties can probably be explained - at least qualitatively - by a corotating interaction region or a tilted confined corotating wind.

Astron. Astrophys. 335, 995–1002 (1998)

ASTRONOMY AND ASTROPHYSICS

Line profile variability in the spectrum of the O(f) supergiant HD 192639⋆

G. Rauw and J.-M. Vreux

Institut d'Astrophysique et de Géophysique, Université de Liège, 5, Avenue de Cointe, B-4000 Liège, Belgium

Received 16 January 1998 / Accepted 16 March 1998

Abstract. We report the results of a medium-resolution spectroscopic investigation of the O(f) supergiant HD 192639. Particular attention is paid to the He II λ 4686 line. This line displays strong profile variability on time scales of a few days, changing from a P-Cygni profile with a double-peaked emission component to a pure blue-shifted emission line. It appears that the variability of most of the absorption lines present in our spectra is correlated to the deformation of the He II λ 4686 line and arises probably from a large scale structure in the low-velocity part of the stellar wind rather than from a photospheric phenomenon. We find that the time scale of the variability could be consistent with the estimated rotational period of HD 192639.

Key words: line: profiles – stars: early-type – stars: mass loss – stars: individual: HD 192639 – stars: variables: other – supergiants

1. Introduction

Spectroscopic variability in the optical and ultraviolet wavebands is a widely observed characteristic of early-type stars. However, in most cases, the underlying mechanisms are still rather ill-defined. Only an extensive spectroscopic investigation allows to derive constraints on the time scales and the properties of these variations. The typical time scales range from a few hours to several days (e.g. Fullerton et al. 1996, Kaper et al. 1996, 1997). One of the most controversial issues is the connection between the variability at the photospheric level and in the stellar wind. In some stars, the line profile variability of photospheric absorption lines is attributed to pulsations (e.g. Kambe et al. 1997), whereas Kaper et al. (1997) suggest that a stellar magnetic field may be an essential ingredient for controlling wind variability.

In the present paper, we focus our attention on HD 192639, a rather poorly studied member of the Cyg OB1 association. On the basis of eye inspection of photographic spectra, Walborn (1972) assigned a spectral type O7 Ib (f) to this star; the tag (f) in this classification scheme indicates that the N III $\lambda\lambda$ 4634-41 lines are clearly seen in emission whereas the He II λ 4686 line is seen neither clearly in emission nor in absorption. Using quantitative criteria, namely the ratio of the equivalent widths of selected lines, Conti & Alschuler (1971) assigned a spectral type O7.5 III f to HD 192639. More recently, using the same quantitative criterion on her spectra, Underhill (1995a) derived an O8 spectral type instead of O7 or O7.5. On the basis of the Stark broadening of the He II lines, Underhill (1995b) further assigned a supergiant luminosity class to HD 192639, leading to a O8 I f classification.

In the HR-diagram of the Cyg OB1 association HD 192639 lies at a position typical for a blue straggler, i.e. beyond the turnoff point of the association and in the vicinity of the continuation of the ZAMS (Mathys 1987). The spectrum of HD 192639 shows some indication for the presence of CNO processed material at the surface of the star. In fact, Schild & Berthet (1986) found that the C/N abundance ratio is smaller in HD 192639 than in HD 193514, another member of the Cyg OB1 association with a similar spectral type. Herrero et al. (1992) also derived a slightly enhanced helium abundance in the spectrum of HD 192639.

Variability of the emission lines in the spectrum of HD 192639 has already been reported on various occasions (Mannino & Humblet 1955, Underhill 1995a). Underhill (1995a) noticed line profile variability over a few days in the Hα and He II λ 4686 emission lines. Fullerton et al. (1996) discovered the existence of line profile variability in the C IV $\lambda\lambda$ 5801, 5812 absorption lines and in the He I λ 5876 P-Cygni profile over an interval of about seven days. Finally, in the near infrared, Andrillat & Vreux (1979) reported the variability of the He I λ 10830 emission line, also on a time scale of a few days.

2. Observations and data reduction

A first snapshot spectrum of HD 192639, covering the wavelength range 4530 - 4720 Å, was taken in July 1995 (JD 2449913.54) with the Carelec spectrograph attached to the 1.93 m telescope of the Observatoire de Haute-Provence. The spectrum was obtained in the second order with a 1200 lines/mm grating blazed at 7500 Å, providing a reciprocal dispersion of

Send offprint requests to: G. Rauw

⋆ Based on observations collected at the Observatoire de Haute Provence, France.

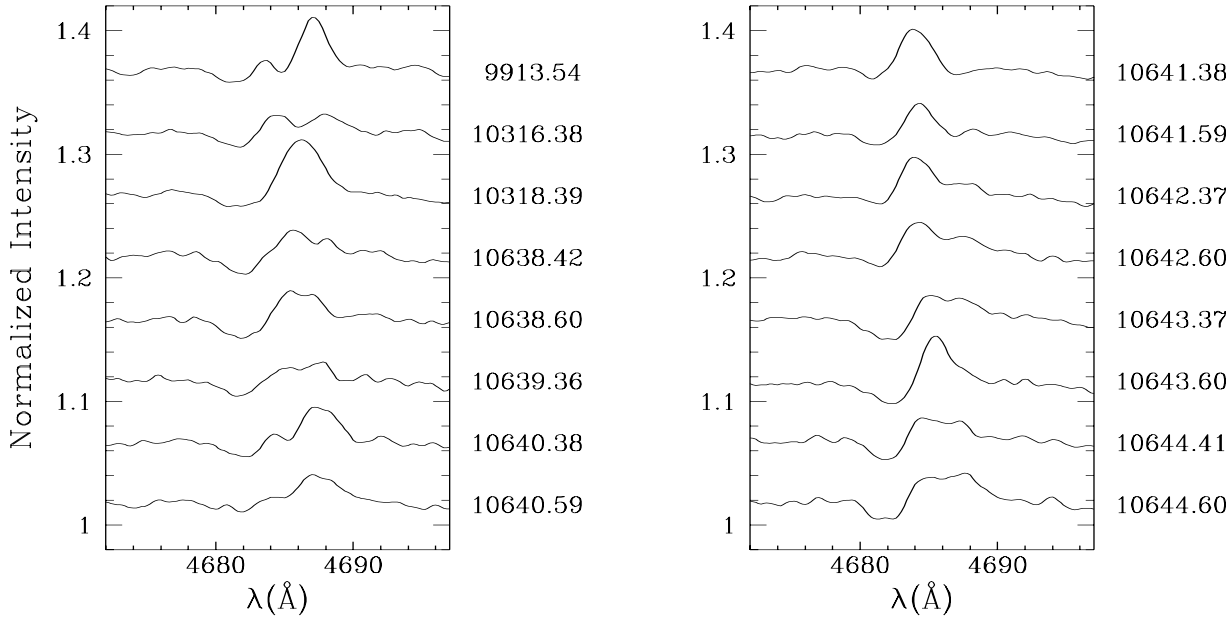

Fig. 1. Examples of the variability of the He II λ4686 line profile in the normalized spectrum of HD 192639 as a function of time. The different spectra are shifted vertically by 0.05 units. The epochs of the observation (JD-2440000) are indicated on the right side of each spectrum.

17 Å/mm. The detector was a Tektronix TK512 CCD with a pixel size of 27μm. The spectral resolution as derived from the FWHM of the lines in the NeAr calibration exposures is $\sim$ 1.0 Å.

A more extensive set of spectroscopic observations of HD 192639 was secured during two observing campaigns in August 1996 and July 1997 with the Aurélie spectrograph (Gillet et al. 1994) fed by the 1.52 m telescope of the Observatoire de Haute-Provence. The data were obtained with a 300 lines/mm grating blazed at 6000 Å providing a reciprocal dispersion of 33 Å/mm over a wavelength range from 4100 to 4950 Å. The detector was a Thomson TH7832 linear array with a pixel size of 13 μm. Two spectra were taken in 1996 (JD 2450316.38, 2450318.39), while a total of 25 spectra of HD 192639 were obtained over seven nights in 1997 (JD 2450638.42 – 2450644.60). The mean exposure time was 30 minutes and the mean S/N ratio in the continuum of the raw spectra is $\sim$ 200. Comparison exposures of a ThAr lamp were taken for each stellar spectrum. The spectral resolution as derived from the FWHM of the calibration lines is $\sim$ 1.2 Å.

All the data were reduced in the standard way using the MIDAS software developed at ESO.

The spectra were normalized using properly chosen continuum windows. As for many Of stars, there is a broad emission bump between λ4600 and λ4700 in the spectrum of HD 192639. The normalized line profiles shown in Figs. 1 and 3 therefore include a weak contribution from this underlying emission feature.

3. Results

3.1. The He II *λ4686 line*

The profile variability of this line is illustrated in Fig. 1. We notice different kinds of P-Cygni profiles. On several occasions, we can see a double peaked emission with varying intensities of the components. Sometimes both have the same intensity (e.g. JD 2450316.38, 2450638.60,...). On other spectra either the red component (e.g. JD 2449913.54, 2450640.38,...), or the blue component (e.g. JD 2450642.37) is the dominant one. Normal P-Cygni profiles are also observed (e.g. JD 2450318.39, 2450643.60). On the spectra taken during the night JD 2450641, we observe a blue-shifted emission line with weak absorption components on both sides. An even more extreme blueward excursion of the emission component was observed by Underhill (1995a) on 1991 September 24. At that time, the profile consisted of a weak broad emission feature with a very weak absorption component on the longward edge.

We have measured the equivalent widths of the absorption and the emission components of the line. The EWs of the entire profile display some variability, during each night and from night to night. In July 1997, the maximum total EW is observed around JD 2450642.5.

Fig. 2a displays the variability of the equivalent width of the absorption component. This measurement includes the very weak red absorption component that appears when the emission line reaches its most negative radial velocity. One notices that the intensity of the absorption component progressively decreases over five nights before it jumps back to its initial high value (JD 2450643).

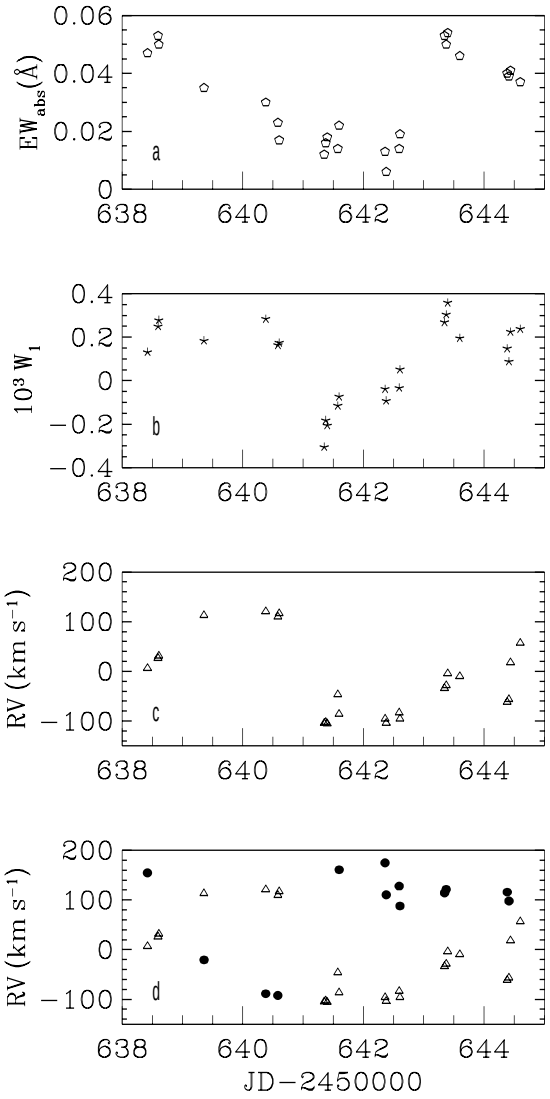

Fig. 2. a Equivalent width of the absorption component of the He II λ 4686 line in the spectrum of HD 192639 as observed during our campaign in July 1997. **b** First order moment of the profile of the He II λ 4686 line integrated between λ 4675.8 and λ 4695.8 (see text). **c** Radial velocity of the strongest peak of the emission component of He II λ 4686. **d** Same as **c** but this time we have also plotted the RVs of the second highest peak in the emission component (filled circles).

An easy means to quantify the line profile variability is through the so-called moments of the line. Let us recall that the nth order moment of a line is defined by (e.g. Castor et al. 1981):

$$W_n = \left(\frac{c}{\lambda_0\, v_\infty}\right)^{n+1} \int_{\rm line} \left(\frac{F_\lambda}{F_c} - 1\right) (\lambda - \lambda_0)^n \, d\lambda \qquad (1)$$

where F_λ is the flux of the line and F_c is the corresponding continuum flux. λ_0 and v_∞ designate the rest wavelength of the line and the terminal velocity of the wind respectively. In our present analysis, we focus on the first order moment, since it provides a direct measurement of the asymmetry of the line. We adopt a terminal velocity of 2180 km s^{-1} (Prinja et al. 1990) and we integrate the profile between λ 4675.8 and λ 4695.8.

The variations of W_1 as a function of time are shown in Fig. 2b. W_1 shows no systematic trend except during the blueward excursion of the dominant emission peak when the first order moment becomes negative.

The radial velocities of the dominant peak of the emission component, determined by fitting a gaussian, are displayed in Fig. 2c. We observe variations over a range of some 200 km s^{-1}. Finally, for those spectra on which the emission component appears double-peaked, the radial velocities of both peaks are shown in Fig. 2d. The latter figure indicates that the RV variations of the strongest peak shown in Fig. 2c seemingly result from the alternating intensities of the two peaks.

3.2. Other emission lines

The normalized spectrum of HD 192639 between λ 4625 and λ 4660 is illustrated as a function of time in Fig. 3. The relatively intense N III $\lambda\lambda$ 4634-41 emission lines do not display the same behaviour as the He II λ 4686 line. In particular, the radial velocities of the N III emission peaks remain nearly constant (see Table 1 below). We notice some intensity variations, that are only slightly correlated to the variations of He II λ 4686 (see Fig. 5) and present a much lower relative amplitude than for the latter line.

The formation of the N III $\lambda\lambda$ 4634-41 ($3p\ ^2\mathrm{P}^0 - 3d\ ^2\mathrm{D}$) lines in the atmospheres of O stars has been discussed by Mihalas & Hummer (1973). These authors have shown that in the photosphere of O((f)) and O(f) stars, the $3d\ ^2$D level of the N^{2+} ion is overpopulated as a result of dielectronic recombination, leading to photospheric emission of the $\lambda\lambda$ 4634-41 lines. In the case of HD 192639, the lower amplitude of variation and the different behaviour of the N III lines compared to the He II λ 4686 wind feature probably confirm that the former emission lines arise mainly in the photosphere of the star rather than in the stellar wind.

In order to measure the line profile variability in a quantitative way, we have computed the time variance spectrum (TVS, Fullerton et al. 1996) of our Aurélie observations. For the most variable lines in the spectrum of HD 192639, Table 1 provides the value of the highest peak of $(TVS)^{1/2}$ over the entire line profile, the velocity interval $\Delta\, v$ over which the detected variations are significant at the 99% confidence level, as well as the mean amplitude of the deviation $(TVS)^{1/2}$ evaluated over $\Delta\, v$. For the N III $\lambda\lambda$ 4634-4641 emission lines, the severe blending of the TVS features of these lines and the proximity of the variable C III $\lambda\lambda$ 4647-50 absorption lines prevent a reliable evaluation of the mean amplitude. Nevertheless, the TVS parameters given in Table 1 confirm that the N III $\lambda\lambda$ 4634-4641 blend displays a lower variability than e.g. the He II λ 4686 line.

Brucato (1971) claimed to detect irregular variations in the equivalent width of the N III emission lines on a time scale of

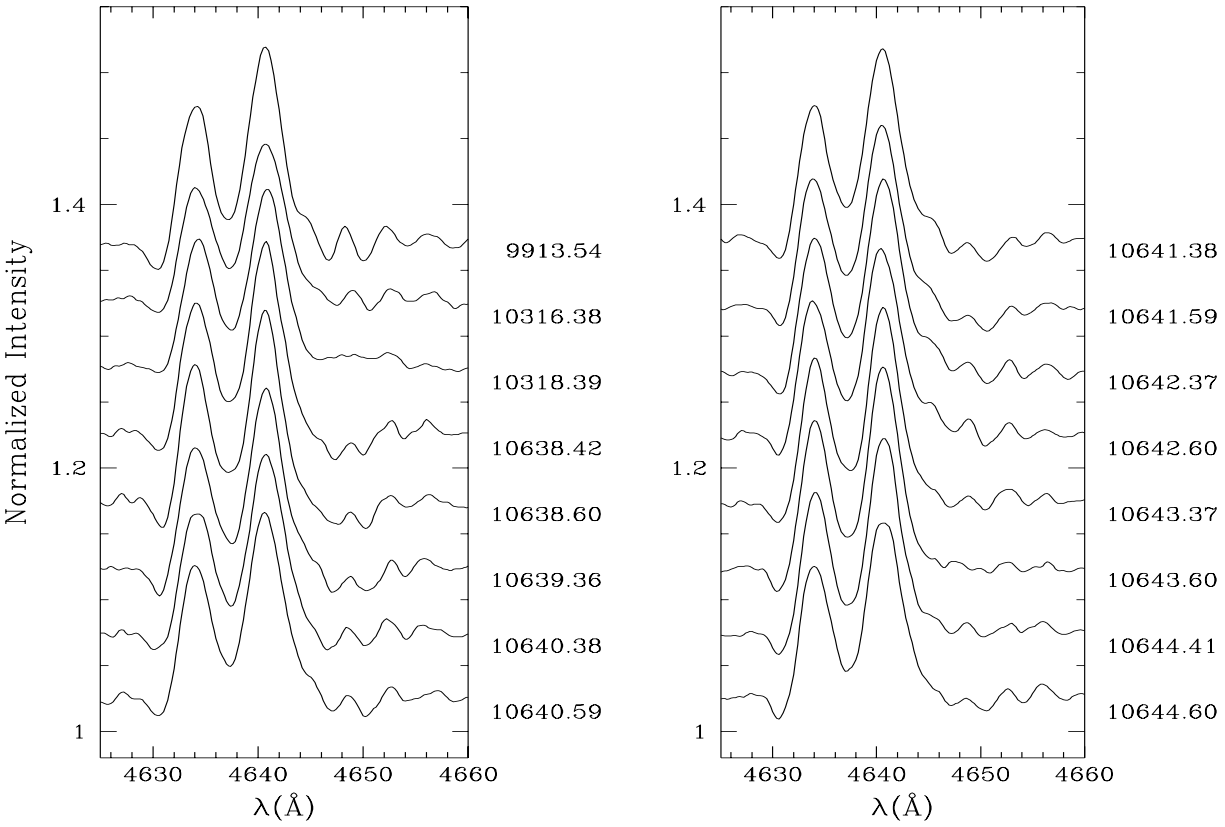

Fig. 3. Same as Fig. 1, but for the blend around the N III $\lambda\lambda$ 4634-41 lines in the spectrum of HD 192639. The absorption line shortward of the N III emissions is due to Si IV λ 4631. One notices also the important variability of the C III $\lambda\lambda$ 4647, 4650 absorptions (see text).

about 20 minutes. Even if the sampling of our time series is not well suited to detect such rapid fluctuations, it appears that the reliability of Brucato's discovery is rather difficult to assess. In fact, Brucato (1971) noticed these rapid variations only during one night, whereas he found only marginal variability during the other nights. Moreover, these results were derived from photographic plates and the author does not provide error estimates for his measurements.

Concerning the two unidentified emission lines at λ 4486 and λ 4504, we detect no significant variability and no correlation with the variability of the Hβ line (Fig. 5). We conclude therefore that these lines are probably not produced in the stellar wind, but may arise in the same physical region as the bulk of the N III emission.

3.3. The absorption lines

All the absorption lines in the observed spectral domain display variations to some extent. Part of the intensity variability may result from uncertainties in the normalization of the spectra. We will therefore focus our attention on the strongest lines that show the most stringent variations, as indicated by the TVS analysis (Table 1), and which are the least sensitive to the uncertainties of the normalization.

Fig. 4 displays the variability of the Hβ absorption line in the spectrum of HD 192639. During the observing run in July 1997, the equivalent width of this line varies over a range of $\sim$ 7% (1σ) around the mean value. Larger deviations from the mean equivalent width are observed in August 1996, when the line appears some 18 - 26% weaker than on the average.

Besides the variations of its intensity, the Hβ line displays also important profile variability (Fig. 4). The core of the line changes from a symmetric nearly gaussian shape to a rather sharp asymmetric minimum, that appears either red-shifted or blue-shifted. Occasionally, we also observe a flat minimum.

We have constructed a dynamical spectrum by assembling quotient spectra obtained after division of the individual data by the mean spectrum. A close inspection of this dynamical spectrum reveals a tight resemblance between the deformation pattern of the Hβ, Hγ, He I λ 4471 and He II λ 4686 lines, in the sense that the stronger is the He II λ 4686 emission component, the weaker are the absorption lines.

To quantify this impression, we have used the local pattern cross-correlation technique discussed by Vreux et al. (1992) and by Gosset et al. (1994). Some results obtained using the Hβ line

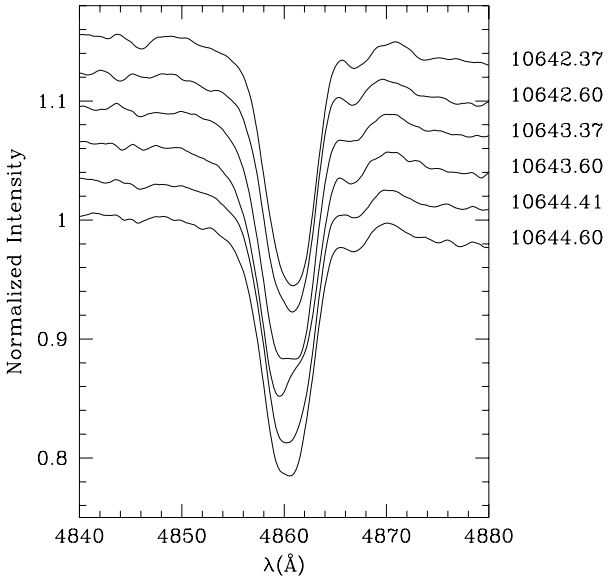

Fig. 4. Illustration of the variability of the shape and strength of the Hβ line as observed during the last three nights of the July 1997 observing campaign. For each night, we show the mean spectrum of the first and second half of the night. The different spectra are shifted vertically by 0.03 units.

as a reference are shown in Fig. 5. This figure underlines the strong correlation between the mean deformation pattern of the different lines in the spectrum of HD 192639.

In Fig. 3 we notice the strong changes in the visibility of the C III $\lambda\lambda$ 4647-50 absorption lines. On JD 2450318.39 and JD 2450643.60, these lines have nearly disappeared, whereas they present their maximum intensity on JD 2449913.54 and JD 2450640.59. The cross-correlation method indicates that the deformation pattern of these lines is correlated to the one of the Hβ line (Fig. 5).

The correlations between the profile variations of the absorption lines and those of the He II λ 4686 emission suggest that the bulk of the variability of the absorption line profiles in the spectrum of HD 192639 is produced by a variable stellar wind emission rather than by a genuine photospheric phenomenon.

Our results are in good agreement with the conclusions of previous studies. Underhill (1995a) noticed that the leading members of the He I series are displaced shortwards by some 11 km s^{-1} indicating that the cores of the strong He I lines are formed in the wind. The same holds true for the Balmer lines Hβ and Hγ. Herrero et al. (1992) also noticed a strong dilution effect of the He I λ 4471, Hγ and Hβ lines due to a stellar wind. In the same context, Fullerton (1990) noticed the strong resemblance between the variations of the C IV $\lambda\lambda$ 5801, 5812 absorption lines and those of the absorption trough of the He I λ 5876 P-Cygni profile. From these results, Fullerton et al. (1996) conclude that the variability of the C IV doublet in the spectrum of HD 192639 is probably not consistent with a purely photospheric origin.

We have measured the equivalent widths of several strong, unblended lines in the spectrum of HD 192639. The average values and the standard deviations are listed in Table 1. Of particular interest are the classification lines He I λ 4471 and He II λ 4542. During the 1997 observing campaign, the standard deviations of the EWs of these lines amount respectively to 7% and 5% of their intensity (Table 1). As for most of the absorption lines, the EWs of the He I λ 4471 and He II λ 4542 lines are the weakest in August 1996, when the intensities deviate by some 14% from their mean values. Considering our whole dataset, the O-star classification criterion $\log_{10} W' = \log_{10}\left(\frac{EW(4471)}{EW(4542)}\right)$ (Conti 1973) varies between 0.066 and 0.173, i.e. around the border line between spectral types O7.5 and O8, with an average value of $0.115 \pm 0.029(1\sigma)$ corresponding to spectral type O8. However, one has to bear in mind that at least the He I λ 4471 line and possibly also the He II λ 4542 line are partially filled in by emission from the stellar wind and their EWs therefore do not depend on the temperature of the photosphere alone.

Since the cores of most of the absorption lines are formed in the wind, one has also to be careful when deriving the chemical composition of the star using a plane parallel model atmosphere. As a matter of fact, the optical depth of the wind for different transitions not only depends on the abundances of the corresponding ions, but also on the physical conditions in the wind.

In order to search for long-term changes, we have compared the equivalent widths listed in Table 1 to the average values reported in the literature (Oke 1954, Mannino & Humblet 1955, Underhill 1995b). We find a very good agreement between our values and the EWs of Underhill (1995b). On the other hand, the older determinations yield systematically larger EWs than our data, although the various datasets usually agree within the limits set by the estimated errors and the observed range of variability. The most outstanding differences concern the He I $\lambda\lambda$ 4471, 4713 and He II λ 4542 lines that appeared some 15 - 40% stronger during the older observations (Oke 1954, Mannino & Humblet 1955). Whether or not these differences reflect a genuine long-term change is however not clear since a reliable estimate of the error bars on the oldest photographic EW determinations is lacking.

3.4. Radial velocities

Conti et al. (1977) found that the radial velocity of HD 192639 was probably variable over a small range. Later on, Underhill (1995a) suggested that HD 192639 could be a single-lined spectroscopic binary with an orbital period of a few days.

Binarity could be a possible interpretation of the observed deformations of the He II λ 4686 line. Strong line profile variability in this line is indeed expected to occur as a consequence of colliding winds in early-type binary systems (Rauw 1997). However, the small range of radial velocity variations would probably indicate a low orbital inclination and the expected line profile variability drastically decreases for lower inclinations. Therefore, it seems unlikely that wind interactions in a binary

Table 1. Measured characteristics of the most prominent lines in the blue-violet spectrum of HD 192639. The second column gives the time-averaged radial velocities, whereas the fourth column lists the equivalent widths of the strongest unblended absorption lines. The last three columns provide the results of the TVS analysis for those lines that display significant variability (see text). The amplitude of $(TVS)^{1/2}$ is expressed as a percentage of the normalized continuum flux. The velocity intervals labelled with a colon are uncertain due to the severe blending of the N III emission lines.

Line	Mean RV ($\mathrm{km\,s^{-1}}$)	σ(RV) ($\mathrm{km\,s^{-1}}$)	Mean EW (Å)	σ(EW) (Å)	$\max (TVS)^{1/2}$ [%]	$\Delta\, v$ $\mathrm{km\,s^{-1}}$	Mean $(TVS)^{1/2}$ [%]
	absorption lines						
He II λ4200	-3.8	9.1	0.435	0.036	0.95	-270 , $+260$	0.69
Hγ	-33.8	7.0	1.457	0.086	1.84	-385 , $+390$	1.04
He I λ4388	-8.1	7.1					
He I λ4471	-15.8	6.2	0.621	0.044	1.21	-460 , $+330$	0.62
N III λ4511	7.1	7.6					
N III λ4515	-3.4	5.9					
He II λ4542	0.9	3.3	0.476	0.025	0.82	-315 , $+215$	0.49
He I λ4713	-5.1	4.1	0.187	0.013			
Hβ	-41.2	11.3	1.355	0.127	2.56	-430 , $+600$	1.14
He I λ4922	-6.9	5.9	0.216	0.017			
	emission lines						
N III λ4634	-0.2	4.6			0.61	-290 , $+110$:	≤ 0.45 :
N III λ4641	-13.2	5.1			0.78	-235 , $+115$:	≤ 0.57 :
He II λ4686					1.37	-440 , $+265$	0.69

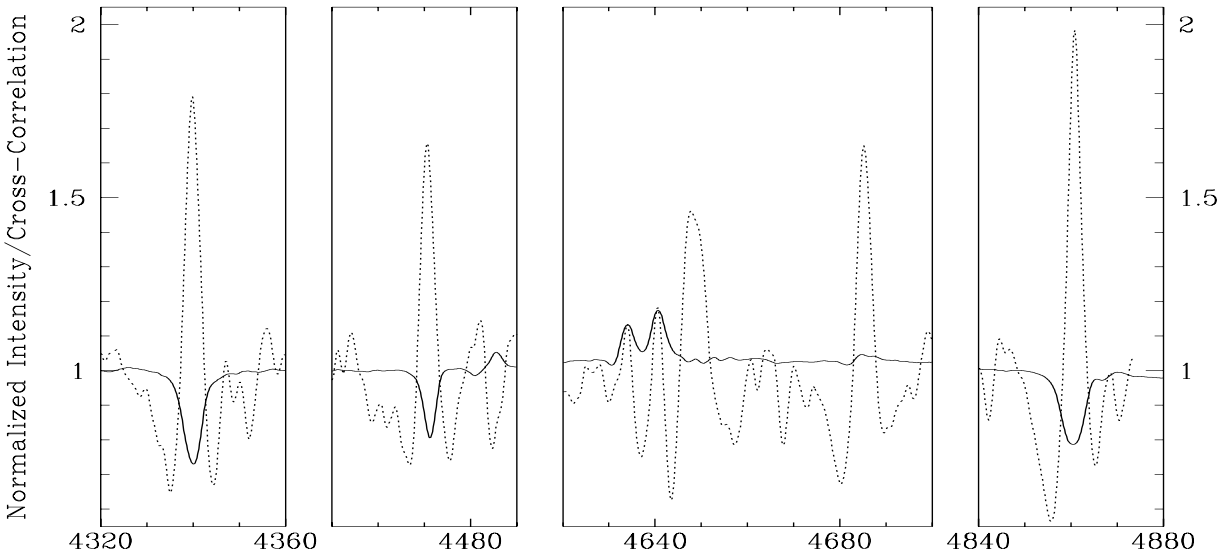

Fig. 5. Mean result of the local pattern cross-correlation on the dynamical quotient spectra using the deformation pattern of the Hβ line as a reference (see Sect. 3.3 for details). The cross-correlation has been shifted up by one unit and is superimposed on the mean spectrum of HD 192639 (continuous line). The broad peak around λ4650 in the cross-correlation spectrum is due to the C III $\lambda\lambda$4647-50 lines. The width of the reference Hβ pattern (12Å) does not allow to separate the individual cross-correlation peaks of the two C III lines.

system could account for the deformations of the He II λ4686 line observed in the spectrum of HD 192639.

We have measured the radial velocities of the most prominent absorption lines in our spectra. The central wavelengths of the absorption lines are determined by fitting Gaussian profiles and the radial velocities are computed with respect to the effective wavelengths tabulated by Conti et al. (1977). The results are given in Table 1 and the mean radial velocity of ten absorption lines is shown as a function of time in Fig. 6. This mean radial velocity has an average value and a standard deviation of respectively $-8.1\,\mathrm{km\,s^{-1}}$ and $5.0\,\mathrm{km\,s^{-1}}$. The range of radial velocity variability of the different lines, quoted in Table 1, is in good agreement with the results of Fullerton (1990). Fig. 6 shows that the radial velocity of the absorption lines is slightly more positive during two nights (i.e. JD 2450641-642) than on the average. This more positive velocity occurs simul-

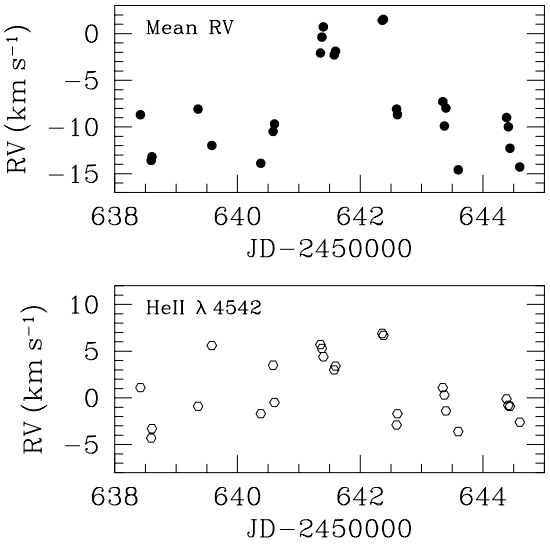

Fig. 6. Upper panel: variations of the mean radial velocity of ten absorption lines in the blue-violet spectrum of HD 192639 during the observing run in July 1997. Lower panel: same as above, but for the He II λ 4542 line only.

taneously with the minimum of the first order moment of the He II λ 4686 line, i.e. when the emission component of the latter line reaches its maximum blueward excursion. However, it seems rather unlikely that the effect seen in Fig. 6 reflects a true velocity variation in a real binary system. In fact, in most of the absorption lines, at least part of the radial velocity variations result from the line profile variability. As discussed above, this variability is probably due to a changing stellar wind emission. On the other hand, the lower panel of Fig. 6 illustrates the radial velocity of the He II λ 4542 line as a function of time. This line presents a slightly lower line profile variability and is probably less affected by emission from the stellar wind (Herrero et al. 1992) than some of the other lines used to compute the mean velocity. One can see on this figure that the amplitude of velocity variation is also smaller than for the mean of the RVs.

We conclude therefore that the present analysis does not provide any clear indication in favour of a binary nature of HD 192639.

4. Discussion

The variability of early-type stellar winds is usually attributed to inhomogeneities or large-scale structures evolving on time scales of several hours to a few days. Large-scale structures in the wind may be connected to photospheric variability through a modulation of the stellar wind by the combined effect of stellar rotation and a moderate magnetic field. An alternative explanation for a photospheric connection could be the instability inherent to radiatively driven stellar winds in the case of a photosphere undergoing non radial pulsations.

Kaper et al. (1997) suggest that the variability in their sample of bright O stars is related to so-called Corotating Interacting Regions. Such corotating stream structures are expected as a result of azimuthal variations in the properties of the outflow as would arise near bright or dark spots on the stellar surface (Cranmer & Owocki 1996). A large-scale wind structure could also result from a strong magnetic field that would confine the wind towards the magnetic equator (Babel & Montmerle 1997). If the magnetic axis is tilted with respect to the rotational axis, the line emitting region near the magnetic equator will be seen under varying inclinations, resulting in periodic line profile variability. Such a configuration is suggested by Stahl et al. (1996) to explain the strictly periodic variability found in the case of HD 37022 (O7 V).

Our observations reveal strong line profile and intensity variations in the spectrum of the O8 I(f) star HD 192639. The changes seen in the absorption lines appear to be correlated to the variability of the He II λ 4686 line, suggesting that the phenomenon probably arises in the stellar wind.

The double-peaked shape of the He II λ 4686 emission component as well as its variability indicate that the wind of HD 192639 is not spherically symmetric. The variability in the wind of HD 192639 affects the entire He II λ 4686 profile and is therefore most probably related to large-scale structures in the low velocity part of the wind rather than to small-scale inhomogeneities.

The characteristic timescales are a key issue for the study of variability in early-type stars. The present data are clearly not sufficient to perform a detailed time series analysis and to find out if the phenomenon observed in the spectrum of HD 192639 is periodic or not. Nevertheless, some of the He II λ 4686 profiles we have observed were already seen during earlier snapshot observations by other observers (Underhill 1995a, Herrero et al. 1992), suggesting that the phenomenon is stable over several years. Furthermore, the properties of the He II λ 4686 line during the 1997 observing campaign (Fig. 2) suggest that the recurrence time scale could be of the order of 4 - 6 days, although we cannot exclude a somewhat longer time scale. A crude Fourier analysis of the characteristics of the He II λ 4686 line over our entire dataset (i.e. including the 1995 and 1996 snapshot observations) yields a recurrence time of ~ 5 days. However, since this time scale is comparable with the total time spanned by our 1997 dataset, the meaning of the Fourier analysis is rather difficult to assess. We find no trace of the 2 day recurrence marginally present in the 1986 observations of the C IV $\lambda\lambda$ 5801, 5812 doublet by Fullerton (1990). On the other hand, during the same limited observing run (6 nights), Fullerton (1990) derived a time scale of 4.15 ± 0.37 days for the variations of the He I λ 5876 line, a value which is more compatible with our results.

Herrero et al. (1992) derive a radius of $19.5\,R_\odot$ for HD 192639. Estimates of the projected rotational velocity $v \sin i$ range from $103\,\mathrm{km\,s^{-1}}$ (Conti & Ebbets 1977) over $110\,\mathrm{km\,s^{-1}}$ (Penny 1996) to $125\,\mathrm{km\,s^{-1}}$ (Herrero et al. 1992). From the two most extreme estimates of $v \sin i$, we derive an upper limit on the actual rotational period of 7.9 to 9.6 days respectively. Considering the critical break-up velocity and using the stellar parameters derived by Herrero et al. (1992), we can set a lower limit on the rotational period of 3.10 days. The

variability of HD 192639 might therefore well be connected to the stellar rotation.

Additional observations over a longer time span are needed to further investigate the properties of the variability seen in the spectrum of HD 192639 and to find out whether or not the phenomenon can be explained by one of the above mentioned scenarios.

Acknowledgements. We are grateful to Drs. E. Gosset and J.-P. Swings for their helpful remarks. We wish to thank the referee, Dr. L. Kaper, for his careful reading of the manuscript and his constructive suggestions. We are greatly indebted to the Fonds National de la Recherche Scientifique (Belgium) for multiple supports. This research is also supported in part by contract ARC 94/99-178 "Action de recherche concertée de la Communauté Française" (Belgium) and by contract P4/05 "Pôle d'Attraction Interuniversitaire" (SSTC-Belgium). Partial support through the PRODEX XMM-OM Project is also gratefully acknowledged. The travels to OHP for the observing runs were supported by the Ministère de l'Enseignement Supérieur et de la Recherche de la Communauté Française. The SIMBAD database has been consulted for the bibliography.

References

Andrillat Y., Vreux J.-M., 1979, A&A 76, 221
Babel J., Montmerle T., 1997, ApJ 485, L29
Brucato R.J., 1971, MNRAS 153, 435
Castor J.I., Lutz J.H., Seaton M.J., 1981, MNRAS 194, 547
Conti P.S., 1973, ApJ 179, 181
Conti P.S., Alschuler W.R., 1971, ApJ 170, 325
Conti P.S, Ebbets D., 1977, ApJ 213, 438
Conti P.S., Leep E.M., Lorre J.J., 1977, ApJ 214, 759
Cranmer S.R., Owocki S.P., 1996, ApJ 462, 469
Fullerton A.W., 1990, PhD Thesis, University of Toronto
Fullerton A.W., Gies D.R., Bolton C.T., 1996, ApJS 103, 475
Gillet D., Burnage R., Kohler D., et al., 1994, A&AS 108, 181
Gosset E., Vreux J.-M., Andrillat Y., 1994, Ap&SS 221, 181
Herrero A., Kudritzki R.P., Vilchez J.M., et al., 1992, A&A 261, 209
Kambe E., Hirata R., Ando H., et al., 1997, ApJ 481, 406
Kaper L., Henrichs H.F., Nichols J.S., et al., 1996, A&AS 116, 257
Kaper L., Henrichs H.F., Fullerton A.W., et al., 1997, A&A 327, 281
Mannino G., Humblet J., 1955, Ann. Ap. 18, 237
Mathys G., 1987, A&AS 71, 201
Mihalas D., Hummer D.G., 1973, ApJ 179, 827
Oke J.B., 1954, ApJ 120, 22
Penny L.R., 1996, ApJ 463, 737
Prinja R.K., Barlow M.J., Howarth I.D., 1990, ApJ 361, 607
Rauw G., 1997, PhD Thesis, University of Liège
Schild H., Berthet S., 1986, A&A 162, 369
Stahl O., Kaufer A., Rivinius Th., et al., 1996, A&A 312, 539
Underhill A.B., 1995a, ApJS 100, 433
Underhill A.B., 1995b, ApJS 100, 461
Vreux J.-M., Gosset E., Bohannan B., Conti P.S., 1992, A&A 256, 148
Walborn N.R., 1972, AJ 77, 312

A&A 366, 585–597 (2001)
DOI: 10.1051/0004-6361:20000106

Astronomy & Astrophysics

The spectral variability of HD 192639 and its implications for the star's wind structure⋆

G. Rauw[1,⋆⋆], N. D. Morrison[2], J.-M. Vreux[1], E. Gosset[1,⋆⋆⋆], and C. L. Mulliss[2]

[1] Institut d'Astrophysique et de Géophysique, Université de Liège, 5 avenue de Cointe, 4000 Liège, Belgium
[2] Ritter Astrophysical Research Center, Toledo, OH 43606, USA

Received 7 August 2000 / Accepted 9 November 2000

Abstract. We report the analysis of an extensive set of spectroscopic data of the O(f) supergiant HD 192639. A Fourier analysis of our time-series reveals a recurrent variability with a "period" of roughly 4.8 days which is most prominent in the absorption components of the He II λ 4686 and Hα P-Cygni profiles. The same periodicity is also detected in the blue wing of several absorption lines (e.g. Hβ). The variations of the absorption components correspond most probably to a cyclical modulation of the amount of stellar wind material along the line of sight towards the star. The 4.8-day period affects also the morphology of the double-peaked He II λ 4686 and Hα emission components, although these emission components display also variations on other (mainly longer) time scales. The most likely explanation for the 4.8-day modulation is that this cycle reflects the stellar rotational period (or half this period). We find that the most important observational properties can be explained – at least qualitatively – by a corotating interaction region or a tilted confined corotating wind.

Key words. line: profiles – stars: early-type – stars: mass loss – stars: individual: HD 192639 – stars: variables: general

1. Introduction

Over the last decade, extensive observing campaigns have been organized to monitor the spectroscopic variability of early-type stars (e.g. Fullerton et al. 1996; Massa et al. 1995; Kaper et al. 1997, 1999). Most of the observed O-stars display line profile variability on time scales of a few days. Some well studied objects were found to exhibit cyclical variations in their stellar winds that are believed to be related to the rotational period of the underlying star. Such a rotational modulation is nowadays usually attributed to large scale structures in the wind that could be generated by photospheric processes affecting the mass outflow at the base of the wind (for a review see e.g. Fullerton 1999).

Understanding the physical mechanisms responsible for this modulation of the mass loss has become one of the primary goals of research in the field of hot stars. Nowadays, the most commonly invoked phenomena are magnetic fields and non-radial pulsations. An oblique magnetic rotator model has been used to explain the cyclical variations of the peculiar O7 V star θ^1 Ori C (= HD 37022, Stahl et al. 1996), although we still lack any firm direct detection of the magnetic field of an O-star (Mathys 1999). On the other hand, non-radial pulsations have been detected in photospheric absorption lines of six O-stars so far (de Jong et al. 1999), but these pulsations have periods that are usually significantly shorter than the observed time scales of the stellar wind variations. Thus a variety of processes may be at work and there is a definite need for additional constraints on the stellar wind structure of early-type stars. This issue can best be addressed by extensive monitoring of selected stars.

In this context, Rauw & Vreux (1998, hereafter Paper I) have started a detailed investigation of the O8 I f star HD 192639 in the Cyg OB1 association. In Paper I, we showed that the He II λ 4686 line displays a rather unusual double-peaked P-Cygni type profile that undergoes strong variability. The shape of this line indicates that the wind of HD 192639 is not spherically symmetric. In Paper I, we further showed that the variability of the He II λ 4686 profile is correlated to that of the Hβ absorption line. This led us to the conclusion that the variations seen in the spectrum of HD 192639 arise probably from a large scale structure in the stellar wind rather than from a photospheric phenomenon. Based on these preliminary results, we tentatively suggested a recurrence time of the variations of ∼5 days.

Send offprint requests to: G. Rauw
⋆ Based on observations collected at the Observatoire de Haute Provence, France and the Ritter Observatory, Toledo, USA.
⋆⋆ Postdoctoral Researcher FNRS, Belgium.
⋆⋆⋆ Research Associate FNRS, Belgium.

To further constrain the properties of the spectral variability of HD 192639, we have obtained new data and we have extended our analysis to the spectral region around the Hα emission line.

2. Observations and data reduction

The bulk of our new spectroscopic observations of HD 192639 were collected during two observing campaigns in September 1998 and August 1999 with the Aurélie spectrograph fed by the 1.52 m telescope of the Observatoire de Haute-Provence (OHP). In 1998 we used a 600 lines/mm grating blazed at 5000 Å providing a reciprocal dispersion of 16 Å/mm. Two wavelength settings ranging from 4460 to 4880 Å and 6360 to 6740 Å were covered. The detector was a Thomson TH7832 linear array with a pixel size of 13 μm. A total of 25 blue and 18 red spectra were obtained over a ten night run. The mean exposure time was about 45 min and the mean S/N ratio in the continuum was ∼200 and ∼400 in the blue and red wavelength ranges respectively. The spectral resolution as derived from the FWHM of the ThAr calibration lines is ∼0.6 Å. Whenever the atmospheric conditions allowed us to do so, we obtained a set of blue spectra at the beginning and at the end of each night in order to study shorter time scale variations.

The 1999 data set was obtained with a 300 lines/mm grating blazed at 6000 Å providing a reciprocal dispersion of 33 Å/mm over a wavelength range from 4100 to 4950 Å. The instrumental configuration used in 1999 yielded a spectral resolution of ∼1.2 Å. We obtained 14 spectra with a $S/N \simeq 200$ over a 15 night run. Typical exposure times were 30–45 min.

All the OHP data were reduced in the standard way using the MIDAS software developed at ESO. The spectral domain between 6420 and 6640 Å is affected by strong absorption bands of telluric water vapor. A template of the telluric spectrum was constructed by observing the rapidly rotating star HD 177724 (A0 Vp, $m_V = 2.99$, $v_e \sin i = 295$ km s^{-1} Abt & Morrell 1995) at very different airmasses. This template was then used for a first order correction of the telluric features. Finally, the spectra were normalized using properly chosen continuum windows.

Eight spectra of HD 192639 were also obtained with the echelle spectrograph attached to the 1-m Ritchey-Chrétien reflector of the Ritter Observatory (Toledo, USA). Five of these spectra were obtained concurrently with the September 1998 run at OHP as part of a multi-site campaign. The instrument was equipped with a liquid nitrogen cooled CCD camera system supplied by Wright Instruments Ltd. The detector was a 1200×800 EEV CCD chip with pixel dimensions of 22.5 μm × 22.5 μm. The resolving power was 26 000 and the typical S/N ratio was about 75 for a typical exposure time of one or two hours depending on the weather conditions. The data reduction used the Interactive Data Language (IDL) with a specific program written for Ritter Observatory data. The individual echelle orders of the Ritter data cover a rather narrow spectral range and we therefore used the lower resolution OHP spectra as templates to normalize the Ritter spectra.

Table 1. Summary of our observing runs. The violet, blue, red and Hα wavelength ranges stand respectively for 4100–4460 Å, 4460–4880 Å, 6360–6740 Å (except Hα) and 6560–6590 Å

	violet	blue	red	Hα
$\Delta T^{\rm tot}$ (days)	1094.09	1094.09	9.07	36.91
N	40	65	18	28
$\overline{\Delta t}$ (days)	0.081	0.098	0.052	0.069
$\Delta T_{\rm run}^{\rm max}$ (days)	13.93	13.93	9.07	13.95
$\Delta\ \nu_{\rm nat}$ (d^{-1})	0.001	0.001	0.110	0.027
$\nu_{\rm max}$ (d^{-1})	6.2	5.1	9.6	7.2
$\nu_{\rm min}$ (d^{-1})	0.072	0.072	0.110	0.072

In addition to these new observations, we have also included the 1996 and 1997 Aurélie data discussed in Paper I in our analysis. A summary of the characteristics of our various data sets is presented in Table 1. $\Delta T^{\rm tot}$ gives the total time elapsed between our first and our last observation, while N is the total number of observations. $\overline{\Delta t}$ provides the average time interval between consecutive exposures obtained during the same night. $\Delta T_{\rm run}^{\rm max}$ yields the time spanned by the longest observing run in our data set. In light of the Fourier analysis in Sect. 3.1, we further list the typical width of a peak in the power spectrum $\Delta\ \nu_{\rm nat} = 1/\Delta T^{\rm tot}$. Due to the occurrence of bundles of aliases with nearly identical amplitude, the actual uncertainty on the peak position is larger than $\Delta\ \nu_{\rm nat}$ for the blue and violet data set; typical uncertainties are of the order of 0.005 d^{-1}. $\nu_{\rm max} = 1/(2\ \overline{\Delta t})$ provides a rough indication of the highest frequencies that could safely be studied with the present time series. Finally, $\nu_{\rm min} = 1/\Delta T_{\rm run}^{\rm max}$ yields the shortest frequency that could possibly be fully sampled within the longest data subset.

3. Results

To start, we have identified those lines in the spectrum of HD 192639 that display the most prominent variations. To this aim we have computed the temporal variance spectrum (TVS, Fullerton et al. 1996) of our entire data set. Although we rectified our spectra in a homogeneous way, small amplitude discrepancies in the normalization procedure cannot be ruled out and they might induce some artificial "variability". We have evaluated an upper limit on this apparent variability due to the normalization by computing the TVS over the broad diffuse interstellar band at 4430 Å and over the narrow DIB at λ 6614. In this way we find that the normalization errors should be limited to $TVS^{1/2} \leq 0.004$[1]. A Fourier analysis of the artificial

[1] Due to the broad wings of the Hα emission line, the residuals of the telluric features and the rather narrow spectral range covered by the Ritter data, the normalization errors at Hα could be slightly larger.

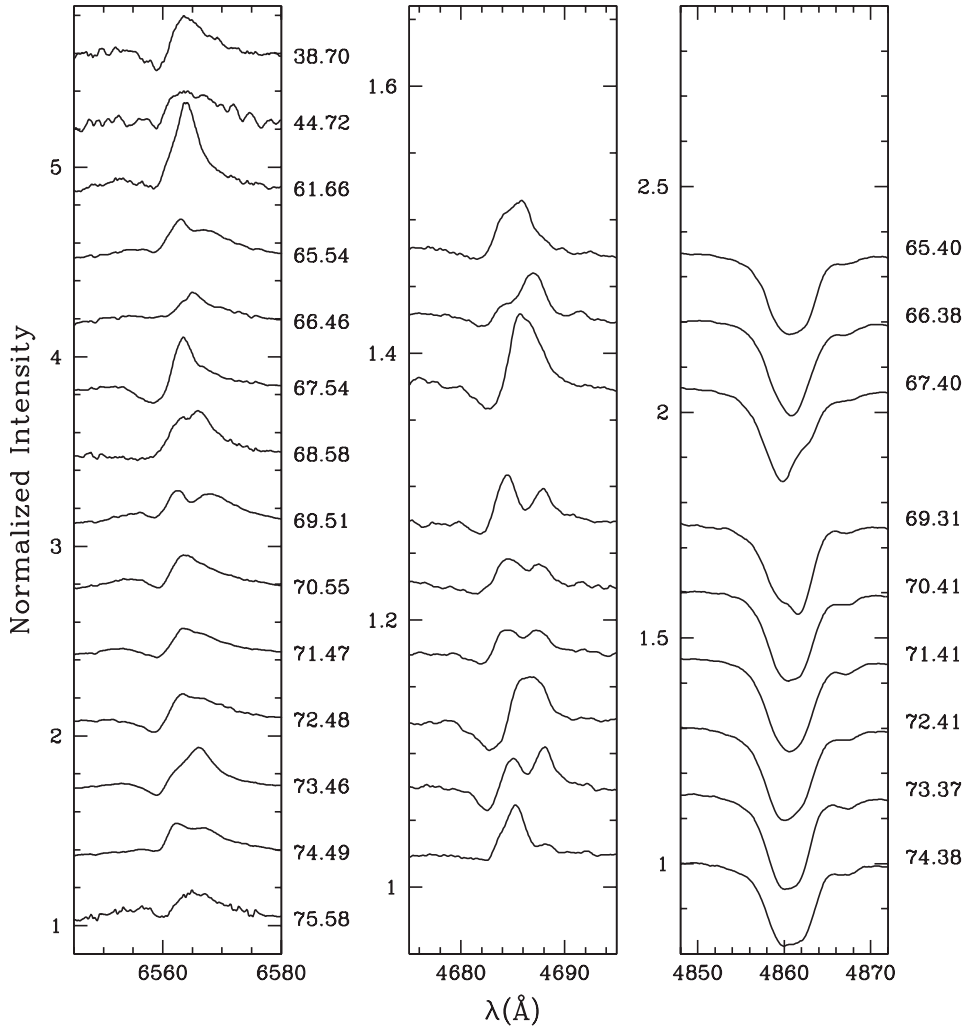

Fig. 1. Examples of the night to night variability of the Hα (left), He II λ 4686 (middle) and Hβ (right) line profiles in the normalized spectrum of HD 192639 as observed in September 1998 from OHP and Ritter Observatory. The various spectra are shifted by 0.35, 0.05 and 0.15 units respectively for the Hα, He II λ 4686 and Hβ profiles. The labels yield the mean date of the observation in the format JD-2451000.0. Note the very different vertical scales of the different panels

variability of the interstellar features reveals that this effect mainly appears as a long-term trend.

As already discussed in Paper I, the most significant profile variations in the blue-violet wavelength range are found in the He II λ 4200, Hγ, He I λ 4471, C III $\lambda\lambda$4647-50 and Hβ absorption lines as well as in the He II λ 4686 P-Cygni type profile and, to some extent, the N III $\lambda\lambda$ 4634-41 emission line. To this list we can now add the He I λ 6678 absorption line and the Hα P-Cygni type profile in the red wavelength range. Our new data confirm the low amplitude of the variations in the He II $\lambda\lambda$ 4542, 6406, 6527 and λ 6683 absorption lines ($TVS^{1/2} \leq 0.007$ for the blue line and ≤ 0.005 for the red lines) and the lack of variations in the Si IV $\lambda\lambda$ 6668, 6701 emission lines ($TVS^{1/2} \leq 0.003$).

The night to night profile variability of the Hα, He II λ 4686 and Hβ lines in the spectrum of HD 192639 as observed in September 1998 is shown in Fig. 1. Although subtle changes on time scales of a few hours are certainly present, the most prominent variations occur over time scales of a few days.

The Hα line consists of a P-Cygni type profile overlying a broad emission component extending from 6530 to 6590 Å. The wings of the broad emission component exhibit very little variability (see Fig. 5), whereas the P-Cygni like core of the profile displays prominent variations. The absorption component varies between a well defined trough and a very discrete, hardly noticeable absorption. The emission component changes from a sharp single-peaked normal P-Cygni emission to a double-peaked

somewhat broader structure. The intensity of the emission peak varies between 1.16 and 1.28 times the intensity of the continuum. On one occasion (JD 2451061.66), we observe an increase of the peak intensity to 1.45 times the continuum.

The variations of the He II λ 4686 and Hβ lines are very reminiscent of those already described in Paper I. The He II λ 4686 line displays various kinds of P-Cygni profiles quite similar to what we observe for the Hα line, although the correspondence between the profiles of the two lines is certainly not perfect. Usually, the double-peaked structure of the emission component is more pronounced in the He II λ 4686 line. The core of the Hβ line displays strong variations and changes from a more or less symmetric profile to a strongly asymmetric shape. At the same time we notice that the width of the line is also variable; for instance the line appears slightly broader on JD 2451067.40 than on JD 2451066.38. To quantify this effect, we have measured the width of the Hβ line profile at a normalized intensity of 0.9, i.e. at about half the line intensity (the FWHM cannot be used here since the depth of the line is itself slightly variable). Figure 2 illustrates the variation of this parameter and shows that the width increases by about 10% on ∼JD 2451067.4 and JD 2451072.4. These width increases mainly result from a shift of the blue wing by about 30–40 km s^{-1} towards shorter wavelengths. These events occur at epochs when the P-Cygni absorption components of the Hα and He II λ 4686 lines exhibit their strongest intensity and the strongest blueward extension. Conversely, when the strongest peak of the P-Cygni emission component reaches its maximum redward excursion, we notice a weakening of the red wing of the Hβ absorption line.

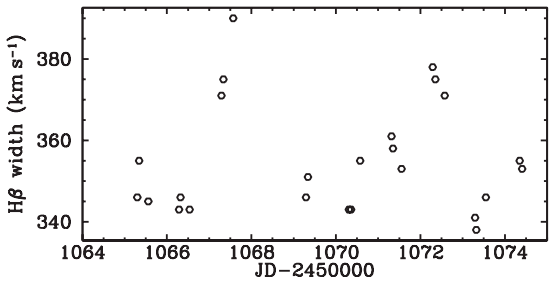

Fig. 2. Variations of the width of the Hβ absorption line at 0.9 times the intensity of the continuum

3.1. Searching for periodic line profile variability

Our time series contains data subsets from different epochs and different instrumentations. In order to improve the S/N and to avoid spurious effects in the time series analysis due to the different spectral resolutions, the Ritter data were filtered using a running average filter to achieve an effective resolution roughly matching that of the 1998 OHP data. For the Fourier analyses, the spectra from the different subsets were rebinned onto a heliocentric frame of reference using a uniform wavelength step of 0.2 Å.

We have used the "generalized spectrogramme" Fourier method of Heck et al. (1985; see their Sect. 2.2) to derive the power spectrum of our spectroscopic time series[2]. This method allows a proper estimation of the power spectrum in the case of an uneven sampling.

The resulting 2-D power spectrum of the He II λ 4686 line is displayed as a grey-scale representation in Fig. 3. The most outstanding feature of the power spectrum is a peak at $\nu_1 = 0.210 \pm 0.005$ d^{-1} ($P = 4.76 \pm 0.10$ days) with its aliases at 0.18, 0.24, 0.76, 0.79 and 0.82 d^{-1}. Although this structure is visible over the entire profile, it is most prominent in the wavelength range [4681.5, 4684.5] Å (i.e. over the velocity range $[-270, -77]$ km s^{-1}). Figure 4 shows the 1-D power spectrum obtained by integrating the 2-D periodogram over the latter wavelength range as well as the same 1-D power spectrum "prewhitened" for ν_1 (see below) and the spectral window up to 5.0 d^{-1}. Above 5.0 d^{-1}, the power spectrum is essentially featureless without any further prominent peak. In Fig. 4, we see that the aliasing of the ν_1 frequency can account for all the significant peaks in the 1-D power spectrum. To check this, we have prewhitened the data for the ν_1 frequency. This means that at every wavelength-step (or radial velocity-step v) we have fitted an expression

$$F(v,t) = c_0(v) + a_1(v)\ \sin(2\ \pi\ \nu_1\ [t - t_0]) + b_1(v)\ \cos(2\ \pi\ \nu_1\ [t - t_0]) \quad (1)$$

to our time series. The sinusoidal variation of frequency ν_1 was then subtracted from our data and the Fourier technique was applied to the resulting time series. The corresponding prewhitened power spectrum reveals no trace of any other significant peak in the [4681.5, 4684.5] Å wavelength range (see Fig. 4).

The situation is a bit less clear for the red emission component of the profile. There is still a peak at ν_1, but it no longer provides the dominating feature in the power spectrum over that part of the line profile. Prewhitening the data for ν_1 according to Eq. (1) reveals two peaks at $\nu_2 = 0.086 \pm 0.010$ d^{-1} and $\nu_3 = 0.38 \pm 0.20$ d^{-1}. The highest peak at ν_2 is rather close to $\nu_{\rm min} = 0.072$ d^{-1} i.e. the shortest frequency that could possibly be fully sampled within our longest data subset. The significance of this peak is therefore highly uncertain. In the following we will refer to this feature as "long term variability". The bundle of peaks in the prewhitened power spectrum around ν_3 is quite broad and asymmetric. We notice that the position of the ν_3 feature is at least not inconsistent with the first harmonic of the ν_1 frequency though one should not overinterpret this result.

[2] To assure that our time-series analysis is not affected by systematic effects due to the rather heterogeneous data set, we have also performed Fourier analyses of the individual data subsets. The resulting power spectra are very similar to those obtained for the entire data set, though the peaks have of course different widths.

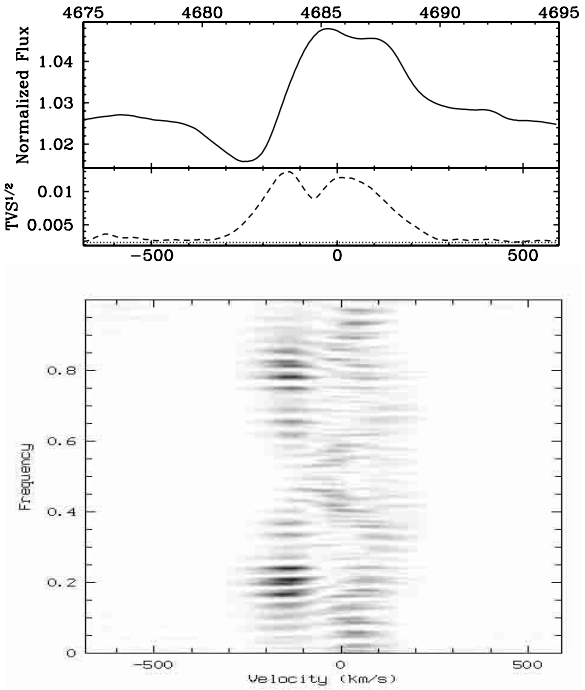

Fig. 3. Mean profile of the He II λ 4686 line in the spectrum of HD 192639 as observed with the Aurélie spectrograph at OHP from 1996 to 1999. The top axis of the upper panel indicates the wavelength whilst the bottom axis provides the corresponding radial velocity. The middle panel displays the square root of the temporal variance spectrum and the lower panel provides a grey-scale image of the power spectrum in the range $[0.0, 1.0]$ d^{-1} computed using the Fourier technique of Heck et al. (1985). The power spectrum reveals a family of peaks around $\nu_1 = 0.21$ d^{-1}

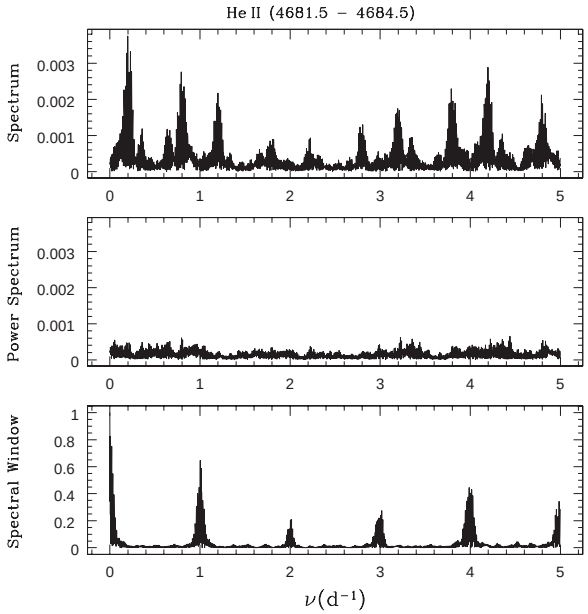

Fig. 4. Upper panel: power spectrum of the absorption component of the He II λ 4686 line profile integrated over the wavelength range 4681.5 to 4684.5 Å. Middle panel: power spectrum prewhitened for $\nu_1 = 0.21$ d^{-1}. Lower panel: power spectral window corresponding to our data set in the blue range

The power spectrum of the Hα line is shown in Fig. 5. The temporal variance spectrum indicates that the variability is concentrated in the P-Cygni core of the line, whereas the extended wings of the line show no sign of variability. Though the natural width of the peak is of course much larger for the Hα data set (see Table 1) than for the He II λ 4686 data, one clearly sees that the highest peak in the blue part of the profile is again found near $\nu \sim \nu_1$ with its $1-\nu$ alias around 0.8 d^{-1}. This peak dominates in the wavelength range $[6553, 6562]$ Å. Figure 6 further demonstrates the lack of power at higher frequencies and the decreasing amplitude of the aliases. The situation in the red emission component is again more complex. The highest peaks are 0.97 d^{-1} and its alias at 0.03 d^{-1}. We notice however that these peaks vanish if we omit the spectrum taken on JD 2451061.66, while the power spectrum over the blue part of the line profile remains unchanged. On the JD 2451061.66 spectrum HD 192639 displays an unusually strong Hα emission component (see Fig. 1). Again we will consider the 0.97 and 0.03 d^{-1} features as an indication of a, most probably non-periodic, long-term variability.

Finally, the power spectrum of the Hβ line (Fig. 7) reveals a clear dichotomy between the behaviour in the blue wing (4856 – 4860 Å, i.e. $[-330, -80]$ km s^{-1}) compared to the core of the line and its red wing. In the blue wing, the highest peak is once more found at $\nu_1 = 0.21$ d^{-1}. On the other side, the highest peaks in the core of the line correspond to 0.02 d^{-1} and its aliases. Most of the absorption lines in the blue spectrum of HD 192639 display a power spectrum similar to that of the Hβ line. A summary of our Fourier analyses is given in Table 2. In most cases, we find the dominant peak in the blue wing of the line either at $\nu_1 = 0.21$ d^{-1} or at the 0.18 d^{-1} alias. The power spectra of the red wing and the core of the absorption lines exhibit their highest peaks in the range $[0.01, 0.02]$ d^{-1} with the corresponding – nearly equally strong – aliases near 0.98 d^{-1}. The low-frequency peaks probably reveal either the existence of a long-term trend in the spectrum of HD 192639 or the occurrence of an exceptional event in the present time series. Conversely, we find no peak at higher frequencies that could be indicative of a photospheric variability on shorter time scales (e.g. due to non-radial pulsations). We caution however that many of the absorption lines of HD 192639 might – at least partially – be filled in by stellar wind emission. Moreover, our time series is not well suited to investigate variability on time scales of several hours as expected for non-radial pulsations.

In summary, our Fourier analysis reveals a roughly "periodic" behaviour especially in the blue-shifted absorption component of the Hα and He II λ 4686 P-Cygni

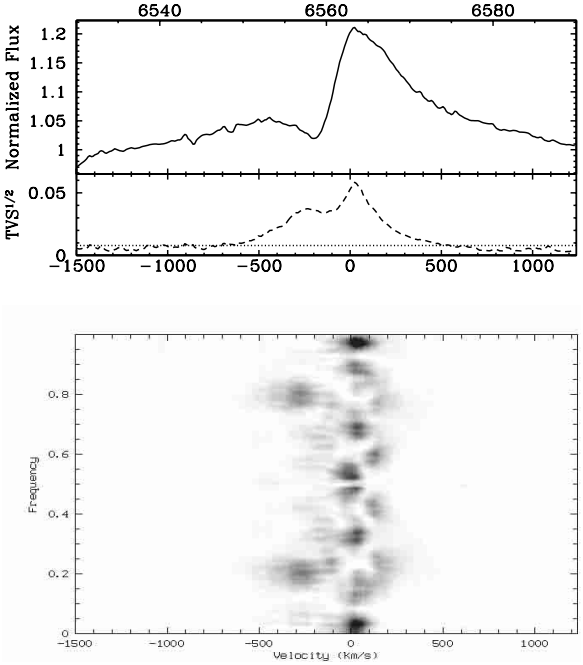

Fig. 5. Same as Fig. 3 but for the profile of the Hα line in the spectrum of HD 192639 as observed at OHP and at the Ritter Observatory in 1998. The power spectrum indicates a peak near $\nu \sim 0.2$ d^{-1} and another one near 1.0 d^{-1} in the emission component. The latter feature is strongly dependent upon the inclusion of the JD 2451061.66 spectrum in the analysis (see text)

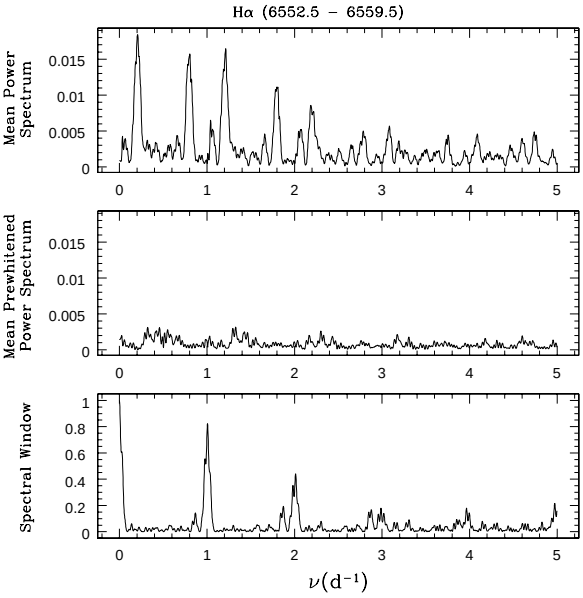

Fig. 6. Same as Fig. 4 but for the Hα line profile integrated over the wavelength range 6552.5 to 6559.5 Å

profiles on a recurrence time of 4.8 days. This result is in very good agreement with our previous suggestion

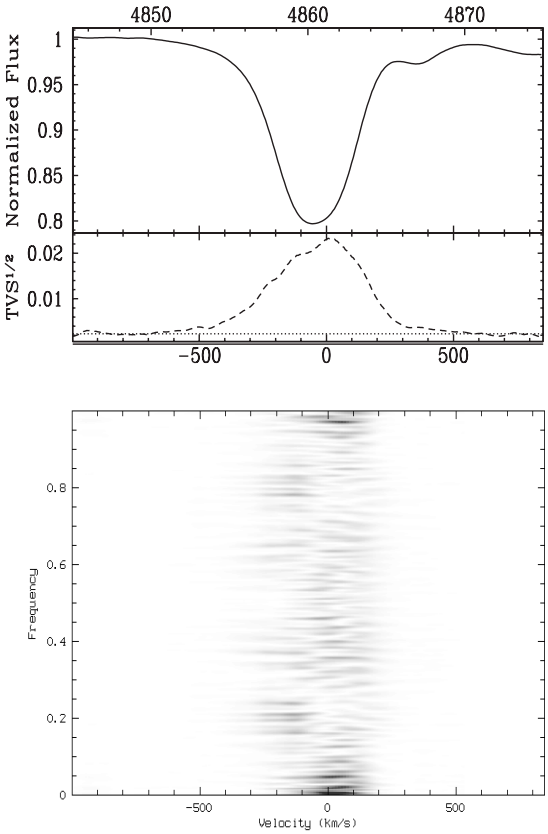

Fig. 7. Same as Fig. 3 but for the profile of the Hβ absorption line

(Rauw & Vreux 1998). The periodogram of the emission component of the He II λ 4686 line reveals also some power near the first harmonic of this period, but the latter detection is not secure. We find also strong evidence for long-term variability in the red part of the line profiles, but the corresponding "periods" are longer than our individual observing runs and no consistent result is found for the different lines.

3.2. The variations with the ν_1 frequency

In order to sample the complete 4.76-day cycle, we have binned the blue data set into twenty equal phase intervals, each containing at least two spectra. The resulting dynamical spectrum of the He II λ 4686 line is displayed in Fig. 8. This figure illustrates the modulation of the intensity of the absorption component of the P-Cygni profile as well as the changes in the relative intensity of the two peaks of the emission component.

In principle, we can use the information from our Fourier analysis to restore the pattern of variability associated with the ν_1 frequency. To this aim, we have fitted

Table 2. Summary of the Fourier analyses of our time series of spectra. Columns (2) and (3) list the frequency of the highest peak in the power spectrum respectively over the entire profile and in the blue wing. The flag given in Col. (4) refers to the data sets described in Table 1. The 0.97 d^{-1} peak in the power spectrum of the Hα line is obtained including the "unusual" spectrum on JD 2451061.66 (see text)

Line	Highest peak entire profile	Highest peak blue wing	Data set
He II λ 4200	1.00 d^{-1}	–	violet
Hγ	$\leq$ 0.005 d^{-1}	ν_1	violet
He I λ 4471	0.02 d^{-1}	0.18 d^{-1}	blue
He II λ 4542	0.02 d^{-1}	–	blue
N III λ 4640	0.18 d^{-1}	0.18 d^{-1}	blue
C III $\lambda\lambda$ 4647-50	0.04 d^{-1}	0.18 d^{-1}	blue
He II λ 4686	ν_1	ν_1	blue
Hβ	0.02 d^{-1}	ν_1	blue
Hα	(0.97 d^{-1})	ν_1	Hα
He I λ 6678	0.20 d^{-1}	0.20 d^{-1}	red

an expression

$$F(v,t) = c_0(v) + \sum_{i=1}^{n}\{a_i(v)\ \sin(2\ \pi\ \nu_i\ [t-t_0]) + b_i(v)\ \cos(2\ \pi\ \nu_i\ [t-t_0])\} \quad (2)$$

to our time series at every velocity step. Equation (2) differs from Eq. (1) in the sense that we simultaneously fit up to three frequencies ν_i. By this means, we are able to account for the specific sampling of the most prominent other frequencies that contribute to the power spectrum and to properly isolate the ν_1 variations from the effects of the other trends that exist in the emission component of the P-Cygni profile. The amplitude $\sqrt{a_1(v)^2 + b_1(v)^2}$ and the phase $\phi_0(v) = \arctan[b_1(v)/a_1(v)]$ of the ν_1 sine-wave are shown as a function of radial velocity v in Fig. 8. Figure 9 shows the reconstruction of the ν_1 periodic modulation in Eq. (2) over the He II λ 4686 line.

We caution that the phase constant ϕ_0 has physical meaning only if the period is clearly detected at the specific velocity. Since ν_1 is not the dominant frequency in the emission component, one could expect a priori that ϕ_0 might be slightly more uncertain there than in the absorption component. We have tested the restoration technique (Eq. (2)) with $n = 1, 2$ and 3. These calculations reveal that the overall behaviour of ϕ_0 is quite robust over the entire velocity range where ν_1 is clearly detected.

The phase diagram and the reconstruction technique reveal several interesting features:

- the phase of the modulation $\phi_0(v)$ remains roughly constant over the absorption component but changes dramatically over the emission component. The overall behaviour of $\phi_0(v)$ is independent of the number of additional frequencies included in the fit of Eq. (2);
- there is a local minimum in the amplitude of the sinusoidal variations near $v \sim -40$ km s^{-1};

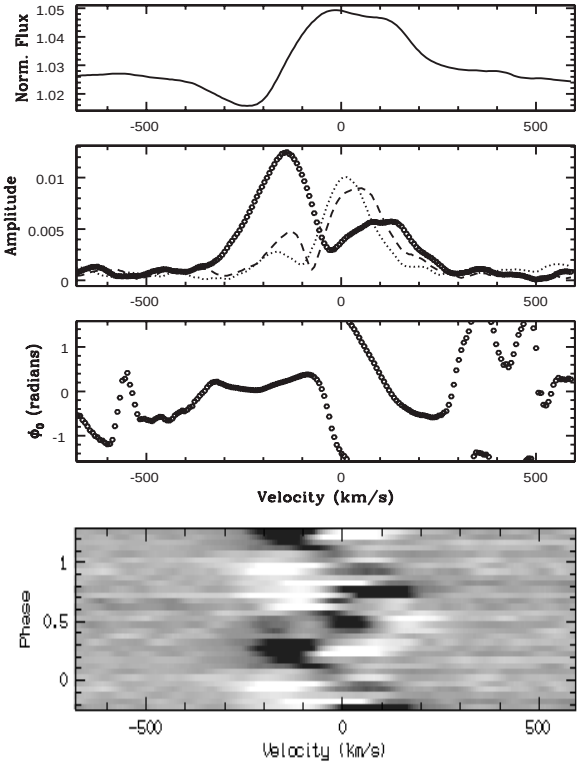

Fig. 8. Variability of the He II λ 4686 line as a function of phase assuming a period of 4.76 days. The three upper panels display the mean line profile, as well as the amplitude and the phase of a sine wave of frequency ν_1 fitted to our data. The reference date for the phase was arbitrarily chosen on JD 2450000.00. The amplitude of the two other frequencies that were fitted simultaneously are shown for comparison: 0.086 d^{-1} (dotted line), 0.38 d^{-1} (long-dashed line). The grey-scale image displays the ratio of the actual spectrum to the mean profile. The black pixels correspond to a ratio $\leq$ 0.99, whereas the white pixels indicate a ratio $\geq$ 1.01

- the intensity of the emission component seems to vary roughly in phase with the strength of the absorption component i.e. the phase-lag between maximum emission strength and maximum absorption is less than 0.08 cycle. At the phase of maximum emission, we observe a single-peaked, flat-topped emission component centred on a velocity of $v \sim +50$ km s^{-1};
- conversely the visibility of the blue emission peak decreases when the strength of the absorption increases. In fact, near maximum absorption strength, the blue peak vanishes and the line displays a "normal" P-Cygni type profile.

We have applied the same techniques to the Hα data set but using only ten bins in the phase diagram to sample the complete 4.76-day period (since the phase-coverage is less complete for this data set). The resulting dynamical

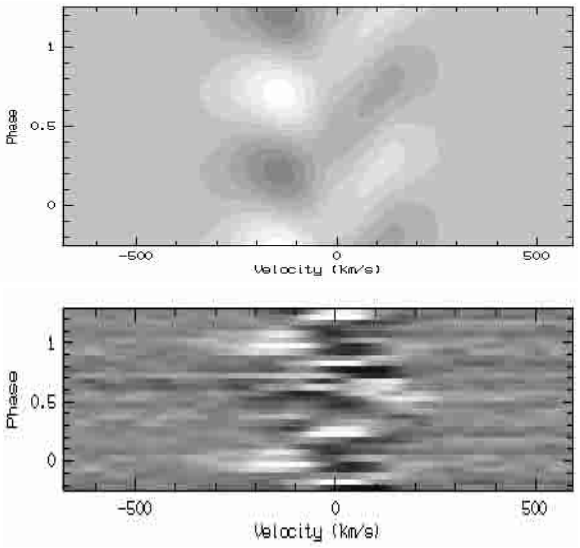

Fig. 9. Upper panel: reconstruction of the modulation of the He II λ 4686 line as a function of phase assuming a period of 4.76 days. The amplitude and phase constant used in the reconstruction are obtained from Eq. (2) and are displayed in Fig. 8. The black pixels correspond to a deficit in the normalized intensity of more than ≥ 0.012 compared to the mean profile, whereas the white pixels indicate an excess intensity of ≥ 0.012. Lower panel: grey-scale image of the residuals (observed – calculated) as a function of phase. This image shows that the variations in the velocity range $[-300, -50]$ km s^{-1} are very well matched by our restoration of the ν_1 frequency, whereas the variations in the emission component are heavily affected by the other frequencies

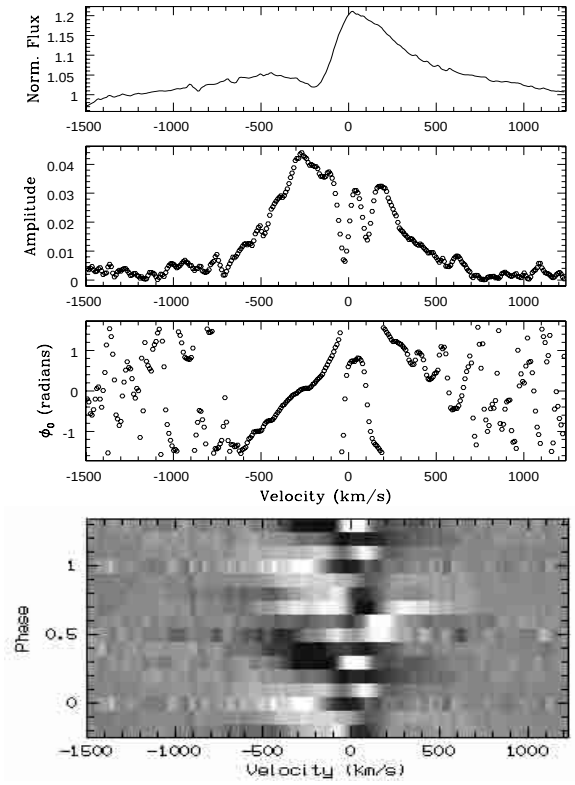

Fig. 10. Same as Fig. 8 but for the Hα line. The black pixels in the dynamical spectrum correspond to a ratio ≤ 0.96, whereas the white pixels indicate a ratio ≥ 1.04

spectrum and reconstruction are shown in Figs. 10 and 11 respectively. We notice the following characteristics:

- contrary to the situation of the He II λ 4686 line, the phase constant $\phi_0(v)$ shows a steady decrease towards more negative velocities across the Hα absorption component;
- there are two local minima in the amplitude of the sinusoidal variations near $v \sim -25$ km s^{-1} and $+100$ km s^{-1};
- the variations of the intensity of the emission peak are less clearly related to those of the absorption component than in the case of the He II λ 4686 line.

We have measured the equivalent widths of the absorption components in the Hα and He II λ 4686 P-Cygni profiles. A Fourier analysis of the *EW*s of the He II λ 4686 absorption yields the strongest peak at 0.2075 d^{-1}, which is an alias of ν_1 (ν_1 itself being the second highest peak). The phase diagram of the *EW*s is shown in Fig. 12. Although there is considerable scatter in this diagram, we notice that the *EW*s of the absorption components of both lines undergo variations by more than a factor of three. The *EW*s are larger between phase ∼0.1 and ∼0.45 and are in fact maximum around phase 0.3. The duration and amplitude of the absorption enhancement reveal an increase of the density and/or the opacity in a significant fraction of the wind column towards the stellar surface. There is no evidence for a significant phase-lag between the variations of the equivalent widths of the absorption components of the two lines.

The pattern of the variability of the Hβ line with the ν_1 frequency is very similar to the one of the He II λ 4686 line. This similarity is not unexpected given the correlation between the variability of both lines found in Paper I. This result indicates that the variations in the blue wing of the Hβ line with ν_1 are most probably due to a changing amount of wind absorption and emission rather than to a genuine variability of the underlying photospheric absorption.

3.3. Radial velocities and equivalent widths of the absorption lines

In Paper I, we concluded that binarity was not a likely explanation for the variability of the He II λ 4686 line observed in the spectrum of HD 192639. To check this conclusion, we have measured the radial velocities of the most prominent absorption lines on our new data by fitting Gaussian profiles. The results confirm the very small range of variability of the radial velocities already found in

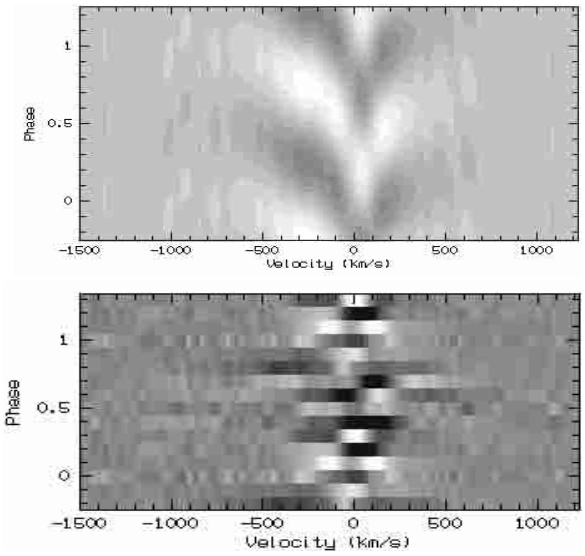

Fig. 11. Same as Fig. 9 but for the Hα line. The amplitude and phase constant of the ν_1 modulation were obtained from Eq. (2) including a simultaneous fit of the 0.03 d^{-1} frequency. The black pixels in the dynamical spectrum correspond to a deficit of more than ≥ 0.044, whereas the white pixels indicate an excess of ≥ 0.044

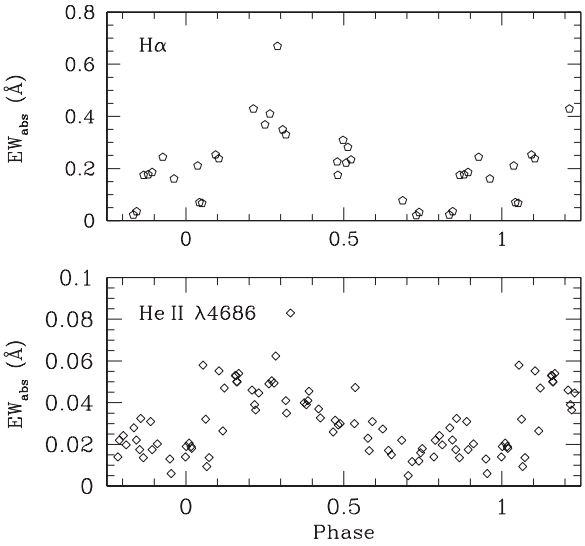

Fig. 12. Phase diagram of the *EW*s of the absorption components of the Hα and He II λ 4686 lines assuming a period of 4.76 days. Phase 0.0 was arbitrarily chosen on JD 2450000.00

Paper I. For instance, for the He II λ 4542 line we can set an upper limit of 5 km s^{-1} on the semi-amplitude of any radial velocity variation in a putative single-lined spectroscopic binary.

We applied a Fourier analysis to the RVs of the individual absorption lines. It turns out that the RVs of different spectral lines yield quite different power spectra with the most prominent peak occurring usually at frequencies below 0.02 d^{-1}. None of the power spectra displays a significant peak near ν_1. Nevertheless, we have folded the RV data with the 4.76-day "period" determined above. The result is shown in Fig. 13. There is no systematic trend in this phase diagram.

Assuming HD 192639 was a binary system made of two nearly identical stars seen under a low inclination angle, one could expect that the lines of the two stars would remain heavily blended all over the orbital cycle. In this case, the variations of the width of the absorption lines would provide the only "finger-print" of an orbital motion. The broadening of the Hβ line observed around JD 2451067.4 and JD 2451072.4 yields therefore an upper limit of $\sim$50 km s^{-1} on the radial velocity separation between the two components in a putative binary system around quadrature. However, the fact that the He II and N III absorption lines (which are expected to be less affected by stellar wind emission and absorption than the Hβ line) exhibit no trace of a broadening or any other significant variability at the ν_1 frequency argues against a binary explanation for the ν_1 modulation.

In summary, there is no consistent periodicity in the RVs of the different absorption lines and although we cannot completely rule out a binary system seen under a very low inclination angle, it seems more likely that the line profile variations with the ν_1 frequency arise in the stellar wind of a single star.

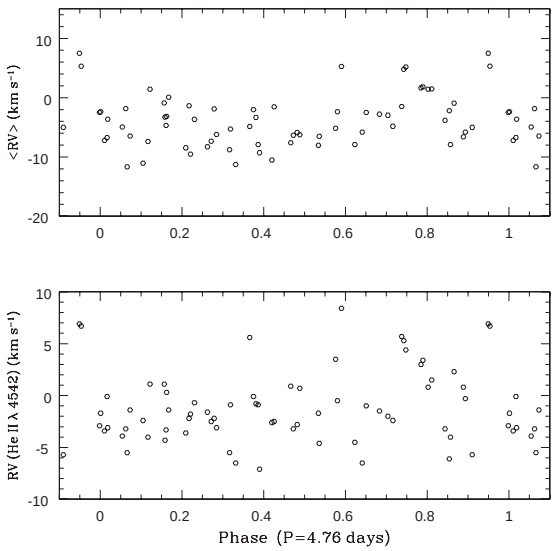

Fig. 13. Upper panel: phase diagram of the mean radial velocity of the He I $\lambda\lambda$ 4471, 4713 and N III $\lambda\lambda$ 4511, 4515 absorption lines assuming a period of 4.76 days. Lower panel: same but for the RVs of the He II λ 4542 line

We have measured the equivalent widths of the He I λ 4471 and He II λ 4542 lines to search for any phase-dependence of the intensity ratio of these lines. According to Conti (1973) the ratio $\log W' = \log\left(\frac{EW(4471)}{EW(4542)}\right)$ provides an efficient temperature classification criterion for O-stars, provided that both diagnostic lines are formed in the photosphere. Assuming that the structure in the wind of HD 192639 results from some kind of "hot" or "cold spot" at the level of the star's photosphere that covers a significant fraction of the stellar surface, we could in principle set an upper limit on the difference in temperature between this "spot" and the ambient photosphere. We obtain an average value of $\log W' = 0.045$ for HD 192639 which corresponds to an O7.5 star. The equivalent width ratio displays some variations corresponding to an apparent spectral type between O7.5 and O8. However, these variations are not "phase-locked" with the 4.76-day cycle. Moreover, in the case of HD 192639, the use of the Conti criterion as a diagnostic of the photospheric temperature is probably ambiguous because of the contamination of the photospheric absorption lines by a variable wind emission and/or absorption. Indeed, the variations of the W' criterion reflect mainly those of the equivalent width of the He I λ 4471 line which is most probably partially formed in the wind (see also Paper I). Therefore it seems likely that the variations discussed hereabove do not reflect a genuine change of the local effective temperature but are rather due to a change in the optical depth in the wind.

4. Discussion

Our spectroscopic time series reveals the existence of a cyclical modulation of the P-Cygni profiles in the visible spectrum of HD 192639 with a period of $P_{\rm obs} \simeq$ 4.8 days (assuming that ν_1 is indeed the right alias). The phenomenon persisted over at least four years.

Nowadays, the most popular explanation for periodic variability of the stellar wind features in OB-type stars assumes that the observed period corresponds to a meaningful fraction of the rotational period (i.e. $P_{\rm obs} = P_{\rm rot}/n$, where n is an integer). Assuming a radius of 19.5 $R_\odot$ (Herrero et al. 1992; Puls et al. 1996), we can derive an upper limit on $P_{\rm rot}$. Using the most recent determinations of the projected rotational velocity $v_e \sin i = 96$ km s^{-1} (Howarth et al. 1997) and 110 km s^{-1} (Penny 1996), we obtain upper limits of 10.30 and 8.99 days respectively. Therefore, in the framework of a rotational modulation hypothesis, the 4.8-day time scale could correspond either to $P_{\rm rot}$ or $P_{\rm rot}/2$. In the former case, the recurrent modulation could be produced by a single feature in the wind, whereas in the latter configuration the lack of a significant signal in the power spectrum near $\nu_1/2$ implies two very similar wind features which would have to be roughly symmetric about the rotation axis. If we assume that $n = 1$, we find that $i \sim 30° \pm 3°$, while $n = 2$ yields $i \geq 68°$.

4.1. Comparison with other stars

The line profile variations detected in the optical wind features of HD 192639 are reminiscent of those detected by Kaper et al. (1997) in the Hα line profile of α Cam (O9.5 Ia) and ζ Ori (O9.7 Ib). It is worth noting that these authors found that Hα variability is usually concentrated in the low velocity ($0.0-0.2 \times v_\infty$) part of the line profile. Kaper et al. (1997) also report an episodic strengthening of the emission component in the Hα profile of 19 Cep (O9.5 Ib) that is reminiscent of the one we observe in the spectrum of HD 192639 on JD 2451061.66.

So far, the most prominent examples of rotationally modulated winds were found from extensive observations of UV resonance lines with the IUE satellite (see e.g. Howarth et al. 1995; Fullerton et al. 1997; Henrichs et al. 1998; Kaper et al. 1999). In the case of HD 64760 (B0.5 Ib), Fullerton et al. (1997) report a periodic ($P \sim$ 1.2 days) modulation of the mean flux level over most of the P-Cygni absorption trough of the prominent Si IV, C IV and N V doublets. An interesting feature of these structures is that a particular phase of the modulation occurs first at an intermediate velocity before it simultaneously reaches higher and lower velocities. This "phase bowing" effect is interpreted by Fullerton et al. (1997) as evidence for a significant azimuthal extent of the structures in the wind of HD 64760. Kaper et al. (1999) report a similar effect for the discrete absorption components (DACs) seen in the resonance lines of ξ Per (O7.5 III). At this point, it is worth noting that the He II λ 4686 and Hα lines in HD 192639 show no trace whatsoever of such a bowing of the phase constant. Instead, the phase constant $\phi_0(v)$ remains roughly constant over the He II λ 4686 absorption component while it undergoes a systematic decrease towards more negative velocities in the Hα absorption trough. The latter situation is slightly similar to what is seen in the UV resonance lines of most of the O-stars observed by Kaper et al. (1999). As far as the DAC features in the UV lines are concerned, this phase behaviour is usually attributed to an outwards moving accelerating structure.

The difference in phase behaviour between the He II λ 4686 and Hα lines of HD 192639 is somewhat surprising. The roughly constant ϕ_0 of the He II λ 4686 absorption component is easily understood in terms of a corotating line forming region confined to the inner region of the wind. On the other hand, the rough similarity between the phase behaviour in the Hα line and typical UV lines (in other stars) points toward a significantly larger radial extent of the Hα line forming region.

The cyclical modulation of the absorption component of the P-Cygni profiles in the visible spectrum of HD 192639 extends to velocities of $\sim$–350 and -600 km s^{-1} for the He II λ 4686 and Hα profiles respectively. Assuming that we see the wind modulation head-on and adopting the terminal velocity $v_\infty = 2150$ km s^{-1} determined by Puls et al. (1996), these velocities correspond to $0.16 \times v_\infty$ and $0.28 \times v_\infty$ respectively. Using the $\beta = 0.95$

"standard" velocity law of Puls et al. (1996) we find that the variability of the P-Cygni absorptions of the two lines probes the base of the wind out to 1.17 R_* and 1.35 R_* respectively. It seems unlikely that such a small difference in the radii of the line forming region could actually account for the different phase behaviour of Hα and He II λ 4686. It seems therefore likely that the velocity law in the line forming region deviates from a standard law and there could be a velocity plateau associated with the structure that generates the line profile modulation. Such plateaus are predicted for instance in the case of corotating interaction regions (Cranmer & Owocki 1996).

The most straightforward interpretation of the phase behaviour of the He II λ 4686 and Hα lines seems to be that the wind rotates roughly as a rigid body out to some distance and then reverts to a Keplerian rotation plus an outwards acceleration due to the radiation pressure. Such a behaviour could be caused by a magnetic field. Indeed, if we adopt the mass loss rate, radius and velocity law derived by Puls et al. (1996) as a first approximation, we find that a bipolar magnetic field of $B_* \simeq 115$ G yields an Alfvén radius of 1.17 R_*, whilst $B_* \simeq 200$ G yields an Alfvén radius of 1.35 R_*. Therefore a moderate magnetic field could be sufficient to force the inner wind region, where the bulk of the He II λ 4686 emission forms, into a rigid body corotation.

4.2. Towards a possible explanation

If we accept the idea that the stellar rotation sets the timescale of the variability, we need to imagine a wind geometry that can produce the modulation observed in the spectrum of HD 192639. In this section, we review the pros and cons of two rather simple models that could account for some of the observed properties of the spectral lines discussed hereabove.

Let us first consider the possibility of a structure resulting from a localized "bright spot" on the stellar surface. Such a spot is expected to produce an enhanced mass flux resulting in a localized slow wind stream. Fast wind streams from adjacent regions will collide with the slower wind generating a so-called corotating interaction region (CIR; Cranmer & Owocki 1996; Owocki 1999). These CIRs are thought to produce the cyclical modulation of the P-Cygni absorptions in UV resonance lines (e.g. Fullerton et al. 1997). The increase of the wind density in the CIR (Cranmer & Owocki 1996) will allow the He II λ 4686 and Hα line formation regions inside the CIR to extend farther away from the star than would be expected for a smooth wind with a $\beta \simeq 1$ standard velocity law. Nevertheless, the formation of the lines probably occurs still rather close to the stellar surface so that the azimuthal extension of the line formation region (at least for He II λ 4686) due to the bending of the CIR structure should remain small.

Harries (2000) presented simulations of synthetic line profiles produced by a corotating spiral density enhancement. He finds that this feature generates an S-wave like pattern as a function of rotational phase. The variations of the He II λ 4686 line displayed in the grey-scale image in Fig. 9 are slightly reminiscent of the synthetic variations simulated by Harries (2000; see his Fig. 4). We note however that the variations observed in the He II λ 4686 profile of HD 192639 occur over a much smaller velocity range and that the behaviour of the Hα line in the spectrum of HD 192639 is quite different from the predictions of this model. Another important difference concerns the time dependence of the modulation. At a given wavelength, the simulations presented by Harries (2000) yield a rather abrupt and short-lived increase of the intensity, whereas our observations reveal a rather smooth (roughly sinusoidal) variation of the intensity (see our Figs. 8 and 10).

A single CIR would be sufficient to account for the observed modulation of the P-Cygni absorption component. However, if the azimuthal extension of the line formation region in the CIR is indeed small, then a second structure is probably required to account for the simultaneous variability of the emission component. If we assume that these structures arise from diametrically opposite spots on the stellar surface, we are confronted with the problem that the second CIR should essentially be occulted by the stellar core when the first one crosses the line of sight. In this case, we would expect the emission component to be significantly reduced at maximum absorption, which is not the case. The observed variability can thus be explained with a CIR scenario if either the spots that generate the CIRs are not symmetric about the center of the star or the formation region of the He II λ 4686 and Hα lines extends along the CIRs out to distances where the azimuthal extent becomes quite significant allowing both CIR features to be visible at maximum absorption (see Fig. 14). However, we recall that the phase behaviour of the He II λ 4686 absorption argues against a noticeable azimuthal bending.

Alternatively, we can imagine a "confined corotating wind" to explain the double-peaked emission component. Conti & Leep (1974) suggested that the double-peaked He II λ 4686 emission line profiles observed in Oef stars are produced in a rotating wind. Assuming that such a corotating wind actually exists in the case of HD 192639, the only way to account for the observed modulation of the absorption component is to consider that the rotating wind is confined in latitude and that its symmetry axis is tilted with respect to the rotation axis. A situation like this could result for instance if HD 192639 were an oblique magnetic rotator. Such a model has been suggested to explain the line profile variability observed in the spectra of ζ Pup (Moffat & Michaud 1981) and θ^1 Ori C (Stahl et al. 1996). Babel & Montmerle (1997) found that a strong enough magnetic field ($B_* \simeq 270-370$ G) can indeed confine a significant fraction of the wind of θ^1 Ori C into a "circumstellar cooling disk" located in the plane of the magnetic equator. The variations of the absorption component of the He II λ 4686 line in HD 192639 (Fig. 9) are indeed a bit reminiscent of the behaviour of this line in θ^1 Ori C (Stahl et al. 1996). The amplitude of the

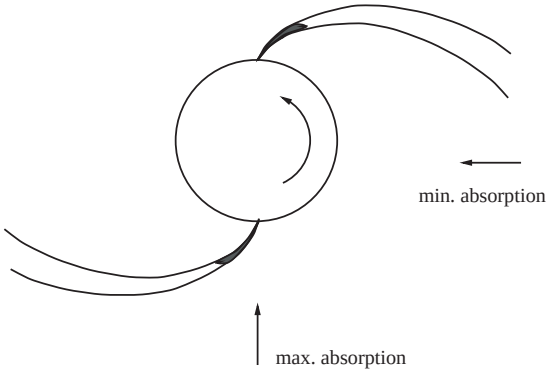

Fig. 14. Schematic view of a CIR structure in HD 192639. The star is shown pole-on and the lines of sight are projected on the equatorial plane. The line formation region along the CIRs is shown by the dark regions. In this cartoon, we have arbitrarily assumed that the spots that generate the CIR are located on the stellar equator. If the spots are diametrically opposite, we find that for reasonable values of the inclination of the rotation axis (and the latitude of the spots), the second CIR should be occulted by the stellar core when the first one passes in front of the star (i.e. at maximum absorption strength)

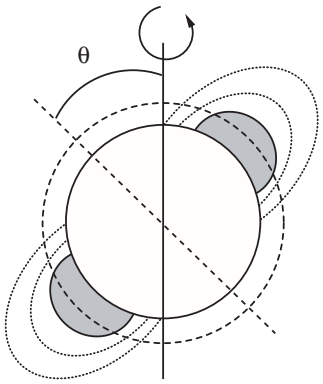

Fig. 15. Schematic view of the confined corotating wind model. The cartoon shows a cross-section across the star by the plane defined by the rotation axis and the magnetic axis. The dashed line indicates the magnetic axis tilted by an angle θ with respect to the rotation axis. The dashed circle corresponds to the Alfvén radius. The confined wind region is schematically represented by the dotted surfaces. The line formation region in the confined wind is shown by the hatched regions

variations in θ^1 Ori C is however about a factor of 10 larger than in HD 192639. Another difference between the two stars is that the lines in the optical spectrum of θ^1 Ori C do not display a P-Cygni type profile.

Let us assume that the line-forming region is a kind of corotating torus tilted with respect to the rotation axis (see Fig. 15). In this configuration, we expect a priori to observe a double-peaked emission line morphology at all rotational phases. Assuming a solid-body rotation law (star + torus), the separation between the two emission peaks would vary roughly between $2\,v_{\rm rot}\,\sin i$ and $2\,v_{\rm rot}\,\sin i\,\cos\theta$ where $v_{\rm rot}$ stands for the rotation velocity of the torus at the intersection between the torus and the stellar (rotational) equator and where θ is the tilt angle of the torus (i.e. the angle between the symmetry axis of the torus and the rotation axis). Of course, the strongest P-Cygni absorption is expected when the torus crosses the line of sight. If $i \sim 30°$ (as expected for $P_{\rm obs} = P_{\rm rot}$), then maximum absorption is predicted to occur when the separation between the two emission peaks is maximum. One would therefore expect to observe a well defined double-peaked emission component around maximum absorption, which is not the case. If instead $i \geq 68°$, then the overall picture depends on the value of θ and maximum absorption can actually occur when the separation between the two peaks is about minimum whilst minimum absorption happens when the two peaks are clearly separated. For reasonable values of the tilt angle θ, we can expect that the separation between the peaks near maximum absorption becomes so small that the peaks are no longer seen as two individual features. Adopting an inclination above 68° and assuming that the wind is confined into a tilted torus allows thus to account qualitatively for most of the observational properties of the P-Cygni profiles in the visible spectrum of HD 192639.

5. Concluding remarks and future work

In this paper, we have shown that the absorption components of the P-Cygni profiles in the optical spectrum of HD 192639 display a periodic modulation with a period of roughly 4.8 days. This period is also found in the emission component of the profiles though with a significantly lower amplitude.

Although we cannot completely rule out a binary system seen under a very low inclination angle, the most likely explanation for the 4.8-day clock is that this period reflects the rotational period (or a meaningful fraction of it) of a single star. Beside the variability of the profile, further evidence for a non-spherical stellar wind comes from the double-peaked structure of the He II λ 4686 and (to some extent) Hα lines. We have discussed two rather simple geometries for the stellar wind in HD 192639. Both a corotating interaction region produced by a local enhancement of the mass loss or a tilted confined corotating wind can be in qualitative agreement with the most important observational properties of the spectral lines discussed in this paper. Detailed simulations of the line profiles adopting the geometries discussed above are needed to further constrain the origin of the phenomenon and to estimate its impact on the accuracy of the mass-loss rates derived from standard model atmosphere codes (Puls et al. 1996). Such quantitative simulations are beyond the scope of the present paper.

If we accept the idea of rotational modulation, we still need to specify the mechanism that generates the structure (be it a CIR or a tilted confined corotating wind) responsible for the observed variation. A magnetic field anchored in the star offers an attractive way to produce such a structure. However, as stated in the introduction, so far there has been no direct detection of such

a magnetic field in a massive star. On the other hand, we can look for other indirect evidence. For instance, it has been suggested that the non-thermal radio emission observed in some OB stars is due to synchrotron radiation of relativistic electrons in the stellar winds (Chen & White 1994 and references therein). Unfortunately, HD 192639 is too faint to be detected in the radio domain and only an upper limit on the flux density at 8.45 GHz is available (Scuderi et al. 1998). Another, maybe more promising, way to learn more about the nature of this intriguing star could be through phase-resolved high resolution spectropolarimetric observations. Finally, high spectral resolution ($\geq$ 50000), high signal to noise and high time resolution spectroscopy of a "wind-free" photospheric absorption line such as He II λ 4542 would allow to search for non-radial pulsations that might play a key role in generating the wind variability.

Acknowledgements. We wish to express our thanks to Tracy L. Smith and David C. Knauth for taking some of the Ritter spectra and to Asif ud-Doula for helpful discussions. We are also grateful to the referee Dr. Alex W. Fullerton for his helpful report. GR would like to thank the staff of the Observatoire de Haute Provence for their technical support during the various observing runs. GR, JMV and EG are greatly indebted to the Fonds National de la Recherche Scientifique (Belgium) for multiple assistance including the financial support for the rent of the OHP telescope in 1999 through contract 1.5.051.00 "Crédit aux Chercheurs" FNRS. This research is also supported in part by contract P4/05 "Pôle d'Attraction Interuniversitaire" (SSTC-Belgium). Partial support through the PRODEX XMM-OM Project is also gratefully acknowledged. The travels to OHP for the observing runs were supported by the Ministère de l'Enseignement Supérieur et de la Recherche de la Communauté Française. The SIMBAD database has been consulted for the bibliography.

References

Abt, H. A., & Morrell, N. I. 1995, ApJS, 99, 135
Babel, J., & Montmerle, T. 1997, ApJ, 485, L29
Chen, W., & White, R. L. 1994, Ap&SS, 221, 259
Conti, P. S. 1973, ApJ, 179, 181
Conti, P. S., & Leep, E. M. 1974, ApJ, 193, 113
Cranmer, S. R., & Owocki, S. P. 1996, ApJ, 462, 469
de Jong, J. A., Henrichs, H. F., Schrijvers, C., et al. 1999, A&A, 345, 172
Fullerton, A. W. 1999, in IAU Coll. 169, Variable and Non-spherical Stellar Winds in Luminous Hot Stars, ed. B. Wolf, O. Stahl, & A. W. Fullerton, Lect. Notes Phys., 523, 3
Fullerton, A. W., Gies, D. R., & Bolton, C. T. 1996, ApJS, 103, 475
Fullerton, A. W., Massa, D. L., Prinja, R. K., Owocki, S. P., & Cranmer, S. R. 1997, A&A, 327, 699
Harries, T. J. 2000, MNRAS, 315, 722
Heck, A., Manfroid, J., & Mersch, G. 1985, A&AS, 59, 63
Henrichs, H. F., de Jong, J. A., Nichols, J. S., et al. 1998, in Ultraviolet Astrophysics Beyond the IUE Final Archive, ESA-SP 413, 157
Herrero, A., Kudritzki, R. P., Vilchez, J. M., et al. 1992, A&A, 261, 209
Howarth, I. D., Prinja, R. K., & Massa, D. 1995, ApJ, 452, L65
Howarth, I. D., Siebert, K. W., Hussain, G. A. J., & Prinja, R. K. 1997, MNRAS, 284, 265
Kaper, L., Henrichs, H. F., Fullerton, A. W., et al. 1997, A&A, 327, 281
Kaper, L., Henrichs, H. F., Nichols, J. S., & Telting, J. H. 1999, A&A, 344, 231
Massa, D., Fullerton, A. W., Nichols, J. S., et al. 1995, ApJ, 452, L53
Mathys, G. 1999, in IAU Coll. 169, Variable and Non-spherical Stellar Winds in Luminous Hot Stars, ed. B. Wolf, O. Stahl, & A. W. Fullerton, Lect. Notes Phys., 523, 95
Moffat, A. F. J., & Michaud, G. 1981, ApJ, 251, 133
Owocki, S. P. 1999, in IAU Coll. 169, Variable and Non-spherical Stellar Winds in Luminous Hot Stars, ed. B. Wolf, O. Stahl, & A. W. Fullerton, Lect. Notes Phys., 523, 294
Penny, L. R. 1996, ApJ, 463, 737
Puls, J., Kudritzki, R.-P., Herrero, A., et al. 1996, A&A, 305, 171
Rauw, G., & Vreux, J.-M. 1998, A&A, 335, 995, Paper I
Scuderi, S., Panagia, N., Stanghellini, C., Trigilio, C., & Umana, G. 1998, A&A, 332, 251
Stahl, O., Kaufer, A., Rivinius, T., et al. 1996, A&A, 312, 539

HD 192639: some additional remarks

Recently, Markova et al. (2005) discussed the Hα variability of a sample of 15 O supergiants, including HD 192639. They found significant line profile variability arising in the stellar wind. Interpreted in terms of a variable mass-loss rate, the observed variations of the Hα line of HD 192639 correspond to $\Delta\dot{\mathrm{M}} = 16\%$. However, their sample consists of only 7 snapshot spectra spread over 18 months (from June 1997 to December 1998) with at least one month between two consecutive observations. Therefore, the authors caution that their dataset is not suited to characterize the time scale and variability pattern of the wind variability. Despite this caveat, the authors claim that they find no evidence for deviations from spherical symmetry or homogeneity in contrast to our finding reported above. Markova et al. (2005) accordingly suggest that the variability pattern that we observed might have been produced by a transient rather than a permanent structure.

Without a new dedicated campaign it is quite difficult to prove that the 4.8-day modulation that we have discussed above is indeed strictly periodic and stable over long time scales. However, in my opinion, the conclusion of Markova et al. (2005) must be considered with caution. Indeed, their sample is by no means suited to prove the existence or absence of a modulation on a time scale of less than five days! Only an intensive monitoring of the star over at least ten consecutive nights, such as the one that we have performed in 1998, would be helpful in this context. In addition, their conclusion must be questioned because most of our He II λ 4686 data were also taken in 1997 and 1998 (i.e. at the same epoch as their snapshot observations) and indicate a consistent behaviour between these two years. It would be quite strange to imagine that HD 192639 only displayed a regular variability during our own observing campaign and not at other times! Finally, it should be stressed that the line profiles shown in the literature (and sometimes taken many years before our observations) are remarkably similar to the kind of profiles that we have observed.

Markova et al. (2005) found that the Hα profile variability occurs at velocities below 0.3 v_∞ and hence at radii below 1.5 R_*. This is in reasonable agreement with the results reported by Rauw et al. (2001a). Using the stellar and wind parameters derived by Markova et al. (2005, see Table 4.1), one can re-estimate the magnetic field strength assuming the Alfvén radius of HD 192639 to be equal to either 1.17 or 1.35 R_* (as in Rauw et al. 2001a). In this way, one finds $B_* = 104$ and 191 G for $\mathrm{R_A} = 1.17\,R_*$ and $1.35\,R_*$ respectively. These figures are in very good agreement with the estimates in Rauw et al. (2001a). Finally, it is interesting to note that to produce a rigidly corotating wind extending out to $1.5\,R_*$ (i.e. the outer limit of the variability according to Markova et al.), a magnetic field strength of 270 G would be required.

As a next step in the study of HD 192639 ($V = 7.1$), it would thus be highly desirable to obtain spectropolarimetric observations of the star to constrain its magnetic field strength (e.g. Donati et al. 2002). While such observations were previously restricted to very bright O-type stars (such as θ^1 Ori C, $V = 5.1$; Donati et al. 2002), the recent detection of a moderate (220 G) line-of-sight magnetic field (which, for a dipolar geometry, translates into a polar field of 1500 G; Donati et al. 2006) in the Of?p star HD 191612 ($V = 7.8$ very much comparable to HD 192639) is quite encouraging in this sense.

Table 4.1: Stellar and wind parameters of HD 192639 as derived by Markova et al. (2005).

$T_{\rm eff}$ (kK)	R_* ($R_\odot$)	$\log g$	$\log \frac{L}{L_\odot}$	v_∞ (km s^{-1})	β	$\dot{M}$ ($M_\odot$ yr^{-1})
34.7	17.2	3.39	5.59	2150	1.09	5.05×10^{-6}

4.3 The spectroscopic variability of Oef stars

Since rotation has been suggested to play a major role in the spectroscopic variability of O-type stars, the next logical step is to investigate the behaviour of those O stars that have the largest rotational velocities. Such stars are found in the category of Oef stars (also known as Onfp stars in the classification scheme of Walborn). The main distinctive feature of these stars is a double-peaked He II λ4686 emission line, whilst no Balmer line emission is observed. The particular He II λ4686 line morphology is interpreted as a result of the rotation of an expanding wind. The classical picture for line formation in the winds of Of and Oef stars is illustrated in Fig. 4.1.

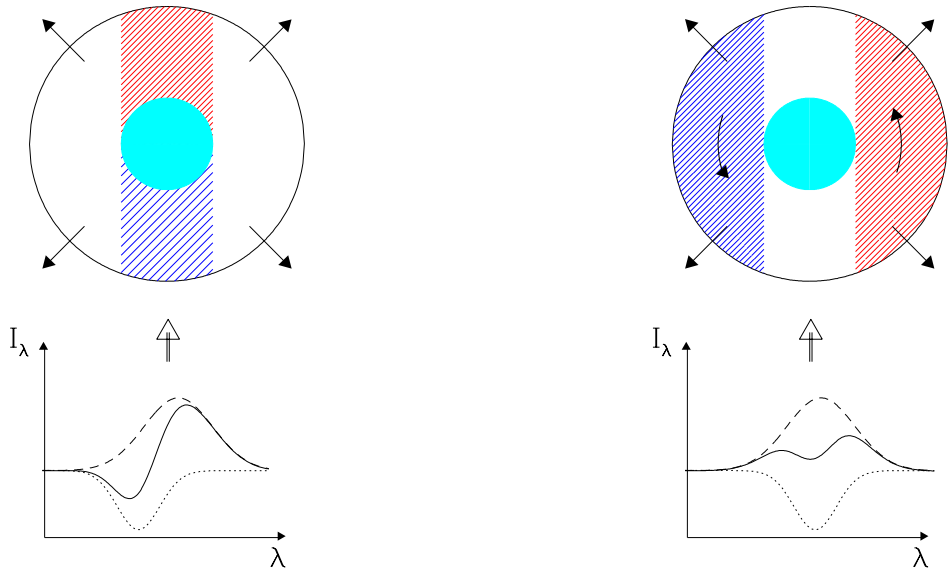

Figure 4.1: Schematic view of the way P-Cygni and double-peaked emission lines are formed in expanding Of stellar winds (left) and rotating expanding winds (proposed to be valid for Oef stars, right) respectively.

P-Cygni profiles are produced by an accelerating outflow that is superimposed onto a bright background. Along the line of sight towards the photosphere, scattering by resonance lines removes photons from the continuum thus producing a blue-shifted absorption component. Simultaneously, the scattering events that take place in the side lobes of the wind send photons in the direction towards the observer, thus inducing a flux excess centered on the systemic velocity of the star.
In the spectra of Oef stars, the He II λ4686 line displays a profile consisting of a blue- and a red-shifted emission peak along with a central reversal. This so-called type III profile morphology in the classification scheme of emission lines introduced by Beals (1950) is interpreted as the result of the

combination of the rotation velocity field with the radial outflow velocity field of the wind (see Fig. 4.1). In our Galaxy, only half a dozen Oef stars are known. However, 16 new ones have been discovered over the last years in the Magellanic Clouds. Interest in these objects has recently grown following the suggestion by Walborn (2006) that their large rotational velocities could indicate them to be the results of stellar mergers and/or the progenitors of γ-ray bursts.

4.3.1 BD$+60^\circ$ 2522

In the following pages, I reproduce the analysis of a long term spectroscopic monitoring campaign of the Oef star BD$+60^\circ$ 2522 (Rauw et al. 2003a). The double-peaked He II λ 4686 emission undergoes strong profile variability on time scales of 2 – 3 days, although the time scale as well as the pattern of these variations turn out to be epoch dependent and the phenomenon is thus most likely not ruled by a single stable clock. It is tentatively proposed that the beating of several non-radial pulsation modes could trigger transient large-scale density perturbations in a confined stellar wind.

A&A 399, 287–296 (2003)
DOI: 10.1051/0004-6361:20021776

Astronomy & Astrophysics

Line profile variability in the spectra of Oef stars

I. BD + 60° 2522⋆

G. Rauw⋆⋆, M. De Becker, and J.-M. Vreux

Institut d'Astrophysique et de Géophysique, Université de Liège, Allée du 6 Août, Bât. B5c, 4000 Liège (Sart Tilman), Belgium

Received 5 November 2002 / Accepted 14 November 2002

Abstract. We report the analysis of a long term observing campaign designed to monitor the spectroscopic variability of the Oef star BD +60° 2522. We find that the double-peaked He II λ 4686 emission line undergoes strong profile variability on time scales of 2–3 day. However, the time scale as well as the pattern of these variations turn out to be epoch dependent and the phenomenon is thus most likely not ruled by a single stable clock. On the other hand, the absorption lines in the spectrum of BD +60° 2522 display line profile variability on time scales of a few hours that might be related to non-radial pulsations. We tentatively propose that the beating of several non-radial pulsation modes triggers transient large-scale density perturbations in a confined stellar wind that produce the 2–3 day time scale variability.

Key words. line: profiles – stars: early-type – stars: mass-loss – stars: individual: BD +60° 2522 – stars: variables: general

1. Introduction

Almost thirty years ago, Walborn (1973) and Conti & Leep (1974) called attention to a group of Of stars where the He II λ 4686 emission line is found to display a double-peaked profile. These objects were classified as Onfp stars by Walborn (1973), whereas Conti & Leep (1974) favored an Oef naming (we shall adopt the latter terminology throughout this paper). In both papers, it was pointed out that the stars in this category are rapid rotators (as derived from their broad absorption lines) and that the occurrence of the Oef phenomenon may be related to rotation. More specifically, Conti & Leep (1974) suggested that the peculiar morphology of the He II λ 4686 profiles results from a combination of a roughly central emission and a slightly blueshifted absorption in stars having stellar winds with appreciable rotational rates (see also Petrenz & Puls 1996).

Oef stars usually do not display emission in the Balmer lines, but they have broad absorption lines indicative of large projected rotational velocities. All known Oef stars are of early spectral type. Conti & Leep (1974) listed a total of six stars belonging to this category; all of them, except ζ Pup, being located in the northern hemisphere. The brightest and hence best studied representatives of this group are ζ Pup (O4 ef) and λ Cep (O6 ef). The remaining four objects (HD 14434, HD 14442, HD 192281 and BD +60° 2522) have received little attention over the last three decades.

Considerable progress in our understanding of the stellar winds of early-type stars has been achieved through extensive monitoring of their spectroscopic variability and the discovery that some of the cyclical variations could be related to a rotational modulation of the stellar wind (for a review, see e.g. Fullerton 1999). Since rotation is believed to shape the winds of Oef stars, these objects appear a priori as good candidates to search for a rotational wind modulation. In fact, part of the line profile variability observed in the spectra of ζ Pup and λ Cep has been attributed to the effect of rotation (Moffat & Michaud 1981; Howarth et al. 1995; Kaper et al. 1999). In order to investigate the spectroscopic variability of the other, poorly known, Oef stars, we have started an extensive observing campaign to collect spectra of these objects. In the present paper, we focus on the results of our seven year observing campaign of BD +60° 2522. The spectroscopic variability of HD 14434, HD 14442 and HD 192281 will be discussed in a forthcoming paper (De Becker et al. 2003, in preparation).

BD +60° 2522 (V = 8.7) is the ionizing star of NGC 7635, the so-called "Bubble Nebula" (see e.g. Christopoulou et al. 1995). NGC 7635 lies at the edge of a low-density clumpy molecular cloud and the nebula can be interpreted as a wind-blown bubble created by the interaction of the stellar wind of BD +60° 2522 with the ambient interstellar medium (Christopoulou et al. 1995; Chavarría-K. et al. 1987). While many investigations have focused on the nebula, little attention has been paid to the star itself.

The paper is organized as follows. Section 2 briefly summarizes our observing campaign and the data reduction. In Sect. 3 we present the results of our radial velocity and line profile

Send offprint requests to: G. Rauw,
e-mail: rauw@astro.ulg.ac.be

⋆ Based on observations collected at the Observatoire de Haute Provence, France.

⋆⋆ Research Associate FNRS (Belgium).

variability analyses. The origin of the line profile variability is discussed in Sect. 4 and our conclusions are highlighted in Sect. 5.

2. Observations and data reduction

Spectroscopic observations of BD +60° 2522 were collected during several observing campaigns between August 1996 and September 2002 at the Observatoire de Haute-Provence (OHP).

Our observations were obtained with the Aurélie spectrograph fed by the 1.52 m telescope at OHP (Gillet et al. 1994). Until 1999, Aurélie was equipped with a Thomson TH7832 linear array with a pixel size of 13 μm. From 2000 on, the detector of the Aurélie instrument was replaced by a 2048×1024 CCD EEV 42-20#3, with a pixel size of 13.5 μm squared.

Table 1 provides an overview of the various instrumental configurations. All the data were reduced in the standard way using the MIDAS package developed at ESO. The spectra were normalized using properly chosen continuum windows.

Table 1 also yields some information about the sampling of the various observing campaigns. For each campaign, ΔT gives the total time elapsed between our first and our last observation, while N is the total number of observations. $\overline{\Delta t}$ provides the average time interval between two consecutive exposures during the same night. In light of the Fourier analysis, Table 1 further lists the natural width of a peak in the power spectrum $\Delta\nu_{\rm nat} = 1/\Delta T$, while $\nu_{\rm max} = 1/(2\,\overline{\Delta t})$ provides a rough indication of the highest frequencies that could be sampled with our data set.

3. Results

3.1. The spectrum of BD + 60° 2522

The blue-violet spectrum of BD +60° 2522 is shown in Fig. 1. Besides the typical absorption lines of H I, He I and He II, this spectral domain contains the complex emission blend of N III $\lambda\lambda$ 4634-41 and C III $\lambda\lambda$ 4647-50 as well as the double-peaked He II λ 4686 emission. The latter emission lines are found on top of a broad emission extending from about 4610 to 4720 Å, a feature that is quite common among Of stars (Underhill et al. 1989). We also note the faint Of emission lines at 4485 and 4505 Å attributed to S IV by Werner & Rauch (2001). We caution that the Balmer absorption lines might be contaminated by nebular emission from the Bubble Nebula.

The ratio of the equivalent widths (*EW*s) of the He I λ 4471 and He II λ 4542 lines, $\log W' = \log(EW(\mathrm{HeI}\,\lambda\,4471)/EW(\mathrm{HeII}\,\lambda\,4542)) = -0.18 \pm 0.03$, as measured on our spectra (Table 2), points towards an O6.5 spectral type for BD +60° 2522 according to the classification scheme of Conti (1973). This result is in excellent agreement with previous classifications. Doroshenko (1972) inferred an O5 spectral type[1], while Walborn (1973) and Conti & Leep (1974) classified BD +60° 2522 as O6.5 (n)(f)p and O6.5 IIIef respectively.

[1] Although we note that the equivalent widths of the He I λ 4471 and He II λ 4542 lines quoted by Doroshenko (1972) yield an O5.5 spectral type according to the classification criterion introduced lateron by Conti (1973).

The giant luminosity class quoted by Conti & Leep was first proposed by Conti & Alschuler (1971). Since none of the conventional luminosity criteria (mainly based on the nature and strength of He II λ 4686) can be applied to BD +60° 2522 in a straightforward manner, we refrain from proposing a luminosity class ourselves.

3.2. Radial velocities

Doroshenko (1972) noted an apparently "abnormal energy distribution" and suggested that this could be the signature of a binary system with the secondary being of spectral type F5 Ib. Subsequent investigations revealed however that flat energy distributions are common among Of stars and can be attributed to the effect of atmospheric extension (see e.g. Kuan & Kuhi 1976).

To investigate the multiplicity of BD +60° 2522, we have measured the radial velocities (RVs) of the two most prominent absorption lines in the 4455–4905 Å domain (i.e. He I λ 4471 and He II λ 4542) by fitting Gaussians. The results indicate a rather small range of variability. For the He I λ 4471 and He II λ 4542 lines we find standard deviations around the mean RV of respectively 9.4 and 7.1 km s^{-1}.

We applied a Fourier analysis to the entire *RV* data set of each of the two absorption lines. The most prominent peaks in the power spectra occur at frequencies below ~0.03 d^{-1}. The amplitudes of the sine waves fitted to the data at the "highest-peak" frequencies are 7.2 and 5.4 km s^{-1} respectively for He I λ 4471 and He II λ 4542. These amplitudes are of the same order as the typical errors on a single *RV* point (~10 km s^{-1} for the 33 Å mm^{-1} data) and we do not regard them to be significant. Moreover, both absorption lines undergo profile variations (see Sect. 3.3.2) that may account for the small amplitude *RV* variations discussed here.

Since no significant short-term variability was found, we have averaged the *RV*s from each observing campaign (see Table 2). Most of these values overlap within the errors with the mean of the entire data set (Fig. 2).

In summary, there is no consistent and significant periodicity in the RVs of the different absorption lines and although we cannot completely rule out a long period binary system seen under a very low inclination angle, it seems more likely that BD +60° 2522 is indeed a single star.

3.3. Line profile variability

To identify the features in the spectrum of BD +60° 2522 that display significant variability, we have computed the time variance spectrum (*TVS*, Fullerton et al. 1996) of our entire data set over the spectral range 4465 to 4800 Å. The largest amplitude of the *TVS* is found over the He II λ 4686 line. Significant variability occurs also in the He I λ 4471 and He II λ 4542 lines. On the other hand, the *TVS* of the entire data set yields some marginal variability in the N III $\lambda\lambda$ 4634-41 and C III $\lambda\lambda$ 4647-50 blend, but this variability disappears when we consider the *TVS* of individual observing campaigns. The variability in the entire data set could either result from long term changes or

Table 1. Overview of our observing campaigns. The third column indicates the detector used with the Aurélie spectrograph (see text). N yields the number of spectra. ΔT, $\overline{\Delta t}$, $\Delta\,\nu_{\rm nat}$ and $\nu_{\rm max}$ provide for each campaign respectively the total time elapsed between the first and the last observation, the average time interval between consecutive exposures during the same night, the natural width of a peak in the power spectrum and the highest frequency that can be sampled with our data set (see text). $(S/N)_0$ stands for the average signal to noise ratio evaluated over a line-free region of the spectrum.

Run	Epoch	Detector	Spectral range (Å)	Recipr. disp. (Å mm^{-1})	N	ΔT days	$\overline{\Delta t}$ days	$\Delta\,\nu_{\rm nat}$ (d^{-1})	$\nu_{\rm max}$ (d^{-1})	$(S/N)_0$
[1]	Aug. 1996	TH 7832	4100–4950	33	13	3.124	0.051	0.320	9.8	320
[2]	Jul. 1997	TH 7832	4100–4950	33	18	6.109	0.044	0.164	11.4	430
[3]	Sep. 1998	TH 7832	4455–4905	16	6	9.008	0.058	0.111	8.6	230
[4]	Jul. 1999	TH 7832	4100–4950	33	14	6.029	0.040	0.166	12.5	215
[5]	Aug. 1999	TH 7832	4100–4950	33	12	13.008	–	0.077	1.0	210
[6]	Sep. 2000	CCD	4455–4905	16	18	10.998	0.024	0.091	20.8	470
[7]	Sep. 2001	CCD	4455–4905	16	14	7.053	0.026	0.142	19.2	320
[8]	Sep. 2002	CCD	4455–4905	16	9	5.006	0.028	0.200	17.6	380

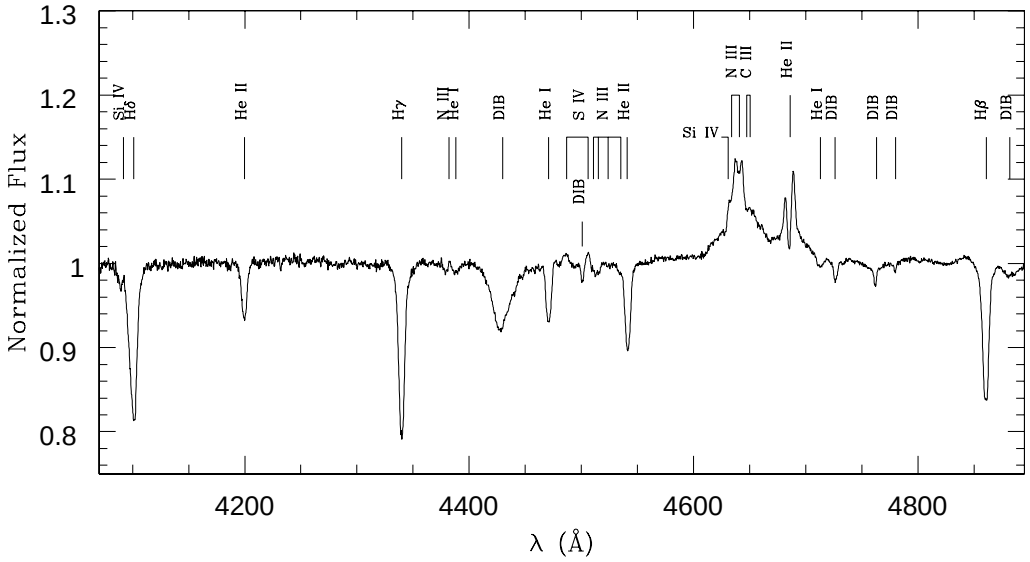

Fig. 1. Mean spectrum of BD +60° 2522 as observed in August 1996.

from small normalization discrepancies between the various data sets. Indeed, some variability is also detected over the narrow diffuse interstellar bands (DIBs) at 4502, 4726, 4763 and 4780 Å. The apparent variability in these features most probably results from small normalization discrepancies between different observing campaigns. During a single observing campaign, these normalization errors are always limited to $TVS^{1/2} \leq 0.004$.

3.3.1. Profile variability of the He II λ4686 line

A simple inspection of the data during the observing runs suggested that the He II λ4686 line varies on time scales of a few days (see Fig. 4). However, when we compare the variations as observed during the various campaigns, we find significant epoch-dependent differences (see Fig. 5).

The overall level of profile variability changes with time. Our *TVS* variability estimator reached its maximum in July 1999 and September 2000, whereas it was lowest in August 1996. Also the wavelength range over which the $TVS^{1/2}$ exceeds the 99% significance level varied from one observing campaign to the other and reached its largest extent in September 2000. But most of all, it is the morphology of the $TVS^{1/2}$ that varies. During observing campaigns [1], [2], [7] and [8], the variability reaches its maximum in the core of the absorption component, whereas the TVS is larger over the emission components during campaigns [5] and [6].

If the line profile variability of the He II λ4686 line were periodic, some of the differences discussed hereabove might actually result from the sampling of the cycle during the various observing campaigns. We have applied the 2-D Fourier techniques described by Rauw et al. (2001) to the time series of each campaign. The results are indicated in Table 3 below. Most of the time the periodograms display one dominant peak together with its one-day aliases. However, in August 1999 (campaign [5]), we find no clearly dominant peak.

Table 2. Properties of the He I λ4471 and He II λ4542 lines in the spectrum of BD +60° 2522. The second column yields the mean observation date in HJD−2450000. Typical standard deviations on the mean equivalent widths are of order 0.03 Å.

Run	$\overline{T}$	He I λ4471		He II λ4542	
		RV (km s^{-1})	*EW* (Å)	*RV* (km s^{-1})	*EW* (Å)
[1]	312.1	−20.9 ± 8.7	0.39	1.1 ± 6.3	0.65
[2]	641.5	−14.3 ± 4.9	0.45	6.4 ± 5.3	0.61
[3]	1071.1	−20.0 ± 5.3	0.42	−2.7 ± 8.6	0.67
[4]	1376.5	−22.6 ± 10.7	0.46	−3.0 ± 9.6	0.66
[5]	1403.7	−28.3 ± 8.9	0.45	−1.1 ± 5.7	0.67
[6]	1815.7	−28.9 ± 7.7	0.46	−5.1 ± 3.8	0.70
[7]	2167.0	−26.1 ± 8.0	0.46	−3.9 ± 4.2	0.72
[8]	2522.4	−28.8 ± 8.8	0.46	−8.6 ± 2.8	0.70

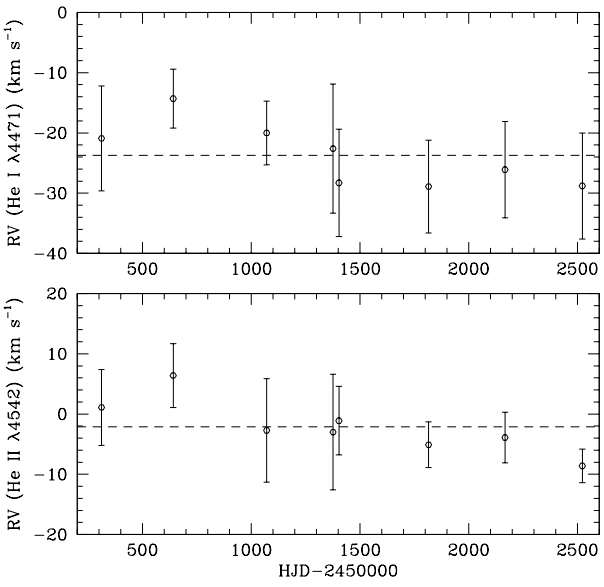

Fig. 2. Epoch-dependent mean *RV*s of the He I λ4471 and He II λ4542 lines in the spectrum of BD +60° 2522. The dashed lines yield the average *RV* over the entire data set. The error bars correspond to the 1-σ *RV* dispersion during a specific run.

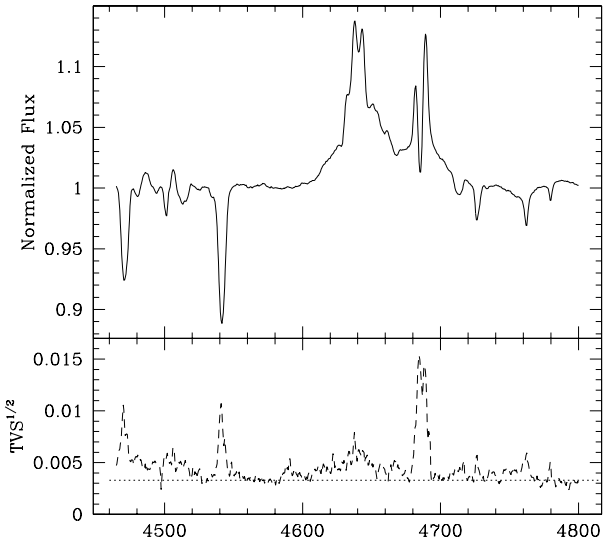

Fig. 3. Top panel: mean spectrum of BD +60° 2522 as observed with the Aurélie spectrograph at OHP from 1996 to 2002. Bottom panel: square root of the time variance spectrum. The dotted horizontal line corresponds to the threshold for variations significant at the 99% level for a total of 104 spectra and an average S/N ratio of 350 (see Fullerton et al. 1996).

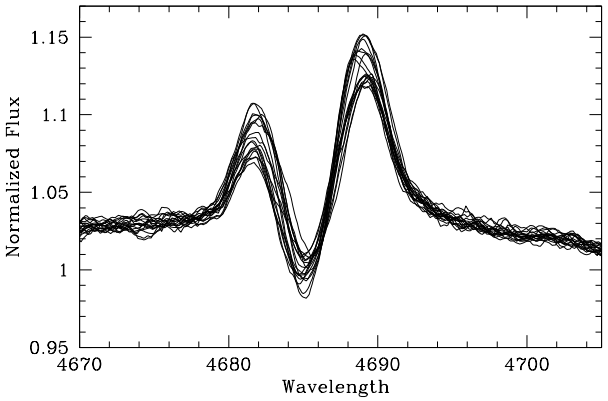

Fig. 4. Variations of the He II λ4686 profile as observed in September 2000. During this campaign, the variations mainly resulted from changing relative intensities of the violet and red emission component.

Most intriguing is the fact that the position of the dominant peak changes from somewhere around 0.34 d^{-1} (or 0.66 d^{-1} depending on which alias is the right one, if any) to somewhere between 0.40 and 0.45 d^{-1}. To illustrate this situation, Fig. 6 displays the 2-D power spectra of three different data sets corresponding to a dominant peak at 0.34 d^{-1} (July 1997), no dominant peak (August 1999) and a dominant peak found in both emission components around 0.40 d^{-1} (September 2000).

Since each observing campaign contains only a limited number of data, one may wonder about the robustness of the Fourier analyses. Therefore, we have performed some trials to evaluate the impact of specific spectra on the aspect of the TVS and the location of the highest peaks in the periodograms. To do this, we have removed the different data points one at the time from the time series and repeated the analysis of the remaining data set. These tests showed that the periodograms are usually very stable except for campaigns [3], [5], [7] and [8] that turned out to be quite sensitive to the presence or absence of individual spectra. For campaigns [3] (September 1998) and [8] (September 2002) this is indeed not unexpected given the very limited number of spectra obtained during these runs. For campaign [5], we cannot blame the number of spectra or the sampling. In this latter data set, the periodogram does not reveal a clearly dominating peak and the poor stability of the

Table 3. Properties of the 2-D periodogram of the time series consisting of the He II λ 4686 line profile as observed during various observing runs. The second column yields the maximum value of $TVS^{1/2}$ and the wavelength where this maximum occurs. The third column indicates the wavelength range over which $TVS^{1/2}$ exceeds the 99% significance level. The fourth and fifth columns yield the highest and second highest peaks in the periodogram over the $[0.0, 1.0]\,d^{-1}$ frequency range. The last column provides the mean equivalent width of the line as integrated between 4675 and 4700 Å. The maximum $1-\sigma$ dispersion of this *EW* during a specific run amounts to ~0.1 Å.

Run	$TVS^{1/2}_{max}$	λ – range (Å)	ν_1 d^{-1}	ν_2 d^{-1}	$\overline{EW}$ (Å)
[1]	0.009 at 4685.1	4683–4691	0.66	0.33	−1.26
[2]	0.014 at 4686.4	4681–4693	0.34	0.66	−1.48
[4]	0.017 at 4684.3	4681–4690	0.45	0.55	−1.38
[5]	0.013 at 4684.1	4683–4690	0.35[a]	0.65[a]	−1.46
[6]	0.016 at 4683.2	4679–4692	0.40	0.60	−1.42
[7]	0.015 at 4684.6	4682–4690	0.43[b]	0.57[b]	−1.24
[8]	0.013 at 4686.9	4682–4692	0.42[a,c]	0.85[a,c]	−1.38

[a] There are a number of other "peaks" in the periodogram that have only slightly lower amplitudes than ν_1 and ν_2.
[b] These frequencies correspond to the highest peaks over the wavelength interval 4682–4685. Over the entire range given in Col. 3, the highest peaks are found at 0.13 and 0.86 d^{-1}.
[c] The periodogram for this run is very sensitive to the inclusion of individual spectra in the time series and the highest peak frequencies are very unstable.

periodogram is yet another indication that the variability was most probably not periodic in August 1999. Finally, the periodogram of the September 2001 campaign ([7]) turned out to be quite sensitive to the spectra obtained during the night of September 11–12 (HJD 2452165.431 and 2452165.455). If we omit these data from our analysis, we recover peaks at 0.34 and 0.66 d^{-1}, pretty close to those found for campaigns [1] and [2]. However, there is no reason a priori to discard these data.

In the case of the He II λ 4686 line profile in the spectrum of BD +60° 2522, it seems therefore more appropriate to talk about time scales rather than periodicities. Indeed, a search for a stable coherent periodicity over the entire data set turned out to be illusory: the periodogram of the combined data set is dominated by very low frequencies and their daily aliases. The same conclusion holds for the He I λ 4471 and He II λ 4542 lines (see below). Also interesting to note is the fact that observations separated by only one month (July and August 1999) produce different power spectra. Finally, we note that the periodograms usually do not reveal strong peaks at frequencies higher than 1.0 d^{-1}, except for some daily aliases of the peaks from the $[0.0, 1.0]\,d^{-1}$ interval.

Another illustration of the epoch dependence of the He II λ 4686 profile variations can be obtained by fitting an expression

$$F(\lambda, t) = c_0(\lambda) + A(\lambda)\,\sin\left(2\,\pi\,\nu_1\,[t - t_0] + \phi_0(\lambda)\right) \quad (1)$$

to the time series of an individual campaign at every wavelength step. Here, ν_1 corresponds to the dominant peak found in the Fourier analysis of the specific data set, while $c_0(\lambda)$, $A(\lambda)$ and $\phi_0(\lambda)$ are fit parameters that represent the mean profile, the amplitude of variability and the phase constant at wavelength λ respectively (see also Rauw et al. 2001). These parameters are illustrated in Fig. 7 for observing campaigns [2] and [6]. We remind the reader that the phase constant ϕ_0 has physical meaning only if the period is clearly detected at the specific wavelength.

This reconstruction technique reveals that the profile modulation in July 1997 is mainly concentrated in the central absorption component (4683–4689 Å). In addition the phase of the modulation ϕ_0 remains roughly constant over this wavelength interval. Therefore, the variations of the profile in July 1997 can be described as a sinusoidal modulation of the depth of the absorption component with a "period" of 2.94 days. Such a variation might result for instance from a periodic modulation of the optical depth along the line of sight towards the stellar core.

On the contrary, the September 2000 data reveal a completely different picture. The amplitude peaks in the emission components of the line and ϕ_0 varies strongly across the peaks of the amplitude. In summary, the variations in September 2000 can be described as a modulation of the strengths of the two emission peaks with a "period" of 2.50 days; the red peak reaching its maximum intensity when the violet peak is minimum and vice versa.

3.3.2. Profile variability of the absorption lines

We have applied the Fourier techniques to the profiles of the He I λ 4471 and He II λ 4542 absorption lines. It turns out that the level of variability during a specific observing run is usually rather low ($TVS^{1/2} \leq 0.007$ on average). However, visual inspection of the spectra indicates profile variability in the line cores for those nights where we have obtained spectra separated by several hours (this is essentially the case for the August 1996 campaign, see Fig. 8, and for one night of the September 2002 run).

While the Fourier analysis of the entire data set fails to reveal a stable period, we find nevertheless that the Fourier periodograms of individual campaigns suggest that the line cores are variable on rather short time scales of the order of hours. Unfortunately, our data set was designed to search for variability on time scales of days rather than hours and hence does not allow us to study these short term variations in detail. From the analysis of the best suited data set (August 1996), we tentatively propose a time scale of about 4–5 hours. A more intensive monitoring of the star with a good time resolution and a good S/N ratio is required to eventually establish the period(s) or time scale(s) of the phenomenon. Figure 8 suggests that the variations of the absorption line profiles may be due to non-radial pulsations (NRPs). This would not be surprising since NRPs have already been reported for the two brightest members of the Oef class (see Sect. 4 below). It seems very likely

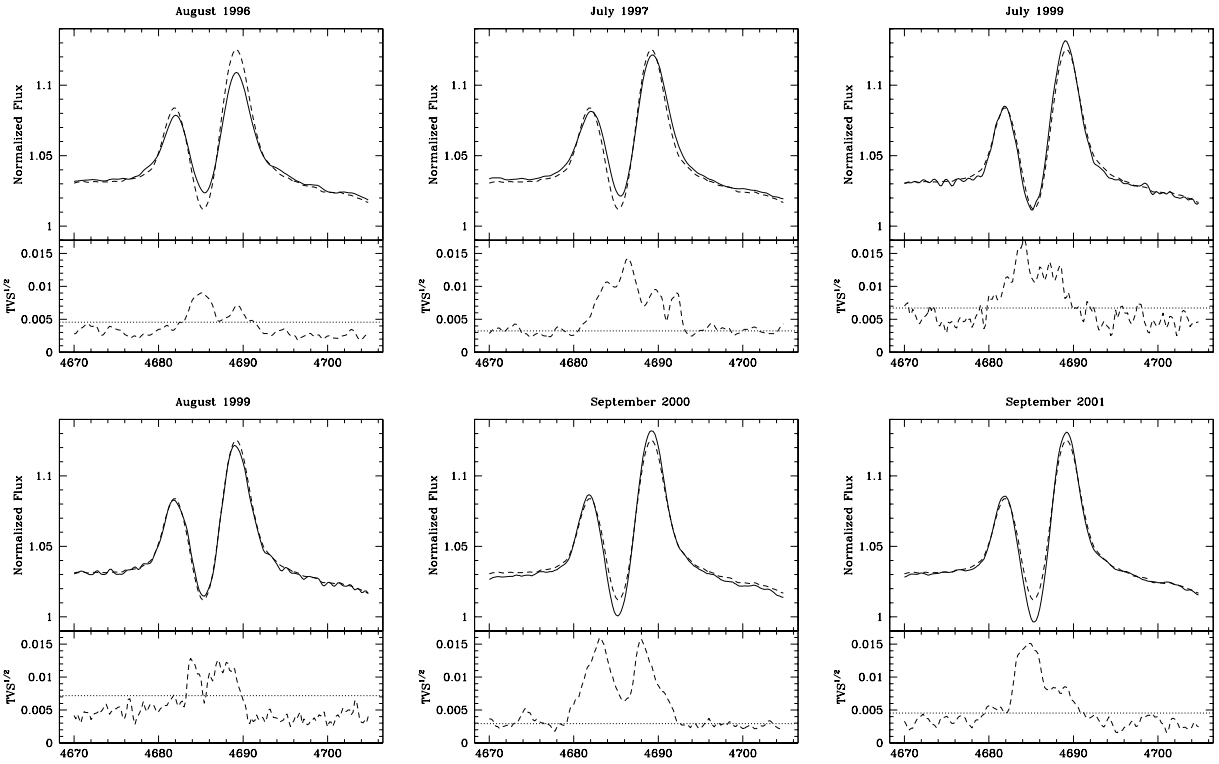

Fig. 5. The top three panels correspond to the variability of the He II λ4686 line profile during campaigns [1], [2] and [4] from left to right, while the lower three panels correspond to campaigns [5], [6] and [7] (also from left to right). Each panel is divided into two subpanels. The upper subpanels yield the mean profiles as observed during a specific observing campaign (solid line) compared to the mean profile as evaluated from the entire data set (dashed line). The bottom subpanels yield the square root of the *TVS* while the dotted lines correspond to the thresholds for variations significant at the 99% level.

that the low amplitude *RV* changes discussed in Sect. 3.2 are in fact a result of the absorption line profile variability.

4. Discussion

4.1. Comparison with ζ Pup and λ Cep

At this stage it is worth comparing the variability of BD +60° 2522 with that of the two most prominent members of the Oef class: ζ Pup and λ Cep.

Optical and UV observations of ζ Pup revealed appreciable variability on different time scales. Moffat & Michaud (1981) and Howarth et al. (1995) detected a modulation of the stellar wind of ζ Pup with a period of 5.0–5.2 days thought to be the stellar rotation period. Moffat & Michaud (1981) accordingly suggested that the inner regions of the stellar wind are forced into corotation by a magnetic field and ζ Pup could thus be a decentered oblique magnetic rotator.

In addition to the rotational modulation, the spectrum of ζ Pup displays also variations on two shorter time scales. The discrete absorption components (DACs) in the UV line profiles appear with a recurrence time of about 19 hrs (Howarth et al. 1995). A perhaps related time scale of 16.7 hrs was reported by Berghöfer et al. (1996) from an analysis of the variations of the Hα line and the *ROSAT*-PSPC count rate in the 0.9–2.0 keV energy range. On the other hand, photospheric absorption lines exhibit moving bumps on time scales of ~8.5 hrs. These features are usually interpreted as due to non-radial pulsations (e.g. Baade 1988; Reid & Howarth 1996).

Finally, the existence of small scale clumpy structures in the wind of ζ Pup was suggested by Eversberg et al. (1998). These authors obtained a set of high quality high resolution spectra of the He II λ4686 emission line that show stochastic variable substructures that they interpret as a manifestation of turbulent clumps propagating outward with the wind.

Henrichs (1991) reported covariability between the equivalent width of the He II λ4686 line and the blue steep edge of the C IV resonance lines in the spectrum of λ Cep. He found a time scale of about two days for the variations of these lines, whereas the photospheric He I λ4713 line displayed variations, likely due to non-radial pulsations, with a period of about 6.5 hrs. Variations in the Hα line on time scales of 4.8 days and 1.2 days were found by Kaper et al. (1997), whereas de Jong et al. (1999) confirmed the existence of NRPs with periods of 6.6 and 12.3 hrs. The latter authors suggested that beating among multimode NRPs could lead to cyclical surface amplitude enhancements that may eventually generate wind perturbations.

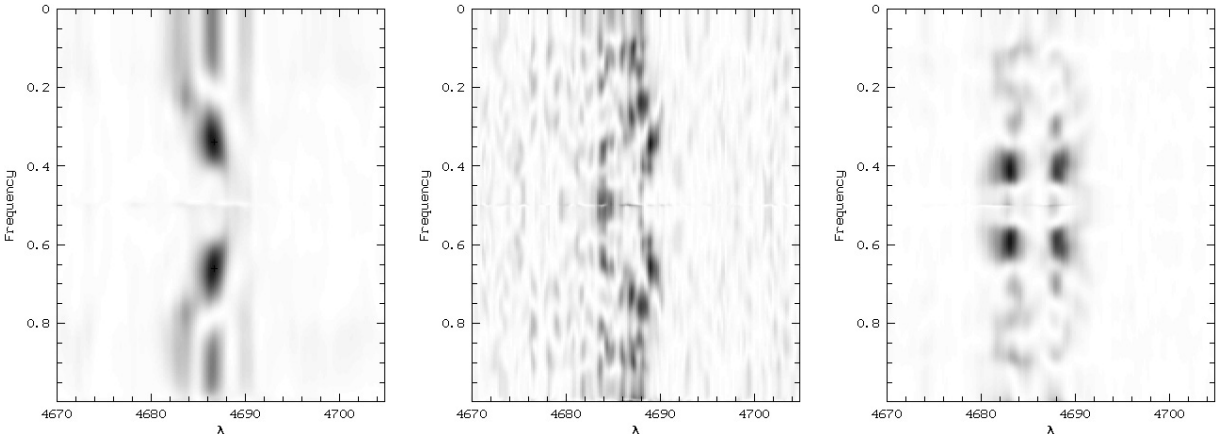

Fig. 6. Grey-scale images of the two-dimensional power spectra of the time series of the He II λ 4686 line in the frequency range [0.0, 1.0] d^{-1}. The power spectra were computed using the Fourier technique described by Rauw et al. (2001). From left to right, the three panels correspond respectively to the data sets from July 1997 (campaign [2]), August 1999 (campaign [5]) and September 2000 (campaign [6]).

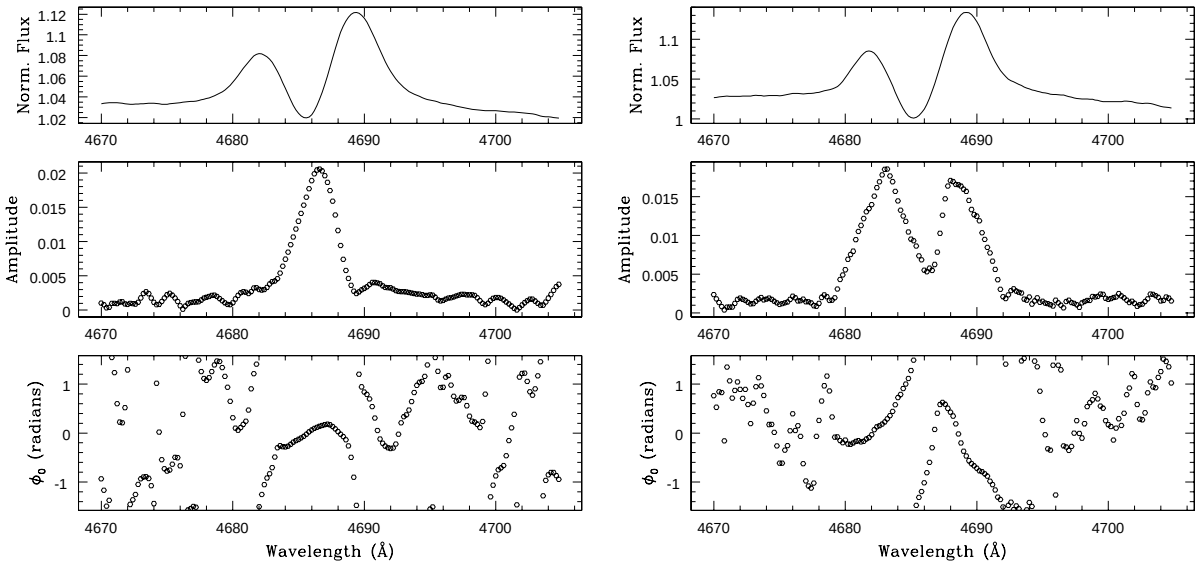

Fig. 7. Left: variability of the He II λ 4686 line in July 1997 (campaign [2]) as a function of phase assuming a "period" of 2.94 days (ν_1 = 0.34 d^{-1}). The three panels display the mean line profile, as well as the amplitude and the phase of a sine wave of frequency ν_1 fitted to our data. The reference date for the phase (t_0) was arbitrarily chosen on JD 2450000.00. Right: same for the September 2000 (campaign [6]) data and assuming a "period" of 2.50 days (ν_1 = 0.40 d^{-1}).

From their analysis of several observing campaigns with the *IUE*, Kaper et al. (1999) noted that the recurrence time of DACs in the UV spectrum of λ Cep changed with time. From the October 1989 data, they found a time scale around 2.2–2.5 days, while the February 1991 and October 1991 data yielded time scales of 4.3 and 1.4 days respectively. This situation is somewhat reminiscent of the results of our Fourier analysis of the He II λ 4686 line of BD +60° 2522. Kaper et al. suggest that the wind of λ Cep is modulated by rotation and the different time scales might correspond to different integer fractions of the rotational period.

In summary, it appears that NRPs are a common feature among Oef stars and that, for lines formed in the stellar wind, profile modulation on several, sometimes variable, time scales is not unusual either.

4.2. The role of stellar rotation

Our analysis of BD +60° 2522 reveals profile variability of the double-peaked He II λ 4686 line on time scales of a few days. Both the time scale and shape of the variability pattern change

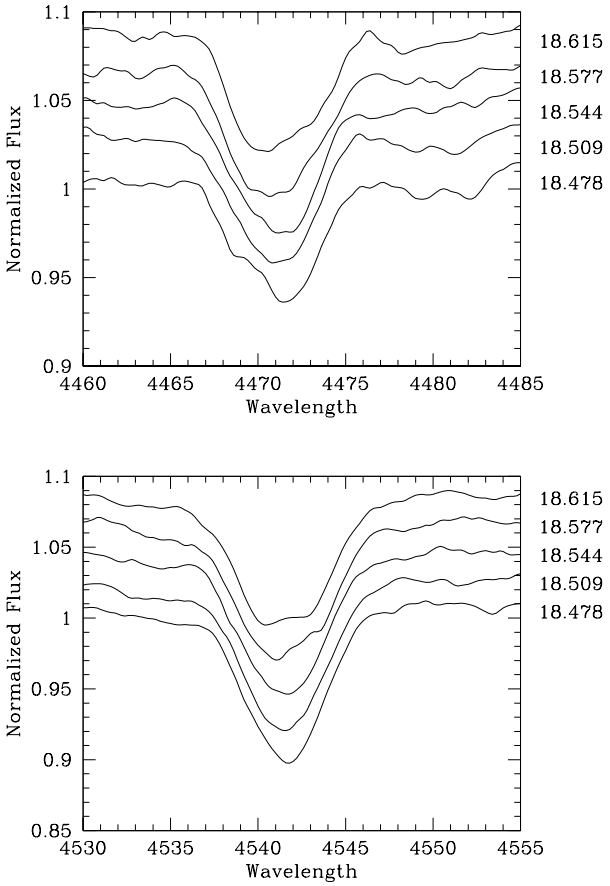

Fig. 8. Top: variations of the He I λ 4471 and Mg II λ 4481 line profiles during the night of 22–23 August 1996. The labels on the right yield the time of the observation in HJD−2450300. Consecutive spectra are shifted vertically by 0.02. Bottom: same but for the He II λ 4542 line.

as a function of time. Therefore, it seems unlikely that the phenomenon is governed by a (single) stable clock such as the rotation of the star. Nevertheless, it is interesting to briefly consider the constraints on the rotational period of BD +60° 2522.

Conti & Ebbets (1977) quoted a projected rotational velocity of 240 km s^{-1}. More recently, Penny (1996) and Howarth et al. (1997) used *IUE* spectra to infer $v \sin i$ of 214 and 178 km s^{-1} respectively. Though these values are not exceptionally large, we note nevertheless that they place the star in the extended high velocity tail of the distribution of observed projected rotational velocities as presented by Penny (1996). This conclusion holds true regardless which of the above values we actually consider. Assuming a radius of 15 $R_\odot$ (Howarth & Prinja 1989), we derive an upper limit on $P_{\rm rot}$ in the range 3.17–4.27 days depending on the actual value of $v \sin i$. We note that the morphology of the He II λ 4686 line in the spectrum of BD +60° 2522 closely ressembles the synthetic Hα profiles simulated by Petrenz & Puls (1996) for large values of i. This suggests that the true rotational period could be pretty close to the upper limit derived hereabove.

A lower limit on $P_{\rm rot}$ can be obtained from the critical rotational velocity. Adopting $\log L/L_\odot = 5.6$, $T_{\rm eff} = 37\,500$ K and $M = 44\,M_\odot$ (Howarth & Prinja 1989) and using the relation from Lamers & Leitherer (1993) to evaluate the ratio of the stellar luminosity to the Eddington luminosity, we derive a critical rotational period of 1.17 days.

The modulation of the line profile could occur with a period representing an integer fraction of the rotational period $P_{\rm rot}/n$ if there were n corotating structures in the stellar wind. The changes in the time scale of the variations might then reflect a change in the number of structures n creating the modulation. However, the above constraints on $P_{\rm rot}$ leave little room for any combination of integer numbers that might suit the various observed time scales.

These results do not imply that rotation does not contribute at all to the observed variability of the He II λ 4686 line, but they indicate that rotation cannot be the sole cause of the phenomenon at all epochs. For instance, we note that the frequency that turns up most often in our Fourier analysis ($\nu = 0.34\,{\rm d}^{-1}$) yields a "period" of 2.94 days that is rather close to the upper limit on $P_{\rm rot}$ and this frequency might well be related to the rotational frequency.

4.3. Towards a possible interpretation

Let us now consider some possible scenarios that could explain the observed variability of the He II λ 4686 emission line in the spectrum of BD +60° 2522. First, we note that a binary scenario is rather unlikely because we find no significant *RV* variations. Also, such a scenario would not provide an explanation for the changing periodicity. A single non-radial pulsation seems equally unlikely. In fact, the time scales observed in the variations of the He II λ 4686 line are much too long compared to the time scales of the variations of the absorption lines.

It seems therefore most likely that the phenomenon is associated with some transient large scale structure in the stellar wind. The lack of a single time scale in the modulation of the He II λ 4686 line suggests that the phenomenon might not be related to corotating structures. Such corotating structures are predicted for instance by the so-called corotating interaction region model (Cranmer & Owocki 1996; Owocki 1999) and are believed to generate the cyclical modulation of the P-Cygni absorptions in UV resonance lines observed for a number of OB stars (e.g. Fullerton et al. 1997).

Let us emphasize that the double-peaked morphology of the He II λ 4686 line clearly suggests that the stellar wind must be rotating at an appreciable velocity out to at least the radius of the formation region of this line. For instance, the wind could be forced to corotate with the star through the effect of a moderate stellar magnetic field. This situation could lead to some confinement of the stellar wind in latitude (see e.g. Babel & Montmerle 1997) and there is some observational evidence for an equatorial compression of the stellar wind of Oef stars. In fact, such a compression of the wind of ζ Pup was put forward by Harries & Howarth (1996) based on their spectropolarimetric observations of the Hα line in the spectrum of this star.

A variation of the global mass loss rate would change the extent of the corotating confined wind and could therefore induce some changes in the time scale of the variability. However, in case of a change of the overall mass loss rate, we would also expect to see epoch dependent changes in the emission strengths. The mean profiles displayed in Fig. 5 and the lack of a clear long term trend in the *EW*s listed in Table 3 do not support this idea.

It is worth pointing out that the pattern of the emission line profile variability in September 2000 is very much reminiscent of the model calculations of recurrent line profile variations presented by Lépine (2002). In these simulations, Lépine assumes a large number of discrete locally optically thick wind inhomogeneities moving around a common rotation axis. This model is designed to simulate the line profile variations arising from a perturbation at the surface of a rotating Wolf-Rayet star core that triggers waves that propagate outwards in the wind and create several overdense rotating "spiral arms". The main difference between the Lépine model and our observations of the He II λ4686 line in the spectrum of BD +60° 2522 is the lack of a single stable period in the observed modulation.

A possible explanation of the modulation of the He II λ4686 line in the spectrum of BD +60° 2522 might be a density perturbation propagating across (rather than just rotating with) the confined part of the wind. We could imagine this as some sort of analogue of the large scale oscillations of Be-like disks. This density perturbation could be triggered by an episodic enhancement of the local mass loss at the tip of a large amplitude NRP wave. A slightly similar mechanism, "NRP wave breaking", was proposed by Osaki (1999) to explain the episodic mass loss in Be stars. Such a large amplitude NRP wave could arise e.g. from beating among various NRP modes. While this scenario could easily account for the lack of a single stable period (through the effect of the propagation velocity of the perturbation and the interplay of various clocks: pulsations, rotation...), it seems more difficult to explain the changing pattern of the *TVS*. For instance, if a density wave moves around the star, why would it not affect the absorption and the emission components in a similar manner? One possibility could be that the density perturbation affects the absorption column only as long as it remains close to the stellar surface whilst the impact on the emission lines would be larger when the perturbation has moved outwards, but this is admittedly still rather speculative.

5. Summary and concluding remarks

Our time series of spectra of the O6.5ef star BD +60° 2522 show that the double-peaked He II λ4686 emission line undergoes strong profile variability on time scales of 2–3 days similar to the variations seen in two other Oef stars, ζ Pup and λ Cep. Both the time scale as well as the pattern of the variations in BD +60° 2522 turn out to be epoch dependent, suggesting that the phenomenon is not related to the sole effect of stellar rotation. On the other hand, the absorption lines display line profile variability on time scales of a few hours which are probably indicative of non-radial pulsations. Dedicated observations with a better time resolution are needed to confirm the latter finding and to quantify the time scales of these pulsations.

It seems very likely that the wind of BD +60° 2522 is not spherically symmetric. Out to the formation region of the He II λ4686 line, the wind appears rather as some sort of corotating equatorially confined envelope. In this context, it would be extremely interesting to investigate the possible presence of a stellar magnetic field in BD +60° 2522. Evidence for a stellar magnetic field might be obtained through the detection of a synchrotron (i.e. non-thermal) radio emission. A detection of a non-thermal radio emission from any of the Oef stars might therefore be of primary importance for our understanding of the Oef phenomenon. We note however, that at least for ζ Pup, the VLA observations by Bieging et al. (1989) revealed a purely thermal radio spectrum.

Acknowledgements. We wish to express our thanks to Dr. Jean Manfroid for taking some of the spectra of the September 2000 campaign and to the referee Dr. P.S. Conti for the careful reading of the manuscript. We are greatly indebted to the Fonds National de la Recherche Scientifique (Belgium) for multiple assistance including the financial support for the rent of the OHP telescope in 1999, 2001 and 2002 through contract 1.5.051.00 "Crédit aux Chercheurs" FNRS. The travels to OHP for the observing runs were supported by the Ministère de l'Enseignement Supérieur et de la Recherche de la Communauté Française. This research is also supported in part by contracts P4/05 and P5/36 "Pôle d'Attraction Interuniversitaire" (SSTC-Belgium) and through the PRODEX XMM-OM Project. We would like to thank the staff of the Observatoire de Haute Provence for their technical support during the various observing runs. The SIMBAD database has been consulted for the bibliography.

References

Baade, D. 1988, in O Stars and Wolf-Rayet Stars, ed. P. S. Conti, & A.B. Underhill, NASA SP-497, 137
Babel, J., & Montmerle, T. 1997, ApJ, 485, L29
Berghöfer, T. W., Baade, D., Schmitt, J. H. M. M., et al. 1996, A&A, 306, 899
Bieging, J. H., Abbott, D. C., & Churchwell, E. B. 1989, ApJ, 340, 518
Chavarría-K., C., Jäger, C., & Leitherer, C. 1987, in Circumstellar Matter, ed. I. Appenzeller, & C. Jordan (Reidel, Dordrecht), Proc. IAU Symp., 122, 445
Christopoulou, P. E., Goudis, C. D., Meaburn, J., Dyson, J. E., & Clayton, C. A. 1995, A&A, 295, 509
Conti, P. S. 1973, ApJ, 179, 181
Conti, P. S., & Alschuler, W. R. 1971, ApJ, 170, 325
Conti, P. S., & Leep, E. M. 1974, ApJ, 193, 113
Conti, P. S., & Ebbets, D. 1977, ApJ, 213, 438
Cranmer, S. R., & Owocki, S. P. 1996, ApJ, 462, 469
de Jong, J. A., Henrichs, H. F., Schrijvers, C., et al. 1999, A&A, 345, 172
Doroshenko, V. T. 1972, SvA, 16, 402
Eversberg, T., Lépine, S., & Moffat, A. F. J. 1998, ApJ, 494, 799
Fullerton, A. W. 1999, in Variable and Non-spherical Stellar Winds in Luminous Hot Stars, ed. B. Wolf, O. Stahl, & A. W. Fullerton, Lecture Notes in Physics, 523, 3
Fullerton, A. W., Gies, D. R., & Bolton, C. T. 1996, ApJS, 103, 475
Fullerton, A. W., Massa, D. L., Prinja, R. K., Owocki, S. P., & Cranmer, S. R. 1997, A&A, 327, 699

Gillet, D., Burnage, R., Kohler, D., et al. 1994, A&AS, 108, 181
Harries, T. J., & Howarth, I. D. 1996, A&A, 310, 533
Henrichs, H. F. 1991, in Rapid variability of OB stars: Nature and diagnostic value, ed. D. Baade, Proc. ESO Workshop 36, 199
Howarth, I. D., & Prinja, R. K. 1989, ApJS, 69, 527
Howarth, I. D., Prinja, R. K., & Massa, D. 1995, ApJ, 452, L65
Howarth, I. D., Siebert, K. W., Hussain, G. A. J., & Prinja, R. K. 1997, MNRAS, 284, 265
Kaper, L., Henrichs, H. F., Fullerton, A. W., et al. 1997, A&A, 327, 281
Kaper, L., Henrichs, H. F., Nichols, J. S., & Telting, J. H. 1999, A&A, 344, 231
Kuan, P., & Kuhi, L. V. 1976, PASP, 88, 128
Lamers, H. J. G. L. M., & Leitherer, C. 1993, ApJ, 412, 771
Lépine, S. 2002, in Interacting Winds from Massive Stars, ed. A. F. J. Moffat, & N. St-Louis, ASP Conf. Ser., 260, 185
Moffat, A. F. J., & Michaud, G. 1981, ApJ, 251, 133
Osaki, Y. 1999, in Variable and Non-spherical Stellar Winds in Luminous Hot Stars, ed. B. Wolf, O. Stahl, & A. W. Fullerton, Lecture Notes in Physics, 523, 329
Owocki, S. P. 1999, in Variable and Non-spherical Stellar Winds in Luminous Hot Stars, ed. B. Wolf, O. Stahl, & A. W. Fullerton, Lecture Notes in Physics, 523, 294
Penny, L. R. 1996, ApJ, 463, 737
Petrenz, P., & Puls, J. 1996, A&A, 312, 195
Rauw, G., Morrison, N. D., Vreux, J.-M., Gosset, E., & Mulliss, C. L. 2001, A&A, 366, 585
Reid, A. H. N., & Howarth, I. D. 1996, A&A, 311, 616
Underhill, A. B., Gilroy, K. K., & Hill, G. M. 1989, AJ, 98, 1063
Walborn, N. R. 1973, AJ, 78, 1067
Werner, K., & Rauch, T. 2001, in Eta Carinae and Other Mysterious Stars: The hidden opportunities of emission spectroscopy, ed. T. R. Gull, S. Johansson, & K. Davidson, ASP Conf. Ser., 242, 229

4.3.2 Other Oef stars

Following the study of BD+60° 2522, De Becker & Rauw (2004d) investigated the spectroscopic variability of three more Oef stars: HD 192281, HD 14442 and HD 14434 of spectral types O5 (ef), O5.5ef and O6.5(ef) respectively[1]. Here, I shortly summarize the main results of this study. For further details, the reader is referred to the paper by De Becker & Rauw (2004d).

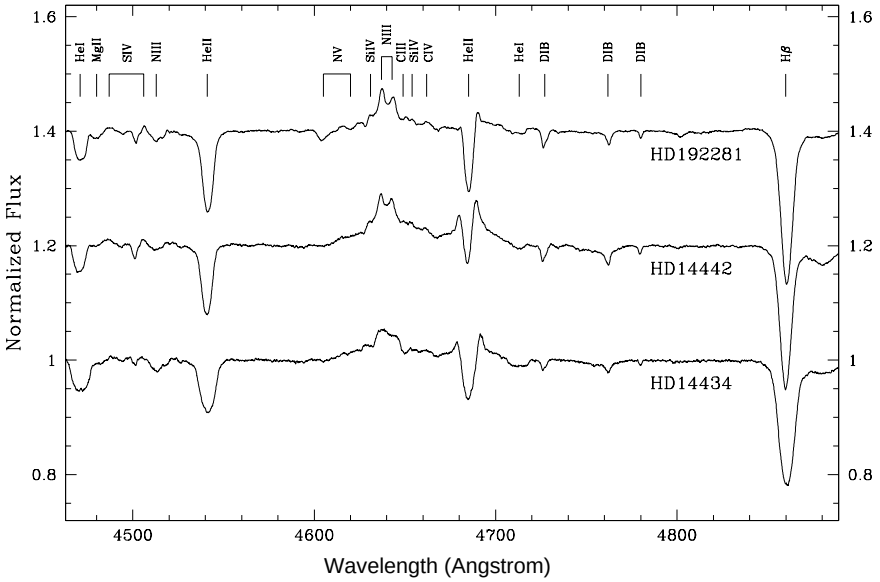

Figure 4.2: Mean normalized spectra of the three Oef stars studied by De Becker & Rauw (2004d).

The data were taken with the same instrumentation as for BD+60° 2522. Figure 4.2 illustrates the mean spectra of the three program stars. Apart from the characteristic double-peaked He II λ 4686 lines, other remarkable features are the N V $\lambda\lambda$ 4605, 4620 absorption lines in the spectrum of HD 192281 and the absorption lines that are heavily broadened by the large projected rotational velocities of 270, 273 and 400 km s^{-1} for HD 192281, HD 14442 and HD 14434 respectively.

No significant radial velocity variations were found for any of the targets and our value of the peculiar radial velocity of HD 192281 does not confirm the runaway status that had been suggested previously.

In all three stars, the He II λ 4686 and Hβ lines display significant line profile variations. However, while HD 192281 and HD 14442 display variations on recurrence times of 1.5 ± 0.1 and 1.6 ± 0.1 days respectively (or their 1-day aliases), this 'periodic' modulation affects only part of the line profiles. Indeed, the variability pattern, the wavelength range over which the recurrent behaviour is seen and the significance level of the modulation are epoch dependent. For instance, the recurrent behaviour can shift from one wing of the line to the other.

The case of HD 14434 is more complex: no obvious time scale emerged from our observing campaign. An intensive monitoring of HD 14434 was performed over one night in October 2003 to search for short-term variations that could result e.g. from non-radial pulsations. No significant variability was detected over 6 hours neither in the absorption nor in the emission lines. This result is at odds with the suggestion of Rauw et al. (2003a) who proposed that beating between several non-radial pulsation modes could

[1] Apart from these three objects and BD+60° 2522, there only two other Galactic Oef stars, λ Cep and ζ Pup.

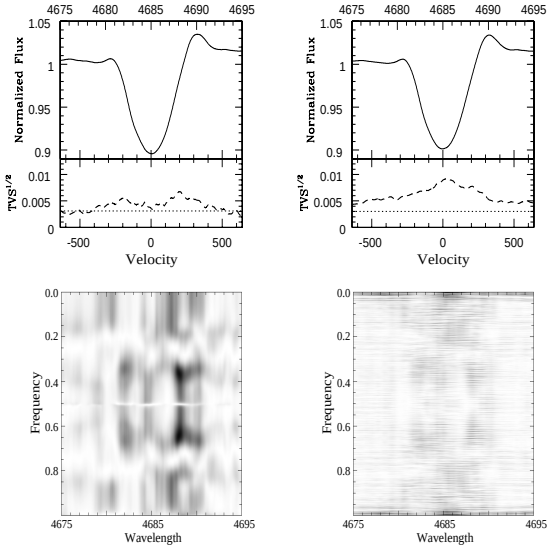

Figure 4.3: Mean spectrum and square root of the time variance spectrum of the He II λ 4686 line of HD 192281 for the September 2001 observing run (left) and for the combined data set (right). The lower grey-scale images show the corresponding two-dimensional Fourier periodograms (from De Becker & Rauw 2004d).

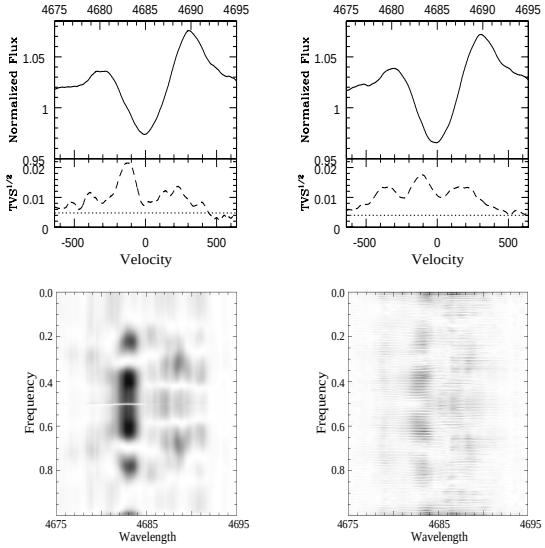

Figure 4.4: Same as Fig. 4.3 but for HD 14442.

trigger structures in the confined wind of Oef stars.
De Becker & Rauw (2004d) suggested that the recurrence times in HD 192281 and HD 14442 could actually be the rotational periods of the stars. However, whilst an oblique magnetic rotator model might account for some aspects of the variations, we also noted that such a model cannot explain the fact that the variability occurs only over a limited wavelength range.

4.4 Conclusions on non-spherical winds

In this chapter, I have presented some results related to the variability of presumably single O-type stars. In the case of HD 192639, periodic modulations are found that are most likely produced by a co-rotating large scale structure in the wind. The study of Oef stars revealed a more confused picture: while some variations actually occur on specific time scales that could be related to a stable clock (such as the stellar rotation), the characteristics of the variability change with time, and the 'periodic' modulation occurs only over a restricted wavelength range.
As stated above, the magnetically confined stellar wind model (ud-Doula et al. 2005) could a priori provide an explanation for the morphology of the He II λ 4686 line in the spectra of Oef stars. Indeed, a sufficiently strong magnetic field could funnel the wind from both hemispheres towards the magnetic equator, thereby producing a disk-like corotating structure, where the double-peaked He II λ 4686 line could arise. Hydrodynamical simulations of this situation (e.g. ud-Doula et al. 2005) indicate that the equatorial structure should be highly unstable and these instabilities could then be responsible for the rather erratic and epoch-dependent variability of the Oef stars in our sample.

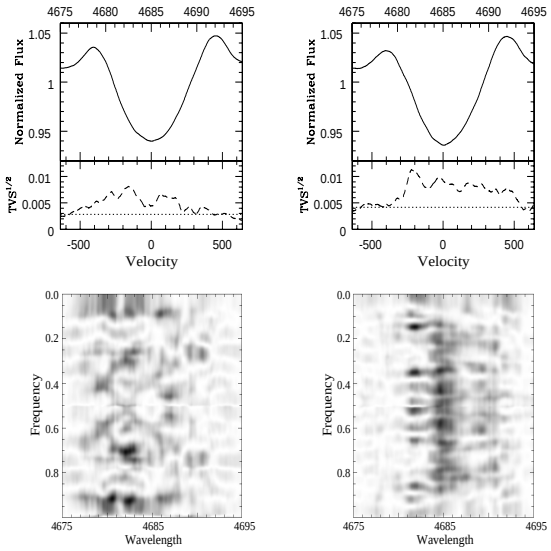

Figure 4.5: Same as Fig. 4.3 but for HD 14434 and the September 2002 (left) and October 2003 observing runs (right). From De Becker & Rauw (2004d).

However, this interpretation faces one major difficulty. In fact, the confined wind model has first been developed for the peculiar O5.5 star θ^1 Ori C. *Chandra*-HETG high-resolution X-ray spectra of this star indicate rather narrow and symmetric emission lines, in excellent agreement with the predictions of the magnetically confined stellar wind model (Gagné et al. 2005). On the other hand, the X-ray line profiles of the O4 Ief star ζ Pup are much broader, asymmetric and blue-shifted (Kahn et al. 2001), in agreement with these lines arising in a spherically symmetric expanding wind. It seems therefore quite difficult to account simultaneously for the modulation of the He II λ 4686 emission and the morphology of the X-ray emission lines of Oef stars within the confined wind model. Therefore, a more complex model perhaps involving jets of material flowing from some part of the stellar surface towards a magnetically confined wind region or clumps of material that pile up near some specific location in the confined stellar wind might actually be necessary. However, so far, this is only speculation and more observations (e.g. spectro-polarimetric measurements of the magnetic field and high-resolution X-ray spectroscopy) are required to derive further constraints.

Finally, it is interesting to note that two of the Oef stars (ζ Pup and λ Cep) are in fact runaways. While it seems likely that λ Cep was produced in a binary supernova event in the Cep OB3 association about 4.5 Myr ago, the parent cluster of ζ Pup is still unknown (Hoogerwerf et al. 2001). A binary supernova scenario could account for the rather large rotational velocities of these stars. In fact, the current Oef stars could have been the secondary components of a massive binary system. During the Roche lobe overflow of the primary component, the transfer of mass and angular momentum could have resulted in a speed up of the secondary's rotational velocity. However, as pointed out above, De Becker & Rauw (2004d) showed that the runaway status of HD 192281 could not be confirmed (at least not from its peculiar radial velocity).

Chapter 5

Star formation activity in very young open clusters

It is the stars,
The stars above us, govern our conditions.

William Shakespeare, *King Lear*

Studies of open clusters provide important clues on many aspects of stellar evolution. Obviously, rich open clusters allow us to investigate the properties of a large sample of stars drawn from a relatively homogeneous population (same metallicity, similar ages, same environment, same distance,...). Moreover, observations of these clusters provide insight into the way stars form. Very young open clusters (ages $\leq$ 4 – 5 Myr) still harbour a stellar population essentially unaffected by stellar evolution effects and their present-day mass function should hence be very close to the initial one.

In this chapter, I discuss the results of the study of a sample of Galactic open clusters using X-ray and optical observations. Since the main objective is to gain insight into the star formation activity, I will first recall our current knowledge of star formation in clusters, with a particular emphasis on the poorly known mechanism of massive star birth.

5.1 Introduction

5.1.1 Young open clusters

Observations of open clusters of different ages show that the distribution of stars in their interior is often non random. Clusters such as the Pleiades, the Hyades or M 11 display evidence for mass segregation, i.e. the more massive stars appear more concentrated towards the cluster centre (see e.g. Raboud & Mermilliod 1998). In addition, binary and multiple systems are also found to be more concentrated in the cluster core than single stars. For clusters whose age is significantly larger than their dynamical relaxation time, the segregation is attributed to the equipartition of the kinetic energy among cluster members via two-body interactions. Therefore, the importance of mass segregation due to this mechanism is expected to increase with cluster age. However, there are exceptions to this rule. In fact, some old clusters (such as M 67) present only weak evidence for segregation, whereas some very young clusters (NGC 6231,

IC 1805, NGC 6530,...) display a pronounced segregation for stars more massive than $\sim 20\,M_\odot$, although their ages (3 – 4 Myrs) are significantly smaller than their relaxation times (~ 10 Myrs, see Raboud & Mermilliod 1998). The latter effect points towards an *initial mass segregation*, resulting from the formation process of the massive stars. Raboud & Mermilliod (1998) accordingly suggest that the initial mass segregation be erased once the most massive stars (that represent a sizeable fraction of the total cluster mass) disappear due to stellar evolution. For older clusters, the mass segregation would then merely result from the dynamical evolution of the cluster.
Observations indicate that most OB stars are formed in open clusters. Among the OB stars that are not found in open clusters (e.g. high Galactic latitude OB stars), a large fraction are runaway stars that have large peculiar velocities and proper motions (see e.g. de Wit et al. 2005). OB stars can be ejected from their parental cluster either through dynamical interactions (Leonard & Duncan 1990) or as a result of a supernova explosion in a close binary system (Blaauw 1961). Runaways created by a binary supernova should have an increased helium abundance, a large rotational velocity and their kinematic age should be less than the age of their parent cluster (e.g. Hoogerwerf et al. 2001). On the other hand, since dynamical ejection runaways are mostly formed in a high-density environment of an extremely young cluster, their kinematic age should be roughly equal to the age of their parent cluster. Dynamical interactions in open clusters can significantly impact the properties of the binary population of these clusters. Binaries that interact can exchange their components, form (temporarily) stable hierarchical multiple systems and/or eject stars from the cluster. As a result, young open clusters can be surrounded by a halo of dynamically ejected runaways produced in binary - binary interactions. N-body simulations by Leonard & Duncan (1990) indicate that the fraction of binaries among these escapees should be very low ($\sim 10\%$). From an observational point of view, the best example of dynamically ejected runaways are probably the two single stars AE Aur (O9.5 V), μ Col (O9.5 V/B0 V) and the binary system ι Ori (O9 III + B1 III). These stars probably originate from a dynamical interaction event that took place about 2.5 Myr ago in the Orion Trapezium cluster (Hoogerwerf et al. 2001). On the other hand, ζ Oph (O9.5 V) and λ Cep (O6 Ief) were probably produced in a binary supernova explosion (Hoogerwerf et al. 2001). Finally, we note that the ejection of runaways modifies the mass function of the parent group at the high-mass end, where the total number of stars is small. For instance, it is thought that in the Trapezium cluster, four stars with total mass of $\sim 70\,M_\odot$ were ejected, leaving only six stars with masses above $10\,M_\odot$ in the cluster core (Hoogerwerf et al. 2001).

5.1.2 Scenarios for the formation of massive stars

The formation of massive stars is one of the major open questions in modern stellar astrophysics. Several scenarios have been proposed and I briefly review the most important ones in this section.

The accretion scenario

Low-mass stars form by accreting gas from a molecular core in which gravity overcomes thermal, magnetic and turbulent pressure gradients. The accretion rates are of order 10^{-6} to $10^{-5}\,M_\odot\,yr^{-1}$. Extrapolating this formation mechanism to higher mass objects (e.g. Shu et al. 1987) would lead to formation time scales of more than 10^6 yrs (i.e. a significant fraction of the main-sequence lifetime). In the classical accretion scenario for the formation of massive stars, the continuously accreting stars rise upwards in the HR diagram along the birthline. For accretion rates of 10^{-6} to $10^{-5}\,M_\odot\,yr^{-1}$, the birthline joins the zero-age main-sequence (ZAMS) around 8 to $10\,M_\odot$. Therefore, massive protostars should evolve along the main-sequence while accreting and their radiation pressure and ionization could halt the accretion, thus

limiting the mass of a massive star formed through this process to $\sim 10\,M_\odot$ (e.g. Beech & Mitalas 1994). From the observational point of view, a major difficulty with these accretion models is that the nascent star is embedded in a dense cocoon of protostellar material that prevents seeing its optical light. It is only once a significant part of the parental cloud has been dispersed that the star becomes visible in the optical band. This emersion could happen after a substantial fraction of the star's nominal main-sequence lifetime, therefore leading to the absence of a proper ZAMS for massive stars (Bernasconi & Maeder 1996). To avoid these problems, the time scale for the formation of massive stars has to be much shorter than for low mass star formation, and the accretion rates must be significantly higher ($\sim 10^{-4}\,M_\odot\,\mathrm{yr}^{-1}$).

Despite these caveats, observations of several deeply embedded objects in the millimetre range suggest that accretion disks actually play a role in the formation of mid- to early B-type stars. Blum et al. (2004) report observations of four massive embedded young stellar objects in M 17 and NGC 3576. CO line profiles are found to be consistent with Keplerian disks with $v \sin i$ between 100 and 260 km s^{-1} in three out of four cases. However, in clusters harbouring mid to early O-type stars, only second-rank late O or early B stars (with masses up to about $30\,M_\odot$) exhibit signatures of circumstellar disks or envelopes. This could indicate that the formation of the most massive objects proceeds in a different way. Observations of CO lines in the millimetre waveband also reveal collimated outflows of molecular material from massive young stellar objects (YSOs). These outflows contain up to a few hundred $M_\odot$ and can thus be more than five times more massive than the final mass of the central star (Lery 2004). The existence of these outflows suggests that non-spherical accretion (due to heat, rotation or magnetic fields) may play a major role in the formation of massive stars. Such a non-spherical accretion could actually help to overcome the radiation barrier. From the theoretical point of view, a major effort has thus been made to develop accretion models that overcome the difficulties outlined in the previous paragraph.

Norberg & Maeder (2000) noted that the mass outflows of PMS stars strongly increase with stellar luminosity, hence with stellar mass. Assuming that a fraction of 1/6 to 1/3 of the infalling mass is accreted, they proposed that the accretion rate may increase relatively quickly with the stellar mass to the power 1.0 to 1.5. For an exponent 1.5, the formation time would be shorter than the main-sequence lifetime for stars up to $\sim 120\,M_\odot$ and half of the accretion time would be spent below a mass of about $2\,M_\odot$. The time needed to evolve from 2 to $120\,M_\odot$ would then be only about 1 Myr. An important question to ask is whether or not such high accretion rates are realistic. Following the work of Wolfire & Cassinelli (1987), permitted accretion rates are determined by the condition that the momentum in the accretion flow must be larger than the outwards directed radiation momentum. On the other hand, the shock luminosity due to the accretion process must remain smaller than the Eddington luminosity. In addition, the dust abundance has to be reduced by at least a factor 4 compared to the 'standard' Galactic gas-to-dust ratio. By setting the maximum stellar mass to be the mass for which the accretion rate is such that the shock luminosity equals the Eddington luminosity, Norberg & Maeder (2000) derived maximum masses of 70 – $300\,M_\odot$ if the accretion shock radius is about $10\,R_*$. Herrero et al. (2007) compared the observed properties of a set of main-sequence O-type stars (both single and in binary systems) to the theoretical ZAMS and birthlines derived by Norberg & Maeder (2000). While they could not reach a firm conclusion for presumably single stars, they found that the properties of binary components are most readily explained by a linearly mass-dependent accretion rate (i.e. an exponent 1.0 in the models of Norberg & Maeder).

These ideas were further developed by Behrend & Maeder (2001) for pre-main-sequence stars with masses from 1 to $85\,M_\odot$. These authors assumed that the PMS objects accrete a constant fraction of the observed outflow rates. Indeed, a relation between outflow rates and stellar bolometric luminosity has been established observationally. To form an $85\,M_\odot$ star, the models of Behrend & Maeder (2001)

require an accretion rate that progressively increases to $8 \times 10^{-3}\,\mathrm{M_\odot\,yr^{-1}}$. Though the latter value seems high, it is apparently not forbidden by the calculations of Wolfire & Cassinelli (1987). The models of Behrend & Maeder (2001) predict that low mass stars form first and high mass stars form slightly later. However, the duration for the formation of an $80\,\mathrm{M_\odot}$ star is only about 10% larger than that of an $8\,\mathrm{M_\odot}$ star. The accretion phase of a massive star expected from these models should typically last about 3×10^5 years. Finally, we note that for objects with masses above $22\,\mathrm{M_\odot}$, the models of Behrend & Maeder (2001) predict that the location of the first optical visibility (i.e. after the dispersion of the prototellar cocoon) should be very close to the ZAMS.

McKee & Tan (2003) suggested a slightly different scenario. As a result of supersonic turbulence, molecular clouds are inhomogeneous on a wide range of scales. McKee & Tan (2003) pointed out that massive stars in the Galaxy form in regions of very high surface density and that molecular clouds where massive stars form are supersonically turbulent. McKee & Tan (2003) argued that the protostellar accretion rate in such a turbulent molecular core should be approximately equal to the instantaneous mass of the star divided by the free-fall time of the gas that is accreting onto the star. The corresponding accretion rate could approach $10^{-3}\,\mathrm{M_\odot\,yr^{-1}}$ and would thus be sufficient to overcome the radiation pressure from the star resulting in a time scale for the formation of a $100\,\mathrm{M_\odot}$ star of about 1.7×10^5 yrs. McKee & Tan (2003) further proposed that the IMF could result from the distribution of masses of molecular cores which is itself determined by the characteristics of the turbulence in the star-forming clump. This mechanism is different from the competitive accretion scenario (Bonnell & Bate 2002, see below) since the turbulent core scenario assumes that the gas that goes into the star was initially bound. McKee & Tan (2003) argued that competitive accretion is suppressed for masses above $10\,\mathrm{M_\odot}$ because radiation pressure prevents Bondi-Hoyle accretion.

Observations of several massive (about 15 – 20 $\mathrm{M_\odot}$) young stellar object candidates surrounded by huge accretion or remnant disks in the Omega Nebula (M 17, Nürnberger 2007 and references therein) provide strong evidence for the accretion scenario. Nevertheless, even though the difficulties due to the radiation pressure of the nascent star might have been solved by assuming non-spherical (i.e. disk-like) accretion structures, there remains the issue of avoiding photo-evaporation of the accretion disk by the radiation of the protostar and how to reach the accretion rates of order $10^{-3}\,\mathrm{M_\odot\,yr^{-1}}$ that are needed to make this scenario work. Another issue is the formation of tight binary systems with mass ratios near unity. Currently, the most likely explanation for the origin of these systems seems to be accretion onto a wide low-mass binary with the separation between the stars shrinking as the masses of the components grow (Zinnecker 2007).

The collision scenario

An important constraint for any theory of massive star formation comes from their environment. In fact, as stated above, they are rarely found in isolation, but occur most of the time in rich stellar clusters. N-body numerical simulations of compact cluster cores including the effects of stellar evolution and physical collisions (Portegies Zwart et al. 1999) show that because of mass segregation physical collisions between stars are frequent in the cluster core. The resulting mergers could lead to the formation of very massive ($\geq 100\,\mathrm{M_\odot}$) stars within 3 – 4 Myrs. The stars are rejuvenated by each new collision, therefore considerably extending their lifetime and they should thus appear as blue stragglers in the Hertzsprung-Russell diagram of the cluster. In these N-body simulations, the massive stars dominate the collision rate, while most previous theories predicted that the majority of collisions should occur between stars of rather low mass ($\sim 0.7\,\mathrm{M_\odot}$). This difference is mainly due to the effect of mass segregation (see also Sect. 5.1.1): the most massive stars sink to the cluster core due to dynamical friction, thereby increasing

the concentration of massive stars in a small volume. In addition, they form close binaries which have larger cross sections for collisions, thereby increasing the collision rates. At maximum a few percent of the total mass of the colliding stars is lost in the collision (Portegies Zwart 1999).
Bonnell et al. (1998) accordingly suggested that accretion-induced collisions in the cores of dense stellar clusters are needed to form very massive stars. Competitive accretion in clusters results in the formation of the highest mass stars in the deepest parts of the cluster potential. Simultaneously, whilst the gas falls on to the cluster, more lower mass stars migrate towards the cluster core (Bonnell et al. 2004): gas accretion therefore causes the cluster to contract and hence affects the stellar dynamics, increasing the number of stellar/protostellar collisions. This idea was further developed by Bonnell & Bate (2002). These authors showed that binaries play a key role in the process, although in a different way than suggested by Portegies Zwart (1999). In fact, gas accretion and interactions with other stars harden the binary up to the point where the periastron separation becomes so small that the components collide. Interestingly enough, the most massive stars formed in the collision scenario are often found in close binary systems. By far the main problem with the collision scenario is that it requires extreme protostellar densities ($\geq 10^8\,\mathrm{pc}^{-3}$) that may only be achieved in some of the most compact clusters. The clusters could subsequently expand and massive stars formed in a dense core could escape the core during the gas expulsion phase (due to the injection of radiative and kinetic energy into the gas through the radiation fields and stellar winds of the most massive stars), provided that the gas fraction in the core is high enough (Vine & Bonnell 2003). A possibility to reach high enough number densities was discussed by Bonnell et al. (2003). These authors studied the formation of a stellar cluster from a turbulent molecular cloud of mass $1000\,\mathrm{M}_\odot$. In their simulation, many small subclusters form independently through the hierarchical fragmentation of the turbulent cloud, leading to the co-existence of several sites of star formation. These subclusters then interact and merge to form the final stellar cluster (see also Bonnell et al. 2004). In the subclusters, the local number density of stars can reach values up to $10^7\,\mathrm{pc}^{-3}$. The high number density of stars in the subclusters coupled with the relatively small number of stars in each subcluster (and thus the small velocity dispersion) result in closer and stronger dynamical interactions than would otherwise occur. Therefore, in this scenario, stellar mergers might well play a role in forming the most massive stars.

5.1.3 The feedback of massive stars on the star formation activity

Since the bulk of the massive stars are found in open clusters, some clues on their formation mechanism can probably be obtained from a study of the star formation processes within young open clusters. Beside their massive star population, such clusters usually harbour a wealth of lower mass objects with the least massive ones not having reached the zero age main-sequence yet. The presence of these objects brings up a sort of *'which came first, the chicken or the egg?'* dilemma: did the massive stars trigger the formation of the lower mass objects or vice-versa? Or did they all form together?
It has alternatively been suggested that the powerful stellar winds and ionizing radiation fields of massive stars can either trigger or inhibit the formation of subsequent generations of stars. For instance, Herbig (1962) suggested that the formation of low and intermediate mass stars in a cluster could continue over some time before more massive stars appear and halt the star formation process. Herbig proposed that this latter effect would result from the heating and ionization of the gas. Today, it is believed that it is rather the stellar winds and supernova explosions of the early-type stars that lead to the dispersal of the gas, thereby bringing the lower mass star formation process to an end.
In the case of triggered star formation, a so-called *two-stage starburst*, the stellar populations should differ in age by several Myr and be spatially separated by 10 – 50 pc. The younger group is usually

surrounded by substantial amounts of gas, whilst the older group lies in an evacuated cavity. Examples of such two-stage starbursts include the 30 Dor and N 11 complexes in the LMC (e.g. Walborn 2002, Nazé et al. 2004 and references therein) as well as the vicinity of WR 48a and the heavily extinguished clusters Danks 1 and 2 (Clark & Porter 2004). Walborn (2002) suggested that whenever there is adequate molecular material in the vicinity of a cluster of O-stars, the second generation star formation takes place in so-called *dust pillars*. These elongated structures appear at the interface between the H II region and the neighbouring molecular cloud (Walborn 2002). The prototypes of these objects are found in the Eagle Nebula (M 16, Hester et al. 1996) where sub-millimetre observations revealed the presence of the cores of massive (10 – 60 $M_{\odot}$) luminous sources in the heads of the pillars. Though the pillars are illuminated and ionised by the OB stars, their orientation is not strictly aligned with these stars. This is at odds with the classical view that the pillars are formed by shadowing from the O-stars by the cores at their heads (Walborn 2002). While it is clear that photo-evaporation of the molecular cloud due to the UV radiation from the massive stars is a key ingredient, the exact formation mechanism of pillars is not yet established. Current scenarios involve either pre-existing higher density cores in the molecular cloud or hydrodynamic (Rayleigh-Taylor) instabilities. Mizuta et al. (2006) recently presented hydrodynamical simulations where the instability of the thin ionization front due to an initial perturbation leads to the formation of pillar-like features.

When studying the influence of massive stars on their surroundings, one has to bear in mind that these clusters are 3-D structures. Therefore, depending on the orientation, the clusters might either appear embedded in a molecular cloud or the two stellar epochs may be superimposed in a single field. Nevertheless, Walborn (2002) noted that triggered star formation sites and remnant molecular clouds are predominantly located in one hemisphere relative to the first generation cluster. Therefore, the original starburst probably occured near the surface of a giant molecular cloud (in response to an external event), rather than from a collapse towards the center of the molecular cloud.

In the case of the Galactic H II region RCW 79, Zavagno et al. (2006) reported the existence of five massive fragments, including an ultra-compact H II region containing newly formed stars, at the border of RCW 79. These authors accordingly suggested that the expansion of the H II region swept up the surrounding material into a dense layer that fragmented into dense clumps, which eventually collapse into new stars. A different explanation for star formation within an OB association was proposed by Clark et al. (2005). These latter authors simulated the formation of clusters in an unbound giant molecular cloud (GMC): they found that individual clusters form as independent OB subgroups and subsequently expand from each other due to the unbound nature of the flows that created the GMC. The clusters in the simulation are not coeval - they exhibit an age spread of ~ 10 Myr, but this feature is not due to triggered star formation. It should be noted that in this scenario, one can expect an age difference of a few Myr between the low-mass stars and the high-mass members. In fact, massive stars will only form once the corresponding star formation centre of the GMC has reached a critical mass. In the simulations of Clark et al. (2005), this happens roughly 2.5 Myr after the onset of the star formation. The star formation will end once the gas is removed from the cluster and the natal GMC is dispersed by the action of the stellar winds and the first supernova explosions.

Obviously, there exist a number of different scenarios, some of which have been tailored to account for the properties of specific star formation sites. Given that different clusters apparently point towards different theoretical interpretations, it is likely that none of the currently available theories can explain all the observed situations. Therefore, it is important to investigate the properties of lower mass pre-main-sequence (PMS) stars in a large sample of very young open clusters. Comparing the ages of PMS stars with those of the early-type stars can help in understanding the feedback of massive stars on their

environment and can thereby also shed light on the way the most massive objects have formed.

5.1.4 X-ray observations versus optical surveys

Classical T Tauri PMS stars display emission in the Balmer lines and can thus be identified either through spectroscopy or through photometric observations with a narrow-band Hα filter. However, foreground dMe stars with Hα emission equivalent widths exceeding 1 Å could also be selected in this way[1] (see e.g. Dahm & Simon 2005). Moreover, many PMS objects do not display a significant Hα emission[2]. With optical photometry only, these would be very difficult to distinguish from field stars lying to the right of the cluster main-sequence. Distinguishing cluster members from field stars is therefore a significant challenge for photometric surveys. Proper motion analyses can provide accurate membership probabilities but the temporal baseline required to study the proper motion of distant Galactic clusters is very long.
An interesting property that can help us identifying these PMS stars is their relatively strong X-ray emission with $\log \mathrm{L_X}/\mathrm{L_{bol}}$ reaching values as large as -3 or even -2 (e.g. Neuhäuser 1997, Feigelson & Montmerle 1999). Moreover, PMS stars often display flares in their X-ray lightcurve on time scales of a few thousand seconds (e.g. Feigelson & Montmerle 1999). X-ray observations thus offer the possibility to identify pre-main-sequence stars in open clusters without the difficulties due to foreground objects. This can be illustrated by a few examples. Consider the open cluster NGC 6231 (Sana et al. 2006a). This cluster lies at a distance of 1585 pc. The field of view of the EPIC instrument onboard *XMM-Newton* has a radius of about 15 arcsec. Using the number densities of stars in the solar neighbourhood tabulated by Allen (1973), one can estimate the total number of foreground objects towards the cluster (see Table 5.1). Very deep optical surveys aiming at the detection of low-mass stars (spectral types G - M) inside NGC 6231 will thus have to cope with a large number of field stars. This can lead to serious trouble in identifying PMS objects belonging to the cluster.

Table 5.1: Total number of foreground objects (i.e. with $d < d_{\mathrm{NGC\,6231}} = 1585\,\mathrm{pc}$) within an angular radius of 15 arcsec towards NGC 6231 estimated following the star number densities from Allen (1973) as a function of spectral type and luminosity class.

	B	A	F	G	K	M
V	8	40	199	501	794	3978
III			4	13	32	3

In the X-ray domain the situation is quite different. This is mainly because of the large $L_{\mathrm{X}}/L_{\mathrm{bol}}$ ratio (up to 10^{-2}, see above) of low-mass pre-main-sequence stars. In the Galactic plane, the population of foreground X-ray sources is dominated by young stars (Guillout & Motch 2003). The general X-ray properties of normal stars can be described as follows:

- $\log L_{\mathrm{X}}/L_{\mathrm{bol}} \simeq -7$ for early B-type stars. Late B stars have usually a significantly lower X-ray luminosity (Berghöfer et al. 1997).

[1] Since the incidence of chromospheric activity increases towards later spectral types, reaching a level of $\sim 60\%$ for spectral types M5 and later (Hawley et al. 1996), dMe stars are more likely to contaminate the lower mass end of the stellar population.
[2] The commonly adopted value of the Hα equivalent width separating classical and weak-line T Tauri stars is 10 Å.

- $< \log L_{\rm X} > \simeq 29.2$ for A and early F stars (Panzera et al. 1999). Whether the X-ray emission from A-type stars is indeed intrinsic to these objects or arises from low mass companions is actually still under debate.

- $\log L_{\rm X}/L_{\rm bol} \simeq -5$ for G V and G III stars. The X-ray emission of low mass stars with spectral types F7 to M5 is attributed to their magnetic activity that results probably from a complex $\alpha\Omega$ dynamo mechanism involving the interaction of convection and differential rotation. As a result, their X-ray luminosity scales roughly with $v_{\rm rot}^2$ and $\log L_{\rm X}/L_{\rm bol}$ can reach a saturation limit of about -3. The largest rotational velocities are observed for young stars in open clusters, while older field stars have usually lower rotational velocities and the results of Pizzolato et al. (2003) suggest $\log L_{\rm X}/L_{\rm bol} \leq -5$ on average for field stars.

- $< \log L_{\rm X} > \simeq 27.8$ for K and M dwarfs as found by Schmitt et al. (1995) for stars within a radius of 7 pc around the Sun. The sample of Schmitt et al. (1995) contains a number of dMe stars that display an enhanced coronal activity compared to normal M dwarfs (Fleming et al. 1995). In fact, dMe stars have $\log L_{\rm X}/L_{\rm bol} = -3.56 \pm 0.10$, whilst normal K and M dwarfs rather have $\log L_{\rm X}/L_{\rm bol} = -5.21 \pm 0.07$ (Fleming et al. 1995). Using the results of Hawley et al. (1996) and assuming an IMF with $\alpha = 1.7$ for M-type stars, I have estimated an IMF-weighted average incidence of chromospheric activity of 48%. The IMF-weighted X-ray luminosity of dMe stars should thus amount to $< \log L_{\rm X} > \simeq 27.6$, whilst normal M stars should have an IMF-weighted X-ray luminosity of $< \log L_{\rm X} > \simeq 26.2$.

- $< L_{\rm X} > \simeq 5 \times 10^{28}$ erg s^{-1} for K and M giants. Observations indicate a sharp decrease in the X-ray emission level of late-type giants around spectral type K1 III which is probably related to the strong decrease in rotational velocity at the same location in the Hertzsprung-Russell diagram (Gondoin 1999).

In addition to the coronal sources discussed hereabove, specific categories of active binaries are usually rather X-ray luminuous and could thus be detected as foreground objects. Indeed, the population of X-ray sources within a distance of 50 pc from the Sun is dominated by RS CVn binaries as well as BY Dra and other long-period binaries (Makarov 2003). For RS CVn systems, $< L_{\rm X} > \simeq 6.6 \times 10^{30}$ erg s^{-1} and 23 such binaries are found within a radius of 50 pc, whilst $< L_{\rm X} > \simeq 2.2 \times 10^{30}$ erg s^{-1} for the 29 long period active binaries in the sample of Makarov (2003).

To estimate the actual contamination of the *XMM-Newton* observation of NGC 6231 (Sana et al. 2006a), we use the $\log N$ – $\log S$ relation for stellar sources at Galactic latitude $b_{\rm II} \sim 0^\circ$ proposed by Motch et al. (2003). This relation was established on the basis of a series of EPIC-pn observations near the Galactic plane, but away from extended diffuse emission or star forming regions.
At the limiting sensitivity of our survey of NGC 6231 of $(1.5 - 2.0) \times 10^{-3}$ EPIC-pn cts s^{-1}, we estimate an average of 180 – 260 sources per square degree. Since the EPIC field of view covers about 0.20 square degrees, we expect about 35 – 51 sources. Therefore, only about 6 – 8 % of the 610 sources in the NGC 6231 EPIC field of view are expected to be due to foreground stars (Sana et al. 2006a).
We can also obtain a rough estimate of the number of extragalactic AGN that might appear as background sources in the EPIC images. The Galactic coordinates of the NGC 6231 cluster are $l_{\rm II} = 343.46^\circ$, $b_{\rm II} = +1.19^\circ$. Because of the proximity to the Galactic Plane, the total neutral hydrogen column density along this direction must be extremely large and should produce a substantial absorption of X-ray photons from extragalactic sources. Although they are in principle not suited for directions at $|b_{\rm II}| \leq 5^\circ$, one can use

the *DIRBE/IRAS* extinction maps provided by Schlegel et al. (1998) to derive a first order estimate of the total column density. In this way, I find a total Galactic $E(B-V)$ of about 5.6 mag. Using the gas to dust ratio of Bohlin et al. (1978), I thus estimate a neutral hydrogen column density of $\sim 3.2 \times 10^{22}\,\mathrm{cm}^{-2}$. Assuming that extragalactic background sources have a power-law spectrum with a photon index of 1.4, and suffer a total interstellar absorption of $3.2 \times 10^{22}\,\mathrm{cm}^{-2}$, the average detection limit $1.9 \times 10^{-3}\,\mathrm{cts\,s}^{-1}$ with the pn camera translates into unabsorbed fluxes of 1.2×10^{-14} and $3.5 \times 10^{-13}\,\mathrm{erg\,cm}^{-2}\,\mathrm{s}^{-1}$ in the 0.5 – 2.0 keV and 2.0 – 10 keV band respectively. Using the $\log N - \log S$ relation from Giacconi et al. (2001), one expects thus about 13 – 16 extragalactic objects among the detected sources. Thus about 2% of the total number of sources could be background AGN. It should be emphasized that these background AGN are expected to appear as rather hard (i.e. heavily absorbed) X-ray sources (see Sana et al. 2006a).
These numbers illustrate the power of X-ray observations compared to deep optical surveys to identify PMS stars down to 0.3 – 0.4 $\mathrm{M}_\odot$ (about spectral type M2-3).
Finally, our method to estimate the number of contaminating sources is validated by *XMM-Newton* observations that do not reveal significant excesses of X-ray sources compared to the expected numbers of background and foreground sources like the field around Plaskett's star (see Linder et al. 2006) and the Southern Coalsack discussed in Appendix B.

5.2 The Lagoon Nebula

The Lagoon Nebula (M 8) is an H II region ionized by the O-stars 9 Sgr (O4 V ((f$^+$)) + O7-8, see Chapt. 3), HD 165052 (O6.5 V + O7.5 V, see Sect. 1.1.2) and Herschel 36 (O7 V) as well as to some extent by the cluster NGC 6530. M 8 is essentially the front end of a molecular cloud into which the H II region is expanding.

Figure 5.1: Left: Three colour image (blue = [O III], green = Hα, red = [S II]) of the Lagoon Nebula as presented by R. Barbá et al. (Astronomy Picture of the Day, 6 October 2002). The image was obtained at the Curtis-Schmidt Telescope at CTIO using a 2048×2048 CCD. Right: same colour coding for an *HST* WFPC2 image presented by A. Caulet (STScI-1996-PR38).

One of the most intriguing features of the Lagoon Nebula is the bipolar Hourglass region resulting from the interaction of the young massive stars Herschel 36 with its surroundings (see Fig. 5.1). Burton (2002) found that the morphology of the Hourglass region is the same in the J, H and K bands, suggesting that this is the intrinsic shape of this blister-type H II region, rather than being a result of variable extinction as had been suggested by Woodward et al. (1986).
The open cluster NGC 6530 embedded in M 8 had previously been observed in optical photometry and for the purpose of identifying the optical counterparts to the X-ray sources, we decided to use the extensive work of Sung et al. (2000) who obtained also Hα photometry allowing them to identify some classical T Tauri PMS stars and PMS candidates.

5.2.1 *XMM-Newton* observations of M 8

Part of the nebula and the NGC 6530 cluster were observed serendipitously in the context of our *XMM-Newton* observation of 9 Sgr. The results of this observation are reported in the paper by Rauw et al. (2002d) that I reproduce hereafter. Our *XMM-Newton* observations of M 8 provided the first study of the X-ray emission from the Hourglass and allowed to significantly extend the list of PMS stars and candidates in NGC 6530 as well as to constrain their properties.
Figure 5.2 presents an overlay of the X-ray contours on a Digitized Sky Survey image of the Lagoon Nebula. This picture was used to illustrate the front page of issue 395 of the Astronomy & Astrophysics magazine.

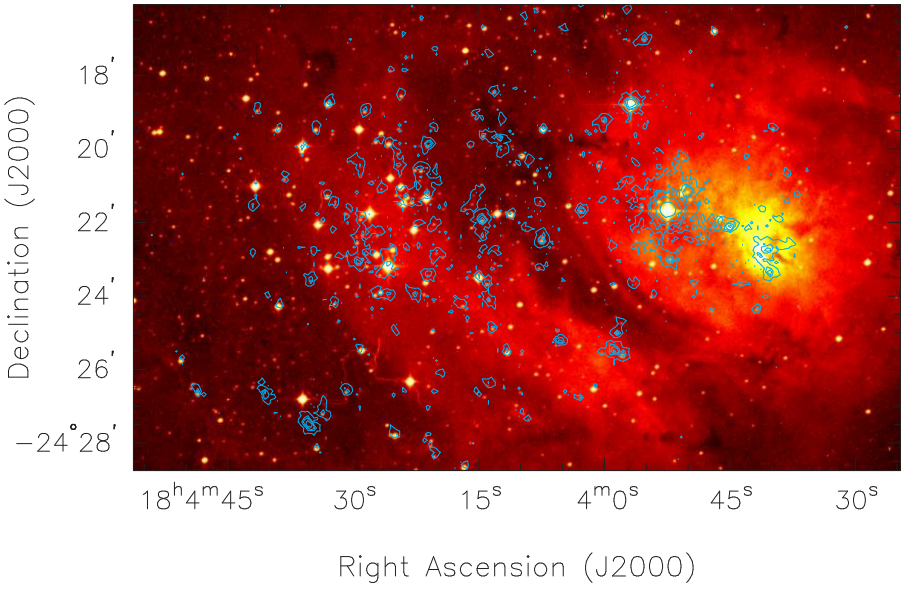

Figure 5.2: EPIC X-ray emission contours overlaid on a DSS image of the Lagoon Nebula displayed in false colours. The brightest source in the field of view (both in the optical and X-rays) is 9 Sgr.

A&A 395, 499–513 (2002)
DOI: 10.1051/0004-6361:20021230

Astronomy & Astrophysics

An *XMM-Newton* observation of the Lagoon Nebula and the very young open cluster NGC 6530⋆

G. Rauw[1,⋆⋆], Y. Nazé[1,⋆⋆⋆], E. Gosset[1,⋆⋆], I. R. Stevens[2], R. Blomme[3], M. F. Corcoran[4], J. M. Pittard[5], and M. C. Runacres[3]

[1] Institut d'Astrophysique, Université de Liège, Allée du 6 Août, Bât. B5c, 4000 Liège (Sart Tilman), Belgium
[2] School of Physics & Astronomy, University of Birmingham, Edgbaston Birmingham B15 2TT, UK
[3] Royal Observatory of Belgium, Avenue Circulaire 3, 1180 Brussels, Belgium
[4] USRA/HEASARC Goddard Space Flight Center, Greenbelt, MD 20771, USA
[5] Department of Physics & Astronomy, University of Leeds, Leeds LS2 9JT, UK

Received 5 June 2002 / Accepted 26 August 2002

Abstract. We report the results of an *XMM-Newton* observation of the Lagoon Nebula (M 8). Our EPIC images of this region reveal a cluster of point sources, most of which have optical counterparts inside the very young open cluster NGC 6530. The bulk of these X-ray sources are probably associated with low and intermediate mass pre-main sequence stars. One of the sources experienced a flare-like increase of its X-ray flux making it the second brightest source in M 8 after the O4 star 9 Sgr. The X-ray spectra of most of the brightest sources can be fitted with thermal plasma models with temperatures of $kT \sim$ a few keV. Only a few of the X-ray selected PMS candidates are known to display Hα emission and were previously classified as classical T Tauri stars. This suggests that most of the X-ray emitting PMS stars in NGC 6530 are weak-line T Tauri stars. In addition to 9 Sgr, our EPIC field of view contains also a few early-type stars. The X-ray emission from HD 164816 is found to be typical for an O9.5 III-IV star. At least one of the known Herbig Be stars in NGC 6530 (LkHα 115) exhibits a relatively strong X-ray emission, while most of the main sequence stars of spectral type B1 and later are not detected. We also detect (probably) diffuse X-ray emission from the Hourglass Region that might reveal a hot bubble blown by the stellar wind of Herschel 36, the ionizing star of the Hourglass Region.

Key words. ISM: individual objects: M 8 – open clusters and associations: individual: NGC 6530 – stars: early-type – stars: pre-main sequence – X-rays: stars

1. Introduction

The Lagoon Nebula (M 8 = NGC 6523) is one of the closest and brightest H II regions in the Galaxy. The nebula is ionized by the O4 V star 9 Sgr and the binary system HD 165052 (O6.5 V + O6.5 V). M 8 harbours also the very young open cluster NGC 6530 as well as a compact H II region, the so-called Hourglass Region (hereafter HG), which is ionized by the O7 V star Herschel 36. NGC 6530 is believed to be at the origin of a sequential star formation process inside the Lagoon Nebula (Lightfoot et al. 1984). NGC 6530 most probably formed from a pre-existing massive molecular cloud. The ionizing radiation of the newly formed hot stars in the cluster then created a cavity allowing us to see inside the parent molecular cloud. Furthermore, NGC 6530 may have triggered the formation of 9 Sgr, which subsequently caused the formation of the massive protostar Herschel 36 (= HD 164740, hereafter H 36).

According to van den Ancker et al. (1997), star formation within NGC 6530 started a few 10^7 years ago and is probably still ongoing. Sung et al. (2000) found that 9 Sgr and H 36 are well fitted to an isochrone of age ∼1.5 Myr, while the age of the stars at the fainter end of the populated part of the main-sequence of NGC 6530 is about 4 Myr and the massive pre-main sequence star LkHα 112 should be only about 0.4 Myr old. Using *UBVRI* and Hα photometry of NGC 6530, Sung et al. (2000) identified 58 pre-main sequence (PMS) stars with Hα emission as well as 17 PMS candidates (PMSc).

Many recent studies of the Lagoon Nebula focused on the Hourglass Region as seen in different wavebands. The HG nebula is believed to be an ionized cavity in an inhomogeneous clumpy molecular cloud. The apparent bipolar structure in the optical band most likely results from a non-uniform extinction along the line of sight. Woodward et al. (1986) proposed a model in which two high-density knots on the eastern side protect the material behind them from the ionizing radiation while

Send offprint requests to: G. Rauw, e-mail: rauw@astro.ulg.ac.be
⋆ Based on observations with *XMM-Newton*, an ESA Science Mission with instruments and contributions directly funded by ESA Member states and the USA (NASA).
⋆⋆ Research Associate FNRS (Belgium).
⋆⋆⋆ Research Fellow FNRS (Belgium).

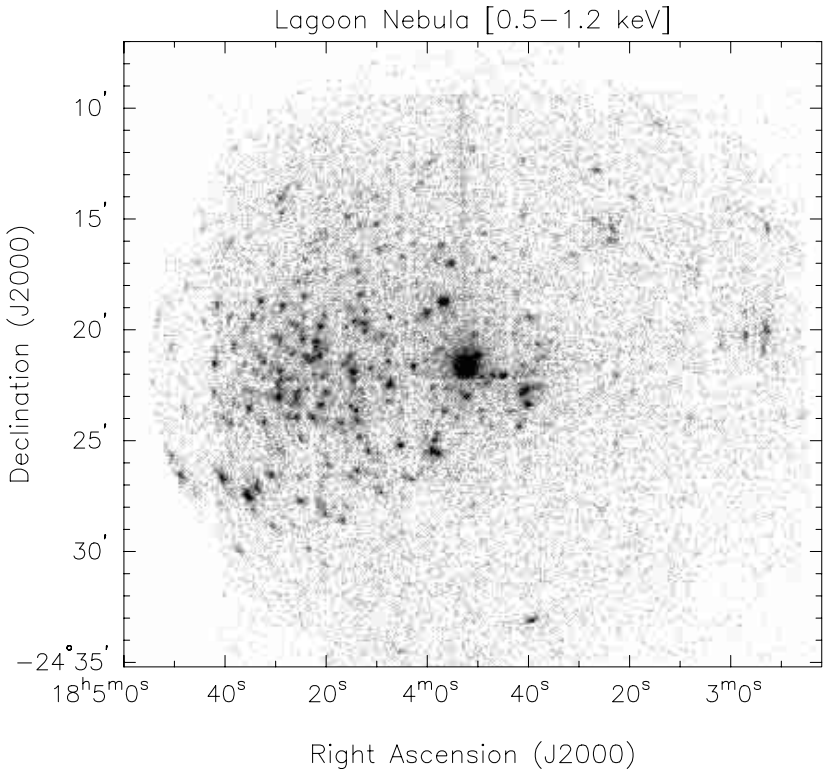

Fig. 1. Combined EPIC-MOS1, -MOS2 and -pn image of the field of view around 9 Sgr. To avoid contamination by the hard straylight photons from GX 9 +1, we restricted the image extraction to events in the soft energy band 0.5–1.2 keV only. The bright source in the center is 9 Sgr. Note that the roughly vertical trail above 9 Sgr is due to events from 9 Sgr that arrived during the readout of the pn detector.

the western edge of the HG would be defined by a foreground cloud obscuring H 36.

In the present paper, we discuss an *XMM-Newton* observation of M 8, that reveals a number of point sources towards the open cluster NGC 6530. In Sects. 2 and 3, we investigate the light curves and spectra of the brightest sources and we discuss their possible association with PMS stars in NGC 6530. In Sect. 4, we discuss also the soft X-ray emission from the HG nebula. Finally, our conclusions are presented in Sect. 5.

2. X-ray sources inside the Lagoon Nebula

The Lagoon Nebula was observed serendipitously for about 20 ksec with the *XMM-Newton* observatory (Jansen et al. 2001) during our AO1 observation of the O4 V star 9 Sgr (JD 2451976.978 – 2451977.239). The two EPIC-MOS instruments were operated in the full frame mode (Turner et al. 2001) whilst the EPIC-pn camera was used in the extended full frame mode (Strüder et al. 2001). All three EPIC instruments used the thick filter to reject optical light. We used version 5.1 of the *XMM-Newton* Science Analysis System (SAS) to reduce the raw EPIC data. More details on the pipeline processing of the data are given in the paper dealing with the 9 Sgr data (Rauw et al. 2002).

The combined EPIC soft band (0.5–1.2 keV) X-ray image around 9 Sgr reveals a number of point-like (and maybe also diffuse) sources (see Fig. 1). Figure 2 displays the EPIC contours of the X-ray sources superimposed on a Digital Sky Survey image of M 8. This image indicates that most of the fainter sources are located in the region of the very young open cluster NGC 6530. One rather bright and apparently diffuse source (to the south-west of 9 Sgr) is associated with the Hourglass Region.

Because of the contamination of the EPIC data by hard straylight photons from the nearby LMXB GX 9 +1, the source detection was performed on the soft band images (i.e. where there is no contamination) only. For details on the properties of the straylight, we refer again to the work of Rauw et al. (2002).

Using the SAS source detection algorithms (see e.g. Hasinger et al. 2001), we find 250 sources that are detected simultaneously in the MOS1, MOS2 and pn images with a combined logarithmic likelihood

$$\sum_{i=1}^{3} -\ln p_i \geq 9.0$$

where the summation runs over the MOS1, MOS2 and pn images. In this formula, p_i stands for the probability that a random Poissonian fluctuation may have caused the observed source counts in the image of the detector i. We then inspected each source manually to reject spurious detections due e.g. to hot pixels. This resulted in a total of 220 confirmed detections. Out of these 220 sources, 117 have a combined likelihood ≥20.0

and are detected in the individual images from all three EPIC instruments with $-\ln p_i \geq 3.0$. With these criteria, the probability of detecting a spurious source within a $15'' \times 15''$ detection element should be $\sim 2 \times 10^{-9}$ and we therefore expect much less than one spurious detection over the entire EPIC field of view. To this list we add two sources that are not detected in at least one of the instruments because they fall outside its field of view, but are clearly detected in the remaining instruments. This gives us a total of 119 highly significant detections. In the following, we will restrict our discussion to these latter objects (see Fig. 3). The faintest sources in this category have about 10^{-3} cts s^{-1} over the 0.5–1.2 keV band of the MOS instruments. Assuming a 1 keV thermal spectrum with a neutral hydrogen column density of 0.17×10^{22} cm^{-2} (see also Sect. 3 below), the faintest sources correspond to an observed flux of about 8.9×10^{-15} erg cm^{-2} s^{-1} and an unabsorbed flux of 13.1×10^{-15} erg cm^{-2} s^{-1} in the 0.5–5.0 keV energy range. Note that the corresponding observed flux in the 0.5–1.2 keV soft band would be 5.2×10^{-15} erg cm^{-2} s^{-1}.

The most complete compilation of optical sources in NGC 6530 is the catalogue provided by Sung et al. (2000). These authors present *UBVRI* and Hα photometry of 887 stars brighter than $V = 17$ and spread over an area from RA = 18:03:20 to 18:04:52 and from DEC = −24:11:45 to −24:32:20 (Equinox J2000.0). They include also a deeper *HST* WFPC2 observation of the Hourglass Region in their analysis.

We find that a total of 111 out of 119 X-ray sources detected with *XMM* fall inside the area covered by Sung et al. (2000). We have cross-correlated the positions of these sources with the Sung et al. catalogue. In order to determine the optimal radius of cross-correlation, we adopted the approach outlined by Jeffries et al. (1997). We generated the cumulative distribution of the number of detected sources as a function of the cross-correlation radius r (see Fig. 4) and modelled this distribution assuming that it can be represented by means of an expression taken from Jeffries et al.:

$$\Phi(d \leq r) = A \left[1 - \exp\left(\frac{-r^2}{2\,\sigma^2}\right)\right] + (N - A) \left[1 - \exp(-\pi\, B\, r^2)\right].$$

Here N, A, σ and B stand for the total number of cross-correlated X-ray sources ($N = 111$), the number of true correlations, the uncertainty on the X-ray source position and the surface density of optical sources respectively. The first term in this expression stands for the cumulative distribution of true correlations whereas the second term yields the cumulative number of spurious correlations. A, σ and B are fitting parameters and were obtained from the best fit to the distribution displayed in Fig. 4. We obtain $A = 87.0$, $\sigma = 2.9$ arcsec and $B = 4.7 \times 10^{-4}$ arcsec^{-2}. The optimal correlation radius, i.e. the radius that includes the bulk of the true correlations while simultaneously limiting contamination by spurious correlations, is found to be around 9 arcsec. For $r = 9$ arcsec, we expect to achieve 86 true and only 3 spurious correlations.

There are two limitations to this procedure. Strictly speaking, the above expression for the spurious detections is downright valid for a uniform distribution of the optical sources over the investigated area. Though this is not the case for the optically brightest objects, Fig. 1 of Sung et al. (2000) indicates that this should be a fairly good approximation for the fainter stars. Another issue is that we assume that a single correlation radius can be used over the entire field of view. A radius of 9 arcsec corresponds roughly to 1.5 times the in-orbit FWHM of the on-axis point spread function (PSF) of the *XMM* mirror modules at 1.5 keV (Jansen et al. 2001). At large off-axis angles, the quality of the PSF progressively degrades and the half energy width increases by nearly a factor of two (Stockman et al. 1998). Our optimal radius should therefore be seen as some sort of weighted average for different off-axis angles.

Within a correlation radius of 9 arcsec, we find that:

- the brightest X-ray source is associated with the O4 V((f$^+$)) star 9 Sgr. The data on this star have been analysed elsewhere (Rauw et al. 2002) and we will not repeat this discussion here;
- a probably diffuse X-ray source is associated with the Hourglass Region. We shall return to the HG in Sect. 4;
- 72 X-ray sources have a single optical counterpart within a radius of less than 9 arcsec. The average angular separation between the X-ray source and the optical counterpart is (4.1 ± 2.1) arcsec. The brightest soft X-ray sources in this category are HD 164816 (O9.5 III-IV) and SCB 731. The latter is a very red 16th magnitude star without outstanding features (such as Hα emission) in its optical photometry. The X-ray source associated with SCB 731 appears elongated since it lies rather far off-axis;
- 17 X-ray sources have two or more optical stars falling within the 9 arcsec radius. Seven of these sources have at least one known Hα emission star inside their "error box";
- 28 sources do not have an optical counterpart in the catalogue of Sung et al. We have cross-correlated these sources with the Guide Star Catalogue (GSC[1]). In most cases, we find one or several GSC objects inside the 9 arcsec radius. These optical counterparts are usually very faint (V or $R \geq 17$) except for sources #91, 92 and 94 that have counterparts with R magnitudes 15.0, 14.6 and 13.3 respectively (note that these sources fall outside the area investigated by Sung et al.). Sources #93, 96, 98, 99, 100, 101, 102 and 112 have no GSC counterpart. Most of the objects in Table 3 are therefore X-ray sources with high L_X/L_{vis} ratios. Given the galactic coordinates of NGC 6530 ($l_{II} = 6.14°$, $b_{II} = -1.38°$), the total galactic column density along our line of sight in this direction must be extremely large and the number of extragalactic sources in our soft detection energy band should be extremely low.

The sources of the last three categories are listed in Tables 1–3 respectively. Along with our own source numbering, we list the source designation following the naming conventions recommended by the *XMM* SOC and the IAU (see the *XMM-Newton* Newsletter #4, April 2001): the XMMU J prefix is followed by the right ascension HHMMSS.s (in hours, minutes, seconds and tenths of seconds) and the declination of the source ±DDMMSS (in degrees, arcminutes and arcseconds).

[1] The Guide Star Catalogue-II is a joint project of the Space Telescope Science Institute and the Osservatorio Astronomico di Torino.

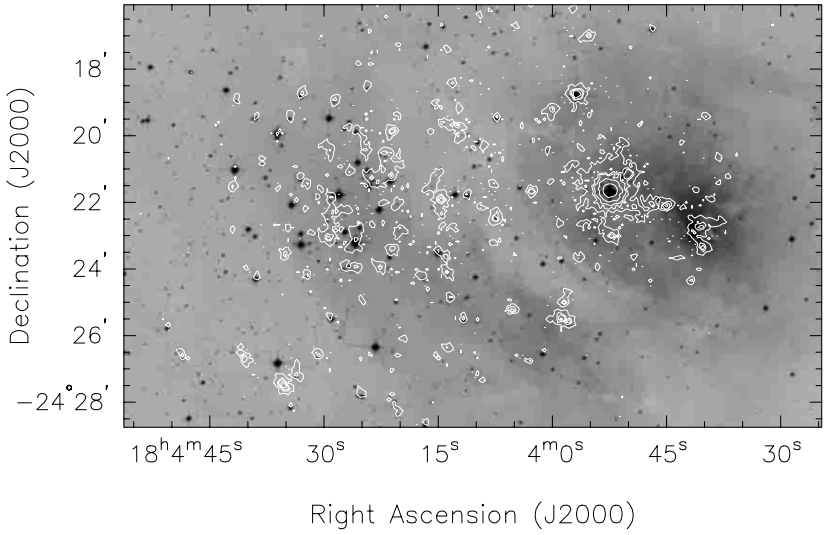

Fig. 2. EPIC X-ray contours (corresponding to the combined MOS1 + MOS2 + pn data in the 0.5–1.2 keV range) superimposed on a DSS optical image of the Lagoon Nebula. The different contours correspond to 5, 15, 24, 50 and 200 counts in the X-ray image.

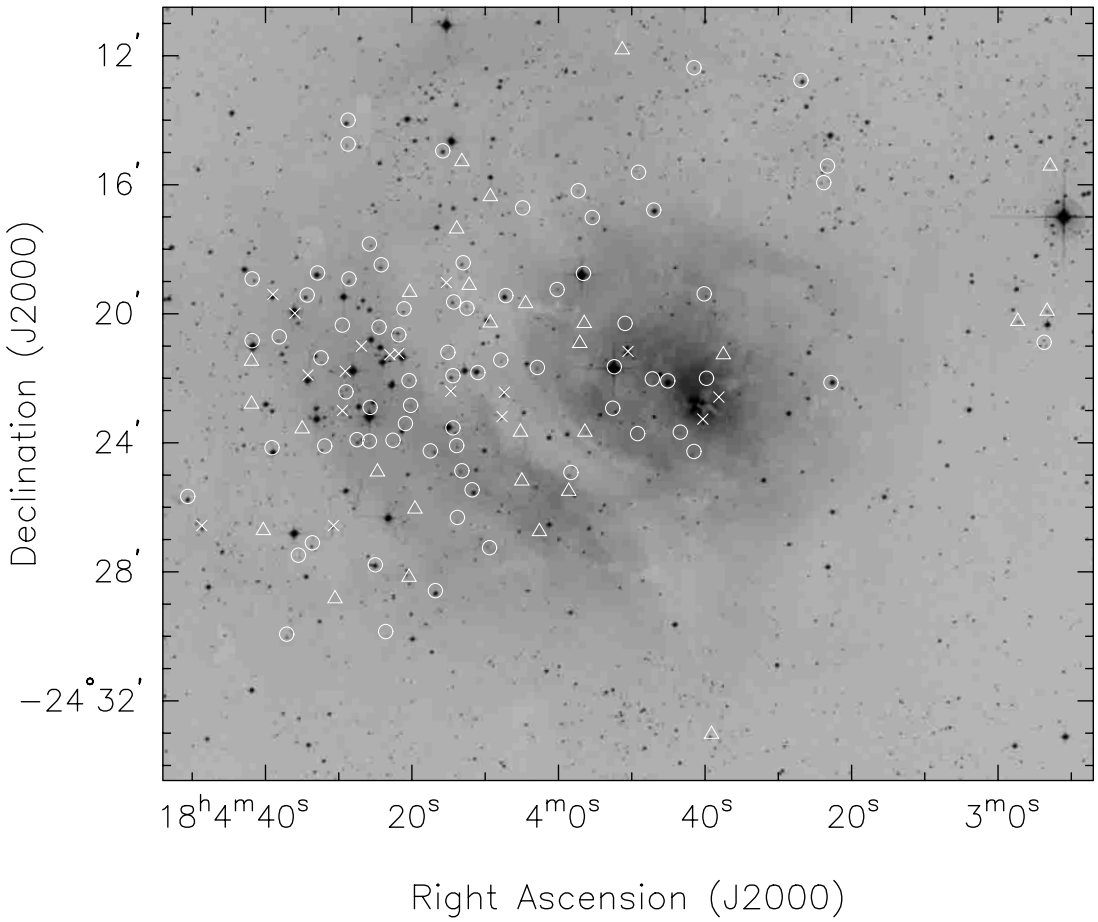

Fig. 3. DSS optical image of the Lagoon Nebula complex together with the positions of the highly significant sources. Open circles and crosses stand for X-ray sources having respectively a single or several counterparts in the Sung et al. (2000) catalogue. The open triangles indicate the positions of sources with no counterpart in the latter catalogue (nor in the SIMBAD database).

Table 1. X-ray sources detected in NGC 6530 and found to have a single counterpart in the catalogue of Sung et al. (2000) or in the SIMBAD database. The first and second columns yield the number of the X-ray source as well as the name according to the conventions for serendipitous *XMM-Newton* sources. Columns [3]–[5] provide the vignetting and background corrected EPIC-MOS and pn count rates in the 0.5–1.2 keV band. For sources affected by the gaps between the detectors, we do not quote the count rate for the corresponding instrument. The number of the optical counterpart from Sung et al. (2000) and the separation from the position of the X-ray source are given in Cols. [6] and [7]. The photometric data are taken from Sung et al. (2000), except for V 1752 Sgr. Column [11] indicates whether variability is detected at the 95% confidence level (Y) or not (N). Those sources flagged with a "?" show some hints of variability in their light curve, but this is not found to be significant by the Kolmogorov-Smirnov test. Finally, the last column yields information about the spectral types, pre-main sequence classification and the membership probability (P_μ) according to the proper motion study of van Altena & Jones (1972).

Source #	XMMU J	MOS1 10^{-3} cts s^{-1}	MOS2 10^{-3} cts s^{-1}	pn 10^{-3} cts s^{-1}	SCB	d (arcsec)	V	$B-V$	$V-I$	Variability	Comments
[1]	[2]	[3]	[4]	[5]	[6]	[7]	[8]	[9]	[10]	[11]	[12]
1	180253.7−242053	4.1 ± 1.0	2.8 ± 1.1	5.2 ± 1.6		8.4	15.80				V 1752 Sgr = PMS
2	180322.8−242208	3.0 ± 0.6	1.4 ± 0.4		7	3.9	10.62	0.96	1.07	N	
3	180323.3−241525	1.4 ± 0.7	1.5 ± 0.7	5.2 ± 1.0	20	7.0	15.17	1.28	1.53		
4	180323.8−241556	2.7 ± 0.6	3.1 ± 0.6	2.0 ± 0.8	28	5.7	15.51	1.25	1.52		
5	180326.9−241246	2.9 ± 0.7	2.1 ± 0.6	6.2 ± 1.2	47	1.4	11.83	0.26	0.45		$P_\mu = 0.80$
6	180339.8−242200	1.6 ± 0.4	1.7 ± 0.4	2.8 ± 0.7	1032	8.8	18.72		2.98		PMS
7	180340.1−241923	1.6 ± 0.4	1.7 ± 0.4	2.8 ± 0.7	138	3.5	15.05	1.24	1.41		
8	180341.5−241222	1.5 ± 0.5	1.0 ± 0.4	1.7 ± 0.7	151	0.8	15.38	1.33	1.58		
9	180341.5−242416	1.9 ± 0.4	2.2 ± 0.4	4.3 ± 0.7	157	5.7	15.44	1.47	1.93		PMS
10	180343.4−242340	2.6 ± 0.5	2.0 ± 0.4	3.8 ± 1.0	174	4.1	16.90	1.44	1.88		
11	180345.1−242205	5.1 ± 0.6	7.3 ± 0.7	11.5 ± 1.2	182	0.5	9.95	0.18	0.41	?	B2.5V, $P_\mu = 0.86$
12	180347.0−241647	0.8 ± 0.3	1.6 ± 0.4	1.6 ± 0.5	199	1.8	10.75	0.09	0.15		
13	180347.2−242201	1.0 ± 0.6	1.8 ± 0.7	3.8 ± 0.9	202	4.5	16.64	1.55	2.13		
14	180349.1−241537	0.7 ± 0.3	0.8 ± 0.3	1.7 ± 0.6	220	4.1	16.87	1.31	1.55		
15	180349.2−242343	0.8 ± 0.4	0.7 ± 0.3	2.4 ± 0.6	223	6.0	16.85	1.35	1.72		
16	180350.9−242018	2.5 ± 0.5	1.7 ± 0.4	3.6 ± 0.9	238	5.6	16.96	1.44	2.07		
17	180352.6−242256	4.3 ± 0.6	4.6 ± 0.6	8.7 ± 1.2	253	6.4	13.80	1.23	1.49	N	$P_\mu = 0.00$
18	180355.4−241701	2.8 ± 0.5	4.7 ± 0.6	7.0 ± 1.1	274	1.8	14.61	1.06	1.18	N	
19	180356.6−241845	14.3 ± 1.0	16.6 ± 1.1	35.8 ± 2.0	282	4.1	6.99	0.02	0.00	N	HD 164816 (O9.5 III-IV)
20	180357.3−241611	1.3 ± 0.4	1.3 ± 0.4	4.2 ± 0.8	285	1.2	16.27	1.20	1.41		
21	180358.3−242455	3.7 ± 0.5	3.4 ± 0.5	3.7 ± 0.9	295	5.6	15.51	1.40	1.84	N	
22	180400.2−241915	3.2 ± 0.5	4.0 ± 0.6	6.9 ± 1.0	314	3.4	15.28	1.14	1.36	N	
23	180402.9−242140	4.4 ± 0.6	5.4 ± 0.6	5.3 ± 0.9	340	0.1	14.85	1.35	1.59	N	
24	180404.9−241643	1.3 ± 0.4	0.7 ± 0.3	2.5 ± 0.6	360	4.3	16.31	1.40	1.64		
25	180407.2−241926	1.5 ± 0.5	1.3 ± 0.4	3.6 ± 0.7	379	2.7	10.76	0.25	0.48		$P_\mu = 0.00$
26	180407.9−242126	1.7 ± 0.4	2.0 ± 0.4	3.5 ± 0.8	387	0.6	16.43	1.32	1.68		
27	180409.4−242715	2.4 ± 0.5	2.1 ± 0.5	3.8 ± 0.8	410	6.2	16.69	1.60	1.86		
28	180411.0−242149	2.0 ± 0.4	1.6 ± 0.4	3.8 ± 0.8	426	4.7	10.37	0.12	0.23		B3Ve, $P_\mu = 0.84$
29	180411.8−242527	1.7 ± 0.4	2.6 ± 0.5	4.2 ± 0.9	432	4.1	11.69	0.24	0.44		A0, $P_\mu = 0.52$
30	180412.5−241950	4.0 ± 0.6	2.9 ± 0.5	11.1 ± 1.5	440	7.0	15.99	1.32	1.70	N	PMS
31	180413.0−241825	1.8 ± 0.4	1.7 ± 0.4	3.8 ± 0.9	450	2.7	14.34	0.98	1.22		
32	180413.2−242452	1.8 ± 0.4	1.8 ± 0.4	4.0 ± 0.9	452	2.8	15.31	1.35	1.65		
33	180413.8−242619	1.4 ± 0.5	1.3 ± 0.5	5.3 ± 0.9	457	5.4	16.32	1.53	1.98		
34	180413.9−242405	2.6 ± 0.5	2.6 ± 0.5	3.8 ± 1.0	454	1.4	15.59	1.40	1.68		

Table 1. continued.

Source #	XMMU J	MOS1 10^{-3} cts s^{-1}	MOS2 10^{-3} cts s^{-1}	pn 10^{-3} cts s^{-1}	SCB	d (arcsec)	V	$B-V$	$V-I$	Variability	Comments
[1]	[2]	[3]	[4]	[5]	[6]	[7]	[8]	[9]	[10]	[11]	[12]
35	180414.3−241938	0.8 ± 0.5	1.3 ± 0.5	4.3 ± 1.0	465	3.0	14.39	1.22	1.46		
36	180414.4−242155	7.6 ± 0.7	7.2 ± 0.8	15.9 ± 1.7	470	4.2	13.45	1.20	1.48	N	$P_\mu = 0.00$
37	180414.4−242332	2.2 ± 0.6	1.8 ± 0.6	7.8 ± 1.2	458	7.9	14.61	1.08	1.29		
38	180415.1−242112	1.6 ± 0.4	2.5 ± 0.5	3.3 ± 1.1	480	8.3	16.83	1.49	1.90		
39	180415.8−241457	1.9 ± 0.5	1.3 ± 0.5	3.9 ± 1.0	481	1.8	12.79	0.27	0.42		$P_\mu = 0.76$
40	180416.8−242835	2.4 ± 0.6	1.7 ± 0.5	4.4 ± 1.0	502	2.3	11.56	0.23	0.42		A0, $P_\mu = 0.60$
41	180417.5−242415	2.0 ± 0.5	3.2 ± 0.5	2.4 ± 0.9	504	6.8	14.26	1.22	1.44		
42	180420.2−242250	2.7 ± 0.5	2.8 ± 0.5	6.0 ± 1.1	540	2.3	16.17	1.26	1.76		PMS
43	180420.4−242204	1.2 ± 0.5	1.6 ± 0.6	6.8 ± 1.1	546	3.4	15.43	1.33	1.58		
44	180420.9−242324	2.7 ± 0.5	4.3 ± 0.6	10.8 ± 1.3	556	4.3	16.98	1.41	2.11	N	PMS
45	180421.1−241951	4.2 ± 0.6	4.1 ± 0.6	11.2 ± 1.4	557	2.7	14.71	1.11	1.44	N	
46	180421.8−242039	4.2 ± 0.6	4.7 ± 0.7	13.4 ± 1.6	571	5.9	13.92	0.84	1.06	N	
47	180422.6−242355	5.2 ± 0.7	6.2 ± 0.8		586	4.4	16.81	1.47	1.82	N	
48	180423.6−242951	1.4 ± 0.4	0.8 ± 0.5	2.3 ± 0.8	592	4.3	16.76	1.42	1.79		
49	180424.2−241829	3.2 ± 0.6	1.7 ± 0.5	4.7 ± 0.9	600	2.6	14.19	1.04	1.34		
50	180424.5−242025	2.6 ± 0.5	2.4 ± 0.5	6.7 ± 1.2	607	3.1	16.47	1.45	1.80		
51	180425.0−242747	2.6 ± 0.6	1.3 ± 0.6	7.7 ± 1.3	611	2.0	11.43	0.21	0.41		$P_\mu = 0.70$
52	180425.7−242254	1.9 ± 0.7	3.7 ± 0.9	8.8 ± 1.5	614	6.1	16.32		1.88		
53	180425.8−241750	1.3 ± 0.5	1.3 ± 0.5	2.4 ± 0.9	617	2.7	15.36	1.22	1.50		
54	180425.8−242357	2.8 ± 0.8	2.3 ± 0.7	6.3 ± 1.3	627	8.4	16.69	1.43	1.93		
55	180427.5−242354	1.9 ± 0.6	2.0 ± 0.6	3.6 ± 1.1	641	2.5	13.77	1.09	1.33		
56	180428.6−241855	1.9 ± 0.6	3.9 ± 0.7	6.9 ± 1.3	654	2.3	14.17	0.97	1.19	N	
57	180428.7−241400	1.1 ± 0.6	2.6 ± 0.8	6.6 ± 1.5	656	3.8	11.99	0.52	0.70		$P_\mu = 0.83$
58	180428.7−241444	1.7 ± 0.5	1.2 ± 0.5	6.9 ± 1.4	655	3.0	15.39	0.63	1.52		
59	180429.0−242225	5.1 ± 0.7	6.5 ± 0.8		658	6.5	15.12	1.26	1.57	N	
60	180429.5−242021	3.7 ± 0.6	2.8 ± 0.6	7.3 ± 1.4	665	6.8	16.86	1.54	2.10	N	
61	180431.9−242406	2.6 ± 0.6	2.7 ± 0.6	6.0 ± 1.3	700	7.1	14.59	1.18	1.46		
62	180432.4−242122	2.9 ± 0.6	2.5 ± 0.6	3.1 ± 1.3	698	6.5	16.11	1.41	1.79		
63	180432.9−241844	3.4 ± 0.7	3.1 ± 0.6	9.8 ± 1.6	707	1.5	10.42	0.12	0.19	N	B2.5Vne, $P_\mu = 0.75$
64	180433.6−242706	6.8 ± 1.0	3.5 ± 0.7	7.6 ± 2.0	718	4.2	14.56	1.23	1.57	N	
65	180434.3−241925	2.2 ± 0.6	3.0 ± 0.6	6.3 ± 1.3	725	3.1	12.85	0.87	1.02		$P_\mu = 0.01$
66	180435.5−242729	15.5 ± 1.5	15.7 ± 1.5	50.9 ± 3.7	731	2.0	16.53	1.50	2.03	Y	
67	180437.1−242956	2.2 ± 0.6	1.2 ± 0.6	5.2 ± 1.4	747	2.7	15.02	1.40	1.63		
68	180438.1−242043	1.9 ± 0.6	2.1 ± 0.6	4.0 ± 1.2	761	4.1	15.41	1.40	1.74		
69	180439.1−242409	1.4 ± 0.7	2.3 ± 0.7	6.3 ± 1.4	763	5.7	10.21	1.21	1.27		K0III, $P_\mu = 0.00$
70	180441.8−241855	2.5 ± 0.7	2.6 ± 0.7	6.4 ± 1.4	786	4.1	14.62	1.04	1.24		
71	180441.8−242050	1.4 ± 0.5		2.8 ± 0.9	787	5.9	9.76	0.09	0.18		HD 164947, B2.5 V
72	180450.6−242540	4.3 ± 1.0			879	2.5	11.94	0.39	0.75		LkHα 115 (B4Ve), $P_\mu = 0.79$

Table 2. Same as Table 1 for X-ray sources with two or more counterparts from Sung et al. (2000) inside a radius of 9 arcsec around the position of the X-ray source.

Source #	XMMU J	MOS1 10^{-3} cts s^{-1}	MOS2 10^{-3} cts s^{-1}	pn 10^{-3} cts s^{-1}	SCB	d (arcsec)	Variability	Comments
[1]	[2]	[3]	[4]	[5]	[6]	[7]	[8]	[9]
73	180338.1−242235	1.8 ± 0.5	1.3 ± 0.5	4.4 ± 0.9	1039/1028	1.7/3.3		[a]
74	180340.3−242316	4.9 ± 0.6	5.1 ± 0.8	9.7 ± 1.3	142/146/1019	4.2/5.5/6.8		[b]
75	180350.5−242110				240/228/229			240 = LkHα108[c]
76	180407.4−242226	7.8 ± 0.8	7.8 ± 0.8		382/380	3.7/4.0	N	
77	180407.7−242311	1.7 ± 0.4	1.4 ± 0.4	1.8 ± 0.7	388/390	2.8/3.2		390 = PMS
78	180414.7−242224	1.5 ± 0.6	3.2 ± 0.6		468/1005	3.2/3.3		1005 = PMS
79	180415.3−241902	0.8 ± 0.4	1.7 ± 0.5	2.6 ± 0.9	478/482	5.0/6.9		482 = PMSc
80	180421.8−242114	1.4 ± 0.8	1.8 ± 0.8	9.7 ± 1.4	573/561/558	5.5/8.0/8.4		
81	180423.0−242116	7.5 ± 0.8	8.3 ± 0.9	14.5 ± 2.1	582/593/587	6.5/8.3/8.7	N	
82	180426.9−242100	2.0 ± 0.5	2.3 ± 0.5	4.5 ± 1.1	631/635	7.1/7.2		
83	180429.1−242147	1.5 ± 0.6	2.0 ± 0.7	4.5 ± 1.5	657/663	5.3/6.1		
84	180429.5−242300	7.7 ± 0.9	7.0 ± 0.9	25.4 ± 2.3	671/659	4.4/7.2	N	
85	180430.7−242634	4.6 ± 0.8	3.7 ± 0.7	7.8 ± 1.4	681/682	2.9/4.1	N	
86	180434.2−242154	1.7 ± 0.5	1.6 ± 0.6	2.8 ± 1.0	723/720/716	4.1/7.0/8.3		
87	180436.0−241959	1.0 ± 0.6	2.3 ± 0.7	3.4 ± 1.0	740/738	3.5/6.8		
88	180439.0−241924	2.0 ± 0.6	2.0 ± 0.6	3.4 ± 1.0	765/773	1.9/8.6		
89	180448.7−242634	10.5 ± 1.4	9.3 ± 1.4		864/862	1.9/6.8	N	862 = PMS

[a] SCB 1028 is classified as a PMS star, while SCB 1039 is a PMS candidate (Sung et al. 2000).
[b] SCB 142 is a Hα emitting star (LkHα106) while SCB 1019 is a PMS star (Sung et al.).
[c] Source #75 (XMMU J180350.5−242110) lies within the wings of the PSF of 9 Sgr. Therefore no accurate count rates can be provided.

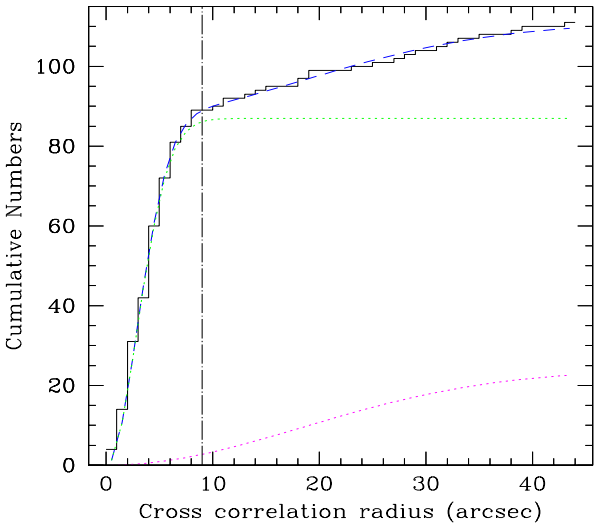

Fig. 4. Cumulative numbers of correlations between the X-ray detections and the Sung et al. (2000) catalogue as a function of correlation radius. The dotted curves correspond to the best fitting expressions for the real and spurious correlations. The dashed curve yields the sum of these terms and the dash-dotted vertical line corresponds to the optimal correlation radius of 9 arcsec.

Note that the coordinates refer to equinox J2000 and are truncated, not rounded.

2.1. Light curves

We have extracted light curves and spectra for the brightest objects. Except for sources near the edge of the field of view, we used a circular extraction region with a radius between 19 and 40 arcsec depending on the angular separation between neighbouring X-ray sources. For sources near the edge of the field of view, we used elliptical extraction regions to match as closely as possible the shape of the point spread function. The light curves and spectra were accumulated over the PI range 200 to 10000 (corresponding roughly to $E \in [0.2, 10.0]$ keV), except for objects that are contaminated by the straylight. In the latter cases, we extracted light curves only (i.e. no spectra) over the PI range 200 to 1500 (i.e. $E \in [0.2, 1.5]$ keV).

For all the light curves we adopted time bins of 400 s. The light curves were tested for variability using a Kolmogorov-Smirnov test against a model of constant count rate. Among the sources with a single optical counterpart, SCB 731, the second brightest X-ray source, is clearly variable: the light curve (extracted over an elliptical region adapted to the shape of the PSF) reveals a strong X-ray flare towards the end of our observation (Fig. 5). The X-ray flux suddenly rises by nearly two orders of magnitude and after about 2000 s starts to decline again.

SCB 182 and source #99 show some marginal variability in their light curves. The behaviour is the same in all three EPIC instruments, but the variability occurs at a rather low level so that it is found not to be significant by the Kolmogorov-Smirnov test (at the $P > 95\%$ confidence level). A Fourier

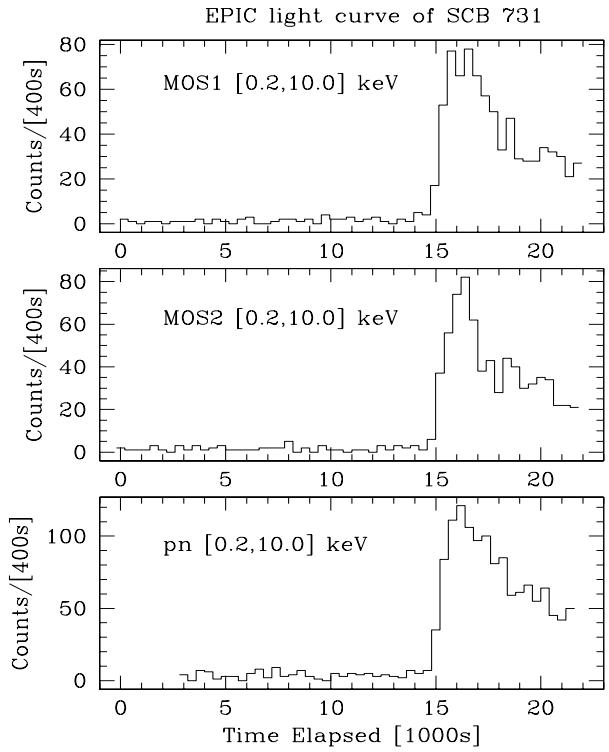

Fig. 5. EPIC light curves of the X-ray source #66 (XMMU J180435.5−242729) associated with SCB 731. We have also extracted the light curve of a nearby background region (not shown here). The latter does not display any variability. The zero time in our light curves corresponds to JD 2451976.982.

technique detects slow variability in the light curve of source #99 at the 99% confidence level.

None of the other relatively bright sources turned out to display significant variability (95% level) over the duration of our observation.

We also reduced a *ROSAT*-PSPC observation of M 8 (rp900374n00, integration time 10.4 ksec, JD 2449078.532 – 2449079.569) using the XSELECT software. In this exposure, SCB 253 appears as the third brightest source (after 9 Sgr and HD 164816) with a net count rate of $(6.9 \pm 1.0) \times 10^{-3}$ cts s^{-1} over the entire energy range of the PSPC instrument. Other sources that are detected in this PSPC image are the Hourglass Region, SCB 7, 28, 47, 182, 274, 340, 452/454, 470, #76, #95, #91, #94 as well as a source which is not seen with *XMM* at RA = 18:04:03.2, DEC = −24:31:08.5 (equinox J2000).

2.2. Spectra

For the spectra, we adopted the redistribution matrices provided by the EPIC instrument teams (versions available in May 2001) and we used the SAS to build the appropriate ancillary response files for each EPIC instrument. The spectra were binned to reach a minimum of 10 counts per channel and the background corrected spectra were analyzed using the XSPEC software (version 11.00). Because of the strong noise in the pn detector below 0.2 keV and the uncertain calibration of the EPIC instruments at low energies, we ignored the binned energy channels below 0.3 keV for the XSPEC fits. Note that for the X-ray sources associated with HD 164816 and SCB 731, we have a total of respectively 300 and 800 net counts for each MOS spectrum. The pn spectra contain about twice as many counts.

We fitted the spectra using either an absorbed one-temperature `mekal` thermal plasma model (Mewe et al. 1985; Kaastra 1992) or an absorbed power law model. The best fitting model parameters are listed in Table 4. In several cases, the fits with a power law with a rather large photon index Γ are slightly better than those with the thermal plasma model. However, these models yield systematically larger $N_{\rm H}$ than the value 0.17×10^{22} cm^{-2} expected from the mean $E(B-V)$ color excess (see Sect. 3 below). More complex models, such as two-temperature `mekal` or `mekal` + power law models could also improve the χ^2_ν. For instance, the spectrum of source #76 is better fitted ($\chi^2_\nu = 0.99$) with a 2-T thermal model with $kT_1 = 0.84$ and $kT_2 = 5.55$ keV. However, we caution that the quality of our spectra is usually not sufficient to distinguish a very hot ($kT \sim$ a few keV) multi-temperature thermal plasma emission from a power law spectrum.

For the 1-T `mekal` fits, we are usually left with a number of nearly equivalent solutions corresponding to either intrinsically harder, but less absorbed or more absorbed but intrinsically softer plasma models. Apart from the late O-star HD 164816 (source #19), all the sources have rather hard spectra with $kT \geq 0.65$ keV.

The spectrum of HD 164816 could be better fitted by adding a second (harder) component to the model, but the properties of this second component are not well constrained by the data. We note that the best fit model yields $N_{\rm H} = 0.43 \times 10^{22}$ cm^{-2} which is significantly larger than the value of the interstellar column density $0.15^{+.05}_{-.04} \times 10^{22}$ cm^{-2} derived by Diplas & Savage (1994) from the interstellar Lyα line. This suggests that part of the fitted absorption could actually arise in circumstellar (i.e. stellar wind) material. Correcting the X-ray flux for the pure interstellar column density only[2], we infer an "intrinsic" (i.e. at the top of the stellar wind) X-ray luminosity of 5.7×10^{31} erg s^{-1}. Adopting a bolometric correction of −3.00, we infer $\log L_{\rm X}/L_{\rm bol} = -6.96$ which is in pretty good agreement with the empirical $L_{\rm X} - L_{\rm bol}$ relation for O-stars proposed by Berghöfer et al. (1997). It is worth pointing out that Howarth et al. (1997) suggested that this star could be an SB2 binary (although no orbital solution exists so far). Provided that the interstellar column alone properly accounts for the low energy absorption, we find that the $L_{\rm X}/L_{\rm bol}$ ratio yields no evidence for an excess X-ray emission attributable to a wind interaction in a colliding wind binary.

If we assume that $N_{\rm H} = N_{\rm H,ISM} = 0.17 \times 10^{22}$ cm^{-2} for the other sources, we find that most fits yield kT of a few keV. Note

[2] If we correct for the entire (i.e. fitted) column density, we obtain a corrected intrinsic flux that would be about 7 times larger (although a proper wind absorption model, accounting for the ionization of the wind material would be required, see e.g. Waldron et al. 1998).

Table 3. X-ray sources detected in NGC 6530 that have no counterpart in the Sung et al. (2000) catalogue and the SIMBAD database within a radius of 9 arcsec.

Source # [1]	XMMU J [2]	MOS1 10^{-3} cts s^{-1} [3]	MOS2 10^{-3} cts s^{-1} [4]	pn 10^{-3} cts s^{-1} [5]	Variability [6]
90	180252.9−241525	[a]	[a]	11.4 ± 2.3	
91	180253.3−241955	6.4 ± 1.4		12.7 ± 2.3	N
92	180257.3−242014	3.9 ± 1.1	2.9 ± 1.1	10.4 ± 1.7	
93	180337.5−242116	0.5 ± 0.4	1.1 ± 0.4	2.4 ± 0.7	
94	180339.1−243302	5.1 ± 1.0	6.9 ± 1.1	12.9 ± 1.9	N
95	180351.3−241149	1.8 ± 0.5	1.8 ± 0.6	1.6 ± 0.8	
96	180356.4−242340	1.3 ± 0.4	2.3 ± 0.4	3.9 ± 0.8	
97	180356.5−242018	0.8 ± 0.4	0.4 ± 0.4	1.6 ± 0.8	
98	180357.1−242055	1.8 ± 0.4	1.4 ± 0.5	1.8 ± 0.7	
99	180358.6−242530	6.4 ± 0.7	6.5 ± 0.7	16.0 ± 1.6	?
100	180402.6−242645	2.3 ± 0.5	2.2 ± 0.4		
101	180404.5−241941	0.7 ± 0.3	1.2 ± 0.4	1.2 ± 0.5	
102	180405.0−242511	2.9 ± 0.5	3.4 ± 0.5	9.1 ± 1.1	
103	180405.2−242340	0.8 ± 0.3	1.1 ± 0.4	1.1 ± 0.5	
104	180409.3−241622	1.2 ± 0.4	0.8 ± 0.4	2.6 ± 0.8	
105	180409.3−242017	1.7 ± 0.5	1.4 ± 0.4	2.6 ± 0.8	
106	180412.2−241907	1.5 ± 0.5	1.3 ± 0.5	1.9 ± 0.8	
107	180413.2−241517	1.4 ± 0.5	1.0 ± 0.5	2.2 ± 0.8	
108	180413.9−241722	0.8 ± 0.4	1.3 ± 0.5	3.2 ± 0.9	
109	180419.6−242603	1.1 ± 0.4	1.1 ± 0.4	3.6 ± 1.0	
110	180420.3−241920	0.9 ± 0.4	1.6 ± 0.5	2.6 ± 1.0	
111	180420.4−242810	2.3 ± 0.6	2.4 ± 0.6	5.0 ± 1.2	
112	180424.7−242454	1.9 ± 0.6	1.5 ± 0.5	3.0 ± 0.8	
113	180430.5−242850	1.2 ± 0.5	1.9 ± 0.6	3.4 ± 1.1	
114	180435.0−242334	3.3 ± 0.7	4.2 ± 0.7	10.0 ± 1.6	N
115	180440.3−242643	7.3 ± 1.1	6.9 ± 1.1	19.0 ± 2.4	N
116	180441.9−242248	2.0 ± 0.7	1.9 ± 0.7	7.8 ± 1.4	
117	180441.9−242128	3.8 ± 0.9	1.7 ± 0.7	12.5 ± 1.8	

[a] Source #90 (XMMU J180252.9−241525) lies outside the field of view of the MOS instruments, but is detected as a rather bright source with $(1.14 \pm 0.23) \times 10^{-2}$ cts s^{-1} in the pn image.

that the spectrum of SCB 731 (Fig. 6) corresponds to the X-ray emission during the flare event, the contribution of the quiescent time intervals to the spectrum being essentially negligible.

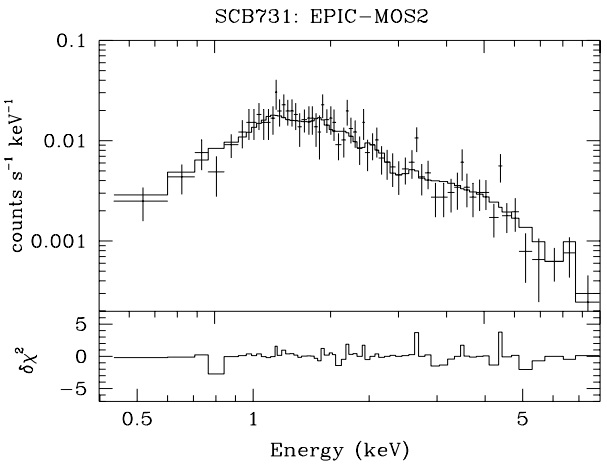

Fig. 6. EPIC-MOS2 spectrum of the X-ray source # 66 associated with SCB 731. The solid line yields the best fitting absorbed `mekal` model.

3. The nature of the X-ray sources in NGC 6530

We have plotted the X-ray sources with a single optical counterpart in a $(B-V, V)$ colour-magnitude diagram (Fig. 7). For this purpose, we adopted $< E(B-V) > = 0.30, R_V = A_V/E(B-V) = 3.1$ and DM = 11.25 (van den Ancker et al. 1997). Although they found that some highly reddened stars show anomalous extinction, van den Ancker et al. (1997) proposed that the average extinction law of the intercluster material is normal ($R_V = 3.1$).

We caution that there could be a number of foreground (or background) sources that contaminate our sample. Nevertheless, for the sake of simplicity, we have adopted the distance of NGC 6530 for all the sources. In Table 1, we include the membership probability from the proper motion study of van Altena & Jones (1972) whenever this information exists. However, Sung et al. (2000) caution that the proper motion study might be problematic since low membership probabilities were assigned to some early-type stars. In their study, Sung et al. therefore favour purely photometric criteria.

Table 4. Best fitting parameters for absorbed thermal plasma `mekal` and absorbed power law models fitted to the EPIC spectra of the brightest X-ray sources in NGC 6530. The observed fluxes quoted in Cols. [5] and [9] are evaluated over the energy range 0.5–5 keV. The quoted uncertainties correspond to formal errors on the spectral fits.

	`wabs*mekal`				`wabs*power`			
Source #	$N_{\rm H}$ 10^{22} cm^{-2}	kT keV	χ^2_ν (d.o.f.)	flux erg cm^{-2} s^{-1}	$N_{\rm H}$ 10^{22} cm^{-2}	Γ	χ^2_ν (d.o.f.)	flux erg cm^{-2} s^{-1}
[1]	[2]	[3]	[4]	[5]	[6]	[7]	[8]	[9]
11	$0.22^{+.07}_{-.05}$	$3.18^{+.66}_{-.55}$	0.98 (60)	1.09×10^{-13}	$0.43^{+.12}_{-.13}$	$2.49^{+.30}_{-.26}$	1.05 (60)	1.07×10^{-13}
19	$0.43^{+.12}_{-.13}$	$0.23^{+.04}_{-.04}$	1.08 (152)	0.77×10^{-13}				
36	$0.16^{+.08}_{-.06}$	$3.05^{+.65}_{-.53}$	1.30 (59)	1.09×10^{-13}	$0.49^{+.11}_{-.09}$	$2.78^{+.33}_{-.29}$	1.07 (59)	1.08×10^{-13}
47	$0.15^{+.06}_{-.04}$	$2.95^{+.66}_{-.41}$	1.02 (61)	1.17×10^{-13}	$0.43^{+.12}_{-.10}$	$2.92^{+.46}_{-.37}$	0.82 (61)	1.13×10^{-13}
59	$1.06^{+.16}_{-.19}$	$0.70^{+.27}_{-.10}$	1.55 (40)	0.65×10^{-13}	$0.42^{+.14}_{-.11}$	$2.99^{+.54}_{-.40}$	1.01 (40)	0.83×10^{-13}
66	$0.26^{+.04}_{-.04}$	$6.64^{+2.27}_{-1.35}$	0.82 (130)	5.24×10^{-13}	$0.34^{+.07}_{-.06}$	$1.80^{+.15}_{-.15}$	0.78 (130)	5.27×10^{-13}
76	$0.11^{+.04}_{-.04}$	$3.54^{+.91}_{-.60}$	1.67 (65)	1.05×10^{-13}	$0.32^{+.08}_{-.07}$	$2.66^{+.33}_{-.29}$	1.35 (65)	1.05×10^{-13}
81	$0.95^{+.05}_{-.13}$	$0.65^{+.17}_{-.06}$	1.54 (66)	0.89×10^{-13}	$0.41^{+.12}_{-.09}$	$3.15^{+.52}_{-.40}$	0.95 (66)	1.19×10^{-13}
84	$0.15^{+.05}_{-.05}$	$2.92^{+.74}_{-.52}$	1.20 (90)	1.13×10^{-13}	$0.35^{+.09}_{-.07}$	$2.62^{+.29}_{-.25}$	1.21 (90)	1.14×10^{-13}
89	$1.04^{+.16}_{-.17}$	$1.01^{+.11}_{-.27}$	1.51 (45)	1.26×10^{-13}	$0.42^{+.13}_{-.10}$	$2.80^{+.23}_{-.36}$	0.75 (45)	1.58×10^{-13}
94	$0.14^{+.11}_{-.09}$	$1.78^{+.64}_{-.34}$	1.07 (36)	0.67×10^{-13}	$0.72^{+.91}_{-.33}$	$4.87^{+2.56}_{-1.72}$	1.24 (36)	0.55×10^{-13}
99	$0.29^{+.11}_{-.08}$	$3.59^{+1.07}_{-.65}$	1.08 (48)	2.22×10^{-13}	$0.43^{+.13}_{-.11}$	$2.22^{+.28}_{-.25}$	1.19 (48)	2.22×10^{-13}
115	$0.18^{+.05}_{-.04}$	$3.49^{+.79}_{-.64}$	0.91 (106)	1.71×10^{-13}	$0.40^{+.10}_{-.05}$	$2.65^{+.34}_{-.29}$	0.79 (106)	1.67×10^{-13}

Apart from a group of rather bright ($V \leq 12$) stars that are probably either early-type OB stars, Herbig Ae/Be stars (see below) or foreground objects, we find a group of objects lying to the right of the ZAMS (by about 0.5 in $B - V$). Note that this result is preserved if we adopt the reddening properties suggested by Sung et al. (2000) instead. Five of these objects display Hα emission and are classified as PMS stars (Sung et al. 2000). It seems therefore very likely that this family of X-ray sources corresponds to intermediate- and low-mass PMS objects.

3.1. A population of pre-main sequence stars?

Low-mass PMS stars are classified according to their infrared properties into classes 0, I, II and III (see e.g. Feigelson & Montmerle 1999). Class 0 and I objects are deeply embedded in their nascent molecular cloud and due to their heavy circumstellar extinction, the X-ray emission from these objects is strongly attenuated. These protostars have X-ray luminosities that range from 10^{28} to 10^{30} erg s^{-1} with occasional flares of order 10^{31} erg s^{-1} (Carkner et al. 1998) and are best detected in the hard X-rays (e.g. Feigelson & Montmerle 1999). Class II pre-main sequence stars are surrounded by a thick disk. The most distinctive feature of these so-called classical T Tauri stars is their Hα emission. Sung et al. (2000) used this criterion to identify 58 PMS stars in NGC 6530 with strong Hα emission and 17 PMS candidates with weak Hα emission. As the PMS stars evolve, it is thought that their disks dissipate and the PMS stars become Class III objects (or weak-line T Tauri stars) that have weaker or no Hα emission. At least in the Taurus-Auriga-Perseus complex, the weak-line T Tauri stars are found to be X-ray brighter than the classical T Tauri stars (Stelzer & Neuhäuser 2001).

The X-ray emission of T Tauri stars is probably due to solarlike magnetic activity or a magnetic interaction with the surrounding protostellar disk. However, the X-ray luminosities are up to 10^3 times larger than that of the Sun (Neuhäuser 1997). Low-mass PMS stars in the T Tauri stage have multi-temperature thermal X-ray spectra with a soft component in the range $kT_1 \in [0.2, 0.45]$ keV and a harder component with $kT_2 \in [1.3, 2.6]$ keV. These objects are usually variable X-ray emitters that exhibit flare events with a fast rising curve followed by a slower decay (see e.g. Feigelson & Montmerle 1999 for a review on their high-energy properties).

In the lower panel of Fig. 7, we have plotted the unabsorbed luminosities (in the 0.5–5.0 keV band) as a function of V. For the brightest sources, we used the luminosities inferred from the spectral fits in Table 4 and assuming a distance modulus of 11.25. For those sources for which we were not able to perform a spectral fit, we have converted the observed count rates into unabsorbed fluxes assuming a thermal plasma model with $kT = 2$ keV, an interstellar column density of $N_{\rm H} = 5.8 \times 10^{21}\, E(B-V) = 0.17 \times 10^{22}$ cm^{-2} (Bohlin et al. 1978) and DM = 11.25. Note that $kT = 2$ keV is in better agreement with the mean temperature inferred from our spectral fits than the "usual" $kT = 1$ keV. Adopting $kT = 1$ keV instead of 2 keV would reduce the luminosities by a factor 0.56 (−0.25 dex).

In summary, among the objects with an intrinsic luminosity exceeding 10^{31} erg s^{-1} and having a single optical counterpart, there are 57 X-ray sources with an optical counterpart fainter than 12th magnitude and we suggest that most of these objects are good candidates for T Tauri stars. The strong flare that we

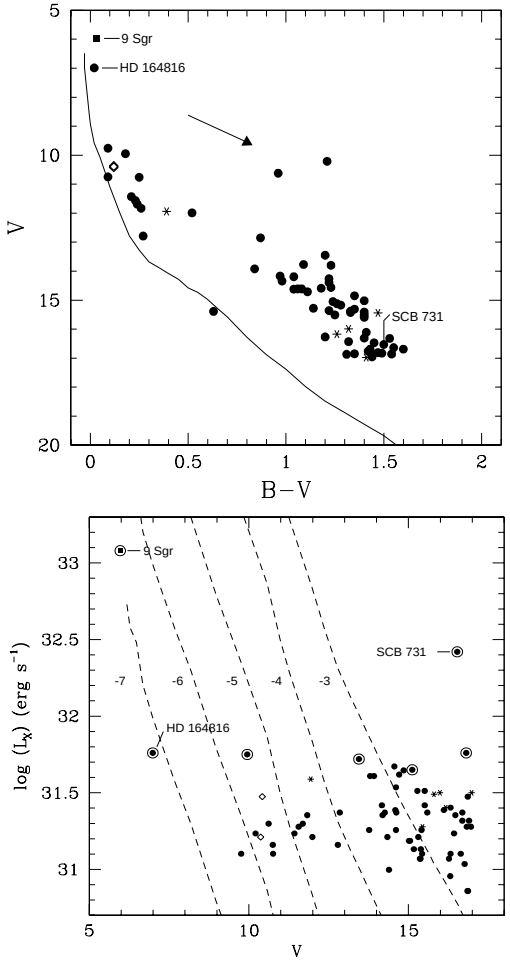

Fig. 7. Top: colour-magnitude diagram of the X-ray sources in the very young open cluster NGC 6530. The reddening vector with $R_V = 3.1$ is indicated and the solid line shows the ZAMS relation taken from Schmidt-Kaler (1982) with a distance modulus DM = 11.25 and reddened with $E(B-V) = 0.30$ (see text). Black dots stand for stars from Sung et al. (2000) without Hα emission, asterisks stand for pre-main sequence stars or PMS candidates from Sung et al. and the (overlapping) open diamonds indicate two stars classified as Be stars by van den Ancker et al. (1997). Bottom: unabsorbed X-ray luminosity (in the energy range 0.2–5.0 keV) as a function of the observed V magnitude. The MOS count rates were converted into luminosities assuming a 2 keV thermal plasma model, a uniform interstellar column density of $N_{\rm H} = 0.17 \times 10^{22}$ cm^{-2} and a distance of 1.8 kpc, except for the sources for which a detailed spectral fit is available. For these sources (symbols surrounded by an open circle) we used the flux from the actual fit. The luminosity of 9 Sgr is taken from Rauw et al. (2002). The dashed lines yield different values of $\log(L_{\rm X}/L_{\rm bol})$ (indicated by the labels) corresponding to main sequence stars of magnitude V in NGC 6530.

observe in the light curve of SCB 731 provides further evidence that at least some of these sources are related to PMS stars. The fact that only a few X-ray selected PMS candidates display an Hα emission is in agreement with the suggestion that weak-line T Tauri stars are intrinsically X-ray brighter than the classical T Tauri stars (Stelzer & Neuhäuser 2001).

The unabsorbed X-ray luminosities of the brightest sources are found to cluster around a few times 10^{31} erg s^{-1}. Let us emphasize that these values are slightly larger than expected for weak-line T Tauri stars and much larger than those of classical T Tauri stars (Neuhäuser 1997). It seems unlikely that this result is due to uncertainties on the distance of NGC 6530; most of the recent determinations of the cluster distance agree nicely (Sung et al. 2000; van den Ancker et al. 1997). In any case, a sizeable fraction of our sources have $L_{\rm X}/L_{\rm bol}$ exceeding 10^{-3}. The most likely explanation for these extreme values is that our data only reveal the tip of the X-ray luminosity function of PMS stars in NGC 6530. The cluster could harbour many more PMS stars with X-ray fluxes below our detection threshold ($\sim$4–8 $\times 10^{30}$ erg s^{-1}). Assuming $L_{\rm X}/L_{\rm bol} \sim 10^{-3}$, this X-ray luminosity threshold corresponds to $M_{\rm bol} \sim 4.3$. Most PMS stars less massive than 1.0 $M_\odot$ were therefore not detected in our observation.

We have constructed the Hertzsprung-Russell diagram of the X-ray selected stars in NGC 6530 using the $T_{\rm eff}$ versus $V-I$ calibration and the bolometric corrections for main-sequence stars from Kenyon & Hartmann (1995). Figure 8 compares the location of the objects with the pre-main sequence evolutionary tracks of Siess et al. (2000) for $Z = 0.02$ and without overshooting (note that these evolutionary models include neither rotation nor accretion).

We find that the bulk of the X-ray selected PMS stars appear to have masses between 1.0 and 2.0 $M_\odot$. A comparison with the isochrones indicates that most of these objects have ages ranging from 4 to 20 Myr. Only a few more massive objects appear to have ages below 1 Myr. We caution that a comparison of these results with other age determinations of PMS stars in NGC 6530 would be difficult because of the use of different calibrations and to the uncertainties related to the evolutionary calculations (see e.g. the discussion in Siess et al.). However, in Fig. 8, we have also included the PMS stars and candidates selected from their Hα emission and which do not appear as X-ray sources in our data. The two samples of PMS stars do not reveal significant age differences, most of the Hα selected objects also fall between the 4 and 20 Myr isochrones. This result is quite interesting: at least in NGC 6530 there is no clear evidence for an age difference between weak-line and classical T Tauri stars. This conclusion is in line with the finding of Stelzer & Neuhäuser (2001) that the overall age distribution of weak-line and classical T Tauri stars in the Taurus-Auriga-Perseus region is mixed.

Let us emphasize that there could be a difference in the mass distribution of these two categories of PMS stars. First of all, with the present data sets it is impossible to compare the lower mass limit of the two samples since the Hα selection criterion allows to identify fainter (and hence less massive) PMS objects than the X-ray criterion. However, we note that while both categories contain more or less the same number of objects in the 1.0–1.5 $M_\odot$ range, there are many more X-ray selected PMS stars in the 1.5–2.0 $M_\odot$ interval.

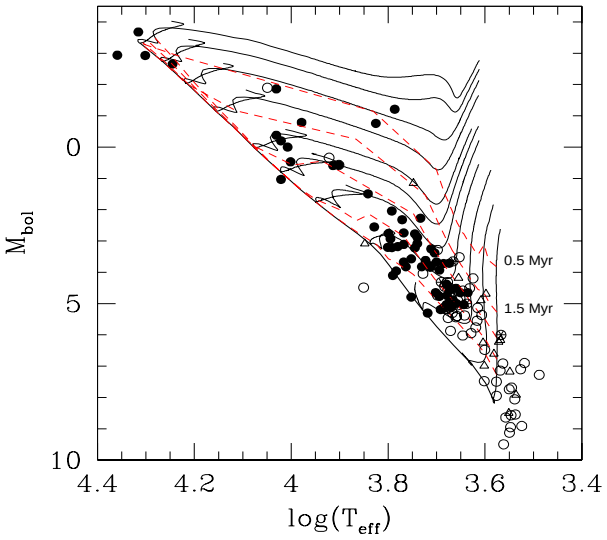

Fig. 8. Hertzsprung-Russell diagram of the X-ray selected stars in NGC 6530. Evolutionary tracks from Siess et al. (2000) for masses of 0.5, 0.7, 1.0, 1.5, 2.0, 2.5, 3.0, 4.0, 5.0, 6.0 and 7.0 $M_\odot$ are overplotted. Filled symbols indicate X-ray detected objects without Hα emission, whereas encircled asterisks stand for PMS stars selected from their Hα emission. The open circles and open triangles stand for Hα selected PMS and PMSc stars from Sung et al. (2000) respectively. The thick solid line shows the ZAMS, while the dashed lines correspond to isochrones for ages of 0.5, 1.5, 4.0, 10.0 and 20.0 Myr (for clarity only the first two isochrones are labelled).

3.2. Early-type stars

Five Be stars in NGC 6530 were found to exhibit a strong IR excess and were suggested to be Herbig Ae/Be stars by van den Ancker et al. (1997): LkHα 108 (SCB 240), LkHα 112 (SCB 583), LkHα 115 (SCB 879), Walker 29 (SCB 427) and Walker 303. These stars are believed to be intermediate-mass (~5.5–14 $M_\odot$, van den Ancker et al.) young stellar objects (YSOs). X-ray emission from Herbig Ae/Be YSOs has been reported by Hamaguchi et al. (2001). The objects observed by Hamaguchi et al. (2001) were found to display high temperature thermal emission ($kT \sim$ 1–5 keV) with luminosities in the range 10^{30}–10^{32} erg s^{-1}.

Walker 29 and Walker 303 are not detected in our soft-band X-ray images. LkHα 112 is marginally detected (with a combined likelihood of 9.9), but another star (SCB 581) lies also inside the 9 arcsec radius around the position of the *XMM* source. LkHα 108 lies inside the "error box" of source #75, together with SCB 228 and 229. The only unambiguous detection of X-ray emission from a Herbig Ae/Be star in our sample concerns LkHα 115 (source #72), which is detected with an unabsorbed X-ray luminosity of 3.9×10^{31} erg s^{-1}. We also note that the X-ray spectrum of source #11 (SCB 182, B2.5 V) yields a surprisingly high temperature ($kT \sim$ 3.2 keV) for a B-star. This suggests that SCB 182 could also be an intermediate-mass YSO, despite the fact that van den Ancker et al. (1997) did not classify it as a Herbig Be star.

High-mass young stellar objects could also emit X-rays. *Chandra* observations of the Orion Nebula Cluster revealed a huge number of X-ray emitting PMS stars over a broad range of masses (Garmire et al. 2000) including the detection of emission from massive stars that are just settling down on the ZAMS. Rho et al. (2001) reported on *ROSAT* and *ASCA* observations of the Trifid Nebula (M 20) which is thought to be in a "pre-Orion" star forming stage. Two massive YSOs as well as one low-mass PMS star were identified as counterparts of *ROSAT* sources. Kohno et al. (2002) obtained a *Chandra* observation of the Monoceros R2 cloud and detected X-ray emission from four massive YSOs which were found to have a mean temperature of $kT \sim$ 3 keV and to display flare-like events, much like their low-mass counterparts. This led Kohno et al. (2002) to suggest that the massive YSOs produce X-rays through the same magnetic activity as low-mass PMS stars. This activity would continue until the ZAMS phase and the onset of the stellar wind.

In NGC 6530 it seems rather unlikely to find high-mass YSOs that have not yet reached the ZAMS (at least outside the HG region). In fact, the earliest star in our field of view (apart from 9 Sgr and H 36) is HD 164816 (O9.5 III-IV) which has probably already evolved off the main sequence. Accordingly, van den Ancker et al. (1997) suggested that the formation of stars more massive than 8 $M_\odot$ has already stopped in NGC 6530. An exception to this rule could be the Hourglass Region which we shall discuss in the next section.

Finally, it is quite remarkable that some of the optically brightest ($V \leq$ 10.0) stars in NGC 6530 are not detected in our EPIC data. These include the late-type stars HD 164584, HD 164948 and SCB 444, as well as a number of main-sequence B-type stars (HD 164865, SCB 466, 588, 599, 647, 667 and 708) that have spectral types B1 or slightly later according to van den Ancker et al. (1997). The latter result is somewhat surprising. In fact, *ROSAT* all-sky survey results reported by Berghöfer et al. (1997) suggest that stars of spectral type B1 can have X-ray luminosities of order a few times 10^{31} erg s^{-1} and most of them should therefore be detected in our data. We conclude that most of the early B-type main sequence stars in NGC 6530 may have X-ray luminosities on the lower side of the L_X/L_{bol} relation proposed by Berghöfer et al. (1997).

4. The Hourglass Region

Our EPIC data also reveal X-ray emission from the Hourglass Region in M 8. Beside the ionizing star Herschel 36, the HG also harbours the ultra-compact HII region G 5.97–1.17 as well as a number of infrared sources some of which are believed to correspond to embedded massive stars. In fact, Woodward et al. (1990) performed near infrared imaging of the HG, unveiling a Trapezium-like stellar cluster of very young hot stars at the core of the HG. G 5.97–1.17 could be a YSO (probably a late-B star) surrounded by a circumstellar disk that suffers photoevaporation by the radiation from Herschel 36, similar to the so-called proplyds in the Orion Nebula (Stecklum et al. 1998). Herschel 36 is probably a massive YSO that is more evolved than the exciting stars of ultra-compact HII regions. In fact,

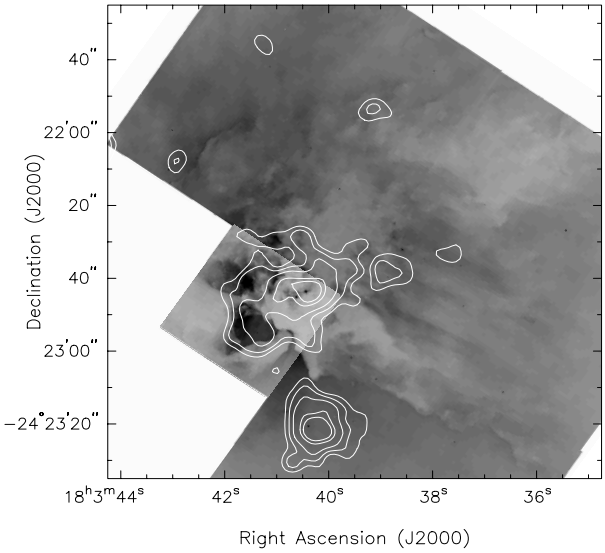

Fig. 9. EPIC X-ray contours superimposed on a *HST* WFPC2 Hα image of the HG region in the Lagoon Nebula. The X-ray contours reveal an elongated X-ray source at the location of the O7 V star Herschel 36 and of the UC HII region G 5.97 −1.17 as well as an emission lobe extending over the southern part of the optical HG nebula. The EPIC contours were smoothed by convolution with a Gaussian of σ = 2 pixels (1 pixel = 1 arcsec^2) and the contour levels correspond to 0.3, 0.4, 0.55, 0.81 and 1 EPIC (MOS1 + MOS2 + pn) count per arcsec^2 in the 0.5–1.2 keV band. The X-ray source below the HG is associated with SCB 142 and 146 (see Table 2).

Stecklum et al. (1995) reported infrared and *HST* Hα images that reveal an elongated jet-like structure associated with H 36 oriented roughly perpendicular to the elongated dust structure around the star that could be indicative of a circumstellar disk.

Woodward et al. (1986) proposed a "blister" scenario of the star formation in the HG where the massive star H 36 formed near the edge of the molecular cloud. This picture is also supported by the results of Chakraborty & Anandarao (1997, 1999). These authors studied the kinematics of the HG and found the H II bubble around H 36 to be expanding which suggests that the ionization front is still destroying the surrounding molecular cloud and pressure equilibrium has not yet been reached. In addition, these authors reported high velocity flows to the south of H 36 that indicate a Champagne flow.

The EPIC soft-band image of the HG region (Fig. 9) reveals an extended X-ray emission probably due to the contributions of the young stellar object H 36, the UC HII region and possibly a diffuse emission from a hot bubble created by the wind of Herschel 36. In particular, we find no correlation between the soft X-ray emission and the embedded IR sources discussed by Woodward et al. (1990). While the X-ray emission peaks around the position of H 36, it presents also an enhancement towards the south-east of H 36 (roughly coincident with the southern lobe of the optical HG nebula).

Woodward et al. (1986) found that the electron density (4000 cm^{-3}) on the eastern side of the ionized cavity is about ten times larger than the electron density on the western side (see their Fig. 15). Therefore, we find that the X-ray emission is enhanced over the higher density part of the HG region.

We have extracted EPIC-MOS spectra of the Hourglass in the energy range 0.2–1.2 keV and fitted them simultaneously with the *ROSAT*-PSPC spectrum extracted from observation rp900374n00. The source counts were extracted over an elliptical area designed to avoid contamination from neighbouring sources. The background-corrected spectra can be fitted (χ^2_ν = 1.25, 55 d.o.f.) with an absorbed `mekal` model with $N_{\rm H} = (1.11^{+.15}_{-.17}) \times 10^{22}$ cm^{-2}, $kT = 0.63^{+.07}_{-.05}$ keV. The observed and unabsorbed fluxes in the energy band 0.2–2.0 keV are respectively 1.1×10^{-13} and 1.7×10^{-12} erg cm^{-2} s^{-1}. The latter value corresponds to an integrated intrinsic luminosity of 6.6×10^{32} erg s^{-1}. Assuming that the X-ray emission from H 36 roughly follows the $L_{\rm X}/L_{\rm bol}$ relation proposed by Berghöfer et al. (1997), we expect H 36 to contribute 1.5×10^{32} erg s^{-1}, i.e. about one fourth of the total X-ray luminosity of the HG region.

Although we cannot completely rule out that the shape of the contours in Fig. 9 might result from the superposition of the PSFs of several faint point sources, it seems very tempting to associate the soft X-ray emission of the HG with a diffuse emission from a hot plasma around H 36. Diffuse X-ray emission has been observed in a few H II regions only. For instance, Seward & Chlebowski (1982) found an extended diffuse X-ray emission in the Carina Nebula. They attributed the heating of the emitting gas to the interaction of the stellar winds of the rich population of early-type stars with a dense cooler cloud. Wang (1999) reported diffuse X-ray emission arising in blister shaped regions of the 30 Dor complex outlined by loops of H II gas. Such a description could also suit the X-ray emission from the Hourglass Region. On the other hand, recent *Chandra* observations of the massive galactic starburst NGC 3603 revealed an extended diffuse X-ray emission in the immediate surroundings of the cluster core (Moffat et al. 2002). Moffat et al. suggest that the diffuse X-ray emission may arise from multiple merging/colliding hot stellar winds, with a rather low contribution of unresolved PMS stars. Since the HG region is a much less extreme star formation region, a superwind scenario (as in NGC 3603) that would require a large concentration of hot massive stars, is less likely to account for the X-ray emission seen in the HG.

As pointed out above, the density distribution in the vicinity of the Hourglass is believed to be highly non-uniform (Woodward et al. 1986) and a sophisticated numerical model such as the one developed by Comerón (1997) is therefore needed for a detailed comparison. In fact, simulated X-ray maps of a blister model presented by Comerón show that the X-ray emission consists of two components: an extended one from the bubble expanding into the intercloud (low-density) medium and a compact one in the vicinity of the star (i.e. in the high density part still contained in the molecular cloud). The simulations of Comerón (1997) indicate that the intrinsic soft X-ray emission from the compact component should dominate the extended emission component. The observed enhancement of the extended emission over the high density part of the HG is at least in qualitative agreement with this description.

Could the stellar wind of Herschel 36 (O7 V) account for the X-ray luminosity of a wind-blown bubble? The theory of these bubbles has been considered by Castor et al. (1975) and Weaver et al. (1977), with further additions by Mac Low & McCray (1988) and Chu et al. (1995) amongst others. The stellar wind sweeps up a dense shell of material, but within the shell there will be a region of hot shocked gas (see e.g. Strickland & Stevens 1999 for a schematic view of the structure of a wind-blown bubble). Within the framework of this theory, the parameters of the bubble depend upon the wind luminosity of the star, the density of the ambient medium and the age of the bubble (see e.g. Chu et al. 1995).

To derive an order of magnitude estimate, we adopt $T_{\rm eff}$ = 39 000 K and $\log(L_{\rm bol}/L_\odot) = 5.31$ for H 36. From these parameters, we expect a mass-loss rate $\dot{M} = 4 \times 10^{-7}\,M_\odot\,{\rm yr}^{-1}$ and a terminal wind velocity $v_\infty = 2300\,{\rm km\,s}^{-1}$ (Howarth & Prinja 1989; Prinja et al. 1990). This yields a kinetic luminosity of the stellar wind ($L_{\rm wind} = 1/2\,\dot{M}\,v_\infty^2$) of $6.7 \times 10^{35}\,{\rm erg\,s}^{-1}$. For simplicity, we assume that the ambient density is constant at the higher value derived by Woodward et al. (1986) with $n_{\rm e} = 4000\,{\rm cm}^{-3}$. Adopting an expansion velocity of the HG of $\sim$10 km s^{-1} (Chakraborty & Anandarao 1997, 1999) and an angular radius of the cavity in the molecular cloud of about 25″ (corresponding to 0.2 pc at a distance of 1.78 kpc), we infer a dynamical age of about 20 000 yrs.

From these values, we derive the theoretical properties of the bubble surrounding H 36. The central temperature of the bubble should be $\sim 5 \times 10^6$ K (i.e. $kT \sim 0.44$ keV), the predicted radius is 0.4 pc and the expected X-ray luminosity amounts to $L_{\rm X} \sim 10^{35}\,{\rm erg\,s}^{-1}$.

We note that the predicted radius is larger than the observed radius. This discrepancy is reminiscent of similar problems reported in the literature when the wind luminosity – age – radius relation from the bubble theory is compared to actual observations (see e.g. Oey 1996; Nazé et al. 2001 and references therein). The most outstanding discrepancy between the model and our observations of the HG region concerns the expected X-ray luminosity which is more than a factor 175 larger than the observed one. Note that mass-loading of the bubble cannot explain the discrepancy since one expects a mass-loaded bubble to be even more X-ray bright (Arthur et al. 1996). Part of this discrepancy may instead be due to our estimate of the kinetic luminosity of the wind of H 36. For instance, Stecklum et al. (1998) noted that the *IUE* spectra of H 36 are similar to those of θ^1 Ori C (HD 37022) and suggested hence that H 36 is close to the ZAMS and has a less developed wind than a typical O7 main sequence star. Assuming a mass-loss rate four times lower and a wind velocity half the values used above, the discrepancy would be reduced to a factor ~12. Note however that Leitherer (1988) derived $\dot{M} = 7.6 \times 10^{-7}\,M_\odot\,{\rm yr}^{-1}$ and $v_\infty = 1650\,{\rm km\,s}^{-1}$ for θ^1 Ori C which yields about the same value of the kinetic luminosity than derived hereabove. Another parameter that might account for some of the discrepancy is the density of the ambient medium. We have adopted a rather large value which should be appropriate for the molecular cloud. However, in the blister scenario, part of the bubble expands into the much lower density intercloud medium and the X-ray luminosity of the bubble around H 36 may be set by the density of the latter.

Although the theoretical values are much higher than the observed X-ray luminosity, we conclude that the kinetic luminosity of the stellar wind of Herschel 36 is most probably sufficient to account for the existence of a wind-blown bubble.

5. Summary and conclusions

Our *XMM-Newton* observation of the Lagoon Nebula (M 8) reveals a cluster of rather faint point-like X-ray sources in addition to the bright O4 star 9 Sgr. We have shown that most of these sources have optical counterparts inside the very young open cluster NGC 6530. We suggest that an important fraction of these sources are associated with low-mass pre-main sequence stars (most probably weak-line T Tauri stars) which were not previously identified as PMS objects because of the lack of strong Hα emission. Our results suggest that the true number of low-mass PMS objects exceeds by more than a factor two the number of objects identified by Sung et al. (2000).

The X-ray selected PMS candidates in NGC 6530 are found to have rather hard spectra with kT of a few keV and their X-ray luminosities (of order of a few times $10^{31}\,{\rm erg\,s}^{-1}$) are apparently in the higher part of the luminosities of T Tauri stars in the literature. The large number of X-ray sources associated with PMS stars in NGC 6530 may shed some light on the origin of apparently diffuse emission in more distant starburst clusters (e.g. NGC 3603) where source confusion becomes a serious issue.

As to intermediate and high-mass young stellar objects, we found that at least one of the known Herbig Be stars in NGC 6530 exhibits a relatively strong X-ray emission, while most of the early-type main sequence stars of spectral type B1 and later are not detected.

We also report X-ray emission from the massive protostar Herschel 36 as well as probably diffuse emission from the Hourglass Region that might reveal a bubble of hot gas produced by the interaction of the stellar wind of Herschel 36 with the denser part of the molecular cloud. Higher spatial resolution observations of the HG with *Chandra* are needed to confirm the diffuse nature of this emission and to further constrain its morphology.

Acknowledgements. We thank the referee Dr. R. D. Jeffries for valuable comments that helped to significantly improve our manuscript. The Liège team acknowledges support from the Fonds National de la Recherche Scientifique (Belgium) and through the PRODEX XMM-OM and Integral Projects. This research is also supported in part by contracts P4/05 and P5/36 "Pôle d'Attraction Interuniversitaire" (SSTC-Belgium). MCR acknowledges support from ESA-Prodex project No. 13346/98/NL/VJ(ic). This research has made use of the SIMBAD database, operated at CDS, Strasbourg, France and NASA's Astrophysics Data System Abstract Service.

References

Arthur, S. J., Henney, W. J., & Dyson, J. E. 1996, A&A, 313, 897
Berghöfer, T. W., Schmitt, J. H. M. M., Danner, R., & Cassinelli, J. P. 1997, A&A, 322, 167

Bohlin, R. C., Savage, B. D., & Drake, J. F. 1978, ApJ, 224, 132
Carkner, L., Kozak, J. A., & Feigelson, E. D. 1998, AJ, 116, 1933
Castor, J., McCray, R., & Weaver, R. 1975, ApJ, 200, L107
Chakraborty, A., & Anandarao, B. G. 1997, AJ, 114, 1576
Chakraborty, A., & Anandarao, B. G. 1999, A&A, 346, 947
Chu, Y.-H., Chang, H.-W., Su, Y.-L., & Mac Low, M.-M. 1995, ApJ, 450, 157
Comerón, F. 1997, A&A, 326, 1195
Diplas, A., & Savage, B. D. 1994, ApJS, 93, 211
Feigelson, E. D., & Montmerle, T. 1999, ARA&A, 37, 363
Garmire, G., Feigelson, E. D., Broos, P., et al. 2000, ApJ, 120, 1426
Hamaguchi, K., Koyama, K., & Yamauchi, S. 2001, Astronomische Gesellschaft Abstract Series, 18, Abstract of Contributed Talks and Papers JENAM 2001, MS 07 12
Hasinger, G., Altieri, B., Arnaud, M., et al. 2001, A&A, 365, L45
Howarth, I. D., & Prinja, R. K. 1989, ApJS, 69, 527
Howarth, I. D., Siebert, K. W., Hussain, G. A. J., & Prinja, R. K. 1997, MNRAS, 284, 265
Jansen, F., Lumb, D., Altieri, B., et al. 2001, A&A, 365, L1
Jeffries, R. D., Thurston, M. R., & Pye, J. P. 1997, MNRAS, 287, 350
Kaastra, J. S. 1992, An X-ray spectral code for optically thin plasmas, Internal SRON-Leiden Report
Kenyon, S. J., & Hartmann, L. 1995, ApJS, 101, 117
Kohno, M., Koyama, K., & Hamaguchi, K. 2002, ApJ, 567, 423
Leitherer, C. 1988, ApJ, 326, 356
Lightfoot, J. F., Deighton, D. W., Furniss, I., et al. 1984, MNRAS, 208, 197
Mac Low, M.-M., & McCray, R. 1988, ApJ, 324, 776
Mewe, R., Gronenschild, E. H. B. M., & van den Oord, G. H. J. 1985, A&AS, 62, 197
Moffat, A. F. J., Corcoran, M. F., Stevens, I. R., et al. 2002, ApJ, in press
Nazé, Y., Chu, Y.-H., Points, S. D., Danforth, C. W., Rosado, M., & Chen, C. H. R. 2001, AJ, 122, 921
Neuhäuser, R. 1997, Science, 276, 1363
Oey, M. S. 1996, ApJ, 467, 666
Prinja, R. K., Barlow, M. J., & Howarth, I. D. 1990, ApJ, 361, 607
Rauw, G., Blomme, R., Waldron, W. L., et al. 2002, A&A, submitted
Rho, J., Corcoran, M. F., Chu, Y.-H., & Reach, W. T. 2001, ApJ, 562, 446
Schmidt-Kaler, T. 1982, Landölt-Bornstein Catalogue VI/2b
Seward, F. D., & Chlebowski, T. 1982, ApJ, 256, 530
Siess, L., Dufour, E., & Forestini, M. 2000, A&A, 358, 593
Stecklum, B., Henning, T., Eckart, A., Howell, R. R., & Hoare, M. G. 1995, A&A, 445, L153
Stecklum, B., Henning, T., Feldt, M., Hayward, T. L., Hoare, M. G., Hofner, P., & Richter, S. 1998, AJ, 115, 767
Stelzer, B., & Neuhäuser, R. 2001, A&A, 377, 538
Stockman, Y., Barzin, P., Hansen, H., et al. 1998, in Proceedings of the First XMM Workshop on Science with XMM held at Noordwijk, The Netherlands, ed. M. Dahlem (`http://xmm.vilspa.esa.es/news/ws1/ws1_papers.html`)
Strickland, D. K., Stevens, I. R. 1999, MNRAS, 306, 43
Strüder, L., Briel, U., Dennerl, K., et al. 2001, A&A, 365, L18
Sung, H., Chun, M.-Y., & Bessell, M. S. 2000, AJ, 120, 333 (SCB)
Turner, M. J. L., Abbey, A., Arnaud, M., et al. 2001, A&A, 365, L27
van Altena, W. F., & Jones, B. F. 1972, A&A, 20, 425
van den Ancker, M. E., Thé, P. S., Feinstein, A., et al. 1997, A&AS, 123, 63
Waldron, W. L., Corcoran, M. F., Drake, S. A., & Smale, A. P. 1998, ApJS, 118, 217
Wang, Q. D. 1999, ApJ, 510, L139
Weaver, R., McCray, R., Castor, J., Shapiro, P., & Moore, R. 1977, ApJ, 218, 377
Woodward, C. E., Pipher, J. L., Helfer, H. L., et al. 1986, AJ, 91, 870
Woodward, C. E., Pipher, J. L., Helfer, H. L., & Forrest, W. J. 1990, ApJ, 365, 252

5.2.2 More results on NGC 6530

Simultaneously with or shortly after our study of NGC 6530, several other investigations of the Lagoon Nebula were published. The most relevant results in the context of this habilitation thesis concern the interaction between the current population of massive stars and the molecular cloud, a deep *Chandra* observation of NGC 6530, age determinations of the cluster and the circumstellar environment of the PMS objects in the cluster.

Evidence for the stellar wind of Herschel 36 interacting with the surrounding molecular cloud came from the H_2 line emission detected by Burton (2002). In fact, this line emission probably traces a thin layer of shock-heated material at the interface between the wind or a bipolar outflow from Herschel 36 and the ambient molecular cloud. However, while the Lagoon Nebula is clearly a site of recent and ongoing star formation (as indicated by the youth of the stars in NGC 6530 and the very young O-star Herschel 36), it is not clear whether the clumps in the surrounding molecular cloud are sites of future star formation. Indeed, Tothill et al. (2002) found that the time scale over which these clumps may be destroyed by photoevaporation could be shorter than the characteristic time scale for gravitational collapse.

Damiani et al. (2004) presented the results of a deep 60 ksec *Chandra* observation of NGC 6530. Thanks to the much better angular resolution of the ACIS instrument onboard *Chandra* compared to the EPIC cameras onboard *XMM-Newton*, these authors were able to detect 884 X-ray sources. Damiani et al. (2004) argued that between 90 and 95% of them are low-mass PMS cluster members of ages 0.5 – 1.5 Myr. Damiani et al. therefore regarded the high- and low-mass stars in the same NGC 6530 subregion as essentially coeval. They also found evidence for an age gradient across the field from northwest to south, suggesting a sequential star formation. According to their results, the southwest subregion, close to Herschel 36 and the Hourglass region, contains a heterogeneous stellar population with an age spread larger than elsewhere in the cluster. At this point, we note that the discrepancy between the ages determined by Rauw et al. (2002d) and those given by Damiani et al. (2004) is due to an error in the `Vizier` database. In fact, in Rauw et al. (2002d), we used the $UBVRIH\alpha$ photometry of Sung et al. (2000) to derive the temperatures and luminosities of the optical counterparts of the *XMM-Newton* X-ray sources. Whilst the `Vizier` database indicates that the colours are expressed in the Johnson photometric system, they are in fact expressed in the Johnson-Cousins $UBV(RI)_C$ standard system (Sung 2005, private communication). Therefore, the luminosities derived by Rauw et al. for the PMS objects in NGC 6530 are too low, leading to an overestimate of their ages. I have thus repeated the derivation of these quantities and the results are given in Fig. 5.3. More than 80% of the PMS stars are now found to be younger than about 3 Myr, with some objects being apparently as old as 10 Myr.

Evidence for an older (≥ 5 Myr) sub-population in the cluster was also reported by Kumar et al. (2004). These authors noted the presence of two possible post-AGB stars. If the evolutionary status as well as the cluster membership of these stars were confirmed, then the age of the oldest stars in NGC 6530 would have to be at least ~ 30 Myr. Prisinzano et al. (2005) analysed archive WFI BVI photometry of NGC 6530 down to $V \sim 23$. They derived a cluster distance of 1250 pc, significantly lower than the 1800 pc distance inferred by Sung et al. (2000). Using the Siess et al. (2000) evolutionary tracks, they found that the X-ray selected PMS stars identified by Damiani et al. (2004) are included between the isochrones of 0.3 and 10 Myr with a median age of 2.3 Myr. Whilst these ages apparently agree with the results given in Fig. 5.3, one has to bear in mind that they correspond to a distance two third of the value that I have used! Regarding this lower distance, it should be emphasized that assuming such a reduced distance towards M 8 will probably lead to a problem with the spectro-photometric parallax of 9 Sgr and other O-type stars believed to ionize the H II region.

Concerning the circumstellar environment of the PMS stars in NGC 6530, Damiani et al. (2004) noted

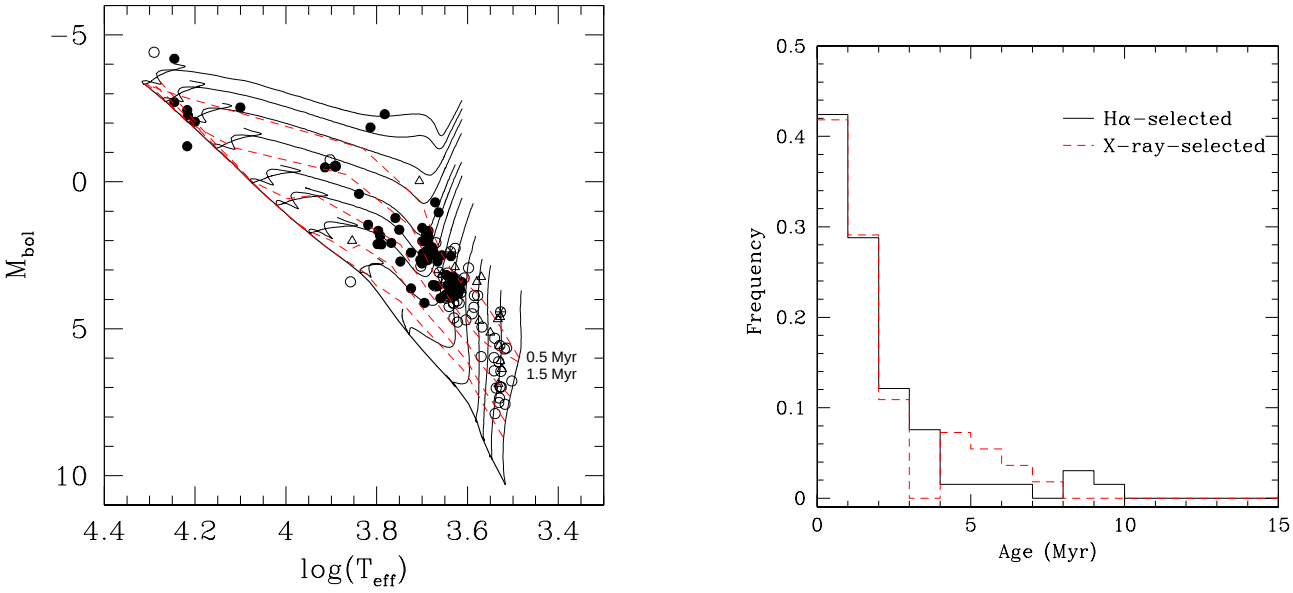

Figure 5.3: Left: revised Hertzsprung-Russell diagram of the *XMM-Newton* or Hα selected PMS objects in NGC 6530 (see Rauw et al. 2002d). We have assumed an $E(V - I_C)$ colour excess of 0.560 and a distance modulus of 11.25 towards the cluster. Evolutionary tracks from Siess et al. (2000) for $Z = 0.02$ and for masses of 0.2, 0.3, 0.4, 0.5, 0.7, 1.0, 1.5, 2.0, 2.5, 3.0, 4.0, 5.0, 6.0 and 7.0 $M_\odot$ are overplotted. Filled symbols indicate X-ray selected objects without Hα emission whereas encircled asterisks stand for PMS stars selected from X-ray and Hα emission. The open circles and open triangles stand for Hα selected PMS and PMS candidate stars from Sung et al. (2000) respectively. The thick solid line shows the ZAMS, while the dashed lines correspond to isochrones for ages of 0.5, 1.5, 4.0, 10.0 and 20.0 Myr. Right: distribution of the ages of X-ray selected PMS objects in NGC 6530 as interpolated from the isochrones derived from the Siess et al. (2000) evolutionary tracks. PMS stars and candidates with $H\alpha$ emission are indicated by the solid line, whilst those selected by their X-ray emission are indicated by the dashed line.

that a sizeable fraction of the X-ray selected stars also display a moderate Hα emission (in excess of the main-sequence star level). These authors suggest that this might be due either to an enhanced chromospheric activity that is often associated with an enhanced X-ray activity in very young stars, or to interactions with a residual circumstellar disk. Damiani et al. further suggested that X-ray flaring is mainly associated with the youngest PMS stars and declines at ages of a few Myr. While 2MASS IR photometry indicates that there are a large number of highly absorbed (up to $A_V \sim 30$) objects inside M 8, only about 60 of them are detected as X-ray sources with *Chandra*.

5.3 NGC 6383

5.3.1 *XMM-Newton* observations of NGC 6383

NGC 6383 is a small, rather poorly studied cluster concentrated around the massive binary HD 159176 (see Sect. 2.3.1). The cluster was observed serendipitously in the context of our *XMM-Newton* observation of HD 159176. The analysis of these X-ray data is presented below (Rauw et al. 2003b).
Using the $\log N - \log S$ relation for field stellar X-ray sources of Motch et al. (2003) for $|b| = 0°$, the

detection limit of Rauw et al. (2003b) translates into an expected number of 34 foreground sources. At the galactic coordinates of NGC 6383 ($l_{II} = 355.67°$, $b_{II} = +0.05°$), the extinction maps of Schlegel et al. (1998) yield $E(B-V) = 27.66$ which translates into a total galactic neutral hydrogen column density of $N_H = 1.6 \times 10^{23}$ cm^{-2} (Bohlin et al. 1978). The $\log N$ – $\log S$ relation for extragalactic X-ray sources of Giacconi et al. (2001) then allows to estimate a total number of 6 – 8 extragalactic objects among the X-ray sources in the field of NGC 6383. These background AGN are expected to have rather hard X-ray spectra and five sources indeed display a rather hard (heavily absorbed spectrum). Among these, source #5 is the only source with no optical nor near-IR counterpart. It has a very hard X-ray emission indicating that it is a likely background object.
About half of the sources detected by Rauw et al. (2003b) are therefore in 'excess' compared to the expected number of background or foreground sources. In the paper reproduced below, we argue that the majority of these objects are pre-main sequence stars belonging to NGC 6383. Figure 5.4 indeed reveals that some of the sources populate the expected locus of PMS stars. This figure also reveals that some of the sources apparently display a reddening of up to 30 mag in A_V.

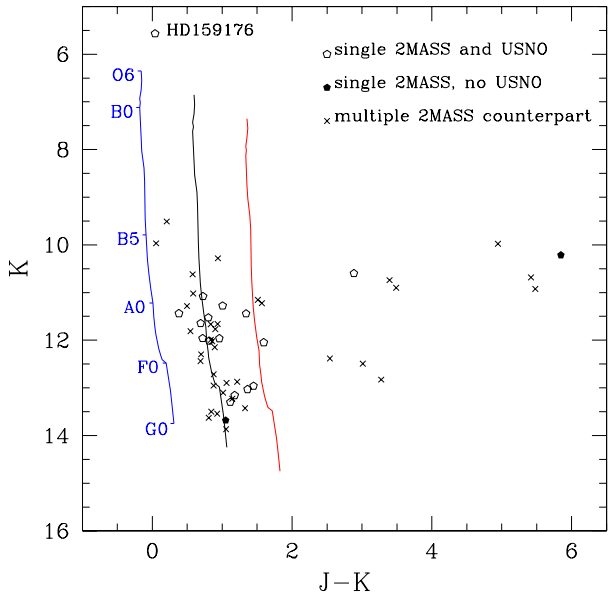

Figure 5.4: Near-IR colour-magnitude diagram of the 2MASS counterparts of the X-ray sources detected by Rauw et al. (2003b) in the core of NGC 6383. The location of the main-sequence is shown for a distance of 1.3 kpc and for three different values of the reddening: from left to right, $A_V = 0$, 5 and 10 mag.

A&A 407, 925–934 (2003)
DOI: 10.1051/0004-6361:20030910

Astronomy & Astrophysics

An *XMM-Newton* observation of the very young open cluster NGC 6383⋆,⋆⋆

G. Rauw[1,⋆⋆⋆], M. De Becker[1], E. Gosset[1,⋆⋆⋆], J. M. Pittard[2], and I. R. Stevens[3]

[1] Institut d'Astrophysique, Université de Liège, Allée du 6 Août, Bât. B5c, 4000 Liège (Sart Tilman), Belgium
[2] Department of Physics & Astronomy, University of Leeds, Leeds LS2 9JT, UK
[3] School of Physics & Astronomy, University of Birmingham, Edgbaston Birmingham B15 2TT, UK

Received 13 February 2003 / Accepted 16 June 2003

Abstract. We report the detection of a number of X-ray sources associated with the very young open cluster NGC 6383. About two thirds of these objects are correlated with a rather faint optical source and all but one have at least one infrared counterpart within a correlation radius of 8 arcsec. Although NGC 6383 is not associated with a prominent star forming region, the overall properties of many of the X-ray sources suggest that they may be candidates for low-mass pre-main sequence stars. The number of X-ray sources increases towards the cluster center suggesting that there exists a close relation between the massive O-star binary system HD 159 176 in the cluster core and the population of X-ray bright low-mass objects in NGC 6383.

Key words. stars: pre-main sequence – X-rays: stars – open clusters and associations: individual: NGC 6383 – stars: early-type

1. Introduction

NGC 6383 is a relatively small young open cluster centered on the massive binary HD 159 176 (O7 V + O7 V). The fundamental properties of NGC 6383 (age, distance, ...) are still somewhat controversial. FitzGerald et al. (1978) derived a reddening of $E(B-V) = 0.33 \pm 0.02$, a distance of 1.5 kpc and an age of 1.7 Myr. On the other hand, Lloyd Evans (1978) inferred a smaller distance of 1.3 kpc and an upper limit on the cluster age of 4–5 Myr.

Unlike many young stellar clusters, NGC 6383 is not embedded in a bright emission nebula harboring large amounts of dust. However, a weak nebula S 11 (Sharpless 1953) of 1 degree radius is centered on HD 159 176 and the cluster lies right in front of the dense dust clouds that divide the Milky Way at this galactic latitude (Lloyd Evans 1978). Although the cluster is not associated with a prominent star-forming region, there is evidence for ongoing star formation in the cluster core. Eggen (1961) presented *UBV* photometry of 27 stars in NGC 6383. He pointed out that the cluster displays a normal main sequence to about spectral type A0 while redder stars fall above the main sequence in the $(B-V, V)$ colour-magnitude diagram. Eggen predicted that if T Tauri variables were present in NGC 6383, they should be found at $V \sim 14.6$. FitzGerald et al. (1978) identified eight probable pre-main sequence (PMS) stars. Lloyd Evans (1978) identified six variable stars that might be in a PMS evolutionary stage. Observations by Thé et al. (1985) and van den Ancker et al. (2000) revealed an infrared excess in the spectra of several cluster members. These excesses are most probably produced by thermal emission from circumstellar dust grains. However, unlike the situation in other young open clusters (see e.g. NGC 6530, Sung et al. 2000), a very deep survey for Hα emission is lacking for NGC 6383. Thé (1965) examined Hα photographic plates that went as deep as $V \sim 16.0$, but he failed to detect faint Hα emission stars. So far, only one Hα emitting object was reported in this cluster (van den Ancker et al. 2000). These authors suggested that this star might be a Herbig Ae/Be object.

In the present paper, we report the results of an *XMM-Newton* observation of NGC 6383. A detailed discussion of the X-ray spectrum of HD 159 176 is presented by De Becker et al. (2003). HD 159 176 and NGC 6383 were already detected in X-rays during the *ASCA* galactic plane survey with a GIS count rate of 0.060 cts s^{-1} in the 0.7–10 keV energy band (Sugizaki et al. 2001). However, our *XMM-Newton* observations have a far better spatial resolution and sensitivity and allow us therefore to perform a detailed investigation of the population of X-ray sources in the cluster. Since low and intermediate mass pre-main sequence stars are known to be prominent X-ray sources (see e.g. Neuhäuser 1997), we can take advantage of our data to investigate the star formation process in NGC 6383.

In Sect. 2, we discuss the detection of X-ray sources in NGC 6383, we summarize their X-ray properties and cross-correlate their positions with various catalogues in Sects. 2.1

Send offprint requests to: G. Rauw, e-mail: rauw@astro.ulg.ac.be

⋆ Based on observations with *XMM-Newton*, an ESA science mission with instruments and contributions directly funded by ESA member states and the USA (NASA).

⋆⋆ Table 1 is only available in electronic form at http://www.edpsciences.org

⋆⋆⋆ Research Associate FNRS (Belgium).

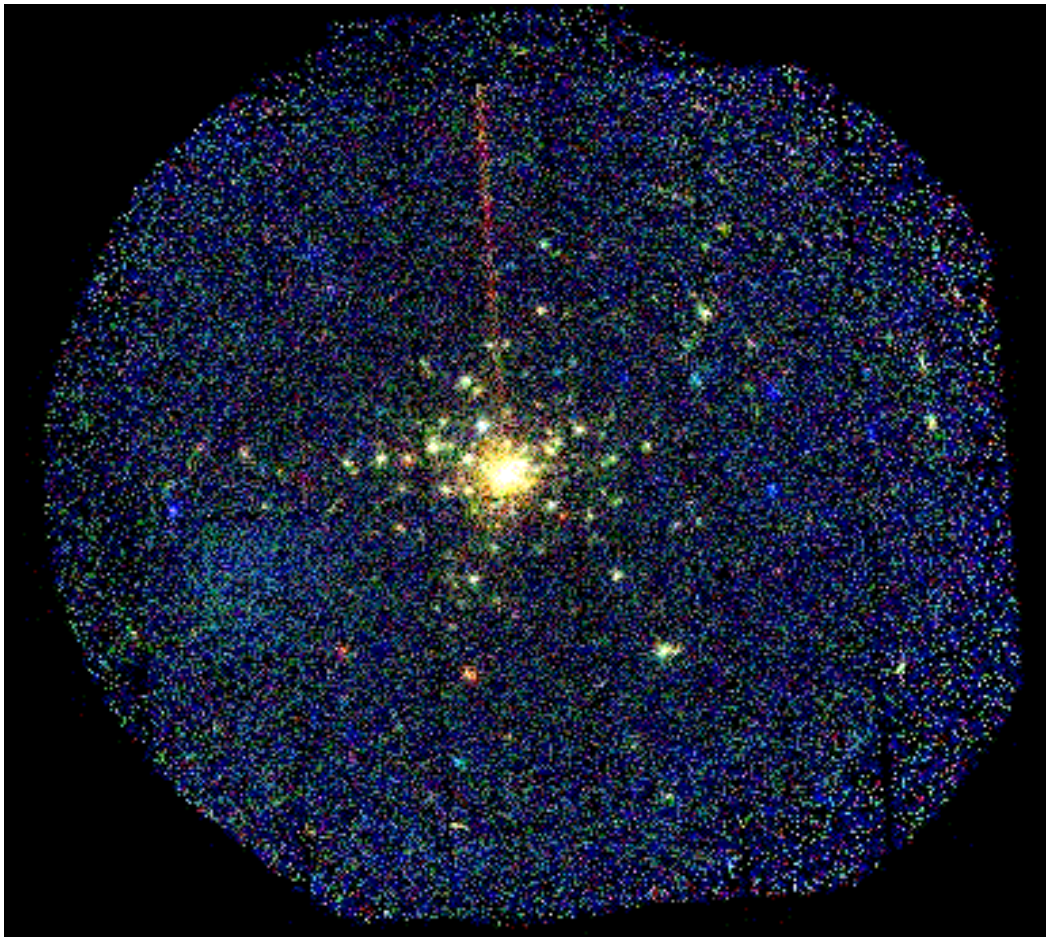

Fig. 1. False colour image of NGC 6383 as derived from the combined EPIC data. The red, green and blue colours correspond to the energy ranges $500 \leq PI \leq 1000$, $1000 < PI \leq 2000$ and $2000 < PI \leq 8000$ respectively. The images in the different energy bands were exposure-corrected before they were combined. North is up, east is left. The radius of the field of view corresponds to about 15 arcmin. The roughly vertical trail above HD 159 176 is produced by events that arrived during the readout of the pn detector (see e.g. Strüder et al. 2001). (This figure is available in color in electronic form.)

and 2.2 respectively. In Sect. 2.3, we investigate the nature of the X-ray sources. Section 3 summarizes our results and presents a discussion of the star formation process in NGC 6383.

2. X-ray sources in the open cluster NGC 6383

NGC 6383 was observed serendipitously with *XMM-Newton* (Jansen et al. 2001) during our AO1 pointing of the massive O-star binary HD 159 176. The observation took place in March 2001 (JD 2 451 977.903 – 2 451 978.338). The two EPIC MOS instruments were operated in the full frame mode (Turner et al. 2001) whilst the EPIC-pn camera was used in the extended full frame mode (Strüder et al. 2001). All three EPIC instruments used the thick filter to reject optical light. We used version 5.2 of the *XMM-Newton* Science Analysis System (SAS) software to process the raw data. Unfortunately, the observation was significantly affected by a high background episode, most probably due to a soft proton flare. While this does not impact on the analysis of the bright central source HD 159 176 (see the discussion by De Becker et al. 2003), it could nevertheless affect the detection and analysis of much fainter sources. Therefore, we filtered out time intervals with a high background level and the remaining useful exposure times were about 15.1, 16.1 and 13.8 ksec for the MOS1, MOS2 and pn detectors respectively. For further details on the observations and the pipeline processing, we refer to the work of De Becker et al. (2003).

The combined EPIC X-ray image around HD 159 176 reveals a number of faint discrete sources displaying a strong concentration towards the O-star binary. Figure 1 shows a false colour image of NGC 6383 where the red, green and blue colours correspond respectively to photons in the pulse invariant (PI) energy channel bands $500 \leq PI \leq 1000$, $1000 < PI \leq 2000$ and $2000 < PI \leq 8000$ (approximately corresponding to energies of [0.5−1.0],]1.0−2.0] and]2.0−8.0] keV)[1]. Most

[1] Hereafter we refer respectively to the soft, medium and hard energy bands.

sources have their spectral distribution peaking between 1.0 and 2.0 keV. Two sources have softer spectra whilst about six sources have significantly harder spectra.

We used the SAS source detection algorithms (see e.g. Hasinger et al. 2001) to derive a list of X-ray sources. We then inspected each source manually to reject false detections due to instrumental artifacts. In this way, we found 77 sources that were detected simultaneously in the MOS1, MOS2 and pn images with a combined logarithmic likelihood given by

$$\mathcal{L} = \sum_{i=1}^{9} -\ln p_i$$

where the summation runs over the three energy band images for each of the MOS1, MOS2 and pn detectors. Here, p_i stands for the probability that a random Poissonian fluctuation of the background may have produced the observed source counts in the image i. This combined logarithmic likelihood $\mathcal{L}$ is then renormalized to a logarithmic likelihood for a single experiment and is finally constrained to be ≥20.0. With this probability threshold, we expect less than one spurious detection due to background fluctuations over the entire EPIC field of view.

The faintest sources in this category have about 2×10^{-3} cts s^{-1} over the entire energy range of the pn camera. Assuming a 1 keV thermal spectrum with a neutral hydrogen column density of $N_{\rm H}^{\rm ISM} = 5.8 \times 10^{21} E(B-V) = 1.91 \times 10^{21}$ cm^{-2} (Bohlin et al. 1978), the faintest sources correspond to an observed flux of about 3.6×10^{-15} erg cm^{-2} s^{-1} and an unabsorbed flux of 5.6×10^{-15} erg cm^{-2} s^{-1} in the 0.5–10.0 keV energy range.

The 77 sources are listed in Table 1. The source designation in this table follows the naming conventions recommended by the *XMM* SOC and the IAU: the XMMU J prefix is followed by the right ascension HHMMSS.s (in hours, minutes, seconds and tenths of seconds, equinox J2000) and the declination of the source +/−DDMMSS (in degrees, arcminutes and arcseconds, equinox J2000), both truncated not rounded.

2.1. X-ray properties

For those sources that have a pn count rate of at least 5×10^{-3} cts s^{-1}, Table 1 lists two hardness ratios defined as

$$HR_1 = (M-S)/(M+S)$$

and

$$HR_2 = (H-M)/(H+M)$$

where S, M and H stand respectively for the EPIC-pn count rates in the soft, medium and hard energy bands defined hereabove. Only a few sources (#4, 5 and 6) display hard spectra as indicated also by their blue colours in Fig. 1. To these we can add sources #8 and 18 that display blue colours in Fig. 1, but have no hardness ratio either because they fall close to a gap in the pn detector (#8) or because their pn count rate is below the limit set hereabove (#18). From the analysis of the infrared counterparts of two of these five sources (see below), it appears that these hard spectra are essentially the result of the absorption by large column densities.

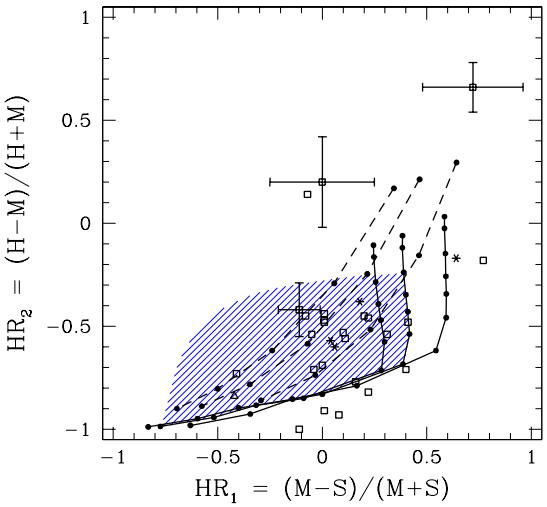

Fig. 2. Hardness ratios HR_1 and HR_2 for the X-ray sources in the field of NGC 6383 (open squares). The open triangle corresponds to HD 159 176, while the asterisks yield four sources for which we studied the spectra (see text). The filled dots exhibit the results for the model simulations described in the text; the lower temperature (or the larger photon indices) correspond to the softer spectra (i.e. the more negative values of HR_1 and HR_2). The solid lines correspond to the simulated thermal plasma models whereas the dashed curves yield the results for power law spectra. For each set of models, the larger hydrogen column density ($2 \times N_{\rm H}$) corresponds to the rightmost curve. For clarity error bars have only been indicated for three sources (#6, 14 and 25). Finally, the shaded area yields the region where objects with $kT_1 \in [0.25–1.0]$ keV and $kT_2 \in [1.0–4.0]$ (as found for confirmed T Tauri stars) should be found if they suffer an absorption by $N_{\rm H}^{\rm ISM} = 1.91 \times 10^{21}$ cm^{-2} (see text).

The hardness ratios that have an accuracy better than 0.3 are plotted in Fig. 2. In an attempt to relate these hardness ratios to the spectral properties of the sources, we have simulated the values of HR_1 and HR_2 for a grid of simple models. Within XSPEC, we have used the EPIC-pn response matrices to generate fake spectra corresponding either to optically thin thermal plasma MEKAL models (Mewe et al. 1985; Kaastra 1992) or power law energy distributions. For the thermal models, we considered plasma temperatures of kT = 0.25, 0.50, 0.75, 1.0, 1.5, 2.0, 2.5, 3.0, 4.0, 6.0 and 8.0 keV, whilst we simulated power law spectra with photon indices of 1.0, 2.0, 3.0, 4.0 and 5.0. Both types of models were combined with neutral hydrogen column densities of $N_{\rm H}^{\rm ISM} = 1.91 \times 10^{21}$ cm^{-2}, $0.5 \times N_{\rm H}^{\rm ISM}$ and $2 \times N_{\rm H}^{\rm ISM}$. These fake spectra were used to generate the hardness ratio curves displayed in Fig. 2.

Although the error bars on most of the observed hardness ratios are quite large, it can be seen from Fig. 2 that many sources have hardness ratios that are apparently roughly consistent with simple one-component models. However, this does not imply that such models actually fit the spectra of these objects. In fact, the spatial distribution of our sources, as well as the properties of their counterparts (see below), suggest that many of them may belong to the low-mass stellar population of NGC 6383. It is nowadays well known that the

Table 2. Spectral and variability analyses of the brightest X-ray sources in the field of NGC 6383. The neutral hydrogen column density was frozen in the spectral fits at the interstellar value (1.91×10^{21} cm^{-2}). Columns 2 and 3 list the resulting best fit temperatures of the MEKAL components, whilst column 4 provides the reduced χ^2 along with the number of degrees of freedom. Columns 5 and 6 yield the observed and absorption corrected fluxes respectively. The quoted uncertainties correspond to formal errors on the spectral fits.

#	kT_1 (keV)	kT_2 (keV)	χ^2_ν (d.o.f.)	$f_{\rm X,obs}$ (10^{-13} erg cm^{-2} s^{-1})	$f_{\rm X,unabs}$ (10^{-13} erg cm^{-2} s^{-1})	Variability
16	$0.87^{+0.23}_{-0.14}$	$3.17^{+1.68}_{-0.97}$	1.08 (55)	0.81	1.08	No
50	$0.61^{+0.24}_{-0.25}$	$5.52^{+1.98}_{-1.31}$	1.02 (84)	1.27	1.53	Yes
55	$0.33^{+0.34}_{-0.05}$	$2.16^{+0.72}_{-0.43}$	1.18 (73)	0.70	1.06	No
65	$0.73^{+0.13}_{-0.12}$	$2.22^{+0.50}_{-0.38}$	1.04 (71)	0.72	1.02	No

coronal X-ray emission of active late-type stars is generally not monothermal. For instance, Tsujimoto et al. (2002) and Favata et al. (2003) find that the *Chandra* and *XMM-Newton* spectra of confirmed T Tauri stars in the Orion Molecular Cloud and in the L 1551 star formation complex are best represented by 2-T thermal models with kT_1 and kT_2 in the ranges ∼0.25−1.0 keV and ∼1.0–4.0 keV respectively. In this context, one should note that the actual energy distribution of a 2-T thermal plasma might mimic the hardness ratios of a pure power law model. Indeed, for a 2-T thermal plasma, the observed hardness ratio should be a linear combination of the hardness ratios corresponding to the individual temperature components:

$$HR_i = \alpha_i\, HR_i(kT_1) + (1-\alpha_i)\, HR_i(kT_2)$$

where α_i is the ratio between the count rate of the kT_1 component and the total rate over the two energy bands used in the definition of HR_i. The shaded area in Fig. 2 illustrates the region of the HR_1–HR_2 diagram where objects with $kT_1 \in [0.25{-}1.0]$ keV and $kT_2 \in [1.0{-}4.0]$ keV (as found for confirmed T Tauri stars, see above) should be found if they suffer an absorption by a column density $N_{\rm H}^{\rm ISM} = 1.91 \times 10^{21}$ cm^{-2}. We see that most of our NGC 6383 EPIC sources lie inside the shaded area. While this is by no means a proof that these objects have indeed 2-T thermal spectra, it shows that at least their properties are not inconsistent with such a model.

The properties of HD 159 176 (source #44) have been discussed by De Becker et al. (2003) and we will not repeat this analysis here. Let us simply recall that the EPIC and RGS spectra could neither be fitted with a 1-T thermal model nor a pure power law energy distribution. A 2-T MEKAL model yielded a better fit with $N_{\rm H} \sim 0.53 \times 10^{22}$ cm^{-2}, $kT_1 \sim 0.20$ and $kT_2 \geq 0.60$ keV. The location of HD 159 176 in Fig. 2 reflects the rather soft spectrum of this source. It should be noted that although the position of HD 159 176 in the $HR_1 - HR_2$ plane falls close to the locus of pure power law models, such a model is clearly at odds with the RGS and EPIC spectra of this star (De Becker et al. 2003).

In addition to HD 159 176, four sources (#16, 50, 55 and 65) have sufficiently large count rates for a more detailed study of their spectra and light curves. Background corrected spectra were rebinned to have at least 9 counts per energy channel and the three EPIC spectra were analysed simultaneously using the XSPEC software. We attempted to fit the spectra with 1-T thermal plasma MEKAL models. The reduced χ^2 values are quite large. Better fits are obtained if we consider 2-T MEKAL models. Table 2 lists the results of the 2-T fits with the neutral hydrogen column density frozen at the mean interstellar value (1.91×10^{21} cm^{-2} see above). Alternatively, we have also allowed the hydrogen column density to float as a free parameter. The best fit parameters are always very close to those listed in Table 2, except for source #55. For this source, a slightly better fit is achieved with a neutral hydrogen column density $\leq 0.06 \times 10^{22}$ cm^{-2} and the corresponding best fit temperatures are 0.83 and 3.15 keV. This result suggests that source #55 might be a foreground object (see also below) affected by a lower column density than the actual cluster members. The four sources have X-ray spectra that consist of a component with a temperature between 0.5 and 1.0 keV and a second much hotter component with kT_2 of order 2−5 keV. The hottest component is observed for source #50, i.e. the source that undergoes a flare during our observation (see below). The average EPIC-pn count rate to unreddened flux conversion factor for the three sources #16, 50 and 65 amounts to 5.1×10^{-12} erg cm^{-2} count^{-1}. Assuming that this conversion factor applies to all the sources in the field of view, our lower detection count rate of 2×10^{-3} cts s^{-1} corresponds to a limiting sensitivity of 10^{-14} erg cm^{-2} s^{-1} on the unabsorbed flux.

X-ray light curves corrected for good time intervals were extracted for the four brighter sources and for all three EPIC cameras. We checked these light curves for variability and for consistency between the various instruments. The only source that displays a strong and well correlated variability in the light curves of all three instruments is #50. This source undergoes a strong X-ray flare towards the end of our observation (see Fig. 3). At the onset of this flare, the X-ray flux rises by about an order of magnitude within about 3000 s. This feature is quite reminiscent of the flare observed on the pre-main sequence star SCB 731 in NGC 6530 (Rauw et al. 2002) and on other PMS objects (see e.g. Feigelson & Montmerle 1999; Preibisch & Zinnecker 2002). We note that the spectrum of the source appears significantly harder during the eruption. In fact, whereas the soft band dominates the count rate during the quiescence, Fig. 3 indicates that the medium and, shortly after, also the hard band overtake the soft band during the flare. This spectral hardening is again quite similar to the behaviour of other flaring PMS stars (e.g. Preibisch & Zinnecker 2002).

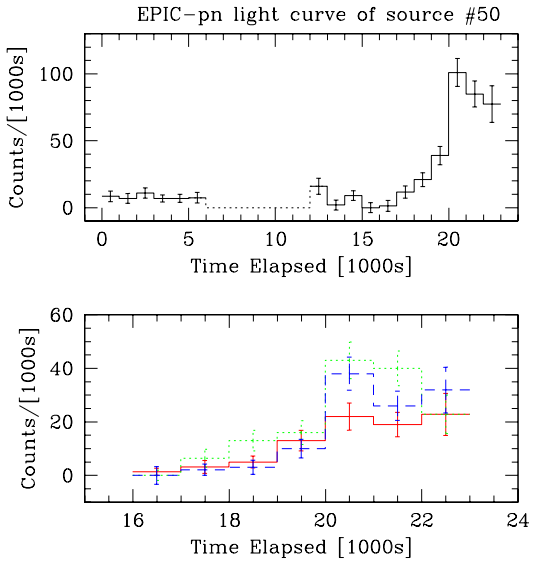

Fig. 3. EPIC-pn light curve of source #50. Upper panel: corrected source count rate as a function of time elapsed since JD 2 451 978.072. The source counts have been binned into intervals of 1000 s corrected for the good time intervals and have been corrected for the background variations. Note that the interval with zero count rate (dotted line) corresponds to a soft proton flare that was discarded from our data set. Lower panel: zoom on the flare as seen in different energy bands. The soft, medium and hard band light curve are displayed by the continuous, dotted and dashed line respectively. Before the flare, the mean count rates were respectively 3.8×10^{-3}, 1.2×10^{-3} and 1.2×10^{-3} cts s^{-1} in the *S*, *M* and *H* energy bands.

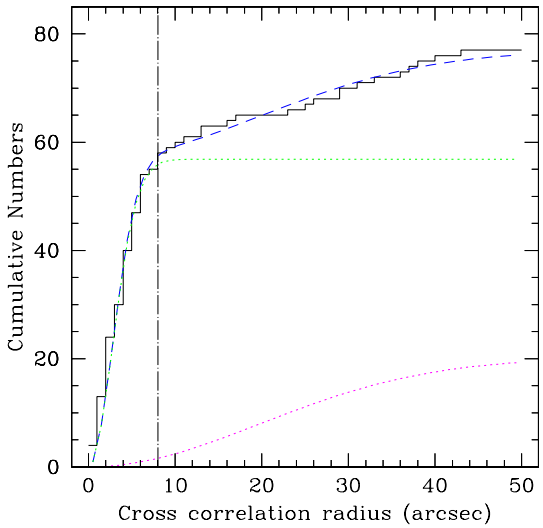

Fig. 4. Cumulative numbers of correlations between the X-ray detections and the USNO catalogue objects as a function of the correlation radius. The dotted curves correspond to the best fitting expressions for the real and spurious correlations. The dashed curve yields the sum of these terms and the dash-dotted vertical line corresponds to the adopted correlation radius of 8 arcsec.

2.2. Optical and infrared counterparts

We have cross-correlated the positions of the 77 sources with various catalogues. Unfortunately, there exists no dedicated very deep photometric survey of NGC 6383 in the literature. Therefore, we used the US Naval Observatory (USNO, Monet et al. 1998), the Guide Star Catalogue (GSC, version 2.2)[2] and the Two Micron All Sky Survey[3] (2MASS, Skrutskie et al. 1997) catalogues. In order to determine the optimal radius of cross-correlation, we adopted the approach outlined by Jeffries et al. (1997) and applied to the *XMM-Newton* data of the very young open cluster NGC 6530 by Rauw et al. (2002): the distribution of the cumulative number of catalogued sources as a function of the cross-correlation radius r (see Fig. 4) is modelled by

$$\Phi(d \le r) = A\left[1 - \exp\left(\frac{-r^2}{2\,\sigma^2}\right)\right] + (N - A)\left[1 - \exp\left(-\pi\,B\,r^2\right)\right]$$

where N, A, σ and B stand respectively for the total number of cross-correlated X-ray sources ($N = 77$), the number of true correlations, the uncertainty on the X-ray source position and the surface density of catalogue sources. The first term in the expression of $\Phi(d \le r)$ stands for the cumulative distribution of true correlations whereas the second term yields the cumulative number of spurious correlations (see Jeffries et al. 1997). A, σ and B are fitting parameters and were obtained from the best fit to the actual distribution displayed in Fig. 4. For the USNO catalogue, we derive $A = 56.9$, $\sigma = 2.8$ arcsec and $B = 4.1 \times 10^{-4}$ arcsec^{-2}. The optimal correlation radius, i.e. the radius that includes the majority of the true correlations while simultaneously limiting contamination by spurious correlations, is found to be around 8 arcsec. For $r = 8$ arcsec, we expect to statistically achieve 56 true and less than 2 spurious correlations. For the 2MASS catalogue, we obtain very similar numbers and therefore we consider an optical or infrared source as a possible counterpart if it falls within 8 arcsec of the coordinates of the X-ray source.

The degradation of the point spread function (PSF) of the *XMM* mirror modules with increasing off-axis angle (Stockman et al. 1998) could bias the value of the optimal correlation radius. For a uniform distribution of sources over the entire field of view, one might have to consider the correlation radius as a function of the off-axis angle. However, in the case of our data set, most of the sources lie within less than 6 arcmin from the center and using a constant correlation radius should therefore provide a fairly good approximation.

The results of the correlations with the USNO and 2MASS catalogues are listed in Table 1:

- 57 EPIC sources have a single USNO or GSC optical counterpart within a radius of less than 8 arcsec. The average angular separation between the X-ray source and the optical

[2] The Guide Star Catalogue-II is a joint project of the Space Telescope Science Institute and the Osservatorio Astronomico di Torino.

[3] We used the 2MASS all-sky point source catalogue released in March 2003 and available at `http://irsa.ipac.caltech.edu/`

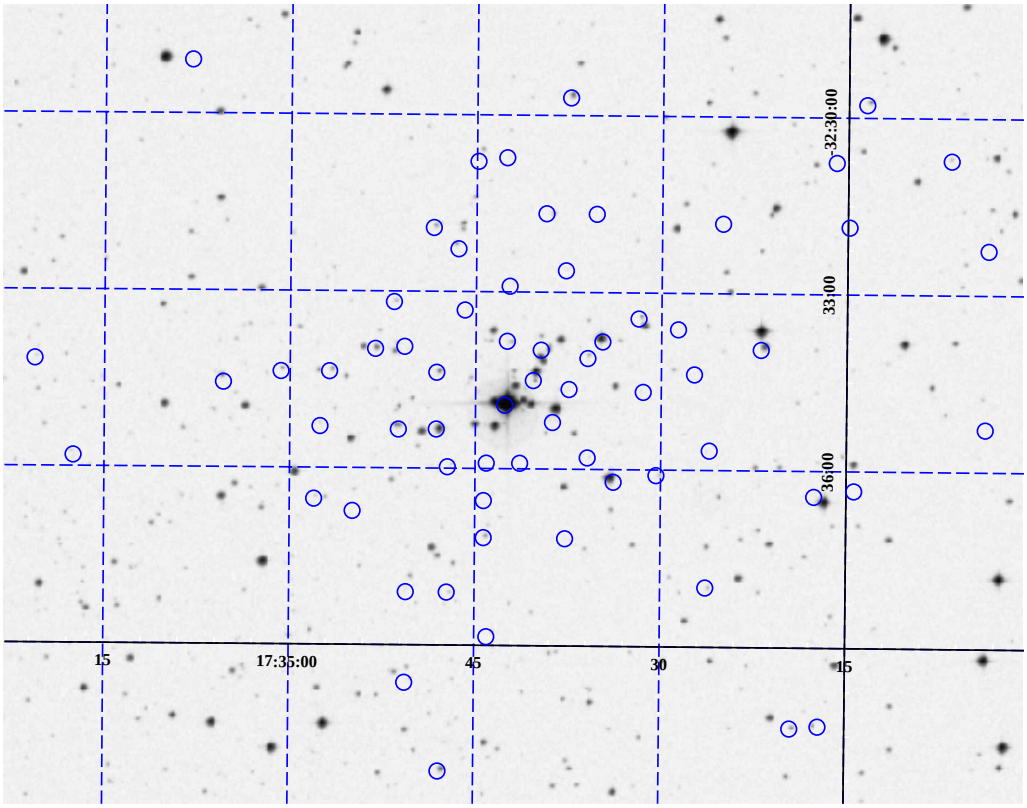

Fig. 5. Location of the X-ray sources detected with *XMM-Newton* around HD 159 176 overlaid on a Digital Sky Survey *V* image. The circles have radii of 8 arcsec corresponding to the optimal cross-correlation radius.

counterpart is (3.6 ± 2.0)″. Most optical counterparts are faint and only a few objects have HD numbers or a number in one of the Thé (Thé 1985), FJL (FitzGerald et al. 1978) or LE (Lloyd Evans 1978) catalogues (see Table 3). Except for the latter objects, the photometric data are taken from the GSC and USNO catalogues and refer hence to photographic magnitudes. All of these 57 sources have at least one 2MASS infrared counterpart, but only 23 X-ray sources have a single USNO and a single 2MASS counterpart[4].

- 29 EPIC sources are found to have a single 2MASS counterpart.
- 11 EPIC sources are found to have two or more USNO or GSC sources in the 8 arcsec radius. The number of EPIC sources having more than one 2MASS counterpart is much larger (47).
- 9 EPIC sources have neither an USNO nor a GSC counterpart, while there is only one source (#5) that has neither an optical nor an infrared counterpart. Note that this object has a very hard X-ray spectrum as revealed by its blue colour in Fig. 1 and its HR_2 value (≥0.91) in Table 1. This source is therefore likely a heavily absorbed background object.

[4] Since the positional errors on the USNO sources are of order 0.3″in both RA and DEC whilst the corresponding errors for the 2MASS catalogue are of order 0.1″, the small positional discrepancies between the optical and IR counterparts are probably not significant.

Table 3. X-ray sources with bright optical counterparts that are known from other catalogues than the USNO or GSC. The last column yields the reference for the spectral type (FJL = FitzGerald et al. 1978, vdA = van den Ancker et al. 2000). The photometric data are taken from FJL, except for Thé 7 and 26 for which we adopt results from Eggen (1961).

#	cross-ID	V	$B-V$	Spect. type	Ref.
17	Thé 7	12.73	0.32		
24	Thé 26	12.87	0.76	A1 IV	vdA
26	HD 317 857	10.30	0.29	B8 IV/B9 IV	FJL, vdA
27	HD 317 847	10.33	0.10	B2 V	FJL
38	FJL 7	12.62	0.28		
39	FJL 9	10.84	0.14		
42	FJL 11	15.10	1.06		
44	HD 159 176	5.64	0.04	O7 V + O7 V	FJL
55	FJL 23	13.79	0.95	G5 V	vdA
56	FJL 24	11.35	0.18	B8 Vne/B7 V	FJL, vdA

2.3. The nature of the X-ray sources

Most of the optically bright sources (except HD 159 176, HD 317 847 and HD 317 857, see Table 3 and Fig. 5) are not detected in our EPIC images. The bulk of the entries in Table 1 are therefore X-ray sources with a large L_X/L_{vis} ratio. Given the position of the cluster very near the direction of the galactic center (l_{II} = 355.69°, b_{II} = +0.04°), the total galactic column

density along the line of sight in this direction must be extremely large. At low energies the total galactic column probably prevents us from detecting background sources, but maybe some of the very hard sources (like #5) might be associated with extragalactic objects.

It is interesting to compare the list of X-ray sources with a single optical counterpart to the list of PMS candidates listed in the literature. First of all, we note that none of the variable sources from Lloyd Evans (1978) is detected with *XMM*. On the other hand, three of the PMS candidates listed by FitzGerald et al. (1978) are clearly seen in our EPIC images. These are FJL 11 (#42), FJL 23 (#55) and FJL 24 (#56). FJL 23 and 24 are known to display near IR excess emission (Thé et al. 1985; van den Ancker et al. 2000) and star FJL 24 was suggested to be an early-type flare star with episodic Balmer emission lines in its spectrum (FitzGerald et al. 1978). The spectral type of FJL 23 (G5 V) as proposed by van den Ancker et al. (2000) suggests that this might be a foreground object unrelated to NGC 6383. This result is in good agreement with our finding that the source #55 associated with this star might have a smaller hydrogen column density than the average value of the cluster. Thé et al. and van den Ancker et al. noted the presence of a strong IR excess associated with FJL 4, 5 and 6 (all classified as A-type stars) making these three stars other PMS candidates. We note that none of the latter three objects is detected in our data.

Figure 6 illustrates the JHK_s colour–colour diagram of the 2MASS infrared counterparts. The diagram includes only those objects that were detected in all three filters J (1.25 μm), H (1.65 μm) and K_s (2.17μm) with a decent photometric accuracy ($\sigma \leq 0.10$). The intrinsic colours of dwarfs and giants (taken from Bessell & Brett 1988) are indicated by the solid lines, whereas the two upper dashed lines delimit the reddening band for normal dwarf stellar atmospheres adopting the reddening law quoted by Rieke & Lebofsky (1985). While most 2MASS counterparts cluster near the loci of unreddened main sequence and giant stars, sixteen IR sources correspond clearly to heavily reddened objects with A_V up to ∼28 mag in the most extreme cases.

Lada & Adams (1992) have shown that the location of a pre-main sequence object in the infrared colour–colour diagram is determined to a large extent by its evolutionary state. Deeply embedded class I protostars were found to lie in the region of the J–H vs. H–K_s plane characterized by a large extinction and for the most part to the right of the reddening band. On the other hand, classical and weak-line T Tauri stars suffer a much lower circumstellar extinction. The weak-line T Tauri stars (wTTs) lie within the reddening band of main sequence stars, whereas the classical T Tauri stars (cTTs) have infrared excesses produced by circumstellar disks and fall therefore mostly to the right of the reddening band. Meyer et al. (1997) emphasized that the locus of dereddened JHK colours of PMS stars with circumstellar material is surprisingly narrow and can be described by a simple linear relation between $J-H$ and $H-K$. This relation is shown in Fig. 6 by the dotted straight line[5].

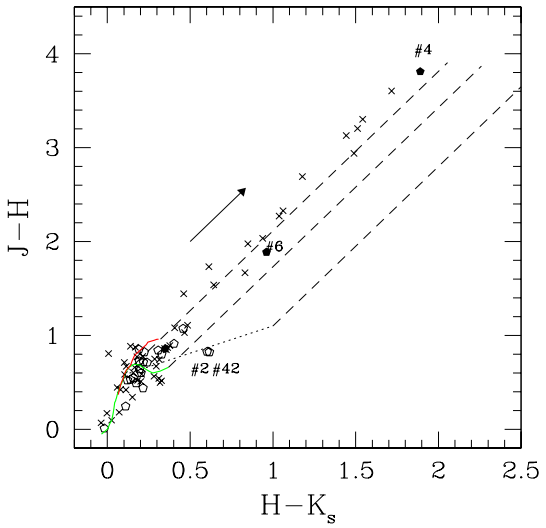

Fig. 6. JHK_s colour–colour diagram of the IR counterparts falling within the 8 arcsec correlation radius from an X-ray source. The heavy solid lines yield the intrinsic colours of main sequence and giant stars, whereas the reddening band is illustrated for up to 30 mag of visual extinction from the position where it intersects the locus of unreddened main sequence stars. Single counterparts of X-ray sources are displayed by pentagons. Open pentagons stand for stars that have also an USNO or GSC counterpart, whilst filled symbols correspond to IR stars without optical counterpart. The crosses indicate IR objects associated with X-ray sources having multiple 2MASS counterparts. The dotted straight line yields the locus of dereddened colours of classical T Tauri stars according to Meyer et al. (1997). See the text for further details.

Inspection of Fig. 6 suggests that only two sources (#2 and 42) fall near the locus of stars with IR excesses revealing the presence of circumstellar material. One of them (#42) is FJL 11 that was already classified as a PMS candidate by FitzGerald et al. (1978). On the other hand, sixteen IR sources suffer a large optical extinction and could therefore be candidates for deeply embedded class I objects. The most extreme reddening ($A_V \simeq 28$ mag) is found for source #4 that has no optical counterpart and displays a very hard X-ray emission. Source #6, another hard X-ray source, suffers a less extreme, but still quite substantial, extinction ($A_V \simeq 11$ mag). The other fourteen objects with $A_V > 5$ mag are not unique counterparts and most importantly the X-ray sources were not found to display extremely hard spectra. Therefore, some of these latter IR objects might actually be unrelated to the X-ray sources.

In summary, our analysis of the 2MASS counterparts indicates that at least two X-ray sources (#2 and 42) are probable PMS objects surrounded by circumstellar material whilst at least two other objects (#4 and 6) are either candidates for deeply embedded class I protostars or are heavily absorbed background objects perhaps unrelated to NGC 6383.

[5] Note however that Preibisch & Zinnecker (2002 and references therein) showed that for the young open cluster IC 348 there exists no strict one-to-one relation between PMS stars with IR excesses and cTTs detected through their strong Hα emission: while all known cTTs in IC 348 are found to have IR excesses, many wTTs also display IR excess emission.

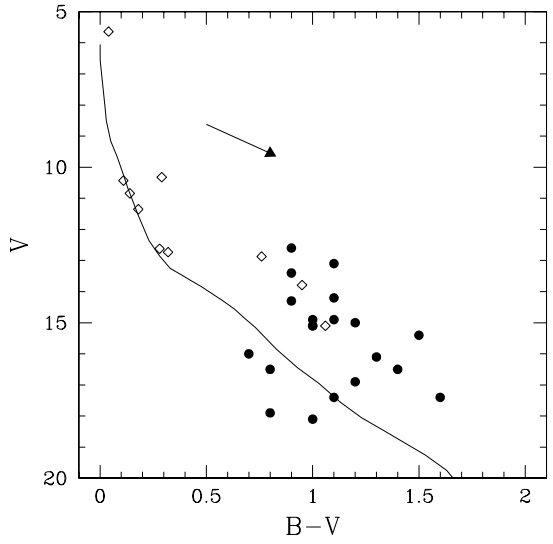

Fig. 7. Colour–magnitude diagram of the X-ray sources with a single optical counterpart and with an existing $B-V$ colour in the very young open cluster NGC 6383. Filled dots indicate stars with USNO/GSC photometry, while the photometric data for the open diamonds are taken from Table 3. The reddening vector with $R_V = 3.1$ is indicated and the solid line shows the ZAMS relation taken from Schmidt-Kaler (1982) shifted by a distance modulus $DM = 10.73$ and reddened with $E(B-V) = 0.33$.

We have plotted those objects for which we have V magnitudes and $B-V$ colours in a colour–magnitude diagram (see Fig. 7). While the optical counterparts brighter than $V \sim 13$ fall mainly on the NGC 6383 main sequence, it appears that most of the sources that are optically fainter lie above the zero age main sequence. Although it is likely that our sample is affected by a number of field interlopers, the strong concentration of faint X-ray sources towards the cluster core together with their optical photometry suggest that many of the EPIC sources with faint optical counterparts are indeed associated with low- and intermediate-mass pre-main sequence stars.

Using the $T_{\rm eff}$ versus $(B-V)_0$ calibration and the bolometric corrections for main-sequence stars from Kenyon & Hartmann (1995), we can construct the Hertzsprung-Russell diagram of the X-ray sources with a single optical counterpart. Comparing this diagram with the pre-main sequence evolutionary tracks of Siess et al. (2000) for $Z = 0.02$, we could in principle infer the masses and ages of the PMS stars. The available USNO and GSC photometry suggests that the bulk of those stars having a location consistent with a PMS status would appear to have masses between 1.0 and 3.0 $M_\odot$ and ages ranging from ∼1.5 to 10 Myr. However, we caution that more accurate optical photometry is needed to firmly establish the properties of these objects. For instance, many X-ray sources with a single optical counterpart are too weak in B to have $B-V$ colours in the USNO or GSC catalogues and they are therefore not considered here. Deeper optical photometry, including also a search for faint Hα emission, is thus needed for a more complete investigation of the nature of the X-ray sources and of the PMS content of NGC 6383.

It is worth noting that out of the twelve B-type stars listed by Thé (1965) and van den Ancker et al. (2000) only three are detected. These are HD 317 857 (B9 IV), HD 317 847 (B2 V) and FJL 24 (B8 V ne). The bulk of the other B-stars in NGC 6383 classified in the literature are later than B5. HD 317 857 is believed to be a foreground object (Thé et al. 1985). FitzGerald et al. (1978) further noted that HD 317 857 has a faint close (∼2 arcsec separation) companion. Whether the X-ray emission comes from the late B-star or from its faint companion is impossible to tell with the present data.

3. Discussion and conclusions

From the previous section, it turns out that an important fraction of the X-ray sources in NGC 6383 might be candidates for PMS objects. Evidence for this interpretation comes from

- The concentration of X-ray sources towards the cluster center indicating that the X-ray sources are actually associated with the cluster.
- The flaring behaviour of source #50: T Tauri PMS stars are usually variable X-ray emitters that exhibit flares with a fast rising light curve followed by a slower decay (Feigelson & Montmerle 1999).
- The spectral properties of the X-ray brightest sources: indeed, T Tauri PMS stars display multi-temperature thermal X-ray spectra with (on average) a soft component in the range $kT_1 \in [0.25{-}1.0]$ keV and a harder component with $kT_2 \in [1.0{-}4.0]$ keV (Feigelson & Montmerle 1999; Tsujimoto et al. 2002; Favata et al. 2003).
- The X-ray luminosities: assuming a distance of 1.4 kpc and an EPIC-pn count rate to unreddened flux conversion factor of 5.1×10^{-12} erg cm^{-2} count^{-1}, we find that the faintest sources should have luminosities of 2.4×10^{30} erg s^{-1} (if we adopted the $kT = 1$ keV model instead, the luminosity would be half this value), whilst the flaring source #50 reaches 3.6×10^{31} erg s^{-1}. Indeed, PMS stars are known to have X-ray luminosities of order 10^{30} erg s^{-1}, i.e. about 10^3 times larger than that of the Sun (Neuhäuser 1997). For the sources with a single counterpart, $\log(L_{\rm X}/L_{\rm bol})$ increases from about −5.5 for the late B stars to ∼−3 for the low-mass stars, a value quite typical for X-ray bright PMS stars (see Fig. 8)[6].

FitzGerald et al. (1978) suggested that the star formation process in the core of NGC 6383 might be triggered by the massive binary HD 159 176. These authors derived an age of 1.7 ± 0.4 Myr for the stars in the ∼1.25 arcmin radius cluster core, whereas they estimated that HD 159 176 is 2.8 ± 0.5 Myr old. The concentration of faint X-ray sources around HD 159 176 suggests indeed that there must be a connection between the PMS objects and the massive binary. However, the way massive

[6] The apparent trend of $\log(L_{\rm X}/L_{\rm bol})$ with M_V seen in Fig. 8 should not be over interpreted. In fact the X-ray production in the objects at the higher luminosity end (shocks in the winds of B-type stars or unseen low-mass companions?) and those at the fainter end (coronal sources and late-type PMS-like emission) arises most probably through quite distinct physical mechanisms.

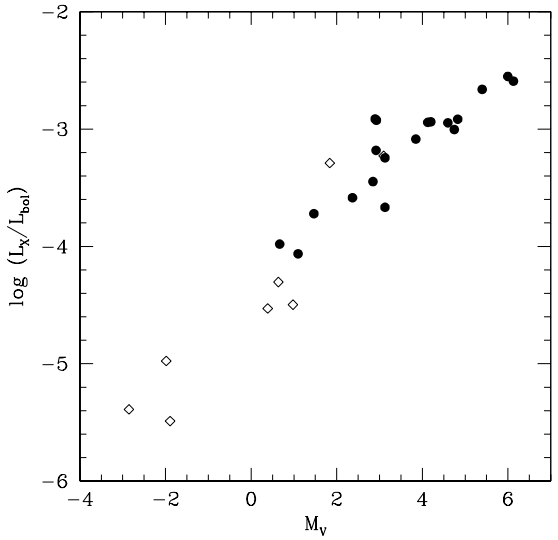

Fig. 8. Ratio between the X-ray luminosity and the bolometric luminosity of the EPIC sources with a single optical counterpart as a function of the absolute magnitude M_V (assuming the stars belong to NGC 6383). The symbols have the same meaning as in Fig. 7. Note that we have omitted sources #27 (no reliable X-ray count rate) and #44 (HD 159 176, discussed by De Becker et al. 2003).

stars form is still a controversial question and another scenario might equally well account for the possible connection between HD 159 176 and the PMS stars in NGC 6383. Bonnell & Bate (2002) performed *N*-body simulations of an open cluster containing 1000 protostars and a large amount of gas. They found that gas accretion leads to a strong contraction of the cluster and hence the stellar density in the simulated cluster core becomes sufficient for a significant number of stellar collisions to occur. In this scenario, the most massive stars of the cluster are formed through a combination of gas accretion and stellar mergers. The massive objects formed this way in the simulations are generally members of binary systems. NGC 6383 might fit rather well into this scenario: HD 159 176, the most massive object of the cluster is a binary system sitting in the core and the concentration of low-mass young stellar objects as revealed by their X-ray emission is much larger in the core than in the outer regions of the cluster. A crucial issue to address in future studies of this cluster will therefore be an accurate determination of the ages of its various components.

Finally, let us emphasize that, so far, there is evidence for only a few PMS stars with circumstellar material among the PMS candidates detected in our EPIC data. In fact, 2MASS colours of their infrared counterparts reveal the infrared excesses that would be expected for such objects only in two cases. It should be stressed that the modest number of 2MASS counterparts displaying a clear IR excess related to circumstellar material does not rule out that the X-ray sources might be associated with magnetically active PMS stars. Indeed, in the Chamaeleon I cloud, Feigelson et al. (1993) found that most X-ray selected PMS stars were wTTs without prominent circumstellar material. Similar results were obtained for the Orion Molecular Cloud (Tsujimoto et al. 2002).

Also there is little known about Hα emission among the cluster members of NGC 6383. At first sight, this observation suggests that most of our PMS candidates may be weak-line T Tauri stars and that they may be intrinsically X-ray brighter than classical T Tauri stars. Similar conclusions were reached for the T Tauri stars in the Taurus-Auriga-Perseus complex (Stelzer & Neuhäuser 2001) and NGC 6530 (Rauw et al. 2002). However, Preibisch & Zinnecker (2001, 2002) pointed out that *Chandra* observations of IC 348 provide no evidence for a significant difference in the X-ray properties of both classes of T Tauri stars and the apparent difference in the luminosities of the Taurus-Auriga-Perseus and NGC 6530 objects might in fact be a pure selection effect. Deep Hα photometry is therefore urgently needed to identify classical and weak-line T Tauri stars in NGC 6383.

Acknowledgements. Our thanks go to Mathias Ehle (*XMM*-SOC) for his help in processing the EPIC data, to Alain Detal (Liège) for his help in installing the SAS and to the referee, Dr. M. van den Ancker, whose comments helped to significantly improve our manuscript. The Liège team acknowledges support from the Fonds National de la Recherche Scientifique (Belgium) and through the PRODEX XMM-OM and Integral Projects. This research is also supported in part by contracts P4/05 and P5/36 "Pôle d'Attraction Interuniversitaire" (SSTC-Belgium). JMP gratefully acknowledges funding from PPARC for a PDRA position. This research has made use of the SIMBAD database, operated at CDS, Strasbourg, France and NASA's Astrophysics Data System Abstract Service. This publication makes also use of data products from the Two Micron All Sky Survey, which is a joint project of the University of Massachusetts and the Infrared Processing and Analysis Center, funded by NASA and the NSF.

References

Bessell, M. S., & Brett, J. M. 1988, PASP, 100, 1134
Bohlin, R. C., Savage, B. D., & Drake, J. F. 1978, ApJ, 224, 132
Bonnell, I. A., & Bate, M. R. 2002, MNRAS, 336, 659
De Becker, M., Rauw, G., Pittard, J. M., et al. 2003, A&A, submitted
Eggen, O. J. 1961, Roy. Greenwich Obs. Bull., 27, 61
Favata, F., Giardino, G., Micela, G., Sciortino, S., & Damiani, F. 2003, A&A, 403, 187
Feigelson, E. D., Casanova, S., Montmerle, T., & Guibert, J. 1993, ApJ, 416, 623
Feigelson, E. D., & Montmerle, T. 1999, ARA&A, 37, 363
FitzGerald, M. P., Jackson, P. D., Luiken, M., Grayzeck, E. J., & Moffat, A. F. J. 1978, MNRAS, 182, 607
Hasinger, G., Altieri, B., Arnaud, M., et al. 2001, A&A, 365, L45
Jansen, F., Lumb, D., Altieri, B., et al. 2001, A&A, 365, L1
Jeffries, R. D., Thurston, M. R., & Pye, J. P. 1997, MNRAS, 287, 350
Kaastra, J. S. 1992, An X-ray spectral code for optically thin plasmas, Internal SRON-Leiden Report
Kenyon, S. J., & Hartmann, L. 1995, ApJS, 101, 117
Lada, C. J., & Adams, F. C. 1992, ApJ, 393, 278
Lloyd Evans, T. 1978, MNRAS, 184, 661
Mewe, R., Gronenschild, E. H. B. M., & van den Oord, G. H. J. 1985, A&AS, 62, 197
Meyer, M. R., Calvet, N., & Hillenbrand, L. A. 1997, AJ, 114, 288

Monet, D., Bird, A., Canzian, B., et al. 1998, USNO V2.0, A catalogue of Astrometric Standards, U.S. Naval Observatory Flagstaff Station (USNOFS) and Universities Space Research Association (USRA) stationed at USNOFS
Neuhäuser, R. 1997, Science, 276, 1363
Preibisch, T., & Zinnecker, H. 2001, AJ, 122, 866
Preibisch, T., & Zinnecker, H. 2002, AJ, 123, 1613
Rauw, G., Nazé, Y., Gosset, E., et al. 2002, A&A, 395, 499
Rieke, G. H., & Lebofsky, M. J. 1985, ApJ, 288, 618
Schmidt-Kaler, T. 1982, in Physical Parameters of the Stars, Landolt-Börnstein Numerical Data and Functional Relationships in Science and Technology, Group VI, vol. 2b
Sharpless, S. 1953, ApJ, 118, 362
Siess, L., Dufour, E., & Forestini, M. 2000, A&A, 358, 593
Skrutskie, M. F., Schneider, S. E., Stiening, R., et al. 1997, in The Impact of Large Scale Near-IR Sky Surveys, ed. F. Garzon et al. (Dordrecht: Kluwer Acad. Pub.), 25
Stelzer, B., & Neuhäuser, R. 2001, A&A, 377, 538
Stockman, Y., Barzin, P., Hansen, H., et al. 1998, in Proc. First XMM Workshop on Science with XMM, ed. M. Dahlem, (`http://xmm.vilspa.esa.es/external/xmm_science/1st_workshop`)
Strüder, L., Briel, U., Dennerl, K., et al. 2001, A&A, 365, L18
Sugizaki, M., Mitsuda, K., Kaneda, H., et al. 2001, ApJS, 134, 77
Sung, H., Chun, M.-Y., & Bessell, M. S. 2000, AJ, 120, 333
Thé, P. S. 1965, Contr. Bosscha Obs., Lembang, 32
Thé, P. S., Hageman, T., Westerlund, B. E., & Tijn A Djie, H. R. E. 1985, A&A, 151, 391
Tsujimoto, M., Koyama, K., Tsuboi, Y., Goto, M., & Kobayashi, N. 2002, ApJ, 566, 974
Turner, M. J. L., Abbey, A., Arnaud, M., et al. 2001, A&A, 365, L27
van den Ancker, M. E., Thé, P. S., & de Winter, D. 2000, A&A, 362, 580

Online Material

Table 1. X-ray sources detected in our EPIC images of NGC 6383. The first and second columns yield the number of the X-ray source as well as the name according to the naming conventions for serendipitous *XMM-Newton* sources. Columns 3, 4 and 5 provide the vignetting and background corrected EPIC-pn and MOS count rates in the 0.5–10.0 keV energy range, whilst Cols. 6 and 7 yield the HR_1 and HR_2 hardness ratios evaluated from the pn data (see the definition of HR_1 and HR_2 in the text). Columns 8 to 12 and 13 to 17 summarize the results of the cross-correlation with the USNO (and GSC) and 2MASS catalogues respectively. Columns 8 and 13 yield the numbers of optical and IR counterparts within 8 arcsec from the X-ray source, while Cols. 9 and 14 provide the angular separation for single counterparts.

#	XMMU J	pn	MOS1	MOS2	HR_1	HR_2	USNO (and GSC)					2MASS				
							Nr.	d	B	V	R	Nr.	d	J	H	K_S
		10^{-3} cts s^{-1}	10^{-3} cts s^{-1}	10^{-3} cts s^{-1}				($''$)					($''$)			
[1]	[2]	[3]	[4]	[5]	[6]	[7]	[8]	[9]	[10]	[11]	[12]	[13]	[14]	[15]	[16]	[17]
1	173 340.4−323 310	18.6 ± 3.1	7.9 ± 2.5	12.0 ± 2.7	−0.05 ± 0.17	−0.54 ± 0.28	1	1.7	15.9	14.9	14.3	4				
2	173 341.6−323 121	7.4 ± 2.6	2.5 ± 1.8	7.3 ± 2.5	0.19 ± 0.26	−0.42 ± 0.41	1	3.3	16.1	15.1	14.5	1	3.2	12.7	11.9	11.3
3	173 344.8−324 052	11.4 ± 3.0	9.4 ± 2.8		0.41 ± 0.22	−0.48 ± 0.28	1	0.6	14.3	13.4	13.0	2				
4	173 349.0−323 332	6.4 ± 1.6	0.9 ± 1.2	2.9 ± 1.5	0.58 ± 0.42	0.69 ± 0.17	0					1	3.6	15.9	12.0	10.1
5	173 403.5−323 214	6.4 ± 1.5	3.8 ± 1.4	4.2 ± 1.3		≥0.91	0					0				
6	173 403.7−323 516	10.2 ± 1.6	4.6 ± 1.3	4.5 ± 1.2	0.72 ± 0.24	0.66 ± 0.12	0					1	2.1	13.3	11.5	10.5
7	173 406.6−323 043	5.5 ± 1.5	2.9 ± 1.2	2.8 ± 1.1	−0.37 ± 0.35	0.39 ± 0.36	1	2.2	17.4	16.1	15.5	4				
8	173 413.4−322 946		9.0 ± 1.7	16.9 ± 2.0			1	3.6	15.3	14.2	13.9	1	3.4	12.2	11.7	11.6
9	173 414.2−322 317	7.3 ± 1.9	3.2 ± 1.6	1.8 ± 1.7	−0.33 ± 0.33	0.41 ± 0.31	2					2				
10	173 414.3−323 620	3.8 ± 1.1	1.0 ± 0.6	1.8 ± 0.7			0					2				
11	173 414.8−323 151	8.1 ± 1.5	4.1 ± 1.0	3.0 ± 0.9	0.77 ± 0.19	−0.18 ± 0.21	1	3.5			17.9	1	3.4	13.5	12.4	12.0
12	173 415.9−323 046	3.3 ± 1.1	1.6 ± 0.8	1.6 ± 0.7			1	2.3	19.0	17.4	16.6	1	2.3	(14.4)	13.2	12.9
13	173 417.1−324 020	2.8 ± 1.4	1.8 ± 1.1	2.6 ± 1.1			1	6.8	16.1	15.1	14.6	2				
14	173 417.5−323 626	6.1 ± 1.1	2.6 ± 0.9	1.8 ± 0.7	−0.00 ± 0.25	0.20 ± 0.22	0					1	1.6	15.2	14.4	(14.0)
15	173 418.8−324 455	5.9 ± 2.0	3.5 ± 1.6	3.6 ± 1.3	−0.09 ± 0.37	≤0.35	1	2.2			17.6	1	2.1	14.2	13.4	13.1
16	173 419.3−324 022	19.6 ± 2.3	15.6 ± 2.1	13.7 ± 1.8	0.18 ± 0.12	−0.38 ± 0.15	1	1.8	16.0	14.9	14.2	1	1.6	12.5	12.0	11.8
17	173 421.9−323 357	6.4 ± 1.1	4.4 ± 1.0	3.5 ± 0.9	0.08 ± 0.16	≤−0.67	1	3.8		12.3	12.4	1	3.5	11.6	11.4	11.2
18	173 425.0−323 149	2.2 ± 1.0	2.2 ± 0.8	1.9 ± 0.7			0					3				
19	173 426.0−323 540	4.7 ± 1.0	0.9 ± 0.7	2.1 ± 0.8			2					3				
20	173 426.2−323 759	10.4 ± 1.5	7.2 ± 1.2	5.4 ± 1.0	0.00 ± 0.14	−0.69 ± 0.24	1	1.5	16.9	15.4	14.9	1	1.5	12.8	12.1	11.9
21	173 427.2−323 422	9.3 ± 1.4	2.7 ± 1.0	2.0 ± 0.9	0.40 ± 0.16	−0.71 ± 0.18	1	5.4		17.1	16.1	1	5.5	13.5	12.7	12.4
22	173 428.6−323 337	2.1 ± 0.9	1.0 ± 0.6	2.3 ± 0.7			2					2				
23	173 430.3−323 605	6.2 ± 1.3	2.7 ± 0.8	2.9 ± 0.7	0.22 ± 0.18	≤−0.52	1	2.5		15.1	14.7	1	2.5	12.7	12.1	11.9
24	173 431.4−323 441	3.0 ± 0.9	0.8 ± 0.6	0.7 ± 0.6			1	4.3		17.1	16.3	1	4.6	14.1	13.4	(12.3)
25	173 431.8−323 326	17.0 ± 1.6	7.7 ± 1.2	8.0 ± 1.2	−0.11 ± 0.10	−0.42 ± 0.13	1	2.4		14.7	14.1	1	2.2	12.2	11.5	11.2
26	173 433.7−323 612	4.3 ± 1.1	1.6 ± 0.7				1	6.6		10.2	10.2	2				
27	173 434.7−323 350						1	4.2		10.3	10.3	3				
28	173 435.2−323 140	3.8 ± 0.9	2.1 ± 0.7	1.9 ± 0.6			0					1	5.4	(16.4)	14.3	12.9
29	173 435.8−323 548	11.3 ± 1.5	5.6 ± 1.1	5.0 ± 1.0	0.20 ± 0.13	−0.45 ± 0.15	1	1.6		17.3	16.7	3				
30	173 435.9−323 407						1	2.8		15.2	14.6	3				
31	173 436.9−322 737	6.0 ± 1.4	2.5 ± 0.9	3.5 ± 1.0	0.31 ± 0.21	−0.54 ± 0.28	1	0.8	16.2	15.0	14.5	2				
32	173 437.4−322 942	7.3 ± 1.3	4.1 ± 0.9	5.5 ± 1.0	−0.29 ± 0.17	−0.31 ± 0.31	1	2.7	14.2	13.1	12.8	2				
33	173 437.4−323 438	2.1 ± 1.6	1.4 ± 1.2	4.1 ± 1.3			2					2				
34	173 437.6−323 710	2.8 ± 1.0	2.4 ± 0.7	1.2 ± 0.6			1	4.2		17.6	17.0	3				
35	173 437.7−323 238	2.0 ± 0.9	1.4 ± 0.6	1.5 ± 0.6			1	0.7		17.5	16.8	1	0.9	14.3	13.5	13.3
36	173 438.7−323 512	7.3 ± 2.0		2.7 ± 1.4	0.47 ± 0.48	−0.60 ± 0.28	0					1	3.4	14.1	13.3	12.9
37	173 439.3−323 140	3.0 ± 0.8	0.5 ± 0.5	0.9 ± 0.6			1	6.2		15.5	15.0	3				

Table 1. continued.

#	XMMU J	pn	MOS1	MOS2	HR_1	HR_2	USNO (and GSC)					2MASS				
							Nr.	d	B	V	R	Nr.	d	J	H	K_S
		10^{-3} cts s^{-1}	10^{-3} cts s^{-1}	10^{-3} cts s^{-1}				($''$)					($''$)			
[1]	[2]	[3]	[4]	[5]	[6]	[7]	[8]	[9]	[10]	[11]	[12]	[13]	[14]	[15]	[16]	[17]
38	173 439.6−323 359	4.8 ± 1.9	3.9 ± 1.4	5.0 ± 1.2			1	6.7		13.2	13.2	4				
39	173 440.3−323 430	13.1 ± 3.3	8.4 ± 2.1	9.4 ± 2.4		≥0.40	1	1.2		14.8	14.0	1	0.9	12.4	11.8	11.6
40	173 441.3−323 554	5.9 ± 1.5	1.4 ± 0.9	2.4 ± 1.0	0.32 ± 0.36	−0.28 ± 0.25	1	7.0		16.7	16.2	3				
41	173 442.2−323 254	5.2 ± 1.4	1.7 ± 0.8	2.1 ± 0.8	−0.34 ± 0.29	−0.63 ± 0.63	1	4.9		17.6	16.7	4				
42	173 442.4−323 350	7.9 ± 2.0	2.8 ± 1.3	4.0 ± 1.3	0.16 ± 0.26	≤−0.47	1	3.9		14.3	14.1	1	4.3	12.6	11.8	11.2
43	173 442.5−323 043	2.1 ± 1.2	2.5 ± 0.8	2.5 ± 0.8			1	4.3	19.1	18.1	17.3	2				
44	173 442.5−323 455	1188.5 ± 13.0	519.5 ± 8.4	534.8 ± 8.2	−0.42 ± 0.01	−0.84 ± 0.01	1	1.8		5.71	5.73	1	1.7	5.53	5.52	5.54
45	173 443.9−323 851	3.8 ± 1.1	1.4 ± 0.7	1.2 ± 0.7			1	6.9	17.3	16.5	15.6	1	6.8	13.3	12.6	12.4
46	173 444.0−323 554	7.3 ± 1.5	2.3 ± 1.0	2.1 ± 1.6	−0.07 ± 0.29	0.14 ± 0.24	1	7.0		17.9	17.2	7				
47	173 444.2−323 710	6.3 ± 1.2	2.5 ± 0.8	1.3 ± 0.7	0.04 ± 0.21	≤−0.54	1	2.0		15.1	14.8	3				
48	173 444.2−323 632	2.3 ± 1.2	0.9 ± 0.7	3.0 ± 0.8			1	5.9			18.0	3				
49	173 444.8−323 047	2.6 ± 1.2	2.5 ± 0.8	2.7 ± 0.8			1	2.2	18.7	17.9	16.8	1	1.9	14.2	13.3	13.1
50	173 445.8−323 318	26.6 ± 2.3	15.6 ± 1.6	11.9 ± 1.5	0.64 ± 0.11	−0.17 ± 0.10	2					1	0.7	14.3	13.6	(13.8)
51	173 446.3−323 216	8.0 ± 1.4	3.0 ± 1.0	1.2 ± 0.8	0.01 ± 0.17	≤−0.65	1	5.9		15.2	14.9	2				
52	173447.1−323 558	4.1 ± 1.2		2.4 ± 0.9			1	3.0		16.9	15.8	3				
53	173 447.2−323 806	12.2 ± 1.6	5.1 ± 1.1	5.9 ± 1.0	0.22 ± 0.14	−0.46 ± 0.16	3					3				
54	173 447.8−324 108	13.1 ± 1.8	5.8 ± 1.2	5.8 ± 1.2	−0.70 ± 0.10	−0.48 ± 0.39	1	3.1	13.5	12.6	12.3	2				
55	173 448.1−323 422	21.9 ± 2.2	13.9 ± 1.5	11.4 ± 1.5	0.04 ± 0.11	−0.57 ± 0.11	1	2.0		13.4	13.2	1	1.9	11.7	11.2	11.0
56	173 448.1−323 520	15.2 ± 1.8	4.1 ± 1.2	5.0 ± 1.1	0.10 ± 0.13	−0.53 ± 0.13	1	2.2		11.2	11.2	3				
57	173 448.4−323 155	14.4 ± 1.7	8.0 ± 1.2	7.8 ± 1.2	0.01 ± 0.12	−0.48 ± 0.17	1	1.7		15.2	14.7	5				
58	173 449.4−324 351	3.5 ± 1.4	6.0 ± 1.4	2.6 ± 0.9			1	4.3	18.5	17.4	16.4	5				
59	173 449.5−324 548	2.2 ± 1.4	2.8 ± 1.1	3.5 ± 1.2			2					3				
60	173 450.5−323 806	2.4 ± 1.0	1.6 ± 0.7	1.9 ± 0.7			1	4.3		17.7	16.6	2				
61	173 450.5−323 938	2.9 ± 1.0	1.7 ± 0.7	1.4 ± 0.7			1	5.9	18.1	16.9	16.2	3				
62	173 450.7−323 356	1.4 ± 1.5	3.2 ± 1.0	3.1 ± 1.0			2					2				
63	173 451.1−323 520	11.8 ± 1.6	5.8 ± 1.1	5.7 ± 1.0	−0.04 ± 0.13	−0.71 ± 0.20	1	3.6		13.1	13.9	5				
64	173 451.5−323 310	8.9 ± 1.4	2.3 ± 0.8	2.2 ± 0.8	0.01 ± 0.17	−0.44 ± 0.21	1	1.5		15.8	15.4	2				
65	173 453.0−323 358	25.8 ± 2.1	11.4 ± 1.4	12.5 ± 1.4	0.06 ± 0.09	−0.60 ± 0.10	1	1.0		13.7	13.2	1	0.8	11.7	11.2	11.0
66	173 454.8−323 643	2.6 ± 0.9	1.8 ± 0.7	0.9 ± 0.7			1	7.0			17.1	2				
67	173 456.7−323 421	13.0 ± 1.7	4.9 ± 1.0	5.7 ± 1.0	−0.41 ± 0.12	−0.73 ± 0.27	1	2.7		14.0	13.8	3				
68	173 457.5−323 517	3.7 ± 1.1		2.8 ± 0.8			1	2.8		15.7	15.1	3				
69	173 457.9−323 631	5.6 ± 1.2	2.8 ± 0.7	3.2 ± 0.8	−0.11 ± 0.20	≤−0.49	1	2.1		16.9	16.4	1	2.0	14.3	13.4	13.0
70	173 500.6−323 422	14.1 ± 1.7	6.2 ± 1.1	8.1 ± 1.2	−0.08 ± 0.12	−0.45 ± 0.17	2					2				
71	173 505.3−323 433	6.8 ± 1.5	3.0 ± 0.9	3.9 ± 0.9	0.01 ± 0.20	−0.47 ± 0.28	1	6.9	15.2	14.3	13.9	1	6.7	12.4	11.9	11.7
72	173 507.9−322 905	4.2 ± 1.3	1.9 ± 0.9	2.1 ± 0.9			0					2				
73	173 517.4−323 548	3.2 ± 1.2	2.4 ± 0.8	1.2 ± 0.8			2					4				
74	173 520.5−323 410	5.6 ± 1.5	5.0 ± 1.1	3.0 ± 0.9	−0.47 ± 0.26	0.03 ± 0.45	1	1.7	17.9	16.5	15.9	4				
75	173 526.6−323 356	5.9 ± 1.7	1.0 ± 0.9		−0.25 ± 0.31	−0.01 ± 0.42	1	6.6	16.7	16.0	15.0	1	4.2	(12.8)	11.4	10.3
76	173 530.9−323 558	15.6 ± 2.3	7.5 ± 1.4	6.7 ± 1.5	≤−0.47	≥0.93	1	5.4		17.5	16.2	3				
77	173 531.5−323 512	2.5 ± 1.3	2.7 ± 1.0	1.6 ± 0.9			2					4				

No hardness ratio could be derived for source #39, since it lies inside the wings of the PSF of the bright central source HD 159 176 (#44).
IR magnitudes between brackets were flagged as uncertain in the 2MASS database because of band filling or diffraction spikes.

5.3.2 Star formation in the NGC 6383 cluster

In the context of the preparation of the *Handbook of Star Forming Regions, Vol. II: The Southern Sky*, to be published by the ASP, M. De Becker and I have been invited by the editor Prof. Bo Reipurth to prepare a chapter reviewing the star formation activity in the NGC 6383 cluster. This document (Rauw & De Becker 2007b) is included below.
In the meantime, some more results have become available. Paunzen et al. (2007) recently published new Strömgren *u v b y* CCD photometry of five fields in the cluster. They analysed the photometry of 272 stars and identified 44 probable cluster members that are still in the PMS stage. The PMS candidates include several Herbig Ae/Be stars as well as classical T Tauri stars. Correlating their sources with the 2MASS catalogue, these authors identified five stars with near-IR excesses. Three of these objects were known before (FJL# 4, 6 and 20), while the other two were reported for the first time. Paunzen et al. (2007) derived a reddening of $E(B-V) = 0.29 \pm 0.05$ and a distance of 1.7 ± 0.3 kpc (somewhat larger than the majority of the recent distance determinations). They found no evidence for a turn-off point or red giants in the cluster which results in an upper limit on the cluster age of 4 Myr. Unfortunately, at the time of writing this habilitation thesis, the photometric data of Paunzen et al. (2007) are not available (due to a hardware problem on E. Paunzen's computer) and they can thus not be used for a cross-correlation with our X-ray sources.

Handbook of Star Forming Regions
ASP Conference Series, Vol. ..., 2006
Bo Reipurth, ed.

The multiwavelength picture of star formation in the very young open cluster NGC 6383

Gregor Rauw

Institut d'Astrophysique et de Géophysique, Université de Liège, Allée du 6 Août 17, Bât B5c, B-4000 Liège, Belgium
Also Research Associate FNRS (Belgium)

Michaël De Becker

Institut d'Astrophysique et de Géophysique, Université de Liège, Allée du 6 Août 17, Bât B5c, B-4000 Liège, Belgium

Abstract. We review the properties of the very young ($\sim$ 2 Myr) open cluster NGC 6383. The cluster is dominated by the massive binary HD 159176 (O7 V + O7 V). The distance to NGC 6383 is consistently found to be 1.3 ± 0.1 kpc and the average reddening is determined to be $E(B-V) = 0.32 \pm 0.02$. Several pre-main sequence candidates have been identified using different criteria relying on the detection of emission lines, infrared excesses, photometric variability and X-ray emission.

1. NGC 6383 and its surroundings

NGC 6383 ($\alpha_{2000} = 17^h34^m48^s$, $\delta_{2000} = -32°34'0$; $l_{II} = 355.69°$, $b_{II} = +0.04°$) is a rather compact open cluster which could be part of the Sgr OB1 association together with NGC 6530 and NGC 6531. The cluster was originally discovered by John Herschel in 1834, and listed as h 3689 in Herschel's Cape Catalogue published in 1847. Most probably due to a clerical error, it also appears in Dreyer's New General Catalogue as NGC 6374, an identifier that is however not commonly used.

Trumpler (1930) pointed out that NGC 6383 belongs to a category of clusters in which a few dozen faint stars are closely grouped around a bright hot central star that frequently happens to be binary system. In the case of NGC 6383, the cluster is centered on the O-type binary HD 159176 (m_V = 5.7, see Fig. 1) that dominates the emission from the cluster over a broad range of energies from the near-infrared to the X-ray domain. Apart from HD 159176, the cluster currently harbours no stars earlier than B1, although de Wit et al. (2005) suggested that the eclipsing binary candidate HD 158186 (O9.5 V, Marchenko et al. 1998) might have been ejected from NGC 6383 through dynamical interactions in the cluster core.

NGC 6383 and more specifically HD 159176 are likely responsible for the ionization of the H II region RCW 132 (Rodgers, Campbell & Whiteoak 1960) also known as S 11 (Sharpless 1953)[1] or Stromlo 67 (Gum 1955). Rodgers et al. (1960) described

[1] Note that the S 11 identifier is not to be confused with the number of the nebula in the revised catalogue of H II regions published by Sharpless (1959). In the latter catalogue, the nebula corresponds to entry number 12 (in the SIMBAD database, this identifier is referred to as Sh 2-012).

RCW 132 as a 110 arcmin $\times$ 80 arcmin medium brightness crescent-shaped region. Images of this emission nebula can be found for instance on plate 131 of Lyngå & Hansson (1972).

During a survey of the galactic ridge at 1390 MHz, Westerhout (1958) detected a large ($1.5^\circ \times 1.5^\circ$) ring-like radio structure roughly centered on NGC 6383. However, Westerhout cautioned that this feature was difficult to separate from the background emission. Part of this source is likely due to RCW 132.

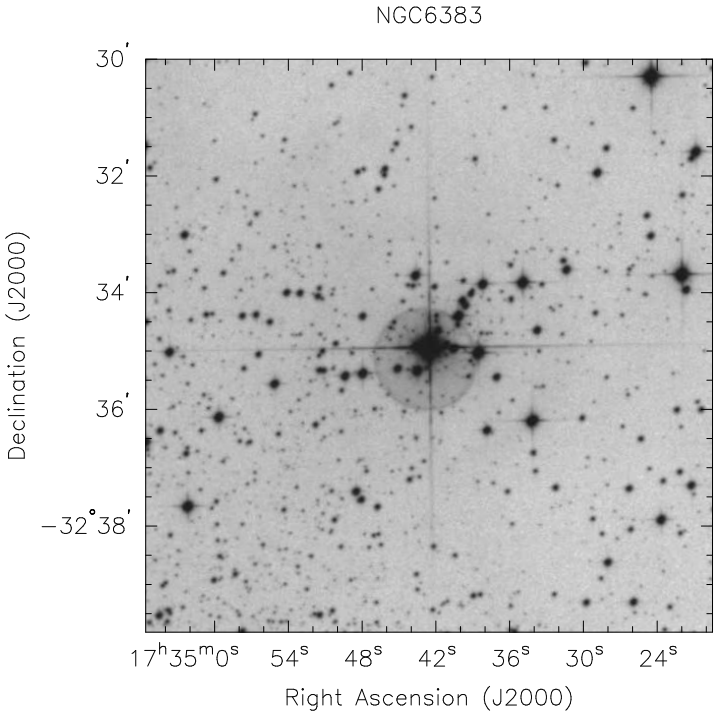

Figure 1. The region around the core of NGC 6383 as seen on the UKSTU survey red plate. The bright star in the middle of the field of view is the massive binary system HD 159176. The field size is 10 arcmin $\times$ 10 arcmin.

2. The massive binary HD 159176 and other early-type stars

According to Lloyd Evans (1978), NGC 6383 harbours a total of 21 OB stars including HD 159176 and V 701 Sco. The spectrum of HD 159176 was described in the *Henry Draper Catalogue* as O5e with very wide lines that were almost double on some occasions. Trumpler (1930) was the first to report the double-lined spectroscopic binary (SB2) nature of the star and proposed orbital solutions for two possible periods of 4.920 and 3.368 days. The first clear determination of the orbital period was performed by Conti, Cowley, & Johnson (1975) on the basis of optical data. The orbital solution was subsequently improved by Seggewiss & de Groot (1976) and Lloyd Evans (1979). Finally, Stickland et al. (1993) derived refined orbital parameters using a series of *IUE* UV spectra. The main result of these spectroscopic studies is that HD 159176 consists of

two very similar main-sequence stars of spectral type O7((f)) V revolving on a circular orbit with a period of 3.367 d.

The photometric monitoring of HD 159176 reported by Thomas & Pachoulakis (1994) revealed low amplitude (~ 0.05 mag) ellipsoidal variations. However, the absence of photometric eclipses prevented these authors from deriving the inclination of the system. The thorough analysis by Pachoulakis (1996) allowed him to determine stellar radii for both components of the order of 25 % of the orbital separation. The stars hence do not fill up their Roche lobe, contrary to the suggestion formulated by Conti et al. (1975).

Pfeiffer et al. (1997) reported on the discovery of a UV emission component produced between the two stars, and interpreted this as a signature of a wind-wind interaction that is slightly wrapped around the secondary star. Pachoulakis (1996) derived mass loss rates of 3.2×10^{-6} and 2.6×10^{-6} $M_\odot$ yr^{-1} respectively for the primary and the secondary. These determinations were based on the fit of the C IV $\lambda\lambda$ 1548-1551 and N V $\lambda\lambda$ 1239-1243 lines with synthetic profiles resulting from the combination of the individual profiles from both stars, and taking into account the effects of wind eclipses depending on the orbital phase. We note that, following a less sophisticated approach and using the same spectral lines, Howarth & Prinja (1989) derived a significantly lower mass loss rate of 6×10^{-7} $M_\odot$ yr^{-1} for both stars.

HD 159176 was detected as a rather bright X-ray emitter by the *EINSTEIN* (Chlebowski, Harnden, & Sciortino 1989) and *ROSAT* (Berghöfer, Schmitt, & Cassinelli 1996) satellites. More recently, the observations performed with the *XMM-Newton* satellite shed new light on the X-ray emission from this close binary system (De Becker et al. 2004). HD 159176 is a rather soft thermal X-ray emitter whose spectrum is dominated by plasma at temperatures of 2 – 3 and 6 – 10 MK. Such temperatures are typical of plasma heated by shocks respectively within individual stellar winds and in colliding winds in close binaries. An additional indication of X-ray emission produced by the colliding winds comes from the X-ray luminosity that is too high to be explained by intrinsic X-ray emission from individual stellar winds alone. The modelling of the X-ray emission from the colliding winds revealed that the previous determinations of the mass loss rates (see above) may have been overestimated. Finally, De Becker et al. (2004) showed that purely thermal emission models failed to fit the X-ray spectrum up to 10.0 keV, although very good results were obtained using an additional power law to fit a high energy tail. This may point to a non-thermal emission component presumably produced by inverse Compton scattering of photospheric UV photons by relativistic electrons accelerated in the wind interaction zone (De Becker 2005). In this context, it is interesting to note that NGC 6383 lies very close to the centre of the error box of the EGRET γ-ray source 3EG J1734 $-$3232 (Torres et al. 2003). Whilst this γ-ray source is usually associated with the supernova remnant G355.6 $+$0.0, a contribution from NGC 6383 and HD 159176 cannot be ruled out (Torres et al. 2003).

The other remarkable early-type star in NGC 6383 is the W UMa-type eclipsing binary V 701 Sco (= HDE 317844, $m_V = 8.05$ at max. light), the second brightest member of the cluster. This system very likely consists of two almost identical and essentially unevolved B1-1.5 stars (Andersen, Nordstrom, & Wilson 1980, Bell & Malcolm 1987) revolving around each other in 0.762 days.

3. General cluster properties

A number of photometric and spectroscopic studies of NGC 6383 can be found in the literature. Photoelectric UBV measurements of 27 stars were presented by Eggen (1961) whilst Thé (1965) obtained photographic photometry of 97 objects down to $V = 13.8$ as well as objective prism plates. Antalová (1972) reported photographic UBV measurements of 32 stars in the neighbourhood of NGC 6383. FitzGerald et al. (1978) analysed photoelectric UBV measurements of 25 stars as well as low and medium resolution spectra of 11 objects within 2 arcmin from the cluster centre. Lloyd Evans (1978) presented photoelectric and photographic UBV measurements of several hundred objects within 12 arcmin from HD 159176, along with spectral classifications for 17 stars and radial velocities for 14 of them. Thé et al. (1985) discussed photoelectric observations of a sample of stars in the Walraven $VBLUW$, Cousins VRI and near-infrared $JHKLM$ bands. Most authors adopted the numbering scheme introduced by Eggen (1961) for the cluster core and extended to the outer cluster regions by Thé (1965) and Lloyd Evans (1978)[2]. A somewhat different numbering scheme for the cluster core was introduced by FitzGerald et al. (1978)[3]. Hereafter we use the notations 'Thé #' for the former and 'FJL #' for the latter.

3.1. The reddening and the cluster distance

Most investigations based on photometric and spectroscopic studies agree within the errors about the reddening: Eggen (1961), FitzGerald et al. (1978), Lloyd Evans (1978) and Thé et al. (1985) inferred an $E(B-V)$ colour excess of 0.30, 0.33 ± 0.02, 0.35 and 0.30 ± 0.01 respectively. Little or no spatial variation of the reddening was found over the central part of the cluster. The only exception is the study of Antalová (1972) who suggested a scatter in A_V between 0.6 and 1.3.

Lloyd Evans (1978) noted that the cluster is probably located right in front of a dust absorption cloud. In fact, some redder stars in the field were found to have a distance modulus only slightly larger than the one of the cluster. There exists also a region of apparently higher stellar density where the dust cloud might be thinner, thus allowing us to see some background objects. In the atlas of dark clouds of Dobashi et al. (2005), NGC 6383 appears indeed located on a thin bridge connecting the two giant cloud complexes DoH 2164 and DoH 2190 (see Fig. 18-1-9 of Dobashi et al. 2005). This position corresponds to the intersection of two large cavities in the Galactic plane which might have been created by the action of early-type stars in NGC 6383 and other young clusters in this region.

While Trumpler (1930) estimated a distance of 2.1 kpc for NGC 6383, more recent studies usually agree about a smaller distance in the range between 1.2 and 1.5 kpc. Distance determinations based on colour-magnitude diagrams are provided by Eggen (1961, $d = 1.25$ kpc), FitzGerald et al. (1978, $d = 1.5 \pm 0.2$ kpc), Lloyd Evans (1978, $d = 1.32$ kpc) and Thé et al. (1985, $d = 1.4 \pm 0.15$ kpc). Using photoelectric measurements of the Hβ index of six likely cluster members with m_V in the range 5.7 – 11.3, Graham (1967) inferred a distance modulus of 10.68 ± 0.54 ($d = 1.37 \pm 0.34$ kpc). Accounting for the binarity of HD 159176 and adopting $R_V = 3.1$ (instead of 3.0 as

[2]In SIMBAD, these identifiers are noted NGC 6383 NNN where NNN is the 3 digit number of the star.

[3]In SIMBAD, these identifiers are noted Cl* NGC 6383 FJL NN where NN is the 2 digit number of the star.

used by Graham 1967), yields $DM = 10.78 \pm 0.34$ ($d = 1.43 \pm 0.22$ kpc). A nice confirmation of these distance estimates comes from the spectroscopic and photometric analysis of the eclipsing binary system V 701 Sco by Bell & Malcolm (1987) who derived a distance of 1240 ± 190 pc. Finally, Rastorguev et al. (1999) used a statistical parallax technique based on the kinematical parameters (proper motions and radial velocities) to derive a cluster distance of 1.18 kpc. To our knowledge, the lowest distance estimate is the one by Kharchenko et al. (2005) who quote 985 pc, although it is not fully clear what technique was used to arrive at this number. In summary, the distance to NGC 6383 thus appears rather well determined at 1.3 ± 0.1 kpc.

3.2. Proper motion and cluster membership

The core of NGC 6383 is rather compact (see Fig. 1). Kharchenko et al. (2005) derived a core radius (defined as the radius where the decrease of stellar surface density drops abruptly) of 4.8 arcmin and a corona radius (where the surface density becomes equal to the average of the surrounding field) of 15 arcmin.

The cluster membership of individual stars has been discussed using photometric criteria (e.g. Lloyd Evans 1978), radial velocities and proper motions. For instance, stars FJL # 3 and 21 of FitzGerald et al. (1978) are likely foreground B9 IV and F stars respectively.

Several authors have investigated the cluster proper motion. Using *Hipparcos* data, Rastorguev et al. (1999) inferred $\mu_\alpha \cos\delta = 2.0\,\mathrm{mas\,yr^{-1}}$ and $\mu_\delta = -0.6\,\mathrm{mas\,yr^{-1}}$. Using the same *Hipparcos* measurements, Baumgardt, Dettbarn, & Wielen (2000) obtained $\mu_\alpha \cos\delta = 2.70\,\mathrm{mas\,yr^{-1}}$ and $\mu_\delta = -0.84\,\mathrm{mas\,yr^{-1}}$, while Kharchenko et al. (2005) derived $\mu_\alpha \cos\delta = 1.66 \pm 0.40\,\mathrm{mas\,yr^{-1}}$ and $\mu_\delta = -1.56 \pm 0.34\,\mathrm{mas\,yr^{-1}}$. Dias, Lépine, & Alessi (2002) used the Tycho2 catalogue to estimate $\mu_\alpha \cos\delta = 1.58 \pm 1.64\,\mathrm{mas\,yr^{-1}}$ and $\mu_\delta = -2.01 \pm 1.64\,\mathrm{mas\,yr^{-1}}$.

Dias et al. (2002) further derived membership probabilities for 41 individual stars brighter than $V_T = 12.2$, and found that 14 of them are most probably members (P $\geq 61\%$), 6 are possible members (P $\in [14, 61]\%$) and the remainder are probable field stars. However, these results critically depend on the actual value of the proper motions and we have seen above that the various determinations are only in coarse agreement.

4. The star formation activity in NGC 6383

Eggen (1961) drew attention to the similarity of NGC 6383 with NGC 2264 in the sense that the colour-magnitude diagrams of the two clusters show a rather normal main sequence down to spectral type about A0 whilst stars of later spectral types are located above the main sequence. This feature was considered as the signature of a population of pre-main sequence (PMS) stars. FitzGerald et al. (1978) identified eight likely cluster members that fall in the region of PMS objects in the colour-colour and colour-magnitude diagram. These authors derived a cluster age of 1.7 ± 0.4 Myr. Given the rather narrow locus of potential PMS stars, they argued that star formation must have been quite coeval, except for HD 159176 for which they inferred an age of 2.8 ± 0.5 Myr, suggesting that this star triggered the formation of lower mass stars in NGC 6383[4]. On

[4]The 5.1 Myr cluster age proposed by Kharchenko et al. (2005) should be considered with caution since this value relies only on the massive binary HD 159176.

the other hand, Lloyd Evans (1978) suggested that the formation of lower mass stars ceased prematurely after the formation of the central cluster of massive stars, resulting in a relative lack of faint stars and the absence of T Tauri stars as bright as those found in regions of continuous star formation. Despite these conflicting interpretations, NGC 6383 is an extremely interesting place to study the interplay between low- and high-mass star formation and it is therefore important to improve our knowledge about the PMS population of this cluster.

The problem with identifying PMS stars from classical colour-magnitude diagrams is the heavy contamination by foreground field stars. Red stars with $B-V \geq 0.7$ are essentially lost in the large population of field stars. Since the original work of Eggen, various other techniques have been applied to identify pre-main sequence stars in NGC 6383 and we review below the main results.

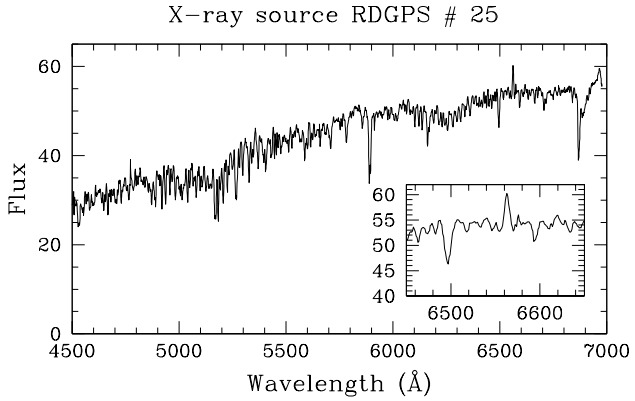

Figure 2. Medium-resolution spectrum of the optical counterpart of X-ray source RDGPS # 25 (Rauw et al. 2003) that we classify as K0 V. The insert shows a zoom on the weak Hα emission (from Rauw et al. 2006, in preparation).

4.1. Emission line objects

Using objective prism spectra, Thé (1965) derived approximate spectral types for 46 objects, but failed to find stars with strong Hα emission down to $V = 16.0$. FitzGerald et al. (1978) noted Hβ emission from star FJL # 24 on one out of six observations. They accordingly classified this star as B8 Vne and suggested that it was a flare star undergoing the final stages of PMS contraction. Lloyd Evans (1978) pointed out that HDE 317861[5] (B3-5 Vne) displayed a pronounced Hβ emission in their observation.

Thé et al. (1985) found that star FJL # 4 (= V 486 Sco, A5 IIIp) displays Hα, He II λ 4686 and [O III] emissions. This star is a probable Herbig Ae star. The Hα emission of FJL #4 was also confirmed by van den Ancker (2000) who classified it as A5 IIIe.

Our knowledge about line emission in cooler stars is much more limited. We recently observed a sample of PMS candidates selected from their X-ray emission (Rauw et al. 2003). The counterparts of X-ray sources RDGPS[6] # 20, 25 and 57 classified

[5]Lloyd Evans (1978) identified this star as Thé # 75, while it should actually be Thé # 76.

[6]These numbers refer to the numbering scheme of Rauw et al. (2003).

as K4-5 V-III, K0 V and K4 III respectively were found to display Hα in slight emission (Rauw et al. 2006, in preparation and Fig. 2). In addition, we are in the process of collecting and analysing deep broad-band and Hα CCD images to identify fainter Hα emission stars that escaped detection during previous surveys (Rauw et al. 2006, in preparation).

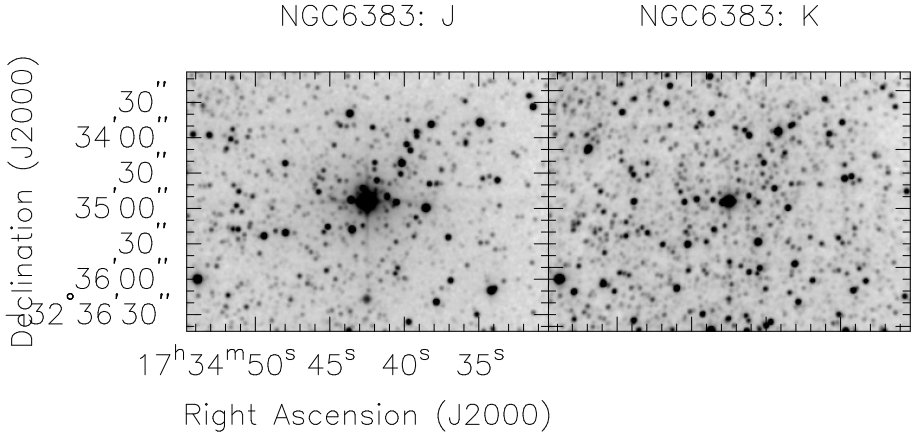

Figure 3. Near-IR images of the core of NGC 6383 as obtained from the 2MASS survey. Note the huge number of sources that appear strongest in the K_s filter.

4.2. Infrared excess emission

Thé et al. (1985) and van den Ancker et al. (2000) identified three stars (FJL #4, 5 and 6) that fall above the ZAMS in the colour-magnitude diagram and show a considerable near-IR excess. While FJL # 4 is the A5 IIIp emission line star discussed above, stars #5 and 6 were classified as A2 Vep and A respectively. According to Thé et al. (1985), the near-IR excess of FJL #4 and 5 is due to thermal emission by circumstellar dust grains that absorb the UV and visible light of the central star. From their analysis, they derived dust shell temperatures of 1700 and 1350 K respectively for FJL # 4 and 5. A few more stars, FJL # 18 (G0 V), 20 (B8 V) and 24 (see above), display a modest near-IR excess (van den Ancker et al. 2000).

The 2MASS images of the region near NGC 6383 reveal a large number of sources that appear most obviously in the K_s filter (see Fig. 3). Some of them are rather heavily absorbed objects without an optical counterpart, but associated to an X-ray source (see below) and could be either background objects or deeply embedded PMS objects.

4.3. Variable pre-main sequence stars

PMS stars often display a high degree of spectroscopic and photometric variability over a wide range of timescales from minutes to months. Several variables have been found from snapshot observations of NGC 6383. FitzGerald et al. (1978) noted that star FJL #10 ($m_V = 15.3$) displayed photometric variability of 0.3 mag. Lloyd Evans (1978) identified six stars that display photometric variability with one object (his star V1) showing a variation of more than 2 mag. Lloyd Evans (1978) suggested that these objects are RW Aur or T Tauri variables. Finally, Thé et al. (1985) drew attention to the star FJL #3 that apparently displays a changing spectral type.

A systematic search for PMS variables was performed by Zwintz et al. (2004; 2005). These authors obtained time series of B and V photometry of NGC 6383 over two weeks. Out of 15 cluster members that are located in the classical instability strip, two A – F type PMS stars were found to display δ Scuti-like pulsations. Interestingly enough, one of them was again the A5 IIIp Herbig Ae/Be star FJL # 4 for which five different pulsation modes with periods between 1.24 and 2.89 hours were identified. For Thé # 55, a single frequency corresponding to 1.26 hours was detected. A third object (Thé # 54) was classified as a suspected PMS pulsator. Several other stars were found to display photometric variations. Some of them are probably foreground or background objects unrelated to the cluster, but four objects were classified as T Tauri stars or T Tauri candidates by Zwintz et al. (2005).

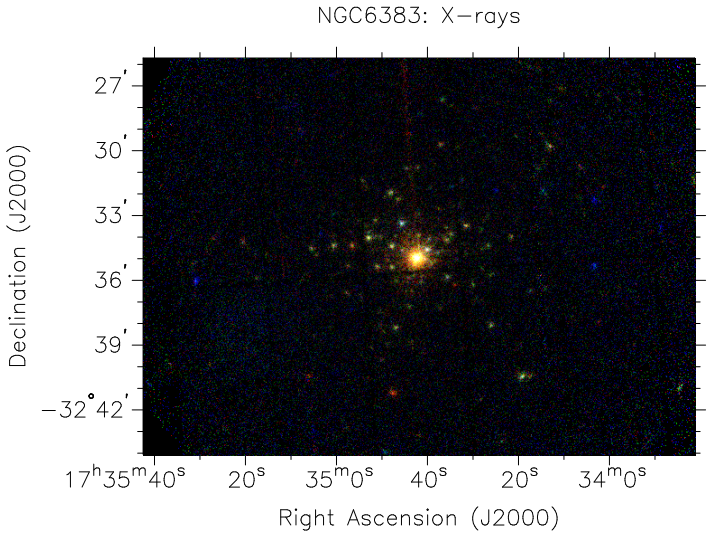

Figure 4. Three colour X-ray image of NGC 6383 as obtained from the *XMM-Newton* EPIC images of Rauw et al. (2003). The colours correspond to different energy bands: the red, green and blue colours stand for emission in the $[0.5, 1.0]$ keV, $[1.0, 2.0]$ keV and $[2.0, 8.0]$ keV energy domains respectively. The brightest source in the image is HD 159176.

4.4. X-ray selected PMS candidates

Relatively bright, hard and variable X-ray emission is another common feature of classical (cTTs) and weak-line T Tauri stars (wTTs). In addition to HD 159176, Rauw et al. (2003) detected 76 secondary X-ray sources in the *XMM-Newton* field of view of NGC 6383. These sources are strongly concentrated towards the cluster centre (see Fig. 4). The coordinates of the X-ray sources were cross-correlated with various optical and near-IR catalogues. Most sources have quite faint optical counterparts indicating that they must have a rather large L_X/L_{vis} ratio. While three PMS candidates of FitzGerald et al. (1978) FJL # 11, 23 and 24 were seen in X-rays, none of the variables of Lloyd Evans (1978) was detected. The three A-type stars (FJL # 4, 5 and 6) that present a strong near-IR excess were also not detected.

The brightest secondary X-ray sources have spectra that can be represented by a two-component thermal plasma model with plasma temperatures in the range 6 –

12 MK and 25 – 60 MK for the cooler and hotter component respectively. Source RDGPS #50 (Rauw et al. 2003) displayed a flare towards the end of the observation with a significant hardening of its emission. These properties suggest that these objects are indeed low-mass PMS stars. Only two X-ray sources were found to have a counterpart with near-IR colours indicating excess emission. This rather low fraction of objects with evidence for circumstellar material suggests that most of the X-ray selected PMS candidates are in fact wTTs rather than cTTs. This is confirmed by the rather low incidence of Hα emitters found in the spectroscopic follow-up observation of the X-ray selected PMS candidates (Rauw et al. 2006, in preparation and Fig. 2). Finally, 16 X-ray sources have possible near-IR counterparts with A_V up to 28 mag, substantially larger than the cluster reddening. These could be either deeply embedded class I protostars or background objects unrelated to the cluster.

Table 1 provides an overview of the properties of the PMS candidate stars discussed hereabove in view of the various selection criteria that have been used.

Table 1. Summary of the multiwavelength properties of the PMS candidates in NGC 6383 discussed in this review. The numbers in the last four columns indicate the references where these features were reported. Note that there are many more X-ray selected PMS candidates, but we decided to focus on those that either display a flaring activity or exhibit a weak Hα emission in their optical spectrum.

Object	α_{2000}	δ_{2000}	Spect. type	V	Em.	IR	Var.	X
HDE 317861	17:34:02	−32:40:40	B3-5 Vne	9.9	1	-	-	-
FJL # 4	17:34:38	−32:36:19	A5 IIIp	13.0	2,3	2,3	4	-
FJL # 5	17:34:34	−32:34:36	A2 Vep	12.9	-	2,3	-	-
FJL # 6	17:34:39	−32:33:59	A6	13.8	-	2,3	-	-
FJL # 10	17:34:40	−32:33:45		15.3	-	-	5	-
FJL # 11	17:34:42	−32:33:52		15.1	-	-	4	6
FJL # 18	17:34:37	−32:35:24	G0 V	13.4	-	2,3	-	-
FJL # 20	17:34:38	−32:33:49	B9 IV	11.4	-	2,3	-	-
FJL # 23	17:34:48	−32:34:22	G5 V*	13.8	-	-		6
FJL # 24	17:34:48	−32:35:20	B8 Vne	11.4	5	2,3	-	6
Thé # 55	17:34:49	−32:37:21		12.9	-	-	4	-
LE V1	17:34:06	−32:32:53			-	-	1	-
RDGPS # 20	17:34:26	−32:37:59	K4-5 V-III	15.4	7	-	-	6
RDGPS # 25	17:34:32	−32:33:26	K0 V	14.5	7	-	-	6
RDGPS # 50	17:34:46	−32:33:18	**		-	-	-	6
RDGPS # 57	17:34:48	−32:31:55	K4 III	15.2	7	-	-	6

(1) = Lloyd Evans (1978), (2) = Thé et al. (1985), (3) = van den Ancker et al. (2000), (4) Zwintz et al. (2005), (5) = FitzGerald et al. (1978), (6) = Rauw et al. (2003), (7) = Rauw et al. (2006, in prep.)

* possible foreground object.

** there are two optical counterparts inside the positional error box of the X-ray source.

4.5. Second-generation star formation?

Through the combined action of their stellar winds and their intense radiation field, early-type stars can sweep up and compress the material of an ambient or nearby molecular cloud. This interaction is thought to trigger the formation of new generations of stars and evidence for such a process has been found in the periphery of several young open clusters (e.g. Westerlund 2, Whitney et al. 2004; NGC 6604, Reipurth, this volume).

ESO red Schmidt films reveal an extended shell like structure to the north of NGC 6383 (see Fig. 5). This shell features several dense clouds and cometary globules. The high-opacity structure in the upper middle probably corresponds to the dark nebula LDN 1734 catalogued by Lynds (1962). These structures are very much reminiscent of the dust pillars seen in well known examples of second-generation star formation sites (e.g. Walborn 2002) and could hence be the result of the interaction between the winds and radiation of the massive stars and their primordial cloud. To our knowledge, none of the structures around NGC 6383 has been investigated in details but they are ideal targets for future studies to search for young stars.

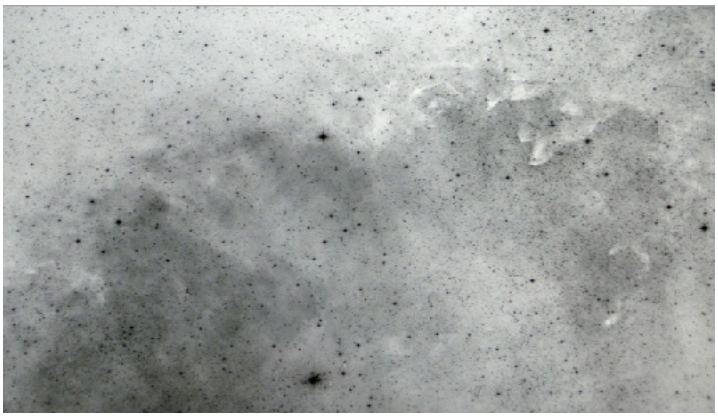

Figure 5. ESO red Schmidt film of the region north of NGC 6383. The cluster is in the lower middle of the image.

Acknowledgements. It is a pleasure to thank Dr. Bo Reipurth for inviting us to prepare this chapter, for extremely valuable suggestions and for providing us with Fig. 5. We are grateful to Dr. Yaël Nazé for assistance in the preparation of Figs. 1, 3 and 4. We acknowledge financial support from the FNRS (Belgium), as well as through the XMM and INTEGRAL PRODEX contract and contract P5/36 PAI (Belspo).

References

Andersen, J., Nordstrom, B., & Wilson, R.E. 1980, A&A, 82, 225
Antalová, A. 1972, Bull. Astr. Inst. Czech., 23, 126
Baumgardt, H., Dettbarn, C., & Wielen, R. 2000, A&AS, 146, 251
Bell, S.A. & Malcolm, G.J. 1987, MNRAS, 226, 899
Berghöfer, T.W., Schmitt, J.H.M.M., & Cassinelli, J.P. 1996, A&AS, 118, 481
Chlebowski, T., Harnden, F.R.J., & Sciortino, S. 1989, ApJ, 341, 427
Conti, P.S., Cowley, A.P., & Johnson, G.B. 1975, PASP, 87, 327
De Becker, M. 2005, PhD thesis, University of Liège

De Becker, M., Rauw, G., Pittard, J.M., Antokhin, I.I., Stevens, I.R., Gosset, E., & Owocki, S.P. 2004, A&A, 416, 221
de Wit, W.J., Testi, L., Palla, F., & Zinnecker, H. 2005, A&A, 437, 247
Dias, W.S., Lépine, J.R.D., & Alessi, B.S. 2002, A&A, 388, 168
Dobashi, K., Uehara, H., Kandori, R., Sakurai, T., Kaiden, M., Umemoto, T., & Sato, F. 2005, PASJ, 57, S1
Eggen, O.J. 1961, Royal Greenwich Obs. Bulletin, 27, 61
FitzGerald, M.P., Jackson, P.D., Luiken, M., Grayzeck, E.J., & Moffat, A.F.J. 1978, MNRAS, 182, 607
Graham, J.A. 1967, MNRAS, 135, 377
Gum, C.S. 1955, Mem. R. Astron. Soc., 67, 155
Howarth, I.D. & Prinja, R.K. 1989, ApJS, 69, 527
Kharchenko, N.V., Piskunov, A.E., Röser, S., Schilbach, E., & Scholz, R.D. 2005, A&A, 438, 1163
Lloyd Evans, T. 1978, MNRAS, 184, 661
Lloyd Evans, T. 1979, MNRAS, 186, 13
Lynds B.T. 1962, ApJS, 7, 1
Lyngå, G. & Hansson, N. 1972, A&AS, 6, 327
Marchenko, S.V., Moffat, A.F.J., van der Hucht, K.A., et al. 1998, A&A, 331, 1022
Pachoulakis, I. 1996, MNRAS, 280, 153
Pfeiffer, R.J., Pachoulakis, I., Koch, R.H., & Stickland, D.J. 1997, The Observatory, 117, 301
Rastorguev, A.S., Glushkova, E.V., Dambis, A.K., & Zabolotskikh, M.V. 1999, Astron. Lett., 25, 595
Rauw, G., De Becker, M., Gosset, E., Pittard, J.M., & Stevens, I.R. 2003, A&A, 407, 925
Rodgers, A.W., Campbell, C.T., & Whiteoak, J.B. 1960, MNRAS, 121, 103
Seggewiss, W. & de Groot, M. 1976, A&A, 51, 195
Sharpless, S. 1953, ApJ, 118, 362
Sharpless, S. 1959, ApJS, 4, 257
Stickland, D.J., Koch, R.H., Pachoulakis, I., & Pfeiffer R.J. 1993, The Observatory, 113, 204
Thé, P.S. 1965, Contribution from the Bossha Observatory, 32, 1
Thé, P.S., Hageman, T., Westerlund, B.E., & Tijn A Djie, H.R.E. 1985, A&A, 151, 391
Thomas, J.C. & Pachoulakis, I. 1994, IBVS, 4115, 1
Torres, D.F., Romero, G.E., Dame, T.M., Combi, J.A., & Butt, Y.M. 2003, Physics Reports, 382, 303
Trumpler, R.J. 1930, PASP, 42, 342
van den Ancker, M.E., Thé, P.S., & de Winter, D. 2000, A&A, 362, 580
Walborn, N.R. 2002, in *Hot Stars Workshop III: The Earliest Stages of Massive Star Birth*, ASP Conf., 267, 111
Westerhout, G. 1958, Bull. Astron. Inst. of the Netherlands, 14, 215
Whitney, B.A., Indebetouw, R., Babler, B.L., et al. 2005, ApJS, 154, 315
Zwintz, K., Marconi, M., Kallinger, T., & Weiss, W.W. 2004, in *The A Star Puzzle*, Proc. IAU Symp. 224, eds. J. Zverko et al., 353
Zwintz, K., Marconi, M., Reegen, P., & Weiss, W.W. 2005, MNRAS, 357, 345

5.3.3 Dark Globules: triggered star formation around NGC 6383?

In the review above (Rauw & De Becker 2007b), we noted the existence of several dark nebulae at some distance from the cluster core and we argued that these features might be associated with triggered star formation. However, the presence of dark nebulae (especially small dark globules) does not unambiguously imply the formation of a new generation of stars (see e.g. Reipurth et al. 1997). To further investigate this issue, I have extracted the near IR photometry of the sources inside the heads of the three most prominent dark nebulae from the 2MASS point source catalogue (Cutri et al. 2003). More specifically, sources were considered inside circular regions of centres 17:32:43.9 −31:46:03.5, 17:32:22.1 −31:52:03.6, 17:32:14.4 −31:56:14.4 and radii 70, 60 and 50 arcsec respectively (see Fig. 5.5). For comparison, sources were also extracted from a neighbouring field free of any dark nebula (centre 17:32:37.8 −31:53:35.5, radius 180 arcsec). The JHK colour-colour diagrams of these regions are shown in Fig. 5.6.

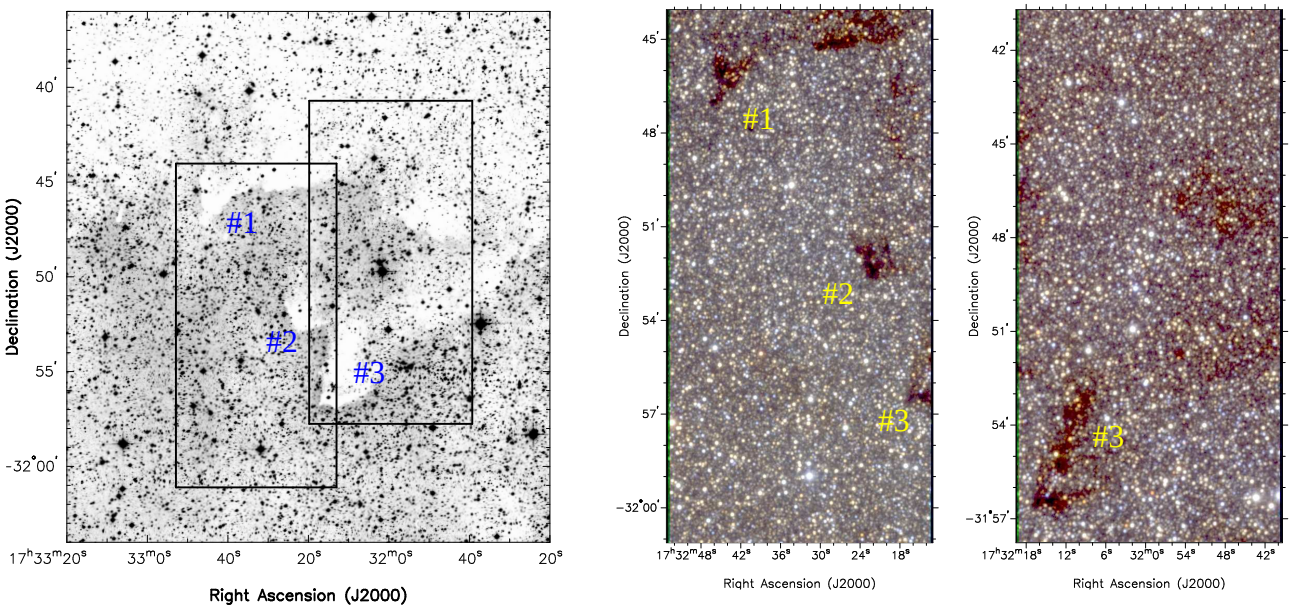

Figure 5.5: Left: Digitized Sky Survey image of the region around the dark nebulae to the North-West of NGC 6383. North is up and East is to the left. The rectangular boxes indicate the areas covered by the 2MASS images on the right. Right: Three-colour images of the dark nebulae to the north of NGC 6383 built from 2MASS images. Blue, green and red colours correspond respectively to the J, H and K_s filters.Note that while there is a slight overlap between the two panels, the left one is shifted northwards compared to the right one as can be seen e.g. from the position of the head of the dark nebula #3 which is present on both pictures.

In the following we only consider good quality (flag 'AAA') data from the 2MASS catalogue. The JHK colour-colour diagram of the comparison field reveals stars over a rather wide range of reddening. The corresponding diagrams of the dust nebulae are generally quite similar (note however that some highly reddened objects might have lower quality photometry and are thus not included in the diagram where only good quality data are shown). Of course, the extraction regions for the dark nebulae include also foreground stars and background stars outside the boundaries of the dark nebulae. Except perhaps for a couple of stars in the third dark nebula that might show a moderate near-IR excess and a few stars with very large reddening in nebulae #1 and #3, there is no strong indication for unusual colours. Therefore,

the question whether or not these dark features are active sites of star formation cannot be answered with the near-IR data currently available.

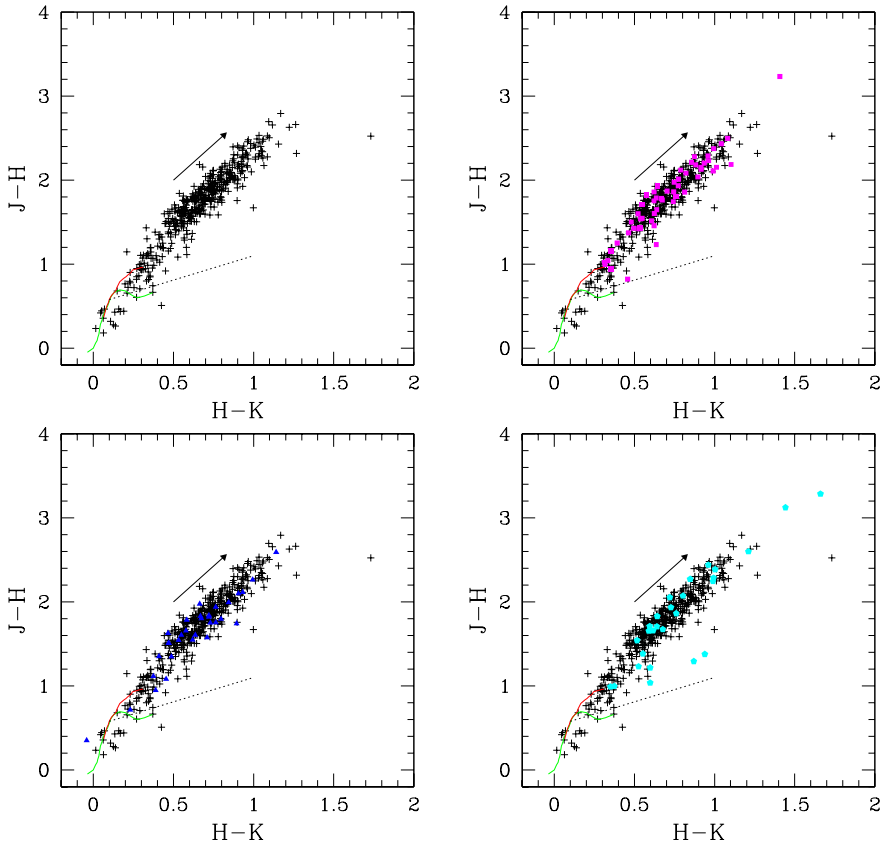

Figure 5.6: JHK colour-colour diagrams of the sources in the comparison field (top left, + signs) and the dark nebulae (#1: top right, filled squares; #2 = bottom left, filled triangles; #3 = bottom right, filled circles). To ease the comparison, the JHK diagram of the comparison fields is overplotted in each panel. The locus of the main sequence and of the giant branch are indicated by the solid lines and the locus of classical T Tauri stars is shown by the dotted line (Meyer et al. 1997).

Another issue concerns the positions of the dark nebulae with respect to the ionizing source. Except for the pillars of the 30 Dor complex, which are 11 – 18 pc away from the ionizing source, all pillars discussed by Walborn (2002) are located at a projected separation of roughly 1 – 6 pc from the ionizing O-star or O-star cluster. Their projected lengths are of order 1 – 3 pc. The axes of these features are often not totally aligned with the ionizing source. Whilst the axes of the three most prominent dark nebulae to the North-West of the cluster are roughly aligned with HD 159176, these structures lie rather far away from the O-type binary. Indeed, if we adopt a distance of 1.3 kpc for the dark nebulae and the O-star binary, we find that the dark nebulae lie at rather large distances between 19 and 21 pc from HD 159176.

5.4 Cyg OB2

The Cyg OB2 cluster appears as one of the most active star forming regions within Cygnus (Odenwald & Schwartz 1993). Evidence for ongoing star formation has been reported in the literature previously.

Parthasarathy et al. 1992 discussed the properties of *IRAS* point sources in the region of Cyg OB2. These authors found 64 sources with positive spectral indices with a steeply increasing flux towards longer wavelength similar to what is found for young stellar objects (YSOs) embedded in thick dust shells (so-called class I sources). In addition, there are a few objects with far IR colours suggesting that they might be class II objects (i.e. embedded T Tauri stars). The far IR luminosities of the class I candidates are between 100 and several 10^3 to $10^4\,L_\odot$, consistent with what is expected from intermediate-mass and massive YSOs. The authors accordingly estimate that this population of cluster members must be very young (probably less than a million years). *IRAS* observations of the Cygnus X region were also analysed by Odenwald & Schwartz (1993) in combination with a ^{12}CO (J=2–1) survey. These authors identified a number of 'first-ranked YSO candidates' among the *IRAS* point sources with far IR luminosities spanning a range equivalent to ZAMS stars of spectral types B4 to O7 (assuming a distance of 2 kpc). Coméron et al. (2002) also noted the existence of a sample of stars displaying an apparent near-IR excess in the 2MASS JHK colour-colour diagram.

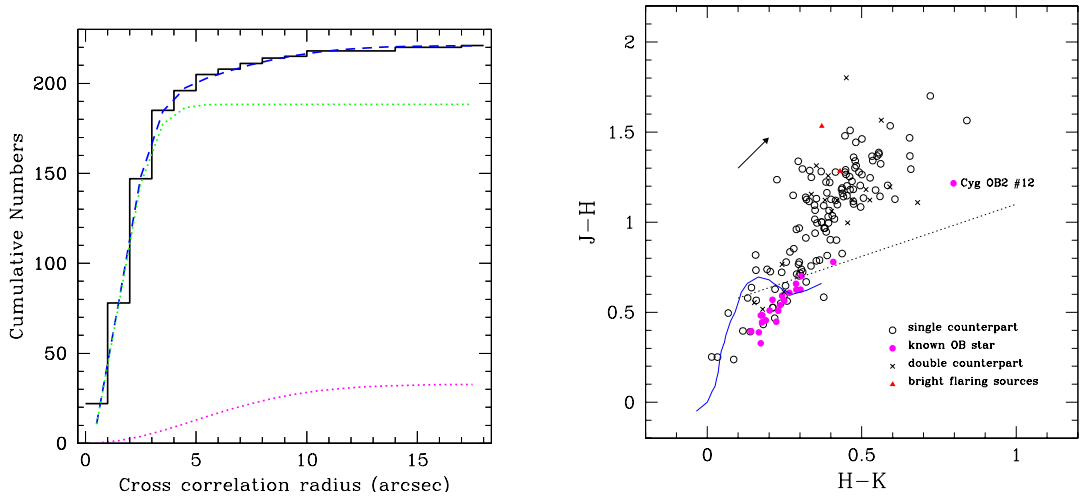

Figure 5.7: Left: cumulative number of correlations between the X-ray detections and the 2MASS catalogue of point sources as a function of the correlation radius. The dashed curve corresponds to the best fitting expression following the approach of Jeffries et al. (1997), whilst the dotted curves indicate the corresponding numbers of real and spurious correlations. Right: JHK colour-colour diagrams of the counterparts of the X-ray sources in the Cyg OB2 field. The locus of the main sequence is shown by the solid line whilst the locus of classical T Tauri stars is indicated by the dotted line (Meyer et al. 1997).

Knödlseder (2000) analysed 2MASS data of Cyg OB2 finding that the association has a spherical form with an angular radius of about one degree and a half-light radius of 13' (6.4 pc at a distance of 1.7 kpc). With an estimated number of 2600 ± 400 OB stars among which 120 ± 20 O-stars, he suggests that Cyg OB2 could be a young globular cluster, and further concludes that the extinction towards Cyg OB2 is in the range[3] $A_V \sim 5 - 20$ mag.

The *XMM-Newton* observation of Cyg OB2 was already discussed in Sect. 3.5. The analysis of these data is still ongoing. A total of 249 sources were detected with the `edetectchain` procedure of the

[3]Note that the absorption towards this association is extremely patchy.

SAS v.6.0 software. All these sources were inspected by eye and 221 of them were eventually retained as real. A few sources could actually be blends of two fainter, spatially unresolved X-ray emitters. The detection limit roughly corresponds to an observed flux of 2×10^{-14} erg cm^{-2} s^{-1} (assuming a thermal plasma with $kT = 3$ keV and $N_H = 10^{22}$ cm^{-2}). The sources were cross-correlated with the 2MASS near-IR catalogue of point-like sources. Using the Jeffries et al. (1997) method, the optimal correlation radius turns out to be 4 arcsec (see Fig. 5.7). A total of 185 near-IR counterparts are identified in this way and they are shown in a colour-colour diagram in Fig. 5.7. The near-IR colour-magnitude (shown by Rauw et al. 2005b, see Sect. 3.5) indicates that most sources have A_V between 5 and 10 mag and actually belong to Cyg OB2 as can be seen by comparing the colour-magnitude diagram to the one obtained by Knödlseder (2000) after correcting for the contamination by field interlopers.

Some of the secondary X-ray sources could be low-mass PMS stars. In fact, three out of the four X-ray brightest non-O star sources display a flare during which the plasma temperatures is high. For instance, the X-ray light curve and spectrum of source XMMU J203246.5+411806 during the third observation (18 November 2004) are shown in Fig. 5.8. During the flare the EPIC spectrum of this source could be fitted by a single temperature thermal plasma model with $kT = 7.3$ keV (80 MK) and an observed flux of 6.0×10^{-13} erg cm^{-2} s^{-1} in the 0.4 – 10 keV band.

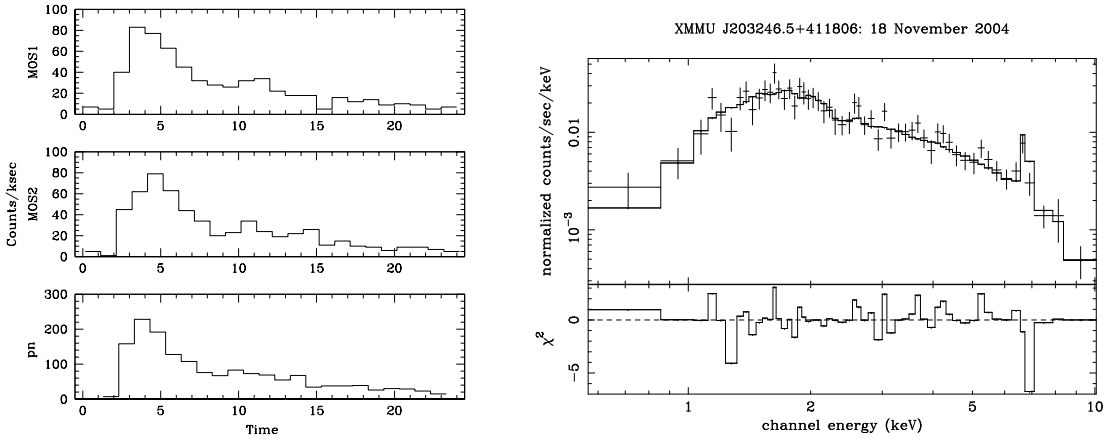

Figure 5.8: Left: X-ray light curve of source XMMU J203246.5+411806 during the third observation (see text). The time is given in ksec after the start of the EPIC-MOS integration. Right: EPIC-pn spectrum of XMMU J203246.5+411806 during the flare. The best fit model is overplotted and corresponds to a plasma temperature of 7.3 keV.

Very recently, Albacete Colombo et al. (2007) analysed a 98 ksec *Chandra* ACIS-I observation of Cyg OB2. The sharp PSF of the *Chandra* telescope allowed them to detect 1003 X-ray sources, 42% of which having less than 20 counts. They cross-correlated their source list with the 2MASS catalogue finding 775 positive identifications, most of which probably correspond to low-mass members of Cyg OB2. Only a small fraction of these objects ($\sim 4.4\%$) was found to fall in the locus of the classical T-Tauri stars, the majority of the other sources being probably weak-line T-Tauri stars. About 10% of the sources with more than 10 counts were found to display a flare in their X-ray light curve.

5.5 Clusters in the Carina OB1 association

In this section, I report my contributions to the analysis of five *XMM-Newton* observations of the Carina OB1 association that will be published by Antokhin et al. (2007). In the first two data sets the primary target was η Car while in the third to fifth pointings the primary target was WR 25.

A total of 242 point sources were detected inside the EPIC field of view with a limiting sensitivity of 1.5×10^{-3} cts s^{-1} for EPIC-pn. The detection of the sources in the Carina region is complicated by the presence of strong non-uniform diffuse emission from the Carina nebula. The line of sight towards η Car ($l_{\rm II} = 287.60°$, $b_{\rm II} = -0.63°$) and WR 25 ($l_{\rm II} = 287.51°$, $b_{\rm II} = -0.71°$) is nearly tangent to the Carina spiral arm. As a result, the neutral hydrogen column density along this direction is quite large and produces a substantial absorption of X-ray photons from extragalactic background sources. To get a rough first order estimate of the total Galactic extinction along this line of sight, we made again use of the *DIRBE/IRAS* extinction maps provided by Schlegel et al. (1998). In addition to the caveats listed by Schlegel et al. for regions with $b_{\rm II} \leq 5°$, a further uncertainty comes from the fact that the interstellar extinction in the Carina region is rather patchy and its properties could deviate from those of the average Galactic extinction curve (e.g. Carraro et al. 2004). With these limitations in mind, we find that the *DIRBE/IRAS* maps indicate a rather large, but highly variable $E(B-V)$ colour excess (between ~ 6.4 on average at the edges of the EPIC field and ~ 14.5 near η Car). Converting these values into neutral hydrogen column densities by means of the gas to dust ratio of Bohlin et al. (1978), we estimate $N_{\rm H}$ in the range $3.7 - 8.5 \times 10^{22}$ cm^{-2}. Based on the Giacconi et al. (2001) $\log N - \log S$ relation, we then expect between 16 and 24 serendipitous extragalactic (AGN) X-ray sources to be detected in the combined EPIC field of view of the five pointings (about 0.27 square degree). On the other hand, using the $\log N - \log S$ relation of Motch et al. (2003) for $b \sim 0°$ one expects about 50 – 70 field stellar sources. Since the Motch et al. (2003) relation was established from fields that do not harbour star formation regions, the significantly larger number of sources detected in the Carina field clearly results from X-ray sources associated with the clusters in the field of view. Among the sources that are clearly associated with the Carina association, 33 are early-type stars: 31 OB-type stars, WR 25 and η Car.

The region covered by the EPIC data harbours several young open clusters that are extremely rich in hot massive stars; the most important ones being Trumpler 14 and 16. Tr 14 is a compact cluster containing three very hot O3 stars. Tr 14 is probably emerging from the eastern and near side of the dense parental molecular cloud (Tapia et al. 2003). Tr 14 might be slightly younger than Tr 16 as suggested by a fainter absolute magnitude and a larger He II λ 4686/ He II λ 4541 ratio in the spectra of early and mid O-type dwarfs (Walborn 1995). Collinder 232 is probably not a physical entity but a condensation of stars in the vicinity of Tr 14 and 16 (see e.g. Walborn 1995 and Tapia et al. 2003). In a similar way, Collinder 228 could actually be part of Tr 16. The apparent distinction between the two clusters might result from obscuration by a dust lane (Walborn 1995). Note an alternative view of Carraro et al. 2004 who argue that Collinder 232 may be a physical aggregate (a rather sparse young open cluster), based on the comparison of its colour-magnitude diagrams and theoretical ZAMS tracks.

Photometric analyses of these clusters are hampered by several problems mainly concerning the reddening and the field interlopers. In fact, the extinction in the Carina complex has been subject to much controversy. Conflicting conclusions ranging from a normal uniformly high to an anomalous and variable extinction have been proposed. This dilemma has important consequences for a consistent determination of the distance moduli (see e.g. the discussion in Walborn 1995). In addition, since the line of sight is along the direction of a galactic spiral arm, there are probably many foreground and background objects that appear projected onto the Carina Nebula. This situation led Kaltcheva & Georgiev (1993) to question the existence of the Tr 16 cluster. These authors suggested that the peculiar orientation of the line of

sight might cause the stars in the Carina arm to appear projected over a comparatively small area of the sky.

The distance to the nebula has been the subject of several studies. Massey & Johnson (1993) and Massey et al. (2001) performed spectroscopic and photometric studies of the clusters in the region and found a distance modulus for Trumpler 14/16 of 12.55±0.1 (which corresponds to a distance of 3.24 kpc). However, the absolute magnitudes determined from the study of three eclipsing binaries in Trumpler 16 (see Sect 1.2) rather suggest a distance modulus of 11.95 ± 0.06 (corresponding to a distance of 2.45 kpc). Allen & Hillier (1993), Meaburn (1999), and Davidson et al. (2001) investigated the geometry and kinematics of the Homunculus Nebula and found the distance to η Car around 2.3± ∼0.3 kpc. In this section we also adopt the distance of 2.5 kpc to all stars in the region.

The star formation history of the Carina complex is another tricky issue. Up to recent years, evidence for ongoing star formation in the Carina Nebula was rather scarce. Using UBV photometry and spectroscopic data for the brightest and bluest members of the Tr 14 and Tr 16 clusters, Massey & Johnson (1993) suggested that the age of both clusters should be about 3 Myr. Based on a $UBVRI$ photometric study of Tr 14, Vázquez et al. (1996) concluded that higher mass members ($\log L/L_{\odot} > 5.0$) have ages of 1.5 ± 0.5 Myr, though several massive stars are still found on the ZAMS and are therefore probably younger. At the lower luminosity end ($\log L/L_{\odot} < 3.5$), Vázquez et al. found a widening of the cluster sequence and a scarity of low-mass stars on the ZAMS. Low mass cluster stars are shifted upwards with respect to the ZAMS consistent with these stars still being contracting pre-main sequence objects. DeGioia-Eastwood et al. (2001) obtained UBV photometry of the Carina clusters. They found a significant population of pre-main sequence stars in Tr 14 and Tr 16 that have been forming over the last 10 Myr whilst the most massive stars in Tr 16 have ages between 1 and 3 Myr (with one exception, a star in the 5-6 Myr range, in each cluster). According to their results, intermediate mass star formation seem to have proceeded continuously over the past 10 Myr and the formation of intermediate mass stars started well before that of OB stars and was apparently not disrupted by the formation of these OB stars. Finally, Tapia et al. (2003) recently performed an extended $UBVRIJHK$ photometric study of the clusters in the Carina Nebula. They infer ages between less than 1 Myr and 6 Myr for Tr 14 and 16. A small number of IR excess stars were found in both clusters. In addition, new generations of stars are being born as the result of the momentum inserted into the ISM by the winds and UV radiation of the older generation of stars. In fact, Tapia et al. detected a population of 19 near-IR sources in the Car I HII region. We note that none of these objects is detected in our EPIC data. Megeath et al. (1996) and Rathborne et al. (2002) reported evidence of star formation triggered in the molecular cloud exposed to the ionizing radiation of the hot stars of the Carina Nebula. Megeath et al. detected a number of young recently formed stars deeply embedded in a molecular globule situated at the edge of the Carina nebula, whilst Rathborne et al. showed that the excitation of these globules is consistent with ultra-compact HII regions harbouring late O or very early B-type stars. None of the three near-IR sources N 1, N 3 and N 4 proposed to be associated with embedded recently born O-stars is detected in our X-ray data. More recently, Smith et al. (2003) reported the discovery of dozens of candidates of so-called proplyds in the Carina Nebula, clearly demonstrating that the formation of low and intermediate mass stars is actively proceeding. We note that none of the objects discussed by Smith et al. (2003) is detected as an X-ray source in our EPIC data.

The positions of the X-ray sources were cross-correlated with various optical and infrared catalogues. For the 2MASS point source catalogue, the optimal radius of cross-correlation was determined to be around 3.5 arcsec (Antokhin et al. 2007). One thus expects to statistically achieve 189 true and 22 spuri-

ous correlations. Fig. 5.9 illustrates the JHK colour-colour diagram of the 2MASS infrared counterparts that were detected in all three filters J (1.25 μm), H (1.65 μm) and K_s (2.17μ m) with a photometric accuracy better than $\sigma \leq 0.10$ and are single counterparts of EPIC sources within a correlation radius of 3.5 arcsec. Only a modest number of the IR counterparts in Fig. 5.9 have colours consistent with these objects displaying infrared excesses and hence being surrounded by large amounts of circumstellar material.

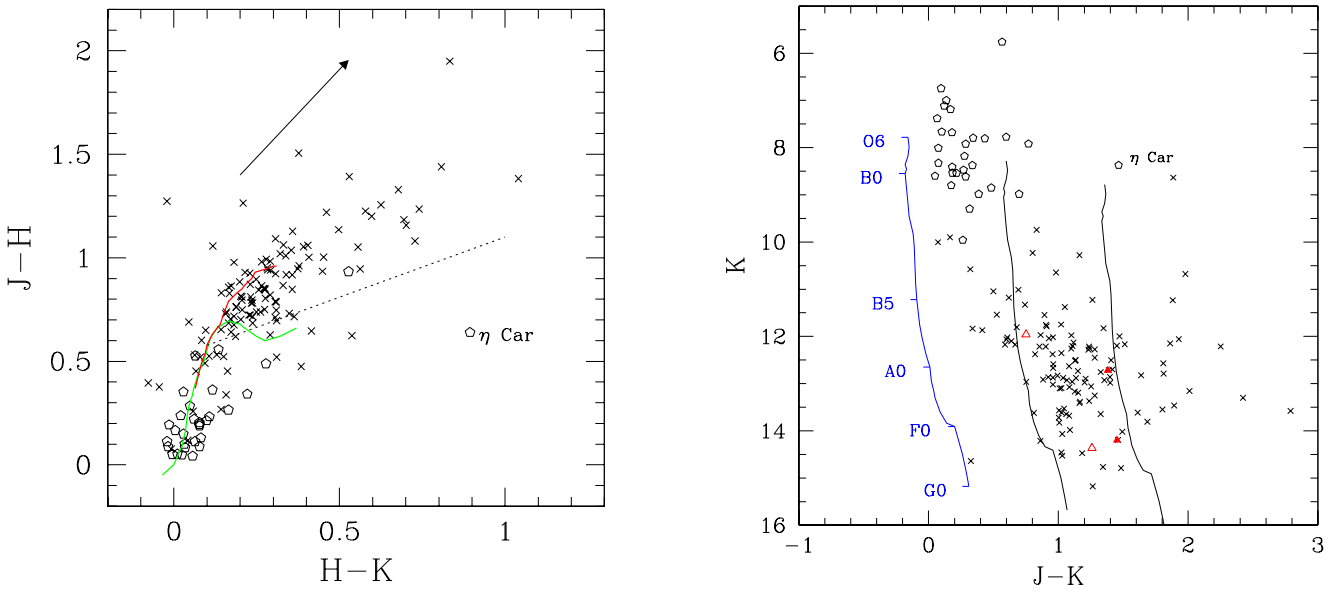

Figure 5.9: Left: JHK colour-colour diagram of the single IR counterparts falling within the 3.5 arcsec correlation radius from an X-ray source. The solid lines yield the intrinsic colours of main sequence and giant stars, whereas the reddening vector is illustrated for a visual extinction of 5 magnitudes. Bright counterparts with $J < 10.0$ are displayed by open pentagons. The crosses indicate fainter IR sources. The dotted straight line yields the locus of dereddened colours of classical T Tauri stars according to Meyer et al. (1997). Right: K vs. $J - K$ colour-magnitude diagram of the 2MASS counterparts with good quality near-IR photometry. The triangles stand for flaring X-ray sources. The locus of the un-reddened main sequence is indicated for a distance modulus of 12.0. The reddened main sequence is indicated for two different reddening values $A_V = 5$ and $A_V = 10$. From Antokhin et al. (2007).

Fig. 5.9 illustrates the K vs. $J - K$ colour-magnitude diagram of the 2MASS counterparts in the EPIC field of view. I used the March 2003 update of the colour transformations, initially derived by Carpenter (2001) and available on the 2MASS website[4], to convert the 2MASS colours and magnitudes into the homogenized JHK photometric system introduced by Bessell & Brett (1988).

Assuming all the sources are at the same distance, the sources to the right of the main sequence could indicate the existence of a population of pre-main sequence stars. The counterparts of three flaring X-ray sources are illustrated by the green triangles (open triangles stand for the two possible counterparts of source #116 of Antokhin et al. (2007), whilst the filled triangles show sources #82 and #88). The flaring X-ray sources with single 2MASS counterparts are clearly located at positions consistent with these objects being PMS stars.

[4] http://www.ipac.caltech.edu/2mass/index.html

Antokhin et al. (2007) studied the variability status of the detected X-ray sources within individual data sets using several variability tests. In three cases the observed variability has the form of a flare with very quick rise of the X-ray flux by a factor of 7-8 followed by exponential decrease to the initial quiet state. The time scale of a flare is about 1 hour. Two more sources experience somewhat similar flares but with a slower increase of the flux. Still the time scale is rather short (about 1.5–2 hours). Three objects show relatively slow and symmetrical increase and decrease of the flux on a time scale of about 1.5–4 hours. The amplitude of these flares is also smaller. Five additional objects display rather slow trends. These may be the tails (or the beginnings) of the slow flares described above. The flare frequency is clearly low: only in one case (source #116 of Antokhin et al. 2007) do we detect significant variability in 2 of 5 data sets. Further insight into the nature of the flare-type sources may be obtained from the analysis of their light curves and spectra during the flare events. The flares occur mostly in the hard energy range which is consistent with these flares being produced by the coronal activity in PMS stars. Assuming that the flaring plasma is confined in a closed coronal loop as is the case for solar flares, we can use the method proposed by Serio et al. (1991). These authors have established a simple analytical relation between the loop half-length l, the maximum temperature at the top of the loop $T_{\rm max}$ and the thermodynamic decay time τ.

$$l \sim 0.129\,\tau\,\sqrt{kT_{\rm max}}$$

where l is expressed in $R_\odot$, kT in keV and τ in ksec. This relation applies to the initial decay phase during which the emission measure decay is roughly exponential (see also Briggs & Pye 2003, Giardino et al. 2004 and Favata 2005). When the temperatures are determined from spectral fits of EPIC data, a correction has to be applied to the observed temperature to derive the maximum temperature at the top of the loop (see Giardino et al. 2004, Briggs & Pye 2003).

I have determined the $1/e$ decay times of the flares of sources # 82, 88 and 116 by a least square fit of the exponential decay phase of the observed light curves (see Fig. 5.10). The decay times derived from the fits of the different EPIC light curves agree within 20% and the results are given in Table 5.2. All three sources have rather short decay times indicating that the X-ray emitting loops must be relatively compact. Antokhin et al. (2007) fitted the spectra of the sources during the flare with an absorbed single temperature `mekal` model. The best-fit column densities of the three sources are found to be 0.26 – $0.39 \times 10^{22}\,{\rm cm}^{-2}$. The best-fit temperatures are quite high ($kT \geq 4.2\,{\rm keV}$) as expected for pre-main sequence stars. The typical flare sizes of the three sources are about one solar radius (see Table 5.2).

Table 5.2: Properties of the flaring sources: τ yields the $1/e$ decay time, $kT_{\rm obs}$ is the best fit plasma temperature during the flare and l is the loop half-length. The X-ray fluxes correspond to the spectrum during the flare.

Source	Rev.	τ (ksec)	$kT_{\rm obs}$ (keV)	l ($R_\odot$)	f_X (0.4 – 10 keV) (erg cm^{-2} s^{-1})	$J-K$	K
82	115	1.5 ± 0.3	13.3 ± 7.5	1.1 ± 0.3	9.3×10^{-13}	1.45	14.20
88	285	2.5 ± 0.6	4.2 ± 1.1	0.9 ± 0.2	2.9×10^{-13}	1.38	12.72
116	115	2.1 ± 0.4	4.6 ± 0.7	0.8 ± 0.1	9.1×10^{-13}		

In summary, the X-ray images of the Carina region are dominated by diffuse emission and strong point sources. The brightest point sources are clearly associated with the hot massive stars in the various clusters that populate this region. The vast majority of the fainter sources are likely to be low-mass stars, either foreground coronal sources or pre-main sequence stars in the Carina complex. The pre-main

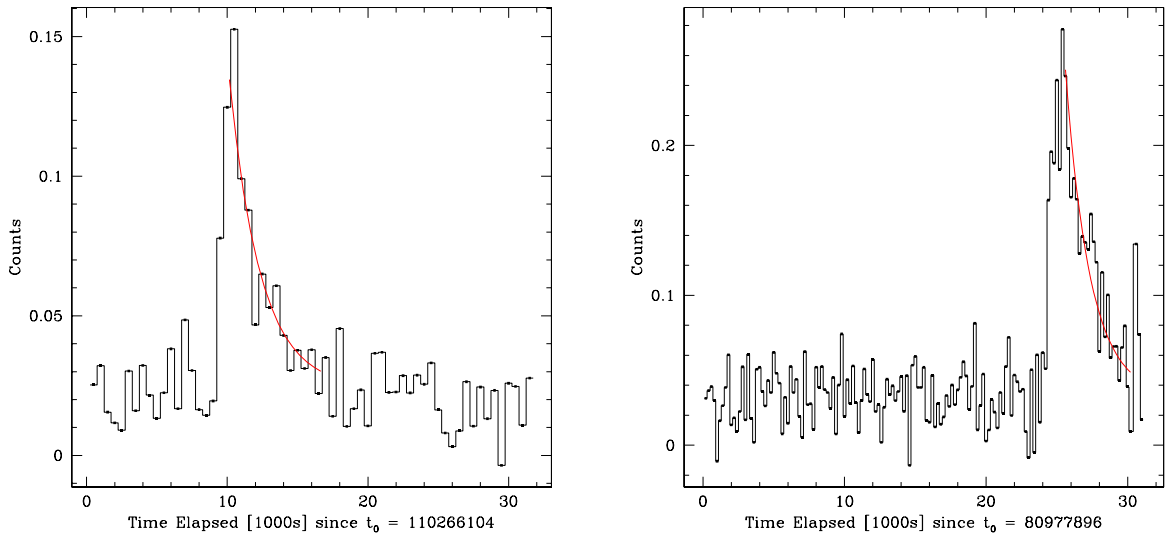

Figure 5.10: Background-corrected EPIC-pn light curves (0.4 – 10 keV energy range) of the flares of sources #88 (left) and #116 (right). The time is shown relative to the start of the exposure. The continous lines show the fits of exponential decays that yield the parameters in Table 5.2. From Antokhin et al. (2007).

sequence objects are likely weak-line T-Tauri stars without strong evidence for circumstellar material. Compared to some other open clusters such as NGC 6231 (see Sect. 5.6), there are less PMS candidates detected. This could be due to a lower detection efficiency (due to the strong diffuse emission) and the larger distance of the Carina complex compared to NGC 6231.

5.6 NGC 6231

NGC 6231 - at the core of the Sco OB1 association - is a very young open cluster, rich in massive O-type stars (Sana 2005). The early-type star population of this cluster contains an amazing fraction of binary or multiple systems, most of which are concentrated in its core. Using $UBV(RI)_C H\alpha$ photometry, Sung et al. (1998, hereafter SBL) found only 12 PMS objects (and 7 PMS candidates) brighter than $V = 17$ and displaying Hα emission. However, there could be a number of PMS stars without Hα emission. With optical photometry only, these would be very difficult to distinguish from field stars lying to the right of the cluster main-sequence.
Sana et al. (2006a) established a catalogue of X-ray sources in the NGC 6231 field based on a set of *XMM-Newton* observations with a total integration time of 120 ksec (see a combined EPIC-MOS image in Fig. 5.11). This catalogue was used by Sana et al. (2007) to analyse the properties of the X-ray sources with faint optical counterparts and I describe here my contributions to this work and its main results.

Although the combined EPIC field of view extends over a wider area than the actual field investigated by Sung et al. (1998), Sana et al. (2007) restrict themselves to the sources with counterparts in the SBL catalogue, because this catalogue provides by far the deepest optical investigation of the NGC 6231 field. 449 X-ray sources have an optical counterpart in the catalogue of Sung et al. (1998) extended down to $V = 21$ (by H. Sung). The V vs. $B - V$ and V vs. $V - I_C$ colour-magnitude diagrams of the optical

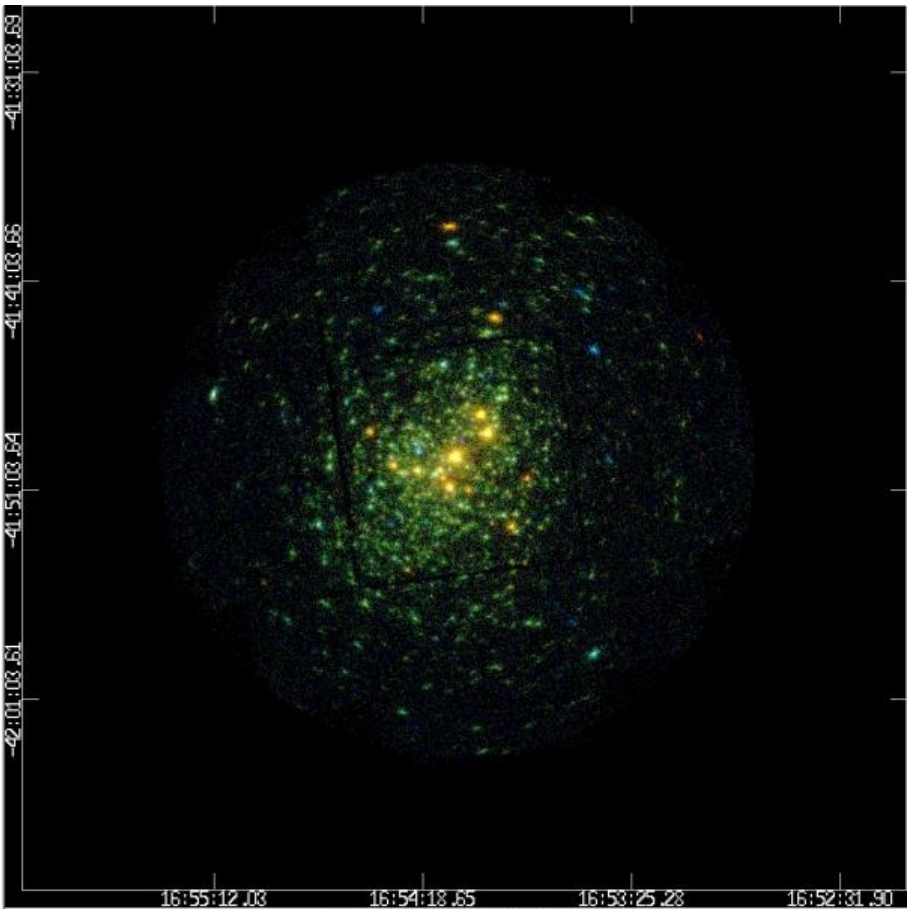

Figure 5.11: Three colour EPIC-MOS image of the NGC 6231 cluster (Sana et al. 2006a). The red, green and blue colours stand respectively for the 0.5 – 1.0, 1.0 – 2.5 and 2.5 – 10.0 keV energy ranges. This image was chosen to illustrate the cover page of issue 454 of the Astronomy & Astrophysics journal.

counterparts are shown in Fig. 5.12. The bulk of the objects in this diagram are rather faint stars mostly located to the right of the main-sequence.

To identify Hα emitting stars among the X-ray selected objects, I compare the $R-H\alpha$ index to its value for main sequence stars using the relation between the $R-H\alpha$ and $V-I_C$ indices for main sequence stars proposed by Sung et al. (1997) and accounting for the effect of cluster reddening on the $V-I_C$ index. A star is considered an Hα emitter if $\Delta(R-H\alpha) = (R-H\alpha) - (R-H\alpha)_{\rm MS} \geq 0.21$ mag, whereas it is considered an Hα emission candidate if $0.12 \leq \Delta(R-H\alpha) \leq 0.21$. About one quarter of the X-ray selected objects are either confirmed or potential Hα emission objects (Fig. 5.13, left panel). This large number of Hα emission candidates compared to the original results of SBL is mainly due to the fact that the photometry used here extends down to much fainter magnitudes (Fig. 5.13, right panel).

Assuming that all X-ray selected stars are located at the distance of the cluster (DM = 11.0) and are all subject to the same reddening ($A_V = 1.538$, Sung et al. 1998), one can build the Hertzsprung-Russell diagram of these EPIC sources using effective temperatures and bolometric corrections interpolated from the dereddened $V-I_C$ colour indices for main sequence stars of spectral types B0 to M6 as tabulated by Kenyon & Hartmann (1995). Figure 5.14 compares the location of the X-ray selected objects to the

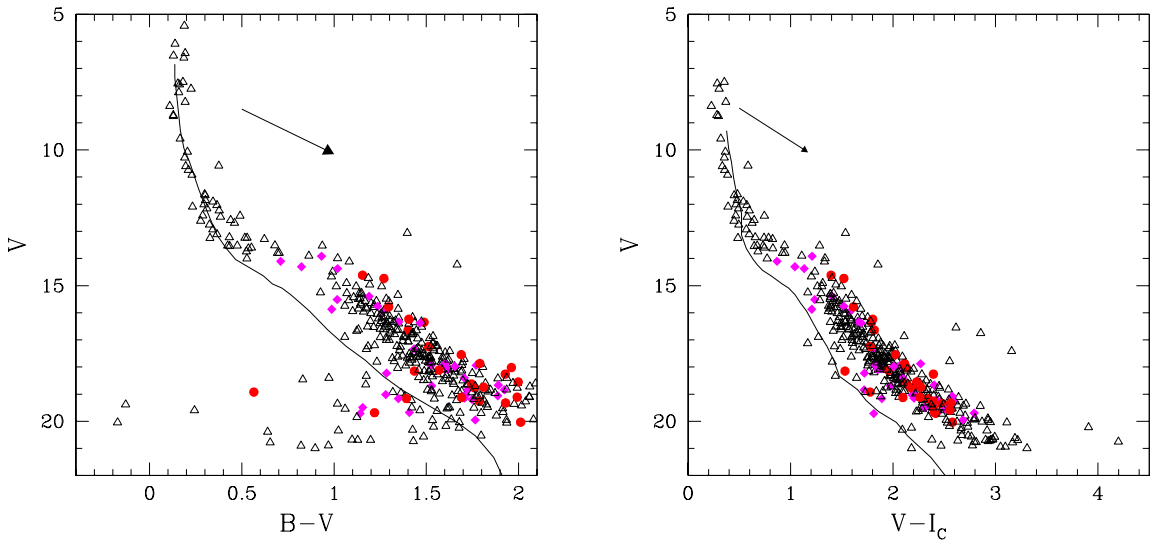

Figure 5.12: Colour-magnitude diagrams of the X-ray sources with an optical counterpart in the SBL catalogue. Filled dots, filled diamonds and open triangles indicate respectively Hα emitting stars, Hα candidates and stars with no evidence for emission (see Fig. 5.13). The reddening vector with $R_V = 3.3$ and $E(V - I_C)/E(B - V) = 1.365$ (Sung et al. 1998) is indicated and the solid line shows the ZAMS relation taken from Schmidt-Kaler (1982) shifted by a distance modulus DM = 11.0 and reddened with $E(B - V) = 0.466$ (Sung et al. 1998). From Sana et al. (2007).

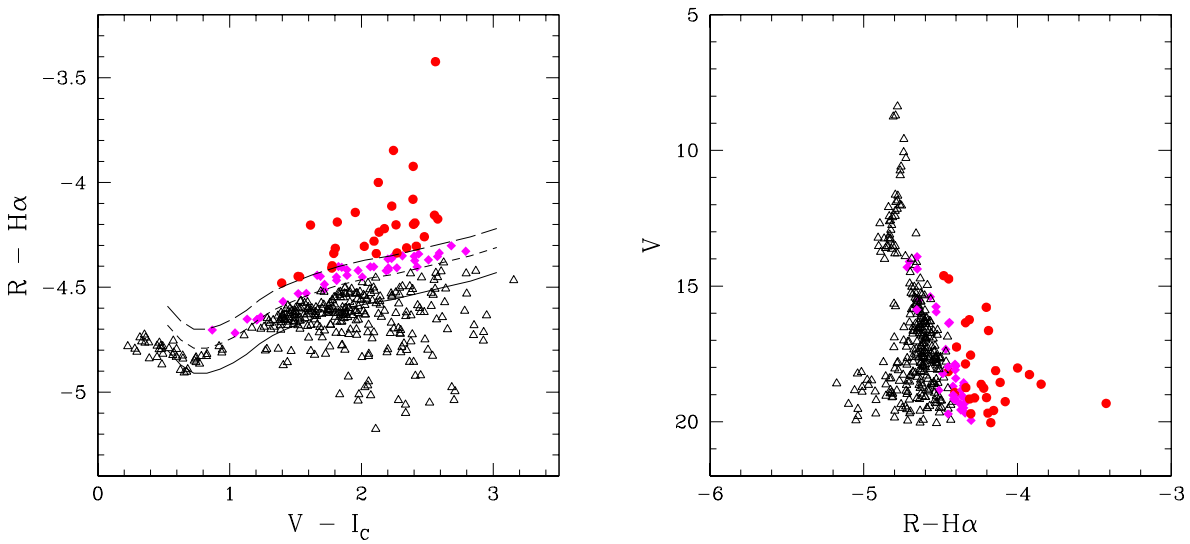

Figure 5.13: Left: $R - H\alpha$ as a function of $V - I_C$. The symbols have the same meaning as in Fig. 5.12. The solid line yields the $R - H\alpha$ versus $V - I_C$ relation for main sequence stars taken from Sung et al. (1997) and reddened with the average reddening of NGC 6231. The short- and long-dashed lines yield respectively the thresholds for Hα emission candidates and Hα emitters (see text). Right: V-magnitude as a function of $R - H\alpha$ for the SBL optical counterparts of our EPIC sources. From Sana et al. (2007).

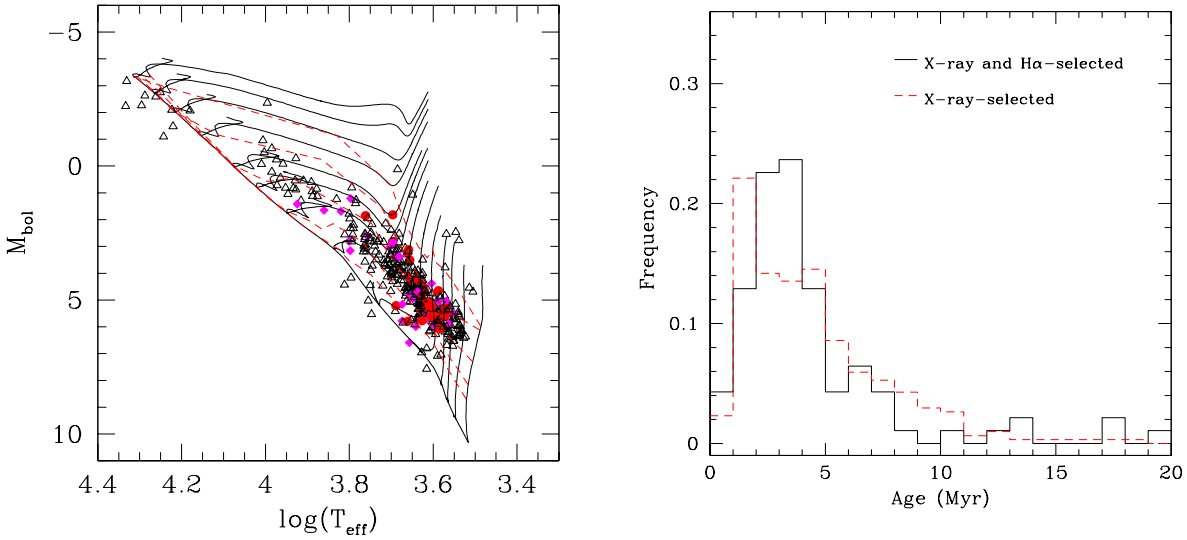

Figure 5.14: Left: Hertzsprung-Russell diagram of the EPIC sources with optical counterparts in the SBL catalogue. Evolutionary tracks from Siess et al. (2000) for masses of 0.2, 0.3, 0.4, 0.5, 0.7, 1.0, 1.5, 2.0, 2.5, 3.0, 4.0, 5.0, 6.0 and 7.0 $M_\odot$ are overplotted. The symbols have the same meaning as in Fig. 5.12. The thick solid line shows the ZAMS, while the dashed lines correspond to isochrones for ages of 0.5, 1.5, 4.0, 10.0 and 20.0 Myr. Right: distribution of the ages of X-ray selected PMS objects as interpolated from the isochrones. PMS candidates with $\Delta(R - H\alpha) \geq 0.12$ are indicated by the solid line, whilst those with $\Delta(R - H\alpha) < 0.12$ are indicated by the dashed line. The total numbers of objects with $\Delta(R - H\alpha) \geq 0.12$ and $\Delta(R - H\alpha) < 0.12$ are respectively 93 and 303. From Sana et al. (2007).

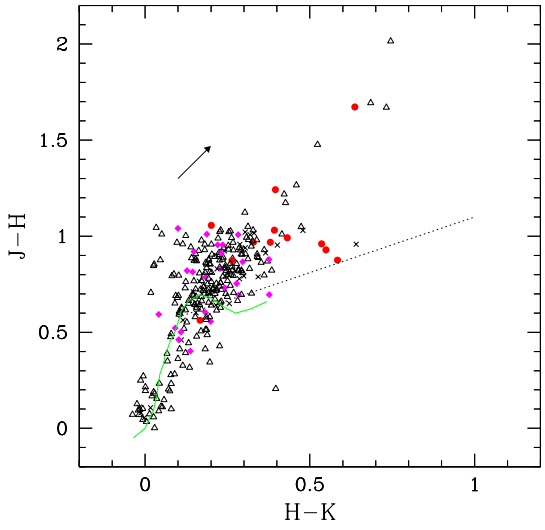

Figure 5.15: JHK colour-colour diagram of the 2MASS counterparts with good quality near-IR photometry of the X-ray sources in the EPIC field of view around NGC 6231. The heavy solid line yields the intrinsic colours of main sequence stars following Bessell & Brett (1988), whereas the reddening vector is illustrated for $A_V = 1.538$ and adopting the reddening law of Rieke & Lebofsky (1985). The crosses stand for 2MASS sources having no counterpart in the SBL catalogue (mainly because they fall outside the field of view investigated by Sung et al. 1998). The other symbols have the same meaning as in Fig. 5.12. The dotted straight line yields the locus of dereddened colours of classical T Tauri stars according to Meyer et al. (1997). From Sana et al. (2007).

pre-main sequence evolutionary tracks of Siess et al. (2000) for $Z = 0.02$ and without overshooting (note that these evolutionary models include neither rotation nor accretion).

Most of the X-ray selected, optically faint objects ($V \geq 14$) fall between the PMS evolutionary tracks

for stars of masses in the range 0.3 to 3.0 $M_\odot$. The majority of these objects should have ages ranging from 1 to 10 Myr (see Fig. 5.14). As for NGC 6530, there does not seem to be a large age difference between those stars displaying Hα emission and those without, though Hα emitters might be slightly older on average. Hα emission seems restricted to X-ray selected stars with masses below about 2.5 $M_\odot$. This is again reminiscent of the situation in NGC 6530.
Binarity affects the distribution of a coeval population of PMS stars in the Hertzsprung-Russell diagram by introducing a band shifted upwards from the true isochrone (Siess et al. 1997) leading to an underestimate of the actual age. Palla (2002) evaluated the average age discrepancy for a realistic distribution of binary mass ratios, finding that age estimates not accounting for binarity can be off by a factor ~ 1.5. Therefore, binarity should not have too large an impact on our age estimates above. In any case, binarity cannot explain the tail of the age distributions towards older ages (see Fig. 5.14).

A total of 384 EPIC sources in the field of view of NGC 6231 have a counterpart in the 2MASS point source catalogue (Cutri et al. 2003). Among these, only 295 have good quality flags (A, B, C or D) for the measurements of all three individual near-IR magnitudes. Their location is consistent with slightly reddened main-sequence or giant stars (see Fig. 5.15). Only a couple of objects display evidence for a moderate IR excess and only about ten objects display strongly reddened IR colours.

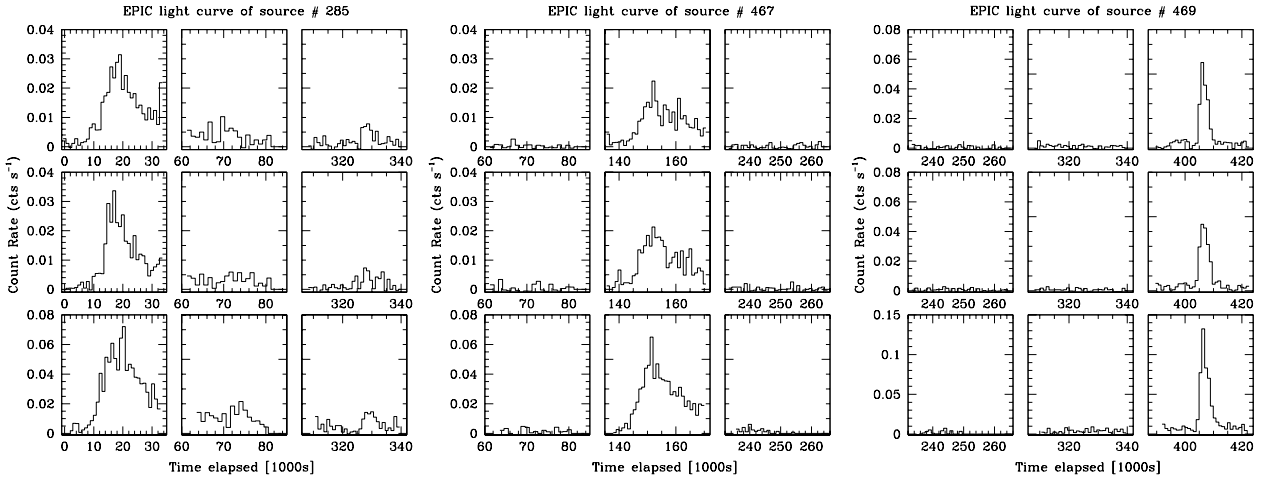

Figure 5.16: EPIC-MOS 1 (top panels), MOS 2 (middle panels) and pn (lower panels) light curves (in the 0.5 – 10 keV energy range) of three flaring sources in NGC 6231. Source #285 (left panel) is shown during observations 1, 2 and 5 (from left to right). Source #467 (middle panel) is shown during observations 2, 3 and 4, whilst the light curves of source #469 (right panel) are shown during observations 4, 5 and 6. The time is given in ksec from the beginning of observation 1. From Sana et al. (2007).

A number of sources display flares in their background-corrected X-ray light curves. Various types of behaviours have been observed (see Fig. 5.16). Most of the flares exhibit an impulsive rise of the source X-ray luminosity within a few ksec followed by a slower decay. Most of the flaring sources display an X-ray spectrum that is best represented by a single temperature `mekal` model with fit temperatures of $kT \geq 3.4$ keV and moderate column densities ($N_H \leq 0.36 \times 10^{22}$ cm^{-2}, in reasonable agreement with the average N_H estimated from the cluster reddening). For the majority of the non-flaring bright X-ray sources, a second temperature is needed to model the spectra. Most of the non-flaring objects have moderate hydrogen column densities (similar to those of the flaring sources) and temperatures of order

0.7 and 2.5 – 3.5 keV for the soft and hard component respectively. The flaring sources thus appear to have significantly harder spectra than the non-flaring objects. Some quantitative insight into the flare events can be obtained from the same technique as in Sect. 5.5. Table 5.3 yields the properties of the flaring X-ray sources with a sufficiently large count rate to study their spectrum and light curve. All flaring sources have rather large temperatures during the flare. The decay times range from about 2 ksec to 16 ksec and the loop half-lengths are in the range 0.3 to 2.4 $R_\odot$. Most loops appear rather compact ($l \leq R_*$) except perhaps for source #467.

Favata (2005) notes that while most flaring structures are indeed relatively compact, extremely slowly decaying flares have been detected in some young stellar objects (with $\tau \sim 40$ ksec) which correspond to rather large loops ($l \sim 14\,R_\odot$). Favata (2005) accordingly suggests that the magnetic structures that produce these large loops link the star to the circumstellar disk. The present dataset is not suited to clearly identify such slowly decaying flares. In this context, it is also interesting to note that among the five flaring objects in Table 5.3 for which a $\Delta(R-H\alpha)$ value can be computed, only source #467 shows a strong Hα emission. Further evidence for circumstellar material around this source comes from its near-IR excess. From Table 5.3 it appears that #467 is also the source with the largest loop half-length ($l \sim 1.4\,R_*$) in our sample.

Table 5.3: Properties of the flaring sources: τ yields the $1/e$ decay time, $kT_{\rm obs}$ is the best fit plasma temperature during the flare (a value between brackets correspond to the hottest component of a 2-T fit) and l is the loop half-length. For comparison the stellar radii computed from the effective temperatures and bolometric magnitudes are provided in the sixth column. Column 7 indicates the value of the $R-H\alpha$ index compared to the value of this index for main sequence stars with the same intrinsic $V-I_C$ (whenever available). Finally, the last two entries correspond to the JHK colours derived from the 2MASS measurements.

Source	Obs	τ (ksec)	$kT_{\rm obs}$ (keV)	l ($R_\odot$)	R_* ($R_\odot$)	$\Delta(R-H\alpha)$	$J-H$	$H-K$
#48	4	8.8	3.43	1.0			.641	.215
#100	3	5.3	4.32	0.7	1.3			
#204	4		(3.64)		2.6	.03	.620	.171
#254	5	7.3	(3.69)		3.7	.08	.388	.067
#285	1	9.4	4.44	1.2			.788	.343
#304	2	5.5	(8.2)		1.6		.204	.071
#442	1	7.6	4.04	0.9	0.8			
#467	3	16.0	5.70	2.4	1.7	.45	.991	.432
#469	6	2.1	4.17	0.3	2.1	$-.04$		
#583	4	5.2	5.58	0.8			.460	.110

Using the bolometric magnitudes derived from the SBL photometry and the vignetting and background corrected EPIC count rates determined by the source detection algorithm, Sana et al. (2007) have built an empirical $L_{\rm X}/L_{\rm bol}$ relation for the sources in the NGC 6231 field. The EPIC count rates were converted into X-ray luminosities in the 0.5 – 10 keV range assuming that the sources have an absorbed optically thin thermal plasma spectrum with a temperature of 1 keV and $N_{\rm H} = 5.8 \times 10^{21} \times \overline{E(B-V)} = 2.7 \times 10^{21}$ cm^{-2} (Bohlin et al. 1978). Adopting a temperature of 2 keV (more typical of the spectra of the brightest sources) would only slightly increase this conversion factor (by 14%). Finally, the unabsorbed fluxes were converted into luminosities, assuming that all sources are members of NGC 6231 ($DM =$

11.0). Figure 5.17 displays the resulting $\log L_{\rm X}/L_{\rm bol}$ as a function of $M_{\rm bol}$. This value increases from about -7 for B0 stars (the hottest objects plotted in this figure) to almost -2 for the lower mass objects. A similar trend was already observed in NGC 6530 (Rauw et al. 2002d).
Of course the results in Fig. 5.17 could be somewhat biased by the fact that some of the sources are detected only during their flaring activity. The same procedure was repeated for the brighter sources discussed hereabove. In the right panel of Fig. 5.17, we distinguish between the flaring and non flaring sources. The average luminosity during a flare can reach up to 3×10^{32} erg s^{-1} and $\log L_{\rm X}/L_{\rm bol}$ can temporarily increase to values as large as -1.00. On the other hand, the brighter steady sources also display rather large X-ray luminosities, up to $\sim 4 \times 10^{31}$ erg s^{-1}, as well as large $\log L_{\rm X}/L_{\rm bol}$, up to ~ -2.4. Therefore, even non-flaring PMS sources in NGC 6231 can be rather X-ray bright.

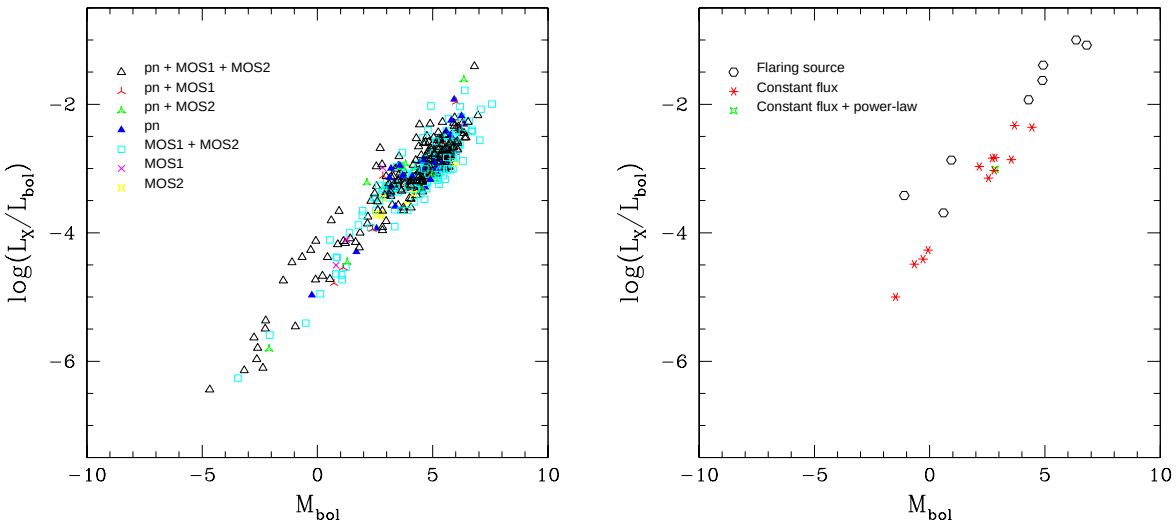

Figure 5.17: Left: logarithm of $L_{\rm X}/L_{\rm bol}$ as a function of the bolometric magnitude for the EPIC sources with optical counterparts in the SBL catalogue. $L_{\rm X}$ refers to the X-ray luminosity in the energy range 0.5 to 10 keV. The various symbols correspond to different combinations of EPIC instruments used in the determination of the X-ray luminosity (see the insert in the upper left corner). Right: $\log L_{\rm X}/L_{\rm bol}$ as a function of the bolometric magnitude for those EPIC sources with optical counterparts in the SBL catalogue and for which a detailed modelling of the spectra was possible (see Sana et al. 2007). Asterisks correspond to sources that have a rather constant flux during the six observations, whereas hexagons stand for flaring sources during the flare. A few constant sources display spectra that are apparently better fitted by a power-law model than the thermal plasma models used for the other objects shown here. From Sana et al. (2007).

In summary, the typical spectra of the optically faint X-ray sources, their flaring behaviour, their X-ray luminosities as well as the location of their optical counterparts in the HR diagram indicate that these sources form a population of PMS stars with masses in the range 0.3 to 3.0 $M_\odot$. Compared to previous optical investigations of the cluster (Sung et al. 1998), the number of PMS stars is increased by a factor 20 at least. An interesting feature is the age spread among the low-mass PMS objects ($\sim$ 11 Myr) that exceeds the main sequence lifetime of the massive O stars in the cluster. This feature was already noted by previous authors. For instance, Raboud et al. (1997) obtained photometry of NGC 6231 in the Geneva system: fitting isochrones to the main sequence and post-main sequence stars believed to be single, these

authors derived an age between 3.2 and 4.5 Myr for the more massive stars, whilst they noted that the PMS stars detected in their observations were mostly older than 3.2 Myr and had ages up to 10 Myr. A similar situation was found by Sung et al. (1998) who derived an age of 2.5 – 4 Myr for the massive stars in the cluster, while they found an age spread of 11 Myr in the PMS objects. Raboud et al. (1997) accordingly suggested that there was a continuous low-mass star formation activity in NGC 6231 at previous times, which came to an end about 3.2 – 4.5 Myr ago when the massive O stars of the cluster formed during a nearly coeval burst. Our results confirm this picture. The age distribution of X-ray selected low-mass stars indicates that low-mass star formation in NGC 6231 started about 15 Myr ago and culminated in a starburst-like event about 2 – 3 Myr ago when the bulk of the low-mass PMS stars as well as the massive cluster members formed. Then, about 1 Myr ago, the formation of stars in NGC 6231 came to end rather abruptly. There is no evidence for a spatial age gradient that could point towards a sequential star formation process.

5.7 Concluding remarks on star formation activity in young clusters

The *XMM-Newton* observations of spatially resolved young open clusters discussed in this section have revealed the existence of an important population of low- and intermediate-mass pre-main sequence stars. In most cases, these objects were found to be weak-line T-Tauri stars. This suggests that these objects might be X-ray brighter than classical T-Tauri stars. However, this could also be a selection effect if the population of pre-main sequence stars in these clusters were dominated by weak-line T-Tauri stars. Further investigations (including especially optical spectroscopy to search for Hα emission) are needed to clarify this issue. It would be interesting to eventually compare this result with the situation in low-mass star forming regions of similar age. Indeed, in the clusters investigated here, the nascent stars are embedded in the ionizing radiation field of the hot early-type stars. This effect might lead to photo-evaporation of accretion structures and might eventually bring the star formation process to an end. Indeed, whenever it was possible to derive the ages of the PMS population, it was found that the star formation activity had peaked during some kind of starburst event when the current population of early-type stars was formed and slowly declined afterwards. There are several reasons why this situation is expected: the formation of massive stars will use up a large fraction of the gas reservoir and the ionizing radiation and the outflow from these objects will erode the molecular cloud. Nevertheless, the action of the massive stars on the periphery of the molecular cloud can also trigger second-generation star formation.
An important consequence of the ubiquity of X-ray bright PMS stars in young open clusters is that spatially unresolved young stellar clusters might display an X-ray halo due to the presence of a population of PMS stars. This could actually contribute to explain part of the apparently diffuse X-ray emission seen in some Magellanic Cloud clusters (e.g. N11 in the LMC, Nazé et al. 2004).

Despite the substantial progresses achieved over the last decades, many details of the formation of stars in various environments (clusters vs. the field, in the vicinity of massive stars or far away from their ionizing radiation,...) are still pretty much open issues. Star formation is thus one of the primary science goals of the far-infrared and millimeter observatories *Herschel* and *ALMA* as well as of the second generation *VLTI* instruments. Substantial progress in this field is thus expected from these facilities. Thanks to its unique capabilities (wide field of view, large collecting area and high-resolution spectroscopic capabilities), *XMM-Newton* has the potential to contribute quite significantly to this endeavour. Combining the spectroscopic diagnostics from *Herschel* and *XMM-Newton* will give unprecedented insight into the

accretion and outflow processes and on the role played by magnetic fields in these processes. Investigating star formation in clusters will be of primary importance because (1) most stars actually form in clusters, (2) this is the key to understand the origin of the initial mass function and (3) clusters are the places where the most massive stars form. The wide field of the EPIC cameras onboard *XMM-Newton* make this the ideal instrument to study star formation processes in open clusters with special attention for triggered star formation. In conjunction with *Herschel* and *ALMA*, *XMM-Newton* will allow to probe successive generations of stars: young massive stars and low-mass pre-main sequence stars are very bright X-ray sources whilst the triggered, deeply embedded next generation stars are best observed with *ALMA* and *Herschel*. Last but not least, the winds and UV radiation of the early-type stars as well as their X-ray emission and that from the PMS stars should impact on the formation of planets around the low-mass stars. All these questions will have to be addressed with the help of the new long-wavelength facilities that will become available at the 2010 Horizon.

Chapter 6

Concluding remarks

Maintenant le principal est fait.
Je tiens quelques évidences dont je ne peux me détacher.
Ce que je sais, ce qui est sûr, ce que je ne peux nier,
ce que je ne peux rejeter, voilà ce qui compte.

Albert Camus, *Le mythe de Sisyphe*

Da steh ich nun, ich armer Tor!
Und bin so klug als wie zuvor;

Johann Wolfgang von Goethe, *Faust*

In this habilitation thesis I have presented my main contributions to the research on massive stars over the last decade. Systematic investigations of specific objects allowed to address some key questions of this field. However, as is always the case in scientific research, the answers that have been obtained also raise new questions that will have to be solved over the forthcoming years. In my opinion, some of the most important issues are:

- Why do certain open clusters display a binary fraction of 70% among their massive star population, whilst other clusters harbour almost no early-type binaries? In other words, what is the physical parameter that governs the formation of multiple systems among the most massive stars in a starburst event? Systematic monitorings (both spectroscopic and photometric) of the O-star population in a large sample of young open clusters need to be performed to answer this question.
- Are the shocks in colliding wind systems collisionless and is the X-ray plasma out of equilibrium? High resolution X-ray spectroscopy with good signal-to-noise of a significant sample of early-type stars should help clarify this issue. This will likely have to await the next generation of high-throughput X-ray observatories.
- What are the mass loss rates of early-type stars and what is the morphology of the stellar winds? There is mounting evidence that the mass loss rates of O-type stars have previously been overestimated e.g. due to the neglect of clumping. The actual structure of the winds remains unknown: are we dealing with small scale clumps or rather with large-scale features resulting in a highly porous wind? This question has potentially important consequences. For instance, in a porous wind the

optical depth at radio and X-ray wavelengths could be substantially reduced. While this could be helpful to explain some of the features discussed in this work (e.g. the detection of the non-thermal radio emission from Cyg OB2 #8a), it has to be stressed that such a conclusion would cast doubt on the 'standard models' for X-ray emission in single O-type stars and non-thermal radio emission. In fact, if the winds are indeed much more transparent to these radiations, the paradigm that X-rays and synchrotron radio emission produced in the lower levels of a stellar wind cannot escape would break down. Therefore, the most popular argument against a base corona as the origin of the intrinsic X-ray emission and the key argument for non-thermal radio emission being solely associated with binary systems would no longer be valid.

Answering the questions above requires both the use of new observing facilities and the intensive use of existing ones. For instance, the spectroscopic monitoring of many stars in open clusters can ideally be done with high-resolution optical multi-object spectrographs, such as those available on the VLT. At the same time, such studies are difficult to perform because they require regular monitoring over rather long intervals of time, which is usually considered incompatible with the high pressure on telescopes of the 8 m class. It is therefore of vital importance to keep a sufficient number of smaller telescopes available that allow to perform this sort of investigation, maybe with a somewhat lower efficiency, but without being subject to such a large pressure and, hence, retaining a higher flexibility. A similar situation holds for photometric monitoring campaigns (see the example of WR 20a described in this work). A small (~ 0.5 m) optical reflector operated by the astrophysics groups of the Liège University to undertake such intensive campaigns would certainly be an interesting starting point.

The results presented in this work, were based on a large quantity of data obtained since the mid 1990s with a number of observing facilities, either ground-based (telescopes in the 0.5 – 4 m class at ESO (La Silla), Observatoire de Haute Provence, Cerro Tololo Interamerican Observatory...) or space-borne (ESAs *XMM-Newton* and *INTEGRAL* satellites, *ASCA*, *ROSAT*,...). To some extent, this period was a kind of "golden age" for research in this field of astrophysics. Today it seems to me that astrophysics has reached a turning point with both exciting perspectives and significant risks at the horizon of the second decade of this century.

Among the exciting prospectives, I would like to emphasize the forthcoming ESA missions *Herschel* and *GAIA*. The first will provide an unprecedented view of the Universe in the far infrared and will help complete the multi-wavelength investigation of massive stars. The second mission will determine the distances and kinematics of a huge number of stars in our Galaxy, allowing, among many other things, a better calibration of the absolute magnitudes and intrinsic properties of early-type stars. On a longer time scale, the *Cosmic Vision 2015 - 2025* programme of the European Space Agency will hopefully allow to build and operate the next generation X-ray telescope *XEUS* which should be over a hundred times more sensitive than *XMM-Newton*. There is no doubt that these future missions will lead to exciting new discoveries and attract many young people into the fascinating field of astrophysics.

Among the potential risks, I would like to point out the editorial policies of some scientific journals as well as the financial constraints on science programmes. Concerning the first point, the increasing importance of the citation index, which is now considered as a major criterion for the quality of a journal, led several editors to adopt a harsh policy with respect to papers that are not dealing with the most "fashionable" topics. Some of these papers are actually rejected by the editors without even having them submitted to a competent referee or substantial shortenings of the papers are requested, regardless of

the potential loss in the scientific content. The consequences are that these research fields could lose their (financial) support and eventually disappear despite their interest. Concerning the second point, the inflation of the costs of the large infrastructures, that are needed to do high-quality science (both from space and from the ground), translates into severe financial constraints. This in turn leads to the setting-up of committees that are asked to take strategic decisions for the future. Again, the obvious threat is that these decisions will be guided by criteria that may be detrimental to some parts of astrophysical research. Often it is the cheapest activities (e.g. operation of small telescopes on the ground, operations of mature space observatories,...) that suffer the most in such exercises.

Our society has to make a choice with respect to the spendings for scientific research. For instance, the annual budget of the ESA science programme amounts to roughly one tenth of the budget available to NASA for their scientific programme. To give another amazing comparison, the *annual* ESA science budget is slightly less than twice the *daily* cost of the present war in Iraq (accounting only for the costs to the budget of the US defense department)! It is the role of the European astronomical community to stand up and convince the politicians that doing science is not a waste of money. Indeed, there remain so many open questions to be answered...

Appendix A

X-ray line profiles from single O-type stars

A.1 Assumptions

To simulate the X-ray line profiles produced in the expanding wind of a single O-type star, I closely follow the approach outlined by Kramer et al. (2003). The main assumptions are:

- the X-ray emission originates from material distributed throughout a spherical wind, above a radius $r \geq R_0 > R_*$. The origin of the X-ray emission (wind-embedded shocks or an extended corona) is not important in this *exospheric* approach.
- the hot (X-ray emitting) plasma follows the bulk motion of the wind.
- 'non-thermal'[1] Doppler broadening due to macroscopic motion provides the main source of line broadening. The latter assumption deserves some considerations. For instance in the case of an oxygen line arising in a plasma at 6 MK (i.e. $kT = 0.5$ keV), the FWHM due to thermal broadening amounts to $2\sqrt{\frac{2\ln 2\, kT}{m_A}} \simeq 130\,\mathrm{km\,s^{-1}}$ (where m_A is the mass of the atom under consideration) which corresponds to about 6% of typical values of v_∞.
- the opacity κ_λ does not vary as a function of radius r. In a stellar wind, the material is ionized by the photospheric UV radiation and the degree of ionization can therefore vary with radius. Since the opacity depends upon the ionization, neutral material being more opaque than ionized gas, the opacity could be somewhat larger in the outer regions of the wind (e.g. Nazé 2003). Adopting a constant value for κ is equivalent to adopting an average opacity.

The line emissivity is assumed to scale as $\epsilon \propto \rho^2\, r^{-q}$. The ρ^2 dependence reflects the fact that the emission results from recombination processes whilst the r^{-q} term accounts for a radial dependence of the filling factor of the X-ray plasma.
At a wavelength λ with $\frac{\lambda}{\lambda_0} - 1 = \frac{v(r)\,\cos\theta}{c}$, the elementary increase of the line intensity can be expressed as

$$dI(\lambda) = \frac{K\, r^{-(q+4)}}{(1 - \frac{R_*}{r})^2}\, \exp\left[-\tau_\lambda(r,\theta)\right] dV \tag{A.1}$$

where K is the emissivity, $dV = r^2\, \sin\theta\, d\theta\, d\phi\, dr$, r_X is the radius where the Doppler-shifted wavelength of the X-ray line equals λ and $\tau_\lambda(r,\theta)$ is the tangential optical depth evaluated along the line of sight from r_X outwards (see below).

[1] Note that the meaning of the term 'non-thermal' in this context has nothing to do with the synchrotron and inverse Compton emissions discussed in Chapter 3.

A.2 Radial and tangential optical depth

For a homogeneous, spherically symmetric wind of mass loss rate $\dot{M}$ and a 'standard' velocity law $v(r) = v_\infty \left(1 - \frac{R_*}{r}\right)^\beta$, the radial optical depth at wavelength λ from a radius R outwards is given by

$$\tau_\lambda = \int_R^\infty \kappa_\lambda \, \rho \, dr \tag{A.2}$$

κ_λ is the opacity at wavelength λ, whilst $\rho = \frac{\dot{M}}{4\,\pi\,r^2\,v(r)}$ is the wind density at radius r. If $R = R_1$ is the radius of radial optical depth unity, then

$$\int_{R_1}^\infty \frac{\kappa_\lambda \, \dot{M}}{4\,\pi\,v_\infty} \frac{dr}{r^2 \left(1 - \frac{R_*}{r}\right)^\beta} = 1 \tag{A.3}$$

Let us define the characteristic optical depth at wavelength λ as $\tau_{\lambda,*} = \frac{\kappa_\lambda \, \dot{M}}{4\,\pi\,v_\infty\,R_*}$. Then, assuming $\beta = 1$, Eq. (A.3) becomes

$$\int_{R_1/R_*}^\infty \frac{du}{u\,(u-1)} = \tau_{\lambda,*}^{-1} \tag{A.4}$$

where $u = \frac{r}{R_*}$. The integration of the latter equation yields

$$\ln \frac{R_1/R_*}{R_1/R_* - 1} = \tau_{\lambda,*}^{-1} \tag{A.5}$$

which finally leads to a very simple expression for the radius of optical depth unity:

$$\frac{R_1}{R_*} = \frac{1}{1 - \exp\left(-1/\tau_{\lambda,*}\right)} \tag{A.6}$$

For $\beta = 2$ and 3, the radius of optical depth unity can be written $\frac{R_1}{R_*} = \tau_{\lambda,*} + 1$, $\frac{R_1}{R_*} = 1 + \frac{1}{\sqrt{1+2/\tau_{\lambda,*}}-1}$ respectively.

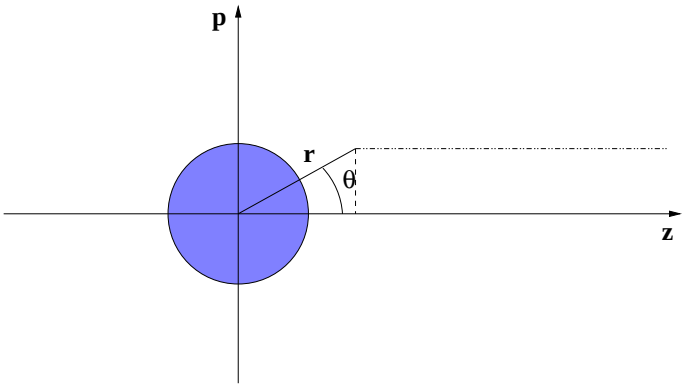

Figure A.1: Schematic view of the coordinates used here. The observer is located at $z \rightarrow +\infty$. The impact parameter p and the z coordinates are given by $p = r\,\sin\theta$ and $z = r\,\cos\theta$.

The tangential optical depth evaluated along the line of sight from r_X outwards can be written

$$\tau_\lambda(r,\theta) = \tau_{\lambda,*}\, R_* \int_{r_X \cos\theta}^{\infty} \frac{dz}{r^2\,(1-\frac{R_*}{r})} \tag{A.7}$$

Here $r^2 = (p^2 + z^2)$ and p is the impact parameter (see Fig. A.1). For $\beta = 1$, this then yields

$$\begin{aligned}
\tau_\lambda(r,\theta) &= \tau_{\lambda,*}\, \ln \frac{r_X/R_*}{r_X/R_* - 1} \quad \text{for} \quad p = 0 \\
&= \frac{\tau_{\lambda,*}}{\sqrt{1-p^2/R_*^2}}\, \ln \frac{\alpha - x_2}{\alpha - x_1} \quad \text{for} \quad 0 < p/R_* < 1 \\
&= \frac{2\,\tau_{\lambda,*}}{\alpha - 1} \quad \text{for} \quad p/R_* = 1 \\
&= \frac{2\,\tau_{\lambda,*}}{\sqrt{p^2/R_*^2 - 1}} \left(\frac{\pi}{2} - \arctan \frac{\alpha\, p/R_* - 1}{\sqrt{p^2/R_*^2 - 1}} \right) \quad \text{for} \quad p/R_* > 1
\end{aligned}$$

In the latter relations, $\alpha = \tan(\pi/2 - \theta) + \sqrt{1 + \tan^2(\pi/2 - \theta)} = \tan(\pi/2 - \theta/2)$, $x_1 = R_*/p + \sqrt{R_*^2/p^2 - 1}$ and $x_2 = R_*/p - \sqrt{R_*^2/p^2 - 1}$.

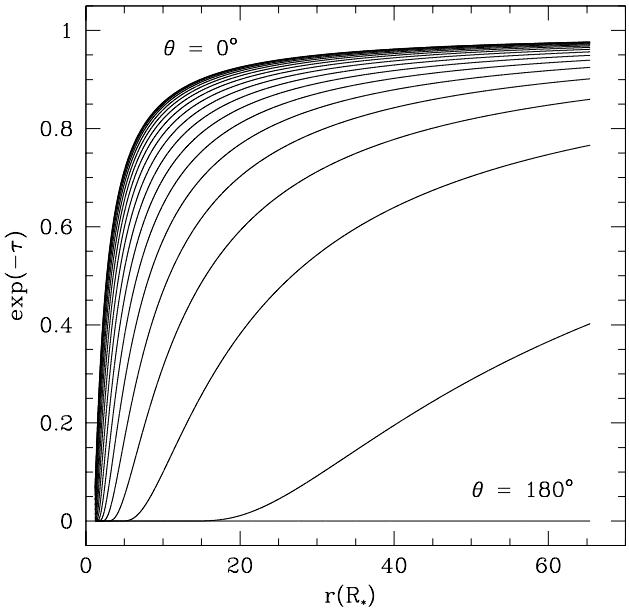

Figure A.2: Tangential transmission of the stellar wind $\exp -\tau_\lambda(r)$ for different values of θ between 0 and 180° in steps of 5°. The parameters used in this calculation are $R_0 = 1.2\,R_*$ and $\tau_{\lambda,*} = 1.5$.

A.3 Synthetic profiles

To simulate theoretical X-ray line profiles, I have written a small FORTRAN code that considers a 2D grid consisting of 10000 nodes in r and 181 steps in θ (from 0 to 180°). Because of the axial symmetry of the problem, no integration on ϕ is needed. I then consider the emission from each cell defined by its central position (r, θ) and its elementary volume dV. For each cell, the velocity projected onto the line of sight is evaluated and the emission increment of the cell is added to the emission at this velocity. The profile is thus built as a kind of histogram (emission vs. projected velocity). Thermal broadening (assuming $kT = 0.5\,\mathrm{keV}$) is accounted for by distributing the emission from a cell over a range of projected velocities set by a Gaussian of $\mathtt{FWHM} = 130\,\mathrm{km\,s^{-1}}$ (see above). Occultations of the emitting region by the stellar body are also accounted for. Some results are illustrated in Fig. A.3 below.

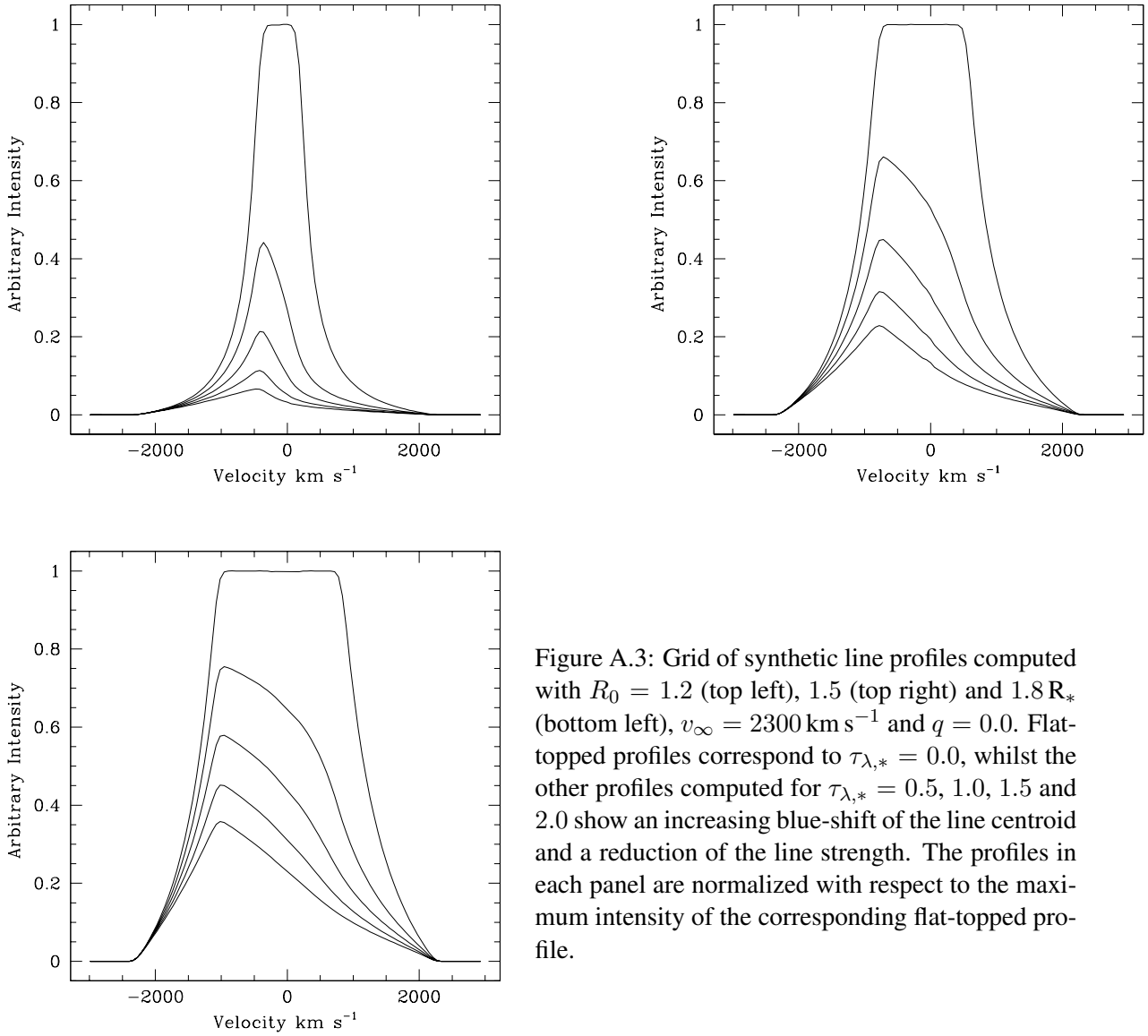

Figure A.3: Grid of synthetic line profiles computed with $R_0 = 1.2$ (top left), 1.5 (top right) and $1.8\,\mathrm{R}_*$ (bottom left), $v_\infty = 2300\,\mathrm{km\,s^{-1}}$ and $q = 0.0$. Flat-topped profiles correspond to $\tau_{\lambda,*} = 0.0$, whilst the other profiles computed for $\tau_{\lambda,*} = 0.5$, 1.0, 1.5 and 2.0 show an increasing blue-shift of the line centroid and a reduction of the line strength. The profiles in each panel are normalized with respect to the maximum intensity of the corresponding flat-topped profile.

Appendix B

A test field in the Southern Coalsack

In this appendix, I will consider the results of an *XMM-Newton* observation of the early-type binary system LSS 3074 (Gosset et al. 2005b). The X-ray emission of the binary itself is discussed by Gosset et al. (2005b) and I shall not repeat this discussion here. LSS 3074 is located behind the edge of the Southern Coalsack, a foreground molecular cloud (see e.g. Marraco & Orsatti 1982). So far, little information is available on the population of X-ray sources in this region[1]. The objective here is to search for serendipitous X-ray sources that could reveal information on the star formation either near LSS 3074 or within the Southern Coalsack.

B.1 Observations and data reduction

LSS 3074 was observed with *XMM-Newton* (Jansen et al. 2001) during revolution 309 on August 17, 2001 (JD 2 452 138.648 – 2 452 138.951). The exposure time with the EPIC-pn camera (Strüder et al. 2001) was 22 778 s. The exposures with the EPIC-MOS cameras (Turner et al. 2001) started 4.5 hours after the pn exposure and their durations were 9982 and 9831 s for the MOS1 and MOS2 instruments respectively. All three EPIC instruments were operated in the full frame mode and used the medium filter to reject optical light. The Optical Monitor (OM) onboard *XMM* observed LSS 3074 in the default fast imaging mode (see Mason et al. 2001). The nominal exposure times were 1200 s and 2760 s per image window in the $UVW1$ and $UVW2$ filters respectively.

I used version 5.4.1 of the *XMM-Newton* Science Analysis System (SAS) software to reduce the raw data. The EPIC data were processed with the `emproc` and `epproc` pipeline chains with default parameters. The raw light curves of the events with pattern 0 and a pulse invariant channel number (PI) above 10 000 reveal no soft proton flaring activity during the *XMM* observation, but the general background level at these energies is quite high: around 0.6 cts s^{-1} for the MOS cameras and around 1.5 cts s^{-1} for the pn camera. Since there is no flaring activity, it is not possible to exclude high-background episodes through selection of good time intervals. The EPIC field of view (FOV) around LSS 3074 contains the background low-mass X-ray binary (LMXB) XB 1323−619 ($d = 10$ kpc, e.g. Boirin et al. 2005). This source does however not contribute in a significant way to the overall count rate at PI $> 10\,000$.

The spectrum and light curve of the LMXB will not be considered here. In fact, the present data of this source are affected by pile-up (especially the MOS data, but also the pn data, at least during the bursts

[1] Andersson et al. (2004) presented a combined *FUSE* and *ROSAT* study of the Coalsack, but this work was mainly focusing on diffuse emission probably arising from the interaction of the Coalsack cloud with the Upper Cen-Lup superbubble.

of the source) and a dedicated *XMM-Newton* observation of this binary was recently analysed by Boirin et al. (2005) and Church et al. (2005).

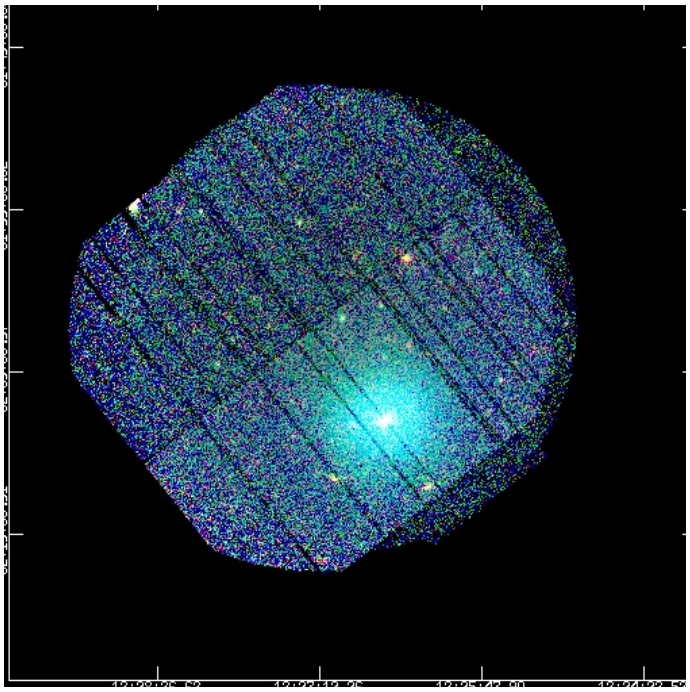

Figure B.1: Combined three-colour image of the EPIC field of view around LSS 3074 (the faint bluish source in the centre of the image). Blue, green and red colours correspond to events in the PI ranges 500 – 1000, 1000 – 2000 and 2000 – 8000 respectively. The EPIC-pn images in the individual energy bands have been corrected for out of time events and were divided by the appropriate exposure maps. Only pattern 0 events were used in this figure.

Due to the shorter exposure times (and the pile-up problem for the LMXB), the MOS data are of limited use here and will not be considered in the following except for the three-colour image in Fig. B.1. In the subsequent analysis of the pn data, I restrict myself to events with pattern 0 – 4. I extracted three images in the PI ranges 500 – 1000 (soft), 1000 – 2000 (medium) and 2000 – 8000 (hard). Due to the brightness of the LMXB, raw EPIC images display a strong tail connected to the LMXB along the read-out direction. This feature is due to so-called 'out of time' events that arrive during the read-out sequence. The images were corrected for the out of time tail by subtracting a second image obtained from an event list where all events are assumed to correspond to out of time events (this file was built through the `epchain` task). As a next step, each image was divided by an appropriate exposure map. Finally, the corrected soft, medium and hard band images were combined into a three-colour image of the EPIC field of view (see Fig. B.1).

The OM data were processed interactively with the SAS routines. The various steps in this reduction include amongst other operations, application of a unity flat field, removal of the modulo-8 fixed pattern (Mason et al. 2001), source detection, photometric measurements, pile-up corrections and astrometric corrections. For the $UVW2$ data, the S/N ratio in the images was too low to perform a correction of the modulo-8 noise. Finally, the individual OM image windows were combined into a mosaic sky image.

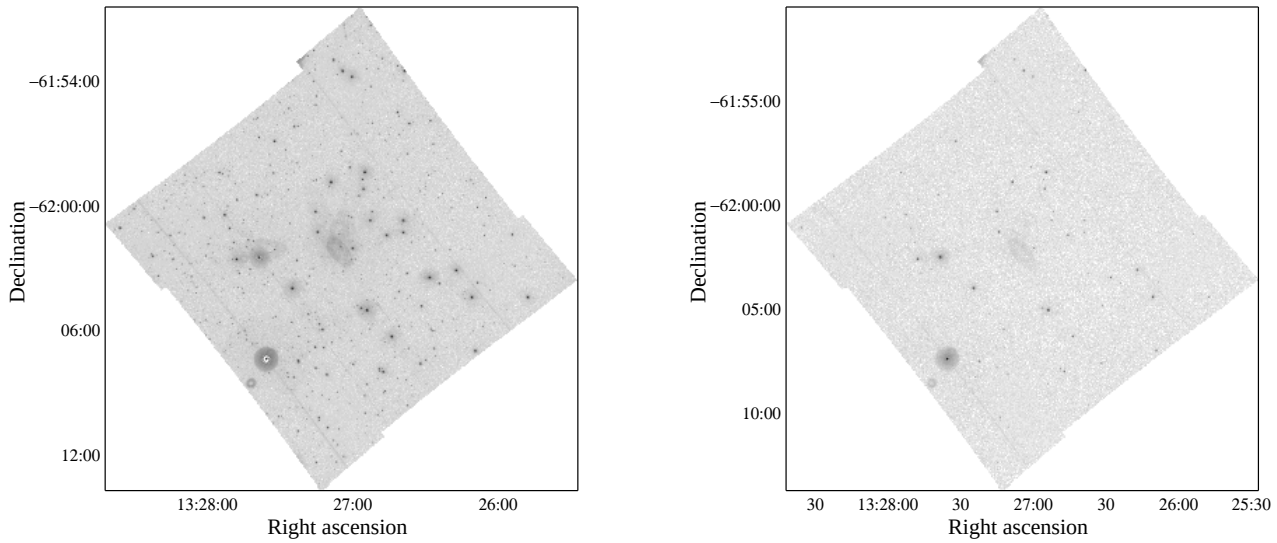

Figure B.2: Mosaic sky images of the OM field of view around LSS 3074 seen through the UVW1 (left) and UVW2 (right) filters. The images are displayed in a logarithmic scale emphasizing the visibility of the straylight artefacts. The very bright source in the lower left is the Be star HD 116827. No OM photometry was obtained for this object because of the large coincidence losses.

B.2 X-ray sources in the field of view

The SAS source detection tasks were used to search for sources simultaneously on the EPIC-pn images from the three energy bands. The different images were then inspected to confirm the reality of these detections. This results in a list of 14 confirmed sources in addition to LSS 3074 and XB 1323−619. These objects are listed in Table B.1 below. The faintest sources in the list have a total pn count rate of about 8×10^{-3} cts s^{-1}. Apart from the X-ray binary, none of the sources in the field of view displays a significant variability.

LSS 3074 lies very close to the Galactic plane ($l_{\rm II} = 307.088°$, $b_{\rm II} = 0.554°$). Therefore, one expects the total neutral hydrogen column density along this direction to be extremely large and to produce a substantial absorption of X-ray photons from extragalactic sources. Moreover, the dark clouds of the Coalsack region probably produce a rather complex and heterogeneous absorption within the EPIC FOV. In order to get a rough first order estimate of the total Galactic extinction along the line of sight, I made use of the *DIRBE/IRAS* extinction maps provided by Schlegel et al. (1998). As pointed out by Schlegel et al., these maps are in principle not suited for directions at $|b_{\rm II}| \leq 5°$. Keeping this limitation in mind, I find that the *DIRBE/IRAS* maps indicate a total Galactic $E(B-V)$ of about 7.4 mag. Using the gas to dust ratio of Bohlin et al. (1978), one thus estimates a neutral hydrogen column density of $\sim 4.3 \times 10^{22}$ cm^{-2}. Assuming that extragalactic background sources have a power-law spectrum with a photon index of 1.4, and suffer a total interstellar absorption of 4.3×10^{22} cm^{-2}, the detection limit 8×10^{-3} cts s^{-1} with the pn camera translates into unabsorbed fluxes of 3.8×10^{-14} and 1.1×10^{-13} erg cm^{-2} s^{-1} in the 0.5 – 2.0 keV and 2.0 – 10 keV band respectively. Using the $\log N$ – $\log S$ relation from Giacconi et al. (2001), one expects about 4 – 6 extragalactic objects among the detected sources. It should be emphasized that background AGN in the FOV around LSS 3074 are expected to appear as very hard (i.e. heavily absorbed) X-ray sources.

Table B.1: X-ray sources detected in the EPIC-pn FOV around LSS 3074 in addition to the LMXB XB 1323−619. The second column yields the source designation following the recommendations of the *XMM*-SOC and the IAU. The third, fourth and fifth columns provide the total background-subtracted and vignetting-corrected pn count rate as well as the hardness ratios HR1 = (M − S)/(M + S) and HR2 = (H − M)/(H + M) respectively. N and d are the number of 2MASS counterparts within a correlation radius of 6 arcsec and the angular separation between the X-ray source and the nearest 2MASS source respectively. The J, H and K_s magnitudes refer to the nearest 2MASS neighbour of the X-ray source.

	Source	pn CR	HR1	HR2	N	d	J	H	K_s	Notes
#	Name XMMU J	(10^{-2} cts s^{-1})				(arcsec)				
1	132535.5−620536	1.31 ± 0.24	$-.35 \pm .23$	$0.48 \pm .21$	2	3.5	15.35	14.61	14.42	
2	132614.1−621212	2.86 ± 0.45	$-.35 \pm .11$	$-1.00 \pm .71$	1	2.0	12.05	11.46	11.27	(1)
3	132615.1−615741	0.84 ± 0.14	$1.00 \pm .62$	$0.72 \pm .13$	3	1.4	15.43	12.48	11.89	(2)
4	132616.3−615852	0.85 ± 0.14	$-.03 \pm .48$	$0.83 \pm .12$	1	5.7	17.76	14.46	13.39	
5	132624.2−620326	0.72 ± 0.15	$-.23 \pm .21$	$0.57 \pm .32$	2	3.6	12.35	12.15	12.06	
6	132626.4−615806	5.36 ± 0.26	$-.50 \pm .04$	$-.69 \pm .10$	2	1.2	10.47	9.84	9.63	
7	132637.4−620413	0.97 ± 0.18	$0.35 \pm .18$	$0.16 \pm .20$	2	0.5	13.50	11.79	10.64	(3)
8	132639.8−620102	0.68 ± 0.12	$0.61 \pm .15$	$-.39 \pm .22$	1	4.9	8.90	8.50	8.34	
9	132651.3−615800	0.66 ± 0.17	$-.42 \pm .21$	$-.45 \pm .77$	0	6.6	15.95	14.98	13.79	
10	132653.5−620821	3.60 ± 0.41	$0.37 \pm .21$	$0.72 \pm .09$	1	4.3	12.66	12.26	12.01	(3)
11	132700.0−620150	1.54 ± 0.16	$0.58 \pm .09$	$-.44 \pm .13$	1	1.4	8.87	8.47	8.24	= LSS 3074
12	132703.8−621145	2.83 ± 0.33	$-.37 \pm .11$	$-.22 \pm .22$	0	10.3	4.05	2.68	2.14	
13	132710.0−621654	1.61 ± 0.30	$-.53 \pm .21$	$0.43 \pm .27$	1	5.8	14.68	14.00	13.74	
14	132825.2−615511	1.87 ± 0.41	$-.26 \pm .23$	$0.23 \pm .29$	1	0.1	12.67	12.03	11.84	
15	132848.9−615443	45.84 ± 1.83	$0.03 \pm .04$	$-.43 \pm .05$	0	6.1	9.09	8.48	8.31	

(1) very soft source
(2) very hard source
(3) source count rate and hardness ratios affected by straylight from the LMXB

Following the approach outlined in Sect. 5.1.4, one can get a rough estimate of the number of foreground stars. The detection limit of 8×10^{-3} cts s^{-1} for EPIC-pn (corresponding to a flux limit of about 2×10^{-14} erg cm^{-2} s^{-1}) yields an estimated number of 6 detected foreground objects.
All in all, more than two thirds of the sources in the field around LSS 3074 are thus expected to be either background AGN or foreground stars.
Due to the rather large extinction in the Coalsack region, optical surveys of this region are certainly far less complete than infrared surveys. I have therefore cross-correlated the list of X-ray sources with the Two Micron All Sky Survey (2MASS) catalogue of point sources (Cutri et al. 2003). Given the limited number of detected X-ray sources, it is not possible to statistically determine an optimum correlation radius (using e.g. the method of Jeffries et al. 1997). In Table B.1, I simply provide the nearest 2MASS source as well as the number of 2MASS sources within a radius of 6 arcsec (comparable to the FWHM of the PSF of the *XMM-Newton* X-ray telescopes + EPIC cameras) around the X-ray source. It turns out that most of the X-ray sources have an IR counterpart within less than 6 arcsec. I used the March 2003 update of the colour transformations, initially derived by Carpenter (2001), to convert the $J - H$ and $H - K_s$ colours to the homogenized photometric system introduced by Bessell & Brett (1988). Following their JHK colours (see Fig. B.3), most of these IR sources are moderately reddened late-type stars.

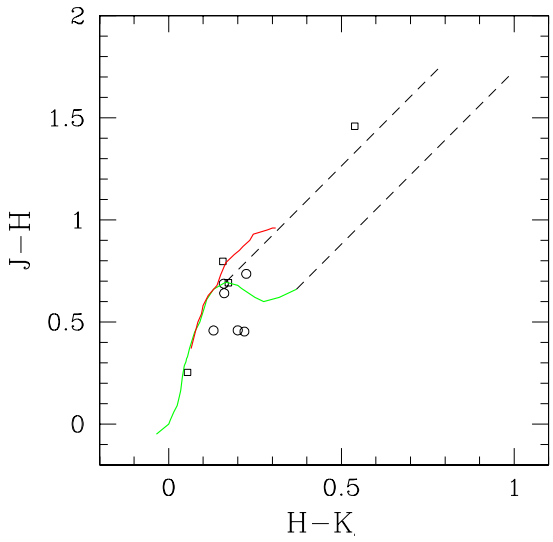

Figure B.3: JHK colour-colour diagram of the IR counterparts of the *XMM* sources. Circles stand for a single IR counterpart within the 6 arcsec correlation radius around an EPIC-pn X-ray source, whilst squares indicate objects with more than one IR source inside the error box. The heavy solid lines yield the intrinsic colours of main-sequence and giant stars (following Bessell & Brett 1988), whereas the reddening band (using the reddening law of Rieke & Lebofsky 1985) is illustrated for up to 10 magnitudes of visual extinction from the position where it intersects the locus of unreddened main-sequence stars.

The case of source #15 deserves a comment: this is a bright X-ray source at the edge of the pn detector and the PSF of this source is thus heavily elongated, which leads to some uncertainties in the definition of its position. Therefore, although the nearest 2MASS source is 6.1 arcsec away, one cannot exclude that this IR object (probably a low-mass foreground star) could indeed be associated with X-ray source #15. Source #15 lies at about 20 arcsec from 1RXS J132850.7-615458. In the *ROSAT* - All Sky Survey

bright source catalogue (Voges et al. 2000), the position of the latter object is quoted with an uncertainty of 13 arcsec and its PSPC count rate is evaluated to be $(5.0 \pm 2.1) \times 10^{-2}$ cts s^{-1}. The *ROSAT*-PSPC and *XMM* EPIC-pn count rates are in reasonable agreement with each other (assuming the model parameters derived below).
Source #12 does not have a 2MASS counterpart within the 6 arcsec radius, but it lies at ~ 10 arcsec from the *IRAS* source IRAS 13237−6156 which is probably associated with an M3 Ia supergiant (Kwok et al. 1997). Given that source #12 is close to a detector gap, it seems likely that its X-ray position is slightly offset and could well be consistent with the *IRAS* source.
It is worth noting that three of the optically brightest stars in the EPIC-FOV are not detected in the EPIC-pn image. These are HD 116826 ($m_V = 10.1$, spectral type B8, Sundman et al. 1974), HD 116827 ($m_V = 9.5$, Be star of spectral type B3 – B5, MacConnell 1981, Sundman et al. 1974) and CPD−61° 3692 (= LSS 3072, $m_V = 9.8$, spectral type B2.5 Ia, Vijapurkar & Drilling 1993).

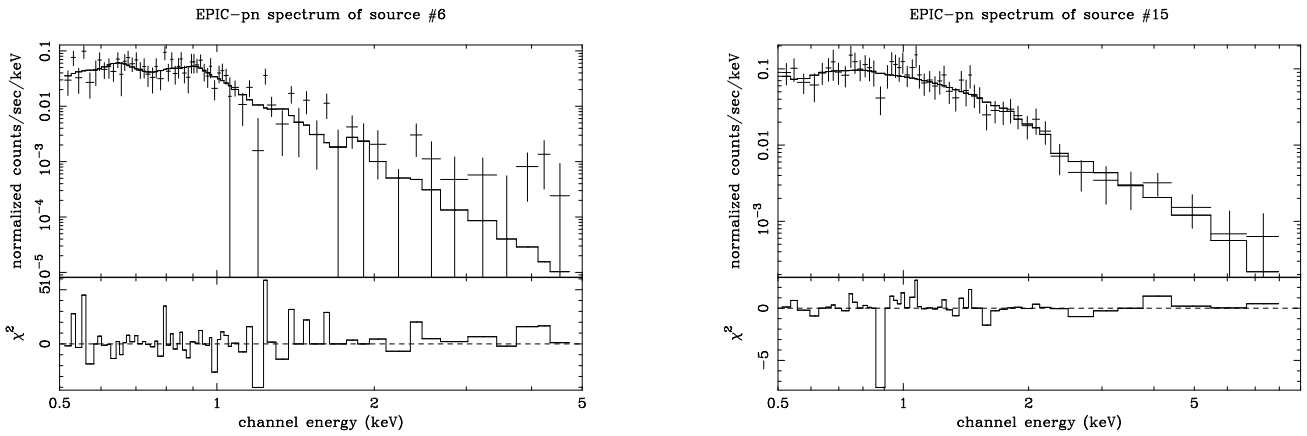

Figure B.4: EPIC-pn spectra of sources #6 (left) and #15 (right) along with the best fit models: an absorbed 2-T `mekal` model for source #6 and an absorbed power-law for #15 (see text).

B.3 X-ray spectra

Spectra of the brighter X-ray sources (#6 and #15) were extracted. Whenever possible, the background spectrum was evaluated in the immediate vicinity of the source. Appropriate redistribution matrix files and ancillary response files were built using the corresponding SAS tasks and the spectra were binned in such a way as to have at least 10 counts per energy bin.

The EPIC-pn spectrum of source #6 displays some residual contamination by the strong background at high energies. In fact, one notes the presence of a weak Cu K fluorescent line at 8.05 keV, whilst the spectrum drops to zero flux level at energies around 5 keV. This is most likely due to the spatial variation of the instrumental background in the copper line near the edges of the chip (i.e. over the source region and the background region, see Lumb 2001) and the high level of the background of this observation in general. The background-corrected source spectrum between 0.5 and 5.0 keV is best fitted ($\chi^2_\nu = 1.00$, 62 d.o.f.) by an absorbed 2-T `mekal` model (see Fig. B.4). This seems plausible since the

source is associated with an optically rather bright (probably foreground) object. The best fit parameters are $kT_1 = 0.18^{+.04}_{-.03}$, $kT_2 \geq 0.58$ keV and $N_H = 0.50^{+.26}_{-.25} \times 10^{22}$ cm^{-2}. Since the fit is restricted to bins below 5.0 keV, the actual temperature of the hotter component is not well constrained, though the best fit is achieved for $kT_2 = 1.03$ keV. The absorbed flux of this source (in the 0.5 – 5.0 keV domain) is of order 10^{-13} erg cm^{-2} s^{-1}. Note that this value is subject to rather large uncertainties because of the proximity of a detector gap.
The spectrum of source #15 is best fitted by an absorbed power-law model ($\chi^2_\nu = 0.61$ for 50 d.o.f.) with a photon index $\Gamma = 2.75^{+.55}_{-.37}$ and $N_H = 0.21^{+.09}_{-.09} \times 10^{22}$ cm^{-2}. The spectrum cannot be fitted by a single temperature thermal plasma model. However, an absorbed 2-T `mekal` model yields a reasonable fit ($\chi^2_\nu = 0.74$ for 48 d.o.f.) with $kT_1 = 1.07^{+.35}_{-.77}$, $kT_2 = 3.71^{+1.92}_{-0.96}$ keV and $N_H \leq 0.1 \times 10^{22}$ cm^{-2}. An absorbed bremsstrahlung model also yields a decent fit with $\chi^2_\nu = 0.70$ (50 d.o.f.) for $kT = 1.69^{+.78}_{-.51}$ keV and a column density $N_H = 0.07^{+.07}_{-.06} \times 10^{22}$ cm^{-2}. The various models all indicate an absorbed flux of about 10^{-12} erg cm^{-2} s^{-1}. Once more this value is somewhat uncertain because of the proximity of the source to the edge of the field of view. The ambiguity about the optical (or IR) counterpart of this source prevents us from using a priori considerations about the best model to be used.

B.4 Discussion and conclusions for this field

An interesting question is whether some of the serendipitous X-ray sources could be associated with pre main-sequence stars either in the Coalsack or near LSS 3074. In this context, it is worth emphasizing that there are no X-ray sources in this field with JHK colours indicating that they were classical T Tauri stars (Meyer et al. 1997, Lada & Adams 1992). Although weak-line T Tauri stars have near-IR colours that are quite similar to those of normal main-sequence stars (Lada & Adams 1992), and might hence not easily be identified as pre main-sequence stars, the *XMM-Newton* data do not provide evidence for an active star formation process in that part of the Coalsack cloud covered by the EPIC field of view. Indeed, assuming a distance of the Coalsack of 175 pc (Nyman et al. 1989 and references therein), the EPIC-pn detection limit corresponds to a luminosity limit of a few times 10^{29} erg s^{-1}, i.e. well below typical X-ray luminosities of PMS stars. This is in line with the results of the CO survey and the analysis of *IRAS* sources in the Coalsack by Nyman et al. (1989). These authors suggested that the Coalsack is a quiescent object where star formation has not started because it has not been triggered yet by an external mechanism. The latter suggestion is somewhat surprising given that Andersson et al. (2004) found the Coalsack to be interacting with the Upper Cen-Lup superbubble.

Assuming that the brightest PMS stars have X-ray luminosities of order 10^{31} erg s^{-1} similar to those found in NGC 6231, the sensitivity of the present *XMM-Newton* observation would allow to detect them out to a distance of about 2 kpc. Therefore, at the actual distance of LSS 3074, only the brightest PMS objects might be detected.
Finally, it should be stressed that neither EPIC, OM nor 2MASS data indicate a clustering of X-ray, UV or IR sources around or near LSS 3074 that could point towards the existence of an open stellar cluster. While a determination of the distances towards the individual stars in this region is necessary before one can definitely conclude about the lack of a parental cluster, this result is nevertheless somewhat surprising. Indeed, as outlined in the introduction of Chapter 5, massive stars are usually not found in isolation and it is believed that most of them actually form in stellar clusters.

Appendix C

Full list of publications (as of January 2007)

C.1 Refereed Journal Papers

1. *WR 22 : The most massive Wolf-Rayet star ever weighed.*
   Rauw G., Vreux J.-M., Gosset E., Hutsemékers D., Magain P., Rochowicz K., 1996, A&A 306, 771

2. *Existence of a short period (3.5–4 hours) in the photometric variability of WR 66.*
   Rauw G., Gosset E., Manfroid J., Vreux J.-M., Claeskens J.-F., 1996, A&A 306, 783

3. *The puzzling Luminous Blue Variable-like object HD 5980 in the Small Magellanic Cloud.*
   Heydari-Malayeri M., Rauw G., Esslinger O., Beuzit J.-L., 1997, A&A 322, 554

4. *The LMC transition star R 84 and the core of the LH 39 OB association.*
   Heydari-Malayeri M., Courbin F., Rauw G., Esslinger O., Magain P., 1997, A&A 326, 143

5. *Line profile variability in the spectrum of the O(f) supergiant HD 192639.*
   Rauw G., Vreux J.-M., 1998, A&A 335, 995

6. *The interacting early-type binary BD+40° 4220. Modeling the colliding winds region.*
   Rauw G., Vreux J.-M., Bohannan B., 1999, ApJ 517, 416

7. *ASCA spectroscopy of the hard X-ray emission from the colliding wind interaction in γ^2 Velorum*
   Rauw G., Stevens I.R., Pittard J.M., Corcoran M.F., 2000, MNRAS 316, 129

8. *Coordinated Monitoring of the Eccentric O-star Binary Iota Orionis. Optical Spectroscopy and Photometry*
   Marchenko S.V., Rauw G., Antokhina E.A., Antokhin I.I., Ballereau D., Chauville J., Corcoran M.F., Costero R., Echevarria J., Eversberg T., Gayley K.G., Koenigsberger G., Miroshnichenko A.S., Moffat A.F.J., Morrell N.I., Morrison N.D., Mulliss C.L., Pittard J.M., Stevens I.R., Vreux J.-M., Zorec J., 2000, MNRAS 317, 333

9. *Coordinated Monitoring of the Eccentric O-star Binary Iota Orionis. The X-ray Analysis*
   Pittard J.M., Stevens I.R., Corcoran M.F., Gayley K.G., Marchenko S.V., Rauw G., 2000, MNRAS 319, 137

10. *A new orbital solution for the massive binary system HD 93403*
    Rauw G., Sana H., Gosset E., Vreux J.-M., Jehin E., Parmentier G., 2000, A&A 360, 1003

11. *Compact star clusters of the LMC H II region N 11C*
Heydari-Malayeri M., Royer P., Rauw G., Walborn N.R., 2000, A&A 361, 877

12. *High resolution X-ray spectroscopy of ζ Puppis with the XMM-Newton Reflection Grating Spectrometer*
Kahn S.M., Leutenegger M.A., Cottam J., Rauw G., Vreux J.-M., den Boggende A.J.F., Mewe R., Güdel M., 2001, A&A 365, L312

13. *The spectral variability of HD 192639 and its implications for the star's wind structure*
Rauw G., Morrison N.D., Vreux J.-M., Gosset E., Mulliss C.L., 2001, A&A 366, 585

14. *The strange case of the massive binary HD 149404*
Rauw G., Nazé Y., Carrier F., Burki G., Gosset E., Vreux J.-M., 2001, A&A 368, 212

15. *HD 152248: Evidence for a colliding wind interaction*
Sana H., Rauw G., Gosset E., 2001, A&A 370, 121

16. *What is the real nature of HD 108?*
Nazé Y., Vreux J.-M., Rauw G., 2001, A&A 372, 195

17. *Optical Spectroscopy of X-Mega targets in the Carina Nebula. II. The massive double-lined O-type binary HD 93205*
Morrell N.I., Barbá R.H., Niemela V.S., Corti M.A., Albacete Colombo J.F., Rauw G., Corcoran M.F., Morel T., Bertrand J.-F., Moffat A.F.J., St-Louis N., 2001, MNRAS 326, 85

18. *Optical Spectroscopy of X-Mega targets in the Carina Nebula. III. The multiple system Tr 16-104 ($\equiv$ CPD -59° 2603)*
Rauw G., Sana H., Antokhin I.I., Morrell N.I., Niemela V.S., Albacete Colombo J.F., Gosset E., Vreux J.-M., 2001, MNRAS 326, 1149

19. *A first detailed study of the colliding wind WR+O binary WR 30a*
Gosset E., Royer P., Rauw G., Manfroid J., Vreux J.-M., 2001, MNRAS 327, 435

20. *Phase-resolved X-ray and optical spectroscopy of the massive binary HD 93403*
Rauw G., Vreux J.-M., Stevens I.R., Gosset E., Sana H., Jamar C., Mason K.O., 2002, A&A 388, 552

21. *The evolved early-type binary HDE 228766 revisited*
Rauw G., Crowther P.A., Eenens P.R.J., Manfroid J., Vreux J.-M., 2002, A&A 392, 563

22. *A multi-wavelength investigation of the non-thermal radio emitting O-star 9 Sgr*
Rauw G., Blomme R., Waldron W.L., Corcoran M.F., Pittard J.M., Pollock A.M.T., Runacres M.C., Sana H., Stevens I.R., Van Loo S., 2002, A&A 394, 993

23. *An XMM-Newton observation of the Lagoon Nebula and the very young open cluster NGC 6530*
Rauw G., Nazé Y., Gosset E., Stevens I.R., Blomme R., Corcoran M.F., Pittard J.M., Runacres M.C., 2002, A&A 395, 499

24. *Optical spectroscopy of X-Mega targets. IV. CPD -59° 2636: a new O-type multiple system in the Carina Nebula*
Albacete Colombo J.F., Morrell N.I., Rauw G., Corcoran M.F., Niemela V.S., Sana H., 2002, MNRAS 336, 1099

25. *Line profile variability in the spectra of Oef stars. I. BD+60° 2522*
Rauw G., De Becker M., Vreux J.-M., 2003, A&A 399, 287

26. *VLT observations of the highly ionized nebula around Brey 2*
Nazé Y., Rauw G., Manfroid J., Chu Y.-H., Vreux J.-M., 2003, A&A 401, L13

27. *XMM-Newton high-resolution X-ray spectroscopy of the Wolf-Rayet object WR 25 in the Carina OB1 association*
Raassen A.J.J., van der Hucht K.A., Mewe R., Antokhin I.I., Rauw G., Vreux J.-M., Schmutz W., Güdel M., 2003, A&A 402, 653

28. *The massive binary CPD −41° 7742. I. High-resolution optical spectroscopy*
Sana, H., Hensberge H., Rauw G., Gosset E., 2003, A&A 405, 1063

29. *An XMM-Newton observation of the very young open cluster NGC 6383*
Rauw G., De Becker M., Gosset E., Pittard J.M., Stevens I.R., 2003, A&A 407, 925

30. *WR bubbles and He* II *emission*
Nazé Y., Rauw G., Manfroid J., Chu Y.-H., Vreux J.-M., 2003, A&A 408, 171

31. *An XMM-Newton observation of the massive binary HD 159176*
De Becker M., Rauw G., Pittard J.M., Antokhin I.I., Stevens I.R., Gosset E., Owocki, S.P., 2004, A&A 416, 221

32. *HD 108: The mystery deepens with XMM-Newton observations*
Nazé Y., Rauw G., Vreux J.-M., De Becker M., 2004, A&A 417, 667

33. *XMM-Newton observations of the giant H* II *region N 11 in the LMC*
Nazé Y., Antokhin I.I., Rauw G., Chu Y.-H., Gosset E., Vreux J.-M., 2004, A&A 418, 841

34. *A phase-resolved XMM-Newton campaign on the colliding-wind binary HD 152248*
Sana H., Stevens I.R., Gosset E., Rauw G., Vreux J.-M., 2004, MNRAS 350, 809

35. *Quasi-simultaneous XMM-Newton and VLA observation of the non-thermal radio emitter HD168112*
De Becker M., Rauw G., Blomme R., Waldron W.L., Sana H., Pittard J.M., Eenens P.R.J., Stevens I.R., Runacres M.C., Van Loo S., Pollock A.M.T., 2004, A&A 420, 1061

36. *WR 20a: a massive cornerstone binary system comprising two extreme early-type stars*
Rauw G., De Becker M., Nazé Y., Crowther P.A., Gosset E., Sana H., van der Hucht K.A., Vreux J.-M., Williams P.M., 2004, A&A 420, L9

37. *Early-type stars in the young open cluster IC 1805. I. The SB2 system BD+60° 497 and the probably single stars BD+60° 501 and BD+60° 513*
Rauw G., De Becker M., 2004, A&A 421, 693

38. *A spectroscopic study of the non-thermal radio emitter Cyg OB2 #8A: Discovery of a new binary system*
De Becker M., Rauw G., Manfroid J., 2004, A&A 424, L39

39. *Line profile variability in the spectra of Oef stars: II. HD 192281, HD 14442 and HD 14434*
De Becker M., Rauw G., 2004, A&A 427, 995

40. *Hard X-ray emission clumps in the gamma-Cygni supernova remnant: An INTEGRAL-ISGRI view*
Bykov A.M., Krassilchtchikov A.M., Uvarov Y.A., Bloemen H., Chevalier R.A., Gustov M.Y., Hermsen W., Lebrun F., Lozinskaya T.A., Rauw G., Smirnova T.V., Sturner S.J., Swings J.-P., Terrier R., Toptygin I.N., 2004, A&A 427, L21

41. *A Period and a Prediction for the Of?p Spectrum Alternator HD 191612*
Walborn N.R., Howarth I.D., Rauw G., Lennon D.J., Bond H.E., Negueruela I., Nazé Y., Corcoran M.F., Herrero A., Pellerin A., 2004, ApJ 617, L61

42. *An XMM-Newton look at the Wolf-Rayet star WR 40. The star itself, its nebula and its neighbours*
Gosset E., Nazé Y., Claeskens J.-F., Rauw G., Vreux J.-M., Sana H., 2005, A&A 429, 685

43. *The spectrum of the very massive binary system WR 20a (WN6ha + WN6ha): fundamental parameters and wind interactions*
Rauw G., Crowther P.A., De Becker M., Gosset E., Nazé Y., Sana H., van der Hucht K.A., Vreux J.-M., Williams P.M., 2005, A&A 432, 985

44. *On the Multiplicity of the O-Star Cyg OB2 #8a and its Contribution to the gamma-ray Source 3EG J2033+4118*
De Becker M., Rauw G., Swings J.-P., 2005, Ap&SS 297, 291

45. *Optical spectroscopy of X-Mega targets. V. The spectroscopic binary HD 93161A and its visual companion HD 93161B*
Nazé Y., Antokhin I.I., Sana H., Gosset E., Rauw G., 2005, MNRAS 359, 688

46. *Non-thermal radio emission from O-type stars. I. HD 168112*
Blomme R., van Loo S., De Becker M., Rauw G., Runacres M.C., Setia Gunawan D.Y.A., Chapman J.M., 2005, A&A 436, 1033

47. *An XMM-Newton observation of the multiple system HD 167971 (O5-8V + O5-8V + (O8I)) and the young open cluster NGC 6604*
De Becker M., Rauw G., Blomme R., Pittard J.M., Stevens I.R., Runacres M.C., 2005, A&A 437, 1029

48. *The massive binary CPD -41° 7742. II. Optical light curve and X-ray observations*
Sana H., Antokhina E., Royer P., Manfroid J., Gosset E., Rauw G., Vreux J.-M., 2005, A&A 441, 213

49. *INTEGRAL detection of hard X-rays from NGC 6334: nonthermal emission from colliding winds or an AGN?*
Bykov A.M., Krassilchtchikov A.M., Uvarov Y.A., Lebrun F., Renaud M., Terrier R., Bloemen H., McBreen B., Courvoisier T.J.-L., Gustov M.Y., Hermsen W., Leyder J.-C., Lozinskaya T.A., Rauw G., Swings J.-P., 2006, A&A 449, 917

50. *New light on the peculiar star HD 108*
Nazé Y., Barbieri C., Segafredo A., Rauw G., De Becker M., 2006, IBVS, 5693, 1

51. *An XMM-Newton view of the young open cluster NGC 6231. I. The catalogue*
Sana H., Gosset E., Rauw G., Sung H., Vreux J.-M., 2006, A&A 454, 1047

52. *The XMM-Newton view of Plaskett's star and its surroundings*
Linder N., Rauw G., Pollock A.M.T., Stevens I.R., 2006, MNRAS 370, 1623

53. *Early-type stars in the young open cluster IC 1805. II. The probably single stars HD 15570 and HD 15629, and the massive binary/triple system HD 15558*
De Becker M., Rauw G., Manfroid J., Eenens P., 2006, A&A 456, 1121

54. *On the Nature of the Hard X-Ray Source IGR J2018+4043*
Bykov A.M., Krassilchtchikov A.M., Uvarov Y.A., Kennea J.A., Pavlov G.G., Dubner G.M., Giacani E.B., Bloemen H., Hermsen W., Kaastra J., Lebrun F., Renaud M., Terrier R., De Becker M., Rauw, G., Swings, J.-P., 2006, ApJ 649, L21

55. *The OB binary HD 152219: a detached, double-lined, eclipsing binary*
Sana H., Gosset E., Rauw G., 2006, MNRAS 371, 67

56. *XMM-Newton observations of the massive colliding wind binary and non-thermal radio emitter Cyg OB2 #8A [O6 If + O5.5 III(f)]*
De Becker M., Rauw G., Sana H., Pollock A.M.T., Pittard J.M., Blomme R., Stevens I.R., van Loo S., 2006, MNRAS 371, 1280

57. *GCIRS 16 SW: A Massive Eclipsing Binary in the Galactic Center*
Martins F., Trippe S., Paumard T., Ott T., Genzel R., Rauw G., Eisenhauer F., Gillessen S., Maness H., Abuter R., 2006, ApJ 649, L103

58. *The atypical emission-line star Hen3-209*
Nazé Y., Rauw G., Hutsemékers D., Gosset E., Manfroid J., Royer P., 2006, MNRAS 371, 1594

59. *An XMM-Newton view of the young open cluster NGC 6231. II. The OB star population*
Sana H., Rauw G., Nazé Y., Gosset E., Vreux J.-M., 2006, MNRAS 372, 661

60. *The first orbital solution for the massive colliding wind binary HD 93162 (≡ WR 25)*
Gamen R., Gosset E., Morrell N.I., Niemela V., Sana H., Nazé Y., Rauw G., Barbá R., Solivella G., 2006, A&A 460, 777

61. *Towards an understanding of the Of?p star HD 191612: Phase-resolved multiwavelength observations*
Nazé Y., Rauw G., Pollock A.M.T., Walborn N.R., Howarth I.D., 2007, MNRAS, 375, 145

C.2 Conference Proceedings

1. *Photometric monitoring of Wolf-Rayet stars: Strömgren uvby and narrow-band photometry.*
Gosset E., Rauw G., Manfroid J., Vreux J.-M., Sterken C., 1994, in *The impact of long term monitoring on variable star research*, NATO ASI Series C, eds. C. Sterken & M. de Groot, 436, 101

2. *A seven year campaign on WR 22.*
Rauw G., Vreux J.-M., Gosset E., Hutsemékers D., Magain P., Manfroid J., Remy M., Rochowicz K., 1995, in *Wolf-Rayet stars: binaries, colliding winds, evolution*, IAU Symp. Nr. 163, eds. K.A. van der Hucht & P.M. Williams, 241

3. *WR 22 as a Core Hydrogen-Burning Wolf-Rayet Star?*
Rauw G., Vreux J.-M., Gosset E., Hutsemékers D., Magain P., 1995, in *Stellar Evolution: What Should Be Done*, 32nd Liège Int. Astroph. Coll., eds. A. Noels, D. Fraipont, M. Gabriel, N. Grevesse, P. Demarque, 463

4. *Spectropolarimetry of WR 66*
Lamy H., Hutsemékers D., Rauw G., 1996, in *Wolf-Rayet Stars in the Framework of Stellar Evolution*, 33rd Liège Int. Astroph. Coll., eds. J.-M. Vreux, A. Detal, D. Fraipont-Caro, E. Gosset, G. Rauw, 247

5. *Line profile variability in the spectrum of WR 22 around periastron: binary interaction or intrinsic variability?*
Rauw G., Vreux J.-M., Gosset E., 1996, in *Wolf-Rayet Stars in the Framework of Stellar Evolution*, 33rd Liège Int. Astroph. Coll., eds. J.-M. Vreux, A. Detal, D. Fraipont-Caro, E. Gosset, G. Rauw, 297

6. *A new orbital solution for the WNL binary system WR 12*
Rauw G., Vreux J.-M., Gosset E., Manfroid J., Niemela V.S., 1996, in *Wolf-Rayet Stars in the Framework of Stellar Evolution*, 33rd Liège Int. Astroph. Coll., eds. J.-M. Vreux, A. Detal, D. Fraipont-Caro, E. Gosset, G. Rauw, 303

7. *Line profile variability and mass-transfer in the early type binary BD+40° 4220*
Vreux J.-M., Rauw G., Bohannan B., Manfroid J., 1996, in *Wolf-Rayet Stars in the Framework of Stellar Evolution*, 33rd Liège Int. Astroph. Coll., eds. J.-M. Vreux, A. Detal, D. Fraipont-Caro, E. Gosset, G. Rauw, 337

8. *Search for interacting winds in the WN7 + O binary WR 22*
Rauw G., Vreux J.-M., Gosset E., 1996, in *Colliding Winds in Binary Stars*, RMAASC 5, eds. V.S. Niemela and N. Morrell, 108

9. *The WN11-like spectrum of HD 5980 during the early stages of the 1994 Eruption*
Heydari-Malayeri M., Rauw G., Esslinger O., 1997, in *Luminous Blue Variables: Massive Stars in Transition*, ASP Conf. Series 120, eds. A. Nota, H.J.G.L.M. Lamers, 243

10. *X-ray spectroscopy with XMM: A new powerful tool to determine fundamental parameters of early-type stars*
Mewe R., Rauw G., van der Hucht K.A., Vreux J.-M., Gosset E., Güdel M., Schmutz W., Stevens I.R., Kahn S., Proceedings of the First XMM Workshop, ed. M. Dahlem, 1998, http://astro.estec.esa.nl/XMM/news/ws1/ws1_papers.html

11. *On the perspective of using XMM to study fundamental parameters of early-type stars*
Rauw G., van der Hucht K.A., Mewe R., Güdel M., Vreux J.-M., Gosset E., Schmutz W., Stevens I.R., in *Wolf-Rayet Phenomena in Massive Stars and Starburst Galaxies*, Proc. IAU Symposium 193, eds. K.A. van der Hucht, G. Koenigsberger & P.R.J. Eenens, 1999, San Francisco ASP, 90

12. *Narrow-band photometry of the eclipsing WN7 + O binary WR 22*
Royer P., Rauw G., Manfroid J., Gosset E., Vreux J.-M., in *Wolf-Rayet Phenomena in Massive Stars and Starburst Galaxies*, Proc. IAU Symposium 193, eds. K.A. van der Hucht, G. Koenigsberger & P.R.J. Eenens, 1999, San Francisco ASP, 94

13. *New observational results on the colliding wind WR + O binary WR 30a*
Gosset E., Royer P., Rauw G., Manfroid J., Vreux J.-M., in *Wolf-Rayet Phenomena in Massive Stars and Starburst Galaxies*, Proc. IAU Symposium 193, eds. K.A. van der Hucht, G. Koenigsberger & P.R.J. Eenens, 1999, San Francisco ASP, 354

14. *Correction of systematic errors in differential photometry*
Manfroid J., Royer P., Rauw G., Gosset E., in *Tenth Conference on Astr. Data and Analysis software and systems*, eds. F.R. Harnden, F.A. Primini & H.E. Payne, 2001, ASP Conf. Series 238, 373

15. *Studying the X-ray Properties of Early-Type Stars*
Vreux J.-M., Rauw G., 2001, in *Space Scientific Research in Belgium*, Vol. II, Part 1, 47

16. *Optical Spectroscopy of Colliding Wind Systems to be observed with XMM*
Sana H., Rauw G., Gosset E., Vreux J.-M., in *Interacting Winds from Massive Stars*, eds. A.F.J. Moffat, N. St-Louis, 2002, ASP Conf. Series 260, 431

17. *Searching for Colliding Wind Signatures in a Sample of O-Star Binaries*
Rauw G., Sana H., Vreux J.-M., Gosset E., Stevens I.R., in *Interacting Winds from Massive Stars*, eds. A.F.J. Moffat, N. St-Louis, 2002, ASP Conf. Series 260, 449

18. *Line Profile Variability in the Massive Binary System HD 149404*
Nazé Y., Carrier F., Rauw G., in *Interacting Winds from Massive Stars*, eds. A.F.J. Moffat, N. St-Louis, 2002, ASP Conf. Series 260, 457

19. *Preliminary results from XMM-Newton observations of the massive Wolf-Rayet binary WR 22 (WN7h + O9 III-V)*
Gosset E., Rauw G., Vreux J.-M., Nazé Y., Antokhin I.I., Sana H., in *A Massive Star Odyssey: from Main Sequence to Supernova*, Proc. IAU Symposium 212, eds. K.A. van der Hucht, A. Herrero & C. Esteban, 2003, San Francisco ASP, 188

20. *Radio continuum observations of massive stars in open cluster NGC 6231 and the Sco OB1 association*
Setia Gunawan D.Y.A., Chapman J.M., Stevens I.R., Rauw G., Leitherer C., in *A Massive Star Odyssey: from Main Sequence to Supernova*, Proc. IAU Symposium 212, eds. K.A. van der Hucht, A. Herrero & C. Esteban, 2003, San Francisco ASP, 230

21. *XMM-Newton high-resolution X-ray spectroscopy of the Wolf-Rayet object WR 25 (WN6ha + O4f)*
Raassen A.J.J., van der Hucht K.A., Mewe R., Antokhin I.I., Rauw G., Vreux J.-M., Schmutz W., Güdel M., 2003, AdSpR 32, 1161

22. *Colliding Wind Binaries: an insight into O-star physics*
Sana H., Rauw G., 2003, in *Collisions*, Revue des Questions Scientifiques, 174 (1-2), 40

23. *Evidence for phase-locked X-ray variations from the colliding winds massive binary Cyg OB2#8A*
De Becker M., Rauw G., 2005, in *Massive Stars and High Energy Emission in OB Associations*, Proc. JENAM 2005, *Distant Worlds*, eds. G. Rauw, Y. Nazé, R. Blomme, E. Gosset, 73

24. *A spectroscopic investigation of the young open cluster IC 1805*
De Becker M., Rauw G., 2005, in *Massive Stars and High Energy Emission in OB Associations*, Proc. JENAM 2005, *Distant Worlds*, eds. G. Rauw, Y. Nazé, R. Blomme, E. Gosset, 111

25. *Preliminary results of an observational campaign aiming at the study of the binary system LSS 3074*
Gosset E., Rauw G., Manfroid J., Antokhina E., Stevens I.R., Sana H., 2005, in *Massive Stars and High Energy Emission in OB Associations*, Proc. JENAM 2005, *Distant Worlds*, eds. G. Rauw, Y. Nazé, R. Blomme, E. Gosset, 77

26. *A survey for γ-ray emission from OB associations with INTEGRAL: some preliminary results*
Leyder J.-C., Rauw G., 2005, in *Massive Stars and High Energy Emission in OB Associations*, Proc. JENAM 2005, *Distant Worlds*, eds. G. Rauw, Y. Nazé, R. Blomme, E. Gosset, 115

27. *The XMM-Newton view of Plaskett's star and its surroundings*
Linder N., Rauw G., 2005, in *Massive Stars and High Energy Emission in OB Associations*, Proc. JENAM 2005, *Distant Worlds*, eds. G. Rauw, Y. Nazé, R. Blomme, E. Gosset, 53

28. *The peculiar Of?p stars HD 108 and HD 191612*
Nazé Y., Rauw G., Walborn N.R., Howarth I.D., 2005, in *Massive Stars and High Energy Emission in OB Associations*, Proc. JENAM 2005, *Distant Worlds*, eds. G. Rauw, Y. Nazé, R. Blomme, E. Gosset, 31

29. *XMM-Newton observations of the Cyg OB2 association*
Rauw G., De Becker M., Linder N., 2005, in *Massive Stars and High Energy Emission in OB Associations*, Proc. JENAM 2005, *Distant Worlds*, eds. G. Rauw, Y. Nazé, R. Blomme, E. Gosset, 103

30. *On the multiplicity of the non-thermal radio emitters 9 Sgr and HD 168112*
Rauw G., Sana H., Gosset E., De Becker M., Arias J., Morrell N., Eenens P., Stickland D., 2005, in *Massive Stars and High Energy Emission in OB Associations*, Proc. JENAM 2005, *Distant Worlds*, eds. G. Rauw, Y. Nazé, R. Blomme, E. Gosset, 85

31. *The young open cluster NGC 6231: five years of investigations*
Sana H., Rauw G., Gosset E., 2005, in *Massive Stars and High Energy Emission in OB Associations*, Proc. JENAM 2005, *Distant Worlds*, eds. G. Rauw, Y. Nazé, R. Blomme, E. Gosset, 107

32. *CPD-41° 7742: an unusual wind interaction*
Sana H., Gosset E., Rauw G., Antokhina E., Royer P., Manfroid J., Vreux J.-M., 2005, in *Massive Stars and High Energy Emission in OB Associations*, Proc. JENAM 2005, *Distant Worlds*, eds. G. Rauw, Y. Nazé, R. Blomme, E. Gosset, 89

33. *Are WC9 Wolf-Rayet stars in colliding-wind binaries?*
Williams P.M., van der Hucht K.A., Rauw G., 2005, in *Massive Stars and High Energy Emission in OB Associations*, Proc. JENAM 2005, *Distant Worlds*, eds. G. Rauw, Y. Nazé, R. Blomme, E. Gosset, 65

34. *Searching for continuum γ-ray emission from OB associations with INTEGRAL, some preliminary results*
Leyder J.-C., Rauw G., 2006, in *Populations of High Energy Sources in Galaxies*, Proc. IAU Symp. 230, eds. E.J.A. Meurs, G. Fabbiano, Cambridge University Press, 338

35. *An exceptional X-ray view of the young open cluster NGC 6231: what XMM-Newton has taught us*
Sana H., Gosset E., Rauw G., Vreux J.-M. 2006, in *The X-ray Universe 2005*, ed. A. Wilson, ESA SP-604, Volume 1, 21

36. *The peculiar Of?p stars HD 108 and HD 191612: the X-ray view*
Nazé Y., Rauw G., Walborn N.R., Howarth I.D. 2006, in *The X-ray Universe 2005*, ed. A. Wilson, ESA SP-604, Volume 1, 99

C.3 Invited Reviews

1. *Non-thermal emission from early-type binaries*
Rauw G, 2004, in *Cosmic Gamma-Ray Sources*, eds. K.S. Cheng, G.E. Romero, Astrophysics and Space Science Library, Vol. 304, 105

2. *Massive binaries and colliding winds*
Rauw G., 2004, in *Evolution of Massive Stars, Mass Loss and Winds*, eds. M. Heydari-Malayeri, P. Stee, J.-P. Zahn, EAS Publication Series, Vol. 13, 293

3. *X-ray emission from early-type stars: new results and new challenges*
Rauw G. 2006, in *The X-ray Universe 2005*, ed. A. Wilson, ESA SP-604, Volume 1, 7

4. *High Resolution X-ray Spectroscopy of Early-Type Stars*
Rauw G., Pollock A.M.T., Nazé Y., 2006, in *High Resolution X-ray Spectroscopy: towards XEUS and Con-X*, ed. Branduardi-Raymont G.,
`http://www.mssl.ucl.ac.uk/~gbr/workshop2/papers/rauw_g.pdf`

C.4 Edited Books

1. *Wolf-Rayet Stars in the Framework of Stellar Evolution*
1996, Proceedings of the 33rd Liège International Astrophysical Colloquium
Editors: Vreux J.-M., Detal A., Fraipont-Caro D., Gosset E., Rauw G.

2. *Massive Stars and High Energy Emission in OB Associations*
2005, Proceedings of a workshop of the JENAM 2005, *Distant Worlds* conference
Editors: Rauw G., Nazé Y., Blomme R., Gosset E.

C.5 Popular Astronomy Publications

1. *Le ciel selon XMM-Newton*
Rauw G., Nazé Y., 2006, Ciel et Terre, 122, 2

2. *L'univers des Hautes Energies dévoilé par Integral*
Nazé Y., Rauw G., 2006, L'Astronomie, 120, 426

C.6 In press

1. *Early-type stars in the core of the young open cluster Westerlund 2*
Rauw G., Manfroid J., Gosset E., Nazé Y., Sana H., De Becker M., Foellmi C., Moffat A.F.J., 2007, A&A, in press, `astro-ph/0612622`

2. *Constraining the fundamental parameters of the O-type binary CPD*-41° *7733*
Sana H., Rauw G., Gosset E., 2007, ApJ in press, `astro-ph/0701574`

Bibliography

[2007] Aharonian, F., et al. 2007, A&A, submitted

[2002] Albacete Colombo, J.F., Morrell, N.I., Rauw, G., Corcoran, M.F., Niemela, V.S., & Sana, H. 2002, MNRAS, 336, 1099

[2007] Albacete Colombo, J.F., Flaccomio, E., Micela, G., Sciortino, S., & Damiani, F. 2007, A&A, in press, astro-ph/0610352

[1973] Allen, C.W. 1973, *Astrophysical Quantities*, 3rd edition, The Athlone Press

[1993] Allen, D.A., & Hillier, D.J. 1993, PASA, 10, 338

[2004] Andersson, B-G., Knauth, D.C., Snowden, S.L., Shelton, R.L., & Wannier, P.G. 2004, ApJ, 606, 341

[2004] Antokhin, I.I., Owocki, S.P., & Brown, J.C. 2004, ApJ, 611, 434

[2007] Antokhin, I.I., Rauw, G., Vreux, J.-M., van der Hucht, K.A., & Brown, J.C. 2007, A&A, submitted

[1996] Bagnuolo, W.G.Jr., & Barry, D.J. 1996, ApJ, 469, 347

[1950] Beals, C.S. 1950, Publ. DAO, 9, 1

[1994] Beech, M., & Mitalas, R. 1994, ApJS, 95, 517

[2001] Behrend, R., & Maeder, A. 2001, A&A, 373, 190

[1997] Berghöfer, T.W., Schmitt, J.H.M.M., Danner, R., & Cassinelli, J.P. 1997, A&A, 322, 167

[1996] Bernasconi, P.A., & Maeder, A. 1996, A&A, 307, 829

[1988] Bessell, M.S., & Brett, J.M. 1988, PASP, 100, 1134

[1961] Blaauw, A. 1961, Bull. Astron. Inst. Neth., 15, 265

[2005] Blomme, R., Van Loo, S., De Becker, M., Rauw, G., Runacres, M.C., Setia Gunawan, D.Y.A., & Chapman, J.M. 2005, A&A 436, 1033

[2005] Blomme, R. 2005 in *Massive Stars and High-Energy Emission in OB Associations*, Proc. JENAM 2005, eds. G. Rauw, Y. Nazé, R. Blomme & E. Gosset, 45

[2006] Blomme, R., De Becker, M., Runacres, M.C., Van Loo, S., & Setia Gunawan, D.Y.A. 2007, A&A, in press, astro-ph/0611768

[2004] Blum, R.D., Barbosa, C.L., Daminelli, A., Conti, P.S., & Ridgway, S. 2004, ApJ, 617, 1167

[1978] Bohlin, R.C., Savage, B.D., & Drake, J.F. 1978, ApJ, 224, 132

[2005] Boirin, L., Méndez, M., Díaz Trigo, M., Parmar, A.N., & Kaastra, J.S. 2005, A&A, 436, 195

[2004] Bonanos, A.Z., Stanek, K.Z., Udalski, A., et al. 2004, ApJ, 611, L33

[1998] Bonnell, I.A., Bate, M.R., & Zinnecker, H. 1998, MNRAS, 298, 93

[2002] Bonnell, I.A., & Bate, M.R. 2002, MNRAS, 336, 659

[2003] Bonnell, I.A., Bate, M.R., & Vine, S.G. 2003, MNRAS, 343, 413

[2004] Bonnell, I.A., Vine, S.G., & Bate, M.R. 2004, MNRAS, 349, 735

[2003] Briggs, K.R., & Pye, J.P. 2003, MNRAS, 345, 714

[2002] Burton, M.G. 2002, PASA, 19, 260

[1992] Campbell, B., Hunter, D.A., Holtzman, J.A., et al. 1992, AJ, 104, 1721

[2001] Carpenter, J.M. 2001, AJ, 121, 2851

[2004] Carraro, G., Romaniello, M., Ventura, P., & Patat, F. 2004, A&A, 418, 525

[1991] Chlebowski, T., & Garmany, C.D. 1991, ApJ, 368, 241

[2005] Church, M.J., Reed, D., Dotani, T., Bałucińska-Church, M., & Smale, A.P. 2005, MNRAS, 359, 1336

[2004] Churchwell, E., Whitney, B.A., Babler, B.L., et al. 2004, ApJS, 154, 322

[2004] Clark, J.S., & Porter, J.M. 2004, A&A, 427, 839

[2005] Clark, P.C., Bonnell, I.A., Zinnecker, H., & Bate, M.R. 2005, MNRAS, 359, 809

[2002] Coméron, F., Pasquali, A., Rodighiero, G., et al. 2002, A&A, 389, 874

[1973] Conti, P.S. 1973, ApJ, 179, 181

[1996] Cranmer, S.R., & Owocki, S.P. 1996, ApJ, 462, 469

[2004] Crowther, P.A. 2004, in *Evolution of Massive Stars, Mass Loss and Winds*, eds. M. Heydari-Malayeri, P. Stee & J.-P. Zahn, EAS Publication Series, 13, 1

[2003] Cutri, R.M., Skrutskie, M.F., Van Dyk, S., et al. 2003, *The 2MASS All-Sky Catalog of Point Sources*, University of Massachusetts and Infrared Processing and Analysis Center (IPAC/California Institute of Technology)

[2005] Dahm, S.E., & Simon, T. 2005, AJ, 129, 829

[2004] Damiani, F., Flaccomio, E., Micela, G., Sciortino, S., Harnden, F.R.Jr., & Murray, S.S. 2004, ApJ, 608, 781

[2001] Davidson, K., Smith, N., Gull, T.R., Ishibashi, K., & Hillier, D.J. 2001, AJ, 121, 1569

[2005] De Becker, M. 2005, PhD-thesis, University of Liège

[2007] De Becker, M. 2007, A&AR, in press

[2004a] De Becker, M., Rauw, G., Pittard, J.M., Antokhin, I.I., Stevens, I.R., Gosset, E., & Owocki, S.P. 2004a, A&A, 416, 221

[2004b] De Becker, M., Rauw, G., Blomme, R., et al. 2004b, A&A, 420, 1061

[2004c] De Becker, M., Rauw, G., & Manfroid, J. 2004c, A&A, 424, L39

[2004d] De Becker, M., & Rauw, G. 2004d, A&A, 427, 995

[2005] De Becker, M., Rauw, G., Blomme, R., Pittard, J.M., Stevens, I.R., & Runacres, M.C. 2005, A&A, 437, 1029

[2006a] De Becker, M., Rauw, G., Manfroid, J., & Eenens, P.R. 2006a, A&A, 456, 1121

[2006b] De Becker, M., Rauw, G., Sana, H., et al. 2006b, MNRAS, 371, 1280

[2001] DeGioia-Eastwood, K., Throop, H., Walker, G., & Cudworth, K.M. 2001, ApJ, 549, 578

[1999] De Marco, O., & Schmutz, W. 1999, A&A, 345, 163

[2000] De Marco, O., Schmutz, W., Crowther, P.A., Hillier, D.J., Dessart, L., de Koter, A., & Schweickhardt, J. 2000, A&A, 358, 187

[2004] Dessart, L. 2004, in *Evolution of Massive Stars, Mass Loss and Winds*, eds. M. Heydari-Malayeri, P. Stee & J.-P. Zahn, EAS Publication Series, 13, 251

[2005] de Wit, W.J., Testi, L., Palla, F., & Zinnecker, H. 2005, A&A, 437, 247

[2002] Donati, J.-F., Babel, J., Harries, T.J., et al. 2002, MNRAS, 333, 55

[2006] Donati, J.-F., Howarth, I.D., Bouret, J.-C., Petit, P., Catala, C., & Landstreet, J. 2006, MNRAS, 365, L6

[2005] Dougherty, S.M., Beasley, A.J., Zauderer, B.A., & Bolingbroke, N.J. 2005, ApJ, 623, 447

[2004] Eggenberger, A., Halbwachs, J.-L., Udry, S., & Mayor M. 2004, RevMexA&A Serie de Conferencias, 21, 28

[2005] Favata, F. 2005, Mem. S. A. It., 76, 337

[1999] Feigelson, E.D., & Montmerle, T. 1999, ARA&A, 37, 363

[1973] Feinstein, A., Marraco, H.G., & Muzzio, J.C. 1973, A&AS, 12, 331

[2005] Figer, D.F. 2005, Nature, 434, 192

[1998] Figer, D., Najarro, F., Morris, M., McLean, I.S., Geballe, T.R., Ghez, A.M., & Langer, N. 1998, ApJ, 506, 384

[1995] Fleming, T.A., Schmitt, J.H.M.M., & Giampapa, M.S. 1995, ApJ, 450, 401

[1978] Forte, J.C. 1978, AJ, 83, 1199

[1999] Fullerton, A.W. 1999, in *Variable and Non-spherical Stellar Winds in Luminous Hot Stars*, eds. Wolf B., Stahl O., Fullerton A.W., Lecture Notes in Physics, Vol. 523, 3

[1997] Fullerton, A.W., Massa, D.L., Prinja, R.K., Owocki, S.P., & Cranmer, S.R. 1997, A&A, 327, 699

[2005] Gagné, M., Oksala, M.E., Cohen, D.H., et al. 2005, ApJ, 628, 986

[2006] Gamen, R., Gosset, E., Morrell, N., et al. 2006, A&A, 460, 777

[2001] García, B., & Mermilliod, J.C. 2001, A&A 368, 122

[1980] Garmany, C.D., Conti, P.S., & Massey, P. 1980, ApJ, 242, 1063

[1981] Garmany, C.D., & Massey, P. 1981, PASP, 93, 500

[1997] Gayley, K.G., Owocki, S.P., & Cranmer, S.R. 1997, ApJ, 475, 786

[2001] Giacconi, R., Rosati, P., Tozzi, P., et al. 2001, ApJ, 551, 624

[2004] Giardino, G., Favata, F., Micela, G., & Reale, F. 2004, A&A, 413, 669

[2003] Gies, D.R. 2003, in *A Massive Star Odyssey, from Main Sequence to Supernova*, Proc. IAU Symp. 212, eds. K.A. van der Hucht, A. Herrero & C. Esteban, 91

[1999] Gondoin, P. 1999, A&A, 352, 217

[2006] González, J.F., & Levato, H. 2006, A&A, 448, 283

[2003] Gosset, E., Rauw, G., Vreux, J.-M., Nazé, Y., Antokhin, I.I., & Sana, H. 2003, in *A Massive Star Odyssey, from Main Sequence to Supernova*, Proc. IAU Symp., 212, eds. K.A. van der Hucht, A. Herrero & C. Esteban, 188

[2005a] Gosset, E., Nazé, Y., Claeskens, J.-F., Rauw, G., Vreux, J.-M., & Sana, H. 2005a, A&A, 429, 685

[2005b] Gosset, E., Rauw, G., Manfroid, J., Antokhina, E., Stevens, I.R., & Sana, H. 2005b, in *Massive Stars and High Energy Emission in OB Associations*, Proc. JENAM 2005, eds. G. Rauw, Y. Nazé, R. Blomme, & E. Gosset, 77

[2003] Guillout, P., & Motch, C. 2003, Astron. Nachrichten, 324, 81 61

[2004] Halbwachs, J.-L., Mayor, M., Udry, S., & Arenou, F. 2004, RevMexA&A Serie de Conferencias, 21, 20

[2003] Harries, T.J., Hilditch, R.W., & Howarth, I.D. 2003, MNRAS, 339, 157

[1996] Hawley, S.L., Gizis, J.E., & Reid, I.N. 1996, AJ, 112, 2799

[2005] Henley, D.B., Stevens, I.R., & Pittard, J.M. 2005, MNRAS, 356, 1308

[1962] Herbig, G.H. 1962, ApJ, 135, 736

[2000] Herrero, A., Puls, J., & Villamariz, M.R. 2000, A&A, 354, 193

[2005] Herrero, A., & Najarro, F. 2005 in *Massive Stars and High-Energy Emission in OB Associations*, Proc. JENAM 2005, eds. G. Rauw, Y. Nazé, R. Blomme & E. Gosset, 21

[2007] Herrero, A., Simón-Díaz, S., Najarro, F., & Ribas, I. 2007, in *Massive Stars in Interacting Binaries*, eds. A.F.J. Moffat & N. St-Louis, ASP Conf. Series, in press

[1996] Hester, J.J., Scowen, P.A., Sankrit, R., et al. 1996, AJ, 111, 2349

[1996] Hilditch, R.W., Harries, T.J., & Bell, S.A. 1996, A&A, 314, 165

[2005] Hilditch, R.W., Howarth, I.D., & Harries, T.J. 2005, MNRAS, 357, 304

[2006] Hillwig, T.C., Gies, D.R., Bagnuolo, W.G.Jr., Huang, W., McSwain, M.V., & Wingert, D.W. 2006, ApJ, 639, 1069

[2001] Hoogerwerf, R., de Bruijne, J.H.J., & de Zeeuw, P.T. 2001, A&A, 365, 49

[1991] Horne, K. 1991, in *Fundamental Properties of Cataclysmic Variable Stars: 12th North American Workshop on Cataclysmic Variables and Low Mass X-ray Binaries*, SDSU Press, ed. A.W. Shafter, 23

[2001] Jansen, F., Lumb, D., Altieri, B., et al. 2001, A&A, 365, L1

[1997] Jeffries, R.D., Thurston, M.R., & Pye, J.P. 1997, MNRAS, 287, 350

[2001] Kahn, S.M., Leutenegger, M.A., Cottam, J. et al. 2001, A&A, 365, L312

[1994] Kaitchuck, R.H., Schlegel, E.M., Honeycutt, R.K., Horne, K., Marsh, T.R., White, J.C., & Mansperger, C.S. 1994, ApJS 93, 519

[1993] Kaltcheva, N.T., & Georgiev, L.N. 1993, MNRAS, 261, 847

[1997] Kambe, E., Hirata, R., Ando, H., et al. 1997, ApJ, 481, 406

[1995] Kenyon, S.J., & Hartmann, L. 1995, ApJS, 101, 117

[2000] Knödlseder, J. 2000, A&A, 360, 539

[2003] Kramer, R.H., Cohen, D.H., & Owocki, S.P. 2003, ApJ, 592, 532

[2004] Kumar, B., Sagar, R., Sanwal, B.B., & Bessell, M.S. 2004, MNRAS, 353, 991

[1997] Kwok, S., Volk, K., & Bidelman, W.P. 1997, ApJS, 112, 557

[1992] Lada, C.J., & Adams, F.C. 1992, ApJ, 393, 278

[1993] Lamers, H.J.G.L.M., & Leitherer, C. 1993, ApJ, 412, 771

[2006] Lanotte, A. 2006, Undergraduate Thesis, University of Liège

[1995] Leitherer, C., Chapman, J.M., & Koribalski, B. 1995, ApJ, 450, 289

[1990] Leonard, P.J.T., & Duncan, M.J. 1990, AJ, 99, 608

[2004] Lery, T. 2004, in *Evolution of Massive Stars, Mass Loss and Winds*, eds. M. Heydari-Malayeri, P. Stee & J.-P. Zahn, EAS Publication Series, 13, 81

[1991] Levato, H., Malaroda, S., Morrell, N., García, B., & Hernandez, C. 1991, ApJS, 75, 869

[2006] Leyder, J.-C. 2006, Master in Science Thesis, University of Liège

[2006] Linder, N., Rauw, G., Pollock, A.M.T., & Stevens, I.R. 2006, MNRAS, 370, 1623

[1962] Lynds, B.T. 1962, ApJS, 7, 1

[2001] Lumb, D. 2001, XMM-SOC-CAL-TN-0016

[2003] Luna, G.J., Levato, H., Malaroda, S., & Grosso, M. 2003, IBVS, 5375

[1981] MacConnell, D.J. 1981, A&AS, 44, 387

[2007] Maíz Apellániz, J., Walborn, N.R., Morrell, N.I., Nelan, E.P., Niemela, V.S., Benaglia, P., & Sota, A. 2007, RevMexA&A Serie de Conferencias, in press

[2003] Makarov, V.V. 2003, AJ, 126, 1996

[1998] Marchenko, S.V., Moffat, A.F.J., & Eenens, P.J.R. 1998, PASP, 110, 1416

[2005] Markova, N., Puls, J., Scuderi, S., & Markov, H. 2005, A&A, 440, 1133

[1982] Marraco, H.G., & Orsatti, A.M. 1982, RevMexA&A, 5, 183

[2005a] Martins, F., Schaerer, D., & Hillier, D.J. 2005a, A&A, 436, 1049

[2005b] Martins, F., Schaerer, D., Hillier, D.J., Meynadier, F., Heydari-Malayeri, M., & Walborn, N.R. 2005b, A&A, 441, 735

[1998] Mason, B.D., Gies, D.R., Hartkopf, W.I., Bagnuolo, W.G.Jr., ten Brummelaar, T., & McAlister, H.A. 1998, AJ, 115, 821

[2001] Mason, K.O., Breeveld, A., Much, R., et al. 2001, A&A, 365, L36

[1993] Massey, P., & Johnson J. 1993, AJ, 105, 980

[2001] Massey, P., DeGioia-Eastwood, K., & Waterhouse, E. 2001, AJ, 121, 1050

[2002] Massey, P., Penny, L.R., & Vukovich, J., 2002, ApJ, 565, 982

[1999] Mathys G., 1999, in *Variable and Non-spherical Stellar Winds in Luminous Hot Stars*, eds. B. Wolf B., O. Stahl & A.W. Fullerton, Lecture Notes in Physics, Vol. 523, 95

[2003] McKee, C.F., & Tan, J.C. 2003, ApJ, 585, 850

[1999] Meaburn, J. 1999, in *Eta Carinae at the Millenium*, eds. J.A. Morse, R.M. Humphreys, & A. Damineli, ASP Conf. Ser., 179, 89

[1996] Megeath, S.T., Cox, P., Bronfman, L., & Roelfsema, P.R. 1996, A&A, 305, 296

[1997] Meyer, M.R., Calvet, N., & Hillenbrand, L.A. 1997, AJ, 114, 288

[2004] Meynet, G. 2004, in *Evolution of Massive Stars, Mass Loss and Winds*, eds. M. Heydari-Malayeri, P. Stee & J.-P. Zahn, EAS Publication Series, 13, 21

[2007] Millour, F., Petrov, R.G., Chesneau, O., et al. 2007, A&A, in press, `astro-ph/0610936`

[2006] Mizuta, A., Kane, J.O., Pound, M.W., Remington, B.A., Ryutov, D.D., & Takabe, H. 2006, ApJ, 647, 1151

[2007] Moffat, A.F.J. 2007, RevMexA&A Serie de Conferencias, in press

[2001] Morrell, N.I., Barbá, R.H. Niemela, V.S., et al. 2001, MNRAS, 326, 85

[2007] Morrell, N.I., Massey, P., Tsitkin, Y., Darnell, E., & Penny, L. 2007, RevMexA&A Serie de Conferencias, in press

[2003] Motch, C., Herent, O., & Guillout, P. 2003, Astron. Nachrichten, 324, 61

[2003] Nazé, Y. 2003, PhD-thesis, University of Liège

[2002] Nazé, Y., Carrier, F., & Rauw, G. 2002, in *Interacting Winds from Massive Stars*, ASP Conf. Ser. 260, eds. A.F.J. Moffat & N. St-Louis, 457

[2004] Nazé, Y., Antokhin, I.I., Rauw, G., Chu, Y.-H., Gosset, E., & Vreux, J.-M. 2004, A&A, 418, 841

[2005] Nazé, Y., Antokhin, I.I., Sana, H., Gosset, E., & Rauw, G. 2005, MNRAS, 359, 688

[1997] Neuhäuser, R. 1997, Science, 276, 1363

[2005] Nomoto, K., Tominaga, N., Umeda, H., Maeda, K., Ohkubo, T., Deng, J., & Mazzali, P.A. 2005, in *The Fate of the Most Massive Stars*, eds. R.M. Humphreys & K.Z. Stanek, ASP Conf. Series, 332, 374

[2000] Norberg, P., & Maeder, A. 2000, A&A, 359, 1025

[2007] Nürnberger, D.E.A. 2007, RevMexA&A Serie de Conferencias, in press

[1989] Nyman, L.-Å., Bronfman, L., & Thaddeus, P. 1989, A&A, 216, 185

[1993] Odenwald, S.F., & Schwartz, P.R. 1993, ApJ, 405, 706

[2005] Oey, M.S., & Clarke, C.J. 2005, ApJ, 620, L43

[2001] Ostrov, P.G. 2001, MNRAS, 321, L25

[2002] Ostrov, P.G. 2002, MNRAS, 336, 309

[1999] Owocki, S.P. 1999, in *Variable and Non-spherical Stellar Winds in Luminous Hot Stars*, eds. Wolf B., Stahl O., Fullerton A.W., Lecture Notes in Physics, Vol. 523, 294

[2002] Palla, F. 2002, in *Physics of Star Formation in Galaxies*, Saas-Fee Advanced Course 29, eds. A. Maeder & G. Meynet, 9

[1999] Panzera, M.R., Tagliaferri, G., Pasinetti, L., & Antonello, E. 1999, A&A, 348, 161

[1992] Parthasarathy, M., Jain, S.K., & Bhatt, H.C. 1992, A&A, 266, 202

[2007] Paunzen, E., Netopil, M., & Zwintz, K. 2007, A&A, 462, 157

[1999] Penny, L.R., Gies, D.R., & Bagnuolo, W.G.Jr. 1999, in *Wolf-Rayet Phenomena in Massive Stars and Starburst Galaxies*, Proc. IAU Symp. 193, eds. K.A. van der Hucht, G. Koenigsberger & P.R.J. Eenens, 86

[2006] Pittard, J.M., Dougherty, S.M., Coker, R.F., O'Connor, E., & Bolingbroke, N.J. 2006, A&A, 446, 1001

[2006] Pittard, J.M., & Dougherty, S.M. 2006, MNRAS, 372, 801

[2003] Pizzolato, N., Maggio, A., Micela, G., Sciortino, S., & Ventura, P. 2003, A&A, 397, 147

[2002] Pojmanski, G. 2002, Acta Astronomica, 52, 397

[1987] Pollock, A.M.T. 1987, ApJ, 320, 283

[2005] Pollock, A.M.T., & Raassen, A.J.J. 2005 in *Massive Stars and High-Energy Emission in OB Associations*, Proc. JENAM 2005, eds. G. Rauw, Y. Nazé, R. Blomme & E. Gosset, 35

[1999] Portegies Zwart, S.F., Makino, J., McMillan, S.L.W., & Hut, P. 1999, A&A, 348, 117

[2005] Postnov, K.A. 2005, in *Proc. Int. Workshop QUARKS - 2004*, ed. V.A. Rubakov et al., in press

[2005] Prisinzano, L., Damiani, F., Micela, G., & Sciortino, S. 2005, A&A, 430, 941

[1997] Raboud, D., Cramer, N., & Bernasconi, P.A. 1997, A&A, 325, 167

[1998] Raboud, D., & Mermilliod, J.-C. 1998, A&A, 333, 897

[2002] Rathborne, J.M., Burton, M.G., Brooks, K.J., Cohen, M., Ashley, M.C.B., & Storey, J.W.V. 2002, MNRAS, 331, 85

[2004a] Rauw, G. 2004a, in *Evolution of Massive Stars, Mass Loss and Winds*, eds. M. Heydari-Malayeri, P. Stee & J.-P. Zahn, EAS Publication Series, 13, 293

[2004b] Rauw, G. 2004b, in *Cosmic Gamma-Ray Sources*, eds. K.S. Cheng & G.E. Romero, Astrophysics and Space Science Library, 304, 105

[2006] Rauw, G. 2006, in *The X-ray Universe 2005*, ESA, SP-604, 7

[1998] Rauw, G., & Vreux, J.-M. 1998, A&A, 335, 995

[2000a] Rauw, G., Stevens, I.R., Pittard, J.M., & Corcoran, M.F. 2000a, MNRAS, 316, 129

[2000b] Rauw, G., Sana, H., Gosset, E., Vreux, J.-M., Jehin, E., & Parmentier, G. 2000b, A&A, 360, 1003

[2001a] Rauw, G., Morrison, N.D., Vreux, J.-M., Gosset, E., & Mulliss, C.L. 2001a, A&A, 366, 585

[2001b] Rauw, G., Nazé, Y., Carrier, F., Burki, G., Gosset, E., & Vreux, J.-M. 2001b, A&A, 368, 212

[2001c] Rauw, G., Sana, H., Antokhin, I.I., et al. 2001c, MNRAS, 326, 1149

[2002a] Rauw, G., Vreux, J.-M., Stevens, I.R., Gosset, E., Sana, H., Jamar, C., & Mason, K.O. 2002a, A&A, 388, 552

[2002b] Rauw, G., Crowther, P.A., Eenens, P.R.J., Manfroid, J., & Vreux, J.-M. 2002b, A&A, 392, 563

[2002c] Rauw, G., Blomme, R., Waldron, W.L., et al. 2002c, A&A, 394, 993

[2002d] Rauw, G., Nazé, Y., Gosset, E., et al. 2002d, A&A, 395, 499

[2003a] Rauw, G., De Becker, M., & Vreux, J.-M. 2003a, A&A, 399, 287

[2003b] Rauw, G., De Becker, M., Gosset, E., Pittard, J.M., & Stevens, I.R. 2003b, A&A, 407, 925

[2004a] Rauw, G., & De Becker, M. 2004a, A&A, 421, 693

[2004b] Rauw, G., De Becker, M., Nazé, Y., et al. 2004b, A&A, 420, L9

[2005a] Rauw, G., Sana, H., Gosset, E., et al. 2005a, in *Massive Stars and High-Energy Emission in OB Associations*, Proc. JENAM 2005, eds. G. Rauw, Y. Nazé, R. Blomme & E. Gosset, 85

[2005b] Rauw, G., De Becker, M., & Linder, N. 2005b, in *Massive Stars and High-Energy Emission in OB Associations*, Proc. JENAM 2005, eds. G. Rauw, Y. Nazé, R. Blomme & E. Gosset, 103

[2005c] Rauw, G., Crowther, P.A., De Becker, M., et al. 2005c, A&A, 432, 985

[2006] Rauw, G., Pollock, A.M.T., & Nazé, Y. 2006a, in *High resolution X-ray spectroscopy: towards XEUS and Con-X*, Proc. 2nd MSSL workshop (March 2006)
`http://www.mssl.ucl.ac.uk/~gbr/workshop2/papers/rauw_g.pdf`

[2007a] Rauw, G., Manfroid, J., Gosset, E., Nazé, Y., Sana, H., De Becker, M., Foellmi, C. & Moffat, A.F.J. 2007a, A&A, in press, `astro-ph/0612622`

[2007b] Rauw, G., & De Becker, M. 2007b, in *Handbook of Star Forming Regions, Vol. II: The Southern Sky*, ed. B. Reipurth, ASP, submitted

[1998] Reed, B.C. 1998, ApJS, 115, 271

[2006] Reimer, A., Pohl, M., & Reimer, O. 2006, ApJ, 644, 1118

[1997] Reipurth, B., Corporan, P., Olberg, M., & Tenario-Togle, G. 1997, A&A, 327, 1185

[1985] Rieke, G.H., & Lebofsky, M.J. 1985, ApJ, 288, 618

[1999] Romero, G.E., Benaglia, P., & Torres, D.F. 1999, A&A, 348, 868

[2005] Sana, H. 2005, PhD-thesis, University of Liège

[2001] Sana, H., Rauw, G., & Gosset, E. 2001, A&A, 370, 121

[2004] Sana, H., Stevens, I.R., Gosset, E., Rauw, G., & Vreux, J.-M. 2004, MNRAS, 350, 809

[2005] Sana, H., Antokhina, E., Royer, P., Manfroid, J., Gosset, E., Rauw, G., & Vreux, J.-M. 2005, A&A, 441, 213

[2006a] Sana, H., Gosset, E., Rauw, G., Sung, H., & Vreux, J.-M. 2006a, A&A, 454, 1047

[2006b] Sana, H., Rauw, G., Nazé, Y., Gosset, E., & Vreux, J.-M. 2006b, MNRAS, 372, 661

[2007] Sana, H., Rauw, G., Sung, H., Gosset, E., & Vreux, J.-M. 2007, MNRAS, in press

[1993] Schaerer D., Meynet G., Maeder A., Schaller G. 1993, A&AS, 98, 523

[1997] Schaerer, D., Schmutz, W., & Grenon, M. 1997, ApJ, 484, L153

[1992] Schaller G., Schaerer D., Meynet G., Maeder A. 1992, A&AS 96, 269

[2004] Schild, H., Güdel, M., Mewe, R., et al. 2004, A&A, 422, 177

[1998] Schlegel, D.J., Finkbeiner, D.P., & Davis, M. 1998, ApJ, 500, 525

[1982] Schmidt-Kaler, T. 1982, in *Physical Parameters of the Stars, Landolt-Börnstein Numerical Data and Functional Relationships in Science and Technology*, Group VI, Vol. 2b

[1995] Schmitt, J.H.M.M., Fleming, T.A., & Giampapa, M.S. 1995, ApJ, 450, 392

[2004] Schröder, S.E., Kaper, L., Lamers, H.J.G.L.M., & Brown, A.G.A. 2004, A&A, 428, 149

[1991] Serio, S., Reale, F., Jakimiec, J., Sylwester, B., & Sylwester, J. 1991, A&A, 241, 197

[1991] Shara, M.M., Moffat, A.F.J., Smith, L.F., & Potter, M. 1991, AJ, 102, 716

[1987] Shu, F.H., Adams, F.C., & Lizano, S. 1987, ARA&A, 25, 23

[1997] Siess, L., Forestini, M., & Dougados, C. 1997, A&A, 324, 556

[2000] Siess, L., Dufour, E., & Forestini, M. 2000, A&A, 358, 593

[2001] Skinner, S.L., Güdel, M., Schmutz, W., & Stevens, I.R. 2001, ApJ, 558, L113

[2003] Smith, N., Bally, J., & Morse, J.A. 2003, ApJ, 587, L105

[1996] Stahl, O., Kaufer, A., Rivinius, T., et al. 1996, A&A, 312, 539

[1996] Stevens, I. 1995, MNRAS, 277, 163

[2001] Strüder, L., Briel, U., Dennerl, K., et al. 2001, A&A, 365, L18

[1974] Sundman, A., Lodén, L.O., & Nordström, B. 1974, A&AS, 16, 445

[1995] Sung, H., & Lee, S.-W. 1995, Journal of the Korean Astronomical Society, 28, 119

[1997] Sung, H., Bessell, M.S., & Lee, S.-W. 1997, AJ, 114, 2644

[1998] Sung, H., Bessell, M.S., & Lee, S.-W. 1998, AJ, 115, 734

[2000] Sung, H., Chun, M.-Y., & Bessell, M.S. 2000, AJ, 120, 333

[2003] Tapia, M., Roth, M., Vázquez, R.A., & Feinstein, A. 2003, MNRAS, 339, 44

[2001] Thaller, M.L., Gies, D.R., Fullerton, A.W., & Kaper, L. 2001, ApJ, 554, 1070

[2004] Tokovinin, A. 2004, RevMexA&A Serie de Conferencias, 21, 7

[2002] Tothill, N.F.H., White, G.J., Matthews, H.E., McCutcheon, W.H., McCaughrean, M.J., & Kenworthy, M.A. 2002, ApJ, 580, 285

[2001] Turner, M.J.L., Abbey, A., Arnaud, M., et al. 2001, A&A, 365, L27

[2005] ud-Doula, A., Townsend, R., & Owocki, S.P. 2005, in *The Nature and Evolution of Disks Around Hot Stars*, eds. R. Ignace & K.G. Gayley, ASP Conf. Series, 337, 319

[2004] Vanbeveren, D. 2004, in *Evolution of Massive Stars, Mass Loss and Winds*, eds. M. Heydari-Malayeri, P. Stee & J.-P. Zahn, EAS Publication Series, 13, 141

[2004] van der Marel, R.P. 2004, in *Coevolution of Black Holes and Galaxies*, ed. L.C. Ho, Carnegie Observatories Astrophysics Series 1, 37

[2005] Van Loo, S. 2005, in *Massive Stars and High-Energy Emission in OB Associations*, Proc. JENAM 2005, eds. G. Rauw, Y. Nazé, R. Blomme & E. Gosset, 61

[2006] Van Loo, S., Runacres, M.C., & Blomme, R. 2006, A&A 452, 1011

[1996] Vázquez, R.A., Baume, G., Feinstein, A., & Prado, P. 1996, A&AS, 116, 75

[1993] Vijapurkar, J., & Drilling, J.S. 1993, ApJS, 89, 293

[2003] Vine, S.G., & Bonnell, I.A. 2003, MNRAS, 342, 314

[2000] Vink, J.S., de Koter, A., & Lamers, H.J.G.L.M. 2000, A&A, 362, 295

[2001] Vink, J.S., de Koter, A., & Lamers, H.J.G.L.M. 2001, A&A, 369, 574

[2000] Voges, W., Aschenbach, B., Boller, T., et al. 2000, IAU Circ., 7432R, 1

[1973] Walborn N.R., 1973, ApJ, 179, 517

[1995] Walborn, N.R. 1995, RevMexA&A Serie de Conferencias, 2, 51

[2002] Walborn, N.R. 2002, in *Hot Stars Workshop III: The Earliest Phases of Massive Star Birth*, ed. P.A. Crowther, ASP Conf. Series 267, 111

[2006] Walborn, N.R. 2006, in *The Ultraviolet Universe: stars from Birth to Death*, Proc. IAU XXVIth GA JD04, eds. A.I. Gomez & M.A. Barstow, #19, `astro-ph/0610837`

[1990] Walborn, N.R., & Fitzpatrick, E.L. 1990, PASP, 102, 379

[2000] Walborn, N.R., & Howarth, I.D. 2000, PASP, 112, 1446

[2002] Walborn, N.R., Howarth, I.D., Lennon, D.J., et al. 2002, AJ, 123, 2754

[1985] Weigelt, G., & Baier, G. 1985, A&A, 150, L18

[1991] Weigelt, G., Albrecht, R., Barbieri, C., et al. 1991, ApJ, 378, L21

[1997] Whiteoak, J.B.Z., & Uchida, K.I. 1997, A&A, 317, 563

[1995] Willis, A.J., Schild, H., & Stevens, I.R. 1995, A&A, 298, 549

[1992] Wiggs, M., & Gies, D.R. 1992, ApJ, 396, 238

[1987] Wolfire, M.G., Cassinelli, J.P. 1987, ApJ, 319, 850

[1986] Woodward, C.E., Pipher, J.L., Helfer, H.L., et al. 1986, AJ, 91, 870

[2004] Wozniak, P.R., Vestrand, W.T., Akerlof, C.W., et al. 2004, AJ, 127, 2436

[2006] Zavagno, A., Deharveng, L., Comerón, F., Brand, J., Massi, F., Caplan, J., & Russeil, D. 2006, A&A, 446, 171

[2007] Zinnecker, H. 2007, RevMexA&A Serie de Conferencias, in press